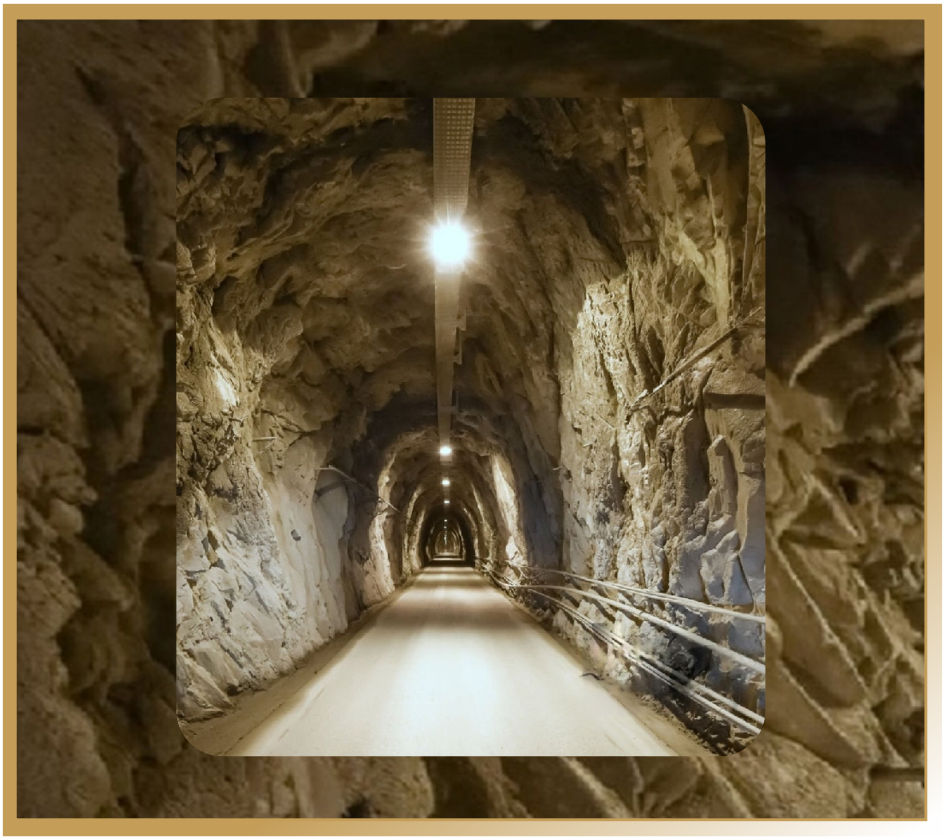
AFRIROCK 2025



Proceeding Book

21-23 JULY 2025

SUN CITY, RUSTENBURG, SOUTH AFRICA

SANIRE
SOUTH AFRICAN NATIONAL INSTITUTE OF ROCK ENGINEERING

SAIMM
THE SOUTHERN AFRICAN INSTITUTE OF MINING AND METALLURGY

THE SOUTHERN AFRICAN INSTITUTE OF MINING AND METALLURGY
JOHANNESBURG 2025

AFRIROCK 2025

21-23 JULY 2025
SUN CITY, RUSTENBURG, SOUTH AFRICA

SAIMM PUBLICATIONS

THE MONOGRAPH SERIES

Ml **Lognormal-De Wijsian Geostatistics for Ore Evaluation**
(2nd ed 1981) D.G. Krige

M2 **An Introduction to Geostatistical Methods of Mineral Evaluation**
(2nd ed 1981) J.-M.M. Rendu

M3 **Principles of Flotation**
(1982) (3rd imp. 1986) Edited by R.P. King

M4 **Increased Underground Extraction of Coal**
(1982) Edited by C.J. Fauconnier and R.W.O. Kersten

M5 **Rock Mechanics in Mining Practice**
(1983) (3rd imp. 1986) Edited by S. Budavari

M6 **Assay and Analytical Practice in the South African Mining Industry**
(1986) W.C. Lenahan and R. de L. Murray-Smith

M7 **The Extractive Metallurgy of Gold in South Africa,**
2 volumes (1987) Edited by G.G Stanley

M8 **Mineral and Metal Extraction — An Overview**
(1994) L.C. Woollacott and R.H. Eric

M9 **Rock Fracture and Rockbursts—an illustrative study**
(1997) Edited by W.D. Ortlepp

THE SPECIAL PUBLICATIONS SERIES

SPI **Proceedings, Underground Transport Symposium**
(1986) Edited by R.C.R. Edgar

SP2 **Backfill in South African Mines (1988)**

SP3 **Treatment and Re-use of Water in the Minerals Industry (1989)**

SP4 **COREX Symposium 1990**
(1990) Edited by H.M.W. Delport and P.J. Holaschke

SP5 **Measurement, Control, and Optimization in Mineral Processing**
(1994) Edited by H.W. Glen

SP6 **Handbook on Hard-rock Strata Control**
(1994) A.J.S. Spearing

SP7 **Rock Engineering for underground coal mining**
(2002) J. Nielen van der Merwe and Bernard J. Madden

SP8 **Second Edition: Rock Engineering for underground coal mining**
(2010) J. Nielen van der Merwe and Bernard J. Madden

SP9 **Theoretical Rock Mechanics for Professional Practice**
(2016) M. Handley

SP10 **Johannesburg and its Holey Mining Heritage 2021**
(2021) T.R. Stacey

SP11 **Mineral and Metal Extraction — An Overview**
(2021) L.C. Woollacott and R.H. Eric

SP12 **The Fall of a Giant: The story of the disintegration of the South African Mining Industry**
(2022/2023) Dr I. Robinsoin

SP13 **COMRO's Legacy: Research and Development of Stoping Mining Machinery and Technologies**
(2023) B. Protheroe

SUPPLEMENT TO THE SAIMM JOURNAL

The Metals and Minerals Industry in South Africa - Part 1 (1989)
Edited by H.W. Glen

THE SYMPOSIUM SERIES

S1 **Mathematical Statistics and Computer Applications in Ore Valuation (1966)**

S2 **Planning Open Pit Mines** (1970) (4th imp.)
Edited by P.W.J. van Rensburg

S3 **Application of Computer Methods in the Mineral Industry** (APCOM 1973) Edited by M.D.G. Salamon

S4 **Infacon 1974** Edited by H.W. Glen

S5 **Proceedings of the 12TH CMMI Congress** 2 volumes (1982)
Edited by H.W. Glen

S6 **Rockbursts and Seismicity in Mines** (1984)
Edited by N.C. Gay and E.H. Wainwright

S7 **The Planning and Operation of Open Pit and Strip Mines** (1986) Edited by J.P. Deetlefs

S8 **GOLD 100: Proceedings of the International Conference on Gold (1986)**
Volume 1: Gold Mining Technology
Edited by H. Wagner and R.P. King
Volume 2: Extractive Metallurgy of Gold
Edited by C.E. Fivaz and R.P. King
Volume 3: Industrial Uses of Gold
Edited by G. Gafner and R.P. King

S9 **APCOM 87: Proceedings of the Twentieth International Symposium on the Application of Computers and Mathematics in the Mineral Industries (1987)**
Volume 1: Mining
Edited by L. Wade, R.W.O. Kersten and J.R. Cutland
Volume 2: Metallurgy
Edited by R.P. King and I.J. Barker
Volume 3: Geostatistics
Edited by I.C. Lemmer, H. Schaum and F.A.G.M. Camisani-Calzolari

S10 **International Deep Mining Conference (1990)**
Volume 1: Innovations in Metallurgical Plant
Edited by G.A. Brown and P. Smith
Application of Materials Engineering in the Mining Industry Edited by B. Metcalfe
Volume 2: Technical Challenges in Deep Level Mining
Edited by D.A.J. Ross-Watt and P.D.K. Robinson

S11 **Infacon 6 (Incorporating Incsac) (1992)**
Edited by H.W. Glen

S12 **Massmin 92**
Edited by H.W. Glen (out of print)

S13 **Minefill 93**
Edited by H.W. Glen

S14 **XVTH CMMI Congress Publications (1994)**
Volume 1: Mining
Edited by H.W. Glen
Volume 2: Metals Technology and Extractive Metallurgy (1994) Edited by H.W. Glen

S15 **Surface Mining 1996**
Edited by H.W. Glen

S16 **Hidden Wealth (1996)**
Edited by H.W. Glen

S17 **Heavy Minerals 1997**
Edited by R.E. Robinson

S18 **The 8TH International Platinum Symposium (1998)**

S19 **Mining in Africa '98**

S20 **Extraction Metallurgy Africa '98**

S21 **Sixth International Symposium for Rock Fragmentation by Blasting (1999)**

S22 **Metallurgy Africa '99**

S23 **Heavy Minerals 1999**
Edited by R.G. Stimson

S24 **Tunnels under Pressure**
Technical Editor T.R. Stacey

S25 **Mine Hoisting 2000**

S26 **Coal–The Future (2000)**

S27 **The Fifth International Symposium on Rockburst and Seismicity in Mines (RaSim 5) (2001)**

S28 **6TH International Symposium on Mine Mechanization and Automation (2001)**

S29 **XIV International Coal Preparation Congress and Exhibition**

S30 **Surface Mining 2002—Modern Developments for the New Millennium**

S31 **IFSA 2002, Industrial Fluidization South Africa**

S31a **APCOM 2003—Application of Computers and Operations Research in the Minerals Industries**

S32 **ISSA/Chamber of Mines Conference—Mines and Quarries: Prevention of Occupational Injury and Disease**

S33 **ISRM—Technology Roadmap for Rock Mechanics**

S34 **Heavy Minerals Conference 2003**

S35 **Safety in Mines Research Institutes (2003)**

S36 **VII International Conference on Molten Slags, Fluxes & Salts (2004)**
Tenth International Ferroalloys Congress INFACONX 2004

S37 **Deep and high stress mining 2004**

S38 **'Platinum adding value' 2004**

S39 **Base Metals—Southern Africa's response to changing global base metals market dynamics 2005**

S40 **Strategic *versus* Tactical approaches in mining 2005**

S41 **Best practices in rock engineering SARES 2005**

S42 **IFSA 2005, Industrial Fluidization South Africa**

S43 **Southern African Pyrometallurgy 2006 International Conference**

S44 **Stability of rock slopes in open pit mining and civil engineering situations**

S45 **'Platinum Surges Ahead' 2006**

S46 **Hydraulic Transport of Solids - Hydrotransport 17 (2007)**

S47 **Fourth Southern African Base Metals Conference 'Africa's base metals resurgence'**

S48 **Heavy Minerals Conference, 2007**

S49 **Cave Mining Conference, 2007**

S50 **International Symposium on Lead and Zinc processing – Lead & Zinc 2008**

S51 **Surface Mining 2008**

S52 **Platinum in transformation 2008**

S53 **IFSA 2008, Industrial Fluidization South Africa**

S54 **Hydrometallurgy Conference 2009**

S55 **Shotcrete for Africa 2009**

S56 **Base Metals Conference 2009**

S57 **Heavy Minerals Conference, 2009**

S58 **Hard Rock Safe—Safety Conference 2009**

S59 **Sampling and Blending 2009**

S60 **World Gold 2009 Conference**

S61 **Physical Beneficiation Conference 2010**

S62 **Second Hardrock Safe—Safety Conference 2010**

S63 **Platinum in Transition 'Boom or Bust' 2010**

S64 **South African Pyrometallurgy 2011 International Conference**

S65 **Minefill 2011 (10TH International Symposium on Mining with Backfill)**

S66 **Base Metals Conference 2011**

S67 **MineSafe 2011 Conference**

S68 **Iron Ore and Manganese Ore Metallurgy 2011**

S69 **Percolation leaching: The status globally and in Southern Africa 2011**

S70 **IFSA 2011, Industrial Fluidization South Africa**

S71 **Southern Hemisphere International Rock Michanics Symposium 2012**

S72 **Platinum Conference 'A catalyst for change' 2012**

S73 **Ferrous 2012—Ferrous and Base Metals Development Network Conference**

S74 **Diamonds - Source to use 2013**

S75 **Sampling and analysis: Best-practice in African mining 2013**

S76 **Base Metals Conference 2013**

S77 **Precious Metals 2013 Conference—The Precious Metals Development Network (PMDN)**

S78 **Physical Beneficiation 2013 Conference**

S79 **21st Century challenges to the southern African coal sector 2014**

S80 **Furnace Tapping Conference 2014**

S81 **Platinum Conference 'Platinum—Metal for the Future' 2014**

S82 **IFSA 2014, Industrial Fluidization South Africa**

S83 **Copper Cobalt Africa 2015**

S84 **The Danie Krige Geostatistical Conference 2015 - Vol. 1**

The Danie Krige Geostatistical Conference 2015 - Vol. 2

S85 **World Gold Conference 2015**

S86 **Slope Stability 2015**

S87 **2nd Annual Young Professionals Conference 2015**

S88 **AMI–Nuclear Materials Development Network 2015**

S89 **MPES–23rd International Symposium on Mine Planning & Equipment Selection 2015**

S90 **Diamonds still Sparkling Conference 2016**

S91 **The SAMREC/SAMVAL Companion Volume Conference 2016**

S92 **New Technology and Innovation in the Minerals Industry Colloquium 2016**

S93 **Theoretical Rock Mechanics for Professional Practice** (Special Publications Series 9) by M. Handley - 2016

S94 **Hydrometallurgy Conference 2016**

S95 **10TH Heavy Minerals Conference 2016**

S96 **MineSafe Conference 2016**

S97 **AMI-Ferrous and Base Metals Development Conference 2016**

S98 **3rd Young Professionals Conference 2017**

S99 **Proximity Detection and Collosion Avoidance Systems in Mining Colloquium 2017**

S100 **6TH Sulphur and Sulphuric Acid Conference 2017**

S101 **Mine Planning Colloquium 2017**

S102 **Chrome Colloquium 2017**

S103 **4TH Mineral Project Valuation Colloquium 2017**

S104 **Water Conference 2017**

S105 **Rapid Underground Mine and Civil Access Engineering 2017**

S106 **MineSafe Conference 2017**

S107 **Uranium 2017 International Conference 2017**

S108 **IFSA 2017–Industrial Fluidization Conference 2017**

S109 **AfriRock 2017–ISRM International Symposium 2017**

S110 **AMI Precious Metals 2017–The Precious Metals Development Network (PMDN) Symposium**

S111 **7TH International Platinum Conference 2017**

S112 **Infacon XV: International Ferro-Alloys Conrgress 2018**

S113 **SOMP–Society of Mining Professors 6TH Regional Conference 2018**

S114 **Digitalization in Mining Conference 2018**

S115 **Diamonds – Source to Use 2018 Conference 2018**

S116 **The 9TH Southern African Base Metals Conference 2018**

S117 **Geometallurgy Conference 2018**

S118 **Mine Safe Technical Conference and Industry Day 2018**

S119 **ASM Conference 2018**

S120 **4TH Young Professionals Conference 2018**

S121 **Furnace Tapping 2018 Conference 2018**

S122 **7TH Sulphur and Sulphuric Acid Conference 2019**

S123 **Mine Planner's Colloquium 2019**

S124 **9TH International Conference on Deep & High Stress Mining 2019**

S125 **New Technology Conference and Trade Show 2019**

S126 **Smart Mining Smart Environment Smart Society Conference 2019**

S127 **The Eleventh International Heavy Minerals Conference 2019**

S128 **Surface Mining Masterclass 2019**

S129 **International Mine Health and Safety Conference 2019**

S130 **Tailings Storage Conference 2020**

S131 **IMPC2020 XXX International Mineral Processing Congress**

S132 **Johannesburg and its Holey Mining Heritage**
(Special Publications Series 10) by T.R. Stacey - 2021

S133 **Mineral and Metal Extraction — An Overview**
(Special Publications Series 11) by L.C. Woollacott and R.H. Eric - 2021

S134 **Diamonds - Source to Use - 2021 Online Conference 2021**

S135 **WorldGold Online Conference 2021**

S136 **APCOM 2021 Minerals Industry4.0-The next digital transformation in mining**

S137 **5TH Young Professionals Online Conference 2021**

S138 **Southern African Rare Earths International Online Conference 2021**

S139 **SAMCODES Conference 2021**

S140 **Global Tailings Standards and Opportunities`For the Mine of the Future Conference 2022**

S141 **The Fall of a Giant: The story of the disintegration of the South African Mining Industry**
(Special Publications Series 12) by I. Robinson - 2022/2023

S142 **Battery Materials Conference 2022**

S143 **32ND SOMP Annual Meeting and Conference 2022**

S144 **SDIMI (Sustainable Development in the Minerals Industry) 10TH International Conference 2022**

S145 **THANOS International Conference 2022**

S146 **Mine Impacted Water Online Conference 2022 (Abstract Book Only)**

S147 **8TH International PGM Conference 2022**

S148 **SANCOT Symposium 2022**

S149 **8TH Sulphur and Sulphuric Acid Conference 2023**

S150 **Southern African Hydrogen and Fuel Cell Conference 2023**

S151 **COMRO's Legacy: Research and Development of Stoping Mining Machinery and Technologies**
(Special Publications Series 13) by B. Protheroe - 2023

S152 **Copper Cobalt Africa in Association with The 10TH Southern African Base Metals Conferenc 2023**

S153 **Digital Transformation in Mining Conference 2023**

S154 **Diamonds Source to Use 2023 Online Conference**

S155 **12TH International Heavy Minerals Conference 2023**

S156 **Geometallurgy Conference 2023**

S157 **Next Generation Tailings Opportunitiy or Risk? Conference 2023**

S158 **6TH Young Professionals Conference 2023**

S159 **Southern African Pyrometallurgy 2024 International Conference**

S160 **The 11TH World Conference of Sampling and Blending 2024**

S161 **SANIRE Symposium 2024**
Technical Applications in Rock Engineering

S162 **2ND International Conference 2024 Southern African Rare Earths**

S163 **2ND Battery Materials Conference 2024**

S164 **Hydrometallurgy Conference 2024**

S165 **Environmental Social Governance Sustainability Conference 2024**

S166 **MineSafe Mine Health and Safety Conference 2024**

S167 **Mintek@90 Conference 2024**

S168 **Mine Closure Conference 2025**

S169 **2ND Southern African Hydrogen and Fuel Cell Conference 2025**

S170 **9TH Sulphur and Sulphuric Acid Conference 2025**

S171 **4TH Digital Transformation in Mining Conference 2025**

Published by The Southern African Institute of Mining and Metallurgy
Minerals Council South Africa, 7th Floor, Rosebank Towers, 19 Biermann Avenue, Rosebank, 2196
Republic of South Africa

© The Southern African Institute of Mining and Metallurgy, 2025

ISBN 978-0-6398820-1-7

The papers in this volume have been for the most part prepared from Word documents supplied by the authors, with additional typesetting and formatting by The Southern African Institute of Mining and Metallurgy.

Organising Committee

K.B. Le Bron, Conference Chairperson
K.Bosman
W.C. Joughin
G. Knox
J. Maritz
S. Mashile
S. Petho
O. Rakumakoe
D. Roberts
B.P. Watson

The Organising Committee would like to thank the reviewers listed below for the efforts in the reviewing process

F. Basson
K. Bosman
G. Betz
K. Brentley
R. Bush
S. Coetzee
R. Durrheim
C. Fietze
L. Gardner
H. Greef
A. Guest
M. Handley
W. Harrison
L. Human
W.C. Joughin
G. Keyter
G. Knox
K.B. Le Bron
L.M. Linzer
P. Linzer
J. Lucas
C. Maduray
D.F. Malan
B. Mashiatshiti
S. Mashile
J. Maritz
M. Matlou
D. Mossop
J.A.L. Napier
M. Nasiri
D. O'Connor
S. Petho
O. Pillay
O. Rakumakoe
T. Rangasamy
D. Roberts
T. Rorke
L. Scheepers
B. Simser
S.M. Spottiswoode
T.R. Stacey
S. Tose
C. Tuitz
B. Vaughn
B.P. Watson
J. Wesseloo

Desktop prepared by Camera Press, Johannesburg

FOREWORD

PIONEERING PROGRESS: THE FUTURE OF ROCK ENGINEERING

It is our great pleasure to welcome you to the Afrirock 2025, themed *Pioneering Progress: The future of Rock Engineering*. This international conference brings together experts, practitioners, and academics from all over the world to share knowledge, exchange ideas, and advance the state of practice in rock engineering.

Two formal workshops are planned prior to the official commencement of formal proceedings of Afrirock 2025, one on pillar design and the other one stress measurements.

The first workshop will be hosted by Prof. Francois Malan, from the University of Pretoria. Presenters include Prof. Nielen van der Merwe, Prof. Bryan Watson, Mr. William Joughin and Dr. Rudi Kersten.

The second workshop will be hosted by representatives from Japanese and South African geoscientists. Since the 1990s, Japanese and South African geophysicists and geoengineers have collaborated to study the mechanisms of seismic events induced by mining activities, through geotechnologies including stress measurements. A Geotech Consortium has now been established based on this collaboration, to accelerate the transfer of the geotechnologies developed not only for deep mining, but potentially also to non-mining applications such as shale gas extraction. The outline, basic theory and practice of stress measurement methods and techniques will be presented by their inventors. Presenters include Prof. Ito Takatoshi, Prof. Yusuke Mukuhira, Prof. Kiyotoshi Sakaguchi, Prof. Yasuo Yabe, Prof. Ray Durrheim, Dr. Dave Roberts, Mr. Willem Meintjies and Mr. Gerhard Hofmann.

We are honoured to host distinguished keynote speakers, each bringing unique expertise and insight:

- Prof. Francois Malan, from the University of Pretoria.
- Dr. John Hadjigeorgiou, from the University of Toronto.
- Mr. Frans Basson, from Newmont Corporation.
- Mr. Brad Simser from Glencore Sudbury Operations.
- Associate Professor Bryan Watson, from the University of the Witwatersrand.
- Dr. Dave Roberts, from Sibanye Stillwater.

These keynote presentations promise to deliver rich and valuable insights that will stimulate discussion and inform best practices in our field. In addition to the keynotes, the symposium features a robust programme of technical papers from industry professionals, consultants, and researchers. These sessions offer attendees an opportunity to learn from the practical experiences of others, explore innovative solutions, and contribute to ongoing dialogue and development within the rock engineering community.

Five technical visits to gold, platinum, diamond and copper mines have been organised, which will take place after the closing of the official proceedings. These technical visits, together with the social events planned at the end of each day, provide conference attendees with further opportunities to network freely in an informal setting.

We extend our sincere gratitude to all those who have contributed to making this conference possible—our keynote speakers, paper authors, reviewers, exhibitors, and sponsors. Your dedication, time, and expertise are the foundation of this event's success. A special note of appreciation goes to the Technical Paper Review Committee and the Organising Committee, comprising members from Sanire and the Southern African Institute of Mining and Metallurgy (SAIMM), for their dedication and hard work in delivering this international conference.

We look forward to a productive and inspiring event and encourage all participants to engage fully, share openly, and collaborate broadly.

On behalf of the Organising Committee,

Afrirock 2025 Organising Committee:
K. Bosman (OHMS)
W.C. Joughin (SRK)
G. Knox (Epiroc)
J. Maritz (ISRM VP)
S. Mashile (SANIRE Honorary Treasurer)
S. Petho (Glencore Coal SA)
O. Rakumakoe (SANIRE VP)
D. Roberts (Sibanye Stillwater)
B. Watson (Wits University)
P. Ntumelang (SANIRE Administrator)
G. Charlie (SAIMM)
C. Jardine (SAIMM)
N. Mamdoo (SAIMM)
S. Moolla (SAIMM)
G. Matsoyane (SAIMM)

K.B. Le Bron
SANIRE President and Afrirock 2025 Chair

Contents

Page No

Ground Support

Controlling tailings backfill leakage through fractured pillars
G.M. Mphike, D. O'Connor, S.M. Sibanda 1

The development of the fast cable anchor
J. Wang, B. Darlington, M. Farrington, P. Young, S. Weaver 13

A review of the stope support system at Impala Bafokeng North Shaft owing to stope closure at shallow mining depths
T. Walsh 25

A proposed method of pre-mining rib pillars and replacing pillars using a cemented aggregate fill
R.M. Arlow, I. Malpartida, J. Nyagumbo 37

Performance and mechanical properties of a styrene-free polyester resin produced with water-based catalyst and a new generation catalyst
G. Smolnik, R. Penczek, J. Franek, D. Bucholc 51

Blast-on-Mesh: Transforming deep-level gold mining – success stories from Kusasalethu
R. van Heerden, M. Phathu 63

Do underground excavations mined by non-explosive mining techniques require less support than when mined by blasting? A challenge to rock engineers to review support design practice
R.G.B. Pickering, D. Arnold, J. Porter 75

Caving

Application of Flac3D to analyse the effects of mining-induced stresses on the behaviour of drawpoint pillars: A case study of a long-hole open stoping mine in Zimbabwe
A. Velempini 91

Geotechnical Data

Rectifying, conforming and extracting value from existing geotechnical data sets - the importance of good data management for optimal value extraction
M.H. van Aswegen, D.H. Mossop 107

Influence of saturation fluids on the elasto-plastic deformation behaviour of shale
L. Chen, L. Wang. 117

Unravelling the past for a safer future: How historic rock mass classification data compare with slope performance monitoring data
M. Pretorius. 127

Slope stability

Stabilisation of highwall instability using numerical modelling and statistical analysis for open pit mining
N.I. Umeh, S. Darries , N.E. Baloyi, T. Rangasamy 139

Integrating monitoring technologies to understand slope deformation in open-pit mines: A case study from Swakop uranium mine
G. Ockhuizen, R. Armstrong, Y. Xiangle, S.Maclennan 161

Rock fall hazard analysis of a natural slope at the Sungun Copper Mine
J.D. Bosman, L. Cilliers, H. Reza Golchin 179

Mitigating pit floor instability above a confined aquifer: Assessing mining block dimensions and sequencing strategies
L. Bruyns, M. Rangasamy, T. Rangasamy 193

Numerical Modelling

3D elastodynamic modelling applied in the design of technical blasts in open pit mines
L.M. Linzer, A.J. Rorke, M.W. Hildyard 211

Key block theory for the miner: A novel simplified method for determining block removability
C. van Rooyen 221

Application of large-scale finite element method simulations to determine geomechanical hazard during room-and-pillar mining under a tectonic fault
K. Fuławka, L. Stolecki, R. Kołodziej 241

Contents

Page No

Seismicity

Application of MEMS accelerometers for continuous near-field monitoring of mining-induced seismicity
L. Stolecki, K. Fuławka, P. Mertuszka 253

Seismic-based live tracking of underground fires and cooling period response
M. Wiggins, L. Scheepers, J. Gerber 267

Subsidence

Modern satellite data provide new insights into surface movements above coal longwall mining
A. Vervoort 289

Modern Analytical Techniques

Machine learning as a catalyst to enhance collaboration across generations and disciplines in South African Rock Engineering
R.T. Masethe, L.N.P. Msimango 301

Transforming geotechnical monitoring data acquisition, 3D visualisation and analytics for modern mining
J.J. Meiring, P.S. Piper 313

Soft computing techniques for predicting mode-ii fracture toughness: A cost-effective approach to advancing rock mechanics' design and sustainability
N.O. Ogunsola, H. Grobler 329

Comparison of machine learning classification for rockburst prediction: A case study of South African gold and platinum mines
N.P. Khumalo, R.T. Masethe 343

Towards ensuring sustainable mining: Application of a pareto-optimized hierarchical structural interaction matrix for prioritizing slope stability influencing factors
N.O. Ogunsola, O. Makinde, H. Grobler 357

Role of machine learning in optimising prediction of blast fragmentation in mines using site-specific geological data
M.S. Kanongovere, R.S. Suglo, M. Masialeti 371

Monitoring

The MDA CHORUS SAR constellation: A unique perspective for improved slope stability monitoring and geotechnical risk assessment
D. Hickson, R. Morin, R. Podmore 385

Klipgat boxcut portal entrance and decline system: Long-term stability assessment and monitoring
S. Vezi, R.T. Masethe 397

Compact radar system for rockmass movement monitoring in underground narrow reef stope
D. van Rooyen, R. Carstens, L. Campbell 415

Monitoring mining-induced subsidence and sinkholes using multi-band InSAR: A case study from Lubambe Copper Mine
P. Chipola, R. Sililo, A. Mkandla, M. Douglas, M. Spreafico 435

Closure and accelerometer measurements to enhance mine safety
L. Scheepers, P. Lenegan, F. Pienaar, H. Hoogenboezem, D. Lamprecht 447

Underground Rock Mechanics

Pillar assessment at Bindura Nickel Corporation's Trojan mine in Zimbabwe
F. Kwangwari, T. Makahamadze, W.C. Joughin 471

Geotechnical design of coal bord and pillar panels: Some complementary suggestions
A. Vervoort 487

Back analysis of ore pass design at Big Gossan sublevel open stope mine, Indonesia
A. Sjadat, J.P.E. Hamman, Y. Irab, D. Putra, W. De Beer, I. Haque 499

Seismological and numerical characterisation of stability pillar behaviour at South Deep Mine
S.M. Sibanda, B.P. Watson 511

Prediction of mine tunnel conditions in a deep Austrian mine by means of numerical back- and forward analysis
P. Gams, B. Moosbacher, H. Wagner, T. Fruehwirt 523

Development of a multi-stage large excavation crusher chamber at Palabora mining company
M. Matsapola, R.B. Khumalo, V.C. Madanda, F.K. Mulenga 539

Effect of pyroxenite layers on the strength of UG2 pillars
T.J. Maphosa, B.P. Watson 553

Improvements in stope designs, and sequencing at the Big Gossan sub level open stope mine, Indonesia
A. Febrian, A. Sjadat, J.P.E. Hamman 565

The organisers of the conference thanks the following sponsors for their support

PREMIUM SPONSORS

BRUGG Geobrugg

DWYKA MINING SERVICES

HEXAGON

HORTS

MACCAFERRI

M and J MINING WE SUPPORT YOUR MINE

MLB CONSULTING

MINE SUPPORT PRODUCTS MSP

New Concept Mining Powered by Epiroc

OHMS

REUTECH MINING

ROCSCIENCE

SANDVIK

STROCAM MINING

BEDROCK Quality. On Time. In Full.

TR TIMRITE UNDERGROUND MINE SUPPORT SOLUTIONS

The organisers of the conference thanks the following sponsors for their support

EXHIBITORS





























The organisers of the conference thanks the following sponsors for their support

NETWORKING COCKTAIL SPONSOR

New Concept Mining
Powered by Epiroc

BANNER SPONSORS

GLENCORE sebotka srk

PENS AND NOTEPADS SPONSOR

M and J MINING
WE SUPPORT YOUR MINE

STUDENT SPONSOR

Rock Mechanics Laboratory

PROMOTIONAL INSERTS

GROUNDWORK
GEOTECHNICAL SENSING AND CONSULTING

Knight Piésold CONSULTING

SABLE®
DATA THAT WORKS

Controlling tailings backfill leakage through fractured pillars

G.M. Mphike[1], D. O'Connor[1], S.M. Sibanda[2]

[1]Minova Africa (Pty) Ltd, South Africa
[2]South Deep Gold Mine, South Africa

A deep level South African gold mine was experiencing leakage of tailings backfill through fractured pillars into the workings, where it created difficult operating conditions. The mine employs a long hole open stoping method, where the orebody is initially extracted using mechanised horizontal destress mining—similar to bord and pillar mining—creating a destress cut. This cut allows for long hole open stoping under reduced stress conditions, enabling the extraction of large mining targets above it. The mining takes place at depths nearing 3000 m, where the destress cut pillars are subject to high stress and are intensely fractured. During the subsequent backfilling operation the fractures provided pathways through the pillars for the highly fluid cemented tailings to migrate into the active workings. Accumulation of the hardening tailings disrupted vehicle and personnel movement, negatively impacting operations of the mine due to the need for rehandling the backfill in the active workings.

Solutions considered were coating the walls of the pillars with an impervious liner; sealing of the migration paths by injection into the pillars and modification of the tailings to increase viscosity. The first two were rejected as they were unlikely to achieve continuous sealing and they required additional crews and equipment to implement.

Viscosity increase was achieved by adding a gelling agent to the tailings stream. This reacted with the cementitious binder in the tailings, to rapidly raise the viscosity to a level that the fill could not permeate through fractures. Setting of the binder then proceeded at its normal pace, over 4 – 6 weeks. The impact of the gelling agent was both significant and swift; migration of the backfill through the pillar fractures was drastically reduced shortly after its introduction and eliminated during the initial pour. Extensive laboratory testing was performed prior to underground trials. Issues investigated included: optimal dosage of the gelling agent; rate of viscosity increase and ultimate viscosity value; permeation rate of gelled tailings through simulated fractured rock and effect of the gelling agent on ultimate compressive strength of the backfill.

The system was then tested underground. Gelling agent was injected by a high-pressure dosing pump into the backfill pipelines, 10 – 30 m before the discharge points. Backfill leakage was significantly reduced or totally eliminated, contributing to a noteworthy increase in operational efficiencies.

INTRODUCTION

Mine location

South Deep is situated approximately 45 km west of Johannesburg in the west Witwatersrand mining region (Figure 1**Error! Reference source not found.**). The mining area covers 4232 hectares and extends for 9.5 km north-south and 4.5 km east-west at its widest points. It is a mechanised mine, extracting a wide reef at depths near 3000 m below the surface. Such wide reefs have not been mined at this depth elsewhere in the world and the production layouts developed at the mine are therefore unique.

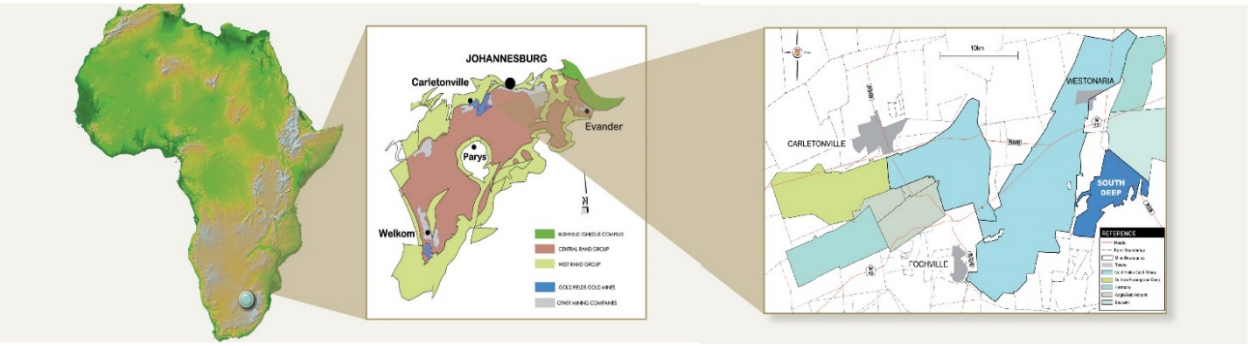


Figure 1. Location of South Deep mine.

Mining method

A series of layered overlapping horizontal de-stress cuts are used to de-stress the large ore body target horizons as shown in Figure 2. Access to the de-stress cut is obtained through a spiral decline, which is sited beneath a previously mined de-stressed area. De-stress cuts consist of 6 m wide and 5.5 m high bords and 7 m wide x 20 m long crush pillars. Mining must be optimally sequenced to mitigate rock burst and stress damage. This destress cut is subsequently integrated with sequential long-hole stoping by utilising the destress cut drives as long-hole drives (Figure 2). This layout allows for selective mining in the massive reefs, where there may be sub-economic quartzite middlings.

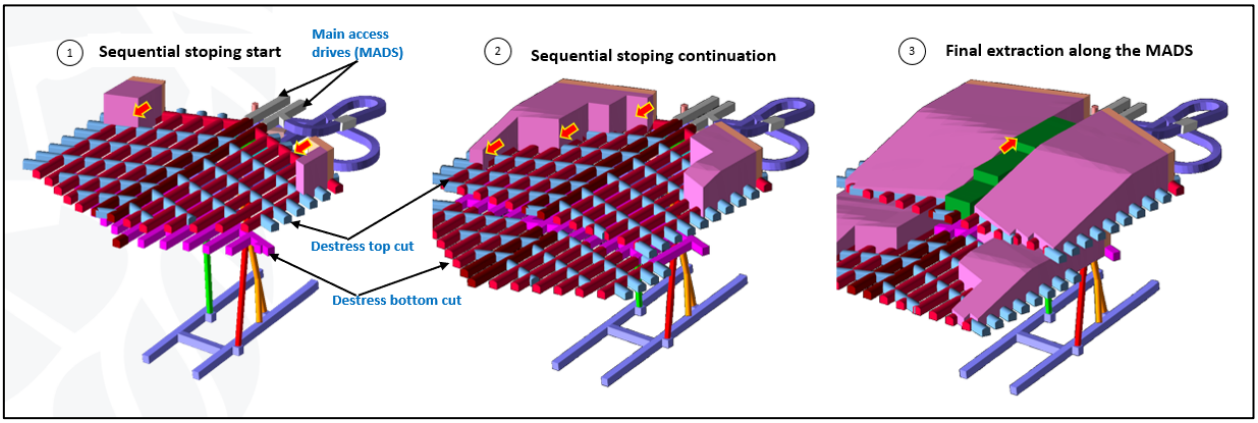


Figure 2. Isometric view of horizontal de-stress and stoping layout.

Backfill operations

The backfilling infrastructure at South Deep Gold mine consists of a surface semi-classified tailings plant and an underground distribution system. The plant supplies backfill material underground for bulk filling of the long-hole stoping voids.

The surface plant has the following major components (Figure 3):

- Tailings receiving plant
- Cyclone section
- Binder preparation plant

In 2024 the mine placed 20 000 m^3 to 60 000 m^3 of backfill per month.

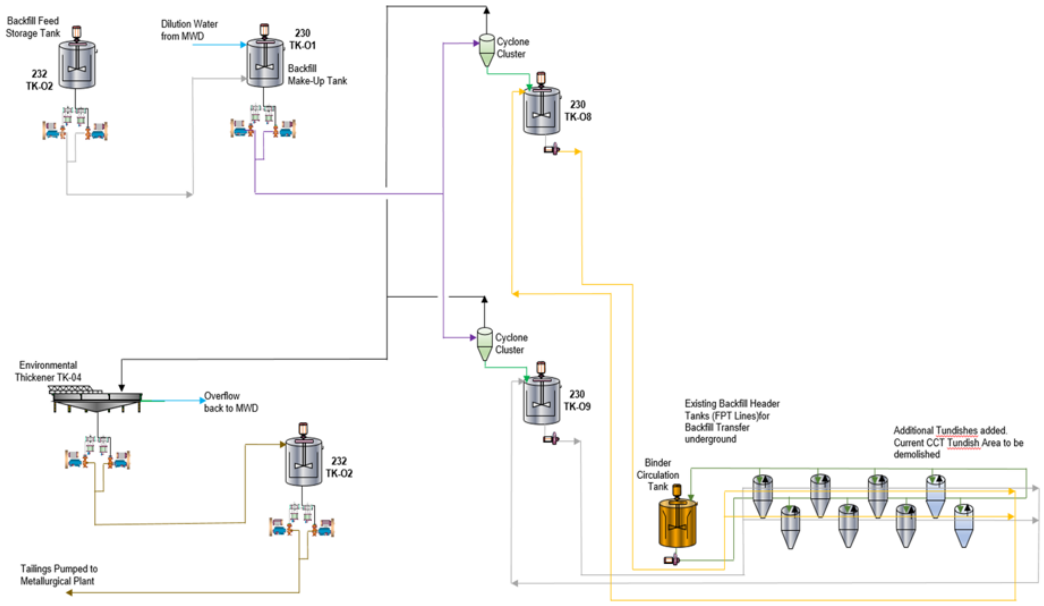


*Figure 3. Semi-classified backfill process flow diagram (*Source: South Deep CPR 2023*).*

Backfill properties

To minimise water and mud in the stopes and drives, and to minimise shrinkage of backfill after placement, an incentive exists to place backfill at the highest possible slurry density. South Deep uses a hydraulic backfill with relative density ranging between 1.70 to 1.80. Particle size distribution is one of the most important parameters controlled, as this determines both the backfill support capabilities and the hydraulic transportation and placement behaviour of the backfill. The target range of fines (<10µm) content is 10% to 20%. Target strengths for backfill are 0.5MPa after seven days and 1.2MPa after 28 days.

The problem - backfill leakage

In the highly stressed areas of the mine, the fractures in the pillars provide fluid pathways. In the several hours between placement and start of setting, the backfill slurry leaked through the fractures into the operating mine workings. The accumulation of backfill obstructed movement of vehicles and people, so had to be removed. In 2024 rehandling of the partially-set backfill became a significant burden on operations (Figure 4). In January 2024 a project was initiated to reduce the amount of backfill leakage.

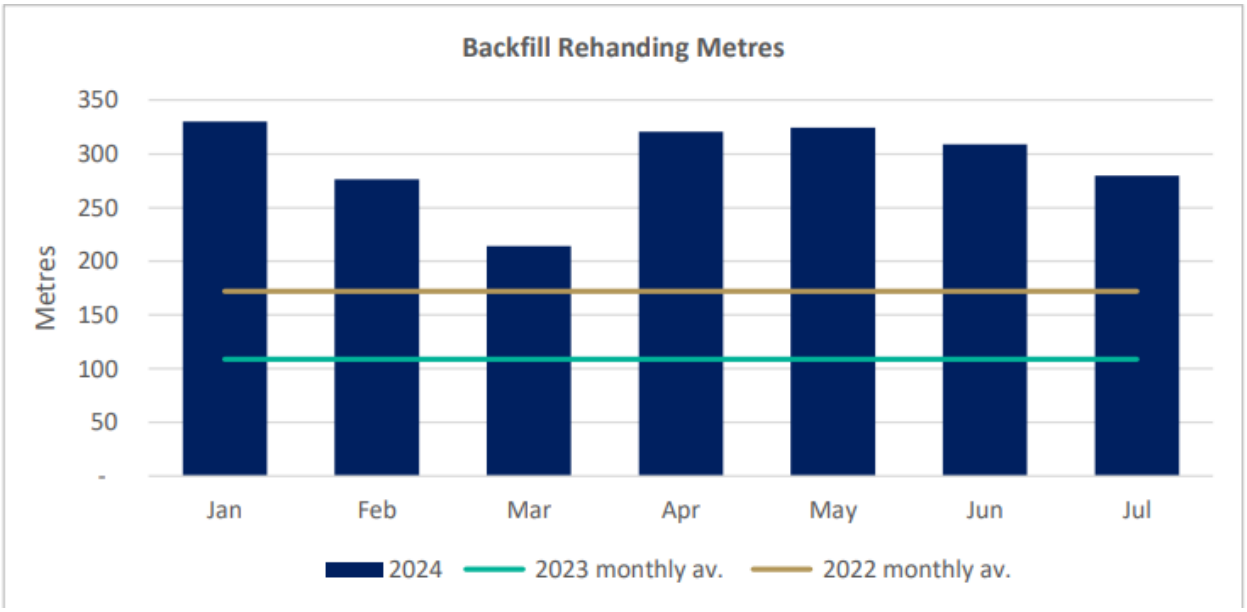


Figure 4. Backfill rehandling (Figure from (Gold Fields, 2024).

Solutions considered
Three potential solutions were identified and examined.

Lining of the backfill paddocks
This required creating an impervious barrier on the inside of the paddocks before filling. Possible impervious barriers were spray-on linings eg., thin sprayed liner or shotcrete (du Plessis & Malan, 2021) or film sheeting. Either needed a large amount of time and labour. Continuity of the lining could not be assured as the pillars were subjected to ongoing deformation and surface scaling.

Injection into the pillars to create an internal barrier
The concept was built on the well-established practice (Hildreth, *et al.*, 2019) of drilling into a rock mass and injecting cement or resin grout to stop water or gas transmission. As the leakage was of a cementitious material, the less costly option of injecting a cement grout would have sufficed. Nevertheless, the concept was rejected as:

- Extensive drilling was required, calling for additional equipment and crews
- Drilling and injection would have taken several days per paddock
- Continuity of the grout curtain could not be assured, especially in the dynamic deformation environment.

Rapid thickening of the backfill slurry after placement
This solution derived from silicated backfill technology, originally developed in 1989 (Smart, *et al.*, 1993). Silicated backfill has been widely used, and investigated by other authors, for example (Kermani, *et al.*, 2015).

With a suitable cementitious binder, addition of an activated sodium silicate gelation agent causes a rapid rise in the viscosity of the backfill slurry ('gelation'). It was expected that the increased viscosity would inhibit flow of the slurry through the narrow fluid channels. Based on favourable results from a small-scale trial carried out in 2018, it was decided to investigate this option further.

Investigation program
An investigation program was set in the Minova Africa laboratories and mine backfill laboratory. The following aspects of the tailings – binder – gelation agent system were examined:

- Nature of the gelation reaction – open time, rapidity and degree of viscosity rise
- Effect of the gelation agent on strength development of the placed backfill
- Optimisation of gelation agent dosage rate
- Effect of the viscosity rise on flow through fractured rock
- Development of a dosing system to inject the gelation agent into the backfill stream.

Mine tailings were used to prepare tailings plus binder mixes with a constant binder addition of 8% and relative density of 1.75. Gelation agent was added over a range from zero (control) to 2% by mass of the tailings – binder – gelation agent mix.

Gelation reaction
Gelation effect was measured by change in flow table spread (ASTM, 2007) of the blend, and visual observation and timing of thickening.

Effect of gelation agent on set strength, and optimisation of gelation agent dosage
The blends were cast into moulds to prepare samples for compression testing. The samples were cured at 35°C for 24 hours, seven days, 14 days and 28 days (later extended to 56 days) then compression tested.

Effect on flow through fractured rock
Permeation of tailings through the fractured rock was simulated by permeation along a column of gravel in 30 mm diameter clear plastic pipe. Static pressure head was kept at 4 m. The gravel grain sizes were 5 – 8 mm and void ratio was measured as 44%. Permeation distance after one hour was compared for backfill slurry with and without gelation agent (Figure 5). The rig is shown in Figure 6.



Figure 5. Backfill (grey) permeating through gravel column.



Figure 6. Permeation test rig - pipe on ground.

Development of dosing system

The gelation agent is typically injected into the backfill stream at 5 – 30 m before discharge. Backfill flow rate depends on the pipe diameter employed at the backfill site and can vary from 60 – 120 m^3 per hour (100 – 200 tonnes per hour). Nominal gelation agent dosing is one percent by mass of backfill slurry (Smart, *et al.*, 1993). At relative density of 1.4, the dosing pump had to deliver 700 – 1500 litres per hour. Pressure at the injection point was unknown.

The dosing system designed for underground trials is shown in Figure 7. It included:

- A two-cylinder, high pressure piston pump, normally used for injection of two-component resins into rock. Pressure can reach 100 bars (10 MPa).
- Pump drive by compressed air from the mine supply. This also controlled the speed of the pump.
- Non-return valves, to prevent entry of backfill slurry into the dosing system.
- A 'static mixer', to disperse the gelation agent into the backfill stream. The static mixer was 2 m of a 25 mm chain, secured at the upstream end and free to flail inside the backfill pipe.
- Supply of the gelation agent in 1 m^3 'flowbins'.

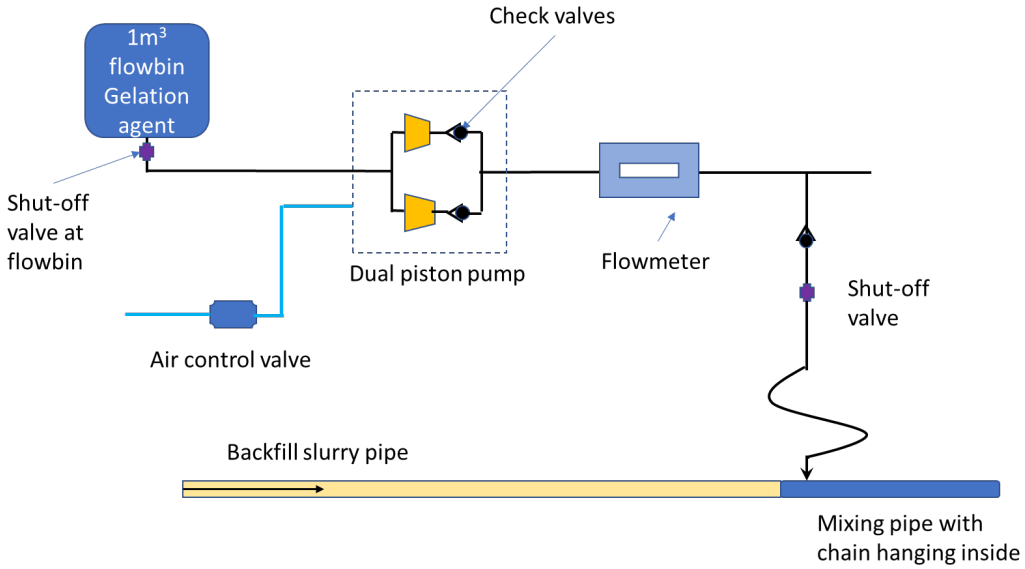


Figure 7. Gelation agent dosing system.

We attempted to measure the gelation agent flow, but this was abandoned as no flowmeter could handle the alkaline environment and high pressure.

Although the mixing method appears rudimentary, it worked well when the silicated system was used on a large scale in the 1990s. (Kermani, *et al*., 2015) found that over-mixing decreases the effectiveness of the silicate.

Laboratory investigation results

Gelation reaction – open time and viscosity rise

Figure 8 to Figure 10 show the effect of gelation agent addition at zero percent (control), 0.5% and 1.0% by mass of the backfill. The backfill slurry comprised full-plant tailings and 8% of cementitious binder, with relative density of 1.75 – 1.79. Gelation took 2 – 8 minutes. Spread' – an indication of flow propensity – decreased progressively from zero addition to being almost completely inhibited at 1% addition. The flow measurements are shown in Table 1. Each result is the average of two measurements at right angles.

Table 1. Flow test results

	Percentage of gelation agent		
	0	**0.5**	**1.0**
Diameter of flow circle (mm) at 2 minutes after addition	172	133	88

This demonstrated the potential for gelation agent addition to stop leakage through the fractured pillars.

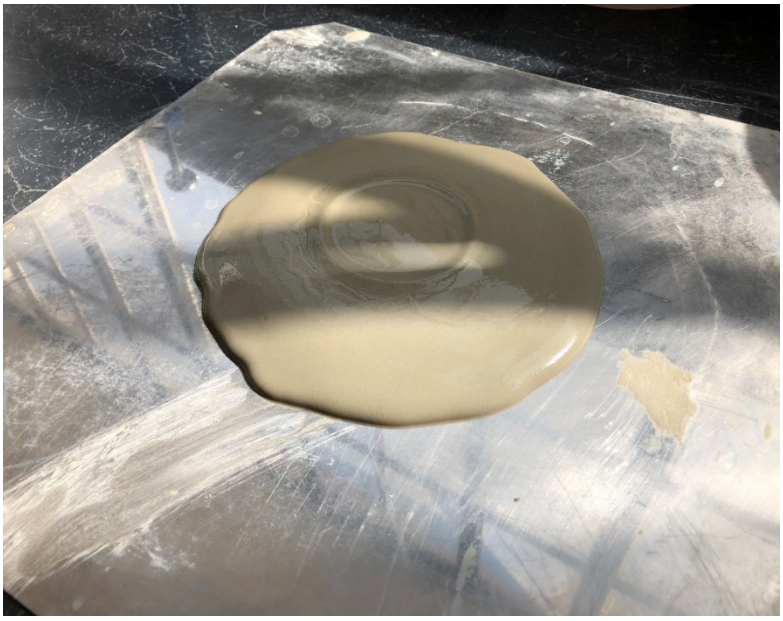


Figure 8. Flow sample with 0% gelation agent.



Figure 9. Flow sample with 0.5% gelation agent.



Figure 10. Flow sample with 1% gelation agent.

Permeation through packed pipe column
Permeation distance was measured after 30 minutes.

- Distance with zero gelation agent: 0.72 m
- Distance with 1% gelation agent 0.25 m

Effect of gelation agent on strength development of the backfill
This testing was essential to ensure that the backfill containing the gelation agent still developed sufficient strength. The same backfill slurry used for the flow tests was poured into cube moulds to prepare specimens for this determination.

The results are summarised in Figure 11.

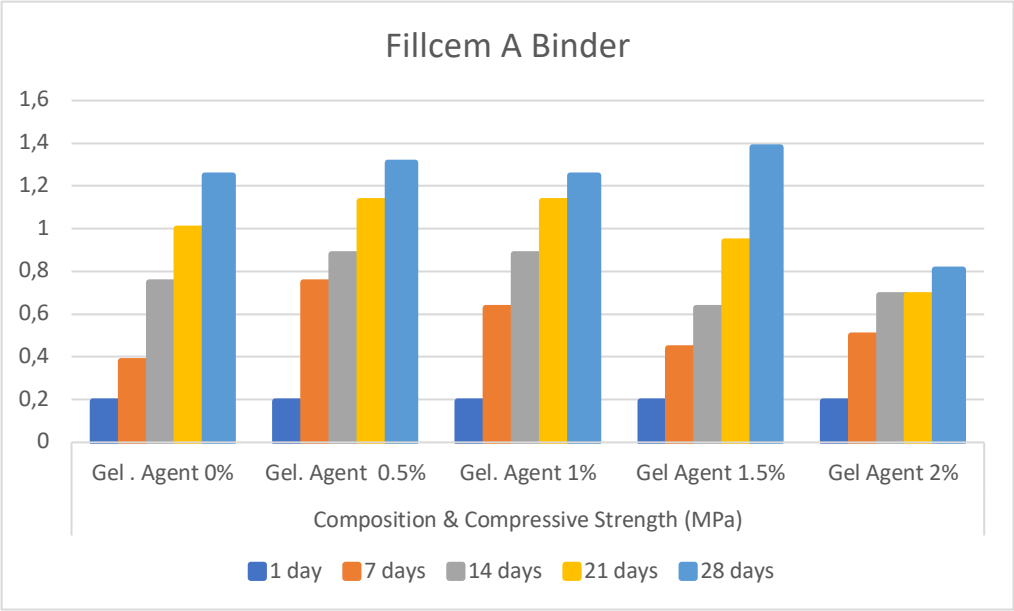


Figure 11. UCS vs time and gelation agent dosage.

The results showed that gelation agent dosage up to 1.5% had little effect on late strength but did cause a decrease in early (seven day) strength. This is most likely due to increased unreacted water retention within the hardening solid. The decrease in strength above 1.5% may be due to syneresis. The possibility of syneresis was noted by (Smart, *et al.*, 1993).

Measurements of 'bleed' water (free water above the solid) support these interpretations:

Table 2. Bleed water accumulation

	Percent gelation agent				
	0.0	**0.5**	**1.0**	**1.5**	**2.0**
% water accumulation after 24 hours	1.10%	0.30%	0.30%	0.30%	0.70%

Underground tests

Based on confidence from the laboratory tests, underground tests were carried out in July and August 2024. Gelation agent dosage of 1% was planned but actual dosing was approximate as backfill flow rate was reported as 60 – 80 m^3/hour, but not accurately known.

The dosing system shown in Figure 7 was set up close to active backfill paddocks. The 105 mm ID backfill pipe was separated and a section containing the chain mixer was inserted, approximately 15 – 20 m before the discharge point (Figure 12).



Figure 12. Gelation agent feed into backfill pipeline.

Output from the pump was measured and set by timing the filling of 10 litre buckets. Flow was approximately 20 – 25 litres per minute, with the pump running at full speed. Air pressure was 4 bar.

Gelling action was observed by filling a 10 litre bucket with the backfill slurry and adding gelation agent to approximately 1% by mass. The slurry in the bucket gelled completely within 10 minutes.

After backfill flow was commenced, the dosing pump was started. Effectiveness was monitored by visual observation of backfill leakage though a fracture into an adjacent excavation. Leakage stopped approximately 10 minutes after commencement of dosing. For confirmation, dosing was suspended. Leakage re-appeared. The pump was then started again; leakage stopped 10 minutes later.

The trials were considered successful.

Operational use

The system has been taken into regular use on the mine and has proven to be effective in eliminating leakages in most cases and significantly reducing them in a few cases. This application has contributed to improving operational efficiencies at the mine.

REFERENCES

ASTM, 2007. *Standard Test Method for Flow of Hydraulic Cement Mortar,* West Conshohocken: ASTM.

du Plessis, M. & Malan, D., 2021. Investigating the use of polymer-modified cementitious thin spray-on liners as stope face support. *International Journal of Rock Mechanics and Mining Science,* Issue 142, pp. 1 - 12.

Gold Fields, 2024. *h1-2024-results presentation-2024.* [Online] Available at: www.goldfields.com [Accessed February 2025].

Hildreth, C., Cybulski, F., Cook, C. & Tadolini, S., 2019. When traditional ground support techniques aren't enough – Chemical injections can solve complex problems. *International Journal of Mining Science and Technology.*

Kermani, M., Hassani, F.P., Aflaki, E., Benzaazoua, M., Nokken, M., 2015. Evaluation of the effect of sodium silicate addition to mine backfill, Gelfil, Part - 1. *Journal Rock Mechanics and Geotechnical Engineering,* Volume 7, pp. 266 - 272.

Kermani, M., Hassani, F.P., Aflaki, E., Benzaazoua, M., Nokken, M., 2015. Evaluation of the effect of sodium silicate addition to mine backfill, Gelfill Part - 2: Effects of mixing time and curing temperature. *Journal of Rock Mechanics and Geotechnical Engineering,* Issue 7, pp. 668 - 673.

Smart, R., Spearing, A. & Harrison, A., 1993. *The Use of Silicated Backfill in South African Gold Mines.* Johannesburg, SAIMM, pp. 289 - 294.



Sifanekiso M Sibanda

Regional Geotechnical Engineer
Goldfields

Sifanekiso M. Sibanda is a geotechnical engineer currently serving as the Regional Geotechnical Engineer at Gold Fields South Deep Mine in Westonaria, where he oversees the entire Rock Engineering function of one of South Africa's most significant deep-level mining operations. With over two decades of expertise in underground hard rock mining across the Bushveld Complex and Witwatersrand Basin, Mr. Sibanda has established himself as a leader in geotechnical engineering, blending operational excellence with innovative research.

Mr. Sibanda holds a BSc in Mining Engineering from the University of Zimbabwe (2002), awarded *cum laude* with Distinction, and an MSc in Mining Engineering from the University of Exeter's Camborne School of Mines (2006), earned *cum laude* with Merit. Currently, he is pursuing a PhD in Rock Mechanics at the University of the Witwatersrand, further cementing his commitment to advancing the field of geotechnical engineering.

Mr. Sibanda's professional journey reflects a progressive ascent through South Africa's mining sector. He began his career in pivotal technical roles before rising to leadership positions at globally renowned firms. As Chief Rock Engineer at Anglo American Platinum's Bathopele Mine (2011–2016), he ensured geotechnical stability in challenging mining environments. His tenure as Manager Rock Engineering at Sibanye Platinum (2016–2023) showcased his ability to lead multidisciplinary teams, optimize safety protocols, and drive operational efficiency. In 2023, he joined Gold Fields, where he continues to shape best practices in rock engineering and risk management.

Committed to lifelong learning, Mr. Sibanda's PhD research at the University of the Witwatersrand focuses on advancing rock mechanics principles, aiming to address complex challenges in deep-level mining. His work underscores a dedication to both practical solutions and scholarly contribution.

The development of the fast cable anchor

J. Wang[1], B. Darlington[1], M. Farrington[2], P. Young[1], S. Weaver[1]

[1]Sandvik Mining & Rock Solutions, Australia
[2]Agnico Eagle, Fosterville Gold Mine, Australia

Mines across the many mining regions are increasingly reliant on both primary and secondary ground control systems. Secondary ground control systems mainly involve the use of deep anchored cable bolts. These cable bolts often require long wait times prior to mine operator re-entry into supported drives. In some current underground cable bolting operations, cable bolting crews must wait up to 12 hours for grout curing before re-entering the work area. This becomes particularly problematic for mine sites working with only one active heading. To reduce re-entry times, and to increase the safety of the work area, a Fast Cable Anchor (FCA) has been developed, which can also accelerate mining development. This FCA allows miners immediate re-entry to the supported work area by securing both the borehole and cable, which can be plated and tensioned immediately after complete insertion. Unlike prefabricated/pre-assembled cable bolts, the FCA device is compatible with bulk coiled cable, increasing the efficiency of the cable bolting process with the use of a Sandvik cable bolter. This paper presents the development of the FCA, and a case study performed at a gold mine in Australia and the Sandvik Test Mine in Finland.

Keywords: Ground support, cable bolting, immediate support, fast re-entry, mine safety, case study

INTRODUCTION

Underground cable bolting is a widely used technique in mining and civil engineering to stabilise rock masses and ensure the safety of underground excavations. This method involves the installation of steel cables, which are grouted into pre-drilled holes in the rock. The primary purpose of cable bolting is to provide deeply anchored secondary support, thereby enhancing the stability of tunnels, shafts, and other underground structures (Hutchinson, 1995).

Since its introduction in the early 1970s, cable bolting has evolved significantly, becoming a cornerstone of underground ground control systems. Its effectiveness in improving load transfer and overall stability has led to widespread adoption in modern mining and civil engineering projects.

The current practice of installing cable bolts in Australian hard rock mines can be performed manually or by mechanised means. Mechanised cable bolting machines are commonly used in large-scale mining operations due to their efficiency and increased operator safety. These machines provide consistent installation, which is crucial for maintaining the stability of extensive underground excavations.

Steps in Mechanised Cable Bolting

Drilling holes

The first step in the installation process is to drill holes into the rock where the cable bolts will be inserted. This is completed using a cable bolting machine, which can accurately and efficiently drill holes to the required depth and diameter. The holes are typically drilled at specific angles and patterns to optimise the support provided by the cable bolts.

Grouting
Grouting is a critical step in the cable bolting process, where the grout is pumped into the hole to fill the space around the cable bolt when it is installed, ensuring secure anchorage to the rock. The grout can be cementitious or resin-based, depending on the specific requirements of the installation. The grouting process can be done using different methods, such as the breather tube method or the grout tube method, to achieve optimal bond strength and load transfer capabilities.

Inserting Cables
Once the holes are filled with grout, the cable bolts are inserted into the holes. The cables are usually made of steel and can be plain or have bulbs (birdcages) to enhance load transfer. Cables can be pre-kinked before insertion to engage with the wall of the hole and thereby prevent cables from falling down vertically-oriented holes.

Plating and Tensioning
After the grout has cured (typically for 12 hours), the cable bolts are tensioned to the required load, which ensures load transfer from the cable bolt through the face plate to the surface or areal support and rock mass. This step is crucial for bulking control and retention of damaged ground following a rock burst or static fracturing and deformation, and in zones of poor or blocky rock mass. The tensioned cable bolt and plate provide active support to minimise the amount of displacement prior to engaging the capacity of the cable bolt.

In mining areas with rock burst damage, weak rock mass, very blocky or poor rock mass, cable bolts can be ineffective in transferring rock mass load to adjacent rock bolts (Bawden 2024). The integrity of surface support and the connection to the cable bolts through the plates is essential in preventing falls of ground (Winder and Maney 2009).

Despite the widespread use and effectiveness of cable bolting in Australian hard rock mining, several bottlenecks can impact its efficiency and overall performance. One of the major bottlenecks in cable bolting is ensuring the quality and consistency of the grout used to anchor the cables. The grout's water/cement ratio and the method of grouting can significantly affect the bond strength and load transfer capabilities of the cable bolts. Inconsistent grouting can lead to weak points in the support system, reducing the overall stability of the rock mass.

Re-entry time is a significant bottleneck in many cable bolting applications. After grouting and installation of cable bolts, there is a mandatory waiting period to allow the grout to cure and achieve the necessary strength before workers can safely re-enter the bolted area. This waiting period removes workers from the area, where a risk exists of cables falling from the boreholes whilst the grout is curing. This curing time can vary depending on the type of grout used, water/cement ratio and environmental conditions; however, it typically takes from several hours to a full day. During this period, mining operations in the affected area must be halted, leading to potential delays and reduced productivity. Innovations in grouting materials, such as fast-setting grout or pumpable resin can help reduce re-entry times, but their adoption is still limited due to cost and other practical considerations.

In the Robbins Hill decline at Fosterville, spanning over 3600 m, the 12-hour waiting period between grouting and tensioning for each of the 84 intersections resulted in a total of six weeks of lost productivity. Given that this is a continuous operation, reducing this waiting period could significantly enhance efficiency, allowing operations to access ore six weeks earlier.

Fast Cable Anchor design development
With the restraints and difficulties of existing cable bolting methods, Sandvik identified an opportunity to improve the safety and efficiency of cable bolting practices. The Sandvik Fast Cable Anchor (FCA) is a mechanical anchoring solution designed for mines aiming to increase safety, speed up processes by significantly reducing re-entry time, and ensure consistent ground support quality. During the development of the FCA, several challenges needed to be overcome.

Tool-free connection required developing a faster way to connect the cable with the FCA without requiring any tools. Insertion in pre-grouted holes was essential and important to ensure the FCA was compatible with the current method of cable bolting; achieving secure engagement with the walls of holes prefilled with grout, whether in sedimentary or igneous rock types. Immediate tensioning is required to enable tensioning to 100 kN upon insertion.

Design features

Barrel and wedge sets are widely used in mining and civil engineering to secure cables. Building on this well-known and well-used concept, the addition of a spring creates a fast-connecting mechanism. The anatomy of the FCA is shown in Figure 1 and the wedges with the additional spring is illustrated in Figure 2.

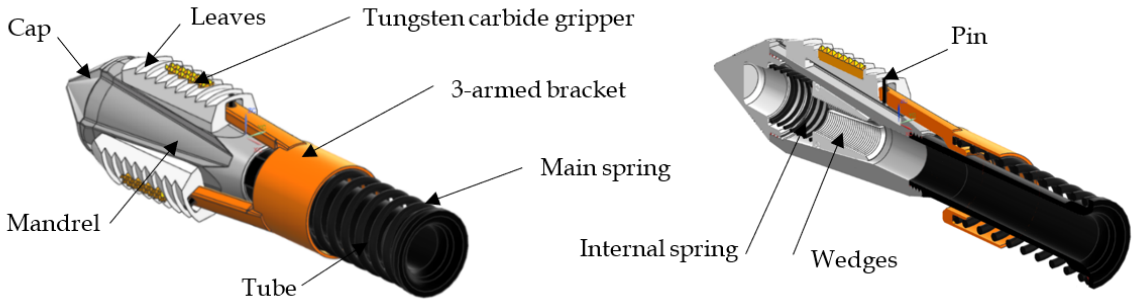


Figure 1. Anatomy of the Fast Cable Anchor.

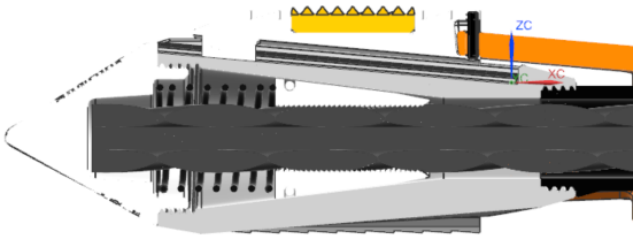


Figure 2. Internal wedges and spring combination to allow fast connection.

During the development phase, the spring load rating was found to be crucial for allowing the wedges to open and let the cable through.

To overcome the challenge of inserting the FCA into pre-grouted holes, the main body of the anchor was specifically designed with a shape that allows maximum grout passage. This design, as shown in Figure 3, ensures that the grout can flow around the anchor, securing it firmly in place while maintaining the integrity of the support system. The use of three leaves helps keep the anchoring system automatically centred inside a round hole.

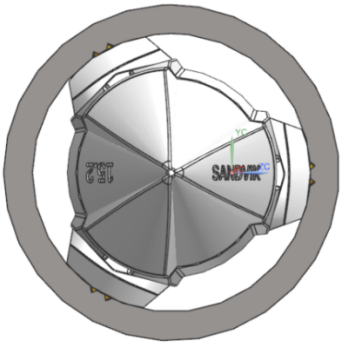


Figure 3. Triangular shaped mandrel compound to allow grout flow.

One of the primary concerns before the development of the FCA was ensuring it securely engaged with the rock wall. Grouting adds to this challenge because wet grout can act as a lubricant, potentially causing slippage of the anchoring system.

Initial engagement of the FCA with the rock is critical for successful and reliable gripping and tensioning. To address this, a mechanical structure comprising a main spring, tube, and a three-armed bracket is used to provide the leaves with the necessary initial engagement, as shown in Figure 4. Once the initial engagement is established between the leaves and the rock, the FCA can take on the load without being pulled out by the pulling force.

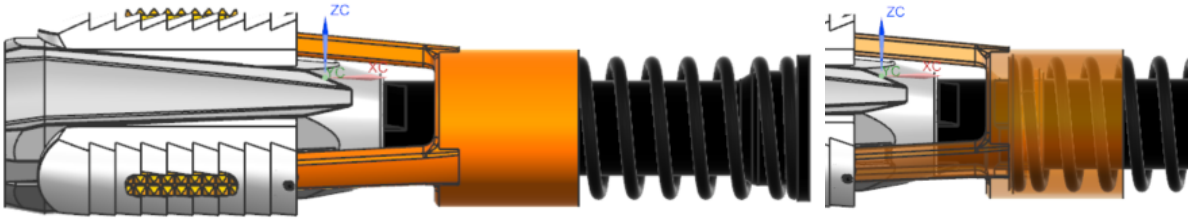


Figure 4. Main spring, tail tube and flexible 3-armed bracket to drive leaves to engage with the rock wall.

At the early stage of the FCA development, slippage occurred due to inadequate grip between the leaves and the test rock. To address this issue, tungsten carbide grippers were brazed onto the leaves, enhancing their gripping capabilities with the rock, as illustrated in Figure 5. This upgrade ensured that the FCA could securely engage with the rock surface, preventing slippage and improving overall performance.



Figure 5. Leaves empowered by tungsten carbide grippers.

Laboratory testing results

Laboratory tests were conducted in the Sandvik Ground Support Research and Development facility in Heatherbrae, Australia, to evaluate the performance of the FCA. Initial testing utilised confinement blocks, cast using Master flow 4600 grout, reinforced with 4 mm basalt aggregate, and allowed to cure for over 28 days. The wet grout used to fill the cast holes was a general-purpose cement mixed with water at a 0.33 water/cement (W/C) ratio.

FCA prototypes were installed into pre-grouted holes, precast to 58 mm and 52 mm diameter. The prototypes were tensioned immediately, as would be expected when used in the underground environment, which showed that both prototypes exceeded the target tension of 100 kN, as shown in Table I. The prototype installed into the 58 mm hole reached a peak load of 190 kN before dropping briefly, then increasing again to 210 kN; whereas the prototype installed into the 52 mm hole reached a peak of 233 kN before dropping slightly to 167 kN. These test results show that the FCA with carbide grippers can grip the rock in a pre-grouted borehole, which deemed it ready for an underground trial.

Testing results

Table I. Fast Cable Anchor pull test in 58 and 52 mm cast holes

58 mm hole			**52 mm hole**		
Load (kN)	**Hydraulic ram extension (mm)**	**Remarks**	**Load (kN)**	**Hydraulic ram extension (mm)**	**Remarks**
0	0		0	0	
25	3		20	4	
42	4		40	7	
60	8		60	10	
80	10		80	12	
100	12		100	14	
125	18		120	18	
140	21		140	22	
160	26		160	23	
190	28	drop to 80 kN	180	26	
210	30	drop to 80 kN	200	28	
			233	30	drop to 167 kN

Case study

With the success of the laboratory grouted hole testing, the next critical phase in a new product development is an in-depth field trial. A successful field trial is key to successfully proving the design of all new ground support products, as the underground environment can often present different challenges to a laboratory environment. In the case of the FCAs, 10 FCA prototypes were tested for installation and tensioning performance.

The trial was conducted at Agnico Eagle, Fosterville Gold Mine in a drive 8 m wide x 6.5 m high, located in the H4770 RAW being developed as part of a major ventilation upgrade project. The location is 400 m below ground level and the rock is an interbedded sandstone and shale turbidite sequence, with typical rock strength of 110 MPa for sandstone and 40 MPa for shale. See Figure 6 for more details.



Figure 6. Core photo from a nearby diamond drill hole.

A Sandvik DS420 cable bolter was used for the trial, including drilling the holes, mixing/pumping grout and feeding cables. The cement mixture used was builders' cement with a water-to-cement ratio 0.3:1. The drill bits used were brand-new button drill bits, with two different diameters: 54 mm and 51 mm. The drilling plan for the two different bits diameter test holes are shown in Figure 7.

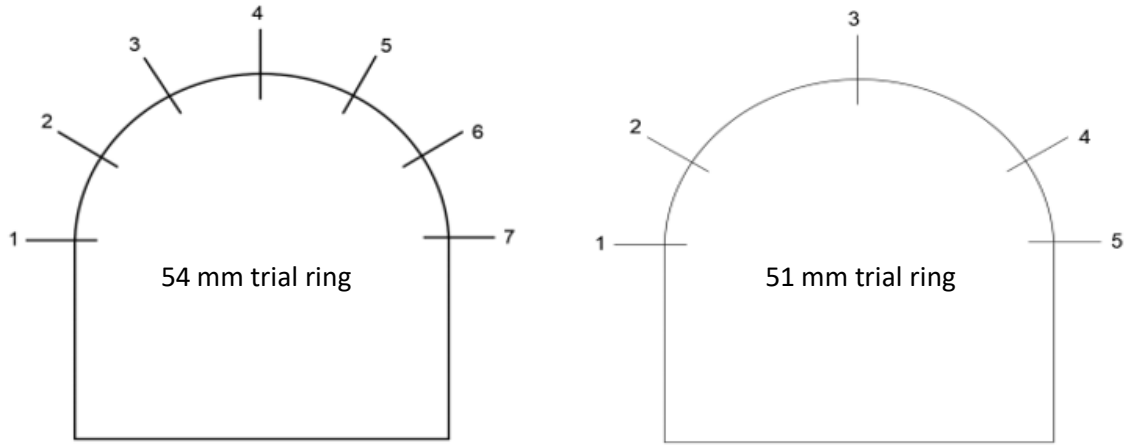


Figure 7. Drilling plan.

Meetings with site engineers and operations teams were arranged before the trial to evaluate the tasks and risks, ensuring a safe testing procedure (see Table II).

During the trial, FCA samples performed well in holes drilled with brand new 54 mm and 51 mm drill bits. Nine out of ten samples could be fully inserted into holes prefilled with grout using the cable bolter. All FCA samples were tensioned up to 100 kN with a relatively short jack extension of around 60 mm, provided the gaps between rock faces and plates were removed prior to tensioning (see Table III). This test validated the use of the FCA in a sedimentary rock.

Table II. Testing procedure

Item No.	Steps
	Holes pre-drilled before trial
1	Cable bolter mixes cement with 0.3 water to cement ratio
2	Pump grout into borehole
3	Manually put anchor onto cable end
4	Insert cable and anchor into grouted hole
5	Cable feeders reverse to test engagement with rock
6	Cable bolter cut cable
7	Cable bolter repeats 2-7 until using up the whole drum of cement mixture
8	Cable bolter leaves the area
9	Cable tensioning rig moves forward
10	Place plate and barrel and wedges against rock face
11	Tension the cable to 100 kN
12	Release tension, relocate jack and re-tension if longer than ~150 mm ram extension is needed

Table III. Testing results

Drill bit (mm)	Hole orientation	Insertion	Plating	Ram extension
54	1	Sample jammed at 3 m depth	ok	100 kN at 42 mm
54	2	ok	ok	100 kN at 90 mm
54	3	ok	ok	100 kN at 50 mm
54	4	ok	ok	100 kN at 50 mm
54	5	ok	ok	100 kN at 58 mm
54	6	ok	ok	100 kN at 40 mm
54	7	ok	ok	100 kN at 36 mm
51	3	ok	ok	100 kN at 58 mm
51	4	ok	ok	100 kN at 55 mm
51	5	ok	ok	100 kN at 59 mm

To understand the FCA performance in an igneous rock type, a series of tests were planned and conducted at the Sandvik Test Mine in Tampere, Finland. This test mine has massive granite rock, which makes it a perfect location to test the FCA performance in an igneous rock. This test was carried out in the F4 area, as illustrated in Figure 8.



Figure 8. Location of the Sandvik Test Mine testing site.

A DS422i cable bolter was used for the trial, which included drilling holes, mixing grout, and installing the samples. The grout used for this trial was Portland cement with a water-to-cement ratio set at 0.33:1. Table IV summarises the various drill bits used to drill the holes for the trial.

Table IV. List of used drill bits

 1 - Drill bit small 53 – 52.5 mm	 2 - Drill bit small 52 – 52.5 mm (Drill bit 3 resharpened)	 3 - Drill bit medium 54.5 – 55 mm	 4 - Drill bit large 57.5 – 58 mm	 5- Drill bit large 57.5 – 58 mm

The testing prototypes for this test included two different spring ratings, a low strength and a high strength, and the assembled samples ready for installation are shown in Figure 9.

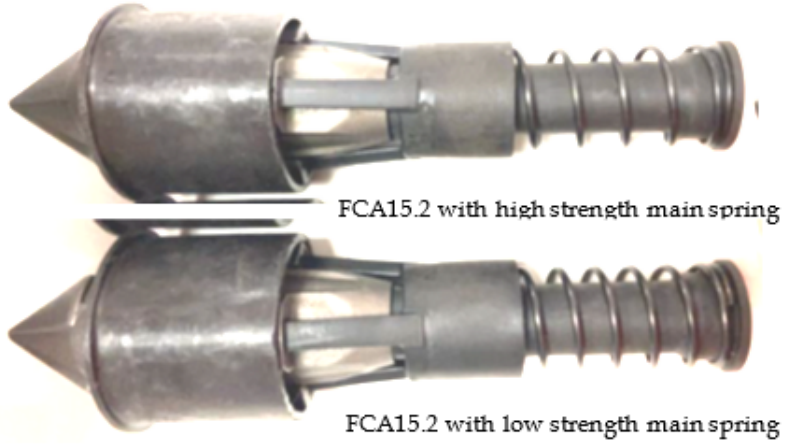


Figure 9. Two types of the Fast Cable Anchor samples were tested.

Three aspects of performance were assessed during the trial:

- FCA samples assembly onto the cable end,
- Assembled FCA full insertion into grouted holes, and
- Installed FCA immediately tensioned to 100 kN.

Additionally, some of the installed cables were planned to be pull-tested to higher loads, above 200 kN, to determine the ultimate strength of the FCA installation prior to grout curing. However, due to a hydraulic cylinder issue encountered, the FCA samples were not tested to destruction; see Table V for the full test results.

Table V. Test mine testing results

Sample	Spring	Bit size (mm)	Hole length (m)	Wall / back	Anchor onto cable	Insertion	100 kN Load	Stroke at 100 kN (mm)	Max load (kN)	Stroke at max load (mm)
15.2	weak	53-52.5 (drill bit No.1)	10	wall	OK	4.7 m	OK	33	209	60
15.2	weak		10	wall	OK	4.8 m	OK	52	N/A	N/A
15.2	strong	52.5-52	10	wall	OK	OK	OK	50	156	75
15.2	strong	52.5-52	10	wall	OK	OK	OK	85	N/A	N/A
15.2	strong	54.5-55	8	back	OK	OK	OK	41	196	66
15.2	strong	54.5-55	8	back	OK	OK	OK	44	199	91
15.2	strong	54.5-55	10	wall	OK	OK	OK	54	199	106
15.2	strong	54.5-55	10	wall	OK	OK	OK	89	N/A	N/A
15.2	strong	57.5-58	10	wall	OK	OK	65 kN	N/A	NA	N/A

The Test Mine test results indicate that the FCA performed well in igneous type of rock holes, with most installations being successful. Failure of insertion on two samples with weak springs was mainly caused by the usage of a worn-out drill bit No. 1, along with drilling through cracked and fractured ground. One FCA experienced slippage in the hole drilled with a 57.5-58 mm drill bit due to its hole size exceeding the FCA design working range. FCAs were all tensioned up to 100 kN before the grout set but were not tensioned to failure due to the capacity of the hydraulic system. This test successfully demonstrated the FCA deployment in an igneous rock.

CONCLUSION

Laboratory tests conducted at the Sandvik Ground Support Research and Development facility in Heatherbrae, Australia, provided a demonstration of the effectiveness of the FCA under controlled conditions. The FCA was successfully inserted into pre-grouted boreholes (precast to 58 mm and 52 mm), and immediately tensioned as is the intended function in the underground environment. These tests showed the FCA was capable of immediate tension exceeding 190 kN, which is above the current cable bolt tension required load (typically 100 kN).

Field tests at Agnico Eagle's Fosterville mine, with sedimentary rock, and the Sandvik Test Mine, with igneous rock, also yielded positive results. These tests demonstrated successful insertion and tensioning of FCA samples in the underground environment. Five samples were also tensioned above the required load (100 kN), reaching peak loads between 156 – 209 kN.

This testing in a variety of ground and borehole conditions confirmed the applicability of the FCA for insertion into pre-grouted holes and immediate tensioning.

The development of the FCA represents a significant advance in underground cable bolting practices, particularly for mechanised cable bolting utilised in Australian hard rock mining. By addressing key challenges such as re-entry time, grouting quality, and secure engagement with rock walls, the FCA will enhance both safety and efficiency in mining operations.

The implementation of FCA can significantly enhance rapid development in mining operations by drastically reducing the waiting period between cable bolt grouting and tensioning. This allows for continuous operation and minimises downtime, leading to increased productivity. FCAs, with their quick-setting properties, enable the immediate application of tension, ensuring that the support system is ready for load-bearing much sooner than traditional methods. This efficiency not only accelerates the overall development process but also supports larger cable bolting campaigns by allowing more intersections to be secured in a shorter timeframe. Consequently, mining operations can advance more rapidly towards ore extraction, optimising both time and resources.

ACKNOWLEDGEMENT

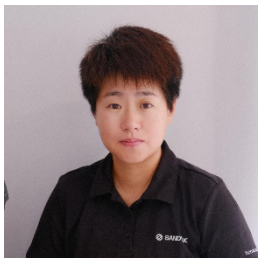
The authors would like to express their gratitude to the geotechnical and operations team at Agnico Eagle's Fosterville gold mine for accommodating the Sandvik Ground Support R&D team during the trial of new products. Special thanks are also extended to the R&D and product management teams at Sandvik Ground Support for their guidance and inspiration throughout the development of the FCA.

REFERENCES

Bawden, W.F (2024). Forgotten critical limitations on cable bolt reinforcement design and guidelines for instrumentation deployment to monitor support behaviour and capacity consumption. *Proceedings of the 10th International Conference on Deep and High Stress Mining*, P Andrieux & D Cumming-Potvin (eds). Australian Centre for Geomechanics, Perth. pp. 403-416

Hutchinson, D.J. and Diederichs, T. (1995). *Cablebolting in Underground Mines*. BiTech Publishers, Richmond, British Columbia.

Winder, K and Maney, B. (2009). The advantages of mechanised cable bolting in the modern underground mine. *Proceedings of the First International Seminar on Safe and Rapid Development Mining.* PM Dight (ed.). Australian Centre for Geomechanics, Perth. pp. 131-138



Jamie Wang

Research and Development Engineer
Sandvik Mining & Rock Solutions, Australia

Jamie Wang is a dedicated and innovative Research and Development Engineer at Sandvik Mining & Rock Solutions, Australia. With a Bachelor of Engineering in Mechanical Engineering, Jamie has consistently demonstrated a strong commitment to advancing technology and improving operational efficiencies within the Ground Support division.

Jamie earned a Bachelor of Engineering in Mechanical Engineering from a respected institution, Tianjin University of Technology and Education, where she developed a robust foundation in mechanical systems, design, and engineering principles. This academic background has been instrumental in Jamie's ability to tackle complex challenges and contribute to cutting-edge research and development projects at Sandvik.

At Sandvik Mining & Rock Solutions, Jamie has played a role in several high-impact projects. Her expertise in mechanical engineering and innovative approach have led to the development of new products that enhance the efficiency and safety of mining operations.

Review of the stope support system at Impala Bafokeng North Shaft owing to stope closure at shallow mining depths

T. Walsh

University of the Witwatersrand, South Africa

Impala Bafokeng's North Shaft is a shallow platinum mine on the western limb of the Bushveld Igneous Complex. Shallow mines experience very little horizontal stress which leads to a support issue of the tensile zone. North Shaft relies heavily on mine pole support due to the requirements for a stiff support system. Elongate support failure in the deeper parts of the mine have occurred due to a change in the loading environment. The support failure has resulted in inadequate support resistance in the back areas and some large falls of ground (FOGs). In this research report the hybrid section stope closure rate was measured. The closure does not appear to be linked to a detachment of a hangingwall parting. The ground penetrating radar scans and borehole data correlate with the observations. The FOGs are structure related and occur in the back areas of the panel after the elongate support had failed. The footwall material is weaker than the hangingwall material and the pillar punches into the footwall. The footwall fractures and tensile cracks in the panel footwall indicate that the stresses are forced to move horizontally due to the Footwall 4 parting plane. The footwall thrusts into the panel causing the high closure observed. The combination of a shorter panel length and pencil sticks would provide adequate support for the high closure rates observed.

Keywords: closure, support failure, footwall thrust

INTRODUCTION

The Bushveld Igneous Complex (BIC) is a layered igneous intrusion that is mined for platinum group minerals. The BIC spans approximately 350 km from east to west and has three major outcrops, the northern, eastern and western limbs. Impala Bafokeng's North Shaft is situated within the western limb of the BIC between the Pilanesberg and Rustenburg (Figure 1). The mine is approximately 30 km north of Rustenburg, in the North-West Province.

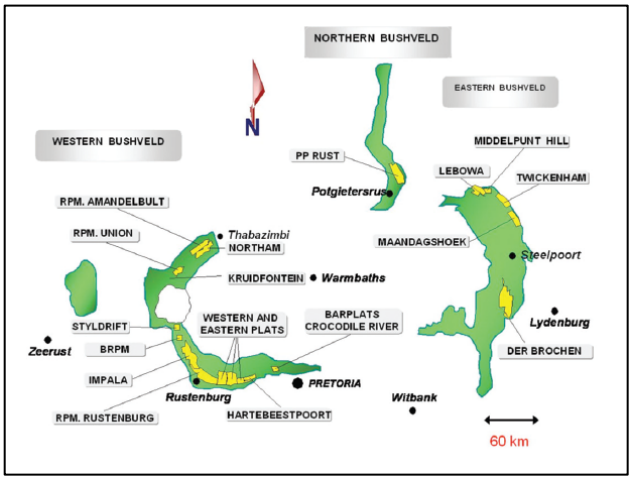


Figure 1. Location of the mine within the Bushveld Igneous Complex (Watson, et al.*, 2010).*

Impala Bafokeng's North Shaft is a shallow tabular hard-rock mine that exploits the Merensky and UG2 reef horizons. A mix of conventional scattered breast mining and hybrid mining takes place. The UG2 reef is currently being mined in the shallower portions of the mine. A reef middling of approximately 70 m is consistent across the workings. The Merensky reef is currently being mined between 400 m and 600 m depth. The shaft bottom is approximately 670 m below surface and the mine is therefore considered a shallow working environment. The hybrid section consists of mechanised on reef development with conventional scattered breast stoping and is located at the deepest workings of the mine (Figure 2). Ore is transported along raise lines using a winch, into a muckbay. A load, haul, dump loader is then used to transport the ore to the strike conveyor belts. The hybrid design was utilised to allow for development on-reef and to reduce capital expenditure and time to access the reef.

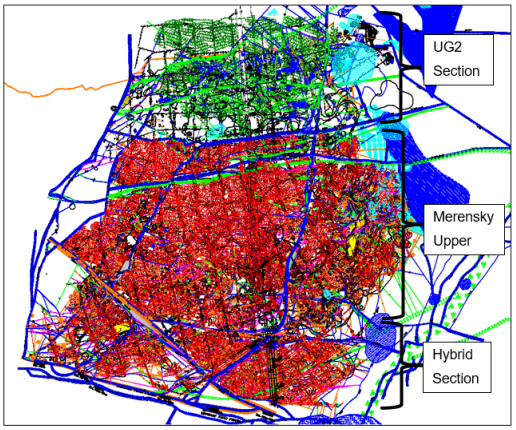


Figure 2. Plan view of North Shaft.

Shallow mines experience very little horizontal stress which leads to the formation of a tensile zone in the hanging wall. When the tensile zone interacts with low angled geological structures, it can lead to instability. North Shaft's support designs have historically been of an empirical nature. The mine relies heavily on elongate support due to the requirements for a stiff support system to prevent any unravelling from taking place. The first raise line that was established and mined at 15 level (Figure 3), experienced higher than expected closure rates which led to the failure of mine pole support units. The safety risk and the loss of reserves necessitated a review of the stope support system.

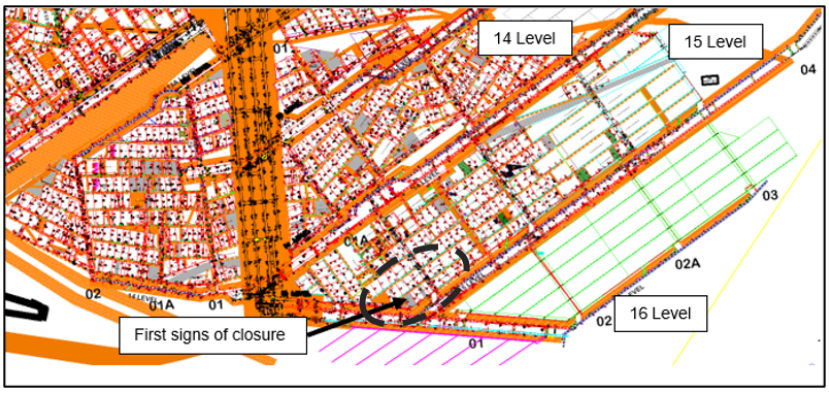


Figure 3. Plan view of the Merensky section on microstation.

The mine pole support was found to be splitting and buckling in the back areas of panels from as little as 20 m away from the face (Figure 4). This led to the finding that the closure rate had increased rapidly from previously mined levels.



Figure 4. Failed mine poles in the back area of stopes.

Support Design Background

A mine pole refers to an unturned elongate (Figure 5). The width of the mine pole is measured diametrically across the end of the pole. The mine poles are installed in combination with a pre-stressing device to make it an active support unit and to reduce blast-outs.

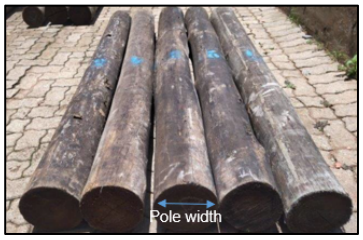


Figure 5. Mine poles (Khosa, 2022).

The face support includes in-stope bolts and temporary support in the form of mechanical props with safety nets. The back area support consists of 'breaker lines' – clusters of three mine poles. The clusters are installed to support the hanging wall up to the tensile zone. The hybrid section is serviced with on-reef mechanised roadways that need to remain stable over the life of the mine. Strike stability pillars were designed on either side of the roadways and belts (Figure 6). The hybrid section's in-stope pillars were designed to crush; they are 6 m long and 3 m wide.

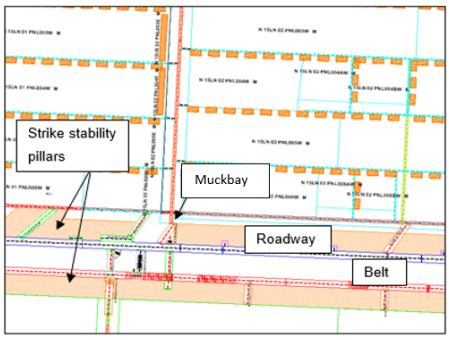


Figure 6. Hybrid section mining layout.

Instrumentation

Closure measurement data was recorded with closure loggers. The data can be used as a predictor for large collapses in mines. Closure data can also be used for improving support designs through the inclusion of the effect of the mining rate (Malan & Napier, 2021). The data can be used to define a new ground control districts with specific support strategies. The installation process is captured in Figure 7. The loggers were used to determine the rate of closure per metre of advance. A total of five loggers were installed across the working places.



Figure 7. Closure logger installation by the author.

Data from the closure loggers were collected using a tablet equipped with a Bluetooth system. This allowed the data to be collected safely without having to enter the back areas of the panel. Borehole camera investigations (Figure 8) was conducted along the roadways. The holes were drilled vertically to approximately 15.0 m into the hangingwall. The 15.0 m depth was chosen as this was the known depth of the 'Bastard Reef' chrome parting, and the contact was examined for any signs of tensile failure.



Figure 8. Rock engineering department borehole camera.

The borehole camera was utilised to assess the condition of potential parting planes such as the Bastard Reef located at 15 m above the Merensky Reef, illustrated in Figure 9. The contact can have a shear plane.

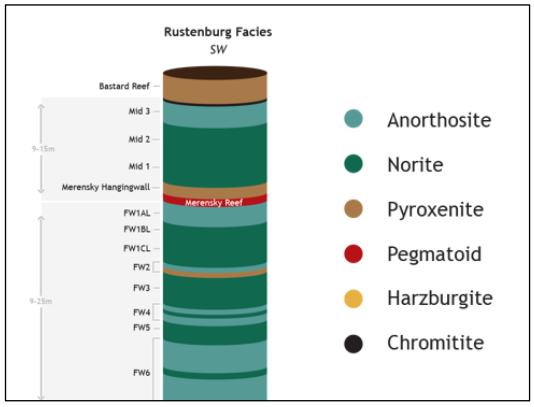


Figure 9. Stratigraphic column of the BRPM mining locality (Impala Bafokeng - Geology Department).

Ground penetrating radar (GPR) scans were conducted along the 14 and 15 level roadways and along the 15 level north 2 raise line. The borehole camera work was used to correlate with the GPR scans. Any observations on the scans were referenced against physical observations (Figure 10).



Figure 10. The author conducting GPR scans along the roadway.

The GPR that was utilised is referred to as a sub surface profiler. The tablet enables the user to check the scans immediately (Figure 11). Technology that is more user-friendly enables scans to take place more regularly.



Figure 11. Sub surface profiler used for GPR analysis (Andrews, et al.*, 2019).*

Visual Observations

The stability of the panels is influenced by the geological discontinuity spacing, infilling, orientation, dip and persistence. Investigations of numerous falls of ground (FOGs) by York *et al.,* (1998) found that almost all FOG events were linked to major geological discontinuities and not due to span alone. Their investigations led to a correlation between a reduction in span and improvement of hangingwall

conditions where shallow dipping discontinuities were present. The crush pillars were inspected and no sign of any pillar failure was found. The taller gully sides of the pillars, along the advanced strike gully showed less scaling than the shorter side at the top of the panels. The gully sidewalls were bolted to reduce scaling along the travelling route which increased the confinement on that side. The hangingwall around the pillars was observed to be competent and no fractures were present. Hangingwall conditions were stable. The footwall around the pillars had fractured significantly and footwall heave had taken place around the pillar (Figure 12).



Figure 12. Footwall fracturing and heave around a crush pillar footwall.

Tensile cracks were observed in the centre of the panel along the footwall. The tensile cracks had an 8 mm aperture and extended for a trace length of more than 20 m (Figure 13). The tensile cracks were orientated near parallel with the mining direction.



Figure 13. Tensile cracks in the footwall.

DISCUSSION

The North Shaft data for the closure loggers is presented graphically in Figure 14. The figure represents the measured displacement in millimetres over time.

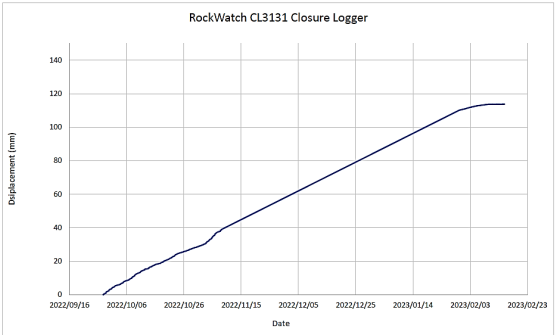


Figure 14. Closure logger data after five months (Unit 3131).

The closure measured on the loggers between the periods of 26/09/2022 and 23/02/2023 was 115 mm. The advance over this period was 64 m.

$$\frac{\text{Closure measured } (115\ mm)}{\text{advance } (64\ m)} = \text{Closure rate } (1.79\ mm/m) \quad [1]$$

Borehole data was compared with the GPR scans that were conducted. The GPR scans show no obvious parting besides the consistent contact at 2.0 m into the hangingwall (Figure 15). The contact was between the Merensky hangingwall pyroxenite and the Mid 1 Norite. The borehole camera was used to confirm the contact.

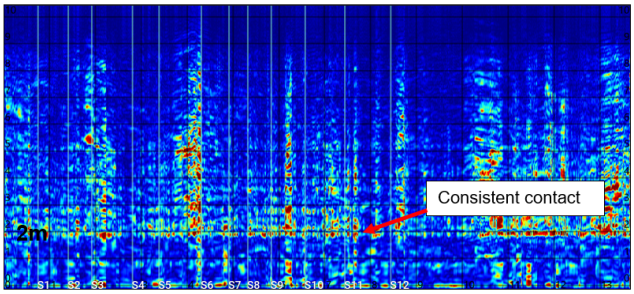


Figure 15. GPR scan of 14 level roadway.

Support Strategy

The mine poles (18 – 20 cm diameter) that are currently installed reach their peak strength after a displacement of 30 mm (Figure 16). This means that after approximately 18 m advance, the closure caused the mine poles to fail.

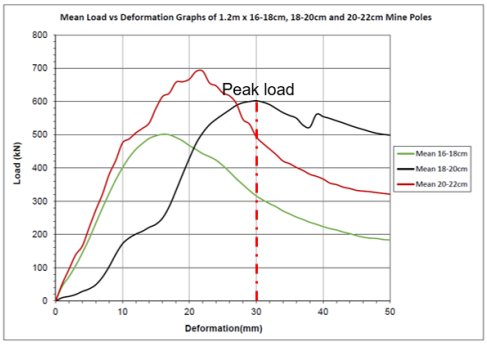


Figure 16. Load-deformation chart of various size mine poles (Khosa, 2022).

Pencil sticks were introduced as an alternative to the mine poles. They provide the benefits of a stiff support system with the yielding capability required for the closure experienced. The profiled portion of the stick brushes/yields (Figure 17) in a controlled manner to allow the load to be shed whilst maintaining the support resistance. The strategy falls in line with those of industry experts: "The problem of premature failure of props caused by footwall heave, resulting from pillar punching, can be overcome by installing yielding elongates" (Jager & Ryder, 1999).



Figure 17. Pencil sticks selected for load deformation testing (Mabitsela, 2023).

Pencil sticks are capable of rapidly reaching peak load, within 10 – 15 mm of deformation. The pencil sticks maintain that load for up to 120 – 150 mm of deformation (Figure 18).

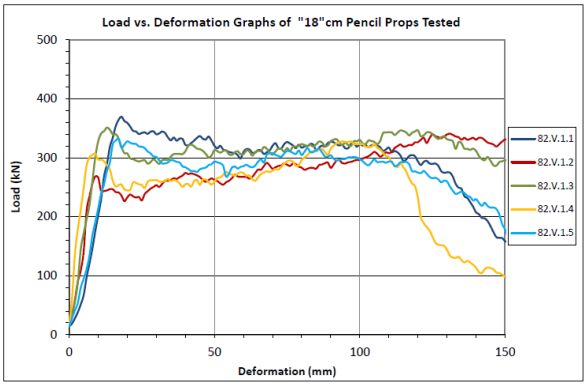


Figure 18. Load-deformation chart of 18 cm pencil sticks, 140 mm length (Mabitsela, 2023).

A short panel length at N15LN01 panel 006W was mined with a 23 m face length from pillar to pillar. The panel was last mined in June 2022, and the condition of the support was fair 12 months after mining was completed to the panel limit. The panel was not redeveloped during its mining cycle and reached the 120 m limit.

Footwall Heave Hypothesis

The high closure rate was initially considered to be due to tensile failure of the hangingwall. The data collected from the borehole camera, GPR scans and visual observations indicated otherwise. The footwall fractures around the in-stope pillars combined with the tensile cracks observed on the panel footwall were indicators of potential footwall heave. The footwall material is weaker than the hangingwall. The presence of layers in the footwall with low cohesion induces foundation instability and pillar punching with heave in the adjacent panels and stope closure (Jager & Ryder, 1999). Exploration drilling data was obtained from the geology department for the contact. The average footwall 4 parting plane elevation was located at 4.65 m below the reef. The potential for the contact to form a parting plane is high due to its 1 – 2 cm thick slickensided and serpentinised contact.

CONCLUSIONS

The GPR scans and borehole data correlate with the observations made that the hangingwall is stable when not affected by low angled geological structures. The FOGs that were analysed are structure related and occur in the back areas of the panel after the elongate support had failed due to high closure. Panels with no prominent structures remained stable after the support failure due to the in-stope crush pillars. The pillar footwall material is weaker than the hangingwall and the pillar punches into the footwall (Figure 19).

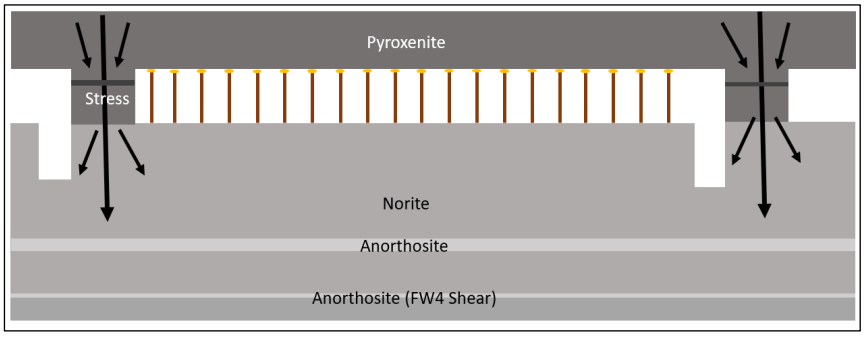


Figure 19. Illustration of stress transfer into the footwall.

The footwall fractures and tensile cracks in the panel footwall indicate that the stresses are forced to move horizontally due to the footwall 4 parting plane. The footwall thrusts into the panel causing the elongate failure and high closure rate observed (Figure 20). The panel length was established as a critical factor in maintaining stability of the workplaces. Reducing the panel length allowed a panel to be mined to completion without any structural failures and with reduced support failure. Panel length was reduced to 25 m for all new panel layouts. The combination of reduced closure within the shorter panel length and the increased yield capability of the pencil sticks provided suitable support for the high closure rates observed. Pencil stick support continued as the primary support.

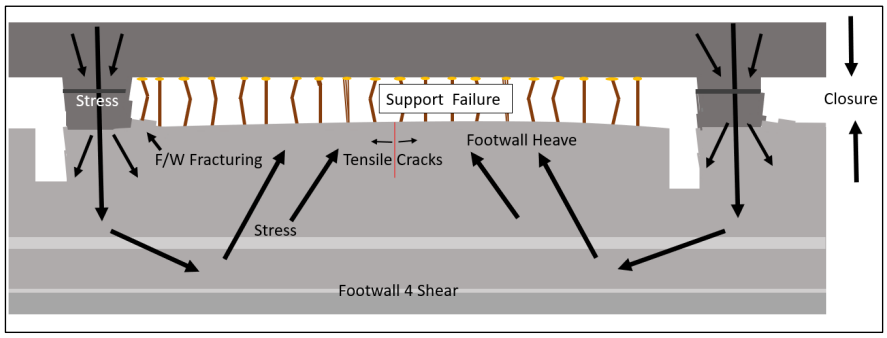


Figure 20. Illustration of footwall failure and heave into the panel.

REFERENCES

Andrews, P. G., Rwodzi, L., Ekkerd, J. & Ratshitaka, N., 2019. *Advanced techniques for the monitoring of pillar and excavation behaviour at a deep level massive mine: Deep Mining 2019.* Johannesburg, The South African Institute of Mining and Metallurgy.

Bieniawski, Z. T., 1992. *Principles of engineering design for rock mechanics.* Rotterdam, 33rd US Symposium on Rock Mechanics.

Daehnke, A., 2001. Addressing the variability of elongate support performance. *The Journal of The South African Institute of Mining and Metallurgy,* 101(2), pp. 83-90.

Daehnke, A., van Zyl, M. & Roberts, M., 2001. Review and application of stope support design criteria. *The Journal of The South African Institute of Mining and Metallurgy,* 101(3), pp. 135-164.

Dunn, M. J., 2013. *Uncertainty in ground support design and implemetation in underground mining. Ground Support 2013: Proceedings of the Seventh International Symposium on Ground Support in Mining and Underground Construction.* Perth, Australian Centre for Geomechanics.

Jager, A. J. & Ryder, J. A., 1999. *A handbook on rock engineering practice for tabular hard rock mines.* Johannesburg: The Safety in Mines Research Advisory Committee (SIMRAC).

Jones, E. & Beck, D., 2017. *The use of three-dimensional laser scanning for deformation monitoring in underground mines: 13th AusIMM Underground Operators' Conference.* Sydney, AusIMM.

Khosa, B., 2021. *Laboratory Testing Report - 75 x 35 - 10cm C-Pack with Mine Pole - BRPM,* Johannesburg: Groundwork Geotechnical Sensing and Consulting.

Khosa, B., 2022. *Laboratory Testing Report - 140 x 18-20cm Mine Poles - BRPM,* Johannesburg: Groundwork Geotechnical Sensing and Consulting.

Le Bron, K., 2015a. *Rock Engineering Analysis of 4m vent holing at BRPM North Shaft 3rd Phase,* Durban: MLB Consulting.

Le Bron, K., 2015b. *Rock Engineering Back Analysis of K-Value at BRPM North Shaft 3rd Phase,* Durban: MLB Consulting.

Lougher, D. R. & Ozbay, M. U., 1995. In-situ measurements of pillar and rockmass behaviour in a moderately deep hard-rock mine. *The Journal of the South African Institute of Mining and Metallurgy,* 74(1), pp. 246 - 249.

Mabitsela, W., 2023. *Laboratory Testing Report - 140 x 18 - 20cm Pencil Props - Rustenburg Section, Sibanye Platinum,* Johannesburg: Groundwork Geotechnical Sensing and Consulting.

Malan, D. F., 2003. *Guidelines for measuring and analysing continuous stope closure behaviour in deep tabular excavations,* Johannesburg: The Safety in Mines Research Advisory Committee (SIMRAC).

Malan, D. F., 2007. *Monitoring of hangingwall stability at BRPM North Shaft,* s.l.: Unpublished internal company document.

Malan, D. F. & Napier, J. A. L., 2011. The design of stable pillars in the Bushveld Complex mines: a problem solved?. *The Journal of The Southern African Institute of Mining and Metallurgy,* Volume 111, pp. 821 - 836.

Malan, D. F. & Napier, J. A. L., 2021. A review of the role of underground measurements in the historical development of rock engineering in South Africa. *The Journal of the Southern African Institute of Mining and Metallurgy,* Volume 121, pp. 201 - 216.

Malan, D. F., Napier, J. A. L. & Janse van Rensburg, A. L., 2007. Stope deformation measurements as a diagnostic measure of rock behaviour: a decade of research. *The Journal of The South African Institute of Mining and Metallurgy,* Volume 107, pp. 743-765.

Ozbay, M. U., Ryder, J. A. & Jager, A. J., 1995. The design of pillar systems as practiced in shallow hard-rock tabular mines in South Africa. *The Journal of The South African Institute of Mining and Metallurgy,* 95(1), pp. 7 - 18.

Pienaar, A., 2017. *The Sub Surface Profiler: a giant leap for ground penetrating radar.* Stellenbosch, Reutech Mining.

Piper, P. S., Malan, D. F., Clements, T. N. & Janse van Rensburg, A. L., 2007. *The real in-situ performance of pre-stressed elongates.* Free State, SANIRE Symposium - Redefining the boundaries II, pp. 15-34.

Roberts, D. P., Roberts, M. K. C., Jager, A. J. & Coetzer, S., 2005. The determination of the residual strength of hard rock crush pillars with a width-to-height ratio of 2:1. *The Journal of The South African Institute of Mining and Metallurgy,* Volume 105, pp. 401 - 408.

Stacey, T. R., 2009. Design - a strategic issue. *The Southern African Institute of Mining and Metallurgy,* Volume 109, pp. 157 - 162.

Swart, A. H., 2005. *Investigation of factors governing the stability of stope panels in hard rock mines in order to define a suitable design methodology for shallow mining operations. MSC Engineering (Mining),* Pretoria: University of Pretoria.

Swart, A. H. & Handley, M. F., 2004. *The design of stable stope panels for near-surface and shallow mining operations. International Platinum Conference ' Platinum Adding Value'*. s.l., The South African Institute of Mining and Metallurgy.

Watson, B. P., 2004. A rock mass rating system for evaluating stope stability on the Bushveld Platinum mines. *The Journal of The South African Institute of Mining and Metallurgy,* 104(4), pp. 229 - 238.

Watson, B. P., Kuijpers, J. S. & Stacey, T. R., 2010. Design of Merensky Reef crush pillars. *The Journal of The Southern African Institute of Mining and Metallurgy,* Volume 110, pp. 581 - 591.

York, G., Canbulat, I., Kabeya, K. K., Le Bron, K., Watson, B. P. &Williams, S. B., 1998. *Develop guidelines for the design of pillar systens for shallow and intermediate depth, tabular, hard rock mines and provide a methodology for assessing hangingwall stability and support requirements for the panels between pillars. SIMRAC Report GAP 334,* Pretoria: CSIR Mining Technology.



Trevor Walsh

Shaft Rock Engineer
Impala Bafokeng Platinum

My career started with a bursary from Anglo American Platinum, I was a graduate at Northam in 2010 where I passed my Strata Control Ticket. I then moved to Rustenburg where I worked as an SCO at Bathopele mechanised mine before joining the team at Thembelani Mine. Whilst at Thembelani in 2012, I passed my Rock Engineering Certificate and was promoted to Shaft Rock Engineer. In 2015 I moved to Royal Bafokeng Platinum, I started my studies at Wits University in 2019 and achieved my Advanced Rock Engineering Certificate in 2022 and my Masters in Rock Engineering in 2024.

A proposed method of pre-mining rib pillars and replacing pillars using a cemented aggregate fill

R.M. Arlow[1], I. Malpartida[2], J. Nyagumbo[2]

[1]Dayenu, South Africa
[2]Alphamin Resources, South Africa

The mine is progressing into deeper regions to access a high-grade tin deposit, unfortunately, due to the mining method, substantial ore remains locked in rib pillars required for stability. An investigation into the removal of the rib pillars was undertaken where replacing rib pillars with cemented backfill is considered. The study assessed 'jig tails' a tailings material, consisting of mica schist and amphibolite materials, as a backfill medium.

Initial testing demonstrated high strengths (12.65 MPa to 27.4 MPa) but revealed that cement content exceeding 20% would be economically unviable. Modified mix ratios (1:3:6, 1:2.25:9 and 1:3:8) with reduced cement content (8%–10%) targeted UCS values between 3 MPa and 10 MPa, aligning with operations of similar approaches. Empirical design methods were used to estimate the backfill strength. A conservative design strength of 32 MPa, was eventually suggested.

Trial mining is planned where it is suggested that cored samples of the backfill from the trial mining site be taken. These samples will undergo further testing, and results will inform discrete element or finite different codes to validate design parameters for deeper mining areas.

INTRODUCTION

Alphamin Resources owns and operates the Bisie Mine in North Kivu, Democratic Republic of Cong. Located approximately 180 km northwest of Goma, the Bisie Mine is one of the World's richest tin producers and accounts for 4% of global tin production (International Tin Association Industry Review, 2022). The mine was established in 2014, with development of Mpama North commencing in 2018, followed by the commissioning of the Mpama South operation in 2022.

Tin ore is extracted using the long hole open stoping method, with stopes backfilled using waste rock fill. Rib pillars are utilised to divide stoping blocks, and sill pillars are used to separate the main levels, referred to as 'echelons.;

Recent exploration has intersected high-grade tin mineralisation at depth within Mpama North, prompting a review of the existing pillar system. The current design limits ore extraction, thus shortening the mine's operational life. As an alternative, a pillar-less system is being investigated, where the existing pillars would be pre-mined and replaced with a cemented aggregate fill made from tailings material 'jig tails' mixed with cement and sand.

A critical consideration in this study is the behaviour of the cemented fill, both during placement and following adjacent stoping activities, including the impact of waste placement on its stability.

BACKGROUND

Geological setting

The Bisie tin deposit is hosted within a N-S trending, steeply east-dipping shear zone in mica schist. Tin mineralisation occurs as botryoidal cassiterite veins, ranging from millimetre to over a metre in thickness. These veins are boudinaged, brecciated, and folded, indicating deformation during and after mineralisation.

The host rock is altered, with chlorite replacing feldspar due to hydrothermal fluid interaction. The mineral assemblage includes muscovite, quartz, and minor amphiboles, but lacks tourmaline and fluorite, suggesting a distal tin source. Tin precipitated from low-pH, high-salinity fluids below 230°C, likely due to fluid mixing and cooling.

The deposit is segmented by NW-SE faults, separating the Mpama North and South ore bodies. Late-stage faulting influenced quartz veining and localised sulfide precipitation, including pyrite, arsenopyrite, chalcopyrite, sphalerite, and galena.

Bisie represents a shear-hosted, structurally controlled tin deposit, with mineralisation influenced by syn-tectonic deformation and late-stage faulting. Shear structures generally define the contacts of the mineralised zones which have weak chlorite infilling and a range of thicknesses.

Mining layout and pre-mining of pillars

The Mpama North orebody has a limited regional strike extent, ranging from 552 m at its shallowest point to 182 m at its deepest point. The orebody generally dips at an average of 70°s, with strike spans between rib pillars varying from 15 m to 45 m, depending on ground conditions and stability factors. Mining depths range from 100 metres below surface (mbs) and will be extending beyond 500 mbs.

The mining layout consists of primary footwall drives, with a ramp system providing access to all sublevels. Each echelon includes five sublevels, with sill pillars spaced approximately 74 m skin-to-skin. From the footwall development, crosscuts are driven to intersect the orebody, with ore drives positioned along the hangingwall contact. This approach facilitates sliping while minimising exposure to the weak hangingwall shear contact.

Figure 1 illustrates a typical stope design, including the planned placement of rib pillars, while Figure 2 presents a cross-section of an echelon showing the ore drives and slipped stopes used to create the undercut.

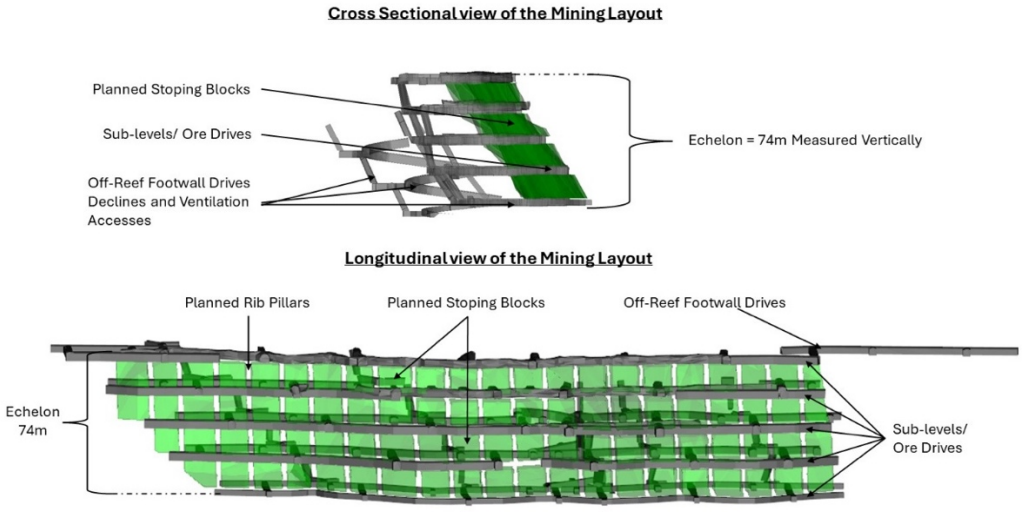


Figure 1. Typical echelon layout implemented at Mpama North.

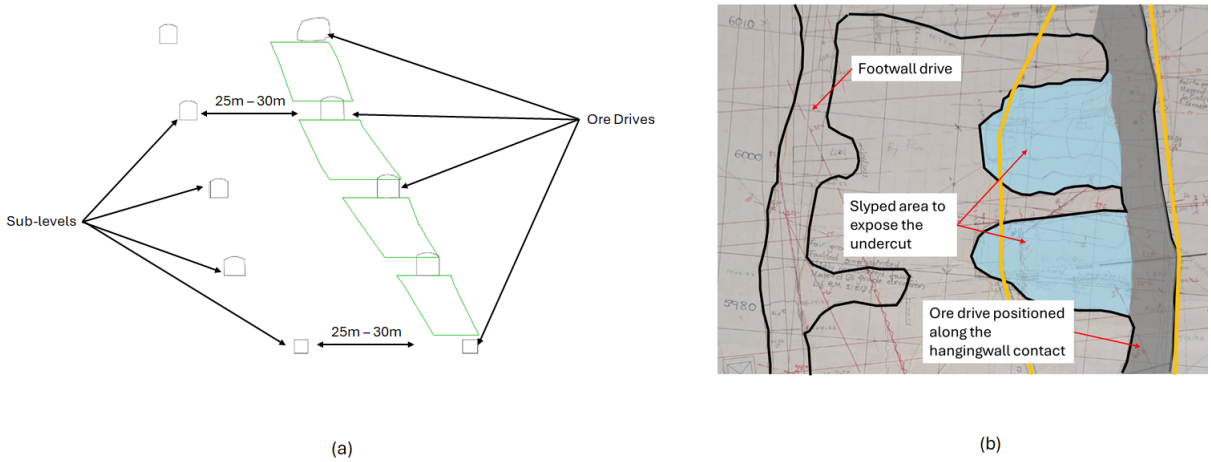


Figure 2: a) Typical cross-section of an echelon showing the footwall excavations and position of the ore drives. b) Stope plans showing the reef contact, sliped area (light blue) and the original position of the ore drives (light grey).

TESTING OF CEMENTED AGGREGATE FILL

Testing program and results

Before conducting any backfill design and backfill exposure assessments, it was essential to evaluate the backfill strengths achievable with the available materials on-site. As is well known, mica schist can reduce the strength of concrete over time by up to 28%. To assess this impact, testing was conducted on mica schist and amphibolite/mica schist tailings material, commonly referred to as 'jig tails'. The particle size distribution of the tailing material is generally uniform, ranging from 19 mm down to 75 µm. Various mix ratios were evaluated, and Table I outlines the range of ratios tested.

Table I: Range of mixing ratios tested and cement content

Material type	Tests	Cement: Sand: Aggregate ratio	Percentage cement content
Jig Tails	1	1:0:2.52	28%
Jig Tails	2	1:0:2.52	28%
Jig Tails	3	1:0:3.26	23%
Jig Tails	4	1:0.5:2.52	25%
Jig Tails	5	1:0.7:2.77	22%
Mica Schist	6	1:0:2.11	32%
Mica Schist	7	1:0:2.73	27%
Jig Tails	8	1:2.25:9	8%
Jig Tails	9	1:3:6	10%
Jig Tails	10	1:3:8	8%

The initial objective of achieving 75% of the host rock strength was based on a practical assumption: the host rock had an average uniaxial compressive strength (UCS) of approximately 47 MPa, and it was considered feasible to produce a cemented aggregate backfill with strengths ranging between 30 MPa and 35 MPa using a high cement content. This target was not derived from numerical modelling or detailed stability analysis, but rather from initial material testing and practical expectations of what could be achieved in a controlled setting.

While these strengths were successfully achieved during laboratory trials, the high cement content required rendered this approach economically unfeasible for large-scale application. Consequently, a lower strength target was considered, guided by the work of Sainsbury (2014) on the Ballarat Gold Project. In that study, through a combination of numerical modelling and empirical testing, backfill strengths ranging from 620 kPa to 1 420 kPa were shown to be sufficient for the replacement of pillars with cemented rock fill under similar operational conditions. This provided a more realistic and cost-effective design target for backfill strength, aligning technical performance with economic viability. Three mix ratios were tested:

- 1:3:6 - yielding a 28-day strength of 3.4 MPa
- 1:2.25:9 - yielding 4.2 MPa
- 1:3:8 - yielding 6.4 MPa

Notably, these strengths are significantly higher than those ultimately proposed for the Ballarat Gold Project, reinforcing confidence in the stand-up capabilities of the lower mix ratios. However, the free-standing stability of the backfill required further evaluation, which is discussed in subsequent sections of this report. Figure 3 below provides the uniaxial strengths achieved throughout the testing phase.

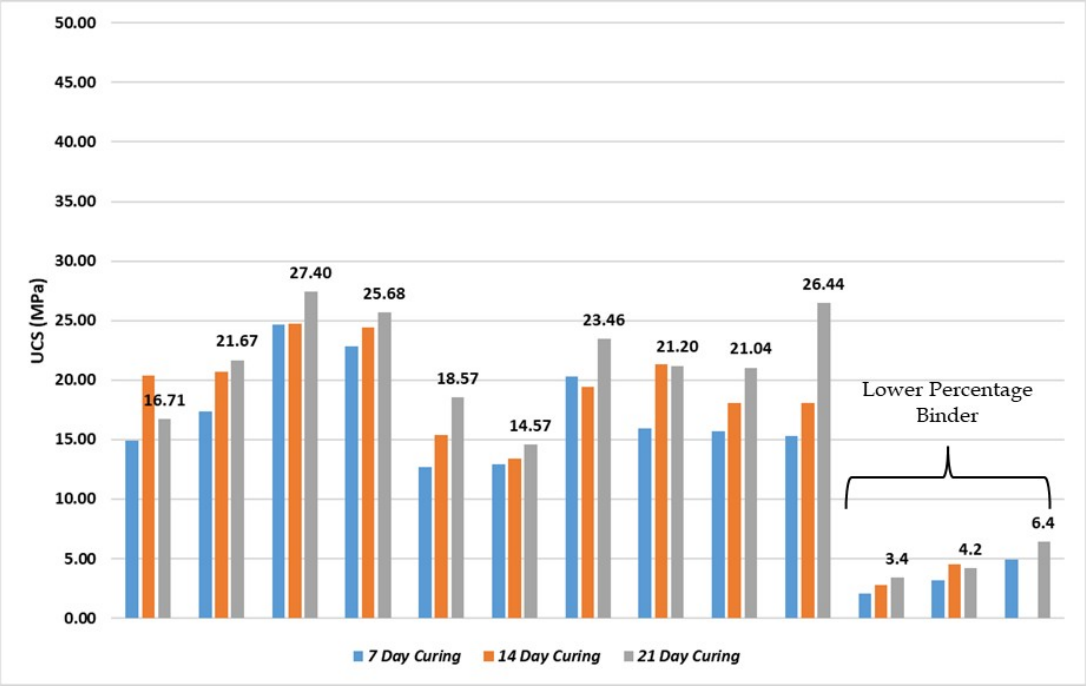


Figure 3. Uniaxial strength estimates based on various cement: sand: aggregate ratios.

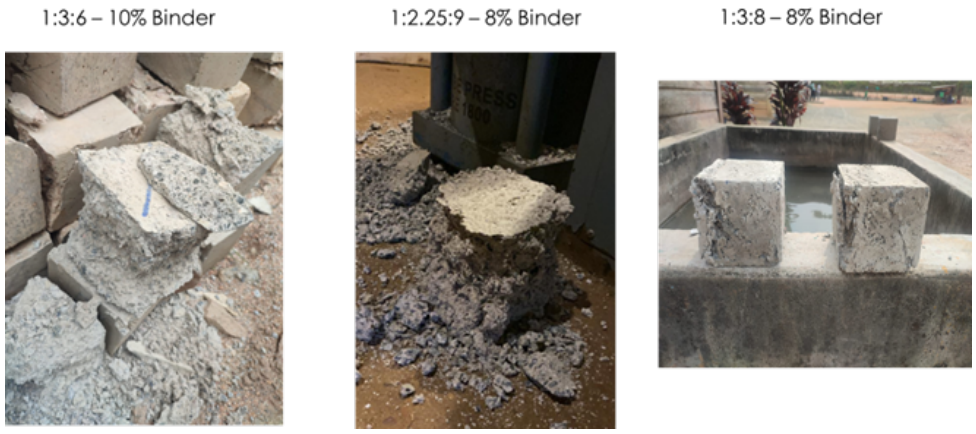


Figure 1. Tested samples after 28 days for various lower-range mix ratios.

No elastic components could be validated, however, and since modelling the behaviour of the cemented rib pillar requires these parameters, an alternative approach was considered. Through personal communication with Patterson and Cooke on tests completed on a cemented aggregate type-fill, the following formula was used to estimate Young's Modulus.

$$E = 150 \times UCS \qquad [1]$$

Where E is the Youngs Modulus (MPa) and UCS (MPa) is the uniaxial compressive strength of the tested sample.

A fixed Poisson ratio (0.25) and friction angle (44°) were assumed, and using Mohr's theory, the cohesion was calculated. While it is acknowledged that this method may not fully represent the tested samples and requires further validation, it provides a first-pass assessment of the relevant elastic parameters. The ratio between Young's modulus and UCS will differ from the materials used, hence actual triaxial strength (TCS) and UCS tests are required. Notably when the backfill is placed, it may result in the layering of weak and strong materials, which will influence the effective strength and stiffness of the fill.

PRE-MINING THE RIB PILLARS

To fully realise the effect of the cemented pillars, it is necessary to pre-mine the pillar and then backfill it with cemented fill. Removing these pillars after the stope block has been mined will be challenging, as the stope blocks will be filled with waste, which could collapse during blasting and development activities. The layout is presented in Figure 6 below. The following outlines the pre-mining sequence for the pre-removal of the pillar:

- During the development of the ore drive, a 'pillar cross-cut' will be created at the location of the planned rib pillar.
- The dimensions of the pillar cross-cut will match the width of the pillar to be backfilled.
- The minimum width that can be created is no less than 4.5m, due to machine and equipment constraint.
- Once the cross-cut is established on both the upper and lower levels, drilling will commence, and a slot will be blasted in the pillar.
- After the blasted ore in slot is removed, the remaining long holes will be charged, and the entire pillar will be blasted.
- Following the removal of the ore, shuttering will be installed in a manner that ensures the ore drive remains open.
- During the construction of the shuttering, a sump mixing chamber will be developed, capable of accommodating up to six pillars. This chamber will only need to be developed once.

- The materials required for the pillars will be transported to the sump mixing chamber according to the mixing ratios.
- Mixing will be carried out using loaders and will be directly delivered into the mined block.
- The fill must cure for a minimum of 28 days before adjacent stope blocks can be mined.

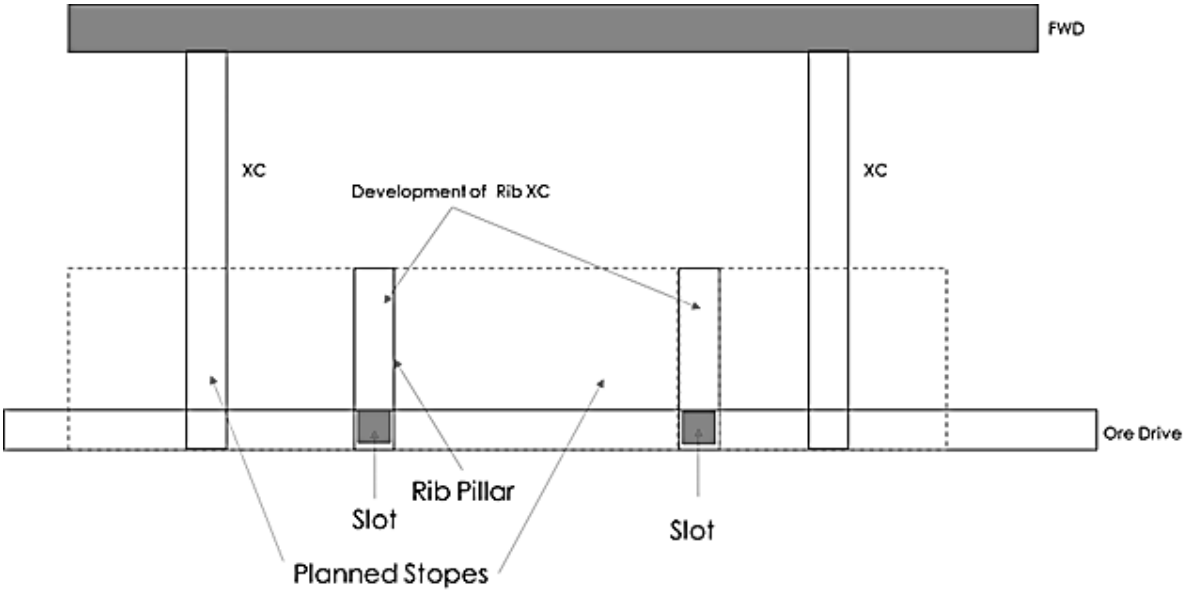


Figure 5. Suggested mining layout (plan view) to excavate the pillar before backfilling.

NUMERICAL MODELLING OF PILLAR STRENGTHS

Model Construction

At the time of compiling this paper, access to distinct element and finite difference codes was not available. Consequently, finite element codes were used to assess the deformations of the backfilled rib pillars considering the fill strength and rib pillar widths.

Rocscience's RS3 software was employed to simulate the planned development and stoping sequence. Figure 6 illustrates the mining steps modelled in RS3. The material properties of the host rock were derived from historical studies at the mine, while the fill strength and stiffness varied based on UCS tests, as presented in Table II.

The planned pillar widths varied between 3.5 m and 6.5 m. The UCS values tested in the models were 0.5 MPa, 2 MPa, and 4 MPa. The mining depth was maintained at 300 mbs, and a maximum ore body width of 10 m was considered.

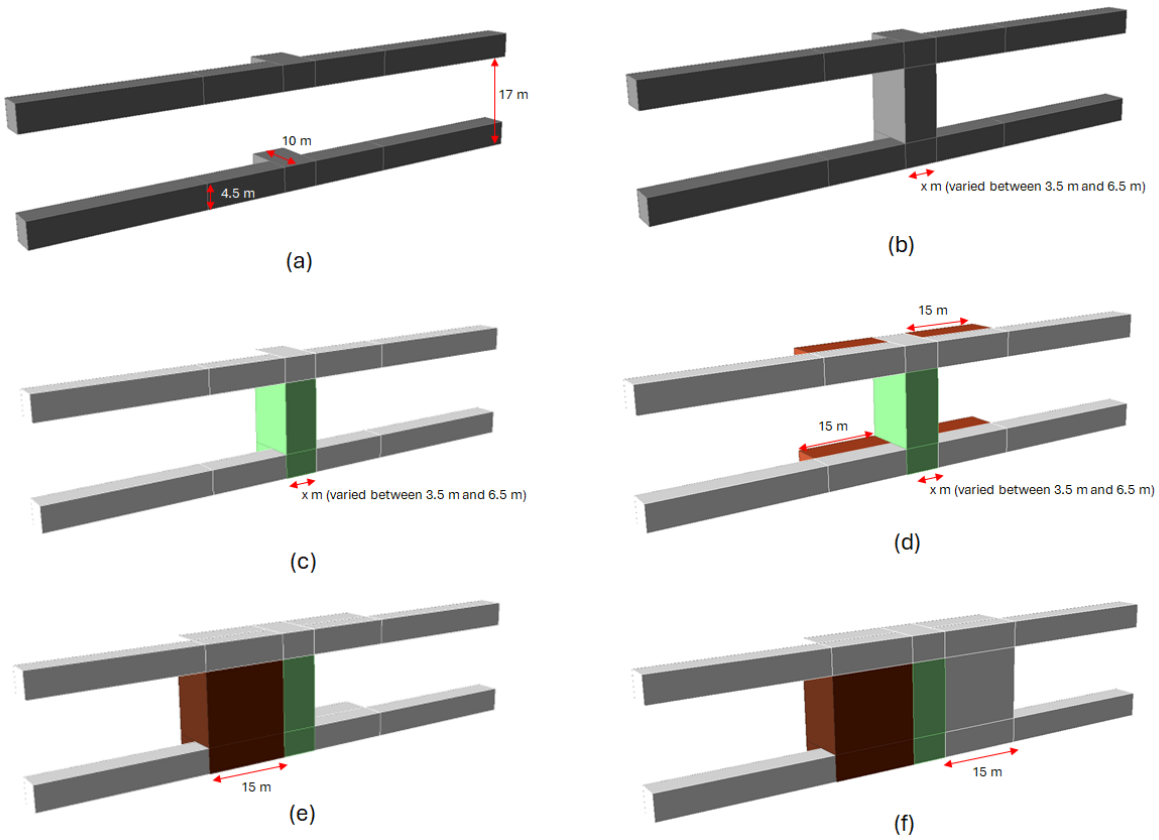


Figure 6: a) Ore drives and pillar drives which are pre-developed. b) Pillar mined to full height. c) Pillar filled with cemented fill. d) Slyping of the stop blocks to their required widths adjacent to the filled pillar. e) Stoping block mined and filled in separate mining steps adjacent to the pillar. f) Second stoping block mined.

Table II: Material properties applied in the model

Material type	UCS (MPa)	Density (kg/m³)	GSI	Youngs modulus (MPa)	Bulk modulus (MPa)	Shear modulus (MPa)	Poisson ratio	Hoek-Brown parameters				Mohr-Coulomb parameters	
								mi	mb	s	a	Cohesion (MPa)	Friction angle (°)
Amphibolite schist	66.9	3040	70	39700	44100	14700	0.35	5	0.97	0.013	0.5	1.80	37.00
Mica Schist	47.3	2820	65	28100	29200	10500	0.34	2.6	0.39	0.007	0.5	1.00	29.00
Waste Backfill	-	2100	-	100	670	400	0.25	-	-	-	-	0.05	30.00
Cemented Fill	0.5	2430	-	75	50	30	0.25	-	-	-	-	0.11	44.00
	2	2430	-	300	200	120	0.25	-	-	-	-	0.43	44.00
	4	2430	-	600	400	240	0.25	-	-	-	-	0.85	44.00

Model Analysis and Results

The numerical analysis conducted at this stage of the study aimed to assess the impact of mining and waste fill, once placed, on the horizontal displacement of the cemented pillar. When analysing the horizontal displacements, increased deformations were observed in the middle of the cemented pillar, resembling the behaviour typically seen in retaining walls (Figure 7).

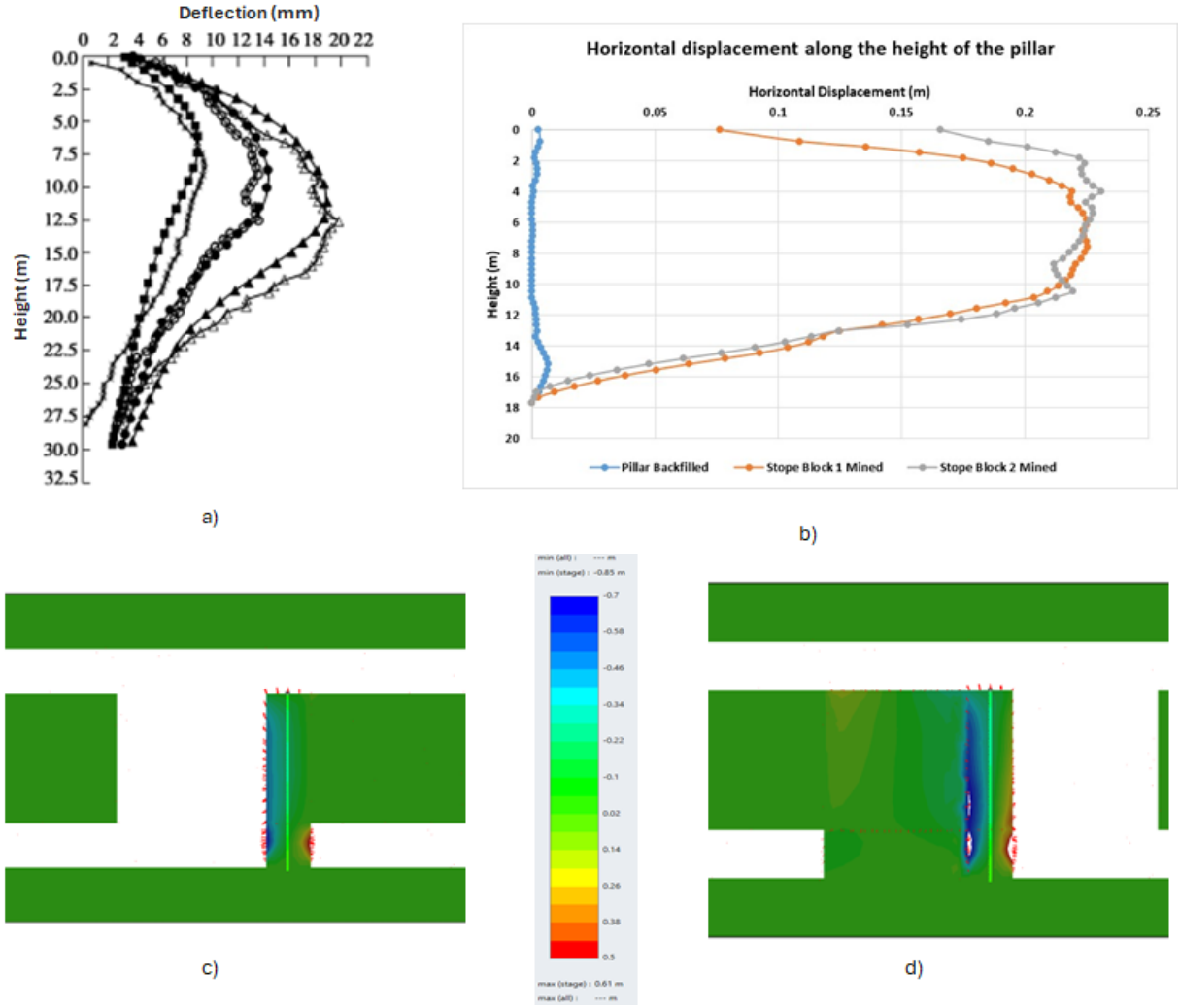


Figure 7: a) Deflection related to retaining wall height (Qiao & Ding, 2012). b) Horizontal displacement of a 4.5 m wide 0.5 MPa cemented fill pillar c) Model outputs showing the horizontal deformation once the adjacent stoping block has been mined next to the cemented pillar. d) Model outputs showing the horizontal deformation once the second stope block is mined and waste fill placed within the first stoping block.

When comparing the horizontal displacements for a 4.5 m wide rib across all assessed fill strengths after the second stoping block is mined (as shown in Figure 8), it is evident that lower strength fills (notably less stiff material) exhibit significantly higher displacements—up to 23 cm for the 0.5 MPa fill—compared to just 3 cm for the 2 MPa fill. Despite the variation in magnitude, horizontal movement is observed in all cases, whether minor or severe. In contrast, the intact pillar and the fill simulating 75% of the intact rock strength (exhibiting a high stiffness) showed negligible displacements, less than 1 mm.

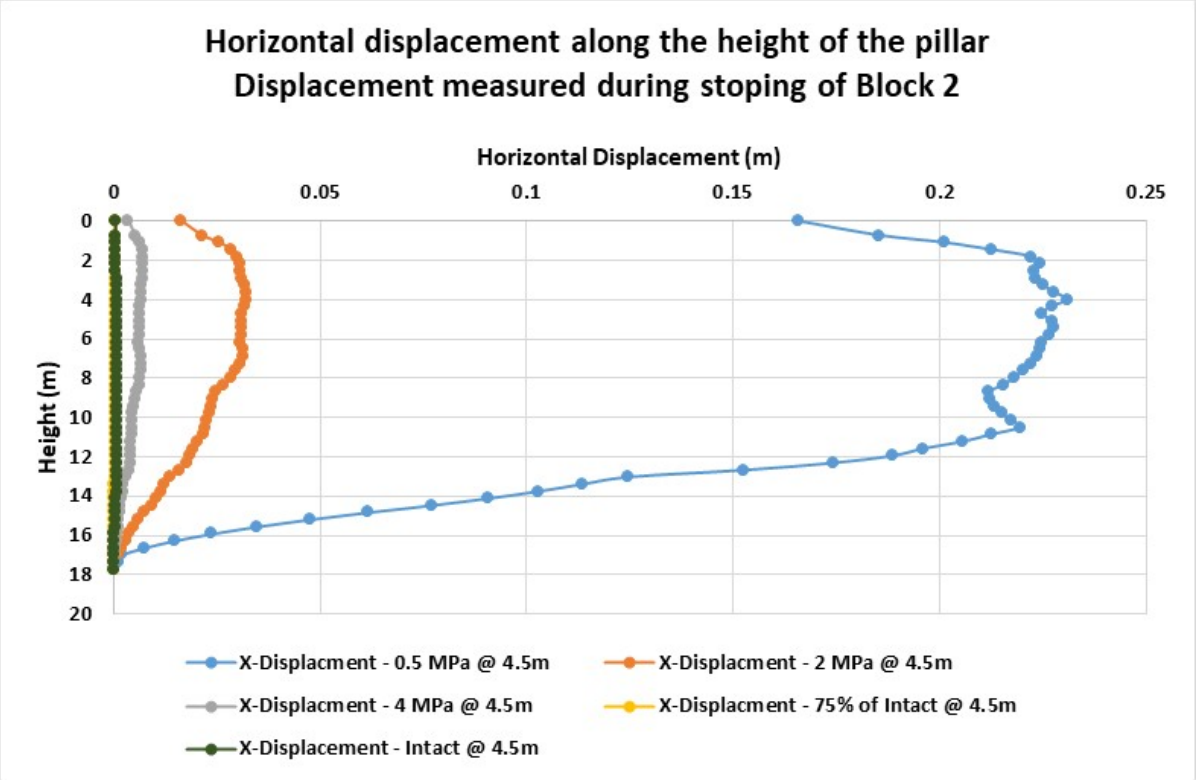


Figure 8. Horizontal displacement measured along the height of the pillar once stoping block 32 has been mined – results represent all material strengths assessed and fixed a 4.5 m rib pillar width.

The maximum horizontal displacements (Figure 9) were compared across various pillar widths, ranging from 3.5 m to 6.5 m. The results indicated that wider backfilled ribs experienced less displacement (although marginal), even when the fill strength was lower (less stiffness). However, increased fill strength within the wider rib pillars did not notably reduce deformation, suggesting that the wider ribs are not so sensitive to the fill strength and stiffness.

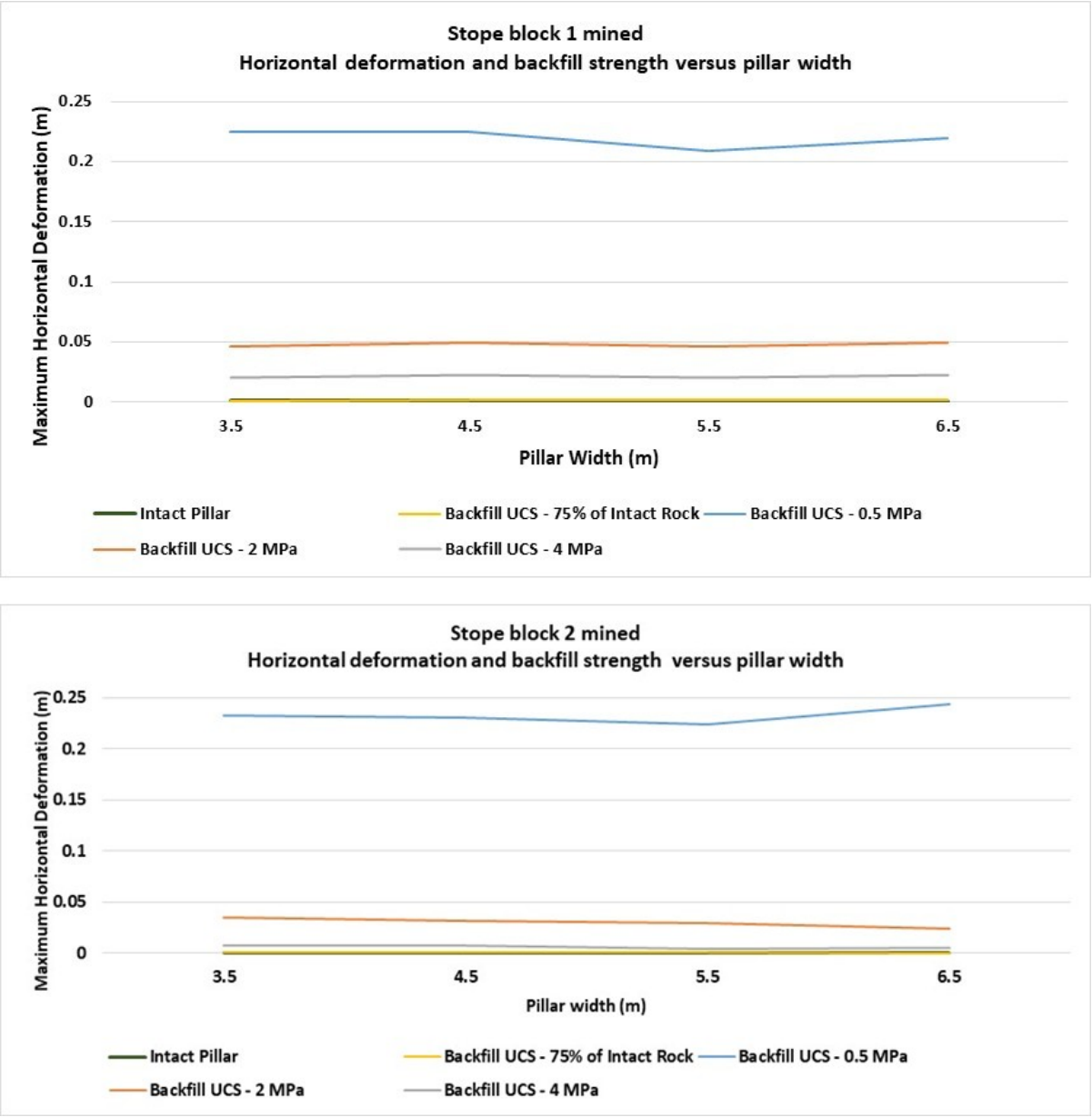


Figure 9: Maximum horizontal deformation for each pillar assessed at various widths once the adjacent mining blocks are excavated.

Notably, during the mining of the second block, while the first stoping block is already filled, the increase in deformation remains marginal (Figure 11) – stiffness is consistent throughout the width and UCS range.

The current model and model package do not provide sufficient results to fully quantify this behaviour. Therefore, further analysis using alternative numerical modelling codes, such as UDEC and FLAC, is necessary to better understand the displacement and overall behaviour of the cemented pillar. It does however provide an insight into the backfill strength (or in this instance the stiffness of the fill) and associated impact on expected deformations.

BACKFILL FREE-STANDING CAPABILITIES: A STRENGTH COMPARISON

Empirical formulae were considered to determine the appropriate strength for the cemented backfilled pillars, based on published work in journal papers and conference proceedings. For example, Askew *et al*. (1987) proposed a strength requirement based on the width-to-height ratio and exposure conditions of cemented backfill, highlighting that single-sided exposures require less strength than double-sided exposures. Mitchell *et al*., (1982) provided guidance on fill stability under different confinement conditions, noting the importance of arching effects in narrow excavations. Belem and Benzaazoua (2004) developed strength classification schemes based on laboratory testing of cemented paste backfill, which helped correlate UCS requirements with fill geometry. Abdelhadi *et al*., (2018) presented an empirical design chart for cemented rockfill pillars, linking UCS requirements to the pillar's width-to-height ratio and expected stress environment, with particular attention to cut-and-fill applications. These studies collectively informed the selection of strength targets relevant to the current rib pillar configuration, which involves narrow exposure faces and low-confinement conditions.

The analysis indicated that backfill strengths ranging from 200 kPa to 1000 kPa may be required to ensure stability. However, when evaluating the modelled deformation and failure modes it was interpreted that a UCS greater than 2 MPa would be required to fully prevent pillar failure under worst-case conditions. To provide context and substantiate this interpretation, the behaviour of backfill pillars was compared to that of an intact in-situ pillar under identical loading conditions. The intact pillar exhibited negligible deformation (<1.5 mm). Similarly, when backfill strength was set to 75% of the intact strength, deformations remained low (<2 mm). In contrast, a backfill with a UCS of 2 MPa—roughly ~4% of the intact rock strength—exhibited horizontal displacements of just under 3 cm for a 4.5 m wide pillar.

Based on these findings, a backfill strength of 2 MPa is recommended for the proof-of-concept trial mining section. This higher strength accounts for the assumptions made regarding friction angle, cohesion, and elastic properties. The trial phase should also be used to validate practical considerations such as material segregation, layering, resistance to horizontal deformation, and stand-up time.

For comparison, Sainsbury and Sainsbury (2014) recommended a maximum backfill strength of 120 kPa for pillar replacement at the Ballarat Gold Project, based on 3D numerical modelling. Table III provides a comparison of the parameters used at the Ballarat mine to that utilised and tested at Alphamin's Bisie Mine and generally shows that the backfill tested at Bisie mine is higher in modulus and has a higher ultimate strength. It must be noted that the geological setting at Ballarat involves narrower, flatter-dipping ore bodies. Despite the lower design strength suggested by the modelling at the Ballarat mine, laboratory tests on backfill samples at Ballarat exceeded 1000 kPa after just seven days of curing. This suggests that the required backfill strength at Mpama North, Bisie Mine, may ultimately be lower than 2 MPa, reinforcing the opportunity for optimisation during detailed design.

Table III: Material property comparisons of Ballarat Gold Mine and Bisie Mine

Operation	Ballarat Gold Mine	Bisie Mine
Host Material	Sandstone/Siltstone and Quartz	Amphibolite and Mica Schist
Backfill type	Cemented Rock Fill	Cemented Aggregate Fill
Maximum Size of Particles	200-400mm	19mm
Depth Range	670mbs	600mbs
Orebody Dip	40-60 degrees	60-70 degrees
Backfill Cement Content	3% to 5%	8% to 10%
Tested Backfill Young's Modulus Range	44 MPa to 274 MPa	75 MPa to 600 MPa
Tested Backfill UCS	881 kPa to 4190 kPa	3200 kPa to 6200 kPa

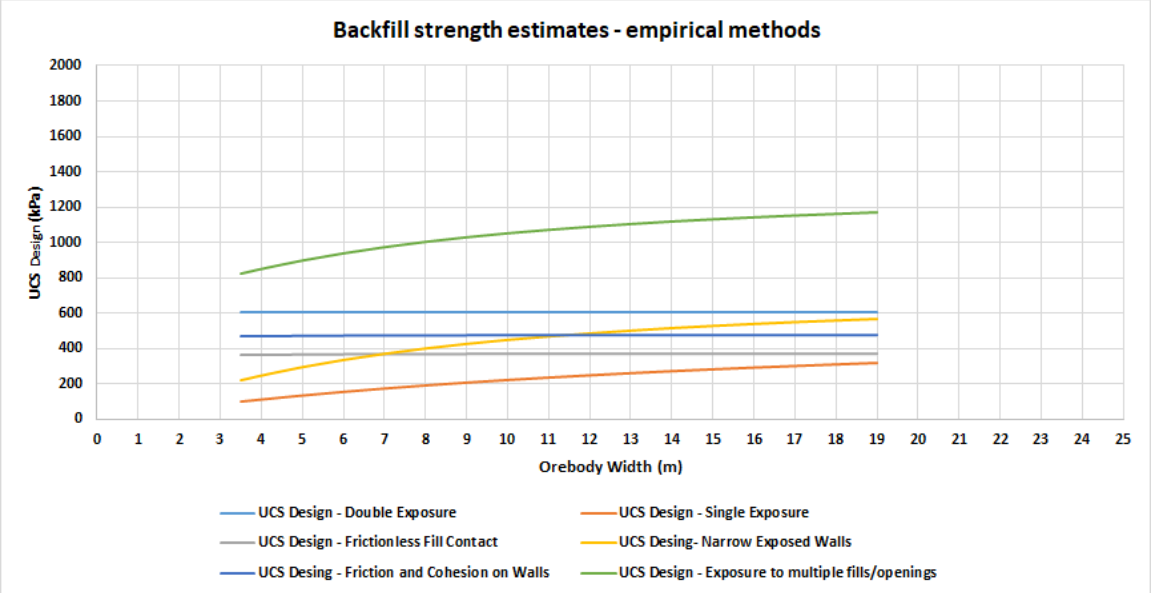


Figure 10: Backfill UCS design strengths based on various methods/formulae used in the industry.

CONCLUSIONS

Pillarless mining is being evaluated for high-grade zones at Alphamin Resources' Mpama North Shaft, Bisie Mine. The concept involves pre-mining rib pillars using existing development infrastructure, followed by replacement with a cemented aggregate-type backfill.

Laboratory tests show that high cement mix ratios can yield strengths exceeding 25 MPa, while lower ratios result in UCS values between 2.4 MPa and 6 MPa. However, the lower-strength mixes exhibited signs of segregation and poor inherent bonding. A 1:3:8 (cement:sand:aggregate) mix ratio, representing approximately 8% binder content, was found to be more consistent and practical for use.

Estimates of elastic properties were applied in the finite element modelling to assess fill performance. Results indicate that displacements were significantly larger for backfill with a lower stiffness (UCS of 500 kPa), while backfill material of higher stiffness (UCS of 2 MPa) resulted in minimal to negligible deformation. The results indicated that wider backfilled ribs experienced less displacement (although marginal), even when the fill stiffness was lower. However, increased fill strength within the wider rib pillars did not notably reduce deformation, suggesting that the wider ribs are not so sensitive to the fill strength.

The modelling incorporated assumptions for friction angle, Poisson's ratio, Young's modulus, and cohesion. Based on these findings and supporting empirical studies, it is recommended to proceed with a trial mining phase using a target backfill strength of 2 MPa.

These modelled results were compared to empirical backfill strength formulae used in pillar recovery. For an orebody height of 10 m and pillar width of 4.5 m, industry-based estimates suggest that UCS requirements should not exceed 1200 kPa.

The following elements are recommended for implementation during the trial mining phase:

- Installation of multi-point borehole extensometers to monitor deformation within both the fill and the surrounding host rock, which will provide input for model calibration and validation.
- Core sampling of placed backfill to assess segregation and layering, particularly in light of the 17 m fall height from upper levels.

- Laboratory testing to confirm the elastic and strength properties of the fill, including UCS, TCS, and tensile strength testing.
- Water management during fill placement, as excess moisture, may reduce backfill performance and long-term strength.
- Advanced numerical modelling using distinct element and finite difference methods (e.g., UDEC, FLAC) to better understand the interaction between the fill, excavation geometry, and host rock conditions.

Initial findings highlight the potential for optimisation in the fill design, which could lead to improved mine economics through enhanced ore recovery, reduced dilution, and better long-term ground control. If successful, this approach may significantly extend the life-of-mine while reducing the need for in-situ pillars.

ACKNOWLEDGEMENTS

The permission of Alphamin Resources as well as Dayenu Mining Consultants, along with the contributions of individuals (Mr. Brian Harbert (Mine Manager) and the mining team, Mr. Noble Chifwaila (Chief Rock Engineer) and the geotechnical team at Bisie Mine who assisted in conducting the backfill strengths, is gratefully acknowledged.

REFERENCES

Abdelhadi, K., Latifa, O., Lahcen, B., & Khadija, B. (2018). Underground Cemented Backfill, a Design Procedure for an Integrated Mining Waste Management. *MATEC Web of Conferences*, (pp. 1-6).

Askew, J., McCarthy, P., & Fitzerald, D. (1987). Backfill research for pillar extraction at ZC/NBHC. *Canadian Rock Mechanics Symposium*, (pp. 100-110).

Belem, T., & Benzaazoua, M. (2004). An overview on the use of paste backfill technology as a ground support method in cut-and-fill mines. *Symposium on ground support in mining and underground construction.* (pp. 637-650). Perth, Western Australia: Tayler & Francis Group.

de Vries, R., Hassel, R., & Player, R. (2015). Geotechnical design considerations for Dugald River — from slot to sequence. (pp. 167-184). Perth: Australian Centre for Geomechanics,.

Mitchell, R., Olsen, R., & Smith, J. (1982). Model studies on cemented tailings used in mine backfill. *Canadian Geotechnical Journal*, 14-28.

Porathur, J., Sekhar, S., Godugu, A., & Bhargava, S. (2022). Stability analysis of a free-standing backfill wall and a predictive equation for estimating the required strength of a backfill material – a numerical modelling approach. *Southern African Institute of Mining and Metallurgy*, 227-233.

Qiao, Y., & Ding, W. (2012). Deformation characteristics of deep excavations for metro stations in Wuxi. *Chinese Journal of Geotechnical Engineering*, 761-766.

Sainsbury, D., & Sainsbury, B. (2014). Design and implementation of cemented rockfill at the Ballarat Gold Project. (pp. 1-15). Perth: Australian Centre for Geomechanics.

Salvoldi, B. (2024). Estimation of Young's Modulus from UCS sampled data; Personal Communication.

Stone, D. (1993). The optimization of mix design for cemented rockfill. *Proceedings Minefill* (pp. 249-243). Johannesburg: Southern African Institute of Mining and Metallurgy.



Ronny Martin Arlow

Rock Engineering Manager
Dayenu Mining Consultants

My mining career began in 2006 when I joined Anglo American as a Learner Miner. During this time, I obtained my blasting certificate and developed foundational mining skills, progressing from PTV to Stope Drilling Operator. In 2008, I enrolled as a Learner Official and gained exposure to all technical departments. My Rock Engineering career commenced in the same year when I took on the role of Strata Control Observer, eventually advancing to Rock Engineer. I continued as an Operations Rock Engineer until 2013 when I transitioned into consulting.

I was appointed as a Consulting Rock Engineer, where I honed my expertise in project management, geotechnical engineering, geotechnical logging, feasibility studies, numerical modeling, and geotechnical reviews. I was subsequently promoted to Senior Rock Engineer and then to Rock Engineering Manager. My career has spanned 18 years, with 7 years in mining and 11 years in consulting, during which I have gained experience in both local South African mining operations and international massive and surface mining methods.

Performance and mechanical properties of a styrene-free polyester resin produced with water-based catalyst and a new generation catalyst

G. Smolnik[1,2], R. Penczek[1], J. Franek[1], D. Bucholc[1]

[1]Sandvik Ground Support, Poland
[2]Silesian University of Technology, Poland

Due to increased knowledge about styrene safety, health, and its environmental impact (especially its effects on humans) a new generation of styrene-free resin cartridges has been recently created. It has been shown that the new styrene-free resin cartridges produced with the so-called oil-based catalyst have superb mechanical parameters. Their compressive strength, stiffness and low creep strain are superior in comparison with standard polyester resin capsules.

As the majority of the resin capsules used in hard rock mines worldwide use the so-called water-based catalyst, the next step in the creation of the new generation of the styrene-free resin cartridges has been made by using a water-based catalyst in their production as well as the development of a novel, new-generation type catalyst.

In this paper we discuss characteristics and performance of these new types of a styrene-free resin. Not only the standard testing results (uniaxial compressive strength, Young's modulus, creep and shear strength) are presented but the procedure of a special push-out test to confirm the effectiveness of the anchoring along the bolt is described. The results of pushing ca. 15 cm cut sections of the bolt embedded in a high strength concrete in a steel pipe are presented as well. The first results of impact (dynamic) loading of Versa bolts embedded in the steel pipes with the styrene-free resin conclude the paper.

INTRODUCTION

Styrene is a key ingredient in polyester resin capsules, commonly used in mining rock bolting applications. Over the last two decades, there has been an increase in research and associated medical knowledge regarding styrene safety, particularly its health impacts upon people. For example, the issue of carcinogenicity and harmful effects on fertility and unborn children has been identified (Vineis and Zeise, 2002; Huff and Infante, 2011). Due to these health concerns, the use of styrene-based resin products in civil construction projects has since been banned in Europe (European Union, 2014). This scenario has further raised safety concerns within resin cartridge production facilities, as well as in the handling and usage of cartridge resin at the end customer's site.

Recent development of styrene-free polyester resin cartridges may become a breakthrough technology for health and safety of miners, with increased mechanical properties and performance of the resin at the same time.

Although the creation of new, safe styrene-free resin cartridges has recently been achieved, the work on the bases for the shift from potentially harmful styrene-based cartridges to styrene-free resin has not been completed.

The first representatives of a new generation of styrene-free resin cartridges were produced with the so-called oil-based catalyst and their superb mechanical parameters have been confirmed (Smolnik *et al.*, 2024, Evans *et al.*, 2025). Their compressive strength, stiffness and low creep strain are superior in comparison with standard polyester resin capsules.

But since the majority of resin capsules used in hard rock mines worldwide use the so-called water-based catalyst our focus was on the creation of the strong, robust yet cheaper version of styrene-free resin cartridges using a water-based type of catalyst. Research during that endeavour was successful – a water-based type of catalyst for the styrene-free resin cartridges was developed but also a completely new generation type of catalyst: emulsified peroxide catalyst (EPC) for the styrene-free resins was created.

After extensive studies performed in the laboratory, both products have been developed and their properties and performance are presented and discussed in this paper.

MECHANICAL TESTING OF THE PROPERTIES OF A STYRENE-FREE POLYESTER RESIN PRODUCED WITH WATER-BASED AND A NEW GENERATION (EPC) TYPE OF CATALYST

In order to enable the comparison of the results and behaviour of the different types of a new styrene-free versions of resin capsules, as well as the existing styrene-based resin cartridges, the results of the laboratory experiments presented were obtained following the requirements of British Standard (2007). These requirements are for strata reinforcement support system components that were used in British coal mines. In general, the requirements of this standard for resin cartridges are more stringent than those that meet local industry standards.

Examples of resin characteristics in uniaxial compression for a basic version of styrene resin cartridges (water-based catalyst) are presented in Figure 1. Typical normal stress – vertical strain curves for styrene- free resin cartridges produced with water-based catalyst are given in Figure 2 and those curves for styrene-free resins created with EPC catalyst are shown in Figure 3.

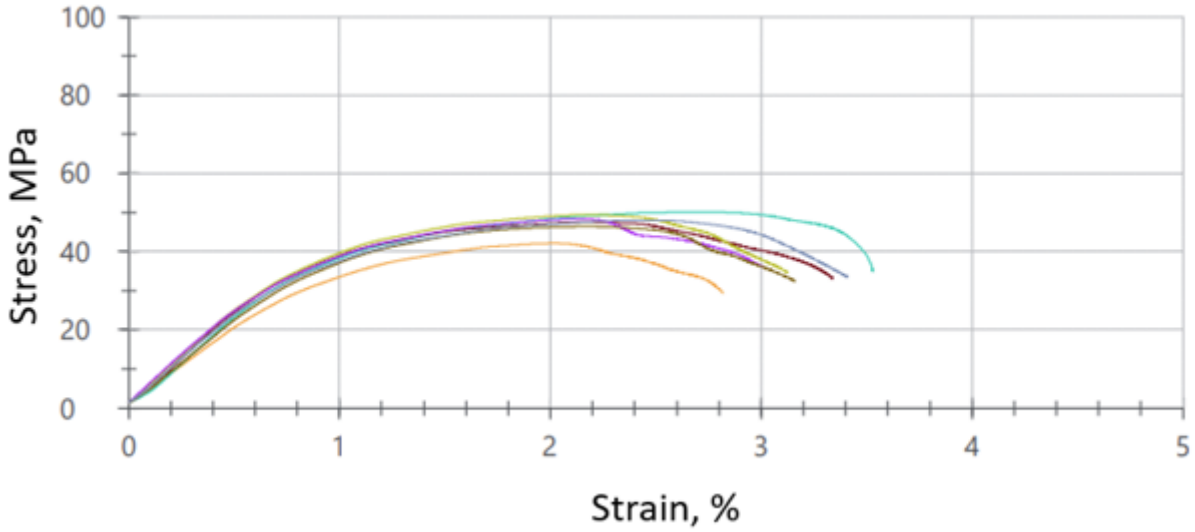


Figure 1. Characteristics of normal stress - vertical strain in uniaxial compression of standard (water -based catalyst) styrene resin cartridges.

In general, the unconfined compressive strength (UCS) of standard formulation styrene resin cartridges is about 50 MPa; for the batch presented in Figure 1, the mean value of UCS is equal to 47.4 MPa (standard deviation 2.63 MPa and coefficient of variation 5.5%). The results (shape of the curves) of all the tested specimens are quite similar, ductility (vertical strain at maximum stress) is about 2.3%.

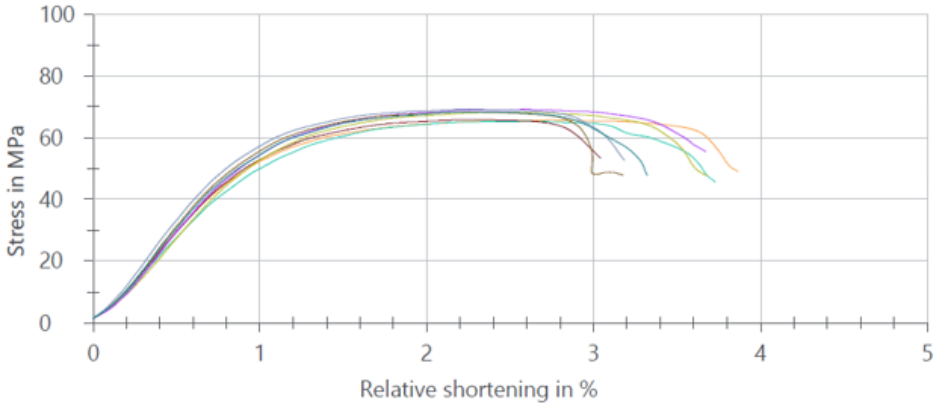


Figure 2. Characteristics of normal stress vs vertical strain in uniaxial compression of styrene-free resin cartridges produced with water-based catalyst.

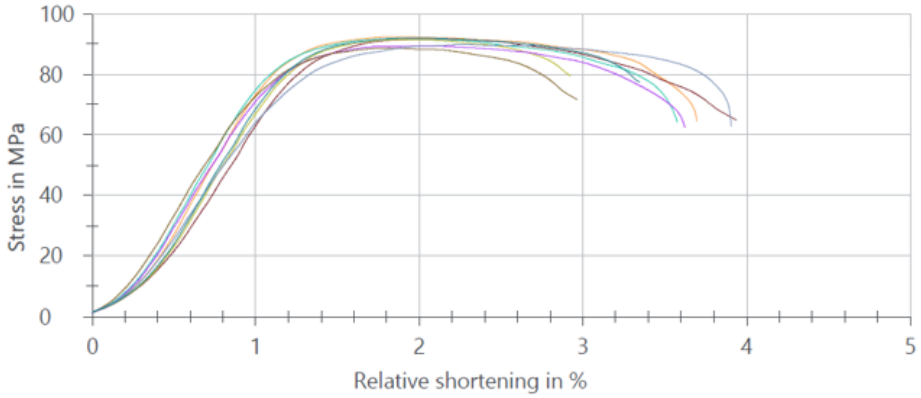


Figure 3. Characteristics of normal stress vs vertical strain in uniaxial compression of a new type of styrene-free resin cartridges created with a new EPC-type of the catalyst.

Mean UCS value for the styrene-free water-based catalyst is equal to 67.5 MPa, and again all the results of the individual tests are similar (UCS standard deviation 1.60 MPa) and ductility is around 2.4%.

New formulation of styrene free resin cartridges based on EPC-type of a catalyst results in significantly higher UCS values. The mean UCS value of the test results presented in Figure 3 is equal to 90.9 MPa (standard deviation 1.39 MPa) and the resin is stiffer (ductility 2.0%). The maximum UCS value determined during testing of eight specimens reached 92.4 MPa and the minimum 88.7 MPa.

UCS of a new styrene-free resin formulation based on EPC-type of catalyst is almost twice as high as standard (water-based catalyst) styrene-based resin cartridges formulation and about 35% higher than water-based catalyst of styrene-free resin.

UCS is not the only mechanical parameter which is important to describe the properties and behaviour of the resin cartridges. BS2007 requires the determination of elastic modulus and creep of resin. Elastic modulus is determined, according to BS2007, in a procedure of loading and unloading cycles between

the 2.5 kN and 7.5 kN load and the elastic modulus is the mean of the three-second moduli measured between the two levels of the applied load.

Since the water-based catalyst styrene resin cartridges do not comply with or do not even give the results close to the requirements of BS2007, the following results and discussion refer to styrene-free resins produced with either a water-based catalyst or a new formulation based on EPC-type of a catalyst. Characteristics of force vs vertical strain in uniaxial compression of styrene-free resin cartridges produced with water-based catalyst are shown in Figure 4. The corresponding curves in the same procedure but for a new type of styrene-free resin created with EPC-type of catalyst cartridges are shown in Figure 5.

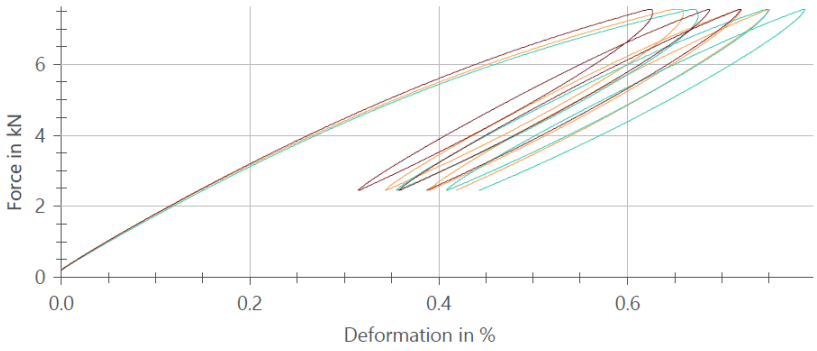


Figure 4. Characteristics of load vs strain in uniaxial compression of styrene-free resin cartridges created with water-based catalyst obtained in the procedure for determining elastic modulus.

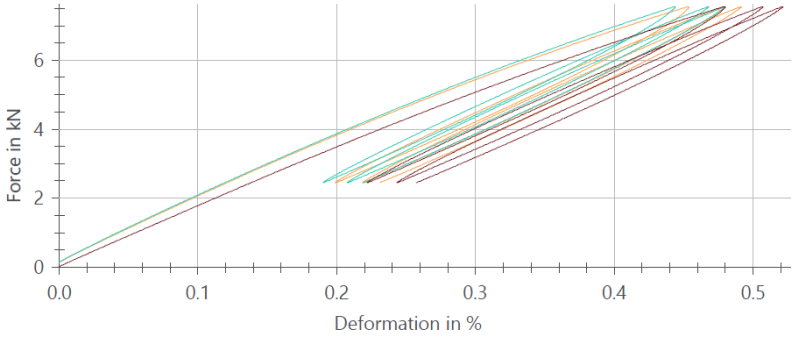


Figure 5. Characteristics of load vs strain in uniaxial compression of a new type of styrene-free resin cartridges based on EPC-type of catalyst obtained in the procedure for determining of elastic modulus described in British Standard (2007).

According to BS2007 the elastic modulus shall be greater than 11 GPa. Although the UCS value for the styrene-free water-based catalyst is in a range of 65-70 MPa and is significantly below the 80 MPa threshold but its stiffness given by the Young's modulus value ≈10.2 GPa is only slightly below the threshold. The mean value for the styrene-free water-based catalyst resin cartridges presented in Figure 4 is 10.20 GPa (standard deviation 0.21 GPa and coefficient of variation 2.04%).

A new type of styrene-free resin cartridges based on EPC type of a catalyst is stiffer and meets the requirements of British Standard (2007), E mean value is equal to 12.93 GPa and the results are quite consistent (standard deviation value 0.25 GPa and coefficient of variation of 1.9%).

Rigidity of the resin is of high importance in rock bolting; E value of a range of about 13 GPa is similar to Young's modulus values of many sedimentary rocks like mudstones and weak, deformable sandstones and more than Young's modulus values of coal and the majority of shales. This means that

even significant loads exerted on the bolt will result in a small deformation (displacement) of the bolt shank.

Rheological properties of the resin cartridges are determined, according to BS2007, in a procedure of loading the specimens to a load of 5 kN and maintaining this load for a duration of 15 min. The resistance to creep is the recorded strain between 0.5 and 15 min expressed as a percentage and it shall be no greater than 0.12%.

Example characteristics for creep determination of styrene-free resin cartridges produced with water-based catalyst and a new type of styrene-free resin created with EPC type of catalyst cartridges are shown in in Figures 6 and 7, respectively.

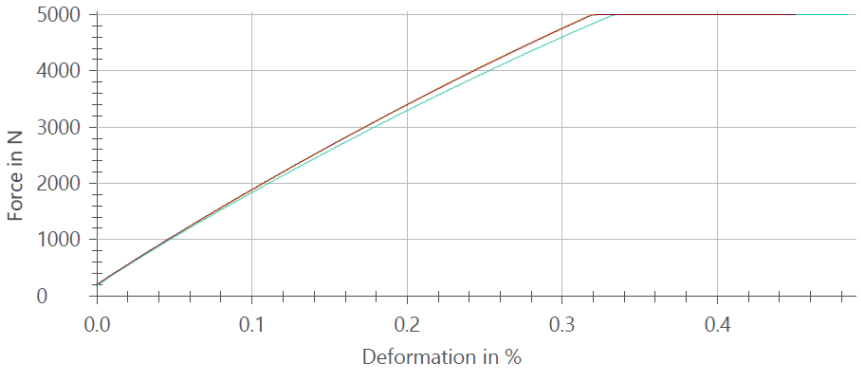


Figure 6. Characteristics of load vs strain in uniaxial compression of styrene-free resin cartridges produced with water-based catalyst obtained in the procedure for determining creep.

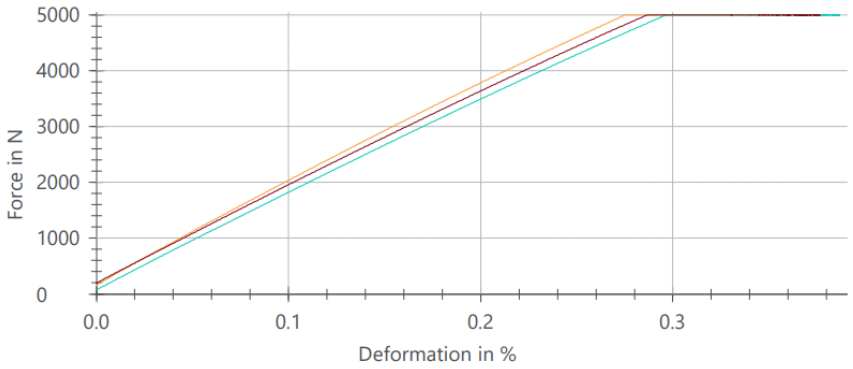


Figure 7. Characteristics of load vs strain in uniaxial compression of a new type of styrene-free resin cartridges based on EPC type of catalyst obtained in the procedure for determining creep described in British Standard (2007).

Resistance to creep of both the water-based and EPC-type of catalyst used to produce styrene-free resins meet the requirements of British Standard (2007). The mean value of the water-based catalyst type of styrene-free resin cartridges presented in Figure 6 is 0.108% (standard deviation 0.009% and coefficient of variation 7.84%).

A new type of styrene free resin cartridges produced with the EPC-type of catalyst has improved creep resistance with a mean creep value of 0.068%. This is almost two times lower than the creep value required (normative) given in BS2007. What's more, the results are uniform and reduced scatter of data is observed (standard deviation ≈0.001% and coefficient of variation 1.94%).

Since in some countries the compressive tests described above are sometimes complemented with or even replaced by testing of the shear strength of the resin, such tests were also conducted for the new

type of styrene-free resin cartridges produced with the EPC-type of catalyst. Tests were conducted according to the South African National Standard (2018).

A sufficient mass of resin mastic and the quantity of catalyst corresponding to the resin mastic-catalyst ratio in the capsule were separately weighed and then cooled in the refrigerator until the samples had reached ≈4°C. The cooled resin mastic and catalyst were mixed together and test specimens were moulded in the 3 mm washer and then conditioned for three hours at 50°C. After cooling the specimens in the room temperature the first specimen was positioned symmetrically in the punching tool assembly which was placed in the loading device (Figure 8a).

The load was applied steadily using the punch and the increasing force fractured (sheared) the test specimen after about 30 seconds. The maximum force values sustained by the test specimens were recorded and the shear strength of the resin was calculated. Example load - deformation curves for shear strength determination are shown in Figure 8b.

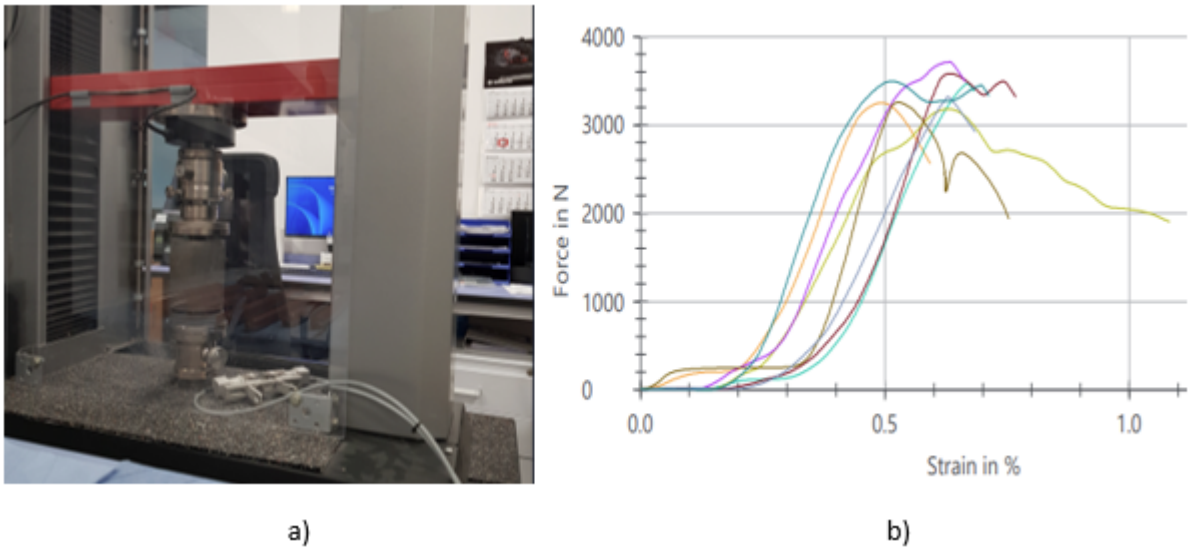


Figure 8. The punching tool assembly positioned in the loading device for shear strength testing (a); characteristics of load vs displacement of a new type of styrene-free resin cartridges based on EPC- type of catalyst obtained in the procedure for determining the shear strength of the resin described in SANS (2018) (b.)

Mean value of the shear strength determined from the eight tests is equal to almost 34 MPa (33.87 MPa). Maximum value reached about 37.7 MPa and minimum value was equal to 30.6 MPa. The results are quite consistent (standard deviation value 2.41 MPa and relative standard deviation of about 7%). Shear strength of styrene-free resin based on EPC-type of catalyst far exceeds the threshold values of 19 MPa and 23 MPa given in the standard; in fact it is almost 50% higher than the value required for the S23 resin.

TESTING BONDING STRENGTH OF A NEW TYPE OF STYRENE-FREE RESIN BASED ON A NEW GENERATION TYPE OF CATALYST

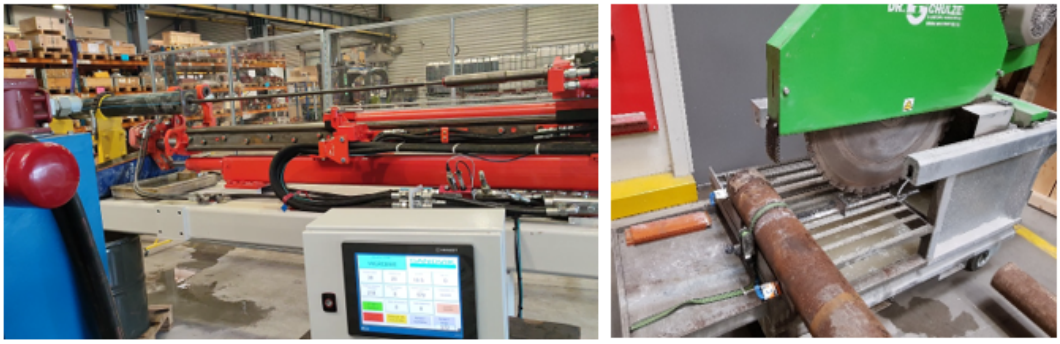
Laboratory tests performed confirmed improved mechanical properties of both types of the new styrene-free resin formulations (water-based and EPC type of catalysts) to the existing styrene-based ones. Those results, although important, are not sufficient to prove the readiness and usefulness of a new type of resin cartridges (styrene-free) for use in underground workings for rock bolting.

It has been decided that an important step to check the performance of the new type of a styrene-free resins would be to test the bonding strength of the assemblies of rock bolts grouted with styrene-free

resin in the holes drilled into high strength concrete embedded in steel pipes. The styrene-free resins based on EPC type of catalysts were selected for this testing and as a first step a pumpable version of that formulation.

One of the reasons supporting the choice of the pumpable version of the new type of resin for rock bolting was its popularity in some parts of the world, but the most important factor was the ability to eliminate possible variabilities related to mixing quality and to test the true bonding strength of the assemblies.

Two steel pipes, diameter ≈ 15 cm and length ≈ 200 cm, were filled with a high strength concrete and left for more than 28 days to allow strength build-up. The pipes were then installed in a Sandvik ground support drilling rig (Figure 9a) and 33 mm holes of were drilled. Canadian 22 mm rebars were subsequently embedded with a pumpable version of the styrene-free resin based on the EPC-type of the catalyst. After curing the resin the pipes were then cut into 15 cm long sections (Figures 9b and 10a).



a) b)

Figure 9. Sandvik ground support drilling rig (a); cutting the assemblies of rock bolts grouted with styrene-free resin in the holes drilled in a high strength concrete embedded in steel pipes (b).

Ambient temperature in the workshop where bolting and curing took place was about 15°C. Cylinders of diameter and length equal to 15 cm were then placed in a standard, 400 kN capacity testing machine. Using a special shape piston of 19 mm diameter, made of hardened steel, a compressive load was gradually applied to determine the bonding strength of the assemblies (Figure 10b).



a) b)

Figure 10. 15 cm sections of the pipes ready for testing (a); one of cylinders placed in a standard 400kN capacity testing machine during push-out tests (b).

A loading rate was in a range of 0.7 kN/s – 0.9 kN/s and bonding strength for almost all sections of the pipe tested reached at least about 20 tons (≈200 kN). The detailed results are presented in Figure

11. As can be seen, the styrene-free resin based on the EPC-type of the catalyst gives superb bonding strength. For pipe number 1 the minimum bonding strength was 200 kN and the maximum reached 234.5 kN. For only the first section of the pipe (collar of the bolt) the bonding strength was a bit smaller (163.5 kN) and this result is believed to be caused by the different boundary conditions, i.e., possible microcracking of the concrete at the end of the pipe.

Maximum loads for pipe number 2 determined during pushing-out of the sections of the bolts grouted with styrene-free pumpable resin were generally even higher. The minimum bonding strength was almost 200 kN (198.5 kN for section number 5) and the maximum reached 270 kN. The load pushing out the bolt was not determined for the first section of the pipe since it was lost due to failure of the equipment during cutting.

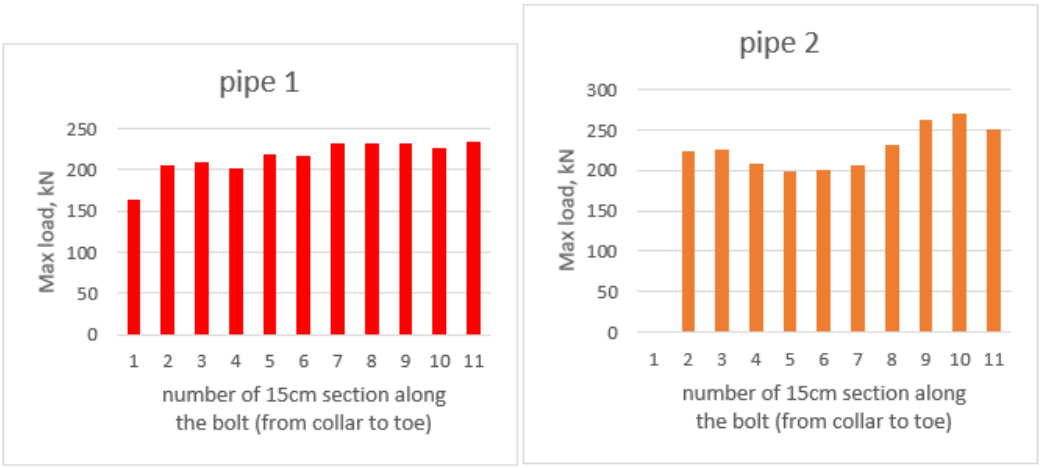


Figure 11. Bonding strength of the assemblies of rock bolts grouted with styrene-free resin based on EPC-type of catalyst in the holes drilled in a high strength concrete embedded in steel pipes cut into 15 cm long sections.

General comment is that the bonding strength is very high for all the sections of both bolts, and although the results are quite uniform, especially for pipe number 1, the differences are noticeable. Since the mixing of the resin is not responsible for this effect it is believed that the local strength of concrete in the pipe is a reason for the behaviour. It was decided that a better concrete embedment in the pipes' techniques should be performed in the future. For now a preliminary study of the concrete revealed presence of some pores and micro open spaces filled with air, especially in those sections of the lowest bonding strength determined.

In each case pushing-out of the bolts embedded with FASLOC styrene-free resin at a loading level of about 20 tons or more occurred due to the failure (sliding) of the resin-concrete interface. The calculated shear bonding strength is in a range of 12.8 – 17.4 MPa.

The results obtained show that the bonding strength of the assemblies of standard rebar bolts embedded with styrene-free resin based on the EPC-type of the catalyst are very high. Just a 15 cm embedment section is needed to transfer a load of 20 tons or more. Although the concrete used to fill the steel pipe was a special type of high compressive strength its UCS is certainly much lower than that of many hard rocks.

Since the bonding strength increases with the strength of the substrate rock, it can be expected with confidence that in those rocks the bonding strength of the rock bolts grouted with a new type of styrene-free resin will be even higher. It means that an embedment length of just 10-25 cm could be enough to cause the failure of steel (and not the grout) of every bolt shank commonly used in the mines. This also confirms that the strength of a new type of styrene-free resin based on the EPC-type of the catalyst is more than sufficient to fulfil the practical requirements for rock bolting in the

underground workings. The tests with different substrate rocks and with resin cartridges, not only a pumpable version of the resin, will be continued.

DYNAMIC TESTS OF THE ASSEMBLES OF ROCK BOLTS GROUTED WITH STYRENE-FREE RESIN IN THE STEEL PIPES

Increasing depth of the mining excavations and extensive extraction in many mines around the world result in complex underground structures' geometries and huge areas or volumes of the extracted ore. All of these cause high seismicity observed in the mines and a high risk related to rockburst hazard.

To mitigate the risk it is important to install so-called dynamic types of support or reinforcement and one of the most popular types of reinforcement used in a seismic/rockburst hazard conditions are dynamic rock bolts fully grouted in the rock mass. The behaviour of a new type of the styrene-free resin based on the EPC-type of the catalyst under dynamic loading conditions was also tested.

For initial dynamic tests Versa bolts of 22 mm diameter and length of 2.4 m were selected. It was decided to follow the recommendations of the recently published ISRM Suggested Method (Li *et al*., 2025). The bolts were embedded with the pumpable version of the styrene-free resin based on the EPC-type of the catalyst directly in the steel pipes and the thickness of the wall of the steel pipes was determined to mimic the deformational properties of the rock mass. Calculations were based on the formulas given in the ISRM Suggested Method (2025) and pipes of the internal diameter of 34.1 mm, wall thickness equal to 7.1 mm and length 2×1135 mm were selected. The so-called spilt tube tests were performed on the rock bolt styrene-free resin grout assemblies at Central Mining Institute (CMI) – National Research Institute's dynamic testing rig in Poland (Fig. 12a).



Figure 12. (a) Versa bolt embedded with styrene-free resin in a split-tube before the impact testing at Central Mining Institute's dynamic testing rig); (b) Versa bolt after the impact testing with 40 kJ of input energy.

The CMI dynamic testing rig uses the so-called free-fall of a mass method, and it has been used for more than two decades to test various types of dynamic bolts from many parts of the world (see Pytlik, 2024; Li *et al*., 2021). The capabilities of the testing rig far exceed the dynamic capacity of any bolt used underground and it is also very stiff, meaning that about 99% of the impact energy is absorbed by the tested bolt assembly and only about 1% is dispersed by the testing rig.

As an example the results of testing of two Versa bolts - styrene-free resin grout assemblies are shown. The first of those bolts was hit by a mass of 2620 kg, released from 1400 mm height, resulting in a 36kJ input energy and a velocity of the impact mass equal to 5.2 m/s. The assembly of Versa bolt styrene-free resin grout behaved very well, the maximum load sustained by the assembly reached 354.3 kN, the bolt deformed and the maximum tubes' split was measured to be 131.1 mm but as there was still an elastic component of the total strain the final displacement of the tubes was reduced to about 117 mm (Figure 13).

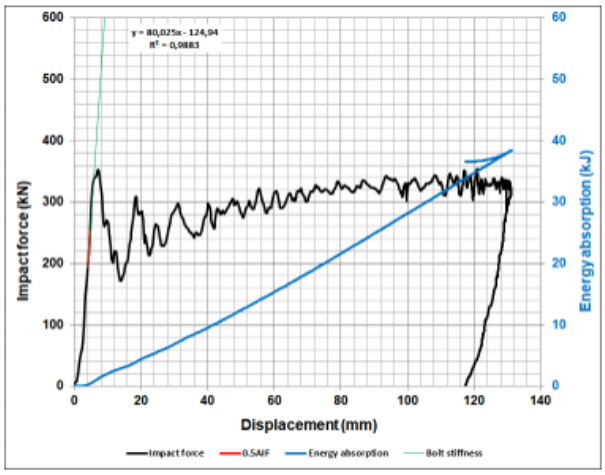


Figure 13. Load – displacement and energy absorption – displacement curves for Versa bolt embedded with styrene-free resin in a split-tube tested with 36 kJ of input energy (first impact).

Although the impact energy was equal to 36 kJ, the total energy absorbed by the embedded bolt was, due to its elongation, about 38 kJ and the average impact force (AIF) was almost 300 kN (299.9 kN). The bolt stiffness and rise time determined by the procedures described in the ISRM Suggested Method were 80 MN/m and 1.4 ms, respectively. The time to the first rebound was below 0.1 s and force measured just before the dropped mass rebounds was equal to 314.5 kN.

It was decided to hit the bolt assembly with the same very high input energy (36 kJ) a second time. As a result the bolt failed but nevertheless it absorbed about 28 kJ of energy. The maximum load in the test reached 486.5 kN, AIF was about 334.7 kN and the force just before the failure of the bolt was 338 kN (Figure 14).

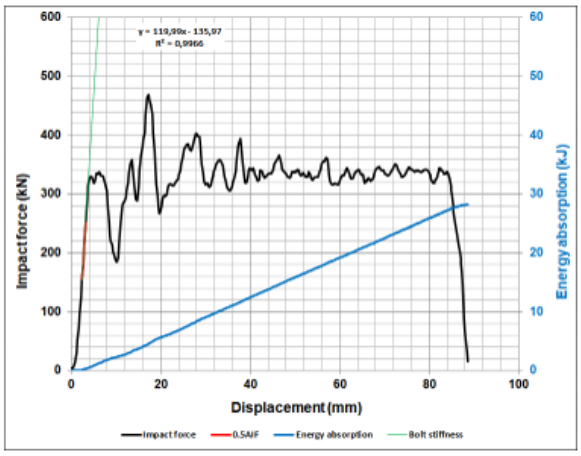


Figure 14. Load – displacement and energy absorption – displacement curves for Versa bolt embedded with styrene-free resin in a split-tube tested with 36 kJ of input energy (second impact).

The bolt deformed and the additional displacement due to the second impact reached almost 84 mm (83.9 mm) and as a result the total energy dissipated by the bolt in two hits reached about 66 kJ before failure.

To test the response of Versa bolt - styrene-free resin grout assembly to the dynamic loading of an even higher input energy a test of 40 kJ input energy on another assembly was performed.

The drop mass was kept constant (2620 kg), but it was released from a 1555 mm height, resulting in a 40 kJ input energy and an increased impact velocity (5.5 m/s). The assembly of Versa bolt - styrene-free resin grout sustained this high energy impact; the maximum load measured in the test reached 346.4 kN, the bolt deformation and the maximum tubes split was a bit bigger, equal to 145.9 mm and again as there was still an elastic component of the total strain of the bolt the final displacement of the tubes was reduced this time to about 131 mm (Figures 12b and 15).

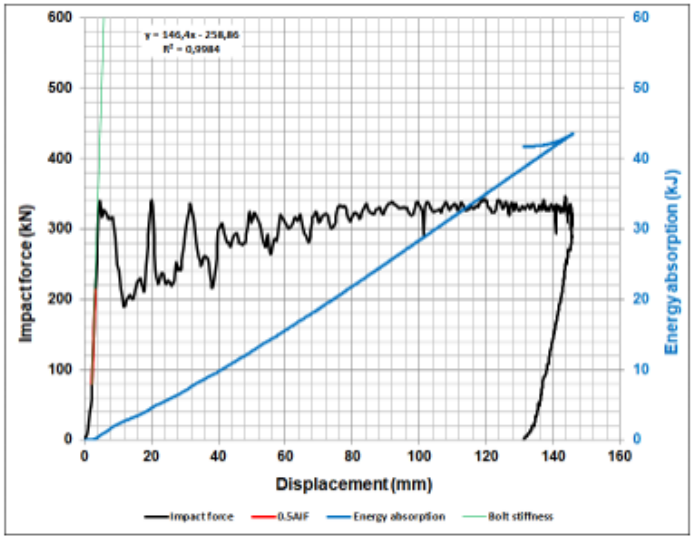


Figure 15. Load – displacement and energy absorption – displacement curves for Versa bolt embedded with styrene-free resin in a split-tube tested with 40 kJ of input energy (first impact).

Although the impact energy was equal to 40 kJ, the total energy absorbed by the embedded bolt was, due to its elongation, almost 44 kJ and the AIF was above 300 kN (304.3 kN). The bolt stiffness and rise time determined by the procedures described in the ISRM Suggested Method were 146 MN/m and 1.0 ms, respectively. The time to the first rebound was again below 0.1 s (0.07 ms) and force measured just before the dropped mass rebounds was equal to 313.7 kN.

CONCLUSION

Development of a new styrene-free polyester resin represents an important step in reducing chemical hazards in underground roof and sidewall rock bolting applications. It is safe for both men and women workers and in the mine it offers increased work comfort, easy waste management and it is hardly flammable. It does not require any special conditions for air, sea and road transport and it can be stored with other materials since it does not require well-ventilated warehouses.

At the same time, the new formulation delivers improved mechanical load transfer properties and the improved product packaging assures reliable pneumatic installation even when using automatic loading systems such as the Sandvik ARI system.

Development of a new generation catalyst (EPC) for the styrene-free resin seems to be an important step forming the basis for the shift from potentially harmful styrene-based cartridges to styrene-free resins.

Results of testing of the mechanical properties both listed in the BS (2007) i.e., uniaxial compressive strength (above 90 MPa), Young's modulus (about 13 GPa) and creep (below 0.07%) as well as the shear strength in the SANS (2018) (about 34 MPa) showed very good behaviuor of the styrene-free resin based on the new generation catalyst.

Push-out tests confirmed its very high bonding strength (generally, above 20 tons per 15 cm long section) and dynamic impact tests showed its usefulness in seismic or rockburst hazard conditions.

REFERENCES

British Standard (2007). Strata reinforcement support system components used in coal mines – Part 1: Specification for rockbolting (BS 7861-1:2007), BSI – British Standards Institution, London.

European Union (2014). Hazardous Substances Subject to Declaration - Construction Product Regulation - Article 6(5), Regulation 305/2011/EU on Marketing of Construction Products, amended by Regulation 574/2014/EU, 28 May 2014.

Evans D., Smolnik G., Penczek R., Drozd J., Franek J. and Bucholc D. (2025). Styrene free polyester resin cartridges – a breakthrough technology for health and safety, with increased mechanical properties. *Proceedings of Resource Operators Conference*. University of Wollongong. Collection.

Huff, J. and Infante, P. (2011). Styrene exposure and risk of cancer. *Mutagenesis*, 26 (5), 583–584.

Li, C.C., Hadjigeorgiou, J., Mikula, P., Knox, G., Darlington, B., Royer, R., Pytlik, A., Hosp, M. (2021). Performance of identical rockbolts tested on four dynamic testing rigs employing the direct impact method. *J Rock Mech Geotech Eng*, 13, 745–754.

Li, C.C., Mikula, P., Hadjigeorgiou, J., Simser, B., He, M., Canbulat, I. and Joughin, W. (2025). ISRM Suggested Method for Determining the Properties of Rock Bolt Assemblies by Mass Freefall Impact Testing in the Laboratory. *Rock Mech Rock Eng*, 58, 165–179.

Pytlik, A. (2024). *Rock Bolt Impact Resistance*, The Publishing House of the Central Mining Institute – National Research Institute, Katowice.

South African National Standard (2018). Resin capsules for use with tendon-based support systems (SANS 1534:2018 Edition 2), South African Bureau of Standards, Pretoria.

Smolnik, G., Penczek, R., Drozd, J., Franek, J., Bucholc, D. and Scolari, F. (2024). A new generation of polyester resin capsules for enhanced health and safety and improved mechanical performance. *Proceedings of the 10th International Conference on Deep and High Stress Mining*. Andrieux, P. and Cumming-Potvin, D. (eds.). Australian Centre for Geomechanics, Perth, pp. 621-630.

Vineis, P. and Zeise, L. (2002). Styrene-7,8-oxide and Styrene, International Agency for Research on Cancer (IARC) Monograph 82, pp. 72–78.

Blast-on-Mesh: Transforming deep-level gold mining – success stories from Kusasalethu

R. van Heerden[1], M. Phathu[2]

[1]Harmony Gold Mining Company Limited, South Africa
[2]Geobrugg Southern Africa

This case study examines the successful implementation of permanent blast-on-mesh (BOM) at Harmony Gold's Kusasalethu Mine and its positive impact on mine safety. The adoption of netting and bolting as a ground support practice began in 2013 as part of the Mine industry Occupational Safety and Health (MOSH) initiative, which aimed to reduce fall-of-ground incidents and enhance safety standards. In 2020, Kusasalethu pioneered the introduction of permanent blast-on-mesh, marking a significant shift in ground support practices. The initiative was met with favourable feedback from underground crew members, who noted the improvement in safety in their working environment.

The introduction of permanent BOM resulted in a marked reduction in gravity-induced fall-of-ground injuries and a significant decrease in overall fall-of-ground incidents. This study highlights the effectiveness of permanent areal support in providing long-term stability to underground workings, with the transition to permanent areal cover support becoming a leading practice by 2023. However, the success was not without its challenges. Issues related to the installation quality of the mesh, as well as damage during routine cleaning and maintenance, were identified as areas for improvement. Despite these challenges, the implementation of netting and BOM proved effective in reducing the severity of fall-of-ground incidents, thus enhancing the overall safety and operational efficiency of the mine.

This case study underscores the critical role of innovative ground support technologies and safety practices in improving mine safety, and it serves as a model for the continued evolution of ground support systems in the mining industry. By detailing both the successes and challenges encountered at Kusasalethu, the study provides valuable insights into the practical application of permanent BOM and its potential to reduce ground-related hazards in deep-level mining operations

INTRODUCTION

The reduction of falls of ground incidents in South African underground mines has been significantly influenced by advancements in areal coverage support systems and other leading practices, reflecting a dynamic response to the challenges of eliminating fall of ground (FOG) injuries and incidents in deep-level mining operations.

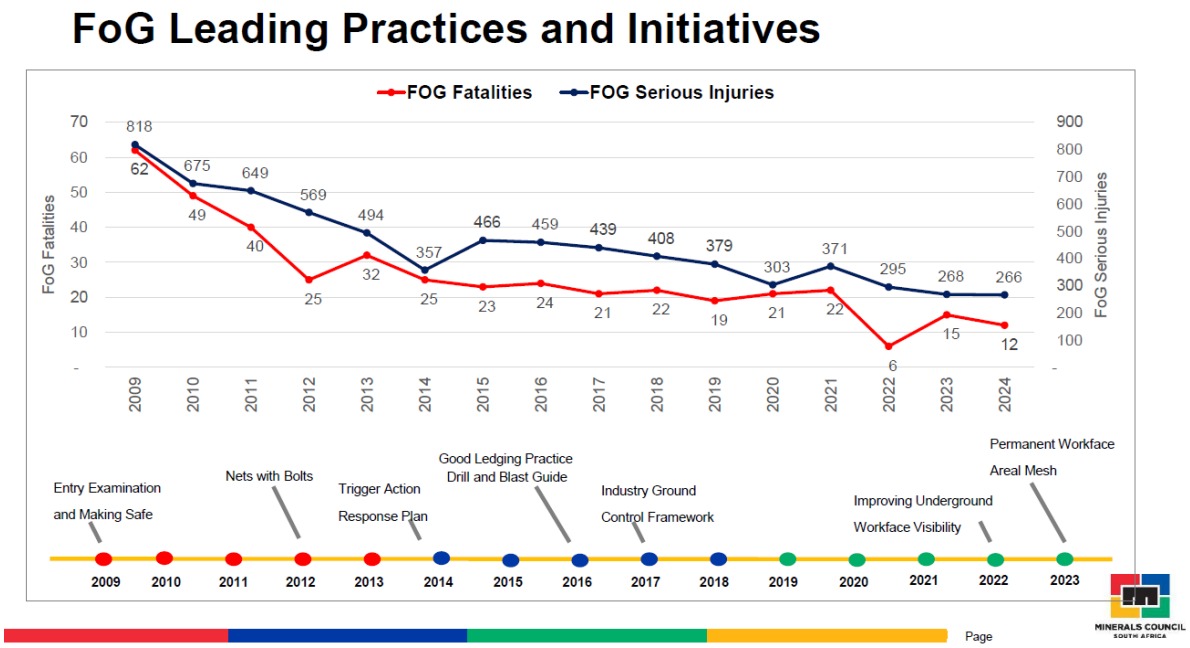


Figure 1. Falls of ground (FOG) leading practices and initiatives (Minerals Council South Africa, 2025).

Leading practices in South African underground mining have evolved significantly over the years, driven by the need for enhanced safety, efficiency, and sustainability in response to the challenges presented by deep-level mining operations. The unique geological conditions and the increased depth of mines have necessitated the development and implementation of advanced support systems designed to maintain the integrity of underground workings while minimising rockfall hazards and optimizing resource extraction (Minerals Council South Africa, 2025).

From the Minerals Council South Africa (2025) it can be seen that the only areal coverage support utilized in the industry by 2012 was safety nets, and it was not an industry-wide practice at the time. That, together with other initiatives or leading practices mentioned on the Minerals Council South Africa website (2025) contributed significantly to the decrease in FOG-related fatalities and injuries. This evolution reflects a commitment to innovative engineering solutions as mining companies strive to balance economic viability with the imperative of protecting their workforce and the environment, as South Africa remains a pivotal player in the global mining sector (Minerals Council South Africa, 2025).

In the past five to ten years, several conventional underground hard rock mines in South Africa have adopted the use of permanent workface areal coverage mesh. This type of areal support is often preferred because it allows the workforce to always work under supported ground, and due to it being permanent, the back areas remain supported from an aerial perspective. The major contributor to most mine's adoption of permanent areal mesh has been the drive from MOSH, which stems from discussions in March 2021, where the CEO zero harm forum discussed the industry's 2020 falls of ground safety performance and tasked MOSH to find ways of mitigating FOG regression in the industry (Minerals Council South Africa, 2025).

Mineral Council South Africa (2025) shows that the study led to MOSH adding permanent work face areal mesh as a leading practice in 2023. Some of the learnings came from different mines that had already started adopting the solution as far back as 2017. Kusasalethu was one of those mines that had already started with this initiative.

The impact of areal coverage support at Kusasalethu mine

Kusasalethu Gold Mine is situated approximately 90 km west of Johannesburg, near the border of Gauteng and the North-West, in the West Witwatersrand Basin (Figure 2). It extracts the Ventersdorp Contact Reef (VCR) which is overlain by the Alberton Porphyry Formation (Ventersdorp Lava). The current mining extracts the orebody at depths of 2700 m – 3388 m below the collar elevation and employs the modified sequential grid mining method. The sequential grid mining method employs a series of raise lines spaced 200 m apart, separated by 30 m wide dip stabilizing pillars. The access/ventilation tunnels are placed 'deep' in the quartzite footwall, >80 m below the reef plane and are excavated ahead of the mining operations. Long cross-cuts every 200 m link the main haulages to the reef plane, where raises are developed (Figure 3). The mining sequence helps to manage the stress levels and limit the incidence of seismicity (van Heerden, 2022).

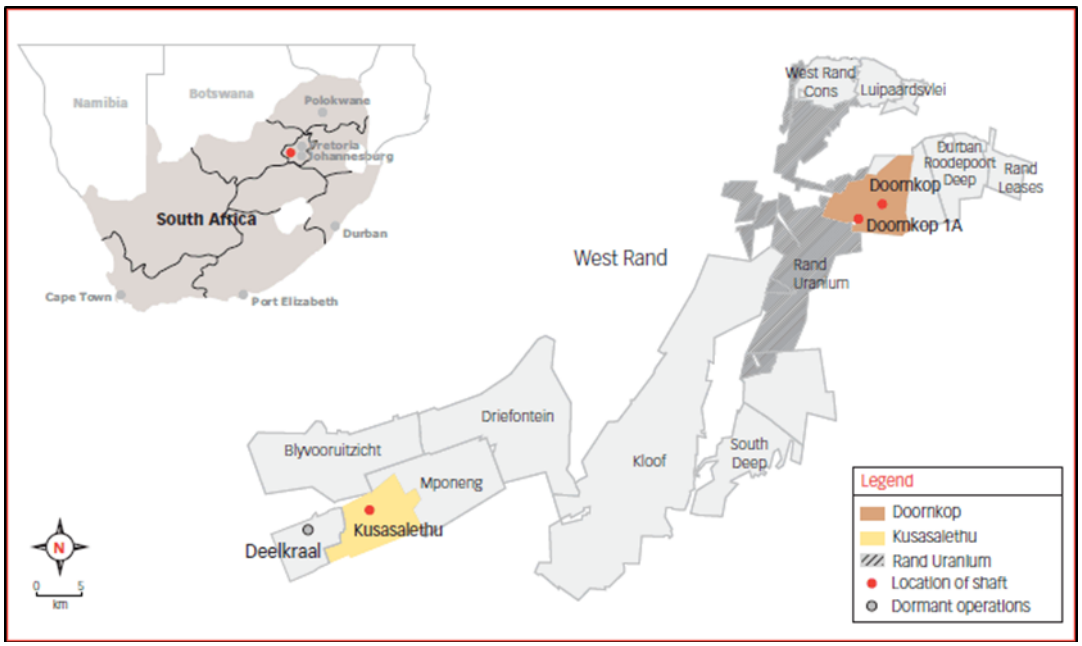


Figure 2. Locality of Kusasalethu Gold Mine (Harmony Gold Mining Company Limited, 2023)

The hanging wall is Ventersdorp Lava, which has a UCS of some 300 MPa. Conditions vary considerably across the above-mentioned reef type. Varying conditions are caused by pilloids; inter-pilloid breccias and joints, associated with slopes and duplicated reef zones. Another contributing factor is a relatively large amount of flat faulting, which extends into the hanging wall, due to the brittle nature of the hanging wall lava. The footwall is competent quartzite, (UCS 180 – 250 MPa) which extends to a depth of approximately 430 m below the reef on the eastern boundary and about 550 m below the reef on the western boundary, enabling haulages and most other primary development to be sited deep in the footwall, in strong competent host rock (van Heerden, 2022). Backfilling is practised to improve the overall stability, to reduce closure rates and improve regional as well as local support when incorporated with additional support units such as pre-stressed timber elongates and packs (van Heerden, 2022). The mine infrastructure includes twin vertical and twin sub-vertical shaft systems, which facilitate the movement of personnel and materials underground. This design is essential for optimizing the efficiency of the mining operations, especially given the depths at which mining occurs (Harmony Gold Mining Company Limited, 2025).

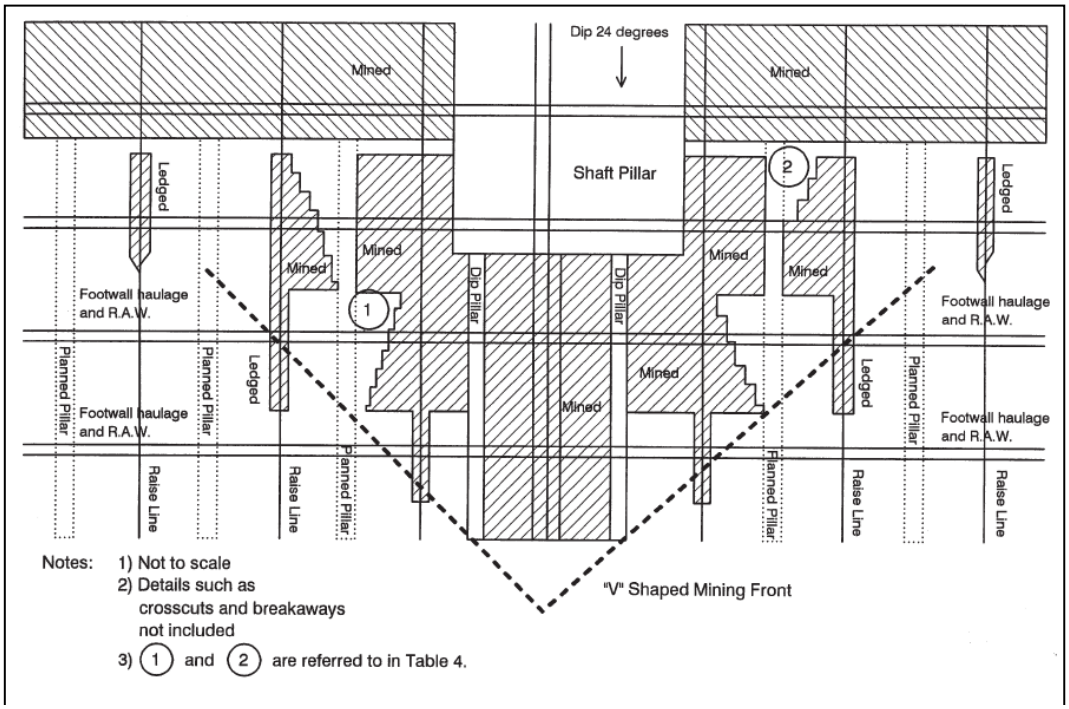


Figure 3. Overall strategy for sequential grid mining (Handley, de Lange, Essrich, & Banning, 2000)

Between the years 2013 and 2018 the mine was utilising temporary safety nets as areal coverage and only started trialling permanent areal mesh in late 2018. The temporary net that was previously used was a nylon-type net with square 100 mm square apertures that was installed during entry examination and making safe and removal of the net before the blast.

On the 10th of July 2018 following a loss of life incident at the operation in a gravity-induced rock fall incident a mandate was given by the then COO of Harmony that permanent net/mesh should be implemented, this informed the transition from a temporary in-stope net to a permanent areal coverage solution. A cable-type net with 100 mm square apertures was selected as the solution, but the overall success of the initiative was hampered as the full change management process as laid out in the 16-step MOSH adoption process, was not fully followed. Figure 4 illustrates the generic process.

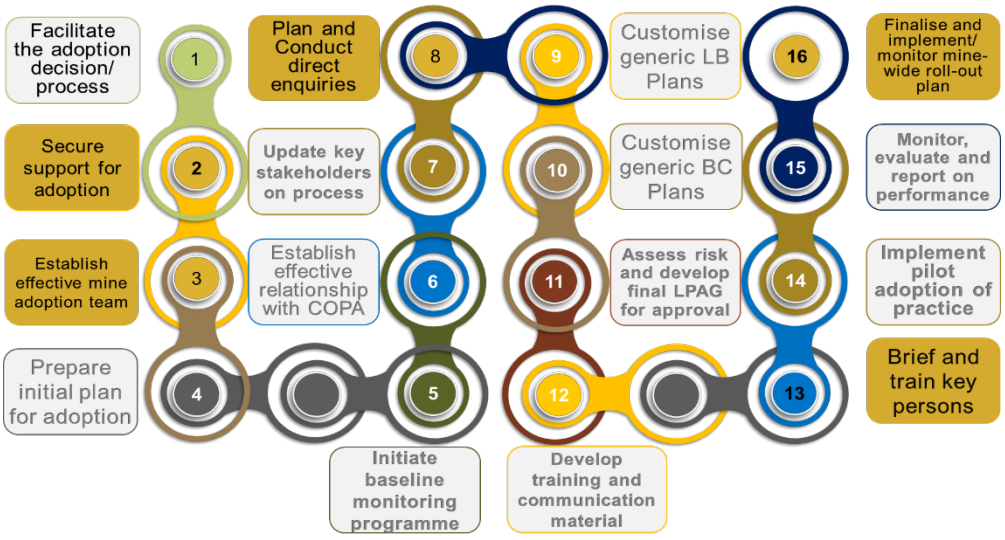


Figure 4. 16-step MOSH adoption process.

Various challenges arose during this time and ranged from were not limited to:

- the size of the net, the mass of the net proving to be cumbersome to handle,
- tensioning and overall installation quality,
- And consistent damage during cleaning operations.

The efficacy of the permanent nets was compromised, and in essence all the relevant stakeholders were not involved and adequately informed. According to the MOSH adoption process, the following seven steps must be followed, updated and refined from the sixteen-step process (Minerals Council South Africa, 2025):

- Secure support for adoption,
- Establish a mine adoption team,
- Confirm my STS (socio-technical system) elements to be addressed,
- Establish mine adoption plan,
- Review, update and monitor operational processes and documentation,
- Execute leading practice adoption and implementation in the pilot site,
- Roll out the leading practice to the rest of the organisation.

In Figure 5 below, a comprehensive summary of total incidents (reported and investigated FOGs) and injuries recorded from July 2018 to June 2024 is presented, with the statistics for 2025 still pending completion over the next four months. Notably, the graph illustrates a significant downward trend in the total number of falls of ground (FOG) incidents since the trial and implementation of permanent areal coverage mesh at the Kusasalethu gold mine. This positive trend highlights the effectiveness of integrating permanent support systems in enhancing mine safety and stability, demonstrating a clear correlation between the adoption of this innovative support solution and a reduction in FOG incidents. As the mining industry continues to prioritise safety and risk mitigation, the ongoing analysis of these statistics will provide valuable insights into the impact of areal coverage mesh on overall operational safety.

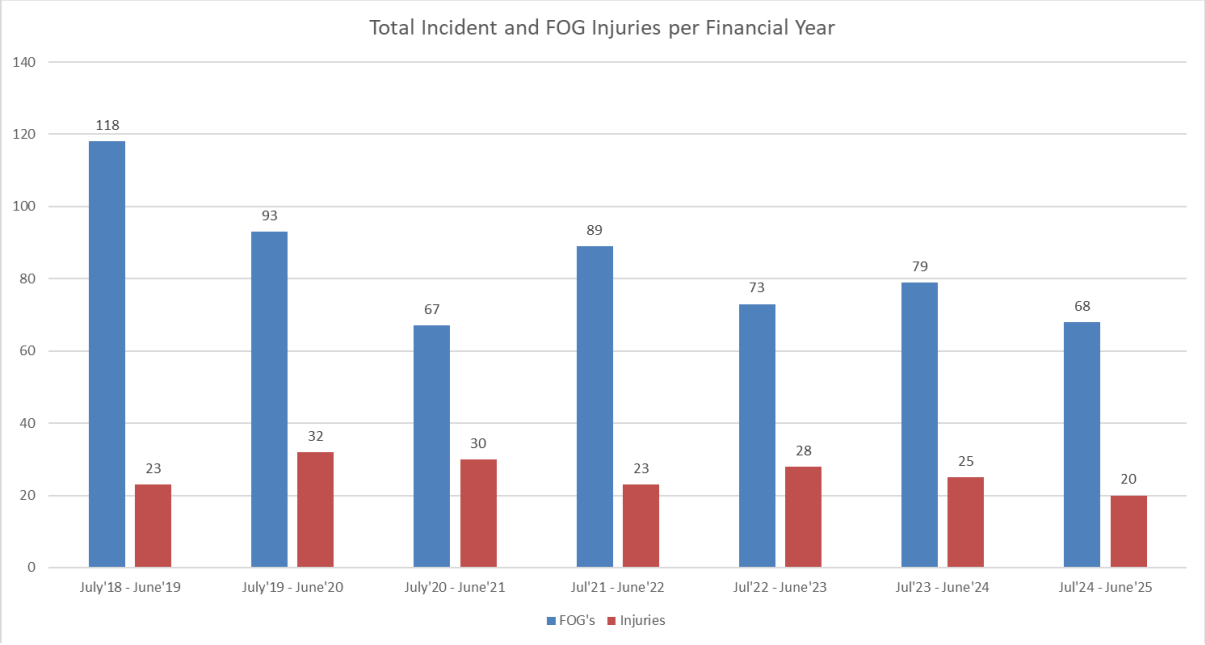


Figure 5. Total falls of ground incidents and injury summary per financial year (van Heerden, Kusasalethu Fall of Ground Stats, 2025).

The main causes for the rock fall-related injuries at Kusasalethu mine are seismicity, entry examination and barring. Figure 5 shows the number of incidents caused by seismicity, entry examination and

barring from the financial year 2018 to 2025. From the statistics, from 2020 the incidents caused by entry examination and barring started flattening out and decreasing towards 2024. The main reason of this decrease was the re-implementation of permanent areal coverage mesh.

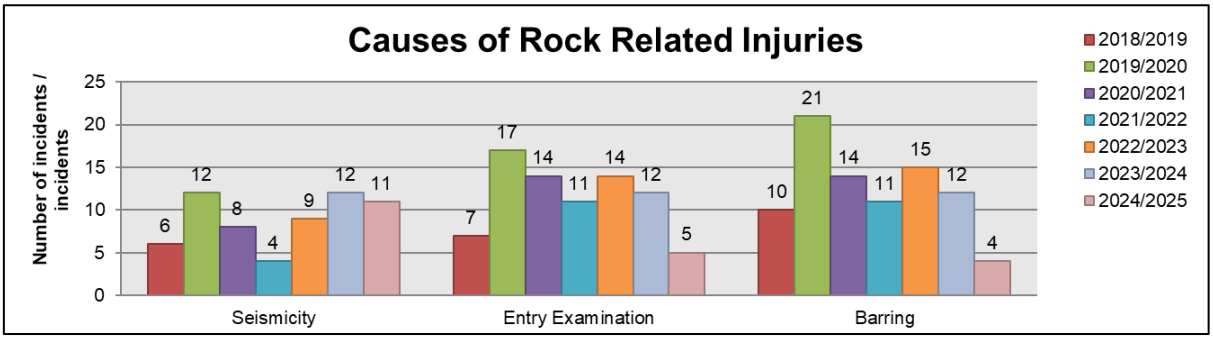


Figure 6. Rock-related Injuries (van Heerden, Kusasalethu Fall of Ground Stats, 2025)

The introduction of permanent areal coverage mesh means that most of the stoping area has areal coverage except for the area from the previous day's blast advance and creates additional cover for the night shift cleaning crews. This leads to less time that the crews must spend barring the panel, because they must only bar the area exposed by the blast advance. The entry examination is also conducted in a panel that has areal coverage, hence less opportunity of being exposed to a FOG.

The Implementation process of Blast-on mesh at Kusasalethu

The operation revisited the adoption process with assistance from the Minerals Council adoption team and implemented the 16-step adoption process at the time. Consultations were held with all the various stakeholders, and underground visits were conducted at Masimong one of Harmony's mining operations in Welkom, Free State. On completion of the aforementioned process, a relevant product was selected which complied with the specifications set out by the company, to hold a 500kg mass with a maximum deflection of 400mm. The product selected was made from high-tensile steel, with a tensile strength of 12.5kN with a blasting cable, and the design of the product ensured that it could withstand the impact of the blast.

Thereafter, training was conducted for every stoping crew on the mine. Upon completion of the training, underground on-the-job coaching was conducted, and the product was rolled out systematically over three months from June 2020 to September 2020. The impact of the newly rolled-out blast-on mesh was followed a reduction in the incidents related to gravity-induced falls of ground. The overall trend for falls of ground incidents and accidents is downward, showing a positive result from the correctly implemented blast-on mesh.

Case studies

Following the full implementation and roll-out of permanent blast-on mesh, several incidents have occurred where, if the blast-on mesh was not installed, a loss of life may have occurred, a lost-time injury may have been a reportable incident or worse. Discussed below are two such examples where, if it was not for permanent areal coverage, the outcome may have been significantly worse.

Case study 1

The incident occurred during the morning shift at 10:26 am on the 9th of April 2023, where five employees were injured when a seismic event with a local magnitude of 1.0 occurred. The employees suffered various injuries, but no one lost their lives. Of the five injured employees, 2 were trapped following the FOG. Following the incident, an in-loco investigation was conducted, and some of the findings are listed below:

- At the time of the incident, support was being installed, including a new installation of permanent blast-on mesh.

- The FOG was significant at the top of the stoping panel and became less severe towards the toe. The fall of ground was large with a total combined mass of 88 tonnes.
- The seismic event was a crush-type event, with the failure (nodal) plane aligning with the face of the panel.
- During the underground investigation and subsequent surface interviews the Team Leader of the crew stated that "if it was not for the blast-on mesh being in place they would never have been able to rescue the Rock Drill Operator as he would've been completey engulfed by the fall of ground".

Without the blast-on mesh being in place regarding this particular incident the outcome may well have been a loss of life.

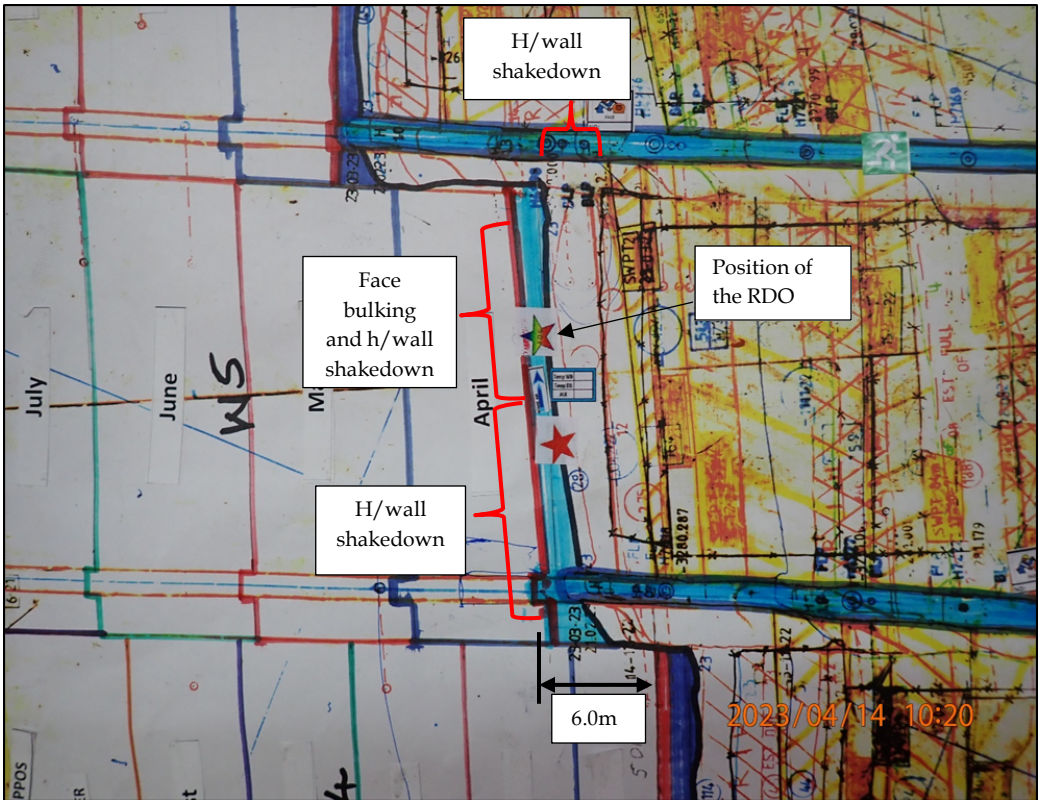


Figure 7. Plan view of the panel in which the incident occurred (van Heerden, 109-40 West 5 - Fall of Ground Incident, 2023).



Figure 8. Position from where the rock drill operator was rescued.

Case Study 2

A rock-related incident occurred at 09:41 on the 7th of February 2025. A seismically induced fall of ground occurred, which trapped an employee. The local magnitude of the event was 1.7, and fortunately, the employee an RDO, was only trapped for a short period. If it were not for the blast-on mesh, the outcome could have been different. Some of the findings during the investigation are listed below:

- The lagging panel had been started up late, which influenced the mining layout.
- The seismic event was a complex-type event, with the failure (nodal) plane aligning with the abutment created with the leading panel to the north.
- In the area where the fall occurred, the steel netting was held in place by two elongates, which prevented further unravelling of the hanging wall.

Potentially life-threatening fall of ground was limited to a lost-time injury.

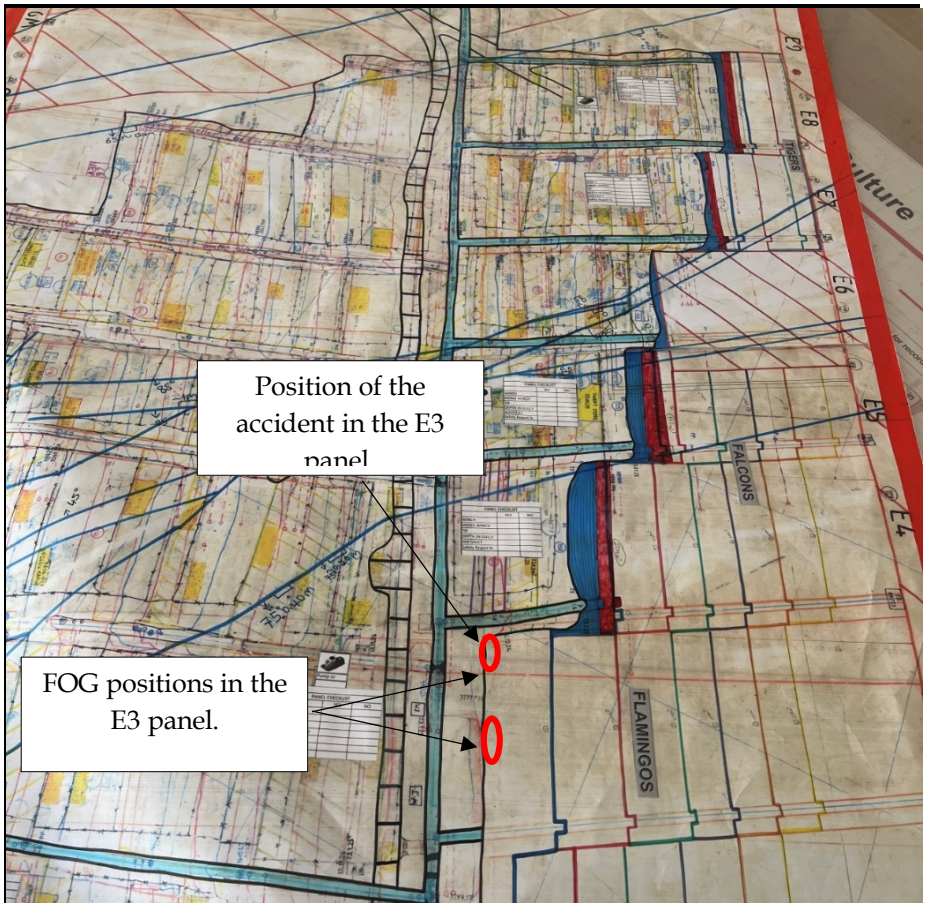


Figure 9. Plan of where the incident occurred (van Heerden, 109-22 E3 Fall of Ground Incident, 2025).



Figure 10. The area from where the rock drill operator was rescued (van Heerden, 109-22 E3 Fall of Ground Incident, 2025).

Advice to industry adopters of blast-on mesh
The experience of rolling out a new product, in this case, permanent blast-on mesh at Kusasalethu mine, has resulted in the following points to note for a successful role-out plan ultimately resulting in the required product being used as intended.

Follow a Proper Adoption Process
- Do not assume end-users will automatically understand and accept the change.
- Adhere to a structured adoption framework such as the **MOSH process.**
- Conduct pilot trials before full-scale implementation.

Involve All Stakeholders from the Start
- Consult mineworkers, supervisors, organised labour, management and the original equipment manufacturer in the process.
- Conduct **site visits** to operations already using BOM to understand best practices with all stakeholders.
- Engage suppliers to ensure the product meets operational needs.

Address Installation Challenges Early
- Ensure proper **training and supervision** for quality installation.
- Consider challenges related to **mesh size, weight, tensioning, and handling.**
- Prevent **damage during cleaning operations** by ensuring proper face cleaning preparation by the production crews and educating crews on proper cleaning techniques.

Integrate BOM into Existing Support Strategies
- BOM should complement other support elements (e.g., **backfill, timber packs and tendons).**
- Ensure that **installation quality is** maintained across different areas of the mine.
- Prevent excessive **lead and lag distances** between supported and unsupported areas.

Ensure Compliance with Standards
- Permanent support must be installed **according to design specifications.**
- Regular **audits and inspections** should be conducted to prevent deviations.
- Address **non-conformances** in real-time to maintain effectiveness.

Plan for Change Management
- Develop a **realistic rollout blueprint** with clear timelines and responsibilities.
- Provide **ongoing coaching** and reinforcement training for underground crews.
- Monitor performance indicators to assess **BOM effectiveness over time.**

Learn from Incident Investigations
- The case studies in the reports should show that BOM helped **reduce injury severity.**
- Even with BOM, **seismicity and incorrect support practices** still posed risks.
- Use lessons from incidents to **continuously improve the support system.**
- Highlight how BOM **reduces fall-of-ground injuries** and enhances safety.
- Use real-world case studies to demonstrate **life-saving potential.**
- The blast-on mesh performance is dependent on the permanent support keeping it in place.

CONCLUSION

The implementation of permanent blast-on-mesh at Kusasalethu Gold Mine stands as a compelling testament to the life-saving potential of proactive and well-structured ground support strategies in deep-level mining. The mine's transition from temporary to permanent areal coverage, driven by both internal commitment and industry-wide safety imperatives, has demonstrated a reduction in the frequency and severity of fall of ground incidents. Real-world case studies underscore how blast-on-

mesh not only limits injury but also prevents fatalities, even in the face of seismic activity. The success at Kusasalethu highlights the critical importance of following a structures adoption process, involving all stakeholders, and continuously learning from incidents to refine and improve support practices. As the mining industry continues its journey towards zero harm, Kusasalethu's experience offers a valuable roadmap for the effective and sustainable integration of innovative support technologies.

ACKNOWLEDGEMENTS

I wish to express my gratitude to the following organizations and people who contributed to this paper:
1. Harmony Gold Mining Company Limited.
2. Geobrugg Southern Africa

REFERENCES

Handley, M. F., de Lange, J. A., Essrich, F., & Banning, J. A. (2000). A review of the sequential grid mining method employed at Elandsrand Gold Mine. *The Journal of The South African Institute of Mining and Metallurgy*, 157-168.

Harmony Gold Mining Company Limited. (2023). Kusasalethu Mandatory code of practice to combat rockfall and rockburst accidents in tabular metalliferous mines. Harmony Gold Mining Company Limited.

Harmony Gold Mining Company Limited. (2025, 03 02). Retrieved from Harmony Gold Mining Company Limited: https://www.harmony.co.za/operations/south-africa/underground/kusasalethu/

Jooste, Y., & Malan, D. (2015). Rock engineering aspects of a modified mining sequence in a dip pillar layout at a deep gold mine. *The Journal of the Southern African Institute of Mining and Metallurgy, 115*, 1097-1112.

Minerals Council South Africa. (2025, 3 1). *Mine Occupational Safety and Health*. Retrieved from www.mosh.co.za: https://www.mosh.co.za/all-categories?task=download.send&id=2054:the-state-of-falls-of-ground-south-african-mining-industry&catid=527

Minerals Council South Africa. (2025, February 28). *Mining Industry Occupational Safety and Health.* Retrieved from www. kosh.co.za: https://www.mosh.co.za/all-categories?task=download.send&id=2004:permanent-workface-areal-mesh-adoption-process&catid=514

Minerals Council South Africa. (2025, February 28). *Mining Industry Occupational Safety and Health.* Retrieved from www.mosh.co.za: https://www.mosh.co.za/all-categories?task=download.send&id=2054:the-state-of-falls-of-ground-south-african-mining-industry&catid=527

Sims, G., Anabalón, J., & Dornbierer, U. (2019, March). MESHA® Installation Handler for MINAX® Mesh USER MANUAL.

van Heerden, R. (2022). *The practicality of using rock mass classification in a narrow tabular orebody at depth.* MSc Dissertation: The University of the Witwatersrand.

van Heerden, R. (2023, 4). 109-40 West 5 - Fall of Ground Incident. *Harmony Gold Mining Company - Kusasalethu In House Fall of Ground Report*.

van Heerden, R. (2025, 2). 109-22 E3 Fall of Ground Incident. *Harmony in House Fall of Ground Report.*

van Heerden, R. (2025, 2). Kusasalethu Fall of Ground Stats.

Do underground excavations mined by non-explosive mining techniques require less support than when mined by blasting? A challenge to rock engineers to review support design practice

R.G.B. Pickering, D. Arnold, J. Porter

Rock Eater (Pty) Ltd, South Africa

In a paper by Olsson *et al,* from the Swedish Rock Engineering Research Unit and entitled 'What Causes Cracks in Rock Blasting', presented at EXPLO 2001 they concluded that:

- Shock waves are mainly responsible for crack lengths in the remaining rock walls.
- Gases are responsible for moving the rock.

It is a given that explosives, by definition, create shock waves, non-explosive mining does not create shock waves. In this paper the authors will:

- Consider the current support design methodology for hard rock underground excavations.
- Investigate the work done to quantify the extent of rock fracturing caused by blasting.
- Provide visual evidence of how excavations mined non-explosively have weathered the ravages of time.
- Identify possible benefits of non-explosive rock breaking to mining (and other) operations.
- Raise the question of how to design support in non-explosively mined excavations

INTRODUCTION

Mining soft rock such as coal, salt and potash, benefitting from new innovations, moved from drilling and blasting in the latter half of the twentieth century, to effective soft rock cutting or ploughing methods of mineral extraction. The corresponding increase in both safety and productivity can be demonstrated with statistics from the British coal mining industry where between 1947 and 1994 (a major period of change due to coal cutting) productivity increased from 270 to 6216 tons per man year. Fatalities were also substantially reduced; with production increasing from 0,35 to 21,5 million tons produced per fatality.

The development of tunnel boring machines (TBMs) also dates from the 1950s and 1960s where their application has mainly been in civil projects. There have been TBMs used in mining but not extensively. It is not the purpose of this paper to discuss productivity or other performance issues related to the different mining machines discussed in this paper but to focus on how excavations created by non-explosive methods withstand the passage of time.

The destructive nature of blasting with explosives, which is the norm in most mining operations, can, and generally does, result in serious damage to the rockmass surrounding that being excavated; while cutting methods, such as boring and wire-lines, inflict little peripheral damage.

The damage caused during explosive rock breaking results from an initial shock wave that fractures the rock, followed by expansion of these fractures by gas pressure. Of course, this damage is not limited to the fractures induced by the shock wave, but also to any and all local pre-existing discontinuities and flaws in the rock.

Literature Survey of Rock Damage
Much of the literature dealing with blast damage concerns establishing the depth of disturbance in crystalline rock using techniques such as electrical resistivity, fluid percolation rates, and seismic tomography. Because they are unable to specifically determine the physical nature of the disturbances, these techniques, while very useful for estimating the potential for 'leakage' of contaminants in nuclear waste disposal facilities, are not germane to general South African mining requirements.

Much less literature deals with actually measuring fractures and discontinuities present in the surrounding rockmass. Methods of visualising hidden rockmass structure include the use of radar, laser and ultra-sonic technology, and, a great deal more fittingly, the application of visual inspection and mapping procedures to exposed rock surfaces and to images obtained from inside suitably positioned boreholes using cameras and photographic recordings.

Although it lacks the ability to actually 'see into' the rockmass, and is innately qualitative rather than quantitative, simple visual inspection and rating of the remaining rock surfaces of an excavation is the easiest way of monitoring inherent and mining-induced rock damage. For example, in the case of smooth-blasting, simply comparing the lengths of half-barrels remaining after the blast with the length of peripheral holes drilled can provide a qualitative damage rating.

Simple visual inspection of the quality of excavation walls leaves no doubt about the stark differences in damage inflicted by conventional straight blasting, cushion- or smooth-blasting and cutting or boring respectively. Some commentators venture to estimates that damage resulting from boring is between 30% and 50% of that due to drilling and blasting. How this translates into their respective support requirements is less easy to establish and requires either quantitative assessment or a trial-and-error approach. Needless to say, the trial-and-error approach is not deemed a suitable method in today's highly risk-averse mining environment – and rightly so.

Although the literature survey failed to provide definitive information about the nature and extent of induced rock wall damage likely to be found in local environments, it did unequivocally point the way towards how this information should be sought. In essence, it will be by means of applying the techniques that will provide information about the actual nature, frequency, orientation and extent of discontinuities in the rock in which non-explosive methods are to operate.

These techniques will include the likes of radar and ultrasound, but in the final analysis, the most important will be the visual inspection and mapping of the discontinuities exposed in rock surfaces and in suitably positioned boreholes. This will lead to the execution of the work that will be required for comprehensive geotechnical evaluation of the pre-existing and post-excavation nature of the host rockmass.

Rockmass Environment
In addition to the destructive power of the breaking methodology itself, the extent to which these various excavation techniques are able to inflict peripheral damage on the surrounding rock is heavily dependent upon the in situ strength and nature of the rockmass being broken.

This, in turn, is controlled by a host of factors.

- First, of course, is the intrinsic strength of the intact rock, which can vary from extremely strong to very weak. But perhaps of more impact is the structure that determines the in situ strength of the rockmass. The nature, strength and frequency of pre-existing discontinuities and flaws are generally of overriding importance. These include features such as bedding, jointing, fractures, faulting, dykes, shear zones and so on. The orientation of these discontinuities with respect to each other and with respect to the excavation walls is also of vital importance.
- Next, but often also of profound importance, is the stress regime, both virgin and induced, be it as a result of external mining activities or that associated with the excavation itself. The sum of these various stress sources gives the total stress environment in which excavation takes place. Once again, in addition to its magnitude and nature, the orientation of the stress field

with respect to the excavation is of vital importance. An example is tunnel boring where high vertical stress causes 'dog-earing' in the sidewalls – see Figure 4.

- Included in the influence of stress on the overall integrity of the rockmass, it must be noted that blast fractures extend preferentially in the direction of the highest stress vector, as that is the favoured direction of tensile failure. Thus, in a high vertical stress regime (the norm), blast fractures will predominate and will extend to greater distances into the hangingwall, which is not the best situation from a stability, rockfall and support perspective.
- Finally, the nature, size, shape and orientation of the excavation itself influences the nature and degree of damage sustained as a result of these various causes. Sometimes excavations are designed and shaped to mitigate the effects of the factors mentioned above, but this is not always possible and is seldom implemented for reasons of practicality.

The Measurement of Damage Induced by Explosive Blasting

Much has been researched and written about actual explosives and their ability to break rock. Much less has been documented about the ability of explosives to damage the rockmass surrounding mining excavations. Most of the quantitative assessment deals with aspects such as its permeability rather than its support requirements. These tend to be more qualitative rather than quantitative.

Of particular interest is determining the severity and the depth of this damage into the rock wall. Several such determinations have been documented (eg., Sperry *et al.*, 1979, Singh 1992, Pusch *et al.*, 1992). They predominantly take the form of the depth of damage vs the size of the charge. Understandably, they confirm the intuitive assessment that the heavier the charge the greater is the depth of damage. A particularly good example of this work is shown in Figure 1. This relationship appears to be logarithmically proportional in the ranges considered, as can be seen in Figure 1.

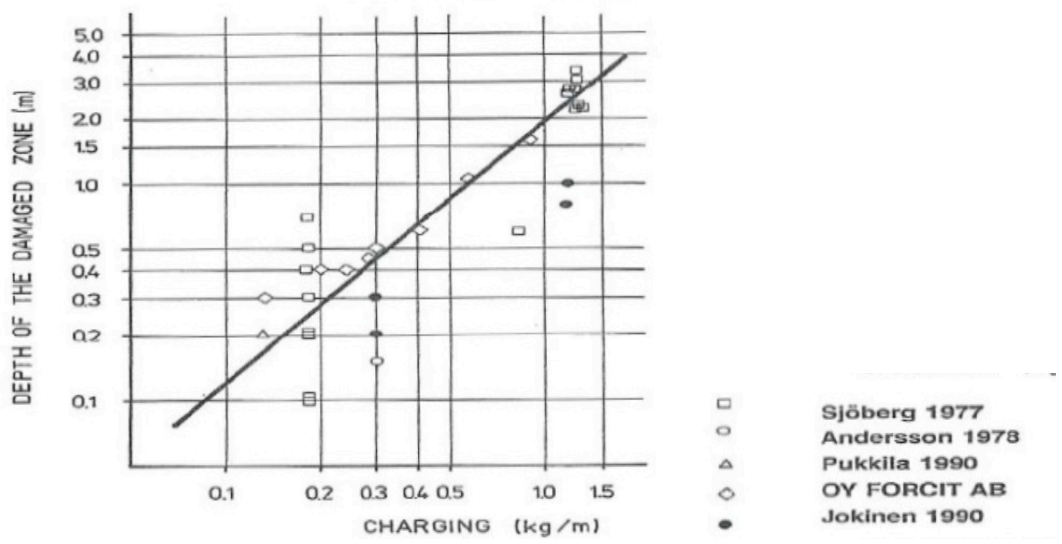


Figure 1. Compilation of empirical data on the influence of charge on the depth of the blasting-disturbed zone in granite (Pusch and Stanfors 1992).

A maximum damage depth of between 2 m and 3 m is suggested for traditional explosive charges in conventional (3 m x 3 m) tunnel blasting operations in hard rock conditions. But this is obviously also a hugely variable function of the in-situ strength of the rockmass and other factors, as mentioned above, and does not explicitly quantify the degree or intensity of damage. For example, much related information has been derived from work in Scandinavian and other nuclear waste repositories sited mainly in crystalline granites, by measuring hydraulic conductivity and electrical resistivity. These can thus be regarded as leaning toward the ultra-conservative. The depth of blast damage in the variety of conventional tunnels in South African mining operations is largely unrecorded in literature available in the public domain, but this is not to say that it does not exist.

In a later summary report by Saiang 1992 of work carried out between 1991 and 2003 and intended to present a synopsis of the important factors that influence the development and extent of the blast induced damage zone, nature and characteristics of blast-induced fractures. It must be emphasised that perimeter blasting techniques, particularly smooth blasting, were employed in all the tests. The thickness of the observed damage ranged between 0,1 and 1,2 m. An average damage thickness of 0.5 m was observed in the Kiruna and Malmberget mine drifts. Figure 2 demonstrates the fracture depth analysis procedure. After blasting, sections of the sidewall were cut out with diamond saws and dye penetrant applied to show up the fractures. The depth of diamond saw cuts was 500 mm.



Figure 2. Dye penetrant in the magnetite ore and waste rock.

It would have been nice to do comparative studies where the rock was mined non-explosively but the authors could find no such information in the literature.

Rock Quality Determination and Rockmass Classification

Rockmass Classification Methods

Terzaghi and latterly Deere (1963) started the ball rolling by considering uniaxial compressive strength (UCS) measurement, Schmidt hardness and Taber hardness determinations. This was soon followed by the development of the simplest rock classification system: rock quality designation (RQD) which classifies the rock mass on the basis of the frequency of discontinuities (usually, but not solely) identified in borehole core. RQD proved to be so useful that it has become an integral part of all the increasingly elaborate classification systems that followed.

This was followed by Barton's NGI Q-System in 1974. This was originally developed primarily for Norwegian applications but has subsequently become the most universally applied classification method. It attempts to refine RQD by not only accounting for, but also characterising the discontinuities (primarily joints), and incorporating evaluation of the stress state. As can be seen in Figure 3 the process involves mapping the rock face to arrive at a rock mass quality Index, inputting the span of the excavation to determine bolt spacing and bolt length.

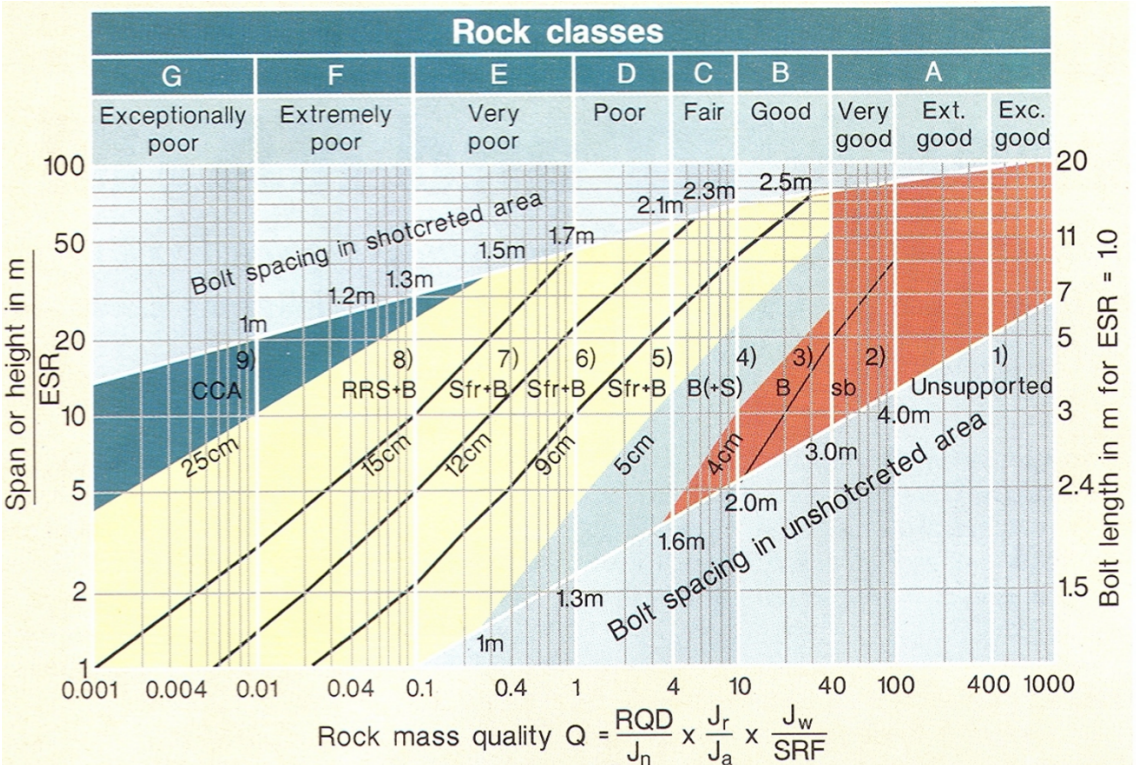


Figure 3. Rock mass quality index.

Bieniowski (1976) and Laubscher (1977) developed rock mass rating systems for evaluating the likely conditions to be encountered in railway and similar tunnels. These systems were further refined for mining operations by the introduction of adjustments relating to factors such as discontinuity orientation and weathering, induced stresses and blasting damage, to become the mining rock mass rating system. This system is capable of use not only for tunnel support design, but also for determining cavability and fragmentation in massive mines, and pit slope angles in open pit operations. What has not been considered is whether the excavation was mined explosively or non-explosively.

The primary output of these systems is a characterisation of the condition of the rockmass under consideration in a range of categories (usually about nine) ranging from exceptionally poor conditions to exceptionally good conditions. Using some measure to account for the dimensions or size (usually span or height) and the purpose (importance and life) of an excavation (usually a tunnel), the support requirements are charted. These are normally of a general nature (suggesting a range of support classes) rather than being dogmatically specific.

Concluding Remarks and Comment Regarding Induced Damage and Support

While there has been a lot of work done on relating rockmass conditions to support requirements, and some work done on rockmass conditions found to be associated with various excavation methods, there is little or no definitive published public domain documentation linking excavation method with support requirements, other than in the broadest of terms based upon the commentator's experience or knowledge of case histories.

There is universal agreement regarding the fact that support requirements for bored tunnels are much less than those for drill and blast tunnels, but once again, nothing specific, although, as mentioned, some commentators venture estimates of between 30% and 50%. The variables appear to be much too broad to allow definitive inferences to be drawn regarding support requirement differences, other than the general, visually-based conclusion made by observers that rock conditions, and thus support requirements, are vastly different between the various excavation methods currently in use.

While common sense says that if rockmass conditions are measurably influenced by the excavation method, and that support requirements are measurably influenced by rockmass conditions, then support requirements must also, ipso facto, be measurably influenced by excavation method. But there does not appear to be any specific documented analysis or comparison in the literature of the different support requirements for directly comparable drill and blast vs tunnel-bored situations.

It appears, thus, in the absence of recorded data, or even adequate anecdotal evidence, regarding the support implications of various excavation methodologies, definitive conclusions about the performance of non-explosive rock breaking in respect of reducing support demand will need to be based upon the measurement of the two important variables (rock condition and support demand) in comparable situations when and while non-explosive rock breaking methods are actually being tested and commissioned.

TBM mining in South African Mines

In 1976 Anglo American Gold Division installed a Wirth TBM in #2 Shaft at Free State Geduld mine on 53 level. The machine holed after a total of 1150 m in February 1979. (Marlow *et al.*, 1983) This tunnel was designed to intersect the Dagbreek fault, where ground conditions were known to be poor. At some time, a parallel tunnel was constructed and used as a haulage and the TBM tunnel was used as a return airway.



Figure 4a & 4b. Bored TBM tunnel return airway after seismic event – minimal damage.



Figure 5a. Neighbouring access haulage after seismic event and 5b after remediation work.

In 1999 there was a seismic event along the Dagbreek fault and the Council of Scientific & Industrial Research was invited to review the impact. The top two pictures in Figure 4a & 4b show very little damage to the TBM tunnel, a little 'dog earing' but no substantial damage. In the upper left picture (Figure 4a) can be seen two roof bolts and there is no frittering of the rock around the load-bearing plates. This clearly demonstrates that there have been absolutely no rock falls. The lower two pictures were taken from the adjacent haulage tunnel driven using drill and blast. The picture in Figure 5a is particularly revealing with substantial lengths of roof anchors exposed by rocks loosened by the seismic event.

It is reasonable to conclude that the blast-induced fractures, interacting with the rock structure, caused a substantial loss of integrity of the surrounding rock and that this was exploited by the seismic event.

Robbins Mobile Miner

In 1983 Mount Isa mine recognised the need for a continuous mining machine which could economically cut hard rock. In 1983 a joint project was undertaken by The Robbins Company and Mount Isa Mines Limited to develop and trial a machine suitable for cutting hard rock (see Figure 6). In September 1984 the Mobile Miner was installed at Mount Isa in the S60 decline to mine an excavation 6,5 m wide and 3,7 m high, with a flat floor. The total length of the drive was 1145 m of which 80% was in hard abrasive quarzitic rock. Over 450 m of the decline was mined by the Mobile Miner, however, reliability was an issue and the balance of the drive was completed by drill and blast. (Grills *et al.*, 1986)



Figure 6. Robbins Mobile Miner.



Figure 7. Tunnel excavated at Mt Isa Mine by Robbins Mobile Miner.

In a paper published at the 13th CMMI Congress the authors' state:

> *The resulting excavation is smooth-walled with no blasting damage to the surrounding rock. This provides a safer working environment than does conventional drill and blast development mining. Ground support requirements are considerably reduced.*

The author had the pleasure of driving down that decline about ten years after it had been mined and in the bored tunnel very little had changed with rock bolts showing no frittering around the collar and no indication that there had been any rockfalls in the bored tunnel. In the length of the tunnel driven by drill and blast the roof bolts were exposed. Unfortunately, there was no information available either from my visit or from the paper as to by how much the ground support requirements were reduced.

A second-generation machine, the MM130 was installed at Pasminco and excavated more than 1400 m in ground having a UCS of between 150 and 250 MPa.

Sandvik Stoping Rock Cutter

The picture below in Figure 8 is of Sandvik's MN330, until recently in operation at Mototolo Platinum mine. The initial version of this stoping machine was developed over 20 years ago and operated in both UG2 at Lonmin and Merensky at Impala. Over 7 100 m² were mined in these early trial (Pickering *et al*., 2006).

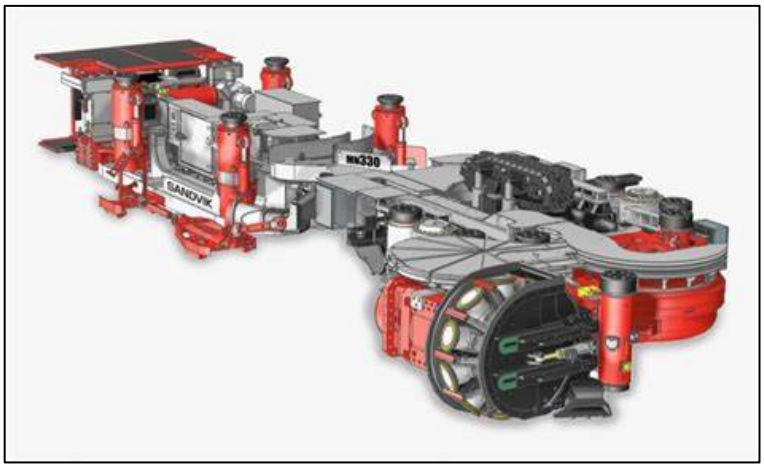


Figure 8. Sandvik's MN330 recently in operation at Mototolo mine.



Figure 9 & 10. Ground mined by Sandvik MN220 and platinum stope mined by blasting.

The picture in Figure 9 shows the hanging cut by the MN220. Bolts were installed as per the mines standard pattern. In the total area mined of 7100 m² not a single rock fell from the hanging. The picture

on the right, Figure 10, was also taken in a platinum mine. The exposed roof bolts were installed to hold up a section of hanging, however, during a subsequent blast that section of hanging fell. Blasting damages the surrounding rock.

Various hard rock tunnelling machines have been developed for mining – Komatsu, Wirth, Epiroc and Sandvik with Caterpillar also developed hard rock cutting machines, mainly for development excavations. There has also been some very successful use of TBMs for access development. The focus of the original equipment manufacturers has been on driving the quest to mine hard rock excavations continuously and consequently non-explosively.



Figure 11 & 12. Komatsu MC51 and Wirth Mobile Tunnel Miner.

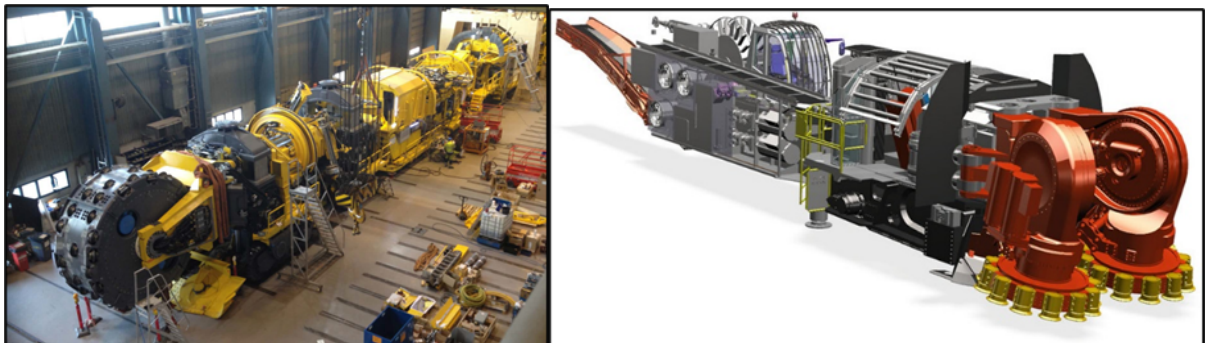


Figure 13 & 14. Epiroc Tunnelling Machine and Sandvik RMDS Undercutter.

For narrow stoping applications as well as the Sandvik MN320 there is the Epiroc Mobile Miner 22H, the Caterpillar Hard Rock Miner HRM 220 and the Placer Dome Mini Mole. At Rock Eater the authors are commercialising controlled foam injection (CFI) as a low capital and operating cost method of rock breaking. A further benefit of CFI is that it can be as flexible as short hole drilling and blasting; whereas cutting machines have limited excavation flexibility.

It can't be long before we have successful non-explosive tunnelling and possibly stoping machines. How and on what engineered basis are we going to design the support systems for these future innovations?

Benefits of non-explosive mining

Imagine one day that an underground hard rock mine did NOT require conventional explosives to conduct mining activities such as shaft sinking, ore reserve development and production stoping. Consider the additional advantages to all of the secondary and peripheral blasting that is often required to create space for infrastructure and the provision of services, if explosives are not required for this work. What would this mine look like?

Explosives are such a critical item that they deserve their very own Act of Parliament: The Explosives Act, Act No. 15 of 2003. There many layers of regulation covering the Built Environment and the chemicals sector that by their sheer number cannot be considered herein.
However, we are interested in the Mine Health and Safety Act, 1996 (Act No. 29 of 1996) and Regulations. After a preliminary review of this document a few points are worth noting just to illustrate a point (it is far from exhaustive):

- The word explosive is mentioned 254 times,
- The word blasting is mentioned 168 times,
- Both enjoy their own definitions,
- Individuals cannot hold any position of responsibility without being the holder of a Blasting Certificate,
- The whole mining extractive process, infrastructure and system is designed around a cycle determined by the need to clear the mine to allow blasting to take place and the harmful products thereof to be cleared.

We need to go no further to illustrate that a mine designed WITHOUT the need to accommodate explosives would be very different across all aspects of mine design, extraction, logistics, staffing, safety and health and environmental compliance. In underground coal mines where the coal is extracted by cutting there are always requirements for blasting for dealing with dykes and other hard rock structures. The requirements for the use of permitted explosives are even more onerous.

Legislative Benefits
Compliance with Environmental Regulations. Non-explosive mining methods often align better with environmental regulations aimed at minimising land disturbance, air pollution, and water quality degradation. This compliance can lead to smoother permitting processes.

Reduced Liability. By avoiding explosives, companies reduce their liability concerning potential accidents, injuries, or damages caused by blasts. Explosives are one of the leading causes of underground fires. This can lead to fewer legal disputes and lower insurance premiums.

Stricter Noise and Vibration Control. Many jurisdictions have stringent laws regarding noise and vibration levels in mining operations. Non-explosive methods typically produce less noise and vibration, making it easier for mining companies to operate within legal limits.

Healthier Underground Environment. Needless to say, the reduction of fine dust particles and noxious gasses can only improve the life expectancy of the mine worker. Despite enormous strides in personal protective equipment, individual compliance remains an issue – far better then to remove the source of the risk.

Community Acceptance. Mining operations using non-explosive techniques are often viewed more favourably by local communities and stakeholders, enhancing public relations and community support. Positive public perception can ease the path for approvals and permissions.

Scalability of Operations. As regulations on explosive use might differ by region, non-explosive techniques offer flexibility, enabling operations to scale according to legislative requirements without the added complexity of managing explosive materials.

Skills Interoperability. Common training platforms can be developed that allow employees to easily move between operations, covering different mining methods in different regions as commodity price and orebody life change over time.

Geotechnical Benefits
Improved Ground Stability. Non-explosive methods typically minimise ground vibrations, which can lead to better overall stability of the surrounding rock formations in the underground workplaces and

will lead to more stable pillars. This is particularly beneficial in sensitive areas or unstable geological formations.

Selective Extraction. These methods allow for more selective and precise extraction, enabling miners to target specific ore zones while leaving surrounding rock undisturbed. This precision reduces waste and decreases the volume of material that requires processing. Specifically, the options for resue stoping a all inclinations improves dramatically with the ability to mine on a continuous basis without flyrock.

Greater Control Over Geological Structures. Non-explosive mining methods afford better control over the resulting geological changes. This can be vital in maintaining the integrity of adjacent structures such as mines, tunnels, and other infrastructure.

Enhanced Resource Recovery. The more uniform fragmentation of rock associated with non-explosive methods can lead to higher recovery rates of valuable minerals and materials, as the intact rock can often be processed more effectively than fragmented rock. Two specific examples:

1. The value of mining gemstones is significantly improved if the larger carat stones are not shattered by the explosive shock.
2. In precious metals, losses can be significant at the workplace if fragmentation is too fine, liberating metal particles that get lost in the footwall.

Improvements to mine call factor translate directly to improved profits or extended life of mine.

Adaptability to Diverse Geological Conditions. Non-explosive techniques can be adapted to work efficiently in various geological settings, including soft sediments, fractured rock, and urban areas where traditional blasting would be impractical or hazardous.

Minimised Groundwater Contamination. By avoiding vibrations and shockwaves from explosions, there is a reduced risk of fracturing permeable layers that could lead to contamination of groundwater resources, safeguarding water quality.

In summary, the legislative and geotechnical benefits of non-explosive mining bolster its appeal as a viable and sustainable alternative to traditional methods, promoting safety, compliance, and responsible resource management. All the above have been amply demonstrated when the underground coal mining industry of the 1940s and 1950s converted to coal cutting.

Financial Aspects of non-explosive mining

Reduced Operational Costs. Non-explosive methods often require less material handling compared to traditional blasting, leading to cost savings in transporting and processing. With the ability to selectively extract materials, non-explosive mining generates less waste, reducing disposal costs and environmental rehabilitation expenses.

Decreased Insurance Premiums. The inherent risks associated with explosives – such as accidents, injuries, and property damage – can lead to higher insurance premiums. Non-explosive operations reduce these risks, often resulting in lower insurance costs.

Fewer Regulatory Costs. Non-explosive mining methods may face fewer regulatory hurdles, which can lead to reduced costs associated with compliance, monitoring, and reporting. By adhering to stricter environmental standards with non-explosive methods, companies can avoid potential fines and penalties associated with violations of environmental laws.

Increased Productivity. Non-explosive techniques such as mechanical and hydraulic mining can lead to faster and more efficient operations, increasing the overall volume of material extracted in a given timeframe. By avoiding the need to conduct safety checks and clear areas after blasting, non-explosive mining can decrease operational downtime, enhancing overall productivity and facilitate continuous operations.

Enhanced Resource Recovery. The ability to selectively mine allows for the extraction of higher-grade ore with less dilution, maximising revenue from the produced materials. With less fragmentation, the extracted materials may require fewer processing steps, reducing costs associated with grinding, classification, and refining.

Long-Term Sustainability. By minimising land disruption, non-explosive methods can lead to lower costs associated with rehabilitating mined areas, as less damage to the ecosystem simplifies restoration efforts. Companies that adopt non-explosive mining are often able to operate longer in a given area due to less detrimental environmental impact, higher extraction ratios and contributing to sustained revenue over time.

Community and Stakeholder Relations. With reduced environmental threats and potential community disruption, companies using non-explosive mining can foster better relationships with local communities, which may lead to additional financial incentives and support. Being perceived as environmentally responsible can facilitate easier access to financing and investment from stakeholders increasingly concerned with sustainability and corporate social responsibility.

Technological Integration. Non-explosive methods often involve the use of advanced machinery and technologies (e.g., automated excavation), which, while initially costly, can lead to long-term savings through enhanced efficiency and reduced labour costs. Many non-explosive techniques can be adapted to various mining scenarios without significant additional investment, allowing companies to pivot quickly, based on market demands. This also applies to the skills needed to support that pivot.

Market Competitiveness. As markets increasingly favour sustainable practices, companies employing non-explosive methods may achieve a competitive edge, potentially commanding higher prices for their products.

In summary, the financial or cost benefits of non-explosive mining encompass a wide range of factors, from reduced operational costs and increased productivity to long-term sustainability and community relations. These advantages contribute to better financial performance and a more resilient business model in the mining industry.

Similarly, in the civil construction industry where there are increased requirements for excavations in urban environments and increased restrictions on the use of explosives, non-explosive rock breaking presents multiple benefits, enhancing safety, efficiency, environmental protection, and community relations. These advantages position the industry for more sustainable development practices and improve overall project outcomes.

COMMENT AND DISCUSSION

The reality, in mining, is that the mining methods practised are based on maximising the benefit of the technology employed. For example, panel length of 30 m because that is the length that can be cleaned by a scraper winch in one shift. Introducing new technology successfully requires that the mining method and layout be changed to extract the maximum benefit from the new technology. The use of explosives is one of the most onerous restrictions on the mining process in South Africa; its use forces the mine to be fully evacuated before the blast and for some time afterwards to allow the dust and noxious fumes to be cleared. This has a major impact on mine productivity. In a recent paper by Fenn, when he was Technical Project Manager at Sibanye Gold, he concluded. *The total time allocated to value-adding activities a combination of drilling and blasting is 6 hours and 30 minutes representing 27% infrastructure utilisation.* (Fenn 2016.)

In this paper we have attempted to describe the potential benefits that are available from non-explosive mining with particular reference to safety and rock support. We can see from the visual evidence

presented, especially from the TBM tunnel at Free State Geduld mine, that ground mined non-explosively is substantially more stable and safer than that mined with explosives. We have conducted an extensive review of the literature to determine if there is a standard procedure for designing rock support where the rock has not been subject to blast damage. We have been unable to identify such a procedure.

The original equipment manufacturers and mining companies have invested millions in developing hard rock mining machines with a number of them undergoing extensive trial periods. The advantages of non-explosive based mining methods have been adequately identified. The challenge now is to quantify those benefits. As we said in the title of this paper, we would like to use this opportunity to present a challenge to rock engineers to review support design practices that are suitable for rock that has not suffered from blast damage.

REFERENCES

https://rockeater.co.za/about/

Adams DJ, Gay NC, Cross M. Preconditioning – A Technique for Controlling Rockbursts. *3rd International Symposium on Rockbursts and Seismicity in Mines, Kingston, Ontario*. 1993

Adams G.R., Jager A.T. Petroscope Observations of Rock Fracture Ahead of Stope Faces in Deep Gold Mines. *SAIMM Journal*. 1980

Autio J, Malmlund H. Properties of Excavation Damaged Zone Caused by Drill and Blast Excavation. *ISRM / SAIMM Technology Roadmap for Rock Mechanics*. 2003

Barker D.B., Fourney WL, Dally JW. Blasting Parallel Hole Cuts with Fracture Plane Control. *NSF Report NSF-RA-770067*. 1977

Barker D.B., Fourney WL, Dally JW. Fracture Control in Tunnel Blasting. *NSF (National Science Foundation)*. 1978

Bieniawski ZT. Rock Mass Classification in Rock Engineering. *Symposium: Exploration for Rock Engineering, Johannesburg* 1976.

Bilim N, Ozkan I, Gokay MK. Determination of Discontinuities at (sic) Rock Materials by Electrical Resistance Method. *Proceedings of the 7th Regional Rock Mechanics Symposium, Ankara*. 2002

Brinkmann J. Rockbreaking Characteristics of Various Explosives in Small Diameter Holes. *5th Annual Research Symposium on Explosives and Blasting Techniques, New Orleans*. 1989

Chitombo G., Scott A. An Approach to the Evaluation and Control of Blast Induced Damage. 3rd International Symposium on Rock Fragmentation by Blasting – *Fragblast '90, Brisbane, Aus*. 1990

Cloete D.R., Collett P.A.G., Cooke N.G.W., Jager A.J., White A.J.A. The Nature of the Fracture Zone in Gold Mines as Revealed by Diamond Core Drilling. *Association of Mine Managers of South Africa, Papers and Discussions*, 1972-1973

Dally J.W., Fourney WL. Fracture Control in Construction Blasting. *NSF/RANN Report, NTIS No. PB264-132*. 1976

Emsley S, Olssen O, Stenberg L, Alheid HJ, Falls S. Study of Damage and Disturbance from Tunnel Excavation by Blasting and Tunnel Boring. *Swedish Nuclear Fuel and Waste Management Company (SKB), Tr-97-30*. 1997

Fenn A. G. Unlocking value by reorganizing the operational value chain through modernization. *Mining Innovation Conference. SAIMM* 2016

Forsyth WW. A Discussion of Blast Induced Overbreak Around Underground Excavations. *4th International Symposium on Rock Fragmentation by Blasting – Fragblast 4, Vienna, Austria*. 1993

Forsyth WW. Blast Induced Overbreak Around Underground Excavations. *4th International Symposium on Rock Fragmentation by Blasting – Fragblast 4, Vienna, Austri*a. 1993

Grady D.E., Kipp M.E. Dynamic Rock Fragmentation. *Fracture Mechanics of Rock, (ed. BK Atkinson, Academic Press, London)*. 1987

Grills R.G., O'Neil T.J., Howarth D.F. Introduction of the Robbins mobile miner to Mount Isa Mines Limited. *13 CMMI Congress – Mining* 1986

Hagan T.N. Controlling Blast Induced Cracking Around Large Caverns. *ISRM Symposium, 'Rock Mechanics Related to Caverns and Pressure Shafts', Achen, WGer*. 1982

Jowsey M., Yu T., Croxall J., Petigrew M., Fisher. Development of a Calibration Technique for HDR Loose Rock Detection System. *93rd AGM, Canadian Institute of Mining and Metallurgy, Vancouver, Canada.* 1991

Kilerbrant M, Norrgart T, Jern M. The Size of the Damage Zone in Relation to the Linear Charge Concentration for Rock Fragmentation by Blasting. (ed. Sanchidrian), *Taylor and Francis Group, London.* 2010

Laubscher DH, Geomechanics of Jointed Rock Masses – Mining Application. *Transactions of the Institute of Mining and Metallurgy (Section A), Volume 86.* 1977

Ladegaard-Pederson A., Fourney W.L., Dally JW. Investigation of Pre-splitting and Smooth Blasting Techniques in Construction Blasting. *University of Maryland Report to the National Science Foundation*. 1974

Lizotte YC, Mohanthy B, Paventi M, Scoble. The Measurement and Control of Blast Damage.
SME Annual Meeting, Phoenix, Arizona. 1996

Marlowe A.C., Littleford I., Grun M. Tunnel Boring in South African gold Mines. *Proceedings from Rapid Excavation and Tunnelling Conference*, Chicago, Illinois – June 12 – 16 1983

Martino JB, Chandler NA. Excavation-Induced Damage Studies at the Underground Research Laboratory. *International Journal of Rock Mechanics & Mining Sciences*. 2004

Mathias A.J. re-split Blasting Research. AIME 1965

Olsson O, Emsley S, Bauer C, Falls S&D, Stenberg L. A Study of the Zone of Excavation Disturbance for Blasted and Bored Tunnels. *Swedish Nuclear Fuel and Waste Management Company (SKB), Stockholm.* 1996. Volumes 1-3, International Cooperation Report ICR-96-03.

Pickering, R.G.B. The optimization of mining method and equipment. *International Platinum Conference 'Platinum Adding Value'.* The South African Institute of Mining and Metallurgy, 2004.

PICKERING, R., SMIT, A. and MOXHAM, K. Mining by rock cutting in narrow reefs. *International Platinum Conference 'Platinum Surges Ahead'*, The Southern African Institute of Mining and Metallurgy, 2006.

Pusch R., Stanfors R. The Zone of Disturbance Around Blasted Tunnels at Depth. *Int.J. Rock Mech. Min. Sci. & Geomeck. Abstr. Vol 29, No 5, pp. 447-456*, 1992

Ricketts T.E. Estimating Mine Damage Produced by Blasting. *4th Mini-Symposium on Explosives and Blasting Research, Society of Explosives Engineers, Anaheim, California*. 1988

Sellers EJ. Controlled Blasting for Enhanced Safety in the Underground Environment. *SAIMM 2nd Hardrock Safety Conference 4-5Aug'10, Emperors Palace, Jhb*. 2010

Saiang D. Blast Induced Damage: A Summary of SVEBEFO Investigations. *Luleå University of Technology*. September 2008

Singh S.P. Alleviation of Blast Damage in Underground Mines. *SME*. 1992

Singh SP. Investigation of Blast Damage Mechanisms in Underground Mines'. *Sudbury Mining Research Directorate Research Report* (1992).

Singh SP. 'Prediction and Determination of Explosive Produced Damage. *4th International Symposium on Rock Fragmentation by Blasting – Fragblast 4, Vienna, Austria*. 1993

Singh SP. Damage-Causing Potential of Different Explosives. *9th Conference on Explosives and Blasting Research, International Society of Explosives Engineers, San Diego, California*. 1993

Singh SP. Blast Damage Control During Underground Mining. *20th Conference on Explosives and Blasting Technique, International Society of Explosives Engineers, Austin, Texas*. 1994

Singh SP, Lamond RD. Investigation of Blast Damage and Underground Stability. *12th Conference on Ground Control in Mining, OSMRE*. 1994

Spathis A.T., Blair DP, Grant JR. Blast Damage Assessment of Rock Using the High Frequency Crosshole Seismic Method. *2nd International Symposium on Rock Fragmentation by Blasting, Keystone, Colorado*. 1987

Sperry P.E., Fourney W.L., Thompson D.E., McKown D.F. Controlled Blasting Experiments in Square Tunnels. *RETC* 1976

Sutherland M. Improving Mine Safety Through Perimeter Blasting at Inco Ltd's Thompson T-3 Mine. *9th Underground Operators Conference, Sudbury, Ontario, Canada*. 1989

Read RS. 20 Years of Excavation Response Studies at AECL's Underground Research Laboratory. *International Journal of Rock Mechanics & Mining Sciences*. 2004

Tsoutrelis CE, Kapenis AP, Theoghili CN. Determination of Blast Induced Damage in Pillars by *Seismic Imaging. Explo '95 Conference, Brisbane*. 1995

Worsey P. Measurement of Blast Induced Damage in Wall Rock for a Selection of Underground Perimeter Blasting Techniques. *Society of Blasting Engineers, San Diego, California*. 1985

Yu T.R., Henning J.G., Croxall JE. Loose Rock Detection with Infrared Thermography. *CIM Bulletin, May 1990* - Underground Mining. 1990

Application of Flac3D to analyse the effects of mining-induced stresses on the behaviour of drawpoint pillars: A case study of a long-hole open stoping mine in Zimbabwe

A. Velempini

Gwanda State University, Zimbabwe

The shift from shallow depth to medium depth operations at mine A resulted in geotechnical challenges. The stability of underground excavations is now more stress control. On 30L, which is 1092 m below surface, the stability of drawpoint pillars is a cause for concern due to pillar size with respect to the depth of operation. The drawpoint pillar width is 7 m, which may be too small to withstand the overburden and mining-induced stresses. Sidewall scaling of drawpoint pillars is observed after every blast in the cone level. This challenge indicates the progressive degradation of the pillar strength, imposing a threat to the safety, stability and overall effectiveness of mining operations. In this paper, the author utilises the Itasca software to analyse the stability of the drawpoint pillars and to compute the average pillar stress for the expected maximum loading. Empirical approaches will be used in conjunction with numerical modelling in order to get the best results. The main purpose of this paper is to confirm the viability of the current pillar size at lower mining depths. The design factor of safety was used to judge the stability of several drawpoint pillar sizes, and to decide upon an optimum size for different mining depths.

Keywords: numerical modelling, drawpoint pillar, factor of safety, spalling, induced stresses, pillar stability

INTRODUCTION

Mine A is a gold mine located in southern Zimbabwe, employing the long-hole open stoping mining method. The mine strives to become the biggest gold producer in the country and is mined at increasing depths. The input of a rock engineer is necessary during this process.

Drawpoint pillars are unmined portions of ground left in-situ along the haulage drift and drawpoint crosscuts to support the roof and overburden. The static loading on the pillars at mine A is a function of the overburden, a haulage drift, a series of drawpoints and an advancing open stope. No support is currently being installed in the drawpoints, except in the roof of the haulage drift. Physical underground observations indicated the occurrence of sidewall scaling and spalling of drawpoint pillars during cone level development. As the mine now operates in the medium depth environment, stress-induced fracturing is a major factor affecting the stability of underground excavations. This phenomenon calls for the implementation of appropriate support systems and pillar designs to ensure safe and cost-effective mining operations. The analysis and revision of the current drawpoint pillar size is the focus of this paper. A sensitivity study involving the Hoek-Brown parameter for intact rock (mi) was also conducted to determine its influence on the plastic zone around the drawpoints.

The underground mine geometry is depicted in Figure 1. The colour distribution in the model represents the following mine excavations:

- Green – existing stopes
- Yellow and red – planned stopes
- Yellow, pink and white background – planned pillars
- White background – unmined solid ground

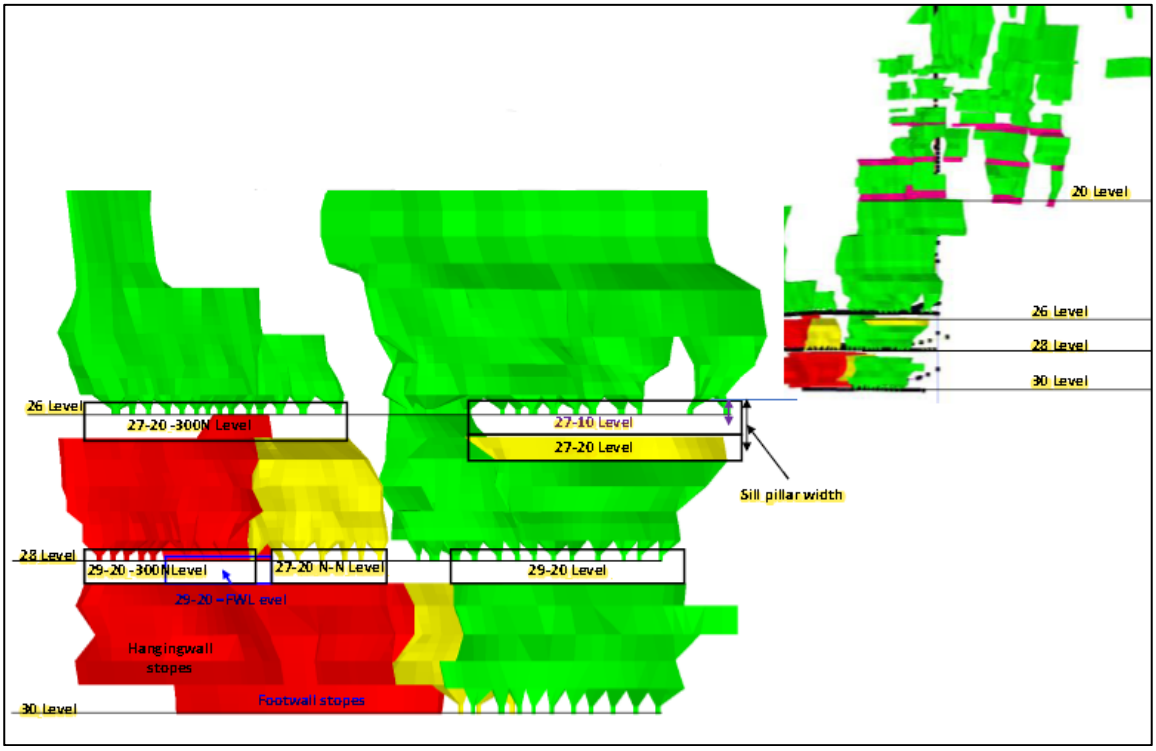


Figure 1. Mine A overall underground mine geometry.

Geometry construction

The Flac3D building blocks tool was used to construct a model resembling the geometry studied. Figure 2 presents the model geometry (left) and a plan view of the drawpoints layout (right).

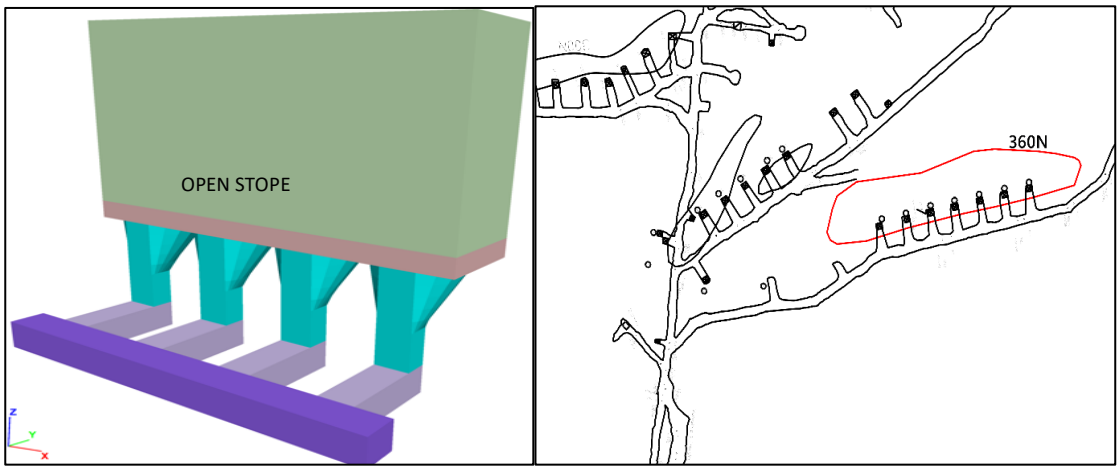


Figure 2. Model geometry showing an open stope, cones, drawpoint crosscuts and a haulage drift (left). Plan view of the drawpoints layout with the 360N orebody outline in red (right).

The mine utilises 3 m x 3 m haulage drifts and a series of 3 m x 3 m drawpoint crosscuts spaced at 10 m centre-to-centre, leaving behind 7 m wide pillars. The 360N drawpoints were the focus of this paper. The steeply dipping 360N orebody is relatively regular and 30 m wide with a strike length of 105 m. The haulage drift is positioned 10 m far from the orebody, with the cone level located at 10 m above the drawpoint crosscuts. A half symmetry geometry, symmetrical on the x-plane, was built to improve computational speed. Roller boundary conditions were applied on the plane of symmetry and artificial boundaries were located 70 m, far from the area of interest.

Geotechnical assessment
The 360N orebody at mine A is hosted in mafic tuff characterised by high intact strength uniaxial compressive strength (UCS) = 180-205 MPa). The rock mass in the area studied appears to be homogenous, to an extent, with no major geological structures nearby. Laubscher's mining rock mass rating (MRMR) of between 45 and 52 reflects a fair quality rock mass. A geological strength index (GSI) of between 60 and 70 was recorded for the mafic tuff, indicating a good geological strength. The rock quality designation was rated between 80% and 90%, with an average joint spacing greater than 0.6 m recorded from scanline surveys. The hydrogeological nature of the area is dry conditions. Judging from this assessment, the rock mass quality was classified as fair to good.

Numerical modelling
Flac3D is a finite difference program that uses an explicit formulation to solve 3D geotechnical problems. The continuum modelling program was used to simulate the current pillar size at 30L. The simulation was first run with the elastic constitutive model to validate the model geometry, and to identify zones of high stress and strain concentrations that needed finer zoning.

The model was then run in stages using the Mohr-Coulomb constitutive model. The 'zone relax excavate' command was used to simulate the gradual excavation of the stages, in order to prevent instability during the excavation. The first stage involved the sequential excavation of the haulage drift and drawpoint crosscuts, followed by the gradual excavation of the cone level and the open stope. Contours were plotted to analyse the stress and strain distribution in the drawpoint pillars. Plasticity indicators were also plotted to observe the types of failure mechanisms occurring in the plastic zone. After simulating and analysing the pillars at 30L, various pillar sizes were simulated at different mining depths. FISH code was used to compute the factors of safety for the respective sizes.

Numerical modelling input properties
Rocscience's Roclab software was used to obtain geomechanical properties for input into the numerical model. The Roclab software scales down the intact rock properties to represent the in-situ rock mass strength. Table I presents the data used as input into the Roclab analysis.

Table I: Roclab input parameters

Input parameter	Value
Uniaxial compressive strength (UCS) [MPa]	180
Geological strength index (GSI)	66
Hoek-Brown intact rock constant (mi)	13
Young's modulus (Ei) [GPa]	100

The UCS, GSI and Ei data were obtained from mine A's rock mechanics department reports. As the mi parameter was not readily available, a median value for tuff was estimated from the Roclab charts. Figure 3 presents the output data obtained from the Roclab analysis.

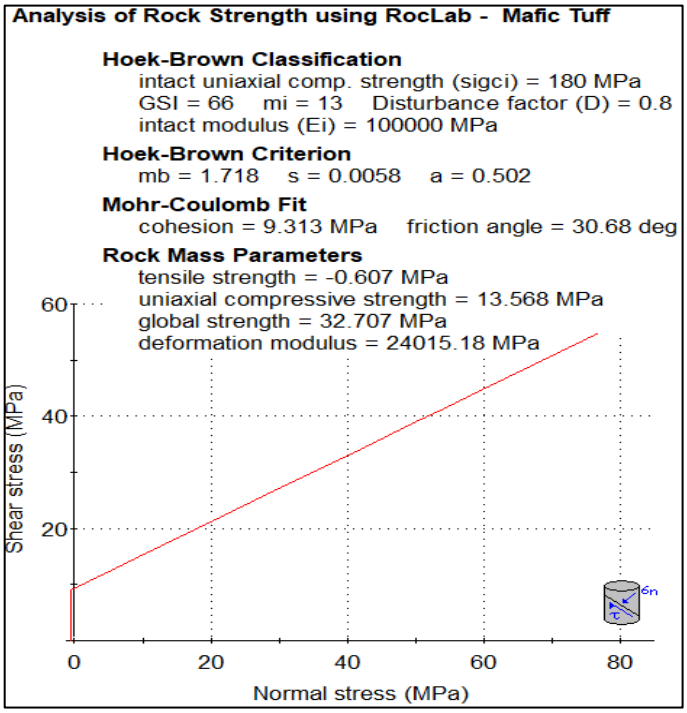


Figure 3. Rock mass properties used in numerical modelling.

The Roclab software best fits a Mohr-Coulomb curve to the Hoek-Brown curve to obtain the cohesion, friction angle, deformation modulus and tensile strength values for the rock mass. Additional input data included a density of 2750 kg/m^3 and a Poisson's ratio of 0.25. The stress field was measured in the problem area using the wireline over-coring method. The horizontal to vertical stress ratio (k-ratio) was established to be 0.78.

Sensitivity study

Engineering design should not be solely based on a single study. Rather, engineering design should be based on a sensitivity study in which significant parameters are varied over a specified range, whilst monitoring the influence on output (Hoek, 2006). Laboratory tested data for the mi parameter was not available during the time of this study and charts in the Roclab software provided a range of 8 to 18 for mafic tuff. The uncertainty in the mi parameter called for a sensitivity analysis to be conducted. Several Flac3D simulations were run with the parameter varied systematically over the provided range, with the plastic zone of the drawpoint pillars periodically monitored.

Empirical approaches

A hybrid approach which incorporates both empirical methods and numerical modelling should be adopted to get the best results (Le Bron, *et al.*, 2024). To use numerical models for future designs, they need to be validated first and this can be done using empirical methods (Bosman & Enslin, 2024). The pillar strength was calculated using the Hedley and Grant formula and the absolute pressure sensor (APS) was obtained from numerical modelling. The pillar strength was used together with the numerically computed APS to calculate the factor of safety (FoS).

Pillar strength determination

The pillar strength is known to be dependent on the strength of the pillar material and the dimensions of the pillar. The strength of the mafic tuff rock mass was determined by adjusting Laubscher's rock mass rating to derive the design rock mass strength (DRMS). A high number of secondary blasts are conducted at mine A with an average of 11 blasts per shift being recorded. These secondary blasts cause damage to drawpoint pillars, thereby contributing to the pillar instability. The MRMR takes into account

of this effect and adjusts the rock mass strength accordingly. A DRMS of 61.12 MPa was calculated for the mafic tuff rock mass at mine A, which is 34% of the UCS.

The Hedley and Grant pillar strength formula was used to calculate the drawpoint pillar strength. The method is based on the pillar width-to-height ratio and the rock mass strength of the pillar material. The empirical pillar strength formula is given by equation 1 as follows.

$$P_s = K * \frac{{W_{eff}}^{0.5}}{H^{0.75}} \quad [1]$$

Where:
Ps = pillar strength [MPa]
K = downgraded UCS/DRMS [MPa]
W_{eff} = effective pillar width [m]
H = pillar height [m]

The drawpoint pillars at mine A have a rectangular cross section, and the effective pillar width was calculated using equation 2. The current drawpoint pillars are 7 m wide and 10 m long.

$$W_{eff} = \frac{4*A_p}{C_p} \quad [2]$$

Where:
W_{eff} = effective pillar width [m]
A_p = pillar area [m^2]
C_p = pillar perimeter [m]

Using an effective pillar width of 8 m, a height of 3 m and a DRMS of 61.12 MPa, a pillar strength of 75.83 MPa was calculated for the current pillar size at 30L.

Factor of safety
The recommendation of a drawpoint pillar size for lower mining depths was based on the design FoS. A FoS is defined as the ratio of pillar strength to APS using equation 5.

$$FoS = \frac{P_s}{APS} \quad [3]$$

The minimum FoS used for pillar design at mine A is 1.6. A pillar with an FoS less than 1.0 is deemed to have failed. A pillar with an FoS in the transition zone (between 1.0 and 1.6) is deemed to be unstable, though it will not fail in its own right. FISH code was used to compute the numerical APSs and the FoSs for various pillar sizes at different mining depths.

Support considerations
Drawpoints are subjected to a range of loading conditions during their lifespan. At mine A, extraction levels are developed in advance of stoping operations, and as a result excavations are initially subjected to development stresses. Stress adjustment due to extraction level development results in the transformation of the surrounding rock mass from elastic zone into plastic hardening zone as shown in Figure 4 below. Cone level development, which is the initial stage of stoping operation, increases the intensity of plastic hardening thus the surrounding rock mass will become seismogenic which is associated with tensile spalling (yielding) of excavation sidewalls. Underground observations indicated scaling and spalling of drawpoint sidewalls during initial stoping activities at the cone level. As stoping operations progress, new set of loading conditions are exerted on drawpoint pillars and the surrounding rock mass, particularly from both primary and secondary blasting activities and the highly stressed abutments. At this stage, the plastic hardening zone is now transformed into plastic softening zone which is associated with fractured ground around drawpoints. The surrounding rock mass is now destressed and prone to fall of ground thus ground support has to be installed to provide confinement to both roof and sidewalls of the drawpoints.

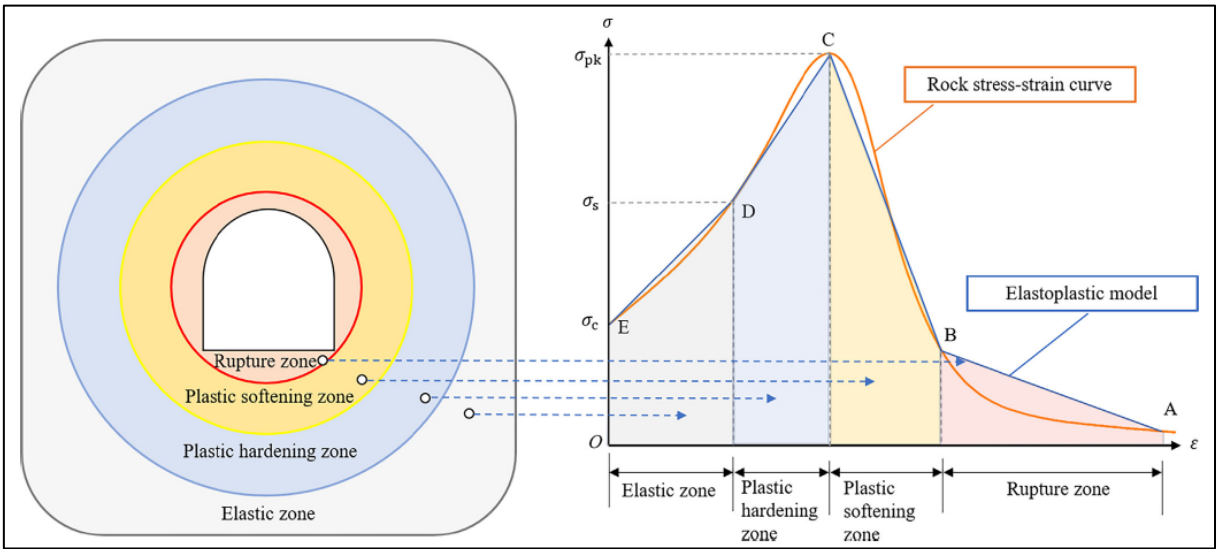


Figure 4. Model of stress adjustment zones of tunnel surrounding rock mass (Weihao, et al.*, 2025).*

Stacey and Stewart (1997) recommended an empirical chart based on the DRMS and stress environment, shown below in Figure 5, for use as a guide on the level of support requirements in drawpoints.

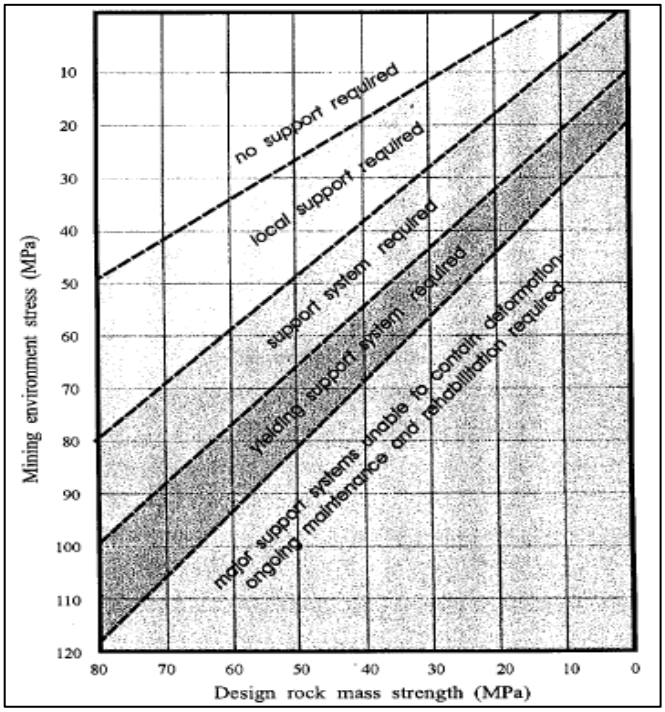


Figure 5. A guide for support requirements in drawpoints (Stacey & Stewart, 1997).

Using the empirical chart with numerical modelling results, a suitable support recommendation was made for the drawpoints at 30L. The support should not only cater for the safety of the development crew, but it also needs to cater for the anticipated changes in the stress field and rock mass conditions as mining advances.

NUMERICAL MODELLING RESULTS AND DISCUSSION

The 30L drawpoints at mine A were developed in advance of stoping operations. The Roclab software estimated the mi parameter value for tuff to be in the range of 8 to 18. The study involved varying the mi parameter systematically over the range, whilst monitoring the changes in the plastic zone around the drawpoints. Stress contours were plotted to analyse the stress redistribution in the drawpoint pillars and plasticity indicators were used to monitor the extent of plastic behaviour around the drawpoints. After analysing the stability of the pillars at 30L, a revised pillar size was recommended for 32L.

State of drawpoints before stoping operations

Footwall excavations are developed in virgin stresses and are later subjected to a changing stress regime as mining takes place (Jager & Ryder, 1999). Under elastic behaviour, high stress concentrations are found in the immediate pillar edges and they are highest at the pillar corners. Figure 6 presents the maximum principal stress contours in plan view for the elastic model (left) and the Mohr-Coulomb model (right).

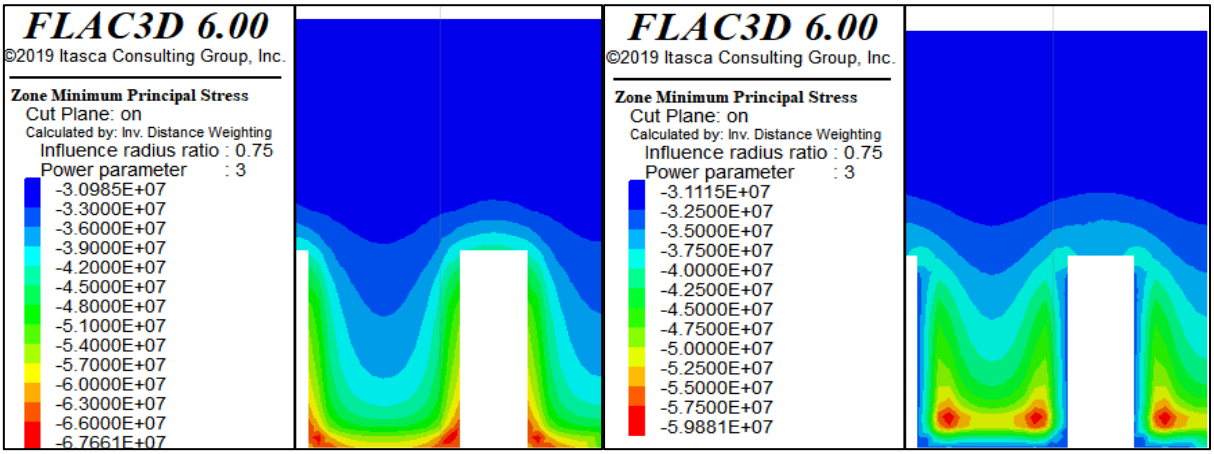


Figure 6. Maximum principal stress for drawpoint pillars. Elastic model (left) and Mohr-coulomb model (right).

The stress contours above indicate load shedding from the pillar corners and edges, due to plastic behaviour which will be later seen in Figure 8. High stress concentrations shifted from the pillar corners back a distance of about 1.5 m into the pillar body. Initially, the corners carried a maximum load of approximately 68 MPa; subsequent shear and tensile failure degraded the load bearing capacity at the corners to approximately 31 MPa. The Flac3D embedded FISH scripting language was used to compute an APS of approximately 44.33 MPa before the commencement of stoping operations. The pillar FoS at this stage was calculated to be 1.71. This FoS is above the recommended minimum design FoS of 1.6, thus the pillars were deemed to be stable before the commencement of stoping operations; though progressive scaling and spalling are likely to reduce the FoS with time.

Maximum shear strain contours in Figure 7 indicate that deformation is highest at the pillar corners where the maximum load was initially carried. High strain gradients are also present on the pillar edges due to unconfinement, but as we move into the pillar body the deformation gradually decreases due to increasing confinement. A strain increment of at least 0.0025 is sufficient to initiate scaling which is shown in Figure 7 by the iso-surface plot in green.

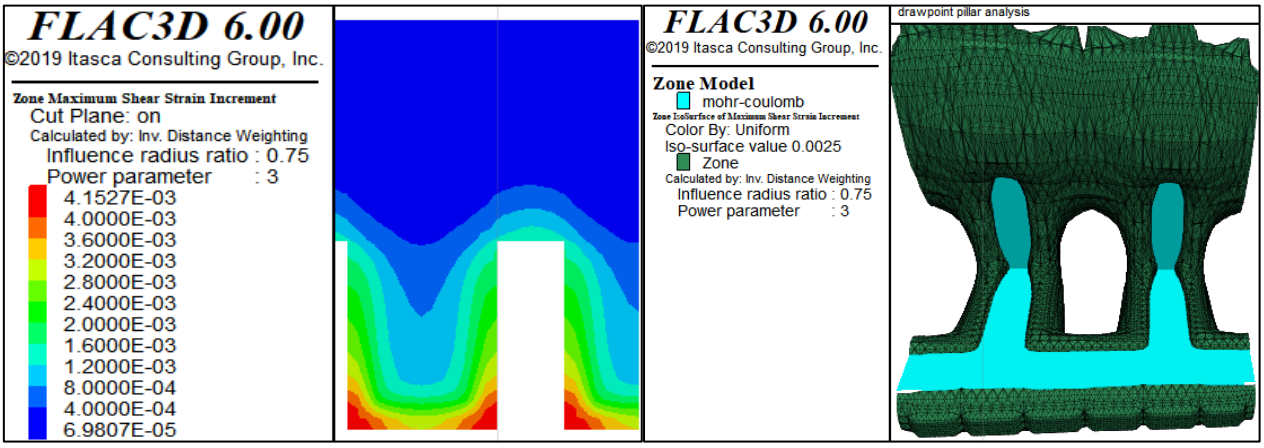


Figure 7. Maximum shear strain increment (left) and iso-surface strain increment = 0.0025 (right). Mi = 13.

Figure 8 shows the plastic zone around the pillars after the development of drawpoint crosscuts and a haulage drift. The plastic zone represents Flac3D zones with a stress state that is tangent to the Mohr-Coulomb failure envelope.

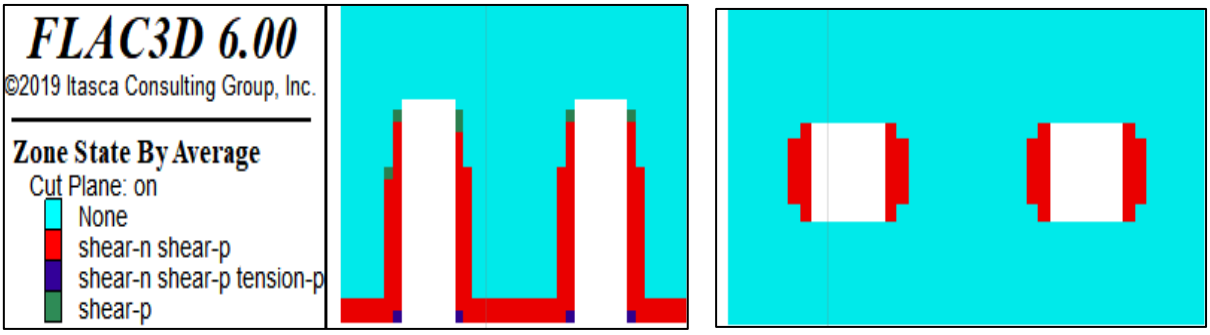


Figure 8. Plasticity state of 7m wide pillars at 30L in plan view (left) and cross section view (right). Mi = 13.

A shear failure mechanism has clearly initiated on the pillar sidewalls prior to stoping operations. The plastic zone around the drawpoints has a depth of approximately 1 m. The transition into the medium depth environment is starting to strain the pillars, loading the sidewalls beyond the elastic limit. The excavation of the drawpoints and haulage drift causes the stresses previously carried by the excavated material to redistribute to the pillar edges. The absolute stresses found on the pillar edges exceed the strength due to low confinement, leading to stress-induced fracturing as physically observed underground. The extent of plastic failure is expected to increase with the advancement of stoping operations at the cone level, giving a rise to hazardous ground conditions in drawpoints. This necessitates the immediate installation of reinforcement of the sidewalls to add confinement to the pillar, thereby increasing its load-bearing capacity and minimising the risk of falls of ground. Reinforcement will also minimise 'self-mining' of the pillar which helps to maintain its size and strength.

State of drawpoints after stoping operations

Stoping operations are at an initial stage at 30L. The advancement of the cone level is associated with sidewall scaling and spalling of drawpoint pillars, as shown by underground observations in Figure 9.



Figure 9. Stress-induced pillar scaling and spalling during cone level excavation.

After simulating the excavation of the haulage drift and drawpoints, the next stage involved the gradual excavation of the cone level and the open stope. The analysis indicated that maximum loading on pillars is expected after the complete excavation of the cone level; subsequent stoping operations will have minimal effect on the stability and loading of drawpoint pillars. Figure 10 shows the maximum principal stress and shear strain contours for the pillars in plan view after stoping operations.

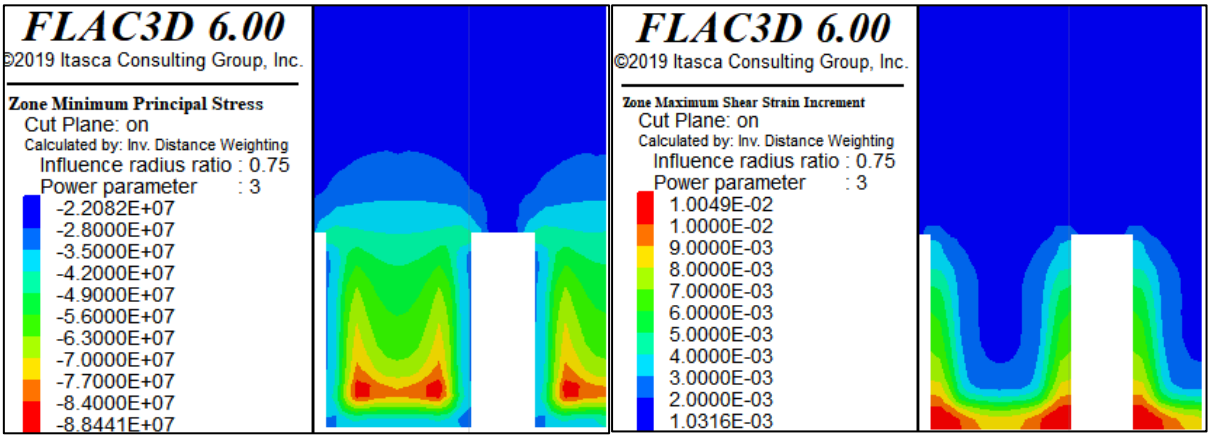


Figure 10. Maximum principal stress (left) and maximum shear strain (right) distribution after excavating the open stope, Mi = 13.

The above contours show an increase in both maximum principal stress and shear strain after the complete excavation of the open stope. The stress contours indicate an increase in the magnitude of stress towards the core of the pillar. Prior to stoping operations, a maximum principal stress of approximately 60 MPa was concentrated at a point located 1.5 m back from the pillar edge, as indicated in Figure 6. Subsequent loading due to stoping operations will increase the stress to a maximum of approximately 88.44 MPa, to a point 2 m back from the pillar edge. The shift in the point of maximum concentration indicates further anticipated load-shedding from the pillar edges due to stresses induced by stoping operations.

Figure 11 shows the stress distribution in the abutment that lies above the drawpoint pillars. The maximum principal stress at the corners of the stope is approximately 3x the virgin vertical stress. There is relatively low stress on the roof of the haulage drift (left) indicating that rock mass has yielded due to destressing (right). A high stress concentration is also present close to the haulage drift footwall causing yielding of the sidewall. Once rock mass is in plastic softening zone, it is prone to rock falls if not supported.

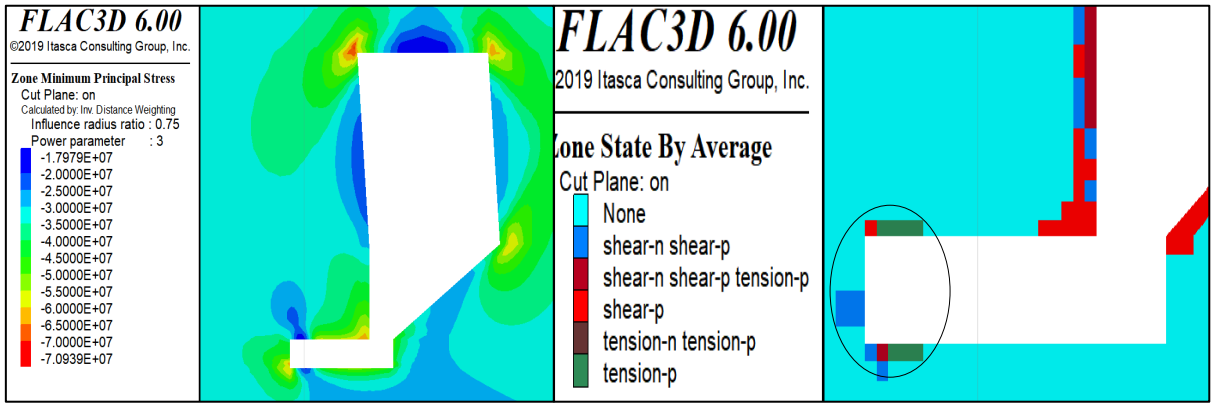


Figure 11. Cross-section through the open stope showing the maximum principal stress distribution in the abutments (left) and the yield zone around the haulage drift (right).

The drawpoints interact with the stress field created by the open stope, resulting in an increase in the APS as indicated in Figure 12. There is a gradual increase in the APS during stoping operations from approximately 44 MPa before stoping.

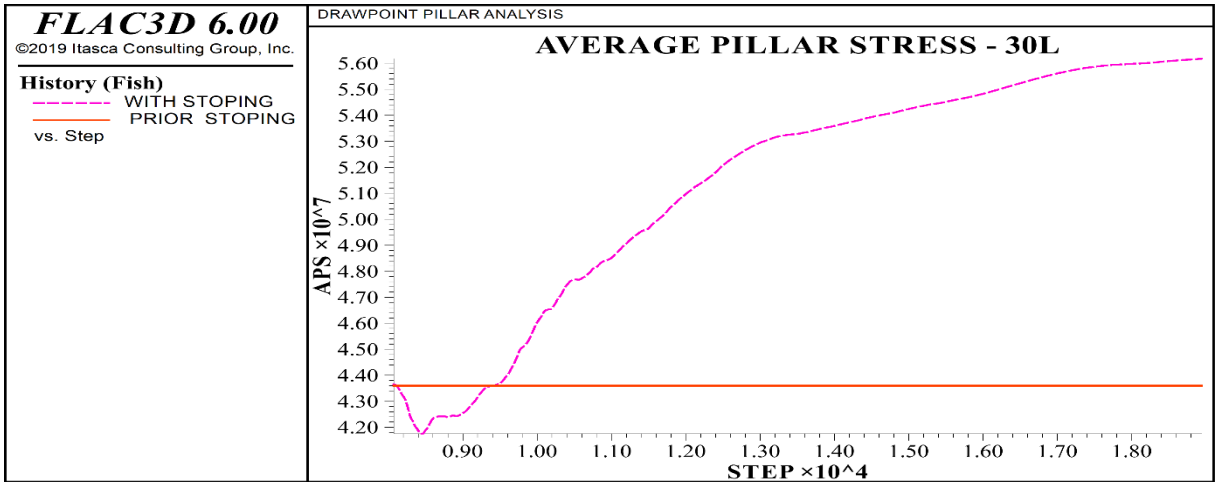


Figure 12. Average pillar stress in 7 m wide pillars at 30L during stoping operations.

An APS of approximately 56 MPa was recorded after the excavation of the cone level in Flac3D. Using the pillar strength of 75.83 MPa calculated from equation 1, a FoS of 1.35 is expected for the drawpoint pillars after the complete excavation of the cone level. This FoS is less than the recommended design FoS of 1.6 at mine A and the pillars will be deemed to be unstable at this stage. The strength-stress ratio (SSR) was used to monitor the diminishing load bearing capacity of the pillars with stoping operations. The SSR is formulated in Flac3D, using the following equation.

$$SSR = \frac{\sigma'_1 - \sigma_3}{\sigma_1 - \sigma_3} \qquad [4]$$

The SSR is used to indicate the current stress state's proximity to failure, in this case the pillars' proximity to failure. Suppose the current principal stresses in the Mohr-coulomb plane are σ_1 and σ_3. By keeping σ_3 fixed, enlarge the Mohr circle so that it is tangent to the failure envelope; the new maximum principal stress is represented by σ'_1 (Itasca Consulting Group, 2024). If a given Flac3D zone representing the pillar is yielding, then SSR = 1 for that zone. Figure 13 shows the mean pillar SSR during stoping operations.

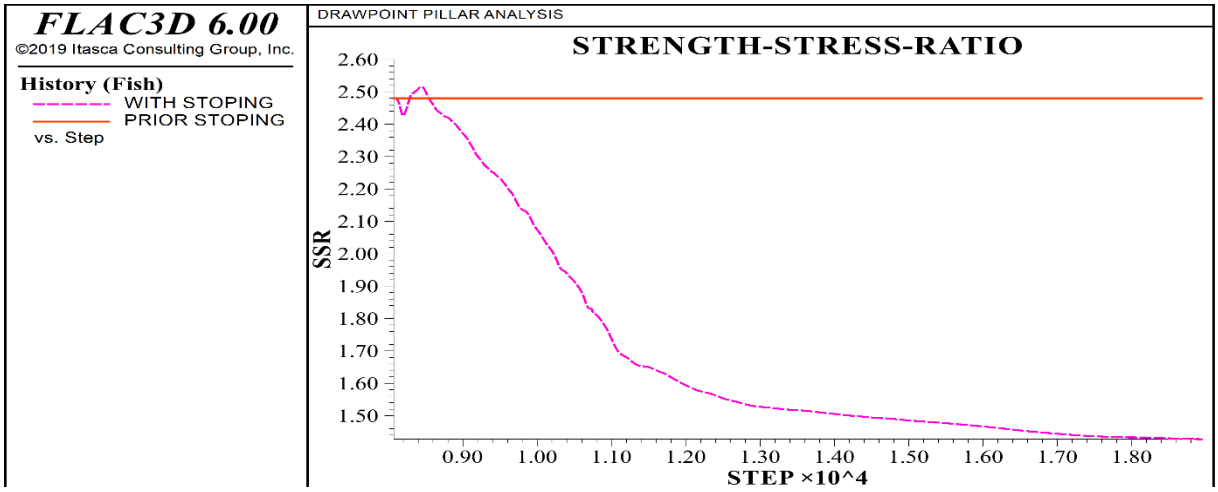


Figure 13. Strength-stress ratio for 7 m wide pillars at 30L during stoping operations.

FISH code was used to sum up the SSR of all zones representing one pillar. The average SSR of the pillar was then computed to be approximately 1.4. The gradual decrease in the SSR from approximately 2.5 (before stoping) down to 1.4 is a result of the expected increase in the APS shown in Figure 12, coupled with a decrease in pillar confinement (σ_3). The reduction in confinement is a result of destressing in the stope floor following the excavation of the cone level, as illustrated in Figure 14.

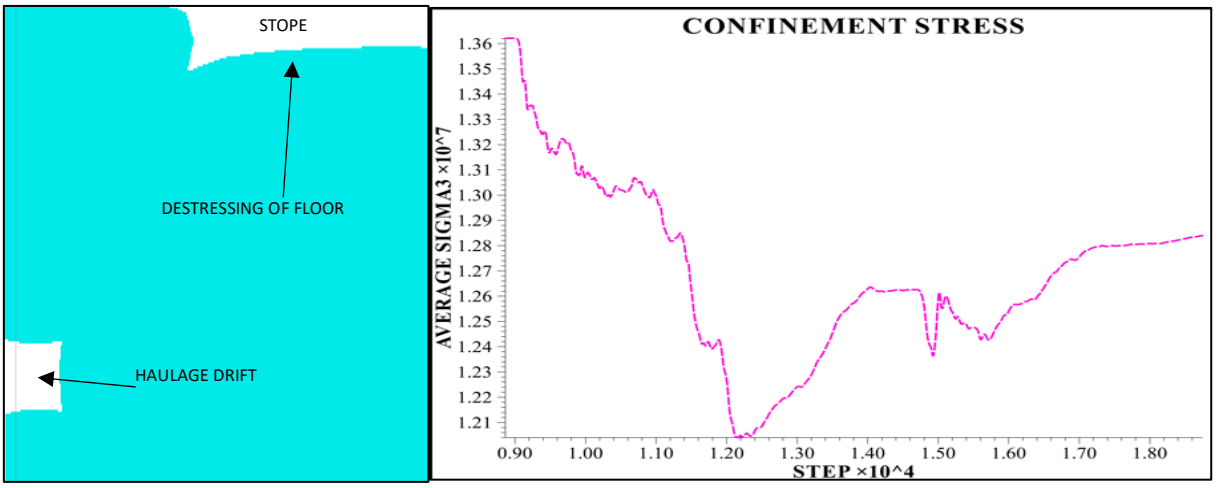


Figure 14. Reduction in the average minimum principal stress in the pillars at 30L. Stope deformed factor: 20.

High confinement stresses are known to build up strength in pillars, helping to limit the extent of plastic behaviour. The numerical modelling results indicate a decrease in the confinement stress coupled with an increase in the APS, resulting in an increase in the plastic zone around the drawpoints as indicated in Figure 15. The confinement in pillars reduced from an average stress of approximately 13.6 MPa to approximately 12.6 MPa after the complete excavation of the cone level.

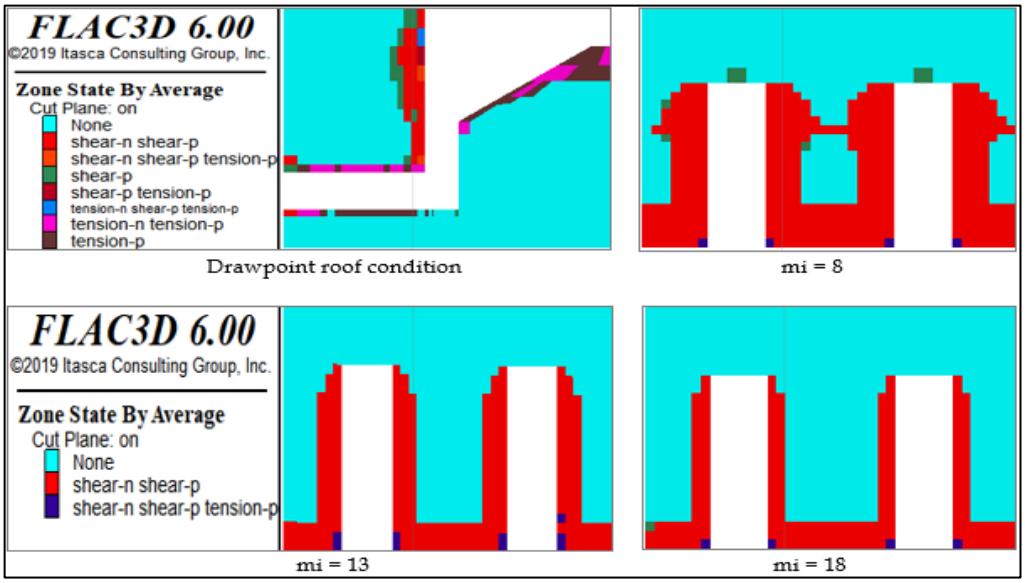


Figure 15. Plasticity indicators for 7 m drawpoint pillars at 30L after stoping operations.

Shear failure has extended further into the pillar sidewalls and tensile failure initiated in the roof of the drawpoints. Prior to stoping, for mi = 13, the depth of shear failure into the pillar body was approximately 1 m. Following the stoping operations, the depth is expected to extend to a point approximately 1.5 m from the pillar skin. Tensile failure is also expected to occur in the roof due to destressing, which will give rise to hazardous ground conditions such as wedge formations in the roof. Therefore, immediate installation of support is necessary before operations commence further in the cone level, in order to minimise the risk of rock falls and to ensure the safety of miners. Adding reinforcement and surface support to the sidewalls and roof will increase the confinement and inherent strength of the pillars, ensuring pillar stability during ongoing stoping operations. The changing extent of the plastic zone around the drawpoints in the sensitivity analysis indicates that the mi parameter has a high influence on the strength of the pillars. The extent of failure has an inverse relationship with the mi parameter, with failure extending to the pillar core for mi = 8. This sensitivity analysis reflects the crucial need to take rock samples for laboratory tests to determine the mechanical properties, and the need to implement pillar monitoring programs in order to validate and calibrate the numerical model.

Pillar size recommendations for lower levels

The 7 m wide pillars have proved to be too small to withstand the overburden and induced stresses. The pillars' FoS of 1.33 is less than the recommended design FoS of 1.6, therefore the pillar size is not recommended for 32L. The pillars should be reinforced and supported to prevent progressive scaling and spalling of sidewalls (time dependent). The confinement will help maintain the pillar size and strength for their operating life.

The pillar sizes listed in Table II were simulated at different mining depths. The pillar strengths for the different sizes were calculated using equation 1, with the APSs computed using FISH code in Flac3D. The pillar strength increases with pillar size, accompanied by a decrease in the APS. As a result, the table shows an increase in the FoS with increasing pillar size.

Table II: Drawpoint pillar factors of safety

Depth [Level]	Drawpoint pillar width (m)			
	7	10	12	14
1015 m [28L]	1.51	1.80	2.02	2.13
1092 m [30L]	1.33	1.66	1.81	1.98
1168 m [32L]	1.22	1.53	1.70	1.83
1245 m [34L]	1.12	1.44	1.59	1.73

The recommended drawpoint pillar width for 32L is 12 m, with an FoS of 1.70. The size is characterised by a higher pillar strength of approximately 89 MPa and a lower APS of approximately 51 MPa, compared to a 7 m wide pillar. Figure 16 shows the approximate APSs for a 12 m wide pillar (before and during stoping) and a 7 m wide pillar after complete stoping operations at 32L.

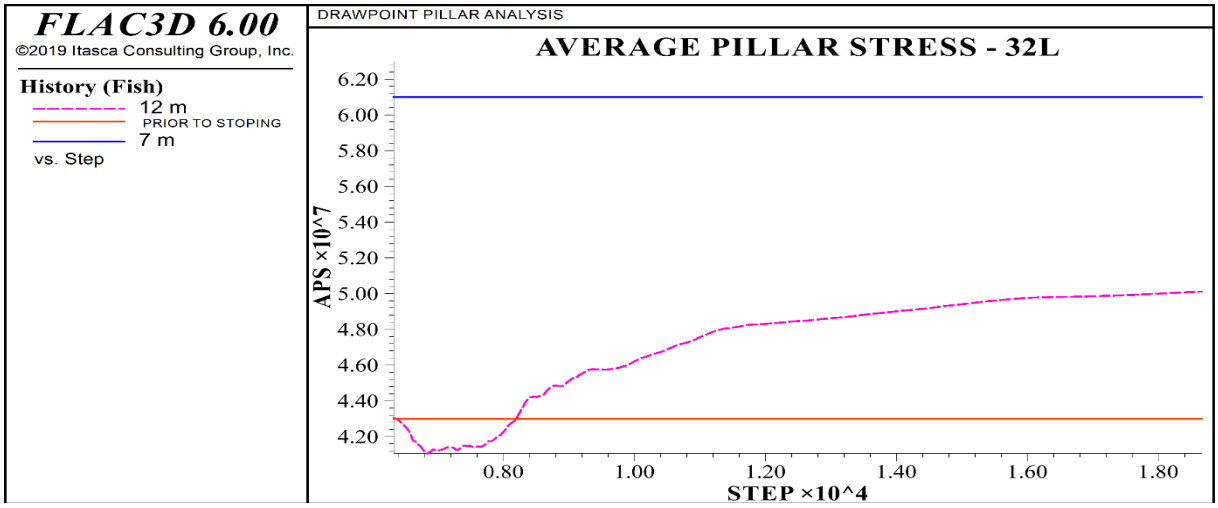


Figure 16. Average pillar stress at 32L. 7 m wide pillar (blue) vs 12 m wide pillar (pink).

CONCLUSION AND RECOMMENDATIONS

The transition from the shallow depth to the medium depth environment at mine A is accompanied by stress-induced geotechnical challenges. Stress induced fracturing in drawpoints raises a safety concern which needs to be addressed with immediate effect. Once scaling initiates on the pillar sidewalls, it will be progressive and the load-bearing capacity of the pillars will diminish with time. The 7 m pillar width was deemed to be too small and unstable with a low FoS of 1.33. There is a need to revise the pillar dimensions and the author has recommended a 12 m pillar width with an FoS of 1.70 for 32L. Additional recommendations are made as follows:

1. 2 m long fully grouted shepherd crooks should be installed in drawpoint sidewalls and roof at 30L. Use a diamond pattern with a 1 m x 1 m grid spacing. At 32L, reinforcement should be installed in drawpoints and haulage drifts during development operations.
2. Install blast-on-mesh to retain slabs and prevent progressive unravelling.
3. Ensure adherence to production blast design in order to minimise hangups and large boulders in drawpoints. This will help reduce the frequency of secondary blasts.
4. Take rock samples for laboratory tests to determine the mechanical properties. This will help increase the accuracy of numerical modelling and improve mine design.

5. Implement pillar monitoring programs. Install multipoint borehole extensometers in some of the drawpoint pillars to monitor dilation. Use a borehole camera or a ground penetration radar to monitor the extent of fracturing around the drawpoints.
6. Continuous barring down of the roof of drawpoint crosscuts and haulage drift must be done as the surrounding rock mass is in the yield zone.
7. An increase in the distance between the open stope and the haulage drift with increasing depth has to be considered to reduce the influence of abutment stresses on haulage drift.

ACKNOWLEDGEMENTS

The author is grateful to Aaron Chagwedera and Tatenda Madziwanzira for their considerable contributions to this paper. This work was supported by the Zimbabwe National Institute of Rock Engineering (ZINIRE).

REFERENCES

Bosman, J. D. & Enslin, Q., 2024. Pillar stability assessment methodology for massive mines. *Proceedings of the SANIRE Symposium 2024.* The Southern African Institute of Mining and Metallurgy. Johannesburg. pp. 123–133.

Hoek, E., 2006. [Online] Available at: https://www.rocscience.com/assets/resources/learning/hoek/Practical-Rock-Engineering-Full-Text.pdf [Accessed 12 February 2025].

Itasca Consulting Group, 2024. *FLAC3D 7.0 Documentation.* [Online] Available at: https://docs.itascacg.com/flac3d700/contents.html [Accessed 10 February 2025].

Jager, A. & Ryder, J., 1999. *A handbook on rock engineering for tabular hard rock mines.* Johannesburg: SIMRAC.

Le Bron, K. B., Gardner, L. J. & Van Zyl, J., 2024. Beyond the empirical design method: The strain criterion and the pillar load inversion concepts. *Journal of the Southern African Institute of Mining and Metallurgy,* 124(5), pp. 293–302.

Stacey, T. R. & Stewart, A. H., 1997. *Booklet on design and operational aspects of drawpoints, tips, orepasses and chutes*.:Safety in Mines Advisory Commitee.

Weihao, X., Chunchi , M., Tianbin , L. Shoudong , S., Feng , P. Ziquan , C. & Hang , Z., 2025. Dynamic interpretation of stress adjustment types in high geostress hard rock tunnels based on microseismic monitoring. *International Journal of Mining Science and Technology,* 35(5), pp. 801–816.



Ama Velempini

Student
Gwanda State University, Zimbabwe

Ama is an aspiring rock engineer holding a National Diploma in Mining from the Zimbabwe School of Mines, and a pass in Strata Control theory. He is currently pursuing a BSc (Hons) degree in mining engineering at the Gwanda State University. He is a very ambitious young man who is eager to begin his career in rock engineering and get the rock rolling. Through persistent practise and autonomous learning, he has become an advanced beginner in numerical modelling and is on the right path to becoming an advanced Flac3D user. He is looking forward to gaining valuable experience in the rock engineering field.

Rectifying, conforming and extracting value from existing geotechnical data sets – the importance of good data management for optimal value extraction

M.H. van Aswegen[1], D.H. Mossop[2]

[1]Independent Consultant - Data Governance, South Africa
[2]SRK Consulting, South Africa

Extracting value from existing geotechnical data sets involves collecting, collating, synthesising, standardising, verifying and presenting the primary data which originates from field and laboratory investigations. These programs produce core logging, outcrop and face mapping descriptions, sampling and resultant tests. Mining method selections, regional and local geological, structural, rock mass and hydrogeological challenges dictate geotechnical programme objectives. The value extraction from the database must inform known and unknown risks. This paper focuses on interactions between source data and state-of-art good data capture and management practice. Traditionally, logged data accumulates on paper and photographs. Data issues include vast quantities of recaptured, missing and duplicated data, and inconsistent logging standards. Solutions must produce usable data and information. Computerised logging was applied to geotechnical investigations by Iscor Mining during the 90s, before developing and proving a methodology across large iron ore (de Beer, 2000) and platinum operations (Little, 2006[2]). Portable database software technology supplied multi-user editing capabilities and data security. Initial implementations ran successfully at Sishen and Thabazimbi Iron Ore mines by 1998 (SABLE®, 1997). Real time validations promoted correction of captured data within its relational context in the field before posting to the final database. The 'hard coded' system rules were subsequently improved to become a configurable software module interfacing directly to the database. Customisable Data Standards allowed geotechnical and rock engineers to define classification systems for individual projects, leading to a standardised methodology for geotechnical data capture and management. This methodology provides a proven approach for optimal value extraction from geotechnical data in general, via sound data capture and data management practices.

INTRODUCTION

A recent example of a feasibility study for a geotechnical mine investigation is discussed, emphasising the data management methods recommended to produce reliable data from the primary field observations and measurements. The field practice for logging the source data included the strategic placement of quality assurance and quality control (QAQC) steps within the process (such as drilling checks, oriented core with photos in v rail-notches, cling wrap after markup of sample runs and orientation line marking with orientation line confidence recorded, before placing in core trays, laying core trays out for QAQC checks before loading to transport etc.), as shown in Figure 1. The workflow for sampling practice in the core yard included its own set of quality assurance measures, photographs and checks.

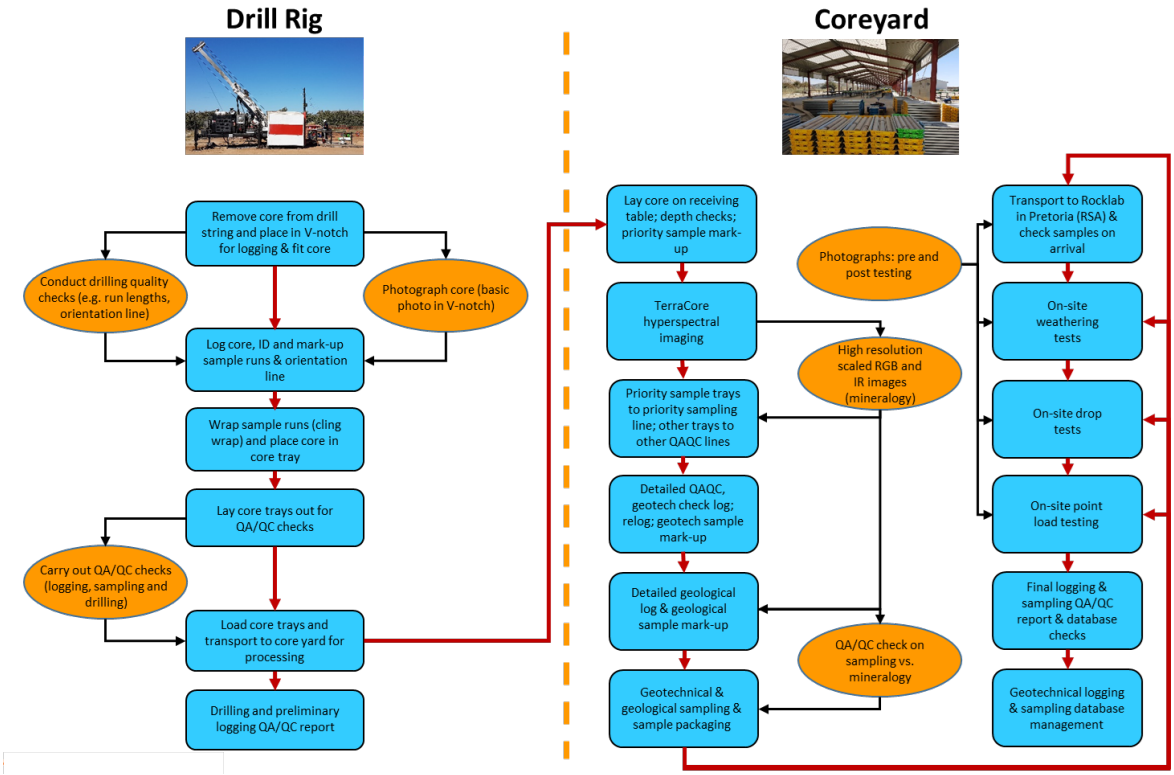


Figure 1. Field data collection workflow.

Hardcopy, manual field logs were quality checked by second loggers and captured digitally with relational validation checks against individual data entries. The purpose of the investigation was to verify and improve the mine design by generating a representative geospatial dataset to improve the confidence in the geotechnical model, as generated from a country rock model, structural model, rock mass model and hydrogeological model. This process relies on varied inter-related datasets as seen below (Figure 2). The importance of a representative validated and relational borehole database to the final geotechnical model is apparent. The regional geology and its related geological challenges were already known and informed the geotechnical programme objectives.

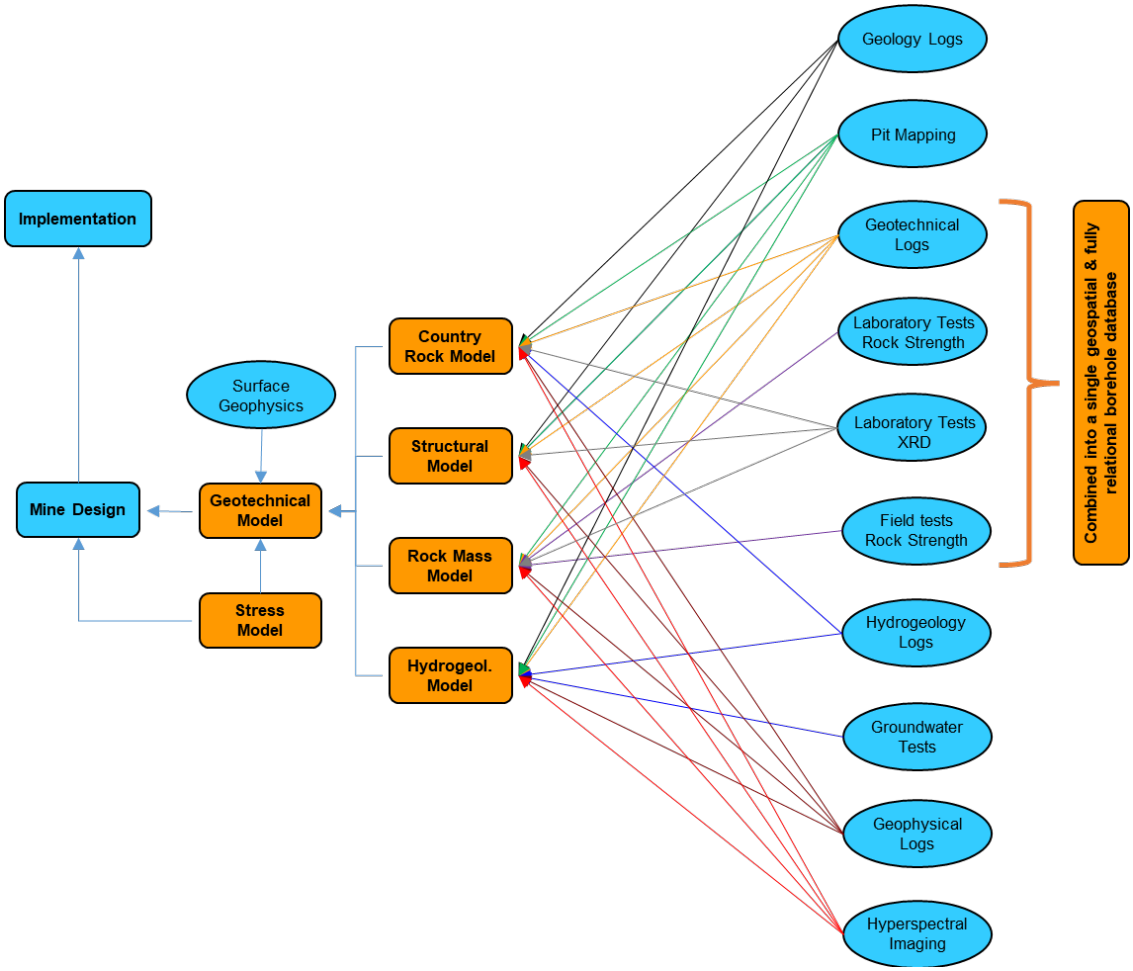


Figure 2. Field data sets involved in a geotechnical investigation, showing the inter-relationship of the data and dependence on a relational borehole database.

Data confidence process

Data confidence compliance was an objective of the feasibility study. This required data integrity through every step in the process (van Aswegen, 2003). The primary data had already been recorded manually and transferred to digital format in spreadsheets, but the system in place at the mine had not supplied the digital result sets required to complete the study by the approaching deadline. A new relational database was needed, and the data management process began by collecting all relevant handwritten paper logs. During the transfer of this data to spreadsheets, the data inputs were verified against the core photographs and QAQC audit logs previously captured systematically in the field, before importing into the relational database for further processing.

Spreadsheets

As the spreadsheets were populated, transparency and auditability were the governing principles. This meant that only spelling mistakes, incorrect units of measure and data recorded in the wrong columns could be modified. Where more than one paper log was discovered for the same record, the best (most legible, most consistent) version was used. An ongoing challenge was to maintain consistent spreadsheet column headers between multiple capturers to facilitate the migration of this data into the final database.

The creation of a working database prototype required a Data Standard. This is a specification of each parameter recorded, together with its data types, conventions, validations and relationships to other data entities. The intelligence to determine this definition evolved as the data management project

progressed. This began with the specification of the data tables to preserve the raw data exactly as recorded in spreadsheets.

Data migration

Once the spreadsheet data had been migrated to the working database clearing tables mentioned above, the first validations could be configured and executed to give a picture of the data quality. Hardcopy data errors included incorrect run depths, inconsistency in descriptors, blanks, duplicate captures etc. These errors increased during the digital data capture to the spreadsheets. During this step, dictionaries could be populated automatically per alphanumeric parameter from the migrated data. Numeric range checks were run, and missing data determined. This intelligence was used to tighten translations and evaluations built into the data migration code. This procedure transformed the data to the loose Data Standard of the clearing area which allowed it to populate the temporary staging tables.

Then followed the setup of the database tables required to organise the varied data sets represented within the relational data model's structure (e.g., per mine /shaft /drillhole /deflection/dataset). This step would make the data usable and compliant with the final Data Standard (SABLE®,2018) required for use during the evaluation of geotechnical parameters to derive rock quality factors. Once completed, these database tables could be created and the data sets loaded from the clearing tables to the primary data tables, as shown in Figure 3. The data structure and logic applied during this step is described in detail by Van Aswegen, 2003[2].

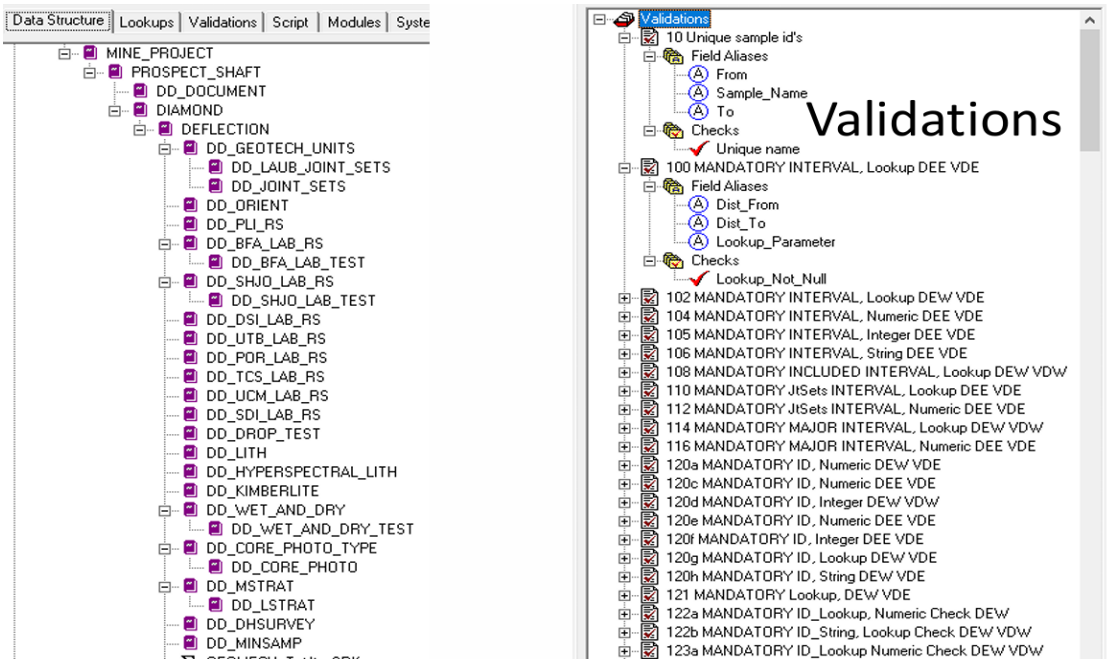


Figure 3. Primary data structures to host and validate source data.

Data quality checks were performed using the predefined rules held in the metadata which is the Data Standard. These rules were adjusted to combat data issues discovered, such as duplicate depth entries, erroneous core descriptors, invalid core recoveries etc. The resulting data validation reports were handed to members of the data management team for verification and correction. Drill core photos were loaded into the database for easy reference and auditability (Figure 4). Data transparency between the data logged at the core yard and what was held in the database was the key principle.



From (m)	To (m)	Core Photo ID	Core Photo File
303.79	307.42	090	~FileStore~
307.42	310.48	091	~FileStore~
310.48	314.00	092	~FileStore~
314.00	317.52	093	~FileStore~
317.52	320.93	094	~FileStore~
320.93	324.20	095	~FileStore~
324.20	327.72	096	~FileStore~
327.72	331.28	097	~FileStore~
331.28	334.85	098	~FileStore~
334.85	338.48	099	~FileStore~
338.48	341.97	100	~FileStore~
341.97	345.49	101	~FileStore~
345.49	348.90	102	~FileStore~
348.90	352.44	103	~FileStore~
352.44	355.93	104	~FileStore~
355.93	359.53	105	~FileStore~
359.53	362.95	106	~FileStore~
362.95	366.51	107	~FileStore~
366.51	370.06	108	~FileStore~
370.06	373.42	109	~FileStore~
373.42	376.85	110	~FileStore~
376.85	380.37	111	~FileStore~
380.37	383.83	112	~FileStore~
383.83	387.40	113	~FileStore~
387.40	390.95	114	~FileStore~

Figure 4. Photos loaded to database for data verification.

Once the data was usable, the dictionaries linked to each logged parameter, for example denoting geotechnical descriptors, some of which are shown in Table 1, reflected a standardised form of the data captured. These lists showed the abbreviation used by the client, together with its associated description (accepted meaning in authoritative relevant publications, such as Laubscher, 1990, Jacubek and Laubscher, 2000, and the Handbook: Using the Q-system, NGI, 2015).

Table 1. Example dictionary for geotechnical descriptors

	MOISTURE	
D	DRY	Absence of moisture, dry
SM	SLIGHTLY MOIST	Minor amount of water present, feels slightly cool to the touch
M	MOIST	Damp but no visible moisture
SW	SLIGHTLY WET	Wet, when soil is compressed water is released
W	WET	Soil is saturated, visible water

	HARDNESS	
X1	VERY SOFT SOIL	Easily penetrated several cm by fist
X2	SOFT SOIL	Easily penetrated several cm by thumb
X3	FIRM SOIL	Can be penetrated several cm by thumb with moderate effort
X4	STIFF SOIL	Readily indented by thumb but penetrated only with great effort
X5	VERY STIFF SOIL	Readily indented by thumb nail
H1	VERY WEAK ROCK	May be broken in hand with difficulty
H2	WEAK ROCK	Cuts easily with a knife
H3	MODERATELY WEAK ROCK	Difficult to cut with knife - pick indents deeply
H4	MODERATELY STRONG ROCK	Cannot be cut with knife - pick indents to 5mm
H5	STRONG ROCK	Requires one hammer blow to break
H6	VERY STRONG ROCK	Requires several hammer blows to break
H7	EXTREMELY STRONG ROCK	Rings when hit with hammer

	WEATHERING	
UW	UNWEATHERED	Parent rock shows no discoloration, loss of strength or any other weathering effects
SW	SLIGHTLY WEATHERED	Rock may be slightly discoloured, particularly adjacent to defects, which may be open and will have slightly discoloured surfaces, the intact rock is not noticeably weaker than fresh rock
MW	MODERATELY WEATHERED	Rock is discoloured, defects may be open and will have discoloured surfaces, with alteration starting to penetrate inwards, intact rock is noticeably weaker than fresh rock
HW	HIGHLY WEATHERED	Rock is discoloured, defects may be open, clay rich and have discoloured surfaces, and the original fabric of the rock near to the defects may be altered. Alteration penetrates deeply inwards, but core stones are still present
CW	COMPLETELY WEATHERED	Rock is discoloured and changed to a soil but original fabric is mainly preserved. The properties of the soil depend in part on the nature of the parent rock
RS	RESIDUAL SOIL	Rock is completely changed to a soil and all original rock fabric has been destroyed. See soil log

	MATRIX TYPE
M1	FAULTS
M2	SHEARS
M3	INTENSE JOINTING
M4	INTENSE MINERALISATION
M5	DEFORMABLE MATERIAL
M6	INTENSE DRILLING FRACTURES

	MICRO ROUGHNESS
1	POLISHED
2	SMOOTH PLANAR
3	ROUGH PLANAR
4	SLICKENSIDED UNDULATING
5	SMOOTH UNDULATING
6	ROUGH UNDULATING
7	SLICKENSIDED STEPPED
8	SMOOTH STEPPED
9	ROUGH STEPPED / IRREGULAR

	MACRO ROUGHNESS
1	STRAIGHT
2	SLIGHT UNDULATION
3	CURVED
4	UNI DIRECTIONAL WAVY
5	MULTI DIRECTIONAL WAVY

	OPEN JOINT SETS
R	Massive, no or few joints
1	One joint set
1+R	One joint set plus random Joints
2	Two joint sets
2+R	Two joint sets plus random joints
3	Three Joint sets
3+R	Three joint sets plus random joints
HJ	Four or more joint sets, random, heavily jointed, sugar-cube, etc
CR	Crushed rock. Earth like

	INFILL TYPE
1	GOUGE THICKNESS > AMPLITUDE OF IRREGULARITIES
2	GOUGE THICKNESS < AMPLITUDE OF IRREGULARITIES
	SOFT SHEARED MATERIAL EG TALC
3	FINE
4	MEDIUM
5	COARSE
	NON-SOFTENING SHEARED MATERIAL
6	FINE
7	MEDIUM
8	COARSE
9	STAINING
10	NONE

	JOINT WALL ALTERATION
1	WALL = ROCK HARDNESS
2	WALL > ROCK HARDNESS
3	WALL < ROCK HARDNESS

Data evaluation process by geotechnical methods

The evaluation system required spatially referenced data. Any distance from a collar (surveyed point of reference) can be converted to an X, Y, Z (northing, easting, elevation) coordinate at a later stage. This calculation requires the inclination angles and bearings recorded in the down/inhole survey log. All data sets are related through their distance from the surveyed collar, as recorded by the mine Survey Department. The survey convention is noted in the database for ease of reference and later conversions as may be required. Therefore, data fields from separate database tables can be mapped as arguments to be evaluated to produce individual factors for separate geotechnical methods (see Figure 5). For this project, the data capture conventions dictated reference Laubscher, 1990, Jacubek and Laubscher, 2000, and the NGI Handbook: Using the Q-system, 2015. It should be noted that the raw data was collected in accordance with these conventions. In this way, the existing data could be validated and evaluated (adjusted) to recognised rock mass and rock quality factors available for building the models necessary to estimate rock parameters for the geotechnical investigation. While the calculations are being performed, a detailed audit trail logs the formulae applied to actual values to determine arguments and factors per geotechnical unit or geomechanical zone (see Figure 6).

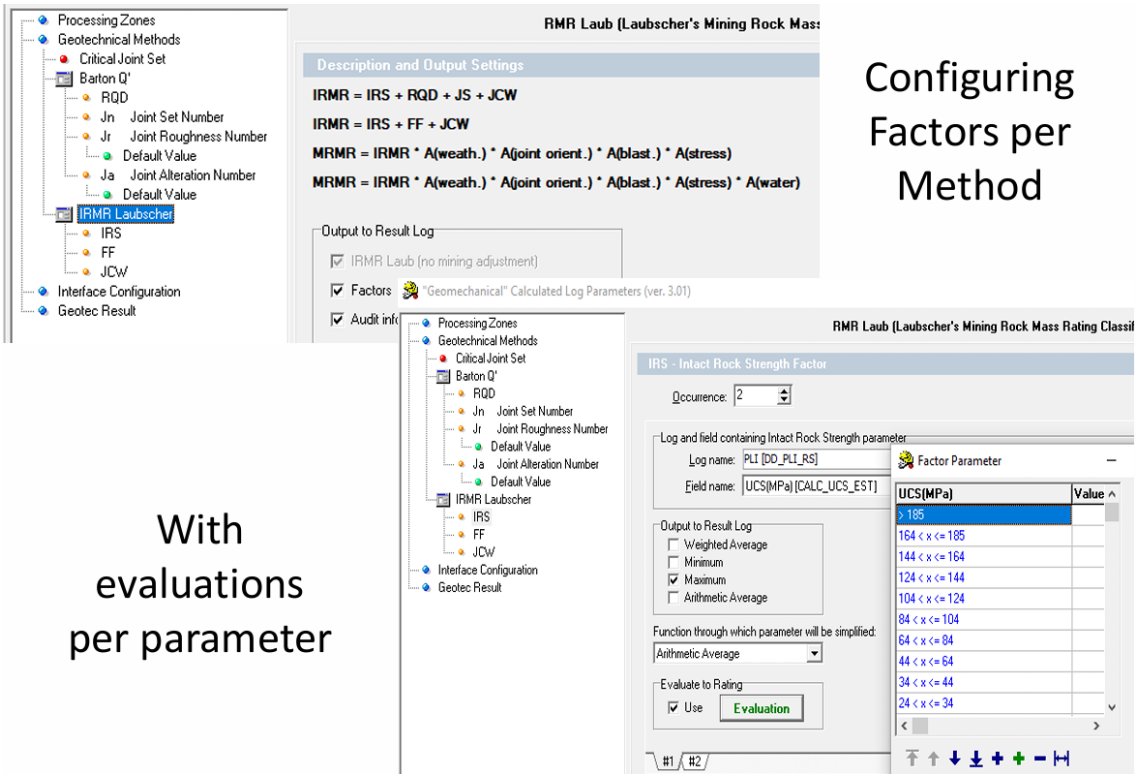


Figure 5. Configuring factors with evaluated arguments.

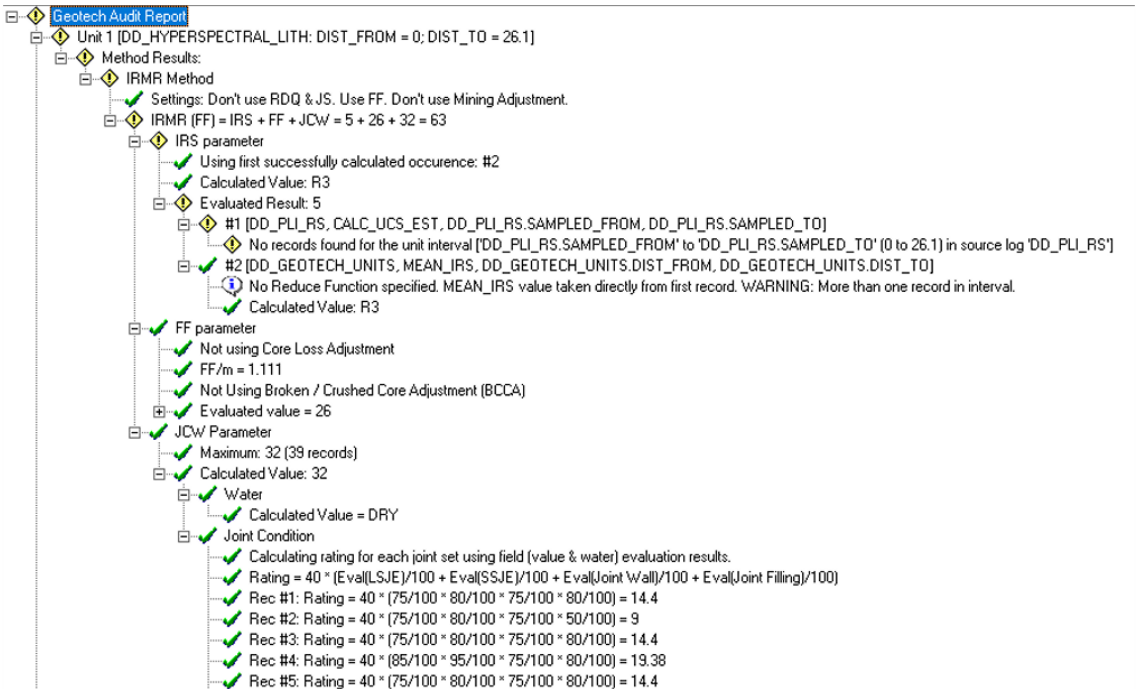


Figure 6. Evaluation process audit trail for validation and determining data sensitivities.

Graphical 'to scale' reports were used to represent the data. Scalable symbols and charts represented primary geological and geotechnical features per discontinuity set, geotechnical unit or geomechanical zone. Alongside the primary parameters and evaluated factors, labelling and charting tools also displayed the rock classifications and primary geology. This provided quality assurance and an

interpretation tool, as shown in Figure 7. These reports were saved back to the database after each drill hole was signed off as a record of the work delivered and can be directly compared to high-resolution core photographs in the database. This also provided evidence that the geotechnical evaluation was completed and correct.

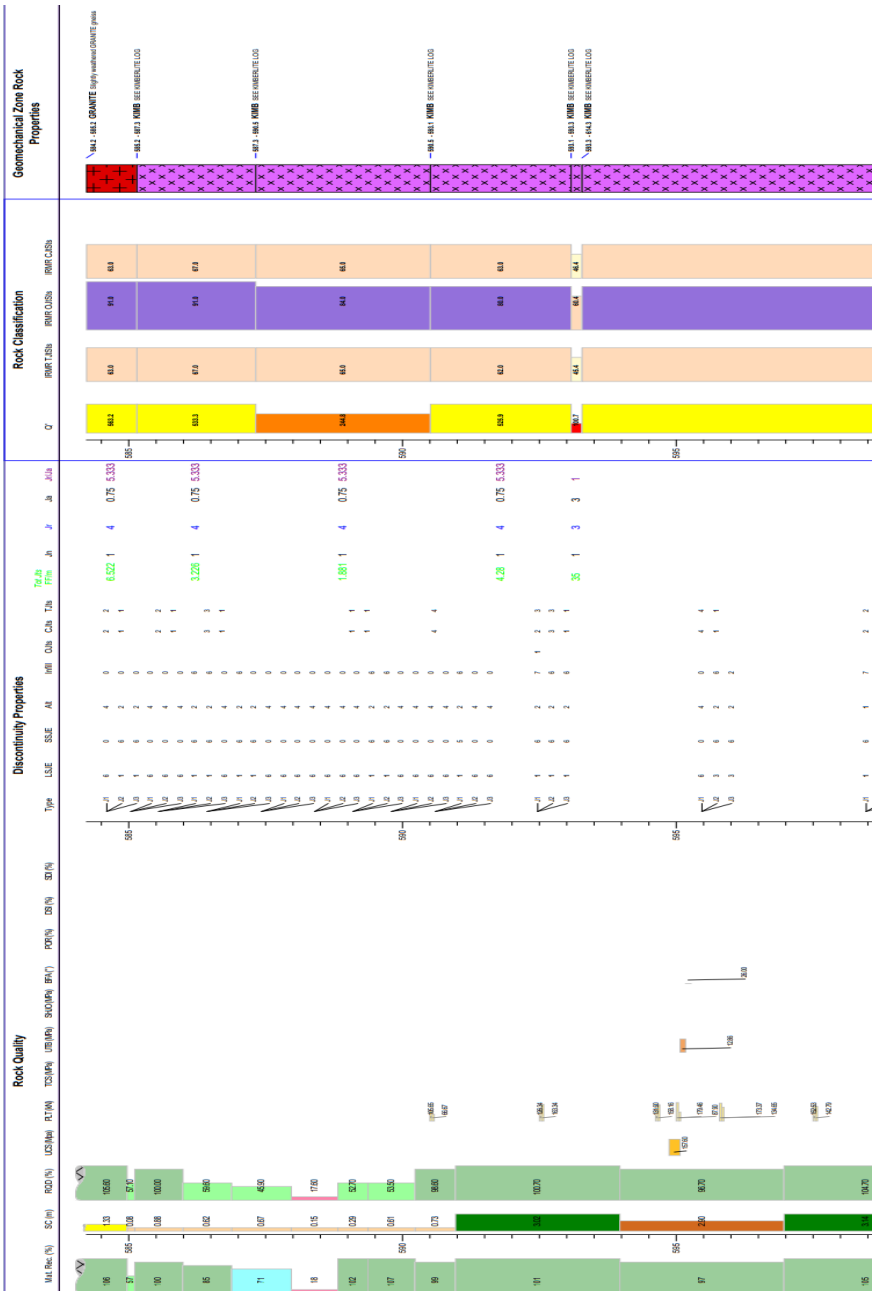


Figure 7. Evaluation process graphical log report for validation and interpretation.

Deliverables

The final open relational database stored all logged entries and delivered reliable data validation. It held representative point load strength data which identified anisotropy in country rock as a result of bedding and unusual uniformity of strength in the host rocks. It allowed open secure access to third party tools to produce analytics, spatial distributions of results, geological and structural models, rock mass block models and mine designs, as shown in Figure 8.

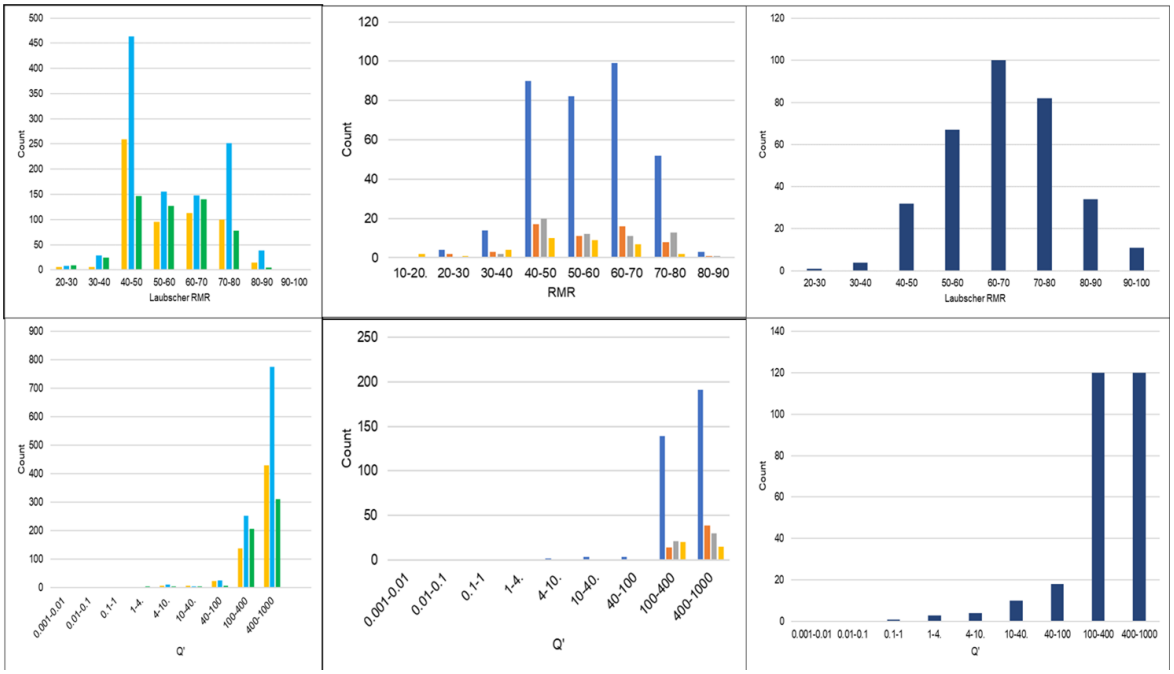


Figure 8. Analysis of data verified and stored.

CONCLUSIONS

The Logging Standard (rules for recording data) must be defined before observations and measurements are made in the field (Van Aswegen, 2003). The objectives of the geotechnical investigation must dictate the Data Standard (SABLE®, 2018) which governs the database structure, data quality assurance and data management processes. This will ensure that essential data is easily available for all necessary calculations. This dictates that there is no 'one size fits all' solution to establishing the Logging and Data Standards but must be suited to the geotechnical environment and end purpose of the information derived from the data.

Good data management in accordance with the above conclusions is applicable to databases and acquisition programmes of all sizes and complexity. For large databases, such as the one in question, it is difficult to provide data integrity within even standardised spreadsheets, and application of a relational database is crucial. The field exercise described provides an example of the complexity and inherent potential for error when transferring data from hardcopy field sheets to digital format in spreadsheets, and promotes the upfront application of a digital database with digital data capture and immediate validation. This ultimately also provides improved data security, portability and auditability.

Furthermore, the database must be 'fit for purpose' and proven within the geoscientific application of interest. It cannot be developed 'on the go' without causing confusion in the field and adversely affecting the integrity of the data. There is more value in less data of good quality than masses of measurements that must be collated and standardised before use. Invest time and expertise up front to prevent long delays in the project delivery.

Adopt a data standard that satisfies more than one geotechnical method. This will create confidence in the data collected by providing verification between the methods. From experience, calculations can produce results for the four separate Q', RMR, MRMR and GSI geotechnical methods using one integrated logging standard which is practical and proven. For the project in question, Laubscher's

rock mass rating and the Norwegian Geotechnical Institute Q-system (Barton, Lien and Lunde) were applied.

During the project the calculation of Laubscher's IRMR and Barton's Q' were validated, auditable and reproducible. The results could be verified graphically alongside the primary measurements and evaluated factors. This process produced data confidence and ultimately, compliant data.

ACKNOWLEDGEMENTS

David Mahlakahlaka, Avhatakali Mulovhedzi and Adelle Mossop are acknowledged for their outstanding dedication to the data integrity and data quality deliverables.

REFERENCES

1. De Beer, C.J. 2000.: An Unbiased Computerised Geotechnical Core Logging System. *Young Geotechnical Engineers Conference*, Stellenbosch

2. Van Aswegen, M.H. 2003: Increasing confidence in geoscientific knowledge for the industry and investor. *South African Institute of Mining and Metallurgy Mineral Resource Management Colloquium*, Johannesburg

3. Little, M.J. 2006: The benefit to open pit rock slope design of geotechnical databases. *Symposium Series S44*. The South African Institute of Mining and Metallurgy, Cape Town. pp. 97–116.

4. SABLE® 1997, 2018: The methodology trademarked in the categories software and mining in South Africa by SABLE Data Works (Pty) Ltd in 1997. This intellectual property was purchased by Datamine Africa (Pty) Ltd in 2018.

Influence of saturation fluids on the elasto-plastic deformation behaviour of shale

L. Chen, L. Wang

China University of Petroleum, China

As a critical component of unconventional reservoirs, shale's mechanical characterisation is essential for hydrocarbon extraction efficiency. Existing research predominantly examines dry or water-saturated conditions, failing to replicate in situ reservoir environments adequately. This paper evaluates three characteristic saturation states (dry, oil-saturated, water-saturated) through multiscale compression testing (uniaxial, triaxial) under variable confining pressures. Experimental results reveal that pore fluids reduce the in situ Young's modulus significantly (about 20% for water, 5% for oil), compressive strength relative to dry specimens, and amplifying plastic deformation capacity. Oil saturation predominantly affects post-yield characteristics through hardening rate reductions, whereas water saturation induces a stronger influence on both elastic and plastic behaviours due to water-rock interactions. During plastic deformation, fluid saturation reduces plastic hardening rate by 46 - 100%, with water demonstrating superior influence. This paper provides practical insights into the role of fluid saturation in controlling shale's mechanical properties and offers guidance for optimising hydraulic fracturing and enhancing wellbore stability in shale gas and oil reservoirs.

Keywords: shale, oil/water saturation, elasto-plasticity, failure

INTRODUCTION

Shale, a fine-grained sedimentary rock composed mainly of clay minerals, quartz, organic matter, and accessory minerals, is a key component of unconventional hydrocarbon reservoirs such as shale gas and shale oil. Despite its low porosity and permeability, its anisotropic and heterogeneous nature, along with sensitivity to fluid saturation and stress state, makes it a challenging yet essential material in petroleum engineering. Internal micropores, microcracks, and mineral composition significantly influence its mechanical properties, stress distribution, and failure mechanisms (Zhang *et al*., 2014; Griffiths *et al*., 2017). Understanding these factors is crucial for applications like drilling, hydraulic fracturing, and reservoir compaction (Sone & Zoback, 2013). Under in situ conditions, shale pores contain various fluids, including water and hydrocarbons. While much progress has been made in studying the mechanical behaviour of shale, further research is needed to clarify how different saturation fluids impact strength and failure processes.

Numerous studies emphasise the weakening effect of water saturation on shale's strength and stiffness, primarily due to water-clay interactions (Chenevert, 1970; Wang *et al*., 2015). Triaxial compression tests show significant reductions in unconfined compressive strength and elastic modulus in water-saturated shale compared to dry samples (Li *et al*., 2016). Despite the presence of substantial movable oil in shale reservoirs, research on oil saturation's impact on elasto-plastic mechanical properties remains limited. Oil saturation modifies pore pressure and effective stress, influencing shale deformation and failure behaviour (Islam *et al*., 2013; Zhang *et al*., 2017).

A deeper understanding of these effects is crucial for optimising shale oil and gas production and reducing geomechanical risks in drilling operations. Quasi-brittle materials such as sandstones, chalks, and argillites have been widely studied to understand fluid-solid interactions and their impact on mechanical behaviour. Water-induced weakening is well-documented in chalk, where interactions with calcite significantly reduce strength and stiffness. Under oil saturation, chalk also experiences a decline in compressive strength. During compression tests, once chalk enters the plastic deformation stage, plastic parameters such as initial plastic yield stress, cohesion, and friction angle are affected differently under water and oil saturation (Xie & Shao, 2006). Fine-grained sandstones similarly exhibit saturation sensitivity, with pore structure and mineral composition playing critical roles in their mechanical properties (Jia *et al.*, 2018). Argillite studies highlight anisotropic swelling and irreversible deformation under varying saturation conditions (Wang *et al.*, 2013, 2014). In the case of shale, it is often characterised by using uniaxial and triaxial compression tests to evaluate mechanical properties under different saturation states. Such tests have been extensively used to examine the effects of water and oil saturation on cohesion, internal friction angle, and energy dissipation (van Oort *et al.*, 1996; Sarout *et al.*, 2014; Xie & Shao, 2012).

This study aims to further investigate the influence of saturation fluids on the elasto-plastic properties of shale, focusing on three characteristic states: dry, water-saturated, and oil-saturated conditions. An established elasto-plastic model is employed to elucidate the role of saturation fluids in influencing mechanical parameters. By synthesising mechanical testing, theoretical parameter analysis, and energy dissipation analysis, this paper advances the fundamental understanding of fluid-shale interactions of elasto-plastic deformation and failure mechanisms, offering critical insights for optimising hydraulic fracturing design and subsurface stability management.

Material and experimental procedure

Material

The shale specimens were obtained from the Fuling shale gas field in Sichuan Province, China—one of the largest gas/oil shale reservoirs within the Lower Paleozoic marine strata. An X-ray diffraction analysis conducted under ambient conditions (25°C) revealed the mineral composition detailed in Table I. Clay mineral analysis identified illite and montmorillonite as dominant phases (constituting over 60% of clay content), with chlorite and kaolinite comprising the remainder. Notably, the carbonate and clay mineral assemblages demonstrate strong water reactivity, inducing substantial mechanical alterations upon water saturation.

Table I: Mineralogical compositions of specimens

Mineralogical compositions	**Clay minerals**	**Quartz**	**Calcite**	**Dolomite**	**Pyrite**
% (by mass)	21.3	45.2	16.4	14.9	2.2

The shale exhibits ultra-low permeability with pronounced bedding-plane anisotropy. Steady-state nitrogen permeability measurements yielded averages of 4.22×10^{-4}mD perpendicular to bedding vs 1.76×10^{-3}mD parallel to bedding, confirming enhanced fluid migration pathways along stratigraphic orientation. This permeability anisotropy may critically influence fluid-mediated mechanical responses during saturation.

Preparation of rock specimens

All tests in this study were conducted on cylindrical shale specimens (25 mm diameter, 50 mm height) following ASTM standards. Specimens were precision-cut from cubic blocks using wire-cutting technology to minimise damage. To reduce anisotropy effects, all specimens were oriented vertically to the bedding. After fabrication, specimens underwent a controlled drying process. The temperature gradually increased from 30°C to 90°C over two days, maintained at 90°C for three days, then lowered back to 30°C over another two days. This protocol minimised internal damage from thermal fluctuations. Throughout drying, specimens were weighed daily to ensure mass stability, confirming full dehydration.

Following complete desiccation, the specimens were categorised into three groups: dry, water-saturated, and oil-saturated. Dry specimens were stored in a temperature-controlled chamber at 30°C. Water and oil saturation were achieved using a triaxial pressure vessel under 30 MPa confining pressure, with distilled water and white mineral oil (ρ = 0.85 g/mL) serving as the saturation fluids. Given shale's ultra-low permeability and porosity, a 30 MPa vacuum-assisted pressure protocol was implemented to ensure complete saturation. Saturation was verified through comparative weight analysis, with water- and oil-saturated specimens showing no mass change after 45 days, confirming full saturation (see Figure 1).

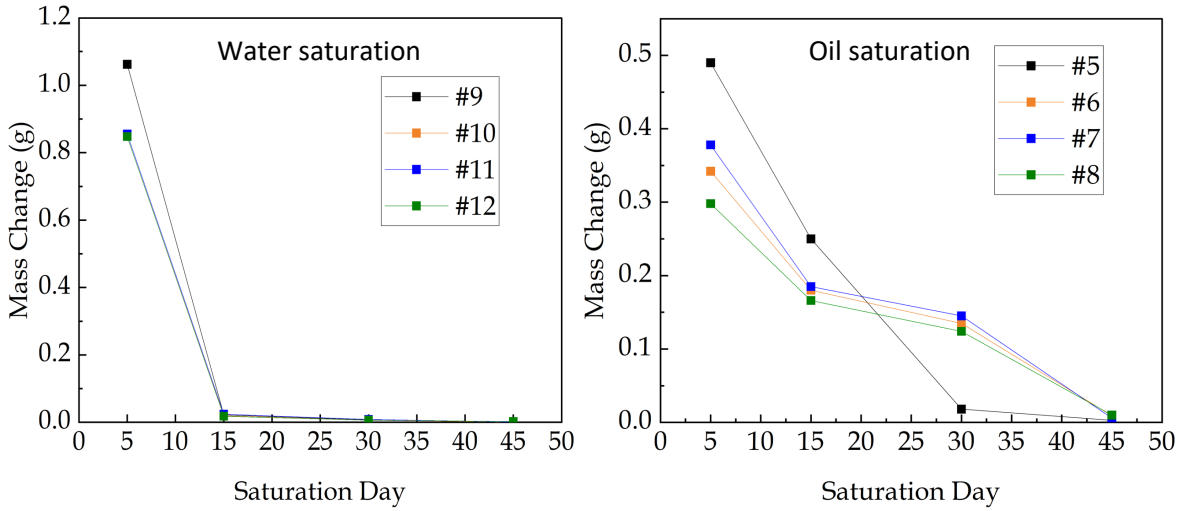


Figure 1. Evolution of specimen mass with saturation time.

Experimental procedure

Mechanical testing employed a servo-controlled triaxial system (see Figure 2) with integrated compression/pressure units and automated data acquisition. Axial displacement was measured via dual LVDTs (LVDT-1/2) on the loading platen, while radial strain was monitored by a circumferential LVDT-3 at mid-height of specimen. Specimens were vacuum-sealed with heat-shrink tubing and end caps to prevent hydraulic oil infiltration. The system's rated capacities include 600 MPa deviatoric stress and 90 MPa confining pressure, hydraulically applied through servo-controlled pumps.

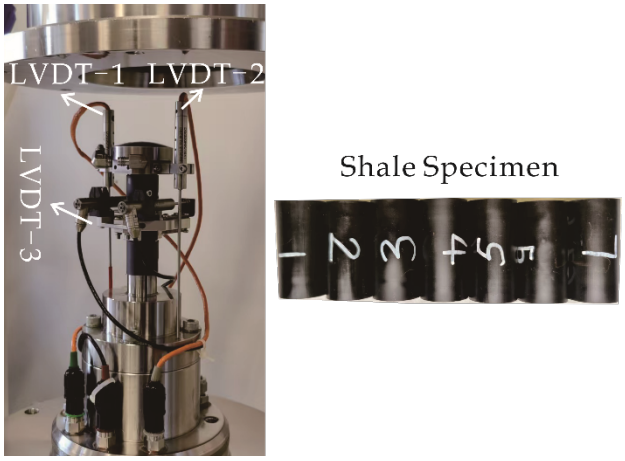


Figure 2. The triaxial test device and rock specimens.

Triaxial compression tests were performed at confining pressures of 10, 20, and 30 MPa following ISRM standards. Specimens were vacuum-sealed with heat-shrink tubing to preserve saturation states. Given the shale's ultra-low permeability, tests were conducted under undrained conditions. Vaseline was applied at the piston-chamber interface to minimise friction. Confining pressure was incrementally increased to target values at 0.5 MPa/min to achieve hydrostatic stress equilibrium. Axial loading was then applied at 0.03 mm/min until failure, with constant confining pressure maintained throughout.

Elastic-plastic models

Macro-mechanics based plastic model

Following the completion of shale specimen preparation and experimental methodology selection, determining an appropriate elasto-plastic model constitutes the first critical step in analysing experimental results and clarifying the influence of different saturation fluids on the mechanical properties of shale. According to a review of the basic mechanical behaviour of rock materials, a key feature is the strong dependency of the plastic shearing process on confining pressure. The mechanical behaviour changes significantly from a brittle regime to a ductile regime with confining pressure increases. The amount of deformation at the failure state also varies greatly with confining pressure. Additionally, there is a large difference between uniaxial tensile strength and uniaxial compressive strength (Risnes & Garspestad, 1998; Colmenares & Zoback, 2002). These findings indicate that classic linear yield surfaces such as the Drucker-Prager (D-P) or Mohr-Coulomb (M-C) yield criteria may not be suitable (Paterson & Wong, 2005). Instead, a curved yield surface is necessary. Based on the plastic model for concrete and chalk proposed by Xie & Shao (2006), the following parabolic yield function is suggested for the plastic model:

$$\left(\frac{\sigma_{\mathrm{eq}}}{p_{\mathrm{r}}}\right)^2 + A\alpha_{\mathrm{p}}\left(\frac{\sigma_{\mathrm{m}}}{p_{\mathrm{r}}} - C\right) = 0 \qquad [1]$$

where σ_{m} is the mean stress defined as $\sigma_{\mathrm{m}} = \sigma_{\mathrm{kk}} / 3$, and σ_{eq} is the equivalent stress given by $\sqrt{3J_2}$, J_2 is the second invariant of the deviatoric stress tensor. Parameters A and C are correlated with the material's internal friction angle and cohesion, respectively. The reference pressure P_{r} = 1 MPa is employed to render the parameters A and C dimensionless. The function a_{p} represents the plastic hardening law governing the yield function:

$$\alpha_{\mathrm{p}} = \alpha_{\mathrm{p}}^0 + \left(1 - \alpha_{\mathrm{p}}^0\right)\frac{\gamma}{B + \gamma} \qquad [2]$$

where the parameter α_p^0 denotes the initial yield threshold, and the parameter B indicates the plastic hardening rate. The variable γ denotes the Von-Mises equivalent plastic strain $\gamma = \sqrt{2/3 * e_{ij}^p e_{ij}^p}$ with $e_{ij}^p = \varepsilon_{ij}^p - \varepsilon_{kk}^p / 3\delta_{ij}$. With the plastic strain increases, a_p increases from 0 to its terminal value 1 at failure.

For most rocks, the plastic volumetric strain transitions from compressibility to dilatancy, marking a fundamental difference from the behaviour of metals. To capture the nuances of plastic deformation, the delineation of a non-associated plastic flow rule is imperative. The plastic potential function is articulated as follows (Xie & Shao, 2012):

$$g = \sigma_{\mathrm{eq}} + \eta_{\mathrm{T}}\left(\sigma_{\mathrm{m}} - C\right)\ln\left(\frac{\sigma_{\mathrm{m}} - C}{I_0}\right) = 0 \qquad [3]$$

where the variable I_0 determines the range of between the two intersections of plastic potential curve along the σ_{m} axis, and the parameter η_T characterises the gradient of the transition boundary in σ_{eq}–σ_{m} plane.

Calibration of the proposed mechanical model for saturated shale

In the framework of a plasticity model, seven parameters are proposed, which can be derived from the results of uniaxial and triaxial compression tests. These parameters include two elastic constants for the material (E and v) and five parameters characterising plasticity (A, C, α_0^p, B and η_T). The elastic parameters are determined from the stress-strain curve obtained in uniaxial compression tests. To identify the failure parameters A and C, peak stress data from triaxial compression tests under various confining pressures are utilised. The initial yield parameter α_0^p can be determined from initial yield stress. Similarly, the hardening parameters B can be extracted by plotting the hardening function α_p against the equivalent plastic strain γ. Finally, the parameter η_T, which defines the rate of transition from plastic compressibility to dilatancy, is determined on the boundary where the condition $\partial g / \partial \sigma_m = 0$ is satisfied in the $\sigma_{eq} - \sigma_m$ plane. For simplicity, it is assumed that this transition boundary can be approximated by a linear function :

$$T_{c/d} = \sigma_{\mathrm{eq}} - \eta_T \left(\sigma_m - C\right) = 0 \qquad [4]$$

Experimental results

Uniaxial and triaxial compression tests

The stress-strain curves of uniaxial and triaxial compression tests are presented in Figure 3. The initial plastic yield stress was determined through the volumetric deformation. The determined initial plastic yield stress and the corresponding axial strain are summarised in Table II, as well as the peak stress. Under uniaxial compression conditions, the stress-strain curves for the water-/oil- saturated shales are both below that for dry shale, shown in Figure 3a. This indicates a reduction of stiffness when fluids are present. In addition, the uniaxial compressive strength decreases significantly when shales are saturated with water or oil. The failure modes also differ among three saturation conditions. The primary failure mode under uniaxial compression is splitting, characterised by one or several macroscopic vertical cracks through cutting the rock specimen. The splitting can explain why the radial strain curves exhibit sudden jumps as well as fluctuations in the axial strain curves.

Table II: Peak strength and initial yield stress of 12 specimens

Saturation condition	Specimen No.	Confining stress (MPa)	Peak deviatoric stress (MPa)	Peak axial strain (%)	Initial yield stress (MPa)	Yield axial strain (%)
Dry	# 1	0	228.8	0.66	/	/
	# 2	10	343.9	1.01	342.1	1.00
	# 3	20	377.3	1.12	351.8	1.02
	# 4	30	459.9	1.52	419.7	1.30
Oil-saturated	# 5	0	170.8	0.65	170.5	0.64
	# 6	10	287.1	0.94	276.8	0.88
	# 7	20	358.8	1.21	348.8	1.11
	# 8	30	427.4	1.36	421.4	1.27
Water-saturated	# 9	0	160.5	0.63	133.2	0.46
	# 10	10	290.2	1.13	275.6	1.05
	# 11	20	336.3	1.32	296.0	1.07
	# 12	30	411.1	1.52	350.2	1.18

The stress-strain curves under confining pressures of 10, 20, and 30 MPa are presented in Figure 3. Both oil- and water- saturation significantly reduce the compressive strength of shale (see Table II), with water having a more pronounced effect. Similar to those in uniaxial compression tests, the stress-strain

curves for water/oil saturated shales are below that for dry shale. Nevertheless, under high confining pressure (above 20 MPa), a considerable portion of the stress-strain curve for oil-saturated shale overlaps with that of dry shale. Quantitatively, the initial plastic stress and corresponding axial strain for oil-saturated shale specimens are comparable with those for dry specimens, as shown in Table II. For instance, this indicates the influence of oil saturation diminishes as confining pressure increases. However, the peak stress for oil-saturated shale is still reduced compared with that for dry shale.

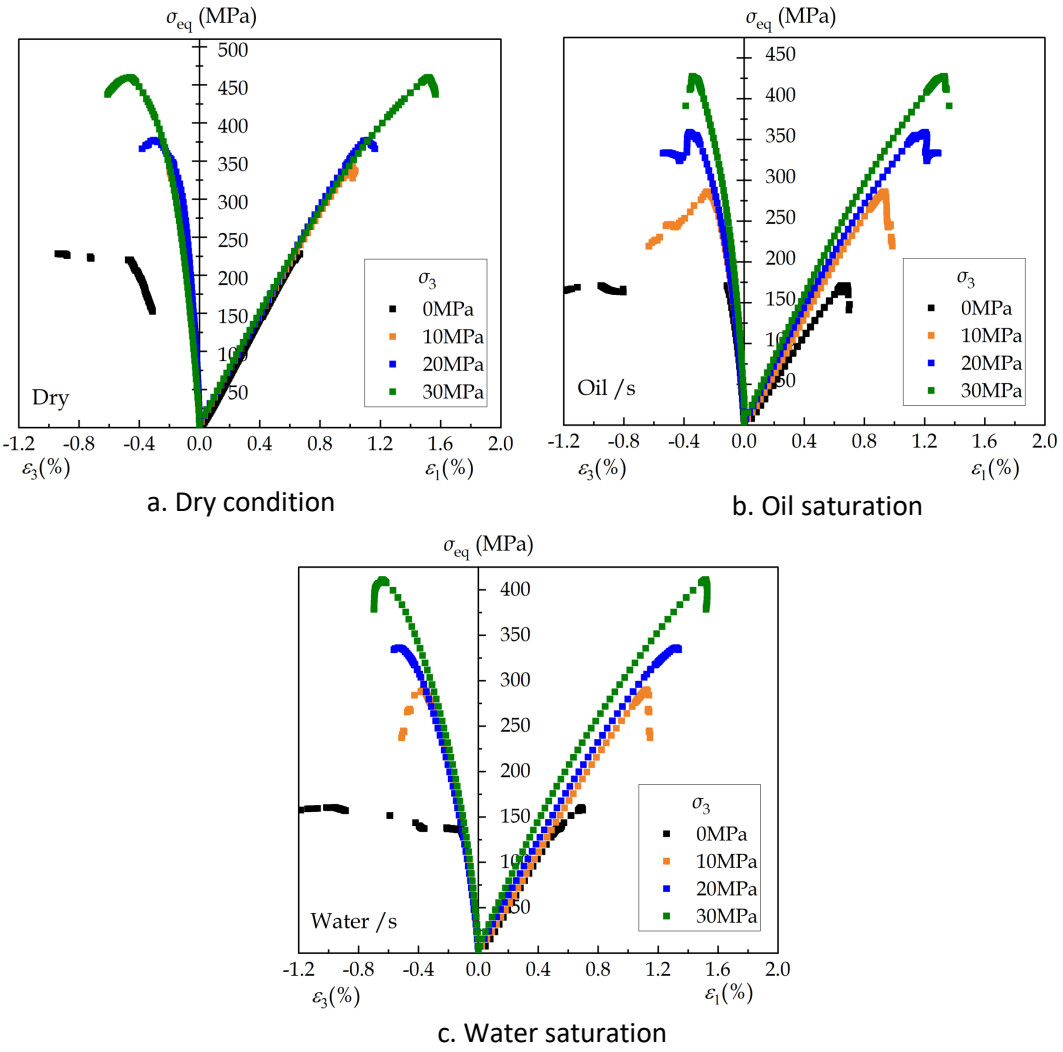


Figure 3. Stress-strain curves of uniaxial and triaxial compression tests.

Influence of saturation fluid on elastic properties

Uniaxial test results show that different saturation fluids influence shale's elastic mechanical parameters. As illustrated in Figure 4, Young's modulus and Poisson's ratio vary under different saturation conditions. Water significantly reduces Young's modulus, decreasing it by nearly 20% compared to dry samples, while oil also lowers Young's modulus but to a lesser extent. In contrast, both saturation fluids increase Poisson's ratio. These findings highlight the significant impact of saturation fluids, particularly water, on shale's elastic mechanical properties.

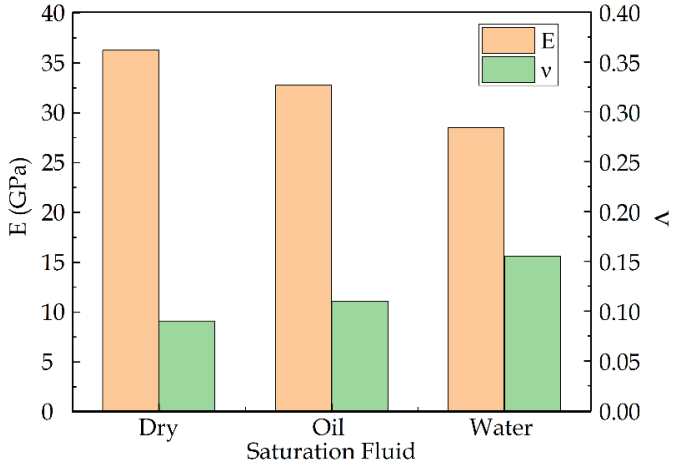


Figure 4. Elastic properties in different fluid saturation.

Influence of saturation fluid on plastic properties

For further evaluation of the influence of saturating fluids, both the macro-mechanical and micro-mechanical models are calibrated using the triaxial compression experimental results. The calibrated plastic parameters of the macro-mechanical model are as shown in Table III.

Table III: Calibrated parameters of macro-plastic model

Saturation Condition	**Failure Parameters**		**Plastic Parameters**		
	A	C	α_0^p	B	η
Dry	1045.4	1.08	0.91474	0.0024	-2.514
Oil	988.2	0.73	0.88055	0.0035	-2.484
Water	921.5	0.21	0.84593	0.0048	-2.425

Table III presents the failure parameters, including the friction angle (A) and cohesion (C). Dry shale has the highest friction angle, while water saturation reduces it by 11.9%, and oil saturation by 5.5%. Similarly, cohesion is highest in dry shale but decreases by 32.4% in oil-saturated shale and nearly 80.5% in water-saturated shale. The results show that saturation fluids also influence the initial yield stress, reducing its corresponding parameter, though the effect is moderate. Like cohesion, the hardening rate is significantly affected by saturation. According to equation 2, dry shale has the smallest B value, indicating the highest hardening rate, while water saturated shale exhibits the lowest hardening rate, with its B value nearly double that of dry shale. Oil saturation reduces the hardening rate by 45.8%. A higher hardening rate indicates a quicker progression to failure, restricting plastic deformation. The results confirm that saturation fluids reduce shale's hardening rate in the plastic phase, promoting greater plastic deformation (see Table II). Regarding the C/D transition boundary, while the overall effect is limited, the steeper slope observed in water-saturated shale suggests an increased likelihood of volumetric strain shifting from compression to dilation under the same confining pressure.

Based on this analysis, the influence of saturation fluids on shale's elasto-plastic properties can be attributed to two main factors:

1. Fluid-clay mineral chemical interactions: Chemical reactions between saturation fluids and shale minerals critically govern their elasto-plastic behaviour. Water saturation induces hydration reactions with clay minerals (e.g., illite, montmorillonite), degrading cementation bonds and structurally altering both microstructure and macroscopic mechanical behaviour. These transformations reduce matrix stiffness while enhancing plastic deformation capacity, as quantified in Table III and Figure 4.

2. Direct influence of fluids on micro-voids and microcracks during the yield stage: pore fluids directly govern microcrack evolution through dual mechanical mechanisms. Fluid presence alleviates local stress concentrations via pressure redistribution while modifying microcrack shear sliding behaviour. Water saturation accelerates crack propagation through bonding-strength reduction at fracture interfaces, reducing plastic hardening rate by 100% compared to dry conditions. Conversely, oil saturation also decreases plastic hardening rate by 45.8% through lubrication-enabled crack sliding, despite limited rock-fluid effects. These findings demonstrate that saturation fluids critically modulate both plastic hardening and failure progression during the plastic deformation phase of shale.

CONCLUSIONS

Uniaxial and triaxial compression tests were conducted on shale to evaluate its mechanical behaviour under different saturation fluids. Experimental results were analysed using established elastoplastic models to examine deformation trends under oil and water saturation. The following conclusions are drawn:

The influence of saturation fluids on the mechanical properties of shale is significant. Whether under water or oil saturation, the compression failure surface and the initial yield surface are lower than those of dry shale. Excluding the effects of water-rock interactions, the primary influence of saturation fluids such as oil or water on shale is greatest in the plastic deformation stage.

The experimental results indicate that saturation fluids significantly reduce the cohesion strength of shale while slightly decreasing the failure friction angle. Both oil and water reduce the hardening rate of shale after entering the plastic stage, thereby strengthening the plastic deformation characteristics of shale, although the effect of oil is less important than that of water. The compression experiments revealed that the presence of saturation fluids significantly increases the plastic behaviour of shale when confined. This indicates that, even without considering the water-rock interactions, the presence of saturating fluids like oil still plays a crucial role in enhancing the plastic deformation characteristics of shale.

REFERENCE

Chenevert, M. E. (1970). Shale alteration by water adsorption. *Journal of petroleum technology, 22(09), 1141–1148*.

Colmenares, L. B., & Zoback, M. D. (2002). A statistical evaluation of intact rock failure criteria constrained by polyaxial test data for five different rocks. *International Journal of Rock Mechanics and Mining Sciences, 39(6), 695–729*.

Griffiths, L., Heap, M. J., Baud, P., & Schmittbuhl, J. (2017). Quantification of microcrack characteristics and implications for stiffness and strength of granite. *International Journal of Rock Mechanics and Mining Sciences, 100, 138–150*.

Islam, M. A., & Skalle, P. (2013). An experimental investigation of shale mechanical properties through drained and undrained test mechanisms. *Rock Mechanics and Rock Engineering, 46, 1391–1413.*

Jia, C., Xu, W., Wang, R., Wang, W., Zhang, J., & Yu, J. (2018). Characterization of the deformation behavior of fine-grained sandstone by triaxial cyclic loading. *Construction and Building Materials, 162, 113–123.*

Li, H., Lai, B., & Lin, S. (2016). Shale mechanical properties influence factors overview and experimental investigation on water content effects. *Journal of Sustainable Energy Engineering, 3(4), 275–298*.

Paterson, M. S., & Wong, T. F. (2005). Experimental rock deformation: the brittle field (Vol. 348). *Berlin: Springer*.

Risnes, R., Garpestad, O. J., Gilje, M., Oland, L. T., Ovesen, M., & Vargervik, E. (1998, July). Strain hardening and extensional failure in high porosity chalk. *In SPE/ISRM Rock Mechanics in Petroleum Engineering (pp. SPE–47581), Society of Petroleum Engineers*.

Sarout, J., Esteban, L., Delle Piane, C., Maney, B., & Dewhurst, D. N. (2014). Elastic anisotropy of Opalinus Clay under variable saturation and triaxial stress. *Geophysical Journal International, 198(3), 1662–1682*.

Sone, H., & Zoback, M. D. (2013). Mechanical properties of shale-gas reservoir rocks—Part 1: Static and dynamic elastic properties and anisotropy. *Geophysics, 78(5), D381–D392*.

van Oort, E., Hale, A. H., Mody, F. K., & Roy, S. (1996). Transport in shales and the design of improved water-based shale drilling fluids. *SPE drilling & completion, 11(03), 137–146*.

Wang, L. L., Bornert, M., Chanchole, S., Yang, D. S., Héripré, E., Tanguy, A., ... & Adams, J. (2013). Micro-scale experimental investigation of the swelling anisotropy of the Callovo-Oxfordian argillaceous rock. *Clay Minerals, 48(2), 391–402*.

Wang, L. L., Bornert, M., Héripré, E., Yang, D. S., & Chanchole, S. (2014). Irreversible deformation and damage in argillaceous rocks induced by wetting/drying. *Journal of Applied Geophysics, 107, 108–118*.

Wang, L., Bornert, M., Héripré, E., Chanchole, S., Pouya, A., & Halphen, B. (2015). Microscale insight into the influence of humidity on the mechanical behavior of mudstones. *Journal of Geophysical Research: Solid Earth, 120(5), 3173–3186*.

Xie, S. Y., & Shao, J. F. (2006). Elastoplastic deformation of a porous rock and water interaction. *International Journal of Plasticity, 22(12), 2195–2225*.

Xie, S. Y., & Shao, J. F. (2012). Experimental investigation and poroplastic modelling of saturated porous geomaterials. *International journal of plasticity, 39, 27–45*.

Zhang, Q. B., & Zhao, J. (2014). A review of dynamic experimental techniques and mechanical behaviour of rock materials. *Rock mechanics and rock engineering, 47, 1411–1478*.

Zhang, S., Xian, X., Zhou, J., & Zhang, L. (2017). Mechanical behaviour of Longmaxi black shale saturated with different fluids: an experimental study. *Royal Society of Chemistry Advances, 7(68), 42946–42955*.



Linghao Chen

Ph.D. student, College of Safety and Marine Engineering
China University of Petroleum (Beijing), Beijing, China

Linghao Chen is a Ph.D. student at the School of Safety and Marine Engineering, China University of Petroleum, majoring in rock mechanics. He earned his master's degree from the University of Texas at Dallas. He has worked as a geological engineer at the Oil and Gas Exploration Institute of the Sichuan Provincial Geological Exploration Bureau, participating in geological drilling and unconventional oil and gas extraction projects.His current research focuses on rock mechanics related to hydraulic fracturing in unconventional oil and gas, such as shale gas and shale oil. He is particularly interested in the effects of different saturation fluids, pore pressures, and multi-field coupling and multi-scale aspects of rock mechanics. His research integrates nuclear magnetic resonance, digital image technology (LD-DIC), and mechanical experiments to analyze the changes in the elastic-plastic mechanical properties of unconventional reservoir rocks like shale under various geological conditions and the main control mechanisms.

Unravelling the past for a safer future: How historic rock mass classification data compare with slope performance monitoring data

M. Pretorius

Vedanta – Gamsberg, South Africa

In this paper the author investigates the correlation between empirically derived deformation threshold values and actual slope monitoring deformation data in open-pit mining, focusing on the Gamsberg mine in South Africa. Two slope failure events within a schist layer were analysed.

Rock mass classification data from borehole logs were analysed and empirical calculations were done to derive predicted deformation values. This data was then compared with real-time deformation measurements from slope stability radar; in particular, where the two failures occurred.

The study revealed a significant alignment between empirical predictions and actual measurements, with both events falling within one standard deviation of the empirical dataset's mean. This validates the utilisation of empirical methods for initial deformation threshold estimations in slope stability monitoring.

This study provides valuable insights into the practical application of empirical deformation thresholds in open-pit mining, offering a foundation for more accurate and reliable slope stability assessments. The findings have implications for enhancing safety protocols, optimising resource extraction, and improving overall operational efficiency in the mining industry.

Keywords: Open-pit mining, Slope deformation, Rock mass classification, Slope stability.

INTRODUCTION

Rock Mass Classification

Rock mass classification is a widely used system for evaluating the quality of rock masses in various geological engineering applications, including slope stability (Hoek, 2023). Some of the most common classification systems include rock mass rating (RMR) (Bieniawski, 1973), Q-System (Barton, Lien & Lunde, 1974), and the geological strength index (GSI) (Hoek, Wood & Shah, 1992). These systems allow engineers to assign numerical values to various aspects of a rock mass, including the strength, joint condition, and spacing, which can then be used to estimate the stability of slopes and other geological features. Each classification system has its strengths and limitations.

Slope Monitoring
Monitoring systems in open-pit mines have evolved with advancements in technology, allowing more accurate real-time measurements of slope deformation. Ground-based radar, interferometric synthetic aperture radar, and laser scanning are widely-used technologies that provide continuous monitoring and early warning of slope failures (Osasan & Afeni, 2010). Slope monitoring aims to detect slope movement at an early stage, allowing operators to take corrective action before a catastrophic failure occurs.

Slope stability radars (SSRs) are essential tools for monitoring and managing slope stability in open-pit mines. These ground-based radar systems provide near real-time deformation measurements over broad coverage areas, allowing geotechnical engineers to observe the spatial distribution of pit-wall movements and their progression over time (Dick, 2015).

Slope Stability Prediction Through Empirical Methods
Brox and Newcomen (2003) provided an influential study on utilising strain criteria to predict high wall stability performance and established a formula for determining deformation thresholds based on empirical data. Their research was instrumental in demonstrating how strain measurements can inform slope stability designs. The authors referenced the work of Zavodni (2001), who proposed that highwalls in open-pit mines could undergo a maximum strain of 0.6% to 1% before transitioning from regressive (self-stabilising) movement to progressive (unstable) movement. The Brox and Newcomen approach focuses on utilising strain criteria to predict high wall stability performance in open-pit mining. The authors suggest that this strain criteria approach, in conjunction with the predictive numerical modelling of strains, may be beneficial for evaluating the proposed highwall modifications and pit expansions during open pit mine design and long-term planning.

Zavodni (2001) also suggested that strains greater than 1% could result in abrupt high wall instability or failure. These thresholds are based on field observations of multiple mining operations that exhibit time-dependent movements. The empirical observations of Brox and Newcomen were used to validate the threshold strain levels proposed by Zavodni (2001). In these case studies, movement data were analysed to determine the strain levels at key points: when tension cracks first appeared (approximately 0.1%), when movement became progressive (0.6%), and when failure occurred (strains over 1%).The authors explained that surface movement monitoring, particularly using prism surveys, was critical in quantifying the total strain experienced by the high walls.

This monitoring data, combined with the rock mass quality (characterised using the RMR system), helped to derive and validate the threshold strain levels for various stages of high wall stability. In summary, the strain levels were derived through a combination of previous research (Zavodni's work) and empirical observations from multiple case histories in open-pit mines, where surface movement and high wall strain were carefully monitored and correlated with actual stability performance.
The following formula was published in the study:

$$\varepsilon = \Delta x / H \qquad [1]$$

where:
ε = strain, presented as a percentage.
Δx = maximum deformation of the high wall
H = total height of the highwall

The study produced a chart as an output that related the different strain percentages calculated to the measured RMRs. Figure 1 shows this chart, and the strain percentages of the different case studies of wedge and planar failures evaluated.

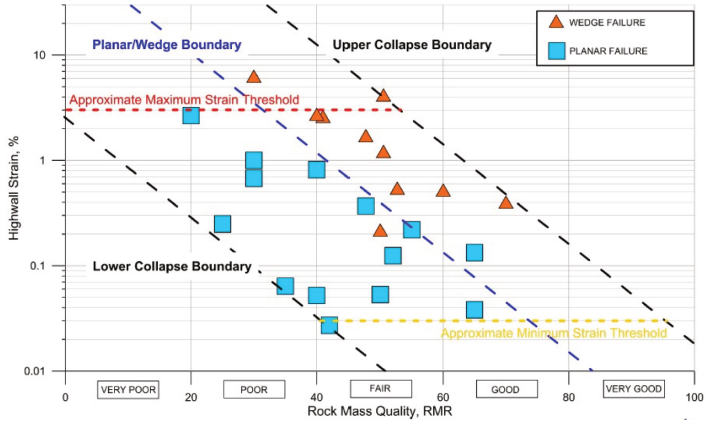


Figure 1. RMR versus pit wall strain for wedge and planar failures at collapse, after Brox & Newcomen (2003).

Newcomen and Dick (2016) built upon the 2003 study by Brox and Newcomen (2003), introducing several key updates in the strain-based approach for predicting pit wall failure. The first major update involved the use of an expanded dataset and refined definitions of failure. The initial study (Brox and Newcomen 2003) was based on a limited dataset of 12 slope failures and included both complete and non-collapsed failures.

In the original publication, the strain threshold for collapse was set at 2%, with general guidance provided for various stages of pit-wall stability. In the 2016 update, the maximum strain threshold for collapse increased to 4%, reflecting findings from the expanded dataset. This was twice the previously suggested 2% strain threshold and four times the 1% threshold proposed by Zavodni (2001). Furthermore, a clear separation of the failure mechanisms was achieved. In the original study, the failure mechanisms were broadly grouped, including wedge, planar, rock mass, and toppling failures. In the 2016 update, the study emphasised the need to differentiate the strain thresholds for different failure mechanisms. Separate analyses were conducted for planar and wedge failures versus rock mass and toppling failures with distinct strain ranges for each type of failure.

- Planar failures typically occurred at lower strains (0.03% to 3%).
- Wedge failures had strains up to 6%.
- Toppling failures exhibited the highest strain values (up to 15%).

Building on this work, Coetsee, Armstrong, and Terbrugge (2020) further refined the empirical methods for determining strain threshold values for slope monitoring in open-pit mines. Their adaptation of Newcomen and Dick's (2016) criteria provided a method for using strain thresholds to develop trigger action response plans in mining operations.

Newcomen and Dick's (2016) strategy involves calculating the strain. Coetsee *et al.*, (2020) modified this formula, allowing displacement to be predicted based on pre-selected strain values and defined slope heights. This adjustment helps provide proactive evaluations of the slope displacement history, making it easier to set alarms and monitor for potential instabilities in mining environments. The original formula was modified as follows:

$$\Delta x = \varepsilon / H \qquad [2]$$

The modification involved re-arranging the formula to obtain the deformation parameter (Δx), where a known strain and slope height is used as input. This approach aims to provide a more comprehensive and adaptable framework for monitoring and responding to slope instability in open-pit mines by integrating strain-based criteria with established movement patterns and stages to enhance early warning capabilities.

Problem statement
Empirical methods have traditionally been used to determine the initial deformation thresholds, particularly at the beginning of mining projects where no historical data are available. By using rock mass classification data, engineers can estimate key parameters such as deformation and rock mass strength (Moser, Wagner, & Schinagle, 2017). Although these methods are widely accepted, they can be prone to biases based on the quality and extent of the data collected during geotechnical investigations.

Once a mine has been in operation for some time, back analysis can be employed to refine the initial deformation thresholds. This technique involves analysing historical deformation data and failure events to better understand the behaviour of the rock mass. According to Sharon and Eberhardt (2020), back analysis is one of the most reliable methods to confirm the validity of slope stability models, particularly when combined with continuous monitoring data.

Furthermore, slope stability monitoring is regarded as an industry best practice, not only for confirming slope designs but also as a key point of risk management for many mines (Osasan & Afeni, 2010; Dixon *et al.*, 2011). A common practice is the use of back analysis of monitoring data to determine threshold values (Sharon & Eberhardt, 2020). A recent study by Mulenga *et al.*, (2022) highlighted the importance of reconciling rockfall and slope safety-critical controls using real-time monitoring data. This study demonstrated that deformation thresholds determined through monitoring can provide more accurate predictions of slope performance than purely empirical methods.

Method

This study used a systematic approach to compare rock mass classification data from an existing database with slope performance monitoring data to examine whether the predictive data correlate with the actual recorded measurement.

Study Area
This study focuses on Gamsberg mine, a zinc mine in South Africa's Northern Cape province, between the towns of Pofadder and Aggeneys. Figure 2 shows the location of the Gamsberg mine.



Figure 2. Location of the study area.

The goal of this study was to quantitatively analyse both datasets – prepopulated rock mass classification data and actual slope performance monitoring data – to determine their relationship and evaluate whether empirical predictions can accurately forecast real-world rock mass behaviour in open-pit slopes.
The data collection process incorporated two primary sources of data:

1. Pre-populated rock mass classification database: This database contains historical data primarily collected through borehole core logging, downhole geophysics, field, and laboratory tests. Key data points include the material strength, fracture frequency, joint orientation and condition, rock mass classification, and other geotechnical parameters.
2. Actual recorded monitoring data: This includes recorded deformation data gathered from slope monitoring equipment (Slope Stability Radar).

The data collection process was conducted in multiple phases. Initially, information was retrieved from the existing database to extract parameters associated with specific rock formations and geographical locations (specifically, the lithological units that comprise the slope surfaces in the region of interest). For the purposes of this study, data from two slope failure events (referred to as Event 1 and Event 2) were selected based on the availability of both rock mass classification and actual recorded deformation monitoring data.

To select only data applicable to the portion of the pit where Events 1 and 2 occurred and within the relevant lithological layer only, borehole data that intersected the specific layer were selected. Data were further extracted from the boreholes to focus only on the selected intervals that intersected the relevant lithology. The extraction criteria were used to select only variables directly applicable to rock mass behaviour and classification. Table 2 presents a sample of the extracted data.

Table I. Sample of the extracted data from selected boreholes

BH ID	Depth From	Depth to	Lith	RQD	ISRM Strength Code	RMR89	GSI	Q
GVD172	183.47	185.5	SCH	97	4.0	70	65	22
GVD185	99.5	101.2	SCH	52	4.0	59	54	8
GVD187	278.39	281.35	SCH	83	5.0	64	59	12

From this data, the RMR and GSI were extracted from all boreholes that intersect the specific lithological layer. The data were grouped for further analysis to calculate the rock mass modulus and further strain calculations, from which the deformation values were calculated. Building on the previous dataset, the rock strength database was used to extract the strength data for the applicable schist layer. A similar approach was adopted in that only the strength data from the relevant lithological layer were analysed. Table 2 shows the rock mass data extracted.

Table II. Rock mass strength data extracted from the database

Lithology	UCS	Poisson's	E (Gpa)	SG
SCH	103	0.24	47.1	2.75

Finally, deformation data from two past failure events were extracted from the slope stability monitoring database. Figure 3 shows the typical deformation data extracted for a failure event from commercially available software used to analyse the data (Monitor IQ).



Figure 3. Typical deformation data extracted from the slope monitoring database (GroundProbe).

Analysis and findings

Rock Mass Classification and Laboratory Test Data Analysis

The data extracted from the two datasets, relating specifically to the schist layer, are summarised. Based on the analysis options selected from the literature, Bieniawski's (1989) RMR, and Hoek's GSI. Table 3 presents the statistical summary of the values extracted from the database.

Table III. Summary of Rock Mass Classification Data

	RMR	**GSI**
Average	52	47
Standard Deviation	10.6	10.6
Minimum	32	27
Maximum	76	71

Using each individual RMR and GSI value, Equations 3 and 4 were used to calculate the Rock Mass Modulus (Erm):

$$Er_m = 10^{(RMR-10)/40} \quad [3]$$

where:
E_{rm} = Rock mass deformation modulus
RMR = Rock Mass Rating

$$E_{rm} = 0.33e^{0.064*GSI} \quad [4]$$

where:
E_{rm} = Rock mass deformation modulus
GSI = Geological Strength Index

From these calculations, a summary of the data is presented in Table 4.

Table IV. Summary of Rock Mass Modulus calculated values.

	Erm from RMR	Erm from GSI
Average	9.88	8.16
Standard Deviation	6.07	5.59
Minimum	2.72	1.90
Maximum	33.50	31.04

Hooke's law was used to calculate the strain values from the rock mass modulus (Equation 5):

$$\varepsilon = \sigma/E \quad [5]$$

where:
E = (Modulus of Elasticity) In this case Rock Mass Modulus
σ = stress (maximum stress; in this case, UCS)
ε = Strain

This calculation assumes that stress versus strain is linear, up to the moment of failure. Table 5 shows a summary of the calculated strain values.

Table V. Summary of Strain Values calculated from the RMR and GSI Rock Mass Modulus

	Strain from Rock Mass Rating Values	Strain from Geological Strength Index Values
Average	14.90	19.57
Standard Deviation	8.83	12.82
Minimum	3.07	3.32
Maximum	37.93	54.21

The last step in the analysis was to use the approach of Coetsee *et al.,* (2020) to calculate the displacement or deformation data (Equation 6):

$$\Delta x = \varepsilon/H \quad [6]$$

The values first calculated are based on the RMR and GSI. For comparison, the same calculation was done for the actual recorded deformation data. Table 6 lists the calculated deformation data from the strain values determined from the RMR and GSI.

Table VI. Calculated deformation values for Strain from RMR and GSI

	Δx = strain/slope height RMR (mm)	**Δx = strain/slope height GSI (mm)**
Mean	42	53
Standard Deviation	29	43
Minimum	10.25	11.06
Maximum	126.44	180.69

For these calculations, the strain is assumed to be surface strain, and not the rock mass strain, as per Brox & Newcomen (2003). The strain direction, or Δx direction is normal for the failure surface, and the slope height is corrected to indicate height of the anticipated failure, and not the entire slope height. The calculated deformation data are now used for comparison with the actual deformation data recorded.

Slope Stability Monitoring Data Analysis
As per the selection criteria, events 1 and 2 were included in this study. For events 1 and 2, slope stability monitoring data were available.

Event 1was classified as a multiple bench scale (two benches of 15 m each) planar failure. As per the mine's standard at the time, a ground-based SSR was used to monitor the high wall. The deformation data leading up to failure were extracted from the slope monitoring database.

Event 2 was classified as a multiple bench-scale wedge failure (two benches of 15 m each). The measured deformation data for Event 1 was 22.84 mm, and for Event 2 was 69.79 mm. As per Brox and Newcomen (2003), deformation data were used to calculate the strain percentage. The result of this analysis is shown in Table 7.

Table VII. Strain percentages calculated from actual measurements

Strain % From Actual Measurement – Planar Failure	**Strain % From Actual Measurement – Wedge Failure**	
0.03%	0.03%	

Data comparison and test for correlation
The analysis compared the actual measured deformation data with empirically determined predictions using statistical methods and visual representations. To assess the correlation between the two datasets, a Z-test was conducted to evaluate the relationship between the actual measurements and empirically predicted values.

A Z-score quantifies how far and in what direction a single data point deviates from the mean of a standardised distribution, measured in units of standard deviation. For Event 1, the Z-test yielded a score of -0.91. In this study, a Z-score of -0.91 indicates that the observed value is 0.91 standard deviations below the mean. Negative Z-scores reflect values below the mean, while positive Z-scores represent values above the mean.

A Z-score of -0.91 places the observed value 0.91 standard deviations below the mean of the distribution. Referring to the Z-distribution table, this corresponds to a cumulative probability of 18.19%, meaning the observed value is greater than approximately 18.19% of the distribution. Given that it lies within one standard deviation of the mean ($-1 \leq Z \leq 1$), the measured value can be considered a good fit to the empirical dataset. Figure 4 shows a visual representation of the Z value distribution on a standard, normal distribution chart.

For Event 2, the Z-test yielded a score of 0.68. In this study, a Z-score of 0.68 indicates that the observed value is 0.68 standard deviations above the mean. The Z-score places the observed value 0.68 standard deviations above the mean of the distribution. Referring to the Z-distribution table, this corresponds to a cumulative probability of 75.17%, meaning approximately 75.17% of the values in the distribution are below this point. Conversely, 24.83% of the values are above it. Given that it lies within one standard deviation of the mean ($-1 \leq Z \leq 1$), the measured value can be considered a good fit to the empirical dataset. Figure 5 shows a visual representation of the Z value distribution on a standard, normal distribution chart.

As a visual comparison, both Z Scores are presented on a distribution graph in Figure 4.

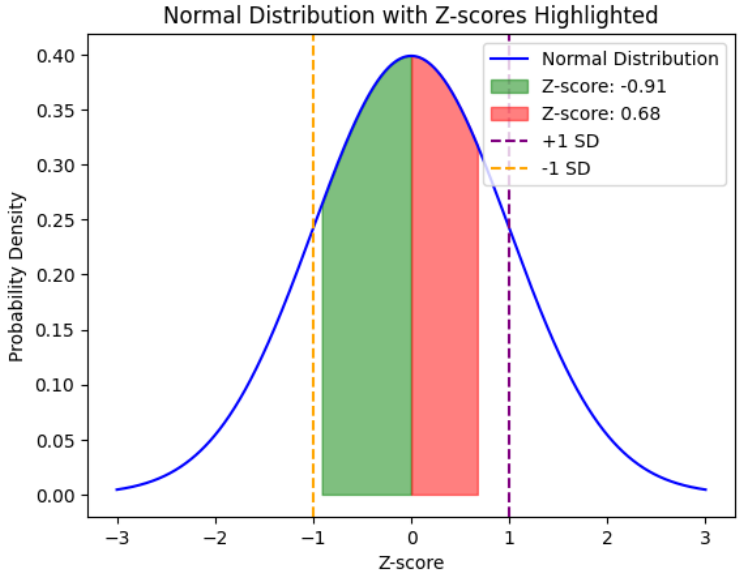


Figure 4. Visual representation of the actual measurements for Event 1 and Event 2 in comparison with the empirical data.

To complement the statistical analysis, the data were also visualised to provide a more intuitive understanding of the relationship between the empirical predictions and recorded values. This visual representation allows for a clear comparison of the range of empirically predicted data with actual observed values. Figure 5 illustrates this comparison for Event 1 and Event 2 with the empirical data. This dual approach of statistical testing and visual representation offers a comprehensive view of how well the empirical predictions align with actual measurements, enabling a more thorough interpretation of the deformation data for both events.

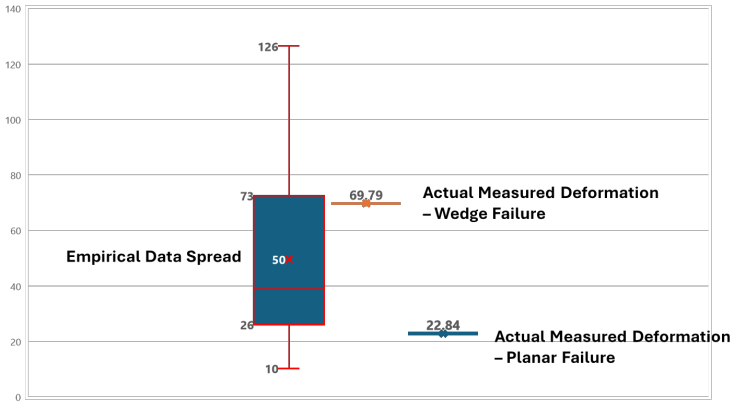


Figure 5. Visual representation of the actual measurements for Event 1 and Event 2 in comparison with the empirical data.

Further analysis was performed, where the deformation data recorded were converted back to strain, as per the work of Newcomen and Brox (2003). Using the original chart produced in their study, where the RMR data were plotted against the pit wall strain at failure, both Event 1 and Event 2 data were plotted. By plotting the results, it can be seen that both events plot well within the range (upper and lower collapse boundary) for planar failures, as compared to the original work of Newcomen and Brox (2003). Figure 6 shows the two case studies evaluated in this research project, plotted on the original chart of Newcomen and Brox.

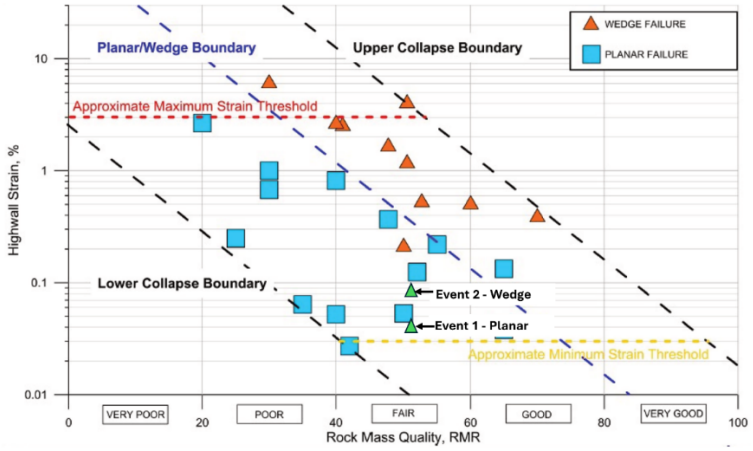


Figure 6. Strain and RMR data for Event 1 and Event 2 plotted against the original published work of Newcomen & Brox (2003).

CONCLUSION

Results indicate a significant correlation between empirical and real-time deformation values. The findings validate the use of combined datasets to enhance slope stability predictions for open-pit mines.

The study revealed that the recorded deformation data falls within one standard deviation of the empirical dataset's mean value. This indicates a good fit of the data. The empirical predictions showed degrees of accuracy within one standard deviation of the actual measured deformation data.

Event 1 demonstrated a slight negative deviation from the predictions, as evidenced by a Z-score of -0.91. This relates to a more than 95% confidence level, as the corresponding Z score would be ±1.96.

The findings suggest empirical predictions may be useful, and that this can accurately reflect real-world deformation events.

These results highlight the importance of comparing empirical models with actual measurements to validate and improve the predictive capabilities of deformation studies. This analysis provides a foundation for refining existing empirical models and developing novel approaches to enhance the accuracy of deformation predictions.

From the data it is concluded that for this particular case, a reliable method to determine monitoring alarm thresholds were derived, based on rock mass classification data.

REFERENCES

Barton, N., Lien, R., & Lunde, J. J. R. M. (1974). Engineering classification of rock masses for the design of tunnel support. Rock mechanics, 6, 189-236.

Bieniawski, Z. T. (1979). The geomechanics classification in rock engineering applications. ISRM.

Bieniawski, Z. T. (1989). 'Engineering rock mass classifications: a complete manual for engineers and geologists in mining, civil, and petroleum engineering'. John Wiley & Sons.

Brox, D. and Newcomen, W. (2003) 'Utilizing strain criteria to predict highwall stability performance', in ISRM 2003 - Technology Roadmap for rock mechanics. Johannesburg: South African Institute of Mining and Metallurgy.

Coetsee, S., Armstrong, R. and Terbrugge, P. (2020) 'The use of strain threshold in slope stability trigger action response plans', in Slope Stability 2020. Perth: Australian Centre for Geomechanics.

Dick, G. J., Eberhardt, E., Cabrejo-Liévano, A. G., Stead, D., & Rose, N. D. (2015). Development of an early-warning time-of-failure analysis methodology for open-pit mine slopes utilizing ground-based slope stability radar monitoring data. *Canadian Geotechnical Journal*, *52*(4), 515-529.

Dixon, R. A., Johnson, T. M., de Graaf, P. J. H., Wessels, S. D. N., & Venter, J. (2011, September). Risk based geotechnical slope reconciliation at rio tinto iron ore, pilbara operations. In *Proceedings International Symposium on Rock Slope Stability in Open Pit Mining and Civil Engineering (Slope Stability 2011), E. Eberhardt and D. Stead (eds)* (pp. 18-21).

Hoek, E., Wood, D., & Shah, S. (1992). A modified Hoek–Brown failure criterion for jointed rock masses. In *Rock Characterization: ISRM Symposium, Eurock'92, Chester, UK, 14–17 September 1992* (pp. 209-214). Thomas Telford Publishing.

Hoek, E. (2023) Practical Rock Engineering (2023 Edition). Hoek's Corner, 21 August. Available at: https://www.rocscience.com/learning/hoeks-corner (Accessed: 21 August 2023).

Moser, A., Wagner, H. and Schinagle, S. (2017) 'Application of rock mass classification systems as a tool for rock mass strength determination', in Deep Mining 2017: Eigth International Conference on Deep and High Stress Mining. Perth: Australian Centre for Geomechanics.

Mulenga, P.A., Ndlovu, X. and de Graaf, P. (2022) 'Rockfall and Reconciliation – Analysis and Reporting of a Slope Safety Critical Control, Venetia Mine', in Slope stability 2022, Tucson, Arizona.

Newcomen, W., & Dick, G. (2016). An update to the strain-based approach to pit wall failure prediction, and a justification for slope monitoring. *Journal of the Southern African Institute of Mining and Metallurgy*, *116*(5), 379-385.

Osasan, K.S. and Afeni, T.B. (2010) 'Review of surface mine slope monitoring techniques', Journal of Mining Science, 46(2), pp. 177-186. Available at: https://doi.org/10.1007/s10913-010-0023-8.

Sharon, R., & Eberhardt, E. (Eds.). (2020). Guidelines for Slope Performance Monitoring. CSIRO Publishing

Stacey, T.R. and Osasan, K.S. (2014) 'Automatic prediction of time to failure of open pit mine slopes based on radar monitoring and inverse velocity method', International Journal of Mining Science and Technology, 24(3), pp. 305-313.

Zavodni, Z.M., 2001. Time-dependent movements of open-pit slopes. In: W.A. Hustrulid, ed. Slope Stability in Surface Mining. Littleton, CO: Society for Mining, Metallurgy, and Exploration (SME), Ch. 8.



Mornè Pretorius

Chief Rock Engineer
Vedanta Zinc International

Mornè is a registered professional scientist (SACNASP, Earth Science) and holds a Chamber of Mines Certificate in Rock Mechanics (Open Pit) amongst other qualifications. He spent 15 years in the consulting space as a Strata Control Officer and later Rock Engineer, gaining valuable experience in various different commodities and mining methods. He is currently the Chief Rock Engineer for the Gamsberg Open Pit.

Stabilisation of highwall instability using numerical modelling and statistical analysis for open pit mining

N.I. Umeh, S. Darries, N.E. Baloyi, T. Rangasamy

Middindi Consulting (Pty) Ltd, South Africa

This study focuses on the geotechnical evaluation of a highwall that experienced a significant slope failure. The primary objective was to thoroughly assess the extent of the failure, identify and evaluate potential trigger mechanisms, and evaluate the risk it posed to a public road situated approximately 100 m from the highwall. Aerial photography and fracture propagation analysis, conducted using QGIS, tracked fracture development over several months. Numerical modelling using Rocscience RS3 and RS2 software enabled a comprehensive stability analysis of the highwall. The results showed that the failed sections had factors of safety below unity (0.82 and 0.81), signalling instability, whereas stable sections maintained sufficient safety margins. The combination of fracture intensity and propagation data coupled with numerical back analyses was able to predict both time to failure and progressive instability. Predictive numerical simulations were subsequently used to derive buttress designs to stabilise the highwall. The study further assessed the potential impact on the public road, which indicated no significant displacement effects.

Keywords: Highwall stability, Fracture propagation, Numerical modelling, Stability analysis, Buttress design

INTRODUCTION AND BACKGROUND

Rock mass stability is influenced by various geological and geotechnical factors, such as discontinuities, material properties, and external loads like seismic activity and mining- induced stresses. Understanding these factors through numerical modelling and field-based observations enables the development of effective engineering solutions for slope stabilisation.

By integrating advanced numerical modelling techniques with field-based observations, this paper provides a comprehensive methodology for assessing and mitigating rock slope instabilities. The findings contribute to a deeper understanding of highwall failure mechanisms and inform the best practices for stabilisation strategies in open pit mining operations. Additionally, the research highlights the importance of predictive modelling in geotechnical risk assessment, offering insights into optimising excavation design and long- term slope management

The objectives of this study are:

- To analyse highwall failure progression using aerial fracture mapping and numerical modelling.
- To assess the impact of slope instability on surrounding infrastructure.
- To develop and validate a buttress support design to enhance slope stability.

The assessment was conducted following the observation of a large-scale failure along the West Highwall of the East Pit. The study aimed to evaluate the failure's extent and progression using aerial photography, assess its impact on a nearby public road, and conduct a stability analysis. Additionally, rock engineering expertise was utilised to develop suitable support measures, specifically a buttress, to ensure highwall stability and safety.

Figure 1 presents an aerial image of the study area, highlighting the area of instability of the highwall, active highwall areas, and the nearby public road.

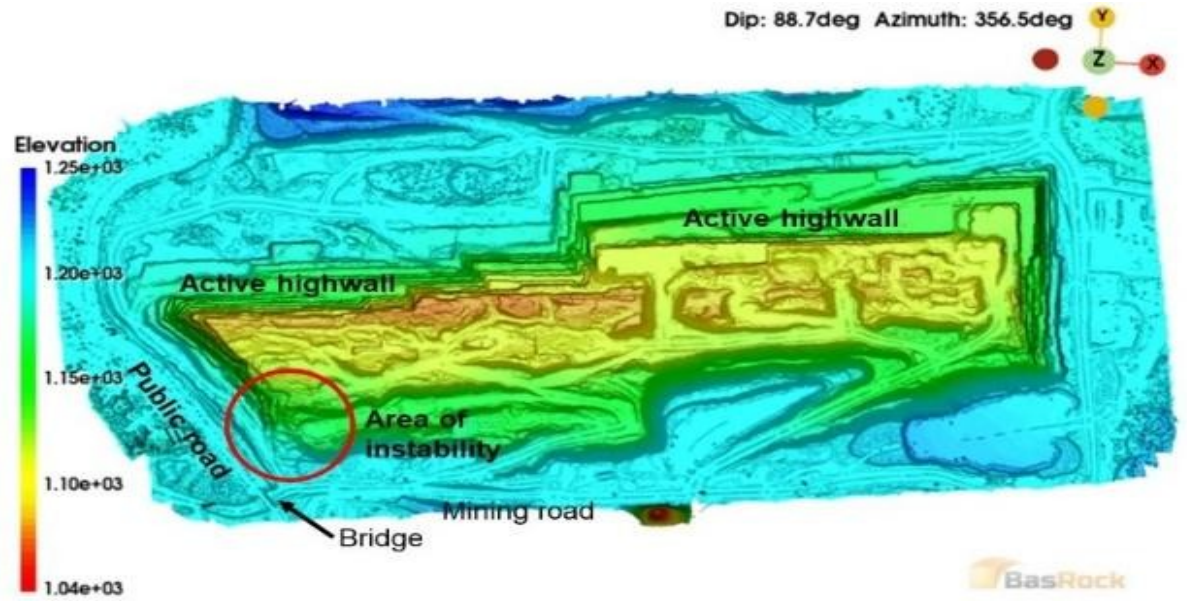


Figure 1. Plan view of the East Pit layout.

The mine is located within the Critical Zone of the Rustenburg Layered Suite in the Western Limb of the Bushveld Igneous Complex. This zone contains three main chromitite packages: the Lower Group (LG), Middle Group (MG), and Upper Group (UG). Mining primarily targets the MG chromitites, which form the basal succession of the Upper Critical Zone. Five major chromitite seams (MG1 to MG4, including MG4A) dominate the lithological succession, with additional sporadic chromitite occurrences. These chromitite layers strike east west and dip northward at approximately 12° to 15° in the East Pit.

Site Inspection

Tensile cracks are surface fractures that develop due to stress redistribution in open pit slopes. They typically form along the crest of highwalls as a result of excessive tensile stress exceeding the rock mass strength. These cracks are early indicators of potential slope failure and can be caused by various factors (Jami & Girard, 2001).

A site inspection was conducted to assess reported tensile cracks and ground displacement along the south-western crest of the East Pit. Observations confirmed prominent tension cracks (Figures 2- 3) and water seepage from the western highwall, southern highwall, and backfill, indicating potential stability concerns.



Figure 2 & Figure 3. Tensile cracks forming the blocks and toppling to the north-east.

Fracture Analysis

Aerial photographs of the East Pit were taken between 1 January, 2023, and 28 June, 2023. A total of eight images were provided, and captured on the following dates:

- 1 January, 2023
- 1 March, 2023
- 1 April, 2023
- 1 May, 2023
- 11 June, 2023
- 18 June, 2023
- 25 June, 2023
- 28 June, 2023

The aerial photographs were analysed for fracture propagation using QGIS, an open- source geographic information system software. QGIS is widely used for spatial data visualisation, analysis, and mapping. It supports a wide range of geospatial formats and provides advanced tools for analysing geological features, such as fracture propagation in rock masses.

The analysis involved mapping visible open fractures and measuring their length and aperture from 1 January, 2023, to 28 June, 2023. Figure 4(A) shows the area on 1 January, 2023, with minimal fractures, while Figure 4(B) illustrates the same area on 28 June, 2023, with increased fracturing. Using QGIS, dip, strike, and random fractures were identified and overlaid on the photographs, along with their corresponding fracture openings.

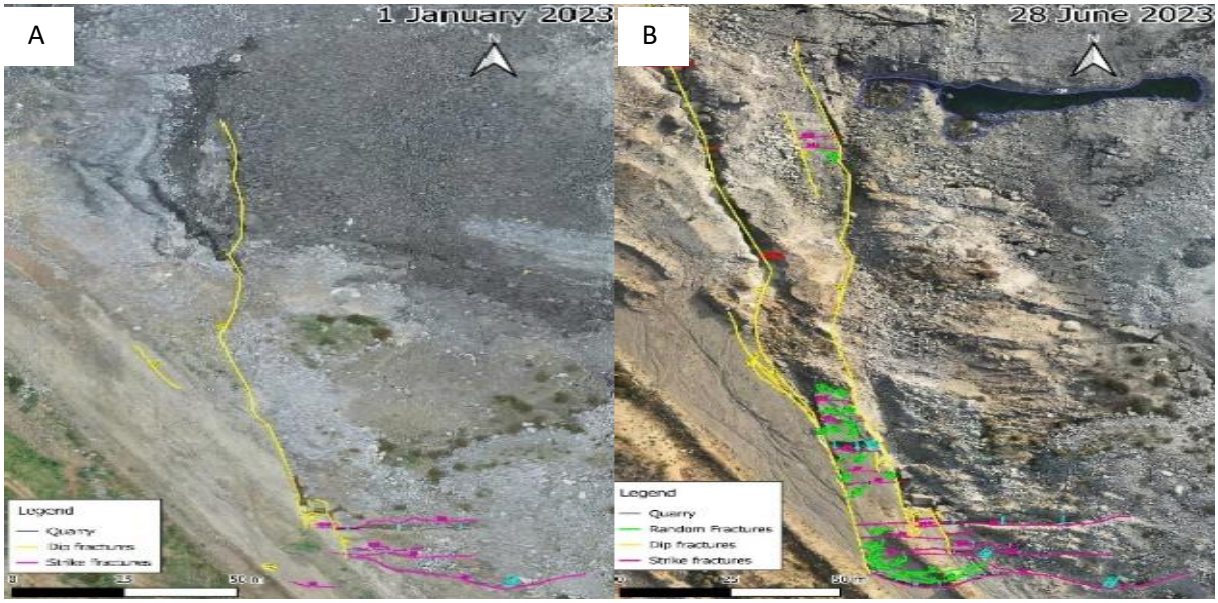


Figure 4. Progression of fractures from (A) 1st January 2023 to (B) 28th June 2023.

The measured fracture lengths and openings are summarised in Table I to Table III. This approach provided a detailed understanding of fracture development and progression over time.

Table I. Summary of dip fractures

Date	**Total Number of Fractures**	**Total Length of Fractures (m)**	**Average Length of Openings of Fractures (m)**
01/01/2023	4	223.57	0.30
01/03/2023	4	243.35	0.37
01/04/2023	4	245.97	0.37
01/05/2023	4	245.73	0.37
11/06/2023	10	630.62	0.67
18/06/2023	10	630.66	0.70
25/06/2023	10	630.66	0.70
28/06/2023	10	630.66	0.75

Table II. Summary of strike fractures

Date	**Total Number of Fractures**	**Total Length of Fractures (m)**	**Average Length of Openings of Fractures (m)**
01/01/2023	6	162.63	0.38
01/03/2023	6	188.25	0.42
01/04/2023	6	188.59	0.67
01/05/2023	6	188.50	0.84
11/06/2023	15	343.15	0.87

18/06/2023	15	343.15	0.87
25/06/2023	15	343.44	0.87
28/06/2023	15	343.44	0.91

Table III. Summary of random/ radial fractures

Date	Total Number of Fractures	Total Length of Fractures (m)	Average Length of Openings of Fractures (m)
01/01/2023	0	0.00	0.00
01/03/2023	0	0.00	0.00
01/04/2023	0	0.00	0.00
01/05/2023	0	0.00	0.00
11/06/2023	27	179.27	0.15
18/06/2023	28	189.02	0.16
25/06/2023	28	191.44	0.18
28/06/2023	28	191.59	0.20

The collected data was graphed to analyse the relationship between time and failure progression. Each data point represents a specific date, with 1 January, 2023, set as the baseline (zero). Parameters such as aperture, length, and fracture count for strike, dip, and radial fractures were plotted against time (Figure 7) to track failure trends and predict potential failure timing.

The graphs indicate a stabilisation trend, with both fracture count and cumulative length plateauing over time. This suggests that further progression of fractures are minimal. Backward projection analysis estimates that the initial movement began six to 12 months prior to January 2023. However, fracture apertures continue to widen and are expected to do so until July–November 2023. Table IV summarises the predicted failure timeline, indicating that the majority of displacements have already occurred, with no significant expansion of the failure footprint.

Numerical Model Setup

Numerical modelling was performed using Rocscience software, RS3 and RS2. The setup and methodology for these models are discussed in the following sections.

Rocscience RS3

Numerical modelling was conducted using Rocscience RS3, a 3D finite element analysis software designed for evaluating stress, deformation, and stability in surface and underground excavations. A model was developed using the provided pit shell and reef material layers in .dxf format (Figure 5). The East Pit shell was refined to focus on the failure area, West Highwall, and adjacent public road. However, material layers were missing in this section, requiring extension in Map3D to generate new reef material planes. Additionally, a 1m MG1 Footwall Shear Zone layer was created and incorporated below the MG1 Chromitite layer to enhance the accuracy of the model.

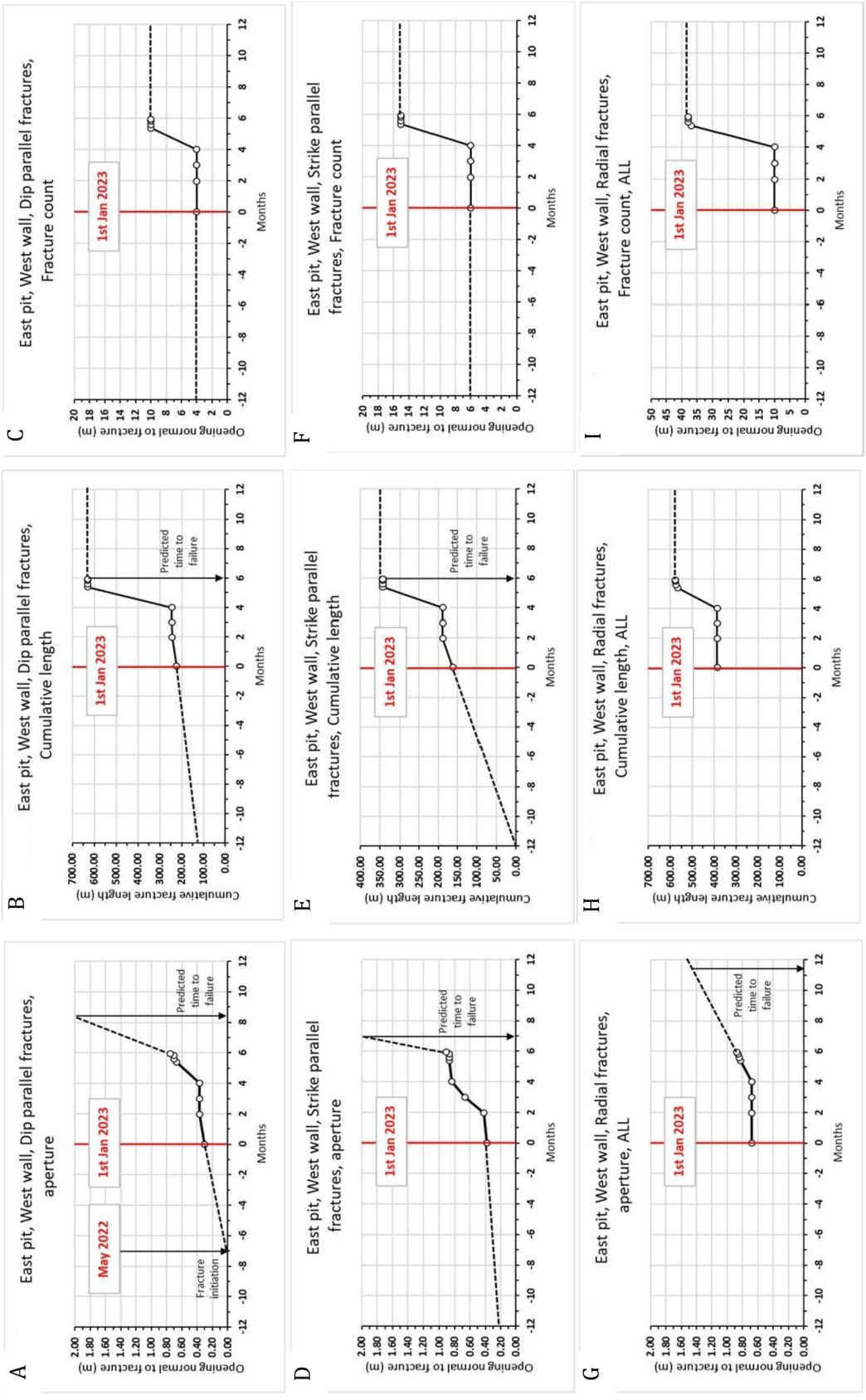


Figure 7. Fracture time to failure graphs

Table IV. Summary of fractures and estimated time to failure

Fracture Set	*Parameter*	*Stabilised*	*Unpredictable*	*Progressing*	*Estimated Time to Failure*
Dip parallel	*Aperture*			x	*Mid-Aug 2023*
	Cumulative length	✓			*Stabilised*
	Fracture count	✓			*Stabilised*
Strike parallel	*Aperture*			x	*Early July 2023*
	Cumulative length	✓			*Stabilised*
	Fracture count	✓			*Stabilised*
Radial	*Aperture*			x	*Mid-Nov 2023*
	Cumulative length		x		*Unknown*
	Fracture count	✓			*Stabilised*
Percentage	*9*	*55.56*	*11.11*	*33.33*	-

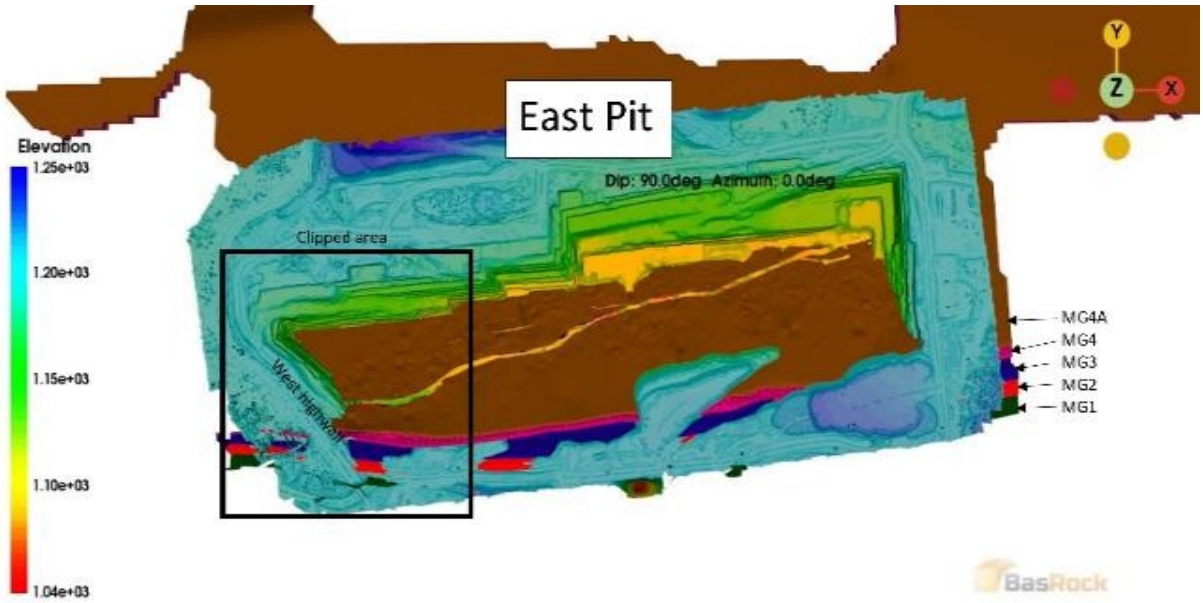


Figure 5. Original .dxf files viewed in GEM4D.

The main objective of the RS3 analysis was to determine and identify the location and extent of displacement along the West Highwall. Figure 6 illustrates a configuration model of the failure area within the East Pit West highwall section.

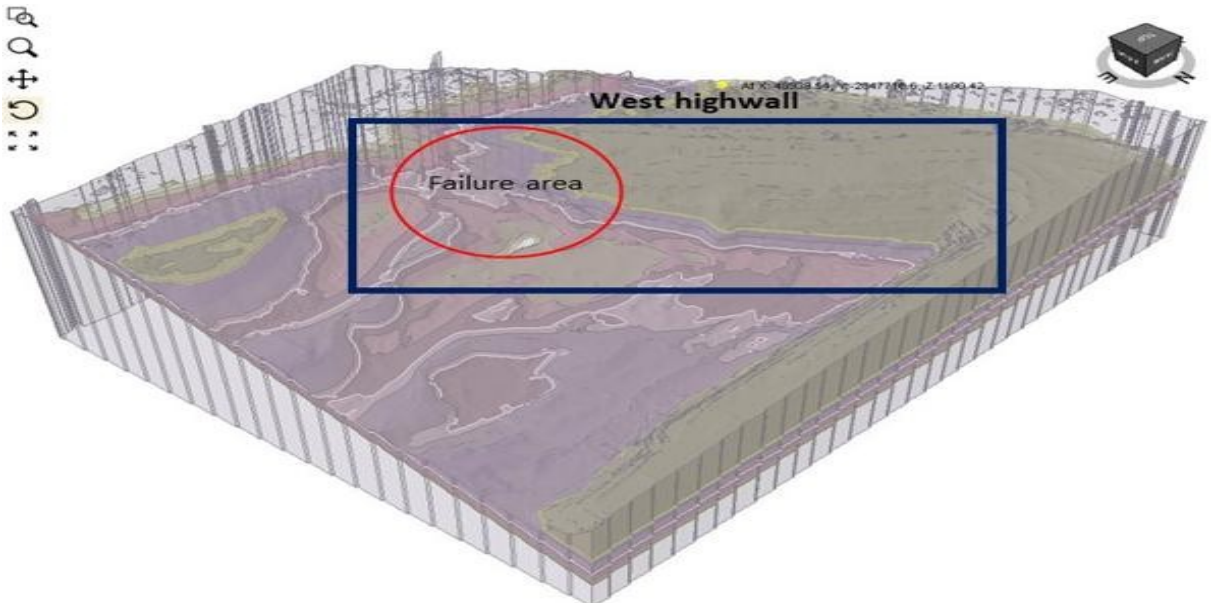


Figure 6. Configuration of East Pit West Highwall section.

Rocscience RS2

Further numerical modelling was carried out using Rocscience RS2, a 2D finite element analysis software suitable for applications such as slope stability, excavation, tunnel support, and groundwater analysis.

Before modelling in RS2, pit shell sections with reef layers were extracted using GEM4D (Figure 8) to generate the necessary profiles for analysis.

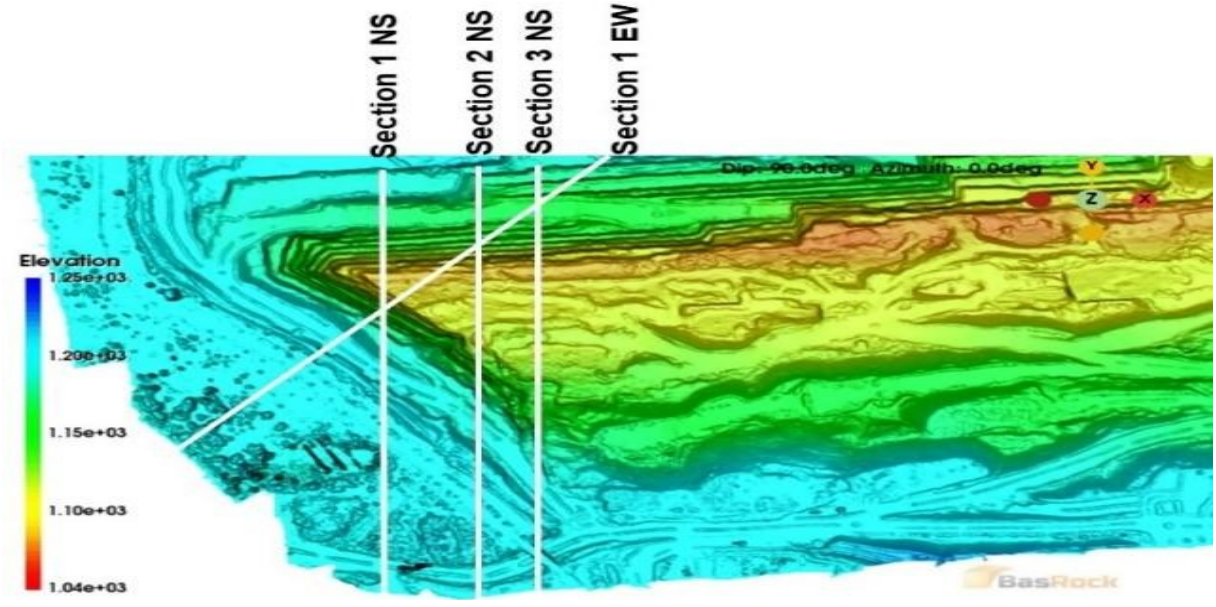


Figure 8. Location of the sections taken for the RS2 modelling.

A total of 29 RS2 models were developed to evaluate the stability of the West Highwall under various geological and structural conditions. These models were categorised as follows:

- West Wall Stability Models (North- South Cross Sections)
  - Only MGs: there are only joints between the materials.

- Vertical Joints (90°): there are joints between the materials and a joint set dipping vertically (90°).
- Sub-Vertical Joints (80°): there are joints between the materials and a joint set dipping sub-vertically (80°).
- Anisotropy (weak joints in layers): modelled rock wall comprised of anisotropic materials.
- Combined Vertical Joints & Anisotropy: materials contain a joint set dipping 90° and anisotropic properties.

North-South Sections: These models utilised cross-sections aligned with the orebody dip, focusing on the influence of the MG1 Shear Zone and the direction of movement towards the north.

- East-West Section: Captured the true slope dimensions, taken perpendicular to the road and western highwall.
- Buttress Models: Analysed varying buttress heights to determine the optimal design for slope stabilisation.

The different constructed models are presented in Figure 9 to Figure 11.

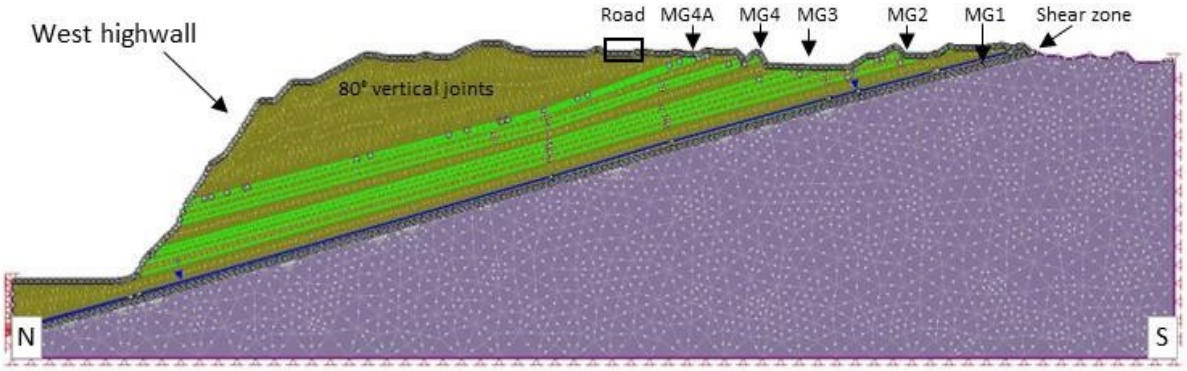


Figure 9. Section 1 NS model with vertical joints.

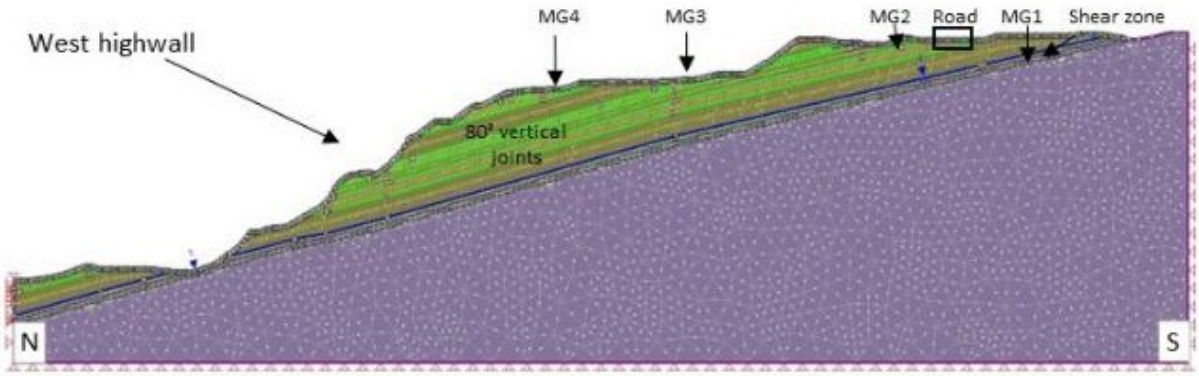


Figure 10. Section 2 NS model with vertical joints.

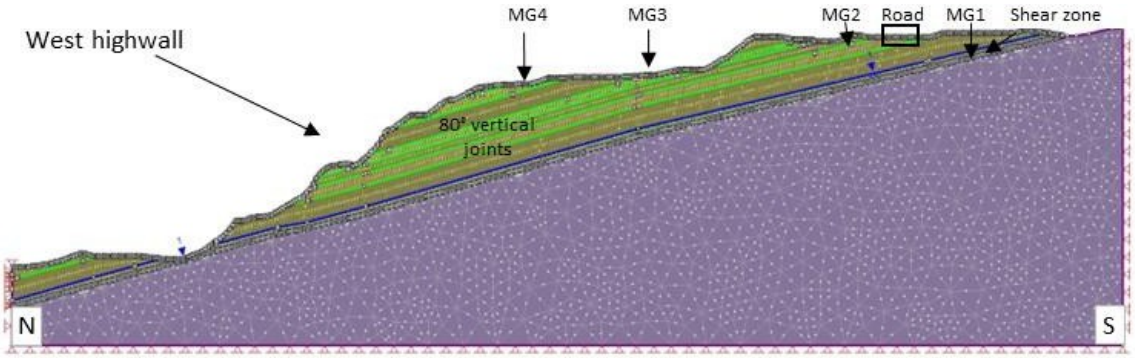


Figure 11. Section 3 NS model with vertical joints.

To determine the optimal buttress dimensions, RS2 models were computed with varying buttress heights from 30 m to 100 m. The buttress was incorporated as a material at the slope's base to assess its stabilising effect. The analysis results are presented in Figure 12 to Figure 16.

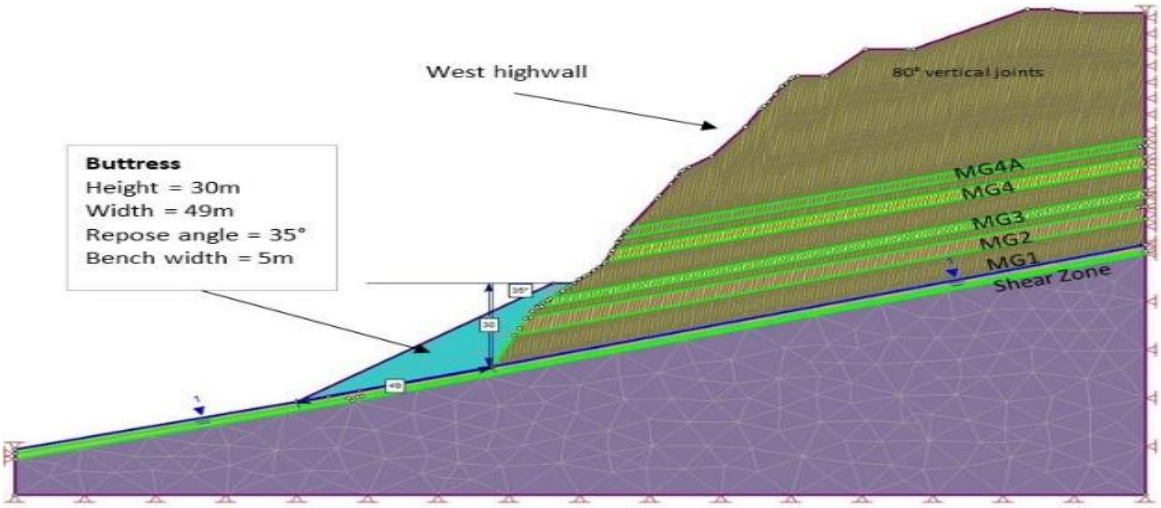


Figure 12. Buttress 30 m high from toe.

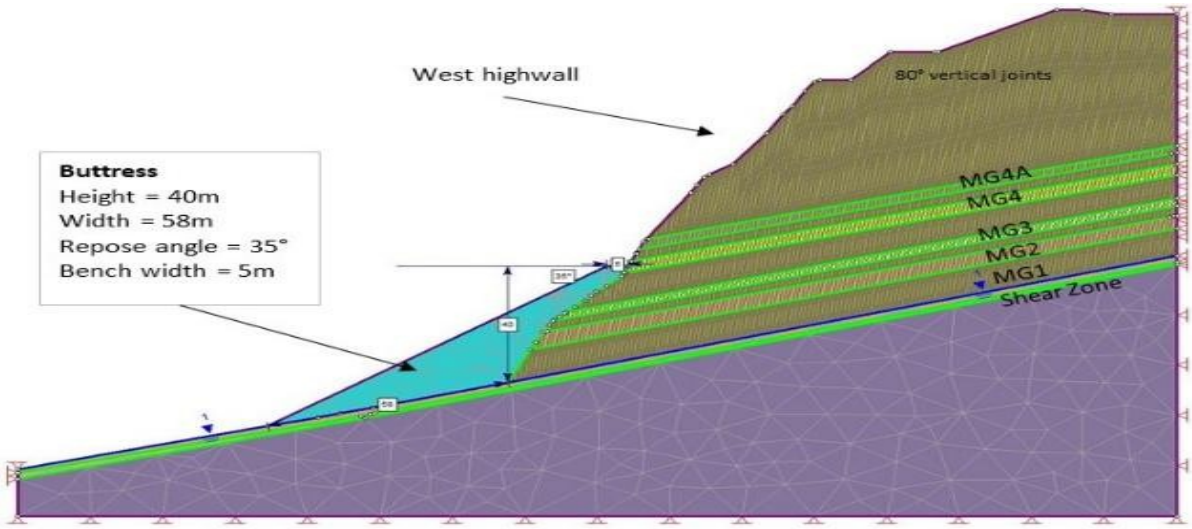


Figure 13. Buttress 40 m high from toe.

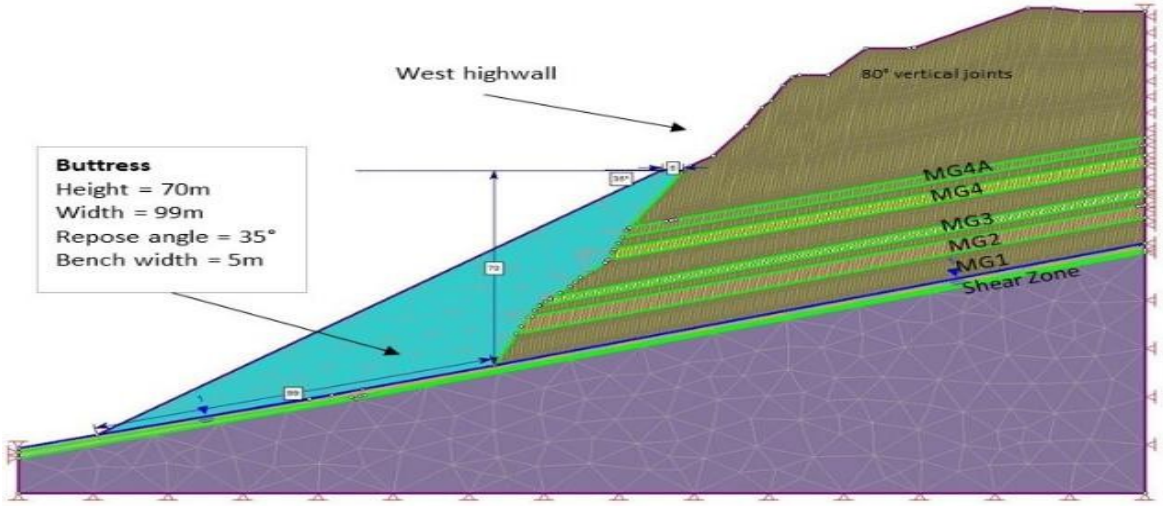


Figure 14. Buttress 70 m high from toe.

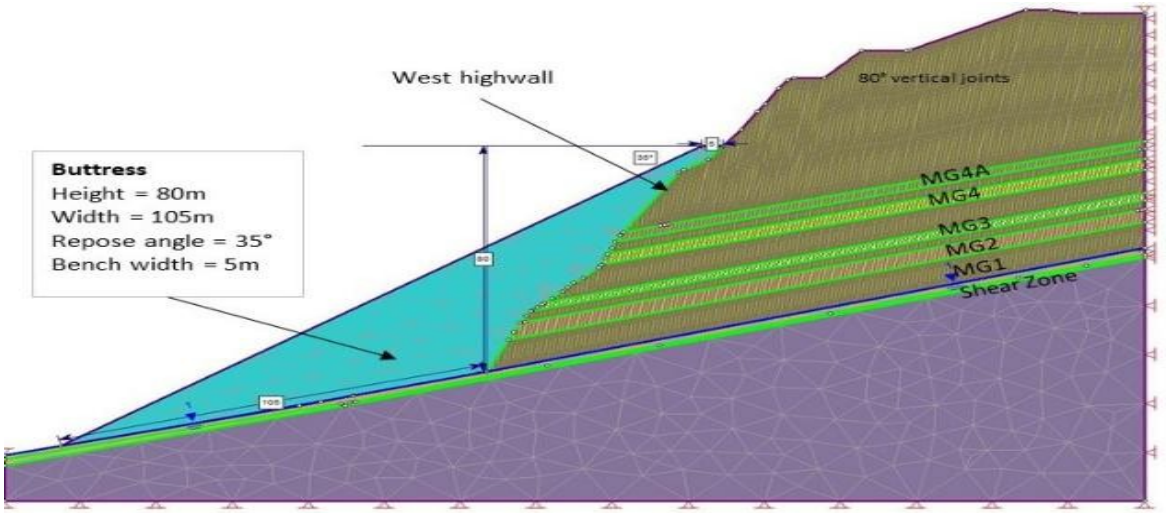


Figure 15. Buttress 80 m high from toe.

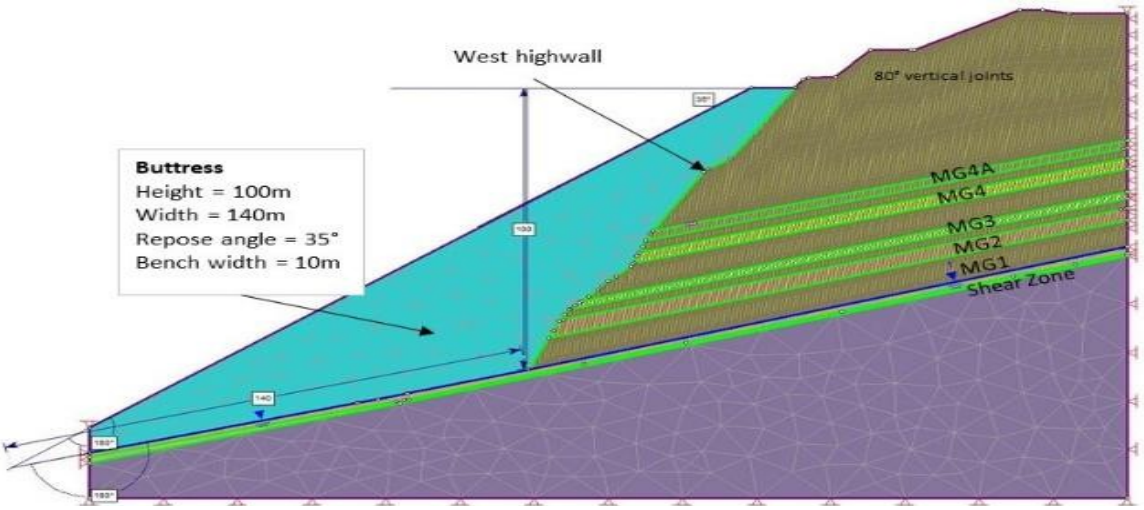


Figure 16. Buttress 100 m high from toe

Model Results

Pit Stability

The southern region of the West Highwall of the East Pit is where instability and failure have occurred. As the open pit develops, the stability of the pit slope may be affected. The stability was assessed by evaluating the safety factor (SF), which is a representation of the factor of safety (FOS):

$$FOS\ (SF) = \frac{Strength\ (MPa)}{Stress\ (MPa)}$$

The SF ranges are described in Table V.

Table V. Description of slope stability per safety factor range

Safety Factor	Description
3.0 – 2.6	Extremely stable
2.6 – 2.2	Highly stable
2.2 – 1.8	Stable
1.8 – 1.4	Within overall stability thresholds
1.4 – 1.2	Within stack scale stability thresholds
< 1.4	Outside overall stability thresholds
< 1.2	Outside stack scale stability thresholds

The RS2 model results were evaluated based on the strength reduction factor, which correlates with the SF. A comparison of SF values across the various models is provided in Table 6. The failed sections showed SFs of 0.82 and 0.81 (Figure 18) and Figure 19), confirming instability. Meanwhile, the currently stable section (Figure 17) demonstrated a higher SF, indicating it is expected to remain intact. This section was used as a reference to determine appropriate remedial measures for the unstable areas.

Table VI. Various model designs' resulting safety factors

Conditions	Safety Factor		
	Section 1	**Section 2**	**Section 3**
Only dipping MGs	2.49	1.03	1.00
Vertical Joints (90°)	2.01	0.97	0.93
Sub- Vertical Joints (80°)	1.60	0.82	0.81
Anisotropy (weak joints in layers)	1.68	0.98	0.86
Vertical Joints (90°) and Anisotropy	1.22	0.95	0.89

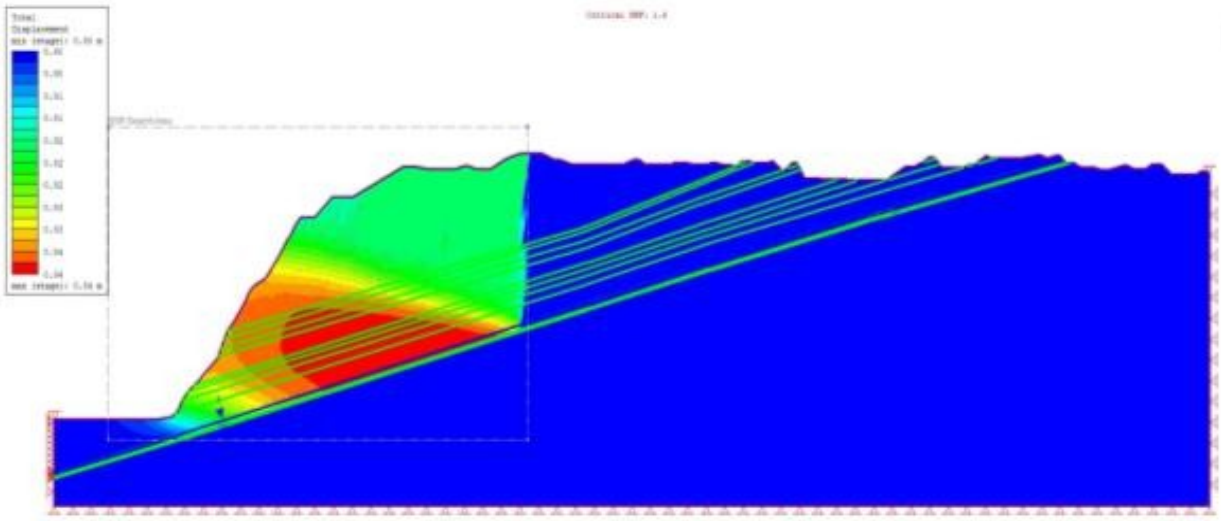


Figure 17. Section 1 NS sub-vertical joints (80°) model (SF = 1.6).

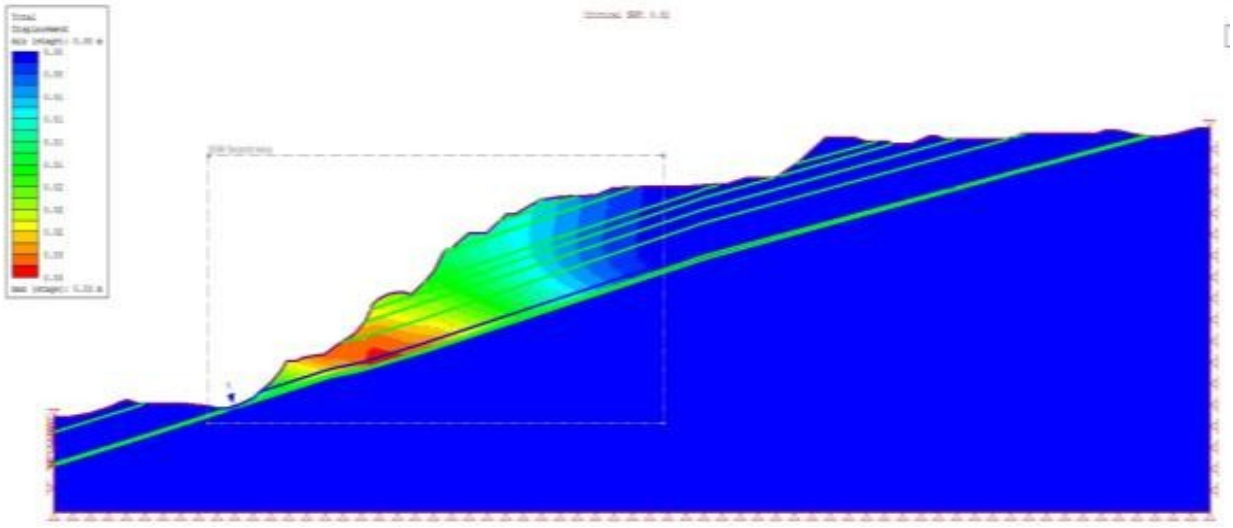


Figure 18: Section 2 NS sub-vertical joints (80°) model (SF = 0.82

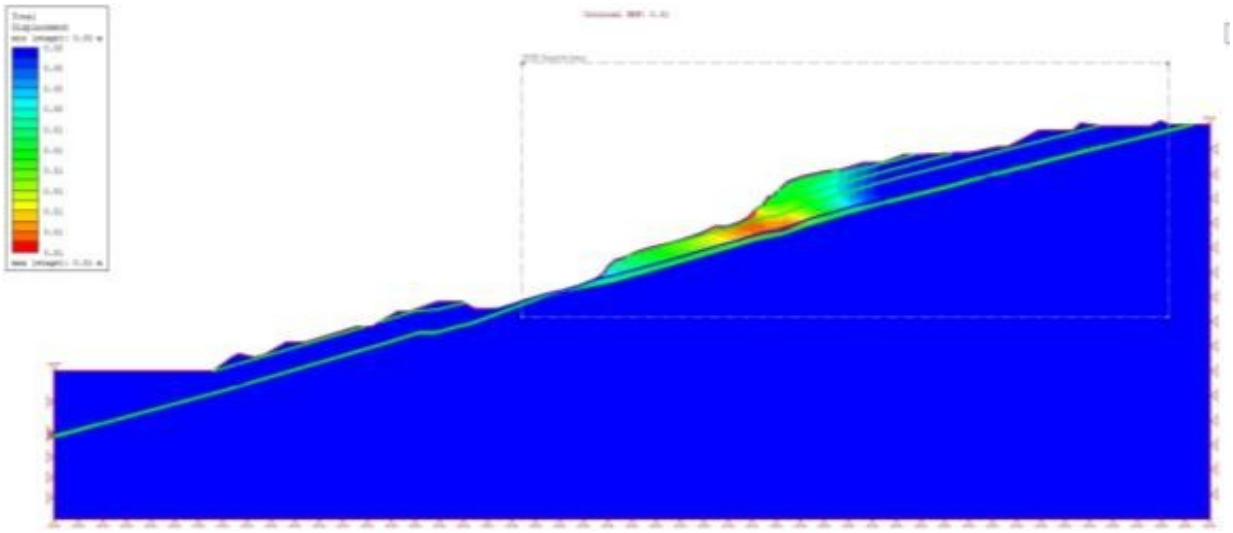


Figure 19. Section 3 NS sub- vertical joints (80°) model (SF = 0.81).

The RS3 model results (Figure 20) highlight the current and observed failure zones within the pit, providing valuable insights into the possible future development of failure along the West Highwall. The red contour represents areas of significant displacement, while the blue contour indicates regions with no displacement.

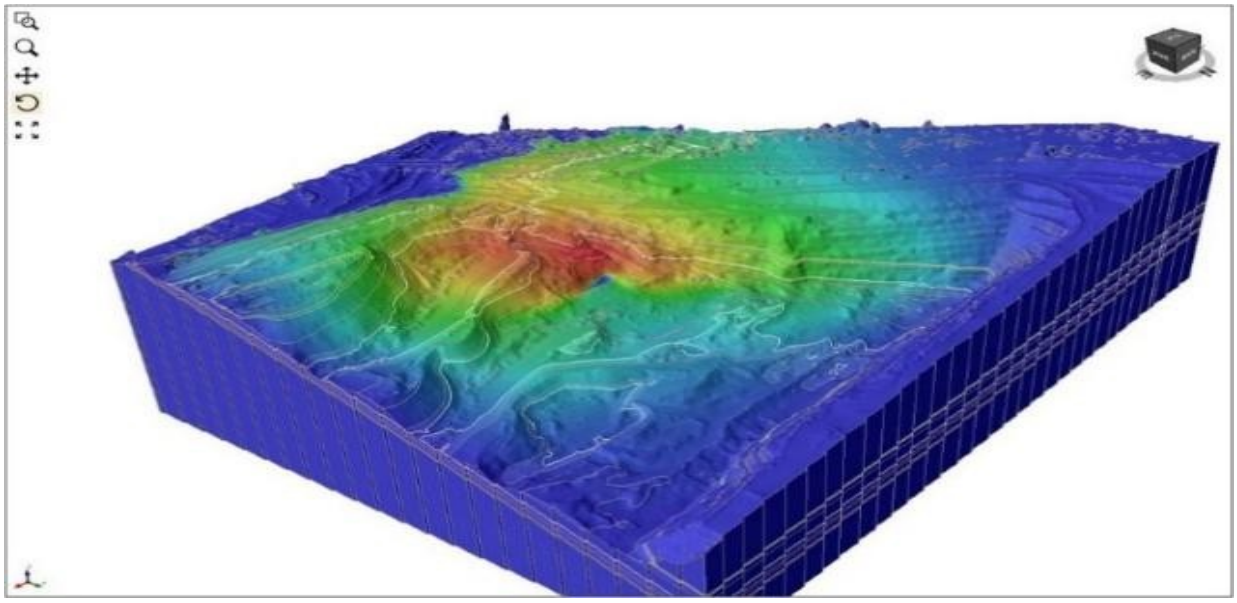


Figure 20. RS3 failure model.

Effect on Public Road

The potential impact of the unstable slope on the public road was evaluated using RS2, with material properties downgraded to simulate a worst-case scenario. This approach has induced failure in areas that are expected to remain stable. The results, shown in Figure 21 to Figure 24, highlight the effects of failure on the road. The red contour indicates the highest displacement, while colour variations reflect displacement magnitudes, with blue signifying no displacement.

In the southern West Highwall (Figure 22 and Figure 23), displacement reached 0.19 m and 0.26 m, with safety factors (SF) of 0.69 and 0.68, respectively. These values are represented by lighter shades transitioning from red to green. In contrast, the northern sections (Figure 21, Figure 23, and Figure 24) exhibited larger displacements of 0.31m and 0.49 m, with SFs of 0.87 and 0.85, represented by darker shades transitioning from red to blue. A detailed summary of the model results is provided in Table 7, offering a comprehensive overview of the slope stability and its potential impact.

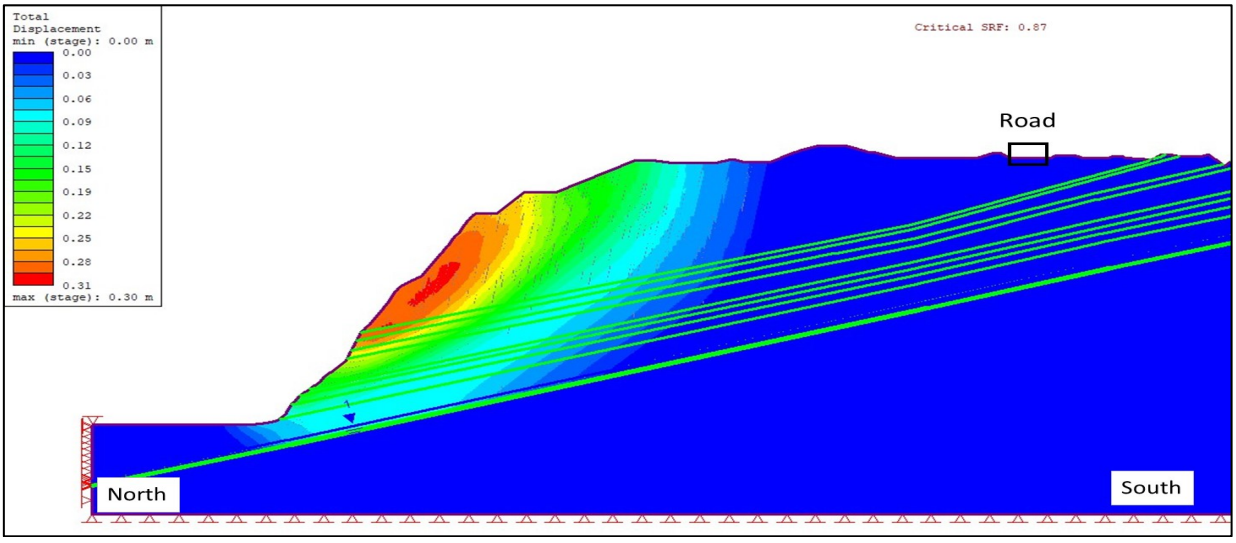


Figure 21. Section 1 NS displacement in relation to the road.

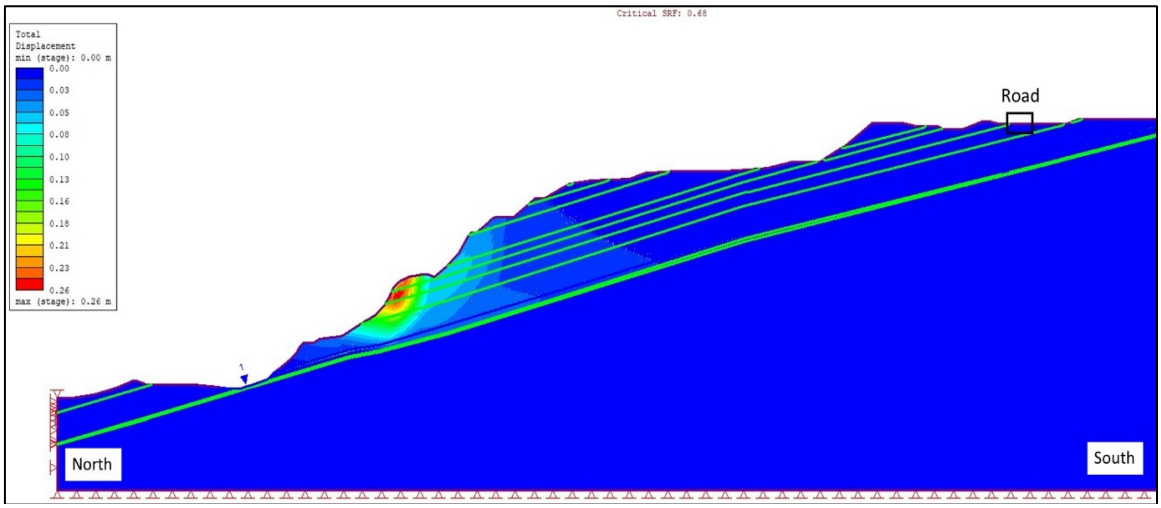


Figure 22. Section 2 NS displacement in relation to the road.

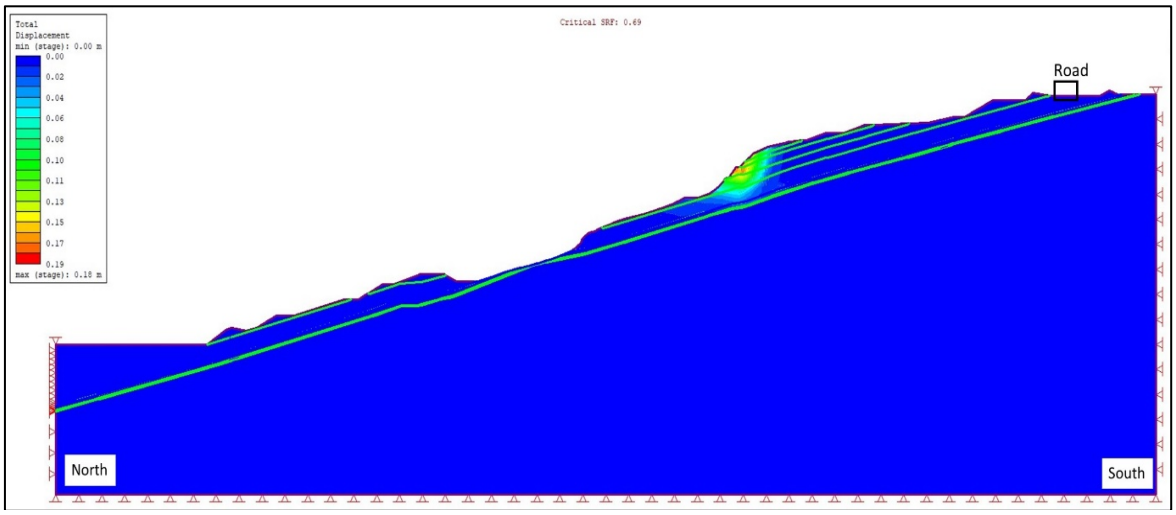


Figure 23. Section 3 NS displacement in relation to the road.

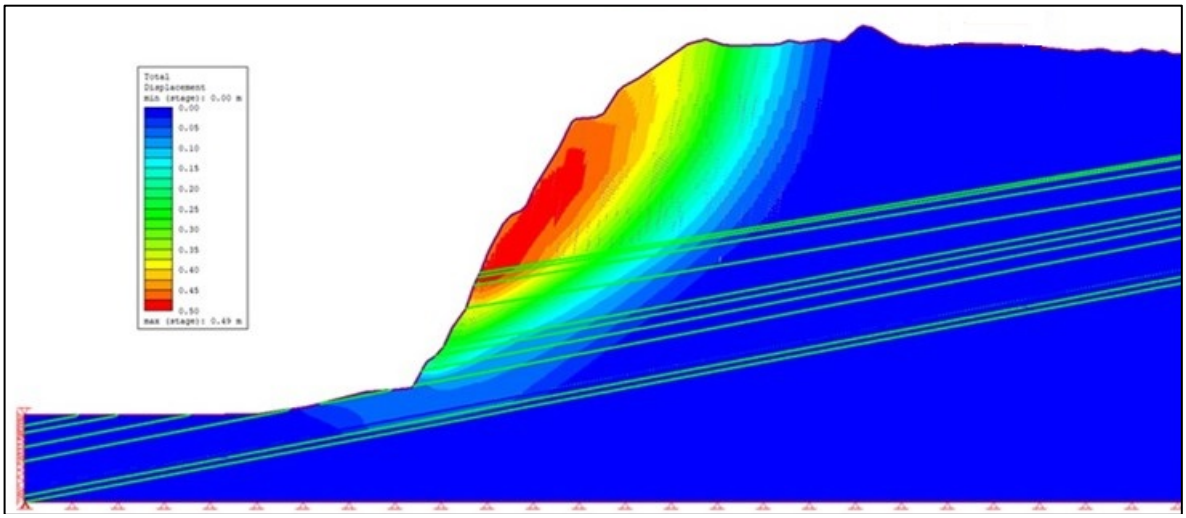


Figure 24. Section 1 EW displacement in relation to the road.

Table VII shows the results of conservative models designed to simulate the worst-case scenario and recreate the failure observed in the southern region of the West Highwall. Despite these conservative assumptions, the road remains stable.

Table VII. Summary of results with effect on the road.

Section	Safety Factor (SF)	Total Displacement (m)	Affects the road?
Section 1 NS	0.87	0.31	No
Section 2 NS	0.68	0.26	No
Section 3 NS	0.69	0.19	No
Section 1 EW	0.85	0.49	No

Buttress

A common method for stabilising a failing pit slope is the construction of a buttress to prevent further movement of the pit wall. The required dimensions of the buttress were analysed and are outlined in Figure 25. The buttress was modelled with heights of 30 m, 40 m, 70 m, 80 m, and 100 m, a repose angle of 35°, and top bench widths of 5 m and 10 m.

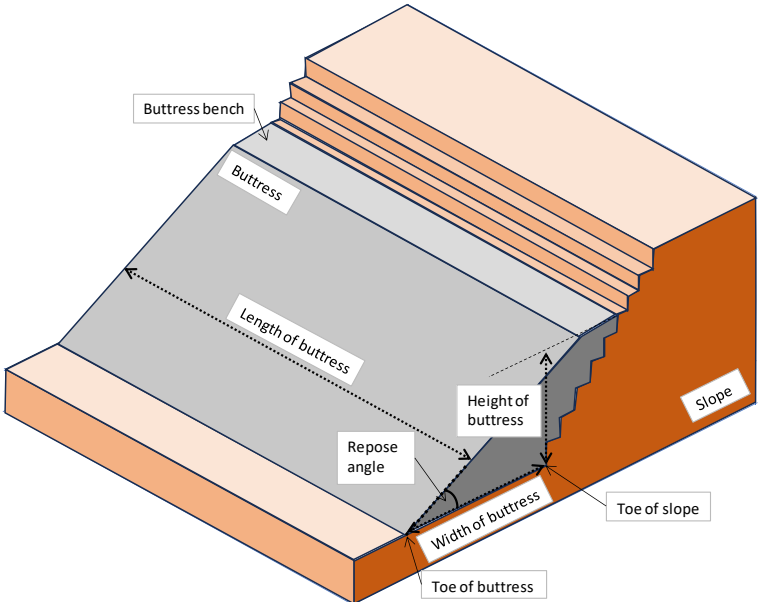


Figure 25. Annotated rough sketch of slope with buttress.

Length of Buttress

The required length of buttress support along the highwall was determined based on the SF of the vertical joints (80°) from the RS2 models, as shown in Table 6. This analysis considered the distance from the failed area to the stable region. The West Highwall spans approximately 579 m in width. Figure 26 illustrates the predicted SF along the highwall, starting from the southwest corner of the East Pit, where the slope failure occurred. For the first 227m, the West Highwall shows a SF below

1 (red), indicating the need for full slope height buttressing. Between 227m and 395m, there is a zone of potential weakness (yellow), requiring partial slope buttressing. Beyond 395 m, no buttressing is needed, allowing for a gradual slope decline.



Figure 26. Buttress length requirements based on SF.

Height of Buttress

To determine the required buttress height along the highwall, a buttress material layer was added to the RS2 models at varying heights. The objective was to achieve full stability of the highwall while minimising displacement.

The strain in the material was calculated using the following equation:

$$\varepsilon = \frac{\Delta L}{L}$$

Where ε is the strain, ΔL is the change in length of the material (represented by the displacement), and L denotes the original length of the material (represented by the original height of the buttress). The total displacement after adding a buttress at a specific height was recorded, and the corresponding strain was calculated, as shown in Table VIII.

Table VIII. RS2 buttress height results

Buttress Height (m)	**Total Displacement (m)**	**Strain**
0	0.38	0.3800000
30	0.21	0.0070000
40	0.18	0.0045000
70	0.05	0.0007143
80	0.05	0.0006250
100	0.00	0.0000010

Figure 27 illustrates the required height for the buttress based on strain in the West Highwall. A strain cut-off of 0.001 was used, as this represents the industry standard for allowable strain limits.

Consequently, an ideal buttress height of 57m was derived.

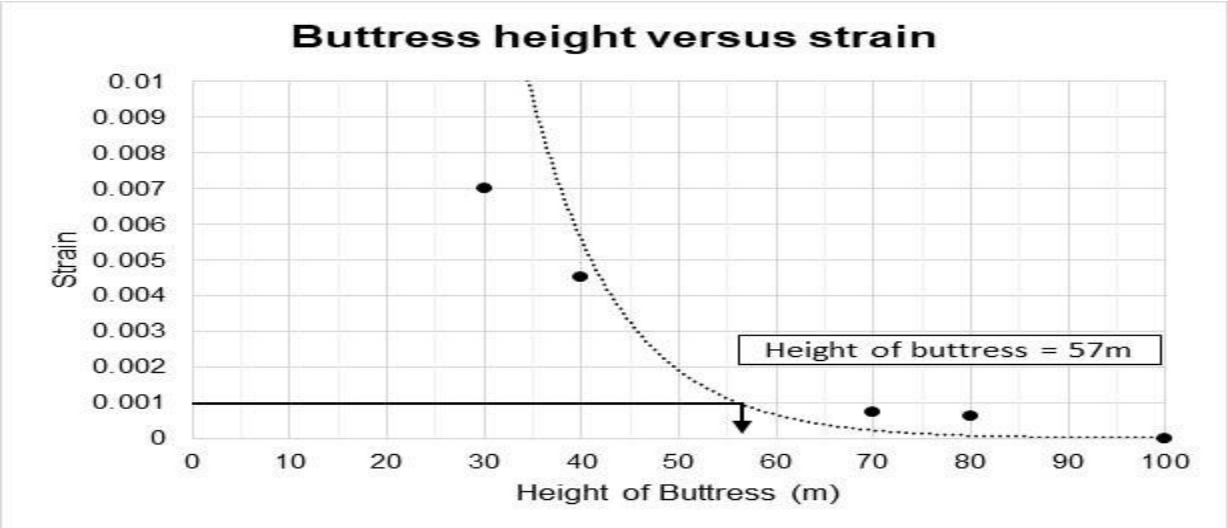


Figure 27. Height of buttress derived from strain threshold.

Width of Buttress

The width of the buttress on the slope floor represents the distance the buttress material must extend perpendicularly from the toe of the slope. This width was determined by measuring the length of the pit floor covered by the buttress in the RS2 models and converting it to the true distance from the toe of the slope. Table IX presents the measured buttress widths for each RS2 model (Figure 12 to Figure 16). The graph in Figure 28 shows the predicted buttress widths as the height increases. Based on the previous section, the recommended buttress height is 57m, resulting in a predicted buttress width of 80 m.

Table IX. Recorded dimensions of buttress width from RS2 models

Buttress Height (m)	**Width of buttress (m)**
30	49
40	58
70	99
80	105
100	140

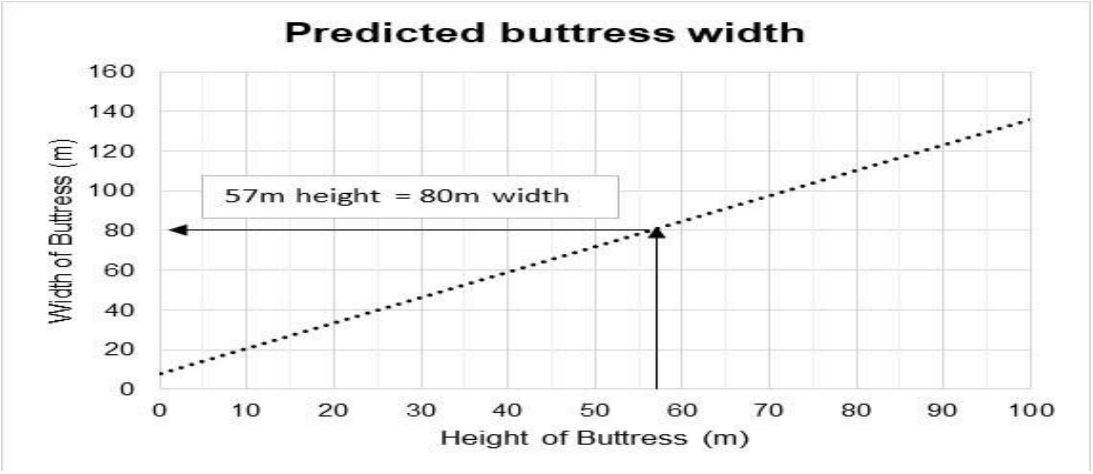


Figure 28. Width of buttress.

Spill Width

Spill width refers to the horizontal distance that debris travels downslope during a mass wasting event, such as a landslide or rockfall. It is an important parameter for assessing the potential hazards and impacts of slope failures. The spill width helps determine a stand-off distance from the highwall to protect personnel and equipment from a potential slope failure. The spill width was calculated using the following equation:

$$Spill\ width = \sqrt[3]{BulkingFactor\ \times\ Failure\ Volume}$$

The bulking factor represents the increase in volume that occurs when excavated materials, such as rocks and soil, are disturbed or transported. During a slope failure, the dislodged material typically experiences bulking due to fragmentation and increased void spaces, resulting in a larger volume compared to its original state.

The failure volume refers to the total volume of material involved in the slope failure event. When a slope fails, a mass of material is detached, and the combined effects of bulking and fragmentation contribute to an increased failure volume.

The bulking factor was assumed to be 1.5, and the failure volume was determined by measuring the failure in the RS2 models (Figure 29). Table X summarises the results for calculating the spill width. The minimum spill width or stand-off distance required is 25 m from the toe of the slope until the buttress is installed. Beyond the 395 m mark (where buttressing is required), it is recommended to maintain a 25 m stand-off.

Table X. Spill width results

Section	Base (m)	Height (m)		Area (m²)	Bulking Factor	Spill Width (m)
Section 1 NS	169	118		9971	1.5	24.64
Section 2 NS	92	55		2530	1.5	15.60
Section 3 NS	71	38		1349	1.5	12.65
Section 1 EW	131	113		7402	1.5	22.31

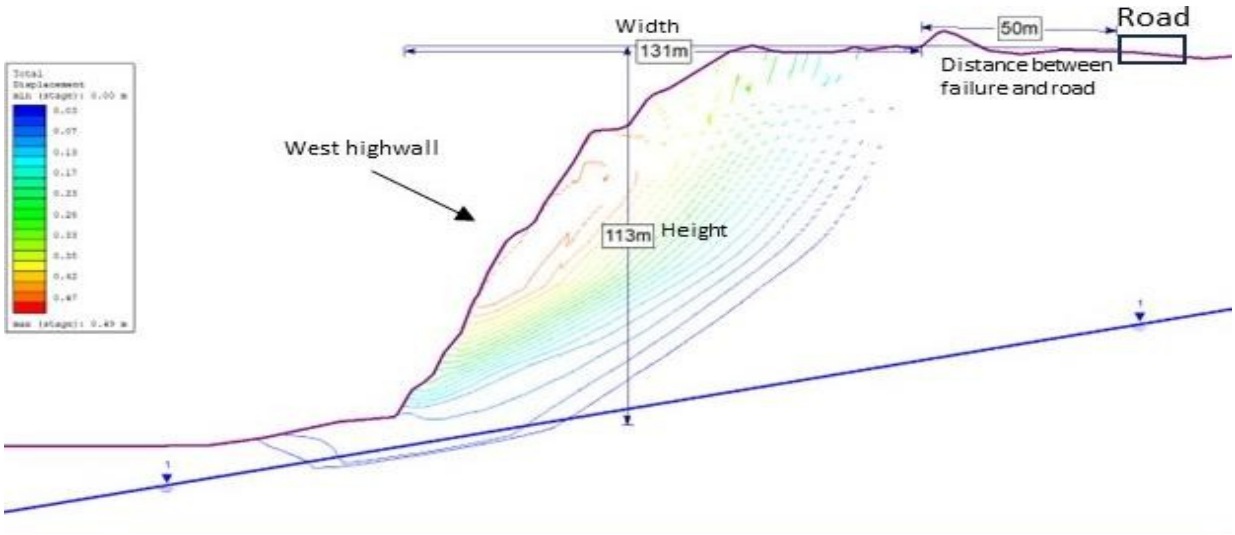


Figure 29. Section 1 EW spill width dimension.

CONCLUSIONS AND RECOMMENDATIONS

Numerical modelling was conducted using Rocscience programs RS3 and RS2. RS3, a 3D finite element program, is suitable for analysing stress, deformation, and stability surfaces, with one model constructed. RS2, a 2D finite element program, is used for slope stability, seepage analysis, and soil-structure interaction, with 29 models created.

Fracture assessment of the southern section of the West Highwall indicated that while the extension of failure across the highwall would cease, the spacing (aperture) would continue to increase in the dip direction of the ore body. Further analysis confirmed that failure should not reach the public road, but these areas should be closely monitored for signs of new failure.

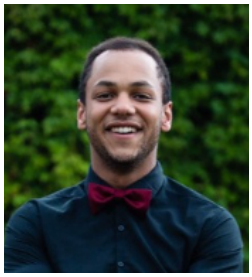
The buttress should be constructed along the full height of the slope for 227 m from the south-west corner of the West Highwall, with a height of 57 m and width of 80 m for the next 168 m. Beyond this, the buttress is no longer necessary, as the remaining highwall does not require additional support. A 25 m stand-off distance from the toe of the highwall is required to protect personnel and equipment from potential slope failure.

Additional measures to ensure the stability of the highwall and the public road include:

- Installing wire extensometers along the crest of the highwall to monitor failure propagation towards the public road.
- Installing wire extensometers every 100 m along the entire length of the west highwall.
- Drilling 10 m to 15 m long horizontal drainage holes to allow water to seep out of the highwall.
- A certified strata control officer should inspect the highwall weekly, covering both failed and stable areas.
- If further movement is observed towards the public road or northern stable areas, the appointed rock engineer should be notified immediately.

REFERENCES

Jami, M. & Girard, 2001. Assessing And Monitoring Open Pit Mine Highwalls. Mining Engineer, National Institute for Occupational Safety & Health, pp. 159-171.



Nicolas Ikenna Umeh

Geohydrologist (Mining Geotechnical).
Middindi Consulting (Pty) Ltd.

I am a Geohydrologist with a focus on Mining Geotechnical applications, blending a solid academic foundation in Geology, Chemistry, and Hydrology from North-West University with practical experience in rock engineering. Over two years at Middindi Consulting, I have refined my expertise in geotechnical analysis, data interpretation, and technical reporting. Skilled in tools like Rocscience, Map3D, QGIS, and GEM4D, I thrive on solving complex challenges in the mining sector. Driven by a passion for innovation, I aim to deliver impactful solutions that advance industry standards and project outcomes.

Integrating monitoring technologies to understand slope deformation in open-pit mines: A case study from Swakop uranium mine

G. Ockhuizen[1], R. Armstrong[2], Y. Xiangle[1], S. Maclennan[3]

[1]CGNPC Swakop Uranium, Namibia
[2]SRK Consulting, South Africa
[3]The University of the Witwatersrand, South Africa

This study investigates the slope deformation characteristics and failure mechanisms on the Western slope of the Zone 1 open pit at the Swakop Uranium Husab mine, Namibia. Slope failures at the Husab Mine are primarily influenced by persistent foliation, sub-vertical joint sets, and intrusive contacts, which collectively define structurally constrained failure zones. Monitoring data obtained from automated prisms and ground-based radar revealed progressive deformation patterns, including rebound effects and stick-slip movement indicative of pre-failure conditions. The observed deformation followed the classic three-stage process consistent with established slope failure models in slope stability research. Two dominant failure modes were identified: rapid wedge failures and slower-moving planar failures, both triggered by excavation-related unloading and blasting-induced vibrations. The blast vibrations contributed significantly to crack propagation and deformation along existing discontinuities. Continuous monitoring enabled early warning and targeted interventions – installation of 10 m catch benches and batter-angle reduction – that effectively mitigated progressive deformation. These findings highlight the critical importance of integrating detailed geological and structural analyses into mine planning and slope design. Overall, the results contribute to the development of predictive models and site-specific stabilisation strategies essential for improving the safety and efficiency of large-scale mining operations. This research contributes to the refinement of slope stability models in highly anisotropic geological settings, with direct implications for mine design and operational safety.

INTRODUCTION

Open-pit mines located in structurally complex geological settings are especially susceptible to slope instability, particularly during dynamic excavation activities such as production blasting and final wall unloading. These instabilities pose considerable safety hazards and have the potential to significantly disrupt the continuity of mining operations. A key challenge in these environments is developing a clear understanding of how structural discontinuities such as foliation planes, joints, and shear zones interact with intermittent mining activities, particularly vibrations induced by blasting, and how these interactions affect slope deformation over time.

The Swakop Uranium (Husab) open-pit mine in Namibia is located within a high-strain regime of the Damara Orogenic belt and is characterised by moderate to steep, persistent structural features that complicate slope stability. In this setting, even localised blasting or excavation can activate pre-existing discontinuities, resulting in progressive deformation that is difficult to anticipate without continuous monitoring. These conditions necessitate the use of real-time geotechnical monitoring systems and robust analytical frameworks to identify early warning signs of instability and inform proactive design interventions.

Recent mining incidents globally and within the region have highlighted the need for slope management strategies that integrate high-resolution monitoring with structural geology and geotechnical modelling. While existing empirical and theoretical models effectively describe multi-stage slope deformation, there is a need to better understand how blasting-induced vibrations, when interacting with complex structural conditions, influence the progression and activation of these failure mechanisms.

This study aims to apply and validate established slope deformation models within a structurally complex open-pit environment, with a specific focus on the role of blasting-induced stress changes as a contributing factor to deformation progression and failure. The central hypothesis is that, even when carefully executed, blasting activities can serve as significant operational triggers in rock masses with persistent discontinuities—amplifying deformation trends consistent with known pre-failure and failure phases.

To address this, the study develops a monitoring-based framework for understanding slope deformation mechanisms associated with mining activities in complex geological settings. Through the integration of field observations, structural mapping, and near real-time monitoring, the research systematically examines deformation progression related to excavation and blasting and evaluates how modifications in mine design can mitigate associated risks.

The specific objectives of the study are to:

1. Characterise slope deformation behaviour using advanced monitoring technologies, including robotic prism surveys and ground-based radar

2. Validate existing multi-stage deformation models by correlating them with field monitoring data, with emphasis on slope movement during and after blasting and excavation-induced unloading, and

3. Recommend practical design interventions—such as slope angle adjustments—based on structural analysis and real-time monitoring insights to enhance slope stability.

By linking observed deformation to both geological structures and operational triggers, this research presents a robust, monitoring-based framework for improving slope stability management in open-pit mines. This study specifically analyses the deformation behaviour, failure modes, and instability mechanisms of the western slope of Zone 1 pit during blasting and excavation activities.

Early research into slope stability established foundational empirical and theoretical models aimed at predicting progressive failure prior to collapse. A particularly influential contribution is the 'Saito Method' (Saito, 1968), which outlines a three-stage deformation process:

1. **Initial creep** – characterised by slow, often undetectable displacements in the absence of a defined failure surface.

2. **Constant-rate (butterfly) deformation** – marked by more noticeable displacement, with the development of cracks and slip surfaces.

3. **Accelerated deformation** – defined by rapid displacement indicative of imminent slope failure.

These stages have been further refined by Zavodni and Broadbent, 1980, Spencer, 1988, Sullivan, 1993, Zavodni, 2001, and Mercer, 2006. (Sullivan, 2007), later expanded these models by categorising slope movement into three overarching phases: pre-failure, failure, and post-failure, thereby improving its relevance to mining contexts.

Although terminology differs slightly among authors—Sullivan (1993) refers to the early stage as the viscoelastic response, while Zavodni (2001) refers to it as elastic rebound, relaxation, or dilation—all models emphasise the progressive nature of deformation leading to failure. These time–displacement

relationships are illustrated in Figure 1, which traces the evolution of slope deformation models from Saito (1968) to Sullivan (2007).

These models remain widely recognised in slope stability analysis and highlights the importance of understanding the interplay between geological structures and operational triggers such as blasting and excavation. However, their direct application to structurally controlled rock masses subjected to blasting requires further field validation. Given the inherent variability of rock mass properties and structural complexity, no two failures behave identically. This study extends the application of established models by examining their relevance to the unique deformation characteristics observed along the structurally complex western slope of Zone 1.

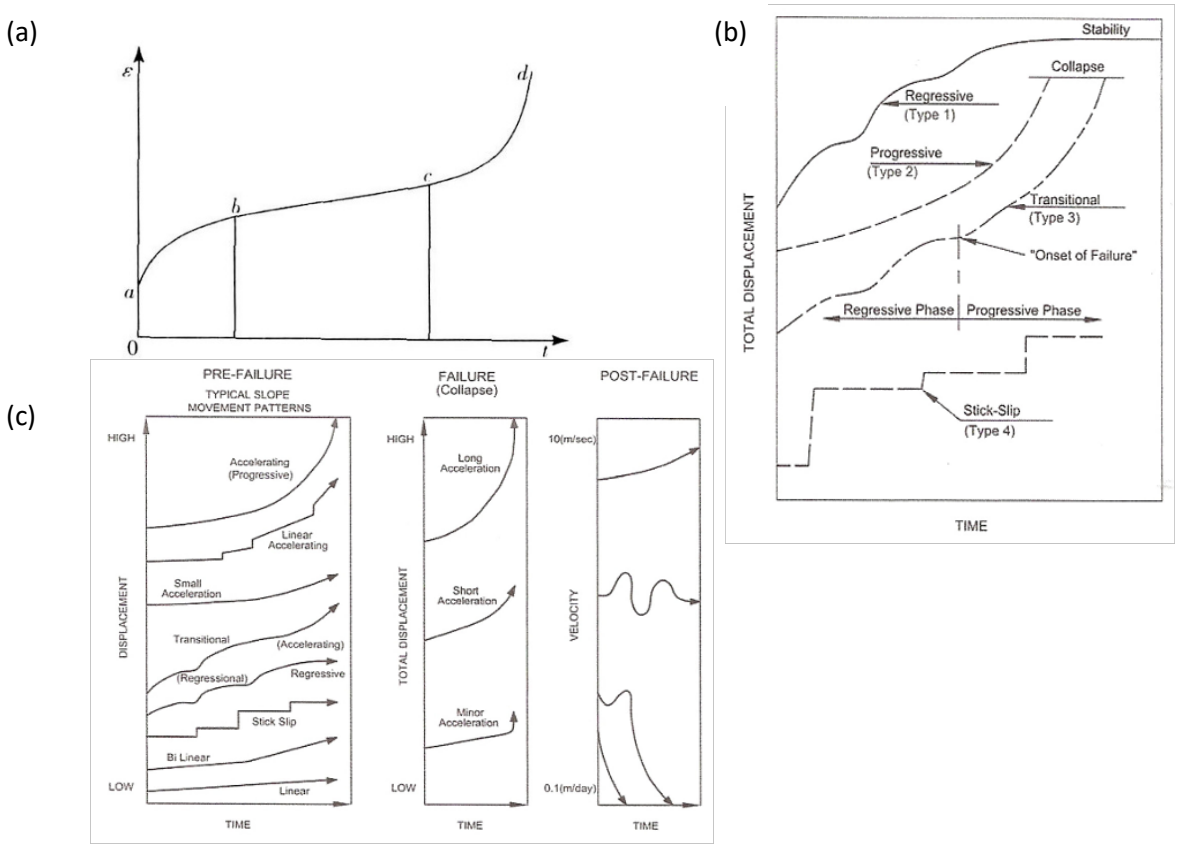


Figure 1. (a) Creep curve introduced by Saito (1968); (b) refinements by Broadbent and Zavodni (1982) and Sullivan (1993), illustrating typical time–displacement behaviour; and (c) model expansion by Sullivan's (2007), dividing pit slope movement into three distinct phases: pre-failure, failure, and post-failure.

Unlike studies that treat blasting and excavation as background processes, this research integrates vibration monitoring with structural and deformation data to quantify the influence of blast energy on slope response. In doing so, it bridges the gap between structural geology, real-time monitoring, and operational practice.

BACKGROUND

The Husab uranium deposit is in the southern central zone of the Damara Orogenic belt in Namibia (Figure 2). The mine is currently in production, with operations focused on two major open pits — Zone 1 and Zone 2. These pits are planned to be developed over nine mining phases throughout the life of mine, with current activities concentrated in Zone 1 Stages 2 and 3, and Zone 2 Stages 3 and 4. A summary of the final pit dimensions and configurations is provided in Table I.

Table I. Final Dimensions and Configuration of Zone 1 and Zone 2 Open Pits

Parameter	***Zone 1***	***Zone 2***
Number of Mining Phases	*5*	*4*
Final Length	*3050 m*	*2055 m*
Final Width	*1030 m*	*1530 m*
Final Depth	*412 m*	*380 m*
Slope Batter Angle Range	*60° – 80°*	*60° – 80°*

The blasting operations onsite consist of pre-split, trim, and production blasting, executed in scheduled, intermittent cycles across the active mining phases in both pits. Pre-split and trim blasts are specifically employed to control/enhance wall stability and clean the slope face. However, these activities, introduce cyclic stress changes into an already structurally complex rock mass., contributing to progressive slope deformation. As a result, continuous monitoring is essential to support effective slope management and risk mitigation.

Uranium mineralisation is hosted within uraniferous leucogranites (Alaskites). The Alaskites were emplaced in an extensional setting, formed under high strain-temperature conditions and are associated with a NW–SE shortening of the Neoproterozoic Damara Orogeny. These mineralised units are closely linked to geological features such as pull-apart zones, fault dilation jogs, pressure shadows adjacent to the domes, and fold hinge dilations (Freemantle, 2015). These emplacement processes and associated structural features influence the geomechanical behaviour of the rock mass, creating zones of weakness that can localise deformation and contribute to slope instability.

The Zone 1 and Zone 2 pits are structurally controlled by sinistral strike-slip fault systems and are bounded by prominent domal features, including the Husab North dome and the Ida domes (Figure 3a). The region is characterised by high-strain structural zones, including the Ida Fault Zone, which runs along the eastern margin of Zone 1 and plays a key role in accommodating regional deformation. Second-order structures, such as thrust and normal faults, are also present. Sub-horizontal slickensides and shear kinematic indicators in the area suggest a left-lateral shear, consistent with fault reactivation during the third deformation phase (D3) of the Damara Orogeny (Maduray *et al*., 2018).

The host rocks consist of amphibolite-facies metasediments from the Swakop Group (Karibib, Arandis, Chuos, and Rössing formations) and the Nosib Group (Khan and Etusis formations), with local Alaskite intrusions. These lithological units have experienced multiple ductile and brittle deformation events (D1–D4), resulting in a complex litho-structural setting that presents significant geotechnical challenges.

Table II. Stratigraphic Units and Lithological Components of the Husab Mine (modified from (Freemantle, 2015)

Group	***Formation***	***Lithology***
	Kalahari (Overburden)	*Sandy soil layer and calcrete layer*
Swakop	*Karibib*	*Marble, dolomite, biotite schist, quartz schist, calcsilicate rocks, shale.*
	Arandis	*Quartzite, schist, pelitic gneiss, calc-silicate, marble*
	Chuos	*Mixite, diamictite, pebble- and boulder-bearing schist, minor quartzite, shale-BIF, schist.*
	Rössing	*Highly variable: marble, quartzite, conglomerate, meta-greywacke biotite schist, biotite-cordierite schist and gneiss, aluminous gneiss, biotite-hornblende schist, calcsilicate rocks.*
Nosib	*Khan*	*Pyroxene-amphibole feldspathic quartzite, amphibole-pyroxene gneiss, aluminous gneiss, biotite-hornblende schist, calcsilicate rocks.*
	Etusis	*Pink-grey well-bedded feldspathic quartzite, arkoses, conglomerate, quartzo-feldspathic gneiss; minor biotite schist, marble, amphibolite, meta-rhyolite and calcsilicate rocks.*
	Intrusives	*Pegmatite, quartz vein, leuco-granite (Alaskites)*

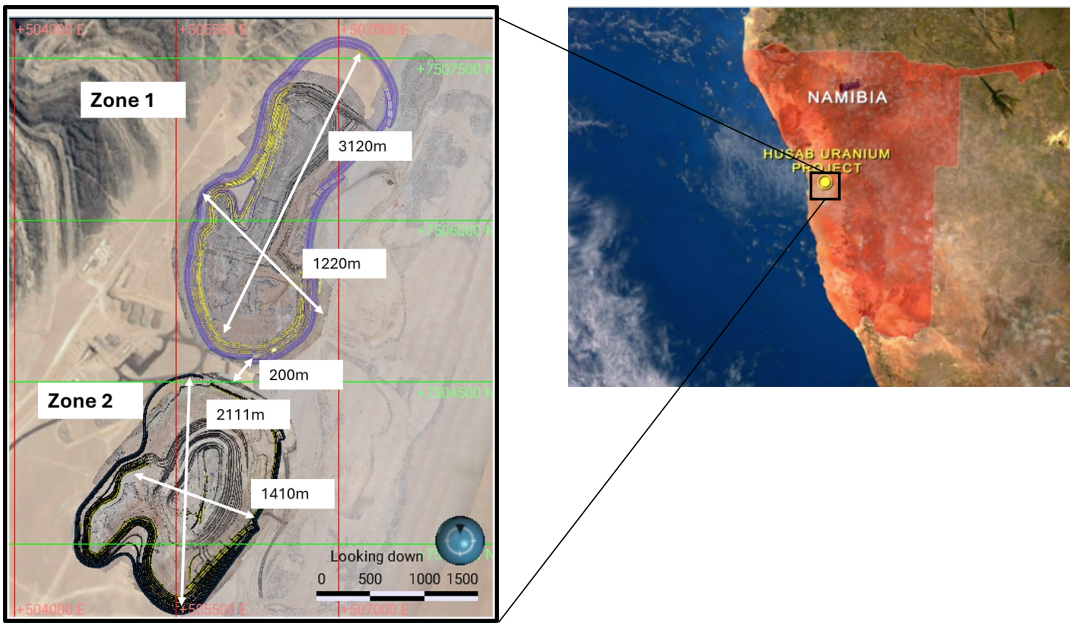


Figure 2. Location of the Swakop Uranium Husab, Namibia and the layout and dimensions of the Zone 1 and Zone 2 open pits.

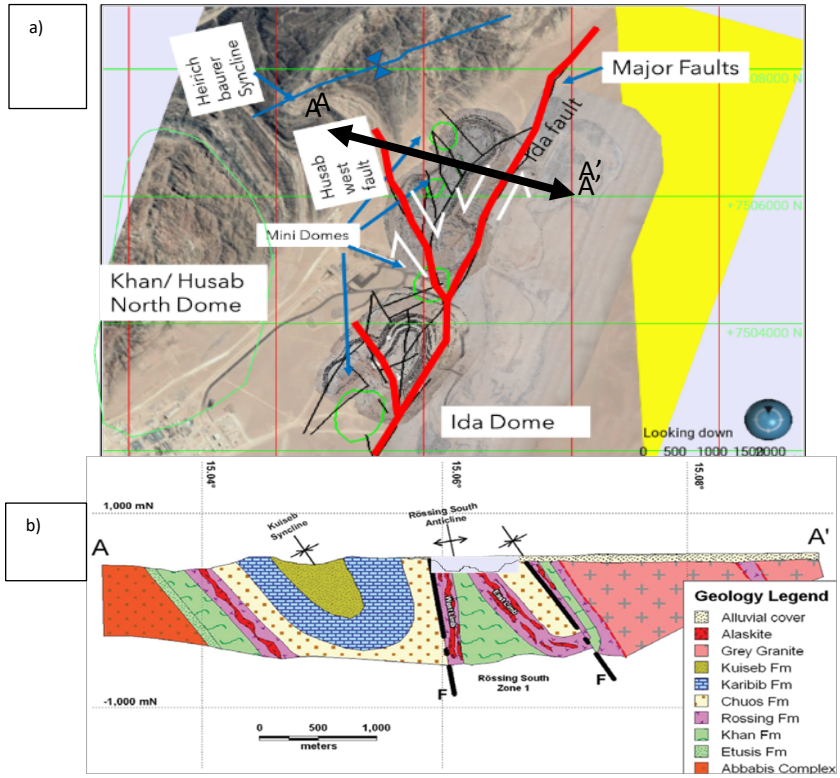


Figure 1. a) Structural framework of the Husab uranium open-pit mine, showing the Zone 1 and Zone 2 pits situated between sinistral strike-slip fault systems and domal interference structures, including the Ida and Khan domes; (b) Geological cross-section A–A' illustrating lithological units and structural features across the pits (modified after Spivey et al.*, 2010)*

METHODOLOGY

This paper presents a monitoring-based analysis of slope deformation associated with intermittent mining activities within a structurally complex rock mass. The primary objective was to assess the deformation response of the slope during periods of excavation and production blasting, using high-resolution geotechnical monitoring systems and field documentation techniques.

Monitoring Configuration and Data Acquisition

Near-real-time deformation measurements were collected using two primary geotechnical monitoring systems, both positioned on the eastern slope of the pit crest with a clear line of sight to the western slope of Zone 1. These systems were deployed to evaluate slope behaviour in response to excavation and blasting activities (Figure 4) and included:

- **Automated prism monitoring**
  A robotic geodetic total station was used to monitor a series of prisms (P6–P19) mounted on the western slope. For this study, prisms P6–P13—installed along Bench 7 at 520 mRL—were selected for detailed analysis due to their location within the structurally sensitive domain. These prisms recorded discrete three-dimensional displacements at sub-daily intervals. The layout of the individual prism points on Bench 7 is illustrated in Figure , highlighting their placement across the area of geotechnical concern.
- **Ground-based real aperture radar**
- The **ground-based real aperture radar** (GB-RAR) unit, also positioned on the eastern pit crest, was configured to continuously scan the western slope every three minutes. This system provided high-frequency, spatially continuous measurements of slope surface deformation, complementing the point-based prism monitoring. Together, the GB-RAR and prism systems were used to quantify displacement patterns and analyse the mechanical behaviour of the slope under intermittent, mining-induced disturbance within the structurally complex rock mass.
- **Blasting Vibration Monitoring**
  Ground vibration levels from production blasts were recorded using peak particle velocity (PPV) measurements collected in proximity to monitored zones. These data sets were used to assess the potential triggering effects of blasting on slope response. In Zone 1, PPV values reached up to 9.4 mm/s, with several blast events showing temporal correlation with observed prism and radar-based slope deformations. The integration of vibration monitoring allowed for evaluation of the relationship between seismic loading and slope deformation phases.
- **Field-Based Visual Documentation**
  Throughout the monitoring period, systematic field photographs were captured from the eastern slope to document progressive surface changes and failure features on the western slope. These images were time-synchronised with monitoring datasets and served to visually correlate observable deformation with real-time instrument readings during key deformation events.

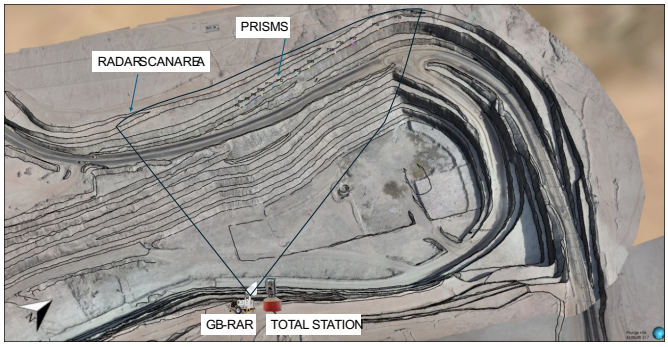


Figure 4. Schematic layout of the monitoring setup on the western slope of Zone 1. The GB-RAR and total station are positioned on the eastern pit crest with direct line-of-sight coverage to the installed prism array (P6–P19). This study focuses on the deformation behaviour recorded by prisms P6–P13, which are located within the area of structural concern. The radar scan area spans the upper benches of the western slope to capture near-real-time slope deformation during excavation and blasting activities.

RESULTS

Observed Deformation During Intermittent Mining Activities

Deformation monitoring focused on capturing slope behaviour during excavation and production blasting cycles on the western slope of Zone 1, characterised by moderately to steeply dipping foliation planes intersecting the pit face. Prism monitoring data from Bench 7 (520 mRL), specifically prisms P6 to P13, indicated the onset of a transitional pre-failure stage beginning around 15 October 2019. This deformation phase correlated with active excavation and the implementation of a 10 m-wide catchment bench (Figure 5) , introduced to reduce basal exposure and mitigate slope instability risks.

Rebound deformation during excavation unloading

Recorded displacement patterns were progressive, notably exhibiting a rebound response following excavation unloading. These patterns reflect the mechanical response of the structurally complex rock mass subjected to excavation-induced stress redistribution. Field observations beneath prism P10 (Figure 7) further supported this interpretation, showing visible displacement along prominent foliation planes. The misalignment of pre-split barrels and shear direction, indicated by red arrows, confirmed excavation-induced activation of structurally persistent discontinuities. These field indicators closely matched recorded prism displacements, reinforcing the link between operational triggers such as blasting and excavation, and the observed deformation dynamics.



Figure 5. Distribution of prism monitoring points (P6–P13) installed on the western slope of Zone 1 to capture deformation in the area of concern. The monitoring focused on Bench 7 (520 mRL), where a design adjustment – a 10 m-wide catchment bench – was implemented to reduce basal exposure and enhance slope

stability. These prism locations correspond to displacement trends discussed in subsequent figures.

Figure 6 (a) and (b), illustrate the vertical displacement trends recorded during the monitoring period. All monitoring points followed a broadly similar trend, initial uplift followed by stabilisation; which is indicative of unloading rebound due to excavation-induced stress redistribution. However, prism P11, located above a previously failed slope section, deviated from this trend, showing significantly higher displacement magnitudes. This anomaly likely reflects localised structural weakening or the reactivation of existing discontinuities. Figure 6(c) and (d) display the horizontal displacement trends, which show similarly consistent behaviour among most prisms. The anomaly in P11 reinforces the interpretation of a structurally sensitive zone reacting differently to unloading and blasting-induced stress changes.

The displacement signature recorded at prism P11 is characteristic of a stick-slip movement regime, aligning with the pre-failure stage illustrated in Figure 1(c) of the modified Sullivan (2007) slope failure model. This interpretation is further supported by field observations beneath prism P10 (Figure 7), where visible offsets along foliation planes and displaced pre-split barrels (highlighted with directional arrows), confirm displacement along an unfavourably oriented structural surface. Together, these observations suggest that excavation-induced unloading has activated pre-existing foliation planes, which remain meta-stable and prone to reactivation under continued mining-induced stress conditions.

Given the proximity of a permanent ramp at the slope toe, a strategic decision was made to install a catch fence below this section of the slope to contain any displaced material in the event of further instability.

Blasting-induced vibrations in Zone 1 have also been identified as a contributing factor to the propagation of existing cracks within the rock mass. Vibration monitoring data indicate that PPV values recorded near Bench 7 range from 4.2 mm/s to 9.7 mm/s—levels that are sufficient to initiate microfracture development in jointed rock, especially where these align with pre-existing structural weaknesses.

These elevated vibration levels likely accelerated deformation and rebound responses along the structurally unfavourable foliation exposed on the western slope. Prism data revealed that vertical displacements increased progressively post-excavation before reaching a plateau, indicative of partial energy release and temporary stabilisation. Horizontal displacements were broadly consistent across the bench, with the exception of P11, further emphasising the influence of structural and blasting-related triggers on localised slope response.

In summary, the rebound deformation observed after excavation unloading corroborates a progressive failure mechanism originating along foliation planes with unfavourable orientations. This deformation was effectively mitigated by prompt design adjustments and continuous real-time monitoring, which successfully prevented the complete exposure of failure surfaces during this critical transitional stage.

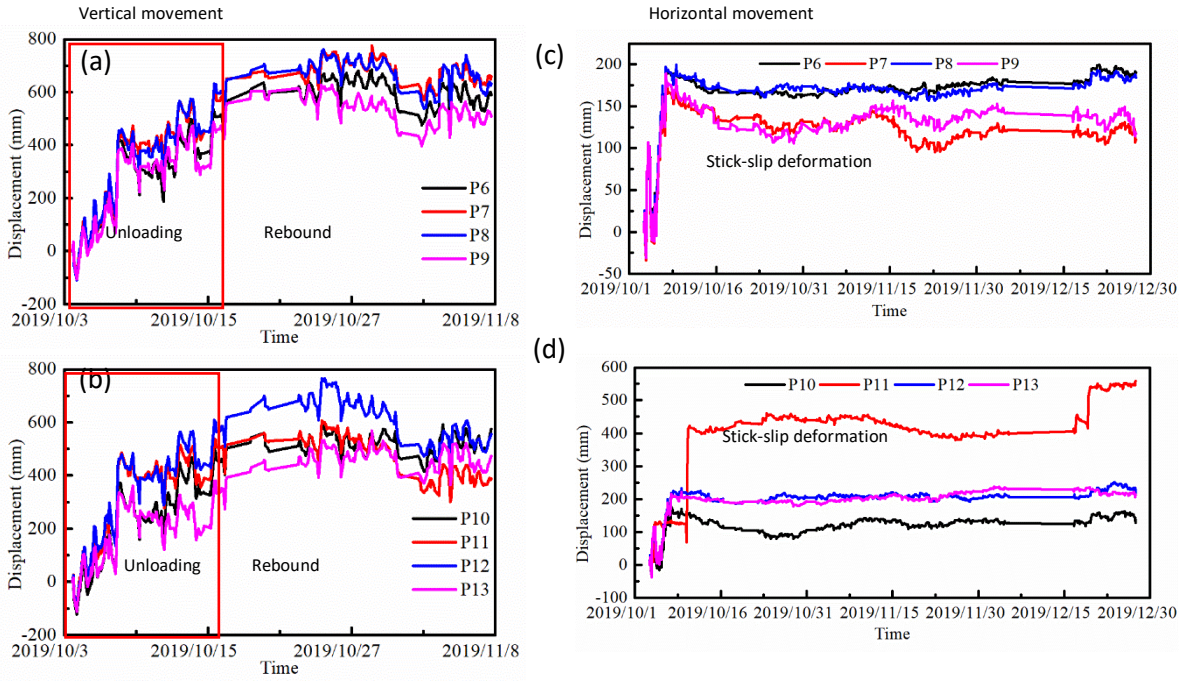


Figure 6. Vertical displacement trends recorded by prisms P6–P9 (a) and P10–P13 (b), illustrating the rebound effect following bench development and unloading. Horizontal displacement trends recorded by prisms P6–P9 (c) and P10–P13 (d), also showing rebound responses post-unloading.

Slope Deformation and Failure Mechanisms

A combination of wedge and planar failures was recorded on Bench 11 of the western slope in Zone 1, following excavation and blasting activities associated with the development of a permanent ramp (Figure 5). These failures occurred within a structurally complex rock mass, characterised by unfavourably oriented foliation planes, intersecting joint sets, and lithological heterogeneity related to intrusive Alaskite bodies.

The initial wedge failure developed rapidly as the result of blasting and scaling, which removed critical support material in front of a pre-defined wedge. Post-event structural mapping confirmed that the wedge was bounded by two intersecting sub-vertical joint sets, oriented 75°/236° and 45°/127°. Although some rebound behaviour was observed, the block did not fully detach until the residual confining material was removed. Once dislodged, the block failed abruptly.

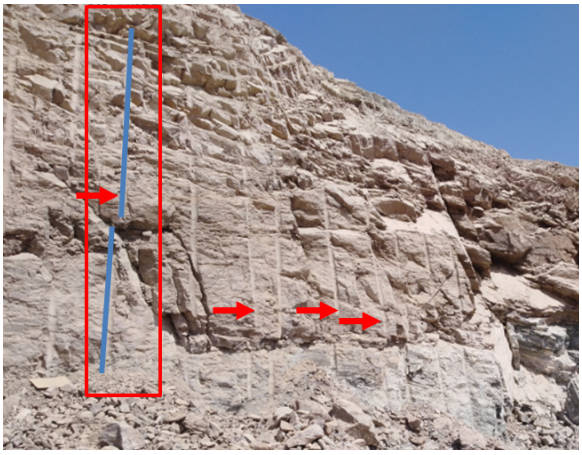


Figure 7. Highwall exposure below prism P10, demonstrating movement along the identified plane. The blue line represents the pre-split barrel, while the red arrows indicate the direction of displacement.

As illustrated in Figure 8, GB-RAR monitoring data show a sharp velocity spike, and time–displacement trends confirm that the wedge failure evolved over a brief period of 1 hour and 45 minutes—consistent with a brittle release. This behaviour corresponds with the lower schematic in Sullivan's (2007) conceptual failure model, which characterises rapid-onset failures with minimal precursory deformation, typical of wedge-controlled mechanisms.

Approximately 12 hours after the initial wedge failure, a planar failure occurred along a foliation surface oriented 45°/110°, which utilised the same bounding joints that had defined the initial wedge. This second failure initiated progressively, driven by continued stress redistribution and excavation-induced unloading. In contrast to the abrupt wedge failure, this collapse exhibited a more gradual acceleration of movement.

Figure 9 shows the GB-RAR heatmaps and prism velocity data, showing an extended 11–12 hour pre-failure acceleration phase. This progressive behaviour aligns with the upper schematic in Sullivan's (2007) conceptual model, which illustrates ductile-to-brittle transitional failure mechanisms with prolonged deformation—characteristic of structurally guided planar failures.

The combined failure geometry measured approximately 37 m in length, 6.3 m in width, and 7.5 m in height. These mechanisms occurred across multiple geological contacts, including the Chuos Formation, transitional layers of the Rössing Formation, the Khan Formation, and areas of Alaskite intrusion—each confirmed through drill core logging and in-pit mapping.

Together, the wedge and planar failures showcase a transition from brittle, rapid failure to a delayed, structurally controlled slide. These events underscore the importance of real-time radar monitoring, detailed structural mapping, and time–displacement modelling in anticipating and managing complex failure sequences in open-pit environments. This dual-mode failure mechanism, captured in real-time, highlights unique structural controls not previously documented in similar mining settings.

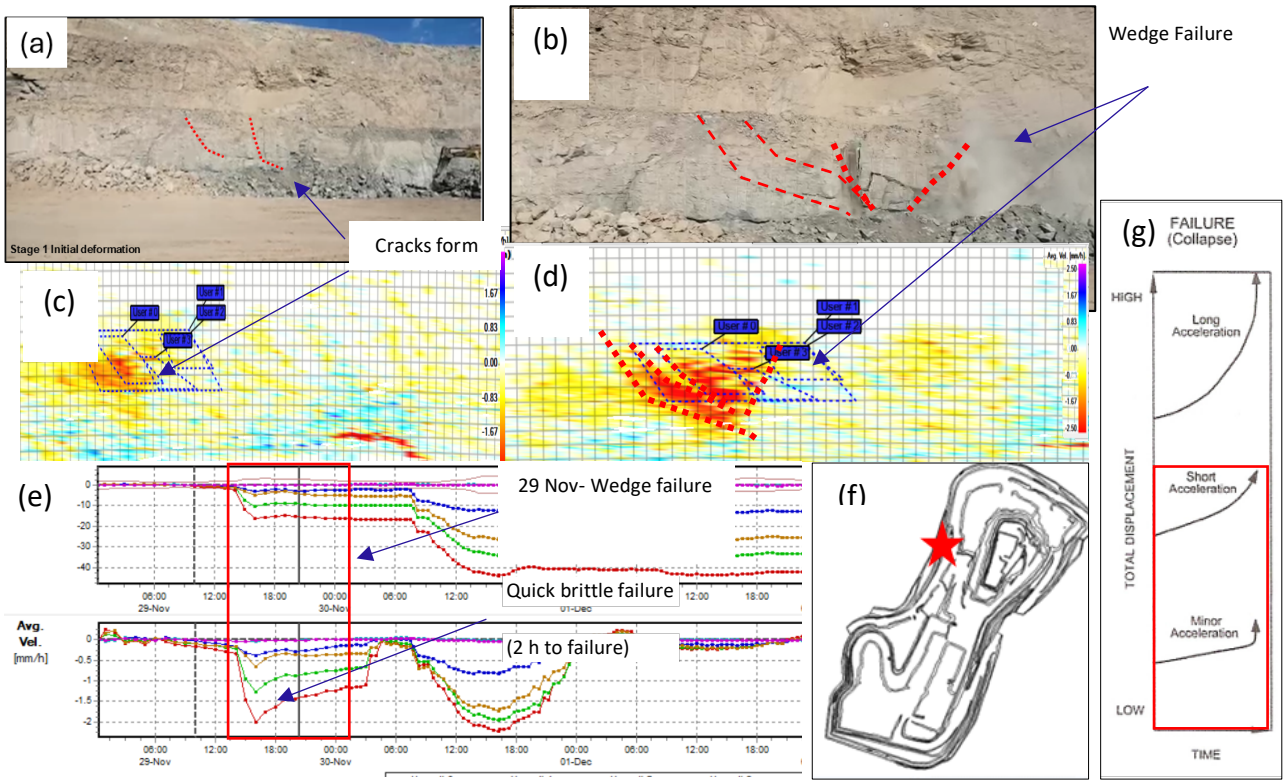


Figure 8. Composite illustration of wedge failure component observed on the western slope of Zone 1, Husab Mine, during the Bench 11 collapse event. (a) Shows the image with the initial crack development and dilation for the formation of the wedge failure (b) The movement stage when the wedge failure has collapsed (c) The radar velocity heat map showing acceleration zones prior to failure (d) The radar velocity heat map showing acceleration zones during the wedge failure (e) Time–displacement plots indicating rapid brittle failure on 29 November. (f) Pit location – a red star marks the point of failure. (g) Failure phase model provides interpretive context, based on time–displacement behaviour described by Sullivan (2007), with the red outline highlighting the brief period of acceleration observed during the wedge failure.

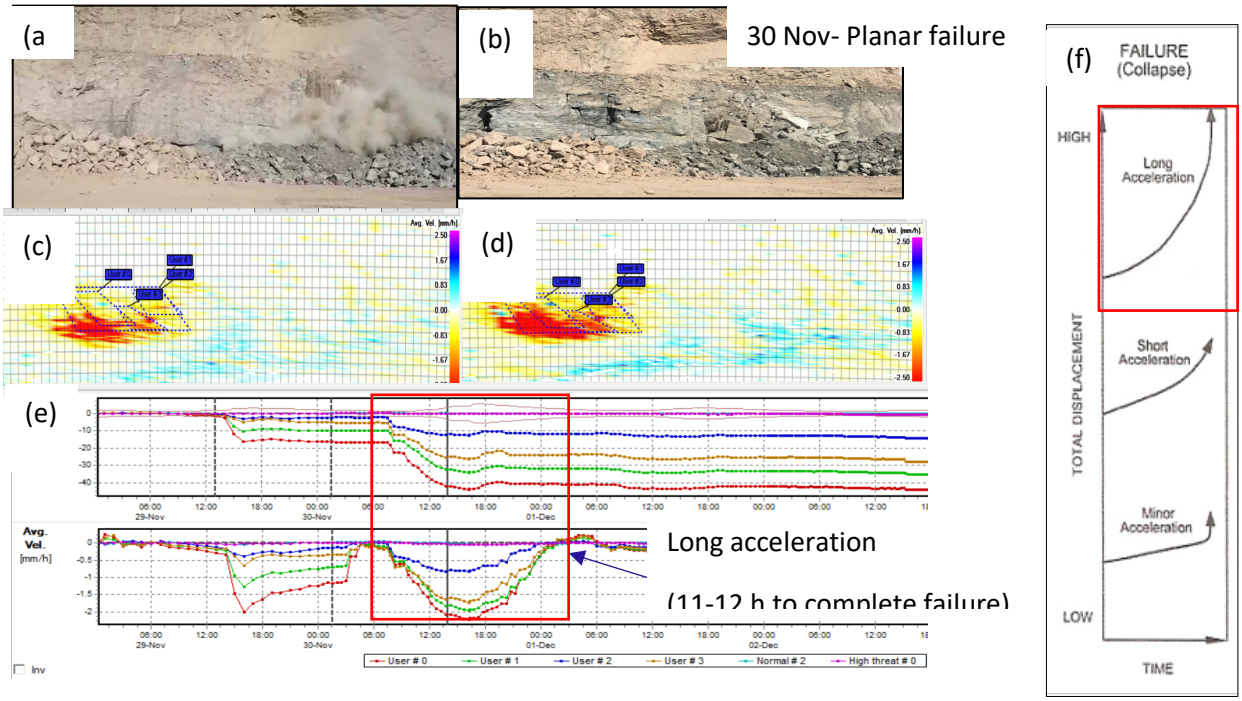


Figure 9. Composite illustration of planar failure component observed on the western slope of Zone 1, Husab Mine, during the Bench 11 collapse event. (a) Field photo showing active planar failure initiation (b)Post-failure image of the exposed failure surface (c) GB-RAR velocity heatmap prior to failure, showing moderate deformation zones (d) GB-RAR heatmap during the failure phase, with acceleration concentrated along the failure plane. (e) Prism time–displacement and velocity trends indicating long acceleration over 11–12 hours prior to collapse. (f) Conceptual failure progression model (after Sullivan, 2007), highlighting the long acceleration regime characteristic of planar failures.

Blast Vibration Characteristics in Zone 1

Blast-induced vibrations were systematically recorded and evaluated to understand their influence on slope deformation along the structurally sensitive western slope of Zone 1. The monitored vibration data focused on PPV measurements near Bench 7, where both prism and GB-RAR monitoring systems were concurrently active.

During excavation and production blasting events, the PPV values recorded in Zone 1 ranged from 4.2 mm/s to 9.7 mm/s, with the highest intensities concentrated near prism P11—a monitoring point situated above a previously failed section of the slope. These vibration levels fall within the range typically associated with microfracture initiation and crack propagation in jointed hard rock, particularly when the structural planes are unfavourably oriented with respect to the direction of blast energy transmission.

The vibration patterns demonstrate that intermittent blasting serves as a periodic dynamic loading mechanism, which, in structurally complex zones, can trigger:

- Rebound deformation following excavation-induced unloading,
- Acceleration of slope movement along foliation planes, and
- Activation of stick-slip failure regimes in meta-stable rock blocks.

These findings highlight the importance of integrating blast vibration monitoring with geotechnical displacement data to establish causality between operational triggers and slope deformation responses in open-pit environments.

Planar failure below the ramp

A planar failure occurred on Bench 17 in 2021 during blasting and unloading activities. The failure measured approximately 40 m in width, 23 m in height, and extended 6 m deep, resulting in significant backbreak into the ramp above. Notably, this ramp lies directly beneath the location of the subsequent Bench 11 failure, further compounding the geotechnical challenges in the area. Due to the extent of the Bench 17 failure, the failed zone was mined out beyond the failure plane and subsequently backfilled to facilitate the re-establishment of the ramp system.

To restore dual access and mitigate associated safety concerns, a series of remediation measures were implemented. These included:

- Construction of a catch fence along the toe of the ramp below Bench 11
- Reduction of the footprint of the sand berm to improve ramp accessibility, and
- Excavation and controlled backfilling of the Bench 17 failure zone to reinstate the ramp alignment and functionality. (Ockhuizen *et al*., 2024.).

Structural data obtained from various drilling campaigns confirm that the foliation planes persist across the entire life-of-mine designed slope, as illustrated in Figure 10. The structural measurements indicate that these foliation planes exhibit average dip angles ranging between 45° and 65°. One such failure plane, which daylighted during mining operations, was mapped with an orientation of 55°/127°, closely aligning with the slope face.

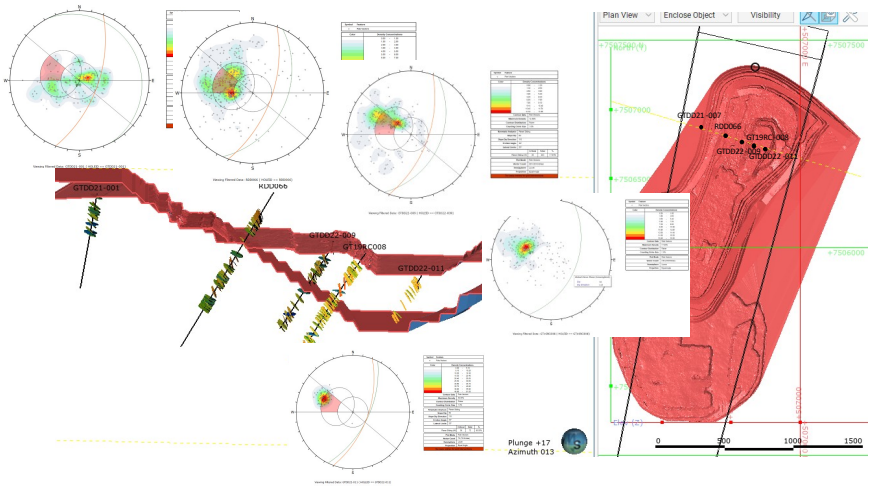


Figure 10. Illustrates the persistent foliation along the western slope from the different holes drilled in Z1 pit (Ockhuizen et al., 2024).

Given these findings, a strategic decision was made to revise the planned batter angle from 80° to 60° to mitigate the risk of further planar failures. This adjustment was driven by the realisation that the original batter design closely paralleled the dip of the foliation, significantly increasing the likelihood of structural failure. As a result, a dip-slope mining approach has been adopted, acknowledging that the foliation orientation is now more closely aligned with the revised slope geometry. This modification is expected to enhance slope stability and reduce geotechnical risk.

Discussion

The study identified several key findings regarding slope deformation and failure mechanisms on the western slope of Zone 1:

Deformation Mechanisms and Structural Controls: Multiple deformation and failure mechanisms were identified, each triggered or accelerated by excavation and production blasting activities within a

structurally complex geological setting. These mechanisms include rebound deformation following unloading, wedge failure, and planar sliding. All of these mechanisms are strongly influenced by the region's tectonic history and lithological variability and do not occur in isolation but rather as sequential or compounding events initiated by excavation-induced unloading and intensified by production blasting.

Failure zones were observed to spatially coincide with major lithological transitions and intrusive contacts, particularly at intersections between the Chuos Formation, intercalated units of the Rössing Formation, and transitions into the Khan Formation. The influence of Alaskite intrusions, particularly where they disrupt schistose units, appears to have further weakened the slope's structural integrity by creating planes of weakness along which failure could localise.

Notably, prism P11—located above a known historical failure zone—recorded higher-than-average displacements, indicative of local structural weakening or the reactivation of pre-existing discontinuities. This behaviour is consistent with expectations in highly anisotropic rock masses, where pre-existing weaknesses are activated by mining-induced stress redistribution.

Collectively, these findings confirm that structural fabric—not just slope geometry or excavation sequence—is a primary determinant of slope performance in this setting. They also point to the importance of integrating detailed structural mapping with deformation monitoring to anticipate zones of elevated risk and guide design interventions.

Different stages in the Deformation behaviour: The observed deformation behaviour follows the progressive stages of deformation illustrated in Figure 5, aligning with established failure progression models by Saito (1968), Spencer (1988), Sullivan (1993), and Zavodni (2001). These stages include:

- *Initial Creep Stage*: Characterised by minor, often undetectable deformations without a clearly defined failure surface, likely marked the early onset of instability but remained below detection thresholds. This underscores the challenge of identifying incipient failures without high-frequency or high-resolution monitoring.
- *Constant-Speed Stage*: was more readily captured, manifesting as measurable displacements and the development of tension cracks. This stage coincided with material removal activities, suggesting a direct link between excavation-induced unloading and the mobilisation of structurally constrained rock masses.
- *Stick-Slip Stage*: particularly evident at Bench 7, is of critical interest. Intermittent displacements recorded at prism P11 reflect a meta-stable state where structural planes are intermittently engaged and disengaged. Importantly, the transition to full failure was interrupted through timely engineering interventions, including design modification and catchment bench installation. This case illustrates the potential of responsive slope design to interrupt the failure progression before full detachment occurs.
- *Accelerated Stage*: as documented on Bench 11, presents a contrasting scenario. Two temporally distinct but spatially linked failures—one wedge-type and one planar—occurred within a 24-hour window. The **wedge failure**, developing over approximately 1 hour and 45 minutes, displayed brittle characteristics typical of sudden energy release along intersecting joint sets. In contrast, the **planar failure** evolved more gradually over a 24-hour period, indicative of ductile deformation controlled by persistent foliation surfaces. These two modes, while adjacent in space, represent fundamentally different mechanical responses, reflecting both the anisotropy and the heterogeneity of the rock mass. While localised, the event underscores the critical importance of combining continuous monitoring with proactive geotechnical design at all bench levels to mitigate the risk of progressive failure escalation. Sullivan's (2007) time–displacement framework distinguishes rapid, brittle failures from slower, ductile ones—each requiring different hazard responses. Brittle failures allow little warning, while ductile events can be mitigated if identified early. Continuous monitoring is vital, as no universal failure model exists; local structural conditions determine how failures occur and should be managed.

Influence of Structural Planes and Blasting Vibrations: The primary cause of slope instability was identified as the presence of multiple unfavourably-oriented structural planes and sub-vertical joint sets. These discontinuities, when activated by blasting-induced vibrations, significantly increased the likelihood of failure. Blasting-induced vibrations—particularly in the 4.2 mm/s to 9.7 mm/s PPV range recorded near Bench 7—likely contributed to crack propagation and displacement along these planes. The location of prism P11, which showed anomalously high displacements, coincided with zones of elevated PPV and a known prior failure area, suggesting a compounded effect of structural predisposition and blasting energy on slope response.

Field observations below prism P10 (Figure 7) visually confirmed this interpretation. The misalignment of pre-split barrels and visible offsets along foliation planes provide compelling evidence of excavation-induced activation of pre-existing structural weaknesses. Although this meta-stable behaviour did not result in immediate failure, it highlights the latent geotechnical risk posed by cumulative energy input in structurally complex rock masses.

Monitoring and Mitigation: The implementation of a comprehensive monitoring system combining GB-RAR and automated prism measurements, proved instrumental in capturing deformation trends in real-time. These proactive responses demonstrate the value of coupling continuous monitoring with an adaptive mine design philosophy. Interventions such as the installation of a 10 m-wide catchment bench and the adjustment of batter angles from 80° to 60° were supported directly by data interpretation. These design changes were not only reactive but also preventative—targeting areas of structural concern before full-scale failure could occur.

Notably, the timely redesign of Bench 7 geometry prevented the full daylighting of critical failure surfaces. On Bench 11, although a collapse occurred, the combined use of GB-RAR velocity maps and prism displacement graphs provided advance warning, enabling safe evacuation and post-failure assessment.

In response to the observed deformation and proximity of a permanent ramp below the unstable section, a catch fence was installed to contain potential rockfall material. Additionally, the remediation strategy on Bench 17—where a previous planar failure was backfilled to restore ramp access—demonstrates the effective integration of structural mapping, monitoring, and engineering design in mitigating slope-related risks.

Integration into Mine Planning and Slope Design: The findings of this study emphasise the importance of integrating detailed geological and structural analysis into mine planning and slope design. Adjustments to slope angles and mining strategies, informed by a thorough understanding of structural controls can significantly reduce the risk of slope failure.

The implementation of a 10 m-wide catchment bench to shield basal planes from direct exposure and the reduction of batter angles from 80° to 60° in areas of high structural anisotropy are examples of design responses rooted in observational data. These changes were validated by subsequent stabilisation of movement trends and the absence of large-scale reactivation in previously unstable zones.

Furthermore, the integration of radar-derived velocity data, prism displacement trends, and vibration monitoring has allowed for back-analysis of failure events, directly informing updates to pit slope hazard zoning and blasting protocols. This multi-source feedback loop supports a more agile mine design process—one that evolves in response to observed rock mass performance rather than relying solely on pre-mining assumptions.

Overall, the integration of structural analysis, real-time monitoring, and responsive design modifications provides a robust framework for identifying and mitigating slope instability risks, especially in structurally complex geological settings. This integration supports a shift from reactive to proactive geotechnical management, embedding observational data and model validation into the full mine planning lifecycle. It promotes safer, more cost-effective mining in complex geologyical environments where standard designs may not adequately address site-specific instability risks.

Future work
Future research should focus on creating calibrated slope failure forecasting models that consider structural orientation and cumulative blast energy. These models will improve predictions and help geotechnical teams refine designs based on actual ground behaviour, enhancing risk management in mining.

At Husab mine, integrating satellite-based InSAR with existing ground monitoring aims to provide a more complete, long-term view of slope deformation. Alongside this, a 3D structural modelling effort—using drone photogrammetry, radar data, and field mapping—is underway to improve failure mechanism understanding and guide proactive design.

The geotechnical team is also gathering detailed rock mass data through core logging, drilling, and lab tests to better understand material responses to dynamic loads and link slope movements to blasting. Combining this information with ongoing monitoring and back-analysis will help define PPV thresholds for microfracture propagation and support robust, predictive stability models for complex sites.

CONCLUSION

This paper provides critical insights into the deformation behaviour and failure mechanisms of open-pit slopes subjected to excavation and blasting in a structurally complex rock mass. At the Husab mine, slope failures were strongly influenced by persistent foliation, sub-vertical joint sets, and intrusive contacts, which collectively define structurally controlled failure zones. Monitoring data captured through automated prisms and ground-based radar revealed progressive deformation patterns, including rebound effects and stick-slip movement, indicative of pre-failure behaviour.

Two key failure modes were identified: rapid wedge failures and more gradual planar failures, both primarily triggered by excavation-induced unloading and blasting vibrations. These vibrations (in the study area), with recorded PPV values ranging from 4.2 to 9.7 mm/s, contributed significantly to crack propagation and deformation along pre-existing discontinuities.

The research findings underscore the value of combining structural geological analysis with real-time monitoring technologies to enhance the detection, understanding, and mitigation of slope instabilities. Practical slope design adaptations—such as catchment bench installations and slope angle adjustments—demonstrated the effectiveness of timely, data-informed responses in moderating deformation and reducing failure risks.

Overall, the study contributes to the refinement of multi-stage deformation models and supports the integration of monitoring-informed design strategies for safer and more resilient slope management in large-scale mining operations. These findings establish a replicable framework for proactive geotechnical decision-making in structurally complex open-pit environments. By integrating structural analysis, real-time monitoring, and responsive design strategies, the study advances safer, more efficient, and geotechnically robust mining practices applicable to similar settings worldwide.

ACKNOWLEDGMENTS

Sincere appreciation is extended to CGNPC Swakop Uranium management for permission to publish this paper. The contributions made by various geotechnical geologist and mine engineers are greatly appreciated.

REFERENCES

Freemantle, G.G., 2015. Primary Uranium Mineralisation Of The Central Damara Orogen , Namibia (PHD). University of the Witwatersrand, Johannesburg.

Maduray, C., Armstrong, R., Pillay, O., Imrie, S., Tuitz, C., Muaka, J., 2018. 2018 Husab Mine_Design Review Report_20180726_Final.pdf (No. 469305). SRK Consulting (South Africa) (Pty) Ltd.

Mercer, K.G., 2006. Investigation into the time dependent deformation behaviour and failure mechanisms of unsupported rock slopes based on the interpretation of observed deformation behaviour (PHD). University of Witwatersrand, Johannesburg, South Africa.

Ockhuizen, G., Maduray, C., Armstrong, R., 2024. The importance of geological understanding in the development of a geotechnical model and its impact on slope design, in: Proceedings of the 2024 International Slope Stability Conference. Presented at the International slope stability conference, Belo Horizonte, Brazil.

Saito, M., 1968. Forecasting time of slope failure by tertiary creep, in: 7th International Conference on Soil Mechanics and Foundation Engineering. Presented at the Stability of Natural Slopes and Embankment Foundations, INTERNATIONAL SOCIETY FOR SOIL MECHANICS AND GEOTECHNICAL ENGINEERING, Mexico.

Spencer, E.W., 1988. Introduction to the Structure of the Earth, 3rd Ed. ed. McCraw Hill Book Company.

Spivey, M., Penkethman, A., Culpan, N., 2010. Geology and Mineralization of the Recently Discovered Rössing South Uranium Deposit, Namibia. 2010 Soc. Econ. Geol. Inc Spec. Publ. v. 15. https://doi.org/10.5382/SP.15.2.17

Sullivan, T., 2007. Hydromechanical Coupling and Pit Slope Movements, in: Proceedings of the 2007 International Symposium on Rock Slope Stability in Open Pit Mining and Civil Engineering. Presented at the 2007 International Symposium on Rock Slope Stability in Open Pit Mining and Civil Engineering, Australian Centre for Geomechanics, Perth, pp. 3–43. https://doi.org/10.36487/acg_repo/708_sullivan

Sullivan, T.D., 2020. Understanding pit slope movements, in: Szwedzicki, T. (Ed.), Geotechnical Instrumentation and Monitoring in Open Pit and Underground Mining. CRC Press, pp. 435–445. https://doi.org/10.1201/9781003077756-54

Sullivan, T.D., 1993. Understanding pit slope movements, in: Szwedzicki, T. (Ed.), Proceedings of the Australian Conference on Geotechnical Instrumentation and Monitoring in Open Pit and Underground Mining. Presented at the Geotechnical Instrumentation and Monitoring in Open Pit and Underground Mining, CRC Press, Balkema, Rotterdam, pp. 435–445. https://doi.org/10.1201/9781003077756-54

Uezawa, H., Saito, M., 1961. Failure of Soil Due to Creep, in: 5th International Conference on Soil Mechanics and Foundation Engineering. Presented at the Soil Properties and their Measurement, INTERNATIONAL SOCIETY FOR SOIL MECHANICS AND GEOTECHNICAL ENGINEERING, Paris, pp. 315–318.

Wessels, S.D.N., 2009. MONITORING AND MANAGEMENT OF A LARGE OPEN PIT FAILURE (Degree of Master of Science). University of Witwatersrand, Johannesburg.

Zavodni, Z., 2001. Time-Dependent Movements of Open-Pit Slopes, in: SME Proceedings. Presented at the International conference; 4th, Stability in open pit mining, Society for Mining, Metallurgy, and Exploration, Denver, Colorado, pp. 81–87.

Zavodni, Z.M., Broadbent, C.D., 1983. INFLUENCE OF ROCK STRUCTURE ON STABILITY. Presented at the 3RD STABILITY IN SURFACE MINING.

Zavodni, Z.M., Broadbent, C.D., 1980. Slope failure kinematics. Bull. Can. Inst. Min. 69–74.



Grantham Ockhuizen

Superintendent: Geotechnical
CGNPC Swakop Uranium

Grantham Ockhuizen is a highly experienced Engineering Geologist with 17 years in the mining industry. He is professionally registered with SACNASP and serves as the Superintendent - Geotechnical at Husab Mine, Namibia, where he leads the geotechnical team and overseeing operational risks, slope design and the execution of monitoring programmes in line with medium and long term mine plans. This includes continual improvement of Department systems to optimise both efficiency and effectiveness in order to maximise production. Support operations and projects with the implementation of best-practise geotechnical standards in mapping, logging, analysis, groundwater conditions and slope stability interpretation

His leadership extends beyond his operational role, having served as the Namibian branch Chairman for the Southern African Institute for Mining & Metallurgy (SAIMM) from 2013 to 2017 and remains an active affiliate member. His extensive expertise and leadership highlight his ongoing commitment to the industry.

Rock fall hazard analysis of a natural slope at the Sungun Copper Mine

J.D. Bosman[1], L. Cilliers[1], H. Reza Golchin[2]

[1]Open House Management Solutions (Pty) Ltd, South Africa
[2]Sugun Copper Mine, Iran

The Sungun Copper Mine is in the mountainous terrain of East Azerbaijan Province in the Islamic Republic of Iran. Following a rockfall incident from a natural cliff, the exposure of the exposed section of a conveyor belt was identified as a potential risk to continued safe operations. A comprehensive rockfall hazard analysis was required to quantify the potential risks to the exposed conveyor belt area. The study aimed to quantify the risk to the belt infrastructure and propose protective measures to prevent damage. Using high-resolution photogrammetry, LiDAR scanning and back analysis, the study determined key input parameters for rockfall simulations.

The photogrammetry approach involved particle size distribution analyses of the natural cliff which enabled the estimation of the size of falling rock blocks. The size, shape, and mass of the falling bodies are essential for creating realistic 3D models used in rockfall trajectory simulations. The LiDAR scan of an actual boulder that had fallen onto the conveyor belt provided critical data on block size and shape. A wireframe model, representing the boulder, was constructed to simulate its movement and impact along the slope. In addition, the topography of the slope was carefully considered, to be used for trajectory simulations, using the Trajec3D software.

Back analysis of an observed rockfall proved valuable in refining simulation input parameters such as the coefficient of restitution, static and dynamic friction angles, and block size. The analysis revealed that the existing fence, on a portion of the slope, provides 93% effectiveness in mitigating rockfall risk. The study concludes with recommendations for the most effective protective measures and providing a robust risk assessment for the exposed conveyor belt infrastructure.

Keywords: Rockfall, conveyor belt, photogrammetry, LiDAR scanning, risk assessment.

INTRODUCTION

In this paper, we present the findings of a rock fall hazard analysis, following a rock fall incident in the exposed conveyor belt area at the Sungun mine. The mine, located in the mountainous terrain of East Azerbaijan province in the Islamic Republic of Iran (see Figure 1), faces a significant hazard from rockfalls, originating from a natural cliff situated approximately 250 m above the main conveyor belt. This belt is used for transporting run-of-mine ore to the reduction works.

The primary aim of this paper is to assess the potential exposure of an open, elevated section of the conveyor belt to rockfall hazards and to propose strategies for mitigating the risk of damage to the belt infrastructure. Hazard quantification is supported by a back analysis of an observed rockfall event, providing insight into the frequency and severity of potential future incidents. This study aims to provide valuable recommendations to ensure the long-term safety and reliability of the conveyor system, minimising the risk of further disruptions or infrastructure damage from rockfall events.



Figure 1. Location map of Sungun mine, Iran.

ROCKFALL SIMULATION INPUT PARAMETERS

Rockfall simulations require several key input parameters to model the trajectory and behaviour of falling rocks. These parameters include fall body characteristics (such as size, shape, and mass), coefficient of restitution (which determines how much energy is lost during impact), static and dynamic friction angles (which affect sliding and rolling behaviour), and topography of the probable travel path. By accurately inputting these parameters, simulations can help predict rock fall paths and assess potential hazards in open-pit slopes.

Topography

The topography of the Sungun mine is a crucial component in simulating the trajectory of a falling body. The rockfall analysis was conducted by considering the mine's topographical features, which were then processed and analysed using the Trajec3D software program to assess the risk of rockfalls. The total area of interest is depicted in Figure 2, showcasing the topographical surfaces deemed optimal for the assessment. The resolution of these surfaces is representative of the actual slopes, as key features such as windrows on recently excavated benches are clearly visible in the topographical data. This high level of detail ensured that the simulations reflected the conditions on the ground.

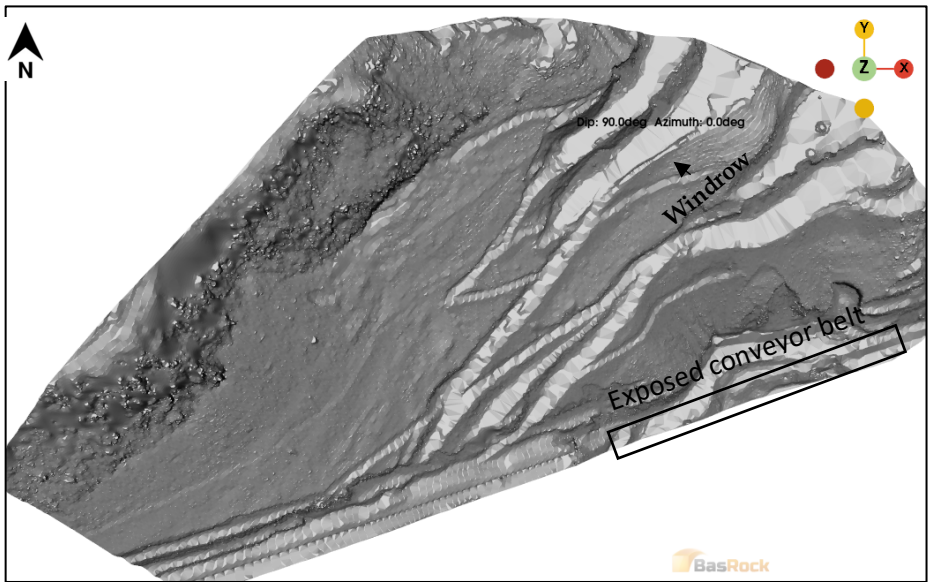


Figure 2. Topography of the slope above the belt.

Fall body shape

A LiDAR scan captured a 3D representation of the rockfall boulder. The scan allowed for precise digitisation of the boulder's shape and size, enabling a thorough analysis of the rock's geometrical characteristics. Figure 3 presents the 3D image generated from the LiDAR scan, providing a detailed view of the boulder.



Figure 3. 3D image of the LiDAR-scanned boulder.

In rockfall simulations, a realistic yet simplified 3D representation of the fall body is used, as excessive detail in the shape does not substantially affect the dynamics of the fall. Instead, it adds unnecessary complexity to the simulation. To convert the LiDAR scan into a usable model for simulation, a point cloud was exported and used to create a smooth wireframe surface (see Figure 4).

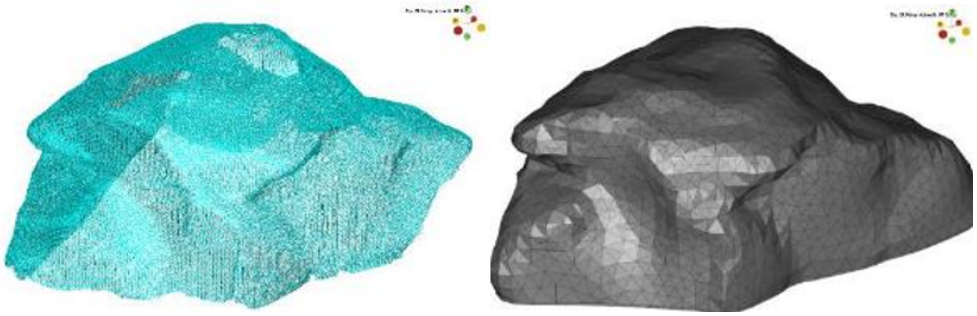


Figure 4. High resolution points cloud (left); wrapped wireframe (right).

This wireframe was wrapped around the scanned data, ensuring that the size and shape of the boulder are accurately represented, while also simplifying the geometry for computational efficiency. The resulting wrapped wireframe CAD model was then used to quantify the boulder's volume, calculated to be 5.12 m^3, yielding a mass of 13.82 tons, based on a density of 2700 kg/m^3. This approach allowed representative yet computationally efficient representation of the rock for further analysis in the simulation.

BACK ANALYSIS

In this study, the rockfall simulation was carried out using the Trajec3D software, which is used to perform 3D rigid fall body analysis. The software computes the trajectory paths of rock blocks or fall bodies traversing a specified topography (Basson, F.R.P., (2012)). For simulation, several key parameters were required, including the slope geometry, fall body size, shape, rock density, coefficient of restitution (COR), and both static and dynamic friction angles. While the first four parameters were derived from available data, the static and dynamic friction angles, which govern the mechanistic behaviour of the

fall, were determined through back analyses. The start location and travel path of the known rockfall were provided by Sungun mine.

The simulation involved repeatedly modelling the fall body's movement over the topography, with different mechanical properties tested to understand their influence on the trajectory. The COR, which defines the elasticity of the interaction between the fall body and the surface, is set based on literature values, with the surface type influencing the chosen COR. The friction angles were also varied, and a range of combinations was tested to determine the most representative parameters. Over 120 fall bodies are dropped from the origin of the known rockfall, and the resulting paths were analysed.

The results reveal that the static and dynamic friction angles had little effect on whether a fall body would reach the conveyor. This behaviour is attributed to the volumetric shape of the fall body, which tends to promote rolling rather than sliding. In contrast, flatter-shaped blocks are more likely to slide, with the friction angle playing a significant role in governing their movement. This suggests that in the case of the observed rockfall the frictional properties in the simulations do not significantly alter the outcome. In the end, the static friction angle of 40° and the dynamic friction angle of 35° are found to provide the best correlation with the actual trajectory of the rockfall. The simulation outcomes were validated by comparing the model predictions with the real-world path. Only minor deviations occur between certain elevation levels.

The properties from the back analysis are used in the baseline risk assessment to determine the current rockfall risk. The following sections provide details on the properties used in the analysis.

Fall body size

An evaluation of the cliff area where rocks are most likely to dislodge utilised drone images to construct 3D orthophotos, which are processed in the 3GSM software. This software is designed to quantify particle size distribution (PSD) for blast muck piles, and is adapted to estimate the likely size distribution of loose rocks on the cliff. The orthophotos generated from the drone scans were used to identify isolated rocks on the steepest part of the cliff, where rockfalls are most probable and analysed to determine their sizes and included in the PSD dataset.

In collaboration with Sungun mine personnel, it was decided to focus on the 99.6 percentile value, representing a rare but critical event with a probability of occurrence of only 0.4%. This was selected due to the higher kinetic energy that large blocks would carry, potentially placing a greater demand on protective systems, if they were to fall.

The size and mass of the fall bodies are quantified using the formula for the volume of a sphere:

$$\text{Mass} = 4/3\pi r^3\rho \qquad [1]$$

where 'r' is the radius of the sphere and 'ρ' is the density of the rock (2700 kg/m^3).

The cliff was divided into four zones (Figure 5), based on their specific geometries. The 99.6 percentile rock sizes were determined for each of the four zones (Zone 1 = 6.95 tons, Zone 2 = 9.7 tons, Zone 3 = 15.1 tons and Zone 4 = 11.3 tons), of which the 9.7-ton and a 15.1-ton fall body sizes are located above the belt.

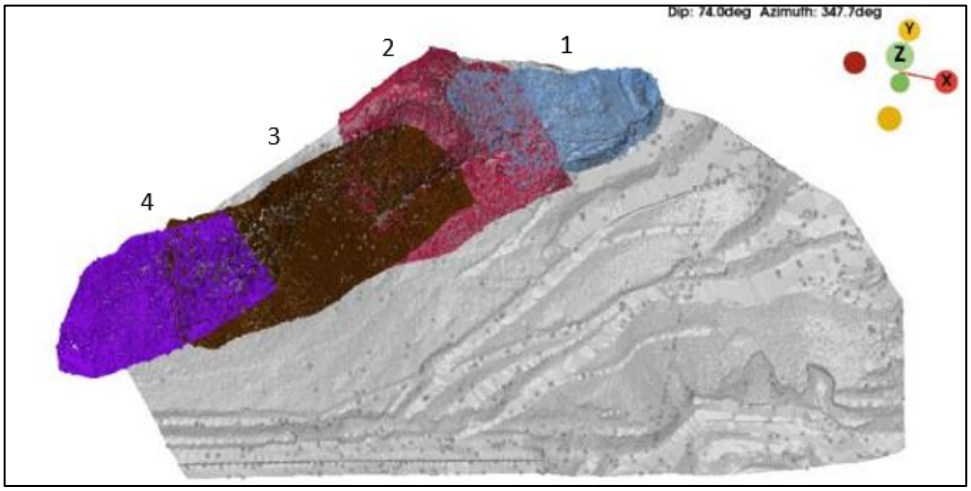


Figure 5. Four zones on cliff.

Mechanical properties

The COR plays a role in simulating rockfall trajectories using the Trajec3D software, which is designed to perform three-dimensional rigid body analysis. COR represents the elasticity or bounciness of a collision, quantified as the ratio of the final velocity to the initial velocity of two objects after impact. It is an essential parameter for determining how a fall body will behave when it strikes a surface, influencing its rebound and overall kinetic energy after collision.

The COR value ranges from 0 to 1:

- A COR value of 1 signifies a perfectly elastic collision, where no energy is lost, and the rock bounces with no reduction in speed.
- A COR value of 0 represents a perfectly plastic collision, where all kinetic energy is absorbed, and there is no rebound.

In the context of rockfall simulations, the COR value is used to assess the extent to which rocks will rebound when they strike surfaces on the slope. To simulate these impacts, real-world data, such as large-scale in situ tests and experimental results, are essential. Published studies, such as those by Basson (2013), have suggested that the minimum COR for surfaces commonly found in mining environments, like catch berms or pit floors, is 0.003, with a rebound of at least 1 mm.

The COR depends heavily on the nature of the impacting surface. For example, surfaces covered in broken rock or soil typically result in a lower COR, as they tend to absorb more kinetic energy from the falling rock. In this study, the natural rock slope above the conveyor installation features soft soils and vegetation, which are anticipated to significantly absorb the kinetic energy of falling rocks. Therefore, a low COR value of 0.001 was chosen to account for the energy absorption by these soft, vegetated surfaces.

By utilising COR and friction values, determined from experimental data and back analyses, the simulation provides a more accurate representation of rockfall behaviour, helping to predict the rock blocks' trajectories and their potential impacts on the surrounding environment.

BASELINE HAZARD QUANTIFICATION

A baseline rockfall assessment was conducted to identify critical areas for rockfall risk and determine appropriate preventative measures to protect the belt at the bottom of the slope (see Figure 5). The assessment incorporates an existing fence on the western side of the slope, which covers approximately 140 m of the slope above the conveyor belt protection canopy.

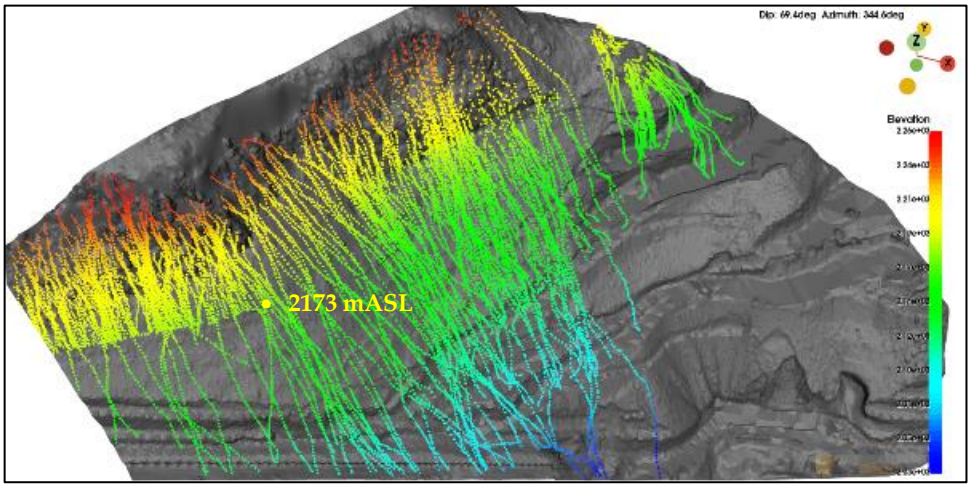


Figure 1. Results of the baseline rockfall assessment.

Using the Trajec3D software, the trajectories of fall bodies of sizes determined through analysis were simulated across the slope. The locations, bounce heights, velocities, and kinetic energies of the fall bodies were recorded at 0.01 second intervals, as the rocks descended the slope.

The bounce height, or the height above the topography that a falling body reaches, is a key parameter to consider when designing protection systems. It is essential to align the height of catch fences with the typical bounce height of rockfalls. For optimal efficiency, the fence should be positioned in areas where the bounce height is generally low, ensuring the fence effectively captures falling bodies.

Kinetic energy, which was determined from the velocity and mass of the falling bodies, is another crucial factor to consider in rockfall assessments. Initially, fall bodies descend slowly, but as they moved further down the slope, they begin to accelerate and become airborne, a phase known as free falling. During this stage, their velocity increases, leading to a rise in kinetic energy. This acceleration significantly impacts the rock's potential to cause damage and should be accounted for when designing protective measures such as catch fences.

The mass of the fall body is a key factor in determining its kinetic energy. A larger mass resulted in significantly higher kinetic energy, as the body accelerates down the slope. Higher kinetic energy means that fall bodies have greater potential for impact, making it essential to consider this factor when evaluating the effectiveness of protective measures such as fences.

Results of Baseline Risk Assessment

The simulation results of the rockfall assessment revealed several key findings regarding the effectiveness of the existing fence and the dynamics of rock falls across the slope (see Figure 6).

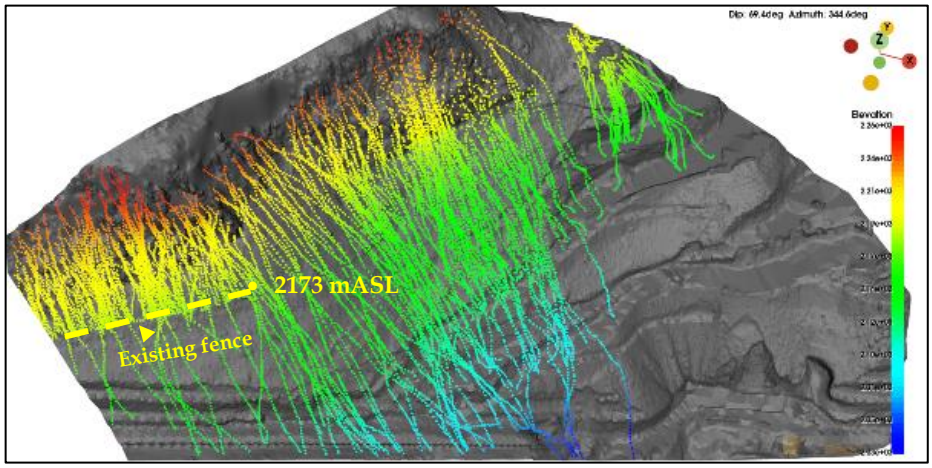


Figure 7. A perspective view of the fall body trajectories looking north-northwest.

The existing fence is largely effective in containing rockfalls. However, 7% of the simulated rockfalls managed to bounce over the fence, with nine reaching the conveyor belt protection canopy. No fall bodies are observed tumbling down the slope in the eastern portion where sufficient catchment berms are constructed.

Bounce heights varied from 0 to 17 m across the slope, with the maximum bounce heights occurring over vertical sections of the cliff. The 95-percentile bounce height was 8 m. Areas where bounce heights were lower (2-3 m) were identified as more suitable for the construction of effective protective measures, such as the 4-m-high fence.

The bottom of the slope and the vertical bench areas were identified as critical zones, with the maximum bounce height at the bottom of the slope reaching 14 m (95 percentile: 10 m). In the vertical cliff area, the maximum bounce height reached 17 m (95 percentile: 13 m), reflecting the high vertical drop.

The simulation also revealed varying velocities as fall bodies descend. The maximum velocity at the bottom of the slope is 38 m/s, with a 95-percentile of 28 m/s. The 95-percentile kinetic energy at the bottom of the slope is 5839 kJ. At the vertical bench, the maximum velocity is 27 m/s (95-percentile: 23 m/s) and the kinetic energy is 2819.21 kJ. High velocities and kinetic energy values were typically found in steeper sections, where fall bodies are more difficult to arrest.

Areas with high velocities, particularly above the canopy near the belt, are difficult to manage with protective measures. Fall body velocity statistics show a 95-percentile of 21 m/s, with a maximum of 38 m/s. High kinetic energy is more prominent with larger fall bodies (up to 15.1 tons), where the increased mass contributes significantly to energy.

Overall, the results emphasise the importance of placing protective measures in areas where bounce height and velocity are lower to enhance their effectiveness in arresting rockfalls before they become problematic.

ASSESSEMENT OF ROCKFALL PROTECTION SYSTEMS

To effectively safeguard the exposed section of the belt, it is crucial to prevent any falling rock from reaching this vulnerable area. The key to achieving this objective lies in arresting rockfalls early, before they travel down the slope to the exposed section. To devise an optimised protection strategy, the results derived from the baseline risk assessment were essential. These results provide valuable insights into the dynamics of rockfall trajectories, such as bounce heights, velocities, and energy levels, allowing for a more informed decision on the protection measures to be deployed.

Equally important is determining the optimal locations for deploying these protection systems. The placement of the protection must align with the specific characteristics of the slope, such as where bounce heights and velocities are lower. By carefully analysing the data on fall body paths and characteristics, protection measures can be placed strategically to maximise their effectiveness. The careful consideration of both the type and location of protection systems will ensure that the exposed section of the belt remains safe from rockfall damage.

Given the results from the baseline assessment, several protection options were evaluated. These options considered various factors, such as the intensity of the rockfall, the location of the highest risk zones, and the effectiveness of different protective solutions in mitigating these risks.

Table I Recommended protection systems

Protection system	**Advantage**	**Disadvantage**
Catchment Two options (See Figure): - Excavating (cut) and construction of a catchment berm. - Dumping (fill) entails placing waste material at an angle of repose and then create a catchment berm.	- Effective, providing that the width is adequate. - Reducing and arresting the velocity of falling rocks. - Waste mining in close vicinity. - Cost effective. - Safety advantage.	- Vertical bench – velocity and kinetic energy of falling rocks increase, before impact with horizontal area. - Drilling and blasting are required. - Working under destabilised slope. - Waste must be load and haul. - Practicality of angle of repose slope on steep topography.
Fence (see Figure)	- Lower waste material production (lower mining expenses). - Tested to be effective. - Absorbs energy. - Flexible design. - Energy absorbing (multiple hits)	- Expensive. - In country availability.

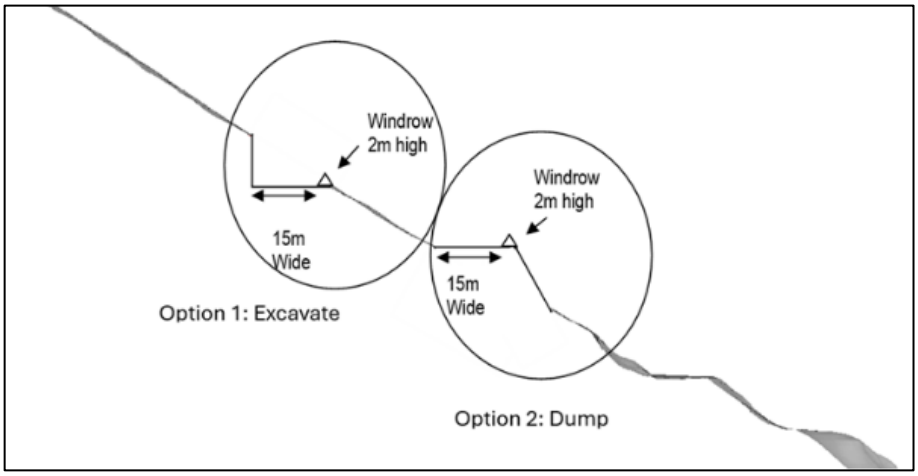


Figure 8. Options for dump or excavate.

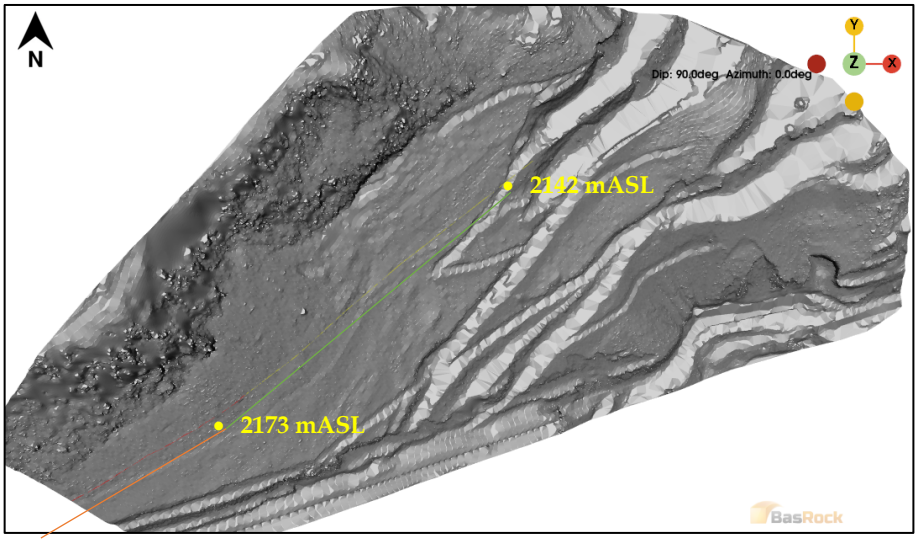


Figure 9. Option for an extended fence.

By considering all these aspects, an appropriate and effective rockfall protection system can be designed, enhancing the safety of the exposed section of the belt and ensuring the integrity of the entire system.

Excavated catch bench

The rockfall assessment was carried out with the integration of a catchment berm. The berm, located between specified markers, was 15 m wide, featuring a 10-m-high vertical bench and a 2-m-high windrow on its crest (see Figure 9).

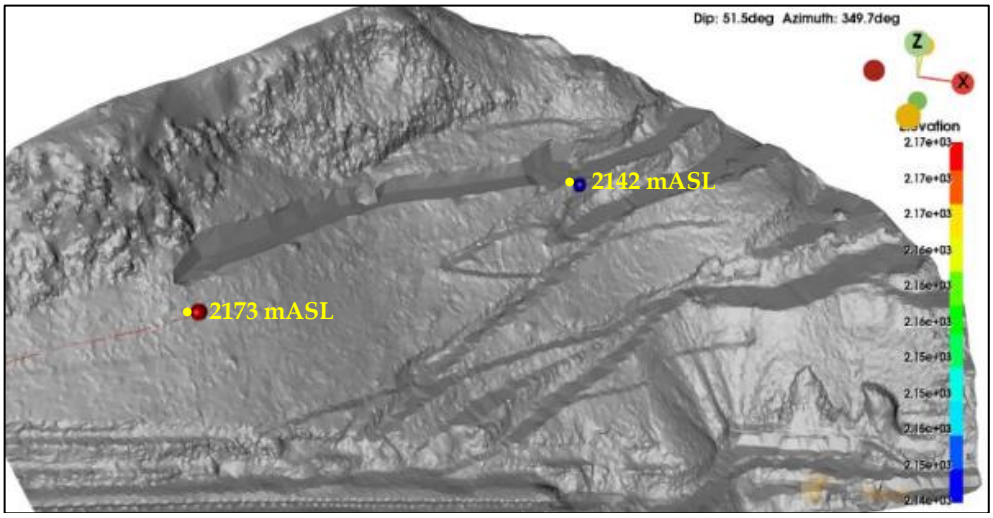


Figure 10. Catchment berm included on the topograph.y

The assessment entailed the evaluation of the bounce height, velocity, and kinetic energy of fall bodies.

For this scenario, 164 fall bodies weighing 9.7 tons (blue), and 298 fall bodies weighing 15.1 tons (red) were placed on the cliff area, and their trajectories were modelled (see Figure 10).

Upon reviewing the fall body trajectories, it was observed that several fall bodies (marked with black oval) reach the bottom of the slope in the area of the existing fence. This may be attributed to a steeper slope in this section of the cliff. The exposed area of the belt is indicated with a yellow rectangle in Figure 10.

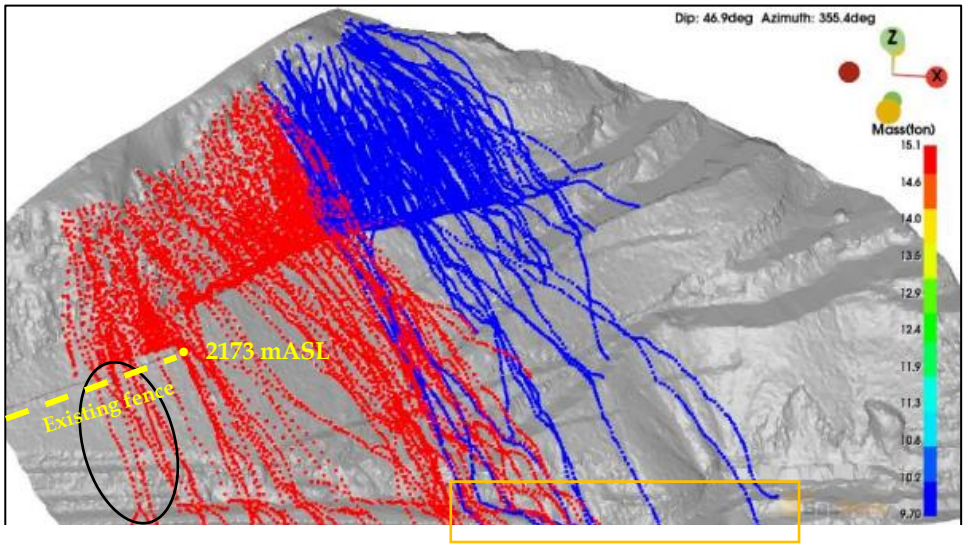


Figure 11. Fall body trajectories for 9.7 tons (blue) and 15.1 tons (red.)

The bounce heights were particularly high in areas with vertical benches and at the cliff overhangs, where free fall is likely more appropriate than typical bounce behaviour. Bounce height statistics showed a minimum value of 0.3 m and a maximum of 15 m, at the vertical benches.

High velocities were observed at the vertical benches. The statistical distribution of velocities reveals a wide range for the fall bodies. The velocities upon reaching the catchment berm are analysed, yielding the following results:

- The 9.7-ton fall bodies reach a maximum velocity of 6 m/s on the catchment berm, while the maximum velocity of the 15.1-ton fall bodies is 17 m/s. In the area of the fence, the maximum velocity reaches 21 m/s.
- For fall bodies travelling before going down the slope, the highest velocities are recorded in the area where the mass is the highest, with values up to 26 m/s before descending further down the slope.

Out of all the fall bodies simulated, 5.5% (9 out of 164 for 9.7-ton fall bodies) and 3.2% (7 out of 217 for 15.1-ton fall bodies) made their way down the slope to the exposed area at the belt. Most fall bodies are arrested either by the berm or fence before reaching the bottom.

Kinetic energy analysis shows that the highest energy was concentrated in the areas where fall bodies have the highest velocities. The goal of the analysis is to assess the need for additional protective systems, especially in cases where a fall body may bypass the catchment berm or fence. The maximum kinetic energy recorded is 6228.64 kJ, just above the conveyor protection canopy.

To summarise, the following is important:
- The catchment berm system effectively captured a significant percentage of the fall bodies, with more 15.1-ton fall bodies travelling down the slope due to the steeper sections.
- Bounce heights and velocities were higher in areas with vertical benches and overhangs.
- The velocities at the catchment berm and fence varied significantly, with the highest recorded in the area with the 15.1-ton fall bodies.
- Despite the effectiveness of the berm and fence, a small percentage of fall bodies still reached the exposed area at the belt, which is crucial for determining if additional protective measures are necessary.
- The kinetic energy at the exposed belt area reached high values, indicating the potential need for more robust systems to manage rockfall incidents.

In conclusion, the catchment berm shows promise in reducing the number of fall bodies that reach the bottom of the slope, but additional protective strategies would have to be considered, especially in areas with high kinetic energy or steeper slope profiles.

Filled catch bench

Another option involves placing waste material on the slope at its angle of repose and creating a catchment berm between the specified markers. The section between the backfill bench and the current fence lacks rockfall protection, as the backfill bench is too short and would need to be extended towards the western side (see Figure 11).

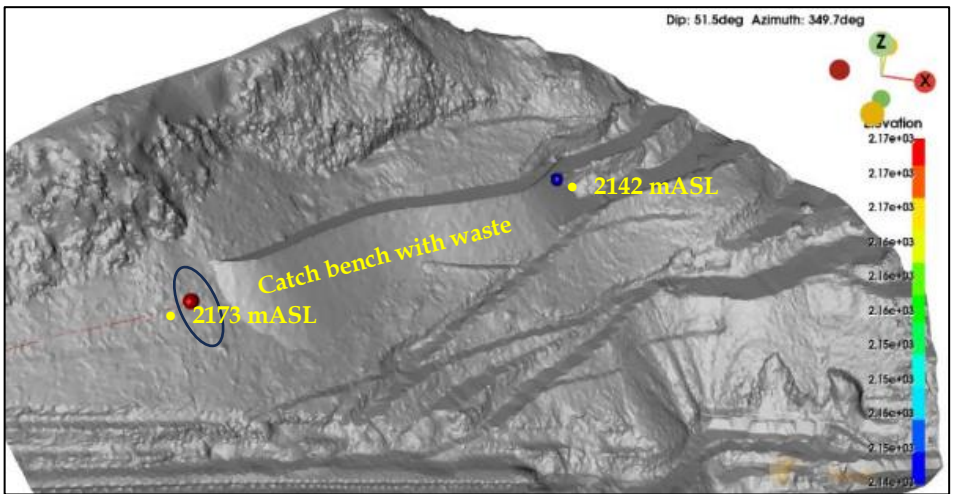


Figure 12. Placement of waste material.

The rockfall assessment for the fill option followed the same methodology used for the catchment berm evaluations, assessing the areas for 9.7-ton and 15.1-ton fall bodies. A total of 285 fall bodies weighing 9.7 tons, and 167 fall bodies weighing 15.1 tons are simulated. The simulation revealed that fall bodies exhibited varying behaviours, with 6% of the 9.7-ton and 8.5% of the 15.1-ton fall bodies reaching the bottom of the slope. Many of the fall bodies travelled through an open area between the fence and the backfill bench, gaining significant momentum as they descend (Figure 12). High bounce heights and velocities were observed, especially on vertical benches and cliffs, with the highest recorded velocities reaching 32.37 m/s. Kinetic energy was also notably high in areas lacking proper rockfall protection, highlighting the need for additional protective measures. The velocity and kinetic energy results are analysed at the catchment berm and fence, revealing critical points where further protection might be required, particularly in exposed areas.

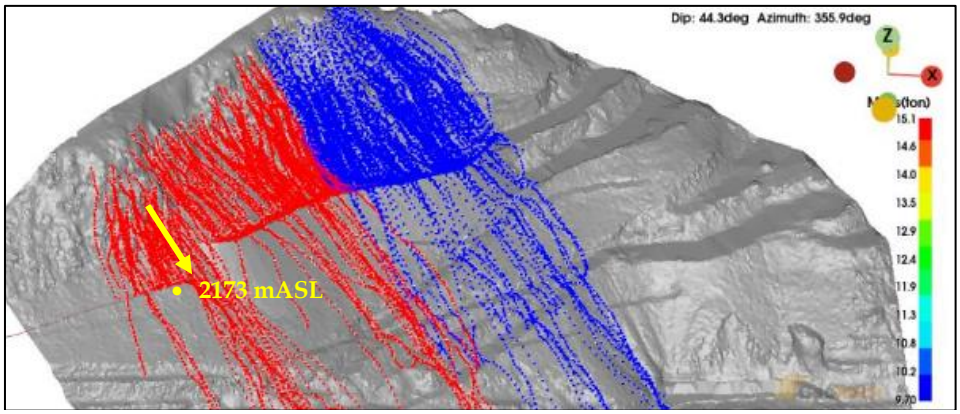


Figure 13. Fall body trajectories for the two fall body masses.

Catch fence

The simulation tested the effectiveness of the placement of a 4-m-high fence from the existing fence towards the catchment berm at 2142 mASL. The effectiveness was tested using 155 fall bodies of 9.7 tons (blue) and 145 fall bodies of 15.1 tons (red) on the cliff of the slope (see Figure 13).

The fence's effectiveness was tested, and the results showed that 2.3% (7 out of 300) of the fall bodies either bounce over the 4-m fence or bypass it on the northeastern side of the slope. One of these fall bodies reached the protection canopy above the belt, while the others were arrested by the catchment berms. The 15.1-ton body that bypassed the fence, reaching the protection canopy, with a bounce height of 5 m and a velocity of 23 m/s, corresponding to a kinetic energy of 4055.98 kJ.

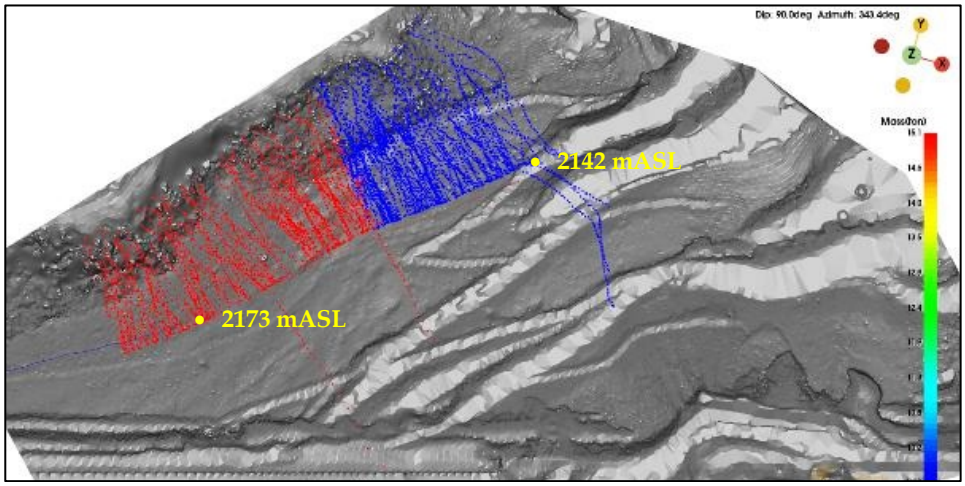


Figure 14. Fall body trajectories.

The bounce height data indicates that the heights were higher where the cliff forms a vertical overhang, with some fall bodies experiencing free fall rather than typical bounce behaviour. Despite these high bounce heights, the fallen bodies were still arrested by the fence. The bounce height varies between 0 and 22 m, with a 95th percentile value of 6 m. The data revealed that bounce heights greater than 7 m were limited to specific sections of the slope, particularly where the cliff is vertical.

As fall bodies descend, their velocities increased, particularly in the steeper sections of the slope below the cliff. The statistical distribution of velocities shows that the velocity just before the fall bodies are arrested by the fence have a 95th percentile value of 17 m/s, with a maximum of 21 m/s. Higher velocities are recorded where the fall body mass is larger.

Kinetic energy values were higher for the 15.1-ton fall bodies, reflecting the increased mass. These higher kinetic energy values were particularly noticeable above the belt protection canopy, where one of the fall bodies reached the bottom at the protection canopy, demonstrating the need to capture rock falls before they reach this critical area. Kinetic energy at the fence showed considerable variation, with higher values for the larger 15.1-ton bodies.

In summary, while the 4-m fence was effective in arresting most fall bodies, some rocks do bypass the fence. None of the rocks that bypassed the fence travelled to the exposed section of the belt. This protection system according to the models is therefore most capable of protecting the section of belt that was most critically required.

CONCLUSIONS

The rock fall hazard analysis utilised specific parameters, such as a static friction angle of 40° and a dynamic friction angle of 35°, with a falling rock mass of 13.82 tons. Key considerations include the absence of vegetation in the model and the software's assumption of hard rock for the slopes, while actual ground conditions are more energy-absorbent.

The particle size distribution was calculated from 3D orthophotos, with masses assigned to falling bodies based on their size. Fall body mass was determined to be 6.95 tons, 9.7 tons, 15.1 tons, and 11.3 tons. The fall bodies above the exposed belt are 9.7 tons and 15.1 tons.

Following a baseline risk assessment, three protection systems were evaluated. The advantages and disadvantages of each system were considered, with catchment berms and fences offering benefits such as energy absorption and cost-effectiveness but facing challenges in steep terrain and safety. The assessment revealed that the existing fence is 93% effective in rockfall protection.

In the comparison of rockfall results across the slope, it was observed that catchment berms and fences successfully absorbed and reduced rock velocities, with the fence being the most effective. The velocity and kinetic energy of falling bodies are analysed, showing that fences can withstand high velocities. The maximum kinetic energy recorded was 4192.17 kJ, helping to inform the design of protective systems for the lower slope.

In conclusion, a 4-m-high fence constructed with high-tensile steel wire and installed from the existing fence at 2173 mASL towards the catch berm at 2142 mASL is expected to provide adequate protection against potential rockfall hazards.

REFERENCES

Paper published in a conference proceeding

Basson, F.R.P., (2012). Rigid body dynamics for rock fall trajectory simulation. *Presentation at the 46th US Rock Mechanics / Geomechanics Symposium held in Chicago, IL, USA*. Newmont Asia Pacific, Perth, Western Australia, Australia. p 2.

Basson, F.P.R, Humphreys, R. and Temmu, A., (2013). Coefficient of restitution for rigid body dynamics modelling from onsite experimental data. *Slope stability, Brisbane, Australia.* Newmont Asia Pacific, Perth, Western Australia, p 1163.



Jacobus Delarey (Koos) Bosman

Managing Director
Open House Management Solutions Pty Ltd

Koos started his mining career as a learner official in January 1987, at the Hartebeestfontein Gold Mine. In 1990, he joined the Rock Engineering Department at Harties, where he obtained relevant industry certificates. He was appointed as the head of Rock Engineering at Harties in 1996. In February 2000, co-founded Open House Management solution, and has spent the last 25 years building the company. Koos currently consults on a wide variety of rock engineering topics to clients in the global mining industry.

Mitigating pit floor instability above a confined aquifer: Assessing mining block dimensions and sequencing strategies

L. Bruyns, M. Rangasamy, T. Rangasamy

Middindi Consulting (Pty) Ltd, South Africa

This study investigated the potential for clay aquitard failure within the floor of an open-pit mine overlying a confined aquifer system. Excavation activities above the clay layer can disrupt the equilibrium between the weight of the overlying material and the upward pressure exerted by the confined aquifer. This can lead to ground movement and, in extreme cases, failure of the pit floor. This paper sought to mitigate the impact of mining activities on the pit floor through establishing an acceptable area of clay aquitard exposure by defining optimal mining block dimensions (width and length) and excavation sequences. Two (2D)- and three- dimensional (3D) numerical models were simulated and analysed to extract vertical displacement data for various geological and mining conditions. Optimal mining block widths (E-W) were determined through 2D modelling. Furthermore, 3D modelling, which included backfilling of excavated areas, provided critical insights into the optimal length (N-S) and sequencing of mining blocks. Strip-mining and checkerboard mining sequences were evaluated through a comparative analysis to identify the sequence that minimises the amount of permanent disturbance to the clay aquitard and mitigates the overall risk of subterranean blowouts. Results indicated that limiting mining blocks to 70 m (E-W) in width and 170 m (N-S) in length, in conjunction with a checkerboard mining sequence, effectively abates pit floor disturbance. This research establishes a robust methodology for ensuring minimal pit floor disturbance in open-pit mines with underlying confined aquifers.

Keywords: clay aquitard, area, numerical models, vertical displacement, mining sequence, pit floor disturbance

INTRODUCTION

An aquifer is a geological formation that has the ability to store and transmit groundwater (Van der Gun, 2022). In order for aquifer formation to take place, the rock mass must be porous and permeable for adequate water perforation and saturation. Aquifers can be unconfined or confined; where an unconfined aquifer is commonly referred to as a water table that is directly connected to the surface. A confined aquifer, however, is confined between two layers of material with significantly low permeability, referred to as an aquitard (Cherry, et al., 2004). The presence of these layers above and below the aquifer restricts water from freely rising and falling, containing it in a state of equilibrium.

If the material overlying a confining bed is excavated during mining activities, the overburden stress exerted on the confined aquifer is reduced and exposes the aquitard to environmental elements such as weathering and wetting-and-drying cycles (Chu, 2021). Not only does this compromise the composition of the aquitard but increases the pore water pressure exerted upwards by the aquifer, as the reduction in overlying weight causes the expansion of the confined water (Chu, 2021).

This research investigated an open pit mine (Figure 1) overlying a confined aquifer system with a 22m thick clay aquitard and a uniform back pressure of 650kPa. Exposure of the clay during pit floor mining creates the potential for dangerous subterranean water blowouts. Subsequently, exposing the clay to moisture fluctuations, such as wetting and drying, will result in pit floor surface deterioration, ultimately leading to an increase in permeability and a decrease in water storage capacity. Thus, leading to the loss of shear strength and predisposing the material to failure (Shah, et al., 2024).

An adapted geological log provided in Figure 2, demonstrates the key materials comprising the mining environment in relation to the confined aquifer. The orebody terminates at the pit floor, directly overlying a low-permeability clay aquitard that forms the basal stratigraphic boundary.

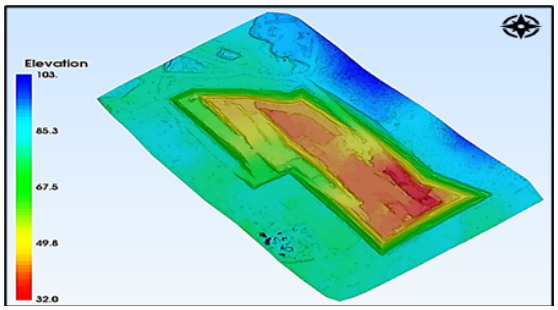


Figure 1. Plan view of the open pit

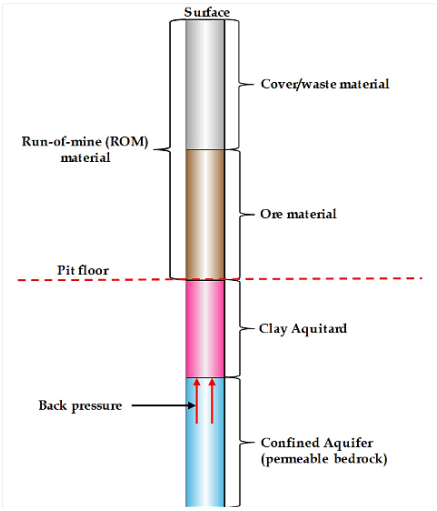


Figure 2. Adapted geological log

This study aimed to establish the following parameters using two-dimensional (2D) and three-dimensional (3D) numerical modelling:

- Maximum mining block width (E-W),
- Maximum mining block length (N-S), and
- An optimal mining sequence that will result in the least amount of permanent disturbance to the underlying clay aquitard.

Soil Classification and Characterisation

The classification of soil plays an important role in predicting and understanding the behaviour of the material. In the case of this study, the behaviour of the clay aquitard material under specific environmental and stress conditions dictated the maximum width and length of a mining block, as well as the optimal mining sequence.

The classification procedure begins with establishing the Atterberg Limits of the soil material as well as conducting a Particle Size Distribution test, which will be used to determine the plasticity and potential expansiveness of the material. These limits aid in determining the soil type (i.e., silt, clay, or non-expansive soils). The Atterberg Limits are basic measures of the critical water contents of a fine-grained soil. The Atterberg Limits include the following (Craig, 2004):

- Liquid Limit (LL)
- Plastic Limit (PL)
- Shrinkage Limit (SL)
- Plasticity Index (PI)

The Liquid Limit (LL) represents the water content at which soil transitions from a plastic to a fluid state. The Plastic Limit (PL) marks the lower threshold, where soil begins to exhibit plastic behaviour. In contrast, the Shrinkage Limit (SL) denotes the water content at which soil changes from a brittle solid to a semi-solid state (Hossain, et al., 2021). These Atterberg limits are graphically illustrated in Figure 3.

The PI, or Plasticity Index, is defined as the difference between the LL and the PL. It is known as the range of water content over which a soil exhibits plastic behaviour. The Plasticity Index (PI)—calculated as the difference between the LL and PL—defines the range of water content over which a soil behaves plastically. These limits are typically expressed as percentages and highlights how moisture content directly influences soil consistency and behaviour (Shakoor, 2018).

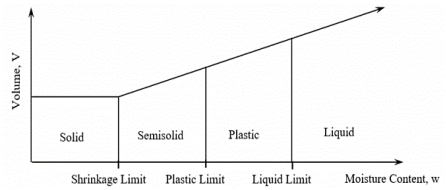


Figure 3: Plasticity chart: British System (BS 1377 – 2: 1990) (Hossain, et al., 2021)

Material Properties

The material properties used in this study (Table I) were derived from laboratory testing of representative rock and soil samples obtained from the site. These parameters were applied in both 2D and 3D numerical models to simulate realistic geotechnical conditions within the mining environment. As illustrated in Figure 2 the waste/cover material comprises topsoil, overburden, calcretized sand, and sand units. These materials vary in thickness from approximately 3 m to 16 m, with a cumulative thickness of ~36 m. The orebody, which underlies the waste units, has an average thickness of approximately 25 m.

Methodology

Two numerical modelling approaches were employed using RocScience software: two-dimensional (2D) modelling with **RS2** and three-dimensional (3D) modelling with **RS3**. The 2D models assessed the limiting mining block width (E–W), while the 3D models evaluated the limiting block length (N–S) and an optimal excavation sequence.

The optimal excavation sequence is one that minimises permanent disturbance to the underlying clay aquitard, which serves as a confining layer above the regional aquifer. Preserving this barrier is critical for maintaining pit floor stability and preventing unwanted hydraulic connectivity between the pit and the aquifer.

The following sections describe the model setup, boundary conditions, input parameters, and analysis objectives.

Table 1. Material properties

Parameter	Unit	Topsoil	Overburden	Calcretized Sand	Sands	Ore	White Sand	Clay (Aquitard)	Bedrock
Unit Weight	kN/m³	18.22	17.48	17.73	17.62	17.49	16.28	19.99	24.53
Friction Angle	°	35.00	36.00	41.00	34.48	28.44	33.00	23.94	40.00
Cohesion	kPa	6.00	3.00	0.00	1.29	20.06	0.00	10.73	10.50
Tensile Strength	kPa	0.00	0.00	0.00	0.00	0.00	0.00	0.00	0.00
Elastic Modulus	MPa	80.00	80.00	80.00	80.00	27131.50	80.00	230.00	750.00
Poisson's Ratio	-	0.30	0.26	0.30	0.28	0.24	0.30	0.35	0.30
Porosity	-	0.38	0.38	0.38	0.38	0.30	0.38	0.36	0.30

Two-Dimensional (2D) Numerical Modelling

Two (2) sections were cut across the pit (Figure 4), one traversing N-S (long section) and the other E-W (short section). These sections were utilised to capture variations across the pit. The long and short cross-sections are schematically presented in Figure 5 and Figure 6, respectively.

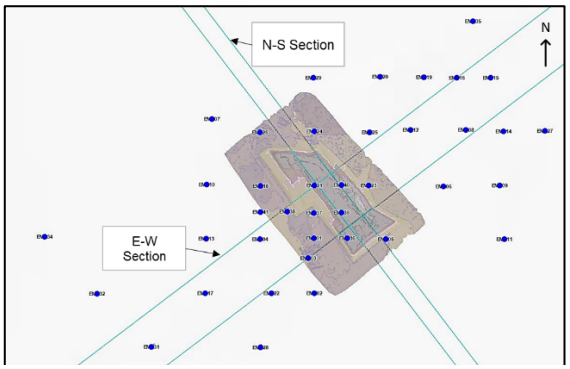


Figure 4. Section clippings through the pit

Each section was assessed under the various conditions summarised in Table II. The clay aquitard varies in thickness across the pit, with a predominant stratum of 22m. The models were simulated to constant back pressure of 650kPa at the base of the clay aquitard using the various clay thickness mentioned in Table II. Vertical displacement was extracted from each computed model and assessed.

Table I. Variation in clay thickness and back pressure, 2D models

Variation in RS2 models	
Variation in thickness of clay (m)	22
	15
	10
	5

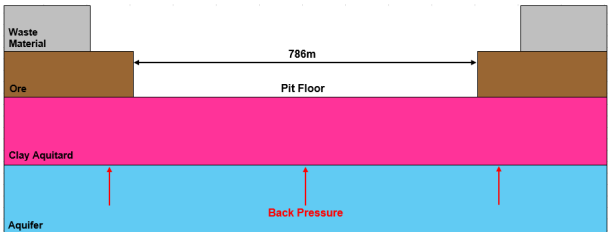


Figure 5. Long section across the pit (N-S)

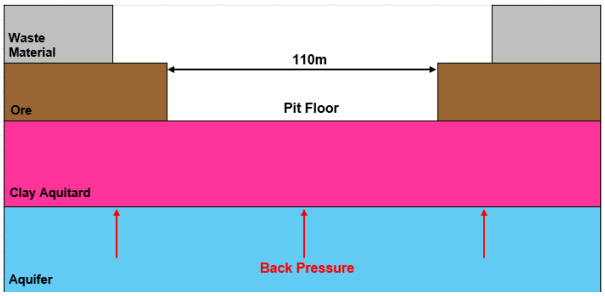


Figure 6. Short section across the pit (E-W)

The Clay Exposure Limit based on vertical displacement for a limiting mining block width, was derived using the following steps:

1. The extracted Vertical Displacement values for each clay thickness (22m, 15m, 10m, and 5m) under a constant back pressure of 650kPa, were converted into Rate of Change of Vertical Displacement.
2. Rate of Change was plotted against length of exposed clay, and limiting lengths were derived by identifying the asymptote value on the x-axis (length of exposed clay) of each graph.
3. These values were then plotted against clay thickness to derive an Optimistic, Conservative and Realistic plot. The point of deviation of the three (3) curves was noted.
4. The point of deviation over the length of exposed clay, as identified in Step 2, was used to derive a Factor of Safety (FoS) which was then converted into Probability of Failure (PoF). The relationship between PoF and clay exposure length was plotted to identify the limiting exposure length at a PoF threshold of 20% (Figure 7).

		Acceptance criteria[a]		
Slope scale	Consequences of failure	FoS (min) (static)	FoS (min) (dynamic)	PoF (max) P[FoS ≤ 1]
Bench	Low–high[b]	1.1	NA	25–50%
Inter-ramp	Low	1.15–1.2	1.0	25%
	Moderate	1.2	1.0	20%
	High	1.2–1.3	1.1	10%
Overall	Low	1.2–1.3	1.0	15–20%
	Moderate	1.3	1.05	10%
	High	1.3–1.5	1.1	5%

a: Needs to meet all acceptance criteria
b: Semi-quantitatively evaluated, see Figure 13.9

Figure 7. Limiting Probability of Failure (PoF) (Read & Stacey, 2009)

Three-Dimensional (3D) Numerical Modelling

The RS3 modelling consisted of two (2) models with different mining sequences. The first model followed a strip sequence. The purpose of Sequence One (1) was to determine the maximum length (in the N-S direction) that the clay layer could be exposed before the risk of blowouts becomes too high. The second model followed a checkerboard sequence. The purpose of Sequence Two (2) was to determine whether a checkerboard sequence would result in less disturbance of the clay layer compared to that of a strip-mining sequence.

The steps followed to derive a limiting mining block length (N-S) were executed as follows:

1. Data from the RS3 Sequence One (1) Model was extracted from six (6) delineated query lines (Q1-Q6), placed from South to North across the centre of four (4) consecutive mining blocks as displayed in 8.

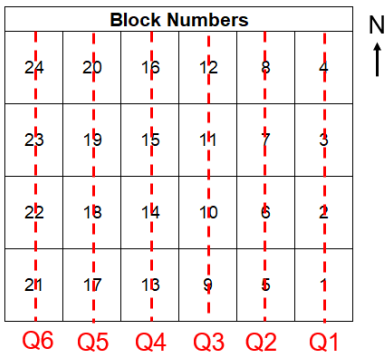


Figure 8. Position of query lines (Q1-Q6) per mining strip

2. The raw Vertical Displacement results obtained for each query line (Sequence One (1)) were converted into Rate of Change of Vertical Displacement (i.e. Vertical Strain). This was carried out to produce a graph that aligns with the RS2 Rate of Change plots utilised in the derivation of the maximum width of exposed clay (E-W).
3. Fully excavated mining blocks length (100m, 200m and 300m) per stage were selected and served as indicative markers for the length of exposed clay.
4. The relationship between the length of exposed clay and the corresponding Vertical Displacement Rate (Vertical Strain) was plotted to produce an acceptable Vertical Displacement Rate curve

Figure 9 and Figure 10 show a side view (section) of the planned mining and backfilling, respectively. The steps have been colour coded from Bottom of Ore (BOO) to Top of Ore (TOO). The 30m thick ore was modelled in 10m stepped intervals. Figure 11 and Figure 12 show a plan view of the mining blocks per strip and checkerboard sequences, respectively. Mining Sequence One (1) consisted of a total of eighteen (18) stages, whereas mining Sequence Two (2) consisted of thirteen (13) stages. Each mining sequence encompassed a backfilling process following clay exposure, this was done to counteract the potential blowouts caused by back pressure. The backfilling was limited to the Top of Ore (TOO) and did not extend to the surface. The backfill properties were considered under worst-case assumptions, as specified in Table III.

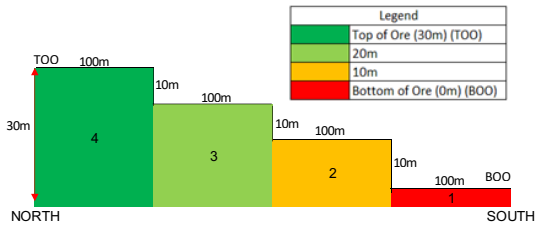


Figure 9. Side view of planned mining

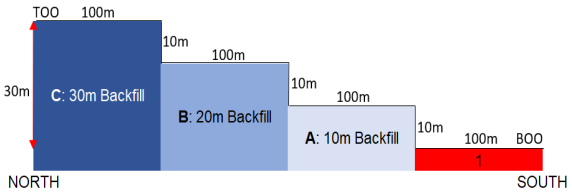


Figure 10. Side view of planned backfilling

Table III. Backfill material properties

Parameter	Unit	Backfill
Bulk Unit Weight	kN/m3	18.22
Friction Angle	°	20.00
Cohesion	kPa	0.00
Tensile Strength	kPa	0.00
Elastic Modulus	MPa	80.00
Poisson's Ratio	-	0.30
Porosity	-	0.38

Similar to the RS2 models, vertical displacement was extracted and assessed as the output parameter.

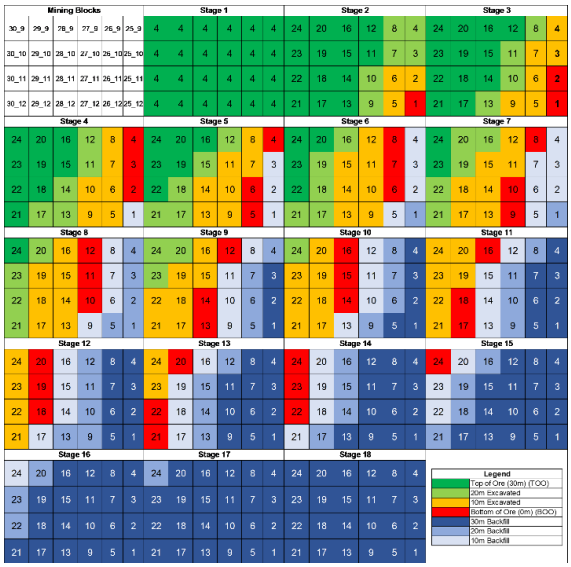


Figure 11. Plan view of blocks following a strip-mining pattern (Sequence 1)

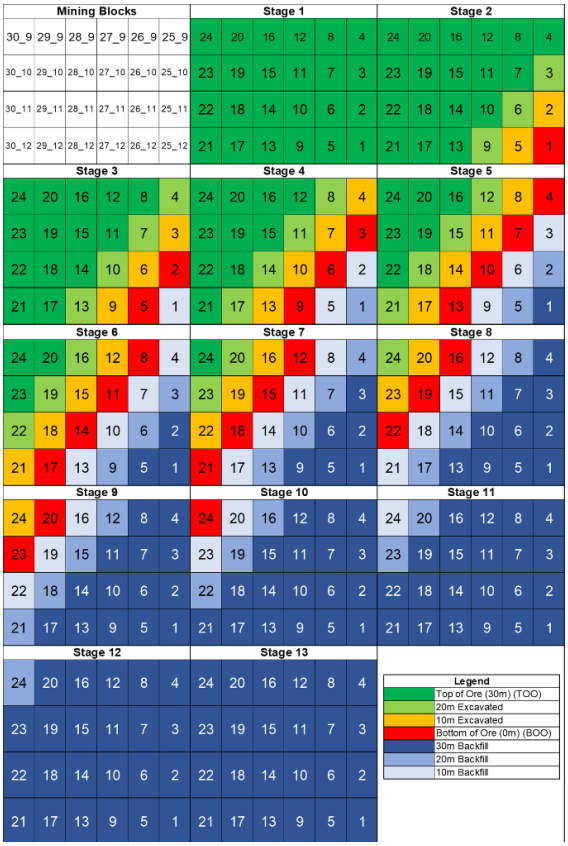


Figure 12. Plan view of blocks following a checkerboard pattern (Sequence 2)

RESULTS AND DISCUSSION

Soil Classification – Results

Figure 13 shows the plasticity chart for laboratory tested clay material with the LL% on the x-axis, and the PI on the Y-axis. The LL% can exceed 100%, hence the x-axis extended past 100%. Table IV provides descriptions of the abbreviations outlined in Figure 13. According to the plasticity chart, the clay classifies as a low to intermediate plasticity clay. This indicates that the water content range at which the clay material can behave plastically is relatively small, making it an important factor to consider in this study.

The A-line represents the boundary between the clay soils (above the A-line) and the silt soils (below the A-line). The A-line can be calculated using the Equation below:

$$\mathbf{I_P = 0.37(w_L - 20)} \qquad [1]$$

I_P : Plasticity Index
w_L : Liquid Limit

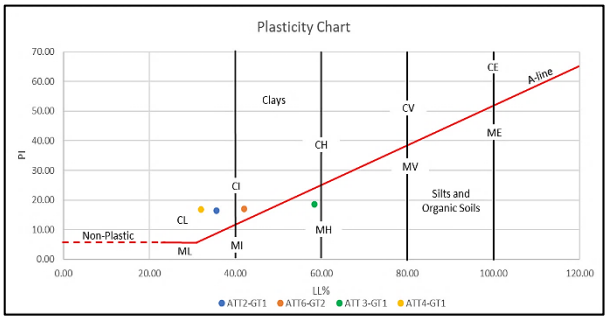


Figure 13. Plasticity Chart: British System (BS 1377 – 2: 1990) for Carbonaceous Clay

Table IV. Abbreviations and descriptions for Plasticity Chart

Plasticity Chart Description	
Abbreviations	**Meaning**
CL	Low Plasticity Clay
CI	Intermediate Plasticity Clay
CH	High Plasticity Clay
CV	Very high Plasticity Clay
CE	Extremely high Plasticity Clay
A-Line	Boundary between Clay and Silt
ML	Low Plasticity Silt
MI	Intermediate Plasticity Silt
MH	High Plasticity Silt
MV	Very high Plasticity Silt
ME	Extremely high Plasticity Silt

RS2 modelling results – mining block width

The long section model, with a pit floor length of 786m, involved a phased excavation, progressing through sixteen (16) distinct stages. Each stage incrementally increased the exposed length of the clay layer. Figure 14 visually demonstrates the progressive impact of staged excavation. By comparing stages 1, 8, and 16, it's clear that vertical displacement within the clay aquitard increases with each subsequent excavation phase. This downward propagation of movement directly correlates with the reduction of overburden pressure above the aquitard.

The short section model, with a 110m pit floor, was excavated in eleven (11) stages. As illustrated in Figure 15 and in concordance with the long section results, a modest, incremental increase in vertical displacement is observed across stages 1, 6, and 11.

The long section results are indicative of an optimistic scenario, while the short section results represent a conservative scenario. The combined analysis of both sections provides a realistic representation of a limiting mining block width. The results from the short section indicate a reduced allowable mining block width, which is attributed to the shorter distance between the slope toes. This reduced spacing likely results in elevated stress concentrations distributed across a larger portion of the pit floor. These scenarios are graphically presented in Figure 16. The point where the three (3) curves deviate from one another occurs at an exposed length of 55m. The Optimistic, Realistic, and Conservative scenarios yield clay limit lengths of 70m, 64m, and 60m, respectively.

Figure 17 displays a limiting clay exposure length at 5%, 10% and 20% PoF thresholds. The corresponding lengths per PoF are 57m, 61m, and 68m, respectively.

Due to the small displacement values, 70m (Optimistic scenario) was selected as the limiting mining block width (E-W).

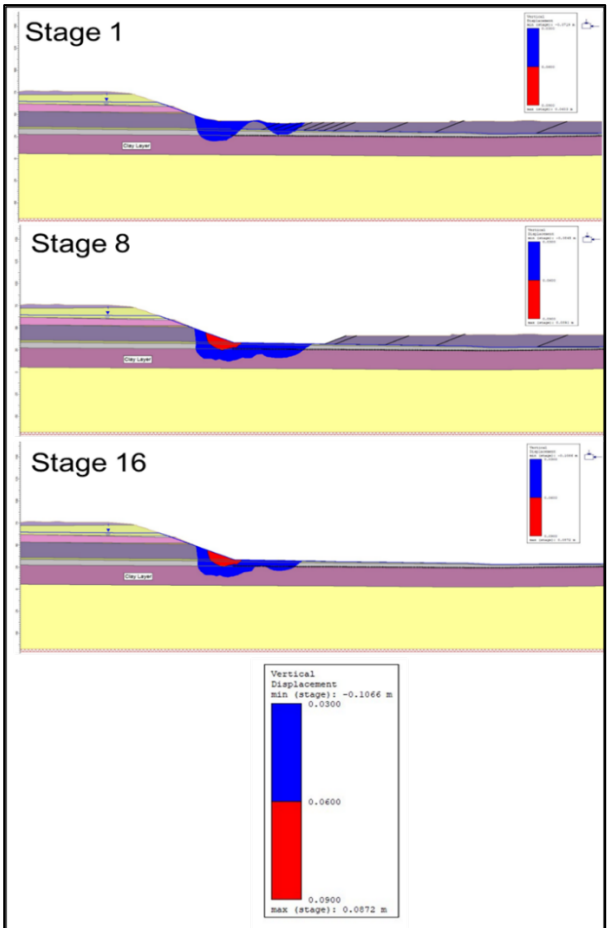


Figure 14. Vertical displacement for the long section (N-S) per stage 1, 8 and 16

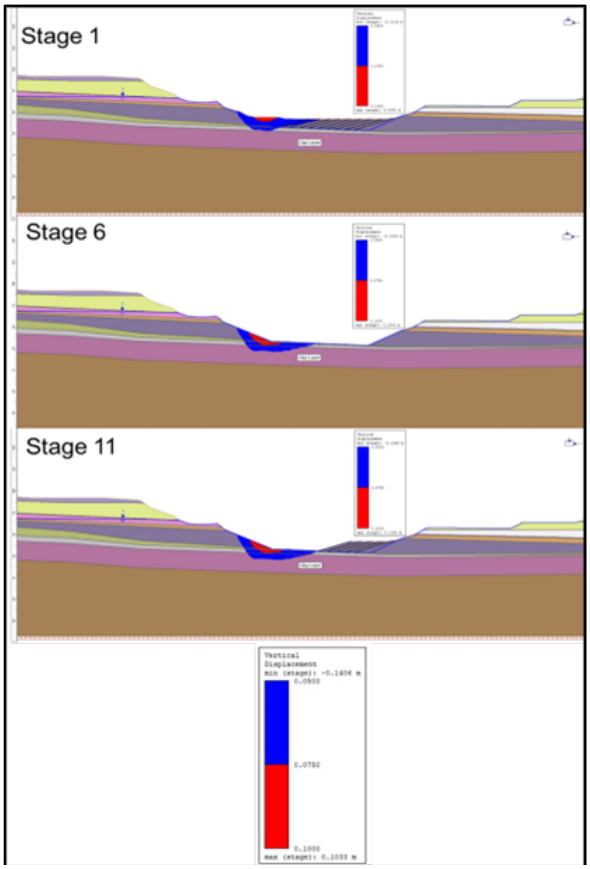


*Figure **15**. Vertical displacement for the short section (E-W) per stage 1, 6 and 11*

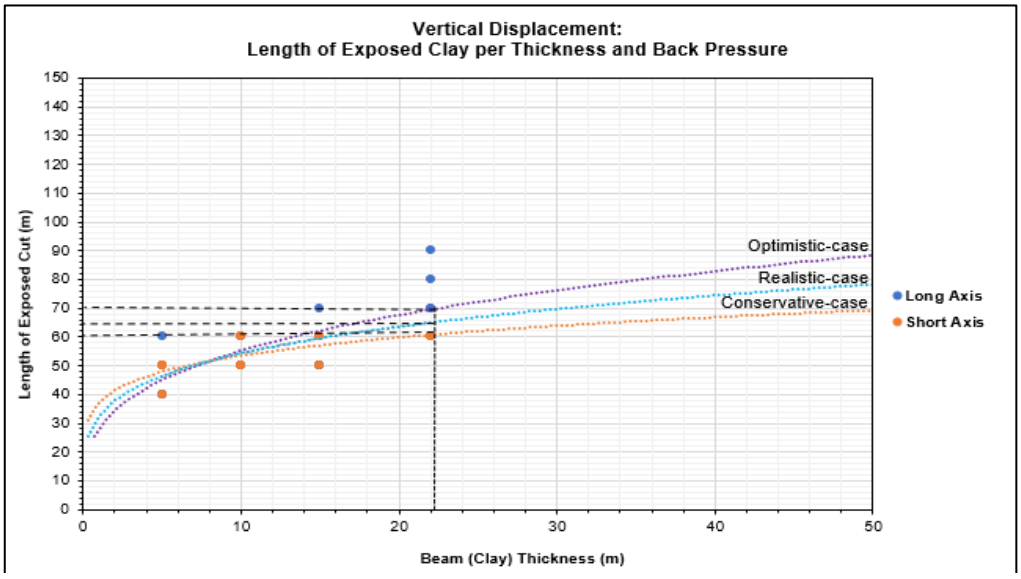


Figure 16. Length of exposed clay per variation in clay thickness and back pressure, vertical displacement (vertical displacement, asymptote).

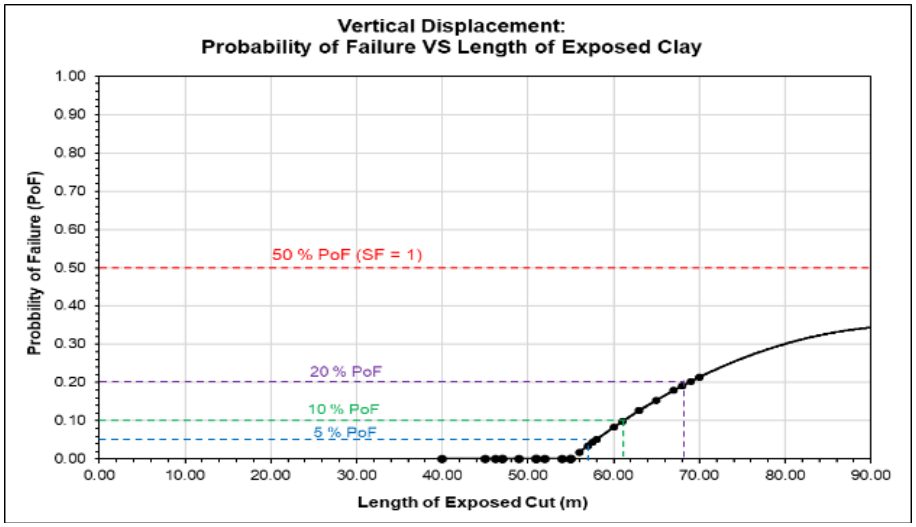


Figure 17. Probability of failure of the clay layer per length (m) of clay exposed, vertical displacement.

RS3 Modelling Results – Mining Block Length and Optimal Mining Sequence

Referring to Figure 18, the RS2 Vertical Strain graph, represented by the 22m thick clay and 650kPa back pressure, the 70m width of exposed clay cut-off (E-W), indicated by the Optimistic scenario was identified. The point where the 70m cut-off length

(x-axis) intersects the curve was used to determine the corresponding vertical strain limit (y-axis). This strain limit was used to identify the corresponding maximum exposed clay (N-S). This length was defined as the lower clay exposure limit. The upper clay exposure limit was determined using the asymptote of the curve in Figure 18, thus establishing a range of risk levels as clay is exposed in length (N-S).

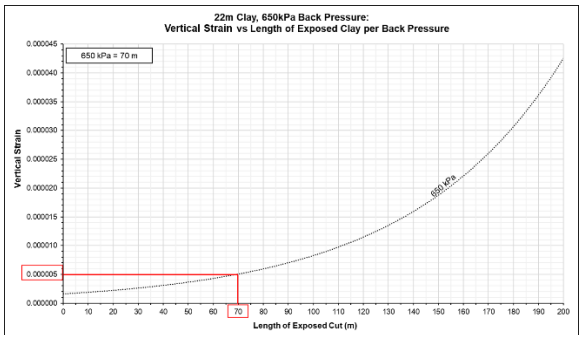


Figure 18. Rate of vertical displacement (Vertical Strain) vs length of exposed clay, 22m thickness, 650kPa back pressure

Figure 19 illustrates the exposure limits of the clay layer in terms of length, across varying risk levels ranging from low to high. This graph demonstrates an inverse relationship between the length of the exposed clay (N-S) and the maximum allowable vertical strain. When 110m of clay is exposed, the maximum acceptible vertical strain is 5×10-6m/m. However, when 170m of clay is exposed, the allowable strain decreases to 2×10^{-6}m/m. Clay exposure lengths of less than 110m are considered low-risk, moderate-risk lies between 110m and 170m, and high-risk is any length greater than 170m.

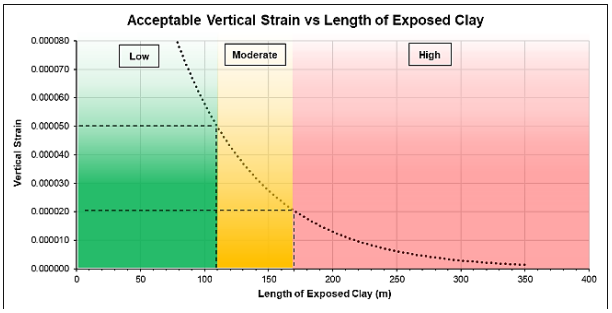


Figure 19. Vertical strain vs. Length of exposed clay plot indicating the Low, Moderate, and High-risk regions

The vertical displacement in Sequence One (1) is visually illustrated in Figure 20, highlighting distinct low, moderate, and high-risk regions corresponding to 100m, 200m, and 300m of exposed clay. The red contour projects towards the 200m and 300m exposed blocks, deviating from the 100m blocks. This suggests that there is a higher blowout risk when more than 200m of clay is exposed. Upon the completion of backfilling all blocks (Stage 18), the elevated vertical displacement diminishes. However, a residual area of high displacement persists along the eastern pit wall, indicating potential disturbance within the clay layer.

A comparison of the results of Sequence One (1) and Sequence Two (2) was carried out, with emphasis on the total disturbance in the form of vertical displacement within specific blocks experiencing analogous stress conditions. These blocks were entirely excavated and encircled by 10m high steps in both sequences. Figure 21 demonstrates the elevated vertical displacement contour (red) moving diagonally behind the fully excavated blocks when evaluating Sequence Two (2). Once backfilling of all blocks was completed (Stage 18), no residual regions of high vertical displacement were observed as opposed to those obtained using Sequence One (1). It is important to note that the increased vertical displacements observed after backfilling may be attributed to a low-density material property and/or limited backfilling up to the Top of Ore, rather than reaching the surface. Consequently, the elevated displacements could be slightly overstated.

The legend indicating the vertical displacement values for Sequence One (1) and Sequence Two (2) is presented in Figure 22.

Numerical data was extracted and compared for each sequence. Figure 23 graphs the comparison between the average vertical displacements for Sequence One (1) and Two (2), respectively. Overall, the checkerboard sequence (Sequence Two (2)) showed less overall disturbance to the clay layer than the strip-mining sequence (Sequence One (1)).

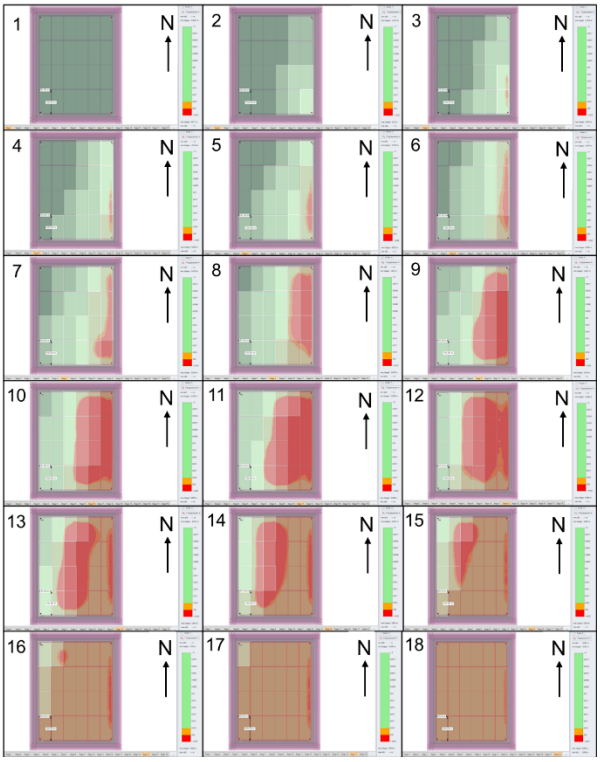


Figure 20. RS3 model of Vertical Displacement per mining block at stages 1-18 (Sequence One (1)); plan view

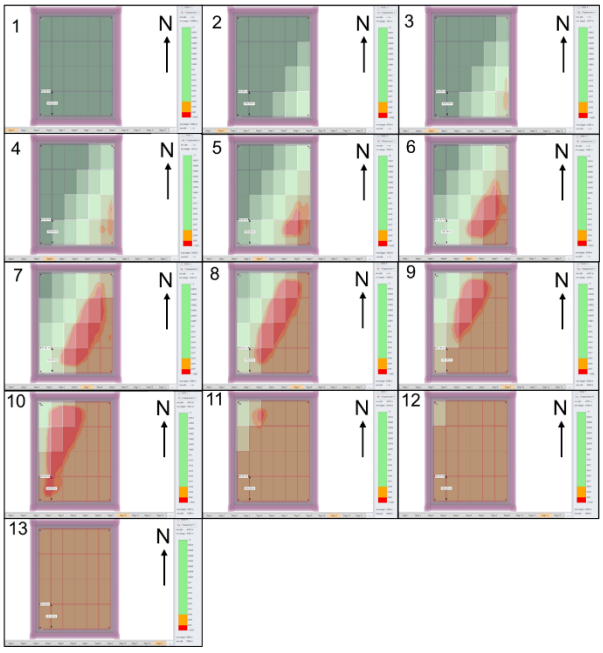


Figure 21. RS3 Model of Vertical Displacement per mining block at stages 1-18 (Sequence Two (2)); plan view

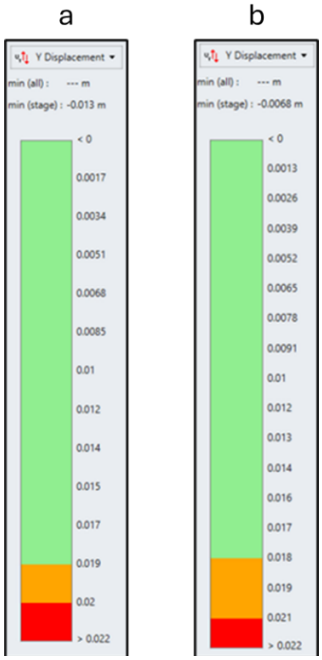


Figure 22. RS3 vertical displacement legend: a) Sequence One (1); and b) Sequence Two (2)

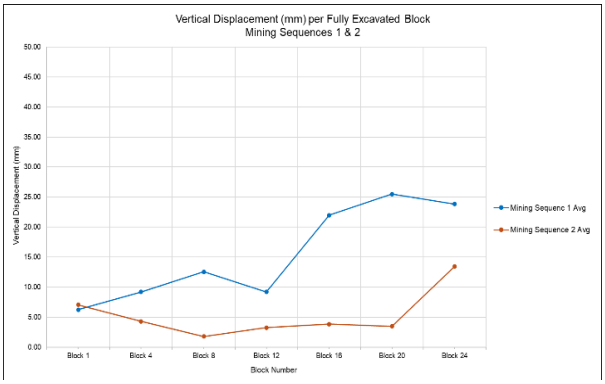


Figure **23**. *Average Vertical Displacement per block for Sequence One (1) (blue), and Sequence Two (2) (orange)*

CONCLUSIONS AND RECOMMENDATIONS

Based on the numerical modelling results, it is advised that the mining blocks should not exceed 70m in width and 170m in length (Figure 24). Furthermore, adopting a checkerboard mining sequence is proposed as a more effective approach for minimising clay disturbance, representing a more conservative alternative.

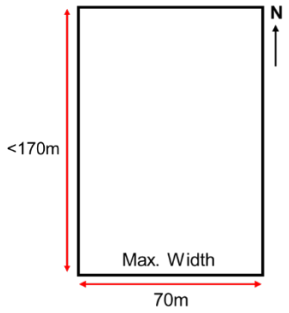


Figure 24: Schematic of limiting mining block dimensions

The 3D models revealed a significant increase in upward vertical displacement after backfilling. This could potentially be attributed to a low-density material. Consequently, it is crucial to ensure that excavated areas are backfilled using a material of adequately high density and compacted to control the rate of vertical movement.

ACKNOWLEDGEMENTS

We wish to express our appreciation to our colleagues at Middindi Consulting (Pty) Ltd for their collaborative support in enabling the completion of this study, through the provision of necessary facilities and software resources.

REFERENCES

Cherry, J., Parker, B., Bradbury, K. & Eaton, T., 2004. *Role of aquitards in the protection of quifers from contamination: a "state of science" report,* Denver: AWWA Research Foundation.

Chu, C., 2021. Investigation on the Responses of Overburden Stress and Water Pressure to Mining under the Reverse Fault. *Geofluids,* pp. 1-11.

Craig, R. F., 2004. *Craig's Soil Mechanics.* 7 ed. London: CRC Press.

Hossain, S., Islam, A., Badhon, F. & Imtiaz, T., 2021. *Properties and behaviour of soil-Online Lab Manual,* s.l.: Mavs Open Press.

Jones, G., 2017. An empirical preliminary prediction of heave. *Journal of the South African Institute of Civil Engineering,* 59(4), pp. 64-66.

Read, J. & Stacey, P., 2009. Acceptance Criteria. In: A. de Kretser, ed. *Guidelines for Open Pit Slope Design.* Collingwood: CSIRO, pp. 221-236.

Shah, S., Turrakheil, K. & Naveed, M., 2024. Impact of Wetting and Drying Cycles on the Hydromechanical Properties of Soil and Implications on Slope Stability. *Atmosphere,* 15(1368), pp. 1 - 18.

Shakoor, A., 2018. Atterberg Limits. In: P. T. Bobrowsky & B. Marker, eds. *Encyclopedia of Engineering Geology.* s.l.:Springer, Cham, pp. 44-47.

Van der Gun, J., 2022. *Large aquifer systems around the world.* Guelph: The Groundwater Project.



Leandi Bruyns

Engineering Geologist
Middindi Consulting (Pty) Ltd

Leandi Bruyns is an Engineering Geologist at Middindi Consulting Pty Ltd, specializing in geotechnical investigations and engineering geology assessments. She completed her undergraduate and postgraduate studies in Engineering Geology at the University of Pretoria, gaining a strong foundation in geological and geotechnical principles.

During her studies, Leandi worked as a demonstrator (Demi) for 1st- and 3rd-year students at the University of Pretoria from 2021 to 2022. This role allowed her to develop mentoring and instructional skills while assisting students in understanding fundamental geological concepts, field techniques, and laboratory analyses.

In 2023, she joined Middindi Consulting as a Junior Engineering Geologist and has since progressed to the role of Engineering Geologist. She is actively involved in a range of geotechnical and engineering geology projects, including site investigations, rock mass characterization, stability assessments, and technical reporting for mining and infrastructure developments. She collaborates with multidisciplinary teams to provide geotechnical recommendations that contribute to safe and efficient design solutions. Leandi has developed proficiency in various RocScience software programs, including Dips, Slide, RS2, RS3, SWedge, and RocPlane, allowing her to conduct advanced stability modeling and rock mechanics analyses. Her expertise extends to data analysis, report writing, and the interpretation of geotechnical data to support engineering decision-making.

Her experience at Middindi Consulting has provided exposure to real-world geotechnical challenges, including slope stability, and underground support design. She continues to expand her knowledge and technical skills in engineering geology, striving to deliver high-quality geotechnical solutions for diverse projects.

Leandi is passionate about applying her geological expertise to practical engineering challenges and contributing to the advancement of geotechnical engineering in mining projects.



Mayuri Rangasamy

Geotechnician
Middindi Consulting (Pty) Ltd

As a Geotechnician specialising in Mining Geotechnics at Middindi Consulting (Pty) Ltd., I have cultivated significant expertise over the past two years. My tenure has been marked by rapid professional development and a commitment to continuous improvement. I am highly adaptable and thrive in challenging environments. My academic background, encompassing a General BSc in Biology and Honours in Human Biology from the University of Witwatersrand, has provided me with a robust analytical foundation. While my initial academic pursuits differed from my current field, I am deeply passionate about Mining Geotechnics and am grateful for the opportunity to contribute to this industry. My immediate goals include enhancing my rock mechanics knowledge through specialised courses at the University of Witwatersrand, obtaining my SCO certification, and pursuing a Master's degree in the discipline. Ultimately, I am dedicated to achieving the Qualified Person (QP) designation in Rock Engineering. I am driven by a belief in the importance of perseverance, as encapsulated by Winston Churchill's sentiment: 'Success is not final, failure is not fatal, it is the courage to continue that matters.'

3D elastodynamic modelling applied in the design of technical blasts in open pit mines

L.M. Linzer[1,2], A.J. Rorke[3], M.W. Hildyard[4]

[1]SRK Consulting, South Africa
[2]University of the Witwatersrand, South Africa
[3]Independent
[4]Leeds University, United Kingdom

Complex blast patterns are both time-consuming and costly to implement in terms of their planning, drilling, charging, stemming, and execution. Moreover, testing different combinations of charge length, blast timing, and sequencing is infeasible for full production blasts, but calibrated models can assist with investigating such variations for the purpose of optimising blasting parameters. 3D elastodynamic blast modelling for large blasting patterns in open pits is a recent innovation that has arisen due to the increasing need for properly designed technical blasts in which the peak particle velocities are carefully controlled so as not to damage critical infrastructure. Since the original modelling code was designed to simulate rockbursts and wave propagation in deep South African gold mines, several adaptations were necessary to apply the code to surface blasting problems. These adaptations are the focus of this paper.

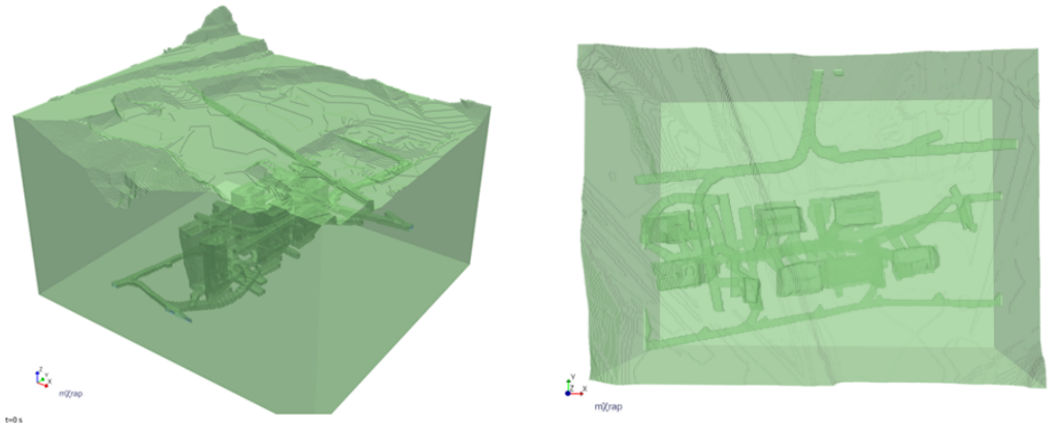
INTRODUCTION

As open pits become deeper and steeper, and in cases where underground mining occurs below a pit, there is an increasing need for properly designed technical blasts in which the peak particle velocities (PPVs) are carefully controlled. The design and execution of complex blast patterns is an expensive and time-consuming process, and involves drilling of the blastholes, charging with explosive, stemming the blastholes to minimise energy loss, verification of the detonation sequence electronically to identify holes inadvertently excluded from the sequence, etc. Field-testing of full blasting patterns in which the charge lengths and timing are varied to test different blast pattern configurations is not practical, apart from posing a risk to critical infrastructure.

Numerical modelling is a powerful tool in simulating the behaviour of physical phenomena, for instance seismic wave propagation. The investigation of multiple, different scenarios is desirable so that an optimal solution can be selected. In this paper, we apply WAVE3D (Hildyard, 2020), a finite-difference full waveform modelling research code originally developed for underground applications, to the simulation of large blasting patterns in open pits. Different configurations of blasting patterns with varying spacings, charge lengths, charge firing delays, etc. are simulated and compared. An added advantage of this approach is that a calibrated model can be used to estimate PPVs in areas of concern where it is impractical or impossible to install an instrument, either due to inaccessibility or proximity to the blast.

Since the original modelling code was designed to simulate rockbursts and wave propagation in deep South African gold mines, several adaptations were necessary to apply the code to surface blasting problems. These adaptations are the focus of this paper.

The technical blast that is the subject of this paper took place at a large open pit mine in South Africa. WAVE3D was used in the design of several mass blasts that were executed to extract crown pillars overlying historical underground mining (Figure 1). The layout comprised six open stopes, a smaller chute, a sill stope, access tunnels and other tunnels. The stopes varied in width from 11 – 24 m, and height from 70 – 75 m. The access tunnels had cross-sectional dimensions of 4 × 5 m^2. The mine had exposed the area above the underground voids and had left a crown pillar 22 – 27 m in thickness to ensure the stability of the pit workings below the pillar. Mass blasting of the crown pillar was intended to fragment the pillar, while keeping the mined voids open, so that the blasted material could fill the voids but without damaging the underground mining layout.



(a) (b)

Figure 1. Historical underground workings underlying a section of the pit (a) side view (b) plan view.

Blasting considerations

A well-thought-out blasting strategy is required to provide enough energy to optimally fragment the crown pillar while keeping the PPV in the sidewalls of the stopes below 250 mm/s. The PPV scales in proportion to the mass of the charge, so as to limit the PPV, the charges were split into three smaller lengths (decks) in each hole (Figure 2).

This type of blasting is complex and requires a number of considerations that are less important in standard bench blasting applications. In the blast that was carried out, it was important to get the following aspects right.

- The fragmented rock from the blast was required to fall into the underlying void. Any hang-up or inter-locking of the fragmented rock would have created a significantly unsafe situation to deal with subsequently. Therefore, the decked charges were timed to fire in a particular sequence with sufficiently long delays (of 250 to 500 ms) to ensure detachment of the fired decks before the following decks fired. These delays could only be achieved with electronic detonators.
- The long delays between charge decks increased the risk that the shockwave from a firing deck would damage the electronic detonators in the unfired adjacent deck, and thus cause a misfired charge which could lead to a combined risk of hang-up and misfired charges.
- It was necessary to protect vertical walls between the stopes from blast induced damage. The newly created walls during the blasting of the crown pillars also had to be carefully blasted to ensure they were stable so that normal work around the exposed stopes could continue safely.

Vibration modelling was critical to the three requirements above, as it was not possible to measure the ground vibration induced by each charge in the critical areas. There was also insufficient time for an empirical study to establish optimal blasting design criteria because of mining schedule requirements.

A basic rule in blast design is that blasting must take place towards the void. In cases where blast holes in the crown pillar overlay the stopes, they needed to be fired from the bottom charge deck upwards, ejecting the blasted rock downwards into the stopes. Conversely, for blast holes in normal benches, with no void below, blast holes containing decked charges needed to be fired from the top deck down to eject the material upwards and sideways into the pit.

The important consideration in decked holes is to protect the detonators from being damaged by the shockwave from the adjacent firing deck in the hole. Electronic detonators are necessary for the long inter-deck delays that are needed, but these detonators are more prone to shock damage than older-type detonators with pyrotechnic delays. The waste deck between the charge deck provides a damping effect on the shockwave and needs to be long enough to ensure the shock wave is sufficiently attenuated to prevent a misfire in the adjacent charge deck. The length of the waste deck and its compositions between the charge decks is therefore an important design element. The waste deck needs to be long enough to prevent the shockwave from one deck prematurely detonating or damaging any neighbouring detonators, thereby disrupting the timing sequence and causing hang-ups. Furthermore, the waste deck could not be too long, because then the fragmentation would be adversely affected and the risk of hang-ups would increase.

Based on laboratory work undertaken by Katsabanis and Ghorbani (1995) on shock wave impact on pyrotechnic detonators and emulsion explosive, a 3 m waste deck between each charge deck in the 165 mm holes was decided and needed to be modelled for the electronic detonators and explosive charge type being used.

Blast source modelling

The standard approach applied in surface blasting is empirical (Devine, 1966) and relies on the well-known scaled (or cubed) distance equation. This relates the PPV (m/s) to scaled distance D ($m/kg^{1/2}$), which is the ratio of the distance from the source of excitation (explosives) R (m) to the square (or cube) root of the charge mass Q (kg).

$$PPV = k \cdot D^{\beta} \quad [1]$$

$$D = R/Q^{1/2} \qquad (\text{or } D = R/Q^{\frac{1}{3}}) \quad [2]$$

Generally, site constants k and β are determined by blast experiments at the site and quantify the effects of attenuation. The scaled distance equation works well for standard blasting problems, provided the blast can be represented by a single point source and the geometry of the problem is simple. In the case where there are multiple blast sources of differing length, with varying time delays between the detonations, where the directionality of the blast propagation is critical, full waveform modelling is more applicable because the complex interactions that occur in a 3D wavefield, for example refraction, diffraction, reflection, superposition, generation of surface waves, etc. can be simulated.

The PPVs excited by a multi-borehole blasting pattern result from a complex combination of factors listed by Linzer *et al.,* (2022) as:

- the charge mass and, therefore, length of explosive charge in each borehole,
- explosive type and velocity of detonation (VOD),
- direction of detonation,
- pressure pulse wavelet shape,
- 3D spatial relationship between charges,
- number of borehole charges detonated,
- delay between charges,
- rock material properties,
- 3D geometry of underground excavation, and
- the 3D pit geometry.

Adaptations to the surface blasting problem

One of the most critical aspects in blast modelling is the correct design of the source because the source characteristics control the propagated seismic wave's amplitude and frequency content (Linzer *et al.*, 2022).

This study required the blast source to model the physics of a real blast as closely as possible, given the functions available in the modelling code. Note that the wave propagation in the near, intermediate, and far fields is modelled—the degree of damage to the rock is not simulated but can be inferred from the levels of PPV excited at the points of interest.

The blast source in these models is an 'equivalent source' to the actual blast. This equivalent source is designed to be sensitive to real blast parameters, in particular the charge mass, charge length, charge density and type, borehole diameter, borehole length, VOD, and direction and position of detonation (Linzer *et al.*, 2022). The explosive type and density together control the peak explosion pressure exerted on the blasthole walls and can be estimated using:

$$Ideal\ detonation\ pressure\ (GPa) = \frac{(\rho_{expl} . VOD^2)}{4} \quad [3]$$

where ρ_{expl} is the density of the explosive (g/cm^3) and VOD is the velocity of detonation (km/s) (Persson *et al.*, 1994). According to Boshoff (2009), the calculated peak explosion pressure should be halved because only a fraction of the ideal detonation pressure is converted into borehole pressure.

$$Peak\ borehole\ pressure\ (GPa) = \frac{(\rho_{expl} . VOD^2)}{8} \quad [4]$$

For computational efficiency, one of the restrictions of the WAVE3D modelling code is that the grid is orthogonal, comprising equal-sized cubes or cuboids. Realistic geometries can be modelled, provided the grid cells are made small enough. To keep runtimes within the timeframe of an active mine project with tight deadlines, a 1 m^3 grid size proved optimal. However, the diameter of a blasthole is a fraction of a metre, requiring an equivalent borehole pressure to be applied – this pressure is lower than the actual peak pressure because the force acts over a much larger area.

A further consideration is that the finite difference scheme suffers from the dispersion of high frequencies, with the result that the disturbance is not propagated through the mesh at a constant velocity. The different frequencies that compose the signal are propagated at different velocities (higher frequencies at lower velocities), resulting in the separation of frequencies with propagation away from the source.

In a prior underground rockburst research project, the validity of the source model was investigated in a simulated rockburst experiment (Hildyard and Milev, 2001). This same source definition was tested in the open pit blasting models but was found to excite PPVs and frequencies that were much higher than those recorded by blasting seismometers in the pit. The original source had been designed and calibrated in blast experiments underground where the blastholes were drilled into competent rock. Blasting in an open pit is a different problem since the confining stresses are much lower and the rock is likely to be fractured due to previous blasting (Linzer *et al.*, 2022).

The new source pulse peak pressure was dropped until the modelled PPVs matched those that were recorded in the pit. The rise time and time profile of the new blast source pulse also required modification to match the frequency content in the modelled seismograms to that of the recorded data.

Another adaptation is the use of the concept 'pseudo-air' to model voids. The modelling code is an elastic one which cannot accurately simulate the propagation of a sound wave through a fluid medium such as air that does not transmit shear waves. 'Pseudo-air' is simply a soft material, with very low density and velocity that greatly retards the wave travelling through this material. The values chosen

were the lowest ones that produced a stable model. The downside of this compromise is that the air-blast that is always produced by blasting is not accurately simulated. Also, the high Poisson's ratio and extremely low stiffness of pseudo-air results in unrealistically large displacements that can alarm an unsuspecting user, especially for long cycle times.

RESULTS

The newly defined and calibrated source pulse was applied to a simple model of a single blast hole consisting of three charge decks, separated by waste decks (Figure 2). The rock density of the material was 2600 kg.m^{-3}, the P-wave velocity was 4000 m/s and the S-wave velocity was 2400 m/s. The aim of this exercise was to simulate the shock pressure from the point of detonation at the lowest charge deck, and then measure its change in amplitude with distance as the shock front propagated up the borehole. The source pulse was propagated linearly upwards along the borehole at VOD = 4900 m/s towards the surface (Figure 3). The pressure of the source pulse was measured at intervals from the point of detonation, at 1 m and then at 3 m from the detonation, in the waste deck (Figure 4).

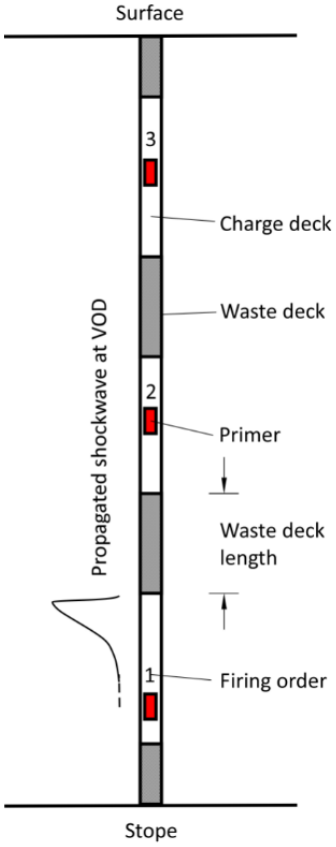


Figure 2. Example of bottom-up firing of a blasthole above a stope.

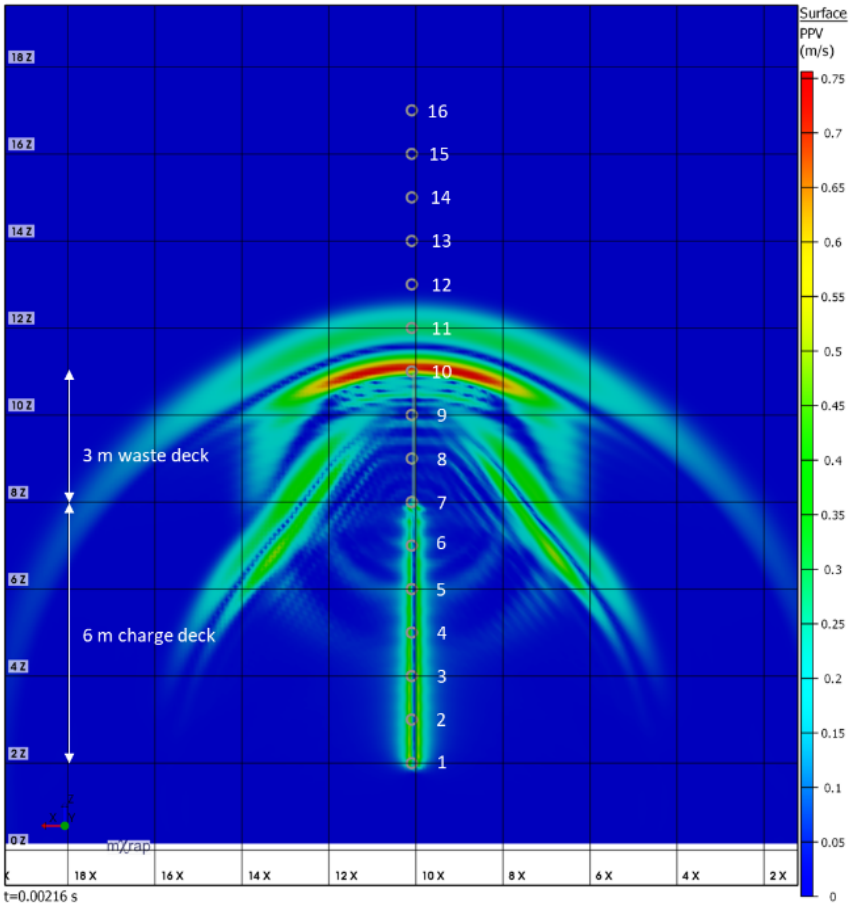


Figure 3. Modelling the shock pressure along the borehole. Numbers indicate points at which the pressure wave was measured. Time of snapshot is 0.00216 s.

The pressure decayed rapidly from a maximum of 2 GPa at the top of the charge (base of the waste deck) to about 4.5 MPa 1 m into the waste deck. It decayed to 2.5 MPa at the top of the waste deck 3 m from the charge deck. A detonator initiates a booster (both of which comprise the primer) that produces an explosion pressure of around 10 GPa which initiates the explosive column, whereas 4.5 MPa is only about 0.1% this value.

The modelling thus showed that there was very little to no risk of sizeable shock-induced sympathetic detonation of the charge in the adjacent charge deck in the hole. The detonators are designed to withstand a dynamic shock impact of 100 MPa. Therefore, they were also safe from being damaged by the impinging shock wave.

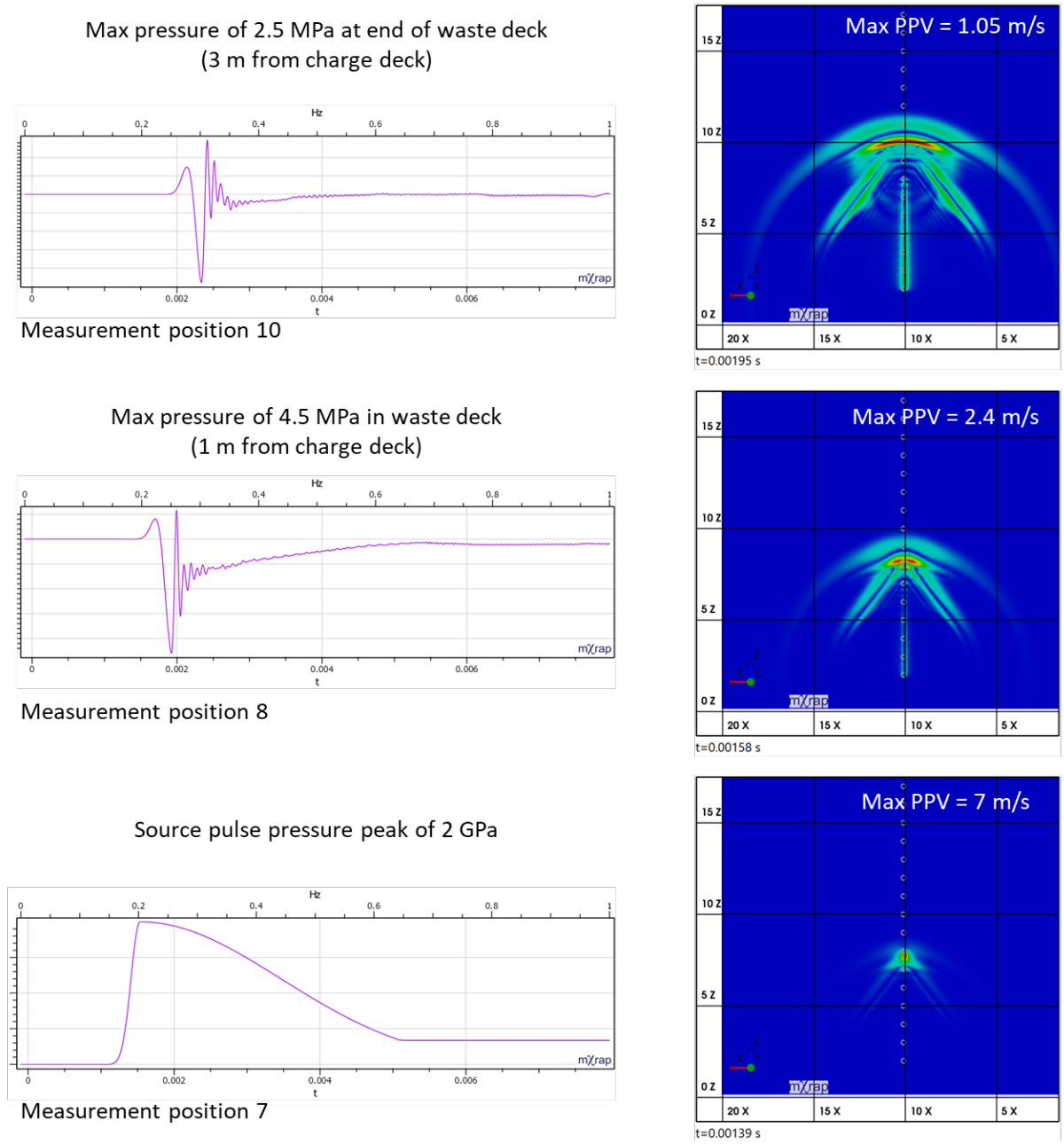
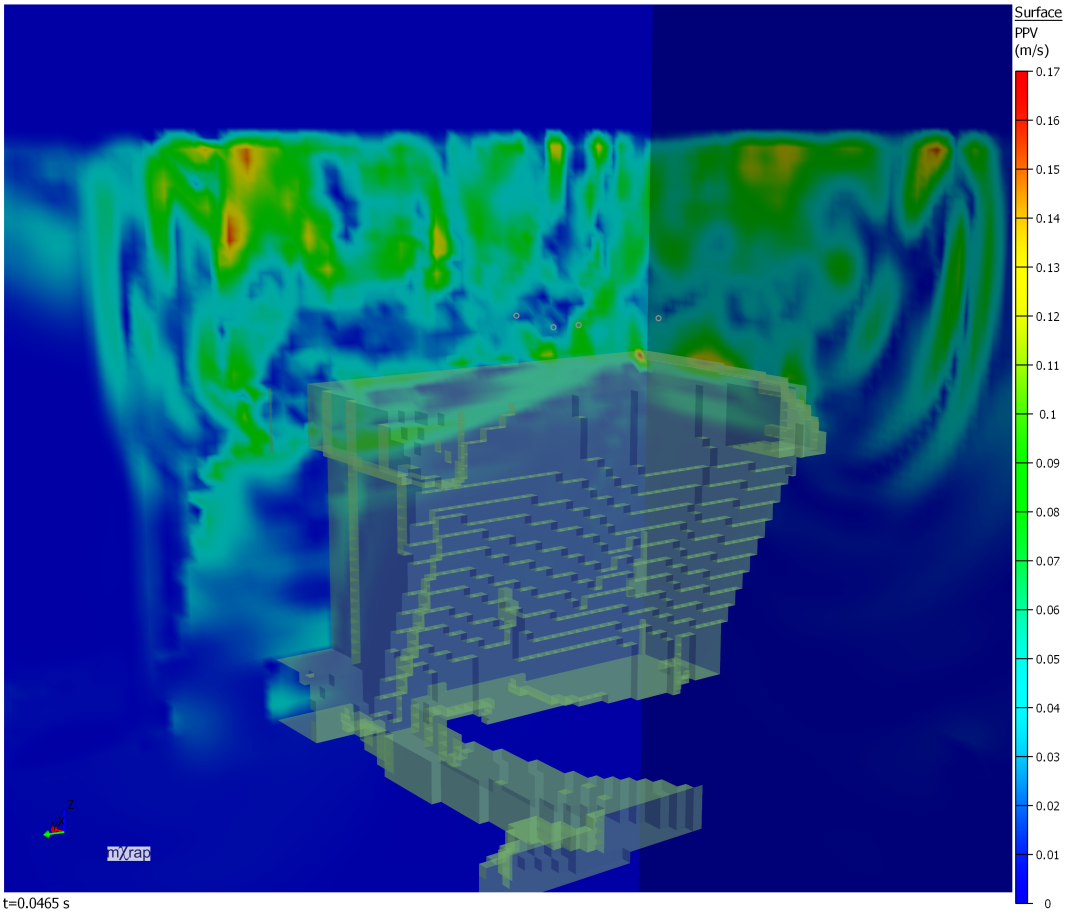


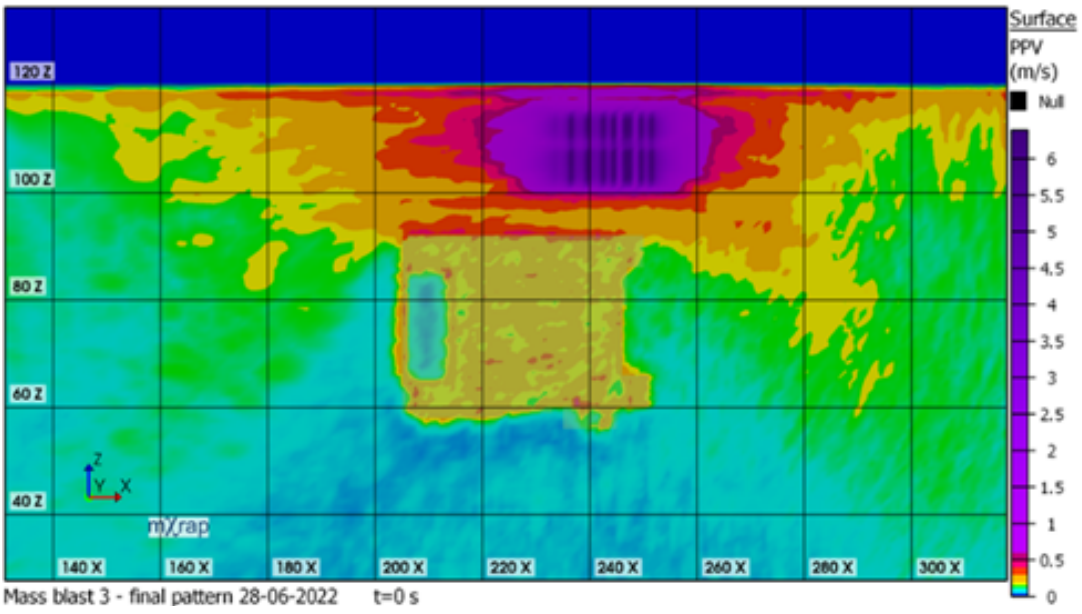
Figure 4. Modelling the shock pressure along the borehole. Graphs on the left show gas pressure vs time. The images on the right show the wave propagation up the borehole.

Once the triple deck concept was verified, the waveforms excited by entire blasting patterns could be simulated and PPVs could be estimated in the stope backs, sidewalls, and tunnel walls. Different blasting sequences were tested, and designs were refined and finalised. The actual mass blasts that were implemented, based on this modelling, all successfully achieved the design objectives.

A snapshot in time showing the wave propagation of the final mass blast of a single stope is shown in Figure 5. The maximum PPVs recorded throughout the duration of the model is also shown. Note that the high PPVs inside the stope are a result of the pseudo-air material inside the stope.



(a)



(b)

Figure 5. (a) Snapshot showing wave propagation 46 ms after the detonation of the first blast in the pattern. (b) Maximum PPV recorded throughout entire duration of the model.

CONCLUSIONS

Full waveform modelling using a properly calibrated source can significantly benefit the prediction of detailed vibration effects of both simple and complex blasts, enabling highly technical blasts to be designed and implemented with heightened confidence. This approach allows both the amplitude (PPV) and frequency content of the waveform to be simulated as a function of all the contributing blast parameters, including charge mass, VOD, spatial distribution of charges, multiple charge decks, detonation directions, and firing sequence.

REFERENCES

Boshoff, D. 2009. The development of a blasthole stemming performance: evaluation model using a purpose-built testing facility, MEng dissertation, University of Pretoria. https://repository.up.ac.za/handle/2263/29843

Devine, JF. 1966. Effect of charge weight on vibration levels from quarry blasting, USBM Report of Invest 6774.

Hildyard, MW. 2020. WAVE3D software. Leeds, United Kingdom, 2020, version 2020, http://homepages.see.leeds.ac.uk/~earmhi/MarkHildyard/WAVE3D/

Hildyard, MW. and Milev, AM. 2001. Simulated rockburst experiment: Development of a numerical model for seismic wave propagation from the blast, and forward analysis
August 2001, Journal- South African Institute of Mining and Metallurgy 101(5):235-245

Katsabanis, PD. and Ghorbani, A. 1995. A laboratory study of explosives malfunctioning, Society of Explosives Engineering Proceedings, V1, pp356 - 371

Linzer, LM. Hildyard, MW and Rorke, AJ. (2022). 3D Elastodynamic modelling applied to complex blasting problems. South African Geophysical Association's 17th Biennial Conference & Exhibition, Sun City, South Africa.

Persson P. Holmberg R and Lee J. 1994. Rock Blasting and Explosives Engineering. Boca Raton: CRC Press



Lindsay Linzer

Corporate Consultant (Geophysics) | Partner
SRK Consulting

Lindsay has 27 years of combined experience in mining seismology, reflection seismics and engineering geophysics. Lindsay's experience ranges from: acoustic emissions recorded in the laboratory; seismic surveys for geotechnical purposes; seismicity induced by shallow and deep level mining; and, seismic reflection data. She has applied state-of-the-art seismic interpretation technology to extract information vital to shaft-sinking, optimal borehole siting, and mine-planning. Lindsay has specialist skills in determining seismic source mechanisms (laboratory tests in rock and concrete and mining seismology) through moment tensor inversion using her own code and expertise in dynamic numerical modelling (2D and 3D) of seismic waves for AE/NDT laboratory tests; mine-seismology problems; geotechnical problems; shaft-sinking, and reflection seismology. Lindsay is an expert user and programmer in mXrap, a geotechnical data analysis and monitoring platform within which data analysis tools have been developed under the ACG's Mine Seismicity and Rockburst Risk Management project. Current interests are applying machine learning techniques to geophysical wireline and hyperspectral data.

Key block theory for the miner: A novel simplified method for determining block removability

C. van Rooyen

University of the Witwatersrand, South Africa

Gravity-driven rock falls cause the most injuries and deaths in the South African underground mines when compared to other agencies. Blocks are primarily defined by the intersection of discontinuities such as joints. Key block theory describes a methodology to determine whether such a rock can move into an excavated space. The complex calculations and multiple iterations required to execute key block analysis, however, restrict its routine use. Although several methods address some of the shortcomings of key block theory, none address the complexity of its underlying calculations. The main drive of this paper was to find a method to judge rock block removability that is simple enough to encourage the routine application of key block theory in daily mining. The novel gravitational removability theorem satisfied the need for simplicity. A comparison between the gravitational removability method and the edge vector method on a large set of synthetic blocks yielded a fair correlation in terms of removability, but less so in terms of non-removability. The definition and application of a set of calibrating geometric conditions in conjunction with the gravitational removability method resulted in a perfect accounting of all the synthetic blocks. The gravitational removability method proved effective in identifying rotational removability as well. The gravitational removability theorem allows for the judgement of the removability of a block with minimal or no calculation.

INTRODUCTION

The single largest contributor to fatalities in the South African mining industry are related to falls of ground (FOG). FOG-related incidents contributed to an average of 36.5% of mining fatalities overall during the 20 years between 2003 and 2022 in the South African mining sector as shown in Figure 1.

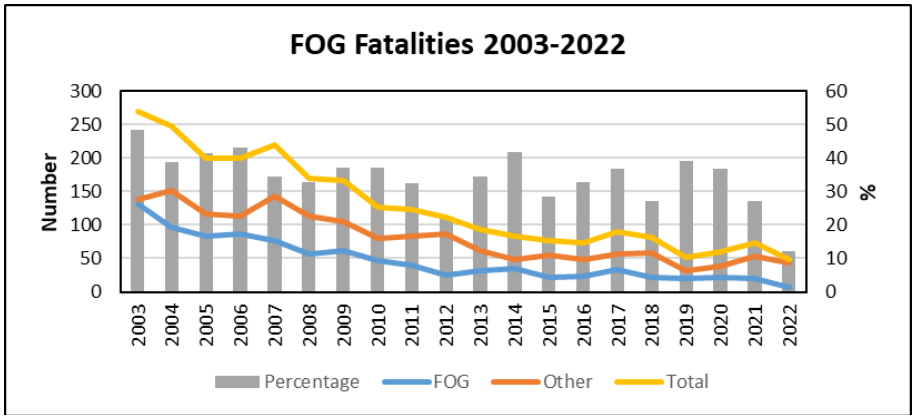


Figure 2. Mining fatalities, 2003 – 2022.

The South African Department of Minerals and Energy classifies FOG-related injuries and fatalities under two primary mechanisms: seismic and gravity. An analysis of the annual reports of the Mine Health and Safety Inspectorate between 2016 and 2020 shows that roughly 60% of all FOG-related fatalities and injuries result from gravity as shown in Figure 2 and Figure 3, respectively (Mine Health and Safety Inspectorate, n.d.).

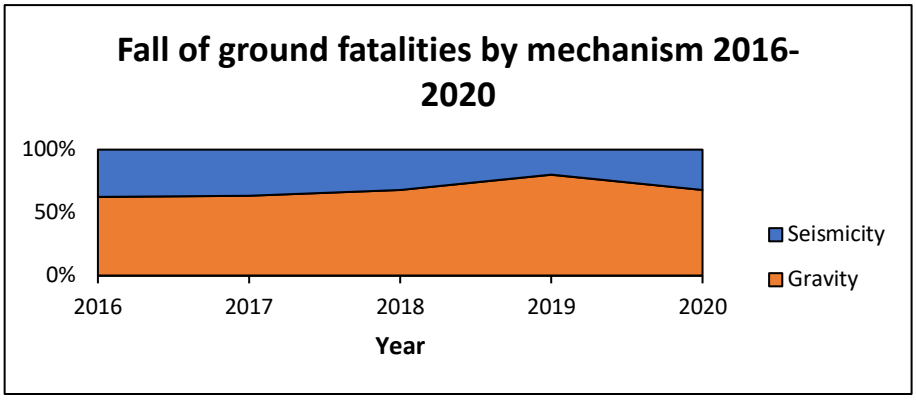


Figure 2. Fall of ground fatalities by mechanism 2016-2020.

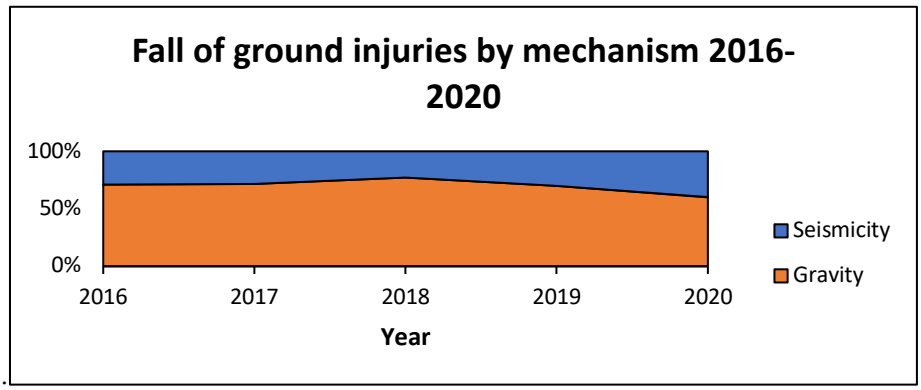


Figure 3. Fall of ground injuries by mechanism 2016-2020.

Goodman *et al.,* (1968) proposed that a jointed rock mass can be represented as a system of connected blocks. This concept was later formalised by Goodman & Shi (1985) through the formal introduction of block theory, commonly referred to as key block theory (KBT). The premise of KBT is that removable blocks contribute the most to excavation instability. Given that most of the injuring FOG in the South African mining industry are gravity-driven, KBT is a well-suited design approach to address gravity-driven FOG.

The application of KBT as a support design tool became popular in the South African mining industry following the release of JBlock (Esterhuizen and Streuders, 1998), a software package specifically designed for probabilistic key block analysis. Several authors have shown the applicability of the probabilistic key block approach (Esterhuizen and Streuders, 1998; Dunn and Stacey, 2008; Dunn, Hagan and Saydam, 2010; Joughin *et al.,* 2012b; 2012a; Nezomba, 2012; Judeel *et al*., 2016; Gardner, Bronkhorst and Ayres, 2017; Sewnun *et al*., 2017; Chikande and Zvarivadza, 2018; Khoza *et al.,* 2019; Netshilaphala and Zvarivadza, 2022). The major disadvantage of the probabilistic approach is that it is not well suited to routine application.

The use of KBT is typically limited to specific projects and is mostly absent in day-to-day mining. Practical constraints such as the cost of software licensing and a certain degree of skill necessary to execute KBT using commercial software contribute to its limited routine application. The computational

complexity to determine block removability is daunting and is therefore mostly done through software programming, which places KBT out of reach of the miner at the face.

This paper presents a summary of the research conducted by the author to develop a method to determine block removability that is sufficiently simple from a computational perspective to promote the utilisation of KBT routinely.

Brief overview of KBT

KBT formed the foundation of the research conducted, therefore a brief overview of KBT as it relates to block removability is provided as a preamble. The concepts, equations and their applications that follow are restated from the work of Goodman and Shi (1985) and reflect only those relevant to block removability.

The rock mass is intersected by a multitude of joints which divide it into discrete blocks resembling a three-dimensional mosaic, referred to as discontinuous rock. This discontinuous rock is constrained in all dimensions in a state of static equilibrium until disturbed by mining. Mining removes constraints from the rock mass within the void of an excavation, which allows blocks to move into the excavated space (Goodman and Shi, 1985). Goodman and Shi (1985) regarded continuum mechanics as a secondary consideration to the identification of key blocks. They recognised that although the identification of key blocks, is limited, the following simplifying assumptions are reasonable:

- Joints are perfectly planar
- Joints extend through the entire rock mass
- Blocks are rigid; and
- Joints and excavation boundaries are input parameters.

The minimum information needed to apply KBT is the dip and dip direction of each joint and an excavation surface. The assumption of planarity allows the joints and excavation surfaces to be expressed mathematically as three-dimensional planes.

Representing a joint as a plane

According to Goodman & Shi (1985) the general form of a plane is given by Equation *1*:

$$Ax + By + Cz = D \qquad \text{Equation 1}$$

where A, B and C are the coordinates of the unit vector perpendicular to the plane and D is the perpendicular distance of the plane from the origin. The values of A, B and C are calculated using Equation *2*:

$$\begin{aligned} A &= \sin(\alpha)\,.\,\sin(\beta) \\ B &= \sin(\alpha)\,.\,\cos(\beta) \\ C &= \cos(\alpha) \end{aligned} \qquad \text{Equation 2}$$

where α is the dip, between 0° and 90°, and β the dip direction of the joint or surface. The range of the dip angle ensures that C is always positive, hence the normal unit vector will always be the upward normal of the plane (Goodman and Shi, 1985).

Planar half-spaces

A plane divides three-dimensional space into an upper half-space (UHS) and lower half-space (LHS). A point lying above a plane lies in the UHS of the plane and conversely, a point below a plane lies in the LHS of the plane. Mathematically the half-spaces of a plane are expressed as inequalities.

The UHS of a plane is defined by Equation *3*:

$$Ax + By + Cz \geq D \qquad \text{Equation 3}$$

The LHS of a plane is defined by Equation *4*:

$$Ax + By + Cz \leq D \qquad \text{Equation 4}$$

The space common to a combination of the UHS and the LHS of three or more planes defines a block. The common space of the planes shown in Figure 4, for example, forms the tetrahedron shown in Figure 5.

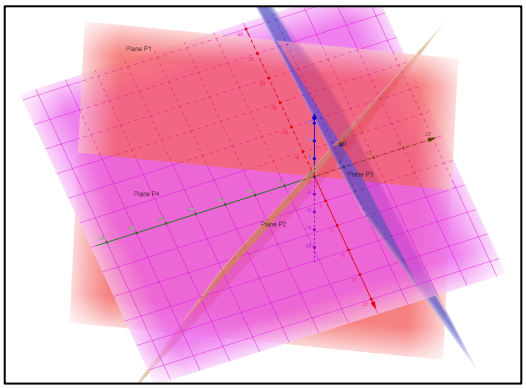


Figure 1. Planes forming a tetrahedron.

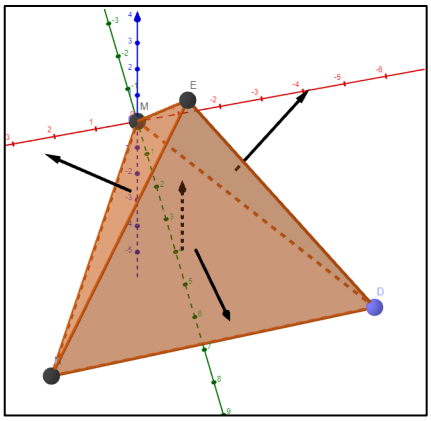


Figure 5. Tetrahedron formed in the planar common space.

Intersection of planes

An edge to a block is the line of intersection of two planes. The unit vector parallel to the line of intersection is the vector cross-product of the normal vectors of the two planes. Consider planes A and B with normal vectors $\hat{n}_A = (x_A, y_A, z_A)$ and $\hat{n}_B = (x_B, y_B, z_B)$, respectively. The vector parallel to the line of intersection is given by Equation *5*:

$$I_{AB} = [(y_A z_B - y_B z_A), (x_B z_A - x_A z_B), (x_A y_B - x_B y_A)] \qquad \text{Equation 5}$$

The intersection vector has two directions shown in Equation *6*:

$$I_{AB} = -I_{BA} \qquad \text{Equation 6}$$

The block pyramid

The block pyramid (BP) is central to judging whether a block is removable or not. The BP is constructed by shifting all the planes that define a specific block through the cartesian origin by setting D=0 in Equation 3 and Equation 4, for the system of inequalities that defines a specific block. The intersection

vectors $\pm I_{AB}$ must then be calculated for each pair of planes that intersect. Each intersection vector is substituted into the system of inequalities and only those intersection vectors that satisfy all the inequalities define the edges of the BP for any specific block. The BP is empty if no intersection vector satisfies the system of inequalities.

Block removability

The fundamental approach of KBT is that the stability of a key block affects the stability of an excavation. Goodman & Shi (1985) classified the geometric configuration of blocks as shown in Figure 6.

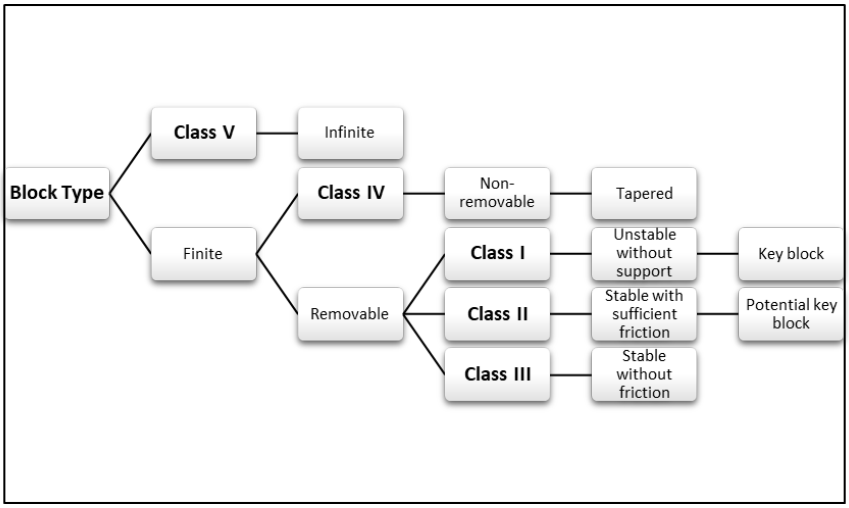


Figure 6. Block types (Goodman and Shi, 1985, p.99).

The definition of a class I or class II block is that the block must be finite, removable, and possibly unstable. The theorem of finiteness is used to determine whether a block is finite. The theorem of finiteness states: "*A convex block is finite if its block pyramid is empty. Conversely, a convex block is infinite if its block pyramid is not empty*" (Goodman and Shi, 1985, p.101). The BP consists of both joints and excavation planes. A joint pyramid (JP) is constructed using the same method as for the BP, but only the joint planes are considered. The theorem of removability then states that: "*A convex block is removable if its block pyramid is empty and its joint pyramid is not empty. A convex block is not removable (tapered) if its block pyramid is empty and its joint pyramid is also empty*" (Goodman and Shi, 1985, p.108).

Edge vector method

The edge vector method is a matrix-based formulation of KBT (Warburton, 1981; Goodman and Shi, 1985; Yan *et al*., 2023). The edge vector method was used to provide the comparative base for the research conducted. An overview of this method is provided here for completeness.

Consider a tetrahedron formed by three joints with planar equations J1, J2 and J3 shifted through the cartesian origin as shown in Equation *7*:

$$\begin{aligned} A_{J1}x + B_{J1}y + C_{J1}z &= 0 \\ A_{J2}x + B_{J2}y + C_{J2}z &= 0 \\ A_{J3}x + B_{J3}y + C_{J3}z &= 0 \end{aligned} \qquad \text{Equation 7}$$

The normal upward unit vector for each plane is shown in Equation *8*:

$$\hat{n}_{J1} = (A_{J1}, B_{J1}, C_{J1})$$
$$\hat{n}_{J2} = (A_{J2}, B_{J2}, C_{J2}) \qquad \text{Equation 8}$$
$$\hat{n}_{J3} = (A_{J3}, B_{J3}, C_{J3})$$

If the block is formed in the lower half-spaces of the planes the inwards normal vectors $\hat{I}_{J1}$, $\hat{I}_{J2}$ and $\hat{I}_{J2}$ are given by Equation *9*:

$$\hat{I}_{J1} = -(A_{J1}, B_{J1}, C_{J1})$$
$$\hat{I}_{J2} = -(A_{J2}, B_{J2}, C_{J2}) \qquad \text{Equation 9}$$
$$\hat{I}_{J3} = -(A_{J3}, B_{J3}, C_{J3})$$

The intersection vector between each pair of planes is determined by the cross product of the pair. The cross-product between J1 and J2 is shown in Equation *10*:

$$I_{J1J2} = \hat{I}_{J1} \times \hat{I}_{J2}$$
$$I_{J1J2} = \begin{vmatrix} \hat{\imath} & \hat{\jmath} & \hat{k} \\ A_{J1} & B_{J1} & C_{J1} \\ A_{J2} & B_{J2} & C_{J2} \end{vmatrix} \qquad \text{Equation 10}$$
$$I_{J1J2} = \begin{vmatrix} B_{J1} & C_{J1} \\ B_{J2} & C_{J2} \end{vmatrix} \hat{\imath} - \begin{vmatrix} A_{J1} & C_{J1} \\ A_{J2} & C_{J2} \end{vmatrix} \hat{\jmath} + \begin{vmatrix} A_{J1} & B_{J1} \\ A_{J2} & B_{J2} \end{vmatrix} \hat{k}$$
$$I_{J1J2} = (B_{J1}C_{J2} - C_{J1B_{J2}}, C_{J1}A_{J2} - A_{J1}C_{J2}, A_{J1}B_{J2} - B_{J1A_{J2}})$$

The intersection vector has two directions, the chosen direction must be towards the free surface. When considering the hangingwall, this will typically be the intersection vector with a negative z-component. Once the intersection vectors are determined, the scalar product as detailed in Equation 10, between the inwards normal unit vector of each plane and each intersection vector is determined. The nine scalar products are shown in Equation *11*.

$$\begin{matrix} \hat{I}_{J1}.I_{J1J2} & \hat{I}_{J1}.I_{J2J3} & \hat{I}_{J1}.I_{J1J3} \\ \hat{I}_{J2}.I_{J1J2} & \hat{I}_{J2}.I_{J2J3} & \hat{I}_{J2}.I_{J1J3} \\ \hat{I}_{J3}.I_{J1J2} & \hat{I}_{J3}.I_{J2J3} & \hat{I}_{J3}.I_{J1J3} \end{matrix} \qquad \text{Equation 11}$$

If any of the scalar products are less than zero the block is not removable (Warburton, 1981; Goodman and Shi, 1985; Yan *et al.*, 2023).

Development of the novel block removability method

Rationale

A joint, or free surface, is represented mathematically as a plane. A plane is defined by its dip and dip direction, which are used to calculate the coordinates of its normal vector. Since the measurement range for the dip of a joint or free surface is always between zero and 90° the normal vector will always have a positive z-component between zero and one, which is the upward normal vector. The fact that the normal vector will always be upward normal is important when considering the planar half-space. If a block lies in the UHS of the plane the normal vector will be in the direction of the block, referred to as the inwards normal. Conversely, if a block lies in the LHS of a plane the normal vector will be in the direction of the rock mass, referred to as the rock mass vector (RMV). The normal vector of a free surface, when considering the hangingwall, will always point into the block, but also into the rock mass. Joints divide the rock mass into a collection of discrete blocks. Each block is held in place by the constraint provided by its neighbours. The two-dimensional view of an arbitrary joint network shown in Figure 7 illustrates this.

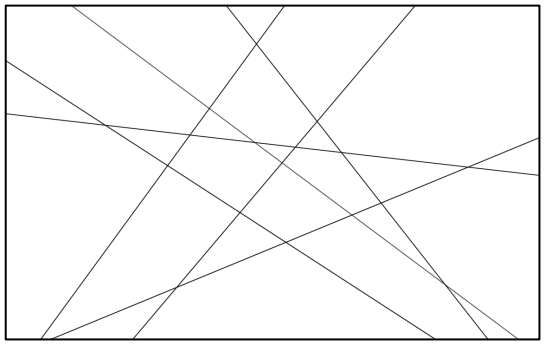


Figure 7. Random joint network.

Several blocks develop where the joints intersect, but in the absence of a free surface, these blocks are simply the rock mass. The introduction of a free surface results in blocks that could potentially move into an excavation. The line that is shown in Figure 8 represents a free surface, the hangingwall in this case, introduced into the rock mass which illustrates this concept. The orientation of the free surface relative to the joints affects the blocks formed as well as the removability of these blocks. Considering the same free surface shown in Figure 8 as a slope, the blocks that could potentially move are quite different as shown in Figure 9.

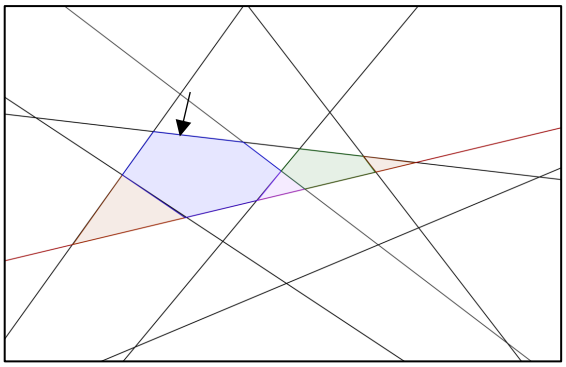


Figure 8. Two-dimensional view of blocks formed above excavation.

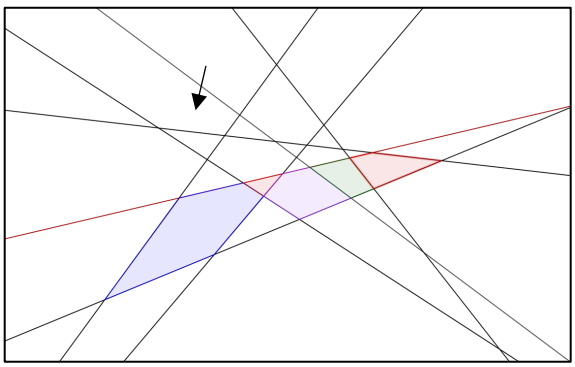


Figure 9. Two-dimensional side view of blocks formed in slope

The orientation of the free surface relative to the excavated space is therefore the primary factor when considering block removability. The secondary factor is the relative orientation between the free surface and each joint that defines a block. The orientational relationship between a free surface and any joint is described by the angle between the RMV of the free surface and the RMV of a joint. The dot product of these two vectors indicates whether the angle is more or less than 90°. Equation *12* is used to calculate this angle where θ is the angle between any two vectors: 'a' and 'b'.

$$\cos\theta = \frac{a.b}{|a||b|}$$ Equation 12

Equation *13* yields the dot product of two vectors, a= (x_a, y_a, z_a) and b= (x_b, y_b, z_b).

$$a.b = (x_a x_b).(y_a y_b).(z_a z_b)$$ Equation 13

Considering that Equation *2* produces a unit vector, Equation *12* simplifies to Equation *14*.

$$\cos\theta = \hat{a}.\hat{b}$$ Equation 14

The maximum angle between two vectors is 180°, or π radians, which implies that the two vectors are directionally opposite.

Consider the two-dimensional removable triangular block formed by three lines in Figure 10. The block is the region where the half-planes coincide. In this case, it is the lower half-planes of the joints (blue) and the upper half-plane of the free surface (red). Removal of the block creates the cavity as shown in Figure 11. The RMV for the three lines are shown in Figure 12. From Figure 12 the angle between the RMV of the free surface and both joints are less than 90°. A non-removable scenario is shown in Figure 13. In the non-removable scenario, the RMV (green) of the joints (blue) do not necessarily coincide with the upward normal vectors (blue). A combination of joint orientations, as shown in Figure 14, is also possible.

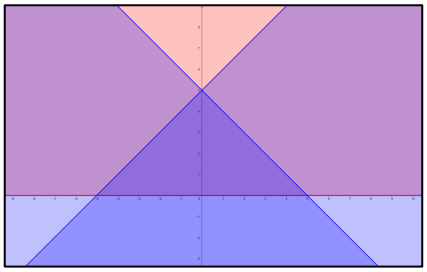


Figure 10., Two-dimensional block.

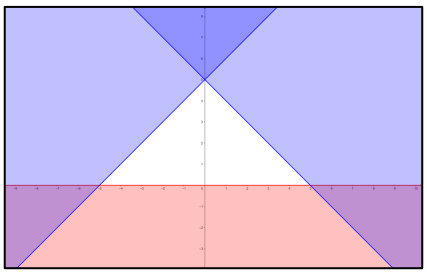


Figure 11. Removable two-dimensional remnant cavity

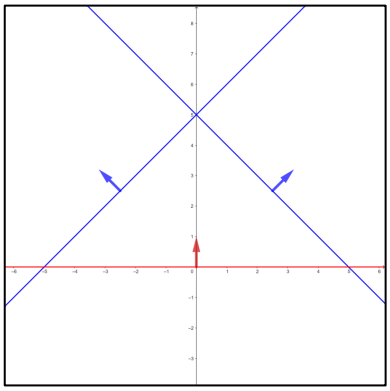


Figure 12. Normal vectors.

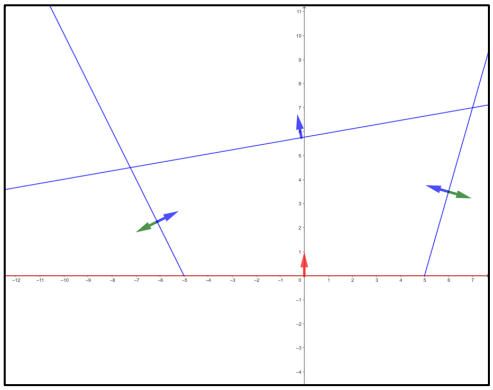


Figure 13. Non-removable two-dimensional block

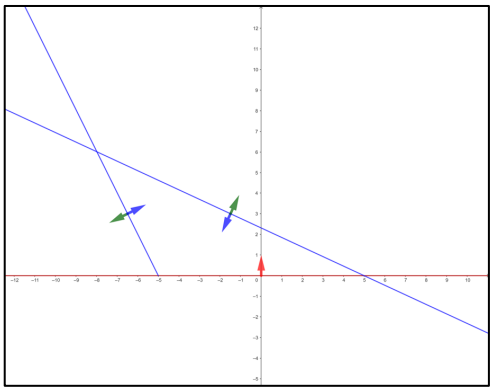


Figure. Two-dimensional combination scenario.

The scenarios presented in Figure 12, Figure 13 and Figure 14 demonstrate that the angle between the RMV of a free surface and that of a joint is an indication of whether a block will be constrained along that joint. An angle of less than 90° will contribute to removability while an angle exceeding 90° will constrain block movement. This concept alone however, is not sufficient to determine removability.

Gravity is the principal force that drives block movement. The unit vector for gravity in cartesian space is $\hat{\mathbf{g}} = (0,0,-1)$. The gravitational vector can be related to the geometric analysis through Newton's third law of motion which states that any applied force is counteracted by an equal force in the opposite direction of the applied force. It then stands to reason that a block is removable when there is insufficient geometric constraint to maintain its static equilibrium under gravitational load.

A free surface is not a physical entity, it is merely a space into which a block may move and is therefore not considered beyond classifying a joint as contributing to or constraining movement. The practical interpretation of a constraining joint is that there is intact rock between the face of the block and the free surface. Conversely, a contributing joint has no intact rock between the face of the block and the free surface. The concept of geometric constraint was used to formulate a set of 'rules of thumb' allowing that removable and non-removable blocks could be identified without the need for any calculations. Geometric constraint is discussed in section 0.

Assumptions and conventions
The assumptions of KBT as set out by Goodman & Shi (1985) were maintained. Concepts introduced by other authors were included as additional assumptions:

- The test for finiteness is discarded (Cheng *et al*., 2021a; 2021b)
- Only those joints intersecting the free surface are considered (Wu *et al*., 2017)
- The actual spatial location of each constituent plane is a secondary consideration to the relationship between the various unit vectors as shown by the construction of the block and joint pyramids (Goodman and Shi, 1985); and
- Only the gravitational movement direction of a block is relevant in determining a block's removability, hence the gravitational unit vector satisfies the removability analysis (Warburton, 1981).
- The method is only applied to those blocks that have not been discarded outright as removable or non-removable based on geometric conditions.

The following spatial orientation conventions are adopted:

- North coincides with the positive y-axis
- East coincides with the positive x-axis
- The dip is measured as the angle below the horizontal to a maximum of 90°
- Dip direction is measured clockwise from north; and
- Up is in the direction of the positive z-axis.

Formulation
A prerequisite to the method is the calculation of the upward normal unit vectors and determination of the RMV of each plane. The set of symbols introduced are stated in Table I.

Table 1. Symbols

Symbol	Meaning
$\hat{n}_{Ji}$	Upward normal unit vector of joint i
$\hat{n}_{FS}$	Upward normal unit vector of the free surface
$\hat{r}_{Ji}$	Rock mass vector of joint i
$r_{Ji}z$	z-coordinate of $\hat{r}_{Ji}$
$\hat{r}_{FS}$	Rock mass vector of the free surface
$r_{FS}z$	z-coordinate of $\hat{r}_{FS}$
S_{Ji}	Absolute value of $r_{Ji}z$ constraining movement
G_{Ji}	Absolute value of $r_{Ji}z$ contributing to movement
RC	Total constraint
RG	Total contribution
GRN	Gravitational removability number

The orientation of the RMV for the free surface is determined by applying Lemma 1 and the RMV for each joint by applying Lemma 2.

Lemma 1: *If the rock mass is situated in the UHS of the free surface, then* $\hat{r}_{FS} = \hat{n}_{FS}$ *. Conversely, if the rock mass is situated in the LHS of the free surface, then* $\hat{r}_{FS} = -\hat{n}_{FS}$.

Lemma 2: *If a block is situated in the LHS of joint, i, then* $\hat{r}_{Ji} = \hat{n}_{Ji}$. *Conversely, if a block is situated in the UHS of joint, i, then* $\hat{r}_{Ji} = -\hat{n}_{Ji}$.

Considering Equation *14*, Lemma 3 is used to classify each joint. A special case arises when the RMV of the free surface and the RMV of a joint are perpendicular to each other, which is addressed by Lemma 4.

Lemma 3: *Joint, i, constrains movement when* $\hat{r}_{FS}.\hat{r}_{Ji} < 0$, *then* $S_{Ji} = |r_{Ji}z|$. *Joint, i, contributes to movement when* $\hat{r}_{FS}.\hat{r}_{Ji} > 0$, *then* $G_{Ji} = |r_{Ji}z|$.

Lemma 4: *When* $\hat{r}_{FS}.\hat{r}_{Ji} = 0$ *and the dip angle of the free surface is not zero joint, i, constrains movement when* $r_{Ji}z < 0$, *then* $S_{Ji} = |r_{Ji}z|$. *Joint, i, contributes to movement when* $r_{Ji}z > 0$, *then* $G_{Ji} = |r_{Ji}z|$.

The total constraint against movement, RC, is calculated by a summation of all the absolute values of the z-components of the joints constraining movement. The total contribution to the movement, RG, is calculated by a summation of all the absolute values of the z-components of the joints contributing to the movement. The gravitational removability number, GRN, is calculated using Equation *15*.

$$\mathrm{GRN} = (1 + \mathrm{RC}) - \mathrm{RG} \qquad \text{Equation 15}$$

The novel gravitational removability theorem then states that: "*A block formed by the intersection of a free surface and several joints is not removable when its gravitational removability number is greater than zero. A block is removable when its gravitational removability number is less than zero*".

The scenario where the joints are not constraining but have steep dip angles introduces a point of contention when considering the gravitational removability number. Slender blocks, however, rarely occur in underground mining as the blocks are often 'trimmed' by a parting plane, such as the Chromatite markers found in the hangingwall of most platinum mines. A fictitious parting plane parallel to the free surface is introduced to 'trim' slender blocks in Equation 15 with its contribution to movement equal to $r_{FS}z$. Equation *15* then becomes Equation *16*:

$$\mathrm{GRN} = (1 + \mathrm{RC}) - (\mathrm{RG} + r_{FS}z) \qquad \text{Equation 16}$$

The effect of gravity on a solid body, such as a block, is to pull it vertically downwards. However, when an obstacle is introduced in the gravitational path, such as a constraining joint, the effect of gravity is to increase the normal load on the constraining surface, effectively clamping a block more firmly to the constraining surface. Although the forces acting on a block are not directly considered, the assumption of rigidity implies that forces will be resolved within the confines of the geometric boundaries of the remnant cavity. Hence, a block will only move if the constraining effect of gravity is overcome.

GRN application example

The GRN can be calculated easily by setting up a spreadsheet with a few simple formulae. The example uses the inputs from an example put forth by Goodman and Shi (1985), as shown in Table 2 (Goodman and Shi, 1985, p.49). Figure 15 presents a three-dimensional plot of the planes assuming D=1 from Equation 1.

Table 2. Example inputs (Goodman and Shi, 1985, p.49)

ID	α	β	½ Space
FS	0	90	U
J1	45	90	L
J2	45	330	L
J3	45	210	L

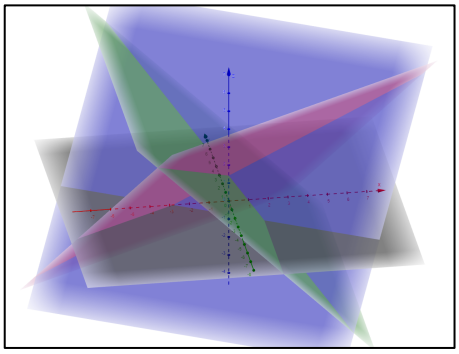


Figure 15. Example planes.

The intersection of the planes shown in Figure 15 results in the tetrahedron shown in Figure 16.

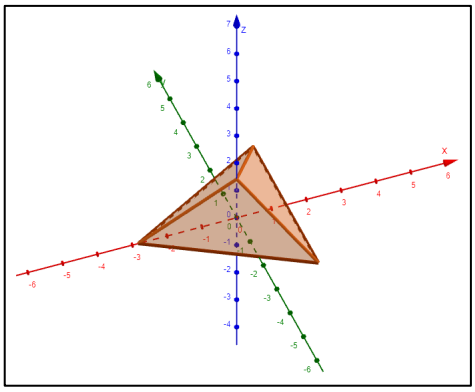


Figure 16. Example tetrahedron.

The tetrahedron is determined to be removable according to the GRN as shown in Figure 17.

GRN Calculator												
Input				Upwards unit normal			RMV					
ID	α	β	½ Space	A	B	C	x	y	z	Dot	Contribute	Constrain
FS	0	90	U	0	0	1	0	0	1			
J1	45	90	L	0.707107	4.33E-17	0.707107	0.707107	4.33E-17	0.707107	0.707107	0.7071068	0
J2	45	330	L	-0.35355	0.612372	0.707107	-0.35355	0.612372	0.707107	0.707107	0.7071068	0
J3	45	210	L	-0.35355	-0.61237	0.707107	-0.35355	-0.61237	0.707107	0.707107	0.7071068	0
Removable											2.1213203	0
											GRN	-2.12132

Figure 17. Example 1 GRN calculation.

Observed joints underground are typically plotted and extrapolated on mine plans as shown in Figure 18. The simplicity of the GRN method is demonstrated by repeating the example by inspection only.

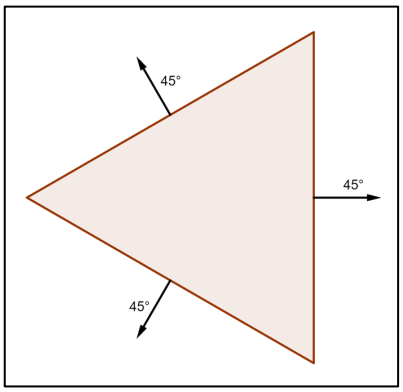


Figure 18. Two-dimensional projection of example tetrahedron.

The dip directions point away from the centre of the block; hence the dip directions are also the RMV of each joint. All the joints contribute to block movement, hence the GRN will be less than zero, and therefore the block is removable.

Experimental design

The necessity to test field data was considered secondary to determining the efficacy of the gravitational removability theorem as field data introduces additional variables, such as roughness and cohesion, which may skew the results. To prove the gravitational removability theorem as a viable method it was necessary to compare the results obtained from the application of the theorem to results on the same data set using an established method. The EV method originally described by Goodman and Shi (1985) as cited by Yan *et al.*, (2023) was used as the comparative base. The reason for choosing the EV method was for computational efficiency.

A spreadsheet was set up to randomly generate the defining parameters of sets of joints to represent discrete blocks having three, four and five sides. A 'rinse and repeat' code was written to generate 100 000 blocks of each shape, resulting in a data set of 300 000 blocks which satisfied the Monte Carlo principle, first described by Metropolis and Ulam (1949). The removability of each block was tested using both the EV and GRN methods.

A direct comparison between the EV and GRN methods yielded Table 3. The base comparison correlated well in terms of removability but significant disagreement in the other areas required further study. The concept of geometric constraint previously mentioned was explored in detail to address the difference in results.

Table 3. Base comparison

Base Comparison			
Number of constituent joints	**3**	**4**	**5**
Base Statistics			
Blocks generated	100,000	100,000	100,000
Removable according to EV	47,417	15,988	4,184
Non-removable according to EV	52,583	84,012	95,816
EV & GRN removable			
Count	42,789	15,480	4,179
Agreement	90%	97%	99.88%
% of total blocks	43%	15%	4%
EV & GRN non-removable			
Count	45,332	49,405	49,927
Agreement	86%	59%	52%
% of total blocks	45%	49%	50%
EV removable / GRN non-removable			
Count	4,628	508	5
Disagreement	10%	3%	0.12%
% of total blocks	5%	1%	0%
EV non-removable / GRN removable			
Count	7,251	34,607	45,889
Disagreement	14%	41%	48%
% of total blocks	7%	35%	46%

Geometric constraint

The GRN method assumes that geometrically constrained blocks are discarded outright before calculation. The fictitious parting plane included in the GRN may also lead to misclassification, especially in instances where the joint dips are steeper, resulting in lower z-components, which may be insufficient to overcome the contribution of the fictitious plane.

Wu *et al.*, (2017) introduced the concept of a 'free domain' to account for the concave corners of a block. Only those joints intersecting a free surface are considered in the determination of removability (Wu *et al.*, 2017). Scenarios arise in practice where a block is non-removable based only on the physical configuration of its constituent joints. Goodman & Shi (1985) stated that a block is removable when it can be moved in some direction that does not cause the block to 'collide' with adjacent rock (Goodman and Shi, 1985). Consider the block formed by a free surface and four joints shown in Figure 19.

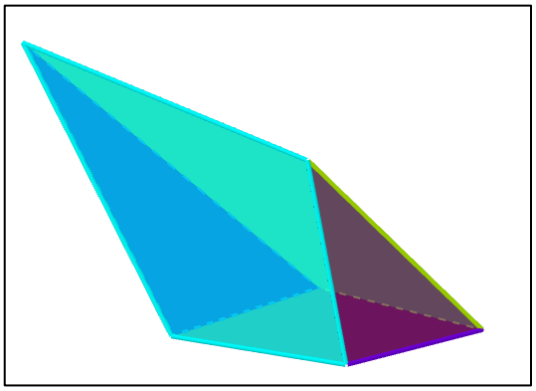


Figure 19. Geometrically constrained four-sided block.

At face value, the block appears to be removable, but it is not. A section plane cut through the block yields the polygon, PNSR, shown in Figure 20. The block lies in the UHS of segment PS and the LHS of segment RN. The dip angle of segment PS is shallower than the dip angle of segment RN as shown in Figure 21. Any movement of the block will result in a 'collision' as described by Goodman & Shi (1985) with the rock mass along segment RN, effectively constraining the movement of the block (Goodman and Shi, 1985).

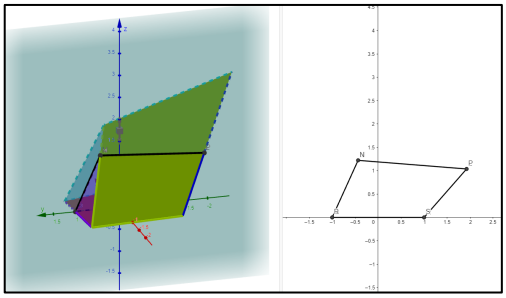


Figure 20. Geometrically constrained block cross-section.

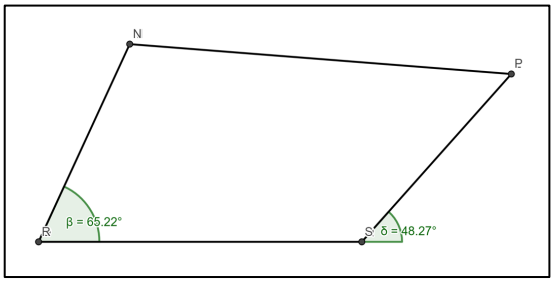


Figure 21. Geometrically constrained block detail.A four-sided block can be classified outright as non-removable under the following conditions, which are graphically represented in Figure 22

- A block lies in the UHS of all the constituent joints
- A block lies in the UHS of two opposing joints; and
- A block lying in the UHS of a joint and in the LHS of the opposing joint where the dip angle of the upper half space joint is lower than that of the opposing joint.

When a block lies in the LHS of all the constituent joints the block is outright removable as shown in Figure 23.

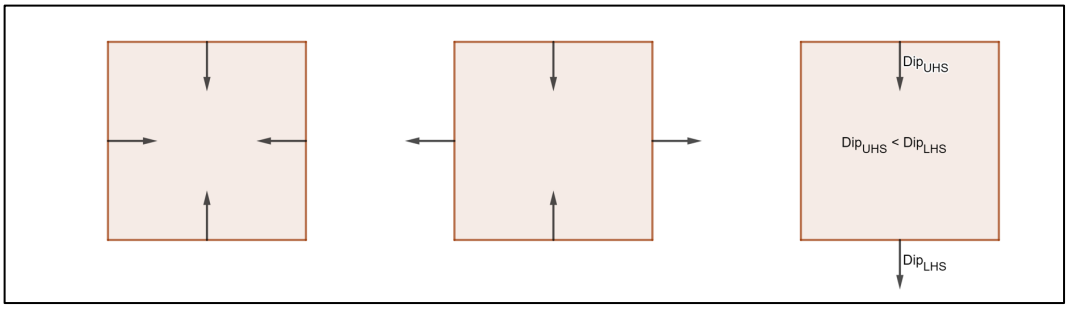


Figure 22. Four-sided non-removable conditions.

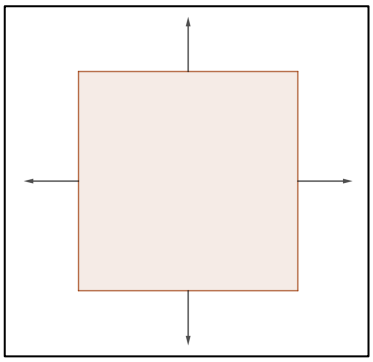


Figure 23. Outright removable four-sided block.

The rationale discussed for four-sided blocks was applied to both the three-sided and the five-sided blocks with similar results. The balance of the disagreement between the EV method and GRN was comprised of blocks formed in the UHS of one constituent joint. Such a geometry implies that at least one apex of the block lies outside of the two-dimensional footprint of the block on the free surface. Such a block will not necessarily be removable through translation, but rather through rotation, which is not addressed by the edge vector method. An example of such a block is given in Figure 24. It is concluded that when a block is formed where it lies in the upper half space of at least one constituent joint the block can be potentially removable through rotation.

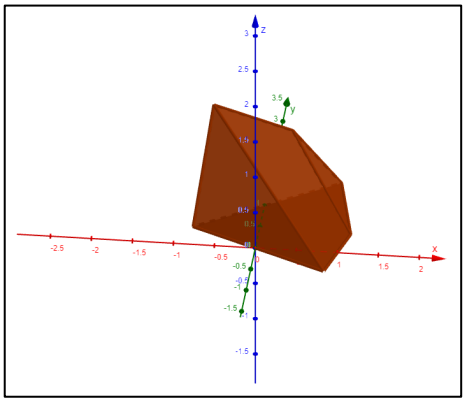


Figure 24. Potential rotationally removable four-sided block.

The blocks regarded as potentially removable through rotation were further analysed. The scenario where the EV method implies removability and the GRN not, yielded 4628 data points for three-sided blocks, two for four-sided blocks and none for five-sided blocks. The results for three-sided blocks are shown in Figure 25. The inverse scenario where the EV method implies non-removability and the GRN implies removability was significantly more prevalent as shown in Figure 26.

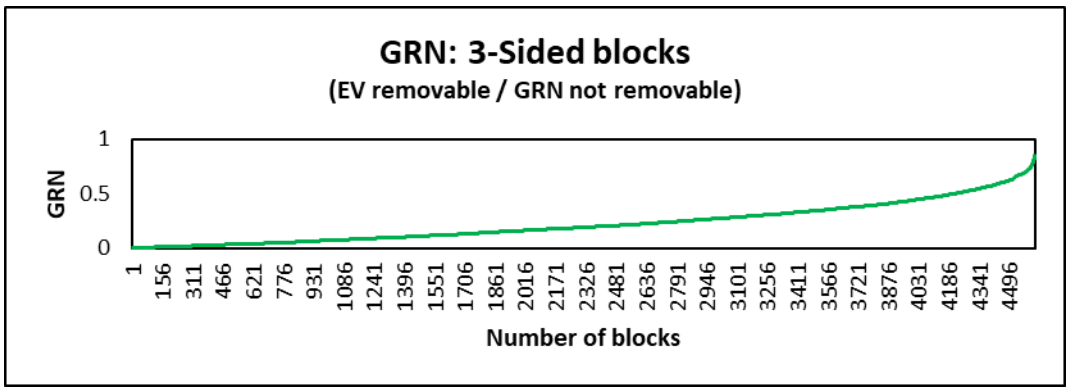


Figure 25. 3-sided plot of GRN (EV removable / GRN not removable).

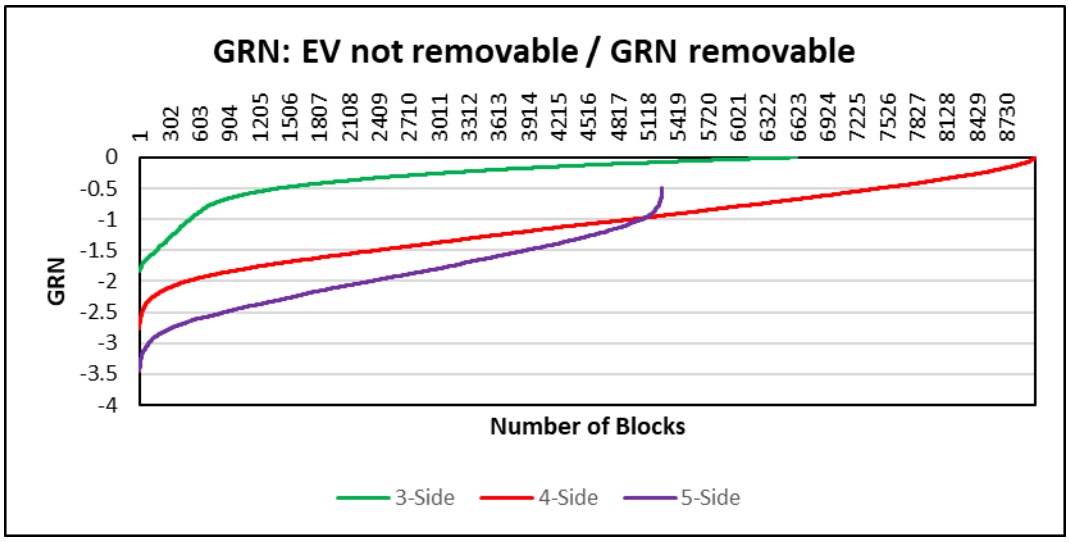


Figure 26. GRN removable / EV not removable.

The GRN values when considering the first scenario were all equal to or greater than zero. The GRN values when considering the second scenario were all less than zero. This clear distinction in the data leads to the conclusion that a block that lies in the upper half space of at least one constituent joint and remains unclassified following the application of the geometric filters is removable when the GRN is greater than zero. Conversely, if the GRN is less than or equal to zero the block is removable by rotation.

Calibrated results

The geometric constraints were used to filter the base data set as the assumption for the application of the gravitational stability method, followed by a comparative run. The results are presented in Table 4.

Table 4. Calibrated balance sheet

Calibrated Balance Sheet					
Number of constituent joints			**3**	**4**	**5**
Number of blocks generated			**100,000**	**100,000**	**100,000**
Geometric calibration					
1.	Outright removable	All LHS	(633)	(1,554)	(1,558)
2.	Opposite constrained	UHS-UHS	0	(7,112)	(18,834)
3.	Constrained by collision	α-UHS < α-LHS	0	(17,430)	(20,236)
4.	Potential rotation	At least 1 UHS	(11,246)	(9,019)	(5,266)
Subtotal			**88,121**	**64,885**	**54,106**
EV & GRN removable			(42,789)	(15,480)	(4,179)
EV & GRN non-removable			(45,332)	(49,405)	(49,927)
Blocks not accounted			**0**	**0**	**0**

DISCUSSION

The data analysis revealed a strong correlation in terms of removable blocks but the correlation with regards to non-removable blocks was unsatisfactory. Further analyses revealed that the source of the misclassification was the disregard for physical geometry in the calculation of the gravitational removability number. The instances where disparity existed offered valuable insights which led to the definition of a set of geometric conditions. These geometric conditions allow for blocks to be regarded as removable or not outright by inspection of a block's two-dimensional footprint and dip direction vectors only. Joints are typically indicated as lines, with arrows indicating dip directions on mine plans. A potential application of the GRN method is to produce a pictorial reference card and with some training any mine worker, even an illiterate one, can, with minimal training, identify potentially dangerous blocks by simply looking at a mine plan.

Application of the geometric conditions on the data set addressed all disparities. In addition, a comparison of the actual GRN with the EV results in the disparate cases revealed that the GRN, when considered in conjunction with the geometric conditions, can indicate rotational removability, whereas the EV method only considers translational removability.

CONCLUSION

The research conducted achieved the primary objective of devising a simple method to determine block removability. In addition, the GRN method introduces an advancement over the EV method in that it allows for the identification of blocks that may be removable through rotation.

REFERENCES

Cheng, X.L., Liu, L.P., Xiao, J., Zhang, Q.H., Jiao, Y.Y., Zheng, F. and Wang, Y., 2021a. Analysing Block Stability under Varying Resultant Force for Arbitrary Shapes. *IOP Conference Series: Earth and Environmental Science*, [online] 861(3), https://doi.org/10.1088/1755-1315/861/3/032062.

Cheng, X.L., Liu, L.P., Xiao, J., Zhang, Q.H., Xue, J. and Wang, Y., 2021b. A General Block Stability Analysis Algorithm for Arbitrary Block Shapes. *Frontiers in Earth Science*, 9. https://doi.org/10.3389/feart.2021.723320.

Chikande, T. and Zvarivadza, T., 2018. Evaluation of tendon support in anisotropic jointed rockmass. In: *ARMA US Rock Mechanics/Geomechanics Symposium*. ARMA. p.ARMA-2018.

Dunn, M.J., Hagan, P. and Saydam, S., 2010. The application of probabilistic keyblock methods for support design in blocky rock masses. In: *Proceedings 2nd Australasian Ground Control in Mining Conference, P. Hagan and S. Saydam (eds)*. pp.23–24.

Dunn, M.J. and Stacey, T.R., 2008. Design of stable spans at Tau Lekoa Mine. In: *SHIRMS 2008: Proceedings of the First Southern Hemisphere International Rock Mechanics Symposium*. Australian Centre for Geomechanics. pp.179–192.

Esterhuizen, G.S. and Streuders, S.B., 1998. Rockfall hazard evaluation using probabilistic keyblock analysis. *The Journal of The South African Institute of Mining and Metallurgy*, (April), pp.59–64.

Gardner, L.J., Bronkhorst, L. and Ayres, N.L., 2017. Optimizing stope panel spans at an eastern Bushveld platinum mine by probabilistic analysis. In: *ISRM AfriRock-Rock Mechanics for Africa*. ISRM. p.ISRM-AFRIROCK.

Goodman, R.E. and Shi, G., 1985. *Block Theory and its application to Rock Engineering*.

Goodman, R.E., Taylor, R.L. and Brekke, T.L., 1968. A Model for the Mechanics of Jointed Rock. *Journal of the Soil Mechanics and Foundations Division*, 94(3), pp.637–659. https://doi.org/10.1061/JSFEAQ.0001133.

Joughin, W.C., Jager, A., Nezomba, E. and Rwodzi, L., 2012a. A risk evaluation model for support design in Bushveld Complex underground mines: Part I-Description of the model. *Journal of the Southern African Institute of Mining and Metallurgy*, 112(2), pp.83–94.

Joughin, W.C., Jager, A., Nezomba, E. and Rwodzi, L., 2012b. A risk evaluation model for support design in Bushveld Complex underground mines: Part II-Model validation and case studies. *Journal of the Southern African Institute of Mining and Metallurgy*, 112(2), pp.95–104.

Judeel, G., Swanepoel, T., Holder, A., Swarts, B., Van Strijp, T. and Cloete, A., 2016. Extension of the Cullinan Diamond Mine No. 1 Shaft underneath the existing operating shaft. *Journal of the Southern African Institute of Mining and Metallurgy*, 116(8).

Khoza, K.R., Hingston, E.D.C., Mtshali, S., Khumalo, C. and Mabogo, N., 2019. The Use of JBlock in the Analysis of Potential Rock Falls at the Magdalena Colliery, Dundee, South Africa. In: *IAEG/AEG Annual Meeting Proceedings, San Francisco, California, 2018-Volume 1: Slope Stability: Case Histories, Landslide Mapping, Emerging Technologies*. Springer. pp.101–109.

Metropolis, N. and Ulam, S., 1949. The monte carlo method. *Journal of the American statistical association*, 44(247), pp.335–341.

Mine Health and Safety Inspectorate, n.d. *Annual reports of the Mine Health and Safety Inspectorate: 2016-2020*.

Netshilaphala, V. and Zvarivadza, T., 2022. Fall of ground management through underground joint mapping: shallow chrome mining case study. *Geotechnical and Geological Engineering*, 40(4), pp.2231–2254.

Nezomba, E., 2012. *Use of joint trace data to evaluate stability of mining excavations, and validation against underground observations*. University of the Witwatersrand.

Sewnun, D., Joughin, W.C., Armstrong, R. and Cooper, A., 2017. Keyblock stability analysis of longhole stopes. In: *ISRM AfriRock-Rock Mechanics for Africa*. ISRM. p.ISRM-AFRIROCK.

Warburton, P.M., 1981. *Vector Stability Analysis of an Arbitrary Polyhedral Rock Block with any Number of Free Faces. Int. J. Rock Mech. Min. Sci.& Geomech. Abstr.*

Wu, W., Zhuang, X., Zhu, H., Liu, X. and Ma, G., 2017. Centroid sliding pyramid method for removability and stability analysis of fractured hard rock. *Acta Geotechnica*, [online] 12(3), pp.627–644. https://doi.org/10.1007/s11440-016-0510-4.

Yan, J., Chen, J., Zhang, Y., Liu, Y., Zhao, X., Xue, J., Zhu, C., Mehmood, Q. and Wang, Q., 2023. Semi-automatic extraction of dangerous rock blocks from jointed rock exposures based on a discontinuity trace map. *Computers and Geotechnics*, 156. https://doi.org/10.1016/j.compgeo.2023.105265.



Christiaan van Rooyen

Rock Engineering Manager
Glencore

I started my mining career at Lonmin Platinum in 2001 and became a miner by 2003. I joined the Rock Engineering team in 2008 and achieved the Strata Control certificate in the same year. I obtained the Rock Mechanics certificate in 2012 and was appointed as a Rock Engineer shortly after. The advanced Rock Engineering certificate came along in 2018. I joined Marula Platinum as Rock Engineering Manager in 2022. I graduated from the University of the Witwatersrand in 2024 with an MSc in mining engineering, specializing in Rock Engineering. I joined Glencore early in 2025 as Rock Engineering Manager.

Application of large-scale finite element method simulations to determine geomechanical hazard during room-and-pillar mining under a tectonic fault

K. Fuławka[1], L. Stolecki[1], R. Kołodziej[2]

[1]KGHM CUPRUM Ltd, Poland
[2]KGHM Polska Miedź S.A, Poland

The issue of geomechanical hazards manifested by roof falls, rock bursts and induced seismicity has been one of the main aspects accompanying the exploitation of copper deposits in the Legnica Glogow Copper Basin region, Poland, in recent years. With the constantly increasing depth of deposits, the scale of hazards increases, negatively affecting the safety and continuity of mining operations. The problem becomes even more pressing in the case of the necessity to conduct exploitation under tectonic faults. Disturbance of the equilibrium state in such areas can often result in the release of high-energy tremors and serious rock bursts. It is therefore important to design exploitation in the safest and most effective way possible, based on the data collected in continuous manner in an underground site. One of the tools enabling the data-driven prediction of the impact of mining operations on the stability of excavations and their tendency to failure as a result of conducted operations are large-scale 3D numerical simulations with the finite element method. This paper presents the results of 3D non-linear finite element method-based numerical simulations of exploitation conducted under a tectonic fault in one of the Polish underground copper mines. The computational assumptions and the method of model validation are described and discussed. Finally, the applicability of the proposed approach in regular exploitation of the room-pillar system at great depths has been defined.

INTRODUCTION

Underground mining of deposits due to the necessity of exploiting large areas of the rock mass significantly disturbs the state of primary equilibrium (Liu, 2011; Askaripour *et al*., 2022, Yetkin *et al*., 2024). Disturbance of this state often leads to instability within the mining excavations and in many cases can lead to phenomena such as mining tremors, rock bursts and local roof collapses (Semenova & Kulkova, 2021). Additionally, with each year the problem becomes more and more critial because many underground mines are forced to operate at greater and greater depths (Fuławka *et al*., 2018a). As a result, the scale and frequency of geomechanical hazards increase with each year, leading to numerous accidents and significantly disturbing the exploitation process. It is therefore important to pay attention to the appropriate monitoring of hazards and, subsequently, to the development of methods for estimating and predicting the risk of adverse events. In geomechanical aspects, numerical modelling may be an appropriate tool. In recent years, many studies have proven the usefulness of numerical simulations in assessing the change in the stress state with advancing mining operations. Pytel *et al*., (2024), based on finite element (FEM) simulations, analysed the potential for rock outbursts in excavations located at depths exceeding 1 km. Fuławka *et al.*

In the research (Fulawka *et al*., 2024a, 2024b; Tomás, 2024) large-scale numerical models were used to determine zones with an increased risk of seismic hazard. In turn, Burtan *et al*., (2024) utilised FEM-based simulations for the purposes of analysis of geomechanical and technical aspects of torpedo blasting in areas subjected to mining-induced seismicity. FEM analyses were also used for dynamic calculations. The study (Baranowski *et al*., 2019) presented an approach to the design of destress blasting based on the results of dynamic simulations in which the ability of seismic waves to amplify and the influence of different timing variants on the safety margin within the roof layers were analysed. Geomechanical problems can also be successfully solved using discontinuous methods such as discrete element method (DEM) and finite DEM (FDEM). In the works (Che *et al*., 2020; Varelija & Hartlieb 2024) DEM simulations were used to determine the interaction of the anchor support with the rock mass and the simulation results were used to optimise the selection of the support for the given geological and mining conditions. Rock mass-rock bolt interaction may be successfully analysed also with the use of FDEM approach both in 2D and 3D (Wang *et al*., 2020; Li *et al*., 2022; Du *et al*., 2025). DEM and FDEM methods, due to the discontinuous nature of calculation, are excellent for geomechanical simulations in which it is necessary to take into account all kinds of cracks and delaminations. Unfortunately, discontinuous methods are also very demanding in terms of computational power, so at least for now they are not an optimal tool for large-scale simulations. Therefore, to prepare models with dimensions of several cubic kilometres, simulations based on continuous methods such as FEM are recommended. In this paper, attempts were made to determine the geochemical hazard associated with the exploitation of the deposit using the room-pillar system under the tectonic fault with the use of 3D FEM-based large-scale numerical simulations. Additionally, based on the simulation results, recommendations were made for the design of mining operations under the tectonic fault with emphasis on the direction of the front advance.

Material and methods

Reliable numerical simulations require calibration of the model. In practice, FEM simulations are most often calibrated based on the results of laboratory tests of rock strength. Unfortunately, as the author's experience shows, this method, although effective for small geometries, is not applicable to the construction of large-scale models with a volume of several cubic kilometres. As shown in the works (Fuławka 2024a, 2024b), calibration of large-scale models can be successfully carried out based on data on displacements recorded at the level of mining excavations. Having information on convergence, one can compare the results at selected points of the numerical model with the results of in situ measurements and then, based on the results of the comparison, try to adjust (usually reduce) the rock parameters to the extent that allows for obtaining correlation of measurements with the results of numerical calculations. Figure 1 shows the process of preparing and calibrating the numerical model for the purposes of this analysis.

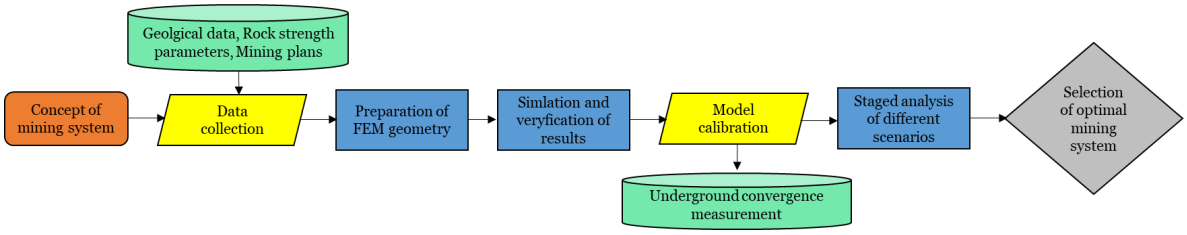


Figure 1. Flow chart of numerical model preparation.

Geology and rock strength

The analysis began with the construction of a 3-dimensional geological model. Information from geological boreholes that were drilled from the surface to several dozen or several hundred metres below the deposits was entered into the model. The locations of the boreholes and their stratigraphic profiles are presented in Figure 2.

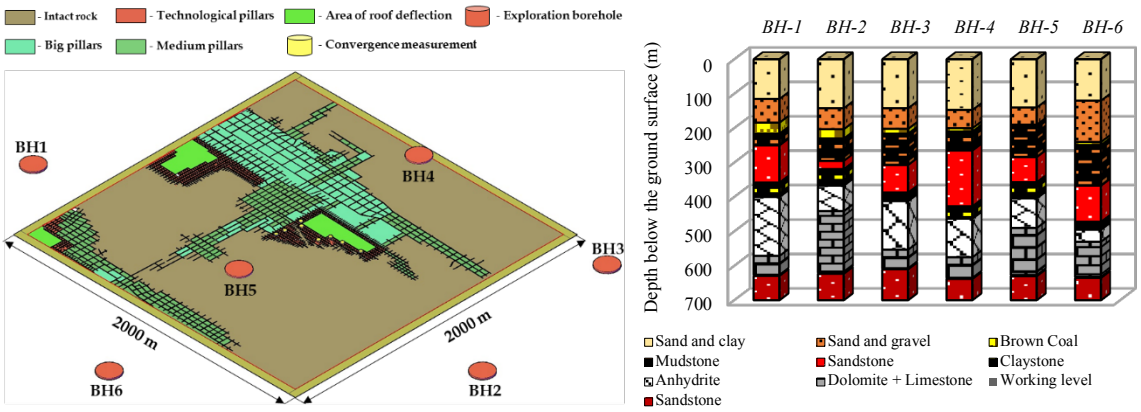


Figure 2. Geometry of workings and location of exploration boreholes (left) and stratigraphic profiles of boreholes located in the surrounding of analysed mining panel (right).

The geometry of the model was prepared in a full-scale system without simplifications. This means that the geometry of the excavations is exactly the same as the geometry of workings periodically determined by the underground geodesy department. Additionally, the model takes into account all geological layers from the level of the floor of the excavations to the ground surface. Strength tests were carried out for each layer, while in the case of the direct floor and direct roof strata, rock samples were taken multiple times at intervals of several dozen centimetres. This ensured proper investigation of the roof and floor conditions in the surroundings of the analysed excavations. Figure 3 shows the strength profiles of rock layers in the roof and floor of the excavations.

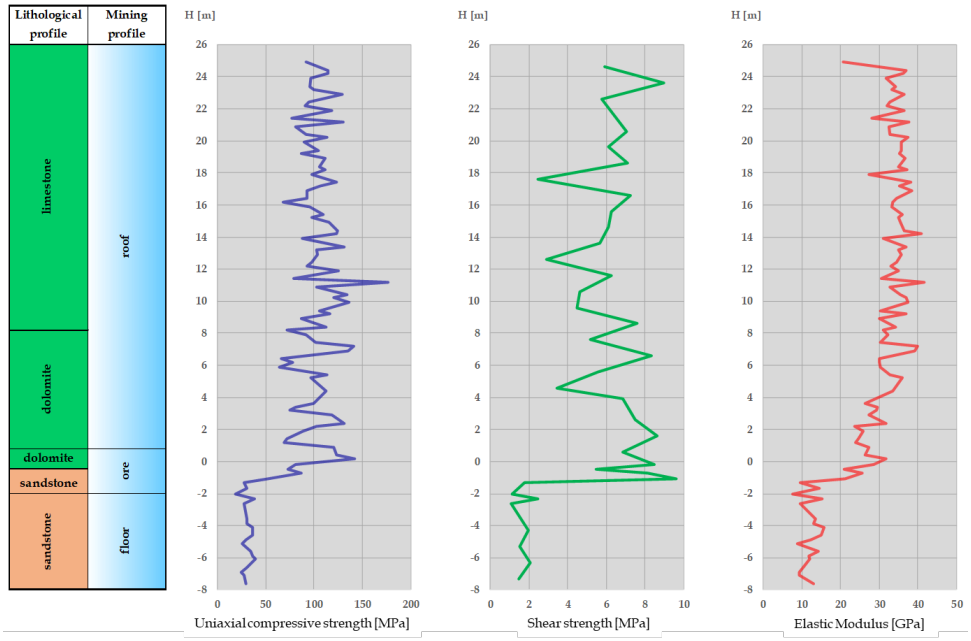


Figure 3. Geometry of workings and location of exploration boreholes (left) and stratigraphic profiles of boreholes located in surrounding of analysed mining panel (right).

Underground data collection

For calibration purposes, convergence measurements were carried out over several months at eight locations. The measurements were carried out using mechanical convergence meters and data readings were performed once a day. The exact operating principle of the convergometers used in Polish copper ore mines has been described in a paper (Fuławka *et al*., 2018b). The measurements were performed in three 3-month time intervals, which correspond to the subsequent stages of numerical simulations.

Period 1 covered months 1-3; Period 2 covered months 4-6 and Period 3 covered months 7-9. Figure 4 shows the location of the convergence meters and the results of 3-month measurements along with the average values for the analysed mining panel.

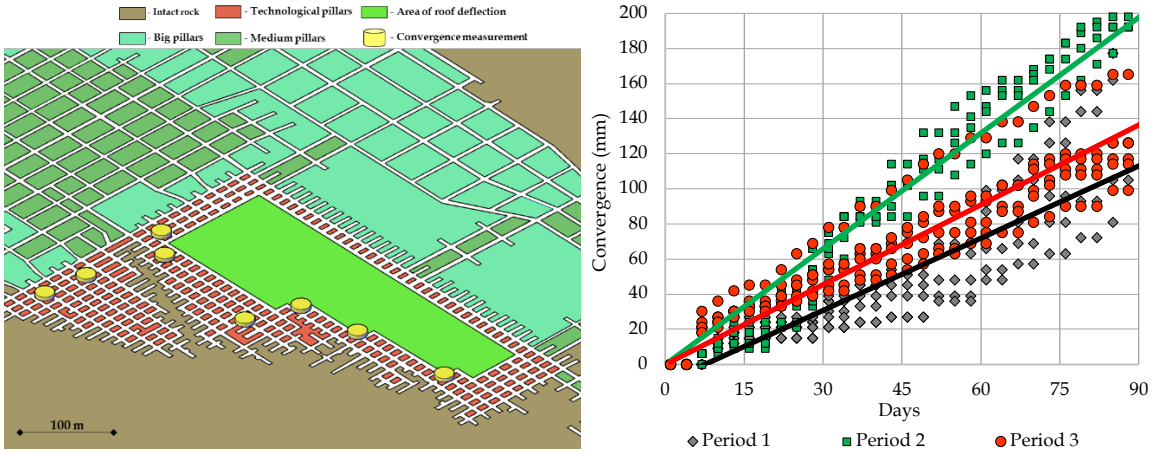


Figure 4. Location of convergence measurement sites (left) and results of long-term convergence measurement (right).

Numerical model preparation and validation

In LGCB area the deposit is located on the boundary of stiff carbonate layers (at the top of the excavations) and hard sandstone layers (at the bottom of the excavations). Therefore, the Generalised Hoek-Brown criterion (GHB) was selected as a representative model for simulating rock behaviour (Figure 5). The GHB criterion allows for combining rock strength parameters with geological observations using rock classification systems such as GSI or RMR.

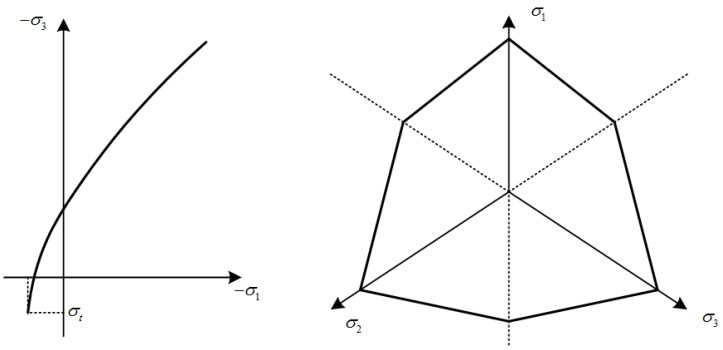


Figure 5. Graphical representation of yield criterion (left) and failure surface in principal stress plane (right) for GHB criterion.

The main nonlinear parameters of the Generalised Hoek-Brown criterion are as follows.

$$m_b = m_i exp\left(\frac{GSI-100}{28-14D}\right) \quad [1]$$

$$s = exp\left(\frac{GSI-100}{9-3D}\right) \quad [2]$$

$$a = \frac{1}{2} + \frac{1}{6}\left(e^{\frac{-GSI}{15}} - e^{\frac{-20}{3}}\right) \quad [3]$$

where: *GSI* – empirical parameter which relates the failure criterion to geological observations in in-situ conditions; m_i - material constant for the intact rock; *D* - disturbance factor which depends on damage level of rock mass (from 0-intact rock mass to 1-very disturbed rock mass).

The calculations were performed using GTS NX software for advanced modelling of three-dimensional, nonlinear geotechnical problems. The model discretisation was carried out based on a hybrid approach, i.e., a mix of tetragonal, pyramidal and hexahedral elements. This allowed for a good representation of the complex geometry of the mining panel while maintaining good quality of the mesh. To increase the accuracy of the analysis, the elements located at the deposit level were divided into backfilling zone, intact rock zone, large pillars zone (area over 1600 m^2), medium-size pillars zone (area between 120 m^2 and 1599 m^2) and technological pillars zone (area under 119 m^2) (Figure 6). Each of these elements had separate strength parameters assigned, and if necessary, modifying the parameters did not generate a global change in the results. Additionally, a series of tectonic faults with a throw of 15 to 25 m were modelled above the deposit. The faults were filled with loose material (sand) to simulate a weak contact at the boundary of two layers.

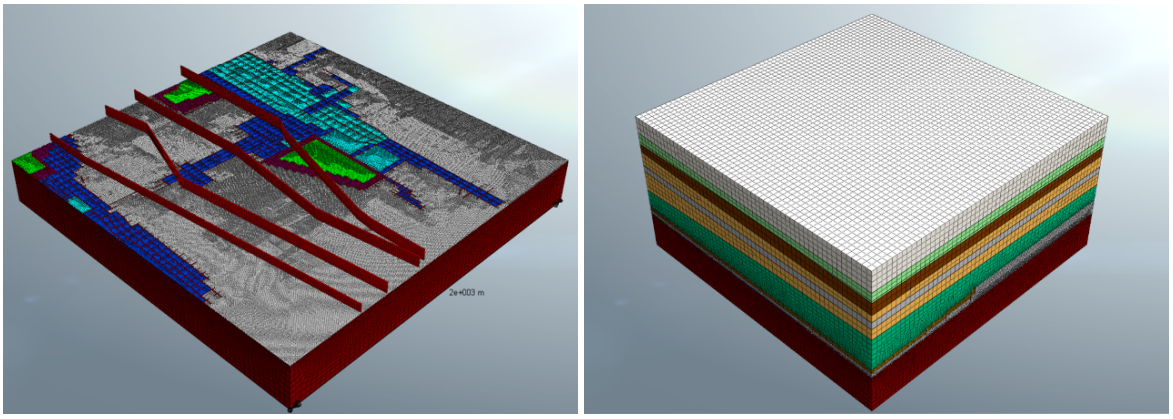


Figure 6. Division of the model into zones with different rock strengths (left) and isometric projection of the entire computational model (right).

Figure 7 shows the analysed scenarios of exploitation under the fault.

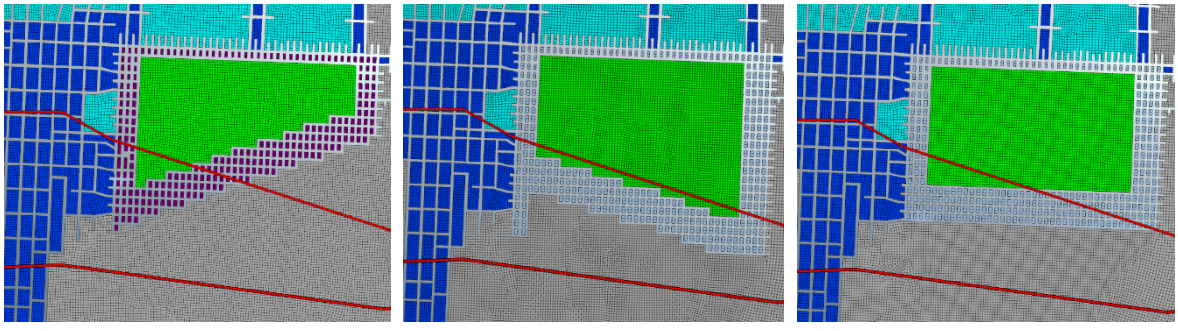


Figure 7. Considered exploitation scenarios: Mining direction along the fault line (left); mining direction perpendicular to the fault line (centre); regular mining front not adapted to the fault line (right).

Results and discussion

In the first phase of calculations, the model was calibrated by comparing the results of underground convergence measurements for three three-month calculation intervals. Then, with calibrated strength data, the influence of different exploitation scenarios on the stability of faults was analysed.

Model calibration

The excavations are located in medium-strength sandstone layers. Therefore, the parameters from the laboratory strength tests of the sandstone rocks were assigned to the elements located at the level of the deposit, such as pillars and intact rock mass. The liquidation zone is filled with dry backfilling, therefore in the model this area was filled with loose material (sand) and the Coulomb-Mohr strength criterion was applied. The input parameters of the sandstone located at the excavation level are presented in Table I.

Table I. Parameters of intact rock mass at the excavation level

Parameter	UCS of Intact rock	Elastic modulus *Es*	Cohesion *c*	Friction angle ϕ	Poisson ratio *v*	Density ρ	m_i
Unit	MPa	GPa	MPa	°	-	g/cm^3	-
Value	40,0	10.6	20.5	32	0.22	2.69	12

The model calibration consists of reducing the strength parameters of rocks by reducing the GSI parameter and increasing the D parameter. These parameters were modified separately for each zone located at the level of the deposit. Details of the Hoek-Brown nonlinear parameters for subsequent calculation iterations are presented in Table II.

Table II. Calculation of non-linear parameter for GHB criteria

Non-linear parameters	**Intact rock mass**	**Big Pillars (area over 1600 m²)**	**Medium-size Pillars (area between 120 m² and 1599 m²)**	**Technological pillars (area under 119 m²)**	**Roof deflection area**
First iteration of calculations					
GSI	100	90	80	70	M-C failure criterion
m_b	12	8.39	5.66	3.6489	
s	1.0	0.3291	0.1003	0.0281	
D	0.0	0.0	0.1	0.2	
a	0.5	0.5002	0.5006	0.5013	
Second iteration of calculations					
GSI	100	90	70	60	M-C failure criterion
m_b	12	8.24	3.65	2.24	
s	1.0	0.3168	0.0281	0.0072	
D	0.0	0.1	0.2	0.3	
a	0.5	0.5002	0.5014	0.5028	
Third iteration of calculations					
GSI	100	80	60	50	M-C failure criterion
m_b	12	5.66	2.2350	1.2876	
s	1.0	0.1004	0.0072	0.0016	
D	0.0	0.1	0.3	0.4	
a	0.5	0.5006	0.5028	0.5057	
Fourth iteration of calculations					
GSI	100	70	50	40	M-C failure criterion
m_b	12	3.88	1.47	0.69	
s	1.0	0.0318	0.0021	0.0006	
D	0.0	0.1	0.3	0.5	
a	0.5	0.5014	0.5057	0.5114	

Figure 8 shows the degree of matching of displacements resulting from successive computational iterations to the convergence measurements carried out in-situ.

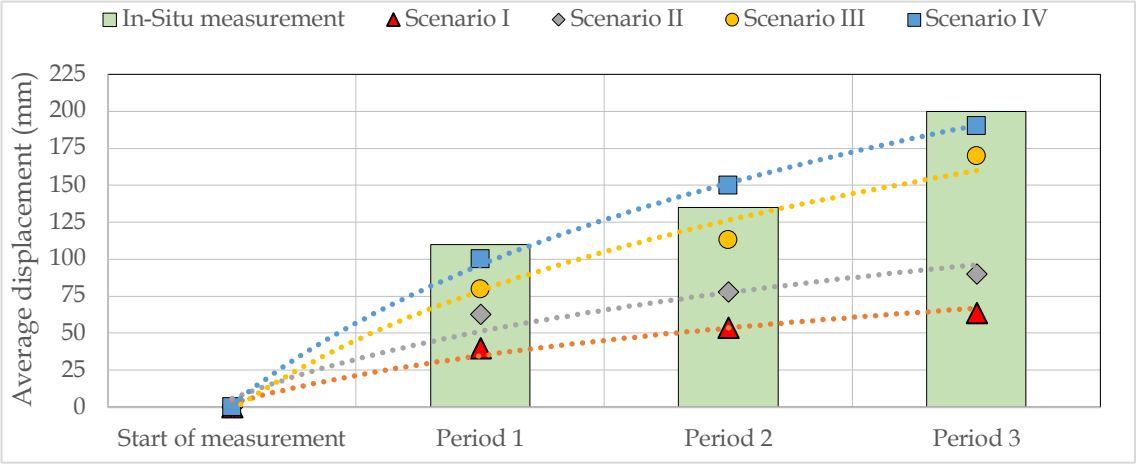


Figure 8. Matching the results of numerical simulations to underground measurements.

Taking the above into account, the parameters used in the fourth calculation iteration were used to calculate the impact of exploitation on the stability of fault zones.

The influence of the mining pattern on the fault zone

The fault that was located in the immediate vicinity of the mining operation at the time of the analysis was subjected to numerical analysis. The fault zone subjected to detailed analysis is shown in Figure 9.

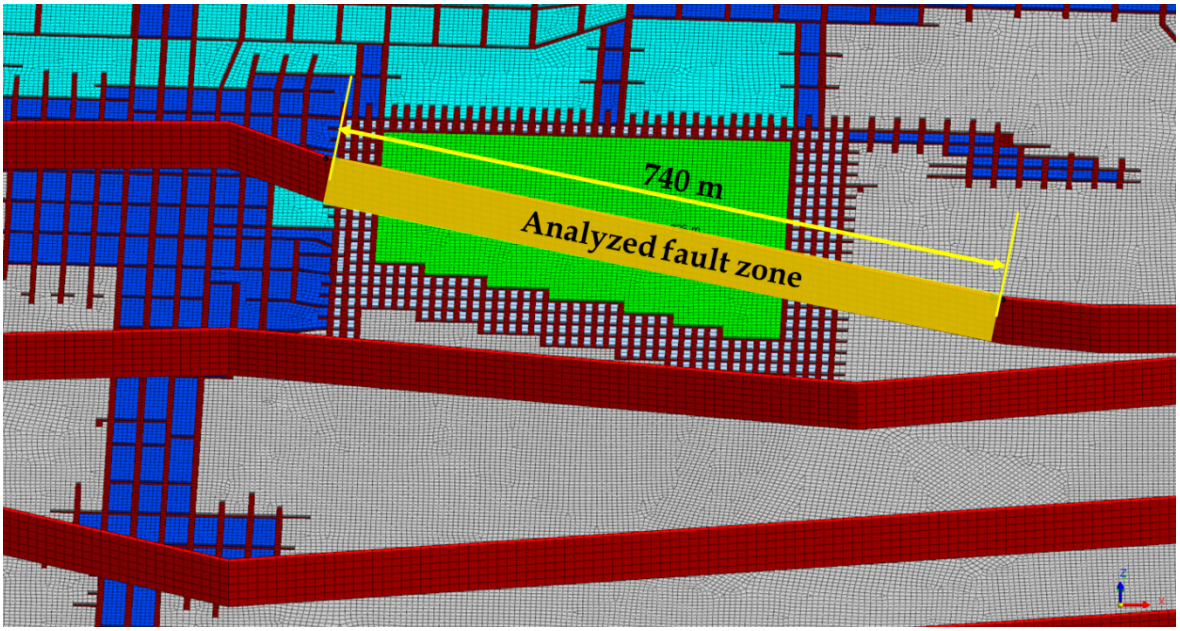


Figure 9. The area of the fault zone (yellow part) was subjected to detailed analysis.

As it results from numerical simulations, conducting mining in the direction along the fault line affects the fault zone, especially in the area located between the mining front line and the backfilling area. Nevertheless, mining with the use of the room-pillar system according to the scheme presented in Figure 10 should not lead to a dynamic loss of stability of the fault and pillars, because all areas of the model are characterised by an appropriate safety margin SF>1.5.

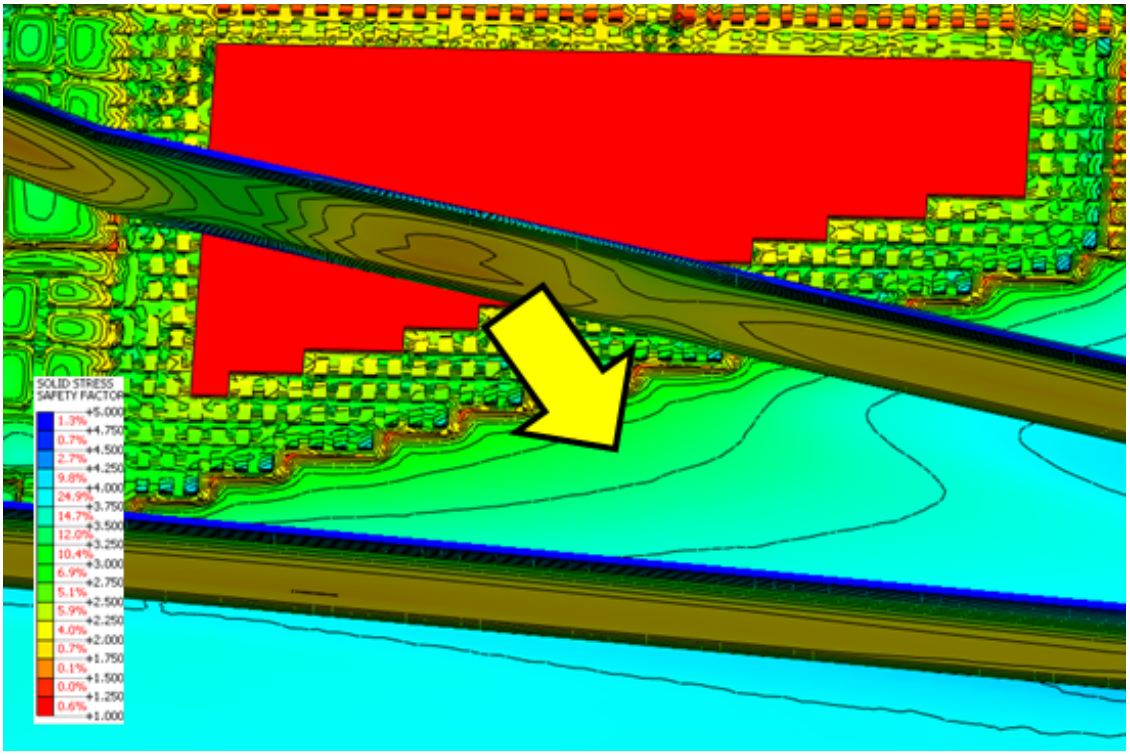


Figure 10. SF distribution for mining with front direction along the fault line.

In the case of mining perpendicular to the fault line, a significant decrease in the SF is observed in the central part of the fault (Figure 11). Such a situation in the long term may lead to local collapses of the roof strata, and in extreme cases may even lead to activation of the fault, as a result of which seismic tremors and rock bursts may occur.

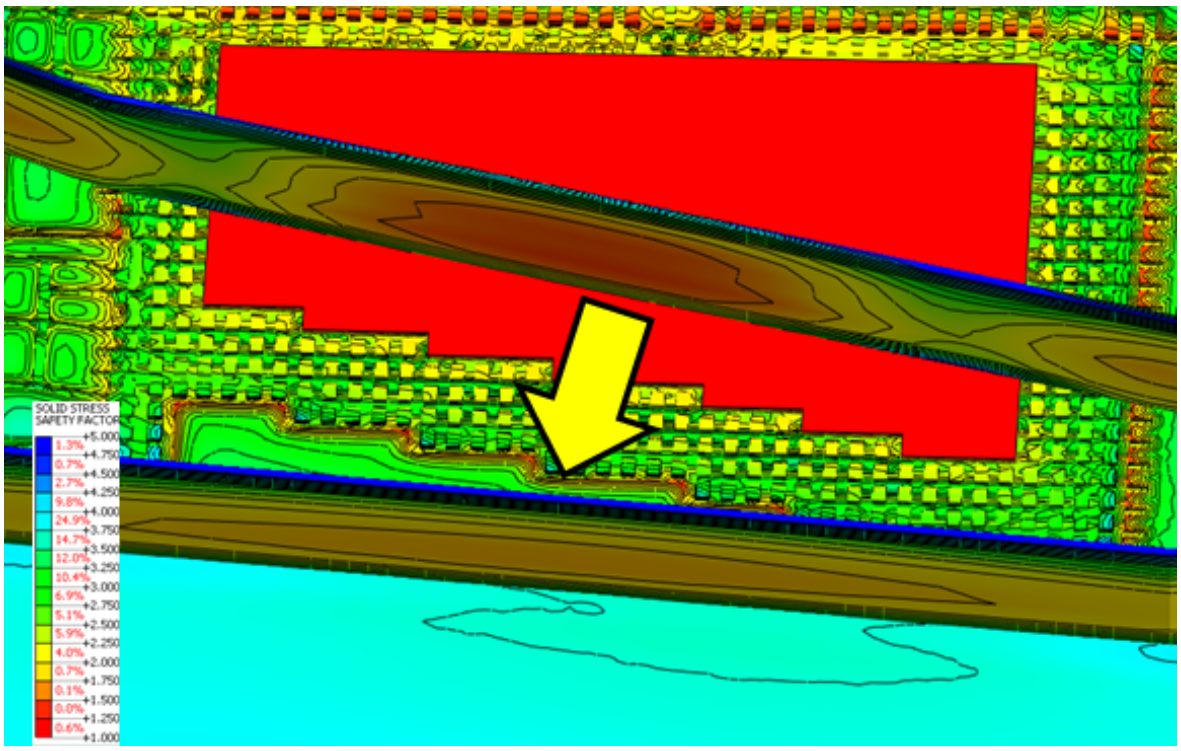


Figure 11. SF distribution for mining with front direction perpendicular to the fault line.

Also, it seems to be disadvantageous to conduct mining operations with a regular front line without taking into account the direction of the fault zones. It is generally assumed that a regular mining front minimises the possibility of generating local zones of increased stress, and consequently has a beneficial effect on the safety of mining operations. Unfortunately, this rule does not apply to situations in which mining is conducted under a tectonic fault. As can be seen from the numerical analysis, the moment the front passes through the fault zone generates a clear decrease in SF in the fault zone, which in turn may translate into an increase in geomechanical hazard (Figure 11).

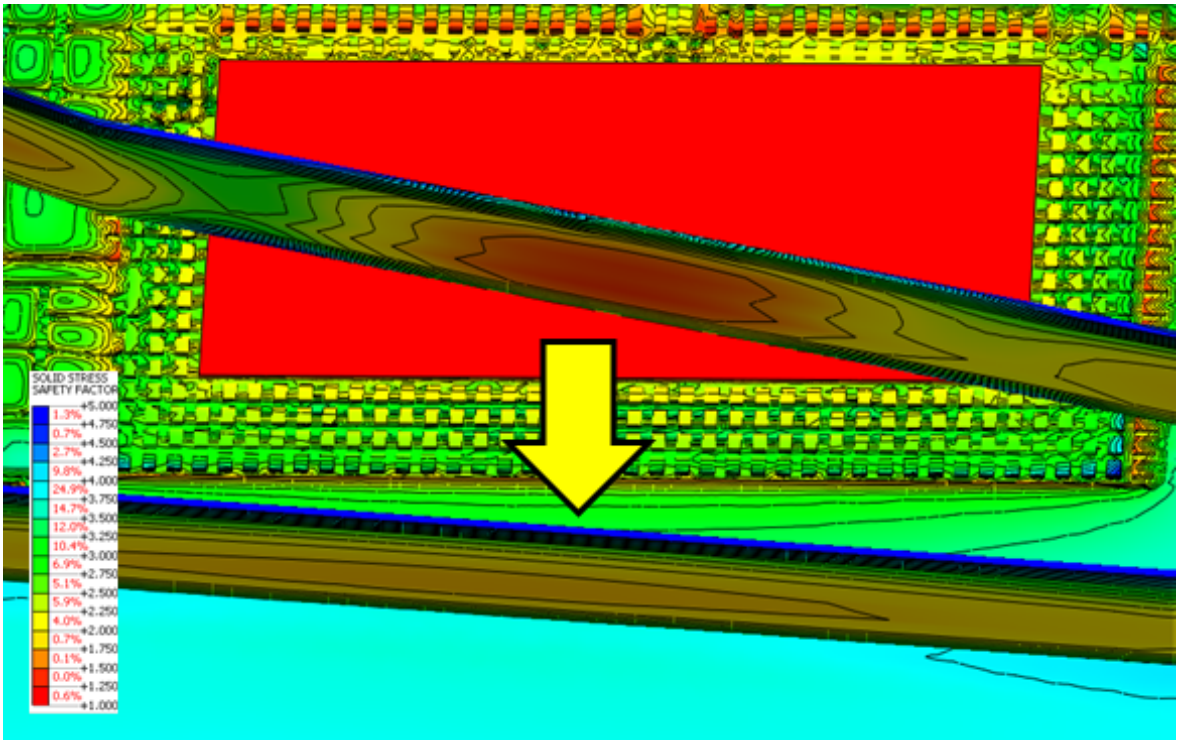


Figure 11. Regular mining front not adapted to the fault line.

Figures 12 and 13 present a detailed comparative analysis of displacements and stability indicators in the analysed tectonic fault zone. As a result of the analysis, mining along the fault generates approximately 10% smaller vertical displacements in the fault zone. Additionally, the observed subsidence is stretched over a smaller distance, which is beneficial from the point of view of stress dispersion in the roof layers of the excavations. On the other hand, scenarios in which mining operations are conducted according to Scenarios II and III generate similar displacements in the fault zone.

In extreme cases, displacements generated by mining according to scenario I were 33% smaller than displacements generated by mining according to Scenario II and 28% smaller compared to Scenario III. This situation was observed in the vicinity of 390 m of the fault.

Interesting conclusions can also be drawn from the analysis of the Safety Factor distribution. In the case of exploitation according to Scenario I, SF is greater than 1.5 over the entire analysed length of the fault. In the case of the remaining scenarios, these values are significantly lower, and in the case of Scenario II, as much as 23% of the fault is characterised by a stability index lower than 1.5 (with a minimum value of SF=1.36), while in the case of Scenario III it is over 21% of the total fault length (with a minimum value of SF=1.29).

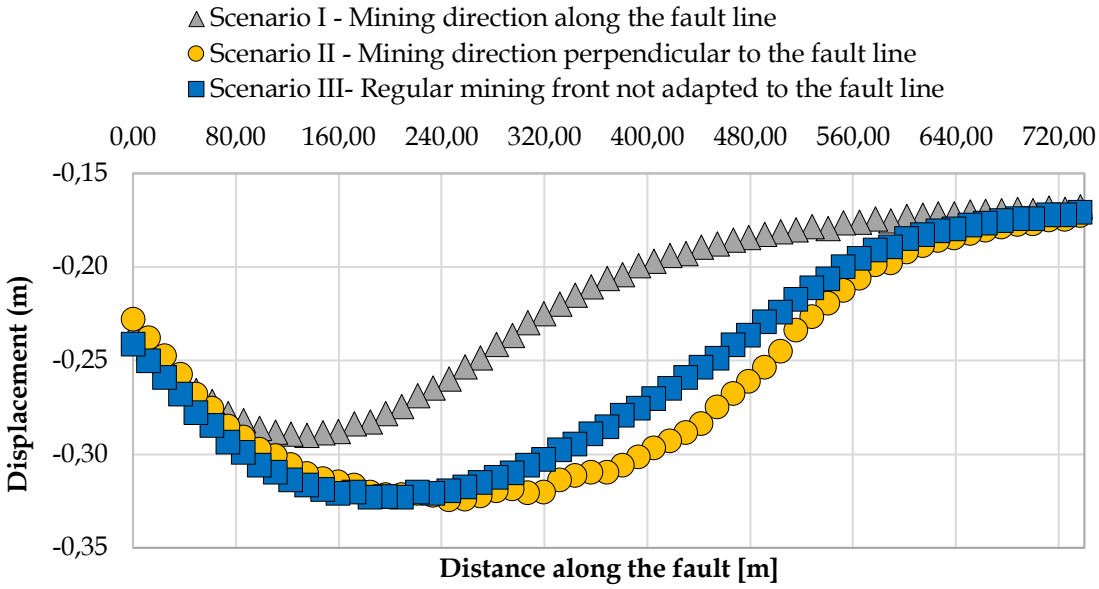


Figure 12. Distribution of vertical displacements along the tectonic fault for the analysed scenarios.

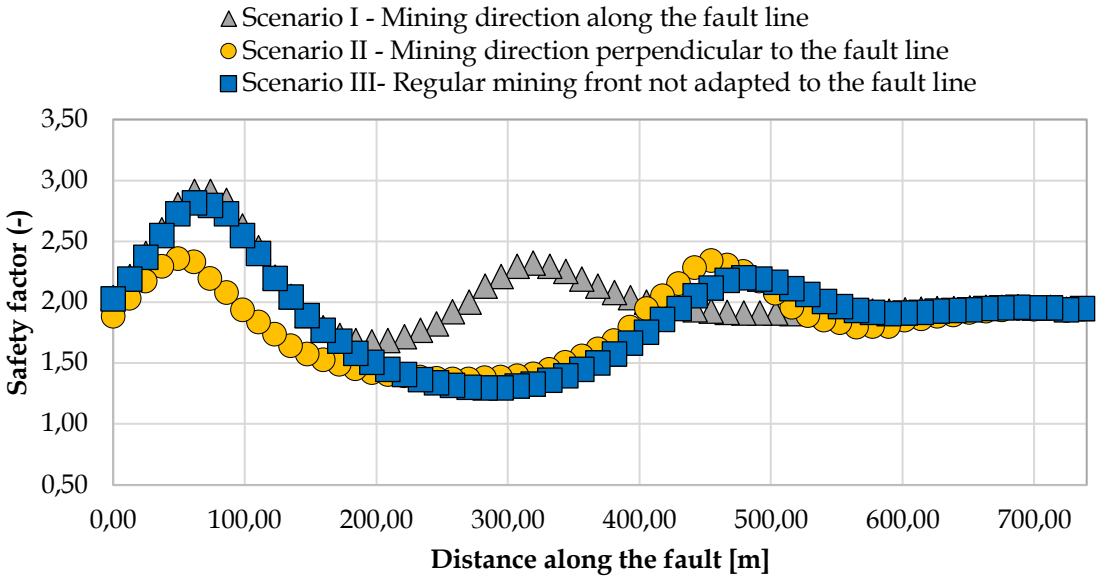


Figure 13. Distribution of Safety Factor along the tectonic fault for the analysed scenarios.

CONCLUSION

In this analysis, attempts were made to determine the effect of different variants of mining using the room-and-pillar system on the stability of a tectonic fault located above the excavation area. The analysis was performed based on a series of large-scale numerical simulations using the 3-dimensional finite element method. In the first phase of the study, attempts were made to calibrate the numerical model by matching the simulation results to underground measurements of displacements within the mining excavations. The matching was carried out by gradually reducing the strength parameters of rocks at the deposit level using the nonlinear parameters of the GHB criterion and the empirical GSI scale. After four computational iterations, a satisfactory fit of the model was obtained, which allowed for making a decision on the final selection of rock strength parameters for further calculations. In the second phase of the study, three different mining systems under the fault were analysed and the effect of individual

solutions on displacements and stability indicators within the fault zone was analysed. As it results from the analysis, the direction of mining affects not only the range of possible fault activation but also significantly affects the value of the SF index. Ultimately, it was found that the optimal solution is to conduct mining with direction along the tectonic fault line. This minimises the zone of possible loss of stability, and in the long term should be beneficial from the point of view of stress dispersion in the fault zone.

Additionally, based on the conducted research, it was found that numerical simulations can be a useful tool for quantitative mining design, provided that the calculation model is properly calibrated beforehand.

Further research will be aimed at attempts to systematise the methodology related to the reduction of rock strength parameters. This is aimed at reducing the required load iterations in the model validation phase while maintaining an appropriate level of simulation accuracy.

ACKNOWLEDGEMENTS

This paper was prepared within the framework of the AGEMERA project 'Agile Exploration and Geo-modelling for European Critical Raw materials'. The project received funding from the European Union's Horizon Europe Research and Innovation Program under grant agreement No. 101058178.

REFERENCES

Askaripour, M., Saeidi, A., Rouleau, A., & Mercier-Langevin, P. (2022). Rockburst in underground excavations: A review of mechanism, classification, and prediction methods. Underground Space, S2467967422000022. https://doi.org/10.1016/j.undsp.2021.11.008

Baranowski, P., Damaziak, K., Mazurkiewicz, Ł., Mertuszka, P., Pytel, W., Małachowski, J., Pałac-Walko, B., & Jones, T. (2019). Destress Blasting of Rock Mass: Multiscale Modelling and Simulation. Shock and Vibration, 2019, 1–11. https://doi.org/10.1155/2019/2878969

Baranowski, P., Mazurkiewicz, Ł., Małachowski, J., & Pytlik, M. (2020). Experimental testing and numerical simulations of blast-induced fracture of dolomite rock. Meccanica, 55(12), 2337–2352. https://doi.org/10.1007/s11012-020-01223-0

Burtan, Z., Cieślik, J., Chlebowski, D., Piasecki, P., & Gzik, K. (2024). Geomechanical and Technical Aspects of Torpedo Blasting under Seismic and Rockburst Hazard Conditions in Legnica–Glogow Copper District Mines. Energies, 17(5), 1174. https://doi.org/10.3390/en17051174

Che, N., Wang, H., & Jiang, M. (2020). DEM investigation of rock/bolt mechanical behaviour in pull-out tests. Particuology, 52, 10–27. https://doi.org/10.1016/j.partic.2019.12.006

Du, C., Cheng, Y., Liu, Q., Cheng, Z., Liu, Y., Lu, Y., & Jiang, H. (2025). A new type of rockbolt model in 3D FDEM and its application to tunnel excavation. Tunnelling and Underground Space Technology, 155, 106210. https://doi.org/10.1016/j.tust.2024.106210

Fuławka, K., Pytel, W., & Mertuszka, P. (2018). The effect of selected rockburst prevention measures on seismic activity – Case study from the Rudna copper mine. Journal of Sustainable Mining, 17(1). https://doi.org/10.46873/2300-3960.1116

Fuławka, K., Mertuszka, P., & Pytel, W. (2018). Monitoring of the stability of underground workings in Polish copper mines conditions. E3S Web of Conferences, 29, 00008. https://doi.org/10.1051/e3sconf/20182900008

Fulawka, K., Mertuszka, P., Solecki, L., Szumny, M., & Kolodziej, R. (2024). Identification Of Areas Prone To Seismic Activity Occurrence Using 3d Fem Numerical Simulations. 311–320. https://doi.org/10.5593/sgem2024/1.1/s03.41

Fuławka, K., Stolecki, L., Jaśkiewicz-Proć, I., & Kołodziej, R. (2024). The Use Of Large-Scale 3D Numerical Modeling to Identify Areas of Increased Seismic Risk in Polish Underground Copper Mines. 7th International Conference on Geotechnical and Geophysical Site Characterization. 7th International Conference on Geotechnical and Geophysical Site Characterization. https://doi.org/10.23967/isc.2024.113

Li, N., Du, Z., Gao, F., Qi, F., Gao, H., Li, M., & Wang, X. (2022). Simulation Study on Mechanical Characteristics of Rock Bolt in Rock Mass with Bedding Separation Based on the Nonlinear Bond Slip Relationship. Geofluids, 2022, 1–11. https://doi.org/10.1155/2022/5279884

Liu, C. (2011). Distribution Laws of in-Situ Stress in Deep Underground Coal Mines. Procedia Engineering, 26, 909–917. https://doi.org/10.1016/j.proeng.2011.11.2255

Tomás, R., Cano, M., Riquelme, A., Pastor, J. L., Benavente, D., & Ordóñez, S. (2024). New Challenges in Rock Mechanics and Rock Engineering (1st ed.). CRC Press. https://doi.org/10.1201/9781003429234

Varelija, M., & Hartlieb, P. (2024). Designing Intelligent Rock Support Systems to Detect Gravity-Driven Wedges. Rock Mechanics and Rock Engineering. https://doi.org/10.1007/s00603-024-04039-6

Wang, W., Liu, Q., Ma, H., Lu, H., & Wang, Z. (2020). Numerical analysis of material modeling rock reinforcement in 2D FDEM and parameter study. Computers and Geotechnics, 126, 103767. https://doi.org/10.1016/j.compgeo.2020.103767



Krzysztof Fuławka

Assistant Professor in Rock Engineering Department
KGHM CUPRUM Ltd. Research & Development Centre

PhD Krzysztof Fuławka works as Assistant Professor in Rock Engineering Department of KGHM Cuprum Ltd Research and Development Centre. He received his doctoral degree in Mining Engineering at Wroclaw University of Science and Technology, Poland. He also obtained a postgraduate diploma in Applied Geophysics at AGH University of Science and Technology, Cracow, Poland. In last few years, Krzysztof has participated in numerous international research and scientific projects financed by Interreg BSR, Polish National Centre for Research and Development, Horizon 2020, Horizon Europe and EIT Raw Materials. He is an author and co-author of numerous research reports, scientific papers and pre-feasibility studies. His background is rock mechanics and numerical modelling as well as risk assessment and blasting technology. Krzysztof Fuławka is also a vice-chair of European Underground Laboratories Association (EUL).

Application of MEMS accelerometers for continuous near-field monitoring of mining-induced seismicity

L. Stolecki, K. Fuławka, P. Mertuszka

KGHM CUPRUM Ltd. Poland

Disturbance of the equilibrium state in rock mass resulting from underground mining often leads to excessive stress accumulation, ultimately leading to seismic activity. Monitoring seismicity in terms of tremor energy, its location and induced vibration parameters is therefore crucial to constructively plan mining operations and manage seismic hazards. However, the problem with most mines is the high cost of building a seismic network. High costs associated with purchasing equipment and installing stations lead to a situation in which the number of measurement stations in networks is often reduced to the necessary minimum. Depending on the layout, the costs of measurement equipment and recorders cover 60-80% of the total network construction costs. These cost constraints can be overcome by using low-cost seismic devices based on micro-electromechanical system (MEMS) technology. This paper presents multi-month measurements of seismic activity generated by mining activities in underground mines in the Legnica Glogow Copper Basin region in Poland. An analysis of the effectiveness of the MEMS-based devices in relation to the results of recording with standard piezoelectric, piezoresistive and force balance accelerometers has been achieved. The results of pilot measurements of the velocity of seismic wave propagation using an underground seismic monitoring network based on MEMS technology are presented. According to preliminary analyses, despite certain limitations, MEMS technology can be successfully used to build a mine seismic network.

INTRODUCTION

Vibrations induced by mining activities have an adverse effect on the safety of the mining crew and generate destructive loads on the surface and underground infrastructure (Cook, 1976; Witkowski *et al*., 2024). In order to establish the exact nature of the threat, it is necessary to develop an appropriate, local seismological network that allows for determining the parameters of tremors such as their location, energy and focal mechanism (Goldswain, 2020). Additionally, a well-developed network of seismic stations allows for determining the vibration magnitude and preparing ground motion prediction equations (Guo *et al*., 2011; Meyer, 2024).

Seismic monitoring can also be used for active measurements such as seismic tomography or seismic profiling (Jian *et al*., 2025). However, taking into account the relatively low energy of the vibration source, the network for this type of measurement must be characterised by appropriate measurement sensitivity. This applies to both the characteristics of the measuring devices and the number of sensors in the area of the monitored location (Kotyrba *et al*., 2023). Therefore, the area covered by the seismic network must be large enough to effectively record even low-magnitude events (Fuławka *et al*., 2020). However, the problem is the high cost of building and maintaining the monitoring network. According to authors' experience, regular seismic networks for monitoring induced seismicity are expensive to build and maintain.

For example, in Polish underground mines — depending on the layout — the costs of measurement equipment and recorders arer 60-80% of the total network construction costs. As a result, when planning a monitoring network, mining operators look for compromises between the ability to record seismic phenomena and the costs of building a measurement system (Fuławka *et al.*, 2022; Stolecki *et al*., 2024). On the other hand, smaller networks used for period active measurements — such as those designed for active seismic tomography — typically require a dense array of sensors and generate high installation and equipment costs. Due to the high cost of the seismic devices themselves, these networks are usually installed temporarily in mining excavations, strictly for the purpose of conducting one or several series of active measurements. Once the data collection is complete, the system is dismantled to minimise eventual expenses related to the destruction of components. This cost-driven limitation results in active tomography being employed only periodically in Polish underground mining, which significantly reduces its potential for continuous assessment of the rock mass condition and long-term monitoring of geomechanical changes. As a result, the very effective process of rock mass based on the velocity of seismic wave propagation becomes a tool used only periodically, which means that the mining operator does not receive current information about the state of the rock mass (Friedel *et al*., 1992; Wang *et al*., 2018). As recent experience has shown, a breakthrough solution in increasing the efficiency of seismic measurements may be devices based on MEMS technology, which is characterised by low energy consumption, satisfactory technical specifications and, above all, low costs compared to standard seismic devices (Fuławka *et al*., 2022; Sarmadi *et al*., 2023; Stolecki *et al*., 2024).

This paper presents the results of pilot measurements of seismicity induced by Polish underground copper mining using MEMS-based accelerometers. The analysis includes determining the applicability of new-generation devices for surface measurements, underground measurements, active seismic tomography and current monitoring of technological processes in underground mines.

MATERIAL AND METHODS

The test site for the purposes of this study was the Legnica Głogów Copper Basin (LGCB) region in Poland, where underground exploitation of copper and silver deposits has been conducted for over 60 years. The exploited area exceeds 500 km^2, and the depth of exploitation ranges from 600 to 1300 m below ground surface. A large exploitation area, constantly increasing depth of extraction and very strong rocks located in the roof layers determine the tendency of the rock mass to generate seismic activity. Figure 1 shows the location of tremors recorded in the LGCB area since 2014 with magnitudes ranging from 0.9 to 4.0. All tremors included in this research were classified as near-field because they were measured in close proximity—typically within a few kilometers—of a source that induces the seismicity (Fuławka *et al*., 2020). This term is especially relevant in contexts where human activity, such as mining, significantly alters subsurface stress distributions, leading to stress release and seismic events. The proximity of seismic sources to the monitoring of affected zones allows for higher-intensity ground motions, resulting from small perturbations in the local stress regime caused by mining operations (Orlecka-Sikora, 2010; Chodacki, 2016).

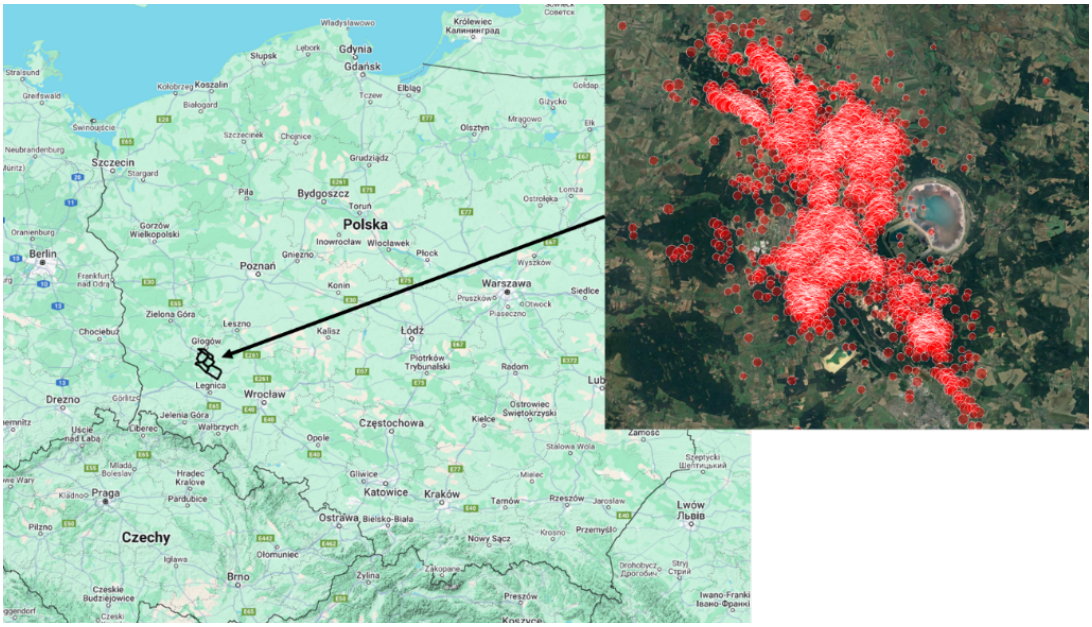


Figure 1. Location of mining-induced seismic tremors in LGCB area in the years 2014-2024 (EPISODES Platform, 2024).

Due to the high intensity of seismic activity in the LGCB area, it was found that this would be an ideal experimental site to determine the applicability of MEMS-based accelerometers for near-field monitoring.

Description of trial site

Excavation level is located at the boundary of Zechstein and Rotliegend and copper minerals are hosted by three main lithological rock types: sandstone, shale and dolomite (Figure 2).

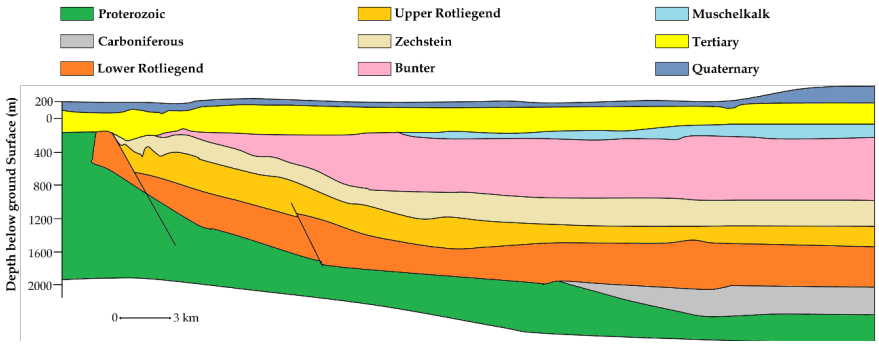


Figure 2. Geological cross-section of copper ore deposit in LGCB area.

Strong dolomite strata with uniaxial compressive strength (UCS) up to 260 MPa is located in the roof of workings, while the floor consists of weaker layers of sandstone characterised by UCS in the range of 80-100 MPa. The deposit is excavated with room-and-pillar mining with roof subsidence. In systems of this type, the deposit is mined by means of perpendicular rooms, creating technological pillars. In Polish copper mining, technological pillars refer exclusively to the pillars formed during the initial phase of mine development, known as the opening-out phase. These pillars are intentionally left unmined to provide immediate structural support as the excavation progresses, ensuring the stability of the roof and surrounding rock mass from the very beginning of mining operations. Then, in the second phase, the technological pillars are cut to the remnant/post critical size, which makes them yield and initiates the process of roof defection (Figure 3).

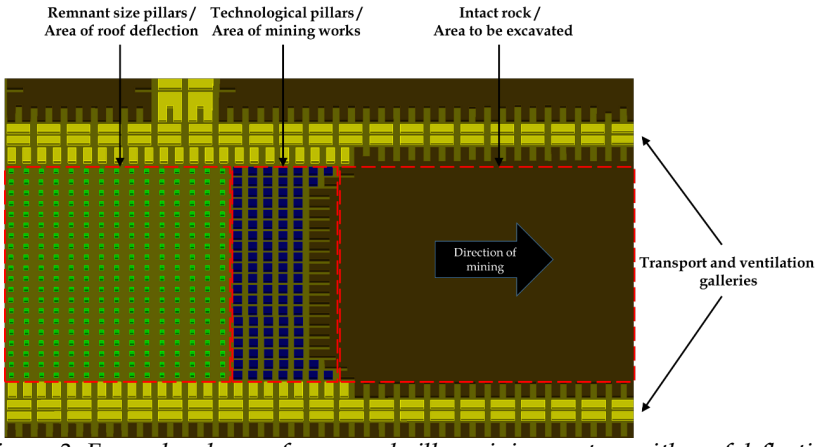


Figure 3. Example scheme of room and pillar mining system with roof deflection.

Selection of suitable devices based on field evaluation results

For the purposes of this analysis, pilot tests were conducted using two types of MEMS technology-based devices. The MEMS-IMU accelerometer ADIS16470 (Figure 4 - left) was used for surface monitoring of mining-induced seismicity in the LGCB region, while the low noise, low drift and low power 3-axis MEMS accelerometers ADXL355 (Figure 4-right) were used for near-field underground measurements. Both devices are manufactured by Analog Devices. During the field validation stage, a comparative analysis was carried out with the use of measuring devices used in mines in the LGCB region. The records of the ADIS16470 accelerometer were compared directly with the waveforms collected with the classic MR3003C accelerometer, while the ADXL355 accelerometers were validated by indirect comparison of results with data recorded by the underground seismic network built with Willmore MK III seismometers.

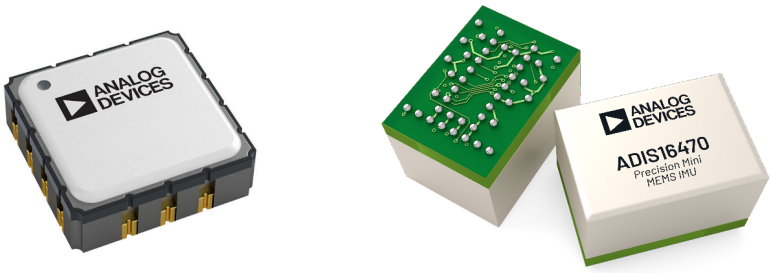


Figure 4. 3-axis MEMS accelerometers ADXL355 (left) and miniature MEMS inertial measurement unit ADIS16470 (right).

The technical parameters of devices used in this analysis are presented in Table I.

Table I. Main parameters of seismic devices used for this analysis

Parameter	Unit	ADIS16470	ADXL355	MR3003C	Willmore MK III
Resolution	Bit	32	20	24	12
Number of recording components	-	3-axial (X,Y,Z)	3-axial (X,Y,Z)	3-axial (X,Y,Z)	1-axial (vertical)
Sampling (set up during measurement)	Hz	250	500	250	500
Measuring range	g *or* mm	±40 g	±2 g	±4 g	± 2 mm
Operating temperature	°C	-25 to +85	−40 to +125	-20 to +70	-40 to +50
Noise density	$\frac{\mu g}{\sqrt{Hz}}$ or $\frac{m/s^2}{\sqrt{Hz}}$	23 $\frac{\mu g}{\sqrt{Hz}}$	25 $\frac{\mu g}{\sqrt{Hz}}$	Not specified	10^{-10} $\frac{m/s^2}{\sqrt{Hz}}$

Field validation of MEMS-based devices

Before the construction of prototype measurement systems, field verification of the effectiveness of low-cost MEMS devices was carried out, based on a comparative analysis of the recorded data with data collected using already existing seismic networks. The measurement methodology was simple: MEMS accelerometers were located in the immediate vicinity of standard seismological devices. Then, at specified distances from the measurement site, ground vibrations were generated by hitting the ground with a 10 g hammer. Vibration parameters such as amplitude, frequency and arrival time of the seismic wave into the measurement area were analysed. More on the data processing process and comparative analysis can be found in the literature (Fuławka *et al.*, 2022 and Stolecki *et al.*, 2024). The preliminary comparison of the MEMS-IMU ADIS16470 accelerometer with the classic MR3003C accelerometer leads to the conclusion that the sensitivity and dynamics of the low-cost devices are sufficient for near-field monitoring of seismic activity. As can be seen from the recorded waveforms, the data recorded by the two types of devices correlate both in terms of the amplitude distribution and enable effective identification of seismic wave arrival times (Figure 5). However, it can be observed that the standard accelerometer is slightly more effective in identifying low-frequency components, while having a lower level of self-noise in the 60-125 Hz range compared to the ADIS16470 accelerometer (Figure 6). Still, the differences are at an acceptable level and the results of the frequency analysis for both devices can be considered convergent.

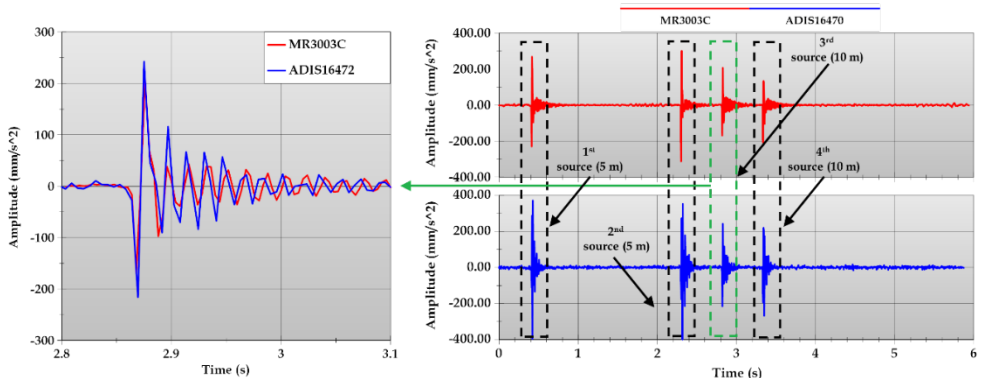


Figure 5. Recording of four hammer blows near the ADIS16472 MEMS-IMU accelerometer and the MR3003C accelerometer on the ground surface.

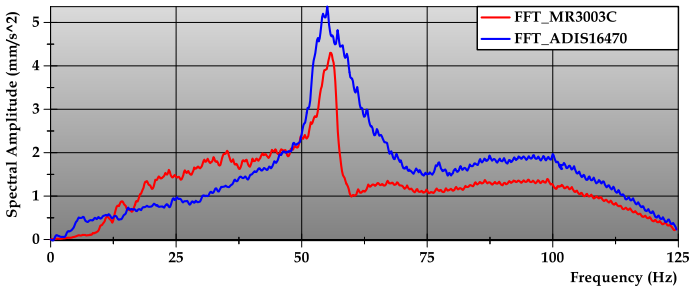


Figure 6. Comparison of Fast Fourier Transform analysis results for MR3003C (red) and ADIS16470 (blue) accelerometers.

Due to the above, a decision was made to start work on the construction of an autonomous surface measurement station using the MEMS-IMU ADIS16470 accelerometer. In the case of comparing data from the MEMS ADXL355 accelerometer with recordings from the Willmore MK III seismometer, vibrations were induced at a distance of 5 and 10 m from the measurement stations. Due to the lower measurement dynamics of seismometers, direct comparison of the time-frequency characteristics of waveforms recorded by different types of devices is pointless. Still, the general nature of the seismic waveform and the ability to identify arrival times on each device can be assessed. At the same time, it should be noted that the ADXL355 accelerometers are planned to be used as elements of a network for

active seismic tomography. In connection with this, the key parameter was the ability to effectively register the arrival times of P and S waves. As it turned out from the pilot analysis, the ADXL355 accelerometers enabled the identification of arrival times of seismic waves with an accuracy equal to or even better than the Willmore MK III seismometer (Figure 7). It should be noted that the tests were carried out in solid rock, i.e., rock salt. Frequency analysis in this case indicates large differences in spectral curves. Nevertheless, this is a situation that should be expected, as seismometers are generally better suited to measuring phenomena with lower frequencies compared to accelerometers. The presented spectral analysis shows that the dominant frequency recorded by the MEMS accelerometer is clearly higher than in the case of the Willmore MKIII seismometer (Figure 8). Additionally, based on the spectral analysis, it can be stated that due to the characteristics of the seismometer used, the measurement of high-intensity phenomena cannot be carried out in a fully efficient manner with its participation. On the other hand, it is clearly visible that the ADXL355 accelerometer is characterised by a relatively higher level of self-noise in the frequency range above 50 Hz compared to the analysed seismometer.

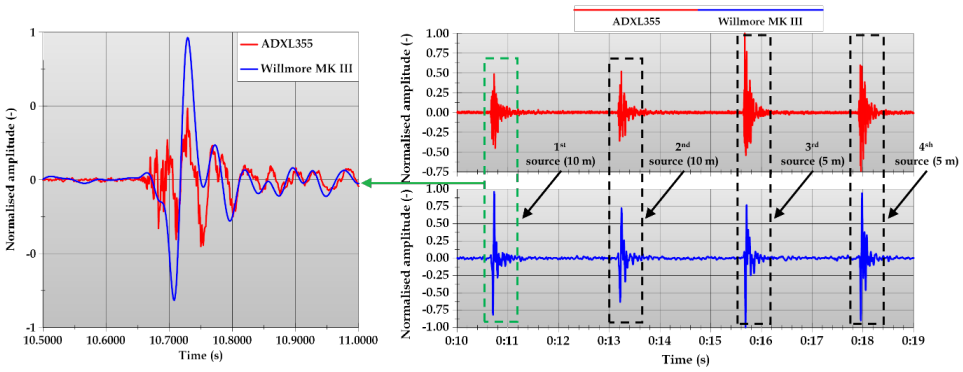


Figure 7. Recording of four hammer blows near the ADXL355 MEMS accelerometer and the Willmore MK III seismometer in underground conditions.

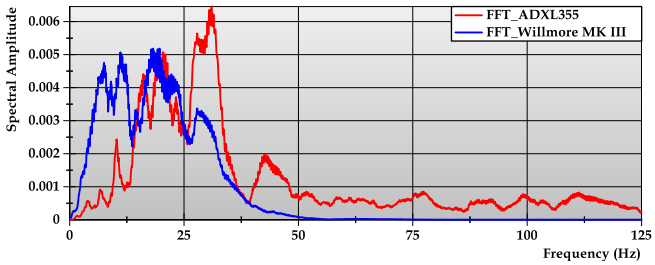


Figure 8. Comparison of Fast Fourier Transform analysis results for ADXL355 (red) and Willmore MK III (blue) accelerometers.

Good efficiency in identifying the arrival times of P and S waves, combined with almost 20 times lower costs of measurement equipment compared to standard solutions used in the LGCB area, determined the decision to build an active seismic tomography system using ADXL355 accelerometers.

Pilot testing of MEMS accelerometers in situ conditions

Monitoring of mining-induced seismicity

During several months of measurements, eight medium-energy tremors were recorded, with the epicentre at a distance of up to 5 km from the autonomous measurement station using MEMS IMU technology. Details of individual phenomena, such as time of occurrence, energy and magnitude, are presented in Table II.

Table II. List of events recorded with the surface seismic monitoring station using an ADIS16470 accelerometer

ID of seismic event.	Date	Time	Energy [J]	Magnitude
1	19 September 2023	10:10:01	5,4E+05	2,3
2	22 September 2023	19:34:31	1,2E+05	2,0
3	28 September 2023	03:45:28	1,7E+05	2,1
4	12 October 2023	03:01:16	2,2E+05	2,1
5	13 October 2023	14:44:40	1,4E+06	2,5
6	17 October 2023	12:04:51	1,7E+05	2,1
7	17 November 2023	20:38:57	2,0E+05	2,1
8	18 November 2023	03:04:12	2,3E+05	2,1

Since the new measuring station was installed directly at the existing measuring system, it was possible to conduct a detailed analysis of the efficiency of the MEMS-IMU ADIS16470 accelerometer in real operating conditions. Results from the pilot measurements show that the registrations in terms of amplitude, frequency and waveform character correspond to the registration collected with a classical accelerometer (Figure 9). Differences are visible in the scope of measurement noise registration, namely the MEMS-IMU accelerometer is characterised by a significantly higher noise level than the classical measuring device (Figure 10). This may be important, among others, in terms of localising low and medium-energy shocks located at large epicentral distances from the measuring station. However, for the monitoring of high-intensity phenomena, this aspect should not be of significance.

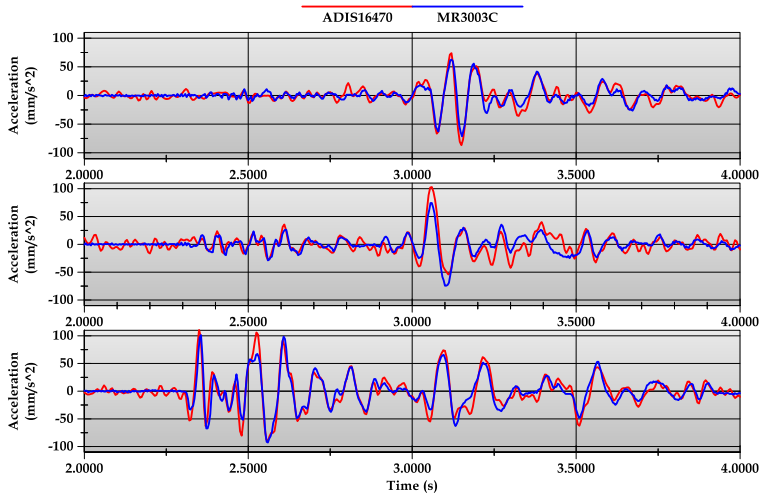


Figure 9. Recording of 4 hammer blows near the ADXL355 MEMS accelerometer and the Willmore MK III seismometer in underground conditions.

As was pointed out in papers (Porębski *et al.*, 2018; Gong *et al.*, 2023) seismic tomography technique is one of most effective methods for spatial evaluation of rock mass condition. Basically the aim of this method is to determine the seismic wave propagation velocities within the area located between sources of vibration and receivers. It should be noted that geotomography requires the use of a large number of monitoring stations (receivers) to cover the area of interest effectively. Therefore, regular seismological networks often turn out to be insufficient to carry out effective, local profiling of the rock mass and it is necessary to install a special network of geophones/accelerometers solely for the purpose of performing the survey. This is a costly and time-consuming process, so it is most often used only in special cases e.g., after an accident or a high-energy mining tremor. Thus, the authors have attempted to design, develop and validate on a pilot scale in operational conditions an innovative continuous real-time underground monitoring system for active geotomography. The system was based on MEMS-based accelerometers ADXL355. It was assumed that this system will help to indicate the time and location of preventive actions that should be taken in order to reduce geomechanical risk, such as destress blasting.

Continuous data processing will enable the evaluation of the effectiveness of the preventive actions taken as well.

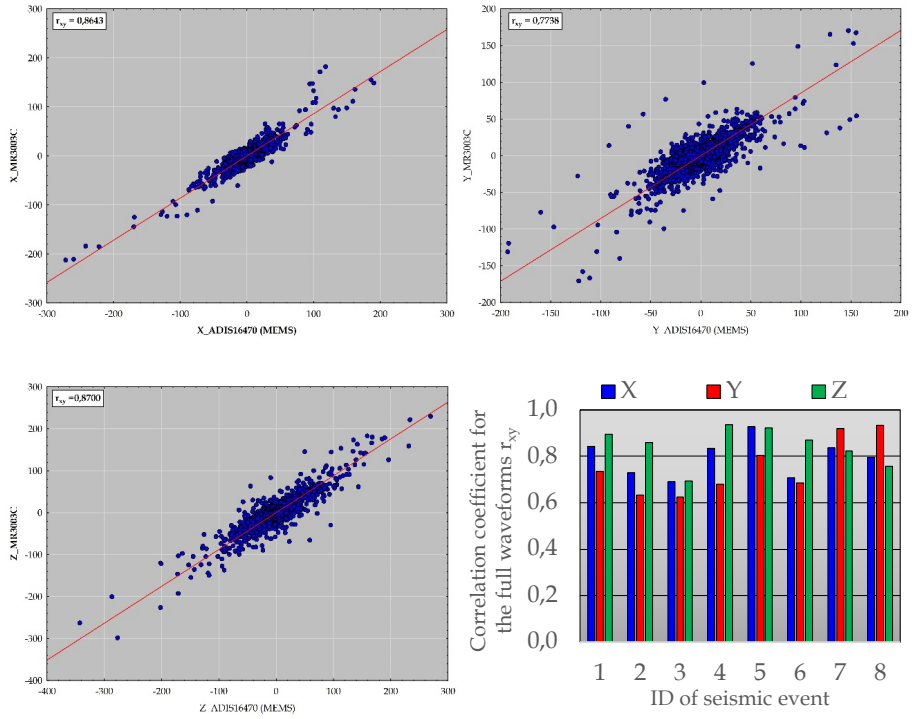


Figure 10. Scatterplots of data recorded in X (top-left), Y (top-right), Z (bottom left) directions and correlation calculated for full waveform of each analysed seismic event (bottom right).

Active seismic velocity profiling

In order to ensure a suitable environment for long-term monitoring (at least several months), a prototype monitoring system was installed in one of the active mining panels in the LGCB area. Accelerometers were mounted to the sidewalls in the location shown in Figure 11. The depth of excavation in this area was approximately 700 m below surface. The scheme of excavations over the analysed panel with locations of MEMS accelerometers, recorder and source of vibrations is shown in Figure 11.

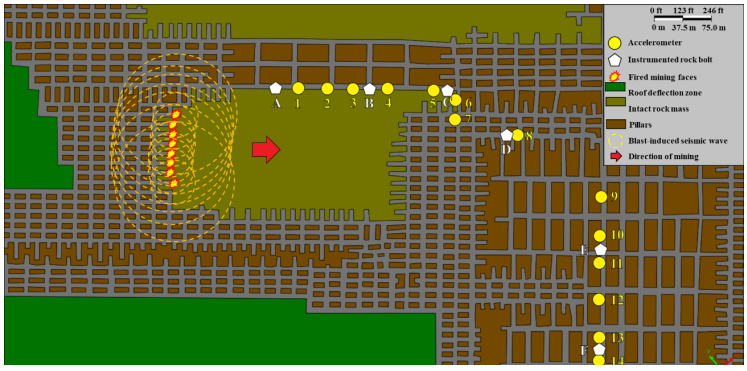


Figure 11. Map of the trial site and location of monitoring devices.

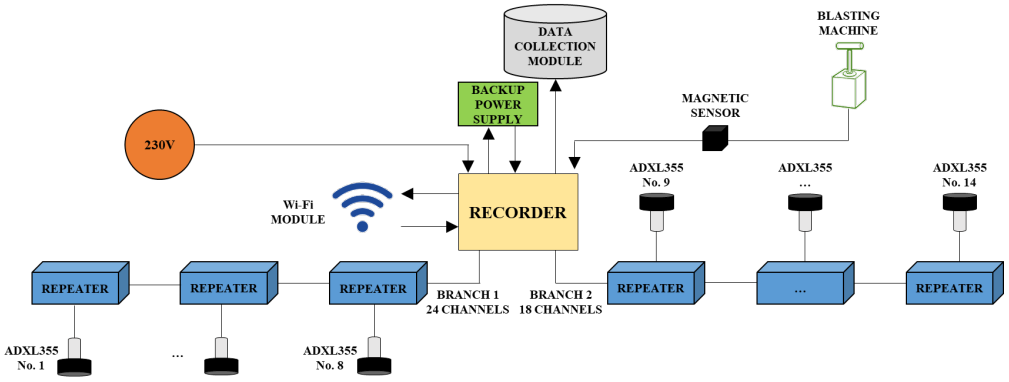


Figure 12. Scheme of MEMS-based monitoring system for active seismic tomography.

Before starting regular monitoring, the system was validated for correct operation. A single explosive charge was detonated at exactly the same location every 20-40 minutes. The seismic wave propagation velocities were then measured at each monitoring point. As shown by the preliminary analysis, the differences in the seismic velocities usually did not exceed 2% (Figure 13).

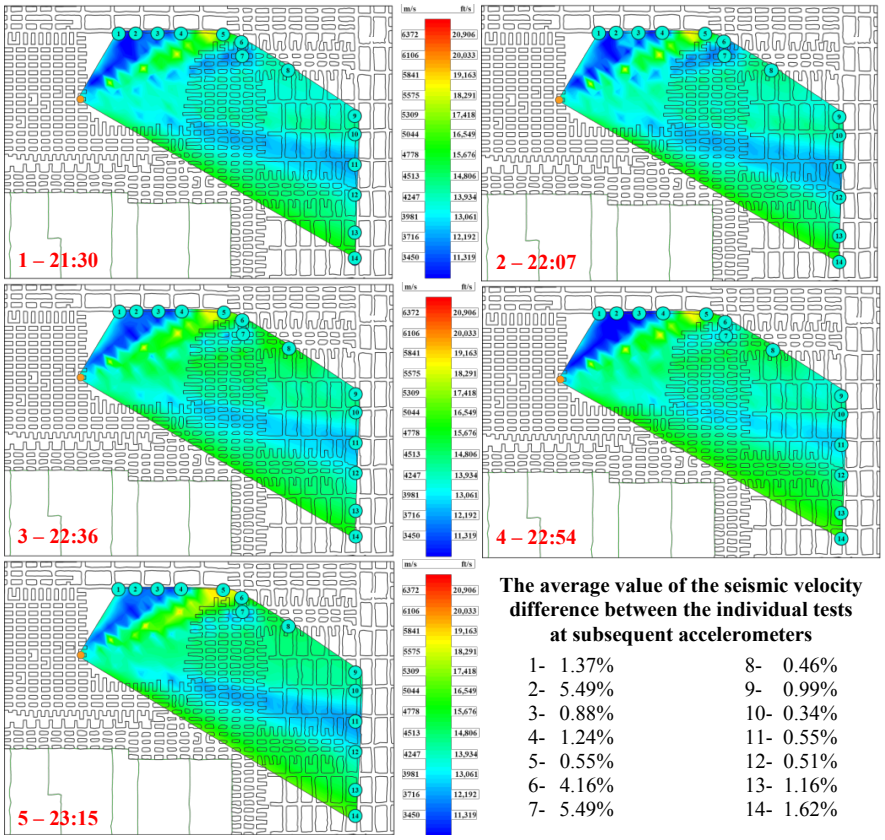


Figure 13. Scheme of MEMS-based monitoring system for active seismic tomography.

Small changes could result from the unstable detonation parameters or a small change in the stress state between subsequent measurements. This may happen while the tests are carried out in an active mining field. As it turned out, the application of MEMS technology to the construction of a monitoring network for fully automated active seismic tomography enabled a significant reduction in costs and the permanent installation of measuring devices in excavations. In the case of damage to one of the sensors, the repair costs are very low, therefore financial constraints can be effectively overcome. The possibility of conducting continuous seismic tomography enables ongoing assessment of the rock mass condition

and is the basis for the implementation of constructive planning of preventive measures, such as destress blasting. Figure 14 shows the distribution of seismic wave velocities in the analysed area before and after destress blasting. In the study, destress blasting was implemented as a targeted rock burst mitigation strategy following the identification of zones with elevated stress concentrations. The blasting design was based on a multi-face blasting approach utilising electronic detonators, which allow for precise control of delay times between individual faces. The delay sequences were carefully calculated to promote constructive interference and amplification of seismic waves in the area of stress accumulation. This controlled amplification was intended to locally exceed the rock mass strength threshold, thereby inducing controlled stress release and reducing the potential for uncontrolled rockburst events. The use of electronic detonators ensured a high level of timing accuracy, which is critical for the effectiveness of the destress blasting method.

Everyday information on the location of stress zones allows for determining when and to what extent the rock destressing should be carried out.

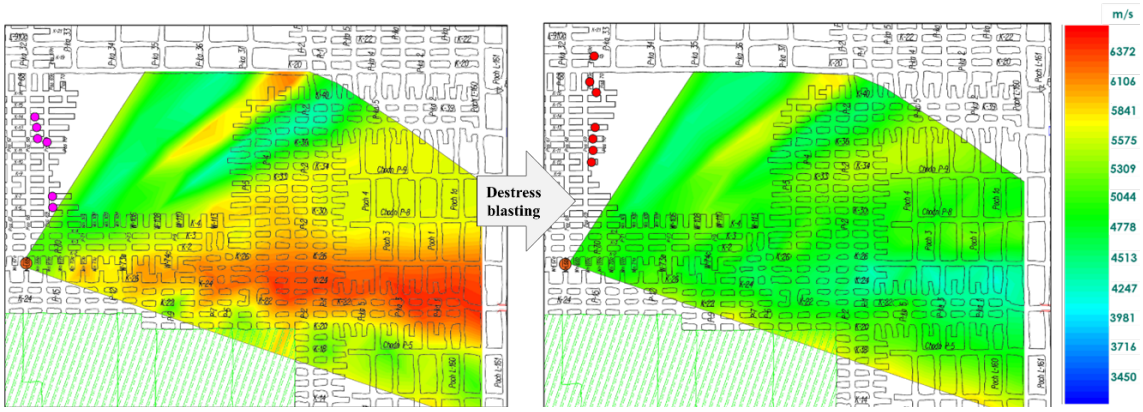


Figure 14. Top-view on active tomography results distribution of seismic wave speeds before (left) and after stress relief blasting (right).

DISCUSSION

Results show that from the pilot seismic measurements conducted over several months in the LGOM region, the use of low-cost MEMS technology can significantly contribute to an increase in the accuracy of seismic measurements. A significant reduction in the costs of individual devices allows for a significant increase in the density of coverage of a given area with seismic devices without affecting the overall economics of the project. Of course, it should be noted that the tested MEMS accelerometers, both the ADXL355 and ADIS16470 models, were characterised by a significantly higher level of self-noise compared to standard seismic devices currently used in the LGCB area. Such a situation determines the less usefulnss of MEMS-based devices in the area of monitoring low-energy phenomena or far-field monitoring. Additionally, the relatively high self-noise of the device may affect the ability to identify the arrival time of seismic waves (mainly P waves). Inaccurate information in this area may translate into a decrease in the accuracy of determining the epi- and hypocentral location of tremors, assuming the same number of measurement stations.

Taking the abovementioned into consideration it is also necessary to analyse the possibility of applying MEMS technology to structural stability assessment based on the seismic noise distribution. In general, this is a topic that may have potential due to the possibility of installing a large number of measurement stations, which theoretically would enable effective localisation of the formation of instability areas in the roof layers, pillars or geotechnical objects located on the surface. However, the question arises whether the ambient noise level and its changes as a result of structure disintegration are large enough for MEMS accelerometers to capture them, despite the device's own noise. From a practical point of view, a dense network of accelerometers in underground conditions can also contribute to increasing

the possibilities of monitoring technological processes in the mine. The 42-channel system, which was developed for the needs of conducting active seismic tomography, continuously recorded data related to the movement of machines. In this way, it was possible to analyse how many machines passed along the measurement line in a unit of time, at what speed they moved and even whether they were loaded with ore or were driving with an empty bucket. Information of this type was unavailable in the mines of the LGCB region. Measurement of the parameters of the machine park can undoubtedly contribute to the optimisation of the process of transport and haulage of ore.

CONCLUSION

This article presents the authors' experience in the construction of local seismic monitoring networks using accelerometers based on MEMS technology. The paper presents two measuring systems: one for surface monitoring using an accelerometer-based on MEMS-IMU ADIS16470 technology; the second system was designed for underground active seismic tomography and monitoring of dynamic phenomena located in the near wave field and utilised the MEMS-based ADXL355 accelerometer. In both cases, the systems were characterised by low construction and installation costs, low energy consumption, as well as stability and reliability of the measurements. In both pilot measurement campaigns, the new generation MEMS accelerometers conducted measurements in parallel with measuring devices used in regular operation in the LGCB area. As demonstrated in the paper and a number of comparative analyses, MEMS technology, although clearly inferior to classical devices, provides data quality that guarantees the possibility of performing detailed seismic analyses, developing predictive patterns or monitoring the velocity of seismic wave propagation. Taking into account the promising results of the pilot work, the authors will attempt to further develop seismic monitoring systems based on MEMS technology. One of the first directions of development will be the construction of a surface wireless network. Additionally, it is planned to perform pilot tests aimed at the possibility of determining the structural stability of objects based on ambient noise characteristics.

ACKNOWLEDGEMENTS

This paper was prepared within the framework of the AGEMERA project 'Agile Exploration and Geo-modelling for European Critical Raw Materials'. The project received funding from the European Union's Horizon Europe Research and Innovation Program under grant agreement No. 101058178.

REFERENCES

Chodacki, J. (2016). New ground motion prediction equation for peak ground velocity and duration of ground motion for mining tremors in upper silesia. Acta Geophysica, 64(6), 2449-2470. https://doi.org/10.1515/acgeo-2016-0109

Cook, N. G. W. (1976). Seismicity associated with mining. Engineering Geology, 10(2–4), 99–122. https://doi.org/10.1016/0013-7952(76)90015-6

Fuławka, K., Pytel, W., & Pałac-Walko, B. (2020). Near-Field Measurement of Six Degrees of Freedom Mining-Induced Tremors in Lower Silesian Copper Basin. Sensors, 20(23), 6801. https://doi.org/10.3390/s20236801

Fuławka, K., Mertuszka, P., Szumny, M., Stolecki, L., & Szczerbiński, K. (2022). Application of MEMS-Based Accelerometers for Near-Field Monitoring of Blasting-Induced Seismicity. Minerals, 12(5), 533. https://doi.org/10.3390/min12050533

Friedel, M. J., Tweeton, D. R., Jackson, M. J., Jessop, J. A., & Billington, S. (1992). Mining applications of seismic tomography. SEG Technical Program Expanded Abstracts 1992, 58–62. https://doi.org/10.1190/1.1822158

Goldswain, G. (2020). Advances in seismic monitoring technologies. Proceedings of the Second International Conference on Underground Mining Technology, 173–188. https://doi.org/10.36487/ACG_repo/2035_05

Gong, S., Li, J., Shangguan, K., Xue, Z. (2023). Improvement of the accuracy of active seismic tomography by eliminating blasting delay in coal mines. Arabian Journal of Geosciences, 16, 154.

Guo, X., Tang, C., Nan, S., Zhang, J., & Wang, W. (2011). Application of Mine Micro-Seismic Monitoring System on Preventing Against Illegal Mining. Procedia Engineering, 26, 2206–2212. https://doi.org/10.1016/j.proeng.2011.11.2426

Jian, Z., Zhao, G., Ma, J., Liu, L., Liang, W., & Wu, S. (2025). Detection of Rock Mass Defects Using Seismic Tomography. Applied Sciences, 15(3), 1238. https://doi.org/10.3390/app15031238

Kotyrba, A., Sokoła-Szewioła, V., & Marwan, A. (Eds.). (2023). Methods on assessment and monitoring of seismic hazards in coal post-mining areas: guidelines: collective work. Silesian University of Technology Publishing House.

Meyer, S. (2024). Seismic Monitoring Systems in Mines, where are we Today? 58th U.S. Rock Mechanics/Geomechanics Symposium, D042S056R005. https://doi.org/10.56952/ARMA-2024-0785

Orlecka-Sikora, B. (2010). The role of static stress transfer in mining induced seismic events occurrence, a case study of the Rudna mine in the Legnica-Glogow copper district in Poland. Geophysical Journal

Porębski, K., Koziarz, E., Anderko, A., Krawiec, K., Czarny, R., Kokowski, J., Harba, P. (2018). Recognition of gasogeodynamic zones in the rock mass using seismic tomography in Rudna copper ore mine. E3S Web of Conferences, 66. 01012. 10.1051/e3sconf/20186601012.

Sarmadi, H., Entezami, A., Yuen, K.-V., & Behkamal, B. (2023). Review on smartphone sensing technology for structural health monitoring. Measurement, 223, 113716. https://doi.org/10.1016/j.measurement.2023.113716

Stolecki, L., Fuławka, K., Frühwirt, T., & Schimmel, M. (2024). In-field Verification of the Applicability of MEMS-IMU Accelerometers for Monitoring of Mining-induced Seismic Activity. Civil and Environmental Engineering Reports, 34(4), 563–581. https://doi.org/10.59440/ceer/196753

Wang, Z., Li, X., Zhao, D., Shang, X., & Dong, L. (2018). Time-lapse seismic tomography of an underground mining zone. International Journal of Rock Mechanics and Mining Sciences, 107, 136–149. https://doi.org/10.1016/j.ijrmms.2018.04.038

Witkowski, W. T., Łucka, M., Guzy, A., Sudhaus, H., Barańska, A., & Hejmanowski, R. (2024). Impact of mining-induced seismicity on land subsidence occurrence. Remote Sensing of Environment, 301, 113934. https://doi.org/10.1016/j.rse.2023.113934



Lech Stolecki

Deputy Department Manager
KGHM CUPRUM Ltd. Research & Development Centre

Lech Stolecki, PhD, is a research worker in KGHM Cuprum Research & Development Centre. He received his M.Sc. at Wroclaw University of Science and Technology in 2000. In 2006 he obtained his Ph.D in mining and environmental protection. His research interests cover protection of land surface and rock mechanics. He is interested mainly in natural hazards accompanying the underground exploitation of copper ores. The research, that he conducted on this subject, enabled to development of a new inclinometer measurement method for assessing the stability of underground workings. This method is based on the measurement of the excavation roof's inclination. The wide and long-term research resulted in the development of the dynamic criterion of assessing the stability of roof layers, where for the first time it was possible to create a quantitative criterion describing the process of the roof fall. This method was patented by its authors and widely published in scientific articles. Measurement system based on this method is applied on an ongoing basis in copper mines belonging to KGHM Polska Miedź S.A. Dr Lech Stolecki is also a co-author of the verification of the seismic intensity scale for mining tremors about the land Surface impact. The research, carried out under his supervision, allowed the development and implementation of a modified GSI-2004/18 scale, which is currently used to assess the impact of mining-induced seismic events on buildings, people's perception and the nuisance of using buildings and apartments in LGOM mining area. One of the appendices to the scale is the standard operation procedure for conducting surface seismic measurements, interpreting the results for the assessment and forecasting of ground vibration parameters caused by mining tremors on the surface of the LGOM area based on the GSI-2004/18 scale, containing guidelines for the implementation of seismic measurements, their interpretation and assessment, and principles of forecasting seismic activity.

Seismic-based live tracking of underground fires and cooling period response

M. Wiggins[1], L. Scheepers[1], J. Gerber[2]

[1]Sibanye Stillwater, South Africa
[2]IMS – Institute of Mine Seismology, South Africa

This paper outlines the monitoring and analysis of an underground fire incident at Hlanganani Shaft, Driefontein Operations, Sibanye Stillwater, Gold Division in 2023. Through the utilisation of Institute of Mine Seismology software and live feed monitoring of seismic responses, the thermal dynamic trend of the fire was tracked from ignition to cooling. This approach facilitated early detection and response, enhancing safety for deployed proto teams (mine rescue brigades men). Although not universally applicable, similar systems could enhance fire containment efforts and enable early interventions through trend analysis of peak particle velocity in high-risk areas.

Keywords: Fire, seismicity, PPV, withdrawal, tracking

INTRODUCTION

Underground mining operations present unique safety challenges; with fire incidents ranking among the most hazardous events that can occur in these confined environments. The complex interaction between fire, ventilation, ground support, and geological structures demands sophisticated monitoring and response systems to ensure worker safety and minimise operational disruptions.

This paper analyses the underground fire incident that occurred at Hlanganani Shaft in the Driefontein Operations in July 2023. The primary objective is to examine how monitoring technologies, particularly the Institute of Mine Seismology (IMS) software and seismic data analysis, contributed to early detection, tracking of fire progression, and informed decision-making during the incident.

The scope of this analysis encompasses the circumstances leading to the fire, the deployment of monitoring systems, the interpretation of seismic data in relation to fire dynamics, and the effectiveness of response actions. By documenting the incident, this paper aims to contribute to improved safety protocols and monitoring strategies across the underground mining industry.

Background

Underground Fire Hazards

Underground mining environments present several specific fire hazards that make fire incidents particularly dangerous:

- *Flammable Materials*
  Underground mines contain various flammable materials, including timber supports, rubber belting, fuel, and hydraulic fluids. In this specific incident, a void fill material bag was compromised during welding operations while installing pipe sets. A spark was not properly treated, leaving it smouldering near hoses, loose chock units, and reef drive packs.

- *Limited Ventilation*
  The confined spaces in underground mines restrict airflow, potentially leading to the accumulation of hazardous gases. In this incident, the crosscut was located in a return airway, acting like a chimney with an accelerated burn rate due to concentrated ventilation flow directed along the timber arteries (ledging packs which are the first line of packs installed when establishing a raise for stoping purposes). This resulted in fast burn rates and high gas loads.

- *Explosive Atmosphere*
  When mixed with air, the presence of gases such as methane creates an explosive atmosphere susceptible to ignition from a single spark or equipment friction. Methane did not play a role in this incident.

- *Difficult Emergency Access*
  The limited access in underground mines complicates firefighting efforts and evacuation procedures. During this incident, five people were safely evacuated from a highly toxic environment with zero visibility and CO concentrations of 12,000 ppm at 250 m^3/ s. Mine Rescue Service (MRS) brigade personnel equipped with Long Duration Self-Rescuers and connected by lifelines helped the group crawl 1.5 km to safety before the temperature window for successful rescue closed.

- *Hot-Work Risks*
  Activities like welding, cutting, and grinding generate sparks that pose significant fire risks if safety protocols are not strictly followed. Hot-work was the primary ignition source in this incident.

- *Fire Detection Challenges*
  Some underground mines lack advanced fire detection systems, which can delay response times. Fortunately, Hlanganani Shaft had an efficient beacon head system that triggered an alarm shortly after the fire started.

- *Limited Escape Routes*
  Fires and smoke can rapidly spread in confined spaces, complicating evacuation. Clearly marked and accessible escape routes are essential, which enabled the safe evacuation of nine additional people to a neighbouring shaft during this incident.

Location of the site

The incident site is situated within the Sibanye Stillwater Driefontein Gold Operations, approximately 70 km west of Johannesburg, near Carletonville and Fochville in the Gauteng Province of South Africa (Figure 1). It can be accessed via the N12 highway between Johannesburg and Potchefstroom. Geologically, it lies along the West Wits Line, a significant part of the Far West Rand Goldfield within the Witwatersrand Basin.

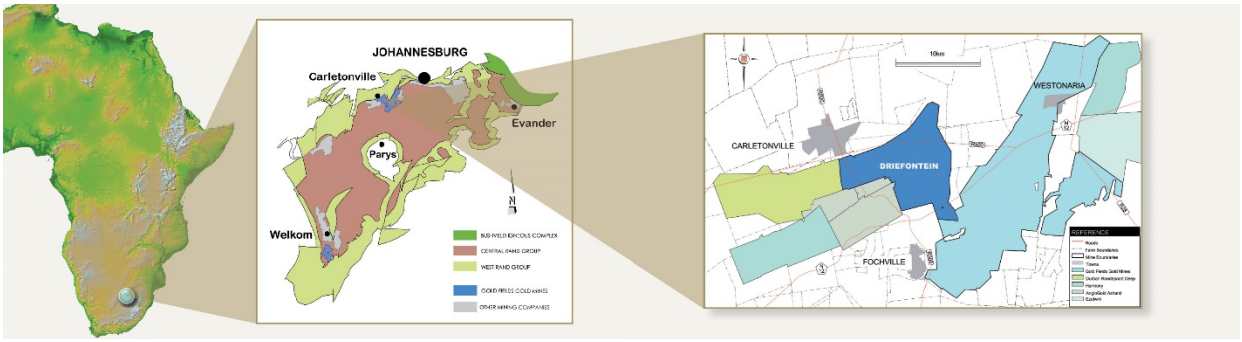


Figure 1. Regional location of the Driefontein Gold Operations.

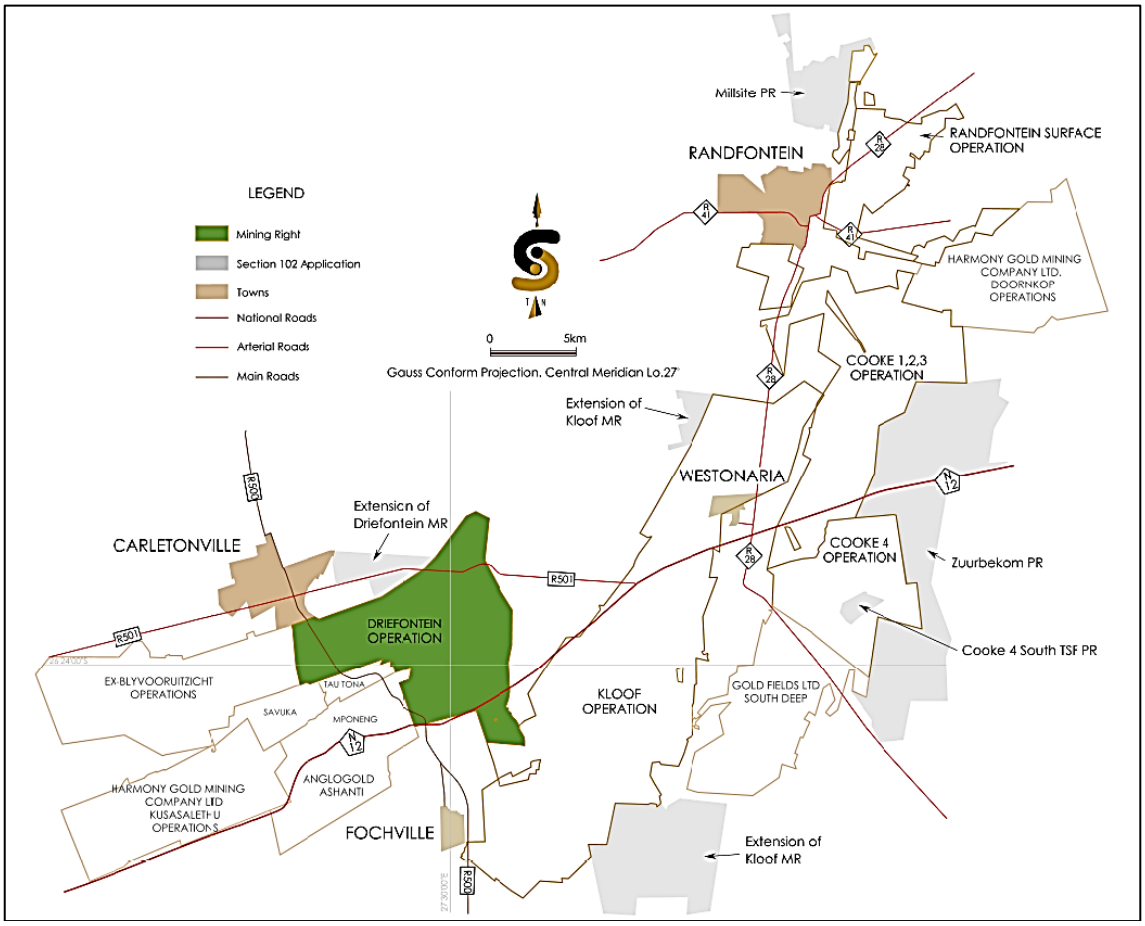


Figure 2. Regional location of the Driefontein Gold Operations.

Location and Geotechnical Setting

Driefontein lies within the West Wits Line, a significant part of the Far West Rand within the Witwatersrand Basin, which remains the most significant gold depository in the history of mining. Geologically, the mine is positioned within the richest formations of the Carbon Leader and Ventersdorp Contact Reefs ever found in South Africa. This area is divided into an Eastern Section and a Western Section, separated by the Bank Anticline and related faulting (Figure 2).

In the Western Section, three primary reefs are exploited (Figure 3):

- The Ventersdorp Contact Reef (VCR) at the top of the Central Rand Group
- The Carbon Leader Reef (CLR) near the base
- The Middelvlei Reef (MVR), positioned some 50 m to 75m above the CLR in terms of stratigraphy

The distance between the VCR and CLR increases from east to west, ranging from 0 m to over 1300 m, due to the relative angle of the VCR unconformity surface to the regional CLR and MVR strike and dip. The CLR itself strikes west-southwest and dips to the south at about 25°.

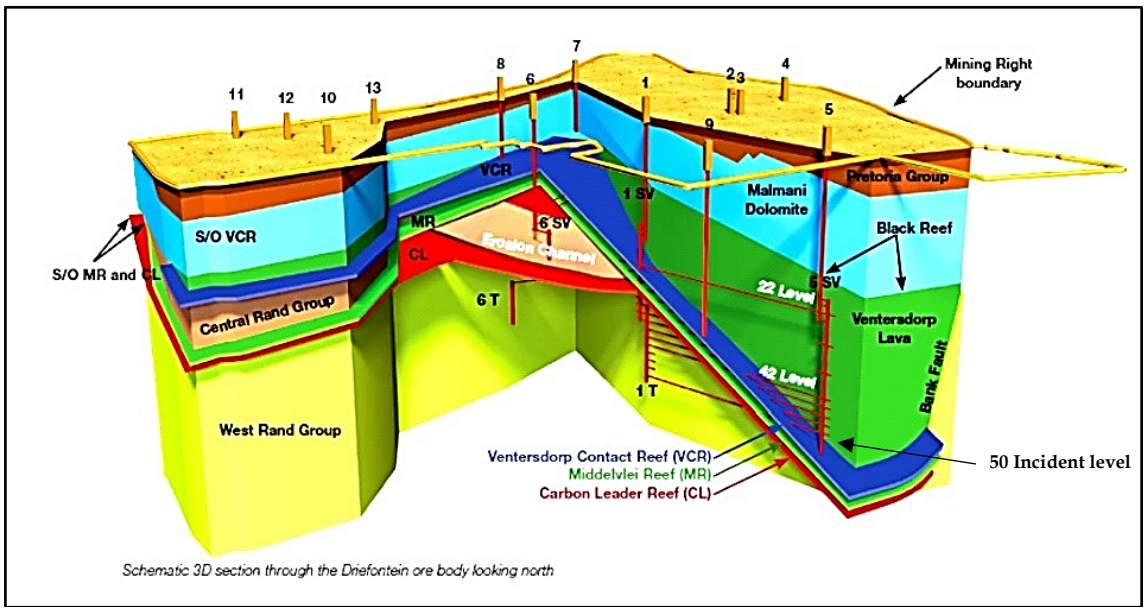


Figure 3. 3D View of Driefontein Operations depicting the Economic Reef Horizons.

Geologically, the mine is situated in an area with disturbed ground featuring significant structures (Figure 4) including:

- Faults averaging 10 m with dips between 47° and 70°
- Dykes ranging between 3 m and 10 m with dips of 70°-80°

Two of these structures have been associated historically with large magnitude seismic events.

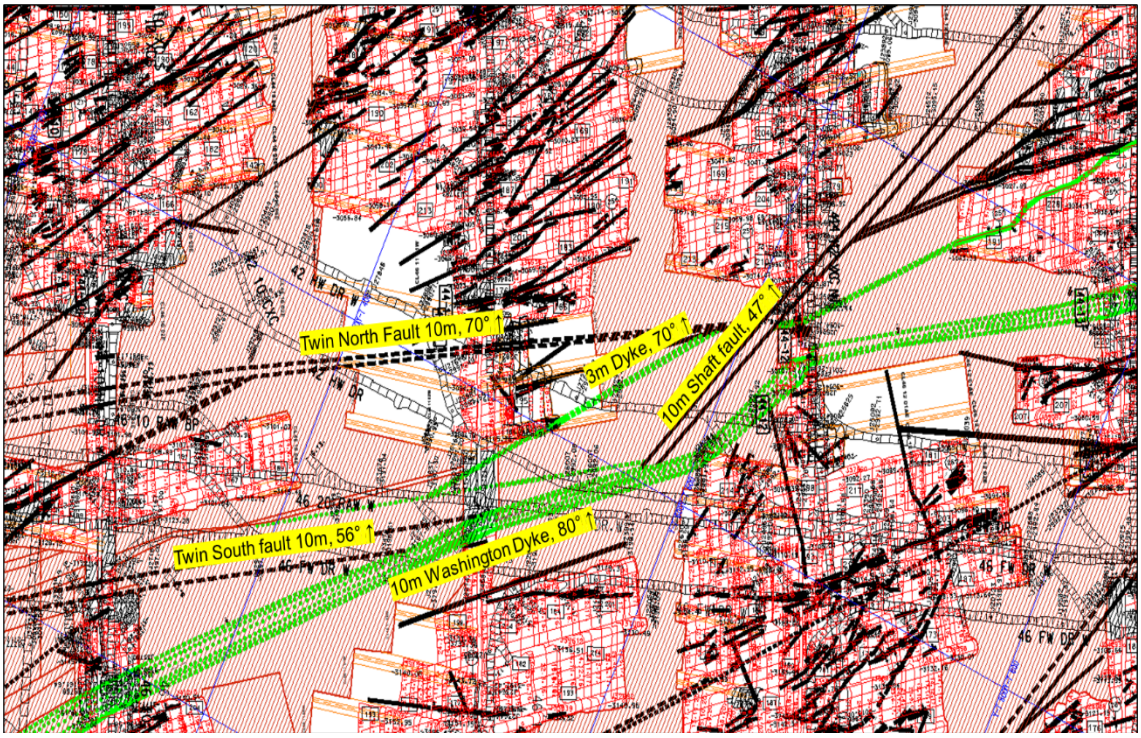


Figure 4. Location plan micro-station) with significant geology highlighted.

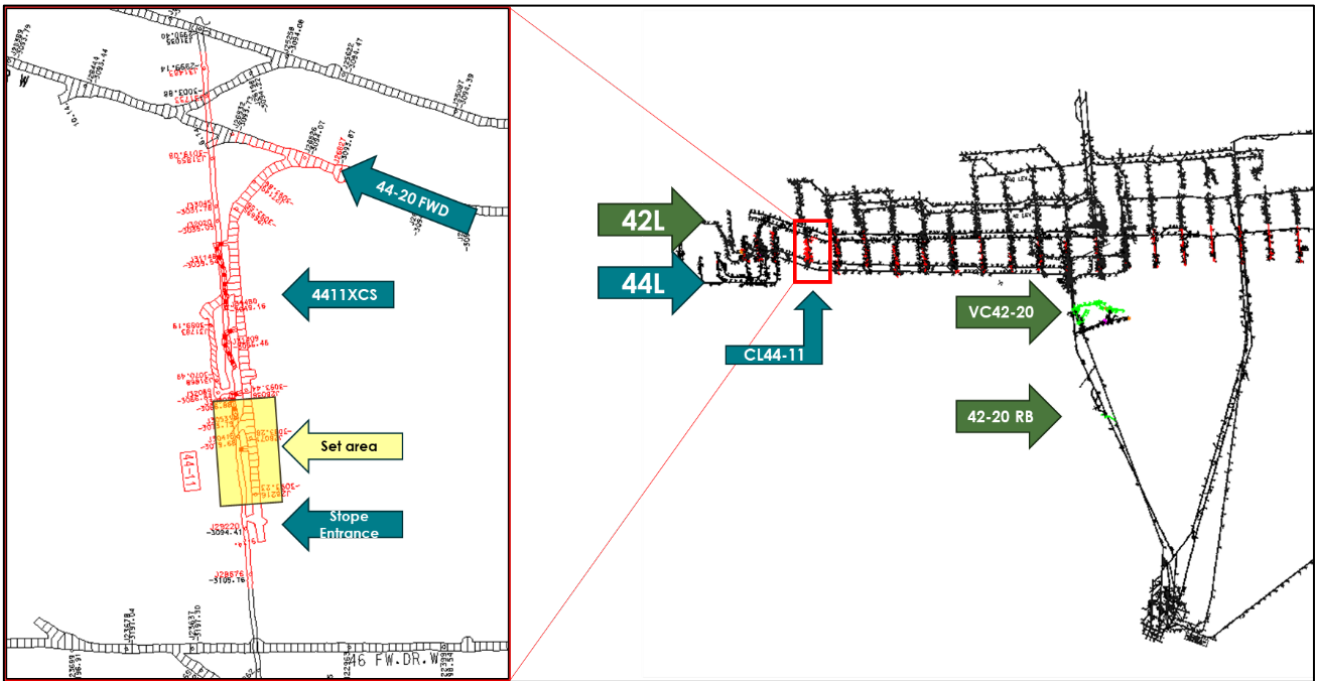


Figure 5. Location area with highlighted infrastructure.

Fire Incident Overview

Rehabilitation work began in the crosscut in April 2023, and the fire occurred in July 2023. The planned work involved installing additional set legs between existing set legs that had been damaged due to historic seismicity associated with delayed overstoping and time-dependent deterioration.

The ignition occurred when flame cutting was performed near combustible materials including timber and void fill bags. Proper fire-safety protocols were not followed as the area was not adequately watered down with a hose, and only a 5-litre paint can filled with water was used by the contractor to attempt to extinguish the initial fire. The spark was not properly treated before the crew knocked off.

On July 12 at approximately 14:07, beacon heads in the CL44-11 crosscut tiggered an alarm (Figure 5). A supervisor passing by the area reported visible smoke to the control room. An emergency control room was established, and emergency protocol was initiated. By 01:00 the following day, 19 employees were brought to surface by the dispatched MRS brigades men. Sadly, one miner was found ±50 m from the refuge bay without his self-rescuer donned as per protocol.

Methodology

Monitoring Systems

IMS Software

In line with standard practice in deep-level gold mining, numerical modelling is employed to interpret and analyse anticipated changes in rock mass stress or strain (Figure 6). The current software utilised in this operation is Vantage II from the Institute of Mine Seismology, which offers a comprehensive visualisation and analysis toolkit, integrating various codes and seismic programs into a full 3-D visualisation package.

Numerical modelling was conducted and peer-reviewed for the working place, with the risk profile for the area falling within the expected range for an excavation situated at 3209 m below the surface. Seismicity is very much part of deep level mining, and the seismic response is monitored continually.

Observations indicated a direct correlation between the burn rate and seismic activity in the affected area.

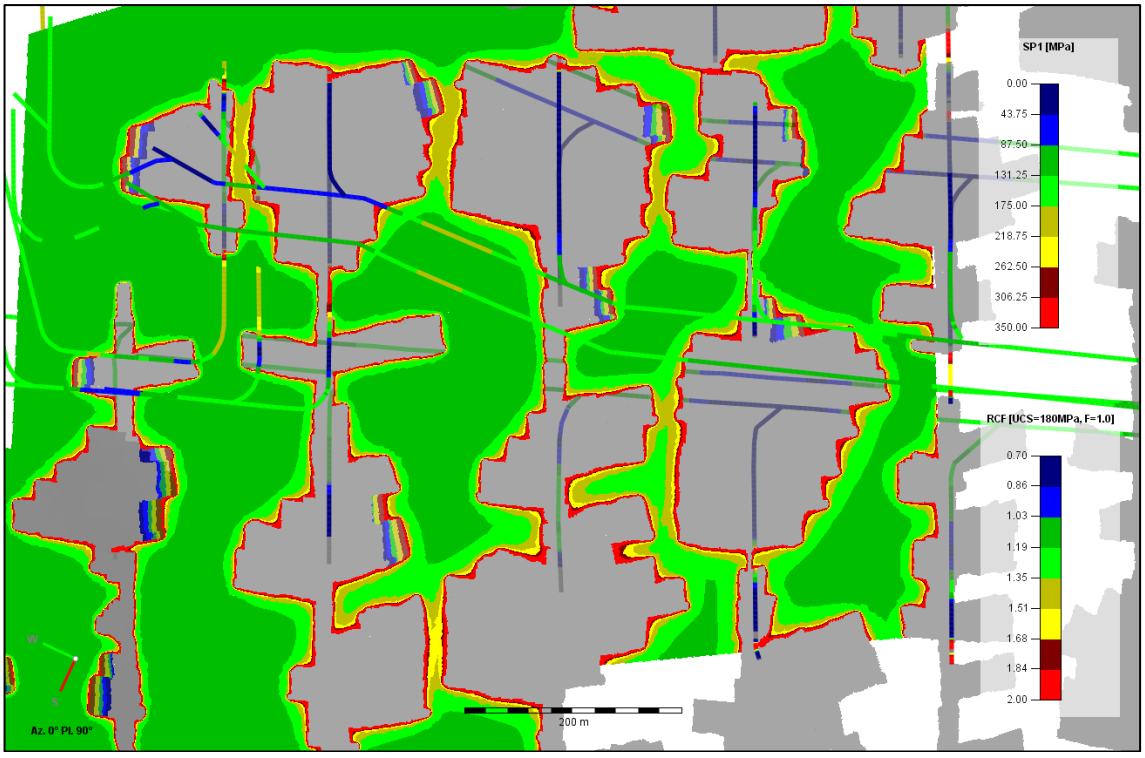


Figure 6. Modelled stress level.

Seismic Monitoring Network

An existing network of geophones throughout the Driefontein district enabled real-time tracking of seismic activity associated with the fire (Figure 7). Geophone placement was sufficient to distinguish between micro and large magnitude events in the region of the zone of influence for the working place affected.

Micro events are seismic events at the lower range of the spectrum at minus magnitude, such as e.g,. M_L-2.0, which have little to no impact with larger events ranging from M_L0.0 and above.

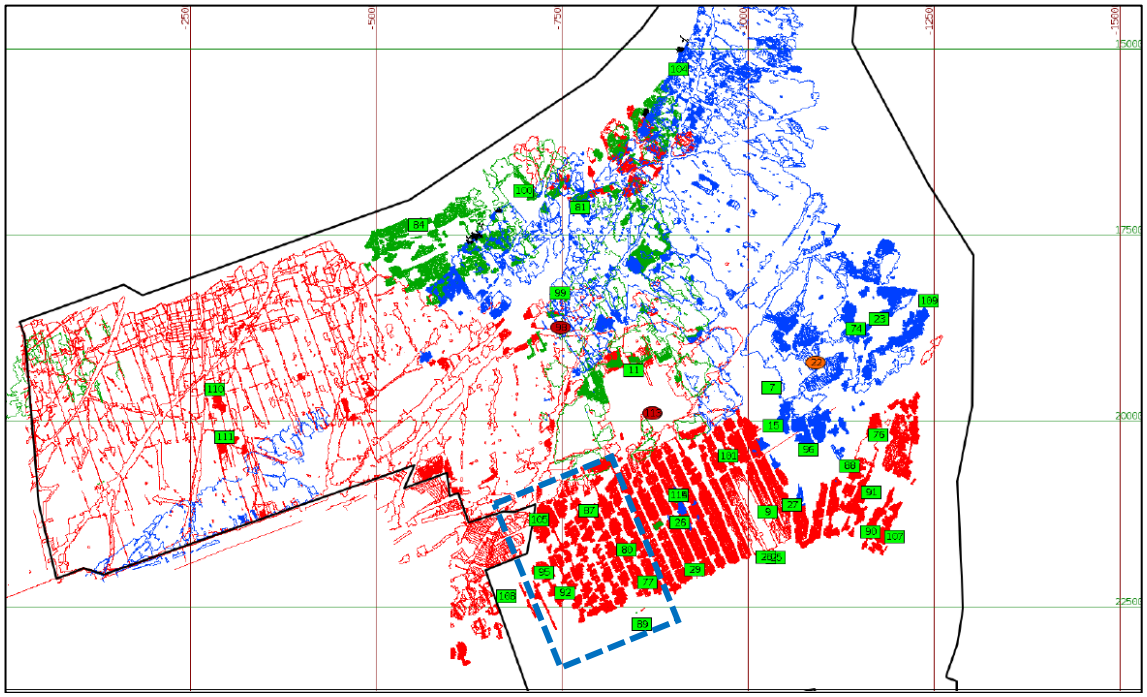


Figure 7. Seismic network of geophones.

Gas Monitoring
Sensors monitoring carbon monoxide and other gases provided data on the fire's progression and intensity. As this paper is written from a rock engineering perspective, the gas reading and subsequent information pertaining to fire is only discussed in highlights.

Data Collection and Analysis
Seismic Data
Seismic responses were clearly detectable from the onset of the fire in the rates of accumulated events, providing a trackable route for the raise line. Data collected included local magnitude measurements, peak particle velocity, and location of events.

Risk Assessment Framework
Prior to continuing with sealing work, a comprehensive seismic risk assessment was conducted, including:

Identification of seismic sources
Stressed mining abutments, pillars, and loaded geological structures were assessed as a potential source of seismic activity, with particular attention to the Washington Dyke (Figure 8).

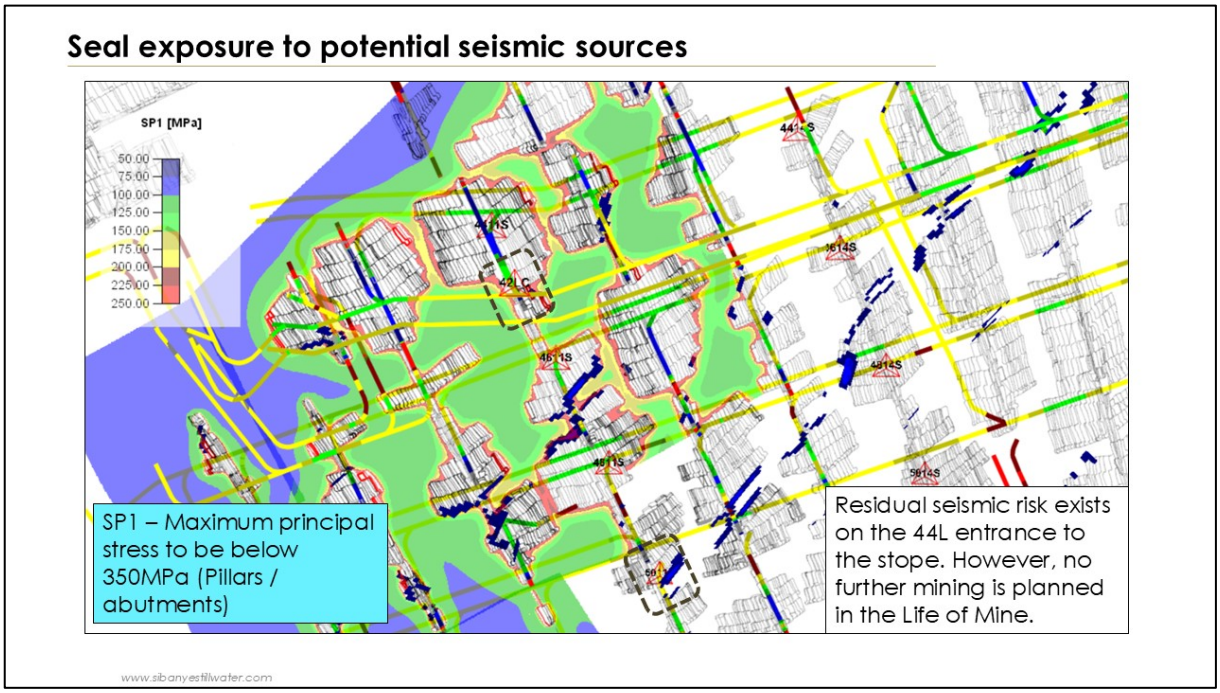


Figure 8. Seal exposure to potential seismic sources.

Vulnerability assessment of stressed tunnels near identified seismic sources
Tunnel vulnerability under seismic loading conditions is shown by modelled rock wall condition factor (RCF), with values higher than 1.4 indicating higher vulnerability. At the planned site, the RCF was between 1.0 and 1.2. (Figure 9).

RCF is a simple stress strength ratio. The numerator is deduced from the calculation of maximum tangential stress acting on the periphery of a circular excavation as suggested by the Kirsch equations. The denominator is a basic rock mass strength parameter obtained from downgrading the UCS by a factor between 1 and 0.4.

$$RCF = \frac{(3x\sigma_1) - \sigma_3}{F\ x\ \sigma_c}$$

Where:

σ_1 = Maximum principal stress

σ_3 = Minimum principal stress

F = Rock mass condition factor

σ_c = Uniaxial compressive strength

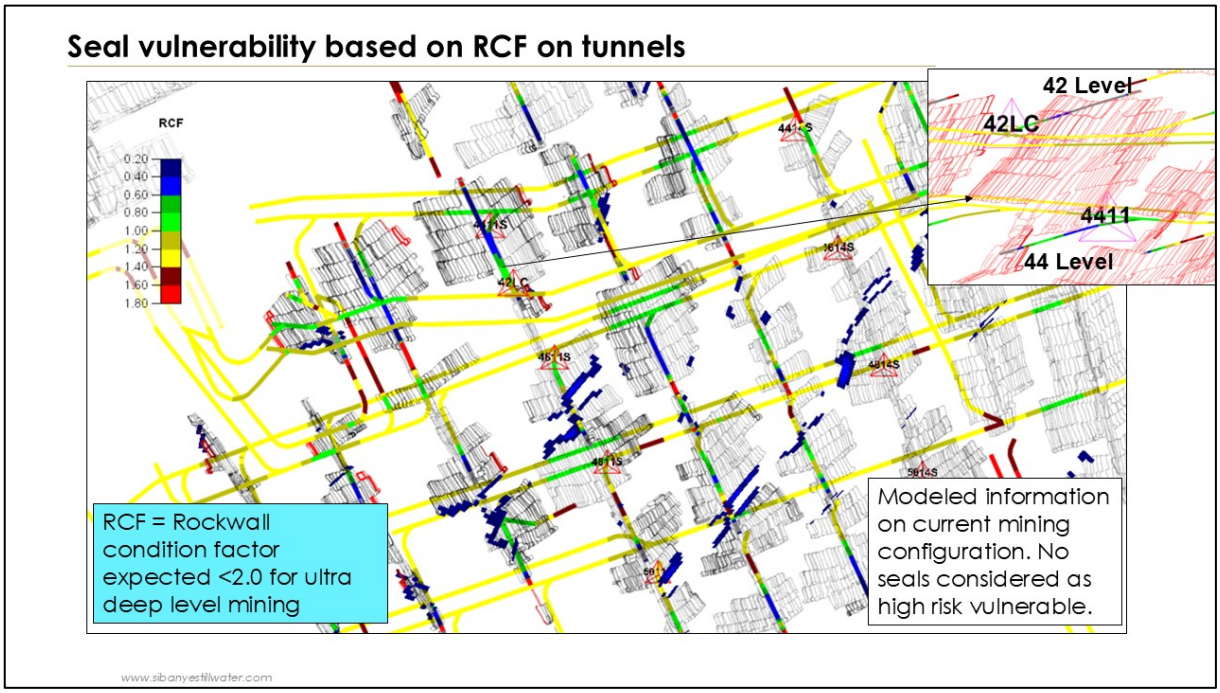


Figure 9. Seal vulnerability based on RCF on tunnels.

Analysis of Seismic Activity Rate (Cumulative number of seismic events)
The regional seismic risk after the increased activity period was similar to the risk prior to the increased risk period, based on the slope of the graph of cumulative number of events over time (Figure 10).

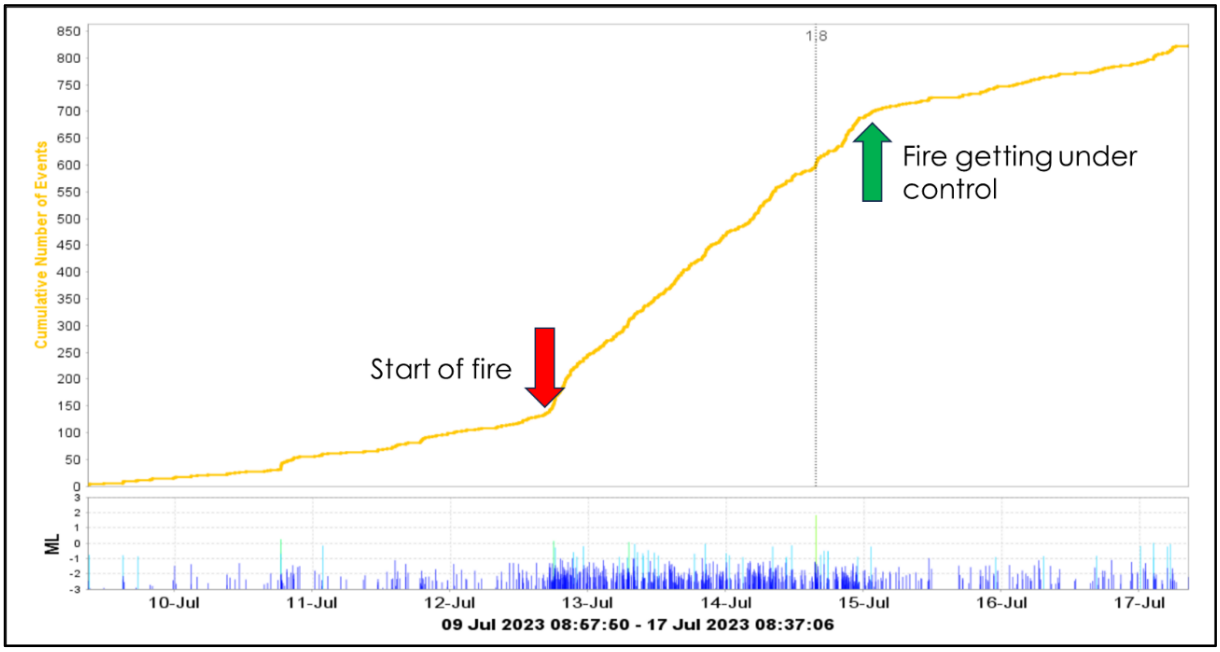


Figure 10. Accumulative number of seismic events (10-07-2023 to 17-07-2023).

Short-term Seismic Ratings

Seismic ratings serve as a simplified yet effective indicator of the current seismic activity within a defined geotechnical region. These ratings are typically represented either numerically on a scale (e.g., 0 to 6) or categorically using a traffic-light system—green (low), orange (medium), and red (high) to denote increasing levels of seismic hazard. The primary function of seismic ratings is to inform operational decision-making by guiding access control to areas experiencing elevated seismicity, thereby supporting proactive risk management.

The seismic rating for a particular region is derived from multiple seismic parameters, including:

- A significant increase in the rate of cumulative seismic displacement , which reflects intensified inelastic deformation within the rock mass.
- Noticeable changes in the Energy Index, indicating shifts in the energy released relative to the deformation scale of seismic events.
- Elevated medium-term (two-day) seismic event rates compared to the baseline average for the region.
- Significant variations in the seismic Schmidt Number, which characterises the spatial clustering of seismic events.
- The occurrence of larger magnitude events (e.g., ML ≥ 0.0), which may suggest escalating instability.

During the preparatory period leading up to the installation of underground seals to contain the fire expansion, seismic ratings remained consistently in the low category (numerical rating <6). This provided a stable operational window for controlled access and safe execution of seal construction activities (Figure 11).

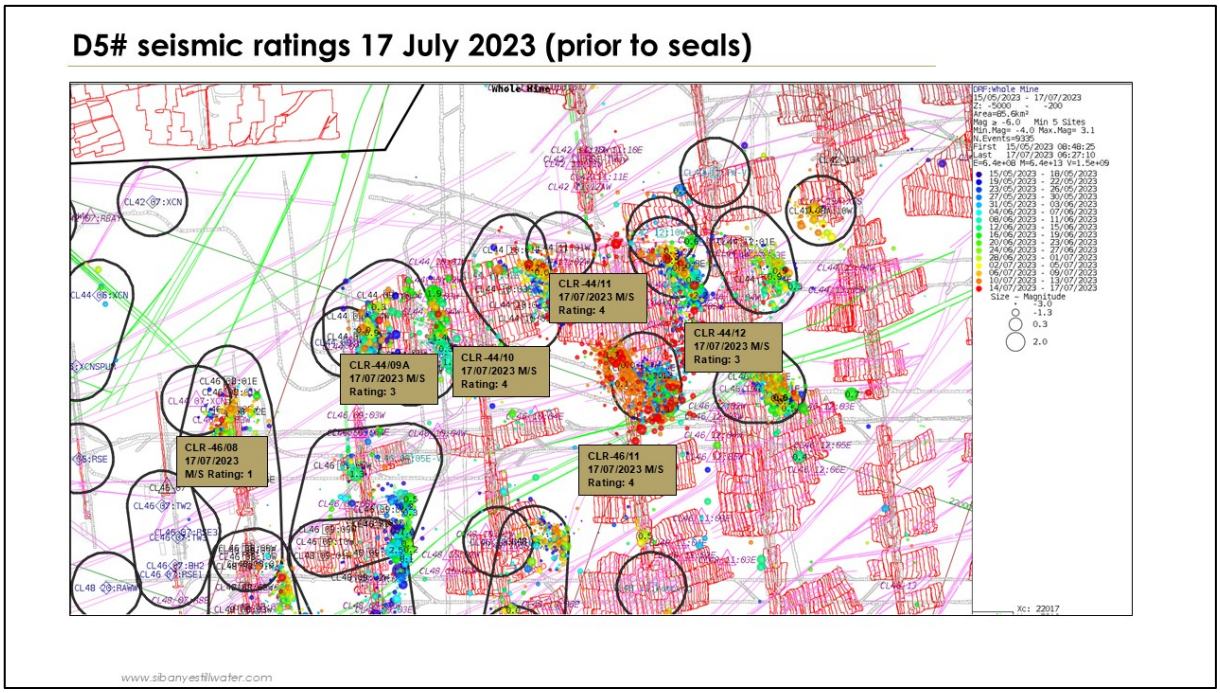


Figure 11. Short-term seismic ratings prior to building seals by Mine Rescue Services (proto).

Continuous monitoring of PPV at seal building sites

Continuous monitoring of PPV proved to be invaluable and resulted in the safe withdrawal of the MRS brigades men on three occasions during the underground intervention of building seals to control the extent of the fire (Figure 12 and 13).

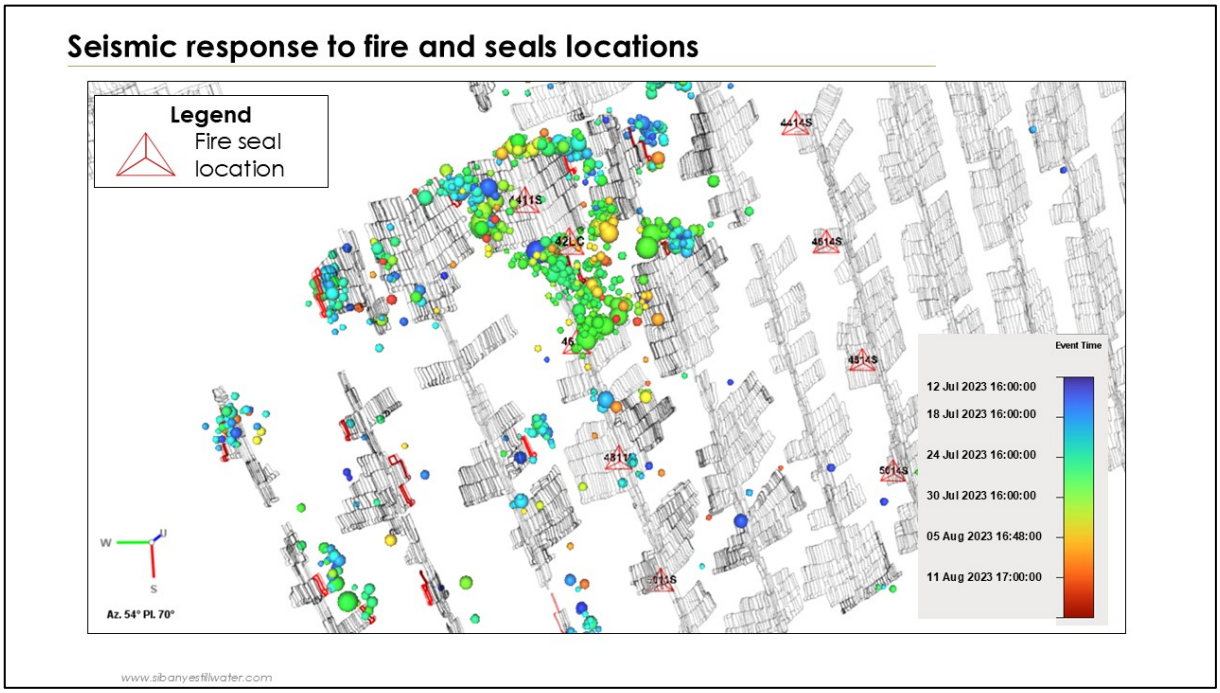


Figure 12. Seismic response to fire and seals location with the event time depicted in the colour legend (12 July 2023 in blue to 11 August 2023 in red).

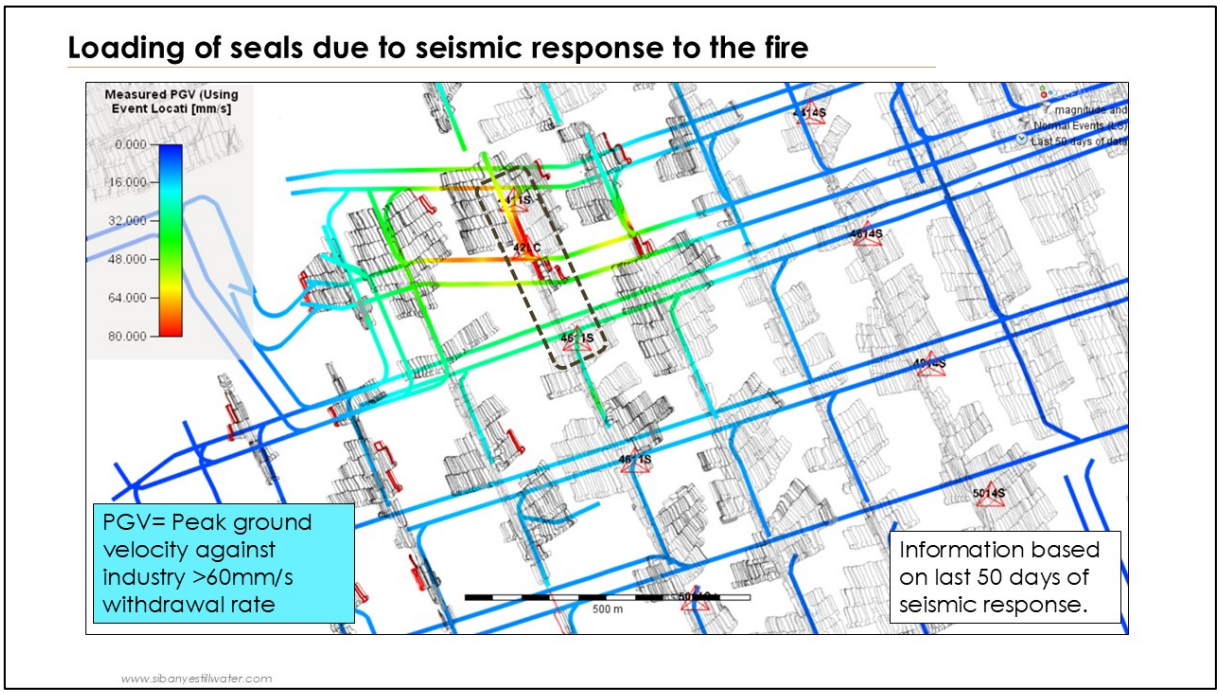


Figure 13. Loading of seals due to seismic response to the fire (PPV = 0 mm/s (blue) to PPV = 80 mm/s (red)) – GMPE (Refer to Paragraph 5).

Technical Parameters and Analysis for GMPE

The ground motion prediction equation (GMPE) gives the peak particle velocity (PPV) at some point as a function of seismic potency (P) and distance to the seismic event (R). For some seismic events with an estimated seismic potency, the PPV is calculated at different points that represent the 'strings' of tunnels

in Vantage and the calculated PPVs are then contoured from PPV=0 mm/s (blue) to PPV=80 mm/s (red) to produce the plot in Figure 13.

In terms of PPV, no correlation was tested. The PPV parameter was simply used as a risk management tool (without calibration) to indicate where risk of exposure to high calculated PPV (due to nearby seismic events) was experienced; as the PPV is a calculated number in the model.

Seismic Monitoring Parameters

Local Magnitude
The local magnitude (ML) is regionally defined to ensure comparability across Sibanye-Stillwater operations, calculated as:

$$\boldsymbol{ML = A0.\log(E) + B0.\log(Mo) + C0}$$

Where:

- Regional coefficients are A0 = 0.344, B0 = 0.516, and C0 = -6.572
- E = seismic energy (Joules)
- Mo = seismic moment (N.m)

Both seismic energy and seismic moment are obtained from recorded waveforms.

PPV expressed in Potency
The PPV expressed in relation to local magnitude and distance from the source (D) and expressed in P:

$$\boldsymbol{\log(PPV) = A2.log(P) + B2.\log\left(D + D2.\frac{P1}{3}\right) + C2}$$

Where:

- A2 = 0.684, B2 = -1.809, and C2 = 1.900
- D2 = 10.000
- PPV is measured in m/s

In the model the tunnel is not excavated and as such the PPV is in solid rock.

Seismic Potency
The seismic potency (P) is used to quantify rock mass strain in response to mining:

$$\boldsymbol{P = \frac{Mo}{G} = A.d}$$

Where:

- G = modulus of rigidity (30 GPa)
- A = area of slip (m^2)
- d = slip displacement (m)

Threshold Values
Based on in situ inspections, a ground motion threshold of approximately 0.08 m/s was identified, below which damage in stopes, tunnels, and ancillary excavations was not visually apparent. This value was reduced to 0.06 m/s with a factor of safety of 1.5 to account for various unknowns and for wider application across operations.

Monitoring Implementation

Vantage is a three-dimensional seismic visualisation and modelling tool designed to enhance the interpretation of seismic data and numerical modelling results within complex underground environments. Within the Vantage platform, a 'string' comprises a sequential array of spatial points that form a line. These strings serve as reference paths along which seismic parameter values—such as PPV or peak ground velocity —can be calculated and graphically displayed in three-dimensional space (Figure 14).

For this application, strings were strategically positioned to represent critical underground infrastructure, particularly planned tunnel excavations and areas where active construction activities—such as seal building—were to occur. The goal was to visualise and evaluate seismic risk in advance of and during these operations.

Monitoring points were specifically placed along the alignment of planned seal sites and their associated access ways. For each recorded seismic event, Vantage was used to calculate the PPV values at these string locations. These values provided a spatially distributed estimate of potential ground motion induced by the event.

A threshold PPV value of 0.06 m/s was adopted as a trigger for safety action. When this threshold was exceeded at any of the designated monitoring points, automated SMS notifications were generated and sent to relevant operational personnel. This real-time alert system enabled prompt risk-informed decisions, including temporary withdrawal from work areas, thereby improving overall workplace safety, and supporting proactive seismic hazard management.

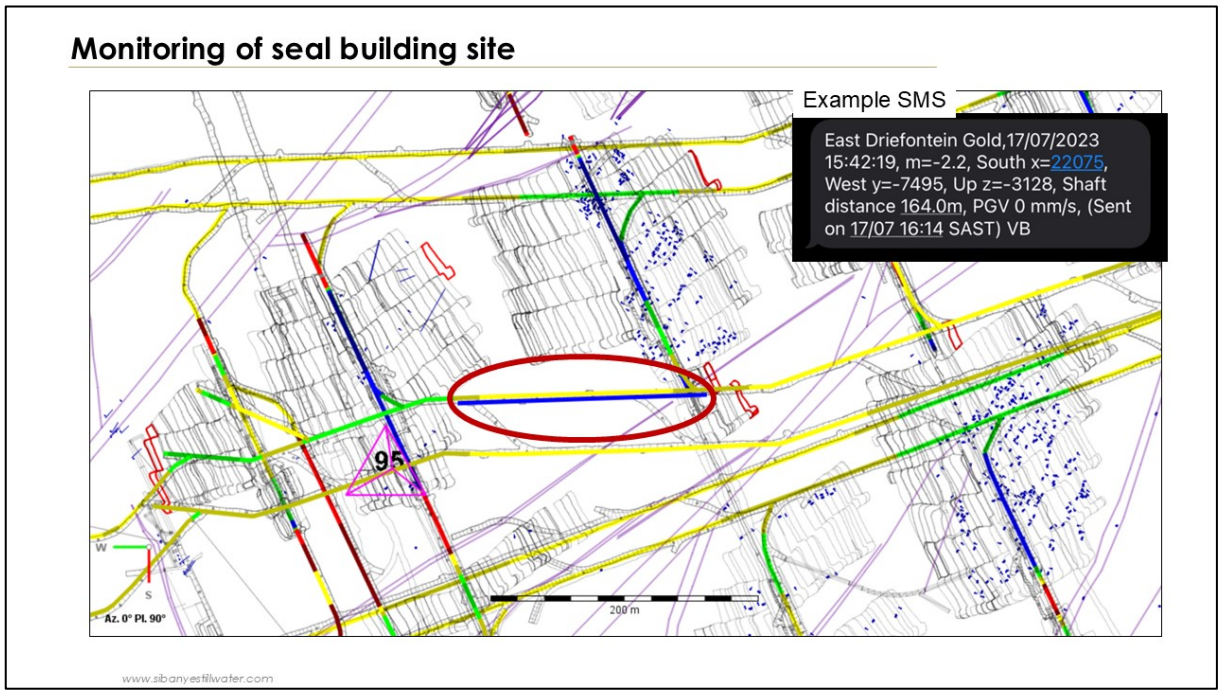


Figure 14. Monitoring of seal building sites (example of SMS).

Fire Dynamics and Seismic Response

Temperature Profiles and Progression

The fire demonstrated significant thermal intensity following this process:

- Initial ignition from hot work operations
- Rapid spread through timber supports and combustible materials
- Intensification due to ventilation flow acting as a chimney effect
- Peak temperatures estimated to exceed 1000°C in the core fire zone

- Gradual cooling after sealing operations restricted oxygen supply

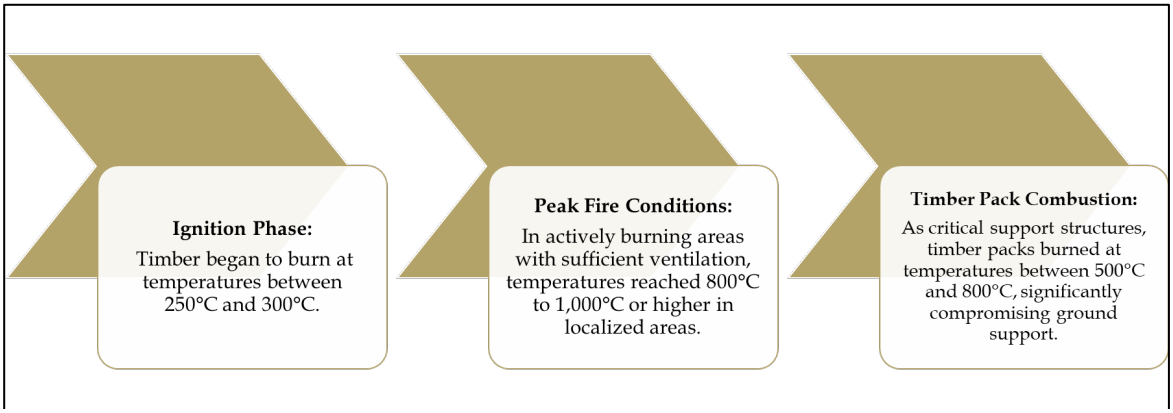


Figure 15. Simplified diagram for the process described.

Thermal Effects on Rock Mass
The intense heat from the fire induced several thermal effects in the surrounding rock:

Thermal Spalling
Rock surfaces began to crack and spall due to rapid temperature changes, typically initiating at 150°C to 200°C, with more significant spalling occurring above 300°C. This varied by rock type, with sedimentary rocks spalling at lower temperatures than granite or basalt.

Support Structure Degradation
Timber supports began to degrade and burn at around 250°C to 300°C, while concrete-based backfill started to break down when exposed to temperatures above 400°C.

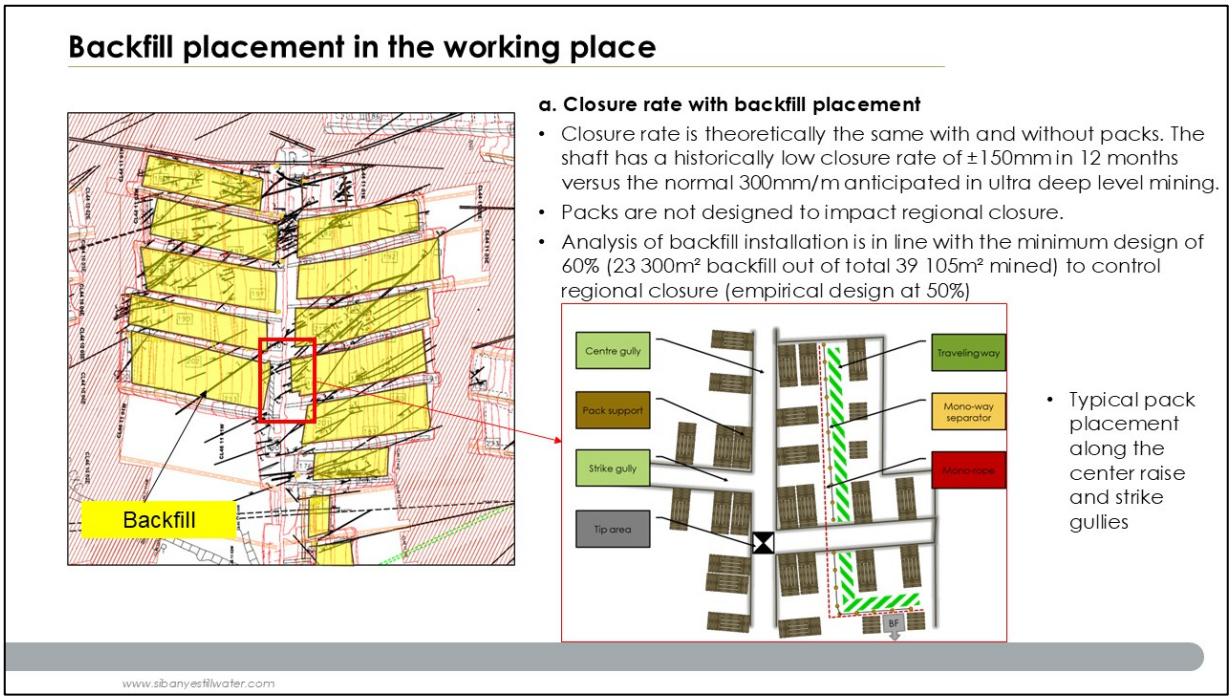


Figure 16. Backfill placement with solid timber packs installed along the arteries such as the centre raise and strike gullies.

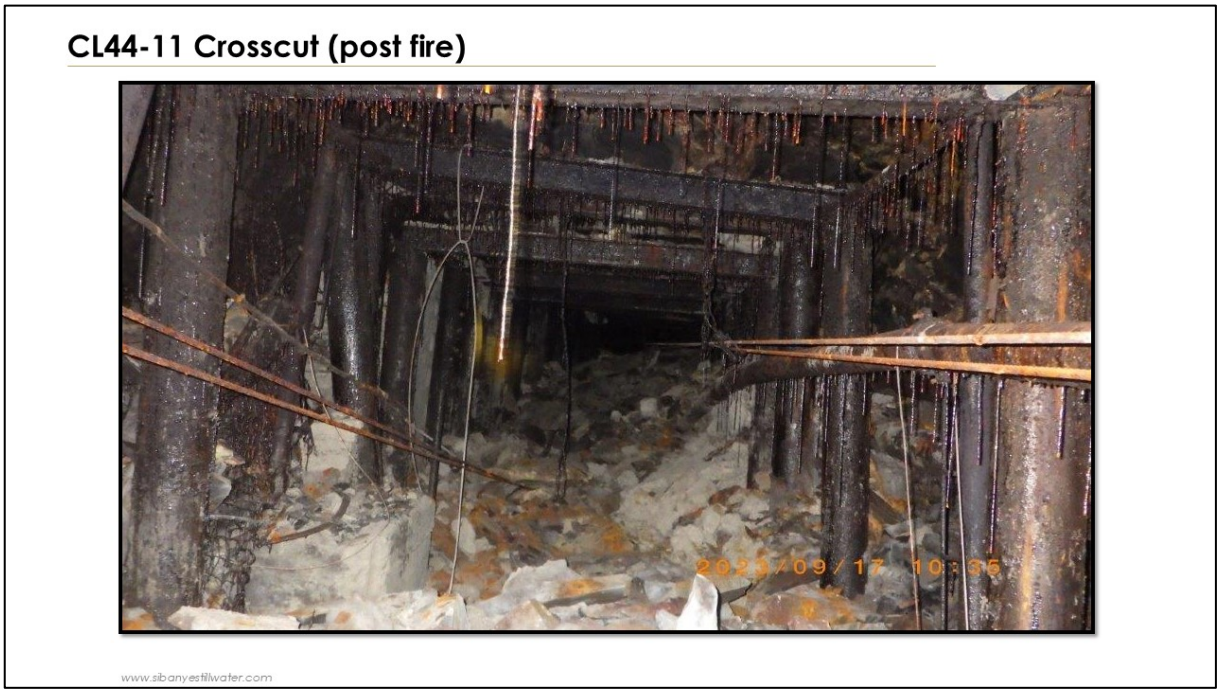


Figure 17. Crosscut conditions post-fire showing structural damage.



Figure 18. Hangingwall conditions close to the dyke intersection showing thermal effects.

Seismic Activity Correlation
A clear correlation between the progression of the fire and seismic activity was observed:

Onset of Seismicity:
Seismic activity began immediately with the onset of the fire, with micro-events ranging from

M_L-6.0 to M_L2.4 in a short period. The sensitivity of the network was well within range to ensure that the network conforms to minimum objective for warnings as prescribed in Jager & Ryder (1999) (Figure 19).

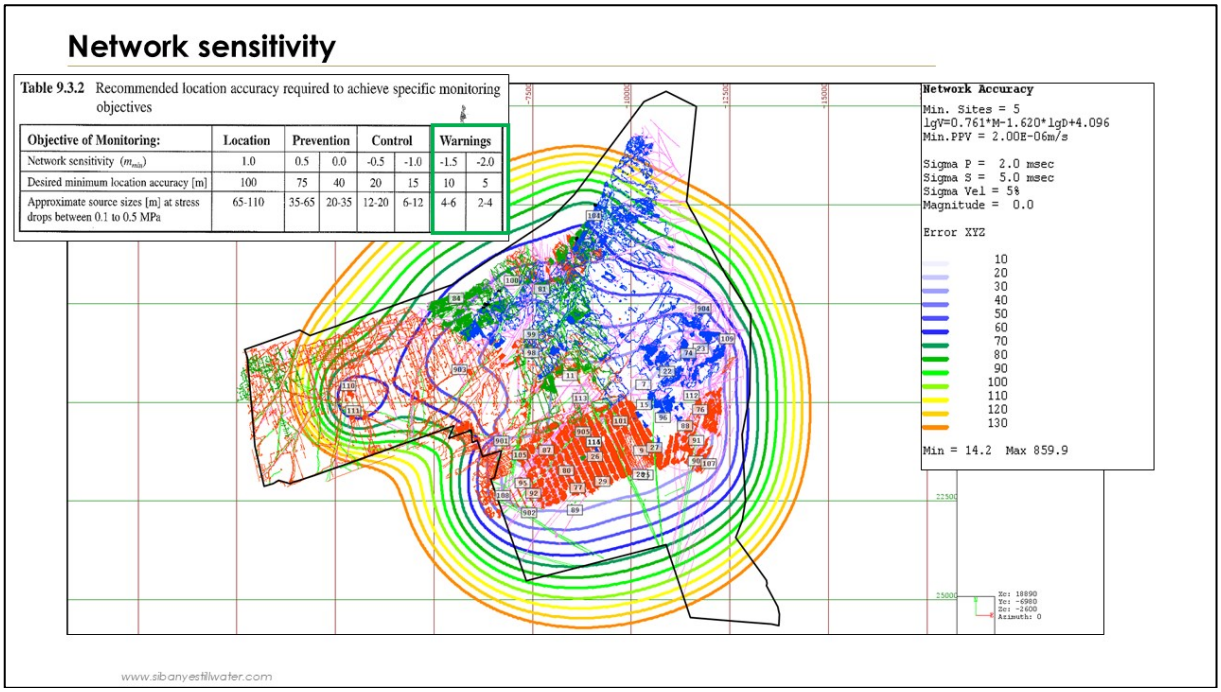


Figure 19. Network sensitivity at the time of the incident.

Spatial Pattern

Initial seismic events indicated the route of the fire, later concentrating along abutments and associated with slips on geological structures, particularly the Washington Dyke (Figure 19).

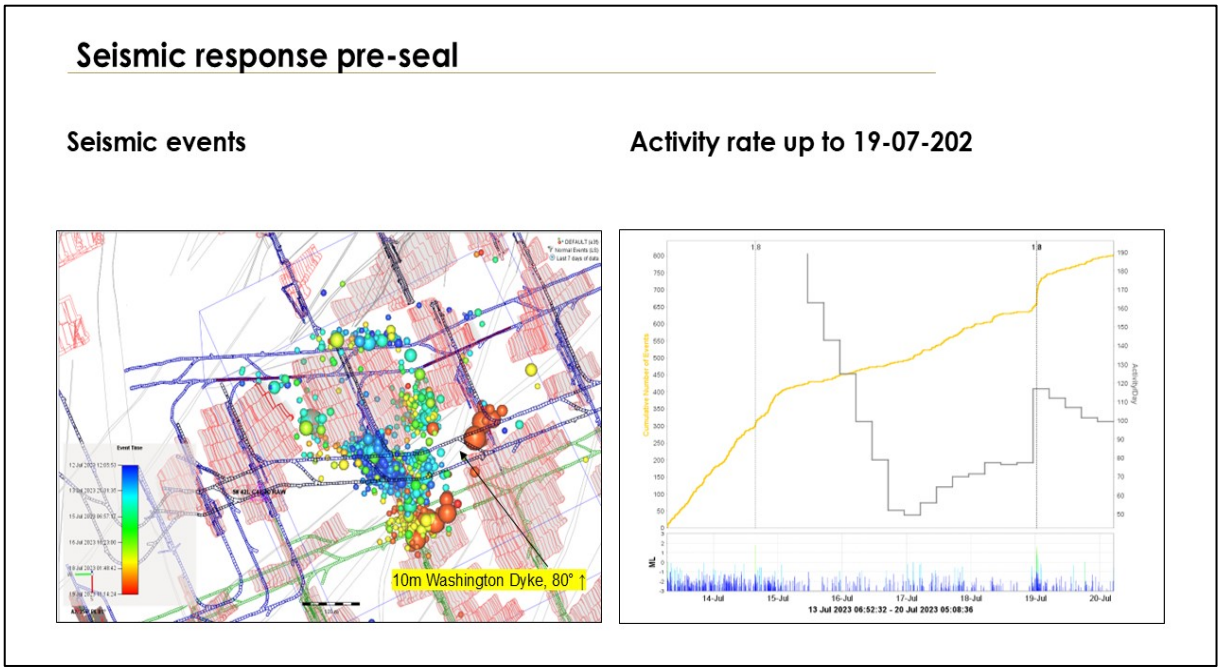


Figure 20. Seismic response pre-seal completion showing fire propagation path.

Causal Mechanisms
The seismic events were attributed to:

- Thermal expansion and contraction of the rock mass
- Thermal alteration of fault and dyke materials
- Gas and pressure build-up in geological structures
- Slippage and rupture along pre-existing weaknesses

Post-Fire Cessation
Seismic activity diminished once the fire was extinguished, as thermal stresses dissipated, and the rock mass began to cool and stabilise. Reference to be made to Figures 20a – 20d, depicting the seismic activity during the period from the onset of the fire to the containment thereof.

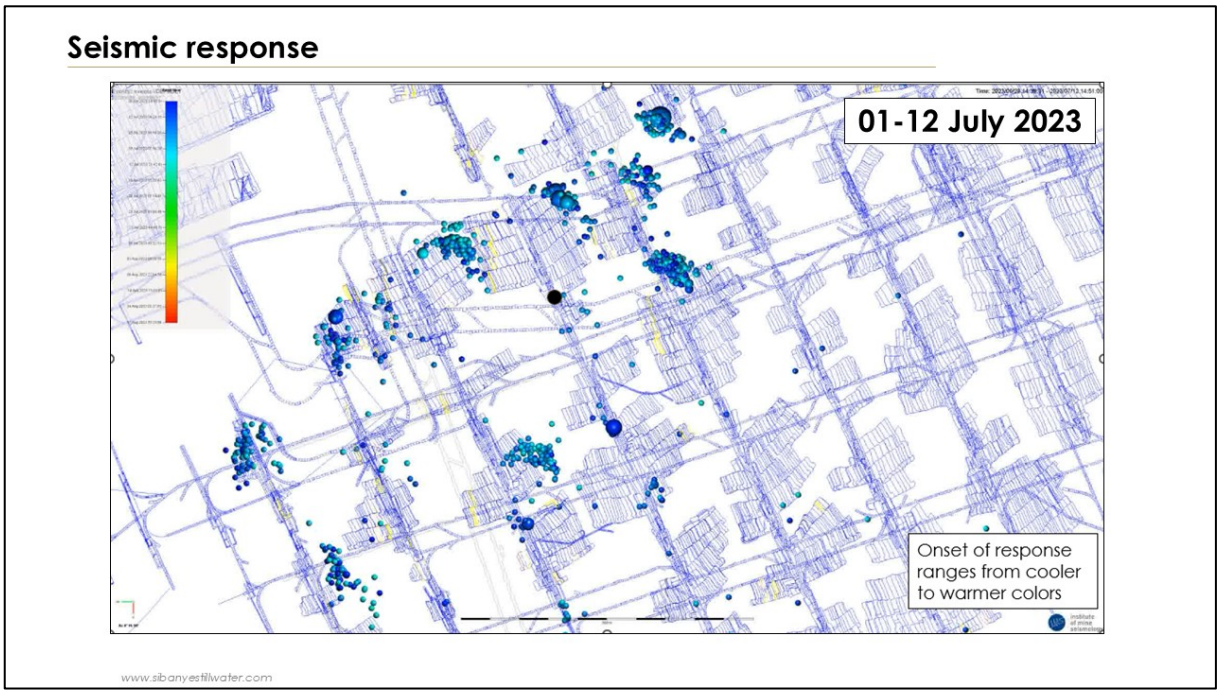


Figure 21a. Seismic response timeline showing pre-fire phase.

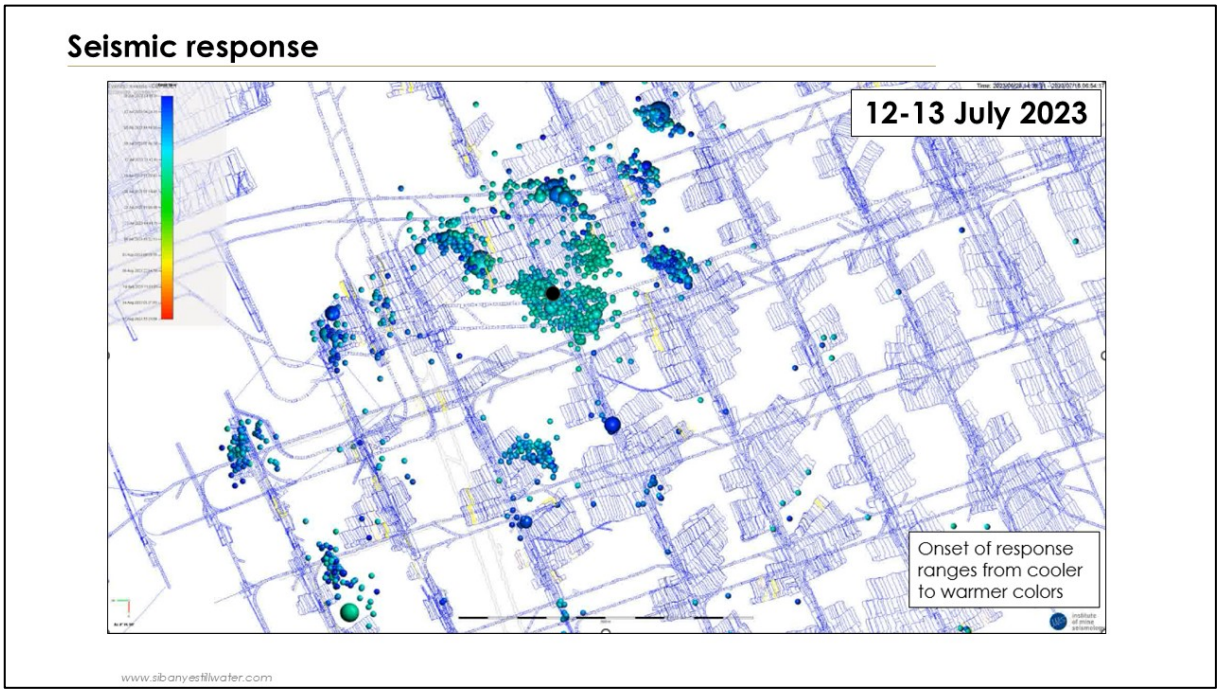


Figure 21b. Seismic response timeline showing start of fire phase.

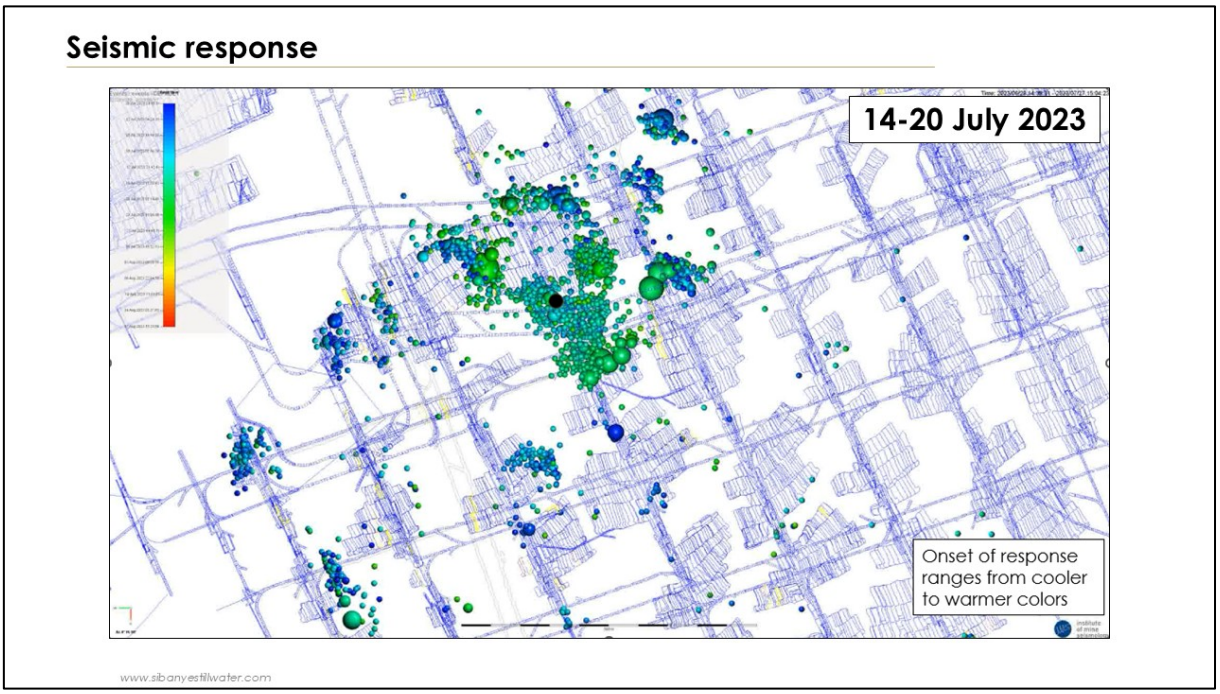


Figure 21c. Seismic response timeline showing height of fire phase with increased response.

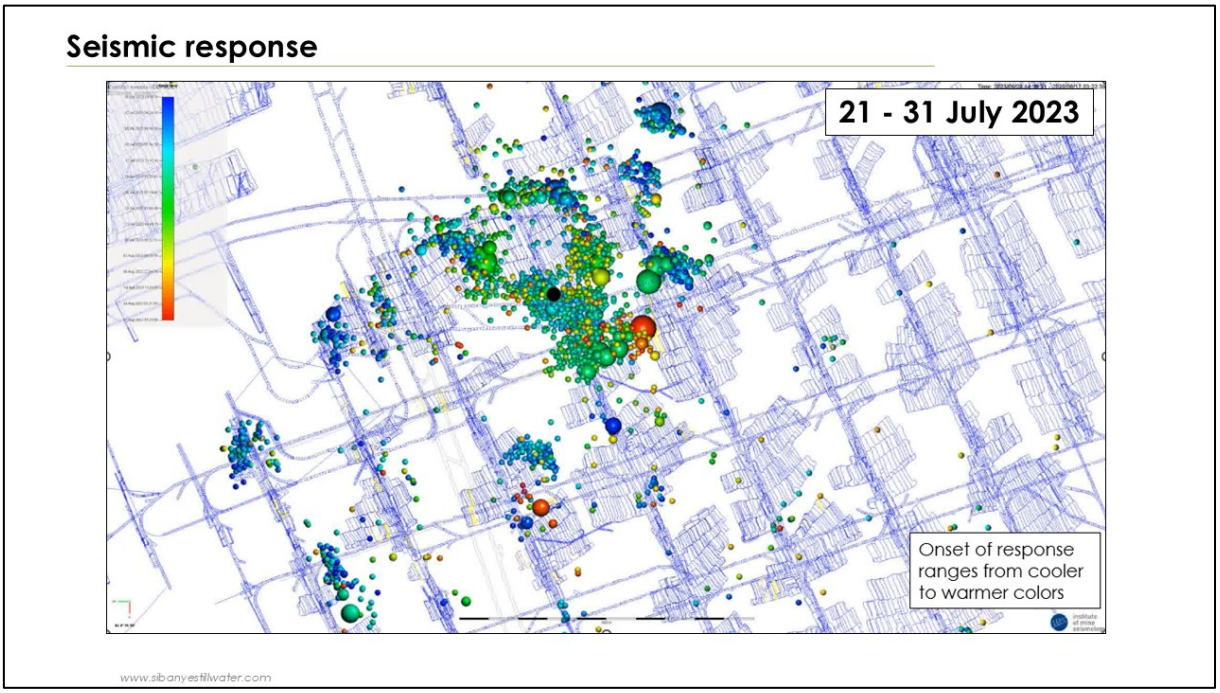


Figure 21d. Seismic response timeline showing response after seals were built.

Monitoring Enhancements

Monitoring systems demonstrated significant value but could be further improved as outlined in Table 1.

Table 1. Monitoring enhancements

Monitoring system	***Potential improvement***
Integrated Monitoring	Develop systems that better integrate seismic, gas, and temperature monitoring for a more comprehensive assessment of fire conditions.
Automated Analysis	Implement advanced analytics to better correlate seismic patterns with fire progression and predict critical thresholds.
Mobile Monitoring	Equip emergency response teams with portable monitoring devices to enhance situational awareness during response operations (not available currently).
Decision Support Tools	Development of decision support systems that incorporate real-time monitoring data to guide response actions.

CONCLUSION

The underground fire incident at Hlanganani Shaft demonstrated the complex interaction between fire, ground support, ventilation systems, and geological structures in underground mining environments. The use of IMS software and seismic monitoring proved invaluable in tracking the fire's progression and guiding response decisions.

Key findings indicate that:

- Underground fires can induce significant seismic activity through thermal effects on rock masses and geological structures.
- Real-time monitoring provides critical data for predicting fire behaviour and optimising response strategies.
- Established threshold values for ground motion (specifically 0.06 m/s PPV) serve as effective triggers for withdrawal decisions during emergency response.
- Integration of multiple monitoring parameters (seismic, gas, temperature) offers the most comprehensive assessment of underground fire conditions.

This paper contributes to the growing body of literature on using geophysical monitoring for safety applications in underground mining (Mendecki, 2016; van Aswegen *et al*., 2018). The findings align with previous research on thermal effects on rock stability (Jager & Ryder, 1999) while providing new insights into the correlation between fire progression and seismic activity patterns.

Future research should focus on developing more integrated monitoring systems and automated analysis tools to further improve response capabilities, particularly in developing predictive models that can anticipate fire behaviour based on early seismic signatures.

These findings underscore the need for continuous innovation in fire monitoring systems to ensure operational safety in deep-level mining.

ACKNOWLEDGEMENTS

The authors wish to acknowledge the contributions of Mine Rescue Services South Africa, the Rock Engineering and Seismic Departments at Sibanye Stillwater Driefontein Operations, and the Institute of Mine Seismology for their support in the response efforts and subsequent analysis of this incident.

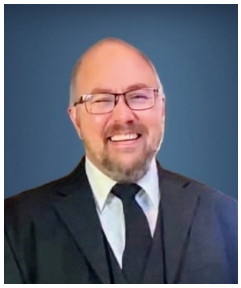
REFERENCES

Ferreira, R. I. L., Masethe, R., & Ndaba, P. (2023). Rationale for the quick withdrawal of the underground workforce following (large) dynamic ground motions – How extensive should the exclusion zone be? In Proceedings of the ISRM 15th International Congress on Rock Mechanics and Rock Engineering & 72nd Geomechanics Colloquium – Challenges in Rock Mechanics and Rock Engineering (W. Schubert & A. Kluckner, Eds., pp. 445–450). Austrian Society for Geomechanics.

Jager, A.J., & Ryder, J.A. (1999). A handbook on rock engineering practice for tabular hard rock mines. The Safety in Mines Research Advisory Committee (SIMRAC), Johannesburg.

Mendecki, A.J. (2016). Mine Seismology Reference Book: Seismic Hazard. Institute of Mine Seismology.

Van Aswegen, G., Mendecki, A.J., & Mountfort, P. (2018). Near-field ground motion decay in constrained rock. Proceedings of the Deep Mining Conference, Perth.



Mitch William Wiggins

Unit Manager Rock Engineering
Sibanye-Stillwater

Mitch Wiggins is an appointed Rock Engineering Practitioner at Kloof Operations, where he applies a blend of practical experience, analytical expertise, and evolving technical knowledge to support safer and more efficient mining practices. His journey into rock engineering began in seismic processing, where he built a solid foundation in rock mass behavior and data interpretation—skills that continue to inform his decisions in high-risk underground environments.

Raised in a mining family, Mitch was immersed from an early age in stories of falls of ground and near misses. These early experiences instilled a deep respect for the earth's complexities and a lifelong passion for understanding its dynamic behavior. For him, rock engineering is not just a profession but a vocation—one rooted in purpose and driven by the goal of protecting lives through the responsible application of geotechnical science.

Mitch's career reflects a hands-on, progressive path through the rock engineering discipline. He has consistently embraced both the lessons of the field and the insights of academic study. Currently in progress of completing his Advanced Rock Engineering Certificate, Mitch views formal accreditation as a natural extension of his commitment to continuous learning and professional development. He is particularly interested in bridging the gap between theoretical models and real-world mining conditions, advocating for solutions that are both technically sound and practically implementable.

Beyond his operational role, Mitch is an active contributor to the broader rock engineering community. He serves on the council of the South African National Institute of Rock Engineering (SANIRE) and is the current Chair of the Free–Vaal Branch. He is also a member of the International Society for Rock Mechanics (ISRM) and the Southern African Institute of Mining and Metallurgy (SAIMM).

Mitch approaches rock engineering with humility and purpose, recognizing both the potential and limitations of current practice. He is committed to collaborative problem-solving, applying modern tools, and sharing experience in service of safer mining. Grounded in the realities of deep-level operations yet inspired by the possibilities of innovation, he continues to strive in shaping the future of rock engineering in South Africa.

Modern satellite data provide new insights into surface movements above coal longwall mining

A. Vervoort

KU Leuven, Belgium

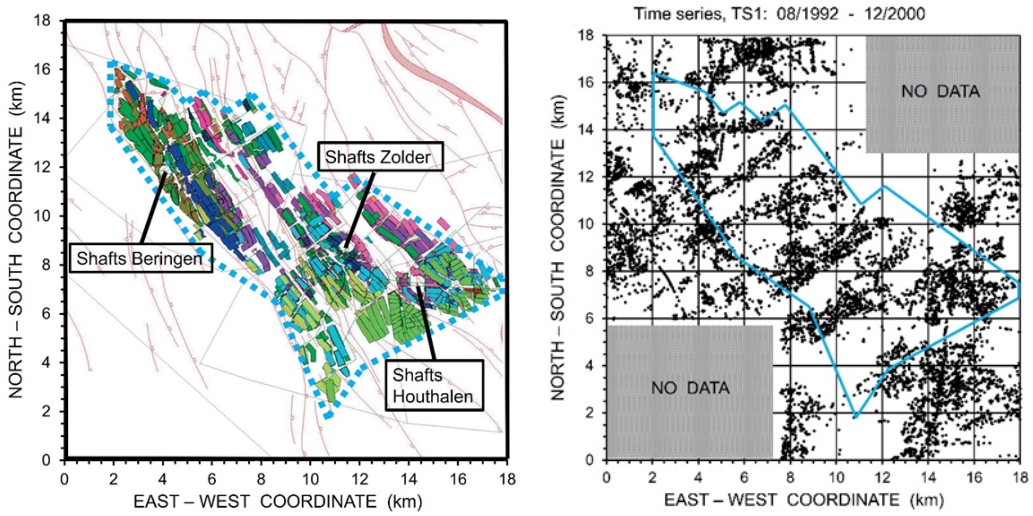
Apart from theoretical considerations and mathematical calculations, most basic concepts of subsidence over coal longwall mining are based on conventional levelling techniques. At the end of the last century, satellite data images became freely available for research. Although this remote sensing technique has its limitations, it offers many advantages over conventional levelling. The datasets are not limited to specific survey lines above the mined area and its immediate surroundings, and the frequency is relatively high (i.e., once a month or, for the more recent datasets, every six days). Furthermore, there is no time limit on the observation period. Analysis of more than 30 years of satellite observations above the Belgian Campine coal district shows that (i) in old mined sub-areas, subsidence continued for several decades after the last longwall panel in that sub-area had been mined, (ii) 12 to 15 years after mine closure, the direction of surface movements reversed and an uplift of the surface above the mined areas was observed, which is still ongoing in 2025, (iii) the horizontal extension of the impact of mining on surface movements is larger than is generally assumed.

Keywords: surface movements, subsidence, uplift, longwall mining, remote sensing

INTRODUCTION

Coal longwall mining with goafing affects the behaviour of the strata and overburden above the mined panels. Surface subsidence is the result of this complex behaviour of underground collapses (goaf), fracturing of the coal strata, deformation of the rock layers and possible relative movements along faults and fractures. The paper focuses not on the initial subsidence, but on the residual subsidence and the long-term movements. The phase of residual subsidence is often assumed to end (i) when an amount of additional subsidence has occurred equal to a certain percentage of the initial subsidence, or (ii) when the increments between successive measurements have become negligible, or (iii) when a predefined fixed time period has been reached (Al Heib *et al.*, 2005; Cui *et al*., 2020; Luo and Peng, 2000; Vervoort, 2020a). After this phase, it is often assumed that the subsidence has stopped and that the ground is stable (Al Heib *et al*., 2005). In the last 30 years, remote sensing satellite data of surface movements became freely available for research (Costantini *et al*., 2021; Crosetto *et al*., 2020; Devleeschouwer *et al*., 2008). This means that surface movements can be studied without the need for large research budgets, and independent of mining companies. Other advantages of this new and modern surveying tool are that (i) the density of datapoints is high and the datasets are not limited to specific survey lines above the mined area and its immediate surroundings, (ii) the frequency is relatively high (i.e., once a month or, for the more recent datasets, every six days) and (iii) that there is no time limit on the observation period, even after the closure of an underground mine. Although this remote sensing technique also has its limitations (Vervoort, 2021a), the three advantages listed above contrast to the characteristics of conventional levelling. The latter are time-consuming, and therefore expensive, the measurements are conducted along a limited number of measurement lines, and the maximum distance away from the mined area is also limited. The frequency between successive measurement moments is normally low, especially after the mining period. In most cases, no further levelling is performed in an area when the differences between successive measurements are of the order of the measurement accuracy.

In the case study presented, an area of 18 km by 18 km is studied above and around three underground coal mines (Figure 1a; based on Van Tongeren and Dreesen, 2004). These mines are the Beringen, Zolder and Houthalen mines, which are situated in the western part of the Belgian coal Campine basin in north-eastern Belgium. Coal production took place in these three mines between 1922 and 1990, 1930-1992, 1939-1992, respectively. Access to the three underground mines was through two central vertical shafts. The underground pumping stations were dismantled, and the shafts were sealed off in the year after production was terminated. The total thickness of the overburden varies between 400 and 600 m. Characteristic of these coal mines is that along a vertical line, numerous coal seams were mined (Figure 1a). At certain locations 10 or more seams were mined. Overall, the mining heights were low. As the Campine coal basin is heavily faulted, the mining lay-out is very irregular. In Figure 1, an approximate (blue) contour is drawn around all the panels mined. This envelope is used further as reference to define whether a datapoint is situated above the mined area or outside the mined area.



(a) (b)

Figure 1. Map of the study area. (a) View on the superimposed longwall panels in the Beringen, Zolder, and Houthalen mines (based on Van Tongeren and Dreesen, 2004), (b) Spatial distribution of datapoints during first time series, TS1, from August 1992 through December 2000. Blue lines present an approximate contour around the panels.

Radar interferometry or interferometry with synthetic aperture radar (InSAR) data are used to study the surface movements since the closure of the last coal mine in the Campine coal basin in 1992 (see Table I). The first two data sets were made available for research through a European Space Agency research proposal (Devleeschouwer *et al.*, 2008). The third and fourth time series are made available through the European Ground Motion Service project which receives funding from the European Commission's Copernicus programme (Costantini *et al.*, 2021). For all these satellite data, complex algorithms are needed to transfer the recording of a pulse of electromagnetic waves travelling through the atmosphere and reflecting on the earth's surface into a measurement of the change in vertical position of the surface (Crosetto *et al.*, 2016; Ansar *et al.*, 2022). One condition for observing the movement is the presence of a reflective surface that can be followed during the entire observation period. In most cases, these surfaces are the top of buildings and other hard surfaces (e.g., roads and paved zones). Agricultural land, woodlands, and unused or semi-natural land seldom have useful reflectors. For the satellites of the first two time series, the algorithms search for reflective surfaces with dimensions of 4 m on 20 m and follow these surfaces through the entire time series. The data for all detected reflective surfaces are available (Figure 1b). For the third and fourth time series another approach is applied. For all nodes on a regular mesh with a spatial resolution in the order of 100 m, the change in vertical position is determined for all reflected waves around the node position (Crosetto *et al.*, 2016; Ansar *et al.*, 2022).

Table I: Overview of all the time series available for the study and sub-periods analysed

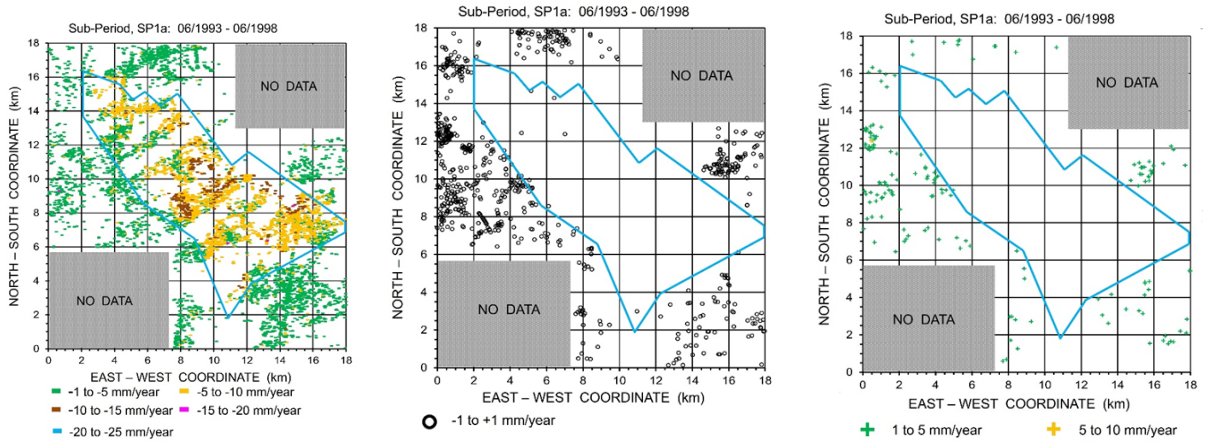
Time Series			Sub-periods	
TS1	08/1992 – 12/2000	ESA: European C-band ERS1/2	SP1a SP1b	06/1993 - 06/1998 07/1998 - 12/2000
TS2	12/2003 – 10/2010	ESA: ENVISAT-ASAR	SP2	01/2005 - 12/2009
TS3	01/2016 – 12/2021	EGMS: Sentinel-1 C-band SAR	SP3	01/2016 - 12/2020
TS4	01/2019 – 12/2023	EGMS: Sentinel-1 C-band SAR	SP4	07/2021 - 12/2023

The evolution of the surface movement rates after mine closure

Analysis of maps representing the surface movement rates

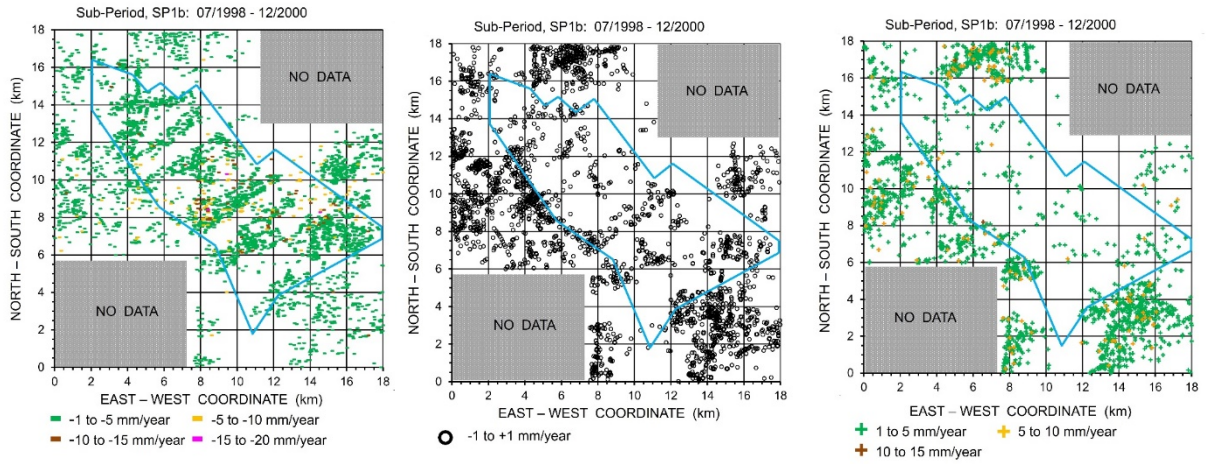
To study the spatial distribution of the additional surface movement, the latter is presented as the average annual movement rate over periods of five or of 2.5 years. In Figure 2, the spatial distribution for the first five-year sub-period (SP1a) is presented. This sub-period follows immediately after the closure of the Zolder and Houthalen mines. In total, there are about 9000 reflectors or datapoints in the study area. These datapoints are grouped in three different classes and each class is presented in a different map. The generally accepted accuracy of the method is considered, i.e., about 1 mm/year when looking at the variation of the rates over a few years (Marinkovic *et al*., 2009; Vervoort, 2021a). The three maps are for the datapoints clearly undergoing subsidence (< -1 mm/year; Figure 2a), the datapoints with an average annual rate within the accuracy limits of ± 1 mm/year (Figure 2b), and the datapoints clearly undergoing uplift (> 1 mm/year; Figure 2c). The group of subsidence and uplift datapoints are further divided and presented by different colours. The movement rates are classed in 5 mm/year intervals (except the first interval which starts from -1 or +1 mm/year). A good interpretation of the data requires that the three maps are looked at together. Above the mined area, i.e., inside the blue contour, there are no reflectors undergoing uplift (Figure 2c) and only a few of them (2 to 4) undergo no significant movement (Figure 2b). This means that the entire surface area directly above the mined zone during this sub-period SP1a is still in the phase of (residual) subsidence (Figure 2a). Within the mined area, the largest portion of the reflectors undergo a movement between -5 and -10 mm/year (orange minus-signs). Above the mined area, the group of reflectors with smaller rates of subsidence are mainly observed close to the blue contour envelope. The group of average subsidence rates between -10 and -15 mm/year (brown minus-signs) are mainly situated in the central part of the mined area. There are five reflectors with an average subsidence rate larger than -15 mm/year. The largest recorded rate is -20.6 mm/year (coordinates of 11.8 km east-west and 11.1 km north-south; blue square). This means that this reflector has moved about 10 cm downwards over this five-year period.

In Figure 3, the spatial distribution for a 2.5-year sub-period (SP1b) is presented. When comparing Figure 3 to Figure 2, it is immediately clear that there is an evolution in the surface movements over time. During the sub-period SP1b, the three different groups of surface movements (i.e., subsidence, movement within accuracy limits and uplift) are observed both outside and inside the mined area. Most of the reflectors undergoing subsidence belong to the class -1 to -5 mm/year (green minus-signs in Figure 3a) and the density of these reflectors is similar inside and outside the mined area. In conclusion, it is clear that the surface movements are in a transition phase six to eight years after the closure of the last two mines. Above the mined area, most reflectors are still undergoing subsidence, but in comparison to SP1a, there are many more reflectors moving within the accuracy limits and even a group of reflectors undergoing uplift.



(a) (b) (c)

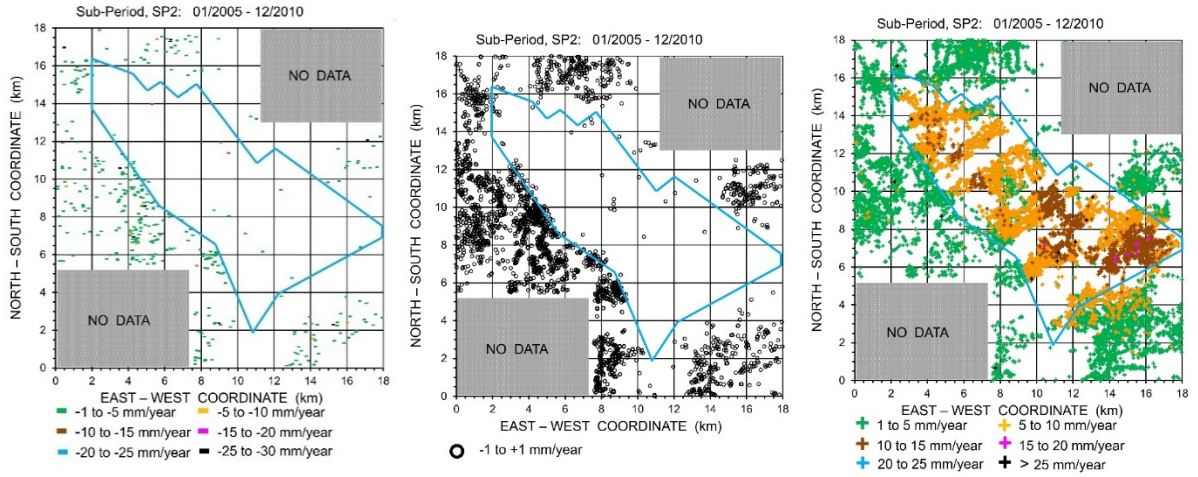
Figure 2. Spatial distribution of average surface movement rates (mm/year) for five-year sub-period SP1a (06/1993 - 06/1998). (a) All datapoints undergoing subsidence (< -1 mm/year); (b) All datapoints with averages within accuracy limits (±1 mm/year); (c) All datapoints undergoing uplift (> 1 mm/year). The blue line presents the approximate contour around the mined longwall panels.



(a) (b) (c)

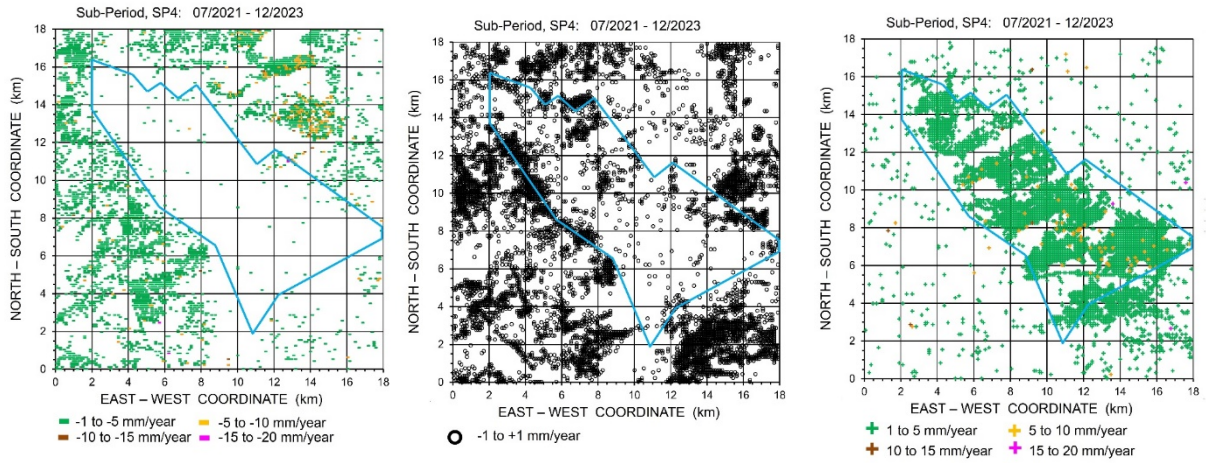
Figure 3. Spatial distribution of average surface movement rates (mm/year) for 2.5-year sub-period SP1b (07/1998 - 12/2000). (a) All datapoints undergoing subsidence (< -1 mm/year); (b) All datapoints with averages within accuracy limits (±1 mm/year); (c) All datapoints undergoing uplift (> 1 mm/year). Blue line presents the approximate contour around the mined longwall panels.

For the sub-period SP2, the overall view (Figure 4) is nearly the opposite as for sub-period SP1a, immediately following the closure. Above the mined area, nearly all reflectors are undergoing an uplift (Figure 4c). The number of reflectors moving within accuracy limits (Figure 4b) is small and only 20 reflectors are still undergoing subsidence (Figure 4a). Above the mined area, nearly the entire surface is moving upwards. The larger rates, e.g., larger than 5 mm/year, occur around a central line running from north-west to south-east. Outside the mined area, the density of reflectors undergoing clear subsidence is smaller (Figure 4a) and the density of uplift is larger (Figure 4c). In conclusion, about 15 years after the closure of the mines, the surface movement direction has fully reversed from downwards to upwards above the mined area. Above the mined area, a similar picture is observed for the 5-year sub-period SP3: nearly no reflectors undergoing subsidence or are moving within accuracy limits. So, nearly all reflectors are moving upwards, i.e., about 25 years after the closure.



(a) (b) (c)

Figure 4. Spatial distribution of average surface movement rates (mm/year) for five-year sub-period SP2 (01/2005 - 12/2010). (a) All datapoints undergoing subsidence (< -1 mm/year); (b) All datapoints with averages within accuracy limits (±1 mm/year); (c) All datapoints undergoing uplift (> 1 mm/year). The blue line presents the approximate contour around the mined longwall panels.



(a) (b) (c)

Figure 5. Spatial distribution of average surface movement rates (mm/year) for 2.5-year sub-period SP4 (07/2021 - 12/2023). (a) All datapoints undergoing subsidence (< -1 mm/year); (b) All datapoints with averages within accuracy limits (±1 mm/year); (c) All datapoints undergoing uplift (> 1 mm/year). The blue line presents the approximate contour around the mined longwall panels.

For the most recent dataset (sub-period SP4), the surface movements characteristics further change (Figure 5). The largest difference from the previous sub-periods is that there are now more reflectors above the mined area that cannot be clearly characterised as moving upwards, i.e., with an average rate within the accuracy limits of ±1 mm/year (Figure 5c). This is most clearly noted above the Beringen mine, i.e., the mine which was closed two years before the Zolder and Houthalen mines were closed. In sub-period SP4, reflectors undergoing an uplift larger than 5 mm/year are relatively rare (Figure 5c).

The main conclusion following the analysis of the various maps presenting the spatial distribution of the surface movement rates above and around the mined zone, is that in the approximately 30-year period after the closure of the underground coal mines, there is still movement, linked to the past mining and flooding of the underground infrastructure and surrounding rock mass. During this period there

is a clear change in the surface behaviour. In the first years following closure, additional subsidence occurred above the mined area. Later, this was replaced by a clear uplift of the surface. Initially the uplift rates were the highest, but they decreased with time. Above the mined area, spatial variation is observed, indicating that the surface movement is not homogeneous. Outside the mined area, the surface movement also shows a systematic variation over time, but the picture is less clear, as the largest density of reflectors is for datapoints with average rates within the accuracy limits of ±1 mm/year. The latter is not illogical.

Variation of surface movement as a function of time

The main aim of the study presented in the paper is to analyse surface movements after the closure of deep underground coal mines. During the phase of residual subsidence and the phase of uplift, the average rates of surface movements are small in comparison to the short-term or immediate subsidence. During sub-period SP1a, the largest subsidence rate was 21 mm/year, averaged over a five-year period (i.e., for the datapoint at east-west 11.9 km, north-south 11.1 km). This means that during this period, the surface has moved further downwards over 0.1 m. During sub-period SP3, the largest uplift rate was 38 mm/year, averaged over a five-year period (i.e., for the datapoint at east-west 11.2 km, north-south 6.8 km). So, just for this five-year period, the uplift totalled nearly 0.2 m. For the entire Campine coal basin, total uplift values of 0.5 m (till now) have been observed. Some researchers apply the rule of thumb that the total uplift corresponds to 5 to 10 % of the total subsidence. However, one should be careful in applying this rule too strictly. It is certainly not valid point per point along a transect (Bekendam and Pöttgens, 1995; Pöttgens, 1985; Vervoort, 2020b), i.e., the zone with the largest (residual) subsidence does not correspond to the zone with the largest uplift. Or, in other words, uplift is not a simple rebound of subsidence.

This is illustrated in Figure 6. This figure presents the variation of the average rate along a north-south transect. The transect runs through the shaft complex of the Houthalen mine (see green rhombus). A moving average is calculated for all datapoints situated within a band of 500 m around a central line corresponding to an east-west coordinate of 14.5 km. The northern and southern border of the mined area along this transect are indicated by blue lines. Curves for the five sub-periods are presented. The subsidence rate is largest for the subperiod SP1a, with a clear maximum around 8.25 km (north-south). The extension of the subsidence profile beyond the mined boundary is large, especially to the south (left side of the graph). In the sub-period SP2, the uplift rate is the largest. Its maximum is situated at about 6.25 km (north-south). For the two later sub-periods, SP3 and SP4, the location of the maximum uplift moves slightly to the north (at 6.75 km for SP4). The extension of the average uplift zone outside the mined area is larger to the south. More than 3 km for SP2, and about 1 to 2 km for the two other subperiods characterised by uplift.

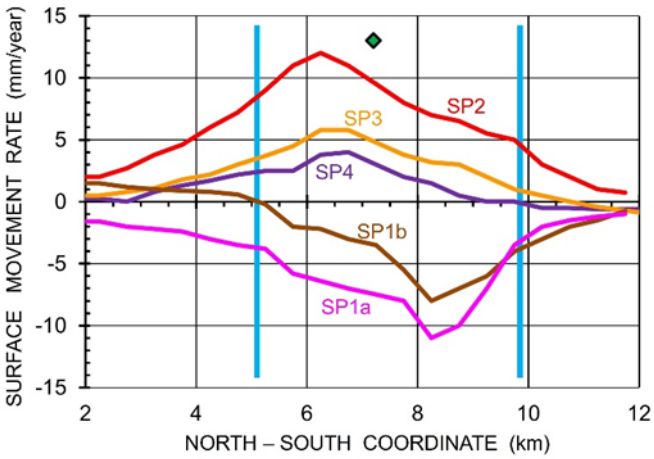


Figure 6. Variation of the average rate of surface movement for each sub-period studied along a 10 km north-south transect at the east-west coordinate of 14.5 km. The limits of the mined area along this transect are indicated by blue lines and location of central shafts is shown by green rhombus.

For a survey line situated around the western limit of the mined area of the Zolder mine, some data are available. The line is 1675 m long and is situated at the north-south coordinate of about 6 km (Figure 7a). To the east of the mined border and in the vicinity of the survey line, longwall panels were mined between 1941 and 1992. In the zone of influence, a total of 159 panels were mined, of which 76 panels were mined before 1966 (i.e., reference date for first survey). The depth of the 159 panels varied between 547 m and 828 m (average about 690 m). The average mining height was 1.57 m). Nine different coal seams were mined. The measured subsidence between 1966 and 1992 was for the three survey points outside the mined area 0 mm (m-3), -50 mm (m-2) and -660 mm (m-1). Above the mined area, these values were -1.61 m (m+1), -3.25 m (m+2) and -3.63 m (m+3). In Figure 7b, some interpolations and extrapolations are applied between the time series, so that full curves can be presented for the entire 32 years following the closure in 1992. All six survey points show additional residual subsidence followed by uplift, even the survey point (m-3), which was classed as undergoing no movement in the conventional survey campaigns. The largest additional subsidence is recorded for the two survey points, furthest into the mined area, i.e., m+2 and m+3. The total additional subsidence after 12 years is -66 mm and -62 mm for m+2 and m+3, respectively. Outside the mined area, the total residual subsidence of the survey points m-1 and m-2 is larger than the one for m+1. For m-1, the largest additional subsidence is reached after 14.5 years and is -34 mm. For m-2, these values are 18.5 years and -45mm, respectively. So, the end of the residual subsidence phase is not the same along this survey line. For the two survey points furthest away from the mined boundary, i.e., m-3 and m-2, the rates of uplift are similar. For the point just outside the mined area (m-1), the additional subsidence after 1992 is completely recovered by uplift at the end of 2023. For the three survey points above the mined area, the rate of uplift is larger than the rate of residual subsidence after 1992. At the end of the 32 years of satellite data observations, the three survey points above the mined area are 21 to 35 mm higher than in 1992. If one compares the uplift after reaching the lowest point in the curves to the total amount of subsidence since 1966, i.e., the year of the first survey, the calculated percentages uplift vs total subsidence are 3.4 %, 2.6 % and 2.6 % for m+1, m+2 and m+3, respectively. For example, for m+3, it is the ratio of 96.5 mm to 3692 mm, i.e., the sum of 3630 mm (until 1992) and 62 mm subsidence afterwards. In conclusion, the analysis of the additional surface movements for six points along a survey line of 1675 m shows again the complexity of the long-term surface movements above and around a mined area. Some observations are easy to understand, others are more difficult to explain. However, the remote sensing satellite data proves to be a powerful and accurate tool, and it allows new insights into the long-term surface movements above closed deep coal longwall mines.

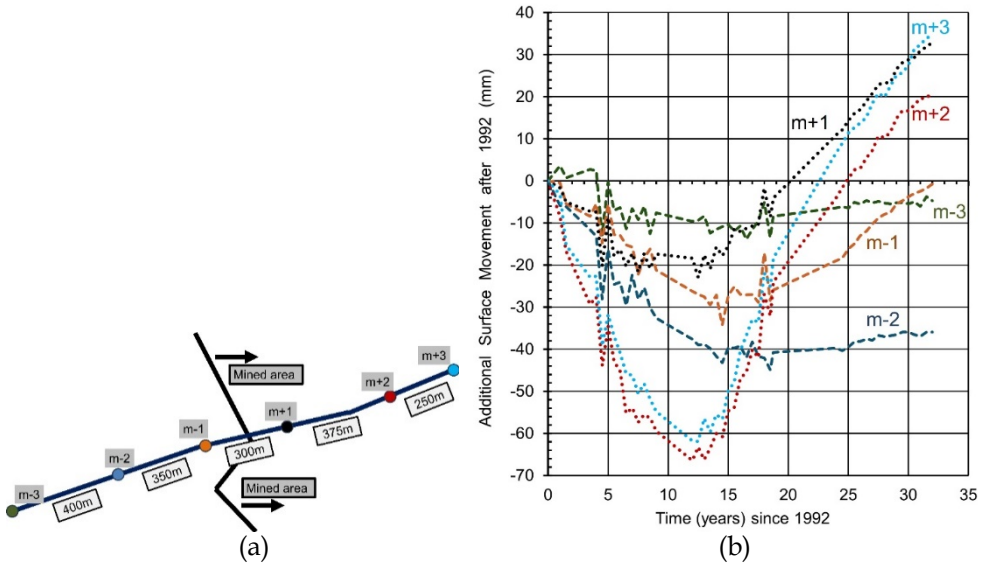


Figure 7. Surface movement of six measuring points after mine closure in 1992: (a) View of survey line, (b) Variation as a function of time.

DISCUSSION OF FINDINGS AND CONCLUSIONS

InSAR's remote sensing satellite data of surface movements opens new opportunities to learn more about the impact of mining and to gain new insights. The research topic presented in the paper focusses on the long-term impact of longwall coal mining, specifically after mine closure. Data covering a period of more than 30 years are studied. The major advantages of satellite data are the high density of the measuring points in a built environment above and around a mined area and the high measuring frequency. These aspects can never be realised by conventional surveys. During the lifetime of a mine, a limited number of survey lines are monitored and the interval between successive monitoring points is mostly 100 m or more. The selection of the survey lines coordinates is often influenced by specific issues (e.g., critical buildings or infrastructure, and the presence of faults below the surface). During the mining of a longwall panel, the frequency of measuring can be high, but only over a limited distance. Once the panel is mined, the frequency normally drops to once a year or every few years. In other words, a small portion of the surface area above and around the mined zones are monitored, and the behaviour between successive surveys remains unknown. The monitoring of the surface movements often stops completely, once all the mining activities have stopped. For the case study presented in this paper, a limited survey was done in 1992, i.e., the year of closure, followed by a last survey (again with a very limited extent) 15 years after the closure. As one can see in Figure 7b, a comparison between these two moments would not indicate the possibility of a phase of uplift movements. So, the most relevant and practical conclusion is that access to satellite data is of cardinal importance to study long-term surface movements.

The analysis of more than 30 years of satellite observations over an area of 18 x 18 km shows that:

- Surface movements continue for several decades after the closure of the underground mine and the dismantling of all equipment such as the underground pumping stations. In specific sub-areas, where the last panel was mined several decades before the closure, the residual subsidence phase covered periods of up to 50 years, much longer than the three to five years usually assumed.
- 12 to 15 years after mine closure in 1992, the direction of surface movements reversed and an uplift of the surface above the mined area is being observed (relative to the end of the subsidence phase), and which is still ongoing in 2025. The rate of uplift is of the same order as the rate of the residual subsidence. The uplift is mainly linked to the expansion of the collapsed, fractured and intact strata due to the increase in water pressure after flooding (see further for details). The maximum uplift to date is in the Campine coal basin, about 0.5 m since the start of the uplift phase.
- The horizontal extension of the impact of mining on surface movements is larger than generally assumed. The zone of influence outside the mined boundaries is several times the mining depth. Although above the mined area, the uplift has been explained (see further for details), outside the mined area and its immediate surroundings the picture of surface movements is less clear.

After the mine closure, the open tunnels, the collapsed goaf volumes and the surrounding rock mass or strata started to be filled with groundwater and the hydraulic gradient started to evolve towards the original hydraulic gradient. Recently, an analytical framework was successfully presented to better understand the different mechanisms and processes involved (Vervoort 2021b; Vervoort 2022a). Good correlation was observed between the measured and the calculated uplift. The crucial aspect for a good match between the two is to take into account the expansion of the goaf material when the water level is increased. However, equally important, is to also include in the calculations the expansion of all the strata between the excavated panels and around the mined area. It is believed that the strata layers are also drained during mining and that, after flooding, the pore pressure values are increased towards their original values before the mining began. A good fit with the measurements was observed for a goaf thickness equal to four times the mining height, and a stiffness ratio between goaf material and the rest of the strata equal to 1 on 10.

One could argue that the overall rates of surface movements are small, i.e., small residual subsidence and uplift rates. In comparison to the short-term or immediate subsidence rates, this is correct. However,

one cannot ignore additional movements of 10s of centimetres, even if the movement rates are low. Such movement values have an influence on surface and ground water, and on the flow in rivulets. As shown on the various graphs and maps, additional movements can significantly differ within relatively small areas. The long-term movements also can lead to new and/or additional damage to buildings and other infrastructure. Damage is caused by the sum of stresses and strains stored within constructions by past movements and loading (Boscardin and Cording, 1989), e.g., by the impact of the short-term subsidence phase, and of the additional loading due to the long-term movements (residual subsidence and uplift). As illustrated in Figure 7b, the sign of the relative movements between two neighbouring points or zones changes over time. In such cases, the impact on the angular distortion and horizontal strain of the various phases must be added in absolute terms, increasing significantly the angular distortions and horizontal strains. This enlarges the radius of the strain Mohr circles, resulting in possible new micro- and macro-fracturing of, e.g., masonry. In (Baglikow 2011; Dudek *et al.* 2021; Vervoort 2022b and 2024), examples are given of damage to buildings and other infrastructure during the uplift phase.

Prior to the various studies of long-term impact of deep coal longwall mining in Europe, based on satellite data (e.g., Caro Cuenca *et al*., 2013; Devleeschouwer *et al.,* 2008; Gee *et al*., 2017; Samsonov *et al.,* 2013; Vervoort and Declercq, 2017), one thought to know and understand the duration of induced surface movements, i.e., a few years after mining. Now, we must recognise that we do not know how long the impact will last. It is reasonable to assume that once all cavities, fractures and pores are again in equilibrium with the original hydraulic gradient, the uplift phase comes to an end. However, two major questions remain. The first question is, how long the physicochemical swelling of the clay minerals in the shale formations carry on (Wakim *et al.,* 2007). And the second question is whether the observed uplift corresponds to the only component of surface movements or if it is the result of a certain amount of subsidence and a larger amount of uplift. The latter would mean that once the causes for uplift are neutralised, e.g., the mechanical expansion of all rock and the physicochemical swelling of the clay minerals, residual subsidence would again be observed. Note that due to the flooding of the underground infrastructure and surrounding rock mass, the strength characteristics of the rock have weakened, and its compressibility capacity has increased. This would mean that even the residual subsidence rate would be larger than before the flooding. In other words, it is nearly impossible to predict today the surface behaviour over the coming decades. Only further monitoring over a sufficiently long period (e.g., an additional 20 years) will tell us if the strata and overburden have reached a full equilibrium.

REFERENCES

Al Heib, M., Nicolas, M., Noirel, J.F. and Wojtkowiak, F. (2005). Residual subsidence analysis after the end of coalmine work. Example from Lorraine colliery, France. *Proceedings of the Symposium Post Mining*, Nancy, France, 16–17 November 2005, pp. 1–9.

Ansar, A.M.H., Din, A.H.M., Latip, A.S.A. and Reba, M.N.M. (2022). A short review on persistent scatterer interferometry techniques for techniques for surface deformation monitoring. *Int. Arch. Photogramm. Remote Sens. Spatial Inf. Sci.*, XLVI-4/W3-2021, 23–31. https://doi.org/10.5194/isprs-archives-XLVI-4-W3-2021-23-2022

Baglikow, V. (2011). Damage-relevant effects of mine water recovery— Conclusions from the Erkelenz hard coal district. *Markscheidewesen,* 118(2), 10 – 16.

Bekendam, R.F. and Pöttgens, J.J. (1995). Ground movements over the coal mines of southern Limburg, The Netherlands, and their relation to rising mine waters. *Proceedings of the Fifth International Symposium on Land Subsidence.* The Hague, the Netherlands, IAHS234, pp. 3-12.

Boscardin, M.D. and Cording, E.J. (1989). Building Response to Excavation-Induced Settlement. *J. Geotech. Engrg.,* 115 (1), 1–21. https://doi.org/10.1061/(asce)0733-9410(1989)115:1(1)

Caro Cuenca, M., Hooper, A.J. and Hanssen, R.F. (2013). Surface deformation induced by water influx in the abandoned coal mines in Limburg, The Netherlands observed by satellite radar interferometry. *J. of Appl. Geophys.*, 88, 1–11. https://doi.org/10.1016/j.jappgeo.2012.10.003

Costantini, M., Minati, F., Trillo, F., Ferretti, A., Novali, F., Passera, E., Dehls, J., Larsen, Y., Marinkovic, P., Eineder, M., Brcic, R., Siegmund, R., Kotzerke, P., Probeck, M., Kenyeres, A., Proietti, S., Solari, L. and Andersen, H.S. (2021). European Ground Motion Service (EGMS). *Proceedings International Geoscience and Remote Sensing Symposium (IGARSS)*, Brussels, Belgium, pp. 1-4. https://doi.org/10.1109/IGARSS47720.2021.9553562

Crosetto, M., Solari, L., Mróz, M., Balasis-Levinsen, J., Casagli, N., Frei, M., Oyen, A., Moldestad, D.A., Bateson, L. and Guerrieri, L. (2020). The Evolution of Wide-Area DInSAR: From Regional and National Services to the European Ground Motion Service. *Remote Sens.*, 12, 2043. https://doi.org/10.3390/rs12122043

Cui, X., Zhao, Y., Wang, G., Zhang, B. and Li, C. (2020). Calculation of residual surface subsidence above abandoned longwall coal mining. *Sustainability*, 12, 1528. https://doi.org/10.3390/su12041528

Devleeschouwer, X., Declercq, P.Y., Flamion, B., Brixko, J., Timmermans, A., and Vanneste, J. (2008). Uplift revealed by radar interferometry around Liège (Belgium): A relation with rising mining groundwater. *Proceedings of Post-Mining*. Nancy, France: GISOS, Groupement d'intérêt scientifique de recherche sur l'Impact et la Sécurité des Ouvrages Souterrains, pp. 13.

Dudek, M., Rusek, J., and Tajduś, K. (2021). Analysis of steel industrial portal frame building subjected to loads resulting from land surface uplift following the closure of underground mines. *Arch. Civ. Eng.*, 67, 283–298. http://dx.doi.org/10.24425/ace.2021.138056

Gee, D., Bateson, L., Sowter, A., Grebby, S., Novellino, A., Cigna, F., Marsh, S., Banton, C. and Wyatt, L. (2017). Ground Motion in Areas of Abandoned Mining: Application of the Intermittent SBAS (ISBAS) to the Northumberland and Durham Coalfield, UK. *Geosciences*, 7, 85. http://dx.doi.org/10.3390/geosciences7030085

Luo, Y. and Peng, S.S. (2000). Long-term subsidence associated with longwall mining—Its causes, development and magnitude. *Min. Eng.*, 52, 49–54.

Marinkovic, P., Ketelaar, G., van Leijen, F. and Hanssen, R.F. (2009). INSAR quality control: Analysis of five years of corner reflector time series. *Proceedings of the Fringe Workshop*, Frascati, Italy, pp. 1–8.

Pöttgens, J.J. (1985). Uplift as a result of rising mine waters. In: The Development Science and Art of Minerals Surveying. *Proceedings 6th Int. Congr. Int. Soc. For Mine Surveying*, Harrogate, UK, 2, pp. 928–938.

Samsonov, S., d'Oreye, N., and Smets, B. (2013). Ground deformation associated with post-mining activity at the French – German border revealed by novel InSAR time series method. *Int. J. of Appl. Earth Obs. and Geoinformation*, 23, 142–154. http://dx.doi.org/10.1016/j.jag.2012.12.008

Van Tongeren, P. and Dreesen, R. (2004). Residual space volumes in abandoned coal mines of the Belgian Campine basin and possibilities for use. *Geol. Belg.*, 7, 157–164.

Vervoort, A. (2020a). The time duration of the effects of total extraction mining methods on surface movement. *Energies*, 13, 4107. https://doi.org/10.3390/en13164107

Vervoort, A. (2020b). Long-term impact of coal mining on surface movement: residual subsidence versus uplift. *Min Rep Glückauf*, 156(2), 136–141.

Vervoort, A. (2021a). Uplift of the surface of the earth above abandoned coal mines. Part A: Analysis of satellite data related to the movement of the surface. *Int. J. Rock Mech. Min. Sci.*, 148, 104896. https://doi.org/10.1016/j.ijrmms.2021.104896

Vervoort, A. (2021b). Uplift of the surface of the earth above abandoned coal mines. Part B: Framework to understand and explain uplift. *Int. J. Rock Mech. Min. Sci.*, 148, 104947. https://doi.org/10.1016/j.ijrmms.2021.104947

Vervoort, A. (2022a). Upward surface movement above deep coal mines after closure and flooding: Analytical modeling results. *Proceedings of the SME 2022 International Conference on Ground Control in Mining*, Canonsburg PA, USA, 26–28 July 2022. Paper 0601.

Vervoort, A. (2022b). Impact of the closure of a coal district on the environmental issue of long-term surface movements. *AIMS Geosci.*, 8, 326–345. https://doi.org/10.3390/en13164107

Vervoort, A. (2024). Additional damage to buildings and infrastructure induced by long-term surface movements above longwall mining. *Proceedings of the 2024 SME Annual Conference & Expo MINEXCHANGE*, February 25-28 2024, Phoenix AZ, United States, Pages 10.

Vervoort, A. and Declercq, P.Y. (2017). Surface movement above old coal longwalls after mine closure. *Int. J. of Min. Sci. and Techn.*, 27(3), 481–490. https://doi.org/10.1016/j.ijmst.2017.03.007

Wakim, J., Hadj-Hassen, F., Tijani, M. and Gordine, D. (2007). Three-dimensional anisotropic swelling of argillaceous rock. *Rev Fr Geotech.*, 118, 23–36.



Andre Vervoort

Professor
University of Leuven

Prof. Andre Vervoort is a mining engineer and obtained his Ph.D. in 1987 at FPMs, Belgium for a study of roof behaviour in coal longwalls. From 1988 to 1992 he was a researcher at COMRO, South Africa and was mainly involved in ground control studies for the South African coal mines. Since 1992 he is a professor at the University of Leuven, Belgium. His academic teaching duties include courses in rock mechanics, geostatistics, mining methods and aspects of sustainable development. The emphasis of his research is on rock mechanics. He has published about 250 technical papers.

Machine learning as a catalyst to enhance collaboration across generations and disciplines in South African Rock Engineering

R.T. Masethe[1], L.N.P Msimango[2]

[1]University of KwaZulu-Natal, South Africa.
[2]Gauteng Department of Education, South Africa

Mining in South Africa presents complex rock engineering challenges, including geological intricacies, high-stress environments, and rockburst risks. Traditional design methods have long been essential to the field, but machine learning (ML) offers new opportunities to enhance accuracy, efficiency, and predictive capabilities. However, integrating ML into rock engineering is impeded by generational divides that hinder knowledge transfer. Overcoming this barrier requires fostering effective knowledge-sharing practices to accelerate artificial intelligence (AI) adoption. Collaboration is vital in merging traditional expertise with AI-driven advancements. A significant challenge arises when essential knowledge remains undocumented or unshared. Older generations, particularly Baby Boomers (1946-1964), have often neglected to impart their wisdom, resulting in lost solutions and repetitive problem-solving by younger professionals. This delay stifles innovation and hinders progress.

To investigate this dynamic, a qualitative study was conducted involving semi-structured interviews with rock engineers and early-career professionals. The interviews, even though designed to be conversational and informal in tone, followed a structured format with guided discussion focused on challenges in knowledge-sharing, perceptions of ML, and collaboration preferences. The responses were thematically analysed to identify barriers and enablers in generational collaboration.

This paper advocates for inter- and multi-generational collaboration, pairing experienced Baby Boomers with technologically proficient Generation Z professionals. This synergy can bridge the gap between legacy methods and modern computational tools, leading to transformative advancements in rock engineering. By strategically aligning the strengths of different generations with their unique training, the sector can improve operational efficiency and resilience. A framework is proposed to implement collaborative strategies, addressing key challenges and opportunities. This approach ensures sustainability and innovation in South Africa's mining sector, positioning it to navigate future challenges effectively. References highlight the role of inter-generational knowledge-sharing in driving progress and securing the industry's future.

Keywords: Machine Learning, ML, Artificial Intelligence, Inter-generation, Multi-generation, Hazard, Risk, Monitoring, Seismic event, Platinum

INTRODUCTION

Rock engineering in South Africa plays a critical role in ensuring the stability and safety of mining operations, particularly in deep-level mining environments. However, the industry faces unique challenges, including diverse geological conditions, generational differences in the workforce, and the integration of modern technologies.

A key concern is a behavioural gap between experienced professionals, who often rely on traditional methodologies, and younger engineers, who are more inclined towards data-driven, technology-based approaches. This disparity can create collaboration challenges, hindering the effective exchange of knowledge and expertise. Additionally, technical difficulties such as slope stability issues, unpredictable ground conditions, and limited visibility behind support systems like shotcrete further complicate rock engineering decision-making. Despite its advantages, numerical modelling is often constrained by insufficient input data and the complex nature of rock mass behaviour (Jager & Ryder, 1999). Moreover, in situ stress measurements at depth remain problematic due to instrument limitations, leading to inaccuracies that impact excavation designs (Jing & Hudson, 2002). The difficulty in predicting excavation conditions and a general lack of comprehensive design information underscores the need for innovative solutions that enhance accuracy, efficiency, and collaboration in rock engineering.

Machine learning (ML) is emerging as a transformative catalyst that addresses these challenges by enhancing collaboration across generations and disciplines within rock engineering. Literature reveals that leveraging ML-driven techniques can significantly improve rock engineering designs by processing vast amounts of geotechnical data, reducing uncertainties, and increasing predictive accuracy, provided ML approaches are applied correctly with appropriate discipline, adequately validated, monitored for ongoing relevance, and recalibrated with fresh data as needed. (Smith *et al*., 2023). The ML paradigm facilitates interdisciplinary partnerships by enabling engineers, data scientists, and geologists to work cohesively to analyse rock mass behaviour, optimise support systems, and refine excavation methodologies. Additionally, ML fosters cross-generational collaboration by creating platforms for knowledge transfer, where experienced professionals contribute domain expertise while younger engineers enhance traditional methods with artificial intelligence (AI)-driven insights. This synergy can revolutionise rock engineering by improving the precision of design processes, similar to how AI has optimised aeronautical engineering (Tafur *et al*., 2025). Integrating AI with conventional expertise allows the mining sector to develop more reliable, efficient, and safer rock engineering solutions. Therefore, embracing ML-driven advancements, alongside collaborative and multi-generational efforts, will shape the future of South African rock engineering, ensuring a more innovative, resilient, and data-driven approach to ore extraction and mine safety.

ML is revolutionising various industries (e.g., medical, agriculture, etc.) by enhancing data-driven decision-making, improving predictive accuracy, and optimising operational efficiency (Smith *et al*., 2023). In rock engineering, ML enables real-time analysis of geological data, facilitating proactive risk management and precision in excavation design (Jing & Hudson, 2002). Beyond technical advancements, ML bridges cross-generational collaboration by integrating traditional expertise with AI-driven insights, fostering knowledge transfer between experienced professionals and younger engineers (Brady & Brown, 2013). Furthermore, ML promotes interdisciplinary (Figure 3a) cooperation by allowing different disciplines (e.g., rock engineering practitioners, geologists, computer programmers, data scientists, etc.) to work cohesively in refining rock mass behaviour predictions and support system designs, further cultivating a culture of continuous learning and innovation (Jing & Hudson, 2002).In contrast, intradisciplinary collaboration involves specialists within the same field, such as various branches of rock engineering, working together to deepen understanding and enhance methodological precision. For example, collaboration between structural geologists and rock mass classification experts within rock engineering can lead to more nuanced interpretations of deformation patterns, complementing broader interdisciplinary efforts. Therefore, ML can be a powerful tool for transforming rock engineering through innovation, collaboration, and improved safety measures, leading to more holistic solutions that address complex challenges in rock engineering. As such, ML serving as a catalyst to enhance collaboration across generations and disciplines is not just a technological evolution; it is a transformative force, radically changing the rock engineering landscape and making it more efficient.

THE SOUTH AFRICAN ROCK ENGINEERING LANDSCAPE

Traditional rock engineering methods in South Africa have long been rooted in empirical design principles, observational techniques, and numerical modelling. These methods rely on extensive field investigations, laboratory testing, and experience-based guidelines to assess rock mass behaviour and to design support systems (Brady & Brown, 2013). Empirical design approaches such as the rock mass rating (RMR) and Q-system remain widely used for classifying rock masses and selecting appropriate support strategies in underground mining and civil engineering projects (Bieniawski, 1989). Additionally, numerical modelling tools like finite element analysis and distinct element modelling have enhanced predictive accuracy for geotechnical designs, allowing engineers to simulate stress distributions and failure mechanisms under various loading conditions (Hoek *et al.*, 2018). Despite their effectiveness, traditional methods often require extensive manual interpretation, and site-specific geological complexities can limit their applicability.

South African rock engineering faces several key challenges, including safety concerns, a widening skills gap, and difficulties integrating emerging technologies. Safety remains a top priority, especially in deep-level hard rock mines where rockbursts, seismicity, and falls-of-ground pose significant risks to workers (Jing & Hudson, 2002). While traditional support systems and monitoring techniques have improved, unpredictable geotechnical hazards continue to challenge the industry. Additionally, there is a growing skills gap as experienced engineers retire, and fewer young professionals enter the field with adequate training in traditional and modern engineering practices. Integrating new technologies like ML, automation, and real-time monitoring can potentially enhance predictive capabilities and operational efficiency. However, many companies struggle with the high costs of implementation, limited technical expertise, and resistance to change within established engineering teams (Singh *et al.*, 2022).

The workforce in South African rock engineering is multi-generational and trans-disciplinary, requiring effective collaboration between rock engineering practitioners, geologists, data scientists, computer programmers, and relevant safety experts. Experienced professionals bring invaluable industry knowledge, while younger engineers introduce new perspectives and technological expertise, creating an opportunity for knowledge transfer and innovation (Hudson & Feng, 2015). However, different technical proficiencies and the adoption vs non-adoption of modern digital tools can create communication and workflow integration gaps. Moreover, the trans-disciplinary nature of rock engineering demands collaboration across various scientific and engineering domains, including geomechanics, civil engineering, geology, geophysics, and materials science (Brady & Brown, 2013). As the industry evolves, fostering interdisciplinary teamwork and upskilling the workforce in emerging technologies will ensure sustainable and safe rock engineering practices in South Africa, working towards the Mine Health and Safety Council slogan, "Every mine worker returning from work unharmed every day, striving for zero harm in our lifetime."

Understanding ML in rock engineering

ML is a subset of AI that enables computers to learn from data, identifying patterns and making predictions or decisions based on the data, often without being explicitly programmed for a specific task (Figure 1). In rock engineering, ML is transforming traditional methods by providing data-driven insights into geological conditions and stability assessments. The integration of ML in rock engineering builds upon existing empirical and numerical methodologies, offering predictive capabilities that enhance decision-making processes. However, these conventional methods rely heavily on expert judgment to integrate categorical and numerical data, leaving room for uncertainty and subjectivity. ML can bridge this gap by identifying complex patterns in rock engineering datasets, improving the accuracy and reliability of predictions.

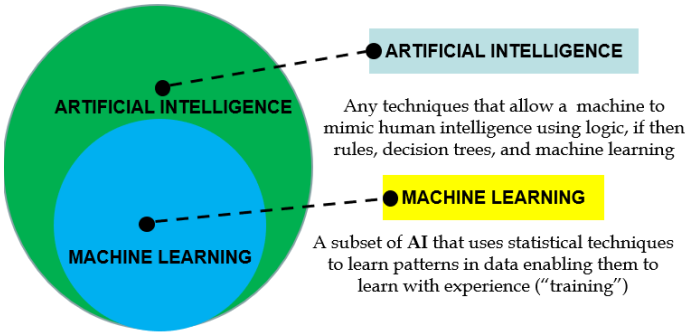


Figure 1. Artificial intelligence and machine learning.

MACHINE LEARNING APPLICATIONS IN ROCK ENGINEERING

Machine learning algorithms (MLAs) are being progressively employed in the field of rock engineering; however, their application remains in early stages. The choice of technique depends on the quality of geotechnical data, similar to other AI fields. The most suitable algorithm for predictions varies, based on the desired outcome. Various MLAs have been applied to classify rock mass properties, rock bursts, and tunnel performance. Mining and tunnelling often face incomplete datasets due to the high cost of field data collection and laboratory testing. In practice, simple statistical analyses can provide conservative estimates, which are then scaled using analytical or empirical methods. In contrast, MLAs tend to provide more accurate correlations between rock mass and laboratory-scale properties, reducing bias. An overview of some MLAs that have been deployed in rock engineering-related problems are shown in Table I. This listing is not exhaustive.

Table I. Overview of some recent ML models and their application to rock engineering

Application	ML Models Used	Applications
Rock Mass Properties Prediction	Artificial Neural Networks (ANNs)	- Predict rock mass properties based on observed site conditions.
		- Estimate large-scale rock mass behaviour using laboratory-scale properties and geological mapping.
		- Enhance rock mass classification (e.g., Q-system, RMR) by integrating multisource geotechnical data (Jing & Hudson, 2002).
Predicting Rock Failure and Stability	Decision Trees, Support Vector Machines (SVMs), Convolutional Neural Networks (CNNs), Ensemble Learning	- Classify rock stability levels, based on historical failure data and stress conditions (Jing & Hudson, 2002).
		- Detect early instability signs through image recognition of rock surfaces using CNNs.
		- Ensemble learning improves the reliability of seismicity analysis and correlates well with actual induced rockburst events (Masethe *et al.*, 2024).
Laboratory Testing & Constitutive Behaviour	ANNs, SVMs	- Predict crack initiation and damage thresholds using geology and peak unconfined compressive strength (UCS).
		- Estimate constitutive behaviour based on laboratory tests and field observations.
Slope Stability Assessment	ANNs, SVMs, Random Forests (RFs), Clustering	- Predict slope movements using geometric and sensor data (e.g., piezometers, inclinometers).
Automated Geological Mapping & Point Cloud		- Estimate volumes of structurally controlled failures based on mapped discontinuities.

Analysis for Tunnel Deformations	RF, k-Nearest Neighbours (kNN), CNNs	- ML-powered image recognition automates geological mapping, improving accuracy in rock classification and fracture detection (Bieniawski, 1973).
		- Process LiDAR and hyperspectral imaging data to estimate rock quality designation (RQD) values.
		- Use successive tunnel scans to detect volume changes and predict time-dependent deformations.
Tunnel Performance Prediction & Mine Support Design	ANNs, SVMs, RFs, Reinforcement Learning	- Predict stress/strain fields for numerical models to refine mine support design.
		- Optimise tunnel support class based on geological conditions, excavation methods, and environmental factors (Barton *et al*., 1974).
		- Use microseismic data to assess rock mass deformation as excavation progresses.
Rock Burst Prediction	ANNs, Naïve Bayes, kNN, RFs, SVMs, Decision Tree	- Predict the magnitude and location of rockburst events using 3D excavation geometry and seismic event data.
		- Estimate failed material volume and rock support performance, based on past rockburst events.
		- Assess rockburst probability using mapped rock classification data (Jing & Hudson, 2002).
Numerical Model Enhancement	ANNs, Reinforcement Learning	- Calculate numerical models (e.g., finite element, discrete element methods) using past simulation results and observed site conditions to improve predictive accuracy.
Blasting Optimisation	ANNs, SVMs	- Predict blast damage and optimise blasting parameters for enhanced safety and efficiency.
		- Estimate blast parameters based on mapped rock classification data, improving precision in rock fragmentation.

Bridging Generational Gaps through ML in the South African Rock Engineering Context

In the South African rock engineering context, integrating ML into traditional methodologies is a pivotal mechanism for bridging generational gaps within the industry. The realm of rock engineering has undergone significant transformation over the decades, with experienced practitioners frequently adhering to time-honoured methodologies, while more recent entrants tend to command sophisticated computational proficiencies and a penchant for innovation. Machine learning technologies offer a unique opportunity to merge these potentially complementary approaches, promoting collaboration and knowledge transfer.

A particularly captivating application of ML resides in predictive modelling, wherein algorithms scrutinise extensive datasets accrued from previous projects to anticipate potential challenges and outcomes in forthcoming undertakings. This predictive capacity not only refines decision-making processes but also instils greater confidence in junior engineers as they participate in intricate problem-solving situations, supported by data-driven insights. As seasoned professionals impart their experiential wisdom alongside machine-generated forecasts, a vibrant tapestry of comprehension unfolds, connecting the expertise of veterans with the innovative viewpoints of the younger generation (e.g., Millennials and Generation Z).

Moreover, reliance on ML tools can potentially mitigate certain ingrained biases that may permeate conventional rock engineering practices. By grounding decisions in empirical data rather than anecdotal evidence, the industry promotes an inclusivity environment where every opinion is valued, regardless of experience. This evolution not only aids in retaining younger talent but also enriches the discipline overall, nurturing a culture that reveres ongoing learning and adaptation in the face of changing geological and environmental circumstances. 'Bridging generational gaps through machine learning in South African rock engineering' refers to leveraging ML technology to enhance collaboration and knowledge transfer across different generations within the field (Purdue Global, 2023). Addressing the technological divide aims to help the younger, digitally native generation work more effectively with older generations who may be less familiar with digital tools and technological advancements. This

approach fosters a more inclusive and efficient working environment, promoting the adoption of modern engineering practices in South Africa's mining and rock engineering sectors.

The rock engineering discipline encompasses various generations, including Baby Boomers (1946-1964), Generation X (1965-1980), Millennials (1981-2000), and Generation Z (2001-2020). Each generation's perspective is shaped by four key factors, as outlined by Purdue Global: (i) the way they are characterised, (ii) their sources of motivation, (iii) their preferred communication styles, and (iv) their worldview. These factors collectively define the dynamics between generations within the different *disciplines/fields (Table II and Figure 2).*

Table II. Generational differences in the workplace (after Purdue Global, 2023)

Generation	Characterised	Motivated	Communication Style	Worldview
Baby Boomers	Optimistic, Competitive, Workaholic, and Team-Oriented	Company loyalty, teamwork, and duty	Efficient methods, including phone calls and face-to-face	Achievement comes after paying one's dues, sacrificing for success
Generation X	Flexible, Informal, Sceptical and Independent	Diversity, work-life balance, and personal-professional interests	Efficient methods, including phone calls and face-to-face	Favouring diversity, quick to leave if the employer fails to meet their needs
Millennials	Competitive, Civic- and Open-minded, Achievement-oriented	Responsibility, quality of manager, and unique work experiences	IMs, texts, and emails	Seeking challenge, growth, and work-life balance; likely to leave if dissatisfied
Generation Z	Global, Entrepreneurial, Progressive, and Less focused	Diversity, personalisation, individuality, creativity	Social media, texts, IMs	Digital device addicts value independence and individuality, and prefer innovative environments

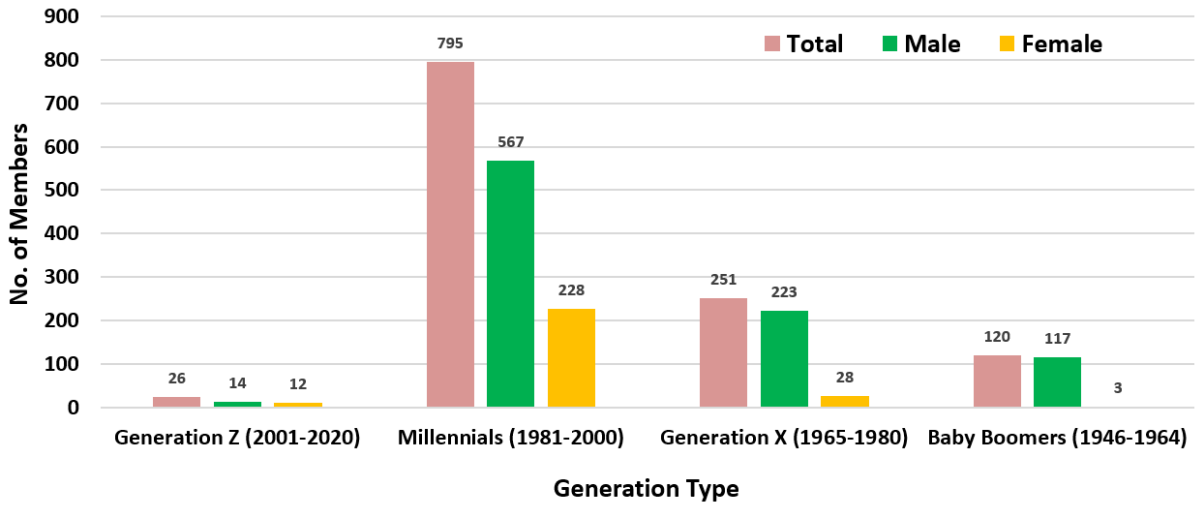


Figure 2. Different generations in the rock engineering fraternity (South Africa).

Depending on what characterises each generation, we can leverage their unique strengths to enhance and accelerate the adoption of ML in rock engineering. Baby Boomers bring years of industry experience and a strong work ethic, making them invaluable in guiding and mentoring younger generations. Generation X's adaptability and appreciation for work-life balance can help integrate technological advancements with practical applications, ensuring a smooth transition. With their tech-savvy nature and inclination toward innovation, Millennials are crucial in implementing new AI tools and pushing

boundaries. Generation Z, immersed in digital environments from a young age, can drive creativity and the use of cutting-edge technology. By fostering multi-generational integration, we can create a knowledge-sharing environment where diverse perspectives and skills come together to fast-track the understanding and implementation of ML and AI in rock engineering. This collaborative approach enhances technological adoption and ensures a more holistic and effective application of these advanced tools across the industry.

INTRADISCIPLINARY COLLABORATION ENABLED BY MACHINE LEARNING

The advent of ML can significantly enrich intradisciplinary collaboration, fostering synergy among diverse knowledge domains within a singular discipline (Figure 3b). The intricacies inherent in addressing challenges within rock engineering can be profoundly comprehended and resolved by deploying ML algorithms (Ahangari *et al.*, 2022). Researchers are empowered to make informed decisions grounded in the empirical insights provided by ML. Furthermore, ML cultivates an iterative research methodology. As teams accumulate additional data, ML models can be enhanced and retrained, perpetually elevating the accuracy of predictions and insights. This dynamic process promotes a culture of collaboration, wherein insights from one subfield can enlighten and refine the methodologies of another, resulting in deeper insights and more useful outcomes (Ahangari *et al.*, 2022).

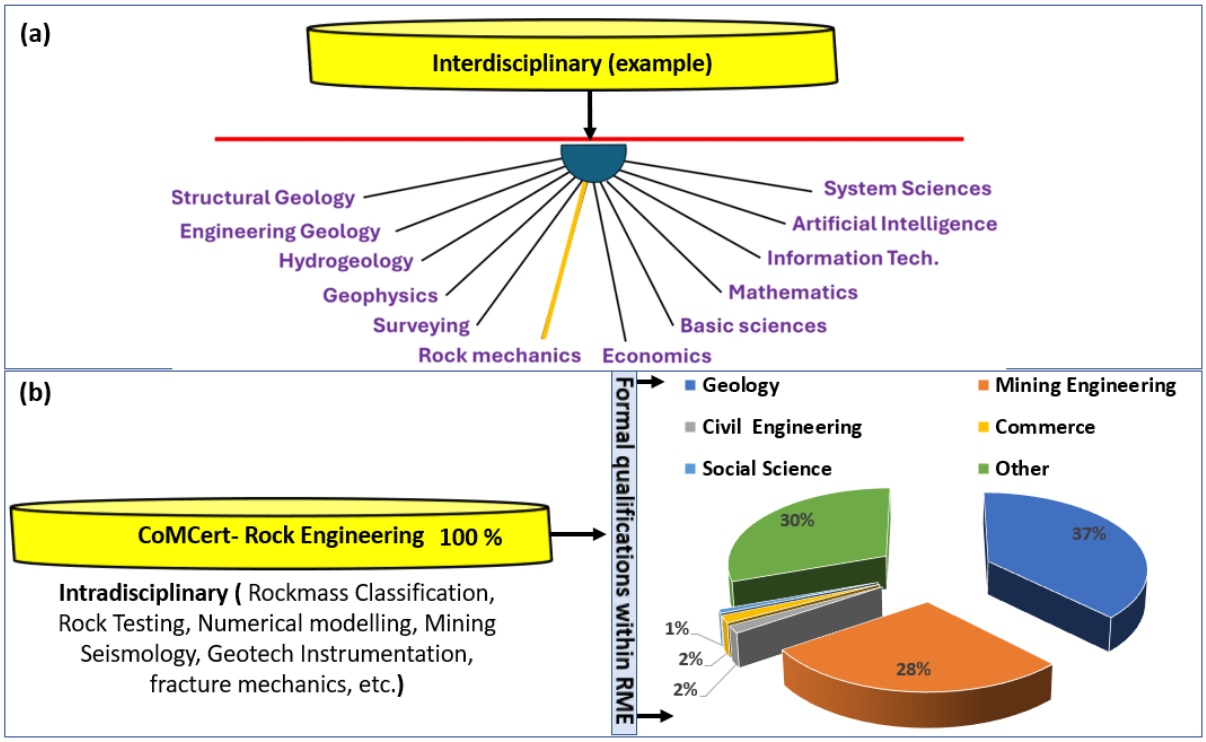


Figure 3. Intradisciplinary vs interdisciplinary composition in the rock engineering discipline within the South African context.

As the research domain becomes increasingly interdisciplinary, the importance of ML in promoting collaboration both within and among disciplines cannot be exaggerated. By effortlessly bridging various fields of expertise, ML empowers teams to tackle challenges with enhanced effectiveness, ultimately leading to breakthroughs that reverberate deeply throughout society.

Intradisciplinary Integration in Machine Learning

Integrating intradisciplinary elements with ML embodies a harmonious synthesis of the field's diverse facets, enhancing algorithms' overall efficacy and applicability. By uniting theoretical foundations, such as statistics and optimisation, with practical applications like natural language processing and computer

vision, researchers and practitioners are equipped to formulate more robust solutions to complex challenges. Intradisciplinary integration encourages the exchange of exemplary practices and methodologies across many subfields. By nurturing a dialogue among the diverse domains of ML, researchers can absorb effective strategies from one area and apply them to another, thereby fostering a culture of continuous improvement and innovation. As the discipline evolves, this collaborative spirit will be crucial in tackling increasingly complex challenges and enhancing the capabilities of ML technologies, especially in rock engineering.

AI-Driven Decision Support Systems in Machine Learning

AI-driven decision support systems (DSS) within the domain of ML have emerged as transformative tools across various industries. By harnessing the power of advanced algorithms and huge datasets, these systems provide invaluable insights that enhance the decision-making process. The primary advantage of integrating ML into decision support is its ability to extract intricate patterns and subtle trends that may otherwise escape human observation in real time. At the core of these systems lies predictive analytics, which leverages historical data to anticipate future outcomes. For instance, in the sphere of healthcare, AI-driven DSS can predict patient admissions, optimise resource allocation, and even recommend personalised treatment plans tailored to individual patient data. This capability not only elevates the quality of patient care but also streamlines hospital operations, consequently reducing costs and enhancing efficiency. Lastly, as industries increasingly embrace these advanced systems, the potential for AI-driven DSS to revolutionise practices and enhance outcomes becomes ever more evident. The future foretells a domain where decision-making is not only enhanced by data but also enriched by the profound insights derived from ML technologies.

Challenges and Ethical Considerations in Machine Learning

The utilisation of ML in the field of rock engineering is gradually gathering momentum. It presents many challenges and ethical considerations that must be meticulously addressed to guarantee responsible and effective utilisation. A prominent challenge relates to the quality and accessibility of data. Rock engineering encompasses intricate geological phenomena, and the datasets necessary for training ML models are frequently sparse, inconsistent, or biased. Insufficient or erroneous data may result in inaccurate predictions, which could endanger safety and compromise project outcomes. As the incorporation of ML technologies into diverse sectors becomes increasingly widespread, a multitude of challenges and ethical considerations have arisen that demand immediate attention. One of the foremost challenges pertains to the quality and bias of data. ML models are profoundly dependent on the datasets used for training, and if these datasets are biased or fail to accurately represent the population, the outcomes may reinforce existing deficiencies and result in flawed decision-making.

Ethical considerations also encompass matters of privacy and surveillance. As organisations increasingly leverage the capabilities of ML to scrutinise extensive collections of personal data, apprehensions surrounding individual privacy and consent intensify. Achieving a harmonious equilibrium between innovation and ethical accountability becomes essential as we traverse the intricacies of this swiftly advancing technological landscape. Ultimately, nurturing a collaborative discourse among technologists, ethicists, and policymakers will be vital in confronting these challenges and ensuring that ML technologies are developed and implemented with the highest degree of responsibility.

Barriers to Adoption in Machine Learning

Despite the transformative potential of ML across diverse sectors, numerous obstacles hinder its widespread adoption. A significant challenge lies in the resistance to change, particularly within entrenched organisations. Employees frequently display scepticism towards emerging technologies, harbouring fears of job displacement or disruptions to established workflows. This reluctance may arise from a deficiency in understanding the advantages of ML, cultivating a cultural inertia that stifles innovation.

The prerequisites for training further complicate the landscape. The successful execution of ML necessitates a workforce equipped with specialised expertise, encompassing areas from data analysis to algorithmic development. However, the existing skills gap poses a significant challenge, as many

employees may not possess the requisite knowledge to proficiently employ ML tools. Training programs can prove to be both time-consuming and financially demanding, and without a clear strategy for upskilling, organisations may hesitate to invest resources in these initiatives.

Ethical Considerations in Machine Learning

With the proliferation of ML systems across diverse sectors, ethical considerations assume paramount importance, particularly concerning data privacy, the dependability of AI predictions, and accountability. Data privacy also holds paramount significance, especially considering the vast quantities of personal information that ML algorithms often require for their training. Equally important is the reliability of AI predictions. As ML systems are progressively entrusted with critical decision-making from healthcare diagnostics to criminal sentencing, the stakes can be extraordinarily high. Erroneous predictions may have catastrophic repercussions. Therefore, these systems must undergo rigorous examination for biases and inaccuracies. Also, validation and periodic recalibration with more recent data when necessary. ML models can lose relevance over time, especially in situations where they are used to guide operational aspects. Utilising diverse datasets and perpetually monitoring AI performance can alleviate these risks, thereby cultivating trust in the technology. Ultimately, accountability continues to be a significant concern.

FUTURE PROSPECTS AND RECOMMENDATIONS FOR MACHINE LEARNING

The future potential of ML in rock engineering is not only promising but also transformative. As the discipline progresses, amalgamating sophisticated algorithms and comprehensive data analytics will enable more accurate predictions and elevate decision-making processes. A pivotal domain where ML can exert considerable influence is in evaluating rockmass behaviour under diverse loading conditions. By leveraging extensive datasets derived from field measurements and laboratory testing, ML models can be cultivated to discern intricate patterns that conventional methodologies might neglect (Kumar *et al.*, 2024). Moreover, the implementation of real-time monitoring systems enhanced by ML capabilities has the capacity to revolutionise risk management in rock engineering. These systems can continuously analyse data from sensors embedded within tunnels, slopes, and diverse structures, providing prompt alerts regarding potential failures or hazards. Such proactive measures enhance safety, optimise maintenance schedules, and reduce costs.

To fully harness these advantages, several recommendations may be proposed. Firstly, fostering intradisciplinary collaboration within the discipline is imperative. Such collaboration will ensure that ML models are firmly rooted in the practical realities of geology and engineering demands. Secondly, investing in educational and training programs emphasising ML applications for geotechnical engineers will cultivate a proficient workforce in leveraging these sophisticated technologies. Lastly, establishing standardised datasets and benchmarks will facilitate the creation of more dependable ML models, promoting consistency and reproducibility within rock engineering practices. Embracing ML in rock engineering presents the prospect of enhanced safety and efficiency and paves the way for innovation within the field.

Strategic Recommendations

Technological advancement is not merely transforming operational methodologies across various industries, but it is also crucial for growth and sustainability. For the widespread integration of ML, managers must foster seamless collaboration and implement best practices to augment its accessibility. Research centred on ML is vital to equip future generations with essential skills. Moreover, ML offers a distinctive opportunity to transfer knowledge between generations and disciplines.

CONCLUSION

The South African rock engineering sector faces significant challenges, including complex geological conditions, high-stress mining environments, and the need to bridge generational divides in the workforce. Traditional methodologies have served the industry well, but their limitations in adapting to modern technological advancements hinder progress. ML offers transformative potential by

improving accuracy, predictive capabilities, and operational efficiency, but generational gaps and resistance to change often slow its integration. Fostering cross-generational collaboration is essential for facilitating the transfer of knowledge and expertise. The use of ML can potentially revolutionise rock engineering practices by leveraging the strengths of experienced professionals and digitally proficient younger rock engineering practitioners. This synergy can enhance both the precision of design processes and the overall safety of mining operations. Embracing this collaborative approach will allow the mining sector to unlock new possibilities, ensuring sustainability and innovation in the face of evolving challenges. Through the amalgamation of traditional expertise and modern technology, South Africa's mining industry can transition toward a more data-driven and resilient future, better equipped to navigate the complexities of deep-level mining. As new challenges arise, collaborative and interdisciplinary approaches will be essential in ensuring the sector's long-term success. Global scientific collaboration has the power to accelerate progress, driving transformative solutions to the industry's most pressing challenges. Research partnerships across the world are dismantling traditional barriers, fostering a more inclusive and impactful scientific community. As nations, institutions, and researchers continue to collaborate across borders, the potential for innovation and discovery becomes boundless.

ACKNOWLEDGEMENTS

The authors express their sincere gratitude to the financial support provided by the University Capacity Development Programme (UCDP) through the University of KwaZulu-Natal, which made this research possible.

REFERENCES

Ahangari Nanehkaran, Y., Pusatli, T., Chengyong, J., Chen, J., Cemiloglu, A., Azarafza, M., & Derakhshani, R. (2022). Application of machine learning techniques for the estimation of the safety factor in slope stability analysis. *Water*, *14*(22), 3743.

Barton, N., Lien, R., & Lunde, J. (1974). *Some new Q-value correlations to aid in site characterization and design*. Rock Mechanics and Rock Engineering, 7(4), 171-179.

Bieniawski, Z. T. (1973). *Engineering classification of jointed rock masses*. Trans. Southern Africa Institute of Civil Engineers, 15, 335-344.

Bieniawski, Z. T. (1989). *Engineering rock mass classifications*. Wiley.

Brady, B. H. G., & Brown, E. T. (2013). *Rock mechanics for underground mining* (3rd ed.). Springer.

Hoek, E., Marinos, P., & Benissi, M. (2018). *Practical rock engineering for underground mining*. Geotechnical Engineering Journal, 51(3), 121-134.

Hudson, J. A., & Feng, X. (2015). *Multidisciplinary collaboration in rock engineering: The key to sustainable mining practices.* Journal of Mining and Geotechnical Engineering, 42(1), 10-20.

Jager, A.J. and Ryder, J.A. (1999). *Rock Engineering Practice for Tabular Hard Rock Mines*. The Safety in Mines Research Advisory Committee (SIMRAC), Johannesburg.

Jermy, C., Harris, L., & Phillips, D. (2023). *Machine learning in geotechnical engineering: Transforming rock engineering design*. Engineering Geology, 45(1), 12-23.

Jing, L., & Hudson, J. A. (2002). Numerical methods in rock mechanics. *International Journal of Rock Mechanics and Mining Sciences*, *39*(4), 409-427.

Kumar, P. R., Muthukkumaran, K., & Sharma, C. (2024). Technological advancements and sustainable practices in rock slope stability–Critical review. *Physics and Chemistry of the Earth, Parts A/B/C*, 103699.

Masethe, R. T., Durapraj, S., & Adoko, A. C. (2024). Mining-induced classification for rockburst prediction: A case study in Siphumelele Platinum Mine, South Africa.

Purdue global: Generational Differences in the Workplace [Infographic] , 2023 https://www.purdueglobal.edu/education-partnerships/generational-workforce-differences-infographic/

Singh, R., Peterson, R., & Williams, L. (2022). *Barriers to the integration of machine learning in South African mining*. South African Journal of Engineering, 34(1), 31-45.

Smith, T., Thompson, R., & Ford, A. (2023). *Leveraging machine learning for better rock mass predictions*. Journal of Geotechnical Engineering, 62(3), 74-86.

Tafur, C. L., Camero, R. G., Rodríguez, D. A., Rincón, J. C. D., & Saenz, E. R. (2025). Applications of artificial intelligence in air operations: A systematic review. *Results in Engineering*, *25*, 103742.



Dr Richard Masethe

Senior Lecturer (Rock Mechanics and Engineering)
University of KwaZulu-Natal

Dr. Richard Masethe is a seasoned professional in the field of Rock Engineering and Mine Seismology, with a career spanning nearly two decades. He has been actively involved in overseeing seismic systems and executing a variety of rock engineering projects across complex underground environments. His academic journey, from undergraduate to doctoral studies, all completed at the University of the Witwatersrand, has provided him with a comprehensive and interdisciplinary foundation that continues to inform his research and teaching practice.

Dr. Masethe holds a BSc in Economic Science, a BSc Honours in Geophysics, a Graduate Diploma in Engineering (Rock Engineering), an MScEng in Rock Engineering, and a PhD in Geophysics and Rock Engineering. This progression through the earth and engineering sciences reflects both depth and breadth in his academic preparation, positioning him uniquely at the intersection of geophysics, rock mechanics, and engineering seismology.

His professional career began in 2007 as a graduate rock engineering trainee at Gold Fields, after which he joined Sibanye-Stillwater, working in the Rock Engineering and Seismology Department. With 19 years of operational experience (Gold and Platinum), he transitioned into academia, where he currently serves as a Senior Lecturer. In this role, he teaches, leads research, and supervises postgraduate students, including those at the Master's and PhD levels at both the University of Cape Town and the University of KwaZulu-Natal. He has also contributed to academic programs as a guest lecturer and visiting academic at the University of Johannesburg and the University of the Witwatersrand.

Dr. Masethe's research interests are grounded in addressing critical challenges within deep-level mining. His expertise spans rockburst phenomena, the application of artificial intelligence in rock engineering, underground support design, geophysics, and the study and control of mine-induced seismicity. He is particularly interested in applying probabilistic and risk-based methods to enhance the reliability and safety of rock engineering designs in seismically active mining environments.
An accomplished researcher, Dr. Masethe has published more than 24 peer-reviewed papers in accredited journals and international conference proceedings. His work is recognized for its practical relevance and scientific contribution to the field. In 2023, he was awarded the prestigious SANIRE Salamon Award for the best rock engineering paper an acknowledgement of his impact in advancing the discipline.

He is an active member of several professional bodies, including the International Society for Rock Mechanics (ISRM), the Southern African Institute of Rock Engineering (SANIRE), EUROCK, and the American Rock Mechanics Association (ARMA). His career continues to bridge academic scholarship with real-world industry application, making him a valuable contributor to both education and the broader rock engineering community.

Transforming geotechnical monitoring data acquisition, 3D visualisation and analytics for modern mining

J.J. Meiring, P.S. Piper

Groundwork Consulting, South Africa

As the deepening of an underground mine occurs, dynamic events (rockbursts) or high In the evolving landscape of rock engineering, the transition from traditional data collection methods to advanced digital solutions is imperative for enhancing safety, planning and design. Historically, reliance on manual data gathering, fixed sensors, and localised storage systems – which often rely on basic tools such as Excel – has led to fragmented information silos and limited analytical capabilities. Such approaches are increasingly inadequate for addressing the complex demands of modern geotechnical projects and for enabling key patterns and relationships to be identified in datasets.

This paper explores the transformative potential of contemporary technologies, notably the integration of Industrial Internet of Things (IIoT) sensors and mobile applications, which facilitate real-time, accurate data collection. These innovations enable seamless transmission of information to cloud-based storage systems, ensuring data integrity and accessibility across various platforms for downstream analytics.

The paper outlines the key advantages of structured, cloud-based data repositories that support sophisticated analytics, including machine learning and artificial intelligence applications. Furthermore, the paper proposes that mobile applications can effectively complement IIoT sensors by providing flexible monitoring solutions in critical locations without requiring extensive infrastructure investment in networks.

Advancements in visualisation software are also discussed, with emphasis on the importance of distilling actionable insights from complex datasets that facilitate data-driven decision-making. Case studies demonstrate that by adopting these cutting-edge technologies, the rock engineering sector can significantly improve safety protocols and optimise design processes.

This comprehensive technological analysis, supplemented with mining examples and case studies, aims to provide rock engineers, mining engineers, safety personnel, and geotechnical professionals with a nuanced understanding of the current state of the technological landscape in this field. Furthermore, it offers practical insights into leveraging these tools to drive the industry towards a safer, more efficient and secure future.

INTRODUCTION

Over the past five years, rock engineering has witnessed significant technological advancements that have revolutionised data acquisition, storage, visualisation, and analytics, thereby enhancing data-driven decision-making processes (Zhu *et al.*, 2011).

A notable development has been the reduction in costs associated with mine-scale monitoring systems, which has enabled the collection of more parameters, increased the prevalence of wide-scale monitoring, and substantially improved both safety and productivity in mining operations. The following technologies stand out to improve mining operations and rock engineering methods.

Industrial Internet of Things Sensors

The availability of IIoT sensors has enabled seamless, real-time monitoring of critical locations within mining environments. These sensors continuously collect and transmit data, allowing for immediate analysis and response (Eleftherios *et al.*, 2024). The increase of IIoT devices and the adoption by rock engineering practitioners has resulted in significant cost reductions, making these technologies more accessible to mining operations of varying scales. Standard sensors and IIoT sensors differ significantly in functionality, connectivity and application.

Standard Sensors

1. Functionality: Traditional sensors primarily perform basic data collection by converting physical phenomena (e.g., temperature, pressure, or strain) into electrical signals usually in an analogue format. The sensors normally require a constant power supply via cabling.
2. Data Processing: The sensors lack onboard processing capabilities, necessitating external systems for data analysis and interpretation.
3. Connectivity: Typically, standard sensors are hardwired into control systems, offering limited or no network connectivity with minimal processing, often resulting in delayed analytics and status warnings.

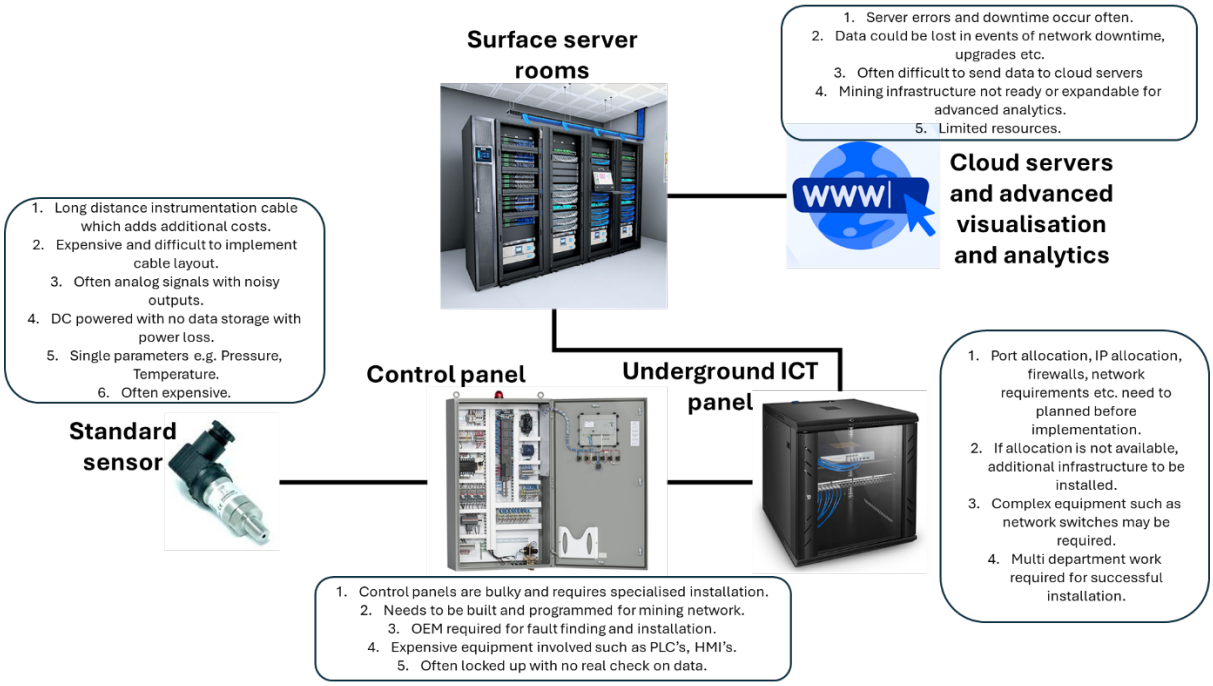


Figure 1. Typical single-point standard sensor setup in an underground application.

IIoT Sensors

1. Functionality: IIoT sensors are equipped with embedded intelligence, enabling the sensors not only to collect data but also to perform real-time processing and analysis.
2. Data Processing: These sensors can execute automatic calibrations, monitor system health, and make autonomous decisions based on predefined parameters. The sensors can store data in the event of connectivity issues.

3. Connectivity: Designed for seamless integration into networks, IIoT sensors often feature wireless communication capabilities, facilitating real-time data transmission to centralised systems or cloud platforms.

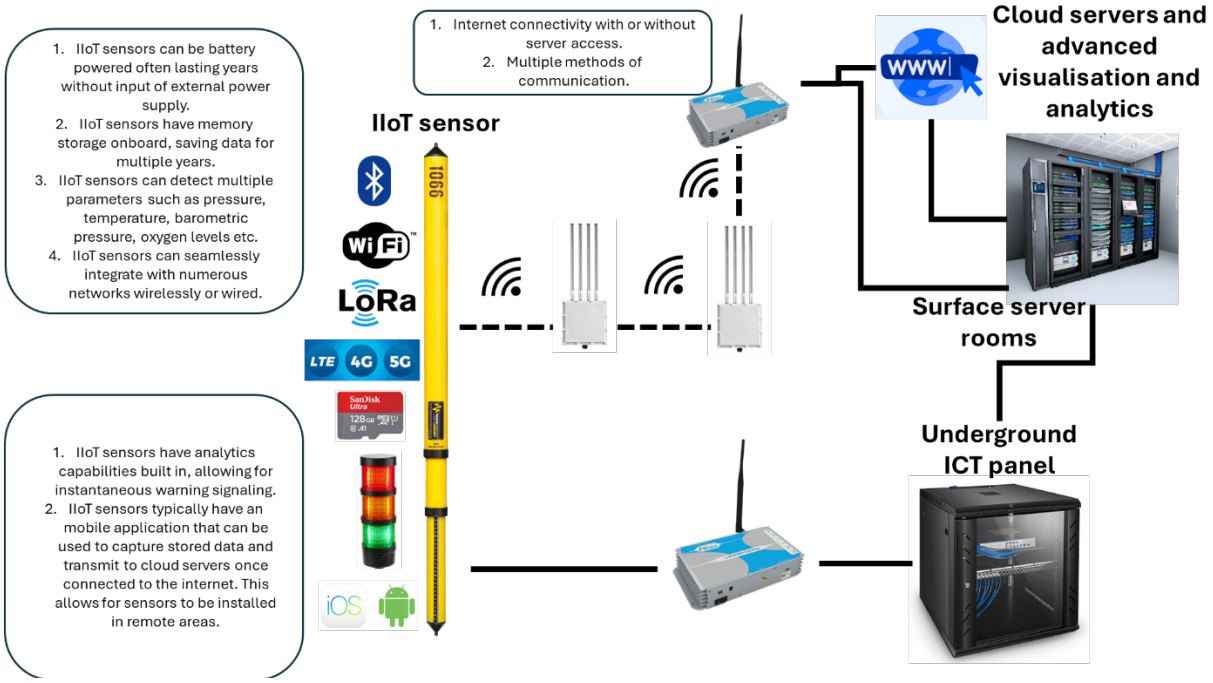


Figure 2. Typical IIoT multi-point sensing setup in an underground application.

However, challenges such as communication latency and bandwidth limitations persist, which can affect real-time data transfer between sensors and the appropriate visualisation platforms resulting in the need for alternative methods such as mobile application for mine-scale data collection.

Mobile Applications for Data Capture

In addition to IIoT sensors, mobile applications specifically designed for rock engineering have emerged as cost-effective tools for mine-scale monitoring. These applications serve as a bridge between manual measurements and digital data processing. They enable the verification of manual measurements, digitisation of the collected data and, where and when internet connectivity is available, enable transmission of this information to visualisation platforms for further analysis. This approach addresses historical challenges associated with manual data collection, which often involves unverified entries and labour-intensive processing, leading to delays and potentially erroneous decision-making. However, it is critical to look at data structuring and storage for effective analytics to be performed.

Data Structuring and Storage for Advanced Analytics

The integration of IIoT sensors and mobile applications facilitates the creation of robust data structures stored in cloud-based databases. Properly structured data is essential for the application of data science (DS) techniques, as well as machine learning (ML) and artificial intelligence (AI). To fully leverage these technologies, data must be stored in formats that support efficient processing and analysis. Key considerations for structuring data include ensuring scalability to accommodate growing datasets, maintaining high performance for rapid data retrieval and processing, and implementing effective data management practices. Scalable storage solutions are particularly important, as AI and ML projects often start small and expand as they prove successful, necessitating storage systems that can expand accordingly (Meiring *et al.*, 2024)

When looking at preparing data for proper analytics, ML and AI, structured models exist that enable rock engineers to make an informed decision on how to approach the transition to the digital future.

Three models stand out for the successful implementation of IIoT technologies and analytics in rock engineering known as the Data, Information, Knowledge and Wisdom (DIKW) model, the IIoT model and the Findable, Accessible, Interoperable and Reusable (FAIR) model. The DIKW and IIoT models were introduced and their applications for rock engineering were discussed in detail by Meiring *et al.*, 2024.

FAIR Model

The FAIR Model focuses on how to share and manage data and ensures that data becomes a digital asset (Asmi *et al.*, 2020). It is often the case that geotechnical measurements are processed manually and that data sits on individual and discrete systems. Data must be collected in a manner where it is findable and reusable by other machines, systems, and people. The FAIR model encompasses the following key elements:

1. Findable: Data sets should be easily findable by humans and machines by using a persistent identifier which is standardised across datasets. The datasets should have rich metadata which describes the data (sensor type, timestamp, location, owner). The data should be properly indexed following a standard. For example, a mining operation stores geotechnical data in a database where engineers can quickly locate historical closure readings.
2. Accessible: The data should be well-documented and stored in accessible repositories such as known cloud storage systems, which adapt to variable data volumes, data collection rates, and which are regularly backed up. Data should be available for the long term. For example, a cloud-based data platform allows rock engineers to access real-time seismic event data from any location with proper credentials.
3. Interoperable: Data should be stored in common, standardised formats (e.g., CSV, JSON, XML) that can be used across multiple software platforms. Metadata schemas that are used to establish and define data elements and the rules governing the use of data elements should align with industry standards. Application programming interfaces (APIs) should be used for seamless integration with other mining software, simulation tools, and ML/AI models. For example, a standardised API allows a mine's geotechnical sensors to send data to different visualisation platforms without manual conversion.
4. Reusable: Data should include rich metadata, describing how it was collected, calibrated, and processed. Well-documented data processing workflows should be maintained to allow future users to reproduce the analyses. Version control should be implemented to track changes in datasets over time. For example, historical stress-strain data from different mining sites are easily retrievable and reusable for predictive ML/AI modelling in future research.

The FAIR model ensures long-term data usability even when technologies change, prevents data loss and the application of the model makes data accessible across teams and ensures seamless integration with future AI and ML models. The FAIR model also allows for cross-domain collaboration that makes geotechnical data useful beyond mining (Bailo *et al.*, 2020).

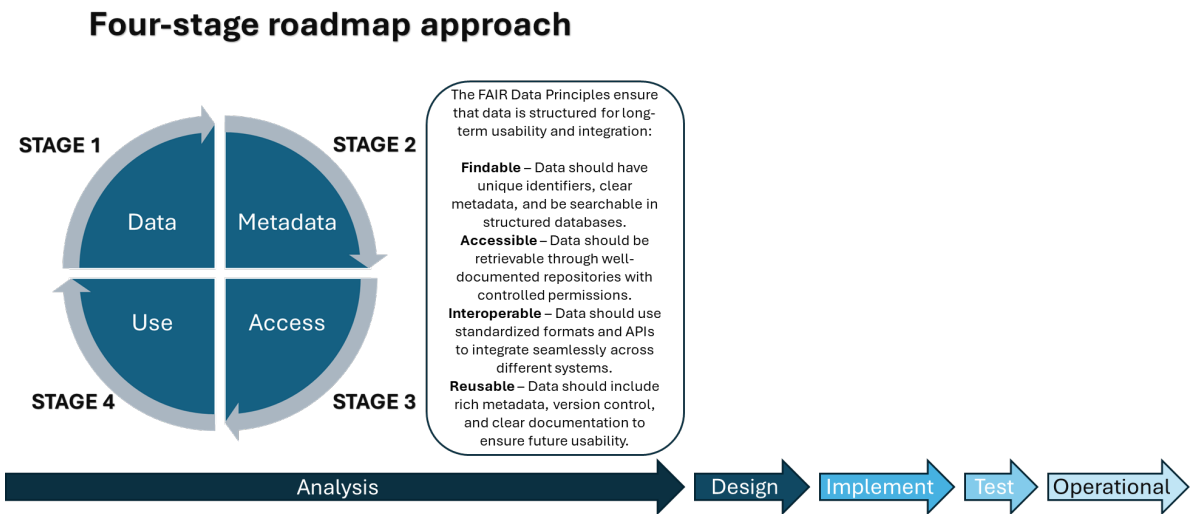


Figure 3. FAIR model 4-stage roadmap.

DATA AS A DIGITAL ASSET

Data is increasingly becoming an important and valuable asset. In order to facilitate the digitisation of manually collected data into a digital asset, user-friendly interfaces for entering data into visualisation and analytics software are essential. These interfaces incorporate validation checks which automate the quality control process and flag potential erroneous data to ensure data accuracy and consistency. Once captured, the data is processed, structured and stored in a robust database schema, enabling long-term accessibility. The key benefits of this approach include:

1. Enhanced data integrity: Built-in validation checks reduce errors and improve data quality.
2. One version one truth: A centralised database ensures that all users access the same accurate and up-to-date data, eliminating discrepancies from duplicated or outdated sources. This fosters consistency, trust, and better decision-making across teams.
3. Advanced visualisation and analytics: Structured data can be visualised in real-time and analysed for insights.
4. Long-term storage and accessibility: Data remains securely stored and accessible to authorised users and integrated systems.
5. Improved interoperability: Ensures compatibility of data with other digital tools and workflows.

This methodology transforms manually collected data into a valuable digital asset, aligning with the FAIR model principles. By doing so, data is no longer restricted to paper records or individual users but becomes a shared resource that enhances decision-making and operational efficiency. The comparative analysis of outdated data collection methods versus modern digital techniques shown in Figure 4 further highlights the advantages of this approach.

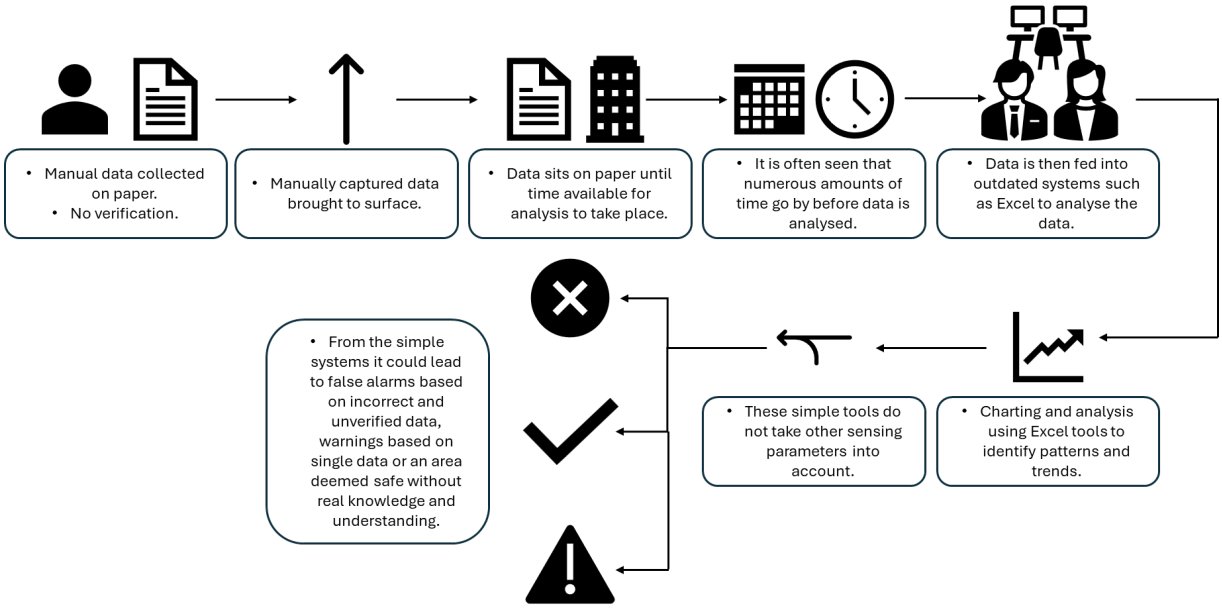


Figure 4. Typical flow of data capturing with outdated methods.

Manually collecting data is traditionally done using pen and paper, with users recording values by hand. This method is prone to several issues:

1. Human error and subjectivity: Data accuracy can be influenced by the user's perception, misinterpretation, or simple mistakes.
2. Physical vulnerability: Paper records are susceptible to damage, loss, or degradation over time.
3. Incomplete or missing data: Points may be unintentionally omitted or inaccurately recorded.
4. Delayed error detection: Errors often go unnoticed until weeks later when the data is reviewed, by which time the original conditions cannot be replicated or re-measured.

Once data is finally analysed, further challenges arise:

1. Limited analytical capabilities: Many organisations rely on standard spreadsheet programmes designed for numerical calculations and graphing, rather than advanced data analytics.
2. Restricted accessibility: These programs are often created and maintained by a single individual, making them difficult for others to access, use or modify.
3. Data silos: If stored on a local machine, the data remains inaccessible to others, preventing collaboration and sharing.
4. Lack of verification: Without cross-referencing against historical data, incorrect assumptions may be made, leading to a false sense of security or inappropriate actions.

This outdated approach highlights the need for a structured digital solution that ensures data integrity, accessibility, and real-time verification. If advanced visualisation and analytics software is used the entire manual data capture process could be changed and adapted as shown in the Figure 5.

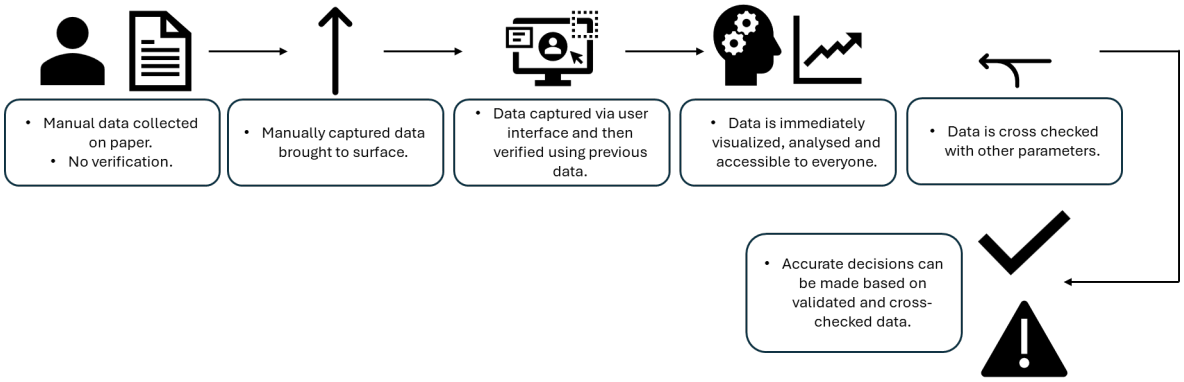


Figure 5. Typical flow of data capturing with modern visualisation platforms.

Figure 5 suggests a significant reduction in processing time compared to the methodology shown in Figure 4. However, the key advantage of using visualisation platforms lies in the ability to validate and cross-check the data against other data sets. By utilising a centralised platform that allows all users to input data, an operator collecting information receives immediate feedback upon entry. This enables real-time validation, with alerts notifying the user if the data deviates from previous records. If the data is valid but exceeds predefined thresholds, stakeholders can be notified immediately upon data entry.

Case study 1 – Visualisation and analysis of mine-scale data collected manually

Background

A mining company in South Africa needed to visualise tunnel convergence consisting of over 120 discrete locations, each containing three measurement points. Previously, a technician manually recorded each data point using a tape measure, documenting it on paper. This data was then taken to surface, where it was manually entered into an Excel spreadsheet, which contained over 120 individual sheets corresponding to each location. Once data entry was complete, an Excel macro was executed to analyse the information and generate visual insights. However, significant challenges soon emerged. The original creator of the Excel macro left the mining company, resulting in the loss of support for the Excel-based visualisation tool and insufficient resources to rebuild it. Additionally, the manual data capture process led to numerous errors, since verifying over 360 measurements before inputting them into Excel was impractical. Furthermore, the macro-generated heatmap, which was designed to highlight excessive movement, provided a false sense of safety due to unverified data. Recognising these issues, the mining company requested a modernised solution that adhered to the key principles of the FAIR model:

1. Validate data before analysis to ensure reliability.
2. Digitally store all collected data for long-term accessibility.
3. Host data in the cloud, ensuring secure, multi-user access.
4. Automate analytics, allowing results to be generated immediately upon data entry.
5. Trigger alerts and notifications via email when thresholds are breached.
6. Provide data insights and analytics through heatmaps, graphs, and advanced calculations to assess tunnel stability.

Solution:

The mining company approached a geotechnical consulting company specialising in advanced data visualisation and analytics to develop a solution. The platform that was developed supported multiple data ingestion methods, including:

1. IIoT sensors for automated data collection.
2. Standard sensors integrated into monitoring systems.
3. Manually entered data, captured and validated through an intuitive interface.

The cloud-based platform leveraged scalable infrastructure on Microsoft Azure and Amazon Web Services, ensuring future-proofing for expanding data needs. The system was also designed to align with FAIR model principles of ensuring findability, accessibility, interoperability, and reusability of all collected data. In order to streamline the process, the client granted access to multiple users, enabling them all to view, download, and input data directly into the database via the platform from any internet-connected device. Upon data entry, the system does the following:

1. Highlights mandatory fields, ensuring completeness.
2. Validates new data against historical records.
3. Triggers a warning if deviations exceed set thresholds, prompting the user to recheck the measurement.
4. Compensates for calibration variations in measurement tapes.
5. Instantly processes and analyses data, eliminating delays in decision-making.

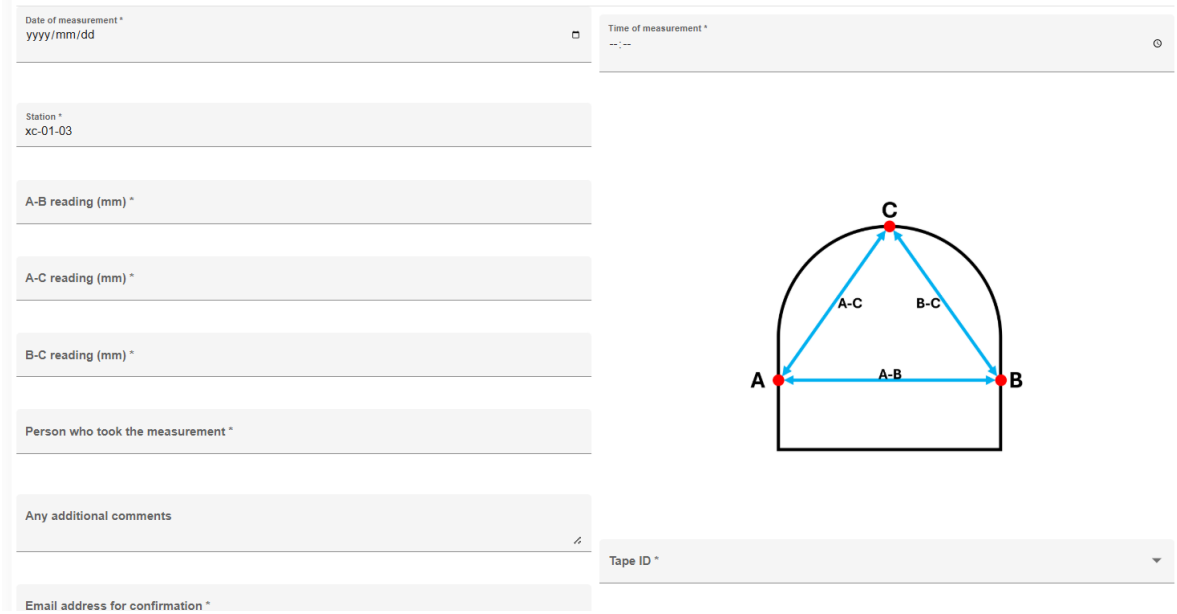


Figure 6. The online user interface for entering manually-captured data.

Automation and Visualisation:

Once validated, the platform automatically:

1. Generates graphs to display trends.
2. Calculates averages for perpendicular measurements.
3. Determines rate-of-change (mm/day) and inverse velocity (day/mm) for assessing ground stability.
4. Updates the heatmap in real time based on alert thresholds.
5. Sends automated email alerts to stakeholders when warning and trigger levels are breached.

The system also allows:

1. Direct data downloads in universally accepted formats.
2. API integrations for seamless interaction with other monitoring systems, including seismic data analysis tools.
3. Permanent secure data storage.

Screenshots:
Figures 7 and 8 show screenshots of the platform, which now provides real-time access to:

1. Horizontal and vertical convergence data.
2. Rate-of-change analytics.
3. Inverse velocity calculations for an indication of possible time-to-failure.
4. Advanced, interactive charts that can be annotated and downloaded for reporting.



Figure 7. A snapshot of the solution platform.

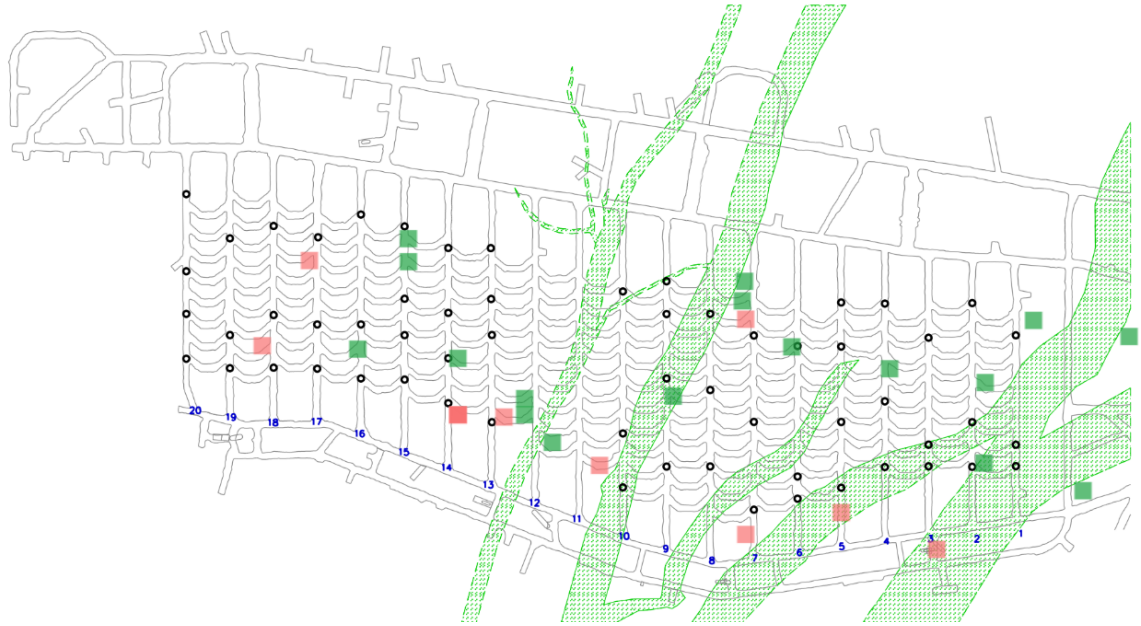


Figure 8. The automatically generated heatmap from the solution platform.

MOBILE APPLICATIONS FOR ADVANCED MANUAL DATA ACQUISITION

The digitalisation of data collection can be further enhanced by transitioning from manual paper-based methods to electronic data capture using mobile applications specifically designed for mining environments, especially underground mining. These applications revolutionise data capture,

verification, and accessibility, also enabling information to be validated at the point of entry based on historical records.

Unlike traditional manual methods, these mobile applications are optimised to function both online and offline, enabling continuous operation without an active internet connection. Through efficient caching and storage mechanisms, the applications can ensure that discrepancies are flagged immediately, reducing errors before they propagate through the system, even without an active internet connection. This is made possible through well-defined APIs that facilitate seamless data exchange between devices, databases, and analytics platforms. Additionally, the applications provide instant access to historical data, allowing users to compare current readings with the date and value of past measurements for better context and decision-making. Key advantages of mobile application-based data collection include:

1. Real-time digital storage:
    a) Measurements are recorded immediately and stored digitally on the mobile device at the time of collection.
    b) The need for manual transcription is eliminated thereby reducing human error.

2. Instant synchronisation and cloud integration:
    a) Once an internet connection is available, whether underground via a mine WiFi network or on the surface, the data is automatically uploaded to the central visualisation and analytics platform.
    b) This ensures that data is available for processing within minutes, enabling rapid decision-making.

3. Enhanced data verification and integrity:
    a) Automated verification algorithms compare new entries with previous values, alerting users to potential anomalies and outliers.
    b) The application enforces structured and complete data entry, reducing inconsistencies and ensuring high-quality data for downstream analytics.

4. Improved accessibility and decision support:
    a) Field technicians can instantly access previous measurements through the mobile application.
    b) This enhances situational awareness, allowing users to track trends in real-time and make informed decisions while at the measurement site.

5. FAIR model compliance and future-readiness:
    a) By structuring data according to the FAIR model principles, the system ensures that data is ready for future integration.
    b) This facilitates advanced ML, predictive analytics, and automation, allowing for continuous improvement in mine safety and operational efficiency.

Figure 9 shows the simplification of the data flow using mobile applications.

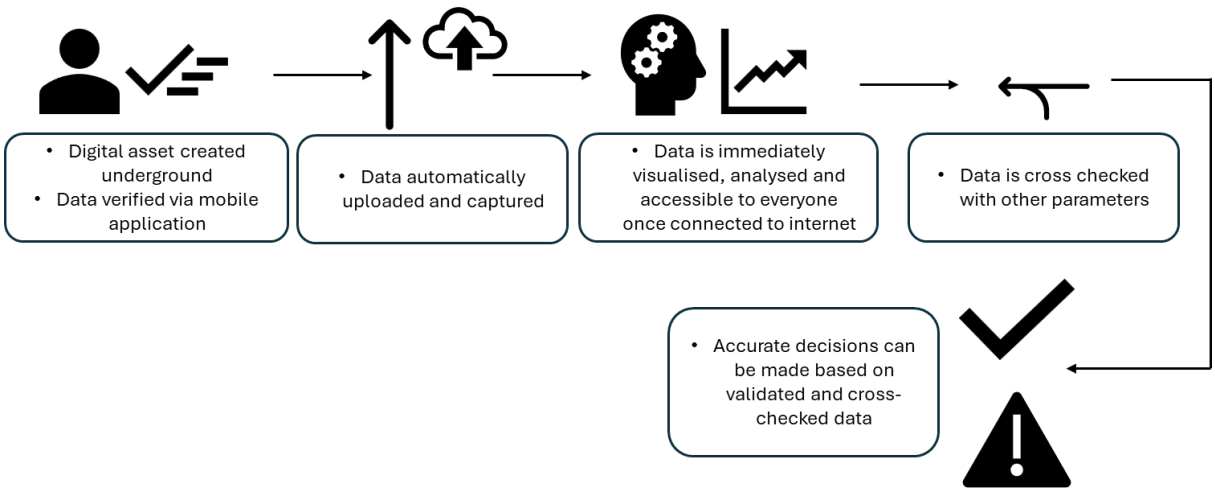


Figure 9. Typical flow of data capturing with mobile applications and modern visualisation platforms.

Case study 2 – Visualisation and analysis of data captured using mobile applications

Background:

A mining company operates multiple tailings dams, each containing numerous piezometers critical for monitoring dam stability. Historically, these piezometers have been monitored manually on a monthly basis, a process that is both time-consuming and resource-intensive. Due to the vast number of piezometers spread across each of many expansive tailings facilities, completing a full monitoring cycle can take over a month. This means that by the time data is collected, conditions in the dam could have significantly deteriorated and critical stability concerns may have gone unnoticed.

The data collection process relied on paper-based methods, where technicians manually recorded readings and later handed over their data sheets to the engineering teams. This data was then entered into spreadsheets, analysed, and reported. If errors were identified in the analysis stage, the engineer would need to request the erroneous measurements to be repeated.

With recent changes to regulations regarding tailings dam safety - Global Industry Standard on Tailings Management - mining companies are now required to adopt proactive monitoring strategies to identify potential risks earlier and mitigate failures before they escalate. Furthermore, insurance providers are now more aware of the potential for real-time, structured data to assess risks more accurately, making modernised data collection and analytics an operational necessity.

Solution:

In order to address these challenges, the mining company partnered with a geotechnical consulting company specialising in advanced data visualisation and analytics. The consulting firm developed an integrated analytics platform with the following features:

1. IIoT sensors deployed at critical monitoring points for real-time data collection.
2. The use of standard digital sensors where real-time monitoring was not feasible.
3. Manual data entry via a mobile application, ensuring structured and verified data collection.
4. Custom-built APIs, enabling seamless communication between the mobile application and the analytics platform.

Although the mining company deployed IIoT sensors at high-risk locations across the tailings facilities, due to the sheer number of measurement points required, ensuring continuous automated monitoring at all locations was not possible. For these areas, the solution incorporated a mobile application that allowed technicians to capture data electronically while ensuring accuracy and efficiency. The mobile application was designed to address key challenges associated with remote monitoring, including:

1. Limited, unreliable or no cellular connectivity in remote tailings locations.
2. Risk of theft and load shedding (rolling power blackouts), affecting real-time communication.
3. Need for data verification at the point of capture.

Automation and Real-Time Verification:
The mobile application was designed to incorporate offline functionality, allowing technicians to download historical data for verification and store new measurements locally until an internet connection became available. The system provided real-time validation, ensuring that:

1. Any data entered is aligned with historical trends automatically via the application.
2. Anomalies were flagged for immediate onsite rectification.
3. Data was structured to eliminate errors before submission to the analytics platform.

Additionally, the application featured GPS tracking and geo-fencing, allowing technicians to easily locate monitoring points while ensuring:

1. Measurement locations were precisely recorded.
2. Only authorised personnel at the correct location could submit readings.
3. The system tracked completed measurement points, preventing duplicate entries and reducing inefficiencies.

Once the device was connected to the internet, data was automatically uploaded to a cloud-based analytics platform, where it was instantly processed and visualised.

Advanced Data Visualisation and Analytics:
The analytics platform provided comprehensive real-time insights into the condition of the tailings dams through:

1. Automated data processing
    a) Instant trend analysis and rate-of-change calculations.
    b) Comparison of current values with historical patterns to identify potential risks.

2. Graphical insights
    a) Live dashboards with colour-coded risk indicators.
    b) Customisable alerts and threshold warnings to notify key stakeholders in real time.

3. Automated reporting and compliance
    a) Monthly and quarterly reports are generated automatically.
    b) Data is stored in a structured format, ensuring compliance with the FAIR model and tailings safety regulations.
    c) Potential for integration with insurance and regulatory monitoring systems.

4. API integration for enterprise-wide access
    a) Integration of the system with third-party monitoring tools.
    b) Access provided to engineers, safety officers, and regulators to the latest data from any internet-connected device.
    c) Integration of the data with compliance software.

Screenshots:
Selected screenshots of the mobile application for tailings dams are given in Figure 10.

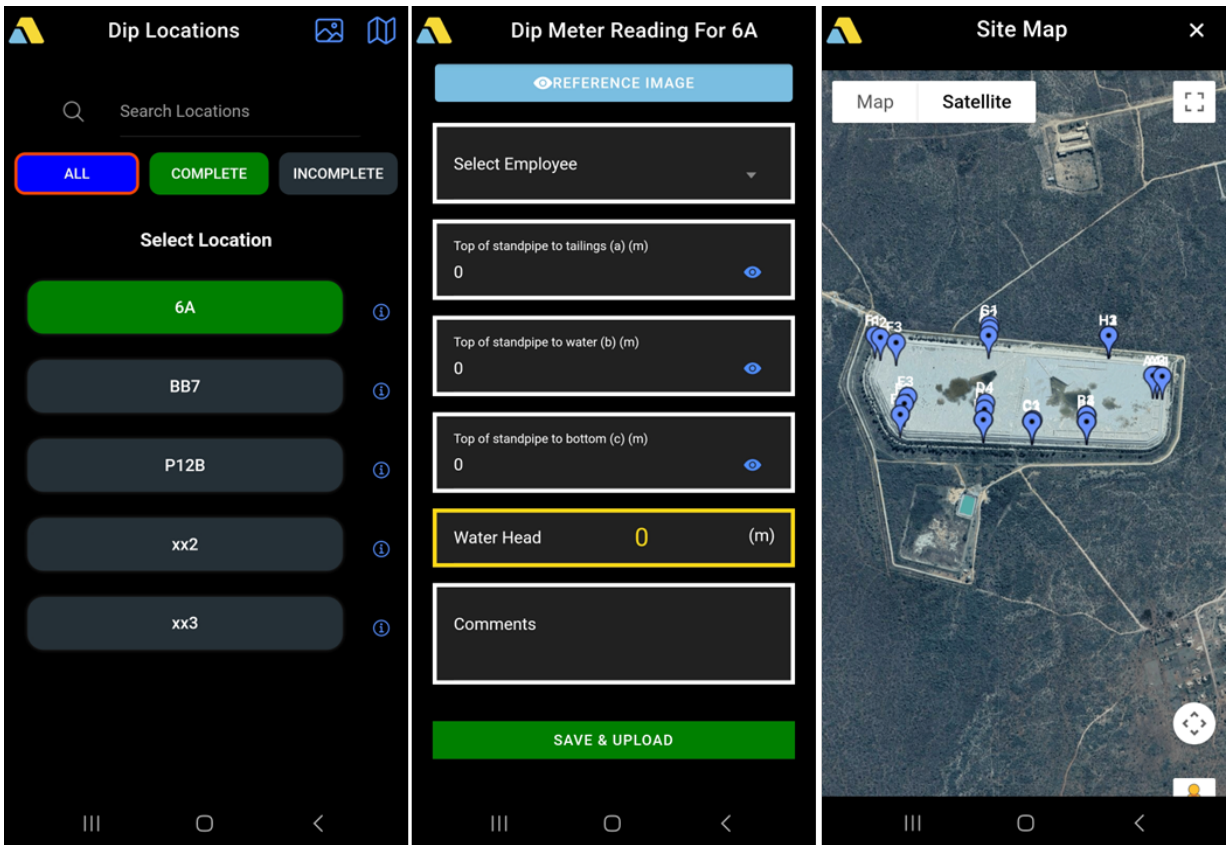


Figure 10. Selected screenshots of the mobile application for tailings dams.

POTENTIAL APPLICATIONS FOR TRANSFORMING DATA CAPTURE METHODS

From the case studies, it is clear that there are numerous immediate applications where advanced data capture methods could be used, and the advantages can be utilised in geotechnical applications. Some of these applications are as follow:

1. MPBX/Extensometers: There are often large quantities of extensometers installed that are manually logged.
2. Shotcrete quality control data: Quality control data could be captured and reported on.
3. Point load testing readings.
4. Rock quality designation, rock mass rating and Q-system.
5. Tailings dam critical controls: This includes slurry density, freeboard, drain flows, etc.
6. Vibrating wire piezometer readings.

CLIENT DATA AND INFRASTRUCTURE SECURITY

As mining operations generate increasingly large volumes of digital data from sensors, automation systems, and digital platforms, the demand for real-time analytics and ML/AI-driven insights has surged. Mining companies recognise the value of leveraging cutting-edge technologies for predictive maintenance, geotechnical stability assessments, and operational efficiency. However, security and integrity for the digital data asset remain paramount, since exposing critical infrastructure to external risks can have severe consequences, including operational disruptions, cyber threats, and regulatory violations.

While some mining companies prefer in-house data processing, keeping pace with the rapid advancements in IIoT, ML/AI, and cloud-based analytics presents them with a significant challenge. Maintaining an internal IT team capable of continuously upgrading systems, integrating new technologies, and ensuring compliance with evolving security standards can be costly and inefficient. As a result, mining companies must balance their need for external expertise with robust cybersecurity measures that protect core infrastructure.

In order to ensure that external analytics providers, ML/AI developers, and geotechnical specialists can access necessary data without compromising internal information and communication technology (ICT) systems, solutions do exist. It is recommended that the following best practices be considered:

1. Dedicated independent networks for IIoT devices
    a) Mining operations often deploy a separate network exclusively for IIoT devices, ensuring that sensor data is isolated from enterprise ICT systems.
    b) These networks are designed to transmit only operational data, preventing the exposure of sensitive company information, such as personnel details or financial records.
    c) For example, LoRaWAN or private LTE networks can be used to transmit piezometer and seismic sensor data independently from the main ICT network.

2. Secure API gateways with authorisation controls
    a) Mining ICT teams can develop secure APIs that allow only authorised external parties to retrieve specific datasets without direct access to internal databases.
    b) APIs include token-based authentication, role-based access control, and encryption protocols to regulate data flow and to prevent unauthorised access.
    c) For example, a mining company implementing an API-based integration with a cloud analytics provider can ensure that only pre-approved data subsets are accessible for processing.

3. Outbound data posting to external platforms
    a) Instead of allowing external systems to query internal databases, mining ICT teams can push relevant data to external analytics platforms at scheduled intervals.
    b) This method eliminates the need for external connections to the mining network, thereby reducing security risks.
    c) For example, a tailings dam monitoring system can send automated daily reports to a cloud-based geotechnical risk assessment platform, where ML and/or AI-driven models process the data.

4. Use of independent cellular networks and edge computing
    a) Mobile applications and IIoT devices can operate on dedicated cellular networks (e.g., 4G, 5G, NB-IoT or satellite connectivity) instead of being connected to a corporate IT infrastructure.
    b) Edge computing solutions allow data to be processed locally on devices before being transmitted securely to external platforms.
    c) For example, a remote mining site using satellite connectivity can collect seismic and water pressure data without linking to the enterprise ICT network.

While ICT security remains a top priority, adopting secure data-sharing frameworks allows mining companies to benefit from advanced AI-driven analytics without exposing critical infrastructure to cyber risks. By implementing robust security measures alongside innovative data accessibility solutions, mining companies can stay ahead of technological advancements and continuously improve rock engineering, geotechnical monitoring, and operational safety.

CONCLUSION

The rapid expansion of IIoT sensors in geotechnical applications is fundamentally transforming the way mining operations collect, process, and utilise data. As digital technologies continue to advance, the volume and complexity of geotechnical data are increasing at an unprecedented rate, making it imperative for mining companies to adopt structured approaches to data acquisition, management, and analysis. Ensuring that geotechnical data is captured correctly, processed efficiently, and visualised effectively is essential for enabling real-time decision-making, predictive analytics, and proactive risk mitigation.

Proper data structuring allows for seamless integration across various platforms, enabling engineers, geotechnical specialists, rock engineers, and decision-makers to access reliable and up-to-date insights. However, managing this data as a valuable digital asset requires robust frameworks that ensure its quality, security, accessibility, and long-term usability.

The role of mobile applications and digital platforms in transforming geotechnical data
The adoption of mobile applications and cloud-based platforms is changing geotechnical data management in mining. These tools enable real-time data entry, automated synchronisation, and seamless integration with visualisation and analytics systems, replacing inefficient paper-based records with more accurate and efficient digital processes. By leveraging digital platforms, mining companies can convert raw geotechnical data into actionable insights, allowing AI-driven models to detect trends, identify anomalies, and predict failures.

Addressing security and accessibility challenges in a digital-first environment
As mining companies increasingly rely on external analytics providers, ML/AI developers, and geotechnical consultants, secure data-sharing frameworks are essential to protect sensitive information. Implementing dedicated IIoT networks, secure API gateways, controlled outbound data posting, and independent cellular networks can help establish strong security measures. These strategies enable controlled data exchange, allowing external specialists to provide insights while safeguarding core ICT infrastructure from cyber threats, operational disruptions, and regulatory risks.

The importance of FAIR data principles in future-proofing mining data assets
To ensure the long-term value of geotechnical data, mining companies must align their data management strategies with the FAIR principles, ensuring that data is Findable, Accessible, Interoperable, and Reusable. Preparing structured, well-documented, and standardised datasets in the present will enable seamless integration with future analytical tools, machine learning, ML/AI models, and evolving technologies.

The role of local geotechnical consultants and visualisation specialists
Specialists in geotechnical visualisation software can develop tailored solutions that enhance data interpretation, risk assessment, and predictive modelling, ultimately improving safety and efficiency in mining operations.

By partnering with local experts who understand the specific challenges of mining environments, companies can ensure that visualisation tools are intuitive, industry-specific, and aligned with operational requirements. Advanced visualisation solutions bridge the gap between raw data and actionable decision-making, providing geotechnical engineers with the tools they need to monitor, analyse, and respond to geotechnical risks in real-time.

Strategic implementation for a data-driven future
A phased and strategic approach is essential for mining companies looking to successfully integrate IIoT-driven geotechnical monitoring, secure data management, and advanced analytics into their operations. This requires a coordinated effort across multiple domains, including:

1. Selecting the right data acquisition techniques to ensure accurate, real-time geotechnical monitoring.
2. Implementing structured data management frameworks that align with FAIR principles.
3. Developing and adopting robust visualisation platforms that make data actionable and accessible.
4. Ensuring cybersecurity and controlled access to protect mining infrastructure from external threats.
5. Collaborating with specialised geotechnical consultants to tailor solutions for operational needs.

By embracing digital transformation, ensuring security, and collaborating with experts, mining companies can create a sustainable, scalable, and future-proofed geotechnical data ecosystem.

REFERENCES AND BIBLIOGRAPHY

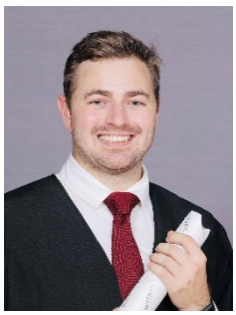
A. Asmi, D. Franz, and A. Petzold, "Building the Foundations for Open Applied Earth System Science in ENVRI-FAIR," Mar. 2020, doi: https://blogs.egu.eu/divisions/gd/2020/07/24/what-is-fair-for-geodynamics/.

D. Bailo, R. Paciello, M. Sbarra, R. Rabissoni, V. Vinciarelli, and M. Cocco, "Perspectives on the Implementation of FAIR Principles in Solid Earth Research Infrastructures," Frontiers in Earth Science, vol. 8, Jan. 2020, doi: https://www.frontiersin.org/journals/earth-science/articles/10.3389/feart.2020.00003/full.

E. Eleftherios, D. Papatsaroucha, and E. K. Markakis, "Leveraging Industrial IoT Infrastructure for Remote Sensing and Edge Computing in the Mining Sector," 2024 5th International Conference in Electronic Engineering, Information Technology & Education (EEITE), pp. 1–6, May 2024, doi: https://doi.org/10.1109/eeite61750.2024.10654424.

J.J. Meiring, P.S.Piper and C.A.Smith, "Transforming geotechnical decision-making using the internet of things and data analytics," 2024 SANIRE Symposium, pp. 77-92, June 2024, doi: https://www.saimm.co.za/Conferences/files/sanire-2024/08_SANIRE16-Meiring.pdf

H. Zhu, X. Li, and X. Zhuang, "Recent advances of digitization in rock mechanics and rock engineering," Journal of Rock Mechanics and Geotechnical Engineering, vol. 3, no. 3, pp. 220–233, Sep. 2011, doi: https://doi.org/10.3724/sp.j.1235.2011.00220.



Johannes Jacobus Meiring

Project Engineer
Groundwork Consulting

Jaco Meiring graduated with a Bachelor's Degree in Electrical Engineering from the University of Pretoria. Since 2020, he has been a valuable team member at Groundwork Consulting, actively contributing to over 30 mining operations, including underground projects and tailings storage facilities.

Soft computing techniques for predicting mode-ii fracture toughness: A cost-effective approach to advancing rock mechanics' design and sustainability

N.O. Ogunsola[1,2], H. Grobler[1]

[1]University of Johannesburg, South Africa
[2]Sibanye-Stillwater Center for Sustainable Mining, South Africa

The pure Mode-II fracture toughness (K_{IIc}) of rocks plays a critical role in understanding shear-dominated failure mechanisms in engineering applications; including tunnelling, slope stability, hydraulic fracturing, and rock mass design. However, experimental determination of K_{IIc} is often complex, expensive, and time-consuming due to the intricate testing procedures involved. This paper examines the application of soft computing techniques, including Levenberg-Marquardt trained artificial neural networks (ANN-LM), adaptive neuro-fuzzy inference system (ANFIS), and multilinear regression (MLR) to predict K_{IIc} of the International Society for Rock Mechanics and Rock Engineering - recommended Punch-Through Shear with Confining Pressure Test using test specimen geometrical and rock geomechanical properties. An experimental database comprising six predictor parameters: inner notch diameter, intact rock portion, specimen height, upper notch depth (a), compressive strength (σ_C), and confining pressure were used to develop and validate the predictive models. The predictive accuracy of the models was assessed using statistical error metrics, including the coefficient of determination (R^2), variance accounted for, and mean absolute error. The results of the predictive performance assessment showed that ANN-LM 6-8-1 model provides a superior predictive accuracy compared to ANFIS and MLR models. The ANN-LM model was later transformed into a user-oriented mathematical formula for easier computation of K_{IIc}. Finally, a sensitivity analysis technique was employed to evaluate the effect of each input parameter on K_{IIc} predictions. This research demonstrates the efficiency of soft computing techniques in predicting K_{IIc}, providing a cost-effective alternative to experiments while advancing rock mechanics design and sustainable practices.

Keywords: Fracture toughness, Soft computing, Punch-Through Shear with Confining Pressure Test, artificial neural network, adaptive neuro-fuzzy inference system

INTRODUCTION

Rock fracture mechanics principles are widely applied in various fields of engineering to prevent catastrophic failures and address specific challenges, including mining excavation, tunnelling, drilling, blasting, cutting, crushing, hydraulic fracturing, and underground construction. Accurate characterisation of rock fracture properties is critical for optimising fracture conductivity, mitigating rock bursts, and assessing rock structure stability. The critical stress intensity factor or fracture toughness (K_c) defines rock resistance to fracture initiation and propagation. Rock fractures occur in three modes: Mode-I (tensile), Mode-II (in-plane shear), and Mode-III (out-of-plane shear) (Dai & Xia, 2013). Mode-I fracture (K_{Ic}) is the most studied fracture mode because most rock engineering challenges involve tensile failure due to the rock's inherent tensile weakness (Wei *et al.,* 2015).

However, despite the wide application of Mode-I fracture in various engineering practices, particularly in rock engineering due to the rock weakness in tension compared to compressive and shear load, pre-existing microcracks or fractures in rock and rock mass geological structures such as bedding planes, unconformities, joints, shear zones, and faults rarely experienced pure tensile loading; instead, they typically experience compressive, shear, or mixed-mode fracturing (Yao *et al*., 2017). An example of Mode-II fracture in rock mechanics is the fracture or disintegration of the rock bridge connecting two adjacent discontinuities due to shearing or sliding. Shear failure is thus one of the most common failure mechanisms in rock engineering, including natural and engineered rock structures. For this reason, understanding Mode-II fracture behaviour is essential for assessing rock stability and designing effective engineering solutions in various engineering applications.

Several test specimens have been proposed to measure the Mode-II fracture toughness (K_{IIc}) of rocks and other geomaterials (Chang *et al*., 2002; Ko & Kemeny, 2006; Backers *et al*., 2002; Jung *et al*., 2016). However, traditional experimental methods for determining K_{IIc} are often expensive, time-consuming, and constrained by complex field and laboratory conditions. Also, many numerical techniques and empirical models have been used to estimate K_{IIc} of rocks (Hua *et al*., 2017; Saeidi *et al*., 2012; Wu *et al*., 2017). However, while numerical simulations are expensive and time-consuming, empirical methods are not often accurate and most of the time underestimate K_{IIc}. These limitations necessitate the development of efficient, cost-effective, and accurate predictive models.

Soft computing techniques, including artificial neural networks (ANNs), support vector machines (SVMs), random forests (RF), and evolutionary algorithms, have emerged as powerful tools for modelling complex nonlinear relationships in rock mechanics. These data-driven approaches have been used to effectively predict the Mode-I fracture toughness (K_{Ic}) of rocks by integrating diverse rock geological, mechanical, and rock specimen geometrical factors, reducing reliance on extensive physical testing (Ogunsola *et al*., 2024a; Afrasiabian *et al*., 2022). However, the techniques have not been explored to predict K_{IIc} of rocks. Thus, this constitutes a research gap that needs to be filled.

This study explores the application of soft computing techniques for predicting K_{IIc} of the International Society for Rock Mechanics and Rock Engineering (ISRM)-recommended Punch-Through Shear with Confining Pressure Test (PTS-CP) using test specimen geometrical and rock geomechanical properties. An experimental database comprising 80 datasets with six predictor parameters, including the inner notch diameter (ID), intact rock portion (IP), specimen height (W), upper notch depth (a), compressive strength (σ_c), and confining pressure (P), was used to develop the models. Three soft computing techniques, including the Levenberg-Marquardt trained artificial neural network (ANN-LM), adaptive neuro-fuzzy inference system (ANFIS), and multilinear regression (MLR), were employed to predict K_{IIc} of rocks. The optimum ANN-LM model was transformed into a user-friendly mathematical equation to aid in an easier and large-scale estimation of K_{IIc} of rocks. This paper provides a sustainable and economically viable alternative to conventional methods. By leveraging machine learning and computational intelligence, this approach enhances the efficiency of rock mechanics design, optimises engineering processes, and contributes to safer and more sustainable geotechnical and mining operations.

DATABASE COMPILATION AND PREPROCESSING OF DATA

Description of the Compiled K_{IIc} Database

We developed soft computing-based prediction models for Mode-II fracture toughness (KIIc) using the ISRM-recommended PTS-CP database. Compiled from Backers *et al*., (2002), this dataset encompasses three rock types— Aue granite, Carrara marble, and Rudersdorf limestone—and contains 80 datasets with six predictor parameters: ID, IP, W, upper notch depth (a), σ_c, and P. The W and ID of the tested rocks varied between 25.00 and 50.22 mm and 22.00 and 50.00 mm, respectively. The upper notch depth (a) and IP of the rock specimens varied between 4.30 and 8.00 mm and 4.00 and 24.70 mm, respectively. The measured confining pressure (P) of the tested rock specimens varied between 0.00 and 70.00 MPa, and the compressive strengths of the three rock types varied between 40.00 and 392.50 MPa. The K_{IIc} of the tested rock specimens varied between 2.20 and 21.10 $MNm^{3/2}$. The statistical overview of the

predictor and predicted parameters used in developing the K_{IIc} soft computing models is detailed in Table I.

Table I: Statistical description of the K_{IIc} predictor and predicted parameters

Model variables	Symbol	Units	Class	Statistics			
				Min	Max	Mean	STD
Specimen height	W	mm	Predictor	25.00	50.22	49.06	4.781
Inner notch diameter	ID	mm	Predictor	22.00	50.00	25.38	3.008
Upper notch depth	a	mm	Predictor	4.30	8.00	5.02	0.591
Intact rock portion	IP	mm	Predictor	4.00	24.70	14.34	3.547
Confining pressure	P	MPa	Predictor	0.00	70.00	17.26	19.796
Compressive strength	σ_c	MPa	Predictor	40.00	392.50	105.28	88.142
Fracture toughness	K_{IIc}	$MNm^{3/2}$	Predicted	2.20	21.10	7.71	3.937

Preprocessing of Compiled Database

Figure 1 illustrates the frequency distributions of both the predictor and predicted parameters, demonstrating that the compiled K_{IIc} database encompasses a broad spectrum of predictor and predicted values. The Pearson correlation matrix presented in Table 2 quantifies the interdependence and correlations between the predictor variables and K_{IIc} for the compiled dataset. According to Table II, the correlations between the predictor parameters and K_{IIc} are substantial, indicating a strong foundation for developing robust predictive models

To develop the ANN-LM, ANFIS, and MLR models, it is essential to mitigate the impact of bias and extreme values (outliers) among both the predictor and predicted parameters, as well as prevent overfitting of the K_{IIc} model. To accomplish this, the compiled database underwent normalisation: for the ANN-LM model, the data was scaled within the range of -1 to 1, as recommended by Lawal *et al.*, (2021), while for the ANFIS model, the data was normalised between 0 and 1 using the generalised normalisation equation (Equation 1).

$$A_{norm} = \frac{(C_{max} - C_{min})(B_i - B_{min})}{(B_{max} - B_{min})} + C_{min} \qquad [1]$$

where A_{norm} represents the normalised variable, B_i represents the actual data to be normalised, C_{max} and C_{min} represent the upper and lower bounds of the normalisation range, respectively, while B_{max} and B_{min} represent the maximum and minimum values of the original dataset.

Table II: Correlation matrix showing the interrelationships between K_{IIc} model parameters

	W	ID	a	IP	P	σ_c	K_{IIc}
W	1						
ID	-0.085	1					
a	-0.294	0.670	1				
IP	0.146	-0.307	-0.329	1			
P	0.122	-0.080	-0.056	0.122	1		
σ_c	0.149	-0.109	-0.097	0.086	0.302	1	
K_{IIc}	0.209	-0.175	-0.155	0.255	0.742	0.490	1

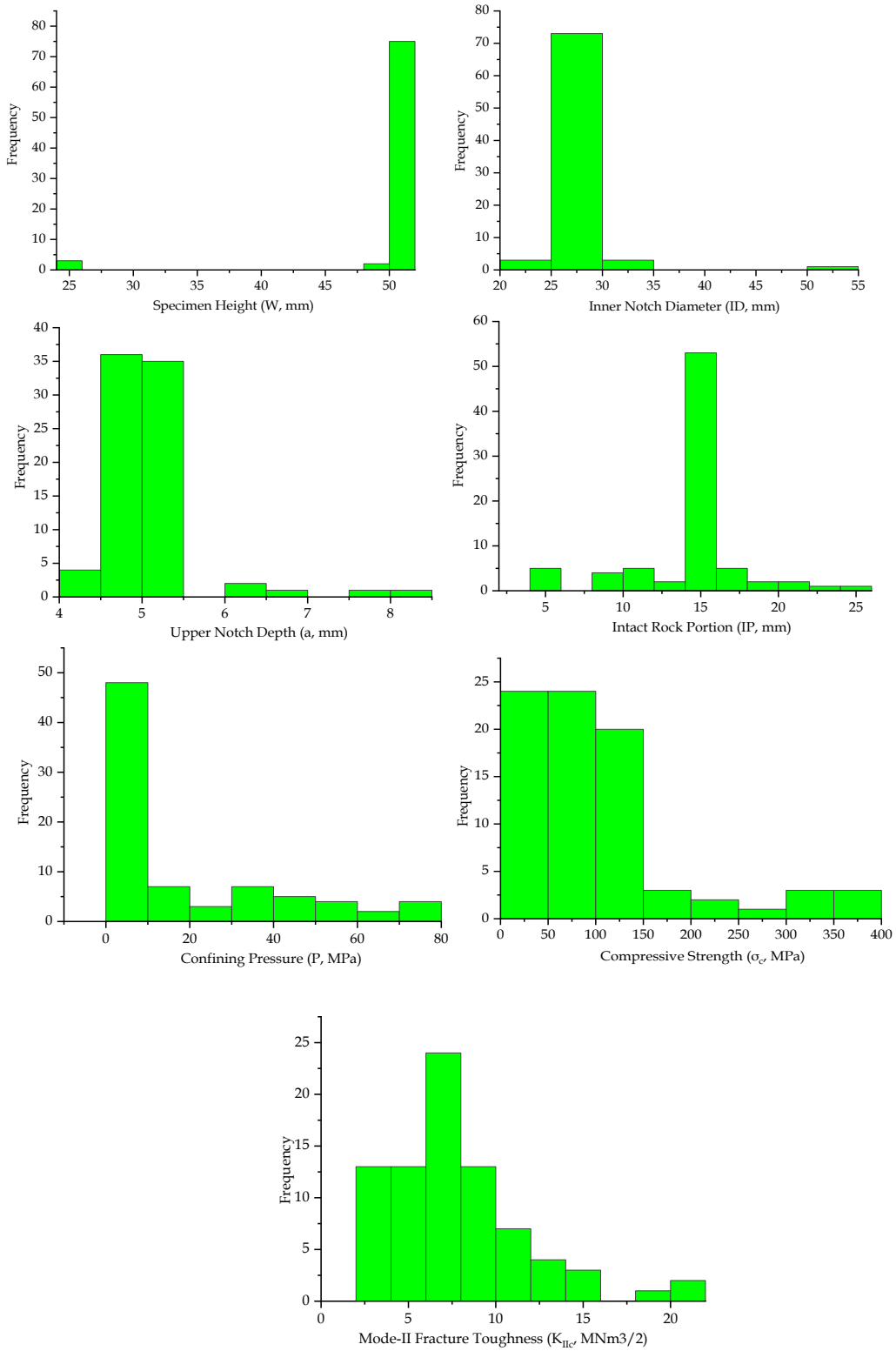


Figure 1. Frequency distribution of the model parameters.

K_{IIc} PREDICTIVE FRAMEWORK DEVELOPMENT

Three soft computing techniques, including an ANN trained with a Levenberg-Marquardt algorithm, an ANFIS, and MLR were employed to develop the K_{IIc} prediction model.

ANN-LM K_{IIc} Prediction Model Development

ANNs represent a subset of machine learning techniques that draw inspiration from the operational mechanisms of the human brain and biological neural systems (Tijani *et al*., 2023). ANNs function analogously to biological neurons by receiving input data, processing it through mathematical functions, and producing an output. The primary components of an ANN include hidden neurons, the learning rate, and equations governing network topology (Ogunsola *et al*., 2024b).

In this paper, ten distinct ANN-LM network topologies were evaluated to develop a prediction model for K_{IIc} of rocks. The performance of each topology was assessed using the correlation coefficient (R) to determine the most accurate and reliable model. Each ANN-LM model was trained on 80 randomly selected datasets, partitioned into 70% for training, 15% for validation, and 15% for testing the model's generalisation capabilities. Table III details the various hyperparameter combinations employed in developing the ANN-LM models.

Table III: Optimal hyperparameter configuration for the ANN-LM model

ANN Hyperparameters	**Values**	**ANFIS Hyperparameters**	**Values**
Training algorithm	Levenberg-Marquardt (LM)	Fuzzy network	Sugeno type
Network type	Feed-forward backpropagation neural network (BPNN)	Initial FIS for training	Genfis2
Normalisation function	Minmax [-1,1]	Normalisation function	Minmax [0,1]
Number of hidden layers	1 or 2	Membership function type	Input: trimf; Output: constant
Number of neurons per hidden layer	1 to 10 by step 1	FIS generation method	Grid partitioning
Train: test: validation ratio	70:15:15	Optimisation method	Hybrid
Hidden layer activation function	Hyperbolic tangent sigmoid (tan-sigmoid)	Train: test ratio	80:20
Output layer activation function	Hyperbolic tangent sigmoid (tan-sigmoid)	Number of epochs	100
Epochs	100	Number of membership functions	333333
Momentum update (mu)	0.001	Cost function	Root Mean Square Error (RMSE)
Minimum performance gradient (min_grad)	1e-07		
Maximum validation checks (max_fail)	100		
Cost function	Mean square error (MSE)		

Table IV presents the performance metrics of the ten trained ANN-LM network topologies, evaluated using correlation coefficients (R-values). The results indicate that network performance is not solely determined by the number of hidden neurons, as certain models with fewer neurons demonstrated superior performance compared to those with more. The most effective model, designated as ANN-LM 6-8-1, features a topology consisting of five input neurons, six hidden neurons, and one output neuron, employing a tan-sigmoid activation function in both the hidden and output layers. The detailed network topology of this optimal ANN-LM 6-8-1 model is illustrated in Figure 2.

Table IV: Various trained ANN-LM network topologies

Network	Training	Testing	Validation	Overall
6-2-1	0.96354	0.94328	0.98565	0.96210
6-3-1	0.97329	0.96576	0.98229	0.97428
6-4-1	0.98029	0.97663	0.99385	0.98075
6-5-1	0.98187	0.98956	0.99007	0.98283
6-6-1	0.96958	0.99255	0.99289	0.98074
6-7-1	0.97002	0.98541	0.99184	0.97650
6-8-1	0.98139	0.99195	0.999446	0.98466
6-9-1	0.97893	0.99386	0.99445	0.98300
6-10-1	0.97777	0.98579	0.99176	0.98179

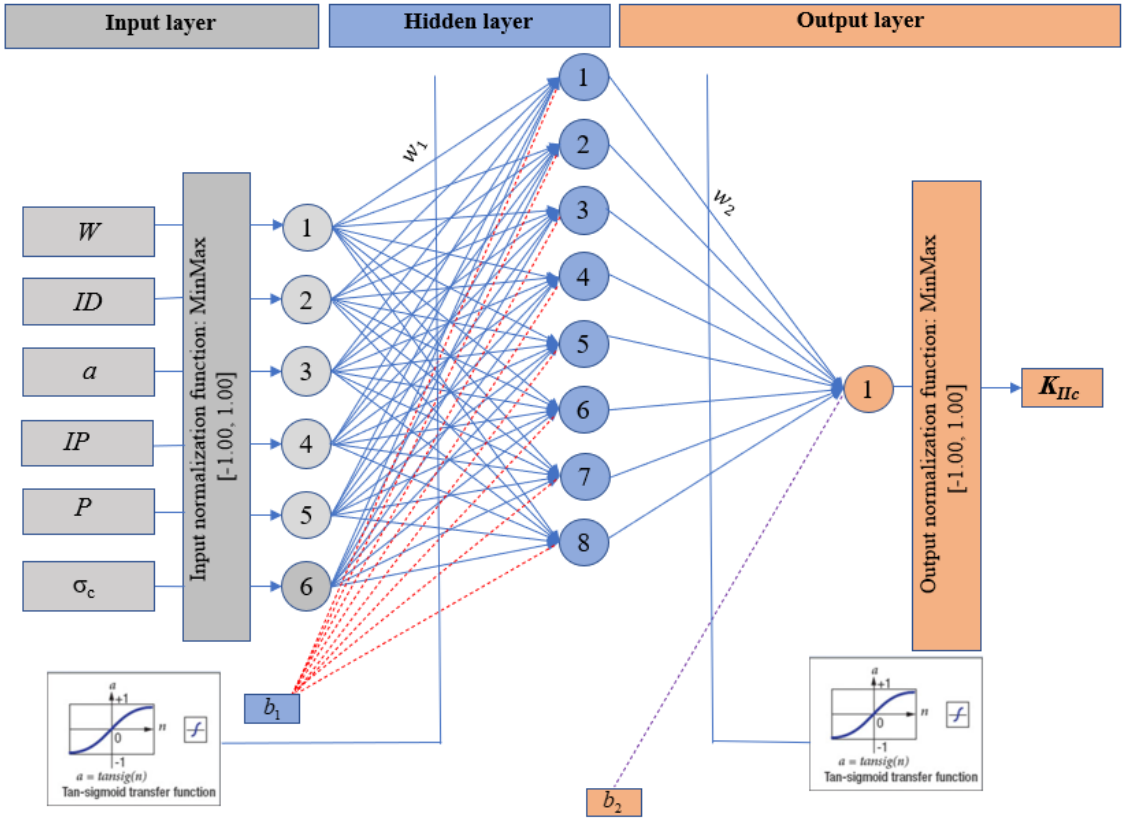


Figure 2. Network topology of the ANN-LM 6-8-1 model.

***ANFIS K_{IIc} Prediction Model* Development**

The ANFIS is a hybrid modeling framework that synergistically combines the strengths of ANNs and Fuzzy Inference Systems (FISs), as initially proposed by Jang (1993). ANFIS is designed to capture complex system behaviours by utilising linguistic variables and handling imprecise relationships. It operates through a five-layer architectural structure, where input-output data pairs from the training dataset are fed into the system. Both premise and consequent parameters are initialised with small values, facilitating the learning process and enabling the system to adaptively refine its parameters based on the training data. Table III provides a detailed overview of the hyperparameters used for training the ANFIS models.

***MLR K_{IIc} Prediction Model* Development**

The MLR model was developed in this study to provide a comparison with the ANN-LM and ANFIS models. MLR is a statistical technique that establishes a linear relationship between a dependent variable and multiple independent variables. It employs the method of least squares to optimise the fit of a linear equation to the measured or observed data. In this framework, each independent variable (x) is associated with a specific coefficient that contributes to the prediction of the dependent variable (y). The mathematical formulation of the MLR model is presented in Equation (2).

$$y = \varepsilon_0 + \varepsilon_1 x_1 + \varepsilon_2 x_2 \varepsilon_3 x_3 + ...\varepsilon_n x_n + \eta \qquad [2]$$

where y represents the predicted output, while x_1 to x_n represent the predictor parameters. ε_0 is the intercept, and ε_1 to ε_n are the coefficients associated with each predictor parameter. Furthermore, η represents the error term that accounts for the variability and uncertainties inherent in the parameters.

The MLR model was formulated utilising the same dataset as the ANN-LM and ANFIS models. The resulting MLR equation, designed to predict the K_{IIc} of rocks, is presented in Equation (3).

$$K_{IIc} = 0.9369 + 0.0572*W - 0.0685*ID + 0.0370*a + 0.1443*IP + 0.1255*P + 0.0121*\sigma_C \qquad [3]$$

ANALYSIS OF MODEL PREDICTION ACCURACY

To evaluate the prediction accuracy of the three developed K_{IIc} models in this study, six statistical error metrics were employed: mean absolute error (MAE), mean absolute percentage error (MAPE), root mean square error (RMSE), relative root mean square error (RRMSE), coefficient of determination (R^2), and variance accounted for (VAF), as defined in Equations (4-9). The coefficient of determination (R^2) ranges from 0 to 1, with values closer to 1 indicating better performance. In contrast, the metrics MAE, RMSE, RRMSE, and MAPE range from 0 to ∞ , where lower values signify superior performance. The VAF ranges from 0 to 100%, with a value of 100% representing optimal performance.

$$MAE = \frac{1}{n}\sum_{i=1}^{n}\left|K_{IIc} - K_{IIci}\right| \qquad [4]$$

$$MAPE = \frac{100\%}{n}\sum_{i=1}^{n}\left|\frac{K_{IIC} - K_{IIci}}{K_{IIc}}\right| \qquad [5]$$

$$RMSE = \sqrt{\frac{1}{n}\sum_{i=1}^{n}(K_{IIc} - K_{IIci})^2} \qquad [6]$$

$$RRMSE = \sqrt{\frac{1}{n}\sum_{i=1}^{n}\sqrt{\left(\frac{K_{IIc} - K_{IIci}}{K_{IIc}}\right)^2}} \qquad [7]$$

$$R^2 = 1 - \frac{\sum_i (K_{IIc} - K_{IIci})^2}{\sum_i (K_{IIci} - \overline{K_{IIc}})^2} \quad [8]$$

$$VAF(\%) = (1 - \frac{\mathrm{var}(K_{IIc} - K_{IIci})}{\mathrm{var}(K_{IIc})}) \times 100 \quad [9]$$

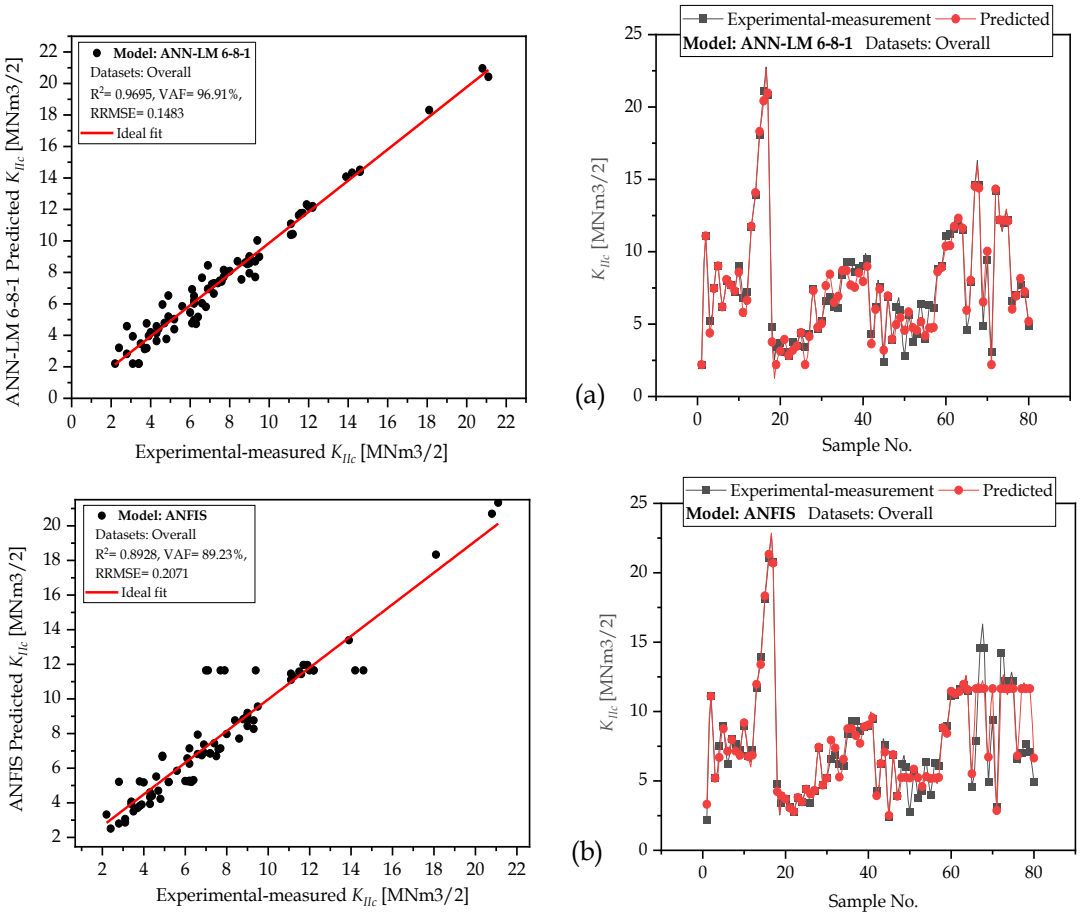
where K_{IIc} represents the experimental-measured Mode-II fracture toughness of rock (MNm$^{3/2}$), K_{IIci} represents the predicted Mode-II fracture toughness of rock (MNm$^{3/2}$), $\overline{K_{IIC}}$ denotes the arithmetic mean of the actual K_{IIcs} (MNm$^{3/2}$), and n is the number of employed datasets.

RESULTS AND DISCUSSION

The performance of the developed K_{IIc} prediction models was comprehensively evaluated using statistical error metrics. A Taylor diagram was utilised to facilitate a comparative analysis of the models, while a sensitivity analysis was conducted to assess the influence of predictor parameters on K_{IIc}. Furthermore, the proposed ANN-LM model was transformed into a user-friendly, closed-form equation to simplify the estimation of K_{IIc}, enhancing its practical applicability.

Evaluation of Model Prediction Accuracy

The prediction accuracy evaluation results for all developed models are presented in Table V. The ANN-LM 6-8-1 model demonstrated superior performance across all metrics, while the ANFIS and MLR models showed progressively lower accuracy. Visual comparisons between experimental and predicted K_{IIc} values for each model are provided in Figure 3(a-c) for ANN-LM, ANFIS, and MLR models, respectively, with ANN-LM showing the closest alignment.



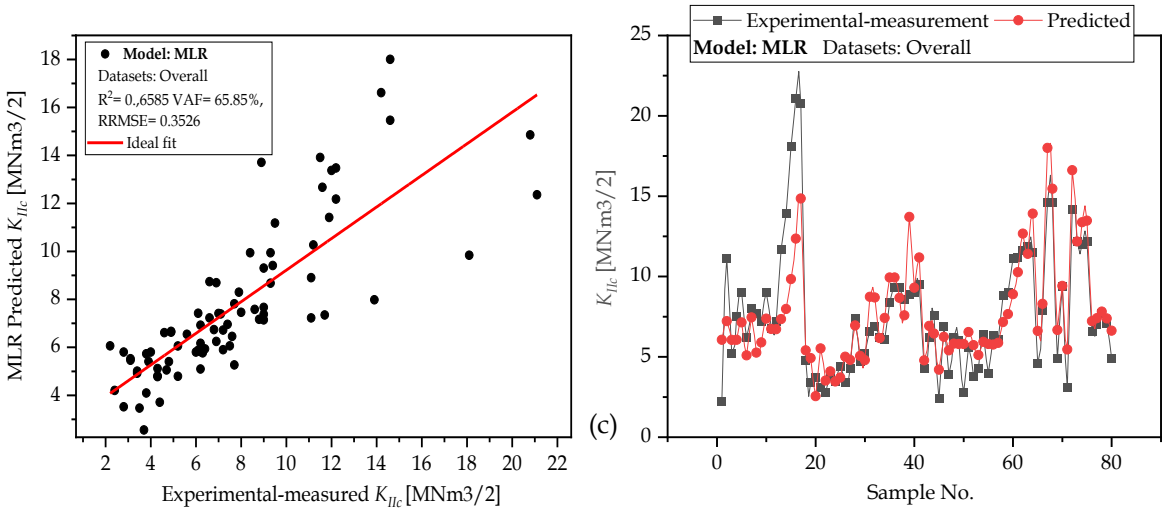


Figure 3. Graphical comparison of experimental-measured and predicted K_{IIc} values using scatter and line diagrams (a) ANN-LM 6-8-1; (b) ANFIS; and (c) MLR.

Table V: Prediction accuracy evaluation results of the K_{IIc} models

Models	**Statistical indices**					
	RMSE	**RRMSE**	**MAE**	**R²**	**VAF**	**MAPE**
ANN-LM 6-8-1	0.6956	0.1483	0.4999	0.9695	96.91	9.2180
ANFIS	1.2953	0.2071	0.7582	0.8928	89.23	11.7821
MLR	2.2862	0.3526	1.5634	0.6585	65.85	23.3656

Comparison of the Developed K_{IIc} Models

The prediction accuracy of the developed models was comprehensively evaluated using various metrics, as presented in Table V. Based on the root mean square error (RMSE) and relative root mean square error (RRMSE), the ANN-LM 6-8-1 model exhibited the highest predictive performance, achieving RMSE and RRMSE values of 0.6956 and 0.1483, respectively. This model outperformed the ANFIS and MLR models by 86.21% and 228.67% for RMSE, and by 39.65% and 137.76% for RRMSE.

When assessed using MAE and coefficient of determination (R^2) as metrics, the ANN-LM 6-8-1 model again demonstrated superior prediction accuracy, with MAE and R^2 values of 0.4999 and 0.9695, respectively. It surpassed the ANFIS and MLR models by 51.67% and 212.74% for MAE, and by 7.91% and 32.08% for R^2.

Furthermore, employing VAF and MAPE as evaluation metrics, the ANN-LM 6-8-1 model maintained its position as the most accurate, achieving VAF and MAPE values of 96.91% and 9.2180%, respectively. It outperformed the ANFIS and MLR models by 7.92% and 32.05% for VAF, and by 27.82% and 153.48% for MAPE.

To further compare the models' accuracy, a Taylor diagram was utilised, incorporating Pearson correlation (R), standard deviation (Std), and root mean squared difference (RMSD) (Taylor, 2001). The most reliable model should be closest to the reference point at the base of the plot. As depicted in Figure 4, the ANN-LM 6-8-1 model achieved the minimum RMSD and maximum R values, indicating superior predictive performance compared to the ANFIS and MLR models. Consequently, the ANN-LM 6-8-1

model is identified as the most robust for estimating the Mode-II fracture toughness (K_{IIc}) of rocks among the developed models.

A key limitation of the ANN-LM 6-8-1 model is its restricted applicability beyond the training data range. Prediction accuracy may decline with different input distributions. Future work will expand the dataset diversity to improve robustness and develop a more universally applicable K_{IIc} prediction.

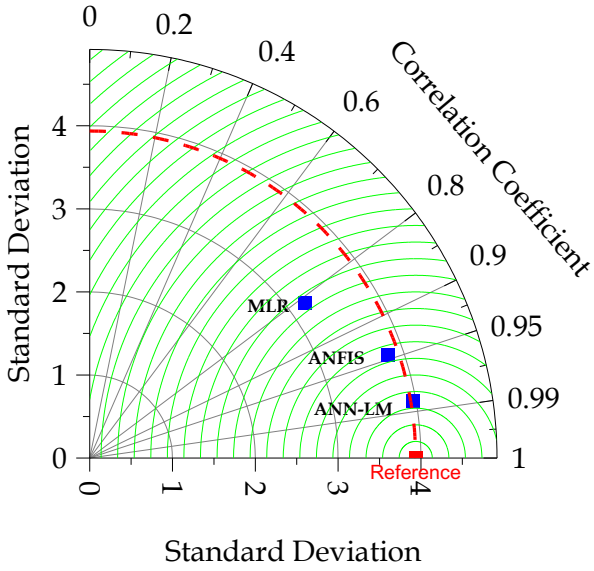


Figure 4. Taylor plot visualisation for K_{IIc} model performance comparison.

Mathematical Transformation of ANN-LM 6-8-1 into an Explicit Equation

To ameliorate the black-box nature of ANNs and other machine learning algorithms, and to enable the practical and large-scale implementation of the optimum ANN-LM 6-8-1 model, its weights and biases were transformed into a user-friendly equation based on the standard ANN formulation. The extracted weights and biases for the ANN-LM 6-8-1 network are detailed in Table VI, facilitating the conversion of the model into a more interpretable and accessible form. The transformed ANN-LM 6-8-1 model can be recreated in a spreadsheet environment such as Excel by researchers without having prior knowledge of ANN.

Table VI: The extracted network parameters (weights and biases) from the ANN-LM 6-8-1 system

Weights							**Biases**	
W	***ID***	***a***	***IP***	***P***	***σc***	***K_{IIc}***	***b1***	***b2***
0.7286	-1.5429	1.5009	-0.9904	0.1793	-2.2231	-9.6070	-1.9673	-1.6537
0.0965	1.0629	1.2954	0.7161	-0.1488	2.3703	0.6355	-2.5823	
0.1995	1.6389	-0.2522	0.0889	-0.0331	3.2217	0.4326	-0.8203	
0.9016	-2.1118	2.0609	-1.0457	0.4350	-2.3663	15.2837	-1.9160	
4.8994	-0.4223	1.3269	5.5055	12.0730	-0.1322	7.3571	6.9182	
-1.1466	2.9128	-3.0038	1.0576	-0.7133	2.7814	5.9239	2.0190	
1.7402	-0.3928	-1.8470	-0.0852	0.0517	-1.9681	1.6591	2.9355	
6.1462	-0.5849	1.4526	6.2147	8.2168	0.2738	-7.1242	2.8797	

The network connection weights and biases of the ANN-LM 6-8-1 model were converted into a user-friendly, closed-form equation, as presented in Equation (10).

$$K_{IIcnorm} = -1.6537 + x_1 + x_2 + x_3 + x_4 + x_5 + x_6 \quad [10]$$

Where $K_{IIcnorm}$ represents the normalised Mode-II fracture toughness of rocks. The unknown parameters in equation (10) are determined using the weights and biases of the ANN-LM 6-8-1 model, as specified in Table VI and mathematically formulated in equation (11).

$$\begin{cases} x_1 = -9.6070.tanhy_1 \\ x_2 = 0.6355.tanhy_2 \\ x_3 = 0.4326.tanhy_3 \\ x_4 = 15.2837.tanhy_4 \\ x_5 = 7.3571.tanhy_5 \\ x_6 = 5.9239.tanhy_6 \\ x_7 = 1.6591.tanhy_7 \\ x_8 = -7.1242.tanhy_8 \end{cases} \quad [11]$$

Furthermore, the unknown parameters in equation (9), denoted as y_1 to y_8, can be calculated using the weights and biases provided in Table VI, as explicitly formulated in equation (12).

$$\begin{cases} y_1 = 0.7286W - 1.5429ID + 1.5009a - 0.9904IP + 0.1793P - 2.2231\sigma_C - 1.9673 \\ y_2 = 0.0965W + 1.0629ID + 1.2954a + 0.7161IP - 0.1488P + 2.37031\sigma_C - 2.5823 \\ y_3 = 0.1995W + 1.6389ID - 0.2522a + 0.0889IP - 0.0331P + 3.2217\sigma_C - 0.8203 \\ y_4 = 0.9016W - 2.1118ID + 2.0609a - 1.0457IP + 0.4350P - 2.3663\sigma_C - 1.9160 \\ y_5 = 4.8994W - 0.4223ID + 1.3269a + 5.5055IP + 12.0730P - 0.1322\sigma_C + 6.9182 \\ y_6 = -1.1466W + 2.9128ID - 3.0038a + 1.0576IP - 0.7133P + 2.7814\sigma_C + 2.0190 \\ y_7 = 1.7402W - 0.3928ID - 1.8470a - 0.0852IP + 0.0517P - 1.9681\sigma_C + 2.9355 \\ y_8 = 6.1462W - 0.5849ID + 1.4526a + 6.2147IP + 8.2168P + 0.2738\sigma_C + 2.8797 \end{cases} \quad [12]$$

The coefficients and constants associated with the predictor parameters in equation (12) are presented in their normalised form, consistent with the normalisation applied during model development. To enhance the practical applicability of the equation for use with experimental measurements, these normalised values must be denormalised. This denormalisation can be achieved using Equation (13), which is specifically designed to transform normalised values within the range of -1 to 1 into their original scale.

$$K_{IIcActual} = K_{IIcnorm} * (K_{IIc\max} - K_{IIc\min}) + K_{IIc\min} \quad [13]$$

Where K_{IIcmax} and K_{IIcmin} represent the maximum and minimum experimental-measured Mode-II fracture toughness values utilised in the development of the models, which are 21.10 ($MNm^{3/2}$) and 2.22 ($MNm^{3/2}$), respectively.

SENSITIVITY ASSESSMENT OF PREDICTOR PARAMETERS AFFECTING K_{IIc}

Sensitivity analysis is a method used to assess how changes in input variables influence a model's output. Several techniques have been proposed for evaluating the impacts of the input parameters on the output. The cosine amplitude method proposed by Jong and Lee. (2004) was used in this study to evaluate the impacts of the six predictor parameters on K_{IIc}. The ranking of predictor parameters by their relative importance, from least to most significant, for predicting K_{IIc} is graphically depicted in Figure 5.

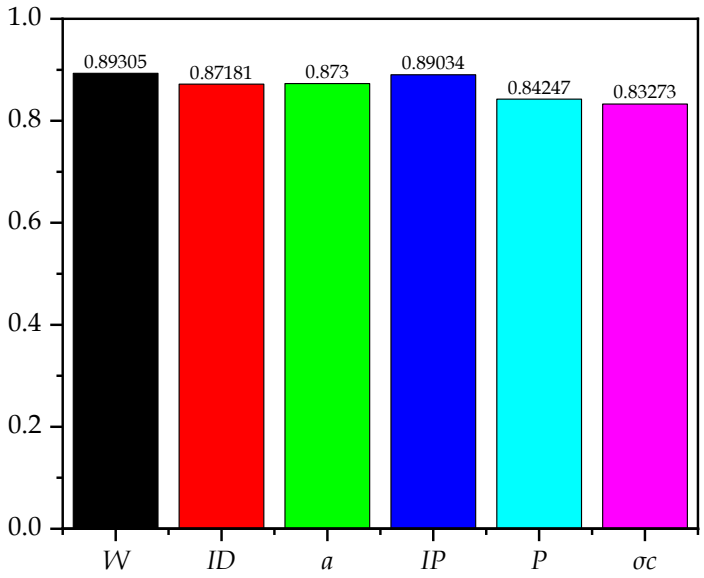


Figure 5. Ranking scores of the predictor parameters on K_{IIc}.

The ranking of predictor parameter significance presented in Figure 5 reveals that all the parameters exert a substantial influence on K_{IIc}. The results indicate that the specimen height (W) has the most pronounced effect on K_{IIc}, followed sequentially by intact rock portion (IP), upper notch depth (a), inner notch diameter (ID), confining pressure (P), and compressive strength (σ_c). The sensitivity analysis confirms that even with limited variance, σ_c and P emerge as consistently influential parameters for the best-performing ANN-LM 6-8-1 model, validating their physical relevance to K_{IIc}.

CONCLUSIONS

The key findings of this study are as follows:

1. The ANN-LM 6-8-1 model exhibited the highest predictive accuracy, achieving an R^2 of 0.9695, RRMSE of 0.1483, RMSE of 0.6956, MAE of 0.4999, MAPE of 9.2180%, and VAF of 96.91%. Based on these performance metrics, the ANN-LM 6-8-1 model is recommended as the most suitable for estimating the K_{IIc} of rocks.

2. The transformed ANN-LM 6-8-1 model, formulated as a user-friendly closed-form equation, is recommended for estimating K_{IIc}, contingent upon the alignment of predictor and predicted parameters, lithological conditions, and the database with those utilised in this study.

3. The outcomes of this study are consistent with and contribute to the objectives of the United Nations Sustainable Development Goals (UN-SDGs), particularly Goals 3, 7, 9, 11, and 15, by advancing sustainable practices and technologies in the field.

REFERENCES

Afrasiabian, B., & Eftekhari, M. (2022). Prediction of mode I fracture toughness of rock using linear multiple regression and gene expression programming. Journal of Rock Mechanics and Geotechnical Engineering, 14(5), 1421-1432.

Backers, T., Stephansson, O., & Rybacki, E. (2002). Rock fracture toughness testing in Mode II—punch-through shear test. International Journal of Rock Mechanics and Mining Sciences, 39(6), 755-769.

Chang, S. H., Lee, C. I., & Jeon, S. (2002). Measurement of rock fracture toughness under modes I and II and mixed-mode conditions by using disc-type specimens. Engineering geology, 66(1-2), 79–97.

Dai, F., & K. Xia. (2013). Laboratory measurements of the rate dependence of the fracture toughness anisotropy of Barre granite. Int. J. Rock Mech. Min. Sci. 60 (Jun): 57–65. https://doi.org/10.1016/j.ijrmms.2012.12.035.

Hua, W., Dong, S., Fan, Y., Pan, X., & Wang, Q. (2017). Investigation on the correlation of mode II fracture toughness of sandstone with tensile strength. Engineering Fracture Mechanics, 184, 249-258.

Jang, J. S. (1993). ANFIS: adaptive-network-based fuzzy inference system. IEEE transactions on systems, man, and cybernetics, 23(3), 665–685.

Jong, Y.H., Lee, C.I. (2004). Influence of geological conditions on the powder factor for tunnel blasting. Int. J. Rock Mech. Min. Sci. 41, 533–538.

Jung, Y., Park, E., & Kim, H. (2016). Determination of mode II toughness of granite by using SCC test. In ISRM EUROCK (pp. ISRM-EUROCK). ISRM.

Ko, T. Y., & Kemeny, J. (2006). Determination of Mode II stress intensity factor using short beam compression test. In 4th Asian Rock Mechanics Symposium, Singapore.

Lawal, A. I., Oniyide, G. O., Kwon, S., Onifade, M., Köken, E., and Ogunsola, N. O. (2021). Prediction of Mechanical Properties of Coal from Nondestructive Properties: A Comparative Application of MARS, ANN, and GA. Natural Resources Research, 1-17.

Ogunsola, N. O., Lawal, A. I., Kim, G., Kim, H., & Cho, S. (2024a). Prediction of Mode-I Fracture Toughness of the ISRM-Suggested Semi-Circular Bend Rock Specimen Using ANN and Optimized ANN Models. Rock Mechanics and Rock Engineering, 1–26.

Ogunsola, N. O., Shin, C., Lawal, A. I., Kim, Y. K., & Cho, S. (2024b). Blasting-Induced Ground Vibration Modeling in Tunnel Excavation: A Comparative Study of ANN, Hybrid ANNs, and Empirical Models. Rock Mechanics and Rock Engineering, 1–27.

Saeidi, O., Torabi, S. R., Ataei, M., & Hoseinie, S. H. (2012). Prediction of rock fracture toughness modes I and II utilising brittleness indexes. International Journal of Mining and Mineral Engineering, 4(2), 163–173.

Tijani, I. A., Lawal, A. I., Ogunsola, N. O., & Kwon, S. (2023). Prediction of ultimate strength of FRP-confined predamaged concrete using backward multiple regression motivated soft computing methods. Scientia Iranica.

Wei M.D, Dai F, Xu N.W, Xu Y, Xia K. (2015). Three-dimensional numerical evaluation of the progressive fracture mechanism of cracked chevron notched semi-circular bend rock specimens. Eng Fract Mech 134:286–303.

Wu, H., Kemeny, J., & Wu, S. (2017). Experimental and numerical investigation of the punch-through shear test for mode II fracture toughness determination in rock. Engineering Fracture Mechanics, 184, 59-74.

Yao, W., Xu, Y., Yu, C., & Xia, K. (2017). A dynamic punch-through shear method for determining dynamic Mode II fracture toughness of rocks. *Engineering Fracture Mechanics*, *176*, 161-177.



Nafiu Olanrewaju Ogunsola

Researcher
University of Johannesburg

Nafiu Olanrewaju Ogunsola is a postdoctoral research fellow at the Sibanye-Stillwater Centre for Sustainable Mining within the Department of Mining Engineering and Mine Surveying, University of Johannesburg, South Africa. Before joining the University of Johannesburg, Nafiu was awarded the Global Korea Scholarship (GKS) by the Korean Government in 2019. He earned his PhD in Mineral Resources and Energy Engineering with a concentration in Rock Mechanics in August 2023 from Jeonbuk National University, Jeonju, South Korea. He also holds a Master of Engineering (M.Eng.) in Mining Engineering (Rock Mechanics) and a Bachelor of Engineering (B.Eng.) in Mining Engineering, completed in 2017 and 2012, respectively, from the Federal University of Technology, Akure (FUTA), Nigeria.

Nafiu is an accomplished mining and rock engineer with a strong passion for studying rock and other geomaterials in situ and through practical application, demonstrated by his extensive industrial and academic experience. He has worked with notable mining and geotechnical companies, including Dangote Mines, China Civil Engineering Construction Corporation (CCECC), and Uniglobe Construction Engineering Limited, all in Nigeria. His recent research activities primarily focus on experimental and computational intelligence methods to deeply understand and predict the multiscale deformation and fracture behaviors of rocks and other geomaterials, addressing challenges in mineral extraction, infrastructure development, sustainability, geohazard mitigation, and energy.

Nafiu's current research focuses on advancing sustainable mining practices and geomechanics, implementing smart mining and monitoring operations through artificial intelligence and machine learning, promoting sustainable and rapid access to orebodies in both surface and underground mines, and applying multi-criteria decision-making (MCDM) methods to address challenges in mining and geomechanics. Contributing to academia and advancing knowledge in his field, Nafiu has published several articles in reputable journals and has been a reviewer for various others.

Comparison of machine learning classification for rockburst prediction: A case study of South African gold and platinum mines

N.P. Khumalo and R.T. Masethe

University of KwaZulu-Natal, South Africa

Rockbursts are one of the most challenging hazards in underground mining, known for their sudden and violent nature, posing significant risks to worker safety, operational continuity, and mining productivity. Accurate prediction of rockbursts is critical for geotechnical risk management, particularly in seismically active gold and platinum mines in South Africa. This study investigates the application of supervised machine learning (ML) algorithms for rockburst prediction, comparing their performance in gold and platinum mines. Models such as support vector machines, random forest, gradient boosting, and ensemble bagged trees were implemented and analysed using similar input parameters, including but not limited to mining-induced seismicity, peak particle velocity, hanging wall, footwall, and geological features. Results demonstrated that the models' classification accuracies and overall performances varied significantly, probably depending on the mining environment. In gold mines, the ensemble bagged trees model achieved the highest accuracy, while in platinum mines, the same ML model type outperformed others, with 84.2% and 95.5% accuracy, respectively. Despite using similar input datasets, these variations highlight the influence of localised geological and operational conditions on model performance. This finding underscores the importance of tailoring ML approaches to the specific characteristics of the mining area under study. The research concludes that while ML algorithms show great potential for rockburst prediction, their effectiveness depends on the mining context. This study emphasises the need for site-specific model development and validation to enhance prediction accuracy, ensuring improved safety and operational efficiency in underground mining.

Keywords: machine learning, ML, rockburst, platinum, gold, geotechnical risk

INTRODUCTION

Rockbursts are among the most dangerous and unpredictable hazards in underground mining, causing sudden and violent failures that threaten worker safety, disrupt operations, and reduce productivity. Their occurrence is primarily influenced by mining-induced seismicity, high-stress conditions, and geological factors, making accurate prediction highly desirable for risk management in a seismically active mine. A recent workshop conducted by the International Society of Rock Mechanics (ISRM) provided a refined definition of a rockburst, characterising it as "a sudden failure of the rock mass surrounding excavations, resulting from the rapid release of stored strain energy when induced stresses exceed the inherent rock strength." (ISRM, 2024). This definition emphasises the dynamic nature of rockbursts as stress-driven instability events within underground mining environments. From a practical and observational standpoint, rockbursts are often associated with seismic events reaching local magnitudes M_L of up to 2.0, accompanied by the violent ejection of rock from excavation surfaces. These events typically occur within the expected range of energy dissipation around excavations (i.e., stopes and tunnels) during active mining operations and are frequently induced by blasting activities (Ferreira *et al*., 2025).

The immediate occurrence of rockbursts following blasting highlights the role of stress redistribution and energy release in triggering these hazardous events, further underscoring the necessity for advanced monitoring and predictive modelling to mitigate associated risks.

In South Africa, deep-level gold and platinum mines experience frequent rockbursts due to the increasing depths, intense stress, irregular pillars, abutments, and complex geological regimes (Masethe *et al.,* 2023). Traditional prediction or forecasting methods often fall short of capturing the complexity of these seismic events (e.g., short-term seismic hazard assessment). This is currently used in the industry with a success rate not much better than random, necessitating the adoption of advanced technologies. The assessment is rooted in the stability analysis methods that have been an integral part of the deep mine culture in South Africa for over 30 years. Despite decades of research and implementation, the approach has not yet yielded reliable predictive results. The core objective of this method is to detect temporal precursory patterns that might indicate changing rockmass conditions, aiming to support proactive safety interventions. True predictive accuracy remains elusive using this system in isolation. Accurate event location (with a plan error under 30 metres) is essential to the viability of this approach, yet even with advanced monitoring systems and daily workplace ratings, the ability to predict large seismic events or rockbursts remains beyond reach. Seismologists and rock engineers alike acknowledge that short-term seismic hazard assessment provides, at best, early warning signals or behavioural trends rather than concrete predictions. These systems can support awareness and comparison against historical seismic responses, but their predictive efficiency is limited and must be quantified. Despite significant investment and technological advancements, the industry still lacks a standardised and comprehensive seismic risk management plan to guide best practices and consistently analyse seismic data across operations.

Artificial intelligence (AI) has gained widespread acceptance across various industries, including e-commerce, media, and finance, due to its ability to process vast amounts of data and improve decision-making (Bhat *et al.,* 2023). However, its integration into geotechnical engineering and rockburst prediction has been relatively slow despite its potential to revolutionise risk management in the mining industry. A subset of AI, machine learning (ML) specialises in learning patterns from data using mathematical functions and rule-based systems to deliver high-precision classification and prediction outputs (Adoko *et al.,* 2013). ML has emerged as a powerful tool in rockburst forecasting, leveraging seismic data and geotechnical parameters to enhance accuracy (Masethe *et al.,* 2024).

This paper explores the application of supervised ML models (e.g., support vector machines, random forest, gradient boosting, ensemble bagged trees, etc.) in comparing mining-induced classification for rockburst predictions in the gold and platinum mines of South Africa. The most successful models will be compared to ascertain whether the mining environment influences their performance. These variations will highlight the critical role of site-specific geological and operational conditions in model effectiveness. This paper underscores the importance of tailoring ML models to specific mining contexts to improve mining-induced classification prediction accuracy. These predictive models need to be dynamic, regularly adjusted, and refined to maintain their reliability and effectiveness. By doing so, they can meaningfully contribute to safer and more efficient underground mining operations. This approach aligns with the vision of the Mine Health and Safety Council, encapsulated in its slogan: "*Every mine worker returning from work unharmed every day, striving for zero harm in our lifetime" (MHSA, 2025*). It is important to recognise that no generic machine learning model can universally apply to all mining environments; instead, models must be tailored to the specific geological and operational conditions of each mine.

Over the past few decades, extensive research has focused on reducing the risks associated with rockbursts, aiming to enhance safety and stability in underground mining operations (Durrheim, 2010; Dong *et al*., 2013; Kaiser & Cai, 2012; Ferreira *et al*., 2023; Masethe *et al*., 2023; Masethe *et al*., 2025). Various engineering strategies and burst-resistant rock support systems have been developed to eliminate, mitigate, or control rockburst hazards, ensuring the protection of personnel, infrastructure, and rock mass stability in ore-extraction areas. In addition to structural reinforcements, advanced monitoring techniques can play a crucial role in rockburst prediction and risk assessment. Seismic monitoring, acoustic emission analysis, and remote sensing technologies are among the key approaches used to

detect, analyse, and forecast rockburst-prone zones. By integrating these proactive measures, mining operations can better anticipate and manage the occurrence of rockbursts, minimising their impact on productivity and worker safety (Masethe *et al.,* 2023).

To address these challenges, ML algorithms have been used recently to supplement existing prediction methods in rockburst hazard prediction tasks (Duan *et al*., 2021; Díaz *et al*., 2022; Anikiev *et al*., 2023). Recent studies suggest that AI-based methods can play a key role in real-time monitoring to help in decision-making during excavation and in promoting a deeper understanding of induced seismicity through appropriate processing of micro seismicity data (Anikiev *et al*., 2023).

BUSHVELD AND WITWATERSRAND BASINS - GEOLOGY AND GEOTECHNICAL SETTING

The Bushveld Complex is the world's largest igneous intrusion, hosting vast deposits of chromium, platinum group elements (PGEs), platinum group metals (PGMs), and vanadium (Viljoen, 2016). This complex underwent multiple intrusive events, with the Rustenburg Layered Suite (RLS) being one of the most significant. Due to crystal fractionation and mineral settling, the RLS is divided into four distinct zones: lower, critical, main, and upper. The Merensky Reef, a PGE-enriched layer, is located within the critical zone of the RLS in both the eastern and western limbs of the Bushveld Complex. This reef is characterised by a chromitite stringer and consists primarily of pegmatoidal feldspathic pyroxenite, with norite, anorthosite, and pyroxenite forming its footwall and hanging wall (Viljoen, 2016; Masethe & Durapraj, 2023). The deep platinum mining in the Bushveld Complex occurs at depths ranging from 1000 to 1400 metres below the surface (Masethe *et al*., 2024).

In contrast, the Witwatersrand Basin hosts some of the world's deepest gold mines. Geologically, the Witwatersrand group is divided into two major units: the lower West Rand group, consisting of quartzite and shale, and the upper Central Rand group, composed of quartzite interbedded with gold-bearing conglomerates (Masethe *et al*., 2023a). The Ventersdorp Supergroup comprises erosional products from the Witwatersrand Supergroup and hosts the extensive gold-bearing quartz pebble conglomerate known as the Ventersdorp Contact Reef (VCR) (Masethe *et al*., 2023a). The VCR is overlain by basalt and is structurally influenced by faults and dykes. Mining of these very deep gold deposits occurs at depths between 1500 and 3900 metres, making them among the world's deepest and most geotechnically challenging operations (Masethe *et al*., 2023a).

SHORT HAZARD ASSESSMENT IN THE SOUTH AFRICAN MINING INDUSTRY

Since the early 1990s, assessing rockburst likelihood has been integral to seismic risk management in the South African mining industry. Short-term seismic hazard assessments (SHA) are routinely conducted to evaluate seismic hazards, as mandated by the Department of Mineral Resources and Energy. This requirement aims to enhance underground safety and minimise the risks associated with mining-induced seismicity. Research efforts have predominantly focused on analysing the temporal variations of key seismic parameters used in SHA, leading to advancements in predictive methodologies (van Aswegen, 2005; Mendecki, 1997; Rebuli & van Aswegen, 2013).

The SHA framework assesses five key seismic parameters within a defined dynamic active working polygon based on neighbouring and strong ground motion, which can be determined automatically or through static analysis. These parameters include the Schmidt number, energy index, seismic activity/clustering index, apparent volume, frequency, and the likelihood of large events, which contribute to quantifying seismic hazard levels ranging from low (0-5) to medium (6-7) and high (8-10) (Figure 1). Additionally, the time interval between significant seismic events (typically, $M_L > 1.0$) is incorporated as a critical metric, acknowledging the periodic nature of seismic activity in deep mining operations. The assessment follows a 24-hour maturity cycle, with seismic hazard ratings being reassessed daily. If the hazard rating increases while miners are underground, immediate evacuation procedures are initiated until a new evaluation is conducted, based on updated seismic data. This structured approach strengthens the industry's ability to anticipate and respond to seismic risks, thereby reducing the potential for rockburst-related incidents. The method could be improved or replaced, as

its success rate is no better than random guessing (within the constraints of the average recurrence time of rockbursts), and the traditional approach is reactive rather than proactive. The rating only increases after the large event has occurred.

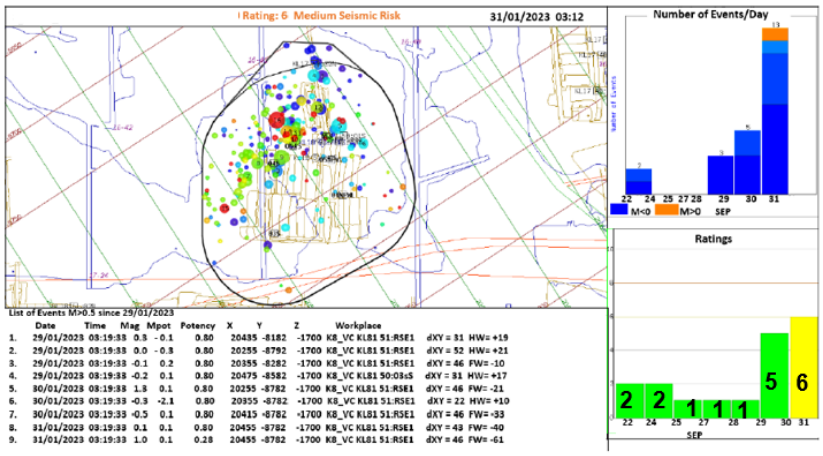


Figure 1. Seismic hazard assessment rating.

The seismic data analysis necessitates a sequence of critical decisions to define spatial and temporal boundaries, to select which seismic and non-seismic parameters to investigate, and to discern hazard-level fluctuations. These procedures must be rigorously evaluated to ensure the most effective SHA methods are applied.

The overall success of the system was evaluated by analysing four key outcomes, as defined in the standard confusion matrix: true positives (TP) instances where a warning was issued and a large seismic event occurred; false positives (FP) cases where a warning was issued but no major event followed; false negatives (FN) situations where no warning was issued, yet a large event occurred; and true negatives (TN) scenarios where no warning was given and no significant seismic activity occurred. These outcomes are summarised in Table I**.**

Table I. Success and failure of the implemented system

	WARNING	NO WARNING
EVENT [M≥1]	0.10 (TP)	0.22 (FN)
NO EVENT [M≥1]	0.38 (FP)	0.30 (TN)
SUM	0.48	0.52

This measure, known as the *threat score* or *critical success index (CSI)*, evaluates the model's ability to correctly identify true positives—the closer the value is to 1, the better the performance. A 'success' in this context includes both accurate warnings and accurate no-warnings. The model's overall accuracy is calculated as the total number of successes divided by the total number of events assessed. For example, with a success rate of (0.10 + 0.30)/ (0.48 + 0.52) = 40.0%, the model correctly classifies only 40% of cases, misclassifying the remaining 60%. Though a true negative is a success, we are concerned with the true positive (where a warning was issued and a large seismic event occurred)

The total success rate was 14.3%. This is expressed using standard classification terminology: true positives (TP), false positives (FP), true negatives (TN), and false negatives (FN). Accordingly, the success rate or threat score/CSI is defined as a ratio of successes to successes and failures using the Equation [1] below

$$Total\ success\ rate = \frac{TP}{TP+FP+FN} \quad [1]$$

representing the proportion of correctly predicted events among all actual and predicted positive cases, excluding true negatives. The efficiency of any operational and implemented system must be both reliable and validated with a high degree of spatial accuracy. In this context:

- Efficiency refers to how effectively the system performs its intended tasks, such as detecting or forecasting seismic activity.
- Reliability implies that the system consistently delivers accurate and dependable results over time.
- Validation requires that the system's performance be tested and confirmed, typically by comparing its outputs against real-world observations or measured data.
- Spatial accuracy ensures that the system can precisely identify the location of seismic events, which is critical for effective hazard assessment and response planning.

SEISMIC DATA ACQUISITION

The seismic event data for this study were recorded using a mine-wide seismic network deployed at both mines. This network encompassed active and operational excavations of interest, ensuring comprehensive seismic monitoring. The system consisted of 4.5 Hz triaxial geophones with a sampling rate of 6 kHz, strategically installed at various locations surrounding the orebody. To enhance the accuracy of hypocentre locations, certain geophones were positioned at sites further from the reef planes, taking advantage of the mine's shaft and development infrastructure.

The recorded seismograms were utilised to identify P- and S-wave arrival times and to compute key seismic source parameters, including origin time, event location, seismic energy, moment, magnitude, and stress drop. Geophone placement was carefully selected to maximise sensitivity and ensure high-precision event location, achieving accuracies within a few metres in the designated areas of interest. However, the minimum detectable event magnitude was influenced by the maintenance status of underground geophone sites, affecting the overall reliability of seismic event recordings.

SEISMICITY DATA CLASSIFICATION APPROACH

In this section, the implementation of several basic M_L algorithms for the classification models of mining-induced seismicity in the mines is presented. The study by Masethe *et al.*, (2023a, 2024) indicates that seismic events with a magnitude greater than 1 (M ≥ 1) are often associated with damage in both gold and platinum mines. Even when these events did not cause visible damage, they frequently triggered precautionary shutdowns of the affected working stopes. As a result, the selection of seismic events for analysis focused on those within the area of interest (M≥1) that are well located and whether they resulted in damage or not.

The used input parameters

Platinum mine study
The study on the platinum mine focused on analysing seismic event parameters and mining-related factors to assess rockburst occurrences. The selected independent variables included elapsed time between events (P1), event magnitude (P2), event location coordinates X (P3), Y (P4), Z (P5), distance from the working face (P6), peak particle velocity (PPV) P7, working wall type hanging wall or footwall P8. The presence or absence of rockbursts served as the dependent variable (simple binary outcome). A dataset of 154 seismic events was compiled and processed, though it represented a very small sample. Predictor importance analysis identified event location, the elapsed time between recorded events, and the footwall location as the most influential parameters for predicting rockbursts in this mining environment.

Gold mine study
Similarly, the gold mine study applied seismic and mining-related parameters to evaluate rockburst occurrences. The independent variables included event magnitude (P1), event location coordinates X (P2), Y (P3), and Z (P4)—distance from the working face (P5), peak particle velocity (PPV, P6), time between seismic events (P7), and working wall type (hanging wall or footwall, P8). Rockburst occurrence was again the dependent variable. A total of 314 seismic events were recorded and analysed for this study.

For both gold and platinum studies, the PPV was estimated using the following Equation [2] (Kaiser *et al.*, 1996):

$$PPV = 1.4\frac{10^{\frac{M_r}{2}}}{r} \qquad [2]$$

where M_r represents the seismic event magnitude, and r is the distance between the hypocentre and the experienced damage.

Standard parameters and key differences
Both studies utilised a set of standard seismic parameters, including event magnitude, event location (X, Y, Z), distance from the working face, PPV, working wall type, and whether there was damage or not. However, key differences were observed in the selection of additional parameters. The platinum mine study incorporated elapsed time (P1) and specific working wall location (P8), whereas the gold mine study included the time between seismic events (P7). The predictor importance analysis in the platinum mine emphasised the significance of event location, elapsed time, and footwall location. In contrast, no such importance ranking was found in the gold mine study.

MODELLING APPROACH

A series of ML algorithms were deployed to predict rockburst occurrences in both gold and platinum mines. The aim is to compare the models listed below to identify the one with the highest predictive performance, particularly in forecasting rockbursts. The objective is to evaluate each model's capability not only in terms of accuracy but also in its adaptability across different mining environments. Once the most effective model is identified, it can be explored further to determine whether it reliably captures environmental controls that influence seismic activity. This evaluation will also assess the model's generalisability across commodities, specifically whether it can be applied effectively in both gold and platinum mining contexts. According to Masethe *et al.*, (2024), model adaptability and contextual sensitivity are critical for seismic hazard forecasting in diverse underground conditions. The selected models included logistic regression (LR), support vector machine (SVM), ensemble boosted trees (ENS boosted trees), ensemble bagged trees (ENS bagged trees), ensemble K-nearest neighbour (ENS KNN), and artificial neural network (ANN). The theoretical background of these methods is well-documented in the literature. Model training and evaluation were conducted using MATLAB's Machine Learning apps, which provided an efficient framework for analysing seismic and mining-related data. To prevent overfitting and improve generalisation, the fivefold cross-validation technique was applied, as recommended in previous studies. For both gold and platinum mine datasets, normalisation was performed by rescaling values to the range [0,1], ensuring consistency and enhancing model performance. The model classification target was defined as a binary outcome, where seismic events associated with rockburst damage were labelled as 1 (Yes) and those without damage as 0 (No). Another categorical parameter was considered in the platinum mine study: wall type (hanging wall or footwall). A numerical encoding was assigned, where 1 represented the hanging wall and 0 represented the footwall. The processed seismic event data samples used in the modelling were compiled into Table II for the gold mine study and Table III for the platinum mine study. These datasets included event magnitudes, locations, elapsed time, peak particle velocity, distance from the working face, and other relevant mining parameters, forming the input features for ML classifications.

Table II. Sample data with normalised values (gold mine)

P1	P2	P3	P4	P5	P6	P7	P8	Damage (Yes/No)
0.52	0.84	0.52	0.22	0.09	0.05	0.25	0	0
0.05	0.51	0.21	0.17	0.11	0	0.25	0	0
0.48	0.49	0.58	0.58	0.08	0.06	0.26	1	0
0.19	0.48	0.56	0.54	0.07	0.04	0.26	1	0
0.1	0.57	0.19	0.21	0.09	0.02	0.27	0	0
0.67	0.84	0.57	0.32	0.01	0.12	0.32	1	1
0.33	0.45	0.45	0.43	0.05	0.09	0.32	1	1
0.05	0.88	0.56	0.31	0.1	0.01	0.32	1	1
0.38	0.5	0.49	0.46	0.07	0.1	0.32	0	1
0.14	0.49	0.49	0.5	0.06	0.02	0.32	1	1
0.62	0.19	0.04	0.41	0.2	0.03	0.34	1	1

Table III. Sample data with normalised values (platinum mine)

P1	P2	P3	P4	P5	P6	P7	P8	Damage (Yes/No)
0.26	0.76	0.35	0.67	0.29	0.05	0.16	0	1
0.01	0.19	0.71	0.10	0.31	0.08	0.18	1	1
0.16	0.05	0.49	0.17	0.33	0.03	0.02	1	1
0.46	0.24	0.35	0.67	0.26	0.04	0.20	0	1
0.77	0.38	0.82	0.35	0.15	0.02	0.46	0	1
0.72	0.05	0.29	0.73	0.31	0.49	0.12	1	0
0.33	0.00	0.23	0.63	0.27	0.12	0.12	0	0
0.80	0.14	0.63	0.83	0.44	0.06	0.12	1	0
0.40	0.00	0.31	0.66	0.31	0.13	0.12	0	0
0.35	0.57	0.32	0.67	0.31	0.10	0.12	0	0
0.82	0.14	0.28	0.71	0.31	0.34	0.12	1	0

RESULTS AND THE DISCUSSION

The performance of various ML approaches in predicting rockburst occurrences was assessed using confusion matrices, receiver operating characteristics (ROC) curves, and area under the curve (AUC) values. The classification accuracies varied across models, with some demonstrating higher predictive power than others. For the best-performing model, the false positive is about 25.2% in gold and 25% in platinum. The results are summarised in Table IV, Figure 3, 5(a), and 6 below.

Table IV. The performance of machine learning models

Mine Type	Model	Accuracy (No Rockburst Case	Accuracy (Rockburst Case)	False Prediction Rate
Gold	ENS bagged trees	84.2%	74.8%	25.2%
Platinum	ENS bagged trees	95.5%	75.0%	25.0%

Additional evaluation metrics, including AUC and ROC curves (Figure 2), were used to assess the models' ability to distinguish between rockburst and non-rockburst events. The **higher the AUC value, the better the model performed** in identifying rockburst events accurately (Figure 2(a) and (b)). AUC has a maximum value of 1; therefore the closer to 1, the better the model.

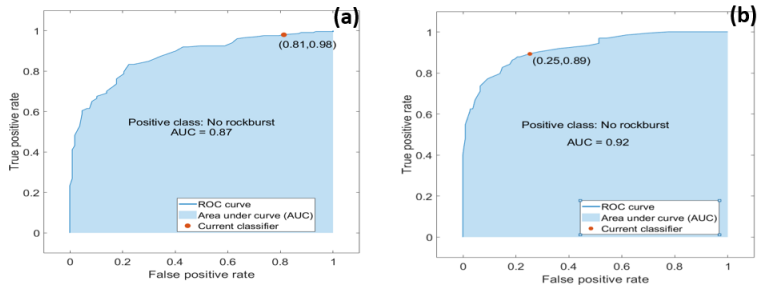


Figure 2. (a) ROC corresponding to the KNN (lower performance) and (b) ensemble trees model (highest performance) – gold mine.

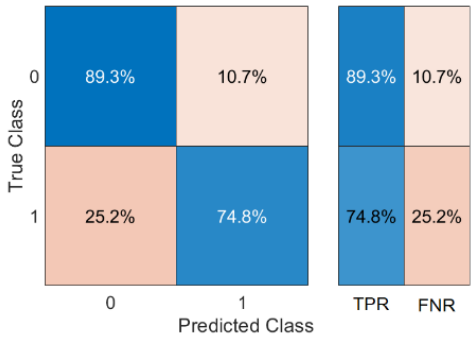


Figure 3. The confusion matrix corresponding to the ensemble trees model (highest performance) – gold mine.

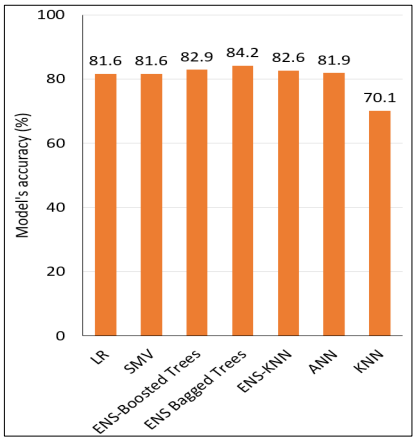


Figure 4. Summary of models' performances – gold mine.

The classification results from the modelling process are presented in the confusion matrices shown in Figure 5(a) for the platinum mine. The accuracy of classification varied depending on the model used. For instance, the ensemble trees model correctly identified 98,5% of events that did not result in rockbursts, while only 75% of rockburst-related events were accurately classified. This corresponds to a false prediction rate of 25%.

Additional performance metrics, including AUC and ROC curves, are shown in Figures 5(a) and (b). The ROC curve represents a probability curve, while the AUC value quantifies the model's ability to differentiate between classes. A higher AUC (closer to 1) indicates a better capability to distinguish between rockburst and non-rockburst events. The AUC values align with the confusion matrices and ROC curves, reinforcing the model's performance evaluation. The overall results are summarised in Figure 5(b).

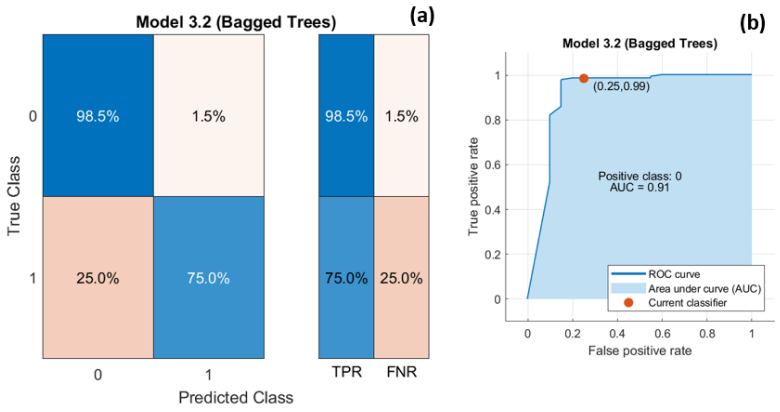


Figure 5(a). Confusion matrix corresponding to the ensemble trees model (higher performance) (b) ROC corresponding to the ensemble trees model (highest performance)- platinum mine.

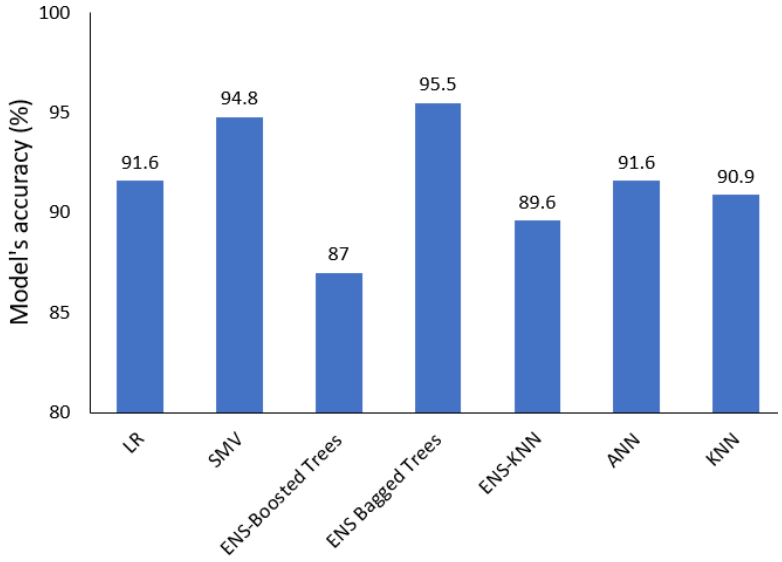


Figure 6. Summary of models' performances - platinum mine.

In summary

- In the **gold mine study**, the **ENS bagged trees** model demonstrated a good balance between predicting rockburst and non-rockburst events, with 84.2% **accuracy for no-rockburst cases** and **74.8% for rockburst cases.**

- In the **platinum mine study**, the **ENS bagged trees model** achieved a high accuracy (**98.5%**) for predicting non-rockburst cases but struggled with rockburst classification, with only **75% accuracy** and a **false prediction rate of 25.0%.**

- The ROC and AUC analyses confirmed the alignment of the models' performances with the confusion matrices. The gold mine model performed more consistently in distinguishing between rockburst and non-rockburst events, while the platinum mine model exhibited a significant imbalance in classification.

T**he ENS bagged trees model in the platinum mines study proved it is the most reliable for rockburst prediction**. In contrast, the same model in the gold mine study was less effective in identifying rockburst cases accurately.

DISCUSSION

The findings from both the gold and platinum mines indicate that event magnitude and distance between the event location and the working face were not among the most significant parameters in the seismic classification models. This observation appears to contradict the conventional understanding of rockburst phenomena, suggesting that these parameters had low weight (sensitivity) in the models, likely due to the nature of the dataset utilised.

The model accuracies varied between the two mine types:

- Platinum mine: Accuracy ranged from 87% to 95.5%, with the best-performing model showing a false positive rate of approximately 25%.

- Gold mine: Accuracy ranged from 70.1% to 84.2%, with a similar false positive rate of around 25% for the best-performing model.

These accuracy levels are consistent with findings in existing literature. However, a key limitation of the current study is that different rockburst features were not analysed separately. Instead, all rockburst occurrences were grouped into a binary classification, disregarding the underlying mechanisms.

For improved classification accuracy and predictive robustness, future studies should consider incorporating additional non-seismic data (e.g., closure loggers), numerical models, other geotechnical data sources, and implementing a multi-class classification approach that distinguishes between different rockburst types. Additionally, established seismicity laws, such as Omori's law (which describes aftershock decay) and other seismicity decay laws, could enhance model reliability and improve the prediction of rockburst events in deep mining environments.

WHAT IS NEXT?

The process of developing a ML model for seismic event classification begins with data collection and preprocessing, where seismic event records are gathered, ensuring key features such as event location, magnitude, time elapsed, and PPV are included. Missing values are handled, duplicates are removed, and numerical features are normalised within a [0,1] range for better model performance. If class imbalance is present, a corrective procedure such as the synthetic minority oversampling technique (SMOTE) can be applied. Next, the data are split into training, validation, and test sets, with 80% allocated for training, 10% for validation to finetune hyperparameters, and 10% for testing to evaluate final model performance (Figure 7). Random shuffling ensures an unbiased split.

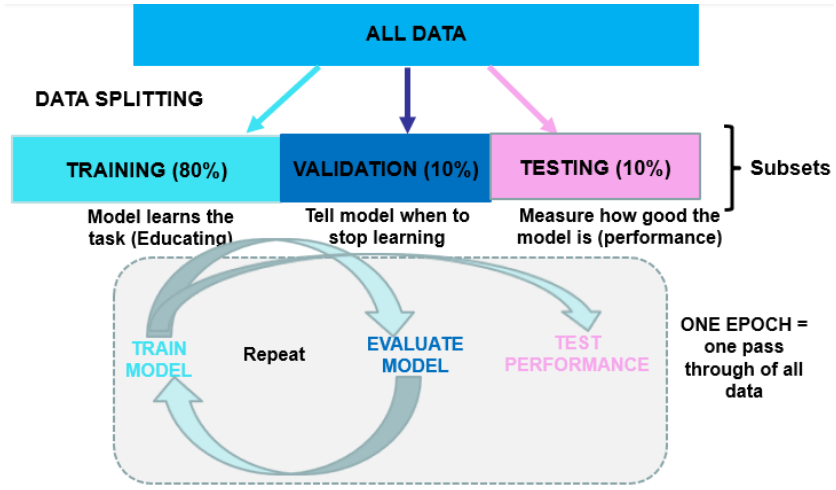


Figure 7. Train, evaluate, and test the model performance (Masethe, 2025).

The subsequent phase of this project is a trained (fitted) model that is generalised well to new and unknown data.

Comparing training, validation, and test accuracy curves allows making informed decisions about adjusting model parameters, applying regularisation techniques, or modifying data to improve the model's performance in real-world scenarios (Figure 8). Model training involves selecting and initialising ML algorithms such as ENS bagged trees, SVM, or ANN, and optimising parameters to classify seismic events effectively. Model validation and hyperparameter tuning are then performed using metrics like accuracy, precision, recall, F1-score, and AUC-ROC. Adjustments to hyperparameters, such as learning rate, number of trees, or kernel functions, improve generalisation. After validation, the model is tested on unseen data, where its predictions are compared against actual labels to measure accuracy and reliability. Finally, deployment and real-time **application** allow the trained model to analyse new seismic data for rockburst prediction. Continuous monitoring and updates ensure that the model remains accurate as more data becomes available.

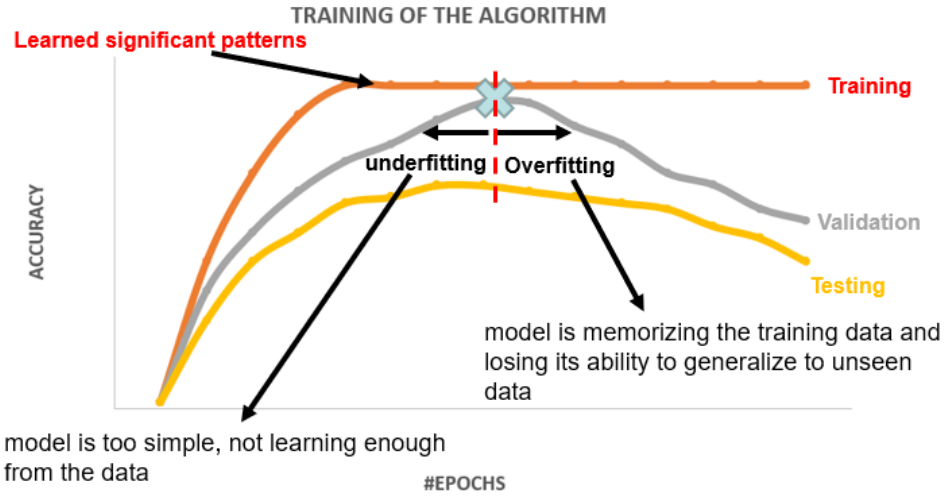


Figure 8. Training of the algorithm (Masethe, 2025).

CONCLUSIONS

This paper applied multiple ML classification algorithms to evaluate their effectiveness in predicting seismicity and rockburst occurrences in deep mining environments. A total of 314 seismic event instances from the gold mine, and 154 seismic event instances from the platinum mine, were analysed. Across both datasets, the most influential parameters identified were event locations, time elapsed between events, and PPV.

ENS bagged trees consistently demonstrated the highest classification accuracy among the tested ML models, making it a promising approach for developing real-time rockburst prediction tools in seismically active mines. Conversely, KNN performed the poorest in the gold mine study, while ENS boosted trees had the lowest accuracy in the platinum mine study. These results suggest that ensemble-based learning techniques, particularly bagged trees, provide greater robustness and predictive performance in differentiating between seismic events associated with rockbursts and those that are not. Applying ML to seismic event classification improves predictive accuracy and enhances decision-making in rockburst risk mitigation. However, a key limitation observed in this study was data imbalance, where models demonstrated higher accuracy in recognising no-damage seismic events compared to correctly identifying rockburst occurrences. This highlights the need for advanced techniques such as data augmentation, synthetic resampling (e.g., SMOTE), and cost-sensitive learning to improve the model's ability to detect rockburst-related seismic events.

Furthermore, the study suggests that expert systems, combined with ML, could enhance predictive capabilities by integrating domain knowledge with data-driven models. Additionally, area-based models demonstrated a potential in identifying regions at greater rockburst risk within the mines, providing a spatial understanding of seismic hazards.

FUTURE WORK AND RECOMMENDATIONS

To refine the predictive power of these models, future research should focus on multi-class classification to distinguish between different types of rockbursts rather than treating them as a binary problem. Incorporating advanced seismicity laws, such as Omori's law and other aftershock decay models, could improve model reliability. Further training of ML models on larger datasets and adaptive learning approaches will enhance the system's ability to recognise patterns towards proactively mitigating rockburst risks in underground mining operations.

ACKNOWLEDGEMENTS

The authors express their sincere gratitude to Mines and to the financial support provided by the University Capacity Development Programme (UCDP) through the University of KwaZulu-Natal, which made this research possible. Special thanks are extended to Dr. Richard Masethe for his invaluable guidance, support, and encouragement throughout the research and writing process. His expertise and continuous motivation were instrumental in shaping the direction and quality of this paper. We are also grateful for the constructive comments from two anonymous reviewers that improved the quality of the manuscript.

REFERENCES

Adoko, A. C., C. Gokceoglu, L. Wu and Q. J. Zuo. (2013). Knowledge-Based and Data-Driven Fuzzy Modelling for Rockburst Prediction. *International Journal of Rock Mechanics and Mining Sciences*. 61: 86–95.

Anikiev, D., C. Birnie, U., b. Waheed, T. Alkhalifah, C. Gu, D. J. Verschuur and L. Eisner. (2023). Machine Learning in Microseismic Monitoring. *Earth-Science Reviews*. 239: 104371.

Díaz, J. P., E. Sáez, M. Monsalve, G. Candia, F. Aron and González, G. (2022). Machine Learning techniques for estimating seismic site amplification in the Santiago basin, Chile. *Engineering Geology*. 306: 106764.

Dong, L. J., Li, X. B., & Kang, P. E. N. G. (2013). Prediction of rockburst classification using Random Forest. *Transactions of Nonferrous Metals Society of China*, *23*(2), 472-477.

Duan, Y., Y. Shen, I. Canbulat, X. Luo, and Si, G. (2021). Classification of clustered microseismic events in a coal mine using Machine Learning. *Journal of Rock Mechanics and Geotechnical Engineering*. 13(6): pp. 1256–1273.

Durrheim, R. J. (2010). Mitigating the risk of rockbursts in the deep hard rock mines of South Africa: 100 years of research. *Extracting the science: A century of mining research*, 156–171.

Ferreira, R.I.L., Lenegan, P., Masethe, R. (2025). Automatic data selection, worker exclusion zones, and an attempt to identify precursory activity in real-time: Routine and research activities in seismology at Sibanye-Stillwater Ltd. *Journal of the Southern African Institute of Mining and Metallurgy*, vol. 125, no. 1,

ISRM (2024). *International Society of Rock Mechanics Commission on Rockbursts*, https://isrm.net/newsletter/show/248#:~:text=From%20February%201st%20to%204th,by%20Professor%20Manchao%20He%2C%20t

Kaiser, P. K. and M. Cai. (2012). Design of rock support system under rockburst conditions. *Journal of Rock Mechanics and Geotechnical Engineering*. 4(3): pp. 215–227.

Masethe, R. (2025). Machine Learning in Rock Engineering Designs, Discipline of Geological Science, University of KwaZulu-Natal.

Masethe, R.T., and Duparaj, S. (2023a). Rockbursts characterization in the Merensky reef: A case study in Siphumelele Platinum mine, South Africa; American Rock Mechanics Association. In proceeding 57th U.S rock mechanics symposium. ARMA 23-100

Masethe, R., Manzi, S.D.M., Durrheim, J.R. (2023). Using legacy 3D seismic data and source parameters of mining-induced earthquakes to mitigate the risk of rockbursting in Kloof gold mine, South Africa; *Geophysical Prospecting*: 71(7): pp.1281-1311

Masethe R.T. Durapraj S., A.C. Adoko (2024). Mining–induced classification for rockburst prediction. *A case study in Siphumelele Platinum mine, South Africa. South Africa national institute of rock engineering*

Rebuli, D. B., & Van Aswegen, G. (2013, September). Short-term Seismic hazard assessment in SA Gold Mines. In *8th International Symposium of Rockburst and Seismicity in Mines (RaSIM 8)* (pp. 323-331).

Vilijoen, M. (2016), The Bushveld Complex; *Hosts to the world's largest Platinum, Chromium and Vanadium resources*; vol .39, no.2. pp.240-268

Towards ensuring sustainable mining: Application of a pareto-optimised hierarchical structural interaction matrix for prioritising slope stability influencing factors

N.O. Ogunsola[1,2], O. Makinde[1], H. Grobler[1]

[1]University of Johannesburg, South Africa
[2]Sibanye-Stillwater Centre for Sustainable Mining, South Africa

Slope stability is a critical factor in ensuring mining and civil engineering operations' safety, efficiency, and sustainability. Characterising rock slope stability and identifying and prioritising its influencing factors is fundamental to achieving sustainable mining operations, proactive risk management, and mining resource optimisation. This study aims to systematically evaluate and prioritise the factors influencing slope stability in mines using a Pareto-optimised hierarchical structural interaction matrix (P-HSIM), whose prioritisation computation is based on the theory of subordination derived through systems thinking. To achieve this aim, the various factors influencing slope stability were identified and collated from the literature. A binary interaction matrix (BIM) that assesses the relative importance and interdependencies among geotechnical, geological, environmental, and other factors was developed. The outcome of the BIM simulation was evaluated numerically using relevant mathematical equations to calculate the intensity rating score of every slope stability influencing factor. A Pareto optimisation technique was then applied to enhance the prioritisation process to ensure that the most significant slope stability influencing factors are appropriately emphasised. The study highlights the versatility of the P-HSIM framework in addressing complex geotechnical challenges and its potential to support sustainable mining practices by reducing geohazards, minimising environmental impact, and enhancing resource efficiency. The findings offer a novel decision-making tool for mining engineers and sustainability practitioners, contributing to developing safer and more environmentally conscious mining operations.

Keywords: Slope stability; Binary interaction matrix; Hierarchical tree structure diagram; Pareto optimisation, Sustainable mining

INTRODUCTION

The demand for minerals and metals, including energy minerals, has continued to increase worldwide due to the surge in human population growth, the need for sustainable energy sources, and technological advancements. Mining is one of the major contributors to global economic development, supporting various sectors, including energy, transportation, communication, etc. However, conventional mining methods such as drilling & blasting, strip mining, hydraulic mining, room & pillar mining, placer mining, etc., are often associated with sustainability and environmental challenges, including environmental degradation, resource depletion, and adverse social impacts (Littleboy *et al*., 2019). Thus, efforts have been made by mining stakeholders and companies at all levels to leverage sustainable mining practices in their operations to ensure efficient resource extraction and enhance a safe environment. Sustainable mining entails reducing the environmental footprints of mining to the minimum by incorporating cutting-edge technologies, efficient resource utilisation, and proactive community engagement.

The stability of rock slopes involves the design of excavated slopes that are safe, economically viable, and functionally optimal, with the goal of achieving equilibrium conditions akin to those of natural slopes (Naghadehi *et al*., 2011). Equilibrium here refers to a stable slope in nature as opposed to a quasi-stable slope under stress equilibrium. Slope failure becomes inevitable when the applied shear stress exceeds the inherent shear strength of the rock, leading to a loss of structural integrity (Gao *et al*., 2017). Rock slope instability is a critical geotechnical risk and safety concern associated with mining operations in open-pit and high-wall mining. The risks associated with slope instability or failure are multifaceted as it affects operational safety, economic efficiency, and environmental sustainability. Examples of risks associated with slope instability or failures include harm or death of humans, physical harm to equipment and mine machineries, delays to mine production, and degradation of the environment (Kolapo *et al.,* 2022). Thus, ensuring the long-term stability of slopes is essential for maintaining sustainable mining practices, as it directly impacts operational safety, environmental integrity, and the overall viability of mining operations.

Analysing slope stability and identifying and prioritising its critical influencing factors is a foundational step in the design of effective slopes, the mitigation of hazards, and the management of risks, as it enables targeted interventions to enhance safety and operational reliability. The most well-established conventional models for evaluating slope stability are grounded in the limit equilibrium (LE) approach and conventional numerical methods rooted in the theories of elasticity and plasticity (Liao and Liao., 2020). However, these two conventional approaches have limitations. A significant limitation of the limit equilibrium (LE) approach is that it yields statically indeterminate equations, necessitating the introduction of simplifying assumptions to render the equations tractable (Xu and Lawal., 2021). On the other hand, stress-strain based numerical models are becoming more popular, but are computationally intensive, which can limit their rapid application for assessing slope vulnerability to natural hazards such as liquefaction (Marrapu *et al.,* 2021; Kolapo *et al.,* 2023). There are also standard approaches such as kinematic analyses and Monte Carlo-type simulations for the assessment of slope integrity/safety (Hoek & Bray, 1981). To address the limitations of conventional approaches, researchers have employed multiple linear regression to evaluate slope stability, aiming to provide models for rapid assessments of slope stability (Cetina., 2014). However, the accuracy of this approach is often compromised due to its inability to capture the nonlinear relationships between the factors contributing to slope failure. More recently, machine learning (ML) models have been proposed to evaluate slope stability (Lawal *et al*., 2023). Nevertheless, the ML models, despite providing accurate solutions, seem too simplistic as they cannot incorporate all the factors influencing slope stability. Also, they are black boxes, and their interpretation of stability problems is cumbersome. To ameliorate these various limitations, advanced decision-making frameworks are required to systematically evaluate and rank the various factors influencing slope stability based on their relative importance and interdependencies.

This paper aims to propose a Pareto-optimised hierarchical structural interaction matrix (HSIM) to prioritise slope stability influencing factors to ensure sustainable mining and environmental stewardship. To the authors' best knowledge, this attempt is the first of its kind in applying the method to mining and rock engineering. The HSIM framework developed by Oke and Ayomoh (2015) integrates multi-criteria decision-making techniques with Pareto optimisation to ensure a balanced consideration of competing factors and has been used in several areas including environmental and health management (Ayomoh *et al*., 2008). By identifying the most critical parameters affecting slope stability, this approach facilitates targeted interventions that enhance safety while aligning with sustainable mining objectives. The application of such frameworks aligns with global sustainability goals, including the United Nations Sustainable Development Goals, by promoting responsible resource management and reducing environmental risks. This study aims to contribute to the broader discourse on sustainable mining by demonstrating how innovative methodologies can support safer and more environmentally conscious mining practices.

SLOPE STABILITY INFLUENCING FACTORS

The factors influencing slope stability can be broadly categorised into natural and human-induced factors. Natural factors include geological, geotechnical or geomechanical, hydrological, environmental,

time-dependent, and slope geometrical conditions (Sha, 2016). Human-induced factors encompass excavation methods, stabilisation measures, monitoring and maintenance, mining activities, and dynamic loading such as blasting (Nicholas and Sims, 2000).

The geological factors affecting slope stability include rock mass structure (orientation, spacing, and persistence of joints, faults, fractures, and bedding planes), lithology (mineral composition and rock type), stratigraphy (layering and sequence of rock units), and weathering or alteration degree. Rock mass structural features like folds and discontinuities significantly influence slope behaviour by either stabilising or destabilising it, depending on their orientation and associated tectonic damage (Stead and Wolter, 2015). The mineral composition also impacts rock strength, while weathering degrades rock quality by weakening potential failure surfaces (Ogunsola *et al.*, 2019; Ogunsola *et al.,* 2017).

The geotechnical or geomechanical factors affecting slope stability include material strength parameters such as uniaxial compressive strength, tensile strength, fracture toughness, elastic properties (elastic modulus and Poisson's ratio), rock mass quality indicators (RQD, GSI, RMR), and in-situ stress conditions. Variability in rock strength parameters significantly affects failure surfaces in slope stability analysis (Ahmed *et al*., 2020). Classification systems like RMR provide reliable estimates of stable slope angles for preliminary and conceptual design purposes (Taheri and Tani, 2010). In situ stress conditions profoundly influence slope stability by dictating deformation behaviour relative to wall height and stress orientation (Kolapo *et al.,* 2022), this in turn leads to more rigorous analysis as slope designs progress towards implementation.

The hydrological conditions such as groundwater presence, pore pressure, seepage, drainage, clays and other water-susceptible mineralisation play a critical role in slope stability. Groundwater infiltration increases pore pressure along potential failure planes, reducing normal stresses and frictional resistance while enhancing driving forces that destabilise slopes (Simataa, 2019). Effective drainage mitigates these risks by lowering pore pressure.

The slope geometrical factors influencing slope stability include angle, height/length, and morphology. Steeper slopes increase gravitational forces that elevate instability risks. Concave slopes are generally more stable than convex ones due to better stress distribution and lateral confinement (Wines, 2016).

Finally climatic effects such as temperature fluctuations, freeze-thaw cycles, precipitation, and erosion progressively weaken slopes. Vegetation can stabilise slopes through root reinforcement or exacerbate instability by retaining moisture.

HYBRID STRUCTURAL INTERACTION MATRIX FOR PRIORITISING SLOPE STABILITY INFLUENCING FACTORS

Introduction to the Hierarchical Structural Interaction Matrix Methodology

The research methodology utilised in this study is anchored in the hierarchical structural interaction matrix (HSIM) framework proposed by Oke and Ayomoh (2005). This framework was selected over other decision-making approaches due to its comprehensive and system-oriented approach. The operation of this methodology is fundamentally rooted in the theory of subordination, as illustrated in Figures 1 and 2. These figures present a flow diagram that outlines the progression toward the creation of the pair-wise comparison matrix and the hierarchical tree structure diagram, which integrates various factor hierarchies into a cohesive hierarchical framework (Ayomoh and Oke., 2006).

The HSIM methodology systematically evaluates the interactions among the factors influencing slope stability through pairwise comparisons guided by a key inquiry. This process constructs a binary interaction matrix (BIM) to represent hierarchical interdependencies within the slope stability prioritisation network. Additionally, HSIM incorporates computational models to quantify factor weights, enabling precise prioritisation.

Critical Factors Contributing to Slope Instability

This section presents the 17 slope stability influencing factors considered in this study, previously described for context. These factors were identified from extensive case studies in literature, including works by Kolapo *et al*., (2022), Cetina (2014), Gao *et al*., (2017), Naghadehi *et al*., (2011), Sha (2016), Stead and Wolter (2015), Simataa (2019), and others.

To enhance understanding, the established slope stability influencing factors are systematically categorised into five distinct classes (Table I) for the purpose of this study. This classification provides a structured framework for analysing the complex interdependencies between these factors, allowing for a more precise evaluation of their roles in causing slope instability.

Table I: Slope stability factors under consideration

S/N	Main Influencing Factor	Influencing Factor	Factor Number
1	Geological	Rock Mass Structure	1
		Lithology	2
		Stratigraphy	3
		Weathering and Alteration	4
2	Geomechanical/ Geotechnical	Material Strength	5
		Elastic Properties	6
		Rock Mass Quality	7
		In-situ Stress Conditions	8
3	Hydrological	Groundwater Presence	9
		Pore Pressure	10
		Seepage and Drainage	11
4	Slope Geometry	Slope Angle	12
		Slope Height and Length	13
		Slope Morphology	14
5	Environmental	Climatic Effects	15
		Erosion Processes	16
		Vegetation	17

HSIM Modelling Framework for Prioritising Factors Influencing Slope Stability

Figure 1 provides a flowchart detailing the pairwise interaction process, leading to the implementation of a BIM for relevant factors. The BIM is a square matrix with designated rows ("*a*") and columns ("*b*"), assigning "*1*" for an affirmative or positive relationship or interdependency between two influencing factors and "*0*" otherwise. The contextual inquiry guiding this assessment is defined by *SQab*, as elaborated below.

$$SQ_{ab} = \begin{cases} 1, if\ the\ influence\ of\ factor\ a\ on\ Rock\ Burst\ occurrence\ can\ be\ directly\ influenced\ by\ factor\ b \\ 0, if\ the\ influence\ of\ factor\ a\ on\ Rock\ Burst\ occurrence\ cannot\ be\ directly\ influenced\ by\ factor\ b \end{cases}$$

The contextual relationship can be mathematically represented in its generalised form as:

If a→b = 1, then there is a direct influence from "a" to "b."

If a→b = 0, then "a" does not influence "b." In this case, "b" may or may not influence "a," i.e., b→a can be either 0 or 1, depending on the specific relationship between the factors.

The contextual inquiry aligns with the specific problem domain. Mapping factor "*a*" to "*b*" requires interpreting the BIM by columns, while the reverse mapping uses rows. Figure 2 illustrates the hierarchical tree structure diagram (HTSD), which organises slope stability factors hierarchically. The highest priority factor is at the apex, and the lowest at the base. A column with more "*0s*" is subordinate to one with fewer, indicating hierarchical relationships.

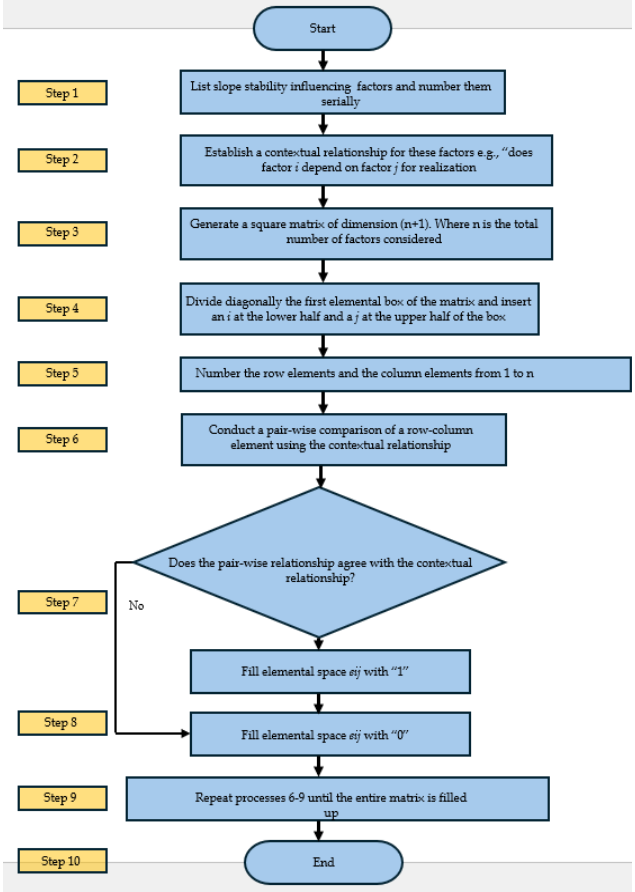


Figure 1. Flowchart for pairwise matrix generation (Modified from Ayomoh and Oke, 2006).

Evaluation of Weight Allocation for Individual Slope Stability Influencing Factors

The weighting model expressed in Equation (1) was utilised to compute the Intensity of Relevance (IR_{F_a}) for each factor influencing the likelihood of slope instability problems in a mining environment. This approach enables a quantitative assessment of the relative importance of each factor in contributing to slope instability occurrences.

$$IIRF_i = \frac{N_{BRF(i)}}{T_{RF}} \text{ x } M_{SR(i)} + \frac{c}{T_{RF}}(M_{SR} - \mu) \quad [1]$$

$$c = N_{BRF} + 1 \quad [2]$$

$$\mu = \frac{M_{BRF}}{T_{RF}} \text{ x } M_{SR}; \quad [3]$$

Where,

N_{BRF} represents the quantity of subordinate slope stability influencing factors linked to a specific factor a, while T_{RF} represents the aggregate number of slope stability influencing factors evaluated in this study. M_{SR} represents the maximum rating scale and M_{BRF} represents the upper limit of subordinate factors.

The weighting model is based on two components: (i) the outcomes of the HSIM exercise, which establishes the count of subordinate factors (N_{SRF}) related to a particular slope stability influencing factor a, and (ii) the assessment of each factor on a scale from 0 to 9, as outlined in the study of Ayomoh and Oke (2006).

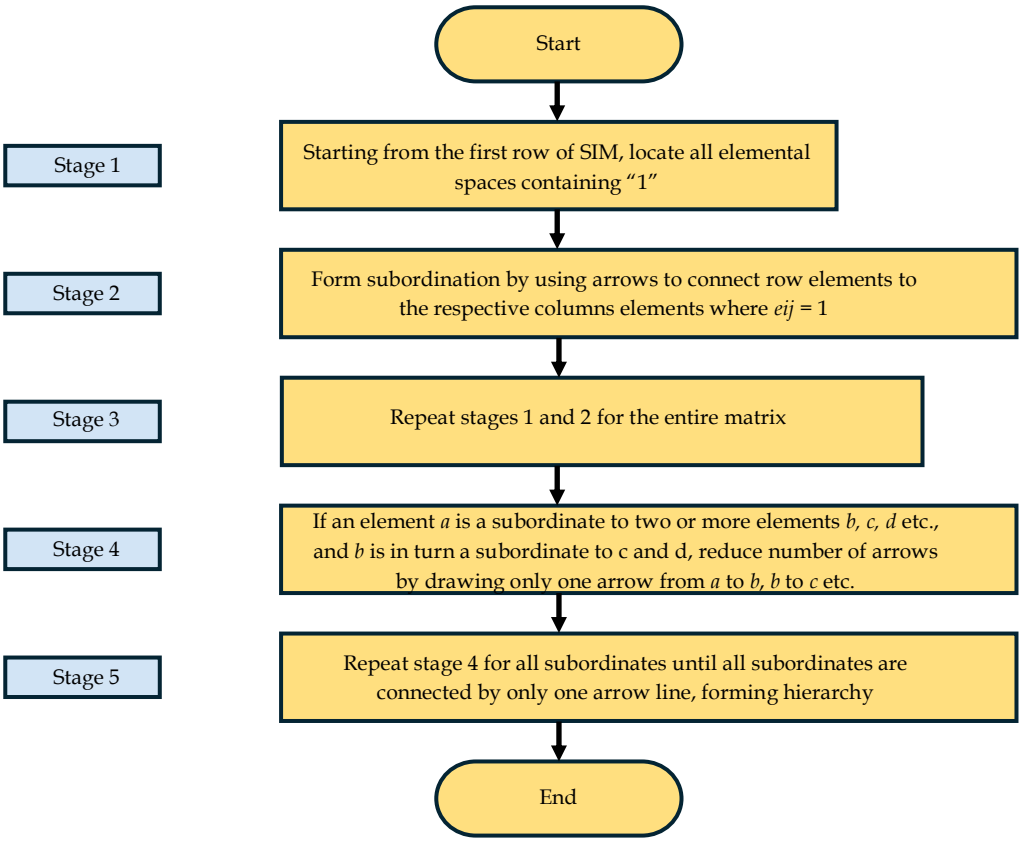


Figure 2. Flowchart for HTSD framework (Modified from Ayomoh and Oke, 2006).

RESULTS AND DISCUSSION

Results of the Binary Interaction Matrix for slope stability influencing factors

This section provides an analysis of the results derived from the BIM presented in Table II, which includes the computed weights for each slope stability influencing factor. The table displays binary outputs of "1s" and "0s," indicating the validity and non-validity of contextual questions related to the interdependencies between factor mappings from "i" to "j." Arrays with "1s" signify valid relationships within the context of the question, while arrays with "0s" denote non-valid relationships.

From Table II, it is evident that factor 1 in the first row is directly influenced by factors {2, 3, 5, 7, 9, 10, 12, and 15}, indicating that factor 1 is subordinate to these factors and its impact on slope stability is contingent upon them to varying degrees. factor 2, in the second row, is subordinate to factors {3, 4, 5, 9, 13, and 15}. factor 3 is influenced by factors {4, 7, 9, 10, and 12}, while factors 4 and 5 are subordinate to factors {1, 5, 7, 9, 10, and 12} and an unspecified set, respectively.

Furthermore, factor 6 is influenced by factor {5}, and factor 7 by factors {5, 6, 8, 9, and 12}. factor 8 is subordinate to factors {1, 5, and 6}, and factor 9 to factors {8 and 10}. factor 10 is influenced by factors {5 and 6}, while factor 11 is subordinate to factors {4, 5, 9, and 10}.

Additionally, factor 12 is influenced by factors {5, 6, 9, 10, 11, and 13}, and factor 13 by factors {8 and 14}. factor 14 is subordinate to factors {4, 6, 9, and 12}, while factor 15 is influenced by factors {4, 5, 7, 9, 10, 11, and 16}. factor 16 is influenced by factors {4 and 8}, and factor 17 by factors {4, 9, 15, and 16}. This hierarchical structure elucidates the complex interdependencies among the factors influencing slope stability.

Table II: Pairwise correlation mapping of slope stability influencing factors

	1	**2**	**3**	**4**	**5**	**6**	**7**	**8**	**9**	**10**	**11**	**12**	**13**	**14**	**15**	**16**	**17**
1	0	1	1	0	1	0	1	0	1	1	0	1	0	0	1	0	0
2	0	0	1	1	1	0	0	0	1	0	0	0	1	0	1	0	0
3	0	0	0	1	0	0	1	0	1	1	0	1	0	0	0	0	0
4	1	0	0	0	1	0	1	0	1	1	0	1	0	0	0	0	0
5	0	0	0	0	0	0	0	0	0	0	0	0	0	0	0	0	0
6	0	0	0	0	1	0	0	0	0	0	0	0	0	0	0	0	0
7	0	0	0	0	1	1	0	1	1	0	0	1	0	0	0	0	0
8	1	0	0	0	1	1	0	0	0	0	0	0	0	0	0	0	0
9	0	0	0	0	0	0	0	1	0	1	0	0	0	0	0	0	0
10	0	0	0	0	1	1	0	0	0	0	0	0	0	0	0	0	0
11	0	0	0	1	1	0	0	0	1	1	0	0	0	0	0	0	0
12	0	0	0	0	1	1	0	0	1	1	1	0	1	0	0	0	0
13	0	0	0	0	0	0	0	1	0	0	0	0	0	1	0	0	0
14	0	0	0	1	0	1	0	0	1	0	0	1	0	0	0	0	0
15	0	0	0	1	1	0	1	0	1	1	1	0	0	0	0	1	0
16	0	0	0	1	0	0	0	1	0	0	0	0	0	0	0	0	0
17	0	0	0	1	0	0	0	0	1	0	0	0	0	0	1	1	0

Analysis of interrelationships among slope stability influencing factors (Binary Interaction Matrix - BIM)

The interdependencies among slope stability influencing factors are analysed in this section. Geological factors, such as orientation, spacing, and persistence of joints, faults, and bedding planes, are influenced by lithology. For instance, sedimentary rocks often display bedding planes acting as weak surfaces, while igneous rocks develop fractures based on cooling history (Kolapo *et al.,* 2022). Lithology also dictates weathering susceptibility; feldspar-rich rocks weather more readily than quartz-rich ones, leading to differential slope degradation. Weathering processes weaken the rock mass structure by widening fractures and reducing cohesion along discontinuities, thereby compromising slope integrity. Hydrological conditions also play a critical role. Groundwater presence elevates pore pressure within slope materials, reducing effective stress and shear strength. This can trigger slope failure by decreasing friction along discontinuities. Poor drainage exacerbates groundwater accumulation, raising pore pressures and destabilising slopes. Conversely, effective drainage mitigates instability risks by lowering pore pressure through water evacuation from slope materials.

Slope geometrical factors further influence stability. Steeper slopes increase gravitational forces acting on the slope, while greater height and length amplify these forces, raising risks of instability. Slope morphology affects stress distribution; for example, concave slopes concentrate stress differently than convex ones. Taller slopes may exhibit pronounced curvature or morphological changes that alter stress patterns. Environmental factors such as temperature fluctuations and precipitation enhance erosion processes. Freeze-thaw cycles weaken rock materials, while heavy rainfall increases runoff and erosion rates. Vegetation stabilises soil with root systems, mitigating erosion, whereas lack of vegetation accelerates erosion and destabilises slopes. Geomechanical factors are also significant. Intrinsic material strength parameters like uniaxial compressive strength and tensile strength are influenced by rock mass quality indicators such as rock quality designation and geological strength index. Higher rock mass quality correlates with greater material strength. Pre-existing tectonic stresses can either enhance or diminish material strength depending on their orientation relative to applied loads and discontinuities.

Interdependencies between geological and hydrological factors reveal that discontinuities like joints and faults provide pathways for water infiltration, increasing groundwater presence within the slope. Water saturation along these planes reduces stability by elevating pore pressure and decreasing friction on potential failure surfaces. Lithology controls groundwater flow; permeable rocks like sandstone allow infiltration, while impermeable layers like shale trap water locally, increasing pore pressure. Geological factors also interact with slope geometry. The orientation of joints and faults influences the effective slope angle; aligned discontinuities create planes of weakness. Stratigraphy impacts steepness

limits; weak layers reduce the maximum safe angle for slopes. Weathered materials further lower safe angles compared to fresh rock. Slope shape affects drainage; poorly draining slopes experience prolonged moisture exposure, accelerating weathering.

Environmental factors interact with geological features as well. Joint and fault orientations influence how precipitation affects water infiltration and drainage within slopes. Climatic conditions like temperature fluctuations drive weathering processes that alter rock strength and stability. Certain vegetation in certain conditions can, in the longer term, weaken rock slopes via strong, expanding, and pervasive root systems, and/or chemical processes. Vegetation can moderate these effects by absorbing soil moisture or enhancing infiltration through root pathways. Hydrological factors also interact with geomechanical properties. Elevated pore pressure reduces effective stress, diminishing material strength and increasing failure likelihood. Rock mass quality influences groundwater interaction; higher-quality rock typically exhibits lower permeability, limiting groundwater presence compared to lower-quality rock that allows more infiltration. Changes in pore pressure affect deformation behaviour; increased pressure leads to greater deformation under load due to altered elastic properties.

These interdependencies highlight the complex interactions among geological, hydrological, geometrical, environmental, and geomechanical factors influencing slope stability. Understanding these relationships is crucial for developing effective mitigation strategies to ensure safe mining operations and infrastructure development in areas prone to slope instability.

Table III is derived directly from the BIM presented in Table II. It quantifies the number of subordinate factors associated with each factor, where a subordinate factor is defined as one that occupies a lower position within the hierarchical structure of interconnected factors. This hierarchical arrangement reflects the dependency relationships between the factors, with subordinate factors being influenced by those positioned higher in the structure.

Table III: Number of subordinate factors for each slope stability influencing indicator

Slope Stability Influencing Factor Number	Number of subordinate factors
1	2
2	1
3	2
4	7
5	10
6	5
7	4
8	4
9	10
10	7
11	2
12	5
13	2
14	1
15	3
16	2
17	0

Slope stability influencing factors Hierarchical Tree Structure Diagram

The HTSD framework depicted in Figure 3 has 14 priority levels. Slope stability influencing factors 5 and 9 (material strength and groundwater presence) are the top hierarchy factors that result in slope instability occurrence in mines while factor 17 (vegetation) is the least prioritised factor due to its high reliance on other factors high up in the HTSD framework, for slope instability to occur in mines. Closely

following is factor 10 (pore pressure). This factor is on the second priority level of the hierarchy diagram and is a direct subordinate to both material strength (factor 5) and groundwater presence (factor 9). With respect to factor 10, the groundwater pore pressure can significantly reduce effective stress, thereby decreasing material strength and increasing the likelihood of slope failure. This phenomenon could have a high impact on a few other slope stability influencing factors, especially on weathering and alteration (factor 4) which could degrade material strength by altering mineral bonds and reducing cohesion within the rock mass and further predisposing the rock mass to failure. Following this are factor 6 (elastic properties) and factor 12 (slope angle), positioned at level 4 and 5 of the hierarchy diagram, respectively. Changes in slope geometry, such as steepness or curvature, can affect how elastic properties manifest under load, influencing deformation behaviour and stability.

Priority level 6 is next, which consists of factor 8 (in situ stress conditions). The pre-existing tectonic stresses within the rock mass can enhance or diminish effective material strength, depending on their orientation relative to the applied loads and discontinuities. It is closely followed by priority level 7 which consists of factor 11 (seepage and drainage), factor 16 (erosion processes), and factor 7 (rock mass quality). The next factor in the prioritised hierarchy is 15 (climatic effects) which is located at priority level 8. Next is priority level 9 which comprises factors 2 (lithology), 3 (stratigraphy), and 14 (slope morphology). The sequence of rock layers (stratigraphy) is inherently linked to lithology since different layers are composed of varying rock types with distinct strengths and mechanical properties. For instance, a strong sandstone layer may overlie a weak shale layer, leading to instability along the interface. Furthermore, factor 1 (rock mass structure) and factor 13 (slope height and length) are at the 10th priority level of the hierarchy diagram. The orientation of joints and faults in the rock mass structure can influence the effective angle and height of the slope; if discontinuities are aligned with the slope angle, they may create planes of weakness. Finally, the last priority level is 11, having only factor 17 (vegetation). Vegetation can mitigate erosion processes by stabilising soil with root systems, while a lack of vegetation can increase erosion rates, further destabilising slopes.

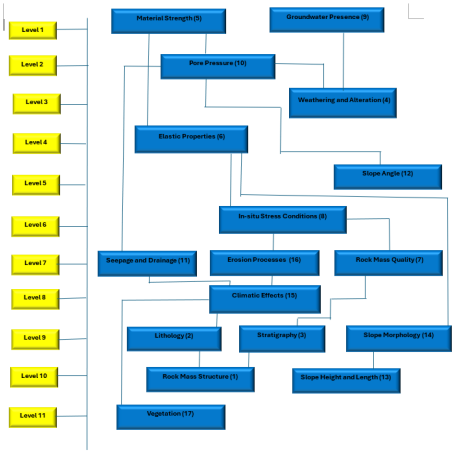


Figure 3. Developed HTSD framework for the prioritised slope stability influencing factors

Slope stability influencing factor intensity ratings

The intensity rating results for each factor, as detailed in Table III and calculated using Equation (1), are presented in Table IV. These results quantify the degree of significance of each factor in contributing to slope instability, providing a comprehensive understanding of their relative importance in influencing slope stability.

As indicated in Table IV, the three highest intensity ratings for the slope stability influencing factors 1 through 17 are 7.695, 5.452, and 3.956, while the lowest is 0.218. These ratings provide a quantitative measure of the relative impact of each factor on slope stability.

Table IV: Slope stability influencing factors weight scores

Slope Stability Influencing Factor Number	Slope Stability Influencing Factor Weight Score
1	1.714
2	0.965
3	1.714
4	5.452
5	7.695
6	3.956
7	3.209
8	3.209
9	7.695
10	5.452
11	1.714
12	3.956
13	1.714
14	0.965
15	2.461
16	1.714
17	0.218

Pareto Analysis of the slope stability influencing factors

The outcomes of the Pareto analysis, derived from the numerical computation of the intensity ratings for each slope stability influencing factor, are presented in Table V and visually illustrated in Figure 4. This analysis provides a detailed insight into the relative significance of each factor in contributing to slope instability phenomena.

Table V: Pareto numerical computation table

Slope Stability Influencing Factor Number	**Reordered Slope Stability Influencing Factor Weight Score**	**Cumulative Factor Weight Score**	**Percentage (%) Cumulative Factor Weight Score**
5	7.695	7.695	14.30
9	7.695	15.390	28.60
4	5.452	20.842	38.74
10	5.452	26.294	48.87
6	3.956	30.250	56.22
12	3.956	34.206	63.58
7	3.209	37.415	69.54
8	3.209	40.624	75.51
15	2.461	43.085	80.08
1	1.714	44.799	83.26
3	1.714	46.513	86.45
11	1.714	48.227	89.64
13	1.714	49.941	92.82
16	1.714	51.655	96.01
2	0.965	52.620	97.80
14	0.965	53.585	99.59
17	0.218	53.803	100

As shown in Table V and Figure 4, the critical factors contributing approximately 80% of the intensity to slope instability are material strength (factor 5), groundwater presence (factor 9), weathering and alteration (factor 4), pore pressure (factor 10), elastic properties (factor 6), slope angle (factor 12), rock mass quality (factor 7), in-situ stress conditions (factor 8), and climatic effects (factor 15). Conversely, the remaining factors collectively contribute about 20% to slope instability and are considered non-vital. The Pareto analysis suggests that mining managers should prioritise their management efforts by implementing targeted initiatives to effectively control these nine critical factors, thereby ensuring stable and safe mining operations.

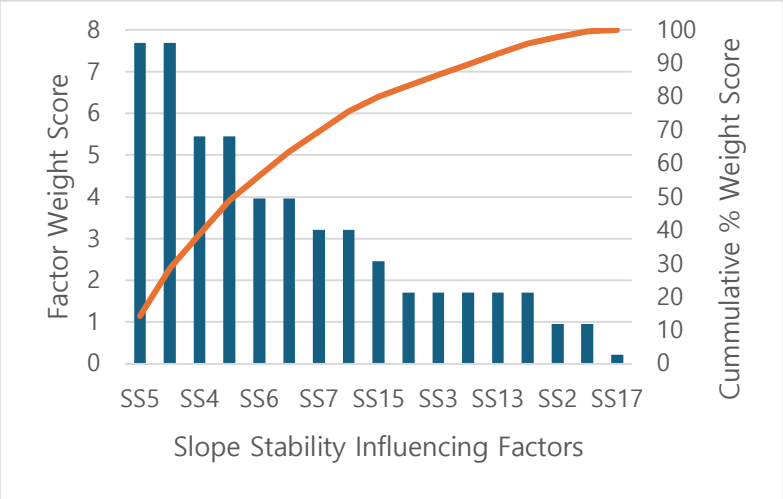


Figure 4. Pareto chart of the slope stability influencing factors.

CONCLUSION

This study introduces a novel HSIM algorithm, designed to prioritise the multitude of factors influencing slope instability in mines, thereby ensuring safe and sustainable mining operations. The method leverages the principle of subordination, integrated with a hierarchical factor tree structure diagram, and is supplemented by Pareto prioritisation computation techniques. The outcome of the Pareto-enhanced HSIM factor weighting exercise reveals that nine critical factors require effective management and control through targeted initiatives to prevent slope instability and to ensure safe and sustainable mining operations. The solution derived from this study is expected to resonate with mining stakeholders, as it pioneers a relatively new area of investigation into the prioritisation of slope instability influencing factors, tailored towards enhancing safety and sustainability in mining operations.

It should be noted that while this study is based on extensive literature research and the resulting hierarchy of elements is true for this literature study, site geotechnical conditions are highly variable and applying the methodology to varying conditions on various sites will lead to different hierarchies and priority elements. However, this study proves the efficacy of the methodology on identifying a representative hierarchy and prioritisation for given conditions, and its ability to provide a guide to managing the associated risk mitigation and control efforts.

ACKNOWLEDGMENTS

The first author gratefully acknowledges the support of the Global Excellence and Stature (GES) Fellowship and the Sibanye-Stillwater Centre for Sustainable Mining in the Department of Mining Engineering and Mine Surveying at the University of Johannesburg, whose postdoctoral research fellowship provided the opportunity to prepare this manuscript.

REFERENCES

Ahmed, Z., Wang, S., Jasim, O. H., Xu, Y., & Wang, P. (2020). Variability effect of strength and geometric parameters on the stability factor of failure surfaces of rock slope by numerical analysis. Arabian Journal of Geosciences, 13, 1-12.

Ayomoh, M. K. O., Oke, S. A., Adedeji, W. O., & Charles-Owaba, O. E. (2008). An approach to tackling the environmental and health impacts of municipal solid waste disposal in developing countries. Journal of Environmental Management, 88(1), 108-114.

Ayomoh MK, Oke SA (2006) A framework for measuring safety level for production environments. Safety Science;44(3):221-39. https://doi.org/10.1016/j.ssci.2005.09.006.

Cetina, T. (2014). The prediction of the critical factor of safety of homogeneous finite slopes subjected to earthquake forces using neural networks and multiple regressions. Geomech Eng, 6(1), 1-15.

Gao, W., Dai, S., Xiao, T., & He, T. (2017). Failure process of rock slopes with cracks based on the fracture mechanics method. Engineering Geology, 231, 190-199.

Hoek, E. and Bray, J. W. (1981). Rock Slope Engineering: The Institute of Mining and Metallurgy, London, England, 358 p.

Kolapo, P., Oniyide, G. O., Said, K. O., Lawal, A. I., Onifade, M., & Munemo, P. (2022). An overview of slope failure in mining operations. Mining, 2(2), 350-384.

Kolapo, P., Ogunsola, N. O., Munemo, P., Alewi, D., Komolafe, K., & Giwa-Bioku, A. (2023). DFN: an emerging tool for stochastic modelling and geomechanical design. Eng, 4(1), 174-205.

Lawal, A. I., Hosseini, S., Kim, M., Ogunsola, N. O., & Kwon, S. (2024). Prediction of factor of safety of slopes using stochastically modified ANN and classical methods: a rigorous statistical model selection approach. Natural Hazards, 120(2), 2035-2056.

Liao, Z., & Liao, Z. (2020). Slope stability evaluation using backpropagation neural networks and multivariate adaptive regression splines. Open Geosciences, 12(1), 1263-1273.

Littleboy, A., Keenan, J., Ordens, C. M., Shaw, A., Tang, R. H., Verrier, B., ... & Hodge, R. A. (2019). A sustainable future for mining by 2030? Insights from an expert focus group. The extractive industries and society, 6(4), 1086–1090.

Marrapu, B. M., Kukunuri, A., & Jakka, R. S. (2021). Improvement in prediction of slope stability & relative importance factors using ANN. Geotechnical and geological engineering, 39(8), 5879-5894.

Naghadehi, M. Z., Jimenez, R., KhaloKakaie, R., & Jalali, S. M. E. (2011). A probabilistic systems methodology to analyze the importance of factors affecting the stability of rock slopes. Engineering Geology, 118(3-4), 82-92.

Nicholas, D.E.; Sims, D.B. (2000). Collecting and Using Geological Structure Data for Slope Design; Hustrulid, W.A., McCarter, M.K., Van Zyl, D.J.A., Eds.; Society for Mining, Metallurgy, and Exploration: Golden, CO, USA, 2000.

Ogunsola, N. O., Lawal, A. I., & Saliu, M. A. (2019). Variations of physico-mechanical, mineralogical and geochemical properties of marble under the influence of weathering. Mining of mineral deposits, (13, Iss. 1), 95-102.

Ogunsola, N. O., Olaleye, B. M., & Saliu, M. A. (2017). Effects of weathering on some physical and mechanical properties of Ewekoro Limestone, South-western Nigeria. Int. J. Eng. Appl. Sci, 4(11), 257336.

Oke, S. A., & Ayomoh, M. K. O. (2005). The hybrid structural interaction matrix: A new prioritizing tool for maintenance. International Journal of Quality & Reliability Management, 22(6), 607-625.

Sha, L. (2016). Analysis of slope instability factors and protection. Int. J. Multidiscip. Res. Dev, 3(4), 181-182.

Simataa, E. (2019). Investigating slope stability in an open pit mine–a case study of the phyllites western wall at sentinel pit (Doctoral dissertation).

Stead, D., & Wolter, A. (2015). A critical review of rock slope failure mechanisms: the importance of structural geology. Journal of structural geology, 74, 1-23.

Taheri, A., & Tani, K. (2010). Assessment of the stability of rock slopes by the slope stability rating classification system. Rock Mechanics and Rock Engineering, 43, 321-333.

Wines, D. (2016). A comparison of slope stability analyses in two and three dimensions. Journal of the Southern African Institute of Mining and Metallurgy, 116(5), 399-406.

Xu, S. Y., & Lawal, A. I. (2021). Deficiencies of the vertical slice method in assessment of the seismic earth pressures. Acta Geotechnica, 16, 959-975.



Nafiu Olanrewaju Ogunsola

Researcher
University of Johannesburg

Nafiu Olanrewaju Ogunsola is a postdoctoral research fellow at the Sibanye-Stillwater Centre for Sustainable Mining within the Department of Mining Engineering and Mine Surveying, University of Johannesburg, South Africa. Before joining the University of Johannesburg, Nafiu was awarded the Global Korea Scholarship (GKS) by the Korean Government in 2019. He earned his PhD in Mineral Resources and Energy Engineering with a concentration in Rock Mechanics in August 2023 from Jeonbuk National University, Jeonju, South Korea. He also holds a Master of Engineering (M.Eng.) in Mining Engineering (Rock Mechanics) and a Bachelor of Engineering (B.Eng.) in Mining Engineering, completed in 2017 and 2012, respectively, from the Federal University of Technology, Akure (FUTA), Nigeria.

Nafiu is an accomplished mining and rock engineer with a strong passion for studying rock and other geomaterials in situ and through practical application, demonstrated by his extensive industrial and academic experience. He has worked with notable mining and geotechnical companies, including Dangote Mines, China Civil Engineering Construction Corporation (CCECC), and Uniglobe Construction Engineering Limited, all in Nigeria. His recent research activities primarily focus on experimental and computational intelligence methods to deeply understand and predict the multiscale deformation and fracture behaviors of rocks and other geomaterials, addressing challenges in mineral extraction, infrastructure development, sustainability, geohazard mitigation, and energy.

Nafiu's current research focuses on advancing sustainable mining practices and geomechanics, implementing smart mining and monitoring operations through artificial intelligence and machine learning, promoting sustainable and rapid access to orebodies in both surface and underground mines, and applying multi-criteria decision-making (MCDM) methods to address challenges in mining and geomechanics. Contributing to academia and advancing knowledge in his field, Nafiu has published several articles in reputable journals and has been a reviewer for various others.

Role of machine learning in optimising prediction of blast fragmentation in mines using site-specific geological data

M.S. Kanongovere, R.S. Suglo, M. Masialeti

Botswana International University of Science and Technology, Botswana

Rock fragmentation by blasting remains a critical challenge in geomechanical engineering, being strongly influenced by geological discontinuities. However, conventional predictive models often fail to account for these discontinuities, leading to inaccuracies in blast performance assessments. This paper introduces a site-specific discontinuity index that quantifies these discontinuities and integrates them into machine learning (ML) models for improved fragmentation prediction. Key parameters such as joint volume, orientation, persistence, infill and alteration were consolidated into the index, providing a structured input for predictive modelling. Validation through Pearson correlation confirmed strong relationships between the index, rock mass rating and fragmentation outcomes, reinforcing its predictive reliability. A dataset of 110 blast events from Eureka Delta gold mine in Zimbabwe was analysed using violin plots and kernel density estimation to identify trends, while feature selection techniques refined critical predictors for fragmentation. Three ML models: Random Forest, support vector regression (SVR)and XGBoost, were applied to predict fragmentation outcomes. XGBoost outperformed the other models, achieving $R^2 = 0.989$, RMSE = 0.692, MAE = 0.484, demonstrating high predictive accuracy. Random Forest showed moderate generalisation ($R^2 = 0.82$), while SVR model exhibited overfitting (R^2 dropping from 0.771 to 0.73). By embedding geological discontinuity effects into predictive models, the site-specific discontinuity index enhances fragmentation prediction, reduces bias, improves generalisation and optimises blast design. These findings highlight the potential of ML in integrating geological heterogeneity into predictive models, offering a robust tool for improving blast design and fragmentation outcomes in mining operations.

Keywords: Fragmentation prediction, site specific discontinuity index, machine learning, blast design optimisation

INTRODUCTION

Accurate rock fragmentation prediction is critical for optimising blast design, enhancing resource recovery, reducing costs and supporting sustainable mining practices. The process involves estimating the size distribution of rock fragments after a blast, which is influenced by, inter alia, blast design parameters, explosive properties and geological conditions (Miao *et al.*, 2021; Zhang *et al.*, 2023; Gebretsadik *et al.*, 2024). However, achieving high prediction accuracy remains challenging due to the complex and unpredictable nature of geological discontinuities such as joints, fractures and faults, which significantly affect fragmentation outcomes (Hekmat *et al.*, 2019; Amoako *et al.*, 2022; Bouterfif *et al.*, 2024). The blasting process as defined by Persson *et al.*, (2018), is the release of explosive energy that generates stress waves propagating through the rock mass. These waves are often disrupted by geological discontinuities which reflect, redirect and absorb the energy leading to uneven stress distribution across the rock. This results in variation in fragmentation outcomes, with some areas experiencing excessive breaking while others exhibit inadequate breakage (Eitzenberger, 2012; Bakar, 2013; Lyana *et al.*, 2016).

To predict these outcomes accurately, a deep understanding of geological discontinuities is essential, as factors such as joint orientation, density, persistence and infill dictate how explosive energy is transferred, dissipated and absorbed within the rock mass.

Despite advances in predictive modelling, conventional fragmentation prediction models struggle to account for geological variability**.** Empirical models, such as the Kuz-Ram model (Cunningham, 1983) and the Kuznetsov-Cunningham-Ouchterlony model (Kuznetsov, 1973; Cunningham, 1983; Ouchterlony, 2005), typically rely on blast design parameters (e.g., burden, spacing, charge weight) while treating the rock mass as a homogeneous entity. Empirical models often fail to account for the complex, nonlinear effects of geological discontinuities, such as joint persistence and orientation on blast-induced stress waves, resulting in inaccurate predictions of fracture propagation and energy dissipation in geologically heterogeneous sites (Ouchterlony, 2005; Ouchterlony and Sanchidrián, 2019; Sharma *et al.,* 2018; Choudhary and Agrawal, 2022; Safak, 2024).

Machine learning (ML) has emerged as a powerful alternative for capturing the complex, nonlinear relationships between geological factors and blast design parameters that traditional empirical models often fail to address. Unlike empirical methods, ML algorithms learn directly from data, identifying hidden patterns and modelling intricate dependencies without predefined equations (Mitchell, 1997). This capability is particularly effective for rock fragmentation prediction, where the variability of geological discontinuities significantly influences blast outcomes (Amoako *et al.,* 2022; Gebretsadik *et al.*, 2024; Taiwo *et al.,* 2024). The application of ML to blast fragmentation follows a structured workflow through data collection, preprocessing, training, validation and testing. During training, models such as Random Forest, support vector regression (SVR) and XGBoost analyse historical blast data to learn the nonlinear interactions between geological parameters and fragmentation outcomes (Chen *et al.*, 2021). This is followed by validation, where hyperparameter tuning optimises model performance and prevents it from making mistakes on new data. Finally, the models are tested on new, unseen data to evaluate their generalisation ability, using metrics like R^2 (coefficient of determination), root mean squared error (RMSE), and mean absolute error (MAE) to measure accuracy. These algorithms consistently outperform traditional empirical models in predicting fragmentation by better capturing the complexities of rock mass behaviour (Tang *et al*., 2020; Chen *et al*., 2021; Zhao *et al.,* 2021).

However, despite these advances, ML-based models still lack a structured way to incorporate detailed, site-specific geological discontinuity effects into their predictive frameworks**.** Many ML models rely on generalised rock mass classification systems, such as the rock mass rating (RMR) (Bieniawski, 1976) and geological strength index (Hoek *et al.,* 1995), which are useful but do not fully capture discontinuity-induced fragmentation variability (Zhang *et al.,* 2018; Ching *et al.*, 2021). Consequently**,** the absence of structured geological discontinuity inputs limits the predictive capability of ML models, reducing their practical applicability in complex rock masses.

This paper aims to address this gap by integrating granular geological data, with a particular focus on discontinuity characteristics, into ML models to enhance fragmentation predictions. To achieve this, a site-specific discontinuity index (ssDI) is developed. It is specifically tailored for the Eureka Delta Gold mine in Zimbabwe, a site characterised by its complex and highly variable geological environment. The ssDI quantifies the combined effects of key geological discontinuity parameters such as joint orientation, density, persistence, alteration and microstructures into a single quantitative rating. These parameters were derived from detailed geological exploration data, field observations and mine pit mapping. A dataset of 110 blast events with their corresponding geological data was analysed and the ssDI was validated through Pearson correlation with RMR and fragmentation outcomes. Key fragmentation predictors were identified through **Pearson correlation** and **feature importance analysis**, based on the criterion that **95% of the fragmented material passes through a 450 mm sieve size**. These predictors were then incorporated into **three ML models: Random Forest, SVR and XGBoost,** to improve fragmentation prediction accuracy and reliability. The outcomes of this study are expected to advance blast design optimisation and improve resource extraction in regions characterised by significant geological variability.

METHODOLOGY

The methods used in this paper include site study, data collection and evaluation of the data.

Study Site

This study was conducted at Eureka Delta Gold, an open-pit mine located within the Guruve greenstone belt of the Zimbabwe Craton, a region with high geological variability. The area features a chromite-rich intrusion (Great Dyke) and a geological composition of granodiorite, greenstone, mafic and pegmatite dykes, forming a complex network of faults, fractures and joints (Soderlund *et al.*, 2010). Figure 1 provides a schematic overview of the mine, highlighting the open-pit layout and major geological discontinuities.



Figure 1. Mine pit (A) showing surface rock mass discontinuities (B and C).

Data Collection

The data collected for this paper comprised both geotechnical and blast data from the Eureka Delta Gold mine. Geotechnical data were sourced from field investigations using clinometers, tape measures and GPS devices, as well as pre-existing mine records. These sources provided insights into geological parameters such as joint volume, orientation, persistence, spacing, infill material type and water content, along with RMR values. RMR assesses rock mass quality based on parameters such as uniaxial compressive strength and rock quality designation (Bieniawski, 1989). The data provided a comprehensive understanding of the geological structures, helping to capture the site's geological complexity and variability (see Table I). These parameters were crucial for developing a ssDI, which consolidates geological parameters into a unified index for fragmentation prediction. Subsequently, blast data was collected from 110 blast events. The data included blast design parameters such as burden (metres), spacing (metres), charge weight (kg) and blast initiation patterns. In addition, fragmentation outcomes were captured through photographs of the muck piles and the fragmentation size was analysed using WipFrag software, which assessed the percentage of material passing a specified size, with a target of 95% passing 450 mm.

Table I: Statistical Summary of key geological parameters

	Joint volume (Jv)	Joint Orientation(o)	Joint Persistence (Jp)	Joint Alteration (A)	Joint Infilling (I)	Water Content (W)	Micro Joint properties (Mi)	Macro Joint properties (Ma)
Minimum	60	-71	1	1	3	1	1	1
Mean	246.74	114.74	3.30	1.49	8.69	1.58	4.70	1.16
Median	60	82.25	3	1	9	1	5	1
Maximum	2000	277	10	3	9	5	8	3

Development and Validation of ssDI

The ssDI formula was developed based on established frameworks (Barton and Choubey, 1977; Hoek and Brown, 1980). It incorporates key geological parameters such as volumetric joint count (Jv), joint persistence (Jp), orientation (O), infill (I), joint alteration (A), water content (W), and micro and macro-structures (Mi, Ma). Jv is the core multiplier, reflecting the amplifying effect of joint density on discontinuity effect. Higher joint densities exacerbate the destabilising effects of other factors, thus making Jv a central element in the formula's design. The approach follows the principles outlined by Lyana *et al.*, (2016), Mulenga (2020) and Ali and Moomivand (2021), who emphasised the importance of assigning higher weights to destabilising factors such as joint orientation. The weights in ssDI were derived from established rock mass classification systems (RMR, GSI, Blastability Index) and assigned based on their relative impact on fragmentation. These systems assign relative impact scores to factors like **joint orientation, persistence, alteration, water content, and infill** based on their observed effects on blast performance. To reflect this, the ssDI formula employs weighted expressions: **1/x** for parameters with inverse fragmentation effects (**P, W, A, I**), **2/x** for j**oint orientation** due to its stronger influence on wave directionality (Lyana *et al.,* 2016), and **0.5/x** for m**icro and macro structures (Mi + Ma)** to represent their secondary contribution (Choudhary and Agrawal, 2022). These weights were directly applied, based on literature findings and validated through **field measurements** at **Eureka Delta Gold mine**, where site-specific geological conditions confirmed their impact on fragmentation efficiency. Importantly, no iterative adjustments were performed, the weight assignments were strictly literature-driven and field-validated to align with geomechanical principles. A scaling factor (**k**) was introduced to **normalise the final index value**, ensuring it is comparable across different geological sites. It is determined by calibrating the raw ssDI output against **field benchmarks** from reference sites, where known fragmentation outcomes are observed. After computing the unscaled ssDI value, it is multiplied by k to adjust it to the expected fragmentation performance, aligning it with real-world blasting results. The ssDI combines original values (joint volume and orientation) for precise measurements and rated values (e.g., joint persistence, infill) for factors that are difficult to quantify directly.

$$\text{Thus, ssDI} = J_v\left(1 + \frac{1}{P} + \frac{2}{O} + \frac{1}{W} + \frac{0.5}{(Mi + Ma)} + \frac{1}{A} + \frac{1}{I}\right) \times k \qquad [1]$$

where: J_v = volumetric joint count; P = joint persistence; O = joint orientation; M_i = micro and M_a = macro structures; A = joint alteration; W = water content; I = joint infill. To validate the ssDI, a Pearson correlation test was performed between the ssDI, RMR and fragmentation outcomes.

The Pearson correlation coefficient (r) measures the strength and direction of the linear relationship between two continuous variables, ranging from -1 to +1 (Soufi *et al.,* 2018). This test assessed the relationship between the ssDI and these established measures, ensuring its predictive accuracy and relevance for rock mass stability and blasting performance.

Exploratory Data Analysis and Preprocessing

The ssDI, RMR, blast design parameters, explosive parameters and corresponding fragmentation outcomes were consolidated into a single dataset using R statistical software (R core Team, 2023), resulting in a total of 13 variables. The dataset consisted of 12 input variables (drilled holes, charged holes, burden, spacing, stemming, charge length, powder factor, hole diameter, hole accuracy, longest delay time, ssDI and RMR) and one output variable (% fragmentation passing, 450 mm sieve size). It was then subjected to exploratory data analysis and preprocessing to understand its structure, identify any relationships and prepare it for machine learning. All analyses were performed using R software, with the dplyr package for statistical analysis, ggplot2 for visualisation and caret for preprocessing and splitting the data. Violin plots (see Figure 2), created using ggplot2, were used to visualise the distribution of both input and output variables. The **horizontal axis** represents the **variable categories** (e.g., ssDI, RMR, burden, stemming), while the **vertical axis** represents the **measurement scale** for each variable. The **width** of each plot indicates the **density of data points**, revealing distribution, spread and potential outliers. For parameter selection, a combination of 2D kernel density plots, Pearson correlation and feature importance from XGBoost was employed. Several 2D kernel density plots helped to identify the relationships between input variables and the output variable. Pearson correlation analysis was used to quantify the strength and direction of these relationships, while also helping to assess

multicollinearity among variables. Lastly, XGBoost (XGBoost package) was used to rank the variables based on their contribution to predictive accuracy.

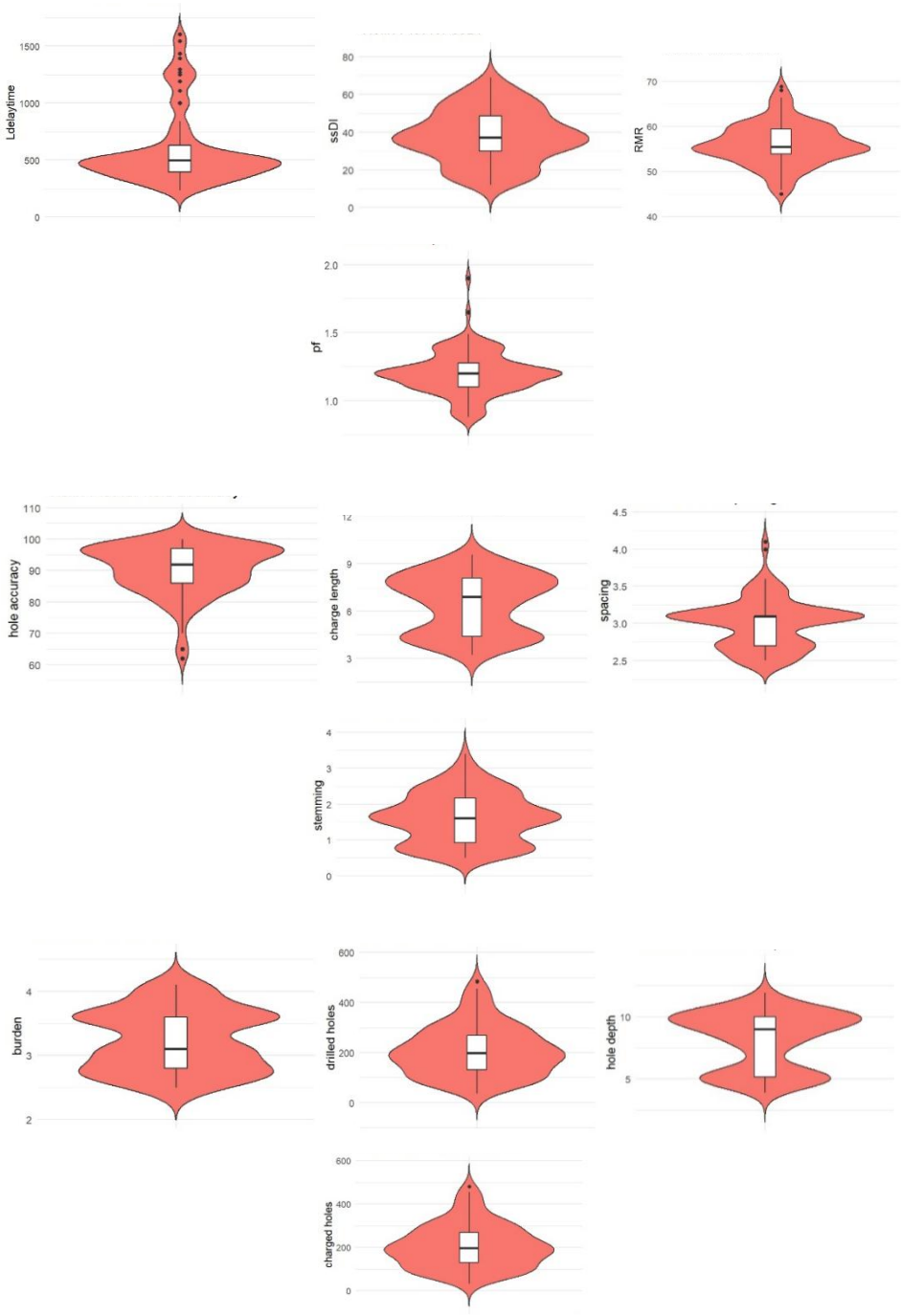


Figure 2. Violin plots of input variables.

Machine Learning Approach

This paper employed **Random Forest, SVR and XGBoost** within **R software**, selected for their ability to model nonlinear relationships in high-dimensional datasets (Fernández-Delgado *et al.,* 2014; Biau and Scornet, 2016; Probst *et al.,* 2019; Qi, 2020; Masoumi *et al.*, 2021; Wright *et al.,* 2022). **Hyperparameter tuning** was performed using the **caret package** in **R software** to optimise model performance. This process involves finding the best settings for a ML model, such as the depth of decision trees, to improve its accuracy. The **caret package** (*Classification and Regression Training*) is an open-source R library that simplifies ML tasks by providing easy-to-use functions for model training, parameter tuning and evaluation (Kuhn, 2008). The tuning process aimed to minimise RMSE and MAE while maximising R-squared (R^2). The algorithms implemented, along with their respective hyperparameter configurations, are summarised in Table II.

Table II: Summary of the hyperparameter settings for the ML models

Model	Key Features	Algorithm	Hyperparameters
Random Forest	Handles complex, nonlinear relationships and large datasets	$Y = \frac{1}{T}\sum_{t=0}^{T} \hat{y}it = \hat{Y}$ t	(n tree = 1000); interaction terms, polynomial features + recursive feature importance
Support Vector Regression	Captures nonlinear interactions using kernel methods	Min $\frac{1}{2}\|\|W\|\|^2$ subject to $\|$- (w.xi +b) $\| \leq \epsilon$	epsilon = 0, c = 8, gamma = 0.5. linear kernel + polynomial features.
XG BOOST	Iteratively optimises weak learners with regularisation	Obj = L(yi, $\widehat{yi}$) + $\sum_{i=1}^{k} \Omega(fk)$	cross validation (best of rounds), polynomial features + interaction terms + logarithmic transformation

The symbols in **Table X** represent key components of the models: Y denotes the predicted output in Random Forest, with predictions averaged across multiple decision trees. For **SVR**, W, w.xi and b represent the weight vector, feature interaction and bias term respectively. In **XGBoost**, L(yi, $\widehat{yi}$) measures prediction error, while Ω(fk) handles regularisation to prevent errors and improve generalisation. The evaluation metrics were selected for their distinct advantages. **RMSE** penalises larger errors, **MAE** provides an intuitive measure of absolute error and **R^2** assesses model explanatory power. Their mathematical formulations are provided in **Equations (2) to (4)**.

$$\text{RMSE} = \sqrt{\frac{1}{n}\sum_{i=1}^{n}(yi - \hat{y}\,i)^2} \quad [2]$$

$$\text{MAE} = \frac{1}{n}\sum_{i=1}^{n}|yi - \hat{y}\,i| \quad [3]$$

$$R^2 = \frac{\sum(yi-\hat{y})^2}{\sum(yi-\bar{y})^2} \quad [4]$$

Where $\boldsymbol{yi}$ are the actual values, $\boldsymbol{\hat{y}\,i}$ are the predicted values, and $\boldsymbol{\bar{y}}$ is the mean of the actual values.

RESULTS AND DISCUSSIONS

This section presents the results of the analysis of site-specific geological data, focusing on the validation of the ssDI and its integration using ML models.

Site-Specific Geological Data

In this study, the complex interplay between rock fragmentation and a range of critical geological factors is explored, with a particular focus on the newly developed ssDI and pre-existing RMR values. The spatial distribution of ssDI values across the Eureka Delta Gold mine open pit areas reveals considerable variability in the geological features across the site (see Figure 3). Areas with higher ssDI values (depicted in red/orange) correspond to regions of more significant geological complexity, characterised by dense faulting and jointing. In contrast, regions with lower ssDI values (shown in blue/green) reflect more homogeneous rock masses with fewer geological discontinuities. Furthermore, the relationship between ssDI, RMR and fragmentation outcomes was further explored through a Pearson correlation matrix (see Figure 4). The analysis revealed a strong negative correlation between ssDI and fragmentation (r = -0.77), indicating that as geological discontinuities increase, the **variability in fragmentation size** also increases, resulting in more irregular and less predictable fragmentation patterns.

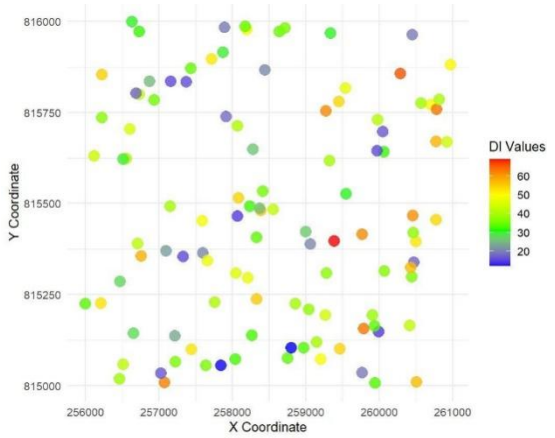


Figure 3. Spatial distribution of ssDI.

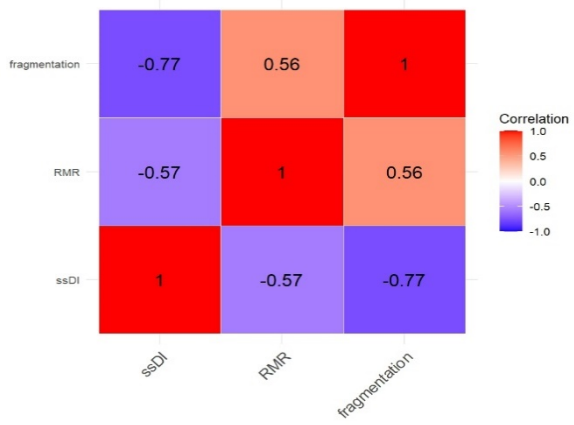


Figure 4. Pearson heat map showing the relationship between ssDI, RMR and fragmentation.

This finding supports prior work which emphasises that increased geological discontinuities tend to disrupt explosive energy transfer, resulting in more unpredictable fragmentation (Bakar, 2013; Moomivand and Azizi, 2021; Hekmatnejad and Crespin, 2022). On the other hand, the RMR exhibited a moderate negative correlation with fragmentation (r = -0.57), suggesting that areas with higher rock mass quality tend to produce more consistent and uniform fragmentation. This aligns with the findings of Bieniawski (1973), who demonstrated that rock mass strength and cohesion are key factors influencing fragmentation efficiency during blasting. A moderate positive correlation was observed between ssDI and RMR (r = 0.56), highlighting that regions with greater geological discontinuities tend to exhibit lower rock mass quality. This correlation shows that ssDI is an effective indicator of geological conditions, capturing essential features of rock mass integrity reinforcing its validity as a reliable predictor for fragmentation.

Variable Selection for Predictive Modelling

A total of 13 variables which consisted of geological, blast design and explosive parameters formed the basis of exploratory data analysis and parameter selection for predictive modelling. Through the 2D kernel density plots, Pearson correlation analysis and feature importance ranking (XGBOOST), the key features that influence fragmentation were identified. The 2D kernel density plots revealed clear

patterns in the relationships between these selected variables and fragmentation (Figures 5). The plots visually represented the density of data points, with colour gradients used to highlight the distribution and strength of these relationships. **Yellow and orange regions** in the plots represent areas of **high density**, indicating more predictable fragmentation outcomes. However, the **effect of this predictability** depends on the **vertical position** along the **y-axis**, which reflects **fragmentation quality**. When high-density yellow regions are located **higher on the axis**, it signifies predictably **good fragmentation**, characterised by a higher percentage of material passing the 450 mm sieve. In contrast, yellow regions appearing **lower on the axis** indicate **predictably poor fragmentation**, with larger particle sizes and reduced sieve passing. Meanwhile, blue and purple regions reflect lower density, indicating more variability in fragmentation. Parameters such as RMR, ssDI, charge weight and hole depth exhibited distinct patterns in these plots, correlating strongly with fragmentation. Hole accuracy revealed a structured relationship with fragmentation. Higher hole accuracy (above 95) consistently aligns with better fragmentation outcomes, as indicated by dense clustering (yellow region) in the kernel density plot. In contrast, lower hole accuracy (deep blue region) results in a more dispersed fragmentation distribution, reinforcing its critical role in blast performance. The use of kernel density plots for visualising relationships between variables has been effectively utilised in similar studies. Gebretsadik *et al.,* (2024) used kernel density plots to identify relationships between blast design parameters and fragmentation, demonstrating how these plots can clearly reveal patterns that might not be immediately evident through simple scatter plots.

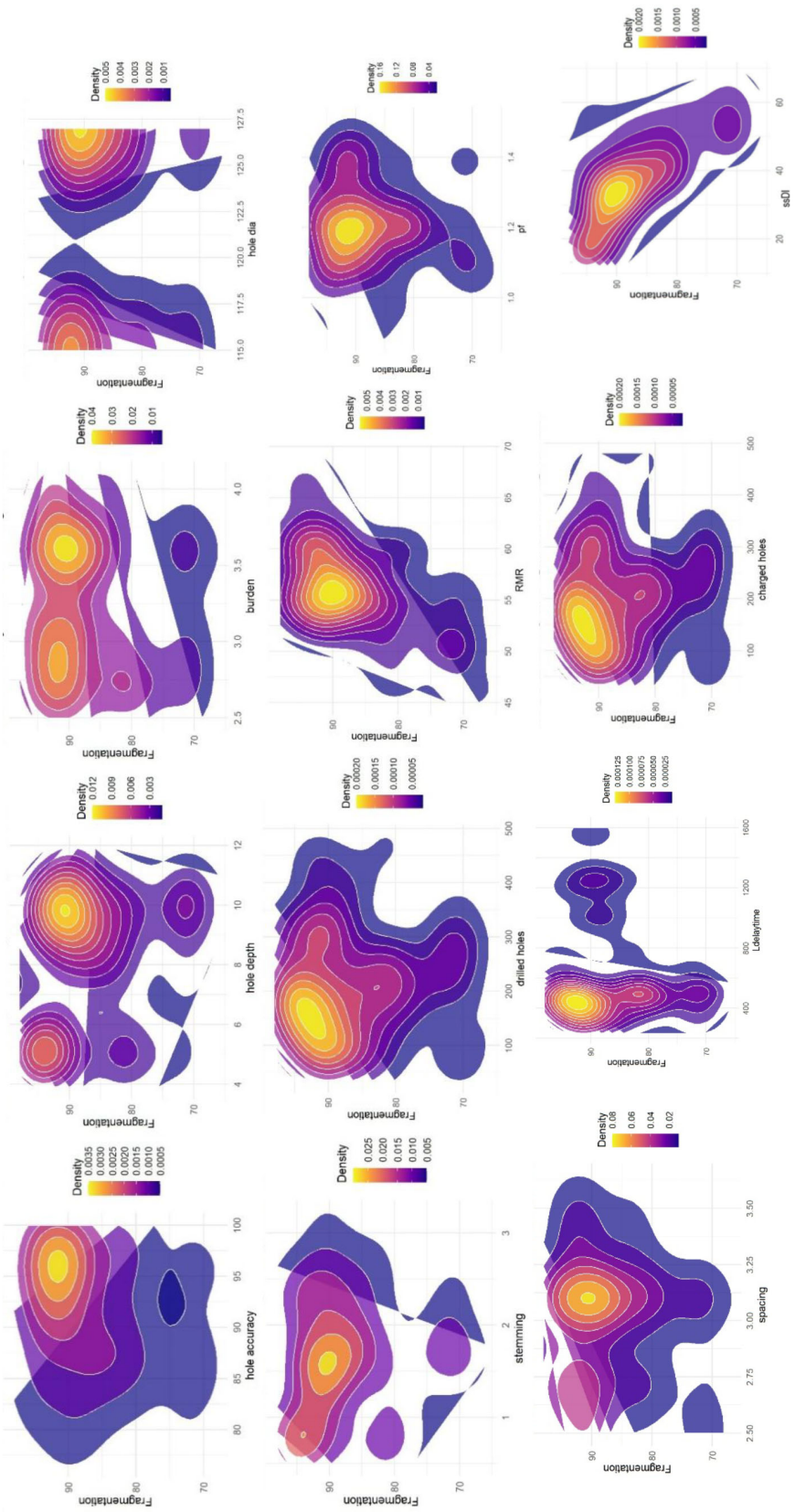


Figure 5. 2D kernel density plots showing relationship between individual input variables (hole accuracy, hole depth, burden, hole diameter, spacing, drilled holes, RMR, pf, charged holes, ssDI) and fragmentation.

The **Pearson correlation matrix** provided critical insights into the relationships between input variables and **fragmentation,** guiding feature selection for the ML model (see Figure 6). **ssDI (r = -0.77) and RMR (r = 0.56)** emerged as the strongest predictors, underscoring the importance of geological factors in fragmentation outcomes. Conversely, **spacing (r = 0), powder factor (r = 0.01), hole diameter (r = 0.02), drilled and charged holes (r = 0.04)** exhibited negligible correlations, indicating minimal predictive value. Removing these weakly correlated variables prevents overfitting and enhances model efficiency by focusing on the most relevant parameters. Additionally, **multicollinearity** was observed between **hole depth and charge length (r = 0.97), hole depth and stemming (r = 0.72), hole diameter and burden (r = 0.73), and spacing and hole diameter (r = 0.64).** Retaining highly correlated variables can inflate variance, leading to instability in coefficient estimates (Dormann *et al.,* 2013). To mitigate these effects, either one variable should be removed, or a ratio-based approach (e.g., stemming-to-hole depth) should be adopted to preserve information while reducing redundancy.

Further feature selection through XGBoost feature importance reinforced the significance of RMR, ssDI, and drilled holes as primary predictors, emphasising the role of rock mass competency, geological discontinuities and blast hole distribution in fragmentation (see Figure 7). However, despite its high ranking, drilled holes showed weak correlation and no significant pattern in 2D kernel density plots, suggesting its importance was due to interactions rather than a direct effect. To ensure robustness and interpretability, it was excluded from the final model. Stemming and powder factor were also identified as critical features in the XGBOOST feature importance, aligning with findings that inadequate stemming can lead to energy loss and inefficient breakage (Olsson *et al.,* 2010; Kahriman *et al.*, 2017). Hole diameter was retained for model stability as it remains constant in blasting designs and ensures consistent fragmentation predictions without introducing variability. The integration of feature selection methods and literature review identified the most influential variables for ML input. Based on these findings, the final selected variables were burden-to-spacing, stemming-to-hole depth, hole diameter, hole accuracy, powder factor, ssDI, and RMR ensuring a robust and reliable predictive model.

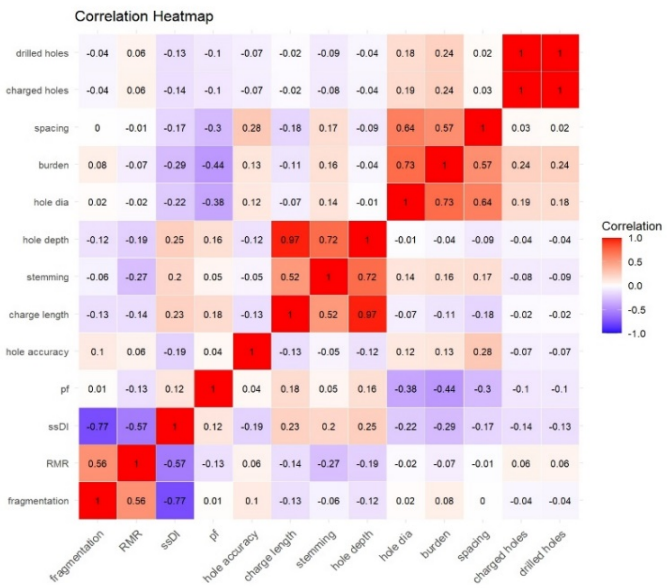


Figure 6. Pearson correlation heatmap.

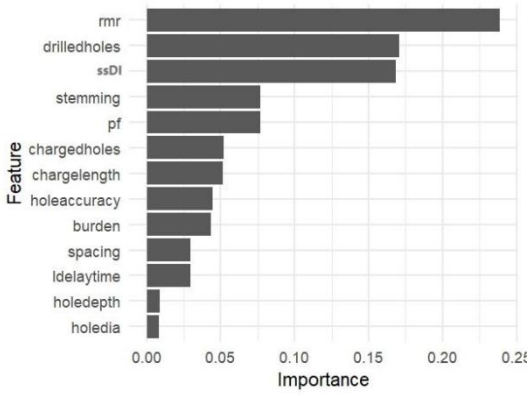


Figure 7. XG BOOST feature importance.

Discussion of Model Performances

The performances of SVR, Random Forest and XGBOOST models are discussed in the next sections. The dataset was divided into **70% for training** and **30% for testing**, following standard ML practices to ensure robust model evaluation.

Support Vector Regression Model

The R-squared value decreases from 0.771 on the training set to 0.73 on the testing set, suggesting mild overfitting (see Figure 8). The SVR model performs reasonably well on both the training and testing datasets, but there is a slight drop in accuracy on the testing data, as evidenced by an increase in MAE, RMSE and MSE as depicted in Fig. 9.

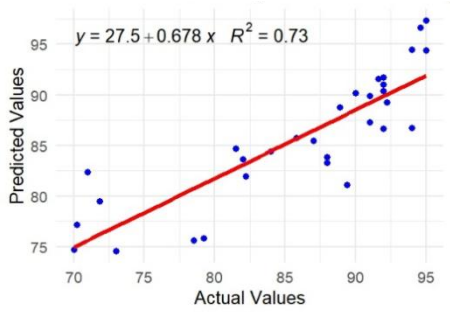


Figure 8. Performance model of SVR.

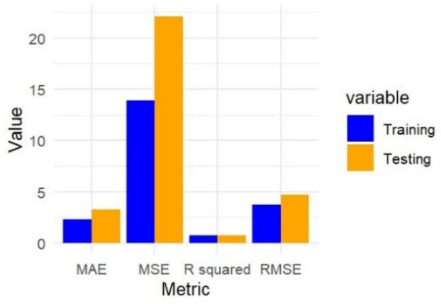


Figure 9. SVR actual vs predicted values.

While the model explains a good portion of the variance in the data, it struggles with generalisation of unseen data. This overfitting could be due to hyperparameter choices or dataset characteristics. Overall, SVR shows moderate accuracy, but further improvements in generalisation could be made through better hyperparameter tuning or feature selection.

Random Forest Model

The Random Forest model outperforms SVR, with an R-squared of 0.895 (training) and 0.82 (testing). This indicates a strong fit to the training data and reasonably good generalisation on the testing data, though there is still a slight drop in performance on unseen data (see Figure 10). The MAE increases from 1.78 (training) to 3.03 (testing), showing a noticeable drop in accuracy when generalising (Figure 11). The RMSE and MSE metrics also show an increase from training to testing, with the training values being lower than testing values, reinforcing the idea that the model performs better on the training set. However, Random Forest is more stable compared to SVR, likely due to its ability to handle more complex relationships and better capture data patterns. Some overfitting remains and improvements could be achieved by tuning more on the number of trees or using cross-validation techniques.

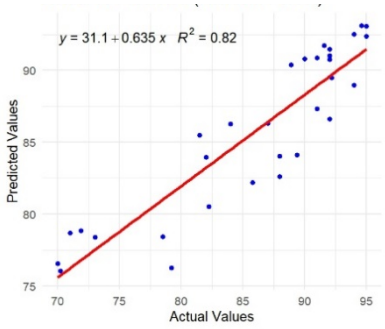


Figure 110. Performance model Random Forest

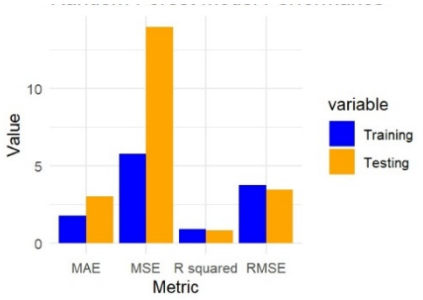


Figure 11. Random Forest actual vs predicted values.

XGBOOST model.

The XGBoost model provides the best performance as it has an exceptionally high R-squared of 0.998 for training and 0.989 for testing (Figure 12). This suggests that the model not only fits the training data well but also generalises excellently to unseen data. The MAE is the lowest among all models, decreasing significantly from 0.723 during training to 0.484 during testing, indicating an overall improvement in performance. Both RMSE and MSE are also the lowest in the testing phase, with values of 0.692 and 6.48, respectively (Figure 13). These low values suggest that XGBoost consistently makes highly accurate predictions across both training and testing datasets. The model's ability to maintain high accuracy in both phases makes it the most reliable and robust model of the three.

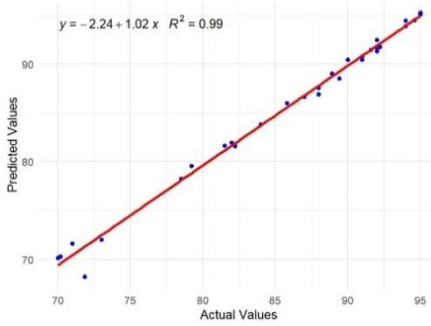


Figure 12. XGBOOST performance model.

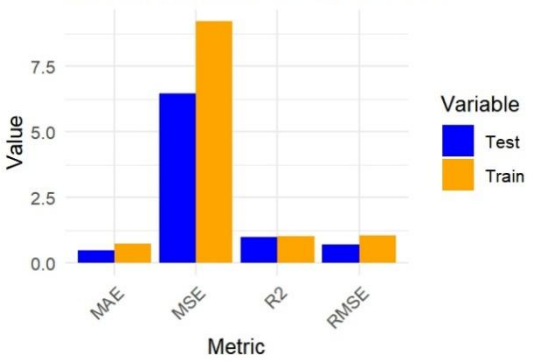


Figure 13. XGBOOST actual vs predicted.

CONCLUSIONS

The integration of site-specific geological data and ML models demonstrates a significant role in predicting rock fragmentation outcomes. The analysis of geological parameters, particularly the site-specific discontinuity index and RMR, revealed key insights into the complex relationship between geological discontinuities and fragmentation variability. The strong negative correlation between ssDI and fragmentation highlights the impact of geological discontinuities on fragmentation patterns. ML models, particularly XGBoost, demonstrated exceptional performance in predicting fragmentation, with R-squared values of 0.998 and 0.989 for training and testing datasets respectively. This suggests that ML, when combined with site-specific geological data, is a robust tool for improving blast design and fragmentation prediction. To enhance **blast design optimisation**, future research should focus on **adjusting controllable parameters**, such as **hole positioning, explosive energy distribution and delay timing** in response to the **site-specific geological conditions captured by ssDI and RMR**. By correlating **controllable parameters** with the **geological constraints** identified by these indices, it should be possible to design blast configurations that are more adaptive to site-specific discontinuities, thereby optimising fragmentation outcomes. This approach would bridge the gap between **predictive**

modelling and **practical blast adjustments**, leading to more precise and efficient fragmentation control in complex geological environments.

REFERENCES

Amoako, R., Ankit J. and Zhong, S. 2022. Rock Fragmentation Prediction Using an Artificial Neural Network and Support Vector Regression Hybrid Approach *Mining* 2, no. 2: 233-247. https://doi.org/10.3390/mining2020013

Azizi, A. and Moomivand, H., 2021. A new approach to represent impact of discontinuity spacing and rock mass description on the median fragment size of blasted rocks using image analysis of rock mass. *Rock Mechanics and Rock Engineering*, *54*, pp.2013-2038. https://doi.org/10.1007/s00603-020-02360-4.

Bakar, M.A., 2013. Influence of geological discontinuities upon fragmentation by blasting. *Pakistan Journal of Science*, *65*(3).

Bouterfif, L., Hafsaoui, A., Zeriri, I., Attia, M. and Idres, A., 2024. Prediction of Rock Fragmentation in the Boukhadra's Mine Conditions. *Scientific Bulletin of National Mining University*, (5).

Cunningham, C.V.B., 1983. The Kuz-Ram model for prediction of fragmentation from blasting. In: *Proceedings of the 1st International Symposium on Rock Fragmentation by Blasting*, Luleå, Sweden, 23-26 August 1983, pp. 439-453.

Djordjevic, N., 1999. Two-Component Model of Blast Fragmentation. In: Proceedings of the 6th International Symposium on Rock Fragmentation by Blasting, SAIMM, Johannesburg, 213-219.

Eitzenberger, A., 2012. *Wave propagation in rock and the influence of discontinuities* (Doctoral dissertation, Luleå tekniska universitet).

Gebretsadik, A., Kumar, R., Fissha, Y., Kide, Y., Okada, N., Ikeda, H., Mishra, A.K., Armaghani, D.J., Ohtomo, Y. and Kawamura, Y., 2024. Enhancing rock fragmentation assessment in mine blasting through machine learning algorithms: a practical approach. *Discover Applied Sciences*, 6(5), p. 223.

Hekmat, A., Munoz, S. and Gomez, R., 2019. Prediction of rock fragmentation based on a modified Kuz-Ram model. In *Proceedings of the 27th international symposium on mine planning and equipment selection-MPES 2018*, Springer International Publishing, pp. 69-79.

https://doi.org/10.1007/978-3-319-99220-4_6

Hekmatnejad, A. and Crespin, B., 2022, June. Rock-Discontinuity-Fragmentation (R-Dis-Frag): a computer package for the characterization of large-scale fractured rock masses in real-time. In *ARMA US Rock Mechanics/Geomechanics Symposium* (ARMA-2022). pp.5 -7.

Kuznetsov, V.M., 1973. The mean diameter of the fragments formed by blasting rock. *Journal of Mining Science*, 9, pp. 144-148. https://doi.org/10.1007/BF02506177

Lyana, K.N., Hareyani, Z., Shah, A.K. and Hazizan, M.M., 2016. Effect of geological condition on degree of fragmentation in a Simpang Pulai marble quarry. *Procedia Chemistry*, *19*, pp. 694-701.

Miao, Y., Zhang, Y., Wu, D., Li, K., Yan, X. and Lin, J., 2021. Rock fragmentation size distribution prediction and blasting parameter optimization based on the muck-pile model. *Mining, Metallurgy and Exploration*, *38*, pp. 1071-1080. https://doi.org/10.1007/s42461-021-00384-0

Mulenga, S., 2020. Evaluation of factors influencing rock fragmentation by blasting using interrelations diagram method. *J Phys Sci*, *2*(1), pp. 1-15

Ouchterlony, F., 2005. The Swebrec© function: Linking fragmentation by blasting and crushing. *Mining Technology*, 114, pp. 29-44. https://doi.org/10.1179/037178405X44539.

Persson, P.A., Holmberg, R. and Lee, J., 2018. *Rock blasting and explosives engineering*. CRC Press.

Safak, S., 2024. A new hyperbolic function approach of rock fragmentation size distribution prediction models. *Symmetry*, 16(8), pp. 979. https://doi.org/10.3390/sym16080979

Sanchidrián, J.A., Segarra, P. and López, L.M., 2007. Energy components in rock blasting. *International Journal of Rock Mechanics and Mining Sciences*, *44*(1), pp. 130-147.

Söderlund, U., Hofmann, A., Klausen, M.B., Olsson, J.R., Ernst, R.E. and Persson, P.O., 2010. Towards a complete magmatic barcode for the Zimbabwe craton: Baddeleyite U-Pb dating of regional dolerite dyke swarms and sill complexes. *Precambrian Research*, *183*(3), pp. 388-398.

R Core Team, 2023. 'R: A language and environment for statistical computing', R Foundation for Statistical Computing, Vienna, Austria. *https://www.r-project.org/*

Taiwo, B.L., Gebretsadik, A., Abbas, H.H., Khishe, M., Fissha, Y., Kahraman, E., Rabbani, A. and Abiodun Akinlabi, A., 2024. Explosive utilization efficiency enhancement: An application of machine learning for powder factor prediction using critical rock characteristics. *Heliyon*, 10(12), p. e33099. https://doi.org/10.1016/j.heliyon.2024.e33099

Zhang, Z.X., Sanchidrián, J.A., Ouchterlony, F. and Luukkanen, S., 2023. Reduction of fragment size from mining to mineral processing: a review. *Rock Mechanics and Rock Engineering*, *56*(1), pp. 747-778.

https://doi.org/10.1007/s00603-022-03068-3



Makomborero Salachi Kanongovere

Post graduate student
Botswana International University of Science and Technology

Currently pursuing a Master of Engineering (MEng) in Mining Engineering by Research at Botswana International University of Science and Technology (BIUST), specializing in blasting engineering and geomechanics. Research focuses on numerical modelling and analysis of blasting performance in discontinuous rock masses, aiming to optimize fragmentation, ground stability, and mine efficiency in structurally complex rock formations. Professional career began in 2020 as a Plant Operator at Chimona Mines, gaining experience in mineral processing operations. In 2021, joined Trade River Investments T/A Progress Mines as a Graduate Trainee, specializing in mine planning, ground control and geotechnical monitoring. In 2022, transitioned into academia as a Teaching Assistant at Manicaland State University of Applied Sciences (MSUAS), contributing to mining research and student mentorship. Since 2023, working as a Teaching Assistant at BIUST, supporting academic instruction and research in rock mechanics, numerical modelling, and geotechnical engineering. With a strong background in both industry and academia, dedicated to advancing sustainable mining practices through rock mechanics and geomechanical innovations.

The MDA CHORUS SAR constellation: A unique perspective for improved slope stability monitoring and geotechnical risk assessment

D. Hickson[1], R. Morin[1], R. Podmore[2]

[1]MDA Space, Canada
[2]Leica Geosystems, South Africa

Satellite synthetic aperture radar observations are integral to a comprehensive monitoring program for ground stability. Interferometric processing of a sequence of images collected over time can provide time series measurements of ground displacement with mm-precision at high resolution over wide areas. The amount of ground displacement that can be measured for a particular target is strongly affected by the orientation from which the target is imaged, which is described by the line-of-sight between the satellite and target. If the direction of ground movement is not aligned with the line-of-sight, the measurement may be significantly underestimated. Furthermore, the side-looking imaging geometry of these satellites introduces imaging distortions, such as foreshortening and shadow, that also depend on the line-of-sight as well as surface topography. These limitations on the quality of interferometric measurements are significant over mining sites with complex accumulation of ground-based deformation. MDA Space will soon be offering MDA CHORUS, a next-generation dual-frequency C- and X-band synthetic aperture radar satellite constellation which will deliver significantly enhanced Earth observation capability. The novel mid-inclination orbit for CHORUS provides unique imaging geometries across the world, increasing measurement coverage in areas with variable topography and enabling high precision three-dimensional ground displacement time series monitoring. In this work, we present simulations of the expected increase in interferometric measurement coverage and performance of three-dimensional processing for the Venetia diamond mine in South Africa. We illustrate how CHORUS will change the way we monitor ground stability to reduce risk and increase the safety of mining operations.

INTRODUCTION

Remote sensing contributes valuable information to geotechnical monitoring of a mine site not possible by conventional in-situ instrumentation. Satellite synthetic aperture radar (SAR) sensors use active microwave radiation to image wide areas at a high-resolution during day or night, through most weather conditions. As a result of their orbital configurations, satellite SAR sensors can image the same area on the ground from the same position in orbit at regular intervals, which is described by that sensors' revisit time, usually on the scale of a few days. A SAR monitoring program therefore provides consistent imaging of an area of interest (AOI) to build a dataset to monitor changes to the AOI over time.

Interferometric SAR (InSAR) provides measurements of surface displacement by isolating the change in the two-way travel distance computed from the phase difference between a pair of SAR images collected at different times. A satellite InSAR monitoring program measures a time series of mm-scale surface displacement, or deformation (the terms displacement and deformation are used interchangeably in this paper) for each pixel in the SAR image..

With image sizes spanning tens of kilometres and pixel resolutions typically on the order of a few metres, InSAR is a powerful technique to monitor surface movement

The surface displacement measured by InSAR is highly dependent on the viewing geometry from the SAR to the target, described by the line-of-sight (LOS) vector. In some cases, the surface displacement can be significantly underestimated, impeding accurate interpretation of the measurements to inform decision-making tools or criteria based on the data being illustrated. InSAR measurements from a diverse range of viewing geometries can be considered together to help reduce this bias. The available viewing geometries to a particular target depends on available SAR satellite orbits; since most SAR satellites are in sun-synchronous orbits (SSO) there is limited diversity in currently available viewing geometries.

MDA Space will soon be offering MDA CHORUS, a next-generation dual-frequency C- and X-band SAR satellite constellation which will deliver significantly enhanced Earth observation capability (Sharma *et al.*, 2022, 2024; Eppler *et al.*, 2023; Greene Gondi *et al.*, 2023). Extensive imaging coverage and a novel mid-inclination orbit will offer unique perspectives for imaging that will revolutionise the way in which SAR data can be utilised for change detection and ground displacement monitoring. The unique viewing geometries enabled by CHORUS will better constrain InSAR analyses to reduce bias in the magnitude of measured surface displacement and resolve the three-dimensional (3D) orientation of ground movement (Wright *et al.*, 2004). Furthermore, CHORUS will improve InSAR coverage over complex topography by illuminating pixels otherwise obscured by SAR imaging distortions resulting from the fixed viewing geometries of SSO SAR sensors.

In this work, we present the results of simulations illustrating InSAR coverage and expected 3D InSAR surface displacement measurement for the Venetia diamond mine in South Africa. We first provide background for measuring 3D surface displacement from InSAR. We then describe the datasets used and details of the 3D simulations. Finally, we present the simulation results and discuss their implications for InSAR monitoring programs for surface displacement.

Background

In this section we provide the necessary context to understand limitations of InSAR measurements that are considered in this study.

Three-dimensional InSAR geometry

Repeat-pass InSAR measures a projection of surface displacement as per the SAR LOS diagram as depicted in Figure (Greene Gondi *et al.*, 2023; Brouwer and Hanssen 2023).

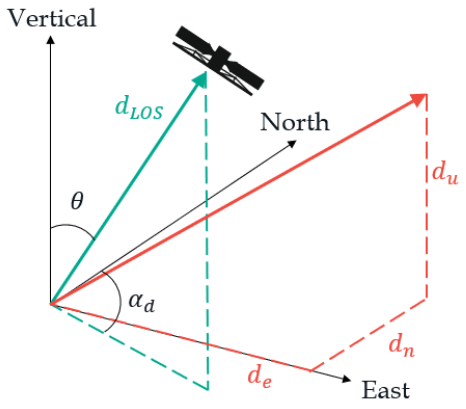


Figure 1. Three-dimensional InSAR geometry with SAR LOS.

In Figure 1, θ is the incidence angle from the target to the SAR sensor and α_d is the azimuth of the zero-doppler plane from the target toward the SAR sensor, following the technique described by Brouwer and Hanssen (2023).

Unless the SAR LOS is perfectly aligned with the surface displacement vector, the displacement measurement using InSAR will be underestimated. To ease interpretation of InSAR measurements, LOS observations are often projected to vertical using the incidence angle alone by assuming there are no horizontal components to the surface displacement. This can result in substantial errors when a horizontal component is present, especially for shallow incidence angles (Furhmann and Garthwaite 2019). This idea can be extended to two-dimensions when there are multiple InSAR LOS observations available from SSO SAR sensors. Since these sensors have LOS typically aligned with the east-west plane, the InSAR LOS measurements are decomposed into vertical and east components by assuming negligible contributions from the north component (i.e., Samsonov and d'Oreye 2017). This can similarly result in large errors when a north-south component of surface displacement is present. These errors can significantly impact the geotechnical interpretation of the InSAR measurements in assessing the amount of ground movement accumulation in magnitude over time.

The full 3D reconstruction of the surface displacement for a target requires at least three distinct InSAR LOS measurements. The process of inverting a set of LOS InSAR measurements to compute the 3D components of the measured surface displacement is termed '3D decomposition'. In this paper, we focus solely on the impact of viewing geometry on the 3D decomposition solution. The accuracy of the 3D decomposition is related to the diversity of InSAR LOS vectors used, where the limited viewing geometries of current SSO SAR sensors results in poor reconstruction of horizontal displacement in the north-south plane (Wright *et al.*, 2004; Greene Gondi *et al.*, 2023).

The MDA CHORUS Mission

The CHORUS SAR constellation consists of two satellites, a C-band SAR (CHORUS-C) built by MDA Space and an X-band SAR (CHORUS-X) supplied by ICEYE. CHORUS builds on the substantial heritage of the RADARSAT program with the addition of new and enhanced features for improved Earth observation capabilities. CHORUS will offer left- or right-looking imaging on both CHORUS-C and CHORUS-X between a 24.5° and 63.9° incidence. This results in a 700 km accessible swath and coverage between ±62.5° latitude (89% global access). The maintained orbital tube supports interferometric exploitation of Stripmap and Spotlight beam modes. With a repeat cycle of 9.85 days, CHORUS will provide high quality repeat-pass InSAR for deformation monitoring. For a more complete description of the mission and available beam modes, the reader is referred to Sharma *et al.*, (2024). CHORUS is currently targeted for launch in mid-2026. The orbit parameters for CHORUS are described in Table I (Sharma *et al.*, 2024; Greene Gondi *et al.*, 2023).

Table I. MDA CHORUS orbit parameters

Orbit Parameter	**Value**
Type	Mid-inclination, non sun-synchronous
Altitude	~600 km
Inclination	53.5° (prograde)
Repeat cycle	9.85 days (147 orbits)
Phasing	Same ground track, CHORUS-X trails CHORUS-C by 1 hour
Orbit control	Maintained in an orbital tube suitable for repeat-pass interferometry

The LOS from CHORUS to a particular target complements those from existing SSO SAR sensors, such as RADARSAT-2. This angular diversity provides much needed information in the retrieval of 3D components of surface deformation using InSAR. The benefits of a mid-inclination orbiting SAR sensor in 3D surface displacement retrieval from InSAR have been theorised as early as Wright *et al.*, 2004.

CHORUS provides an industry first for this technique to be physically realised for routine InSAR monitoring, thereby changing the landscape for InSAR data assessment as it is currently known,

understood and utilised. These advanced 3D displacement and deformation datasets are integral for the stability and performance assessment of pit slopes and other mine-related infrastructure, such as tailings storage facilities (TSF) and waste rock dumps.

METHODOLOGY

In this section, we describe the simulations performed to demonstrate the improvement in recovering 3D surface displacement from InSAR measurements when CHORUS is incorporated in a monitoring plan.

Dataset

The Venetia diamond mine in South Africa was the AOI used for the simulations in this work. The AOI contains variable topological structures including the TSF embankments and open-pit walls (Figure 2).

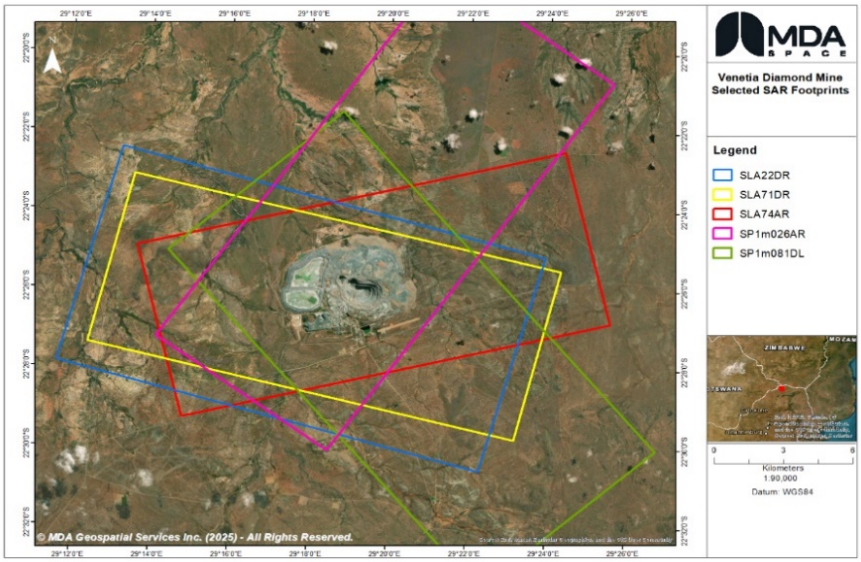


Figure 1. Venetia Diamon Mine AOI with RADARSAT-2 and CHORUS-C swath extents. See Table for a description of beam modes.

The complex topography of the Venetia AOI presents significant challenges to InSAR deformation monitoring. The considerable slopes at varying aspects over the AOI introduce SAR image distortions (i.e., layover, shadow, and foreshortening) that will obscure different areas of the mine when imaged from different directions. Furthermore, the varying slope aspects introduce a wide range of directions in which surface material can move in response to different deformation mechanisms. We used the 5-m WorldDEM Neo digital surface model generated from satellite imagery and interferometric elevation data between 2017 to 2021 to characterise the complex topography over the AOI (Figure 3).

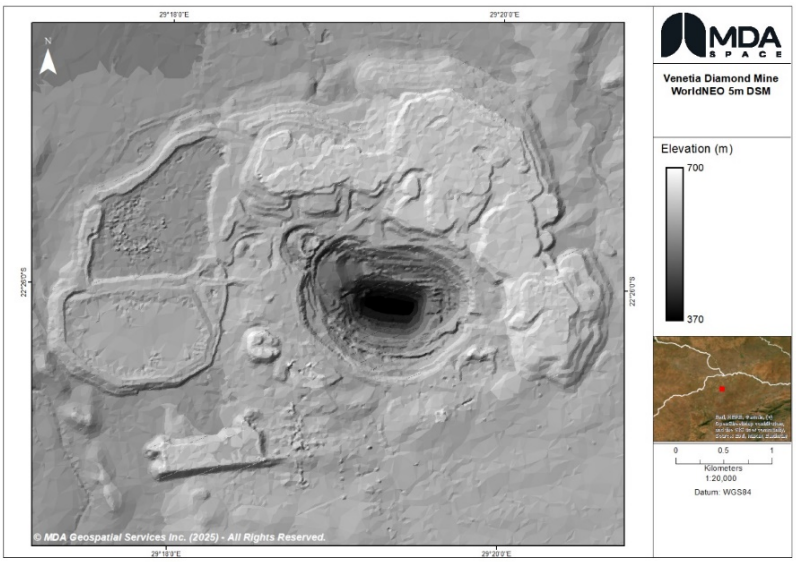


Figure 3. WorldNeo 5m DSM for the Venetia Diamond Mine AOI.

We considered various combinations of SAR images from RADARSAT-2 and CHORUS-C to simulate 3D InSAR results over the AOI. Our analysis is concerned with the viewing geometries offered by the beam modes selected from each SAR sensor to simulate the 3D InSAR performance. As such, the RADARSAT-2 performance is indicative of it's SSO and not the SAR sensor itself; all SSO SAR sensors will be constrained by similar viewing geometries by nature of sharing similar orbits. Table II summarizes the various beam modes considered for this analysis.

Table II. RADARSAT-2 and CHORUS-C beam modes considered for the AOI in our simulation

Beam identifier	SAR satellite	Beam mode	Orbit direction	Look direction	Incidence angle	Beam heading
SLA22DR	RADARSAT-2	Spotlight	Descending	Left	46°	195°
SLA71DR	RADARSAT-2	Spotlight	Descending	Left	21°	194°
SLA74AR	RADARSAT-2	Spotlight	Ascending	Right	24°	345°
SP1m081DL	CHORUS-C	Spotlight	Descending	Left	54°	139°
SP1m026AR	CHORUS-C	Spotlight	Ascending	Right	37°	35°

The selection of beam modes described by Table II was carefully chosen to provide ideal viewing geometries for 3D decomposition of LOS InSAR measurements.

Simulations

We simulated a 5 mm/year deformation rate in the downslope direction for all slopes greater than 5° across the AOI. For each pixel in the DSM, the downslope vector was defined by the azimuth angle of the slope face (i.e. the aspect) and the inclination angle with respect to the horizontal plane (i.e. the slope). This downslope deformation was then decomposed into the east-west, north-south, and vertical components for each pixel. Figure 4 shows the simulated deformation components for the Venetia mine AOI.

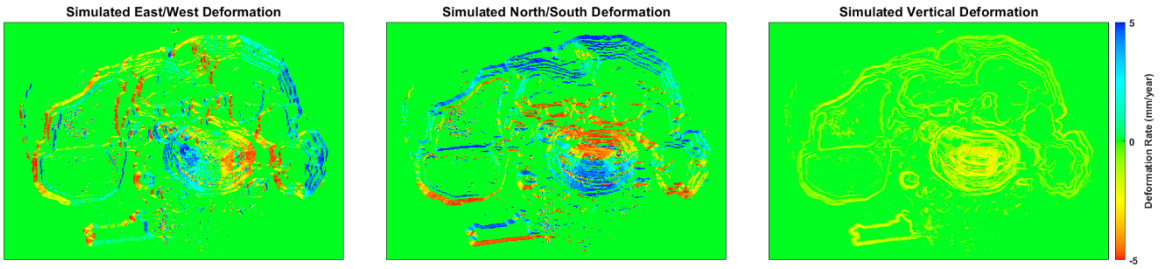


Figure 4. Simulated 3D surface displacement for the Venetia mine AOI using the WorldNeo DSM.

The LOS deformation rate measured by each SAR beam from Table II was computed by projecting the simulated downslope deformation rate to the LOS vector for each beam. Representative noise of 1 mm/year was added to each LOS measurement to analyse the stability of 3D decomposition solutions in the presence of noise.

Two separate 3D decompositions of the LOS InSAR measurements were carried out to investigate how well the 3D surface displacement would be captured in either scenario. The first scenario, Case 1, considers the three RADARSAT-2 beams only, which represents the 3D InSAR capabilities of SSO SAR sensors. The second scenario, Case 2, considers the optimal combination of RADARSAT-2 and CHORUS-C beams to provide the best precision in 3D decomposition of LOS InSAR surface displacement measurements. Through an optimisation procedure, the ideal beam combination for Case 2 was determined to include the SLA22DR, SP1m08DL, and SP1m026AR beams (Table III).

Table III. Scenarios considered in simulating performance of 3D decomposition from LOS InSAR measurements

Simulation Identifier	**Combination of SAR sensors used**
Case 1	RADARSAT-2
Case 2	RADARSAT-2 & CHORUS-C

We computed masks identifying pixels obscured by SAR imaging distortions (i.e., foreshortening and shadow) resulting from the imaging geometry for each beam in Table II. We computed the union of the masks for the beam mode combinations in Cases 1 and 2 to create a combined mask that shows where SAR distortions inhibit 3D decomposition.

RESULTS

LOS InSAR deformation results

Here we present the LOS deformation rate measurements of the simulated deformation rates in Figure 4 by each beam in Table II. Figure 5 shows the LOS InSAR deformation rates for the three RADARSAT-2 beams considered in Case 1.

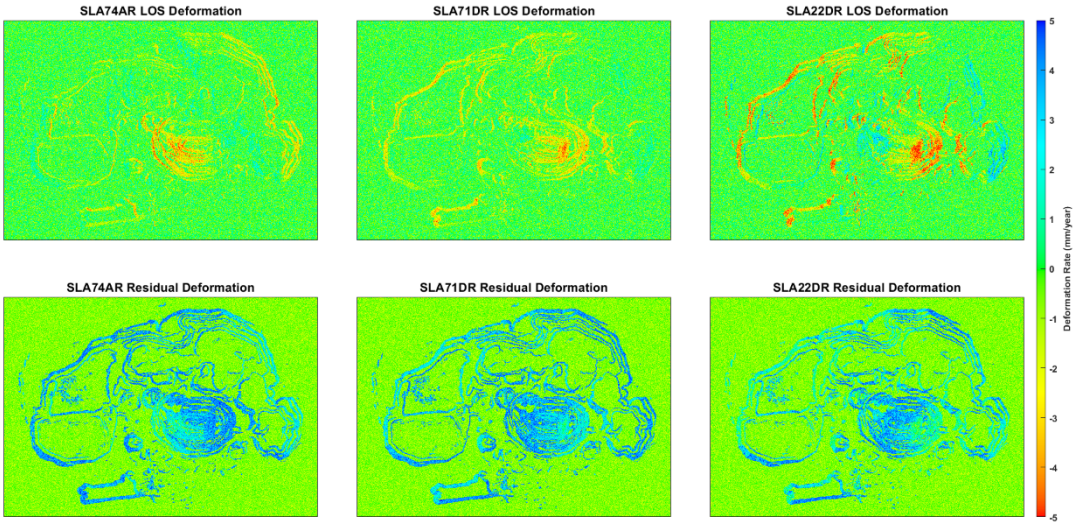


Figure 5. Simulated LOS deformation rate for the RADARSAT-2 beams in Case 1 (top row) and residual deformation between the LOS deformation rate and the simulated deformation.

The residual between the LOS deformation and simulated deformation is provided in the bottom row of Figure 5 to facilitate easier comparison. It can clearly be seen that the sensitivity of the LOS InSAR measurements strongly depends on the surface displacement vectors relative to the SAR imaging geometry. In general, SSO SAR sensors, such as RADARSAT-2, are more sensitive to horizontal surface displacement in the east-west plane as opposed to the north-south plane. The steep incidence angles of the SLA74AR and SLA71DR beams demonstrate this as the steeper west-facing and east-facing slopes show larger surface displacement than north-facing or south-facing slopes. Alternatively, the shallower incidence angle of the SLA22DR provides greater sensivitiy to horizontal motion and captures surface displacement across a variety of slopes in the AOI.

Figure 6 shows the LOS deformation rates and residuals compared to the simulated deformation for the single RADARSAT-2 and two CHORUS-C beams considered in Case 2. There is a significant difference in the measured LOS deformation from CHORUS-C compared to RADARSAT-2 visible between Figures 5 and 6. Similar dependencies on the measured LOS deformation and viewing geometry for the CHORUS-C beams as for the RADARSAT-2 beams is evident.

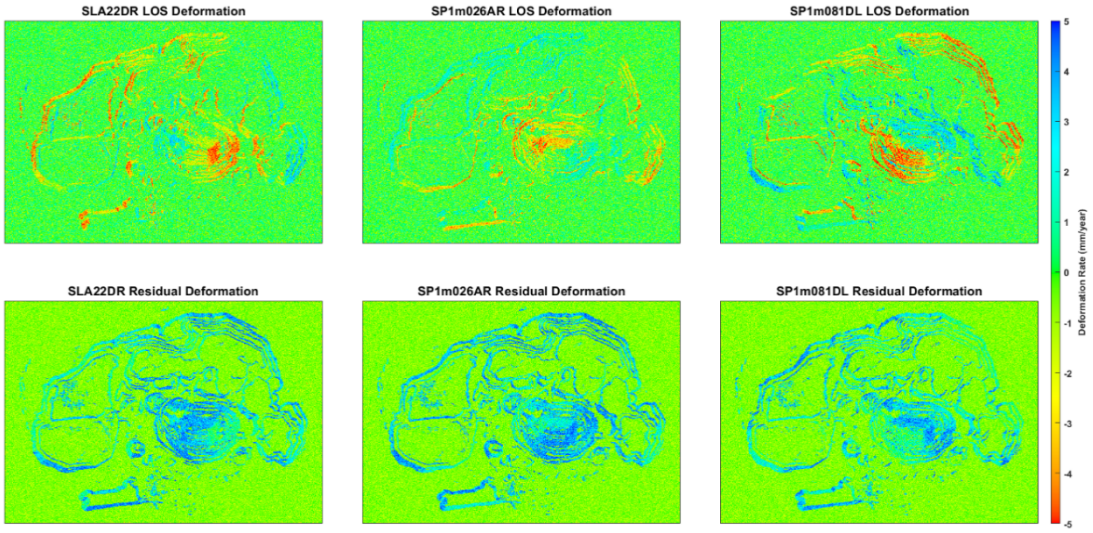


Figure 6. Simulated LOS deformation rate for the RADARSAT-2 SLA22DR and CHORUS-C beams in Case 2 (top row) and residual deformation between the LOS deformation rate and the simulated deformation (bottom row).

3D decomposition

Here we present the results of performing 3D decompositions of the LOS deformation rates for beam combinations in Case 1 and 2. Figure 7 shows the 3D surface displacement results when decomposing the three RADARSAT-2 spotlight modes in Case 1.

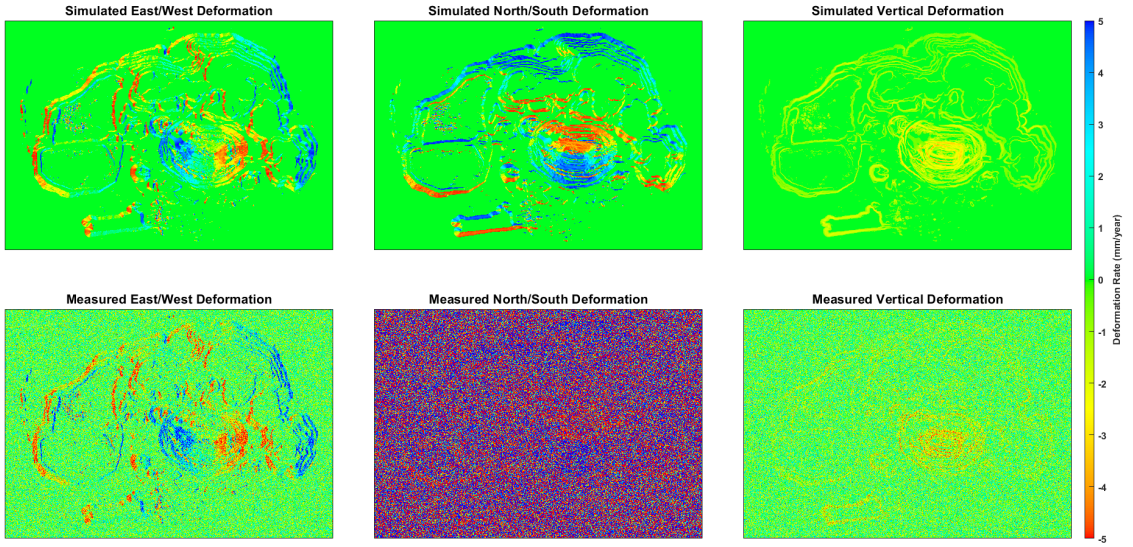


Figure 7. Simulated east, north, and vertical deformation rate components (top row) and corresponding 3D decomposed deformation rates using the LOS InSAR measurements for Case 1 (RADARSAT-2 only) (bottom row).

For Case 1, we see that the RADARSAT-2 LOS InSAR deformation rates provide little to no information on the north-south component of surface displacement. In the resulting 3D decomposition (Figure 7), the measured north-south component is unstable and highly influenced by the noise in the LOS InSAR measurements. Figure 8 shows the 3D surface displacement results when decomposing the RADARSAT-2 spotlight mode with two CHORUS-C spotlight modes in Case 2.

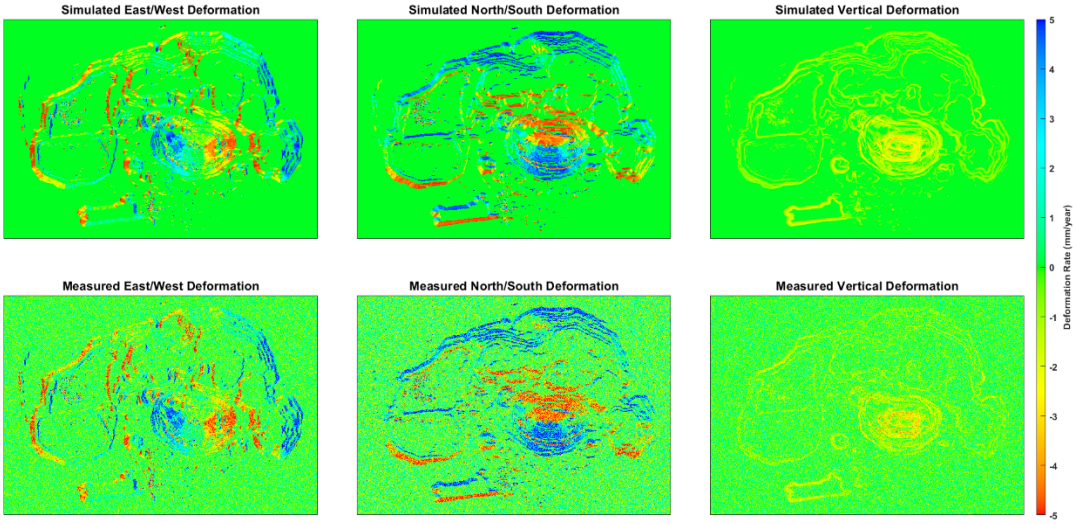


Figure 8. Simulated east, north, and vertical deformation rate components (top row) and corresponding 3D decomposed deformation rates using the LOS InSAR measurements for Case 2 (RADARSAT-2 and CHORUS-C (bottom row).

In Case 2 (Figure 8) we observe a significant improvement in the 3D decomposition of the north-south component of surface displacement enabled by the unique LOS viewing geometries of the incorporated CHORUS-C beams. The overall magnitude of measured surface displacement might be of interest to stakeholders in an InSAR monitoring program. In this case, capturing any north-south oriented surface displacement is paramount to reducing bias in this estimation. Figure 9 shows the residuals between the magnitude of surface displacement obtained by 3D decomposition in Cases 1 and 2 and the simulated deformation. Note that the colour scale has been reduced from ± 5 mm/year to ± 3 mm/year to better highlight the differences in the results.

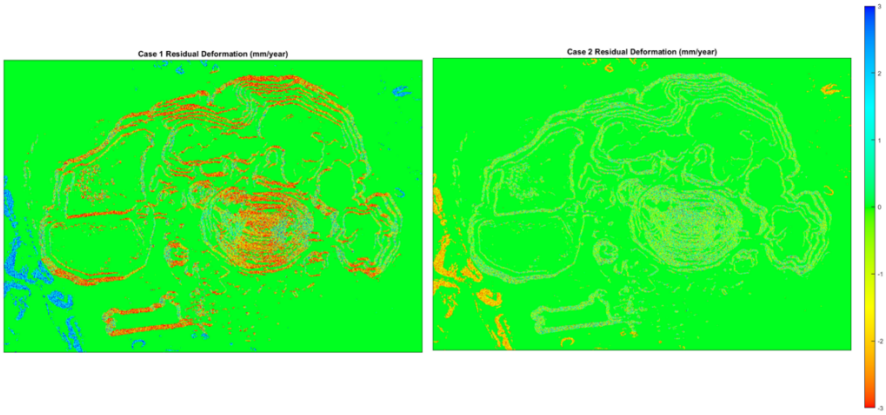


Figure 9. Residuals between the magnitude of the 3D decomposed surface displacement measurements in Case 1 and 2 with the simulated deformation.

Foreshortening and shadow analyses

Figure 10 shows the combined shadow and foreshortening masks for the beam combinations considered in Case 1 and 2. These masks show pixels that would be distorted in at least one SAR image from the different beams comprising either scenarios due to SAR foreshortening or shadow. For Case 1, in which only RADARSAT-2 beams are considered, the dominant contributor to the combined mask is

foreshortening introduced from the relatively steep SLA71DR and SLA74AR beams with minimal shadow masking. Most of the masked pixels are on the east-facing and west-facing slopes. For Case 2, the main contributor to SAR image distortions is shadow from the SP1m081DL CHORUS-C beam. This results in the east-, west-, and south-facing slopes having more masked pixels.

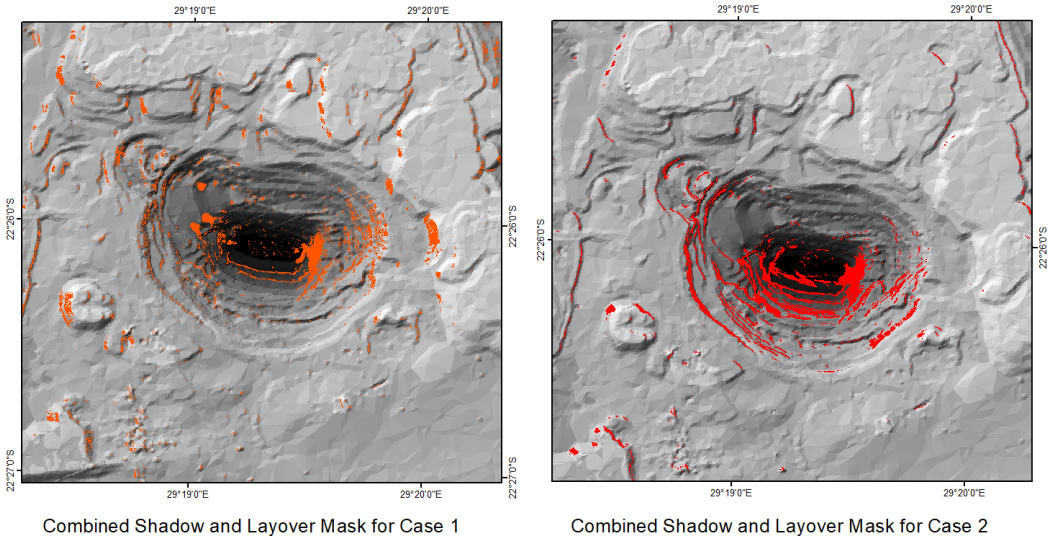


Figure 10. SAR image distortion masks indicating pixels obscured by foreshortening and shadow from the combined LOS viewing geometries of beams considered in Case 1 (left) and Case 2 (right).

DISCUSSION

The LOS deformation results presented in Figures 5 and 6 convincingly show how the magnitude of surface displacement will typically be underestimated by a single InSAR measurement. In all cases, regardless of SAR sensor, simulated motion within the AOI is not fully captured by any individual LOS InSAR measurement. The ability for each independent RADARSAT-2 or CHORUS-C beam mode to capture surface displacement depends on how well the motion is aligned with the LOS vector to the SAR sensor during each image acquisition. By considering LOS InSAR measurements from multiple SAR sensors, it is possible to increase the measurement coverage across the AOI. While the full 3D decomposition necessitates visibility from at least 3 LOS InSAR measurements, separately analysing the LOS InSAR from each of the three beam modes provides some level of indication of surface displacement over a broader range of slopes than is possible with any single beam mode.

The 3D decomposition results presented in Figures 7 and 8 clearly demonstrate the improvement in reconstructing the 3D components of surface displacement from LOS InSAR when incorporating CHORUS into the monitoring plan. In Case 1, which only uses data from SSO SAR sensors (i.e. RADARSAT-2), we see representative reconstruction of the east-west deformation, which highlights the fact that these sensors have LOS vectors typically aligned with the east-west plane. The vertical deformation is also captured well, given the dominance of steep incidence angles in the beam mode combination; however, the noise levels in the LOS measurements obscure this relatively subtle deformation signature. There is virtually no sensitivity to reconstructing the north-south deformation component and the decomposition is highly unstable in this component. In contrast, the 3D decomposition results for Case 2, which incorporates CHORUS-C, shows improved reconstruction of all 3D surface displacement components. The increased angular diversity provided by the CHORUS-C beams results in a much more stable solution that is robust to noise. The difference in the ability to measure surface displacement between Case 1 and Case 2 is illustrated well by Figure 9, which shows that the magnitude of surface displacement measured by SSO SAR sensors will underestimate the total motion if north-south components are present. In contrast, the InSAR monitoring incorporating CHORUS (Case 2) provides a much more accurate depiction of the surface displacement.

The foreshortening and shadow masks for Cases 1 and 2 in Figure 10 illustrate the areas of the AOI where 3D decomposition would not be possible due to the SAR image distortions. The unique LOS vector for each beam considered in this study is associated with a distinct set of pixels experiencing foreshortening and shadow. The increased angular diversity needed for accurate 3D decomposition results in a broader set of pixels distorted in SAR images. However, when only considering LOS InSAR measurements, the set of pixels visible from at least one beam mode will increase measurement coverage with increased angular diversity.

While there are practical constraints (i.e. cost, time) to how many SAR beam modes can be incorporated into an InSAR monitoring program, by increasing this number the resulting 3D decomposition will generally be improved. Added redundancy in the decomposition provides noise suppression. Further, the unique SAR image distortions from each beam mode introduce the opportunity to increase coverage of 3D InSAR over the AOI by considering different beam combinations for each pixel. A comprehensive InSAR monitoring plan includes careful selection of beam modes that balance measurement coverage with 3D InSAR performance, given the unique characteristics of the AOI and requirements in surface displacement monitoring.

CONCLUSION

In this paper, we have presented an analysis of how MDA Space's upcoming MDA CHORUS SAR constellation mission will provide enhanced InSAR capability by enabling precise 3D decomposition of measurements to retrieve the 3D components of surface displacement. We discussed how 3D decomposition performance is strongly affected by the viewing geometry between SAR sensors and targets. Introducing the CHORUS mission, we highlighted that the mid-inclination orbit of CHORUS provides unique viewing geometries that can complement existing InSAR perspectives from SSO SAR sensors. These effects were illustrated by simulating surface displacement at the Venetia diamond mine in South Africa. Our results show how CHORUS-C improves the ability to reconstruct 3D surface displacement from independent line-of-sight InSAR measurements from different SAR beams. This improved InSAR capability is critical to realising the full potential of SAR technology to support safe mining operations and inform geotechnical risk assessment.

REFERENCES

Brouwer, W.S. and Hanssen, R.F. (2023) A Treatise on InSAR Geometry and 3-D Displacement Estimation. *IEEE Transactions on Geoscience and Remote Sensing*, vol. 61, pp. 1-11.

Eppler, J., Mantle, V., Sharma, J. and Caves, R. (2023) CHORUS SAR Constellation: A Mission Capability Overview. *Presented at the 12th International Workshop on Advances in the Science and Applications of SAR Interferometry and Sentinel-1 InSAR – FRINGE 2023.* Leeds, United Kingdom.

Furhmann, T. and Garthwaite, M.C. (2019) Resolving Three-Dimensional Surface Motion with InSAR: Constraints from Multi-Geometry Data Fusion. *Remote Sensing*, vol. 11, no. 3, pp. 1-22.

Greene Gondi, F., Eppler, J., Caves, R. and MDA CHORUS TEAM (2023) Enabling 3D Deformation Monitoring with the CHORUS SAR Constellation. *Presented at the 12th International Workshop on Advances in the Science and Applications of SAR Interferometry and Sentinel-1 InSAR – FRINGE 2023.* Leeds, United Kingdom.

Samsonov, S.V. and d'Oreye, N. (2017) Multidimensional Small Baseline Subset (MSBAS) for Two-Dimensional Deformation Analysis: Case Study Mexico City. *Canadian Journal of Remote Sensing*, vol. 43, no. 4, pp. 318-329.

Sharma, J. and Caves, R. (2022) CHORUS – Changing How and When We Observe Our Planet. *EUSAR 2022; 14th European Conference on Synthetic Aperture Radar.* VDE, Leipzig, Germany, pp 1-4.

Sharma, J., Caves, R. and Mantle, V. (2024) CHORUS Mission Update. *EUSAR 2024; 15th European Conference on Synthetic Aperture Radar*. VDE, Munich, Germany, pp. 1008-1011.

Wright, T.J., Parsons, B.E. and Lu, Z. (2004) Toward mapping surface deformation in three dimensions using InSAR. *Geophysical Research Letters*, vol. 31, no. 1, pp. 1-5.



Dylan Hickson

Senior Member of Technical Staff - Systems
MDA Space

Dylan is a Senior Engineer at MDA Space in the Geointelligence business area with over 11 years of professional experience and graduate education in a wide range of radar applications, geophysical inversion, remote sensing, and data analysis. He obtained two B.Sc. degrees in Earth and Environmental Science and Physical Science from McMaster University in 2014 and his Ph.D. degree in Earth and Space Science from York University in 2019. Prior to joining MDA Space, Dylan was a Preeminent Postdoctoral Scholar with the University of Central Florida researching in planetary radar applications at the Arecibo Observatory and a Research Associate in the Department of Geophysics at the Colorado School of Mines researching in orbital radar sounding applications. In his current role, Dylan develops new capabilities for analyses of interferometric (InSAR) and polarimetric synthetic aperture radar (SAR) data in Earth observation. His efforts support geospatial analysis services offered by MDA Space in environmental monitoring for surface deformation and change detection leveraging InSAR/SAR data. He has published over 65 peer reviewed papers and conference abstracts on various aspects of radar applications, Earth observation, and planetary science. The asteroid 33896 Hickson is named after him by the International Astronomical Union.

Klipgat boxcut portal entrance and decline system: Long-term stability assessment and monitoring

S. Vezi[1], R.T Masethe[2]

[1]African Rainbow Minerals, South Africa.
[2]University of KwaZulu-Natal, South Africa

This study assesses the long-term monitoring of the Klipgat boxcut portal entrance, as well as the long-term stability analyses of the three-decline cluster. The cluster consists of one decline measuring 6 m x 4.5 m and two other declines, each measuring 5 m x 4.5 m, separated by 8-metre-wide pillars. The evaluation focuses on the first 20 m of the declines and the associated pillars, where the rock is classified as competent but still requires an effective support system. Ground conditions range from poor and fair to good. A multi-faceted approach was used to analyse stability, including geological surveys, stress and kinematic modelling, and ground monitoring. The monitoring system employs geotechnical instruments such as early warning extensometers, Bluetooth extensometers, and Interferometric Synthetic Aperture Radar to detect rock movement. Initial monitoring indicates overall stability, with minimal displacement observed. However, localised weak zones due to weathering suggest additional reinforcement may be needed. The support system includes rock bolts, mesh, and shotcrete. Continuous monitoring and adaptive reinforcement strategies are essential to maintaining stability and ensuring safe mining operations.

Keywords: boxcut, portal, kinematics modelling, declines, portal, optimization, long-term stability

INTRODUCTION

Bokoni mine is located 45 km northwest of Burgersfort on the far northern extremity of the eastern limb of the Bushveld Igneous Complex in the Limpopo province. African Rainbow Minerals owns the mine and has a total strike length of approximately 24.5 km in the northwest-southeast orientation. The critical zone layer dips undisturbed to the south. The Merensky and UG2 reefs are the two platinum-bearing reefs and only UG2 is currently being mined. The key economic horizons in the Southern Upper Critical and Main Zones are the platinum group minerals found in the Merensky reef and the underlying UG2 chromitite reef. The high-grade Merensky reef has been extensively exploited, with mining depths between 60 m and 500 m dipping between 15° to 25°. It is a persistent, tabular orebody composed of pegmatoid, chromitite, and pyroxenite layers. Structurally, it consists of an upper feldspathic pyroxenite assemblage within the Upper Group of the Upper Critical Zone, overlying a basal chromitite stringer, followed by an anorthosite-to-norite footwall and a thin (0.1–0.2 m) anorthosite layer underlain by norite (Lougher & Mellowship, 1991). The UG2 reef historic mining depths vary between 40 m and 290 m and dips between 14° to 22° south. The UG2 and Merensky reefs are sub-crops and sometimes outcrops on the mining lease area. The approximate middling between the Merensky and UG2 reefs is about 350 m (Van der Kevie, 2019). A range of pyroxenite hills overlies the north-eastern portion of the mining area, and the south-western portion is below the valley floor, overlain by black turf (Minxcon, 2013). Figure 1 shows the location and geology of Bokoni Platinum mine in the far eastern limb. Figure 2 illustrates the stratigraphical column of UG2 and Merensky.

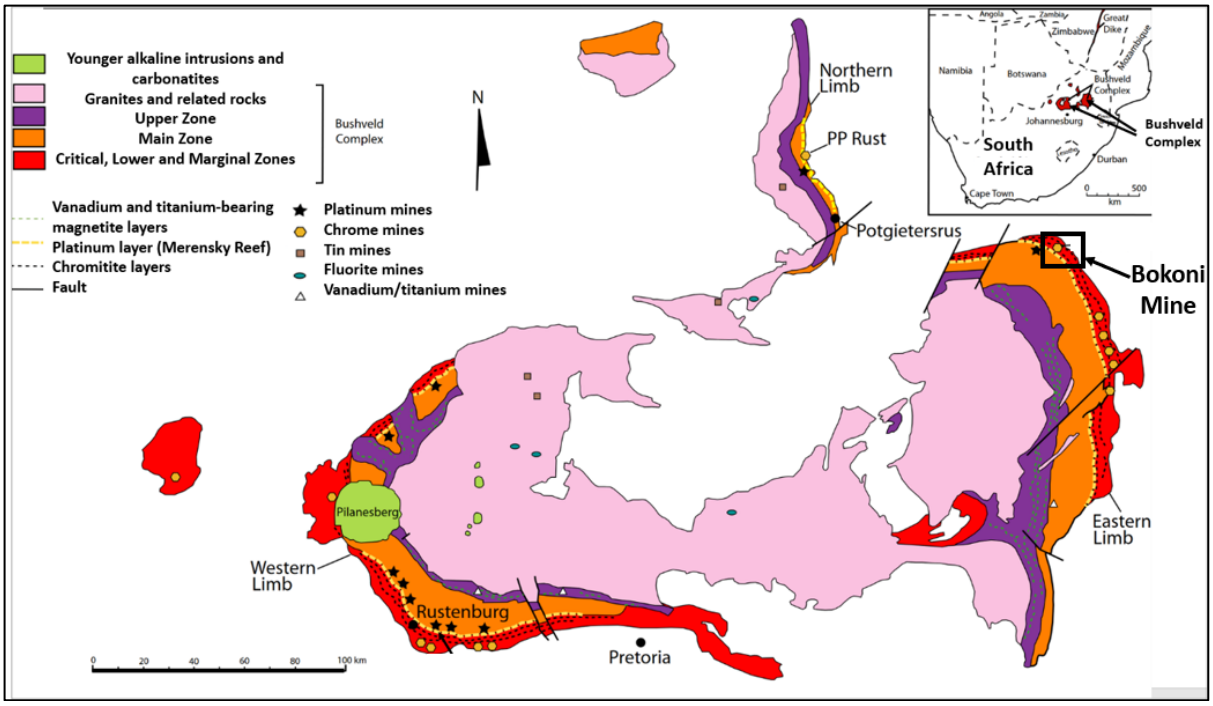


Figure 1. Geological map of the Bushveld Igneous Complex- Bokoni Platinum mine in a red square (Taylor et al.*, 2005).*

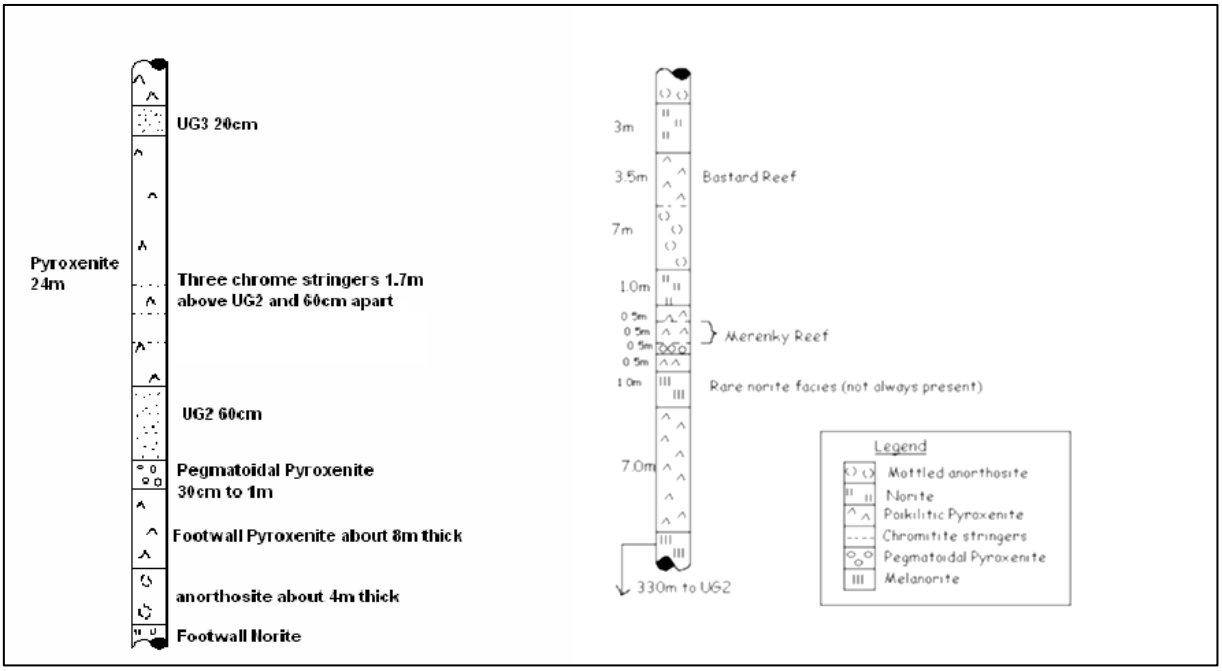


Figure 2. Stratigraphic column for UG2 and Merensky.

The development of the Klipgat boxcut is cut on the waste that will form the boxcut, and the portal entrance and declines are developed toward underground mining of the UG2. It is developed to establish access to the orebody, enhance orebody tramming and handling, and improve ventilation within underground working areas. The design and placement of the portal are critical for the efficiency and safety of mining operations. The long-term stability of underground excavations is essential for safe and efficient mining. The Klipgat portal, consisting of three decline clusters measuring 6 m x 4.5 m and

two clusters of 5 m x 4.5 m, separated by 8-m-wide pillars, creates a complex underground structure that requires detailed stability assessment. The main focus of this study is on the first 20 m of the declines and the associated pillars, where the rock mass is classified as competent but still requires an effective support system to maintain stability.

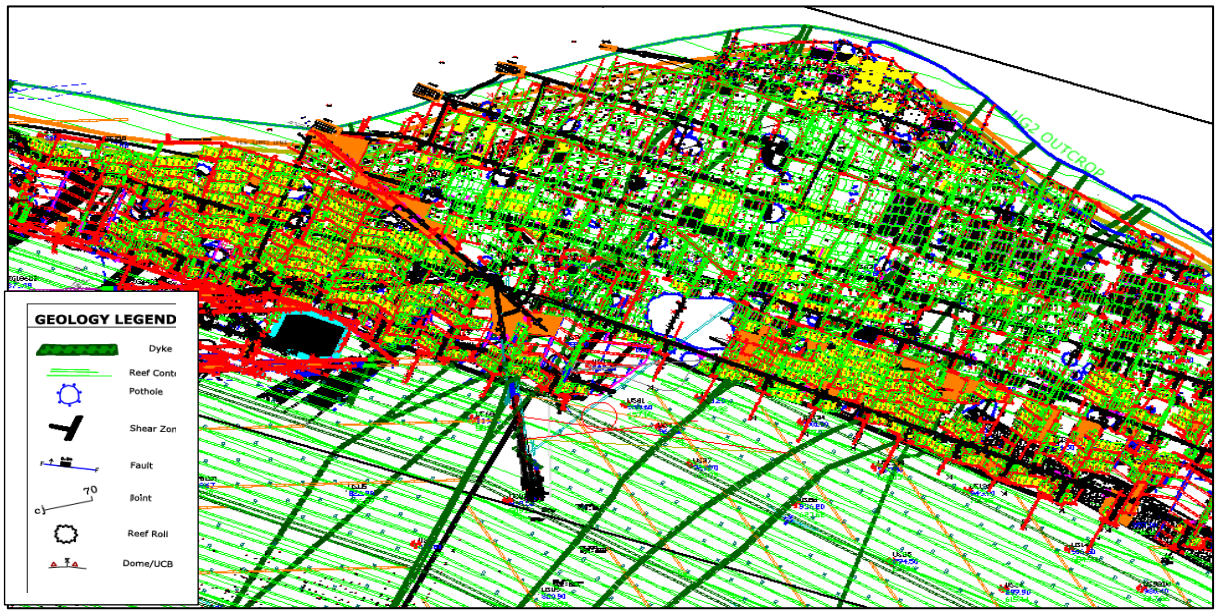


Figure 3. Local geological plan of the Bokoni Platinum mine.

The assessed decline layout reaches a final depth of approximately 20 m by passing the weathered rock mass into norite, with a variable thickness of weathered or overburdened material. The boxcut was divided into three design sectors to evaluate slope stability, each defined by its planned wall orientation. These design sectors are visually represented in Figures 4 and 5. The weathering depth for each borehole was determined using the drilled core. To estimate the average weathering depth in the boxcut and portal area, the values from Geotech boreholes 1 and 2 were averaged. Observations revealed a minimum weathering depth of 4.50 m on one of the benches and a maximum of approximately 6.28 m (Figure 4). As the slope gradient increases, the weathering depth will decrease, necessitating further validation. The benches range between 8.5 m and 10 m in the fresh material. Based on current data and the consultancy reports, the average weathering thickness of 5.50 m represents this analysis's value.

This study integrates geological surveys, stress and kinematic modelling, and ground monitoring to assess structural integrity. The monitoring system utilises advanced geotechnical instruments, including early warning extensometers, Bluetooth extensometers, and interferometric synthetic aperture radar (InSAR), to detect rock movement and provide early warnings of instability. Preliminary findings indicate overall stability with minimal displacement; however, localised weak zones caused by weathering suggest that additional reinforcement may be necessary. The current support system comprises rock bolts, mesh, and shotcrete, which help maintain the structural integrity of the declined entrance and pillars (Nel *et al.*, 2022). Continuous monitoring and adaptive reinforcement strategies ensure long-term stability and safe mining operations. By combining traditional geotechnical analysis with advanced monitoring technologies, this study aims to contribute to the broader understanding of excavation stability in underground mining environments.

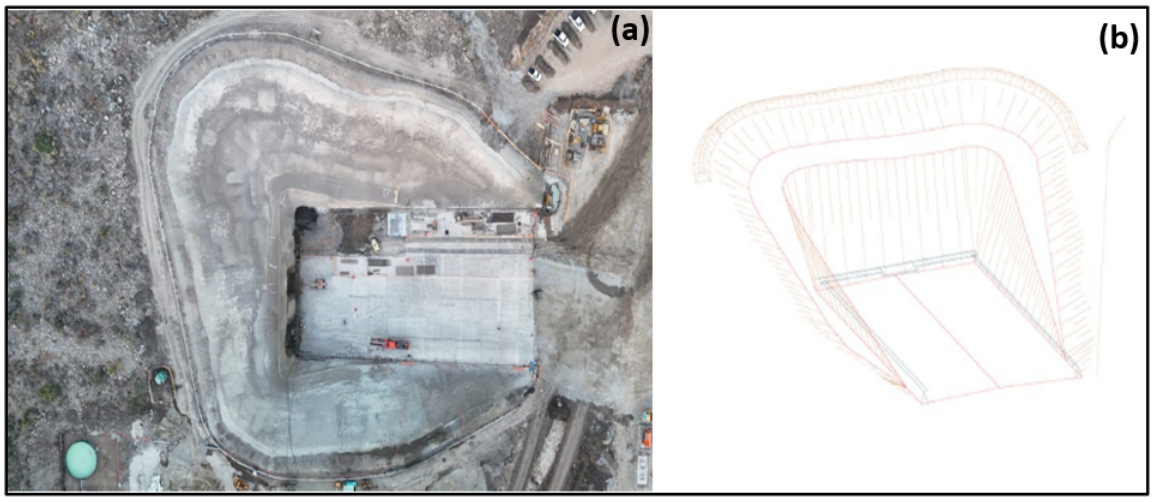


Figure 4. The portal entrance and the Klipgat boxcut.

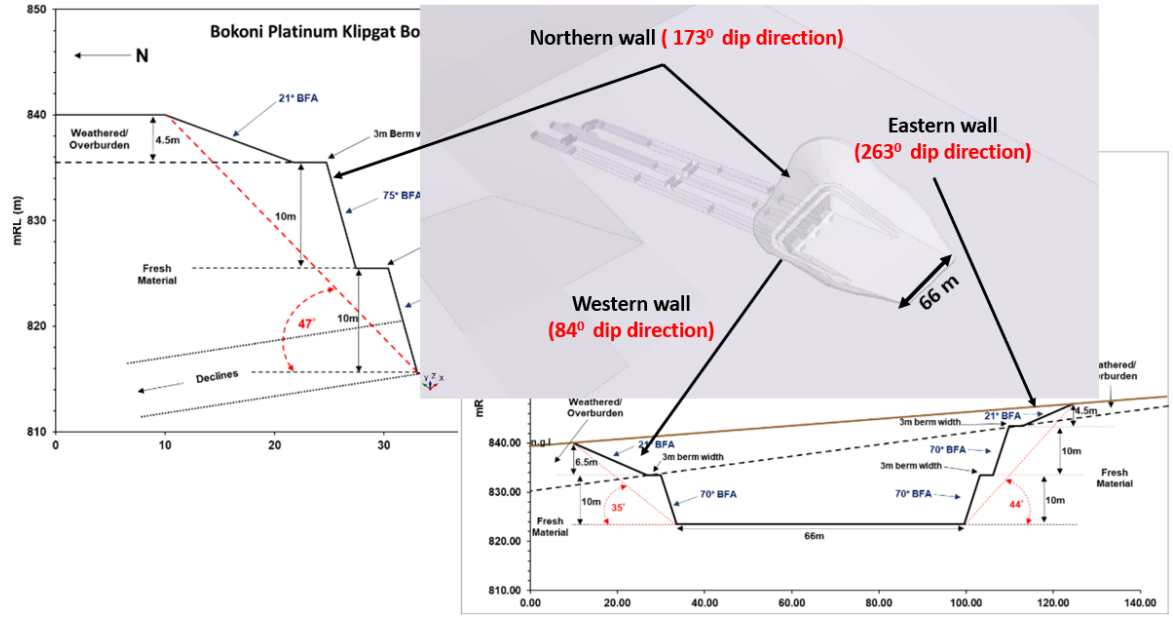


Figure 5. Three design sectors to evaluate slope stability (Western, Northern, Eastern walls) (Nel et al.*, 2023).*

DATA COLLECTION AND GEOTECHNICAL SETTINGS

Data collection methods

Scanline mapping was conducted following International Society for Rock Mechanics guidelines using a measuring tape to record the trend and plunge, though the orthogonal setup was restricted due to safety and access limitations. Data collection included structural characteristics such as weathering, persistence, roughness, infill type, groundwater presence, and dip/dip direction. Boreholes were chosen based on their spatial distribution; however, the core yard limited access to only four boreholes for geotechnical logging. Logging focused on the UG2 orebody zones, with recorded parameters including drill run, rock type, weathering, hardness, core recovery (TCR & SCR), rock quality designation (RQD), and joint/piece counts per run. The data obtained from scanline mapping and core logging were analysed to derive these geotechnical parameters detailed in this section.

Rockmass Classification

In rock engineering design, the rock mass is a highly complex and geological material heterogeneous, with ground behaviour influenced by geological conditions, stress regimes, and tunnel-specific characteristics during tunnel construction (Hoek, 2007). To evaluate and manage these complexities, several rock mass classification systems have been developed, including the rock mass rating (RMR89), tunnelling quality index (Q-rating), modified tunnelling quality index (Q′), and geological strength index (GSI), which provide a standardised framework for characterising rock mass properties, estimating stability, and determining appropriate support measures (Bieniawski, 1989; Barton et al., 1974; Hoek et al., 1995). Since no single classification system is universally applicable, researchers such as Hoek and Brown (1997) emphasise adapting these classifications to site-specific conditions rather than applying them rigidly across all geological environments.

RMR_{89}, originally introduced by Bieniawski (1973), remains one of the most widely applied classification systems for tunnelling and rock engineering. The system has evolved to classify rock masses for pit design and in situ rock property derivation, allowing adjustments for favourable or unfavorable discontinuity orientations relative to excavation geometries (Ryder & Jager, 2002). The RMR_{89} classification is based on six key parameters: uniaxial compressive strength (UCS), rock quality designation (RQD), spacing and condition of discontinuities, groundwater conditions, and discontinuity orientation, with a maximum possible rating of 100.

Barton *et al.*, (1974) of the Norwegian Geotechnical Institute developed the Tunnelling Quality Index (Q) to assess rock mass characteristics and determine tunnel support requirements based on extensive case studies. The Q-value ranges logarithmically from 0.001 to 1000 and is calculated using parameters related to rock quality, joint conditions, and groundwater influence. This system provides a structured approach to evaluating tunnel stability and selecting appropriate support measures. It is represented by equation 1:

$$Q = \frac{RQD}{J_n} x \frac{J_r}{J_a} x \frac{J_w}{SRF} \quad (1)$$

Where: RQD is the rock quality designation, Jn is the joint set number, Jr is the joint roughness number, Ja is the joint alteration number, Jw is the joint water reduction factor, and stress reduction factor (SRF) is the stress reduction factor. The (Q′ in Equation (2) is used for excavation stability analysis, primarily following the Potvin or Matthews methods. Unlike the standard Q-system, Q′ simplifies calculations by assuming that the joint water reduction parameter and stress reduction factor are equal to one, focusing on structural and geotechnical properties. This adaptation makes Q′ particularly useful in mining applications where groundwater and stress adjustments are managed separately.

$$Q' = \frac{RQD}{J_n} x \frac{J_r}{J_a} \quad (2)$$

The Q-system provides a detailed assessment of rock mass conditions, including groundwater and stress influences, making it suitable for tunnel engineering. In contrast, the modified Q′ index removes these variables, focusing on excavation stability, which is critical in mining operations. This simplification allows for a more practical approach in controlled excavation environments, particularly stability assessments in open stoping and ground support design.

Hoek *et al.,* (1995) introduced the GSI as a method for estimating the Hoek-Brown strength parameters (s, a, and mb) by accounting for the reduction in rock strength under varying geological conditions. This system plays a crucial role in determining key geotechnical parameters such as cohesion, friction angle, and deformation modulus of rock masses. The GSI classification is based on two primary factors: rock structure and the condition of block surfaces, providing a systematic approach to characterising rock mass behaviour.

Based on the computed Q-ratings, the UG2 chromitite and the pyroxenite footwall are categorised as 'good' rock types. The Q'-rating for the pyroxenite hangingwall differs from the Q-rating because it incorporates borehole data from a 'medium stress' environment alongside scanline mapping data from a 'low stress' environment. In contrast, the Q and Q' values for the pegmatite and UG2 chromitite remain identical, as their calculations rely solely on borehole data from a 'medium stress' environment (SRF = 1) (Table I).

Table I. Mean Rockmass Classification Values (Nel et al., 2022)

	RMR (Mean)	Q(Mean)	Q'(Mean)	GSI (Mean)
Norite (Hanging Wall)	63.55	2.06	-	58.55
Pyroxenite (Hangingwall)	78.25	11.31	22.79	61.61
UG2 Chromitite	62.75	13.73	13.73	57.75
Pegmatoid (Footwall)	76.75	36.18	36.18	71.75

ROCK MATERIAL STRENGTH AND PROPERTIES

Data on rock strength characterisation at Bokoni Platinum mine is currently limited. The pyroxenite and chromitite have different physical properties. The most important property for rock engineering design is the uniaxial compressive strength (UCS). UCSs for hangingwall pyroxenite and UG2 chromitite were benchmarked from various locations within the Bushveld Igneous Complex to address this. Furthermore, point load tests were performed on core samples collected during a site visit to validate the compressive strength of the UG2 chromitite. A summary of the rock strength parameters used in the design can be found in Table II.

Table II. Rock Strength Material (Nel et al., 2022)

Rock Properties	Units	Pyroxenite (Intact)	Main UG2 Orebody and Chromitite Leaders (Intact)	Source of values
GSI	*N/A*	61.61	57.75	Borehole core logging
UCS	MPa	140.00	84.02	Average between Bokoni Point Load tests, Bokoni Technical Support document, and benchmarked values from neighbouring operations
Tensile Strength	MPa	10	5	Benchmarked from neighbouring operations
mi	*N/A*	18	15	Calculated using RSData
D	*N/A*	0	0	
M_b	*N/A*	4.569	3.317	
S	*N/A*	0.014	0.00915	
a	*N/A*	0.503	0.503	
Rock Density (p)	Kg/m^3	3250	4000	Benchmarked
Unit Weight	kN/m^3	0.03188	0.03924	
Cohesion (c)	MPa	7.914	5.941	Calculated using RSData
Friction angle	degrees	41.895	34.852	

Young's Modulus	MPa	106500	70290	Worley design and benchmarked from neighbouring operations
Poisson's Ratio	-	0.23	0.28	
Rock Mass Modulus	MPa	59270	32969	Calculated using RSData
Bulk Modulus	MPa	65741	53250	Calculated
Shear Modulus	MPa	24089	12881	Calculated

STABILITY ANALYSIS APPROACH

Ground conditions within the excavation area range from poor, and fair to good, warranting a multi-faceted approach to stability analysis. The long-term stability of a decline excavation is crucial for ensuring safe and continuous access for personnel, equipment, and ore transport (Brady & Brown, 2006). Stability considerations begin at the boxcut entrance, where geological and geotechnical factors influence excavation performance, such as rock mass strength and weathering depth (Hoek *et al.*, 2000). Proper ground support systems, including shotcrete, rock bolts, and wire mesh, mitigate potential failures caused by stress redistribution and time-dependent rock deformation (Potvin *et al.*, 1989). Additionally, the decline must be designed to accommodate long-term stress changes due to mining-induced seismicity and ground pressure variations (Hudson & Harrison, 1997). Drainage control is critical to prevent water ingress, weakening rock mass strength, and accelerating deterioration (Singh & Goel, 2011). The decline should follow an optimal alignment with minimal sharp curves or steep gradients to reduce stress concentrations and improve vehicle access (Bieniawski, 1989). Excavation-induced stress fractures and joint dilation require regular monitoring to assess long-term stability and necessary reinforcements (Hoek & Marinos, 2000). Furthermore, geological structures such as faults, shear zones, and dykes should be identified early, as they can compromise stability and necessitate additional support measures (Stacey, 2004). Numerical modelling techniques were used to predict long-term deformation and assess reinforcement requirements (Eberhardt *et al.*, 1999). Finally, ongoing geotechnical assessments and maintenance strategies should be implemented to ensure the decline remains structurally sound throughout the mine's operational life (Read & Stacey, 2009).

Overall slope stability analysis and failure mechanisms

Kinematic analysis is a crucial tool for assessing slope stability, as it evaluates the potential failure mechanisms based on the orientation of discontinuities within the rock mass. The probability of slope failure increases in areas where weathered material forms the top layer, as this weakened zone reduces shear strength and creates pathways for instability, especially under external loading such as rainfall or seismic activity (Duncan & Wright, 2005). **Circular or rotational failures** are widespread in weathered materials, where the loss of cohesion leads to progressive slope movement and potential collapse (Terzaghi, 1943). **Planar and wedge failures** occur when pre-existing discontinuities, such as bedding planes and joints, form weak surfaces along which sliding can occur (Hoek & Bray, 1981). **Toppling failures** may develop in steeply dipping rock masses where near-vertical joints or foliation planes allow rock blocks to overturn due to gravitational forces and excavation-induced stress relief (Goodman, 1989). To accurately assess these risks, **kinematic analysis techniques**, including stereographic projection and limit equilibrium analysis, are essential in identifying potential failure modes and determining the necessary reinforcement measures to improve overall slope stability (Markland, 1972).

To evaluate slope stability, a kinematic analysis was performed on the norite at the planned Klipgat boxcut excavation site. The stability of the slope is influenced by the orientation of discontinuities within the rock mass, with failures or slippage typically occurring along these planes of weakness. The analysis focused on two primary failure mechanisms: planar sliding and wedge failure. Using Rocscience's DIPS software, the probability of failure (PoF) for each failure type was assessed based on the provided discontinuity data and the planned orientation of the boxcut walls. The results of the kinematic analysis for wedge and sliding failures are presented in Table III and Table IV, including their figures that provide graphical representations of slope angles within the norite and their corresponding PoFs. In conclusion, the highwall is designed with slope face angles of 75°, while the sidewalls of the boxcut will

have slope angles of 70°. For the Bokoni Klipgat boxcut slope design, a limiting safety factor of 1.3 and a maximum PoF of 5% were applied to ensure long-term stability (based on Read and Stacey, 2009).

Table III. Kinematic analysis - Wedge failure: Slope angle vs. Probability of failure

Kinematic analysis - Wedge failure					
Northern wall (173°)		Eastern wall (263°)		Western wall (84°)	
Dip angle (°)	PoF (%)	Dip angle (°)	PoF (%)	Dip angle (°)	PoF (%)
40	0	40	0	40	0
50	0	50	0	50	0
60	0	60	0	60	0
70	1.95	70	3.06	70	2.45
80	6.96	80	8.68	80	9.71
90	14.76	90	19.07	90	27.45

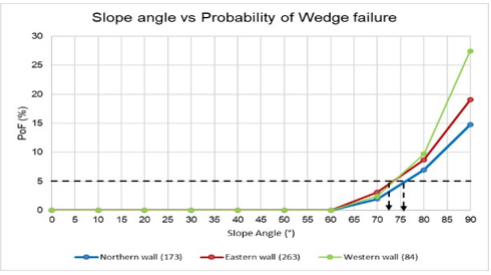
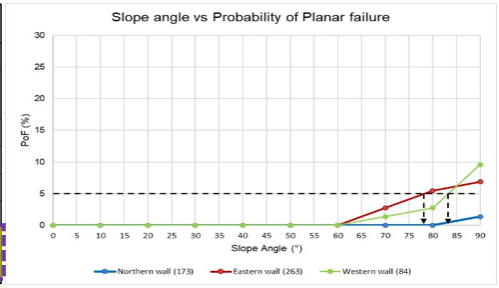


Table IV. Kinematic analysis – Planar Sliding: Slope angle vs. Probability of failure

Kinematic analysis - Planar Sliding					
Northern wall (173°)		Eastern wall (263°)		Western wall (84°)	
Dip angle (°)	PoF (%)	Dip angle (°)	PoF (%)	Dip angle (°)	PoF (%)
40	0	40	0	40	0
50	0	50	0	50	0
60	0	60	0	60	0
70	0	70	2.74	70	1.37
80	0	80	5.48	80	2.74
90	1.37	90	6.85	90	9.59



The overall slope stability of each design sector was assessed using **Rocscience SLIDE 6.0**, a limit equilibrium software that evaluates potential failure surfaces and calculates safety factors under varying conditions (Rocscience, 2023). Both dry and saturated conditions were analysed to determine the impact of water infiltration, as excess pore pressure can weaken shear strength and increase the risk of failure (Duncan & Wright, 2005). The calculated safety factors were compared against the industry-accepted threshold of **1.3,** confirming that all slope angles meet stability requirements under the analysed conditions (Read & Stacey, 2009). By incorporating key geotechnical parameters such as material strength, discontinuity orientation, and slope geometry, the SLIDE 6.0 analysis comprehensively evaluated the excavation site's stability, with the results summarised in **Table V** (*Nel, Arlow, Baloyi, & van der Merwe, 2023*).

Table V. Overall slope stability summary (Nel, et al., 2023)

Slope Stability Analysis						
Hydrology	Non-Saturated (Dry)		Saturated		Method Used	Failure Criteria
Geotechnical Design sector	Overall slope Dip angle (°)	FoS	Overall slope Dip angle (°)	FoS		
Northern wall	47	10.51	47	9.57	Janbu Simplified	Mohr Coulomb + Hoek Brown
Eastern wall	44	11.07	44	10.57	Janbu Simplified	Mohr Coulomb + Hoek Brown
Western wall	35	14.89	35	13.89	Janbu Simplified	Mohr Coulomb + Hoek Brown

Numerical Analysis and the geotechnical assessment

Numerical modelling was employed to evaluate the geotechnical stability of pillars between the three declines, ensuring their long-term structural integrity. The 2023 feasibility study estimated the stress on the decline pillars using the tributary area theory. This theory posits that each pillar supports its portion of the overburden up to the surface. However, the theory has limitations, as it requires the pillars to be arranged in a regular grid and to be of similar size. Consequently, using the tributary area theory in the feasibility study likely overestimates the stress on the decline pillars (Grix, 2024). The analysis considered key factors such as rock mass properties, stress distribution, and deformation behaviour to assess pillar performance under expected loading conditions (Hoek *et al*., 2000). The three-dimensional finite element modelling package from Rocscience was utilised to simulate stress redistribution and potential failure mechanisms, providing a detailed understanding of pillar behaviour (Zienkiewicz & Taylor, 2005). The modelling results were crucial in refining pillar design, optimising dimensions, and implementing appropriate reinforcement strategies to enhance excavation safety and minimise instability risks (Brady & Brown, 2006).

Although the portal and declines are independent of any regional mining activity, and the pillars are anticipated to remain within their elastic range under the proposed mining conditions, an elastic-perfectly plastic material response was simulated. This approach represents the behaviour of rock under stress, where the material initially deforms elastically until reaching its yield point, after which it undergoes plastic deformation without additional hardening (Zienkiewicz & Taylor, 2005). This modelling method ensures that once the rock mass reaches its strength limit, it experiences controlled plastic deformation rather than sudden brittle failure, improving the accuracy of stability assessments (Hoek *et al*., 2000).

The host rock was modelled using the Generalised Hoek-Brown criterion to characterise rock mass strength and failure conditions, considering factors such as intact rock properties and discontinuities (Hoek & Brown, 1997). By integrating this response into numerical modelling, the analysis effectively evaluates stress redistribution and identifies potential failure zones around excavations, contributing to safer and more efficient mine design (Brady & Brown, 2006). The rock strength properties are presented in Table 2.

Figure 6 shows an image exported from the 3D finite element numerical model. The image displays Sigma 3 contours for areas where Sigma 3 is tensile. The highest tensile stress occurs within the first 4.0 m of the middle decline. The model indicates that the dead-weight portion will affect the first bench and extend only 4.0 m up to the first bench. The depth of the tensile zone was used to determine the length of the cable anchor support.

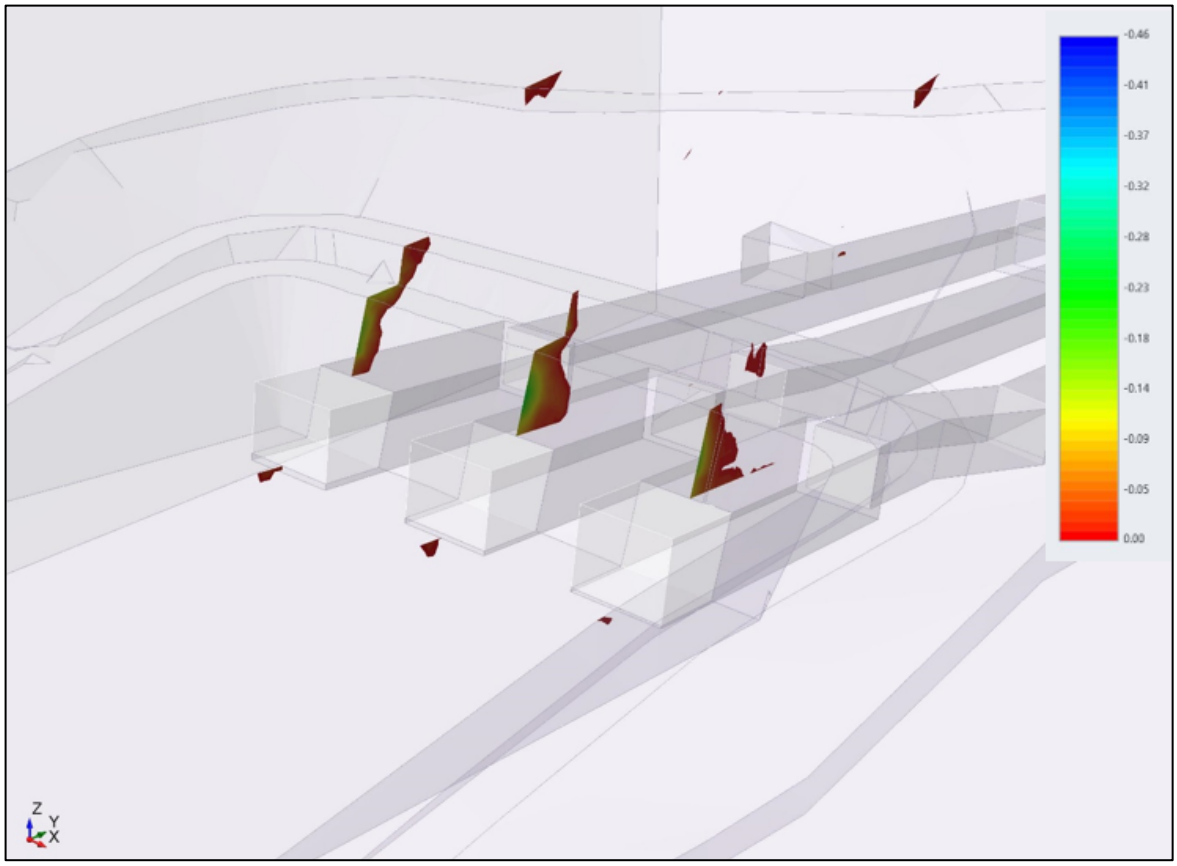


Figure 6. Sigma 3 values along the portal entrance and decline cluster (Grix,2024).

GROUND SUPPORT

The Q-system, developed by Barton *et al*., (1974), is a widely recognised method for classifying rock masses and designing support systems in underground excavations. It evaluates rock mass stability based on a Q-value, which is determined using parameters such as RQD, joint set number (Jn), joint roughness (Jr), joint alteration (Ja), SRF, and water inflow (Jw) (Grimstad & Barton, 1995). Grimstad and Barton (1995) introduced a design chart that refines the Q-system specifically for permanent underground support to enhance its applicability. Based on the calculated Q-value, this chart provides empirical guidelines for selecting appropriate support measures, including shotcrete thickness, rock bolts, and mesh reinforcement.

Since portals are critical access points in mining operations, ensuring their stability is essential for long-term operational safety. Lower Q-values, indicative of poor rock quality, necessitate a combination of shotcrete, bolting, and wire mesh to reinforce the excavation. In contrast, higher Q-values, signifying better rock quality, may require minimal support (Barton & Choubey, 1977). In highly fractured or weathered rock areas, an increased SRF value results in a lower Q-value, highlighting the need for additional stabilisation techniques such as systematic bolting and reinforced shotcrete lining (Grimstad & Barton, 1995). The geotechnical data obtained from photo logging was used to classify the rock mass in the boxcut area into two main geotechnical domains as shown in Table VI.

Table VI. Domains identified within the boxcut and associated Q and ESR values

Domain	ESR	Rock type	Mean Q-rating	Mean RMR_{89}	Planned bench height (m)
Weathered/overburden (Top bench)	1.6	Norite	0.06	29.20	6.5
Fresh Norite	1.6	Norite	2.59	63.55	10.0

To ensure structural integrity, recommended support measures for portals include systematic rock bolting using fully grouted rebar or cable bolts for jointed rock masses, steel fibre-reinforced shotcrete to enhance surface stability and drainage measures to control water ingress and prevent weakening of the rock mass. Slope design for the boxcut relied primarily on RMR, kinematic analyses, and limit equilibrium methods due to the open nature of the excavation. Numerical modelling techniques such as finite element and discrete element methods should be employed to validate the stabilisation strategy and assess its effectiveness under site-specific conditions (Palmström & Stille, 2007).

The primary support strategy was determined using RMR (Bieniawski,1989) values, as Unal (1983) suggested, providing cable anchor length and spacing recommendations. A comprehensive summary of the boxcut support recommendations is presented and illustrated for the different wall sections in Figure 7 to Figure 9. The geotechnical section above discusses the primary support requirements for the decline, while the secondary support requirements for the portal are discussed. To ensure long-term stability, the portal area will require support sets for the first 5.0m at all portal entrances, with sets spaced 1.0 m apart, skin-to-skin.

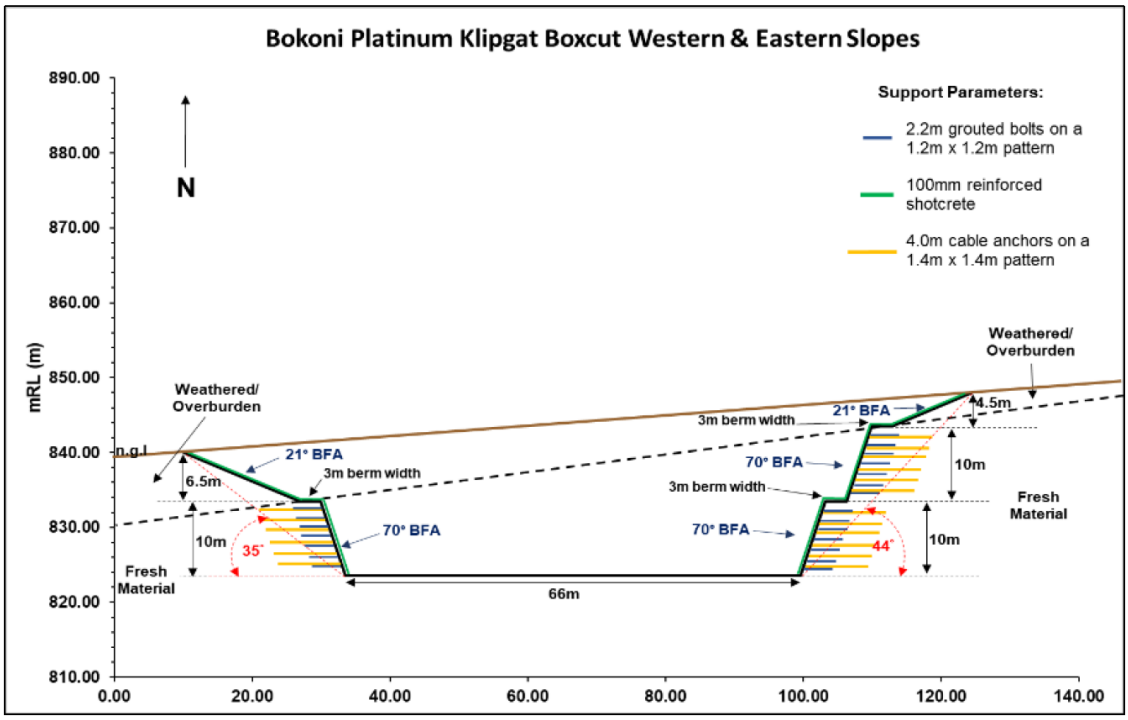


Figure 7. Slope configuration and support strategy for sidewalls of the boxcut (Nel et al.*, 2023).*

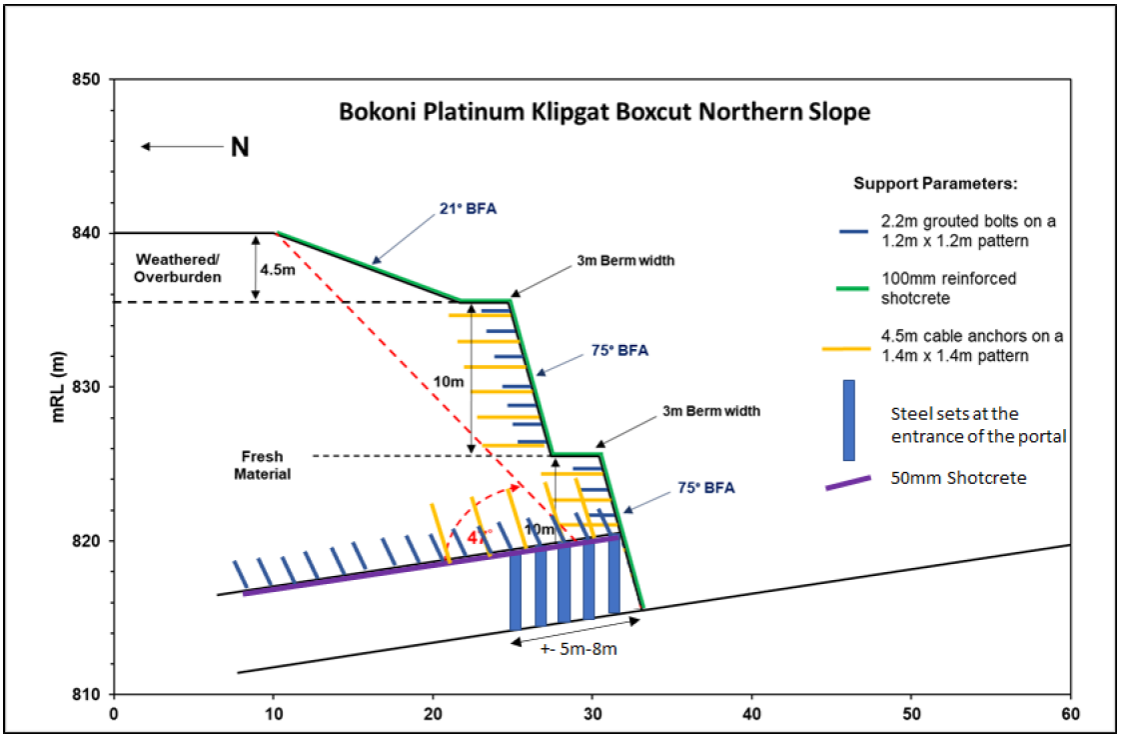


Figure 8. Slope configuration and support strategy for the highwall (Nel et al.*, 2023).*

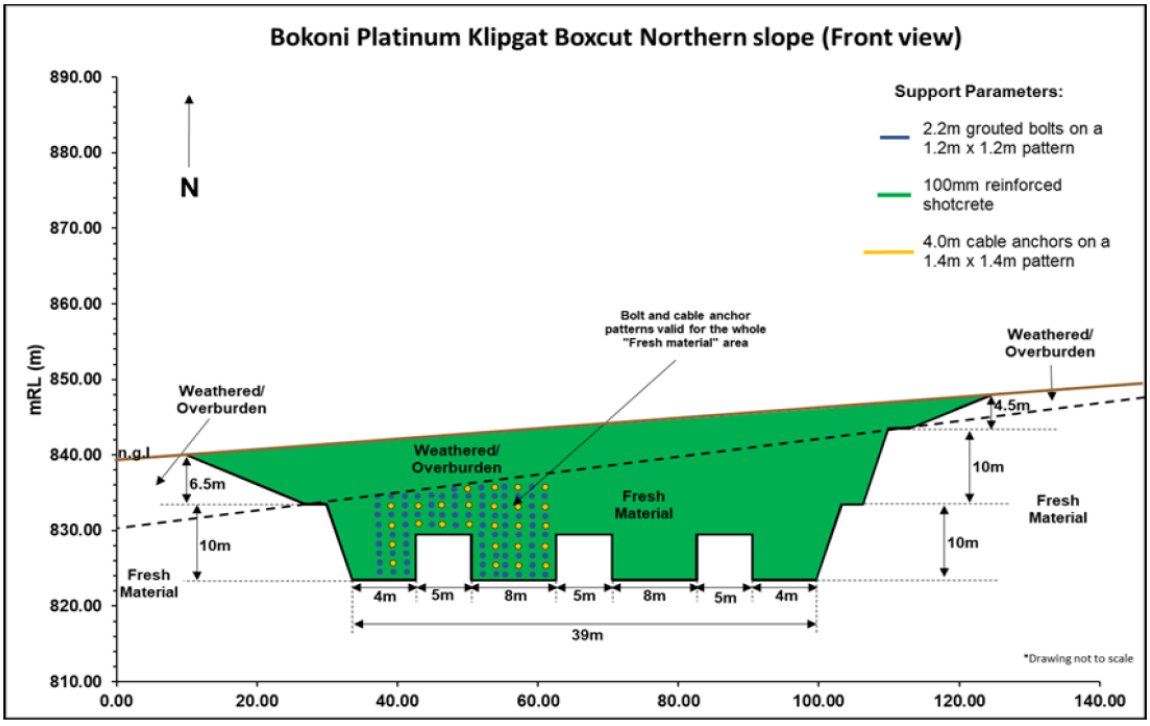


Figure 9. Support strategy schematic for the highwall (front view). (Nel et al.*, 2023)*

STABILITY ANALYSIS AND FAILURE MECHANISMS IN THE TUNNELS

Stability analysis and tunnel failure mechanisms are crucial for ensuring structural integrity, worker safety, and project efficiency. Understanding how stress distribution and geological conditions affect

tunnel stability helps predict potential failures, such as total collapses or deformations before they occur. Rock engineering practitioners can design and implement appropriate support systems by identifying weak zones and failure patterns in advance, reducing risks and costly delays. Proper stability analysis also enhances long-term tunnel durability, minimising maintenance requirements and ensuring safe operation throughout its lifespan. The 3D finite element analysis (described above) and tunnel reflection tomography will be used for future analyses as this project is ongoing.

Tunnel Reflection Tomography

Tunnel reflection tomography (TRT) is a **geophysical imaging technique** that provides real-time monitoring of **adverse geological conditions** ahead of tunnel advancements. By utilising seismic wave reflections, TRT detects **variations in rock properties**, such as weak zones, fractures, or water-bearing structures, which may compromise stability. This method enhances **anticipation of rock conditions and failure modes**, allowing for proactive decision-making. TRT is particularly useful in detecting **hidden discontinuities** and ensuring that support systems are adjusted before encountering unfavorable ground conditions (Figure 10).

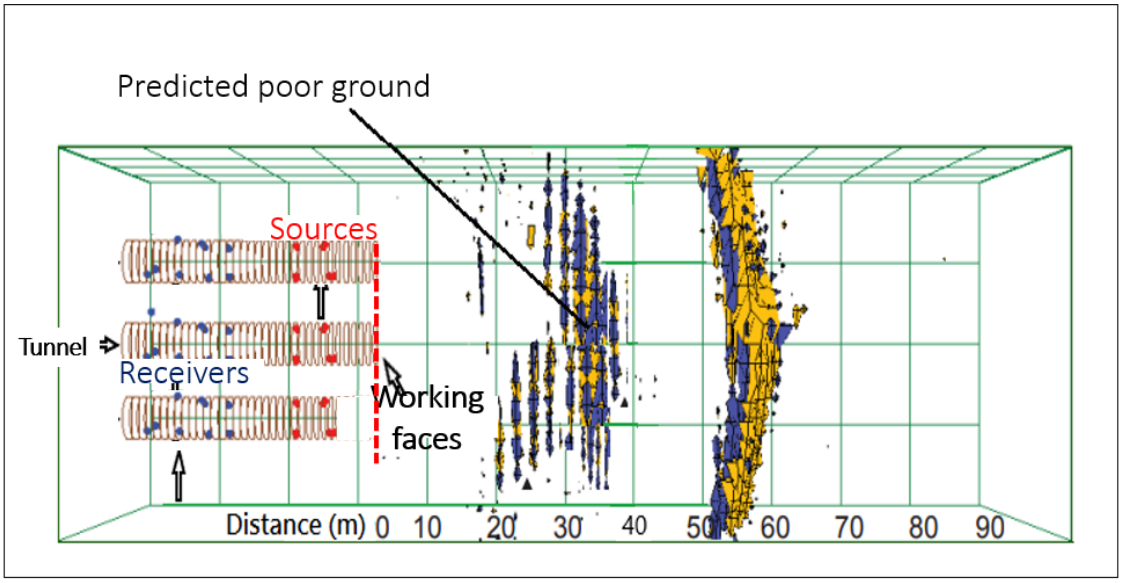


Figure 10. Example of the top view of TRT detection results at 40 m and 60 m in the north direction level (after Dembure et al, 2025).

Combining TRT with RS3's numerical predictions improves **geotechnical design, reduces risks, and enhances tunnel safety and efficiency**.

MONITORING

The monitoring system utilises advanced geotechnical instruments, including early warning extensometers, Bluetooth extensometers, and InSAR, to detect rock movement and assess slope stability (Dunnicliff, 1993). These instruments provide real-time data on displacement trends, enabling proactive decision-making in mitigating geotechnical risks (Mikola & Sitar, 2013). Initial monitoring results indicate overall stability, with minimal displacement observed, suggesting that the current slope design and reinforcement measures are effective (Hoek & Bray, 1981). However, anticipated failure mechanisms such as planar sliding, wedge failure, and toppling could develop due to progressive deformation, stress redistribution, and external factors like rainfall or seismic activity (Read & Stacey, 2009).

Before the failure, precursors such as increasing displacement rates, widening of existing cracks, and differential ground settlement are expected to manifest, signalling progressive instability (Terzaghi,

1943). InSAR technology can detect millimetre-scale ground deformations, making it an essential tool for tracking early warning signs (Colesanti & Wasowski, 2006). Machine learning (ML) algorithms could further enhance monitoring by analysing large datasets from geotechnical sensors, identifying hidden patterns, and predicting failure more accurately (Zhang *et al.*, 2020). By integrating ML with geotechnical monitoring, predictive models can improve risk assessment, reduce false alarms, and optimise mitigation strategies (Reyes-Montes *et al.*, 2018). As mining operations advance, AI-driven predictive analytics in monitoring systems may revolutionise geotechnical risk management, enhancing safety, operational efficiency, and decision-making (Masethe and Adoko, 2024).

Figure 11 illustrates the displacement trends recorded by a 3-point extensometer over one month, providing critical insights into rock mass stability. The primary objective is to monitor ground movement and assess any potential risks to mine safety and operations. Installed adjacent to an early warning extensometer designed to trigger a visual alert upon exceeding a predetermined threshold, the 3-point extensometer captures subtle variations in displacement. The recorded data reveals minimal fluctuations, remaining below 0.1 mm across the three anchor points. These slight deviations are likely attributable to natural stress redistribution, thermal effects, or minor rock mass adjustments. However, as these variations remain within an acceptable range, they do not suggest progressive deformation or instability.

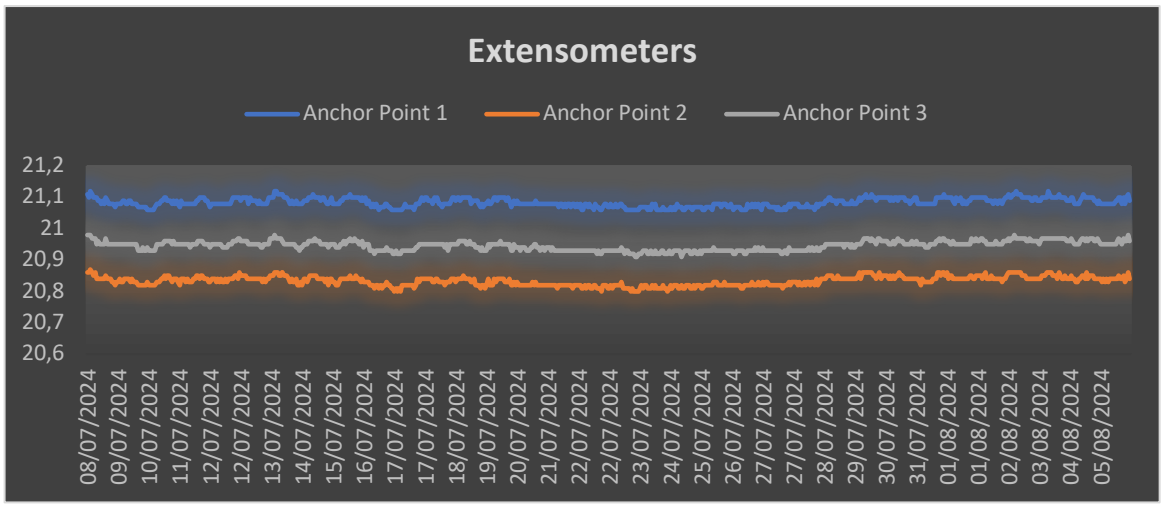


Figure 11. Extensometer displacement trends over time for three-anchor points.

Figure 12 illustrates ground displacement monitoring over a two-year period from January 2022 to December 2024. Ground movement is measured in velocity (millimeters per year). Green areas indicate stable ground based on the selected threshold, while yellow to red signify varying degrees of movement. The image shows some movement near the portal; however, it is not significant and is likely due to vegetation removal, boxcut excavation, natural stress redistribution, thermal stress effects, or minor rock mass adjustments. The graph indicates ground movement of less than 5 mm, remaining consistent throughout the monitoring period. The absence of significant displacement trends or sudden increases suggests that the excavation remains stable under current conditions.

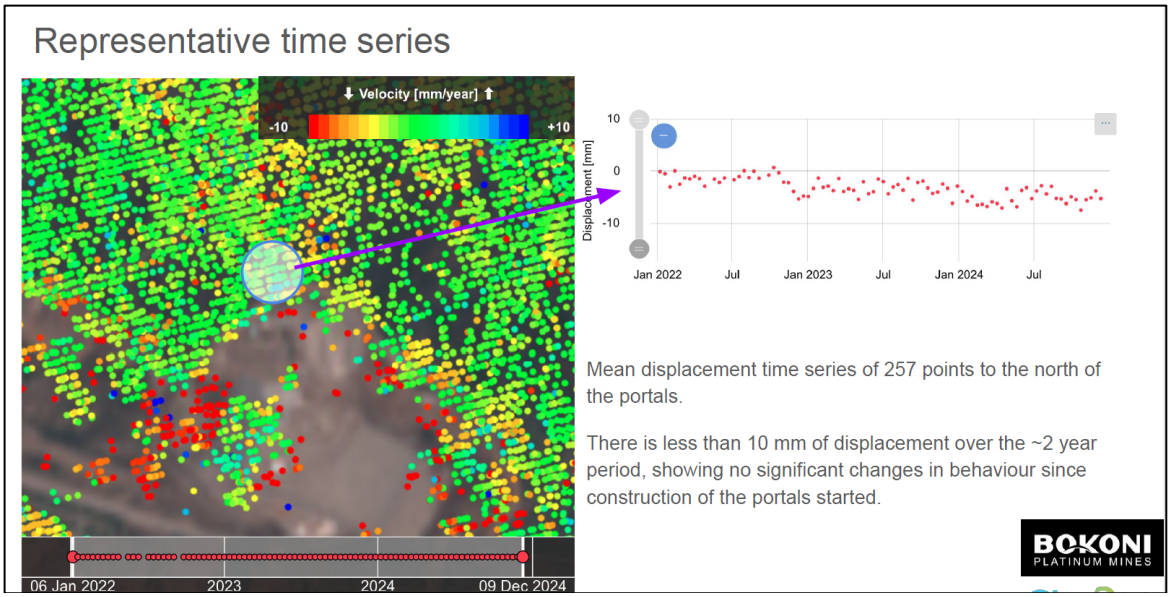


Figure 12. InSAR-derived ground displacement map (Marungwana & Pretorius, 2024).

CONCLUSIONS

This study integrates geological surveys, stress and kinematic modelling, and advanced ground monitoring techniques to assess underground excavations' structural integrity comprehensively. Implementing cutting-edge geotechnical instruments, including early warning extensometers, Bluetooth extensometers, and InSAR, has enhanced the ability to detect rock movement and provide timely warnings of potential instability. Preliminary findings indicate that the rock mass exhibits overall stability with minimal displacement; however, localised weak zones due to weathering necessitate further reinforcement strategies. The current support system, comprising rock bolts, mesh, and shotcrete, has proven effective in maintaining structural integrity, particularly at the decline entrance and pillar areas. Continuous monitoring and adaptive reinforcement measures remain critical for ensuring long-term stability and safe mining operations. The geological conditions within the study area, particularly above the UG2 reef, exhibit gradual transitions between rock types. However, distinct geological contacts, such as those of norite and pyroxenite, chromitite stringers, present potential parting planes that could influence stability. Lithological variations across the Bushveld Complex further underscore the importance of site-specific geotechnical assessments in excavation planning and support design.

By applying 3D finite element analysis (RS3) and TRT, this study has provided a detailed understanding of the excavation's stress distribution, deformation patterns, and potential failure mechanisms. RS3 has been instrumental in simulating stress redistribution, identifying potential failure zones, and guiding reinforcement strategies. Meanwhile, TRT has facilitated the early detection of adverse geological conditions, allowing for proactive decision-making and timely adjustments to excavation methods. Kinematic analysis has further contributed to identifying potential failure mechanisms, including planar sliding, wedge failure, and toppling. Applying empirical rock mass classification systems, such as RMR89, Q-rating, and GSI, has provided a structured framework for assessing rock mass stability and designing appropriate support measures. Given the variability in geotechnical conditions, ongoing refinement of these classification models is essential to ensure their applicability to site-specific challenges.

Integrating numerical modelling, empirical rock mass classification, and real-time monitoring represents a holistic approach to tunnel stability analysis. The findings from this study contribute to a broader understanding of excavation stability in underground mining environments, emphasising the

necessity of continuous geotechnical assessments and reinforcement adaptation. As mining operations progress, applying ML and artificial intelligence in geotechnical monitoring may further enhance predictive capabilities, optimising safety, operational efficiency, and risk management.

ACKNOWLEDGEMENTS

The management of Bokoni Mine is gratefully acknowledged for granting permission to publish these preliminary results. We also extend our sincere appreciation to Open House Management Solutions, SkyGeo, and Middindi Consulting for their invaluable assessment of the stability of the Klipgat decline.

REFERENCES

Barton, N., Lien, R., & Lunde, J. (1974). Engineering classification of rock masses for the design of tunnel support. *Rock Mechanics*, *6*(4), 189–236.

Barton, N., & Choubey, V. (1977). The shear strength of rockfill. *Geotechnique*, *27*(2), 159–185.

Bieniawski, Z. T. (1973). Engineering classification of jointed rock masses. *Transactions of the South African Institution of Civil Engineers*, *15*(12), 335–344.

Bieniawski, Z. T. (1989). *Engineering rock mass classifications: A complete manual for engineers and geologists in mining, civil, and petroleum engineering*. John Wiley & Sons.

Brady, B. H., & Brown, E. T. (2006). *Rock mechanics for underground mining*. Springer Science & Business Media.

Colesanti, C., & Wasowski, J. (2006). Investigating landslides with space-borne synthetic aperture radar (SAR) interferometry. *Engineering Geology*, *88*(3–4), 173–199.

Dunnicliff, J. (1993). *Geotechnical instrumentation for monitoring field performance*. John Wiley & Sons.

Duncan, J. M., & Wright, S. G. (2005). *Soil strength and slope stability*. John Wiley & Sons.

Eberhardt, E., Stead, D., & Stimpson, B. (1999). Quantifying progressive pre-peak brittle fracture damage in rock during uniaxial compression. *International Journal of Rock Mechanics and Mining Sciences*, *36*(3), 361–380.

Dembure, T., Masethe, R., & Zvarivadza, T. (2025). Advanced Optimisation Of Ground Support Systems for Enhancing Underground Tunnel Stability in Geologically Adverse Conditions. *Rock Mechanics Letters*, *2*(1), 9. https://doi.org/10.70425/rml.202501.9

Feng, X. T., Zhang, D., & Wu, W. (2019). Artificial intelligence in geotechnical engineering: Applications and developments. *Georisk: Assessment and Management of Risk for Engineered Systems and Geohazards*, *13*(2), 72–91.

Goodman, R. E. (1989). *Introduction to rock mechanics*. John Wiley & Sons.

Grimstad, E., & Barton, N. (1995). Updating the Q-system for NMT. *Proceedings of the International Symposium on Sprayed Concrete – Modern Use of Wet Mix Sprayed Concrete for Underground Support*, 46, 46–66.

Grix, Q. (2024). Bokoni Platinum Mine Bokoni Platinum Mines Stability Analyses for 3 Decline Cluster. Potchefstroom: Open House Management Solutions.

Hoek, E. (2007). Practical rock engineering. *Rock Mechanics and Engineering*, *40*(6), 729–762.

Hoek, E., Carranza-Torres, C., & Corkum, B. (2000). Hoek-Brown failure criterion – 2002 edition. *Proceedings of the North American Rock Mechanics Symposium*, 267–273.

Hoek, E., & Marinos, P. (2000). Predicting tunnel squeezing problems in weak heterogeneous rock masses. *Tunnelling and Underground Space Technology*, *15*(3), 225–236.

Hoek, E., & Brown, E. T. (1997). Practical estimates of rock mass strength. *International Journal of Rock Mechanics and Mining Sciences*, *34*(8), 1165–1186.

Hudson, J. A., & Harrison, J. P. (1997). *Engineering rock mechanics: An introduction to the principles*. Elsevier.

Masethe, R.T, & Adoko, A. (2024). Algorithms and data: A strategy for the successful implementation of machine learning in rock engineering to enhance safety. Mine Safe Conference, SAIMM.

Markland, J. T. (1972). *A useful technique for estimating the stability of rock slopes when the rigid wedge sliding type of failure is expected*. Imperial College London.

Marungwana, I., Pretorius, J. (2024). Bokoni Platinum Baseline analysis: Analysis of displacements surrounding the newly constructed portal using Sentinel-1 InSAR data. Netherlands: Sky Geo

Mikola, R. G., & Sitar, N. (2013). Seismic earth pressures on retaining structures. *Journal of Geotechnical and Geoenvironmental Engineering*, *139*(12), 2021–2030.

Nel, J., Arlow, R., Baloyi, N., & van der Merwe, J. (2023). *Bokoni Platinum Mine 120ktpm Feasibility Study*. Johannesburg: Unpublished.

Palmström, A., & Stille, H. (2007). Ground behaviour and rock engineering tools for underground excavations. *Tunnelling and Underground Space Technology*, *22*(4), 363–376.

Potvin, Y., Hudyma, M., & Miller, H. (1989). Design guidelines for open stope support. *Proceedings of the CIM Annual General Meeting*.

Read, J., & Stacey, P. (2009). *Guidelines for open pit slope design*. CSIRO Publishing.

Reyes-Montes, J., Young, R. P., & Kwiatek, G. (2018). Machine learning for microseismic monitoring of underground mining operations. *International Journal of Rock Mechanics and Mining Sciences*, *110*, 84–94.

Ryder, J. A., & Jager, A. J. (2002). *A textbook on rock mechanics for tabular hard rock mines*. SIMRAC.

Singh, B., & Goel, R. K. (2011). *Tunnelling in weak rocks*. Butterworth-Heinemann.

Stacey, T. R. (2004). The link between the design process in rock engineering and the code of practice to combat rockfall and rockburst accidents. *The Journal of The South African Institute of Mining and Metallurgy*, *104*(1), 29–34.

Zhang, J., Li, D., & Zhang, L. (2020). Machine learning for geotechnical risk assessment: Current status and future directions. *Computers and Geotechnics*, *122*, 103489.



Siphamandla Vezi

Bokoni Mine, South Africa

I am a certified Rock Engineer with extensive experience in various aspects of mining and rock engineering. My operational expertise spans from surface, shallow, intermediate, and deep-level gold, copper, and platinum operations. I have also had the opportunity to work with different commodities across multiple countries. I gathered geotechnical data from exploration drilling and contributed to pre-feasibility and feasibility studies as part of a project team.

I support mine production teams in managing geotechnical hazards on-site, conducting rock engineering investigations into hazards, falls of ground, excavation stability, and support design. Additionally, I assist in developing risk mitigation strategies that align with Mine Health and Safety regulations and industry standards. As a visible leader in the workplace, I promote a strong safety culture by increasing awareness of geotechnical hazards through clear decision-making and effective communication.

Compact radar system for rockmass movement monitoring in an underground narrow reef stope

D. van Rooyen[1], R. Carstens[1], L. Campbell[2]

[1]Anglo American, South Africa;
[2]Geobotica, Australia.

The introduction of radar technology in open pit mines has made a significant contribution to the prevention of fatalities and damage to equipment from uncontrolled slope failures. This paper introduces a novel way to transfer the same benefits into underground mines. The purpose of the technology is to warn workers of potential instability in the immediate area of their work.

Conventional underground stopes present challenges for geotechnical risk management. The restricted height in which workers have to operate, typically 1 to 1.6 m, makes it difficult to mechanise as drill and blast activities are generally done with conventional hand-held equipment. The mining method is very labour-intensive compared with a mechanised mine, resulting in high exposure to uncontrolled rockfalls.

Current trigger warning monitoring equipment is activated mechanically and drilled into the hangingwall of the stope. This only provides data for a very small surface area relative to a spread area or the complete stope and the likelihood of not identifying anomalous deformation indicating potential instability is very high.

The narrow geometry of stopes combined with the large number of active stopes per mine has meant that traditional radar equipment that is physically large requires significant power and communications infrastructure; and skilled operators are not suitable.

To address this gap, a compact radar system has been developed that offers contactless, continuous, spatial monitoring of rock deformation. Operating on interferometric principles, the system achieves sub-millimetre precision and can be deployed in a distributed configuration across multiple stopes. Its low-power and lightweight design enables extended autonomous operation without complex infrastructure or specialist training, making it well-suited to underground mining environments with limited access and high operational demands.

INTRODUCTION

Background

There are early warning monitoring instruments/devices or tools in the industry that work mechanically or electronically, but the user needs to either drill holes, place the tool next to the workforce, or ensure contact with the hangingwall. These instruments are point information and not continuous spatial monitoring or recording.

Falls of ground remain a leading cause of fatalities and injuries in South African underground mines, with 13 fatalities and 266 injuries recorded in 2024 (Minerals Council South Africa Reporting).

The narrow reef stoping environment presents particular challenges for geotechnical risk management, including confined working spaces typically between 1.0 and 1.6 m in height, high levels of manual labour, and limited mechanisation. These conditions increase exposure to uncontrolled rockfalls and limit the effectiveness of conventional monitoring solutions.

Existing early warning systems in underground operations are generally mechanical or electronic instruments that require installation in direct contact with the rock mass, such as drilling into the hanging- wall. These tools provide point measurements rather than continuous spatial monitoring, increasing the likelihood that precursory deformation may go undetected.

By contrast, radar monitoring technologies have been successfully applied in open pit mines to detect slope movements in real time and improve worker safety. However, traditional radar systems are often too large, power-intensive or infrastructure-dependent for practical use in underground stopes. Previous attempts to adapt radar or LiDAR-based systems for underground environments have been limited by insufficient portability, inadequate robustness in harsh conditions, and an inability to provide early warnings in a contactless manner.

In response to these limitations, a compact radar monitoring system was developed to enable real-time, spatially continuous measurement of rock deformation without requiring direct contact with the monitored surface. The design objective was to create a system capable of deployment in narrow stopes, with minimal infrastructure, low power consumption, and ease of operation by non-specialist personnel.

Research Objectives

The goal was to develop a radar tool capable of monitoring rock movement, providing early warnings to workers, and recording geotechnical data in real-time. This tool must withstand the harsh underground environment while maintaining optimal performance. It was determined the technology must undergo rigorous field piloting to demonstrate its ability to deliver accurate, real-time monitoring, early hazard detection, and long-term geotechnical data, ultimately achieving technology readiness level (TRL) 9 in an actual narrow reef stope production environment.

The operational requirements from Anglo American included:

- Fit for purpose robust, waterproof, compact and portable design
- Alarm trigger (alerts employees to rock movement)
- Simple deployment
- Accurate and precise measurements
- Data integration capabilities
- Continuous real-time monitoring
- User-friendly
- Data recording capability
- Durable and reliable tool
- Monitor larger area
- Long battery life

The capabilities must be able to integrate with wearables such as cap lamps and smart watches; this can be facilitated through collaboration with third-party original equipment manufacturer suppliers.

TECHNOLOGY DEVELOPMENT

Miniaturisation with MIMO Radar Technology
Open pit slope monitoring radars are often large, trailer-mounted devices (Strouth, L. Beckett *et al*.,

2006). In order to miniaturise radar and meet the requirements of operators, it was clear that no moving parts could be used. To solve this problem, multiple-input multiple-output (MIMO) radar technology was explored. MIMO radar, a variant of synthetic aperture radar, uses an array of antennas to transmit and receive multiple coded waveforms, allowing it to synthesise a larger virtual aperture without moving parts. This approach not only reduces the physical size and power requirements of the radar but also enhances spatial resolution and accuracy.

The concept of MIMO radar has been explored extensively over the past two decades for doppler radar systems and military imaging radar, with significant contributions from researchers such as Ilya Bekkerman and Joseph Tabrikian. In their 2006 paper, Bekkerman and Tabrikian introduced a novel space-time coding configuration for MIMO radars, demonstrating its potential for precise target detection and localisation by leveraging virtual sensor arrays.

The MIMO proved robust for a radar imaging technique underground; the next problem was to track rock movement over time. Radar differential interferometry, which analyses phase differences between radar signals, is a method widely used in open pit mining to track sub-mm movement of rocks and detect subtle ground deformation over time. The method is well-described in the 2001 seminal paper by Noon, Stickley *et al*.

Laboratory testing results

After two years of research and development, the following laboratory and controlled field-testing results were obtained using a corner reflector mounted on a mechanical translation stage, where the movement of the corner reflector was controlled in 0.05 mm increments.

Table I. Specifications of NanoRadar

Item	**Specification**
Deformation precision	<0.1 mm
Acquisition time	5 seconds
Scan frequency	Variable, selected by site geotechnical engineer between 30 seconds and 1 hour
Field of view	120° in azimuth and 60° in elevation
Pixel definition	2.5° in azimuth by 0.1 m in range
Range	0.5 m to 20 m (underground version)
Ingress Protection (IP) rating	IP67 – (Dust-tight and water-submersible for 15 minutes at 1 m)
Weight	350 grams
Size	11 cm x 12 cm x 7 cm
Battery life	Internal battery life of 8 days at a 2-minute scan interval, operating 24/7
Communications	Internal WiFi
Alarm notifications	90 dB piezometric siren integrated with LED flashing lights with an illuminated case
User feedback	Integrated e-paper screen, LED lights, and piezometric siren
Data analysis	Deformation, intensity (amplitude), velocity, and inverse velocity data types as heat maps and timeseries

The final underground trial version is presented in Figure 1 and indicates the features on the device.

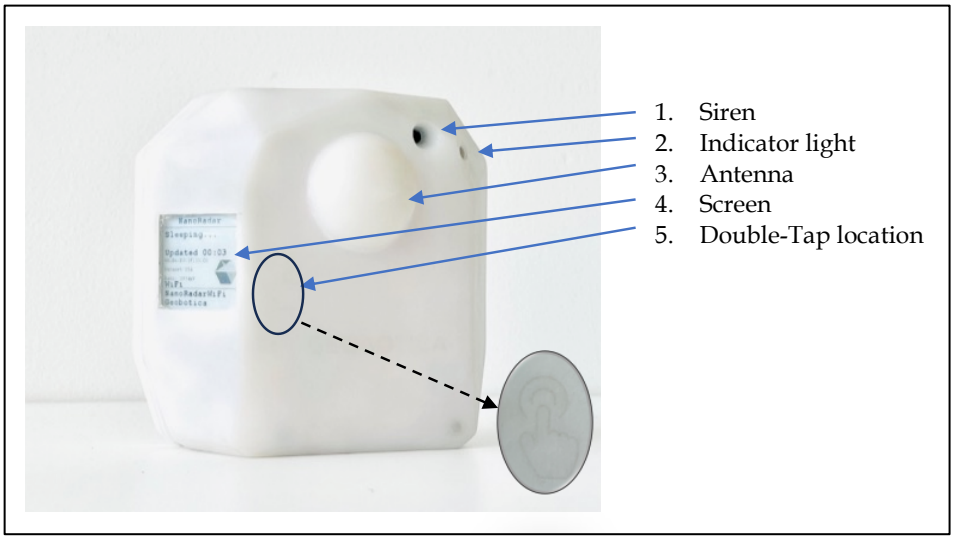


Figure 1. Illustration describing the NanoRadar components.

Development stages

The NanoRadar R&D project commenced in 2022 and achieved deployment testing in a production setting at the Amandelbult mine in 2024. The development process involved nine rounds of hardware prototypes and numerous iterations of alarming and filtering algorithms. The R&D involved concept prototypes and learnings of deployment and robustness that are illustrated in Figures 2 to 6.



Figure 2. Concept radar system with small minicomputer.

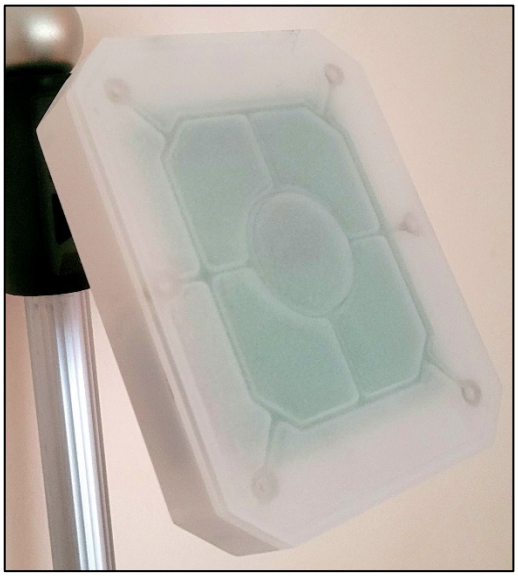


Figure 3. Prototype system 'NanoRadar'.



Figure 4. Underground prototype system testing where brackets broke off after being dropped from an approx. 1.8 m height.



Figure 5. Final trialled underground radar system, NanoRadar.

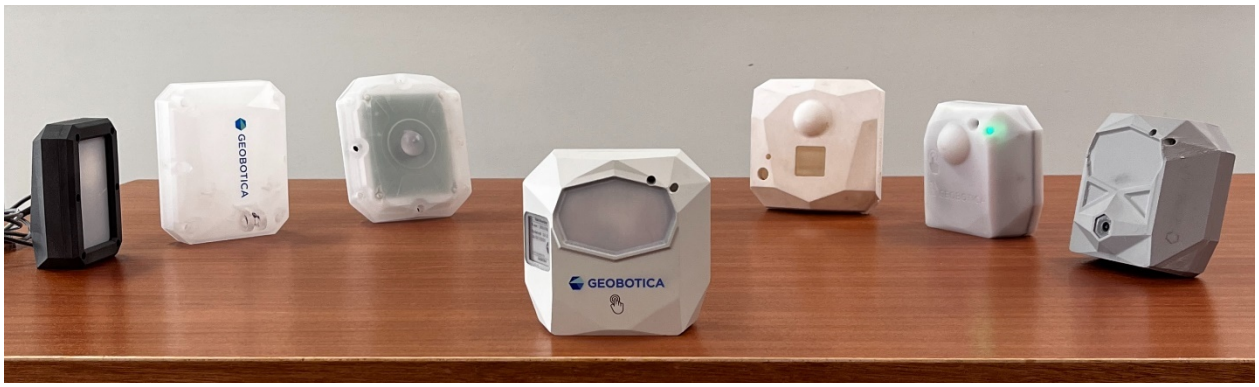


Figure 6. Prototype development line up. The middle version is the latest version available. The version with the green light was the extended trial version that is presented in this paper.

While a detailed review of the development process is beyond the scope of this paper, this section focuses on the practical deployment of the compact radar system in underground mining environments.

Traditional slope stability radar systems typically require extensive setup times of up to 25 minutes, involving complex hardware configurations and specialised software. These requirements are impractical in confined stopes, where time and space constraints are significant.

To address these limitations, the system described here was designed for fully self-contained operation without reliance on external computing devices. The instrument incorporates automatic orientation sensing and motion detection, preventing scanning while being transported or repositioned. A low-power sleep mode is activated when the unit is placed face-down, and the system can be reactivated by repositioning or tapping the housing.

Once deployed and stable for a minimum of two minutes, the radar automatically initiates a new

dataset and begins monitoring for deformation events. This level of automation reduces setup time and operator intervention, supporting deployment in dynamic environments where crews may have varying levels of training and experience.



Figure 7. Final underground NanoRadar instrument with charger and hub as a complete set.

Several deployment methods were evaluated to ensure stable positioning of the radar system in the underground environment. An initial approach involved mounting the device on a telescopic pole anchored to the support holes; however, this configuration transmitted vibrations from drilling activities into the radar, which compromised measurement accuracy.

To quantify the issue, a custom vibration measurement device was created, measuring real-time device vibration via a triaxial accelerometer at 2000 hz, and motion was converted via FFT to total translation of the device in millimetres. This testing found the vibration from face drilling moved the radar by 2.3 mm oscillation when at a 1.5 m radial distance, however when the hangingwall was drilled at the same distance, movement of the sensor reached as high as 4 mm. Measurements of footwall vibration were low, showing the footwall was much less severely impacted than the face and hangingwall during airleg drilling.

To address this issue, an alternative stand was developed consisting of a foldable tripod placed on the footwall of the stope. This setup provided sufficient stability and isolation from operational vibrations and was ultimately selected as the preferred deployment method during field- testing.



Figure 8. Telescopic pole used as deployment method that was placed next to the mechanical prop at the working face area.



Figure 9. Foldable tripod that is placed on the footwall; this was the preferred and workable deployment that was used in the trial period.

Filtering Non-Rock Movements

A significant challenge in underground mining environments, particularly in narrow reef stopes, is the frequent presence of personnel and equipment within the monitoring area. The core problem addressed in this paper was the development of a method capable of detecting sub-millimetre rock movements while excluding signals generated by non-rock sources.

To meet this objective, a custom algorithm was developed, leveraging the capabilities of MIMO radar technology. The system performs rapid scans without moving parts, capturing approximately 192,000 frames of phase data and an equal number of amplitude frames within a five-second acquisition period. This large dataset enables the algorithm to distinguish between true rock deformation and micromovements resulting from human presence (such as breathing and pulse) or equipment vibrations.

The filtering approach was iteratively refined to avoid excluding legitimate rock movements. A factor of safety of 100 was applied to account for the highest theoretical rates of rock deformation, ensuring that early warning capability was preserved while minimising false positives due to non-rock activity.



Figure 10. The system deployed viewing toward the working face while rock drill operator is busy drilling shotholes.

This capability to differentiate between static and dynamic targets allows the system to focus exclusively on stable rock faces, providing reliable deformation monitoring in environments where traditional radar systems would struggle to isolate relevant data.

Subsidence and Deformation Visualisation
The next stage of development was to create a data visualisation tool. While the priority was to create real-time alarms in production environments, it would also be important for members of the geotechnical team to be able to post-analyse alarms to better understand failure mechanisms.

Radar data is visualised in a desktop application into an intuitive 2D or 3D map of the area. An adjustable heatmap highlights changes in movement over time, making it easy to analyse deformation immediately.

FIELD PILOT METHODOLOGY

Site selection
Amandelbult Dishaba mine was selected to pilot the system due to its environment as an underground narrow-stope mine. The underground environment presented uneven and fairly steep conditions (with slopes between 15° and 30°), along with the presence of water and mud. These factors were considered ideal for testing the system under the harshest conditions available within Anglo American. The stope lengths in this mine range between 25 to 35 m, and the stope height is between 1.4 m and 1.6 m, depending on the reef band width. The primary support in the stope is blast on mesh, cable anchors and grout packs. The drilling of blast and support holes is done with precision drilling equipment.

For the long-term monitoring testing a site was selected where rock movement was expected.



Figure 11. Narrow conventional stope environment illustration.

Pilot application
The mine's standard operating procedure for piloting was followed, with all necessary documentation submitted and approval granted.

The following key adoption steps were implemented to introduce the system to the crew:
- Comprehensive operation procedures and training documents were prepared.

- Crew engagement sessions were held before the pilot start date to address questions and concerns.
- The crew received training and a detailed explanation of the process on the pilot start date.
- Time was spent with the crew to ensure proper adoption of the technology.
- Ongoing support was provided by a dedicated member of the geotechnical team.

Deployment and Data Collection
Early warning piloting (short-term, less than a shift):
The system will be positioned at the back, facing forward, approximately 5 to 8 m from the advancing drilling face. The production crew in the stope will move the tool as the drilling operators progress up and down the stope. The tool will be deployed after the entry examination is completed and will be folded away and stored in the waiting place at the end of the shift. The system will be brought to the surface for charging every 14 days, at which point the data will be downloaded to a cloud database. The data will then be interpreted and analysed using the developed analysis software.

The pilot was initially planned for three months, but improvements and modifications to the system allowed the pilot to be extended to six months. Initially, one system was deployed, and this number was gradually increased to a maximum of three systems in one stope to ensure the crew's continued use of the technology and to test the performance of the system.



Figure 12. The system in the stope during the trial period.

Given that this pilot was conducted in a real production environment and the tool will alarm when rock movement occurs, a protocol had to be established to address both real and false alarms. The decision was made that any alarm would follow the same protocol as described in the mine's trigger action response plan (called ABS – HITS on the mine).

The basic steps are as follows:

1. The crew must withdraw to a safe area immediately.
2. The miner must notify the shift supervisor.
3. The shift supervisor, along with the miner, must inspect the stope hangingwall.
4. The trigger may be false or true. A false trigger occurs when the rock monitoring device has been triggered erroneously.
5. If the shift supervisor and miner deem the workplace to be safe and suspect a false trigger, the crew can re-enter after the workplace is declared safe. The decision will be guided by the tables provided below.

6. The shift supervisor must report the trigger to the mine overseer and the geotechnical engineering department for a team inspection of the workplace.
7. If the shift supervisor and miner are in doubt about the safety of the workplace, the area must be barricaded off, and the high-risk trigger (S-trigger) protocol must be followed.

Table II. Manuscript margins

TRUE TRIGGER	
Observations in the vicinity of the triggered unit	**Response**
a. Closure may be visible on grout packs and timber elongates (cracking of packs, buckling/splitting of elongates). b. Triggers on mine standardised instrumentation. c. Excessive scaling of nearby pillars. d. Open joints/fractures. e. Any other reason to suspect hangingwall separation.	a. The area is to be barricaded/abandoned. b. Record findings in the site instruction book. c. Record triggered unit. d. Report to Mine Overseer and Rock Engineering Department of trigger for team inspection of the workplace. e. Remedial action will be issued.

FALSE TRIGGER	
Observations in the vicinity of the triggered unit	**Response**
a. No closure observed on grout packs and timber elongates. b. No triggers on mine standardised instrumentation. c. No excessive scaling of nearby pillars. d. No open joints/fractures. e. No other reason to suspect hangingwall separation. (Inspect from the gully to the top of the panel/over the whole width between the face and pack support.)	a. Record findings in the site instruction book. b. Record triggered unit. c. Reset instruments. d. Report to Mine Overseer and Rock Engineering Department the trigger for team inspection of the workplace.

Geotechnical data recording (long-term, more than a shift recording and integration of LiDAR technology):

The pilot site was an unused haulage where a stope below the haulage was closing, causing the haulage footwall to heave and push, resulting in rocks detaching from the sidewalls and hangingwall. This location was ideal for recording rock mass behaviour. The NanoRadar was particularly suitable for this environment as it allowed for safe distance monitoring, avoiding the need to install other tools in the risky area.

As a safety precaution, a rope was attached to the NanoRadar to allow for its retrieval and data recovery in case the extent of the unstable rock mass increased. Additionally, the developer can research and develop the option of a remote synchroniser to stream the data, ensuring that no data is lost.

The NanoRadar data can be overlaid on LiDAR point cloud data. A drone flight was used to capture LiDAR point cloud data, illustrating the integration of the two data sets to create a visualisation of the results. While this process can also be applied to short-term recordings, the workflow to scan each stope per shift has not yet been implemented.

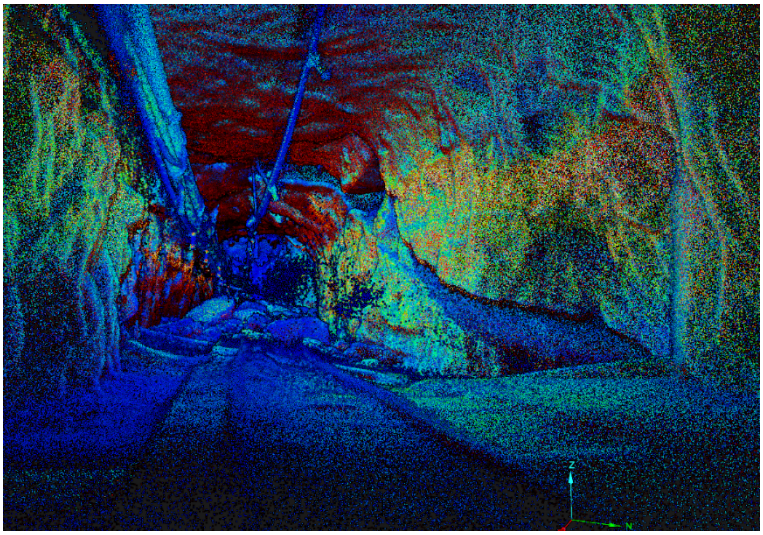


Figure 13. LiDAR scan from a drone flight displayed in a point cloud 3D spatial data software.

RESULTS AND DISCUSSION

Performance Evaluation
Early Warning Piloting Period:

The radar device has an accuracy limitation, with a maximum effective range of 60°
in the upward, downward, and side directions. This means that while the radar can provide valuable real-time monitoring and early warning for potential rockfalls, its coverage is restricted to a 60° angle in all directions. During the preliminary underground testing phase, prior to crew trials, it was observed that although the radar's maximum detection range is 20 m, the underground environment imposes limitations on this range due to the narrow mining width. Specifically, the angle from the hangingwall to the area of interest must not exceed 60° to maintain accuracy, as specified by the developer. Consequently, this reduces the effective detection range to significantly less than the anticipated 20 m. Figure 14 demonstrates this limitation in the radar's field of view within a narrow stope environment.

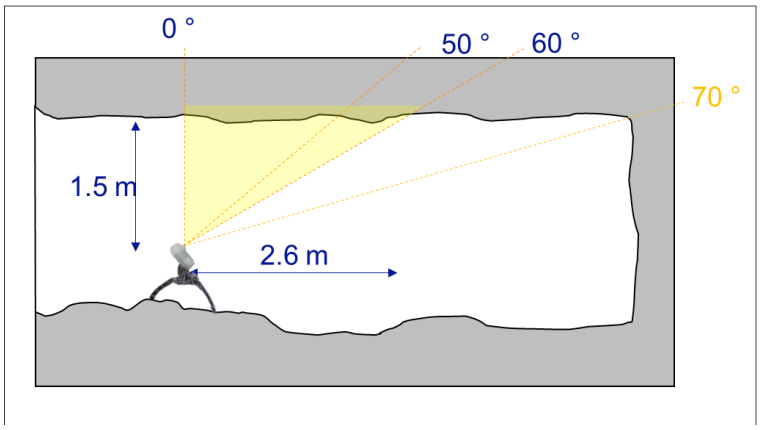


Figure 14. Stope side view: illustration of radar maximum effective range (degree).

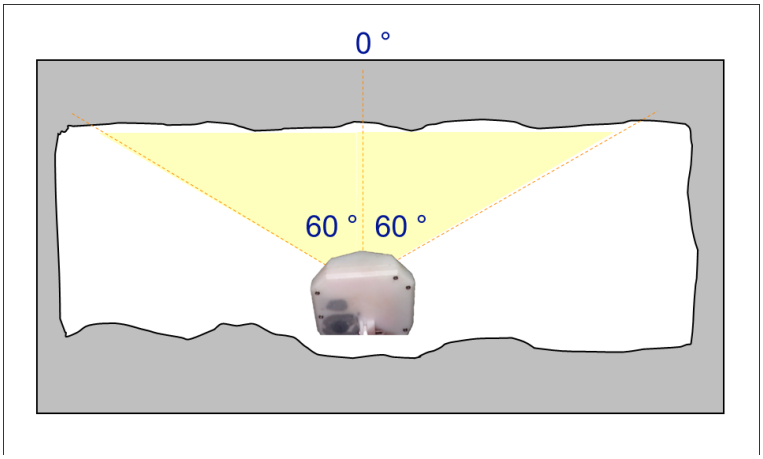


Figure 1. Top view to illustrate the radar maximum effective range (degrees).

During the early warning piloting period, one alarm was triggered. Upon investigation, a small portion of hangingwall rock, estimated to be 0.35 x 0.2 x 0.2 m, dislodged and rested on the blast-on mesh installed as primary support. The data was analysed, and it confirmed that the trigger was true. No other alarms or incidents of uncontrolled fallen rocks were reported by the crew, indicating no false alarms during the pilot period.



Figure 16. Dislodged rocks on top of blast on mesh. The alarm was triggered by the NanoRadar.

Figure 17 shows' the NanoRadar recording data of the rock dislodged in Figure 16 triggering an alarm. Data recording stopped after the 2 mm threshold was reached and the alarm was triggered. After this event, NanoRadar was reprogrammed to continue recording even after alarms were triggered. The 'hot' spheres indicate movements in the recorded resolution cell. The distance from the Nanoradar to the rock was 4.9 m.

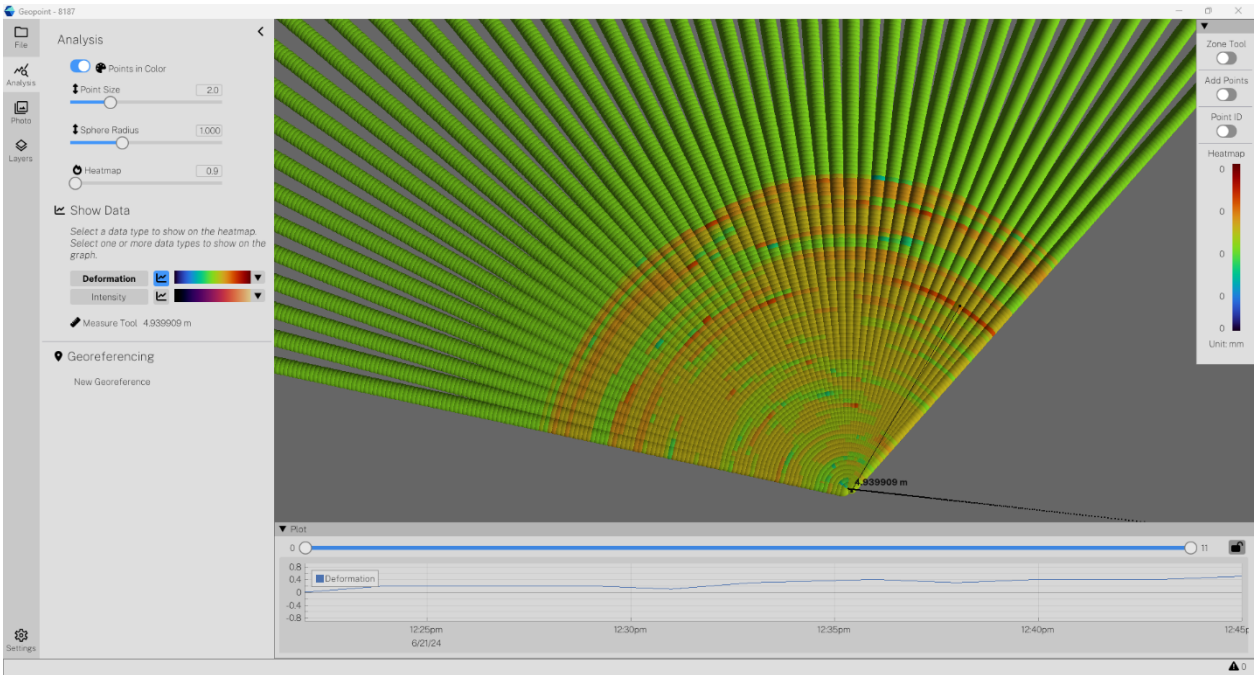


Figure 17. NanoRadar recording data of rock dislodge triggering alarm; note colour pallet of 0 to 1 mm, and cumulative deformation of 0.6 mm in the timeseries graph. Orange represents 0.15 mm of movement. The point selected is the dark red band on the right at 4.33 m range. Green zones are shadows or occlusions.

Throughout the pilot period, the system was used on each shift. Signs of bumping and scratching were observed on the outer body, but the tool's reliability, effectiveness, performance and robustness passed the testing. One issue identified early in the trial was the wireless charging units, which did not last and were subsequently redesigned with a safe waterproof charging port.



Figure 18. NanoRadar after five months in underground trial.

The deployment tripod showed signs of leg bending and may wear out before the system body needs

replacement. However, the wear and tear of the system and tripod could not be fully verified as no parts were replaced during the six-month piloting period except for the improvement of charging.

There were two instances where the batteries drained, and data showed that the system was not stored correctly in an upside-down manner to enable auto-sleep. During the initial stage of the piloting, data was lost when the system was placed on charge. The system was programmed to download data to the hub upon charging, which would then be uploaded to cloud storage. However, the network configuration planned for the pilot stage allowed remote access from the developer to test and investigate the data. The network provider was Vodacom, with a top-up data setup, and when the data airtime ran out, the data was dumped due to the low memory threshold on the system. The memory threshold was subsequently increased to prevent data loss during network instability or downtime.

Long-term Testing:
The long-term testing was successful, with accurate data obtained indicating rock movement in both positive and negative directions. The overlay of point cloud data presented challenges, but the developer rectified these issues and further upgrades are planned. Positioning the radar on the point cloud and rotating the image to achieve alignment was difficult. However, once the system was spatially positioned with georeferenced cloud data, the visualisation was well-developed and clear, providing a better understanding of the rock mass. These user-friendly challenges were being addressed to enhance the user experience.



Figure 19. NanoRadar placed in an old haulage recording movement data.

Analysis in the developed software

Analysis
Data can be converted to 3D via the addition of a background point cloud when available. Otherwise, it is visualised in the radar's native 2D format, with pixels visualised as spheres or as a surface in 2D or 3D. This data is coloured from 'hot' to 'cold' and 'green' areas representing stability. 'Hot' areas of the map indicate large movements of deformation, 'cold' areas show deformation away from the radar, and 'green' areas represent stability. By selecting a point or multiple points, a user can quickly visualise a time series chart showing deformation over time, facilitating data interpretation.

Heatmaps and plots for analysis
Users can measure movement over time, by referring to colour point cloud maps. Clicking any point in the heatmap reveals a timeseries plot showing displacement over time. Selecting multiple points allows for comparing or averaging measurements between points. The rate of change in deformation provides

insights into the rockmass behaviour: a flat trend suggests stability, a regressive trend (slowing down of movement) indicates the rockmass is stabilising; a steady rate of movement shows the rockmass is moving but not yet heading towards collapse, while an accelerating trend indicates an imminent collapse.

Layers
During the analysis and also writing of reports, it was found to be more intuitive to group areas of interest into 'layers' and then hide or display them as needed. This not only ensures clean visualisation but also makes it easier to find interesting data again and generate finding reports.

Real-time data visualisation
The tool is designed for real-time monitoring, enabling data visualisation both on the surface and in a control room. However, this capability could not be tested in this piloting as the mines currently lack the necessary network fibre backbone or wireless meshing infrastructure to support connectivity up to the stopes or working environment. Geobotica tested the concept on a surface operation, successfully visualising NanoRadar data remotely using the developed software.

Long-term testing results in the developed software
In Figure 20 the background point cloud is visualised in red. It can be seen that the rock mass was moving toward the radar and away from the 'hot' and 'cold' colours of the spheres. The results can also be presented in different data types such as deformation, intensity (amplitude), velocity, and inverse velocity. In this location, large tension cracks in the sidewall and footwall were visually observed, so the radar was deployed in the area. In the time series (Figure 20) background creep is visible in positive and negative movements, towards and away from the sensor that matches the location and geotechnical movement of the ground in the matching locations.

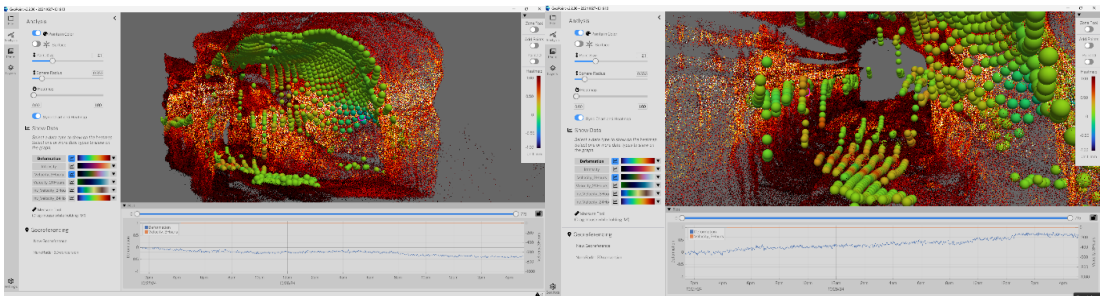


Figure 20. NanoRadar long-term recording data results inside old haulage where rockmass deformation was experienced.

Suggested Workflow:
As the pilot involved a maximum of three systems, the charging and network setup was managed within the geotechnical department office from where the crew supervisor reported daily. The process has not yet been tested for scenarios involving the deployment of a large number of units to production on a daily basis.

The diagram in Figure 21 illustrates the suggested routine integrated workflow for using NanoRadar on a large scale in an operational mine.

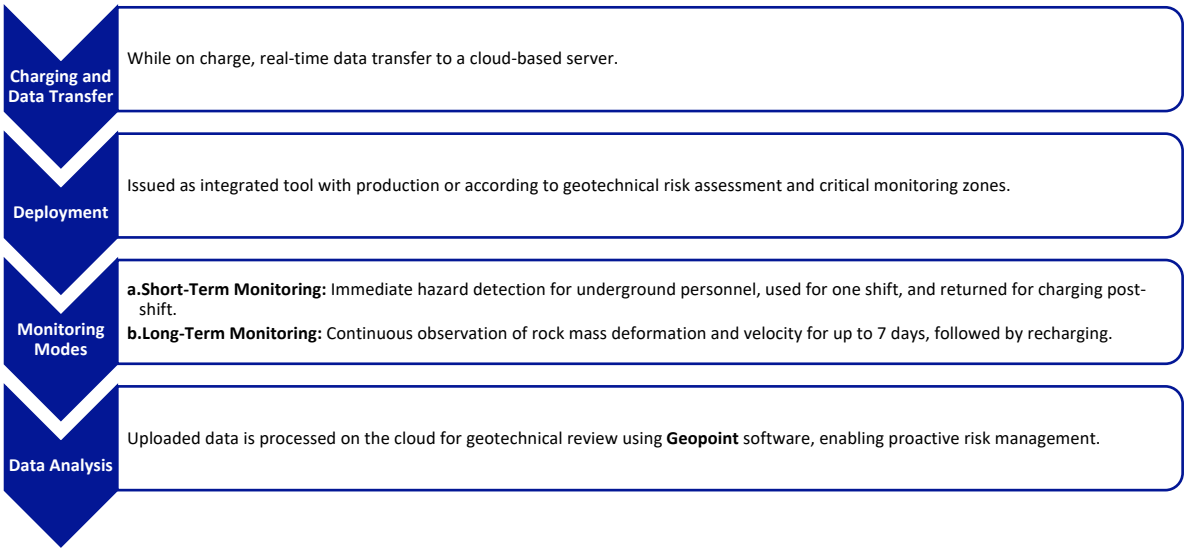


Figure 21. Diagram illustrates the suggested routine integrated workflow for using Nanoradar in a large scale on an operational mine.

Other Application

During the R&D phase, it was identified that the developed radar could be utilised for surface applications, including the recording of any surface slope area. To enhance its capabilities, radar transmission gain was increased to extend its maximum range from 20 m to 80 m. This upgrade allows the system to monitor surface slopes from greater distances and effectively record rock falls or slope movement.

The surface system was also equipped with a self-sustaining solar battery station, which facilitates mobility and remote operation. Additionally, it features built-in network capabilities to record data in real-time, enabling mine operators to monitor the data from a control room. This system was piloted at Anglo American's surface operations in Australia and would be an addition to the surface mine monitoring strategy.



Figure 2. Surface unit that is a solar-battery hybrid system.

CONCLUSION

The piloting process for the system was comprehensive, involving multiple stages of testing to ensure compliance with all required standards. From laboratory assessments to field trials, the system consistently demonstrated its functionality, reliability, effectiveness, performance, and robustness in narrow stope real-mining conditions.

In an operational environment, NanoRadar validated its capabilities, achieving TRL 9, indicating it is ready for full commercial deployment.

It met the operational needs of underground mining by accurately detecting rock movement and providing early warnings. Long-term testing confirmed its accuracy, with data indicating rock movement and enhancing visualisation and interpretation through point cloud data overlay.

Key Advances of the NanoRadar:

- Real-time movement recording: For the first time, the NanoRadar enables the recording of rock movement over time until dislodgement from a safe distance.
- Enhanced safety: This tool significantly enhances safety by providing early warnings of potential rockfalls.
- Rock mass behaviour analysis: It allows for detailed study and understanding of rock mass behaviour.

Additionally, NanoRadar's capabilities were extended to surface applications, making it a versatile tool for both underground and surface mining operations. It has shown potential to replace current early warning tools, offering reusability and the ability to be installed, removed, and redeployed as needed.

LESSONS AND FUTURE DEVELOPMENT

1. Interference from nearby equipment: In highly sensitive submillimetre monitoring technology, other nearby equipment can cause interference. For the system, vibrations from the hangingwall support holes caused interference with the technology when a telescoping pole was used as a deployment method. As a result, the footwall tripod deployment method proved effective in mitigating this issue.
2. Water flowing and atmospheric water particles: Water flowing and particles in the atmosphere reduced signal strength, causing poor recording. The casing and hardware were specially designed to mitigate this effect.
3. Atmospheric water particles: Water running over the antenna reduces signal strength, causing poor recording. The casing and hardware were specially designed to mitigate this effect with good results.
4. Data interpretation: The interpretation of data is similar to that of open-pit radar data.
5. Future development for deployment method: The deployment method needs to be piloted or modified specifically for mechanised operations with high stoping widths, such as 5 m.

REFERENCES

Bekkerman, I., & Tabrikian, J. (2006). Target Detection and Localization Using MIMO Radars and Sonars. IEEE Transactions on Signal Processing, 54(10), 3873–3883.

Bhattacharya1, S., Kumar, V., Nishad, S.N., (2012). Technology Readiness Level: An Assessment of the Usefulness of this Scale for Translational Research. Productivity 2012, 62(2),112-124.

Cecchetti, M., Rossi, M., Coppi, F., Bicci, A., Coli, N., Boldrini, N., Preston, C., (2017). A novel radar-based system for underground mine wall stability monitoring. Underground Mining Technology 2017, Sudbury, Canada pp. 431-444.

Fall of Ground Safety Performance, MOSH FoG, Learning Hub, Minerals Council, Rock Engineering Technical Steercom, 2025.

Noon, D. A., Stickley, G. F., Longstaff, D. (2001). Remote sensing of wall movement using the slope stability radar. In Proceedings of the 10th International Congress of the International Society for Mine Surveying (ISM), Brisbane, Australia, pp. 1–9.

Ryan, B. (2022). New technology aims to stop an old danger in South Africa's mines. Miningmx. Retrieved from https://www.miningmx.com/news/markets/51520-new-technology-aims-to-stop-an-old-danger-in-south-africas-mines/

Strouth, F. T. K. T. F., Beckett, L., Dunnicliff, M. T. (2006). GroundProbe Slope Stability Radar for Monitoring Open Pit Mine Slopes, in Proceedings of the International Symposium on Stability of Rock Slopes in Open Pit Mining and Civil Engineering Situations, Cape Town, South Africa, 2006.



Dewaldt van Rooyen

Specialist Geotechnical Engineer
Anglo American

Dewaldt is a Specialist Geotechnical Engineer at Valterra Platinum. Previously with Anglo American Group Mining he brought 23 years of mining experience to his role with Underground Future of Work and technological improvements within the Group Mining Team. He started as a learner official in 2000 and quickly advanced to eventually managing a number of employees as a Rock Engineering manager. Besides earning the COM Rock Mechanics certificate, his academic achievements include holding six University Post Graduate Competency Certificates in the field of Geotechnical Engineering.

Demonstrating notable leadership and technical skills, some of his key achievements include revising the mine pillar design and support optimisation for a business unit with four operational mines, developing the Trigger Action Response Plan in 2009, integrating a routine monitoring system into operational cycles, and introducing Strata Control technicians to audits before blasting. His innovative side led to the development of a machine learning algorithm to forecast risk areas of fall of ground and UG radar technology.

Dewaldt is an active member of the South African National Institute of Rock Engineering (SANIRE) and the Rock Engineering Technical Counsel (RETC) in collaboration with the Mineral Council of South Africa to combat falls of ground in the mining industry.

On a personal note, Dewaldt has been happily married to his lovely wife, Frieda, for 19 years. They have two children: a 16-year-old daughter and a 12-year-old son. Dewaldt's dedication to excellence and continuous improvement has made him a respected leader in geotechnical engineering field and a sought-after peer to go to for advice. His impeccable sense of humour also makes him all round great guy to work with.

Monitoring mining-induced subsidence and sinkholes using multi-band InSAR: A case study from Lubambe Copper Mine

P. Chipola[1], R. Sililo[1], A. Mkandla[2], M. Douglas[3], M. Spreafico[3]

[1]Lubambe Copper Mine, Zambia
[2]TRE Altamira, South Africa
[3]TRE Altamira, Italy

A holistic geotechnical monitoring approach is vital for ensuring operational safety and minimising risks that could impact production and human lives. Comprehensive monitoring requires the integration of multiple geotechnical sensors and a dynamic adaptive strategy. This technical paper is a multiband interferometric synthetic aperture radar (InSAR) monitoring case study of a shallow underground mine located near critical infrastructure and challenged by the presence of sinkholes and dense vegetation.

The presence of dense vegetation required the use of a multiband InSAR approach to effectively monitor surface deformation across the site, including its impact on adjacent infrastructure. The InSAR data was integrated with ground-based surveys and field inspections to provide further understanding of ground behaviour. This integrated approach enabled the detection of precursor movements, allowing for proactive risk mitigation and enhanced operational safety.

This paper will outline the key challenges faced, the innovative techniques employed, and the tangible benefits of integrating satellite monitoring systems in mitigating geotechnical risks and ensuring operational continuity.

INTRODUCTION

Geotechnical monitoring has become an essential component of modern mining operations, ensuring safety and operational efficiency of mines, including underground mines (Falorni *et al.,* 2018). Over the past decades, advances in remote sensing and geospatial technologies have significantly enhanced the ability to monitor ground deformation, providing critical insights for risk mitigation and mine planning (Wang *et al.,* 2011). Among these technologies, interferometric synthetic aperture radar (InSAR) has emerged as a powerful tool for detecting and analysing surface subsidence and ground movement associated with underground mining activities (Mohamadi, 2024). The integration of InSAR with traditional geotechnical monitoring techniques offers a more comprehensive approach to understanding subsidence dynamics, improving predictive capabilities, and enhancing mine safety (Falorni *et al*., 2018) as in the Lubambe case. This case study provides insights on how InSAR can be incorporated with traditional monitoring techniques and highlights the monitoring benefits that come from multiband InSAR datasets (C-Band and L-Band).

Lubambe mine, approximately 468 km from Lusaka, is located in the north-western extremity of the Zambian Copperbelt province, (Figure 1). The underground mine operation is on two separate orebody limbs referred to as the South Limb and the East Limb. The mine employs a longitudinal overhand longhole retreat (LHR) open stoping (without backfill) mining method, which allows for open or unsupported voids to be left underground after ore extraction, leading to rock collapse and subsequently surface caving (subsidence).

Recognising the challenges posed by poor rock mass conditions and historical near surface stopes, the mine took proactive measures to safeguard the critical infrastructure, such as a government road and electrical transmission lines. Before the year 2020, a surface monitoring system was not in place, which limited the early detection of the first subsidence event. However, following this, the mine promptly responded by implementing a comprehensive monitoring strategy. The Geotechnical Engineering Department deployed three advanced surface monitoring systems comprising drone surveys, InSAR, and Trimble 4D, enhancing both strategic and real-time ground movement tracking.

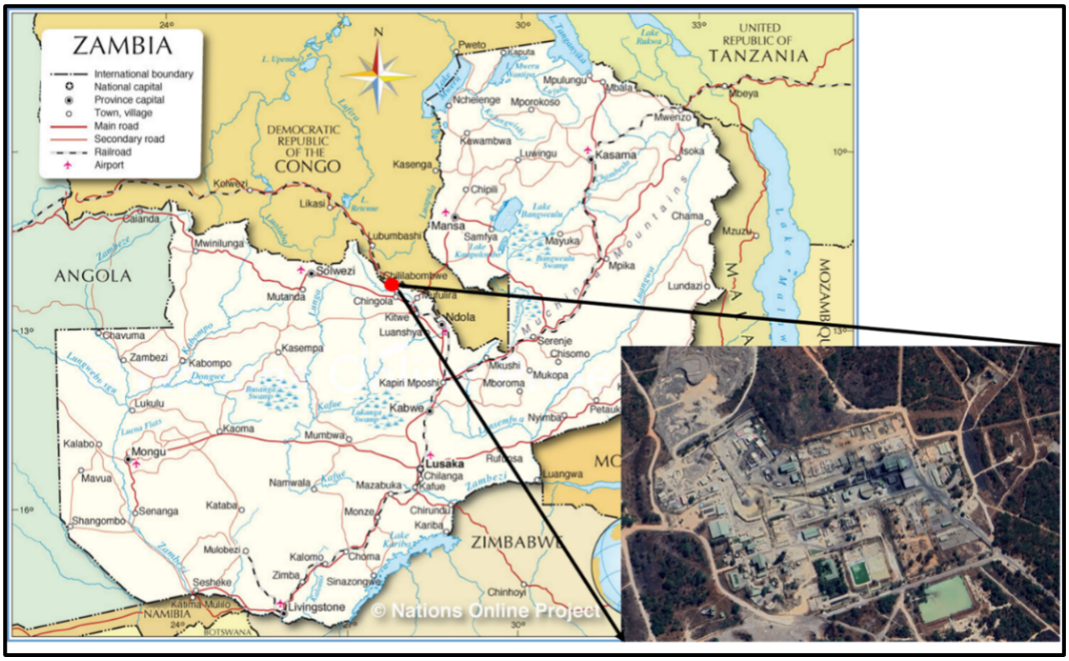


Figure 1. Location of Lubambe Copper Mine Limited in the Copperbelt province of Zambia.

BACKGROUND

Geologic setting

The Konkola North copper deposit, located at the northwestern edge of the Zambian Copperbelt, is an autochthonous 'Zambian-type' deposit within the late-Proterozoic Lufilian Arc fold and thrust belt. It is hosted in intracratonic rift sediments deformed by the Lufilian Orogeny and underlain by the Katanga Sequence of the Roan Group, which comprise thick clastic sediments, primarily arenaceous and argillaceous materials. Copper mineralisation is mainly found in the Ore Shale 1 (OS1) Member of the Nchanga Formation, a key reducing horizon overlying oxidised arkoses and conglomerates. The OS1 Member unconformably overlies the Kafufya Formation, indicating a transgressive event, while mineralisation transitions eastward into the Ore Shale 2 (OS2) Member.

The Konkola North Copper Project hosts stratiform sediment-hosted Cu-Co ore, the shale-type mineralisation, similar to the Nchanga and other Konkola deposits. The OS1 Member, typically 15-20 m thick, extends over 10 km at individual mines, with ore body thicknesses of 5-5.5 m at Lubambe Copper Mine. Mineralisation consists of copper oxides and sulphides, including chalcocite, chalcopyrite, and bornite, while non-sulphide minerals such as malachite, chrysocolla, and native copper occur along fractures and veins. Drilling results confirm continuous mineralisation over an area of 28.2 km², spanning from the Mushoshi orebody in the north to the Konkola Division North orebody in the south. The total geological resource is estimated at 297 million tonnes, with an average grade of 2.57% total copper.

Mine overview and history

Surface infrastructure located within the caving area

The Google Earth image shown in Figure 2 shows the surface infrastructure that is located within the mine caving area. Listings in Table I describe the key infrastructure with respect to operations underground being monitored with InSAR and ground-based instruments. Surface monitoring results over these areas are discussed in the subsequent sections.

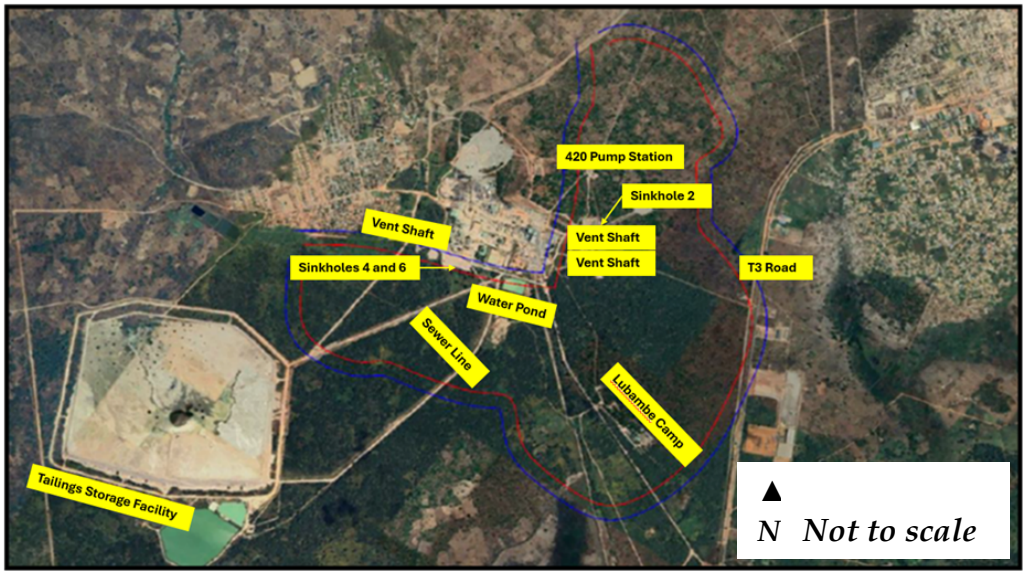


Figure 2. Depicting an aerial view of the Lubambe mine site with key assets overlaying and surrounding the underground operations.

Table I. Main infrastructures being monitored surrounding the mine's underground operations

Asset/High-risk area	Description
420 Pump Station	**Positioned in the east limb caving area but on the footwall side, making mining-induced sinkholes unlikely.**
Tailings storage facility truck routes	**Located ~200m from the cave line. If mining follows stability guidelines (Ohms 2020) and backfill recommendations, the risk remains low.**
Lubambe mine camp	**Positioned on the hanging wall side of the ore body, reducing immediate caving risk. regional pillars have been introduced to slow caving over time. In-stope pillar practices also help mitigate additional risk.**
Main sewer line	**Located beneath ramp 2 in a high-risk zone where six sinkhole events have been recorded. Urgent relocation is necessary to prevent potential damage due to subsidence.**
Ventilation shafts	**The shafts are within the southwest and eastern parts of the limb caving area. The southern ones are most at risk, with sinkhole development occurring 60 m close.**

Evolution of sinkholes and cracks

Over the past five years, Lubambe mine has recorded several sink holes that occurred with the advancement of mining activities. These sinkholes typically occur near surface infrastructure and are backfilled promptly once the area is deemed stable. This backfilling process helps confine the void and inhibits further propagation, which, if not prevented, could pose a risk to the surface infrastructure.

Several sinkholes developed and failed with the progression and advancement of mining activities over the past five years. Sinkhole 2 (Figure 3) formed on the south limb, caused significant damage to surface infrastructure, including the Konkola-Chimfunshi Road passing the Lubambe Camp, which was temporarily closed. After successful backfilling, the road was reconstructed with heavily reinforced concrete and reopened. Later, Sinkhole 4 emerged near the general administrative office's gate (GMO), inducing tension cracks in the reconstructed road. Sinkhole 6 then developed near sinkhole 4, causing severe subsidence of over two metres and rendering the road unsafe. Most recently, the sinkhole close to the GMO reactivated (sinkhole 4), combining with the effects of sinkhole 6 and impacting the areas with key infrastructures (Figure 3 below).



Figure 3. Occurring sinkholes recorded between 2020 and 2025 within the Lubambe mine operating areas.

GEOTECHNICAL MONITORING METHODS

Major infrastructure areas employ enhanced monitoring through InSAR, ground-based instruments (T4D), and routine inspections. Effective monitoring necessitates close collaboration between on-site and off-site teams to integrate and correlate diverse data sources, ensuring the differentiation of false positives from actual threats.

Interferometric Synthetic Aperture Radar

InSAR is a remote sensing technique capable of detecting ground displacement with millimetric precision, making it highly effective for mining applications due to its regular data acquisition intervals (approximately bi-weekly) and extensive coverage compared to ground-based methods. Using microwave frequencies, these satellites can monitor the Earth's surface regardless of weather conditions or time of day, enabling monitoring in areas not easily accessed by the traditional ground-based instruments. InSAR works by emitting electromagnetic waves and analysing their return signals (Figure 4, Ferretti, 2014), which are typically stronger (more coherent) from man-made structures, bare ground,

and rock surfaces, while weaker returns occur over vegetated areas (depending on wavelength), and no signal is backscattered from water bodies (Ferretti, 2014). A limitation of InSAR data that should be considered is unwrapping errors – a measurement point moving more than half of the wavelength in between two images – and the phase shift would not be accurately captured and must be considered with all InSAR datasets.

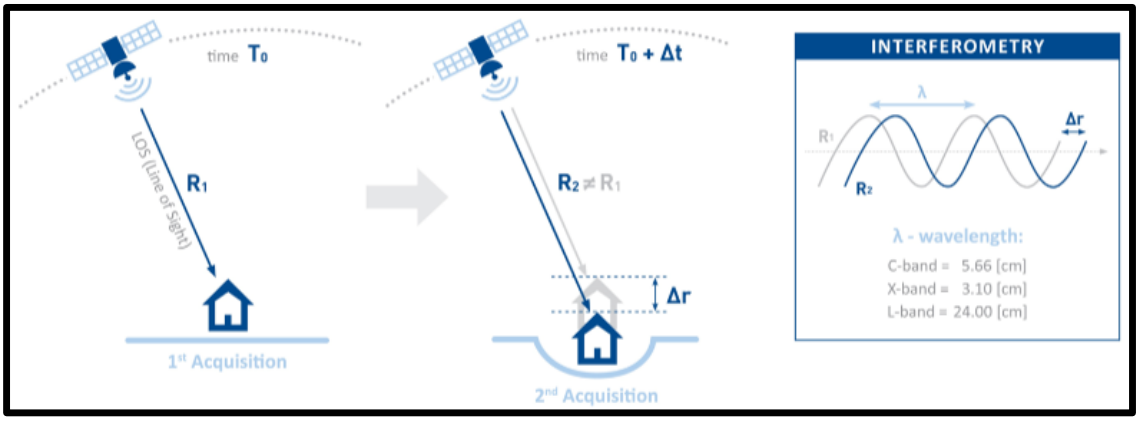


Figure 4. On the left, the InSAR method compares the backscattered signals (R_1 and R_2) from two consecutive radar images then determines the phase shift of the wavelength on the right (Ferretti, 2014).

SqueeSAR, a patent of TRE Altamira, is an advanced multi-temporal InSAR technique developed to improve ground deformation monitoring by analysing both persistent scatterers (PS) and distributed scatterers (DS) in radar images (Ferretti *et al.*, 2011). Unlike traditional PS-InSAR, which relies only on stable, highly reflective targets such as buildings and exposed rock, SqueeSAR extends the analysis to less coherent surfaces, including soil, vegetation, and man-made structures with lower radar reflectivity. By combining information from both PS and DS, SqueeSAR significantly increases the density of measurement points, enhancing its ability to detect and monitor ground displacement in areas with sparse infrastructure or complex terrain.

SAR dataset

Several factors must be considered when selecting a satellite for mine monitoring, including, but not limited to, satellite viewing angle, site topography, wavelength, ground resolution, revisiting frequency and cost. The properties of the SAR satellites used in this project are indicated in Table II. The C-band Sentinel (SNT) with a resolution of 5x20 m is generally more suitable for monitoring man-made objects such as buildings, roads and stockpiles, while, due to its short wavelength (~5.6 cm) is more susceptible to interference from vegetation. Conversely, L-Band ALOS-2 data with a much longer wavelength (~23.6 cm) can penetrate vegetation enabling a better coverage over vegetated areas, however, this wavelength has a lower sensitivity and can have more noise in its time series when compared with C-Band data (see quality parameters listed in Table III).

Table II. SAR image properties used in the monitoring over the Lubambe mine area

Satellite	Orbit	LOS Angle (°)	Wavelength	Cell Resolution
SNT	Descending	32.4	~5.6 cm	5 x 20 m
ALOS-2	Descending	35.8	~23.6 cm	50 x 15 m

InSAR datasets are variable in their quality due to many factors such as atmospheric noise, humidity, vegetation, wavelength, image resolution, number of images in the dataset (Ferretti, 2014). All of these factors affect InSAR datasets and should be considered when comparing the statistics between two SAR

datasets. Some quality parameters are listed in Table III as reference for the datasets used in this case study.

Table III. InSAR dataset quality parameters

Satellite	Minimum Coherence	Maximum Standard Deviation (mm)	Average Standard Deviation (mm)	Average Velocity Standard Deviation (mm/yr)
SNT	0.95	3.0	1.6	3.9
ALOS-2	0.80	14.0	10.4	5.0

Datasets are provided via online platform and checked for any anomalies or changes. This includes looking for accelerations (> 35 mm/yr^2) over the past month of monitoring, or any significant displacement over the last month (> 15 mm). These thresholds have been determined for this specific dataset based on the typically observed displacements and applied for internal purposes.

Ground-Based Monitoring

Trimble 4D is an automated ground monitoring system that utilises robotic total stations to capture, process, and analyse data in real-time. There are currently 18 active monitoring points (prisms) mounted across the mine, with data transmitted to the total station mounted on the shaft headgear for subsidence monitoring.

Sixteen monitoring points are located within or near the south limb caving area, while the remaining two points are positioned in the east limb caving area. The majority of the monitoring points are located on the southern limb for the following reasons:

- Proximity of surface infrastructure: Three-quarters of the surface infrastructure close to the caving area is located on the south limb.
- Historical mining activity: Mining activities dating back to the early 1950s were primarily conducted on the south limb, which has been established as the main contributor to subsidence at the mine.

Table IV shows the monitoring stations distributed throughout the site monitoring specific assets on the south and east limbs.

Table IV. Monitoring points mounted across the mine site

S/N	Location	Number of monitoring points
1	GMO Car park	2
2	CV-185	3
3	South Limb Caving Area	11
4	East Limb Caving Area	2

As seen in the number of stations, the main disadvantage of the ground-based monitoring systems is the coverage. These stations were chosen because of the known displacements that were observed, however, new areas of displacement would be missed because of the sparse number of monitoring stations. Data validation between InSAR and ground-based systems were explored previously (Ferretti, 2007 and Peltier, 2010), but not completed as part of this case study.

RESULTS AND DISCUSSION

L Band vs C band coverage

As previously highlighted, two bands were used for the monitoring of Lubambe mine – the C-Band and the L-Band data. The results of each band over the whole Lubambe area of interest (AOI) are depicted in Figure 6. The C-band with medium resolution provided more points in cleared areas such as the mine

infrastructure, roads, tailings storage facility, and the nearby community neighbourhood. The vegetated area at the heart of the AOI is well covered by the L-Band data showing deformation typically indicative of subsidence. The data coverage complement each other, highlighting different areas of displacement. C-Band and L-Band datasets were compared and areas where there was coverage the displacement rates observed were comparable (eg., within +/- 10 mm/yr) however with the differing time frames, resolution, sensitives, accuracy and wavelength, the datasets were generally used to identify different areas of displacements and have larger coverage. The C-Band dataset was used for higher risk areas where there was coverage and the sensitivity to smaller movements was necessary (eg., surrounding the infrastructure areas and known sinkholes), whereas the L-Band dataset showed larger areas of deformation and the edges of the displacement 'bubbles' within the cave extents were able to be defined with the longer dataset. Some of the areas, e.g., the GMO, have overlapping coverage from InSAR and ground-based instruments, while most of the AOI is only being monitored by InSAR.

One of the main observations looking at the data overview is the correlation between the main areas of displacement and the cave extents seen in Figure 6. The L-Band data shows two large areas of displacement rates less than -50 mm/year which are roughly centralised over the south and east cave limbs, and the SNT data over the cleared areas in these zones also show comparable displacement rates.

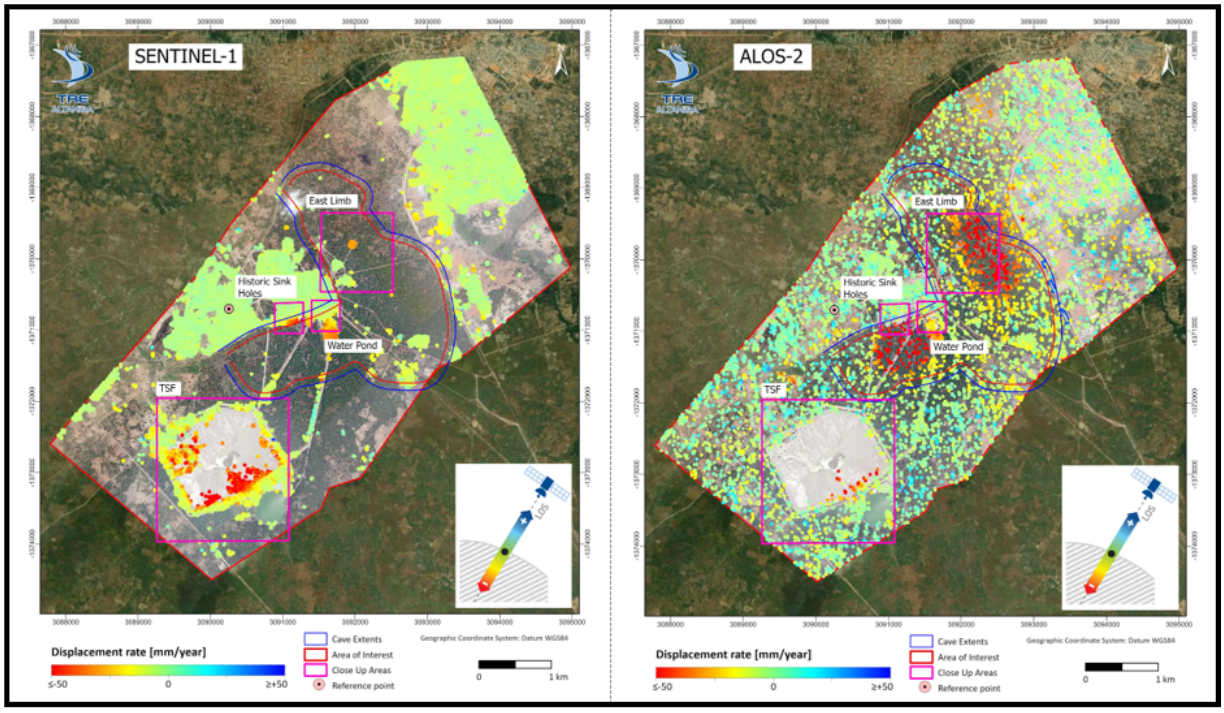


Figure 6. InSAR coverage over Lubambe mine AOI. On the left are the C-Band data; on the right the low-resolution L-Band.

Sinkhole 2 area

Sinkhole 2 occurred above an old historical open stope 65 m below the surface. This old stope was overlain by weak overburden material with high kaolinite concentrations. Ground conditions in this area were further exacerbated by a perpetual collection of stormwater and overflows from Mulonga treatment plant, causing the back of the stope to collapse, and the overlying material migrated into the stope resulting in the formation of sinkhole 2 (Figure 6).



Figure 6. Sinkhole 2 aerial image taken in September 2024, before backfilling in December 2024.

Sinkholes have been filled in and continue to be monitored using both ALOS-2 and SNT dataset (Figures 7, 8 and 9). Figure 8 is a cross-section generated using 100 x 100 m cell size that averages all the points located within the cell along the section line (cross-section line shown in Figure 7). Each blue line in Figure 8 represents an acquired image, the lighter blue represents the older images, while the darker blue lines are more recent images. The red represents the last image in the data set. This section line completely crosses the east limb cave extents, highlighting the increased settlement in the middle portion of the cave and more stable areas at the edges.

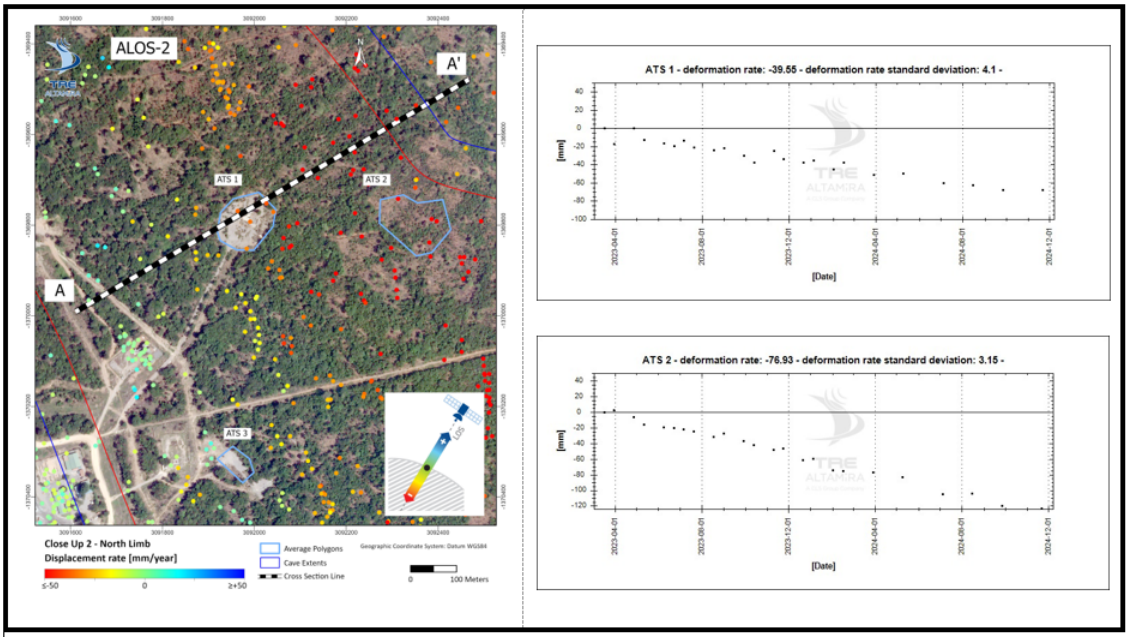


Figure 7. InSAR coverage using the ALOS-2 dataset (L-Band) highlighting large areas of displacement over the vegetated areas within the caving extents.

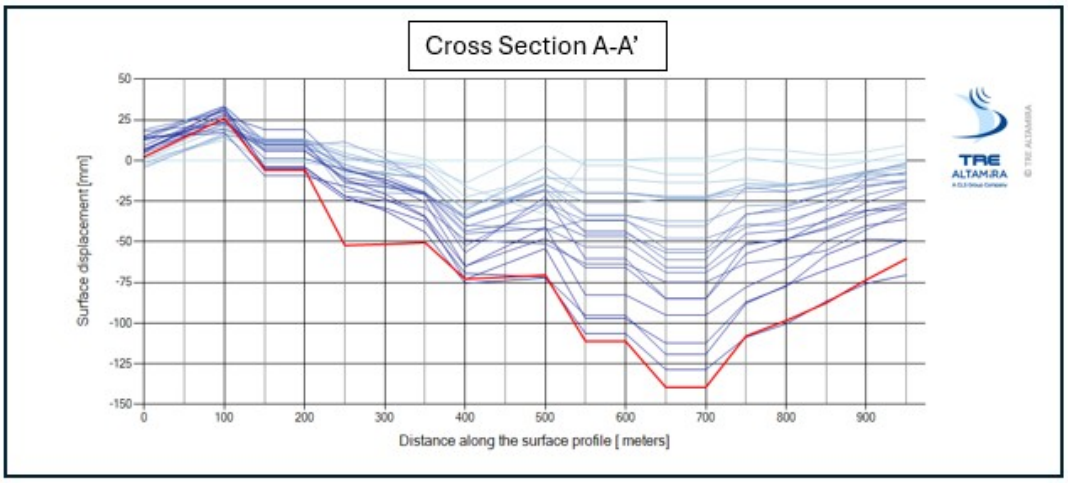


Figure 8. Settlement profile along cross-section A highlighting the larger settlement at the eastern extent of the caving boundary.

The whole area is better covered by L-Band dataset (Figures 7 and 8), while the SNT dataset has a good coverage on the exact location of the sinkhole 2 (Figure 9, ATS 3). In Figure 7, two interesting areas showing settlements were highlighted, ATS1 and ATS2, with their relative average time series (above).

Figure 9 shows the C-band coverage in the same area. As expected, the data mainly covers infrastructure and non-vegetated areas. InSAR data shows approximately -20 mm of settlement between September 2023 and March 2025 in proximity to sinkhole 2 (ATS3). Although no significant surface changes have been observed, this area continues to be monitored for accelerations. For ATS1 area the displacement rates are consistent with those observed with the L-Band satellite (between -31 mm/year and -39 mm/year).

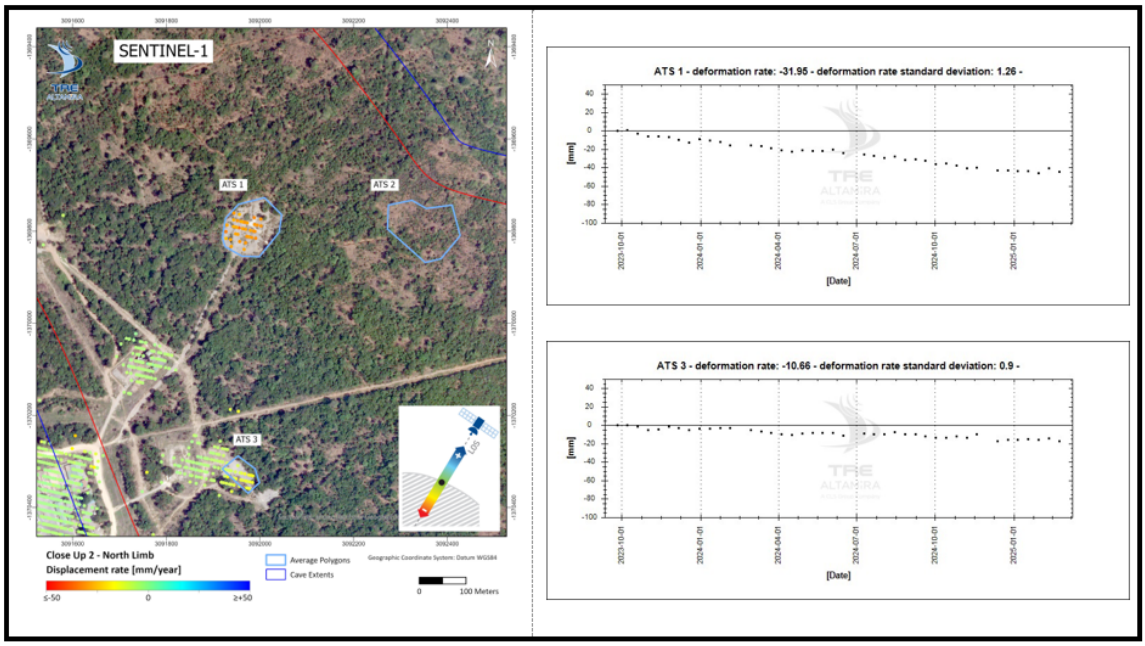


Figure 9. InSAR coverage using the SNT dataset (C-Band) highlighting an area of displacement ATS 1 and continuous monitoring of a previous failure area ATS 3.

Historic Sink Holes and New Cracks

The area surrounding sinkholes 4 and 6 has experienced previous failures and continuing displacements. These failures were monitored primarily using the SNT data and any accelerations were noted and investigated on site. Figure 11 shows an area that has previously experienced cracks and large sinkholes. The polygons indicate the average time series that were chosen based on areas of interest (e.g., existing failure areas at ATS 4) and areas that showed acceleration (> 35 mm/yr^2) over the monitoring period (ATS 5 and 6). ATS 4 shows a relatively linear trend throughout the monitoring period (approximately -40 mm/year). The average time series for polygons ATS 5 and 6 shows an acceleration at approximately mid-August 2024 and an increasing displacement rate. Following the reports from the data in September 2024, where the acceleration was noted, this area was inspected, and new cracks were identified on the ground in the area of ATS 5 and 6 (Figure 11).

Cross-section B (generated with cell sizes of 30 m x 30 m, Figure 12), was selected to follow the path of the well-trafficked road. The western portion is in a relatively stable area (as reported on site), approaches the active sinkhole areas and then ends at the entrance to the administrative buildings. This cross-section was used to highlight differential settlement along the road and monitor whether the sinkholes were progressing towards this highly active area. Differential settlement was observed and upon further inspection on site the cracks reported in Figure 11 were identified.

Further investigations later confirmed that the primary cause of the sinkholes was the failure of the crown pillars, resulting from historical mining activities. These mines operated closer to the surface, at a depth of approximately 90 m below the ground. In addition to legacy mining activities, more recent works involving excessive dewatering for about two months in these areas further exacerbated subsidence. Since October 2024, the InSAR data shows decelerating trends in these areas, and it continues to be monitored as the water conditions change throughout the seasons.

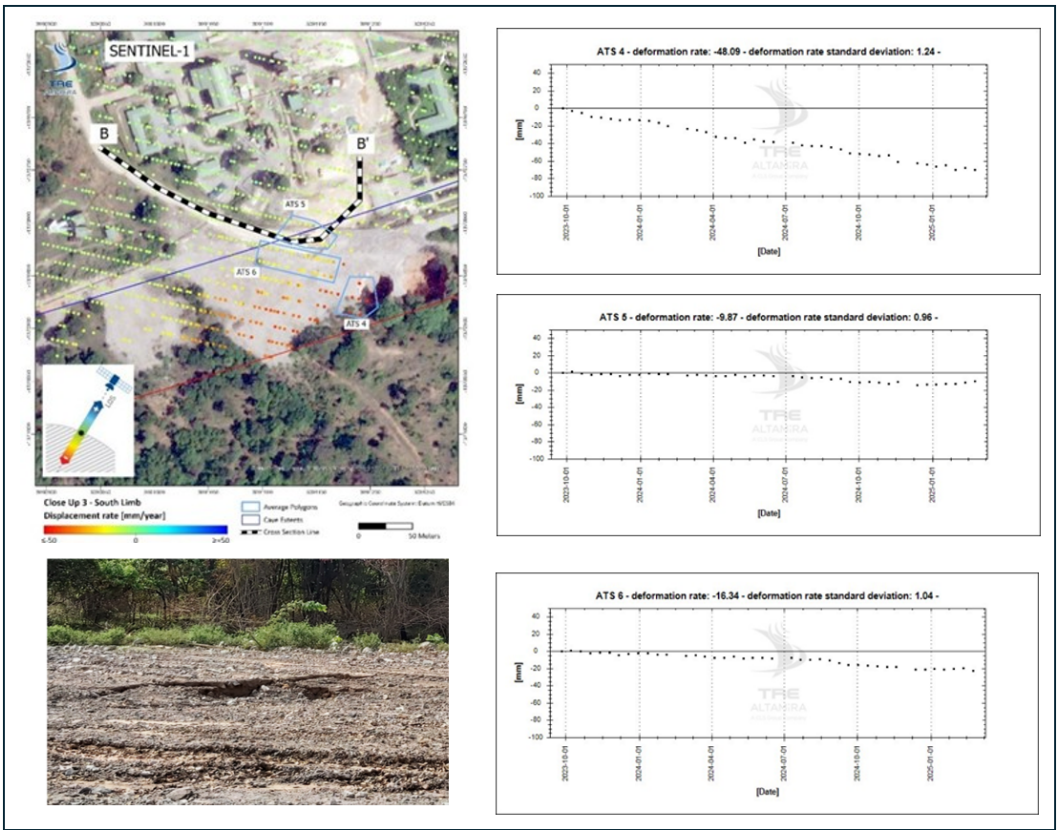


Figure 11. InSAR coverage using the SNT dataset (C-Band) highlighting areas of displacement surrounding the sinkholes (ATS 4) as well as accelerations in the current dataset (ATS 5 and 6). On the bottom left is a crack observed in proximity to ATS 5 and 6 in the area of the existing haul road to the mine facilities.

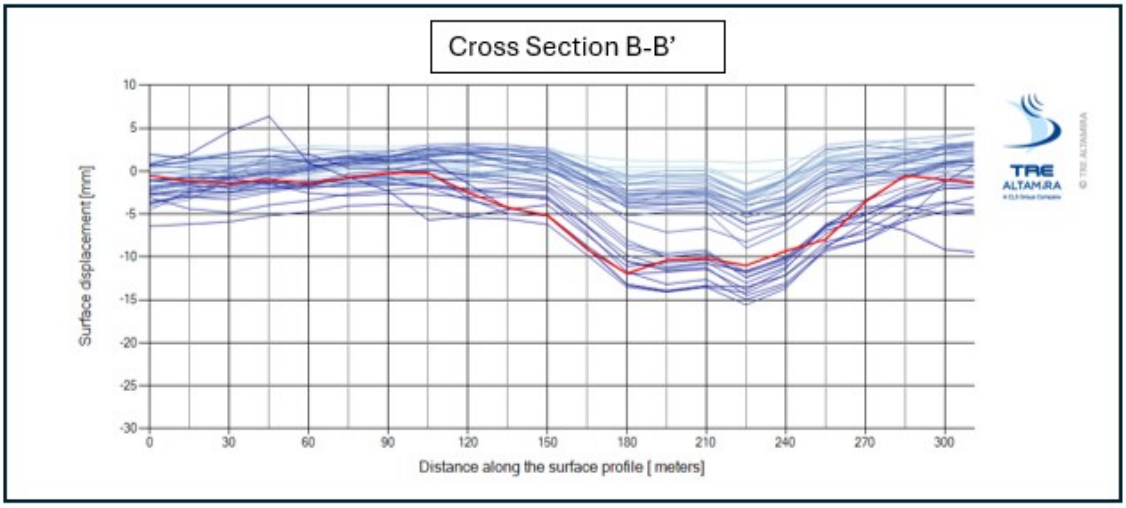


Figure 12. Settlement profile over the haul road area with maximum settlement in the area of ATS 5 and 6.

CONCLUSION

Effective geotechnical monitoring is critical for ensuring safety and operational continuity in mining, particularly in complex environments like Lubambe copper mine, Zambia. The integration of InSAR has significantly improved risk assessment by detecting precursor movements linked to subsidence and sinkholes. Ground based monitoring has been effective in monitoring areas of known displacements, however, these points are sparse and limited to known problem areas. InSAR monitors larger areas and is able to identify millimetric displacements before large surface failures are observed. The use of multi-band InSAR, C-Band for medium-resolution built infrastructure monitoring and L-Band for better penetration through vegetation, enhanced the coverage and accuracy of displacement detection over the entire area of interest. Key infrastructure, including roads, ventilation shafts, and power lines, has been safeguarded through this monitoring approach, allowing for proactive interventions. Study areas show how InSAR provided insights where they were absent, enabling timely mitigation measures across the entire mine. This approach underscores the importance of combining remote sensing with site investigations to enhance mine safety and minimise costly operational disruptions. The following points outline the key takeaways from this paper.

- Multi-Band InSAR Benefits: C-Band provides medium-resolution data for built areas, while L-Band offers better coverage in vegetated regions.
- Integrated Monitoring Approach: Combining InSAR and regular inspections improves risk mitigation.
- Proactive Risk Management: Detection of subsidence and sinkhole precursor movements enables timely interventions, preventing damage to infrastructure.
- Case Study Insights: Monitoring has helped assess and respond to sinkhole reactivations, road damage, and structural risks.

Following this case study, future works could include using a larger dataset to help create more structured acceleration models over known failure areas, taking into consideration the changing rock properties throughout mines. With more data from ground-based monitoring programmes, future works could include calibration between the different wavelength datasets in the known failure areas.

REFERENCES

Falorni, G., Del Conte, S., Bellotti, F. & Colombo, D. (2018) 'InSAR monitoring of subsidence induced by underground mining operations', in Y. Potvin & J. Jakubec (eds), *Caving 2018: Proceedings of the Fourth International Symposium on Block and Sublevel Caving*, Australian Centre for Geomechanics, Perth, pp. 705-712. Available at: https://papers.acg.uwa.edu.au/p/1815_54_Falorni/

Ferretti, A. (2014) *Satellite InSAR Data: Reservoir Monitoring from Space*. CRC Press, Boca Raton.

Ferretti, A., Fumagalli, A., Novali, F., Prati, C., Rocca, F. and Rucci, A. (2011) 'A new algorithm for processing interferometric data-stacks: SqueeSAR', *IEEE Transactions on Geoscience and Remote Sensing*, 49(9), pp. 3460–3470.

Ferretti, A., Savio, G., Brazaghi, R., Borghi, A., Musazzi, S., Novali, F., Prati, C., and Rocca, R. (2007) 'Submillimeter Accuracy of InSAR Time Series: Experimental Validation', *IEEE Transations on Geoscience and Remote Sensing,* 45(5), pp. 1142–1153.

Mohamadi, B. (2024) 'Utilizing InSAR for Surface Stability Monitoring in Mining Sites: A Case Study of Sukari Gold Mine in Egypt', *The International Archives of the Photogrammetry, Remote Sensing and Spatial Information Sciences*, XLVIII-1-2024, pp. 523–528. Available at: https://isprs-archives.copernicus.org/articles/XLVIII-1-2024/523/2024/isprs-archives-XLVIII-1-2024-523-2024.html

Peltier, A., Bianchi, M., Kaminski, E., Komorowski, J., Rucci, A., and Staudacher, T. (2010) 'PSInSAR as a new tool to monitor pre-eruptive volcano ground deformation: Validation using GPS measurements on Piton de la Fournaise', *Geophysical Research Letters,* 37(12) pp. L12301

Sillitoe, R.H. (2017) 'Zoned hydrothermal alteration in porphyry copper deposits', *Mineralium Deposita*, 52(4), pp. 395–424.

Wang, Y., Zhang, Q., Zhao, C., Lu, Z. & Ding, X. (2011) 'Monitoring and inversion on land subsidence over mining area with InSAR technique', *Proceedings of SPIE - The International Society for Optical Engineering*. Available at: https://www.usgs.gov/publications/monitoring-and-inversion-land-subsidence-over-mining-area-insar-technique



McKenzie Douglas

Geospatial Data Analyst
TRE Altamira

Studied at Queen's University in Kingston, Canada. Worked as a geotechnical engineer in the Vancouver area for three years before moving to Italy to work with InSAR data. While working in Vancouver, I was involved in geohazard assessments and seismic design for infrastructure, buildings and deep foundations in the greater Vancouver area. I was involved in the research for the 2025 BC Seismic Building Code and had studied the seismic response in the typical soils in the Victoria area. Since moving to TRE Altamira, most of the work has been focused on safety in mining applications and landslide monitoring. This work has exposed me to projects all over the world and I have thoroughly enjoyed the diverse approaches all of the people I work with have taken to designing slopes and monitoring high risk areas.

Closure and accelerometer measurements to enhance mine safety

L. Scheepers[1], P. Lenegan[1], F. Pienaar[2], H. Hoogenboezem[3], D. Lamprecht[1]

[1]SibanyeStillwater
[2]Mining Product Developments
[3]Hoogenboezem Industries

Mining operations inherently involve risks, and ensuring the safety of workers in underground mines is of paramount importance. In recent years, advancements in instrumentation have provided valuable tools for monitoring and managing risk. In this paper, we review the closure and accelerometer data acquisition techniques described previously and describe two interesting cases.

1. Instrumentation Development: Closure meters
    - A closure meter has been developed as a robust and reliable instrument designed specifically for underground mine use. Its primary function is to measure closure in a narrow tabular stope accurately.
    - Its versatility allows it to adapt to various situations. Whether readings are taken every second or every 10 seconds depends on the specific context.
    - With readings taken every 10 seconds, it can operate for a year on a single battery charge.

2. Data Flow and Real-Time Monitoring
    - Closure readings are collected by intermediate devices, transferring data to the surface via the mining infrastructure.
    - Surface personnel can access real-time closure readings. This capability would allow for timeous response to any anomalies or safety concerns once implemented mine-wide.
    - The accuracy of closure measurements achieved by the SmarTrac is approximately 0.01 mm. Additionally, we capture ride data—the perpendicular movement relative to the instrument's axes—with lower accuracy (around 1 to 2 mm).

3. Insights from Large-Scale Data Collection
    - Deploying multiple closure meters in a test area of the mine yields beneficial insights into the rockmass response. This will be expanded to more areas on the mine.
    - Blasting effects become quantifiable. By analysing closure data before and after blasts, we can assess their impact on mine stability.
    - Seismicity is a critical factor in deep level mines. By correlating closure variations with seismic events, we gain a deeper understanding of safety risks.
    - The challenge lies in aggregating sufficient data to predict unsafe situations reliably. Our ongoing research aims to address this challenge.

In summary, comprehensive data collection using instruments like the SmarTrac empowers mine safety professionals to make informed decisions. By leveraging real-time insights, we move closer to a safer mining environment.

INTRODUCTION

Mining operations inherently involve risks, and ensuring the safety of workers in underground mines is of paramount importance. In recent years, advancements in instrumentation have provided valuable tools for monitoring and managing risk. In this paper, we review the closure and accelerometer data acquisition techniques described previously and describe two interesting cases.

Background

Underground closure had been measured in isolated cases in various mines. Prof Malan (Malan, 2003) reported the following:

"This guide was produced in response to a need identified in the South African gold mining industry for a better understanding of the closure behaviour of tabular excavations. Although references to closure measurements can be found dating back to the early 1930s, research in the SIMRAC fundamental projects GAP332 and GAP601b indicated that continuous closure recordings contain much important data which is lost with the traditional method of closure measurement (which consists of installing closure pegs and taking manual readings on a daily basis or less frequently).

The rate of closure is a very important parameter for support design and therefore impacts indirectly on safety. Continuous closure measurements also appear to be useful to identify different geotechnical areas and the hazards associated with each area. The objective of this guide is therefore to:

- create awareness of the need to do continuous closure measurements on a more regular basis,
- standardise the closure terminology used in the industry,
- illustrate the effect of mining rate on the rate of closure,
- highlight the effect of measurement position on the rate of closure.
- Illustrate the value of the closure ratio parameter to identify different geotechnical areas and hazardous conditions."

Scope

This paper describes the installation of closure meters and accelerometers at SibanyeStillwater, the monitoring of data of these from surface, and the relationship between trends in data observed and physical events such as blasting and seismic events. We focus on data surrounding seismic events on 10 April 2024 and 4 February 2025.

Instrumentation Development: Closure meters

The SmarTrac was developed for use in underground mines to monitor closure to either warn of excessive ground movement or to log closures for separate data analysis.

The device consists of two PVC capped tubes that are spring-loaded for easy installation. Positioned within the tubes is a device that monitors the relative movement of the two ends of the tubes. A flashing light is available to indicate the status of the device.

In the version of SmarTrac used at SibanyeStillwater, there is no on-board logging of data. All data is transmitted live using radio transmitting (LORA). The device can be programmed to specific application requirements and can be programmed to measure deformation at various frequencies from 1 second up to one reading per day. Most instruments at SibanyeStillwater collect and send data every 10 seconds, but there are also some instruments with a one second frequency.

In short:

- A closure meter has been developed as a robust and reliable instrument designed specifically for underground mine use. Its primary function is to measure closure accurately.

- Its versatility allows it to adapt to various situations. Whether readings are taken every second or every 10 seconds depends on the specific context.
- With readings taken every 10 seconds, it can operate for a year on a single battery charge.
- The accuracy of closure measurements achieved by the SmarTrac is approximately 0.01 mm. Additionally, we capture ride data—the perpendicular movement relative to the instrument's axes—with slightly lower accuracy (around 1 to 2 mm).



Figure 1. A SmarTrac

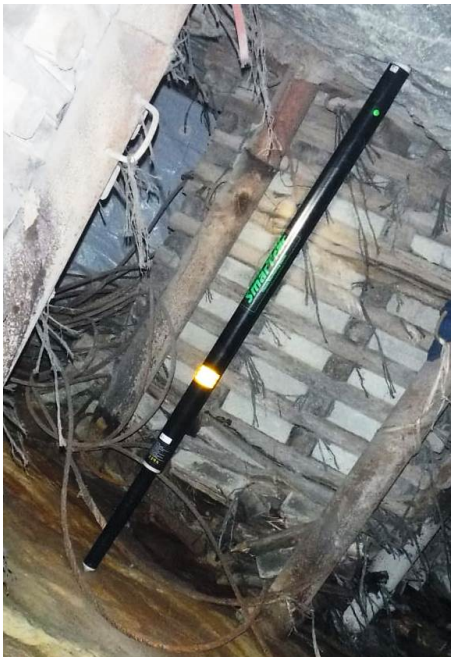


Figure 2. Wide stoping width range is possible.



Figure 3. SmarTrac installed underground.

Instrumentation Development: Accelerometers
An attempt to measure micro-fracturing, possibly related to closure preceding large events, is currently being carried out at Masakhane shaft (Driefontein mine). Traditionally gold mines in South Africa use a seismic network array of mine-wide 4.5 Hz geophones. These arrays of sensors are suitable for measuring larger events but are not ideal for recording fracturing very close to the stope face.

To achieve the recording of micro-seismic events (fracturing), two inexpensive 8 G MEMS accelerometers were installed in a designated project area located in the VCR reef horizon. These accelerometers, located at two different working areas, are approximately 180 m apart. The accelerometers were installed within 50 m of the two stope faces as illustrated in Figure 6.

The upper bandwidth limit of the accelerometer is around 1 kHz. The dynamic range of the 8 G accelerometer is suitable for the recording of small seismic events. The captured waveforms are sampled at 4 kHz.

An additional objective of the project is to observe closure of the stope and the related micro- fracturing of the mining area close to the stope face. To achieve these overall objectives, two technical advances had to be developed. Firstly, close to real time duplex communication from the stope area to surface. Secondly, common time between the closure meters and the associated accelerometer. In-stope wireless communication was successfully designed and implemented. In addition, duplex communication between surface and the underground in-stope hardware was also successfully developed. This development facilitated a common time stamp between the closure and accelerometer data.

A third objective achieved was to design a tri-axial accelerometer sensor array that can fit into a mining stope 'jumper hole.' Traditionally tri-axial sensor arrays are installed in expensive NX (76 mm) diamond drill holes. The development of small tri-axial sensor array is a significant saving on drilling costs

The closure data is visualised on an intranet Grafana graphical display on surface. The display is updated every ten seconds with the latest data from underground.



Figure 4. The 8 G accelerometers.



Figure 5. The installation of the 8 G accelerometer.

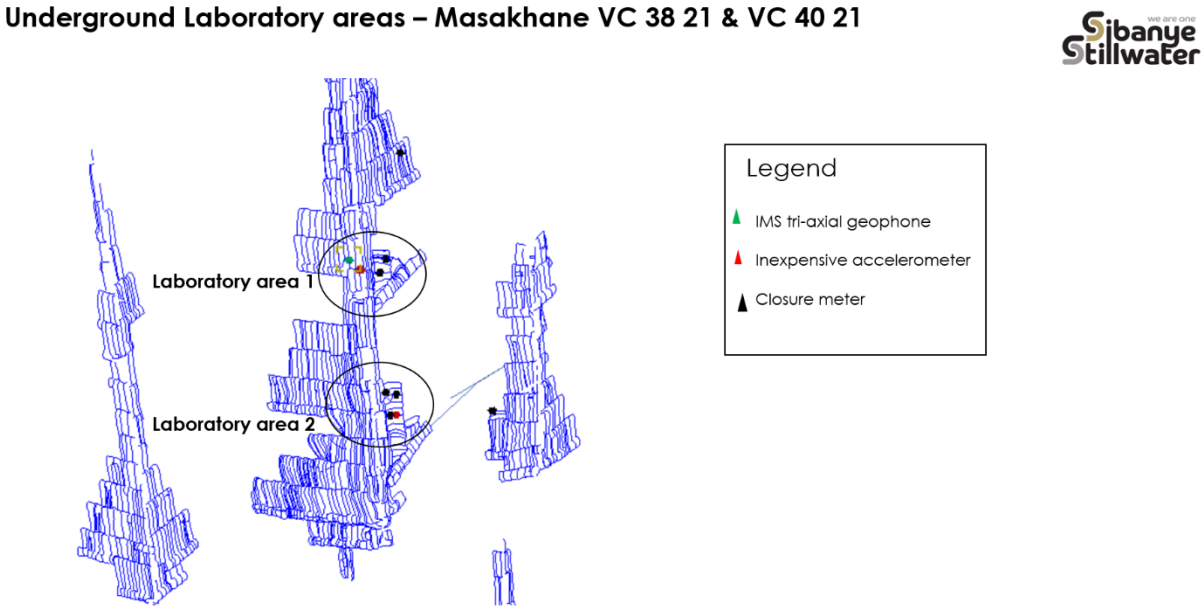


Figure 6. The accelerometers were installed within 50 m of the two stope faces.

Data Flow and Real-Time Monitoring
The communication is described with the aid of Figure 7.

The communication can be divided between two main areas. The first being the existing mine infrastructure going from surface to all levels. This communication medium is normally TCP/IP and has a speed of at least 1 Gb/s, although for closure meters much lower speeds are required. The shaft communication link is connected to the stope area by means of a copper cable. This copper cable is terminated by a power source servicing an in-stope winch. Both ends of the cable are serviced by two Dslam modems. The shaft Dslam modem connects the copper cable to the shaft mine communication infrastructure. In the stope area the Dslam modem interfaces the copper cable to the 8 G accelerometer data logger, and the wireless access point for the closure instrumentation.

The second communication link connects the wireless access point to the closure meters via the gateway as described below.

8 G accelerometer in stope network
The 8 G accelerometer is installed in a jumper hole drilled in the hanging wall. This type of hole is easily drilled in a stope using a conventional stope drill. The accelerometer is connected to the data logger via a thin copper cable.

The in-stope closure meter network
The wireless access point (AP) communicates to the shaft via the Dslam modem for upstream communication. The AP communicates wirelessly to the Gateway (GW) via its own onboard local WiFi. The communication medium used between the GW and the closure meters is LORA. This type of radio frequency communication is suitable for low powered devices and distance for in-stope wireless communication. This is essential in the in-stope areas for conservation of battery power (low consumption) located inside the closure meters.

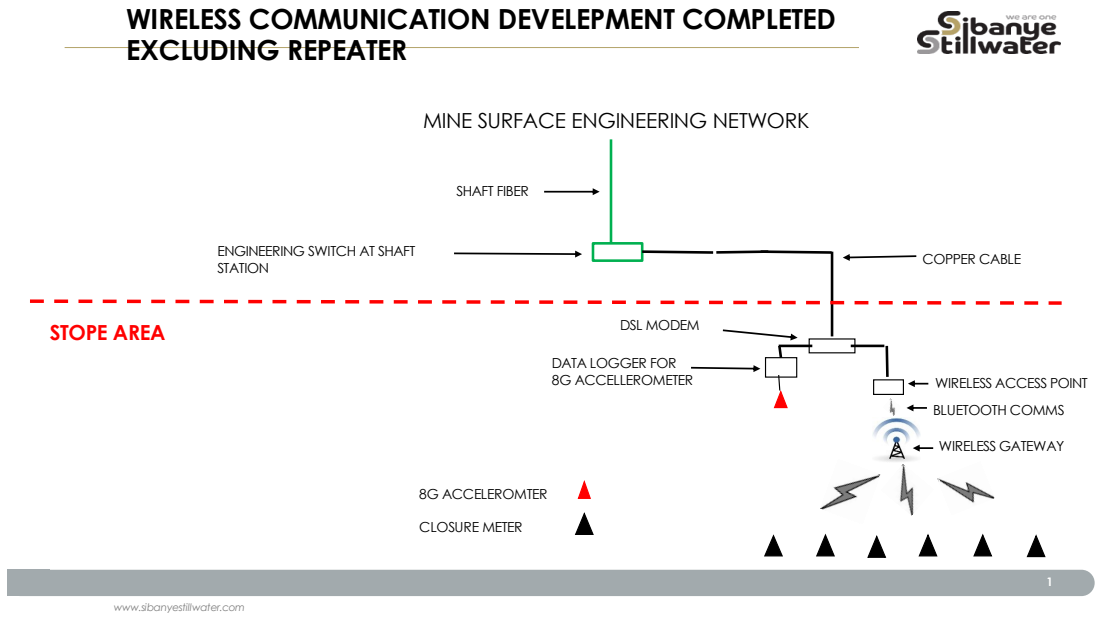


Figure 7. Wireless communication development.

Typical results

From six closure meters

Figure 8 shows typical results obtained with the SmarTrac closure meters over a period of about 16 days. The display is done with Grafana, which gives many viewing options. One or more devices can be selected, time periods zoomed in or out, closure scale and more.

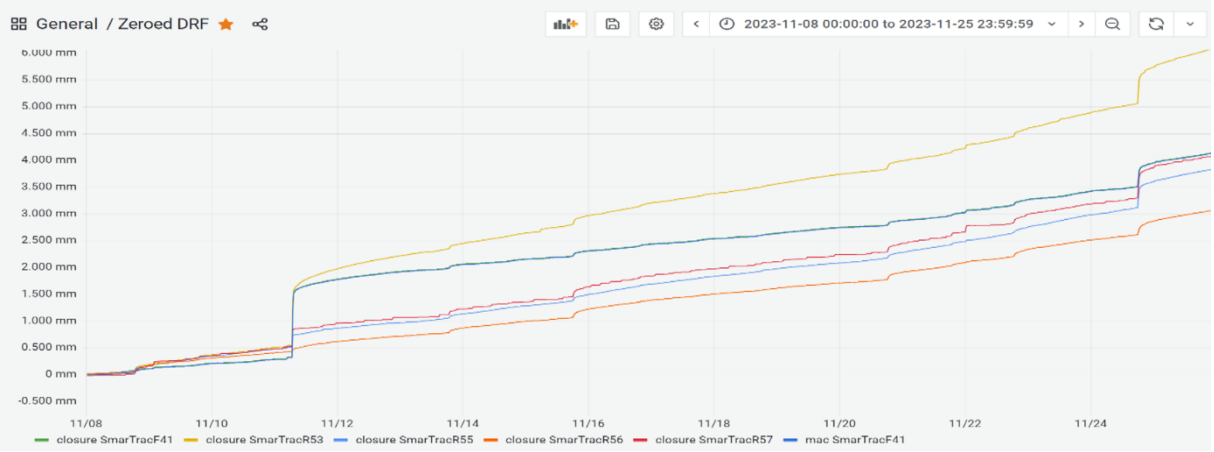


Figure 8. Typical underground closure results from six closure meters over 16 days.

Example 8 G accelerometer data

The results from the 8 G accelerometer contains a large amount of information, as can be seen in the example in Figure 9 below.

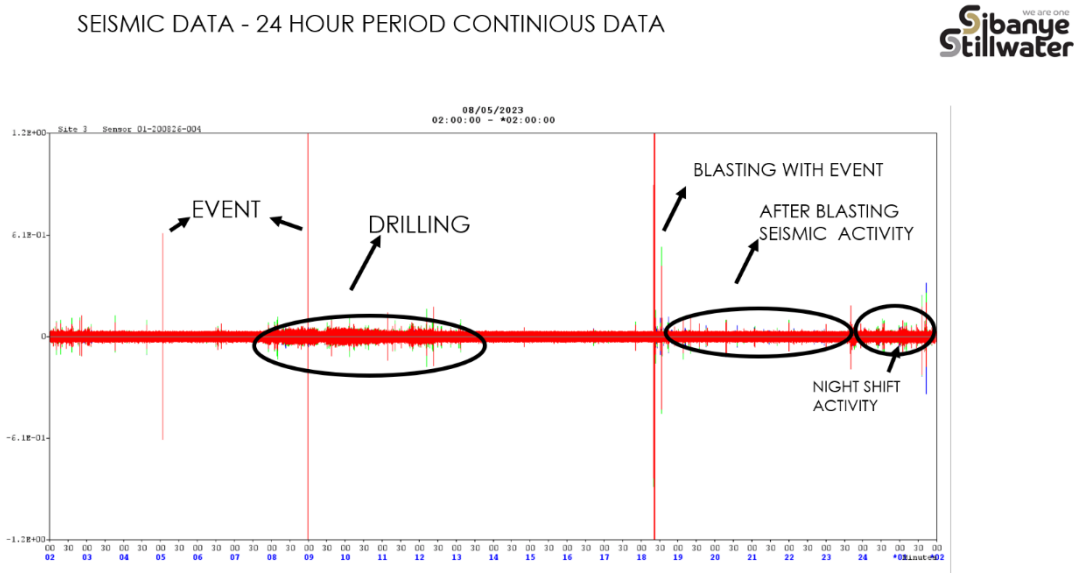


Figure 9. Data recorded with 8 G accelerometer.

Insights from Data Collection: event of 10 April 2024

Installations in project area

Figure 10 shows the plan view of the project area. The three red spheres represent large seismic events that occurred recently close to the stope face where three closure meters (represented by three black dots) and an 8 G accelerometer (red dot) are installed.

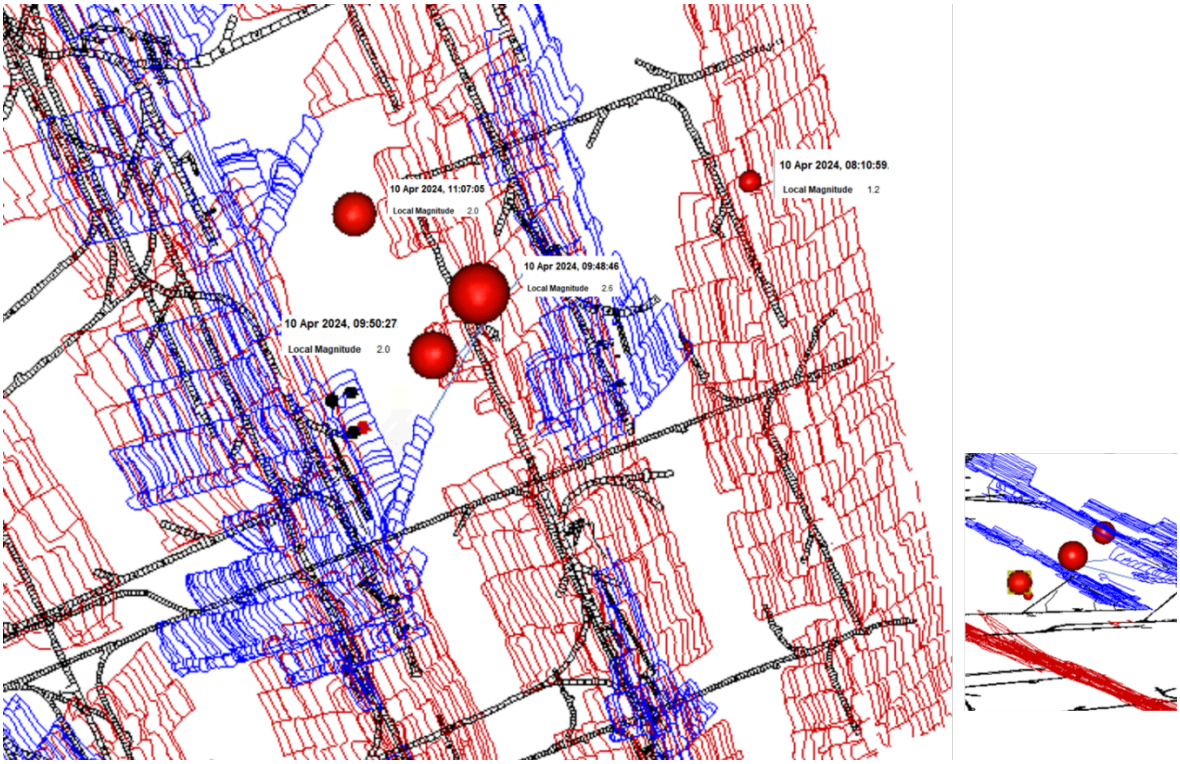


Figure 10. Plan view of the project area where three seismic events occurred.

Results from instrumentation where seismic events occurred

Figure 11 is a graphical representation of data obtained in a period surrounding the seismic events indicated in Figure 10. The representation shows common time interaction between the 8 G accelerometer data (top section) and the SmarTrac data (bottom section).

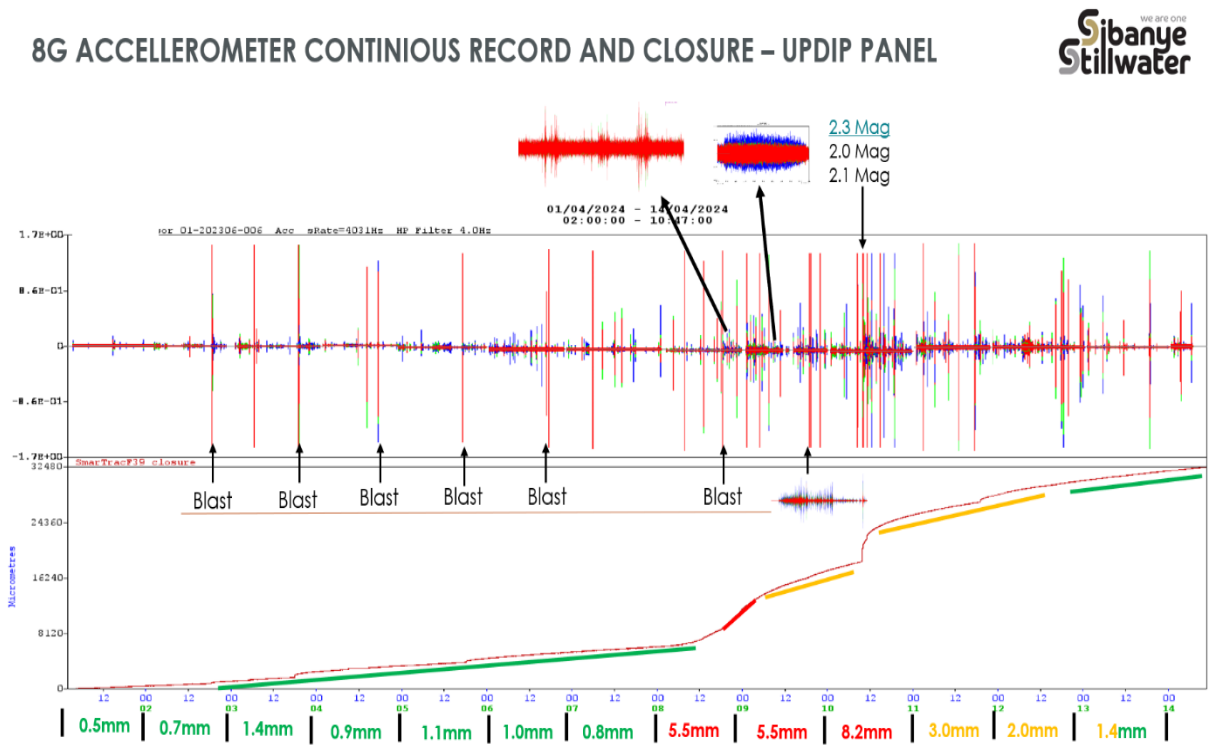


Figure 11. Closure and accelerometer data proceeding large seismic event.

Several interesting and important observations can be made from these results:

- The production blasts are marked in the data. These blasts are on different stope faces within the same mining area. This data is recorded by the 8 G accelerometer.
- The smaller amplitude recordings between the blasts are small seismic events or fracturing of the rock mass, close to the mining area under observation
- A clear increase in fracturing is observed two days prior to the seismic events.
- The first period of closure (depicted in green) represents the normal closure rate observed in the days prior to the events. Average closure rate for this period was 0.9 mm per day.
- Two days prior to the seismic events, the closure rate increased to 5.5 mm per day. The associated increase in seismic fracturing during this increased closure period is also clearly evident.
- At the time of the events, there is rapid closure resulting from permanent deformation of the rock mass.
- In the three-day period after the events, closure rate remains between 3.0 and 2.0 mm per day, gradually slowing down.
- After the three-day period, closure rates in the stope revert to the closure rate observed prior to the events, at around 1.0 mm per day.

Insights from Data Collection: Event of 4 February 2025

Introduction

- Closure stations that report real time data to surface installed at active working panels are part of the non-seismic monitoring research project.
- Three occurrences of large events following accelerated closure rate were observed in the research area in 2024.
- It was decided to monitor closure trends regularly and to consider proactive controls when accelerated closure rates are observed.

On 30 January 2025, an increased rate of closure was detected at one of the panels.

The regional layout and instrument location are given in Figure 12 and Figure 13.

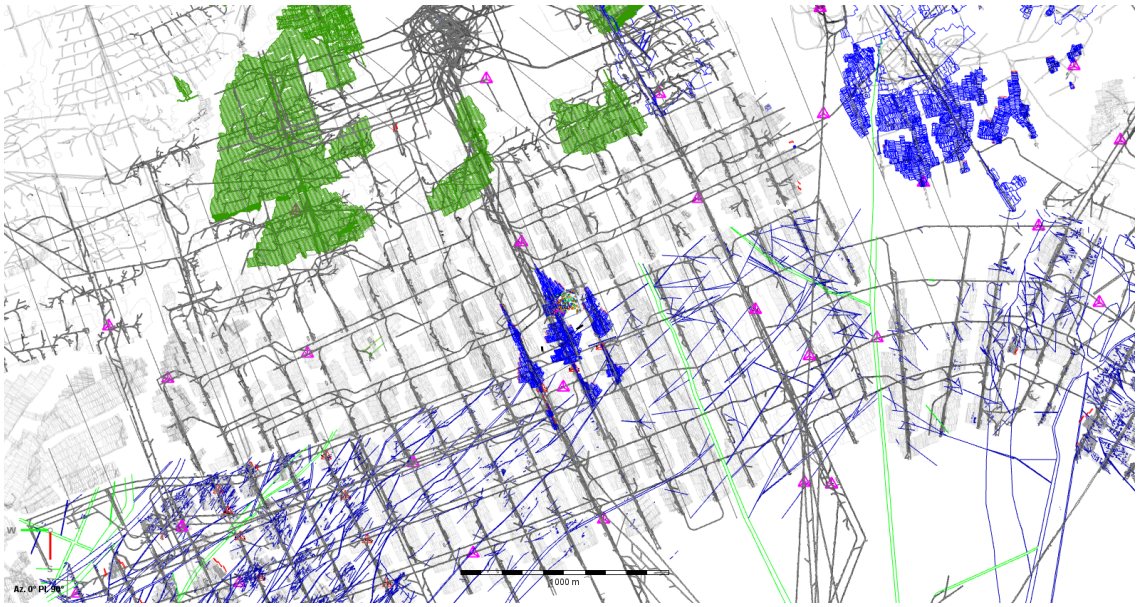


Figure 12. Regional setting.

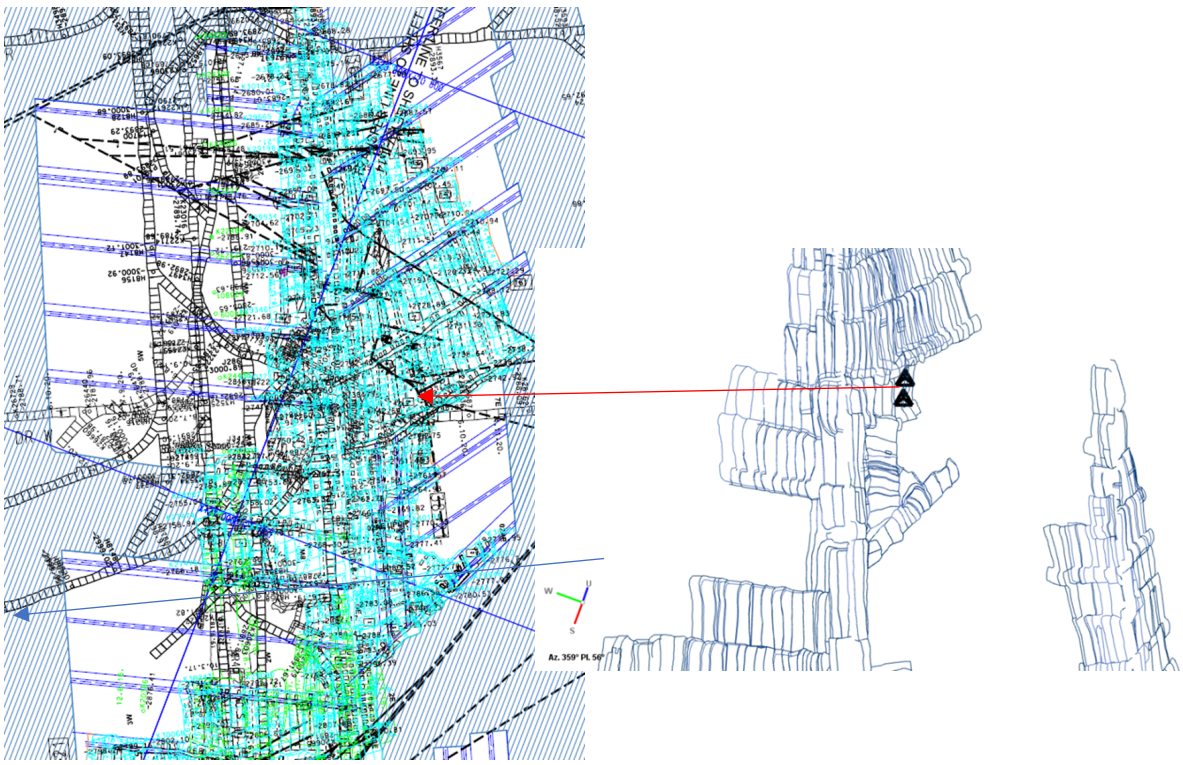


Figure 13. Location of closure instruments.

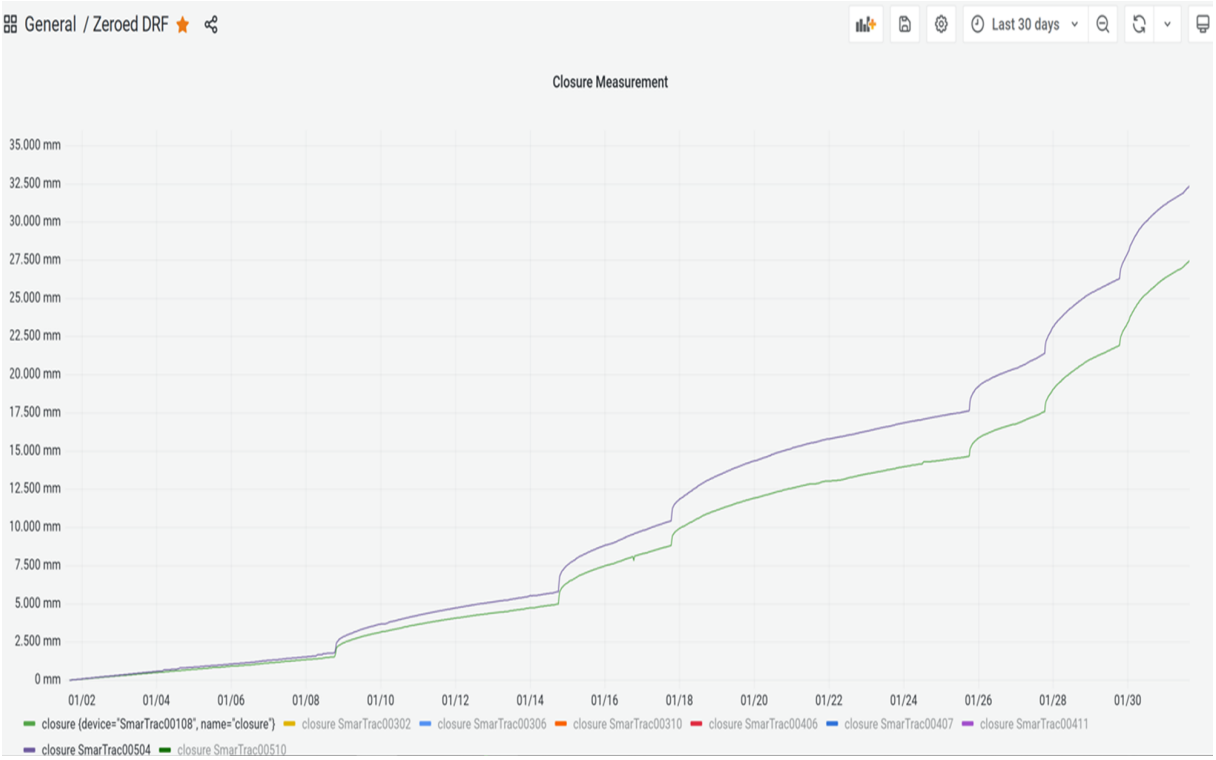


Figure 14. Observed closure.

Figure 14 gives the closure from two closure meters over the period of 1 January to 4 February. It can be seen that the time between blasts varies and that closure rate towards the end of this period increase significantly. This will be analysed further.

Figure 15 shows effectively the same information; but closure that occurred from each blast to two days after the blast, is highlighted for one instrument. In Figure 16 and Figure 17 the highlighted closure is plotted in isolation, in order to compare what happened after each blast. It can then be observed that the closure varies, dependent on the conditions. Further discussion is based on this observation.

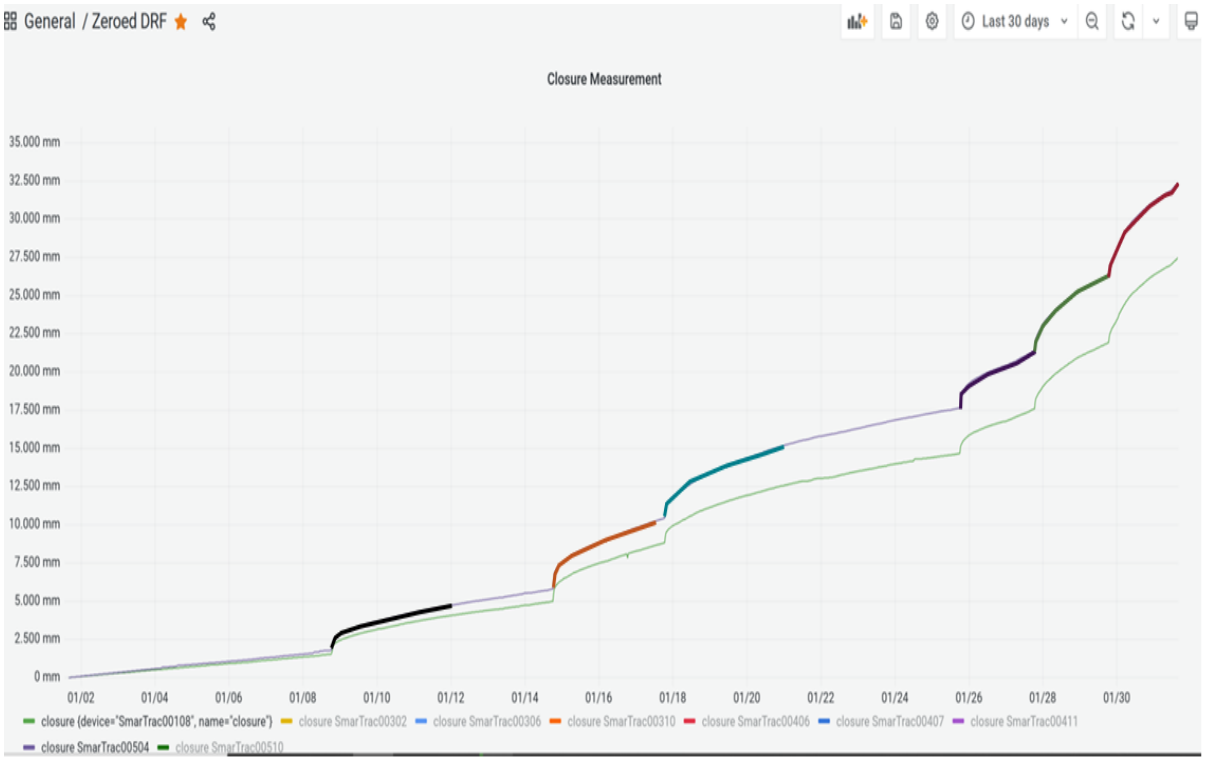


Figure 15. Observed closure – closure trend traced on instrument 504 graph.

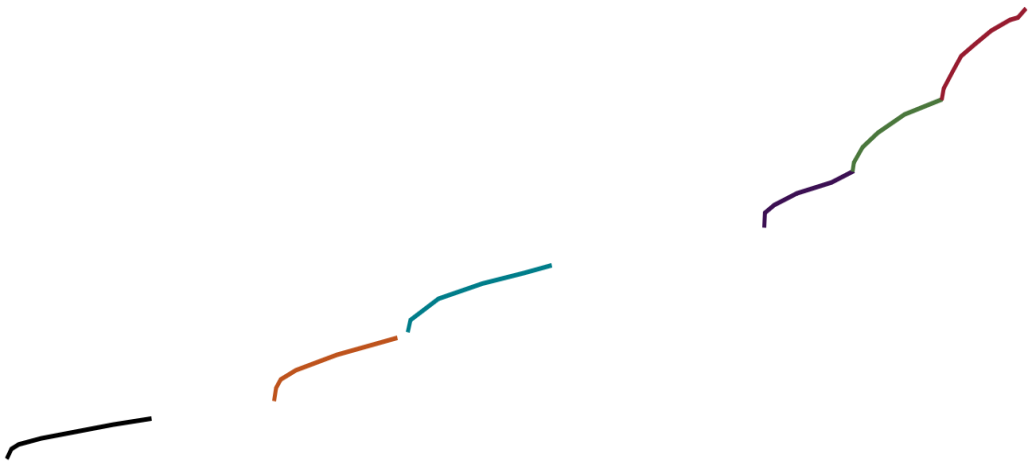


Figure 16. Observed closure – closure trend traced.

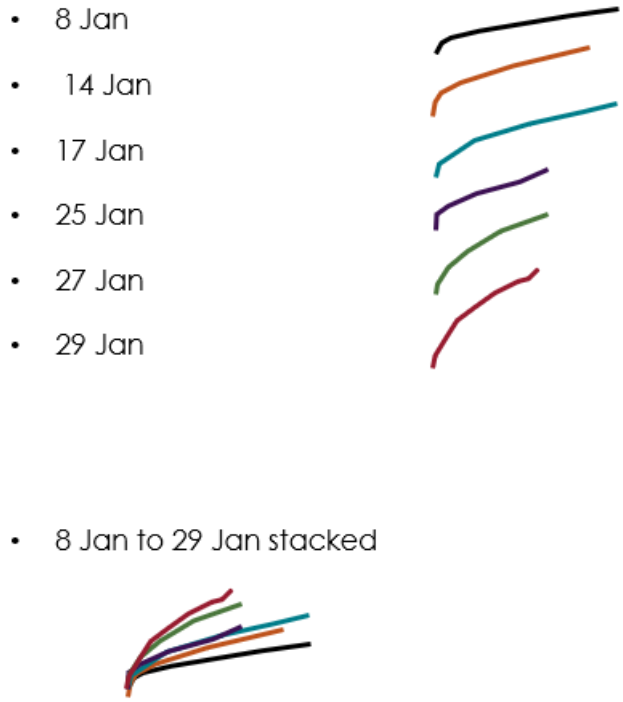


Figure 17. Observed closure after each blast.

Generalised theory

With each blast several changes occur:

- Stress change – a portion of rock that was stressed is removed with the blast and its stress is transferred to the remaining rock in the immediate vicinity, which experiences a rapid increase in stress.
- Closure change – with the face advance associated with the blast, the mining span is increased, and rapid closure occurs.
- Non-seismic deformation – the rockmass in the immediate vicinity of the new face position that experiences the rapid stress increases, will deform, forming new fractures and releasing some energy non-seismically.
- Seismic deformation – some energy release may occur dynamically with an increase in the seismic response.

The changes described above are time-dependent, with rapid commencement immediately after the blast and slowing down as time progresses. This is the basis for establishing a seismic return-period after the blast.

Under certain conditions where the frequency of blasts is such that the next blast is taken before the energy-dissipating processes are concluded, the stress changes of the new blast are superimposed on that of the previous blast and the post-blast response is higher due to the cumulative effect. This can be called excitation, referring to the rock being excited due to cumulation of post-blast response. It is likely that under excited rockmass conditions, the seismic risk is increased.

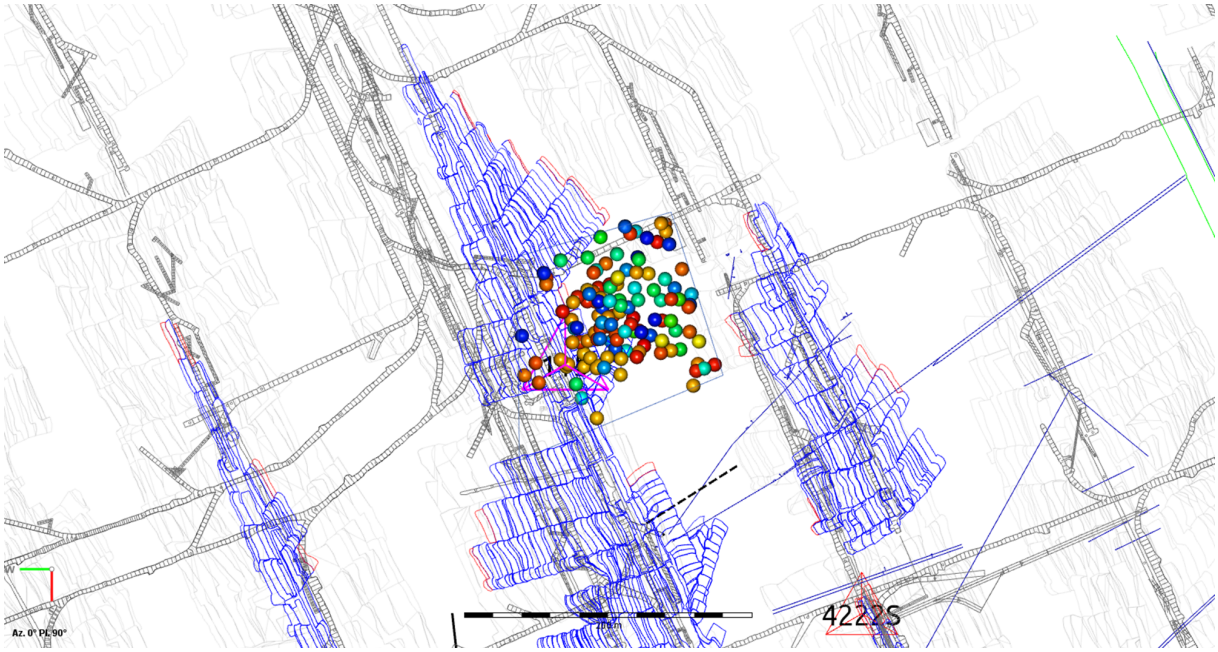


Figure 18. Observed seismic response – last 30 days.

A polygon was created to encapsulate the recent cluster of seismic events associated with the mining of the specific area.

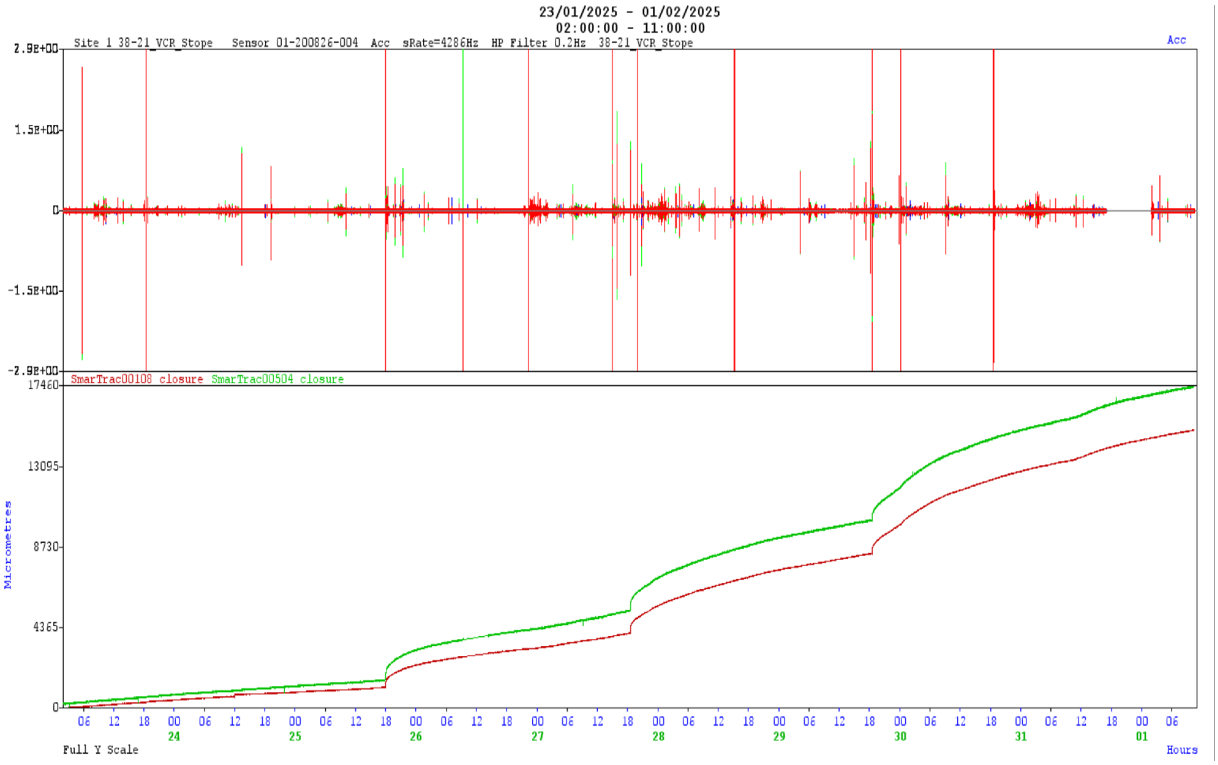


Figure 19. Observed seismic response and closure.

From Figure 19 it can be seen that when there is an increase in the rate of closure, there is an associated increase in seismicity, as is measured by the 8 g accelerometer. In Figure 20 the seismicity is plotted

cumulatively, and the increase in closure rate is seen to be closely linked to seismicity, as is measured by the 8g accelerometer.

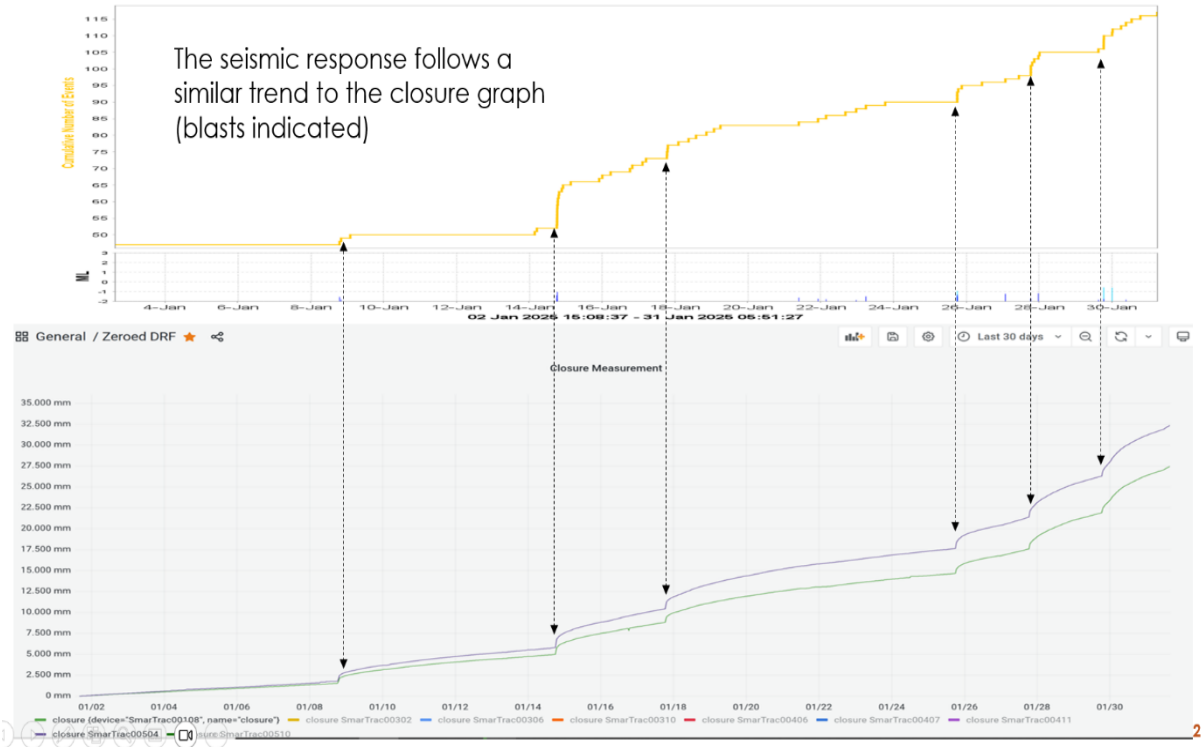


Figure 20. Seismic response (cumulative number of events) associated with blast and closure.

Discussion

The closure trend after each blast is typical

- Steep (near-vertical) closure trends during the blast (rapid closure).
- Period of quick deceleration in rate of closure.
- Near-linear rate of closure trending back to the pre-blast closure rate.

The seismic response (trend of cumulative number of events over time) follows the trend of closure triggered by the blasts.

- For the mining under consideration (30 days), after each blast the post-blast trend is steeper than that of the previous blast. This may indicate an increased seismic risk.
- It is possible that the frequency of blasts in the last 10 days is such that the next blast is taken before the deformation in the rockmass (represented by measured closure) has returned back to the background level, the rockmass is excited and the seismic response may be higher than expected.

On Thursday 30 January 2025, the accelerated closure of the last 30-day period at the research site was reviewed and it was recommended to the rock engineer and mine manager to increase the time to the next blast by two days to allow more time for the energy dissipating processes to occur. The crew was therefore prevented from blasting on the 30th, with blasting set to continue on 3 January 2025.

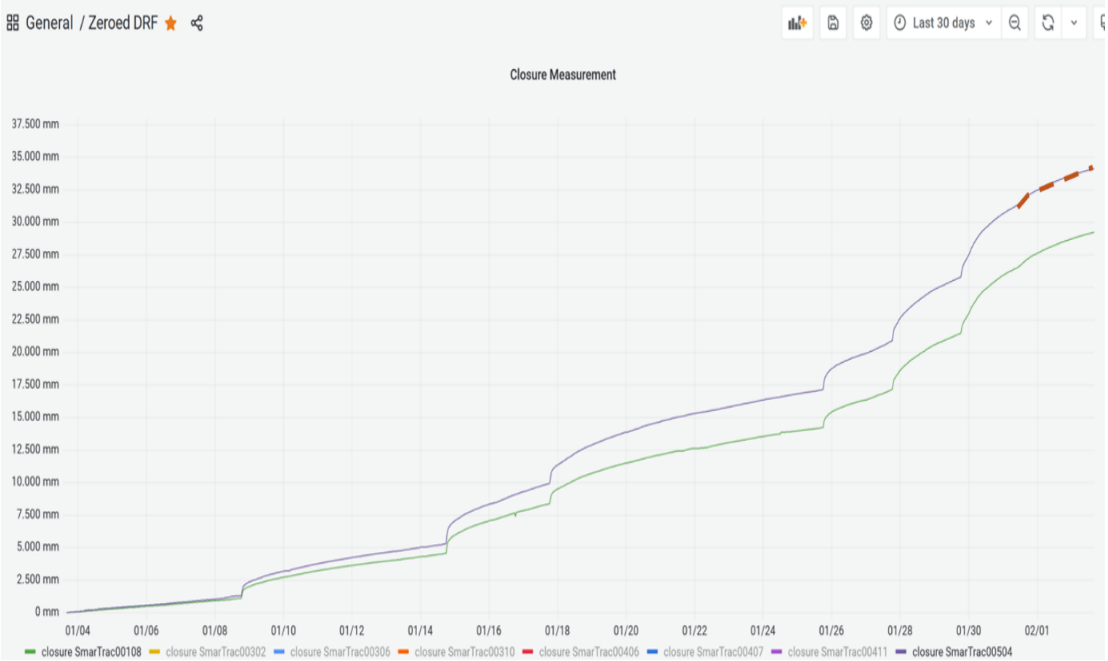


Figure 21. Sunday 2 February 2025 review.

- 8 Jan
- 14 Jan
- 17 Jan
- 25 Jan
- 27 Jan
- 29 Jan
- 2 Feb
- 8 Jan to 2 Feb stacked





Figure 1. Observed closure after each blast.

Figure 21 and Figure 22 show that the rate of closure on 2 February returned to the initial rate of closure.

- The rate of closure was reduced to rates measured between 14 and 17 January.
- It is recommended that mining continues.

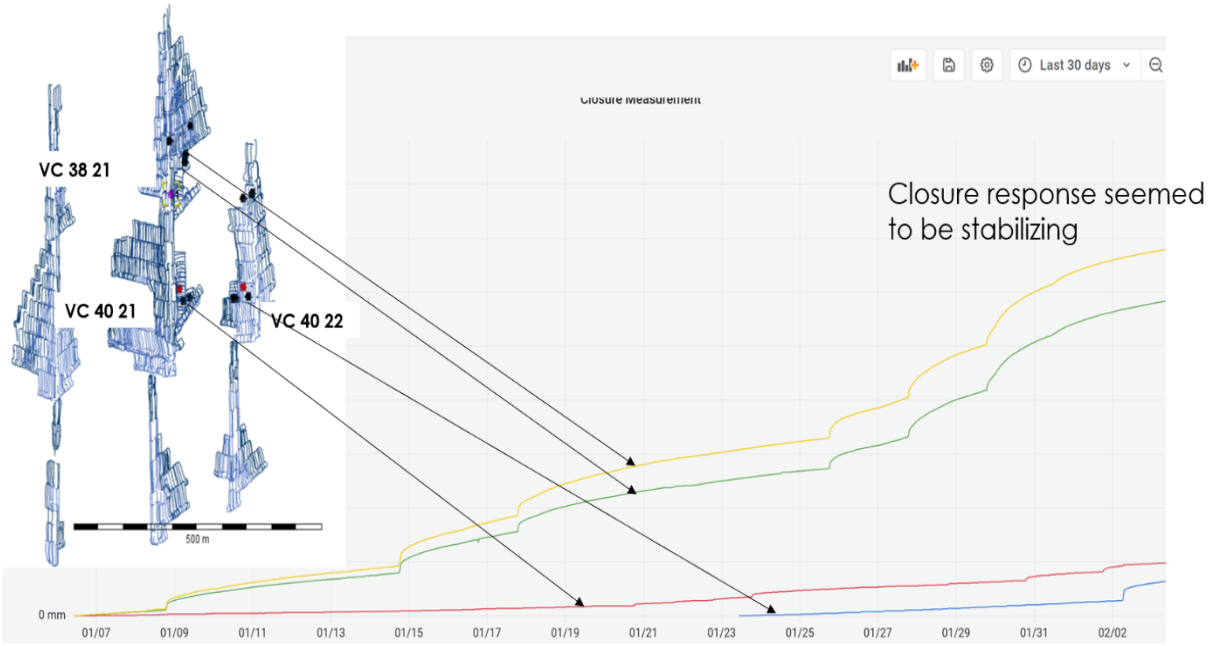


Figure 23. Closure response when mining was continued on Monday 3 February.

Figure 23 shows that the rate of closure stabilised and mining continued on 3 February, but then on 4 February five events occurred, the largest being magnitude 2.2. Figure 24 shows detail.

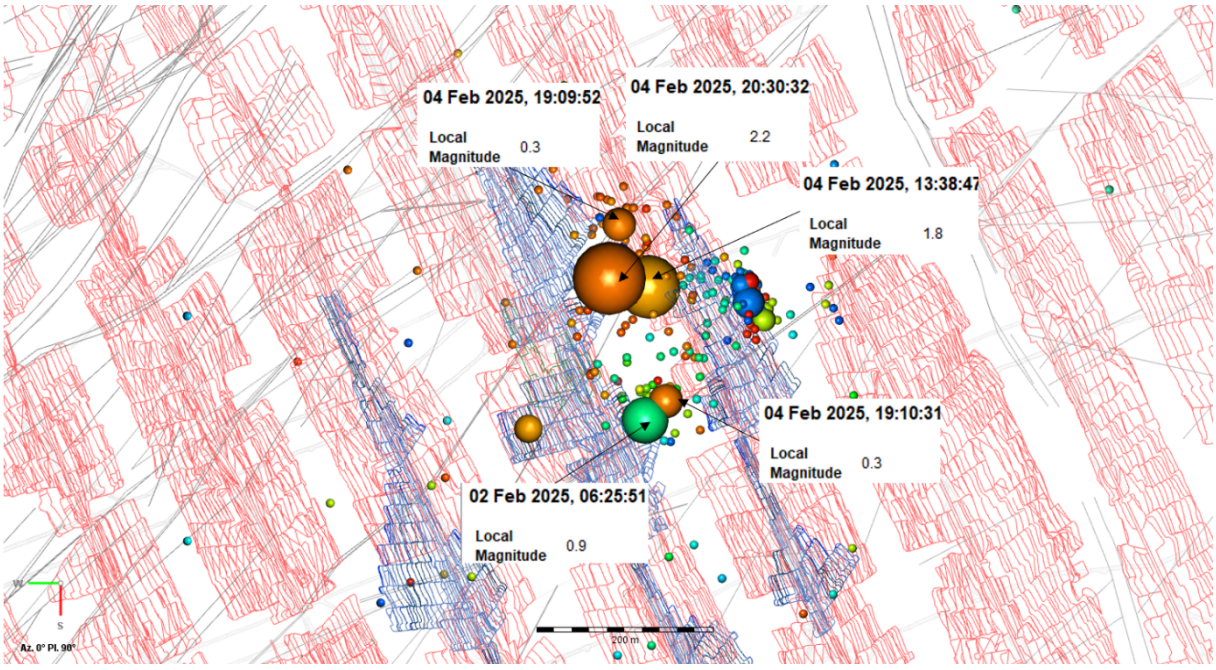


Figure 24. Seismic response.

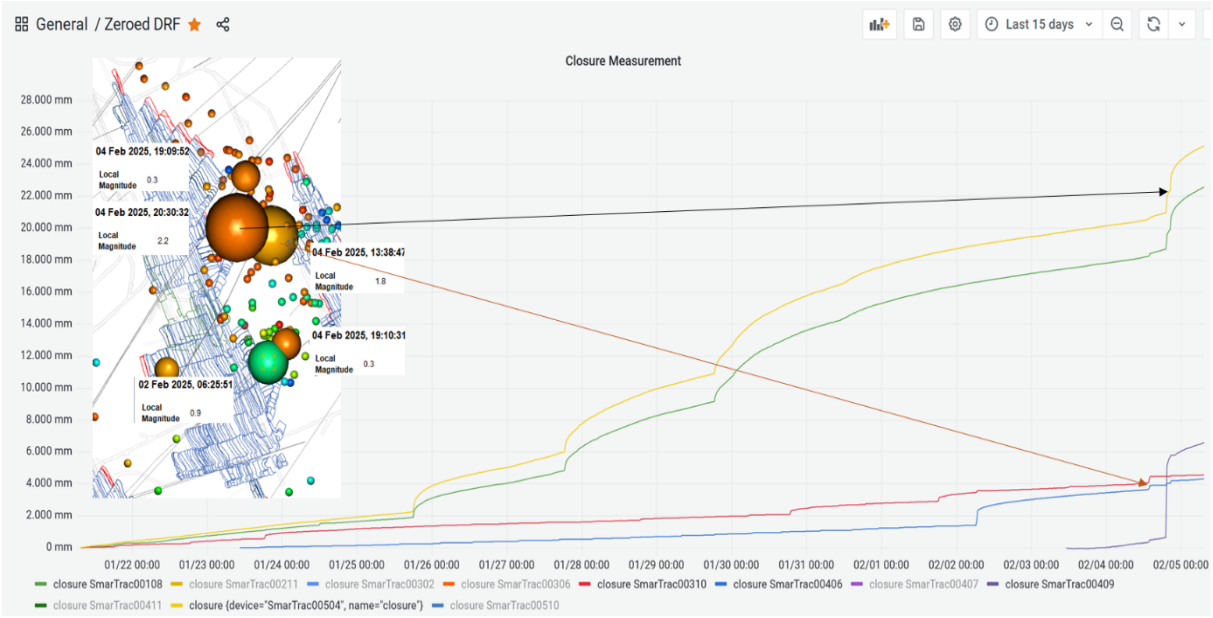


Figure 25. Closure and seismic response post- 4 February.

The rate of closure increases dramatically when the seismic events occur (Figure 25).

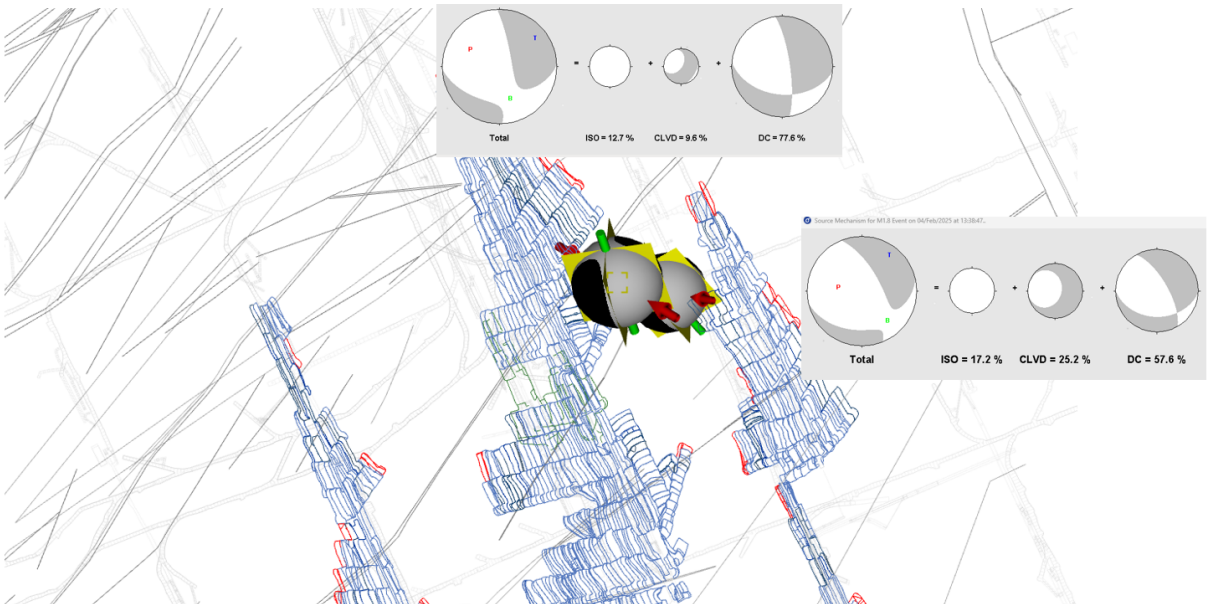


Figure 2. Event mechanism.

Figure 26 refers. The MT QI of 0.63 is indicative of a stable MT solution.
The M2.2 event has a dominant DC component consistent with shear type mechanism. The nodal planes of the DC component aligns with the VCR stope faces.
The MT of the M1.8 is similar to the M2.2.

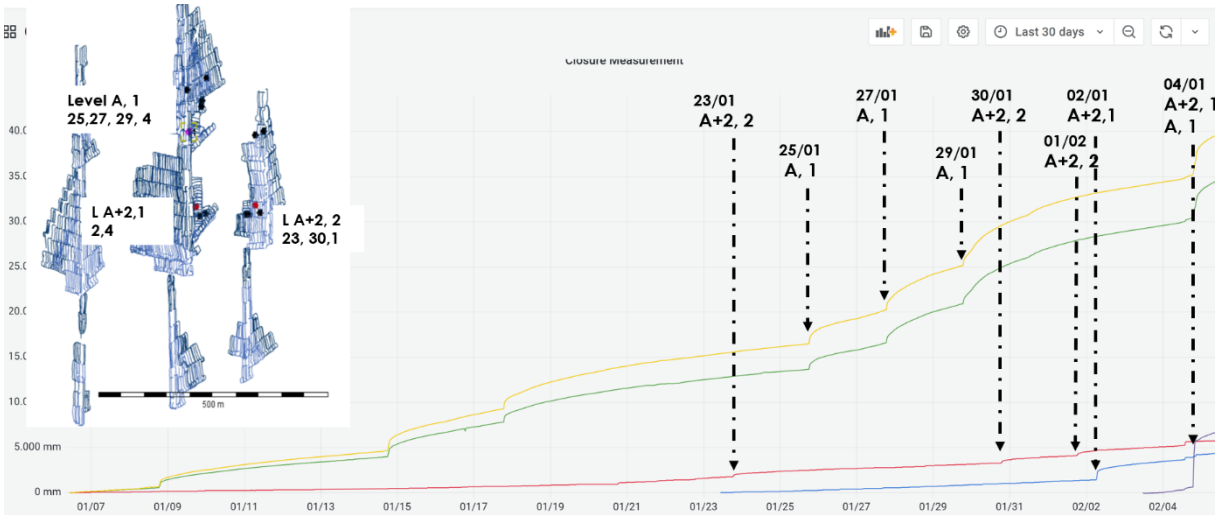


Figure 27. 30 days with blasts represented.

From

Figure : it is clear that the closure increases significantly for days with blasts.

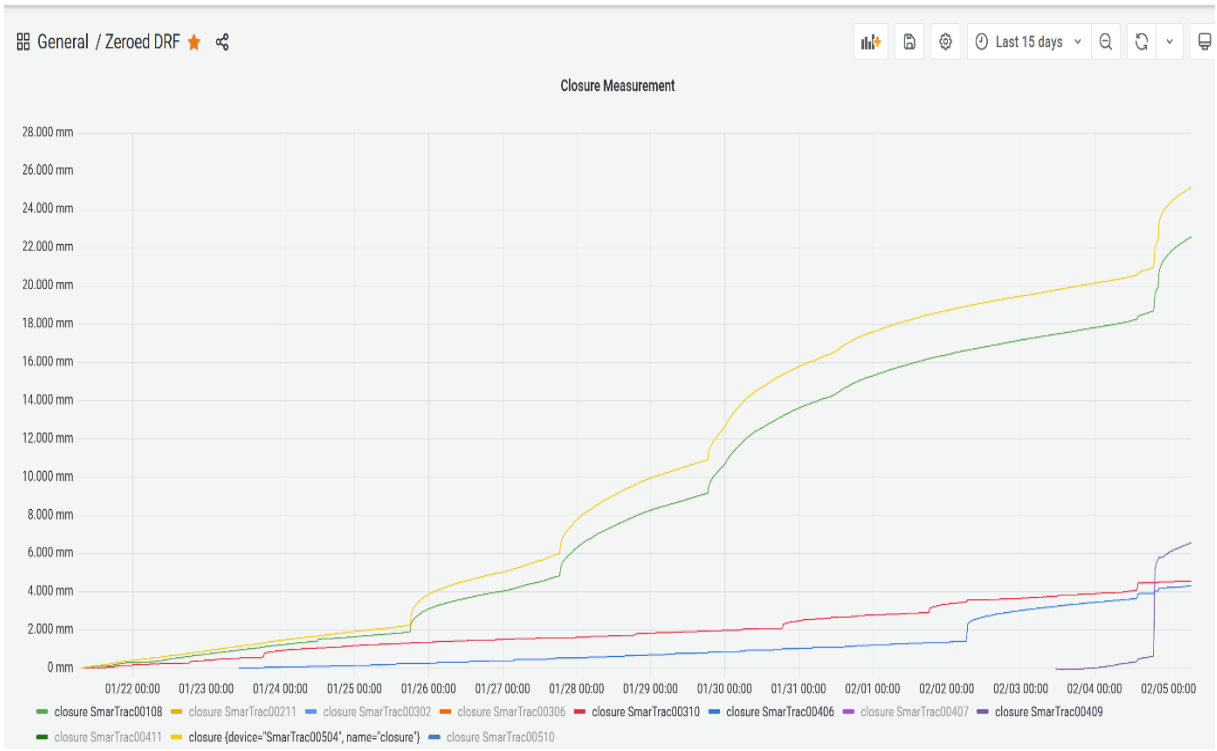


Figure 28. The last 15 days.

The closure per blast significantly increased.

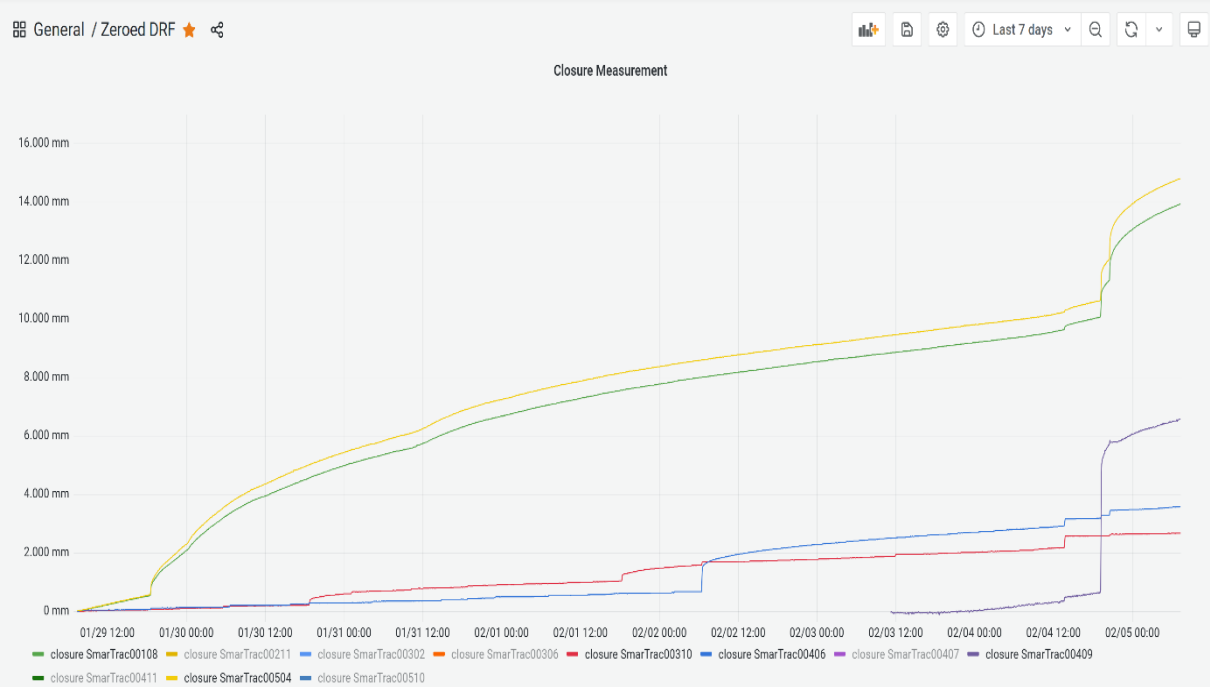


Figure 29. The last 7 days.

The closure per blast is much higher than previously, indicating less stable ground conditions.

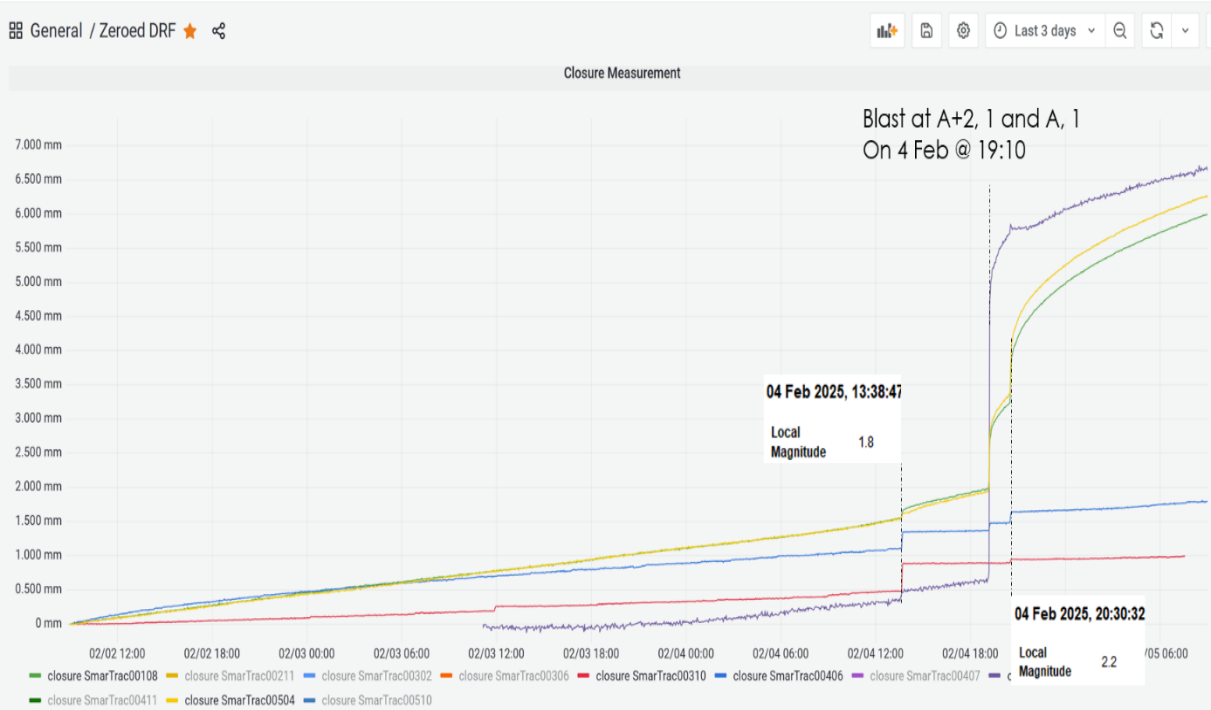


Figure 30. The last three days.

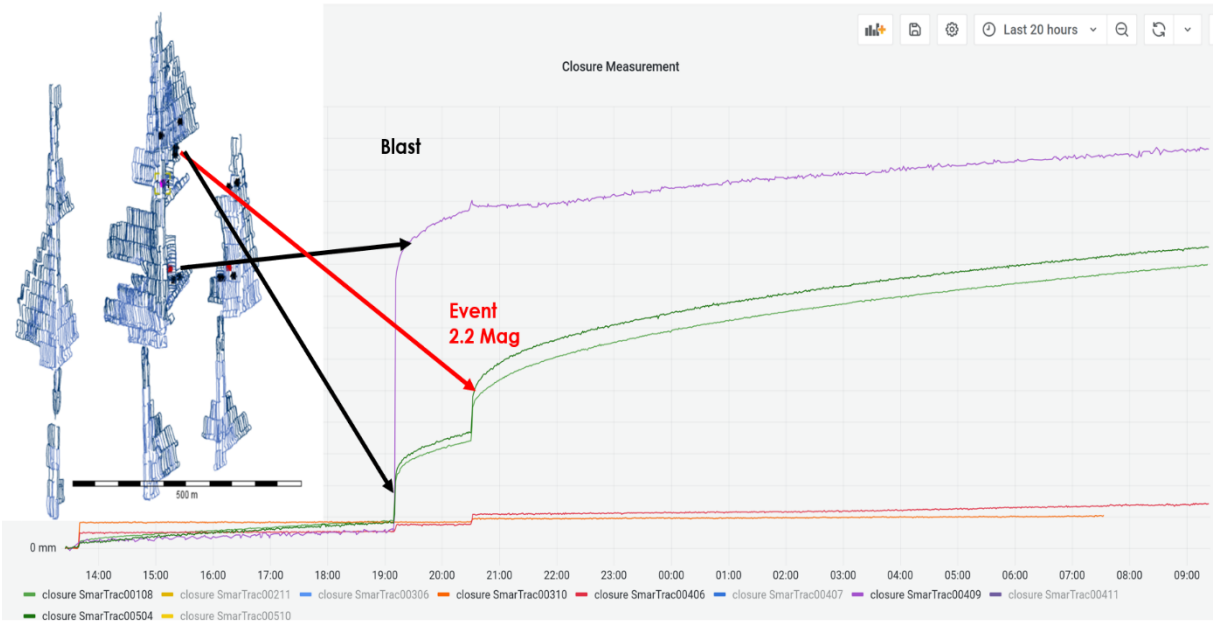


Figure 31. The last 20 hours.

Discussion

- Accelerated closure identified and reported on 30 January proved to be a precursor to a large seismic response (M1.8 and M.2 on 4 February).
- The observed or interpreted reduction in the rate of closure and subsequent continuation of mining proved to be a false sense of non-seismic relaxation and stability.
- Many more examples need to be studied to improve on proactive interpretation of closure and seismic data.
- The M1.8 event occurred at 13:38, before the blast of the day. The M2.2 occurred at 20:30, approximately an hour and a half after the blast of the day.
- The event mechanism is dominated by shear, with little closure or volumetric deformation indicated. This can be interpreted that the mining excavations were not part of the source or event mechanism. This is consistent with the subsequent reports of lack of damage in the stopes.
- The event is most likely associated with Ortlepp shear ahead of and parallel to the VCR mining faces.

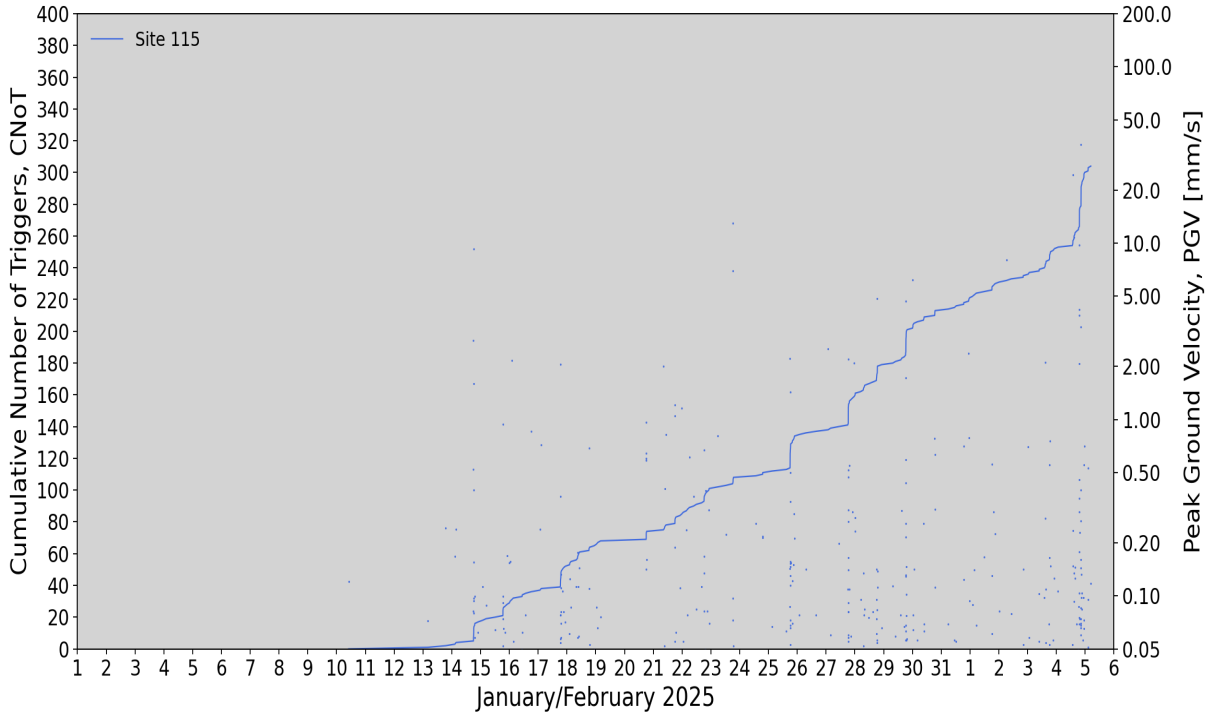


Figure 32. Cumulative number of triggers from accelerometer.

CONCLUSION

The use of complementary monitoring systems (SmarTrac closure monitoring devices along with the 8 G accelerometer) for the acquisition of relevant rock mass data has demonstrated some interesting results that correlate stope closure patterns with rock fracturing that further resulted in a sequence of seismic activity close to the stoping horizon.

Viewing the continuous closure data with continuous recording (seismograms) from the accelerometer on the same timescale, adds significant insight into the rockmass response to mining. In one case study, the rate of closure and fracturing increased significantly prior to a seismic response of three large events (M_L>2.0) near the stopes where the instruments were installed.
More research is required in this area, but initial results are very encouraging, with the end possibility being that warning can be given for an increased likelihood of large seismic events in a specific area , with the resultant increase in safety for mine employees.

For further consideration:

- Deploying multiple closure meters across a significant area of the mine should yield fascinating insights.
- Blasting effects will likely become quantifiable. By analysing closure data before and after blasts, we will be able to assess their impact on mine stability.
- Seismicity can also be studied. By correlating closure variations with seismic events, we gain a deeper understanding of safety risks.
- The challenge lies in aggregating sufficient data to predict unsafe situations reliably. Our ongoing research aims to address this challenge.

In summary, comprehensive data collection using instruments like the SmarTrac and 8 G accelerometers empowers mine safety professionals to make informed decisions. By leveraging real-time insights, we move closer to a safer mining environment.

Lourens Scheepers	Patrick Lenegan	Frans Pienaar	Hanno Hoogenboezem	Dewalt Lamprecht
	National NDip Electrical Engineering	BSc Eng(Civil) MEng(Structures)		

REFERENCES

D.F. Malan (2003) - CSIR Miningtek: SIMRAC- Guidelines for measuring and analysing continuous stope closure behaviour in deep tabular excavations
August 2003

Lourens Scheepers, Patrick Lenegan, Frans Pienaar, Hanno Hoogenboezem(2025) Minesafe2024- Enhancing Mine Safety Through Comprehensive Data and Instrumentation November 2024



Lourens Johannes Scheepers

Manager Rock Engineering
SibanyeStillwater

Mining career start: April 1997 Vaal Reefs (Orkney).

Now 28 years in Rock Engineering, mostly in deep level (seismically active) gold mines. Currently the Manager Rock Engineering in Mining Technical Services for SibanyeStillwater, with a portfolio including the seismic service, modelling service, research and projects.

Pillar assessment at Bindura Nickel Corporation's Trojan mine in Zimbabwe

F. Kwangwari[1], T. Makahamadze[2], W. C. Joughin[1]

[1]SRK Consulting, South Africa
[2]Bindura Nickel Corporation, Zimbabwe

This paper presents the findings of a preliminary geotechnical investigation conducted at Bindura Nickel Corporation's Trojan Mine in Zimbabwe. The study aimed to assess the pillar area between two of its three mineable orebodies: the Main Ore Body (MOB) and the Massives Ore Body (Massives), and to determine optimal pillar sizes between the orebodies, if any. The investigation focused on evaluating the feasibility of mining around historically mined-out areas, highlighting potential geotechnical risks, and assessing the adequacy of existing support systems. The study aimed to evaluate the potential requirement for pillar between the mined-out Massives stopes and the surrounding MOB. The results of the investigation concluded that it was not necessary to leave a pillar between the Massives and the MOB, provided that the proposed extraction sequence and support recommendations were adhered to.
Site investigations were conducted to assess the effect of stress build-up from historically mined-out areas. Thereafter, three-dimensional elastic finite element numerical modelling was carried out, providing more insight and correlating with underground observations. With a better understanding of these stress interactions, site observations and numerical analysis results were then utilised to develop an optimal extraction sequence and recommend adequate support regimes.

The investigation identified significant stress concentrations near mined-out stope abutments, primarily due to historical mining practices, which correlate with damage observed during underground assessment. The findings highlight the importance of strategic stope extraction and support installation to mitigate stress-induced damage and ensure operational safety.

The investigation concluded that with the adoption of the proposed extraction sequence and enhanced support strategies, the Hangingwall Ore Body and the remainder of the MOB could be safely extracted. Recommendations on additional geotechnical drilling, enhanced support strategies, and the implementation of a seismic monitoring system were made to mitigate risks associated with stress-induced damage and to ensure the stability and safety of mining operations.

Keywords: Trojan mine, geotechnical assessment, pillar extraction, stress analysis, mining safety.

INTRODUCTION

The Trojan Mine, operated by Bindura Nickel Corporation, is a brownfields project with a history of mining dating back to the 1960s. The geological setting of the project site is characterised by nickel sulphide mineralisation within the complex structural geology of ultramafic lavas, which form part of the greenstone belt and include three prominent joint sets. Despite the low regional seismicity, the mine has experienced mining-induced seismic events, prompting the need for effective stress management strategies.

Underground mine layout

There are three orebodies targeted, namely, the Hangingwall Orebody (HWOB), the Main Orebody (MOB) and the Massives Orebody (Massives). Figure 1 shows a cross section of the orebodies and major access infrastructure at Trojan mine.

The orebodies are hosted in serpentinite, most of which is unaltered (fair quality rock mass), but there are small pockets of weak altered serpentinite (poor to very poor quality). The footwall comprises basalt (basic lava), which is a good quality, strong rock mass.

The HWOB is irregular, with a strike length of approximately 200 m, and is separated from the MOB by a 20- to 60-m-wide shear zone within the serpentinite and containing lenses of spinifex-textured komatiitic metabasalt, feldspathic schist, and metagabbro. In some areas, these shear zones are entirely within ultramafic rocks, consisting of talc-carbonate schist (Bindura Nickel Corporation, 2018). The MOB is the largest orebody, characterised by massive and near-massive sulphide ores forming a narrow, discontinuous zone along its footwall contact. It extends 250 m along strike, with an average width of 30 m, and has been intersected at a maximum depth of 1440 m below the shaft collar. The Massives, located towards the footwall of the MOB, has a limited strike length of 80 m and an average width of 12 m.

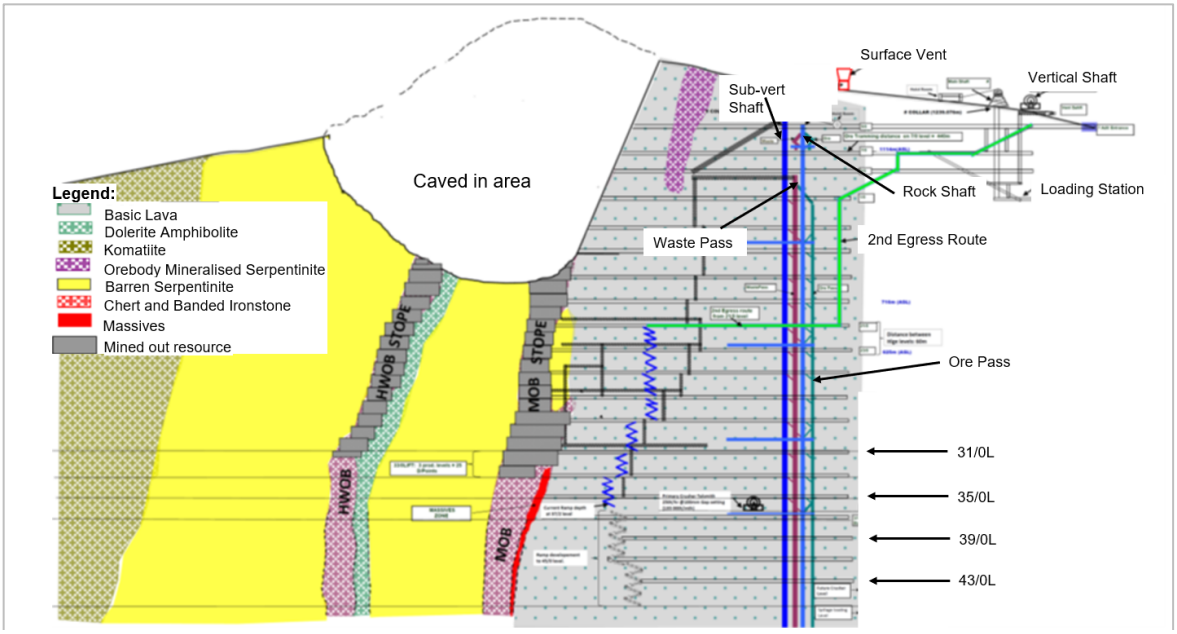


Figure 1. Cross-section of the geology and access infrastructure (Trojan Nickel Mine CoP, 2018).

The mine employs a sublevel caving method, with mining infrastructure extending to 1225 m below surface. All the principal shaft structures and excavations are located in the footwall of the deposit and are therefore not subject to any effect from caving which is confined to subsidence at surface in the hanging wall side of the deposit (Figure 1).

Above the 35L (888-950 mbs), the entire strike length of both the HWOB and the MOB, as well as the Massives, have been mined out (Bindura Nickel Corporation, 2018). As a result, the geological

hangingwall caved, extending to surface and forming a subsidence crater, as illustrated in Figure 2. Large spans were mined, which induced hanging wall caving, making the mined-out zones inaccessible. This suggests that the HWOB must have been mined first on each level; otherwise, caving of the MOB hangingwall would prevent mining of the HWOB. On each level, mining retreated from the hanging wall of the HWOB to the footwall of the MOB to maximise extraction.



Figure 2. Trojan mine project area and subsidence crater.

Below the 35L down to 45 level, only the Massives were mined first, due to the high grade of the orebody, leaving the MOB and the HWOB intact (mined-out areas are indicated in dark blue in Figure 8). Drives on 37/3 level in the hangingwall of the Massives, which include the MOB and HWOB, were observed to be stable during the underground assessment; images of assessed underground sections are presented in the following sections.

As mining progressed through each sublevel, dry, coarse caved material from the upper levels flowed into the massive stope, effectively serving as backfill for the stope. Relaxation of the stope hangingwall was only observed within 5 m to 10 m of the Massives stope. Stress damage was also observed in some of the 37/3 drives, indicating high stope abutment stresses.

Underground visit

Some of the underground areas visited included the 37/3L, and 41/0L levels, as illustrated in Figure 3 and Figure 5, respectively. The brown colour represents the mined-out access drives, the light blue indicates the mined-out stopes, and the green shows the planned access drives and stopes.

The observations at the indicated points (Figure 3 and Figure 5) and observed damage (Figure 4 and Figure 6), are described later on in the article and compared with the stress concentrations from numerical modelling results.

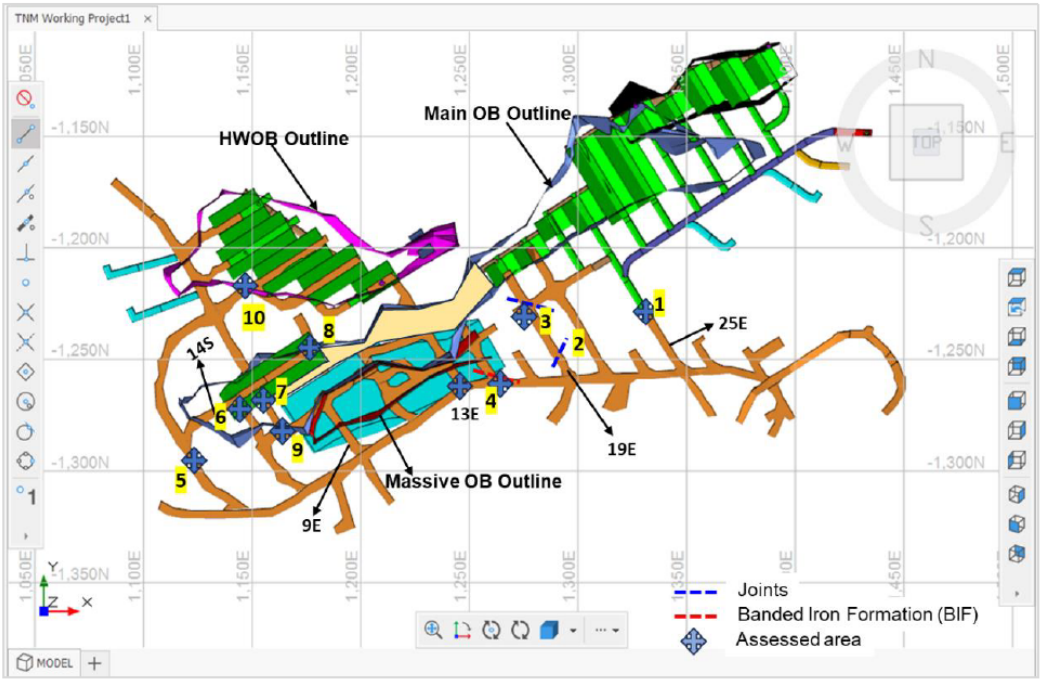


Figure 3. 37/3L Trojan mine- mine plan layout showing assessed areas.

Figure 4 shows stress fracturing and spalling in the sidewalls adjacent to the mined-out stope, particularly at point 4 on 37/3L. Significant spalling was observed at point 9, due to the stope abutment. This spalling is indicative of the stress-induced damage of the rock mass. Drill holes intended for a slot drive at point 8 were reportedly collapsing and significant damage was observed. This hole collapse and damage is likely due to the relaxation in the Massives stope hangingwall.

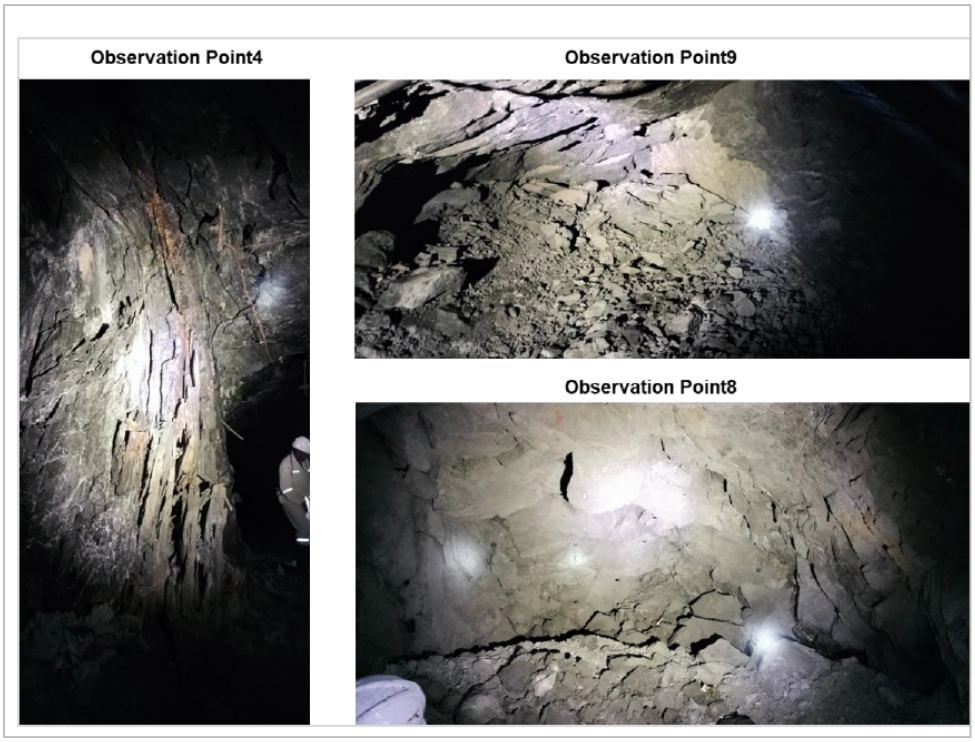


Figure 4. Trojan mine - stress damage observed on 37/3L.

As illustrated in Figure 5, the rock fall there stress damage in the roof on 41/0L (Figure 6) at point 1, indicate high horizontal stresses. Installation of mesh is recommended to provide skin support. At point 2 there is a very thin pillar left between the stope and the drive, which has completely collapsed, causing damage to the gathering drive.

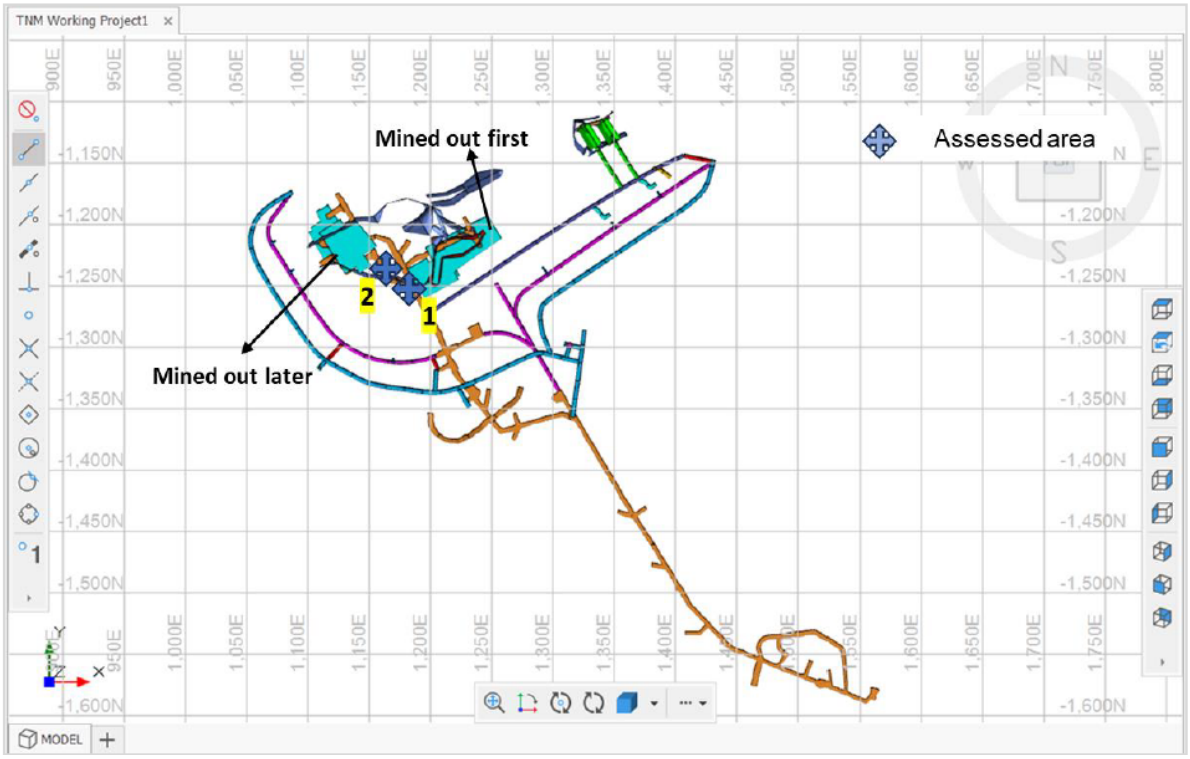


Figure 5. 41/0L Trojan mine- mine plan layout showing assessed areas.



Figure 6. Trojan mine- stress damage observed on 41/0L.

Historical Mining and Proposed 2024 Mine Design

The natural backfilling process supported the mined-out stopes with broken rock, preventing hangingwall failure and enabling safe access in the hangingwall of the Massives stope, which will allow future stoping of the MOB and HWOB. Figure 7 and Figure 8 show historical mining layout and the proposed 2024 mine design to 45/0L MOB and HWOB). In Figure 8, the blue represents historical mining while colourful blocks show the proposed sequenced mine design.

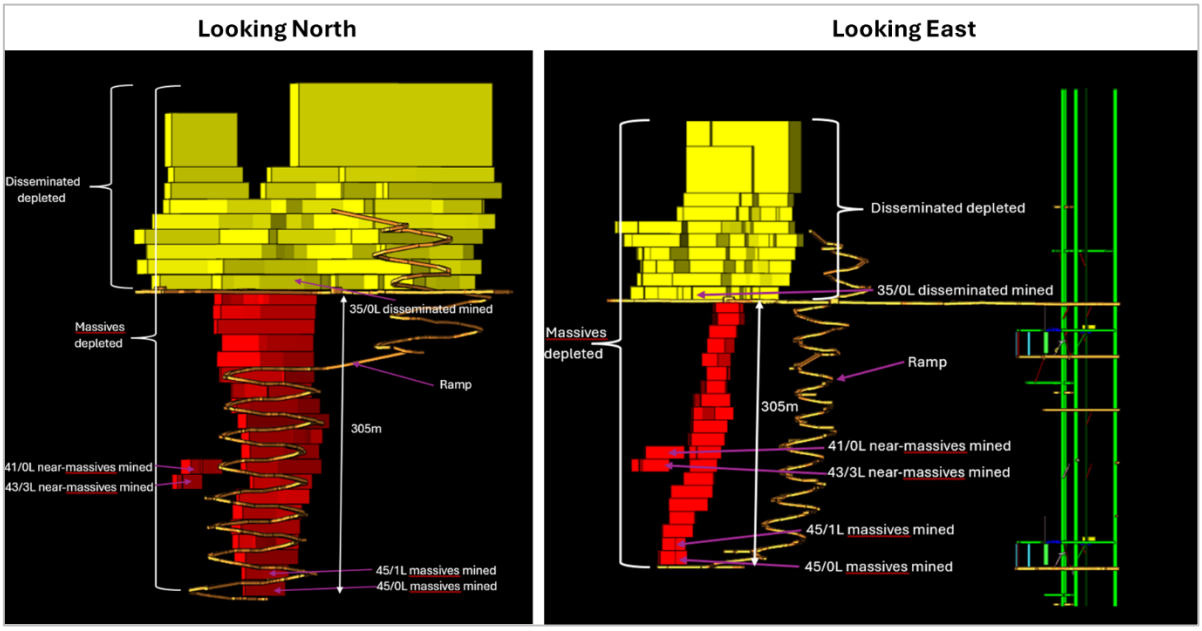


Figure 7. Historical mining configuration.

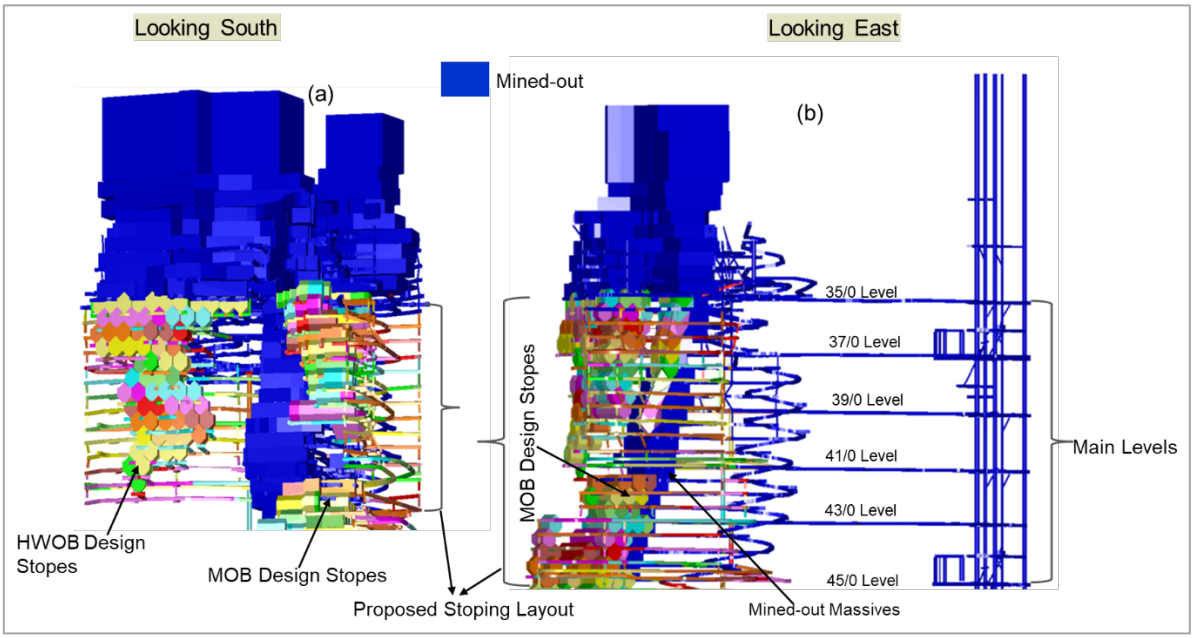


Figure 8. Mined-out stopes and planned layout at Trojan mine.

This study was conducted to address the geotechnical challenges associated with the potential pillar between the Main and Massives orebodies. The primary objectives were to evaluate the feasibility of mining adjacent areas, determine whether a pillar should be left between the mined-out Massives and the MOB (as well as its optimum size), and assess the adequacy of the existing support regime.

Stress regime

No stress measurements have been conducted at Trojan. However, stress-related damage was observed during the site visit, where pillars were formed and excavations were close to abutments as a result of historic mining practice.

Regional information from the Southern African Stress Measurement database suggests that stress magnitudes may have some variability, and the k-ratio (the horizontal to vertical stress) typically ranges between 1.2 and 1.8. High stress levels were not anticipated, and therefore rock engineering designs do not cater for stress damage. The stress state provided in Table I was applied to the elastic modelling.**Error! Reference source not found.**

Table I: Estimated stress state

k1 Trend (°)	Horizontal Stress 1 (k1)	Horizontal Stress 2 (k2)	Vertical Gradient (MPa/m)
161	1.5	1.0	-0.026

Methodology

A preliminary geotechnical investigation was conducted, including a site visit, data collection, and numerical modelling. The investigation commenced with a site visit to assess the existing underground conditions and to identify stress-related damage and any challenges encountered during historical mining. Thereafter, three-dimensional finite element numerical modelling was employed to simulate observed stress interactions and inform the development of an optimal extraction sequence.

The numerical modelling results were calibrated against the stress fracturing observations made during the underground assessment. This calibration was essential to determine the minimum stress threshold that could potentially lead to the onset of instability in the excavations. By back-analysing the progression of stress concentration from historical mining practices, site observations and calibrated modelling results were utilised to develop an extraction sequence aimed at minimising the impact of stress fracturing going forward and to determine support requirements, where stress damage was unavoidable. The optimal offset distances for long-term development drives and haulage drives were determined to reduce stress-related risks and maintain operational safety.

By understanding the stress distribution and potential risks, the study's recommendations aim to assist mine management in making informed decisions about the proposed design and implementation of support systems. This proactive approach helps mitigate the risks associated with stress-induced damage, ultimately contributing to safer and more efficient mining operations.

Numerical Analysis

Numerical modelling was performed using the finite element method with RS3 software to explain the underground observations and inform the development of an optimal extraction sequence. The historical mine design was back-analysed to simulate the stress build-up during mining and assess the potential stress-related risks. Subsequent recommendations were made for input into the proposed future mine design.

The geometry and extraction sequence used in the analysis were derived from the DXF files of the historical mine design and surface topography. The historical mining between level 31/0L and the surface topography was represented by simply extruding the 31/0L footprint upwards to connect with the surface topography, which includes the subsidence crater.

The extraction process was sequenced so that each stoping level was completely mined-out before moving on to the next. The development drives were strategically planned to lead by one level, ensuring that the necessary infrastructure was in place to support subsequent mining activities. Caved waste rock is placed in the stope during the next mining step. Figure 6 shows the mining sequence used in the elastic model. This approach ensured that the extraction process closely aligned with historical mining practices.

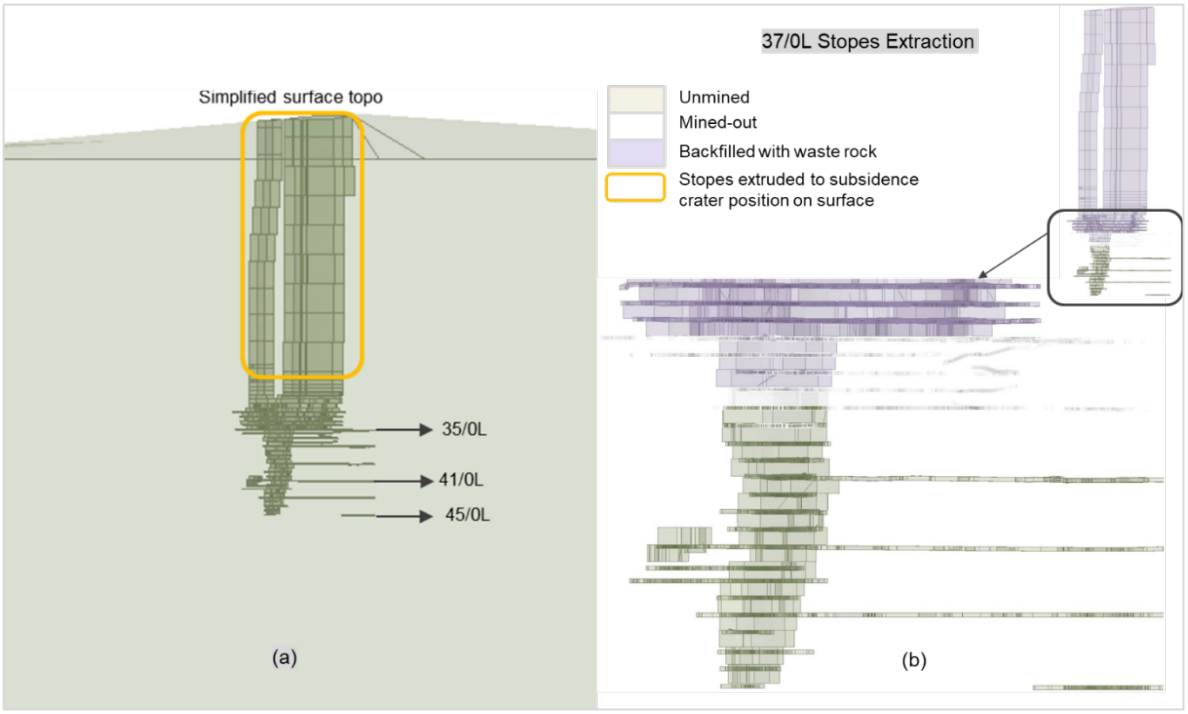


Figure 9. Model layout (a) with extraction of 37/0L stopes (b).

The mining layout, as illustrated in Figure 9, demonstrates the systematic filling of each sublevel with caved material, starting from the top at the subsidence crater, and progressing as mining operations advance to the subsequent stopes.

Material Properties

A digital litho-structural model was not available at the time of the study, which would enable the basalt, serpentinite contact and pockets of altered serpentinite to be included in the numerical model. The material properties of the entire rock mass were simplified to represent unaltered serpentinite properties only. The model interpretation may therefore be conservative where there is basalt and special support strategies will be required when altered serpentinite is encountered in the mine.

The serpentinite material properties required for the numerical analysis were estimated from the Worley Parsons report and Handley (2013), and benchmarked with RocLab data, as site-specific information was not available. The low strength properties of backfill were used to represent that of the caved material filling the mined-out stopes. These properties are summarised in Table II.

Table II: Model Input Parameters

Material	Density (MN/m³)	Ei (MPa)	Poisson's ratio
Serpentinite	0.026	60 000	0.25
Caved Material	0.016	20	0.35

Stress concentrations and observed damage

During the underground assessment, it was observed that the main development and gathering drives situated in basalt were not supported yet remained stable. This stability indicates the competency and inherent strength of the basalt rock mass. However, as the geological conditions transitioned from basalt to serpentinite, the ground conditions noticeably deteriorated. In response to this change, bolt support

was introduced to enhance stability, although the support pattern was not applied consistently across all areas. Significant stress fracturing was noted in the gathering drives and production crosscuts that were near the mined-out stopes. This fracturing highlights the increased stress concentrations in these areas.
The numerical modelling results revealed significant stress concentrations in the gathering drives and production crosscuts located near mined-out stopes. These results correlate with the observations made during the underground assessments. The stress concentrations suggest that these areas are experiencing elevated levels of stress due to their proximity to the extracted stopes. This increased stress can lead to potential instability and damage in the rock mass, highlighting the need for enhanced support measures and careful planning of mining operations.

Based on the underground observations and numerical modelling, major principal stress damage is noted when stress levels surpass 70 MPa in serpentinite. The gathering drives positioned at least 10 m away from stope boundaries are anticipated to experience minimal stress-related damage, as indicated by both underground observations and numerical analysis.

Figure 10 illustrates the stress levels following the extraction of stopes on the 37/3L level. The arrows (black) on the level plan layout with numerical modelling results indicate the path taken during the underground assessment, as there was no access to some sections of the mine. As evidenced by the underground assessment and numerical modelling results, the gathering drive at observation point 4 and the production crosscut at observation point 9 are experiencing severe stress damage. This indicates that these areas are subject to high stress concentrations, rendering them unstable. Observation points 7 and 8 show moderate stress damage and spalling.

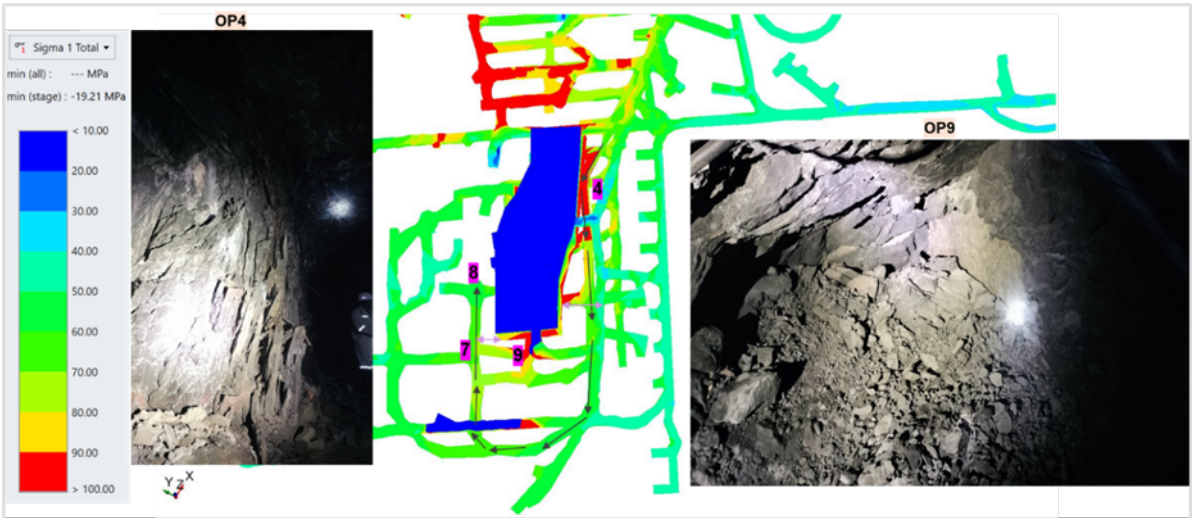


Figure 10. Trojan mine- plan-view of stresses on 37/3L.

The numerical results highlight severe stress damage at both observation points 1 and 2 on the 41/0L level (Figure 11), confirming the observations made during the underground inspections. The currently installed resin bolts and cable anchors at observation point 1 are failing, indicating that they are not effectively supporting the drives. As a result, these support systems will need to be improved to ensure the stability and safety of the affected areas. The installation of mesh is recommended to provide more effective support and to enhance the overall structural integrity of the drives.

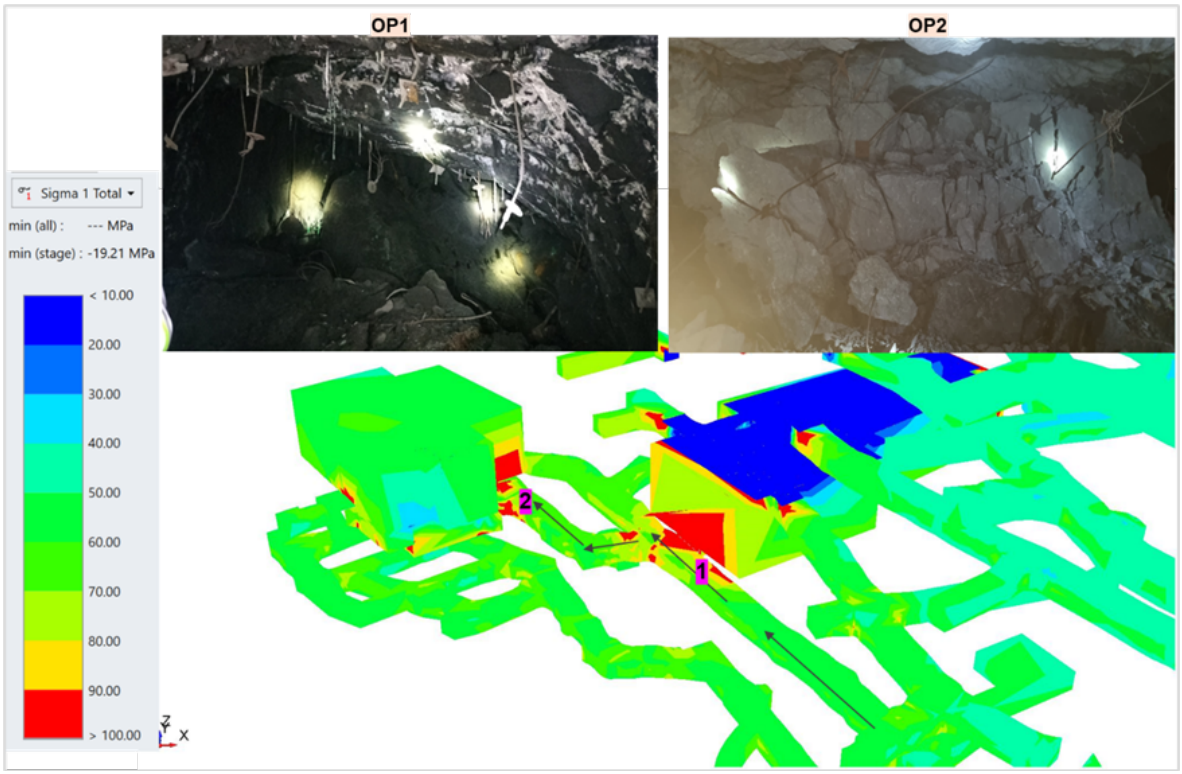


Figure 11. Trojan mine - oblique view of stresses on 41/0L.

DISCUSSION

Massives stope extraction has led to some relaxation of the stope hangingwall, extending a few metres from the stope. The variation in stress impact across different observation points on different levels highlighted the need for targeted support strategies to mitigate potential risks and maintain stability. The existing support regime requires enhancement, particularly in areas of high stress, to ensure safety and stability. The gathering drives are typically located too close to the stope boundaries, resulting in increased stress due to the stope abutments. Significant stress damage has been observed on the roofs and sidewalls of the gathering drives and production drifts, particularly in areas where no mesh has been installed.
To mitigate these issues, it is recommended that the gathering drives be positioned away from high abutment stress zones, at least 10 m from the stope boundary based on the underground observations, and that extra cable anchors and surface support in the form of mesh be installed. This will ensure the structural integrity and safety of the gathering drives, thereby mitigating the impact of stress concentrations. and preventing potential damage.

Recommended stope extraction sequence

The findings highlighted the need for a strategic extraction sequence to prevent the formation of unstable pillars and optimise ore recovery. The study recommended that mining operations progress from the hangingwall towards solid ground, with careful planning to avoid unnecessary stress concentrations. The mining steps have been organised and numbered using the calendar months in a repetitive cycle. The leads and lags for the stopes have been carefully considered to prevent the formation of pillars and to mitigate the time-dependent deterioration of the rock mass adjacent to the mined-out stopes.

The proposed stope extraction sequence for the 37/3L level is presented in Figure 12. The 14S drive in Block 1 will need to be developed and extended, as indicated by the blue dotted outline, to connect with

the drive that links the Block 2 stopes. All the blocks can be mined concurrently, with Block 1 scheduled to lead Blocks 2 and 3. The leads and lags should be planned to limit severe stress damage to the unmined sections. The extraction of all the blocks should aim to adhere to the illustrated sequence. In situations where drilling becomes challenging due to relaxation of the Massives stope hangingwall or excessive stress damage, a few metres ore may be blasted. This ore is already damaged and may be recovered on the active level or from the level below. Some ore loss and ore dilution should be anticipated. A similar sequence should be applied on all levels, except 41/0L and 43/3L, where an additional stope has already been extracted.

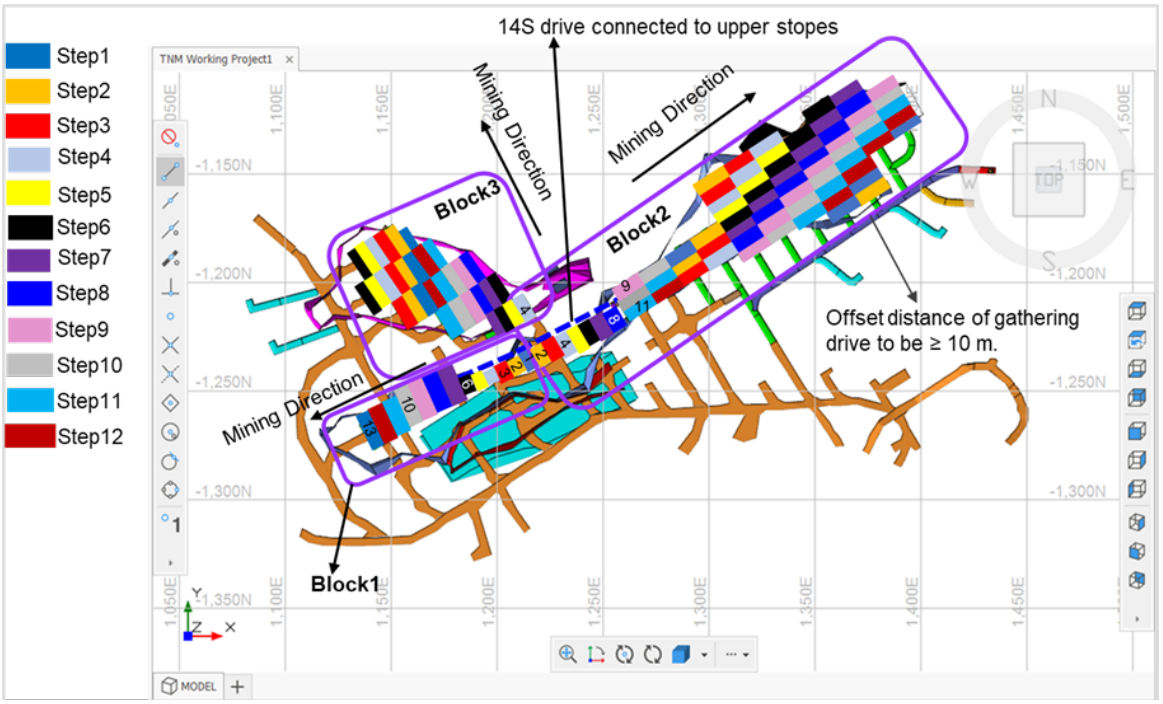


Figure 12. Trojan mine - 37/3L proposed stope extraction sequence.

On level 41/0L (Figure 13), the previous stope extraction sequence aimed at high-grade ore inadvertently led to the formation of a highly stressed pillar, causing severe stress damage in the gathering drive within the pillar. To address this, the planned secondary development and gathering drive should be adequately supported and extended to the orebody boundary, as indicated by the blue dotted lines. The existing damaged gathering drive needs rehabilitation from a safe position, including re-supporting with mesh and primary rebar, using mechanised equipment to minimise personnel exposure. Cable anchors should be installed at intersections with excessive spans and where significant roof breakouts have occurred, following the new primary support to ensure safety. Once rehabilitated, this drive should connect to the secondary drives, as shown by the red dotted outline. The stope panel next to the mined-out stope should be prioritised for extraction using the rehabilitated access. Mining should proceed in two directions, providing two retreat accesses to enhance operational flexibility and safety, allowing for efficient ore extraction while maintaining stability.

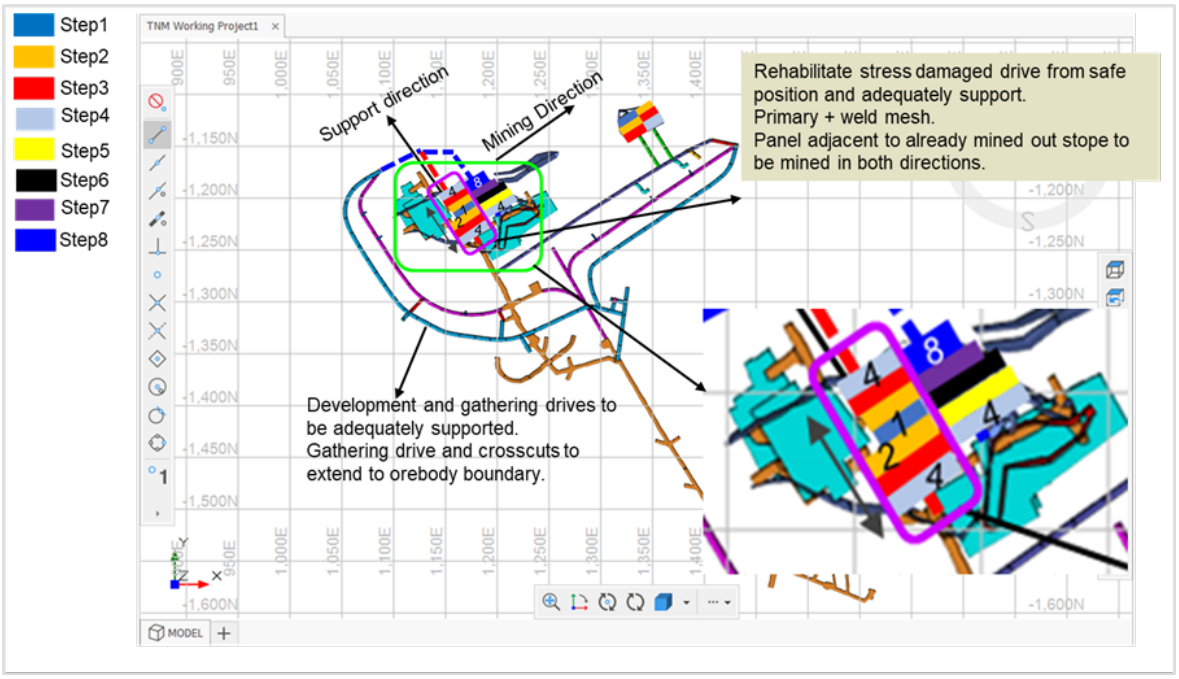


Figure 13. Trojan mine- 41/0L proposed stope extraction sequence.

Recommended support strategy

A review of the logged data indicated that the rock mass ratings (Laubscher RMR) range from 40 to 60 for serpentine and 60 to 80 for basalt, suggesting fair rock mass around the orebody and good in basalt. This corroborated with the underground observations made during the site visit. The serpentine's fair rock mass quality required systematic support measures to ensure excavations stability whilst excavations sited in basalt are anticipated to be more stable and may require no or less reinforcement, depending on their location. The inherent strength and stability of basalt reduces the immediate need for extensive support measures. Therefore, drives in basalt that are not overstressed have not been supported historically and remain in good condition. When the gathering drives in basalt are too close to the stope boundaries, rebar and mesh supported is required. This variability in rock competency between basalt and serpentinite was considered in tailoring support strategies to the specific geological conditions encountered in different areas of the mine.

The currently implemented support system involves using rebars in serpentinite and diamond mesh as secondary support in poor ground conditions, whereas the drives in basalt remain unsupported. The practice of manually installing the diamond mesh is ineffective, as longhole drilling tangles the mesh and installation is not completed in a timely manner. Furthermore, the current diamond mesh is unsuitable for in-cycle installation or subsequent longhole drilling. Due to a significant backlog in secondary support installation, production was allowed to continue without the installation of mesh, but it will not be possible to sustain production safely with this practice.

It is therefore essential to procure the necessary mechanised equipment and train personnel to install bolts and weld mesh in cycle. The recommendation is to spray shotcrete over the mesh, but this would take longer and further exacerbate the backlog. The following are recommended support requirements for various excavation types, tailored to the stress levels and geological conditions encountered:

Table III: Support Requirements for different excavation types

Excavation Type	Support Specifications
Ramp, Main Haulages, gathering drives & tips x/cuts (Basalt-low stress)	• No support required.
Gathering drives, orebody development x/cuts (Basalt-moderate stress)	• Primary support: 3 m tensioned resin fully grouted rebars on 1m x1m spacing (two bolts in back and two bolts in each sidewall per row), to the gradeline. • 5 mm gauge, 100 mm aperture size weld mesh installed in cycle from to grade line.
Gathering drives, orebody development x/cuts (Basalt-high stress)	• Primary support: and • 5 mm gauge, 100 mm aperture size weld mesh installed in cycle from floor to floor. • Pre-tensioned and grouted 6 m cable-anchors on 2 m x1 m spacing in the roof.
Gathering drives, orebody development x/cuts (Serpentinite-moderate stress)	• Primary support: and • 5 mm gauge, 100 mm aperture size weld mesh installed in cycle to grade line.
Gathering drives, orebody development x/cuts (Serpentinite -high stress)	• Primary support: and • 5 mm gauge, 100 mm aperture size weld mesh installed in cycle from floor to floor. • Pre-tensioned and grouted 6 m cable-anchors on 2 m x1 m spacing in the roof and overstressed walls.
Wide areas, Breakaway and Intersection Support	• Primary support: and • Pre-tensioned and grouted 6 m cable-anchors on 2 m x 1 m spacing in the roof.
Large Excavations	• Primary support: and • Pre-tensioned and grouted 6 m cable-anchors (minimum length = half excavation span and maximum spacing = 0.5 x length). • 5 mm gauge, 100 mm aperture size weld mesh installed in cycle to the gradeline.
Large excavation brow support	• Primary support: and pre-tensioned, grouted, cable bolts, in a 2 m x1 m pattern or denser, depending on mass to be supported. Length = brow height. Installed within 1.0 m of the brow.
Bull nose	• Primary support: and • Osro straps across the bull nose for confinement, from the shoulder down to 1.0 m from the floor.

Seismic monitoring

With the planned increase in mining depth, high stress build-up around excavations is inherent. Consequently, it is essential to implement a seismic monitoring system to effectively assess and manage the potential for seismic hazards. The seismic monitoring system should be both sensitive and accurate enough to detect and monitor the progression of rock mass damage. Its location accuracy must be reliable to facilitate the implementation of dependable re-entry protocols following stope blasts.

CONCLUSIONS

The study concluded that leaving a pillar was not necessary, provided that the recommended extraction sequence and support strategies were followed. Additional drilling is recommended to assess the extent of stress damage and inform future mining activities. The implementation of mechanised support installation is crucial to maintaining safe production levels.

Pillar size determination
Leaving a pillar is not necessary, although it should be noted that there may be some losses, because of the relaxation of the rock mass in the Massives stope hangingwall. This may be recovered since the ore is already broken. Targeted drilling can help to establish the extent of the zone of relaxation.

It is recommended therefore to drill boreholes from 35/0L and 37/0L targeting the immediate hangingwall of the mined out Massives stopes in order to determine the severity and extent of the potential damage or fracturing towards the MOB.

Feasibility of mining around the Massives stope
The HWOB and the remainder of the MOB can be extracted, provided that the recommended extraction sequence and support strategies are strictly followed.

The extraction sequence must be carefully planned to prevent the unintentional formation of pillars. Mining operations should commence adjacent to the mined out Massives and progressively move towards solid ground to ensure stability and to maximise resource recovery while minimising the risk of leaving behind unstable pillars.

Gathering drives and production crosscuts, which are sited too close to the stope abutments are experiencing stress damage/fracturing, indicating elevated stress levels. These drives and crosscuts begin to experience damage due to the increased stress concentrations during the extraction of stopes on the level above.

Support Regime Assessment
Current support is not suitable for mining in the moderate to high stress conditions already experienced and anticipated in future. There is therefore a need for mechanised installation of rebar and mesh in cycle where stress damage is required.
Following these guidelines is essential for maintaining stability and safety in mining operations, mitigating risks associated with stress-induced damage, and ensuring efficient ore extraction.

REFERENCES

Bindura Nickel Corporation, 2018. *CODE OF PRACTICE TO COMBAT ROCKFALL ACCIDENTS AND ROCK BURSTS ,* Bindura: Trojan Nickel Mine .

Bindura Nickel Corporation, 2024. *Trojan Mine Presentation,* Bindura: Trojan Mine.

Bindura Nickel Corporation, n.d. *Geological Maps,* Bindura: Trojan Nickel Mine.

Bindura Nickel Corporation, n.d. *GEOMECH 17,* Bindura: Trojan Nickel Mine .

Brady, B. & Brown, E., 2004. *Rock Mechanics for underground mining.* New York: Kluwer Academic Publishers.

Handley, M., 2013. *Pre-mining stress model for subsurface excavations in Southern Africa.* Johannesburg: SAIMM.

Trojan Nickel Mines-LTD, 2018. *Support Standards,* Bindura: Trojan Nickel Mine.

Worley Parsons, 2014. *Numerical Modelling at Trojan Mine,* Johannesburg: s.n.



Fungai Kwangwari

Mining Engineer- Geotechnical
SRK Consulting (SA) Pty Ltd

Fungai Kwangwari is a Geotechnical Engineer with over 15 years of experience in the field of Mining and Rock Engineering. She holds a BSc Degree in Mining Engineering and a Master's degree in Rock Engineering. She has worked and consulted independently for companies such as Zimasco Chrome Mine, Murowa Diamond Mine, SRK Consulting (SA), WorleyParsons RSA, Practara, and MSA Group.

Her experience in the Rock Engineering field includes site geotechnical characterization, underground and open pit slope designs stability analyses, excavations and support designs and analyses, and geotechnical risk assessments. She is conversant with several rock engineering modelling software for analysing rock mass response to mining through stress build-up and rock deformations. She has worked on several Preliminary Economic Assessments (PEA)/scoping studies, Prefeasibility Studies (PFS), and Feasibility Studies (FS), and has carried out due diligence studies for various commodities on different projects. Throughout her career, Fungai has been involved in a wide range of projects and commodities, optimizing them and bringing them to fruition while ensuring sustainability and safety.

She is currently a member of the South African Institute of Mining and Metallurgy (SAIMM), South African National Institute of Rock Engineering (SANIRE), and Zimbabwe National Institute of Rock Engineering (ZINIRE).

Outside of her professional life, Fungai enjoys spending time outdoors, appreciating nature.

Geotechnical design of coal bord and pillar panels: Some complementary suggestions

A. Vervoort

KU Leuven, Belgium

The design of coal bord and pillar workings focuses primarily on the pillars, i.e., the load on the pillar and the strength of the pillar. However, if one were to start a bord and pillar design on a blank piece of paper, one would start with the design of the rooms and first look at the redistribution of the stresses around the rooms. Elastic simulations clearly show that relaxed zones occur in both the roof (and floor) and in the sidewalls. These zones are located within the peak stress arcs. The size of these zones is influenced by the excavation dimensions and by the vertical-to-horizontal ratio of the initial stresses. A second concern is the common reflex to approximate the in situ pillar behaviour with a vertical loading experiment; for example by performing uniaxial compression tests. The latter could be realistic if one were to build a pillar, but that is not the case: one excavates a room. Before mining, the coal is in equilibrium in a three-dimensional stress state and depending on the position within the future pillar, the stress components decrease and/or increase. The various stress paths are illustrated by elastic and elasto-plastic simulations. At the end of the paper, suggestions are formulated for future work and improvements to our knowledge in the design of coal bord and pillar workings.

Keywords: strata control, coal bord and pillar mining, geotechnical design, stress paths

INTRODUCTION

Design of pillars, and more specifically the design of coal pillars, is a topic that has been researched extensively in the past (e.g., Bieniawski, 1981; Esterhuizen, 2000; Galvin, 2010; Mark, 2007; Salamon and Munro, 1967; Sheorey *et al*., 1987; van der Merwe, 1993; Wagner, 1974, 1980; Wagner and Madden, 1984; York and Canbulat, 1998). But it is still studied extensively. The list of references includes a number of papers published during the last few years to illustrate this point (e.g., Bruwer and Stacey, 2023; Chaurasia *et al*., 2025; Doroudgar and Noferesti, 2024; Guner *et al*., 2023; Huang *et al*., 2024; Vlachogiannis and Benardos, 2024; Wu *et al*., 2024). All this means that there is not only substantial interest in this topic, but there also is a need to better understand the behaviour of pillars. The ultimate goal is to optimise the bord and pillar parameters without jeopardising the short-term and long-term safety. An increase in the width of the bord or a decrease in the width of the pillar has a direct effect on the productivity and on the percentages mined. When no pillar extraction is planned (i.e., no retreat mining), the last figure is the complementary part of the percentages of coal that are lost forever. Note that this paper is focused only on bord and pillar panels, and not on retreat mining, pillar extraction, or pillars adjacent to longwall panels.

The aim of this paper is not to summarise, review, or criticise past research. Also, the aim is not to drastically change the current design method. Rather, some complementary suggestions to the ongoing research are formulated and presented here. The two main elements in this paper are (i) the relatively limited focus on the local stress redistribution around the rooms in comparison to the average load over the pillar area and (ii) the use of uniaxial compression experiments as proxies for the in situ pillar behaviour.

Both elements are discussed in detail in the next two paragraphs. At the end of the paper, suggestions are formulated for future work and for improvements to our knowledge of coal bord and pillar design.

Local stress redistribution around the excavations

Elastic simulations

When looking from a certain distance at the design practice of coal bord and pillar workings, one must conclude that the focus primarily is on the pillars, i.e., the average load on the pillar vs. the strength of the pillar. One could argue that this is logical as major incidents in the past involve the collapse of several pillars, even complete panels, e.g., the 1960 Coalbrook disaster (van der Merwe, 2006). However, if one were to start a bord and pillar design from a blank piece of paper (without any prior knowledge), one would start most likely with the design of the rooms and the local stress redistribution around the rooms.

First, results are discussed for an elastic and continuum 2D-model. A depth of 250 m is applied, corresponding to a vertical stress of 6.25 MPa. The standard 6 m width for the bords is modelled, and pillar widths of 34 m are assumed in the first group of simulations. Vertical symmetry planes are introduced in the model mid-way through the bord and mid-way through the pillar. The total height of the model is 60 m, and the seam elements are situated in the middle. For example, for a 3 m high excavation, 28.5 m of roof material and 28.5 m of floor material are part of the model. This means that the average pillar stress in the 2D approach is 7.35 MPa for a pillar that is 34 m wide. Three different values are applied for two parameters, i.e., the height of the pillar is taken to be equal to 1.5 m, 3.0 m (reference), and 4.5 m. The horizontal stress is for the reference case equal to the vertical stress, i.e., an initial isotropic stress state of 6.25 MPa. The two alternatives for the horizontal stress are also plus/minus 50%, i.e., 3.125 and 9.375 MPa. When one wants to focus on the local stress redistribution around an excavation, a sufficiently small mesh is needed. The model is composed of 10 cm square elements in the area surrounding the excavation. As can be deduced from the dimensions of the heights of the seam and the width of the pillar, the first group of simulations models a pillar with high factors of safety, i.e., for a mining height of 1.5 m, 3.0 m, and 4.5 m. The basic formula developed by Salamon and Munro (1967) results in a factor of safety of 3.2, 2.0, and 1.6. The same material is used for the floor, the seam, and the roof, and no interfaces are introduced above or below the seam. This allows to focus on a single aspect in this part of the study, i.e., the local stress redistribution around the rooms. Other aspects are integrated in the model at a later stage. The chosen characteristics for the coal are based on earlier research (Vervoort, 1992a and c), i.e., a Young's modulus equal to 3 GPa and a Poisson's ratio of 0.2.

In Figure 1, the locations of the stress peaks are shown in the roof (half the bord width of 6 m) and in the pillar (half the mining height). The three mining heights are presented in Figures 1a, 1b, and 1c, respectively. In each sub-figure the results for the three different initial horizontal stresses are presented. An ellipse representing the peak stress arches around the excavations are drawn. Inside these arches, there is a zone of stress relaxation in both the roof (and floor) and in the sidewalls. Such a relaxation is one of the reasons that roof support is required because the bedding planes open or fractures are introduced. This mechanism is well known for the roof layers. For the sidewalls, this aspect generally is not considered in the design process. Note that the size of the relaxed zone is determined here for an elastic and continuum model, and this model is independent of fracturing, contacts opening, or spalling. However, also note that, for some displacement discontinuity codes, the relaxed zones at the edges of the pillars are not modelled, and the peak stress occurs at the sidewall. This is not a major problem if the aim of the modelling is to learn more about the average loading of the pillars, but it is a drawback when one investigates the behaviour of a pillar. In Table I, the data are provided for the peak stresses in the pillar, i.e., the peak vertical stress, the corresponding horizontal stress, and the distance of the peak to the sidewall. The overall observation is that the larger the pillar height and the larger the initial horizontal-to-vertical stress ratio, the deeper into the sidewall the stress peak is situated. Or, in other words, the larger the relaxed zone is at the sidewall. If the initial ratio is larger than 1.5 (Aydan and Kawamoto, 1997; Zang and Stephansson, 2010), the relaxed zone would be extended further into the pillar. If the height of a pillar is small, the width of the relaxed zone is also small, i.e., 0.3 to 0.4 m for the cases modelled.

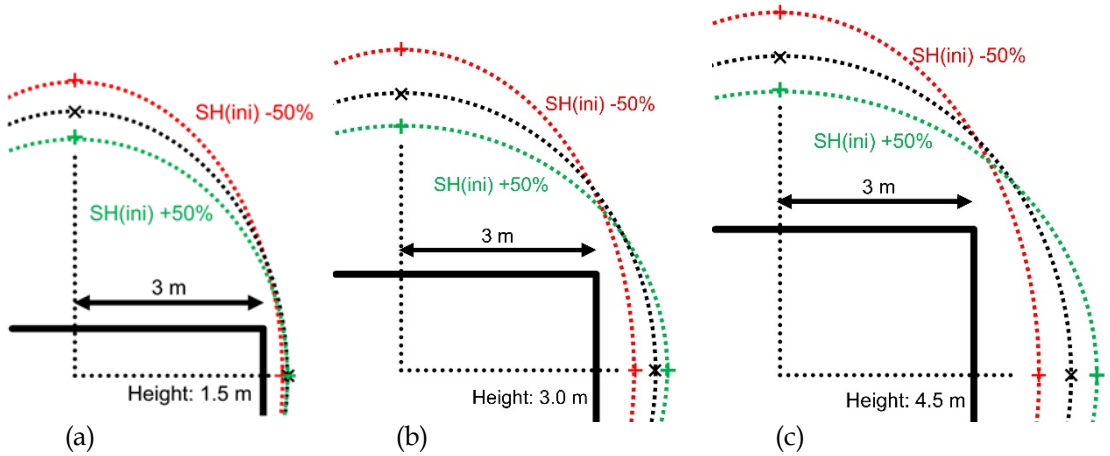


Figure 1. Locations of the stress peaks in an elastic model for three different initial horizontal stresses (pillar width of 34 m): (a) mining height of 1.5 m, (b) mining height of 3.0 m, (c) mining height of 4.5 m.

Table I: Data for the peak stresses in the pillar for different mining heights in an elastic model for three different initial horizontal stresses (pillar width of 34 m), i.e., the peak vertical stress, the corresponding horizontal stress, and the distance of the peak to the sidewall

	SH(ini) -50%	SH(ini) =SV(ini)	SH(ini) +50%
Ia. 1.5 m mining height			
SYY-peak (MPa)	14.93	13.98	13.43
SXX at peak (MPa)	0.64	1.64	1.95
Distance from wall (m)	0.3	0.4	0.4
Ib. 3.0 m mining height			
SYY-peak (MPa)	11.32	10.65	10.37
SXX at peak (MPa)	0.58	1.54	2.69
Distance from wall (m)	0.6	0.9	1.1
Ic. 4.5 m mining height			
SYY-peak (MPa)	9.85	9.38	9.26
SXX at peak (MPa)	0.60	1.64	3.09
Distance from wall (m)	1.0	1.5	1.9

In Figure 2, the stress redistribution in the pillar (at mid-height) is presented for the reference mining height of 3 m. Both the variation of the vertical stress (Figure 2a) and the horizontal stress (Figure 2b) are presented for the three initial horizontal-to-vertical stress ratios. A comparison of both figures shows that the horizontal stresses are low in the zone of larger vertical stresses. Or, in other words, the risk for weakening is larger. Note that introducing interfaces in the model between the seam and the surrounding layers most likely results in lower horizontal stresses, while stiffer roof layers could have the opposite effect. In Figure 3, a zoom-in on the vertical stresses for the first 5 m into the pillar are presented, and this for the 9 combinations, i.e., 3 stress ratios and 3 mining heights. These graphs also illustrate what was observed in the data of Table I. When the width of the relaxed zone is smaller, i.e., for smaller mining heights (Figure 3a), the stress peaks are larger and are more concentrated over a smaller area. Also, the opposite is true for wider relaxed zones (Figure 3c).

The previous simulations were for a relatively large pillar. In Table II, the same information is presented that was presented in Table I, but now three different pillar widths are modelled, i.e., 24 m, 14 m, and 6 m, with a mining height of 3 m. These data clearly show that the widths of the relaxed zones are mainly determined by the geometry of the excavation rather than the width of the pillar. The peak vertical stress

increases for smaller pillar widths, as the average stress is also larger. This influences the behaviour of the various pillars.

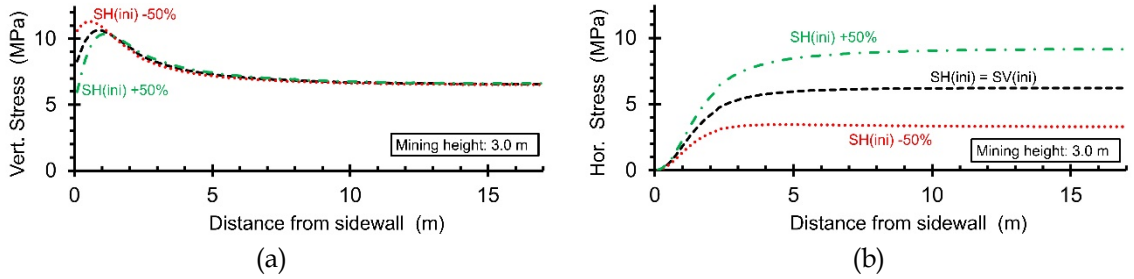


Figure 2. Stress redistribution in the pillar (at mid-height) in an elastic model for three different initial horizontal stresses (reference mining height of 3 m and pillar width of 34 m): (a) variation of the vertical stress, (b) variation of the horizontal stress.

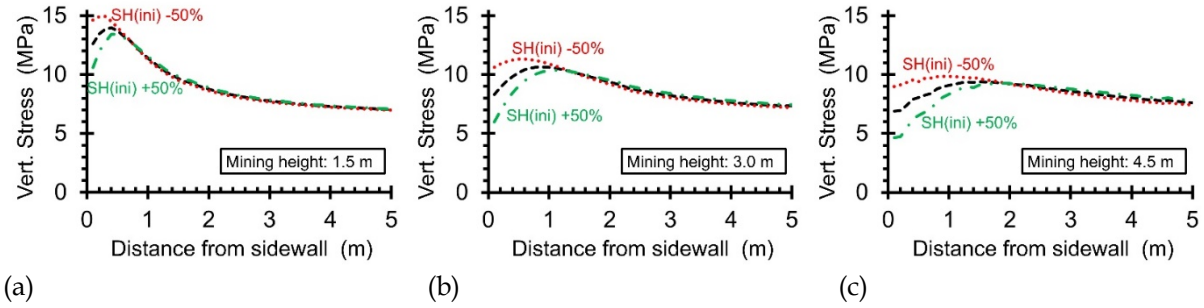


Figure 3. Variation of the vertical stress in an elastic model over the first 5 m into the pillar for three different initial horizontal stresses (pillar width of 34 m): (a) mining height of 1.5 m, (b) mining height of 3.0 m, (c) mining height of 4.5 m.

Table II: Data for the peak stresses for different pillar widths in an elastic model for three different initial horizontal stresses (mining height of 3.0 m), i.e., the peak vertical stress, the corresponding horizontal stress, and the distance of the peak to the sidewall

	SH(ini) -50%	SH(ini) =SV(ini)	SH(ini) +50%
IIa. 24 m pillar width			
SYY-peak (MPa)	11.44	10.80	10.54
SXX at peak (MPa)	0.59	1.54	2.69
Distance from wall (m)	0.6	0.9	1.1
IIb. 14 m pillar width			
SYY-peak (MPa)	11.86	11.30	11.08
SXX at peak (MPa)	0.61	1.58	2.70
Distance from wall (m)	0.6	0.9	1.1
IIc. 6 m pillar width			
SYY-peak (MPa)	13.84	13.58	13.54
SXX at peak (MPa)	0.71	1.36	2.53
Distance from wall (m)	0.6	0.8	1.0

In conclusion, the local stress redistribution around the excavation in a bord and pillar working shows a zone of stress relaxation in the outer part of the pillar. And this zone is larger for a higher initial horizontal-to-vertical stress ratio, and for larger pillar heights. For the various cases modelled, the vertical stress peak can be situated up to nearly 2 m into the pillar, i.e., for an initial stress ratio of 1.5 and a mining height of 3 m. This wide relaxed zone occurs for a linear elastic behaviour of the pillar.

The width of the relaxed zone, defined by the distance between the sidewall and the vertical stress peak, is not really affected by the width of the pillar, even over large intervals, i.e., from 6 m to 34 m. In other words, the stress redistribution around the excavations is mainly influenced by the geometry of the rooms or bords. The impact of the width of the relaxed zone is not directly integrated in the current design formula, nor is the impact of the initial horizontal-to-vertical stress ratio.

Elasto-plastic simulations based on a Mohr-Coulomb constitutive model
In earlier research (Vervoort, 1992a and c), a finite difference continuum model was calibrated using data of in situ fracture depths in coal pillars (Madden, 1989). The in situ fracture depths were compared to the width of the zone with plastic deformation. A good correlation was observed for a Mohr-Coulomb criterium with cohesion values between 1.5 and 4.5 MPa, a friction angle of 27°, and a tensile strength of 0.5 MPa. The maximum in situ depths of fracturing observed for the three case studies varied between 1.5 and 2.6 m (Vervoort, 1992a). In the current model, the same friction angle and tensile strength are chosen, and the cohesion was taken equal to 1.5 MPa. As will be shown below, these values give satisfactory results for the zone of plastic deformation. The mesh and other input characteristics are the same as for the elastic model. Note that for many panels, i.e., at shallow depths, no damage is induced due to the stress redistribution and elastic simulations well present the pillar behaviour.

For the reference case, i.e., a mining height of 3 m and a pillar width of 34 m, the vertical and horizontal stress redistributions through half of the pillar at mid-height are presented in Figure 4 for the simulations with elasto-plastic behaviour. In comparison to the elastic simulations (Figure 2), the peak has moved further into the pillar, enlarging the zone of stress relaxation, due to the plastic deformation. The largest increase is observed for the low initial horizontal-to-vertical stress ratio, i.e., an increase from 0.6 m to 1.9 m. For the three ratios, the ratio of 0.5 results in the largest distance between the peak and the sidewall. This was the opposite for the elastic simulations, where the ratio of 1.5 resulted in the largest distance, i.e., 1.1 m. However, the vertical peak stress remains largest for the small initial stress ratio. The peak of the vertical stress is situated just beyond the plastic deformation zone. Another significant difference between the curves for the elasto-plastic simulations in comparison to the elastic behaviour is that due to the plastic deformation the vertical and horizontal stresses are lower. Note that a perfect linear elasto-plastic constitutive model is applied. Over a width of 1 m, the horizontal stresses are nearly zero (Figure 4b). For an initial stress ratio of 0.5, a maximum is also observed in the graph of the horizontal stress. For the conditions and geometry of the model, it is clear that there is failure in part of the pillar, but, on the other hand, there is a very large portion of this 34 m wide pillar that is still fully in the elastic domain. The distance between the vertical stress peak and the sidewall is for the elasto-plastic simulations larger than for the elastic simulations, which is logical. However, the increase of this distance remains relatively small for this geometry, i.e., between 0.5 m (from 1.1m to 1.6 m for a stress ratio of 1.5) and 1.3 m (from 0.6 m to 1.9 m for a stress ratio of 0.5). The reason for it is that the elastic stress redistribution around the excavation leads to a non-negligeable width for the zone of stress relaxation.

In Figure 5, the vertical stress distributions for three different pillar widths are presented, i.e., for widths of 24 m, 14 m, and 6 m. All other parameters are the same. Except for a 6 m wide pillar, the location of the vertical stress peak is situated at 1.6 m to 1.9 m from the sidewall (Figure 4a and Figures 5a and 5b). For a 6 m wide pillar the maximum stress is situated in the central part of the pillar, confirming earlier simulations (Vervoort, 1992a). For this configuration the variation of the horizontal stresses is similar to the one of the vertical stresses. This is the direct consequence of the constitutive model applied and the plastic flow. Note that for the elastic simulations of a 6 m wide pillar (Table IIc), the vertical stress peak is situated at a distance between 0.6 m (initial stress ratio of 0.5) and 1.0 m (initial stress ratio of 1.5).

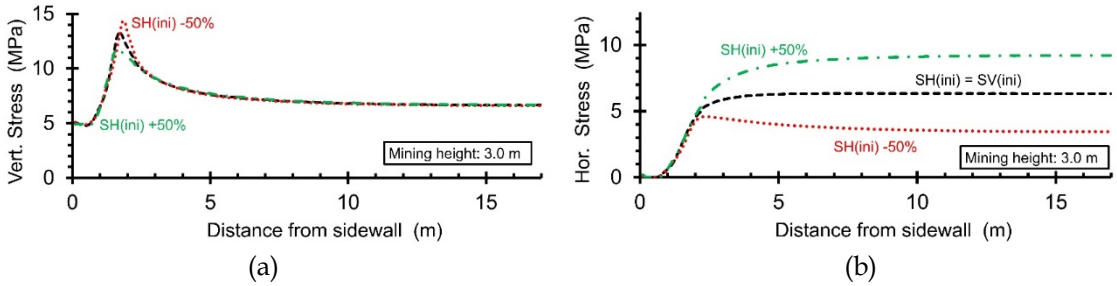


Figure 4. Stress redistribution in the pillar (at mid-height) in an elasto-plastic model for three different initial horizontal stresses (reference mining height of 3 m and pillar width of 34 m): (a) variation of the vertical stress, (b) variation of the horizontal stress.

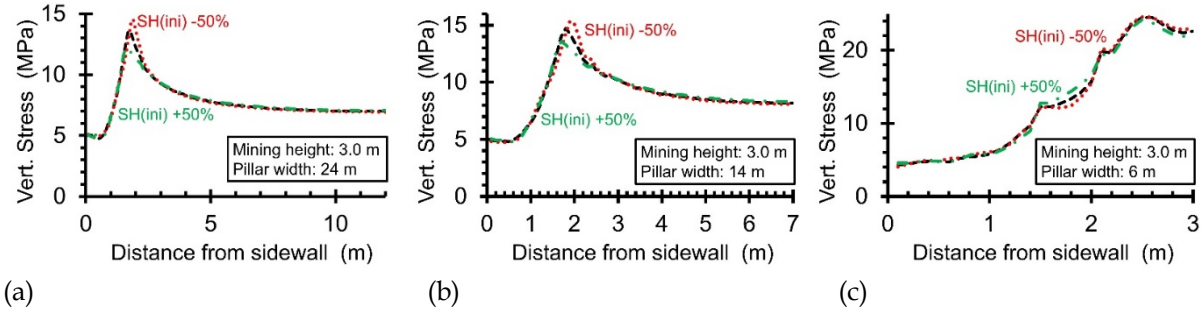


Figure 5. Variation of the vertical stress in the pillar (at mid-height) in an elasto-plastic model for three different initial horizontal stresses (mining height of 3.0 m): (a) pillar width of 24 m, (b) pillar width of 14 m, (c) pillar width of 6 m.

In conclusion, for a geometry in which the stresses in an elastic model close to the sidewall are situated above the failure criterion, plastic deformation occurs in an elasto-plastic model. Due to the plastic deformation, there is a further relaxation, resulting in larger stresses inside the pillar and resulting in larger peak stresses. In comparison to the elastic results, the additional growth of the stress relaxation zone is relatively small. Except for extremely small pillars, the zones of plastic deformation are not enlarged much when the widths of the pillars are decreased. So, although the average vertical pillar stresses and the vertical stress peaks are larger, the stress remains in a large portion of the pillars below the failure criterion.

In situ pillar behaviour vs. uniaxial compression

When discussing pillar behaviour, an association is often made with the uniaxial compression tests. A specimen free of any stress is loaded in one direction until failure occurs. If classic UCS-tests are conducted on core specimens, the axial stresses are clearly the major principal stress and, apart from the influence zone in the vicinity of the platens, the other stress components are zero or very small. Therefore, the classic UCS-tests are not a good representation or proxy for the behaviour of pillars, i.e., for pillars with a width equal or larger than its height (Mark, 2007; Mark and Barton, 1996). However, UCS values of different types of rock can be useful to compare in general the strengths of rock specimens. As an alternative, researchers study specimens with shapes more like the shapes of in situ pillars. The shape effect, like the size effect, is well known, and it has been well investigated from the early days of rock mechanical studies. However, for these specimens, the tests also start from specimens that are free of any stress.

In Figure 6, stress paths are presented for various elements in the elastic model along the horizontal plane at mid-height. The information is for the reference case of a 3 m high and a 34 m wide pillar. The stress paths are presented for the three different initial stress ratios. (See Figure 2.) The results for the initial isotropic stress state are presented in Figure 6b, while the other two sub-figures, i.e., Figures 6a

and 6c, contain the results for the two initial anisotropic stress states. Since the data are for the mid-height plane, the vertical and horizontal normal stresses that are calculated are principal stresses. For a horizontal-to-vertical stress ratio of 0.5 and 1.0, the vertical principal stress is for all elements the major principal stress (and the horizontal principal stress is the minor principal stress). For a ratio of 1.5, the initial horizontal stress is the major principal stress, but the horizontal stress component evolves towards the minor principal stress for some elements. The stress path that corresponds to the stress of the vertical peak is plotted using a ticker line. Not all elements along the central plane are represented, but a selection has been made to the left and to the right of the peak stress, so that one gets a good overall picture without overloading the graphs.

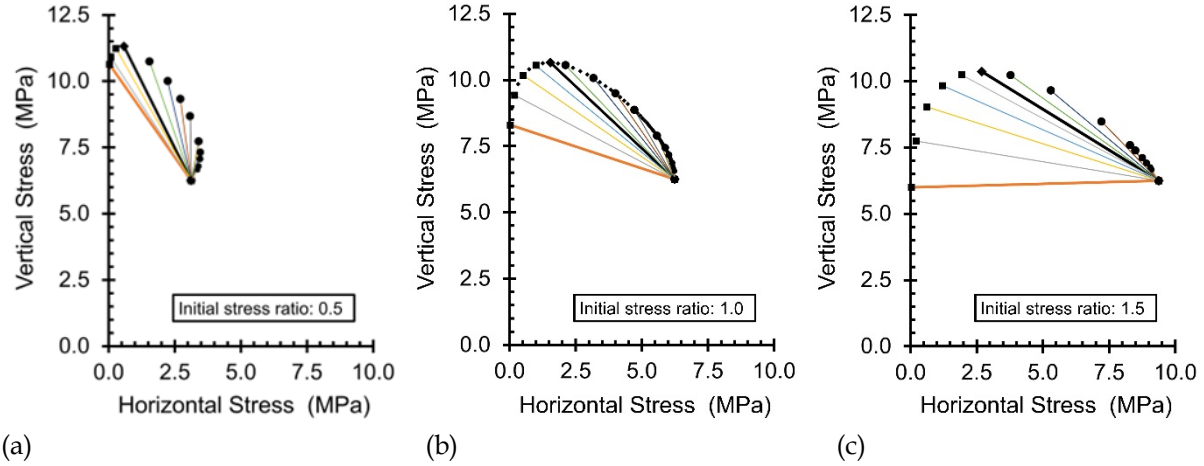


Figure 6. Stress paths in the elastic model along the horizontal plane at mid-height (reference case of a 3 m heigh and a 34 m wide pillar) and for initial horizontal-to-vertical stress ratio of: (a) 0.5, (b) 1.0, (c) 1.5.

As in a real in situ pillar, the starting points of the stress paths for all elements are the homogeneous stress states. The end points correspond to the calculated stress redistribution in the elastic model. In the central part of the pillar, the horizontal stresses do not change a lot. For the initial stress ratio of 0.5, there is a small increase of the horizontal stress. For the ratios of 1.0 and 1.5, there are small decreases. The vertical stresses in the central part increase slightly. Therefore, it is more important to look at the stress paths around the vertical stress peak and close to the sidewall, i.e., the thick black line in the graphs and the points to the left of it, respectively. For the stress paths corresponding to the vertical stress peaks, the vertical stresses logically increase, but there is a significant decrease in the horizontal stress. (See Table Ib for the specific values.) For the stress paths that correspond to the elements that are situated to the left of the stress peak (towards the sidewall), the horizontal stresses decrease significantly following the excavation. For the elements that are adjacent to the sidewall, the final horizontal stresses are zero. When the initial stress state is isotropic, some elements undergo only a small increase in the vertical stress. When the initial horizontal-to-vertical stress ratio is equal to 1.5, even a decrease in the vertical stress is observed adjacent to the sidewall.

The conclusion is that stress paths that occur in uniaxial compression tests do not occur in the pillars during the excavation of the bords or rooms around the pillars. The importance of the stress paths on the failure criteria was discussed in recent research (Vervoort, 2023, 2024). The starting point of the research was the difference between classic laboratory experiments and in situ stress paths. The micro-fracturing that occurs when loading rock (from zero stress or a low stress state) until failure is different from the micro-fracturing that occurs when unloading rock (from the in situ stress state) until failure. Due to this difference in weakening processes, the failure envelopes are significantly different.

In this regard, it is interesting to have a new look at the in situ experiments conducted in South Africa around 1970 (Bieniawski and van Heerden, 1975; Galvin, 2015; Wagner, 1974, 1980). There is no disputing that it was an enormous effort conducting these in situ tests, but more importantly that they provided a tremendous insight concerning in situ coal pillars and a better understanding of their

behaviour. The impact of these tests on the knowledge of pillars cannot be over-estimated. A brief description of the tests (Wagner 1974, 1980): first a narrow corridor was excavated around the to-be-tested pillars (with a horizontal square section of 1 m²); second, a horizontal slot was cut at mid-height in which 5x5 hydraulic cells were placed; and third, the test pillars were loaded in uniform increments of displacement and the required pressures were recorded. This resulted in an average load – displacement curve per test pillar, and data on the variation of the load in each hydraulic cell. More details are available in the publications mentioned above.

Referring to the earlier discussion of the different stress paths between compression tests and the pillar behaviour during the excavation of the rooms, the in situ compression of test coal pillars also starts from a zero-stress state. Hence, the variation of the vertical stresses along the central horizontal slot is different from the variation due to the stress redistribution following the excavation. In Figure 7 the vertical stress is presented along a line in the middle of the pillar, i.e., for a series of five hydraulic cells. These graphs are based on the published results of the in situ tests (Wagner 1974, 1980). The reason for limiting Figure 7 to five hydraulic cells is that it facilitates the comparison with the results of the 2D models. Note that each cell represents a width of 20 cm, or a fifth of the test pillar width. Figure 7a represents the data for the point on the curve with an average load, which is significantly lower than the average peak load of 10.8 MPa. For this example, it is at 67% of the peak value, prior to reaching the peak in the curve. The section in Figure 7b is for the point just before reaching the peak, and the section in Figure 7c clearly is situated in the post-peak part of the average load vs the displacement curve. The average load for the latter point is 75% of the peak value.

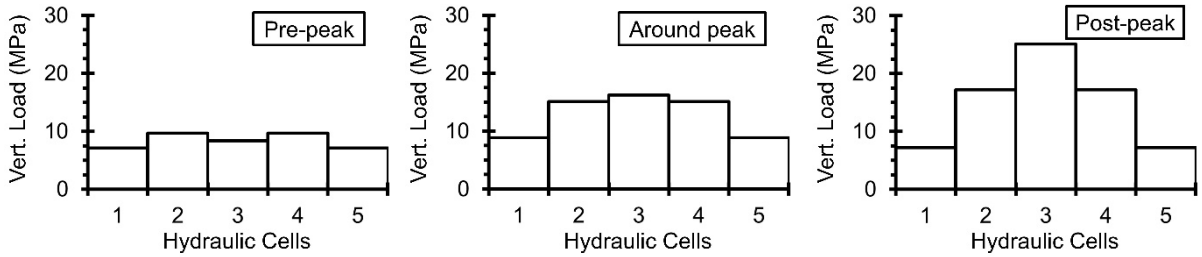


Figure 7. Variation of the vertical load along a line in the middle of the test pillar for a series of five hydraulic cells (based on published results by Wagner 1974, 1980): (a) pre-peak at 67% of the peak value, (b) at or around the peak value, (c) post-peak at 75% of the peak value.

The load distribution in Figure 7c, and to a lesser extent in Figure 7b, shows the influence of confinement on the larger load in the central cell(s). Note that the applied vertical displacements by all hydraulic cells are uniform. It is concluded that the central zone of the test pillar is capable of withstanding extremely high stress, even after failure of the pillar circumference (Galvin, 2015). For loading until about 70% of the average peak load (Figure 7a), the distribution of the load is still relatively uniform. The conclusion that the central zone is strong due to the confinement is without doubt correct. Note that this effect of the confinement is already observed 20 cm from the sidewall. For a real in situ pillar with a larger width than the 1 m wide test pillar, the impact of the confinement must be even larger. The question is whether this finding is relevant or useful in coal pillar design in bord and pillar panels without pillar extraction. First, it is not a good idea to design a pillar that is situated in the post-peak zone. In other applications, e.g., yielding pillars adjacent to a longwall panel, the aim could be to enter the post-peak zone, but in a basic coal bord and pillar panel one should stay away from the average peak strength. Second, and this argument is more relevant, the loading due to the stress redistribution following the mining of the bords or rooms is not uniform. To a certain extent, the stress redistribution is even the opposite of the strength variation determined by the uniform compression of a pillar. The stress redistribution is well illustrated in Figures 2 to 5. When no damage occurs around the sidewalls, there is a zone around the bord that is characterised by a stress relaxation, followed away from the sidewall by larger stresses around the vertical stress peak, and a large central zone with stress states far below the failure criterion. The reasons why there are low stresses around the sidewalls due to the stress

redistribution (Figures 2 to 4) are different from the reasons the strength variation is low along the circumference, i.e., due to the absence of confinement, but with the same vertical compression as in the rest of the test pillar (Figure 7c). When damage occurs around the sidewalls due to the stress redistribution, there is still a large central zone with stress states far below the failure criterion (Figures 4 and 5). The latter zone only disappears when the width of the pillar is very small (Figure 5c) and the entire pillar volume has failed (or, in the model terminology, has undergone plastic deformation).

DISCUSSION OF FINDINGS AND CONCLUSIONS

Numerical models or specifically designed experiments should aim at a single goal or several well-defined goals. The aim should be to get more insights or to gain a better understanding of the rock behaviour. The goal of this paper is to identify how the future design of coal bord and pillar workings can be improved, starting from the insights gained in the past. There is a saying that a numerical model should be made as simple as possible, but not simpler. In overly sophisticated models the focus is often lost. The models presented in this paper are relatively simple, i.e., they are 2D, a continuum is modelled, basic constitutive models are applied (elastic and perfect elasto-plastic), etc., etc. However, it is hoped that the results presented in the paper address the goal described above sufficiently.

In the past, statistical analyses of failed and stable pillars have led to a widely and successfully applied formula for the factor of safety of coal pillars (Salamon and Munro, 1967). The methodology which was applied can be seen as an AI-exercise *avant-la-lettre*, i.e., the data for real in situ behaviour of a large number of bord and pillar panels is used to determine the various coefficients in the strength formula. This requires our respect considering the tools available at that time. Looking at only two parameters (i.e., the height and width of the pillars) and three coefficients seems limited today when taking the current mathematical and computer power into account. As shown in the first part of this paper, the initial horizontal-to-vertical stress ratio is a parameter that has a significant effect on the stress redistribution and thus on the variation of loading along the horizontal central plane in a pillar. In more recent years, further fine-tuning of the Salamon and Munro formula has been implemented, taking for example local conditions into account (Bruwer and Stacey, 2023; Esterhuizen, 2000; Madden, 1989; van der Merwe, 1993). As the value of the coefficients in a statistical strength formula are based on the final criteria safe vs. unstable pillars, such formulas have the advantage that unknown characteristics or conditions are indirectly part of the statistical analysis and thus are indirectly integrated into the formulas. On the other hand, not knowing them is a disadvantage, e.g., if one would like to apply the formula in different environments. Looking at the main theme of the conference, i.e., "Pioneering progress: the future of rock engineering", one could ask the question if further fine-tuning the original statistical formula by Salamon and Munro is the most appropriate way of looking at the future and at the safe design of bord and pillar workings.

This thought leads to the question concerning how the strength of a coal pillar should be defined. And this question goes beyond the choice to raise the mining height to a power of -0.66 or -0.75. The results and discussion presented earlier show a significant and relevant discrepancy between the stress redistribution during the development of bord and pillar panels and the stress variation within test specimens, being lab specimens or underground test pillars, during uniaxial compression tests. Note that the stress variations in test specimens are strongly dependent on the moment within the full loading experiment. However, the observed discrepancy leads to the question concerning whether there are better ways to approach the safety issue of pillars and focusing less on uniaxial compression tests. In a simplified way, one can describe the variation of the vertical stress in a real pillar as: (i) being low at the sides (due to the zone of stress relaxation in the elastic domain and due to a possible damage zone), (ii) the stress peak, and (iii) a large central zone with relatively constant and slightly increased vertical stresses. In bord and pillar panels without pillar extraction, the stress redistribution is relatively symmetric. Note that during pillar extraction, the additional loading is asymmetric and changes significantly over time (Vervoort, 1992b). On the other hand, during uniaxial compression tests of wide lab specimens or of the in situ test pillars, the stress variation is as follows: (i) low stresses at the sides, due to the absence of confinement and the failure of the material and (ii) larger vertical stresses towards

the centre of the test specimens or the centre of the test pillars. The increase in vertical stresses is due to the effect of the confinement, i.e., more load is needed to compress the rock with the same displacement increments. How much larger the vertical stress is depends on the position along the stress–strain curves. This discussion leads to the question whether the integral of the area between both curves, i.e., the curve representing the stress redistribution and the curve representing the stress variation in a uniaxial compression test, could define another type of safety parameter? And, if so, which moment along the stress-strain curve should one take? The most logical moment, and consistent with good practice, should be the pre-peak value, e.g., at 70% of the peak stress.

Note that the horizontal stress variations inside real pillars vs. the variations in wide test specimens or test pillars also are different. In a large central zone of a real pillar, the horizontal stresses are relatively constant and are only slightly increased in comparison to the initial stress state due to the small increase in vertical stresses. On the other hand, in wide test specimens or test pillars the horizontal stresses increase systematically towards the centre due to the confinement effect.

In summary, one could say that the large discrepancy in stress variations between mined pillars and tests specimens or test pillars is caused by the fact that ***one does not build a pillar, but one excavates a room***. And this should be combined with the fact that strength is a non-intrinsic parameter, meaning that it is a function of a large number of parameters and conditions, among others the stress state. In other words, the strength of each volume element in a pillar is as different as the stress state is different. Integrating this essential fact into a simple formula is impossible. Probably the only way to address this is that the full failure curve is determined and used, instead of only the UCS value, and that extensive numerical modelling of real underground cases are conducted. Again, referring to the main theme of the conference, i.e., "Pioneering progress: the future of rock engineering", this should become realistic in the (near) future, and the combination with new geotechnical AI-methodologies currently being developed should facilitate it.

REFERENCES

Aydan, O. and Kawamoto, T. (1997). The general characteristics of the stress state in the various parts of the earth's crust. *Proceedings of International Symposium Rock Stress*, Kumamoto, Japan, K. Sugawara and Y. Obara (eds), A.A. Balkema: Rotterdam, pp. 369–73.

Bieniawski, Z.T. and van Heerden, W. L. (1975). The Significance of In-situ Tests on Large Rock Specimens. *Int. J. Rock Mech. & Min. Sci.*, 12 (4), 101–113. https://doi.org/10.1016/0148-9062(75)90004-2

Bieniawski, Z.T. (1981). Improved Design of Coal Pillars for U.S. Mining Conditions. *Proceedings of 1st Conference on Ground Control in Mining*, Morgantown, WV, pp. 13-22.

Bruwer, F.J.N. and Stacey, T.R. (2023). A proposed method for optimizing coal pillar design using coalfield-specific uniaxial compressive strength. *J. of SAIMM*, 123 (5), 275–286. http://dx.doi.org/10.17159/2411-9717/2063/2023

Chaurasia, A., Walton, G., Sinha, S., Batchler, T.J., Moore, K., Vlachopoulos, N. and Forbes, B. (2025). Large-scale laboratory investigation of pillar-support interaction. *J. of Rock Mech. Geotechn. Eng.*, 17 (1), 71-93. https://doi.org/10.1016/j.jrmge.2024.04.008

Doroudgar, A. and Noferesti, H. (2024). Identifying the prone zones to initiation of unstable failure by numerical simulation of mining pillars under compression. *J. of SAIMM*, 124 (11), 661–672. http://dx.doi.org/10.17159/2411-9717/2265/2024

Esterhuizen, G. (2000). Jointing effects on pillar strength. *Proceedings of 19th Conference on Ground Control in Mining*, Morgantown, WV, Peng, S.S. and Mark, C. (eds), West Virginia University.

Galvin, J. (2010). The Unsw Pillar Design Methodology and Considerations for Using This and Other Empirical Pillar System Design Approaches. *Proceedings of 3rd ICGCM Pillar Design Workshop*, Morgantown, WV, pp. 22–32.

Galvin, J. (2015). Notable Contributions by Horst Wagner to Developing Safe Pillar Systems in Mining. *Berg Huettenmaenn Monatsh*, 160, 163–174. https://doi.org/10.1007/s00501-015-0341-x

Guner, D., Sherizadeh, T., Nowak, S., Karadeniz, K.E. and Sunkpal, M. (2023). Distinct Element Analysis for the Effectiveness of Preliminary Coal Pillar Rib Support Systems Based on the Strength Reduction Method Using Coal Mass Constitutive Model. *Min. Met. & Expl.*, 40, 1535–1546. https://doi.org/10.1007/s42461-023-00815-0

Huang, P., Zhang, Q., Xie, J., Li, J., Zhang, Q., Li, M. and Simao, F.C. (2024), Multiscale study on coal pillar strength and rational size under variable width working face. *Front. Environ. Sci.*, 12, 1338642. https://doi.org/10.3389/fenvs.2024.1338642

Madden, B. (1989). Squat pillar design in South African collieries. *Proceedings of SANGORM Symposium Advances in Rock Mechanics in Underground Coal Mining*, Witbank, RSA, September 12th 1989, pp. 83–90.

Mark, C. and Barton, T.M. (1996). The Uniaxial Compressive Strength of Coal: Should it be used to Design Pillars? *Proceedings of 15th International Conference on Ground Control in Mining*, Golden, CO, August 13-15 1996, pp. 61–78.

Mark, C. (2007). The Evolution of Intelligent Coal Pillar Design: 1981-2006. *Proceedings of 25th International Conference on Ground Control in Mining*, Morgantown, WV, 10p.

Salamon, M.D.G. and Munro, A.H. (1967). A study of the strength of coal pillars. *J. of SAIMM*, 68, 56–67.

Sheorey, P.R., Das, M.N., Barat, D., Prasad, R.K. and Singh, B. (1987). Coal Pillar Strength Estimation from Failed and Stable Cases. *Int. J. Rock Mech. Min. Sci & Geomech. Abstr.*, 24 (6), 347-355. https://doi.org/10.1016/0148-9062(87)92256-X

van der Merwe, J.N. (1993). Revised Strength Factor for Coal in the Vaal Basin. *J. of SAIMM*, 93 (3), 71-77.

van der Merwe, J.N. (2006). Beyond Coalbrook: Critical Review of Coal Strata Control Developments in South Africa, *Proceedings of 25th International Conference on Ground Control in Mining*, Morgantown, WV, pp. 335–346.

Vervoort, A. (1992a). Non-elastic simulations of coal pillar behaviour. *Transact. IMM, Sect. A, Min. Ind.*, 101 (1), A23-A28.

Vervoort, A. (1992b). Sidewall fracturing in coal room and pillar, and pillar extraction panels. *Proceedings of the 11th international conference on Ground Control in Mining*, Wollongong, Australia, July 1992, pp. 58–65.

Vervoort, A. (1992c). Monitoring and simulation of sidewall fracturing in coal mines. *Proceedings of the International Conference EUROCK'92*, Chester, U.K., September 14-17 1992, 6p.

Vervoort, A. (2023) Different Stress Paths Lead to Different Failure Envelopes: Impact on Rock Characterisation and Design. *Appl. Sci.*, 13, 11301. https://doi.org/10.3390/app132011301

Vervoort, A. (2024). In Situ Stress Paths Applied in Rock Strength Characterisation Result in a More Correct and Sustainable Design. *Sustainability*, 16, 4711. https://doi.org/10.3390/su16114711

Vlachogiannis, I. and Benardos, A. (2024). Proposed formulas for pillar stress estimation in a regular room-and-pillar pattern. *Int. J. Rock Mech. & Min. Sci.*, 180, 105826. https://doi.org/10.1016/j.ijrmms.2024.105826

Wagner, H. (1974). Determination of the complete load-deformation characteristics of coal pillars. *Proceedings of 3rd International Congress on Rock Mechanics*, ISRM, Denver, CO, vol. 2B, pp. 1076–1082.

Wagner, H. (1980). Pillar Design in Coal Mines. *J. of SAIMM*, 80 (1), 37–45.

Wagner, H. and Madden, B. (1984). Fifteen Years Experience with the Design of Coal Pillars in Shallow South African Collieries. *Proceedings of Symposium Design and Performance of Underground Excavations*, ISRM, Cambridge, U.K., pp. 391–399.

Wu, Y., Tang, Y., Xie, P., Hu, B., Lang, D. and Wang, H. (2024). Stability analysis of 'roof-coal pillar' structure in longwall multi-section mining of steeply dipping coal seam. *Geomatics, Natural Hazards and Risk*, 15 (1), 2359998. https://doi.org/10.1080/19475705.2024.2359998

York, G. and Canbulat, I. (1998). The scale effect, critical rock mass strength and pillar system design. *J. of SAIMM*, 98 (1), 23–37. http://dx.doi.org/0038-223X/3.00/0.00

Zang, A. and Stephansson, O. (2010). *Stress Field of the Earth's Crust*. Publisher Springer Dordrecht, 324p. https://doi.org/10.1007/978-1-4020-8444-7



Andre Vervoort

Professor
University of Leuven

Prof. Andre Vervoort is a mining engineer and obtained his Ph.D. in 1987 at FPMs, Belgium for a study of roof behaviour in coal longwalls. From 1988 to 1992 he was a researcher at COMRO, South Africa and was mainly involved in ground control studies for the South African coal mines. Since 1992 he is a professor at the University of Leuven, Belgium. His academic teaching duties include courses in rock mechanics, geostatistics, mining methods and aspects of sustainable development. The emphasis of his research is on rock mechanics. He has published about 250 technical papers.

Back analysis of ore pass design at Big Gossan sublevel open stope mine, Indonesia

A. Sjadat[1], J.P.E. Hamman[1], Y. Irab[1], D. Putra[1], W. De Beer[2], I. Haque[3]

[1]PT Freeport Indonesia, Indonesia
[2]ESG Solutions, Australia
[3]Freeport-McMoRan Inc., USA

The Big Gossan sub level open stope mine is part of the Grasberg mining complex at PT Freeport Indonesia that consists of two active cave mines and one cave mine being developed. Access ramps, ore passes, and other infrastructure excavations are planned outside the influence of mining-induced stress around the stopes. The mine design is planned to consist of 23 production levels with nine ore passes. Most ore passes are planned to last for a life-of-mine. In 2022, ore pass 7 (OP 7) lasted only three years before it experienced rock burst damage and stress-related spalling that caused it to be shut down for geotechnical evaluation. A geotechnical assessment was conducted to determine the cause of the elevated stress and seismicity. The assessment included stress measurement, seismic analysis, 3D modelling, geotechnical drilling and numerous observations in and around OP 7. Detail stress analysis also included the evaluation of core discing associated with high stresses as well as the depth of failure in OP 7. During this study, it became clear that a localised elevated stress field associated with a shear zone was present in the vicinity of OP 7. This paper briefly describes the various geotechnical methods used to determine stress orientation and magnitude based on observations and measurements. The design process of a new ore pass system (OP 8) is also discussed.

INTRODUCTION

The Big Gossan (BG) mine is owned by PT Freeport Indonesia (PTFI), located in the Grasberg minerals district of Papua Indonesia (Figure 1). The BG mine uses a sublevel open stope mining method that started development in 2005 and production in 2010. The orebody is vertical, approximately 40 m wide, 1500 m on strike 400 m in depth. The mining method consists of 15 m wide, 40 m high and 40 m long transverse stopes that use cemented paste fill. Stoping is divided into two regions separated by a 20 m wide sill pillar. The BG mine produces approximately 7000 tpd (Casten *et al.,* 2020).

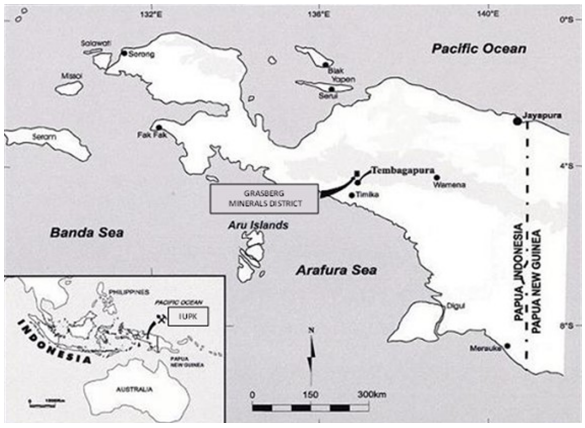


Figure 1. PTFI Grasberg minerals district in Papua, Indonesia.

Ore is transported via ore passes, which are located at the southern footprint of the mine or near the access drifts of each stoping level. OP 7 was constructed in 2019, and after three years, was shut down due to stress-related spalling and rockburst-like damage. OP 7 circular raise was originally 3.6 m diameter in design encompassing from the 3020 m level to the 2540 m level, with cut outs in the 2860 and 2560 m levels.

As illustrated in Figure 2, a survey scan of the overbreak is conducted with comparison to the original design. The overbreak begins and intersects the finger raise in the 2600 m level, carrying down to the 2540 m level. The maximum overbreak is in the 2560 m level and the scaled-out dimension is 8 m by 5 m in diameter.



Figure 2. OP 7 overbreak condition in (A) finger raise, (B) finger raise and OP 7, (C) 2560 m level, and (D) 2540 m level.

GEOLOGY

The BG deposit is tabular in shape and steeply dipping towards the northeast. It is composed of calcium-magnesium silicate skarn. The local geological units are comprised of sedimentary strata metamorphosed of different alteration processes such as skarns, hornfels, and marble. A minor portion of the footprint is characterised by intrusives (PTFI, 2022).

The geological units of OP 7 is predominantly sedimentary strata of the Ekmai formation and a minor seam of diorites of the Tertiary Ertsberg formation, which is a sub-vertical dyke characterised by stockwork or sheeted veins of anhydrite-quartz with local skarn alteration. The Kembelangan Cretaceous Formation (Kke) includes two local members. Kkes is a sandstone member containing fine to medium grained silicified quartz sandstone with weakening of skarn alteration. Kkel is a limestone member comprised primarily of hornfelsic altered limestone and fossiliferous.

Structurally, OP 7 is surrounded by the Shear Zone (SZ), further embedded into Shear Zone 1 (SZ1) and near Shear Zone 2 (SZ2) as shown in Figure 3. The SZ is located at the footwall domain of the ore body steeply dipping and may range between 5 to 80 m. It is rehealed by overprinting the skarn alteration and intrusive diorite. Slabbing is prominent when excavations are advanced parallel to the SZ, given its intense shear structure.

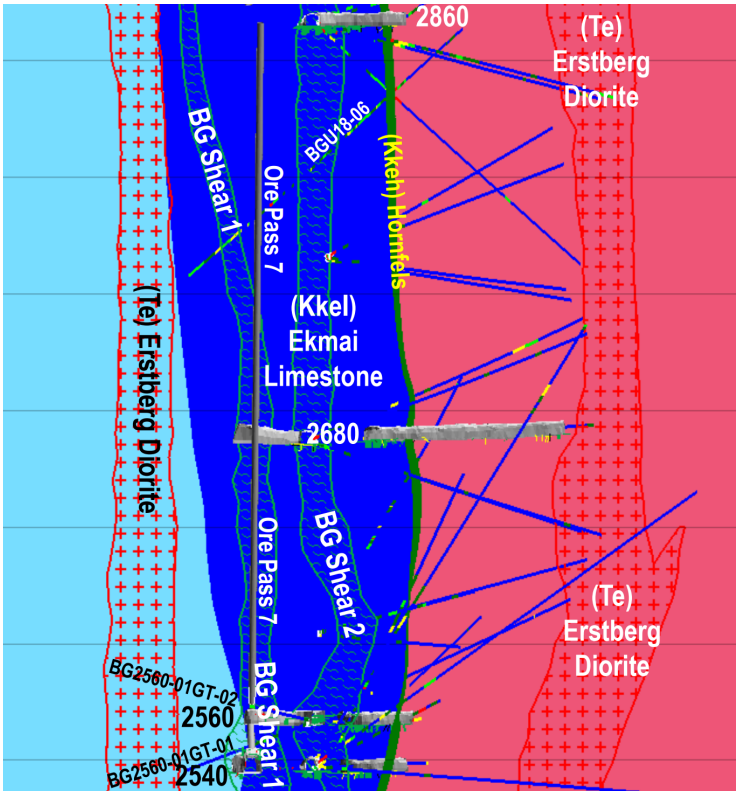


Figure 3. Section view of OP 7 showing lithological and structural contacts.

MECHANICAL PROPERTIES

For numerical and empirical analyses of the surrounding OP 7 rock mass, the existing data of the geotechnical mechanical properties available is insufficient due to the lack of sample sizes in geotechnical domains of interest. We carried out additional drilling with laboratory testing to further assess the confidence of the mechanical properties of each geotechnical domain following the Hoek-Brown criterion (2018). Point load, uniaxial compressive strength (UCS), Young's modulus, Poisson's ratio, and Brazilian tensile strength (BTS) were the parameters for evaluating and concluding the Hoek-Brown criterion.

Point Load Testing

Point load testing is standardised and performed typically every 15 m for each drill hole in the BG mine. Due to the lack of UCS sample data available for a few geotechnical domains, including the introduction of SZ1 and SZ2 domains which required characterisation, existing point load data was assessed to expand and increase the confidence of the database.

According to Bewick *et al.*, (2015), strength distribution of UCS through intact and combined failure types may both be a representative of the rock mass adhering to a coefficient of variance and sample size. Similarly, failure types of only intact and combined (or multiple) were evaluated of the point load data available.

As illustrated in Figure 4, it is not a true normal distribution of intact and multiple failure types. For the basis of this study, a normal distribution of the cumulative frequency between 15 to 30% is applicable. Therefore, Table I summarises the 25% frequency of point load data in addition to -1 standard deviation conservatively.

Applying International Society for Rock Mechanics and Rock Engineering (ISRM) (1985), the UCS may be estimated using a correlation factor. For this exercise on the point load data assessed, an estimated UCS of 150 MPa is justifiable given the strength distribution.

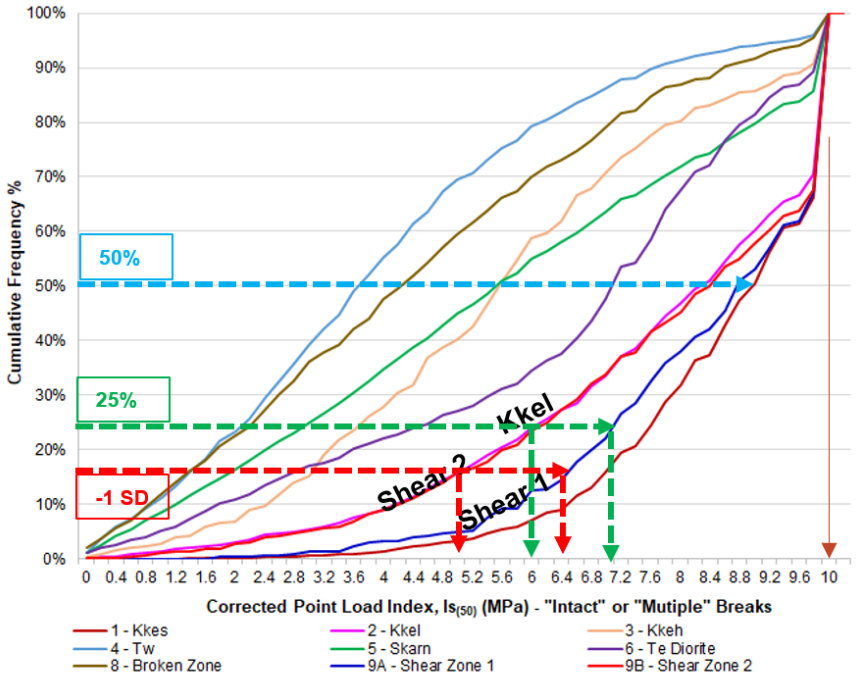


Figure 1. Cumulative distribution of point load data for SZ1, SZ2 and Kkel geotechnical domains.

Table I: Summary of point load testing

Geotechnical Domains	No. Samples (Intact + combined)	Corrected Point Load Index, Is(50) (MPa)			Is(50) * 24 = UCS estimate (MPa)		
		Percentile			Percentile		
		16% (-1SD)	25%	50%	16% (-1SD)	25%	50%
Kkel	2,138	5	6	8.2	120	144	197
Shear Zone 1	304	6.4	7	8.6	154	168	206
Shear Zone 2	2,204	5	6	8.2	120	144	197
Design UCS (MPa)	150						

Rock Mass Characterisation

A drilling program was conducted to collect samples surrounding the OP 7 for geotechnical laboratory testing separated by domain. The samples tested included UCS with Young's modulus and Poisson's ratio, triaxial strength, and tensile strength testing where applicable. Supporting the UCS assessment

on point load testing completed earlier, Table II summarises the laboratory testing results of one representative group data set with design parameters to be applied for numerical analyses:

Table II: Geotechnical mechanical properties

Geotechnical Domain	Mean UCS (MPa)	σ_{ci} (MPa)	E_i (GPa)	GSI	m_i	E_{rm} (GPa)	υ	m_b	s	a	Design UCS (MPa) $\pm$20%
SZ1, SZ2, Kkel	153	178	72	74	10.8	58	0.22	4.3	0.056	0.501	150

ANALYSIS

From the established rock mass parameters derived through existing data and additional laboratory testing, analysis of the OP 7 overbreak was performed to understand the cause and its failure mechanism. A boundary element method (BEM) elastic model was constructed to determine the induced stresses surrounding the OP 7 excavations. Following the results, stress fields and discing were studied and its relationship to tensile strength. Finally, a back analysis on ore pass design and seismicity was assessed to determine the implications on future designs.

Numerical Modelling

BEM was constructed using the Hoek-Brown criterion along with in situ stress parameters available. OP 7 is approximately 50 m from the nearest planned and existing stopes which is a sufficient blasting peak particle velocity distance. The nearby stopes and ore pass development was sequenced accordingly to understand the impact on change in stresses over the life of mine (LOM) .

Based on the model results (Figure 5), a far-field stress of 38 MPa was established (Table III), with an induced stress field of 60 MPa to 70 MPa. The induced stresses did not change over the sequence of the LOM. Model results conclude that the stresses are not high enough to induce overbreak or failure of OP 7.

Table III. Pre-mining stress and orientation at 2540 m level

σ_{Hmax}		σ_v		σ_{Hmin}	
Magnitude (MPa)	Orientation (Trend/Plunge)	Magnitude (MPa)	Orientation (Trend/Plunge)	Magnitude (MPa)	Orientation (Trend/Plunge)
38	359°/25°	19	160°/64°	18	181°/47°

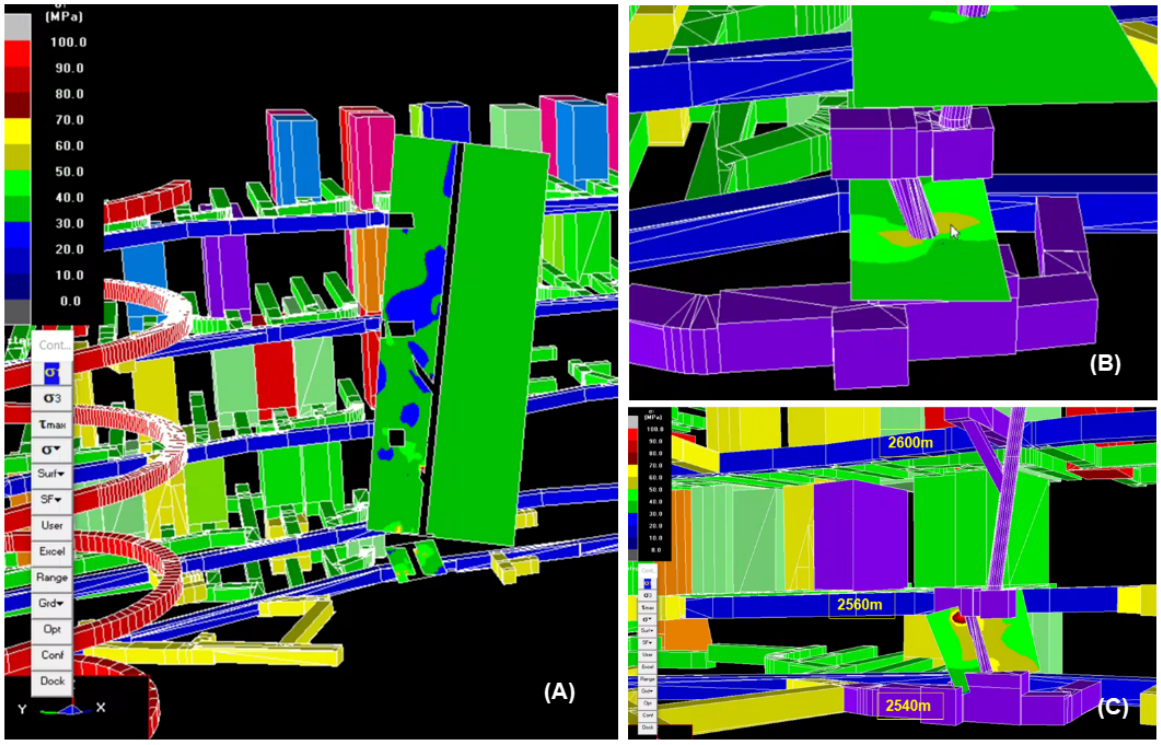


Figure 5. BEM results showing (A) oblique view of model extents, (B) horizontal $\boldsymbol{\sigma_1}$ section of OP 7, and (C) vertical $\boldsymbol{\sigma_1}$ section of OP 7.

Standoff distances are also modelled using a two-dimensional finite element model. The OP 7 location is approximately 50 m from stoping, which results in a zone of influence of 60 MPa (Figure 6).

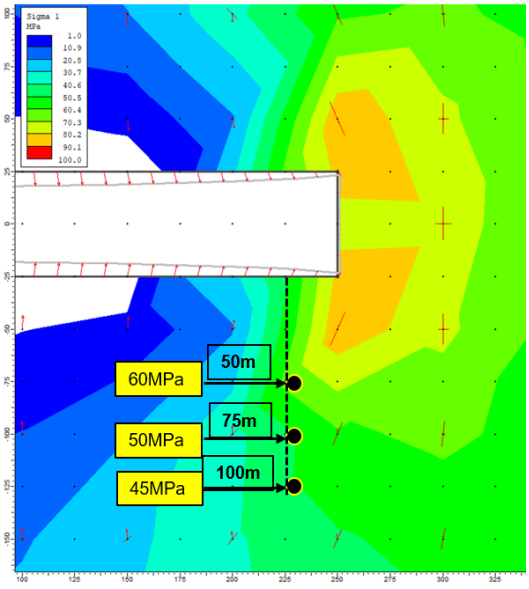


Figure 6. Zone of influence from OP 7 to stoping area.

Stress Field

As defined by Diedrichs (2007), spalling is the development of visible fractures under loading in hard rock or brittle excavations under high stress, creating rock damage and may be time-dependent. Spalling can occur when the maximum stress of the tunnel excavation surpasses 40% of the UCS (Hoek

and Marinos, 2009). Cai *et al.*, (2004) describes crack initiation to start 0.3 to 0.5 times the UCS and the crack initiation thresholds are further expanded to moderately and highly jointed rocks in terms of deviatoric stresses. To understand the OP 7 overbreak, a back analysis of the stress induced field is assessed to determine when spalling must initiate.

To compare the baseline of the projected induced stress and its spalling to the actual overbreak of OP 7, the maximum stress and depth of failure is calculated. The maximum stress, σ_{max}, or also defined as the tangential stress, is given by Equation 1, where σ_1 and σ_2 are the field in situ stresses and σ_c is the average UCS (Martin *et al.*, 1999). Depth of failure (d_f) established empirically by Martin *et al.*, (2001) is defined by the depth of failure normalised to the tunnel radius (a) given by Equation 2:

$$\sigma_{max} = 3\sigma_1 - \sigma_3 \quad [1]$$

$$\frac{d_f}{a} = 1.25\frac{\sigma_{max}}{\sigma_c} - 0.5 \pm 0.1 \quad [2]$$

Given that the original design diameter of the OP 7 is 3.6 m diameter (1.8 m radius) with a scaled distance of 0.9 m, $\frac{d_f}{a}$ is 0.5 m with σ_{max} of 165 MPa (σ_1 and σ_2 is approximately 60 MPa and 15 MPa based on results obtained from Figure 5 and Figure 6). Conversely, overbreak of an 8 m diameter OP 7 equates to a $\frac{d_f}{a}$ of 1.2 m. As illustrated in Figure 7, this would equate to a maximum stress of 266 MPa where σ_1 and σ_2 is approximately 90 MPa and 22 MPa, respectively. Therefore, mining-induced stress of 60 MPa could not be the result of such a large overbreak. Given the depth of failure, residual stress (i.e., 90 MPa) possibly from the SZ1 structure may be the cause of scaling.

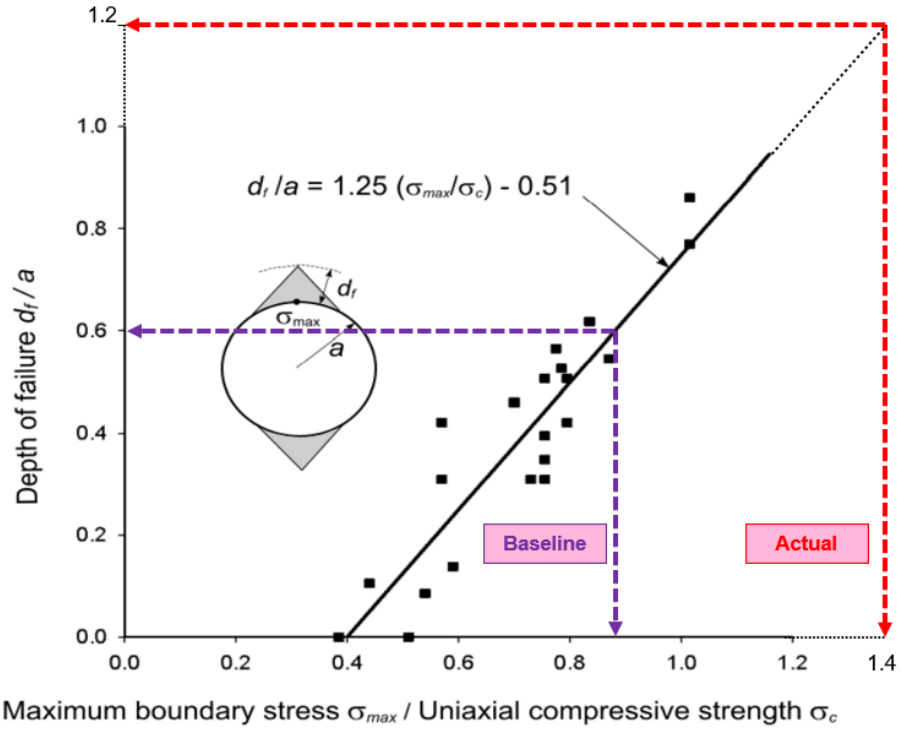


Figure 7. Depth of failure data modified after Hoek and Marinos (2009) comparing OP 7 baseline to actual damage.

Core Discing

Core discing, or the saddle-shaped disc introduced by Dyke (1989), indicates the direction of the maximum and intermediate principal stresses. As mentioned in the previous section, there is a possibility of residual stresses experienced in the OP 7, which can be investigated from core discing.

Core discing was observed from a nearby drillhole approximately 1.8 m from OP 7. Disc thickness varied from 10 mm to 25 mm, where partial discing was also noted. Given the location and condition of the core discing observed, the induced stresses can be back calculated to verify the stress environment.

Lim and Martin (2010) provided guidelines on the relationship of stress magnitude with core discing. The disc thickness t/D (where t is the core disc thickness and D is the diameter of the core) and stress condition σ_1/σ_t (where σ_1 is the maximum principal stress and σ_t is the BTS) are the parameters of study. Applying a tensile strength for OP 7 which is calculated from Kahraman *et al.,* (2012) using a UCS/BTS ratio of 19, the maximum principal stresses range from 130 MPa to 150 MPa due to the range of core dicing thickness.

Based on the calculated range of maximum principal stresses, kirsch equations are applied to verify the stress conditions of the 1.8 m observed core discing location from the OP 7. As shown in Figure 8, an 8 m diameter overbreak raise with a tangential stress influence on 90 MPa on the sidewall, results in a tangential stress of approximately 145 MPa. Therefore, core discing is indicative of a tangential stress of 130 MPa to 150 MPa at 1.8 m away from the 8 m diameter OP 7 location. The trend of the discing follows the SZ1 which may also associate residual stresses from the structure.

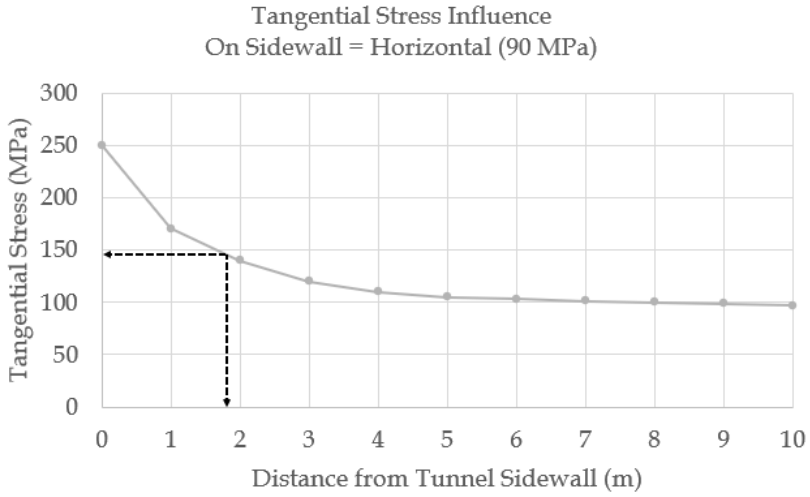


Figure 8. Kirsch equation on tangential stress for sidewall of 90 MPa.

Ore Pass Stability Assessment

Ore pass stability is verified through the McCracken and Stacey (1989) method. Both the wall and face of the 3.6 m diameter raise are deemed stable. It should be noted that the stress reduction factor used for this exercise was approximately 6, which is far lower than the anticipated residual stresses investigated.

Seismicity

Source mechanisms of significant events ($M_w \geq 0.7$) near the bottom of OP 7 and its relationship to the SZ1 was investigated. Although there are too few events to perform a stress inversion, there is a subset of failure planes with an average strike and dip of 300°/73°, which roughly aligns with the orientation of the SZ1 structure (N220°-325°E/45-90°). In addition, one σ_1 direction aligns with the in situ σ_1 inferred direction, albeit with uncertainty.

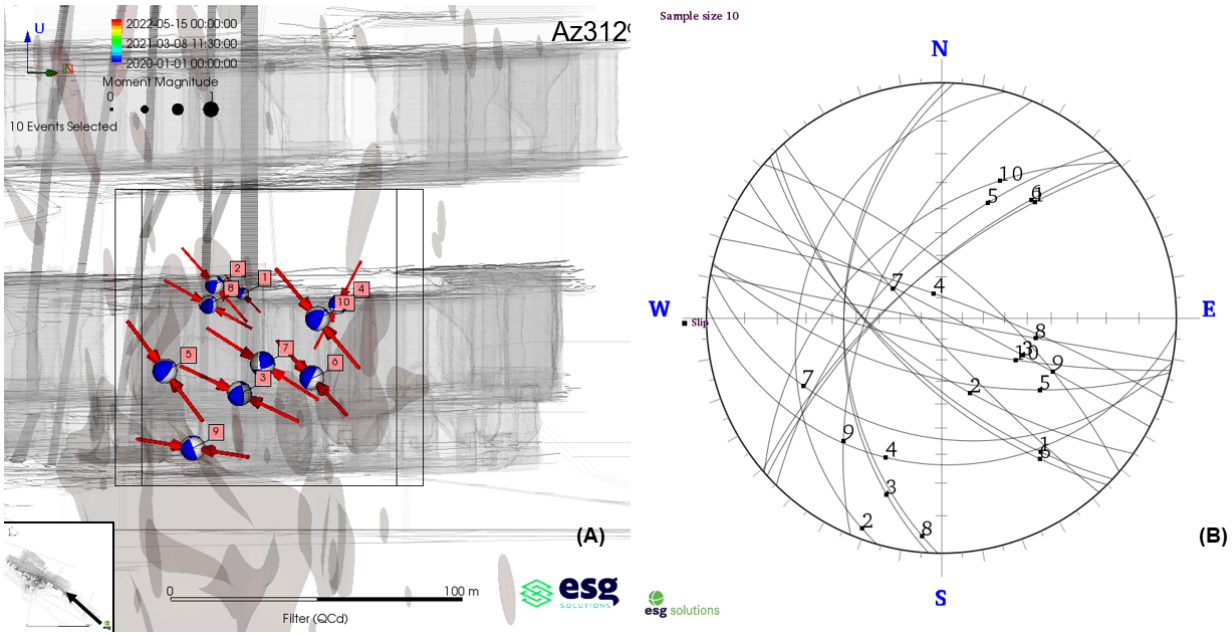


Figure11. (A) Significant events and (B) failure planes at OP 7.

DISCUSSION

OP 7 overbreak and scaled out condition cannot be linked to a single factor but conversely to a combination of attributes. Although induced stresses modelled between 60 to 70 MPa could start the scaling process or crack initiation, the size of the overbreak observed leads to much higher stresses from the back analysis. Residual stresses can be associated with the SZ1 and this is due to the discing observed near OP 7, as well as the seismicity moment tensors parallel to the SZ1 orientation. Furthermore, the high noise or seismicity observed at the bottom of the OP 7 indicates abrasion or impact damage to the ore pass due to operational tipping practices. Therefore, OP 7 scaling is due to mining induced stress, residual stress associated with SZ1, impact or abrasion damage due to tipping, and rockburst damage.

RECOMMENDATIONS

Based on the observations and findings in OP 7, the learnings can be applied to the OP 8 design. OP 8 is located at the far east of the BG mine footprint. It does not have a geotechnical environment similar to the OP 7 due to the location of the SZ1. However, the future mine plan of nearby stoping is not confirmed within close vicinity of OP 8 and this would be ideal for minimal production activities regarding induced stresses.

The recommendation on finalising the best location for OP 8 would be to assess and evaluate the ore pass stability, complete a 5-to-10-year stope plan on numerical model to assess the induced stresses, confirm lithological and structural boundaries, and to evaluate ore tipping procedures to minimise abrasion and impact to ore passes.

From the lessons learned, all future development is to avoid the SZ1 or SZ2 due to residual stresses, and to develop excavations ±20 m outside SZ1 and SZ2 boundaries in the Kkes or Te Diorite domains. Past ore passes developed in similar stress conditions outside the SZ did not result in overbreak except OP 7.

CONCLUSIONS

The back analysis completed for OP 7 at the BG mine indicates several contributing factors on its overbreak. Although mining-induced stresses of 60 to 70 MPa may have initiated the scaling process, the large overbreak suggests high stresses influenced by residual stresses associated with the SZ1. Observations of core discing, seismicity trends, and structural orientations support this hypothesis. Additionally, ore tipping practices likely contributed to further damage the ore pass through impact and abrasion mechanisms.

Lessons from OP 7 are instrumental in guiding the design for OP 8 and future development in the SZ1 and SZ2 domains. To ensure long-term stability, geotechnical assessments such as stress modelling, lithological and structural evaluations, and operational procedures such as ore tipping impact should be conducted. These findings value the importance of future ore pass design stability and longevity in the BG mine.

ACKNOWLEDGEMENTS

The authors wish to thank PT Freeport Indonesia for permission to publish this paper and for providing support. Thank you to the BG mine team and ESG Solutions for their contributions and for their recommendations.

REFERENCES

Bewick, R.P., Amann, F., Kaiser, P.K. and Martin, C.D. (2015). Interpretation of UCS Test Results for Engineering Design. *13th ISRM International Congress of Rock Mechanics*.

Cai, M., Kaiser, P.K., Tasaka, Y., Maejima, T., Morioka, H. and Minami, M. (2004). Generalized crack initiation and crack damage stress thresholds of brittle rock masses near underground excavations. *International Journal of Rock Mechanics and Mining Sciences*, 41(5), pp.833–847. doi:https://doi.org/10.1016/j.ijrmms.2004.02.001.

Casten, T., Johnson, M., Zimmer, C. and Mahayasa, M. (2020). PT Freeport Indonesia – The transition to underground production. *MassMin 2020: Proceedings of the Eighth International Conference & Exhibition on Mass Mining*. doi:https://doi.org/10.36487/acg_repo/2063_0.03.

Diederichs, M.S. (2007). The 2003 Canadian Geotechnical Colloquium: Mechanistic interpretation and practical application of damage and spalling prediction criteria for deep tunnelling. *Canadian Geotechnical Journal*, 44(9), pp.1082–1116. doi:https://doi.org/10.1139/t07-033.

Dyke, C.G. (1989). Core Discing: Its Potential As an Indicator of Principal In Situ Stress Directions. *ISRM International Symposium*.

Hoek, E. and Brown, E.T. (2018). The Hoek–Brown failure criterion and GSI – 2018 edition. *Journal of Rock Mechanics and Geotechnical Engineering*. [online] doi:https://doi.org/10.1016/j.jrmge.2018.08.001.

Hoek, E. and Marinos, P.G. (2009). Tunnelling in Overstressed Rock. *ISRM Regional Symposium EUROCK 2009, Croacia*, 2009, pp.49–72.

International Society for Rock Mechanics Commission on Testing Methods (1985). Suggested Methods for Determining Point Load Strength. *Int. J. Rock. Mech. Min. Sci. and Geomechanical Abstr.*, 22(2), pp.51–60.

Kahraman, S., Fener, M. and Kozman, E. (2012). Predicting the compressive and tensile strength of rocks from indentation hardness index. *The Journal of The Southern African Institute of Mining and Metallurgy*, 112, pp.331–339.

Lim and C. Derek Martin (2010). Core disking and its relationship with stress magnitude for Lac du Bonnet granite. 47(2), pp.254–264. doi:https://doi.org/10.1016/j.ijrmms.2009.11.007.

Martin, C.D., Kaiser, P.K. and McCreath, D.R. (1999). Hoek-Brown parameters for predicting the depth of brittle failure around tunnels. *Canadian Geotechnical Journal*, [online] 36(1), pp.136–151. doi:https://doi.org/10.1139/t98-072.

Martin, C.D., Christiansson, R. and Söderhäll, J. (2001). *Rock stability considerations for siting and constructing a KBS-3 repository Based on experiences from Äspö HRL, AECL's URL, tunnelling and mining*. Stockholm: Svensk Kärnbränslehantering AB.

McCracken, A. and Stacey, T.R. (1989). Geotechnical risk assessment of large-diameter raise-bored shafts. *Proceedings Shaft Engineering Conference*, pp.309–316.

PTFI (2022). *Big Gossan Rock Mass Characterization*. [Internal report] PT Freeport Indonesia, Tembagapura, Indonesia.

Seismological and numerical characterisation of stability pillar behaviour at South Deep Mine

S.M. Sibanda, B.P. Watson

University of the Witwatersrand, South Africa

South Deep Mine operates at depths near 3000 m, where massive mining activities adjacent to stability pillars result in a decreasing pillar width-to-height ratio and the potential for stability pillar yielding. This paper integrated numerical modelling and seismological analysis to characterise the behaviour of a stability pillar during decreased width-to-height ratios with massive mining. Finite element models assessed stress distribution and damage evolution. The results showed gradual pillar yielding with core plastic strains reaching about 2%, indicating the transition from peak strength to strain softening. Seismological tools, including Energy Index (EI) and Cumulative Apparent Volume (CAV), identified distinct strain hardening (high EI, low CAV) and softening (low EI, high CAV) phases. Pillar failure was marked by sustained low EI and reduced seismicity. These findings highlight the value of combining numerical and seismological approaches to monitor pillar stability, offering actionable insights for safer deep-level mining practices.

Keywords: Stability pillars, numerical modelling, seismology, pillar yielding, strain hardening, strain softening, South Deep Mine.

INTRODUCTION

Deep-level mining at South Deep Mine, conducted under high-stress conditions at depths nearing 3000 m, relies on stability pillars to support overburden and ensure operational safety. However, progressive massive mining (long hole open stoping) reduces pillar width-to-height ratios (Figure 1), increasing susceptibility to yielding and failure. Understanding pillar behaviour under such conditions is critical for risk mitigation. This study synthesises numerical modelling and seismological analysis to characterise pillar response, building on methodologies from Ollila and Brown (2022), who demonstrated seismology's efficacy in tracking sill pillar yield.

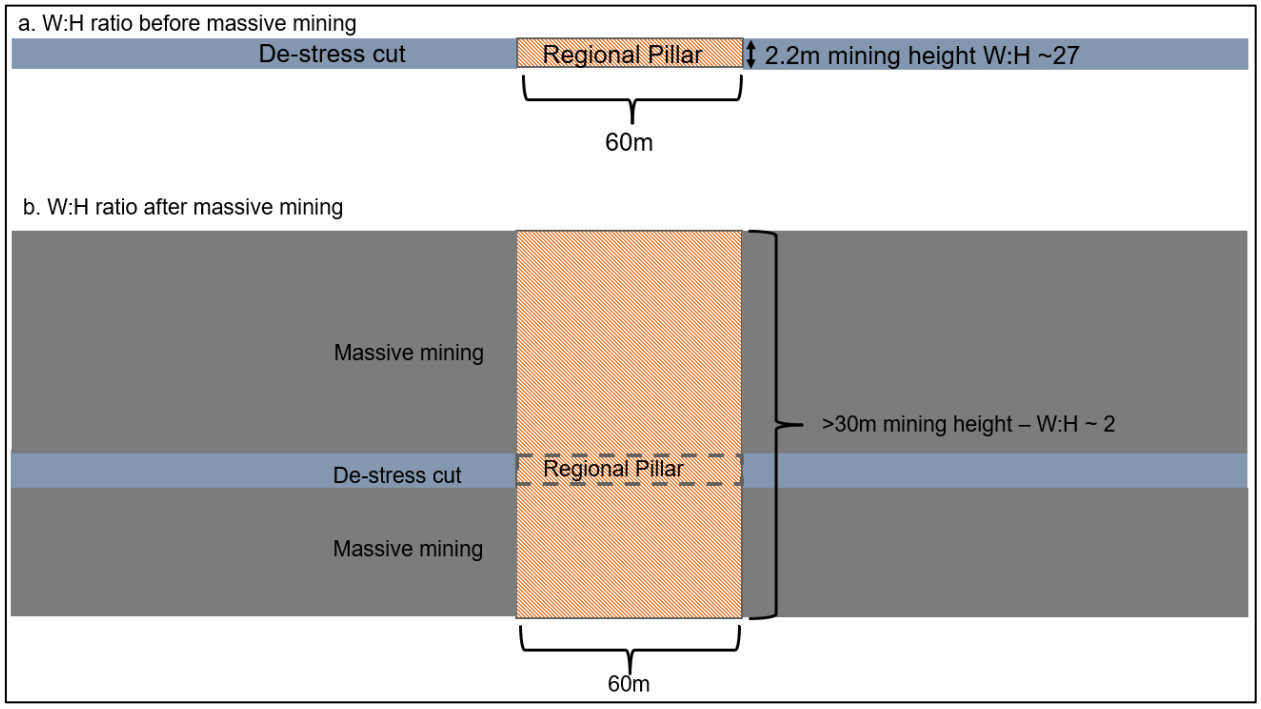


Figure 1. Illustration of the changing width-to-height ratios with massive mining.

Diederichs *et al.,* (2004) illustrated rock damage progression through a simulated stress-strain curve (Figure 2), identifying three stages:

1. Elastic phase (pre-peak), where stress increases within elastic limits, accompanied by rising acoustic emissions.
2. Transition phase (peak to post-peak), where stress plateaus then declines with peak crack rates (acoustic emissions) signalling inelastic strain.
3. Residual phase where stress stabilises at lower levels, with reduced cracking.

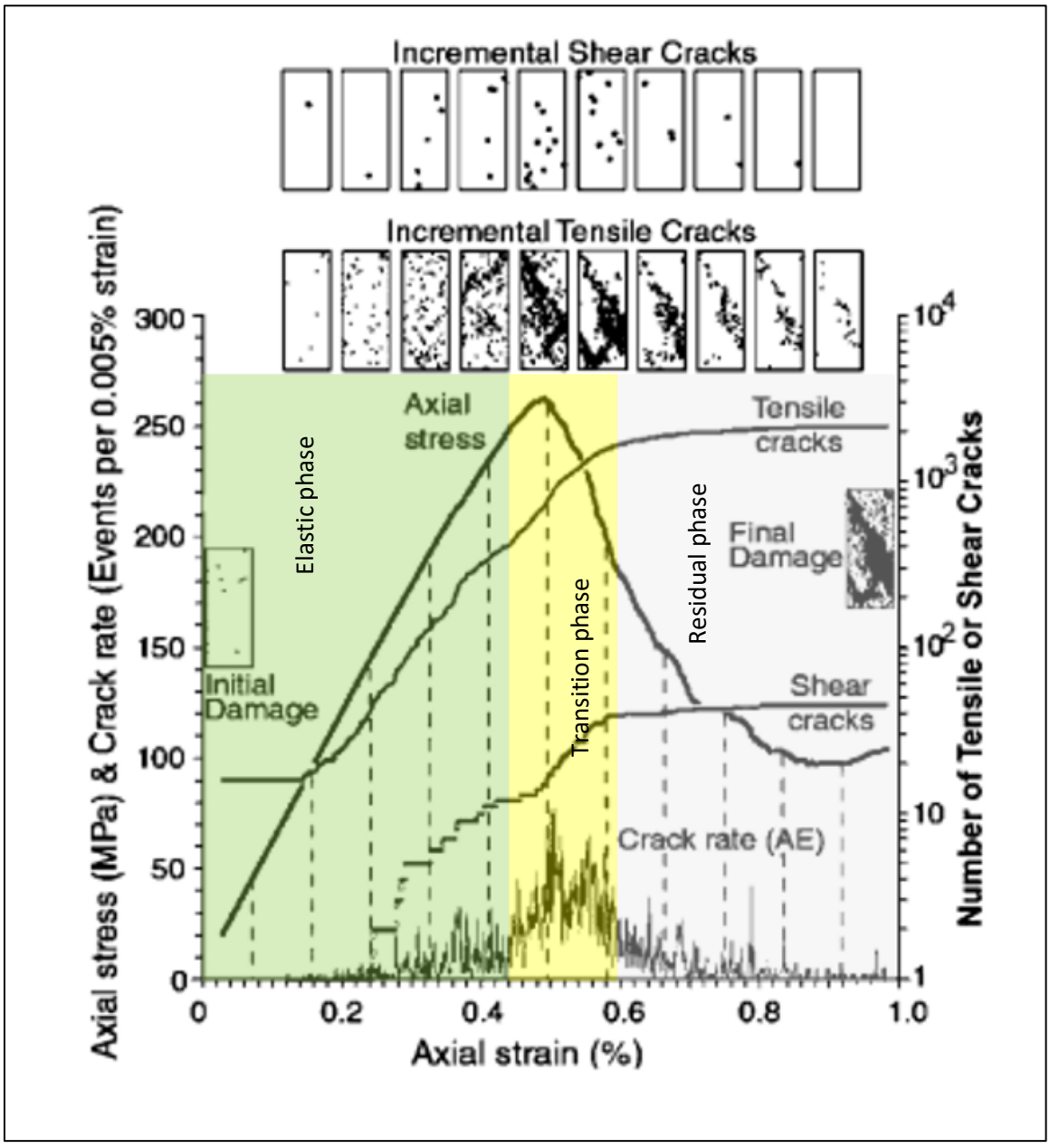


Figure 2. Stress-strain stages (Diederichs et al.*, 2004).*

Ollila and Brown (2022) linked these stages to seismological indicators i.e., strain hardening (high Energy Index (EI), low Cumulative Apparent Volume (CAV) which reflects elastic stress accumulation, while softening (low EI, high CAV) denotes stress release. This study extends their framework by correlating numerical stress-damage models with seismic data to evaluate a stability pillar at South Deep Mine.

OBJECTIVES

The main objectives of the research were to:

1. Quantify stress and damage evolution via finite element (FE) modelling.
2. Identify strain hardening/softening phases in the pillar using EI and CAV.

3. Correlate numerical and seismological findings to predict failure mechanisms.

METHODOLOGY

Numerical Modelling

Non-linear Abaqus FE modelling (Hibbitt *et al.*, 2000) was used to simulate stress and damage for the 2010 to 2016 mining sequences. The stability pillar was 60 m wide, which included a 40 m thick dolerite dyke with 10 m reef margins bracketing the dyke. It underwent width-to-height (w/h) ratio reductions from about 27 (2.2 m high destress slot) to about two when the 30 m high open stopes were mined. The following modelling steps were undertaken:

1. Geometry: 3D CAD database integration of the mine layouts.
2. Mesh Construction: High-order elements for accuracy.
3. Material Properties: Geotechnical domains with calibrated rock properties.
4. Boundary Conditions: Simulated in situ stresses and mining-induced loads.
5. Solution: Large-strain formulation to capture plasticity and deformation.

Input Parameters – Stress field

The initial stress field used in the study was based on stress measurements performed at South Deep mine and is outlined in Table 1.

Table 1. In-situ stress field used in the study

Principal stress component	Magnitude gradient (MPa/km)	Dip	Dip azimuth	σ_i/σ_{zz}
σ_1	27.0	90	000	1
σ_2	24.0	00	000 = 180	0.89
σ_3	16.0	00	090 = 270	0.59

Cartesian stress tensor at 1,000 metres:

$$\begin{bmatrix} \sigma_{xx} & \sigma_{xy} & \sigma_{zx} \\ \sigma_{xy} & \sigma_{yy} & \sigma_{yz} \\ \sigma_{zx} & \sigma_{yz} & \sigma_{zz} \end{bmatrix} = \begin{bmatrix} \sigma_{EE} & \sigma_{EN} & \sigma_{UE} \\ \sigma_{EN} & \sigma_{NN} & \sigma_{NU} \\ \sigma_{UE} & \sigma_{NU} & \sigma_{UU} \end{bmatrix} = \begin{bmatrix} 16.0 & 0 & 0 \\ 0 & 24.0 & 0 \\ 0 & 0 & 27.0 \end{bmatrix} \text{MPa}$$

Input Parameters – Material properties

Material properties used in the study were based on triaxial compressive strength and uniaxial compressive strength tests on selected samples of the orebody quartzites and the hangingwall lava. These properties are presented in Table 2.

Table 2. Material properties used in the study

Number	Domain	Code	Density (kg/m^3)	UCS (MPa)	GSI	Stage	Plastic strain	E (GPa)	ν	s	m	a	d
1	Pretoria Group	PG	2,752	100	65	Peak	ε_0 = 0.0%	20.9	0.25	2.76E-03	1.77	0.5	0.25
						Transition	ε_1 = 2.2%	20.9	0.25	2.76E-03	1.77	0.5	0.25
						Residual	ε_2 = 3.8%	10.5	0.25	1.26E-03	1.16	0.5	0.09
2	Malmani Dolomite	DOL	2,752	100	65	Peak	ε_0 = 0.0%	20.9	0.25	2.76E-03	1.77	0.5	0.25
						Transition	ε_1 = 2.2%	20.9	0.25	2.76E-03	1.77	0.5	0.25
						Residual	ε_2 = 3.8%	10.5	0.25	1.26E-03	1.16	0.5	0.09
3	Ventersdorp Lava	VENT	2,752	100	65	Peak	ε_0 = 0.0%	20.9	0.25	2.76E-03	1.77	0.5	0.25
						Transition	ε_1 = 2.2%	20.9	0.25	2.76E-03	1.77	0.5	0.25
						Residual	ε_2 = 3.8%	10.5	0.25	1.26E-03	1.16	0.5	0.09
4	Westonaria Formation	WAF	2,900	79	54	Peak	ε_0 = 0.0%	16.5	0.25	1.30E-03	1.19	0.5	0.20
						Transition	ε_1 = 2.5%	16.5	0.25	1.30E-03	1.19	0.5	0.20
						Residual	ε_2 = 4.4%	8.3	0.25	7.44E-04	0.92	0.5	0.07
5	Ventersdorp Contact Reef	VCR	2,680	56	57	Peak	ε_0 = 0.0%	11.7	0.23	7.39E-04	1.00	0.5	0.14
						Transition	ε_1 = 2.9%	11.7	0.23	7.39E-04	1.00	0.5	0.14
						Residual	ε_2 = 5.0%	5.9	0.23	3.43E-04	0.65	0.5	0.05
6	Elsburg Reef package	EREEF	2,780	200	75	Peak	ε_0 = 0.0%	50.0	0.20	5.70E-02	3.00	0.5	0.50
						Transition	ε_1 = 0.8%	50.0	0.20	5.70E-02	3.00	0.5	0.50
						Transition	ε_2 = 1.5%	25.0	0.20	1.50E-02	1.23	0.5	0.18
						Residual	ε_3 = 10.0%	1.5	0.20	1.00E-04	1.00	0.5	0.18
7	Footwall quartzite	FWQ	2,780	157	65	Peak	ε_0 = 0.0%	32.8	0.25	1.29E-02	3.12	0.5	0.39
						Transition	ε_1 = 1.6%	32.8	0.25	1.29E-02	3.12	0.5	0.39
						Residual	ε_2 = 2.7%	16.4	0.25	3.49E-03	1.82	0.5	0.14

UCS - uniaxial compressive strength.

GSI - geological strength index.

ε_0 - = 0 = plastic strain at start of peak strength stage.

ε_1 - plastic strain at start of transitional strength stage.

ε_2 - plastic strain at start of residual strength stage.

E - Young's modulus for the rockmass.

υ - Poisson's ratio for the rockmass.

m - Generalised HB yield parameter for the rockmass.

s - Generalised HB yield parameter for the rockmass.

a - Generalised HB yield parameter for the rockmass.

d - rockmass dilation parameter.

Seismological Analysis

In this study, the seismic response of a stability pillar was analysed as its width-to-height ratio was reduced with massive mining. Seismic indicators of stress and strain were used to infer pillar behaviour. The time- scale covered several years during which massive mining occurred around the stability pillar. Its width-to-height ratio was gradually reduced. The stability pillar and the corresponding seismic events are shown in Figure 3.

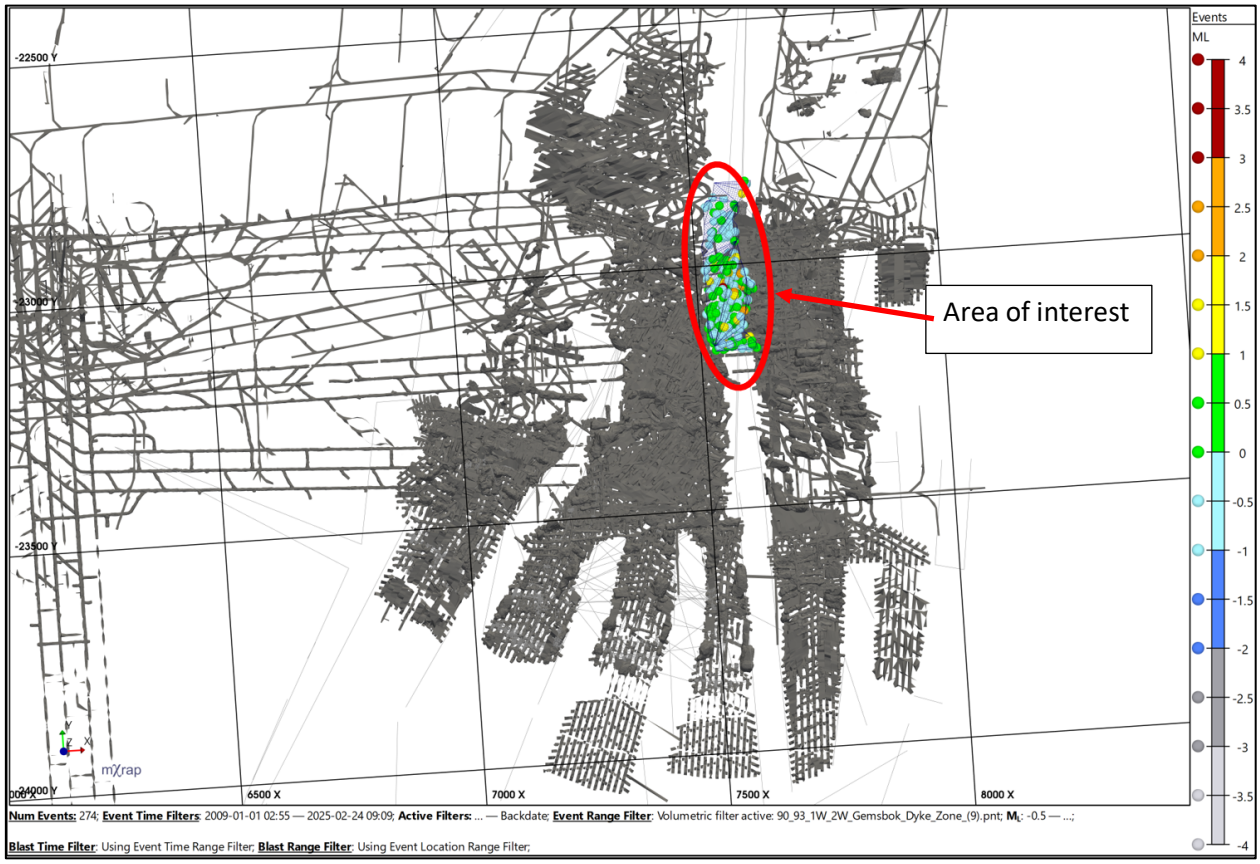


Figure 3. Stability pillar under consideration (area of interest, circled in red) and associated seismic events over 15 years (2009 to 2025).

The seismic data (2009–2025) was filtered on magnitude (ML > -0.5) to exclude non-failure events e.g., blasting. EI and CAV were used to track pillar behaviour and infer stress path changes as demonstrated in Figure 1. Changes in EI and CAV were used as a proxy for changes in stress and inelastic strain rate, respectively following the methodology of Ollila and Brown (2022). Three time periods were selected for the study on the criteria described below:

1. Hardening where there was high EI and low CAV.
2. Transition showing rapid EI decline and CAV rise.
3. Softening where low EI and high CAV were observed.

To further describe the pillar behaviour and progression of rock mass failure, a magnitude-time history plot was plotted and evaluated for the same period. As was found by Jager and Ryder (1999), larger seismic events occurred when the pillar started losing its ability to maintain stress (transition phase in Figure 1).

RESULTS

Numerical Modelling

Figure 4 illustrates the evolution of stress and rockmass damage from 2010 to 2016. For each year, the image on the left depicts the major principal stress, while the image on the right shows the distribution of plastic strain. To provide an unobstructed view of footwall stress, excavations have been hidden in the middle set of images for each year.

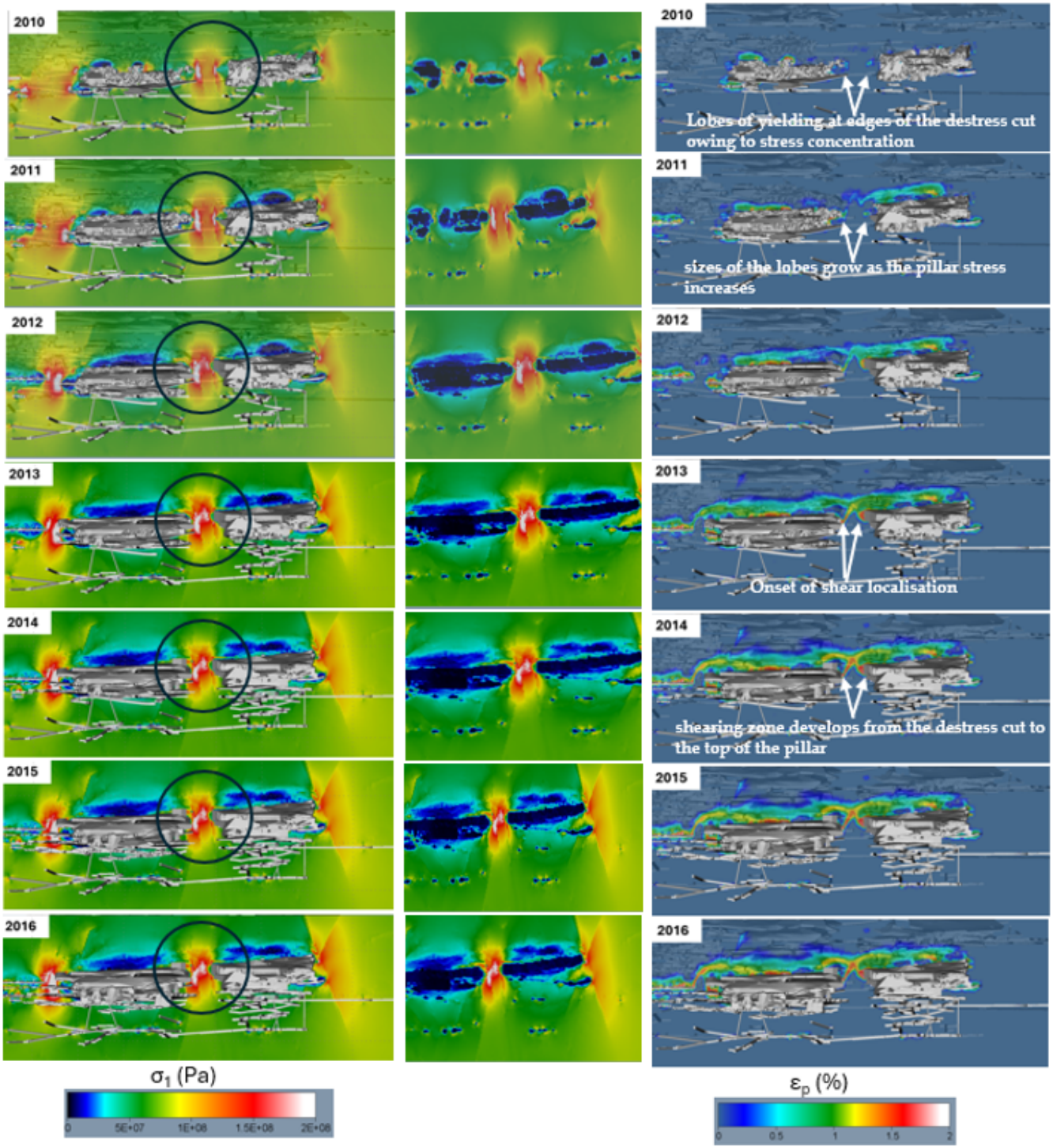


Figure 4. Evolution of major principal stress (left) and plastic strain (right) from 2010 to 2015. Excavations have been removed from the middle images in each year to improve visibility of footwall stress distribution.

Evolution of stress and damage

Stress distribution and damage during the modelled mining steps are shown in Figure 4. The dates on the figure show different snapshots during the simulation process as per the mining sequence. The stability pillar was subjected to relatively lower stresses in 2010, with major principal stress in the core

of the pillar at an average of 100 MPa. At this stage, the predominant mining excavations were the 2.2 m high destress slots. The stresses at the pillar edges exceed 200 MPa. However, as the massive mining increased in extent, from 2012 to 2016, the stress in the pillar increased markedly with stress in the pillar core exceeding 200 MPa while stresses at the pillar edges relaxed.

The evolution of the plasticity state can be described as follows:

Initially (2010 – 2011), lobes of yielding occurred at the edges of the destress slot due to localised stress concentrations. At this stage, the pillar was stable, with failure limited to the edge of the pillar, while the core of the pillar remained intact and was still carrying load.

Moderate damage first evolved in the stability pillar in 2012 and 2013 as massive mining progressed. As damage grew, there were indications of stress relaxation on the pillar edges, particularly on the eastern (right-hand) side of the pillar. The lobes of yielding continued to grow as the pillar stress increased from 2012 to 2016 until shear bands developed from the destress cut to the top of the pillar. The core of the pillar remained intact.

At the same time, damage also evolved in the hangingwall (top of pillar). This shear failure in the hangingwall initiated in the Westonaria Formation (WAF) lava. This may be attributed to the difference in the stiffness and strength of the WAF lava and the reef quartzites.

The coalescing of the plastic zones, as depicted by the shear bands from the destress cut to the top/hangingwall of the pillar represents failure of the hangingwall beam which can be interpreted as a bearing type failure (failure of immediate hangingwall pillar 'foundation'). This bearing type failure could contribute to excessive deformation in the rock mass.

The damage progression was as follows:

- 2010–2011: Edge yielding (elastic/hardening).
- 2012–2013: Core stress accumulation (peak).

2014–2016: Shear banding from destress cut to top of the pillar representative of bearing-type failure.

Seismological Analysis
The behaviour of the stability pillar, as its width-to-height ratio decreased with massive mining, was shown by an EI/CAV chart as provided in Figure 5. The seismological data analysis identified three distinct phases of pillar behaviour:

1. **Strain Hardening Phase**: Characterised by a high energy index and low apparent volume, indicating elevated stress levels with minimal yielding (green region). This is consistent with a confined rock mass under high stress.
2. **Transition Phase**: Indicated by a sharp drop in EI and a corresponding increase in CAV occurring between 2012 and 2014 (yellow region).
3. **Strain Softening Phase**: Marked by a low energy index and high apparent volume, signalling stress release and increased deformation (grey region).

Pillar yielding was inferred when consistently low energy index levels and minimal seismicity were recorded, suggesting that the pillar had reached a state of strain softening. However, the minimal seismicity could also be attributed to the reduction in active mining in the area. This will be investigated in future work using microseismic and active source monitoring to assess pillar behaviour.

The trends observed could be attributed to artifacts of the mine's seismic system. To evaluate this, the EI behaviour in the study area was compared with other geotechnically comparable zones in the mine over the same period. These reference areas did not exhibit similar shifts, supporting the interpretation that the observed behaviour is geomechanically driven rather than a result of system changes.

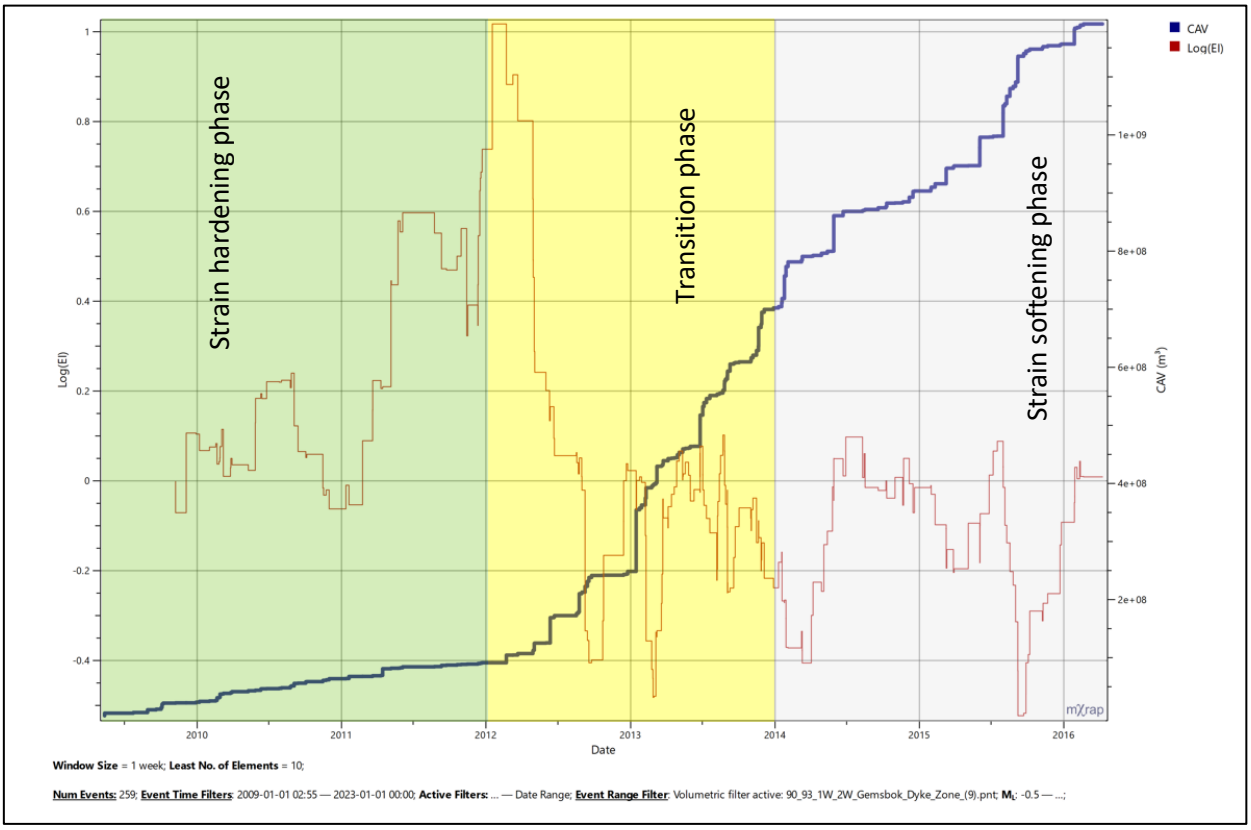


Figure 5. EI/CAV phase transitions.

The magnitude-time plot shown in Figure 6 indicates a rapid acceleration in event rate from early 2012, with some larger magnitude events. A deceleration was noted from early 2014, with relatively smaller magnitude events. This is consistent with a yielding rock mass. The larger seismic events occurred when the pillar started losing its load-bearing ability, similar to the findings of Jager and Ryder (1999).

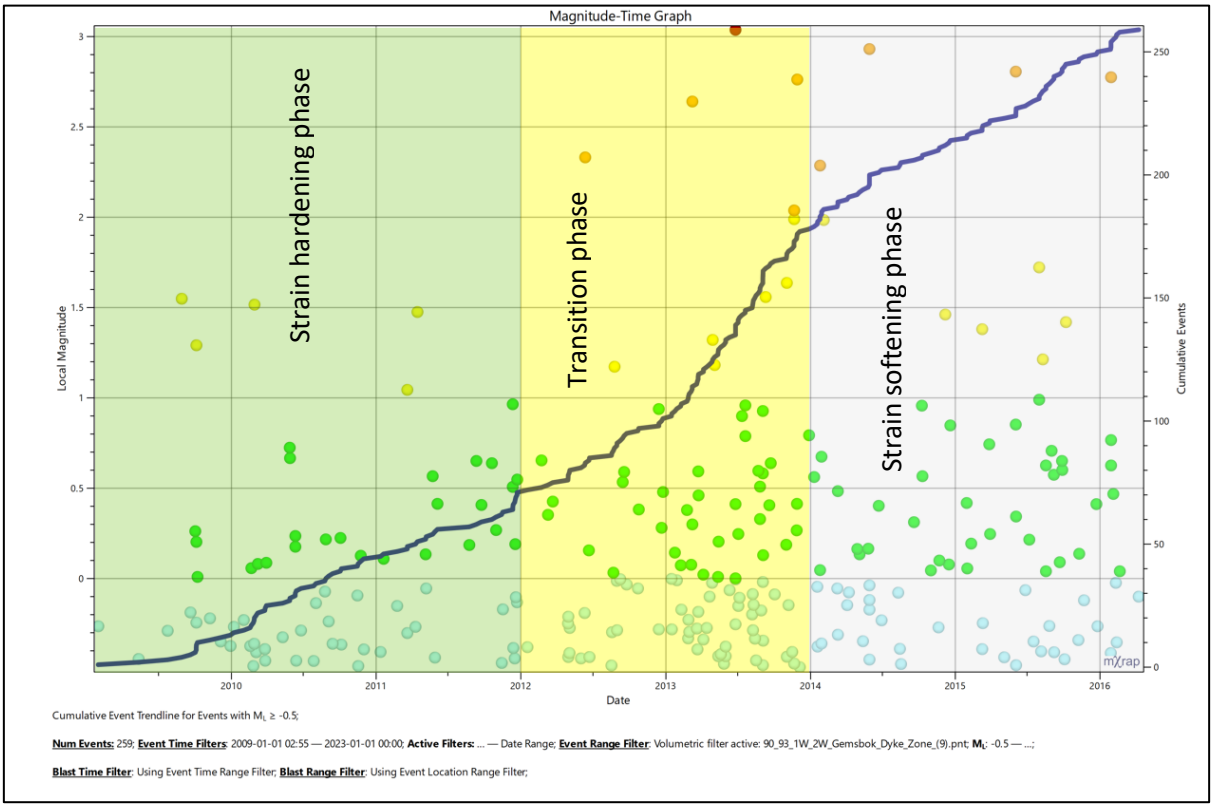


Figure 6. Magnitude-time plot for events in the stability pillar (blue line represents cumulative events).

DISCUSSION

The integration of numerical modelling and seismological analysis provided a comprehensive understanding of the stability pillar's behaviour. Numerical modelling highlighted the importance of the width-to-height ratio in controlling stress distribution and damage evolution, while the seismological data offered real-time insights into the pillar's response to mining-induced stress changes.

The strain hardening phase, characterised by a high energy index and low apparent volume, reflected the pillar's ability to withstand high stress with minimal deformation. In contrast, the strain softening phase, marked by low energy index and high apparent volume, indicated the onset of significant deformation and stress release. These findings aligned with the numerical model's prediction of pillar foundation yielding and bearing failure. The study underscored the value of combining numerical modelling and seismological tools for monitoring, understanding and managing pillar stability in deep-level mining environments.

CONCLUSION

This study provided valuable insights into the behaviour of stability pillars at South Deep mine, demonstrating the critical role of the width-to-height ratio in controlling pillar stability. This study demonstrated that decreasing width-to-height ratios drive stability pillars from hardening to softening, identifiable via EI/CAV trends and numerical damage models. The framework aids in predicting failure and guiding safer mining practices. Future work will integrate additional monitoring tools and model calibration to further enhance the understanding of stability pillar behaviour.

ACKNOWLEDGEMENTS

The author wishes to thank management of South Deep mine for their support and making data available for this study. Special thanks to Dr. David Beck of Beck Engineering for support with the numerical modelling.

REFERENCES

Diederichs, M. S., Kaiser, P. K., & Eberhardt, E. (2004). Damage initiation and propagation in hard rock during tunnelling and the influence of near-face stress rotation. *International Journal of Rock Mechanics and Mining Sciences, 41*(5), 785–812.

Hibbitt, Karlsson & Sorensen, Inclusive (2000) ABAQUS/CAE User's Manual. U.S.A.

Mendecki, A.J., van Aswegen, G. & Mountford, P. (1999). A guide to routine seismic monitoring in mines. In: A.J. Jager & J.A. Ryder, eds. Rock Engineering Practice for Tabular Hard Rock Mines. Johannesburg: Safety in Mines Research Advisory Committee (SIMRAC), 287–309

Ollila, A., & Brown, T. (2022a). Seismological characterization of sill pillar yield. *Journal of Rock Mechanics and Mining Sciences, 45*(3), 112–129.

Ollila, B. & Brown, L. (2022b). Seismological characterization of sill pillar yield. RaSiM10: Proceedings of the Tenth International Conference on Rockbursts and Seismicity in Mines, Society for Mining, Metallurgy and Exploration, Englewood.



Sifanekiso Sibanda

Geotechnical Engineer

Sifanekiso Sibanda is a highly experienced geotechnical engineer with over two decades of expertise in underground hard rock mining, spanning both shallow and deep-level operations within South Africa's most complex geological environments—namely the Bushveld Complex and the Witwatersrand Basin.

He holds a Bachelor of Science and a Master of Science in Mining Engineering, and is currently pursuing a PhD in Mining Engineering at the University of the Witwatersrand, focusing on Stability Pillar Behaviour in deep-level mining. His academic grounding is complemented by a strong track record of applied rock engineering and strategic geotechnical management.

Sifanekiso has held senior technical and leadership positions at major mining companies including Anglo American, Sibanye-Stillwater, and Gold Fields. His experience encompasses operational support, project management of large-scale geotechnical initiatives, execution of feasibility studies, and the integration of geotechnical considerations into safety systems, mine design, and business optimization. He has led multidisciplinary teams and provided expert guidance on seismicity management, backfill strategies, ground control systems, and regulatory compliance.

Currently serving as Geotechnical Engineering Manager at South Deep Mine (Gold Fields), he is responsible for driving the geotechnical strategy for one of the world's deepest and most mechanized gold mines. His role involves leading a high-performing team, ensuring geotechnical input across the mine life cycle, and supporting safe, efficient production through innovation and applied rock engineering principles.

A passionate advocate for knowledge transfer and professional development, Sifanekiso is deeply committed to mentoring and coaching the next generation of mining professionals. He is actively involved in internal talent development programs and often contributes to industry workshops, technical panels, and academic-industry collaborations.

Prediction of mine tunnel conditions in a deep Austrian mine by means of numerical back- and forward analysis

P. Gams[1], B. Moosbacher[2], H. Wagner[1], T. Fruehwirt

[1]Montanuniversitaet Leoben, Austria
[2]RHI Magnesita, Austria

As mining goes deeper and rock pressure problems increase, rock stress management becomes imperative. Advances in rock mechanics knowledge and understanding, together with significant improvements of soft- and hardware available to the rock mechanics practitioner, make it possible to analyse complex mining and geological situations. What is often lacking are reliable rock engineering criteria to convert numerical results into meaningful mine design and operational criteria. In this paper an example is given of how an Austrian industrial mineral mine where an irregular lens type mineral deposit is being extracted at a depth of about 1000 m is dealing with the rock pressure situation. The dimensions of the mineral body are several hundreds of metres in the dip and 100 m to 500 m in the strike direction. The thickness varies from a few metres to more than 100 m. This mineral deposit is situated in a weak shale formation. In the overburden are water-bearing rock formations. For these reasons a sub-level cut and fill stoping method, using pillars to control overall ground movement, is applied. The backfill serves as a working platform and provides stability to the slender, and in instances up to 100 m high, stope-pillars. The geological situation of that mine is very complex and it is predicted that with greater depth more geological formations with weak graphite layers can be expected. A comprehensive geological mapping system is in place. Pillar and ground conditions are monitored regularly. Based on structural geological data it is planned to change the direction of stopes, to intersect these zones of weakness in a more favourable angle. However, already the existing stopes and drifts show that sublevel stoping is an appropriate method to mine in those conditions. Beside several operational advantages, the rock mechanical situation will be improved with the rotation of the stope direction. The actual mining direction is parallel to the strike of the deposit, which is approximately 75° to the north. The new mining direction will be 140° to the north which is approximately perpendicular to the striking direction of the deposit. In this paper a comparison based on numerical simulations of mine layouts with these two different orientations is given. It is pointed out that these simulations are based on the situation in the mine. In a comprehensive study it is shown that the rockwall condition factor (RCF), proposed by Wiseman in 1979, is a suitable criterion for predicting the rock pressure situation in this mine. As a first step the input parameters for the numerical simulations (eg., primary stress situation and the stiffness of so called 'stope-pillars') are determined by means of back analysis. The approach for this calibration procedure is the comparison of the calculated RCF (Wiseman 1979) with in situ observed tunnel conditions in the mine. Based on the determined input parameters, numerical models based on potential future mining layouts are built and analysed. Results gained on models of different types and geometry are introduced and layouts with different orientations are compared against each other. Finally, based on objective criteria, the most favourable layout is selected and proposed for implementation by the mining company.

Keywords: deep mining, design criteria, sublevel stoping, numerical analysis, rock mechanics

INTRODUCTION

The development of mines to greater depths is a common trend in the mining industry and it is predicted that the number of mines in deep mining environments will increase. The growing demand of mineral resources for an economical and sustainable growth is one of the driving forces behind this trend. (OECD 2019)

In the case of deep mines, the most critical issue is the effect of the depth on the magnitude of the rock pressure problems. Whereas the numerical tools are available to calculate the stress environment for most mining situations the same cannot be said for the material properties of the rock mass and the criteria which govern the response of mining excavations to high rock stresses. For realistic and reliable mine planning and evaluation of rock conditions, criteria are needed to describe the rock pressure environment in a manner that is meaningful for mine planners and mine operators (Wagner 2019). Using the example of a deep mine in Austria a process is described as to how this can be done.

Background to the mining situation

General

In this paper an example is given of how an Austrian industrial mineral mine, where an irregular lens-type mineral deposit is being extracted at a depth of about 1000 m, deals with the rock pressure situation. The dimensions of the mineral body are several hundreds of metres in the dip and 100 m to 500 m in the strike direction. The dip angle of the deposit varies between 20° and 35° and the dip direction is approximately 140° towards north. The thickness varies from a few metres to more than 100 m. This mineral deposit is situated in a weak shale formation with water-bearing rock formations in the overburden. To not disturb the water, a sub-level cut and fill stoping method using pillars to control overall ground movement, is applied. The backfill serves as a working platform and provides stability to the slender, and in places up to 100 m high, stope-pillars.

Geology

The lens-type industrial mineral deposit is surrounded by a formation of weak black shale which isolates it from water-bearing limestone formations in the super-incumbent rock strata. Thus, the preservation of this protective black shale formation is crucial for the mine. To achieve this, a system comprising of pillars and backfill is used. Other geological structures which need to be considered are:

- Shear faults which are orientated from north to south with a dip between 70° and 90°. These faults zones tend to occur at intervals of about 20 m. These zones cause only a few problems when they are isolated. In combination with other structures, especially with beddings, rock wedges can develop and require support.
- Beddings are present in the deeper parts of the mine. They differ in their appearance, depending on lithology of bedding planes and filling. Also, the thickness of the bedding and the bedding planes vary. The dip direction of bedding planes is typically 140°. The dip angle is in the range of 25° and 50°. Due to the presence of graphite in the bedding layers, the stability of such beddings tends to be quite low.
- Smaller joints occur everywhere in the mine. In many cases they form rock wedges which are handled easily with support.

Generally, it can be stated that the rock mass of the mineral body is competent in the absence of larger structures such as beddings and shear faults. With support all problems can be managed in a safe manner. For support mechanical end-anchored rock bolts are used. The number of bolts depend on the local situation.

Mine design

The rock engineering design of the deep sections of the mine under discussion is based on the concept of relatively small stoping panels measuring 71 m in width and 80 m in length. The up to 6 m wide stopes are separated from each other by so-called ‘stope-pillars’ of 7 m width. The stoping panels are

separated from each other by 20 m wide barrier pillars (see Figure 7). The stoping method entails developing 6 m wide and 5 m to 6 m high stope drives vertically separated from each other by an 11 m high sill pillar. After the stope has reached its length of about 80 m the sill pillar between the bottom and the top drives is removed by a bench-blasting method. Before this can be done a vertical connection between the two stope drives is developed at the remote end of the stope. The blasted rock of the sill pillar is hauled on retreat by means of remotely operated trackless mining equipment. After removal of the sill pillar a backfill-barrier is erected at the foot-access of the stope and it is backfilled using cemented backfill which is pumped into the empty stope. The primary purpose of the backfill is to provide lateral support to the slender stope-pillars and to serve as a working platform for the operation of mining equipment in the case of extracting another stope on top of the lower stope. The objective of the stope-pillars is to provide local roof support to the stopes. Regional support is provided by the abutments of the mining panel and the barrier pillars. This stoping system has shown to be safe and efficient. A prerequisite is that a new stope will be extracted only once the neighbouring stope has been backfilled and the fill has been given time to build up strength. (Wagner and Froemmer 2005).

This stoping system has been monitored and evaluated over a number of years. The objective of the monitoring and evaluation process has been, amongst others, to establish criteria for the planning and evaluation of future mining layouts. Some of the more pertinent results of this work are presented in this paper.

Rock mechanics program
To deal with the rock pressure situation a comprehensive rock engineering program has been implemented at the mine. It comprises of the design described earlier, i.e., use of backfill, limited size mining panels, use of barrier pillars, adherence to a strict mining sequence and a detailed monitoring program to identify development of critical rock pressure situations and to assess effectiveness of changes to improve the rock pressure situation.

The monitoring measures which are implemented in the mine are:

- Pillar condition rating
- Extensometer measurements
- Photo documentation
- Laserscans

The pillar condition rating is done by the mine geologist on a yearly basis and is described in more detail in a later section.

Extensometers are placed in stope-pillars and in barrier pillars. They measure the horizontal displacement perpendicular to the pillar axes. Thus, they are important to identify and quantify changes in the pillars. Especially for the barrier pillars, this is an important measurement because with this data the internal behaviour of the pillars can be monitored. Larger deformations can indicate a failure of the pillar which can be critical for the overall mine stability. An important aspect is that by using vibrating wire technology it is possible to monitor pillar deformation in backfilled areas which are no longer accessible.

Photos are taken four times a year from pre-defined fixed positions to document the conditions of roof and/or the sidewall as mining advances. This is a simple method with a valuable outcome.

With the help of regularly conducted laser-scans smaller (deformations of sidewalls) and larger (fallouts) deformations can be indicated and analysed.

Rock engineering design approach
In future the ore reserves in the upper levels will be exploited and therefore mineral production focuses on deeper levels. In the particular case of this mine, changes in the orientation of the discontinuity systems were observed in the new mining area. It was found that a change of the stope axis from an

approximately striking direction (75° from the north) to an across-the-strike direction (140° from the north) could be beneficial. The major advantages of the rotation of the stope axis are:

- Improved relative orientation of stopes, drifts and pillars to geological structures, especially beddings
- Better flexibility for changes
- Improvement in quality control

However, there were some questions regarding the stress redistribution in mine elements for barrier pillars and abutments, and the condition of the mine excavations. To clarify these points, it was decided to carry out numerical simulations for the comparison of the different stope axis orientations. To obtain realistic results it is important to work with reliable input parameters. For the comparison of the two mining sequences using numerical simulations it is mandatory to have an idea about the primary stress situation and the residual strength of the pillars. Due to the difficulty of determining those parameters, it was decided to back-calculate the existing stoping area and calibrate it to reality.

For this purpose, numerical simulations incorporating all existing mine openings were performed. The results of these numerical simulations in combination with the application of a design criterion were used for the calibration of the model. The design criterion is necessary to link the numerical results with observations found in the mine. In this particular case, the rockwall condition factor (RCF) (Wiseman 1979) in combination with the correlation to observed tunnel conditions found by Ladinig *et al.*, (2019) was used. The findings of this calibration were subsequently used to simulate and analyse the two different future mine-layouts. This method is shown in Figure 1.

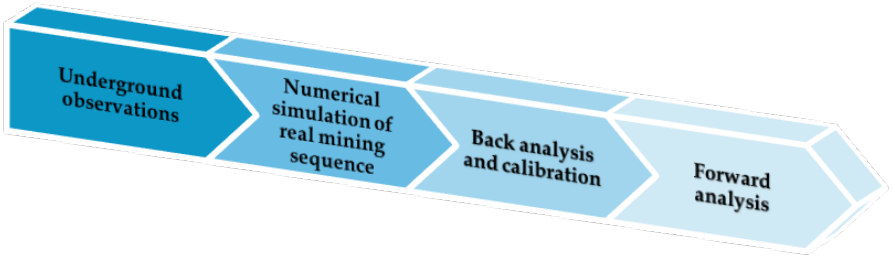


Figure 1. Scheme of the rock engineering approach.

Rockwall condition factor

One of the basic concepts of the whole approach is the RCF (Wiseman 1979). For the description of the condition of the infrastructure this easily understandable design criterion was chosen. The RCF can be calculated by Equation 1:

$$RCF = \frac{3\times\sigma_1-\sigma_3}{UCS\times F} \quad [1]$$

where:

RCF	=	Rockwall condition factor
σ_1	=	Maximum normal field stresses acting perpendicular to the tunnel axis
σ_3	=	Minimum normal field stresses acting perpendicular to the tunnel axis
UCS	=	Uniaxial compressive strength of the rock
F	=	Downgrade factor to account for the discontinuities of the rock mass

Jager and Ryder (1999) created a diagram, see Figure 2, which is based on deep South African mining conditions to determine tunnel conditions based on RCF and installed support. The x-axis describes the RCF value. On the y-axis the observed tunnel conditions can be found. Depending on the type of support and the RCF value the conditions of the tunnel can be determined. A similar approach is used in this paper.

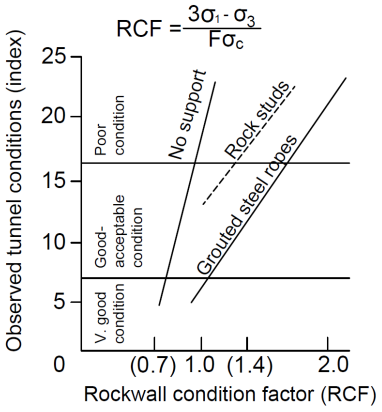


Figure 2. Relationship of RCF value and rock conditions of mine tunnels for different support systems (Jager and Ryder 1999).

Observation of mining conditions

Tunnel condition rating

Ladinig *et al.*, (2019) created a scheme for the classification of underground openings for the prementioned mine. This scheme is shown in Table I. They categorised specific indicators for rock pressure related problem and graded them from 1 to 5, where 1 means excellent conditions and 5 poor conditions.

Table I: Tunnel condition rating after Ladinig et al., (2019)

	Condition rating (1)	Observed tunnel condition
Very Good	1.0–1.5	Excellent tunnel conditions; solid tunnel walls; no support required
	1.5–2.0	See 1.0–1.5; tunnel walls with minor joints or fracturing; occasional spot bolting, where required.
	2.0–2.5	Tunnel walls with more fractures; compared to 1.5–2.0 more frequent spot bolting but no systematic support pattern required; no signs of stress related fracturing or loosening.
Good	2.5–3.0	First signs of stress-induced fracturing; limited strata loosening; isolated rock falls.
	3.0–3.5	Signs of stress induced rock fracturing; strata loosening isolated rock falls; introduction of systematic support systems.
Poor	3.5–4.0	Increased signs of overstressing of tunnel walls, stress damage extends over larger areas of tunnel walls; rock slabbing; formation of rock wedges between supports; visible signs of strata loosening.
	4.0–4.5	Marked signs of rock fracturing extending over full tunnel wall, formation of rock slabs; local overstressing of support; high risk of rock falls from roof and sidewalls of tunnel; tunnel no longer suited for normal operations; special precautions are necessary to enter tunnel.
	4.5–5.0	Tunnel in process of collapse; severe extent of fracturing and loosening; support has failed largely; severe rock fall hazard.

The condition rating was done in 2019 and in 2023. All open mining drifts were rated according to Table I, with special focus was on the roof and sidewalls of the drifts. The tunnel condition is rated and mapped, as Figure 3 indicates.

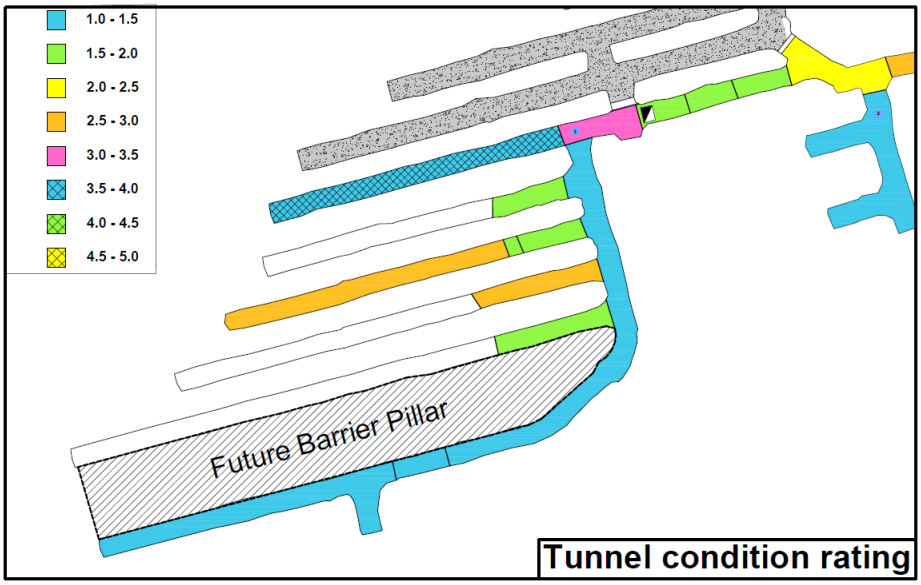


Figure 3. Example of an underground tunnel condition rating map.

Barrier pillar condition rating

The barrier pillar condition rating is conducted on a regular basis by the mine's geologist. It is based on a scheme which includes two different factors, namely the geological structures and stress-related indicators, for example spalling. By doing this developing rock pressure-related problems can be identified early. The barrier pillar is rated at the northern and southern side on three different positions. The analyses of the results of the condition rating show no big changes over the years. One reason for this observation is that at this stage the barrier pillar is actually an abutment area for the mining field to its north. As soon as mining commences south of the barrier pillar, it is expected that changes will be recognised.

Photo documentation

A photo documentation is a simple but powerful tool. The contrast of photos taken on different dates clearly shows changes on the roof or walls of mine excavations. The photo documentation supports the study by an indication of important changes. On the one hand this can be the excavation of new additional drifts, but more important rock pressure-related changes as spalling, fracturing or rock falls. Figure 4 gives an example for identification of rock pressure-related problems.

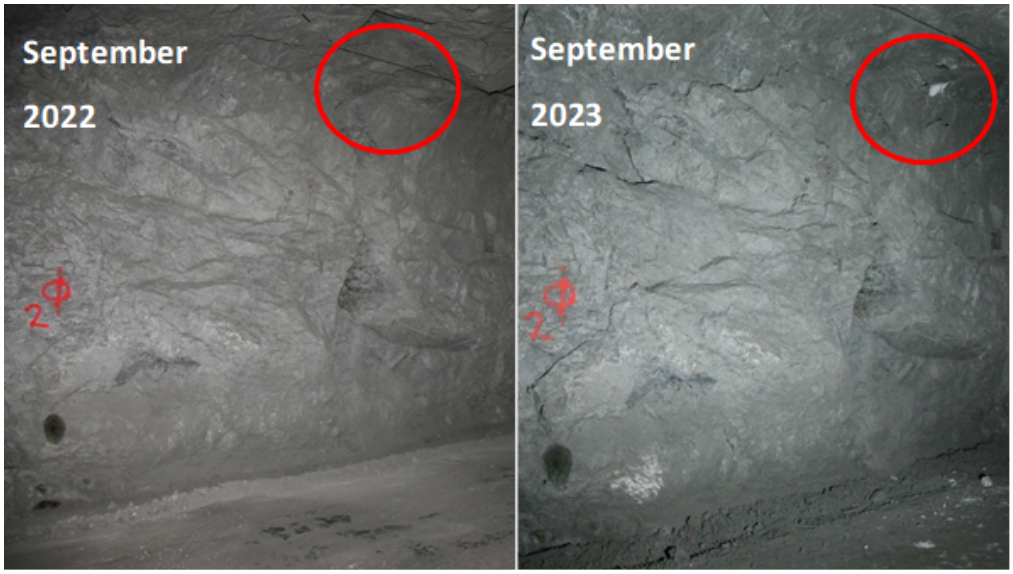


Figure 4. Example for photo documentation. Rock pressure related problems can be found in the image on the right.

Numerical simulation

The main purpose of the numerical simulation is the calculation of the RCF to predict the tunnel conditions for high order infrastructure of the two different future mine layouts. As already described, an additional preceding simulation for the calibration to work later on with a realistic model of the mine is needed. The material behaviour of stope-pillars and the realistic primary stress situation has to be determined. In the subsequent analyses regarding the best layout option, the stope-pillars are modelled with a different Young's modulus, which was determined by the calibration process, to simulate their real behaviour.

All simulations are based on a linear elastic model. This approach is a simplification, but has the following advantages:

- Easier interpretation of results
- Fewer and simpler input parameters which are easily determined in the laboratory
- Quick results of stress and deformations.

The connection between a rather simple linear elastic model and the real situation in the mine is the already-mentioned design criterion. The correlation of the RCF calculated from stresses from the linear elastic simulation and the tunnel condition is superior for the application of a linear elastic approach for such a problem. Processes such as fracturing around a mine excavation are included by the condition rating and the RCF.

Beside the linear elastic material model, some other simplifications were implemented:

- Backfilling of stopes is neglected in the simulations. This leads to a conservative approach.
- Only the stopes including top-and foot drifts are modelled. Infrastructure is not modelled.
- Stopes are excavated to their full length.

Generally, the different simulations have identical input parameters, see Table II. The size of the mesh is variable, which means that the mesh density is high in areas where pillars and drifts are located and lower in outer regions of the model.

Table II: General input parameters for back- and forward analysis

Input parameter	
Young's modulus [GPa]	40
Poisson's ratio [1]	0.25
Density [g/cm³]	2.8

Model for calibration and back analysis
For the calibration it was necessary to create a model of the existing mine. The mesh is created with the help of the software Abaqus (Dassault Systèmes Simulia Corp. 2021). For the simulation itself the mesh is imported into FLAC3D (Itasca 2023). After the implementation of input parameters, the numerical simulation is solved until equilibrium is reached following the historical mining sequence. Therefore one stope is excavated by deleting cells from the model. In case a pillar gets formed, the following assumption based on the real behaviour of stope-pillars is made. Directly after the creation of the pillar the actual stresses at the pillar boundaries are set to zero and Young's modulus is reduced. Due to the reduction of the pillars Young's modulus, the load acting on the stope-pillars is reduced and transferred to the panel abutment and barrier pillars. After one calculation cycle the RCF value is calculated from the simulated stresses. Thus, it is feasible to compare the RCF after each excavation step.

Model for forward analysis
For the forward analysis two models of the future mining layouts including the already mined parts are necessary. There the pre-determined input parameters, namely primary stress situation and stope pillar stiffness, are implemented. At this point it is feasible to make predictions regarding:

- Stress concentration
- RCF and expected tunnel conditions for critical infrastructure
- Barrier pillar stresses
- Appropriate mining sequence
    - Local
    - Regional.

Calibration
Critical for the success of the overall approach is the calibration of the simulation. As already discussed, it is important to have a reliable model of the real mine. In this particular case this means that a model including the real behaviour of the stope-pillars and the correct primary stress situation must be created. Based on historical observations the behaviour of pillars can be characterised. The challenge is to include this behaviour into the numerical model. Also, the primary stress situation must be depicted in the simulations. In the end, it is necessary to determine the overall stiffness (i.e., an elasticity module) for the pillars and a ratio between the vertical primary stresses and horizontal primary stresses.

For that reason, following approach is applied:

At the very beginning it is important to find a criterion that matches the in-situ condition of the mine workings with the results of linear elastic numerical simulations. For that purpose, the RCF (Wiseman 1979) is an ideal solution. The RCF value is based on parameters which can be easily found by numerical simulation, e.g., the minimum and maximum principal stresses acting at the tunnel wall, and from laboratory testing and field observation, e.g., uniaxial compressive strength and F-Factor. The big advantage for that criterion is that it can be connected with the tunnel conditions. Ladinig *et al*., (2019) established a procedure for a condition rating of underground tunnels and connected that with the RCF value; see Table III.

Table III: Correlation between condition rating and RCF found by Ladinig et al. (2019)

Condition rating (1)	RCF <0.7	RCF 0.7–0.8	RCF 0.8–0.9	RCF 0.9–1.0	RCF 1.0-1.1	RCF 1.1-1.2	RCF 1.2–1.3	RCF 1.3-1.4
1.0–1.5	X							
1.5–2.0		X	X					
2.0–2.5		X						
2.5–3.0								
3.0–3.5						X		
3.5–4.0							X	
4.0–4.5							X	X
4.5–5.0								

Based on the chosen criterion, it is now possible to calibrate the simulation in a way that reflects the mine's situation by means of the model. It is important to highlight the excavation steps when a condition rating is done in the underground mine. For these steps a correlation between the RCF and the condition rating can be found. At the beginning the focus was to find an elasticity module of the stope-pillars which reflects the real situation in the mine. Therefore, a number of simulations with different Young's moduli, see Figure 5, were executed to find a value which fits. The RCF was calculated for all mine tunnels where a tunnel condition rating was conducted. Along 20 m segments the average value for the RCF was calculated and compared with the condition rating. The latest tunnel condition rating was done for the last excavation step. Therefore, the condition rating and RCF are compared for the last step, marked by the red box in Figure 5. Moreover, the map in Figure 5 indicates the position for that specific observation. Based on the correlation found by Ladinig *et al.*, (2019), a condition rating of 4.0–4.5, which was found during field observations, correlates to a RCF between 1.2 and 1.4. Simulations stiffnesses of 0.6–1.5 GPa were assigned to stope-pillars resulted in RCF values within the expected range (1.2–1.4). Analyses for additional tunnels showed the same results. Thus, a Young's modulus of 0.6 GPa was chosen for the simulation of stope-pillars in ongoing simulations.

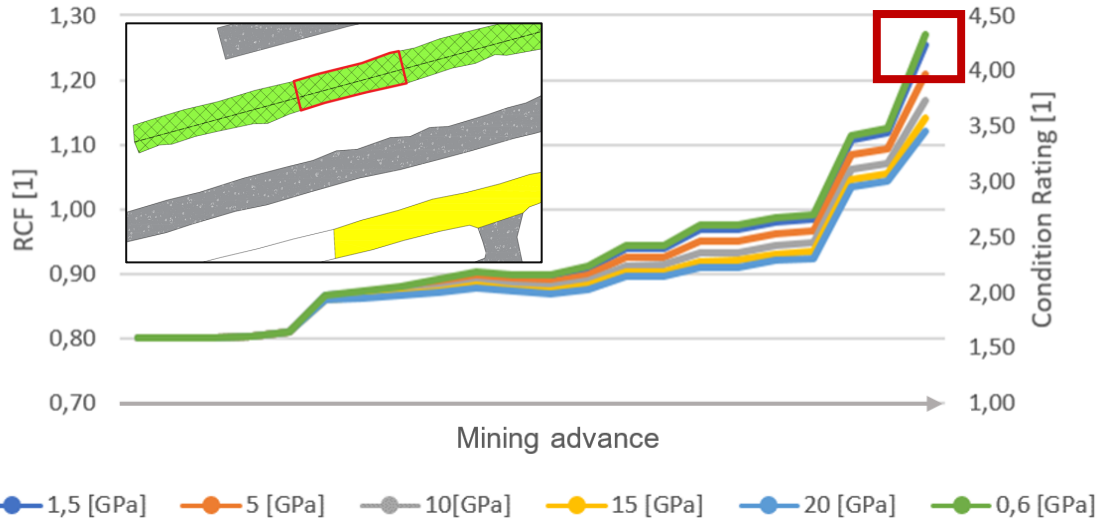


Figure 5. Effect of 'stope pillar' stiffness on the RCF. X-axis shows the mining advance. Left Y-axis gives the calculated RCF. Right Y-axis shows the scale for the condition rating. The red box indicates the observed tunnel conditions after the last mining step. The map shows the position of where RCF-calculation for that specific case was done.

Signs of rock pressure observed in the mine led to the assumption that a non-hydrostatic primary stress situation is present in the mine. The presumption was that the horizontal primary stresses must be lower than the vertical ones. The goal of the calibration was to prove that and to get a better image of the primary stress situation. Therefore, additional simulations were conducted using the new stope pillar Young's modulus. The primary stresses which were used for the first simulations were 28 MPa for the vertical and the horizontal stresses. For the further simulations the horizontal stresses were lowered to 18 MPa in both directions. The results show that the reduction of the horizontal stresses leads to an improved correlation between the RCF and tunnel condition rating. Figure 6 shows the calculated RCF value by the metre along the axis of a mine tunnel. The blue line indicates the RCF value for the non-hydrostatic primary stresses, and the red one for the hydrostatic case. The calculated RCF is in the range of the expected tunnel conditions, which were in this particular case the same for the whole tunnel, marked by a red box. The aberration at the start of the line can be explained with the complex mining sequence and model geometry. Another theory is that the rather bad conditions observed at the end of the tunnel may also have originated from a past high stress environment.

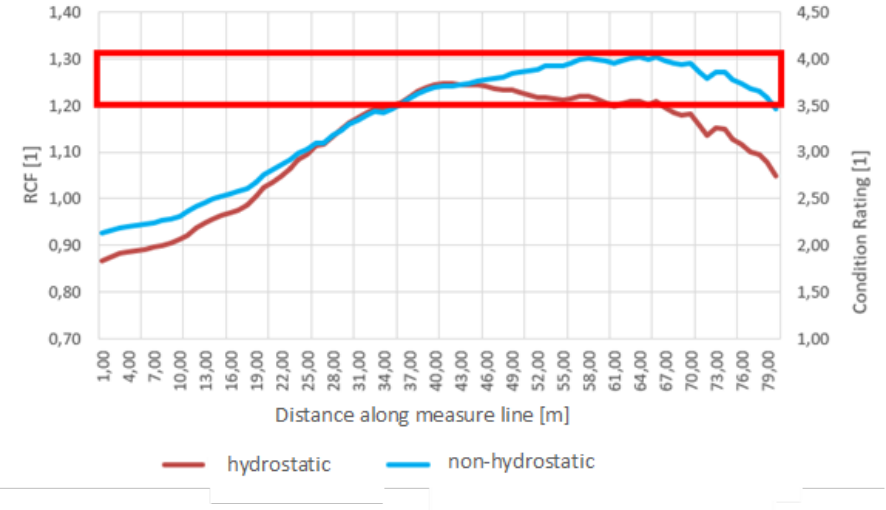


Figure 6. Comparison of hydrostatic (red) and non-hydrostatic (blue) primary stresses based on the correlation between RCF and tunnel condition rating.

The two particular cases regarding the pillars of Young's modulus and the primary cases demonstrate the applicability of a calibration based on the RCF and observed tunnel conditions. The final outcome from the Young's modulus calibration of pillars and primary stresses is shown in Table IV.

Table IV: Results of the model calibration

Parameter	
Young's modulus stope pillars [GPa]	0.6
Vertical primary stress [MPa]	28
Horizontal primary stresses [MPa]	18

The implementation of these parameters into the numerical simulations leads to a realistic model of the mine. This is needed to compare the two different future mine layouts.

Prediction of mining conditions for different mining layouts

The primary goal of the paper is to compare two different mining layouts that differ in the orientation of the stope axis. It is hypothesised that by rotating the stopes, geological structures could be handled better. Additional motivations therefore include operational and rock mechanical advantages related to the mining direction. An aspect which requires further investigation is the evolution of stresses and the conditions of the tunnels.

To answer these open questions numerical simulations are conducted. Based on the performed calibration, and the RCF–tunnel condition correlation, a prediction of tunnel conditions is feasible. The simulations including the two mining layouts are solved elastically and the RCF is calculated. Based on the results, it is possible to compare the two layouts regarding the loads of barrier pillars and abutments. Moreover, it is possible to predict the conditions of the tunnels based on the correlation between RCF and the tunnel condition rating. Furthermore, it is also possible to compare different mining sequences, either on a local basis or on a regional basis. Figure 7a shows a horizontal cut through stopes of the layout where the direction of the stope axis was changed. The major principal stresses are plotted. Figure 7b displays the same situation for the layout where the direction of the stope axis is not changed. Zones of high stresses can easily be indicated. In this particular case the loading of the barrier pillar (B5, black box) between the old and the future mining field is compared. The comparison clearly shows that the pillar stresses are higher if the currently used mining direction is applied in the new mining field; see Figure 7b.

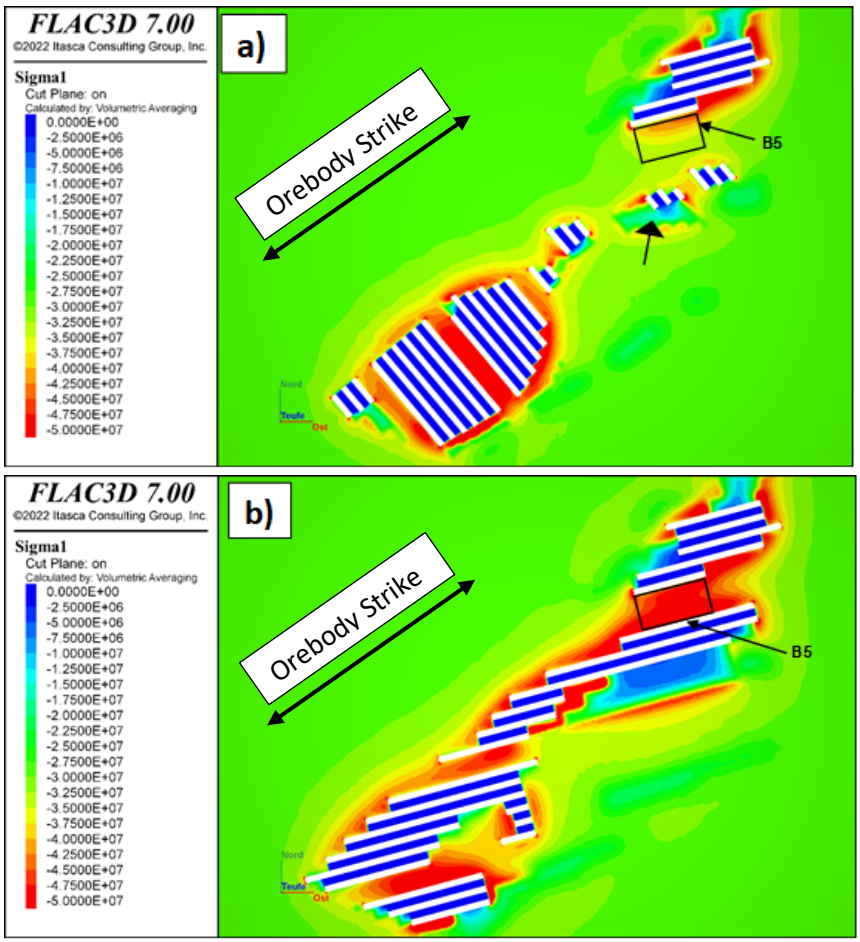


Figure 7. Stress redistribution (maximum principal normal stress) around the stopes for a) mine layout where stope orientation is perpendicular to strike direction of the deposit; b) mine layouts where stope orientation is along the strike direction of the deposit.

Another example where the RCF–tunnel condition criterion can be applied is the judgement of the applied regional mining sequence. Generally there are two mining methods, namely 'sequence 1' where mining of stopes is done in retreat and 'sequence 2' where it develops towards the deposit boundaries at the end of the mining field. The RCF was determined along a 20 m section of a long-term tunnel located at the entrance of the new mining field. It can be stated that the use of 'sequence 1' has advantages regarding long term stability. For quite a long period the RCF was on a low level, which indicated a good situation regarding tunnel conditions. This instance is shown in Figure 8, where the grey line represents 'sequence 1' and the yellow line' sequence 2'.

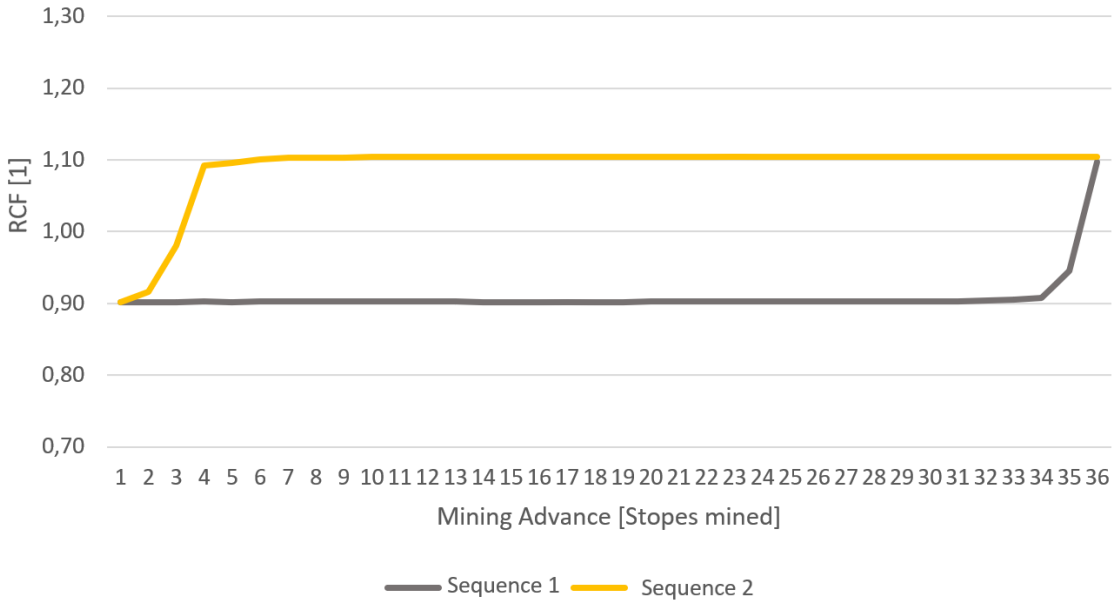


Figure 1. Situation for long term drifts based on the RCF–tunnel condition criterion.

Figure 9 shows the calculated RCF values of the two sequences for a period chosen in an adjusted RCF-tunnel condition diagram which is based on the diagram of Jager and Ryder (1999). For 'sequence 1' a typical RCF of 0.9 and for 'sequence 2' a typical RCF of 1.1 resulted. It is possible that different type of support is necessary to achieve 'good' conditions in the long-term drifts.

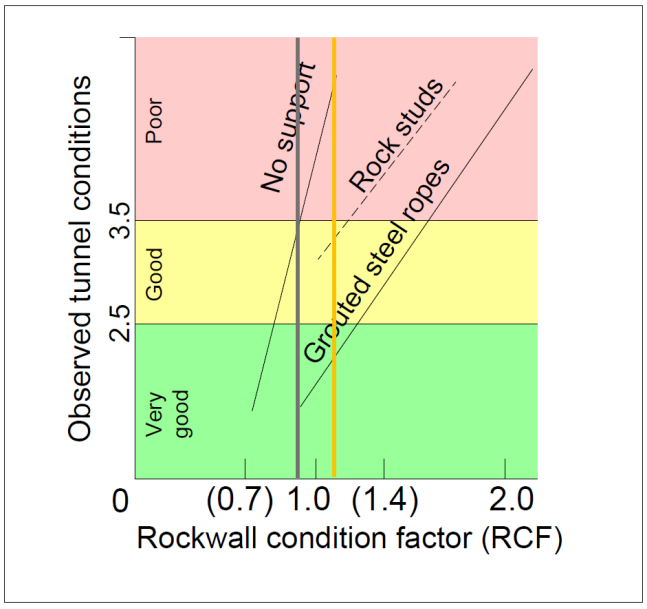


Figure 9. Typical RCF values for long term drift for 'sequence 1' (grey line) and 'sequence 2' (yellow line) an adjusted RCF-tunnel condition diagram which is based on the diagram of Jager and Ryder (1999).

In addition, other important results were found regarding:

- Local mining sequence
  - The local mining sequence should be from one side of a barrier pillar towards the next barrier pillar. In case stability problems occur, it is possible to sacrifice one stope to

create a larger barrier pillar. The neighbouring stope can only be mined if the previous one is backfilled.

- Pillar loadings
    - It was found that load acting on the barrier pillars with the new orientation tends to be lower because of the limited extension of the mining field.

CONCLUSION

This paper shows the applicability of the combination design criteria in mine planning based on field observations and numerical models. The base for such an approach is a proper monitoring program. The rating of tunnel conditions is a suitable tool to assess rock pressure conditions and should be done routinely to obtain a more accurate model. The calibration of the numerical simulations was straightforward and successful. Based on that it was possible to compare two future mine layouts regarding tunnel conditions and stresses.

In future it is suggested the model of the whole mine should be updated and calibrated on a regular basis. In this way confidence can be developed in the value of numerical rock engineering design tools based on design criteria which can be applied readily and are understood by the miners.

REFERENCES

(2019). Global Material Resources Outlook to 2060. Economic Drivers and Environmental Consequences. Paris, OECD Publishing.

Dassault Systèmes Simulia Corp. (2021). Abaqus CAE. Version 2022. Dassault Systèmes Simulia Corp.

Itasca (2023). FLAC3D. Version 7.0. Itasca. Available online at http://docs.itascacg.com/flac3d700/contents.html.

Jager, A. J./Ryder, J.A (1999). A handbook on rock engineering practice for tabular hard rock mines. Johannesburg.

Ladinig, Tobias/Wagner, Horst/Daborer, Andreas (2019). Effects of stoping activities on tunnel conditions in a deep, hard rock mine in Austria. In: Proceedings of the Ninth International Conference on Deep and High Stress Mining, Ninth International Conference on Deep and High Stress Mining. The Southern Africa Institute of Mining and Metallurgy, Johannesburg, 87–96.

Wagner, Horst/Froemmer, Thomas, Changing the mining method in an Austrian magnesite mine, 20th World Mining Congress and Expo, 2005, In: Mining and Sustainable Development (Publ: Geological Survey of Iran), S211-215

Wagner, Horst, (2019): Deep Mining: A Rock Engineering Challenge, Rock Mechanics and Rock Engineering, Vol. 52, No. 5, pp. 1417–1446.

Wiseman, N. (1979). Factors Effecting the Design and Conditions of Mine Tunnels. 01th ed. Chamber of Mines Research Organization. Johannesburg.



Patrick Gams

Junior Researcher
Montanuniversitaet Leoben

Patrick Gams is currently a PhD candidate at Montanuniversitaet Leoben, one of Europe's leading universities in mining and rock mechanics. His doctoral research focuses on design criteria in mining and numerical simulations under the supervision of Prof. Dr. Horst Wagner. He completed his master's degree in Mining Engineering in 2022 with a thesis titled "The Role of Pillars in Raise Caving." As the Chair of Mining Engineering and Mineral Economics at Montanuniversitaet Leoben, he is engaged in various industry projects, working on rock mechanics and mine planning for different operations.

Development of a multi-stage large excavation crusher chamber at Palabora mining company

M. Matsapola[1], R.B. Khumalo[1], V.C. Madanda[2], F.K. Mulenga[2]

[1]Palabora Mining Company, South Africa
[2]University of South Africa, South Africa

Palabora Mining Company (PMC) is extending its life of mine by deepening its operations from the Lift I cave, located 1200 m deep, to Lift II at about 400 m further below. An essential element of Lift II involves the implementation of two high-capacity jaw-gyratory crushers to improve production efficiency. In contrast to Lift I, which required four crushers to manage 1000 tons of ore every hour, Lift II combines this capability into two larger crusher chambers, with each crusher processing 2000 tons per hour. This allows PMC to reach its production target of 32 kilotons per day while enhancing underground operations. Developing the extensive crusher chambers (35 m in length, 30 m in height, 14 m in width) posed considerable geotechnical and operational challenges, necessitating meticulous planning, specialised equipment, and a multi-phase excavation strategy. In spite of the challenges encountered, such as equipment malfunctions, discrepancies from the intended mining configuration, and geological disturbances, the first crusher chamber successfully housed its crusher. In addition to this, no fatalities or injuries were reported during the development phase, demonstrating the success of the strategy. This paper provides valuable insights into the planning, excavation, and ground control of large underground chambers. This is to serve as a replicable framework for similar large excavations, especially in South Africa, where such developments are rare.

Keywords: Crusher chamber, large excavation, underground chamber, excavation stability, massive mining

INTRODUCTION

Palabora Mining Company (PMC), located in the Limpopo Province of South Africa, operates one of the world's leading block cave copper mines. The mine has been in operation since the 1960s, initially as an open-pit before transitioning to an underground block cave. PMC contributes significantly to the global copper market, producing copper along with by-products such as vermiculite, uranium, and magnetite (Nyarela *et al*., 2022). To sustain long-term operations and meet rising global copper demand, PMC is expanding from the Lift I cave, which operates at approximately 1200 m below surface, to Lift II, situated about 400 m deeper, as shown in Figure 1. This expansion is critical to maintaining production targets and optimising ore processing efficiency.

A key component of the Lift II infrastructure is the installation of two high-capacity jaw-gyratory crushers, each capable of processing 2000 tons of ore per hour (Maloma, 2016). This design replaces the setup of four smaller crushers used in Lift I and significantly increases throughput, thereby allowing PMC to meet its production target of 32 kilotons per day (ktpd). However, the development of these crushers required the excavation of large chambers in challenging underground conditions. Given the increased depth and the complex rock mass characteristics, a carefully engineered multi-stage excavation process was implemented to ensure the stability and effectiveness of these chambers.

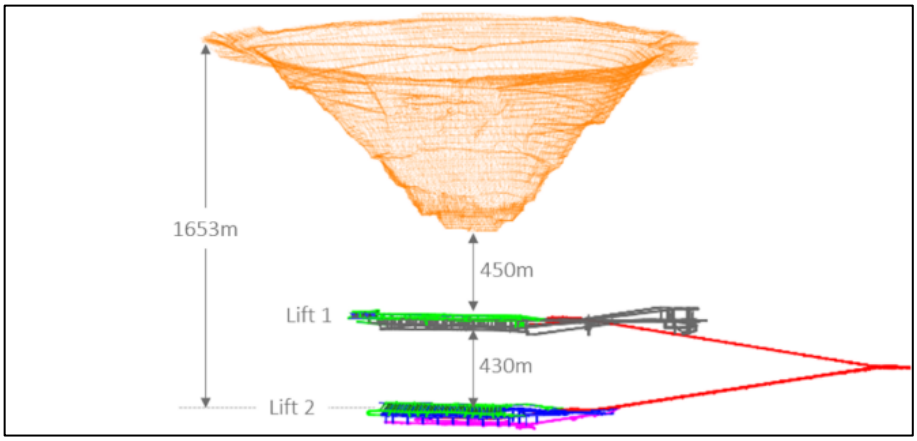


Figure 1. Schematic of PMC mine operation (Maloma, 2016).

The Lift II footprint spans three primary rock formations: Micaceous pyroxenite, fenites, and carbonatites, with dolerite dyke intrusions influencing ground conditions. The crusher chamber was developed in micaceous pyroxenite, between two dolerite dykes, where rock strength varies between 63 MPa and 320 MPa (Handley, 2017). Additionally, the Palabora orebody contains five major geological structures: the Central Fault, the South-West fault zone, the Tree Fault Zone, the Mica Fault Zone, and the Glimmerite Fault (Kuschke and Tonking, 1971; Sainsbury *et al.*, 2016). These geological structures pose geotechnical challenges that require careful excavation planning and ground control measures.

This paper provides a detailed account of the planning, excavation, and construction of the Lift II crusher chambers. Geotechnical considerations, excavation methods, and design strategies that ensured structural stability and operational efficiency are discussed. The insights from this project offer a replicable framework for large-scale underground excavations, particularly in deep-level block cave mining operations.

ENGINEERING INSIGHTS FOR LARGE UNDERGROUND EXCAVATIONS

The development of large underground excavations such as crusher chambers is a vital element of underground mining, especially in massive mining operations like block caving and sublevel caving. These chambers are vital for processing ore, ensuring efficient material handling, and reducing production delays. Nonetheless, their design and development pose considerable engineering challenges, such as stress redistribution, excavation instability, and support system selection. The following subsections highlight the significance of these excavations and present case studies that offer key lessons and best practices from similar global projects.

Importance of large excavations in mining

Large underground excavations are necessary for mining operations to be successful, particularly in complex and deep mining environments. They offer the space required for ore handling and infrastructure. According to Hoek and Brown (2005) and Barton *et al.*, (1974), underground excavations can be classified based on their purpose and durability into several types, including temporary mine openings, vertical shafts, and permanent mine openings. Temporary openings are used during development and are not reinforced for long-term use, while vertical shafts facilitate access for personnel, ore, and ventilation. Permanent mine openings include various infrastructures such as tunnels and chambers that support efficient material handling. Large excavations, like crusher chambers, are also classified as permanent mine openings. They are essential for operations in deep mines but require careful engineering to ensure stability. The stability and design of large excavations rely on various factors such as rock mass properties, stress conditions, sequencing of excavation, and the type of support system used (Lv, 2024; Elrawy *et al.*, 2020).

Large excavations present significant technical challenges due to their size and the stress redistribution they cause in the surrounding rock mass. According to Feng *et al*., (2014), each excavation can alter stress in nearby areas, depending on factors such as depth, rock structure, and excavation sequence. These changes can affect rock stability, potentially leading to rock falls or collapse if not properly managed. The Oyu Tolgoi Crusher #2 Chamber is one example of a large excavation developed at a depth of 1300 m with a stand-off distance of 280 m from the cave footprint (Sharrock *et al*., 2022). The development of this large excavation involved careful engineering and geotechnical analysis to manage stress redistribution and ensure the stability of the surrounding rock.

Challenges with large excavations

Large underground excavations pose considerable challenges owing to diverse geological and operational elements that influence their design and development. Key challenges entail maintaining stability, negotiating geological conditions, and choosing suitable excavation techniques. Hoek and Brown (2005) highlight the importance of minimising reliance on large support systems and conducting thorough geological monitoring. For example, super-large-section tunnels require careful method selection to manage rock deformation (Chen *et al*., 2024). High-stress hard rock formations can lead to stability issues that necessitate adjustments in excavation methods based on observed failures (Liu *et al*., 2024).

Even with meticulous planning, large excavations are still vulnerable to failure in the form of gravity-induced collapses, sliding wedges, and tensile or shear failures. This is because the redistribution of stress can surpass the strength of the host rock. For excavations in coastal areas with abundant water, it is crucial to consider the spatial variability of ground parameters, as this greatly influences structural stability and deformation trends (Xu *et al*., 2023). The existence of interlayer shear weakness zones in rock masses with columnar joints can complicate stability management and lead to different failure modes (e.g., wedge failure and planar sliding) during excavation (Zhao *et al*., 2022).

To reduce these risks, Hoek (2006) recommends employing numerical modelling to predict rock mass behaviour and adjusting support as needed. Effective excavation plans should include trial excavations, regulated blasting, prompt support installation, and continuous monitoring to enhance stability and success in large-scale excavations. Through tailored excavation strategies, comprehensive geological assessments, and continuous monitoring, engineers can address these challenges and enhance the stability and success of large-scale excavations.

Case studies and lessons from literature

This section presents a few case studies (see Table I) that provide valuable insights into the planning, development, and maintenance of large-scale underground excavations. These examples illustrate a variety of techniques and solutions applied in different mining projects. This facilitates the understanding of best practices and lessons learned in preserving the stability and security of large excavations.

Table I: Case studies and key lessons learned from large underground excavations

Case Study	Key Insights	Design and Mitigation Strategies	References
Ernest Henry Crusher Chamber	The chamber at 1000 m depth showed no adverse ground conditions after a feasibility study.	Adoption of civil engineering standards, stringent quality control for excavation and support installation.	Campbell *et al*., (2013)
Tangshan Mine	Extra-large chamber construction in solid backfill mining with active support measures.	Bolting, anchor cables, reinforced floor structures, and numerical analysis using ABAQUS to control rock mass deformations.	Feng *et al*. (2014)
New Level Mine – El Teniente	Geomechanical evaluation of large excavations under high stress led to recommendations for crusher caverns.	Development of empirical, 2D, and 3D models to assess mechanical responses to excavation-induced stress.	Hormazabal *et al*., (2014)
Longhole Stoping Excavations	Large spans (15 m x 15 m) required specialised support design.	Integration of empirical rock mass classification, stability graphs, and numerical modelling for stability validation.	Zvarivadza and Sengani (2018)

The above tabulated case studies offer practical examples and perspectives that can guide the planning and execution of large underground excavations. Applying these concepts and solutions helps address the risks and challenges of complex underground environments, leading to safer, more stable, and efficient operations in future projects.

EXCAVATION METHODOLOGY

This section describes the methodological approach adopted to ensure the safe excavation and support of the crusher chambers at Lift II. It emphasises the positioning, excavation sequence, modelled excavation strategy, and equipment selection for optimal performance and safety. The excavation sequence and support design were modelled using FLAC3D.

Positioning using geotechnical information

Positioning crusher chambers based on geotechnical information is essential for stability and operational efficiency. For the Lift I cave feasibility study, exploration boreholes were drilled from the surface into the ore body and surrounding rock, extending below the Lift I level for additional data. This information was analysed for geotechnical assessment, cost evaluation, and assessing the feasibility of underground mining. Similarly, exploration holes for the Lift II cave were drilled from Lift I, with supplemental holes ensuring complete coverage of the Lift II footprint (Maloma, 2016).

A thorough geotechnical evaluation was performed. It comprised core logging, structural mapping, rock mass characterisation, empirical and kinetic stability analysis, and numerical modelling (FLAC 3D). These tools were used for support design and quantifying the stresses when the cave has fully propagated (Sainsbury, 2017; Masole, 2018). Additionally, benchmarking of the size of the chamber and its possibility to be developed, including having more than one tipping point, was conducted against chambers at Northparkes Mine in New South Wales, Australia. At PMC, the original mine design positioned the chamber within a dolerite dyke and foskorite contact; see position 1 in Figure 2. This position would have created sympathetic jointing, resulting in a weak rock mass that is not ideal for large chamber excavations. Position 2 (see Figure 2) would have had most of the chamber within the dolerite dyke and a similar contact as in position 1. Although dolerite is recognised for its significant strength, its brittle characteristics render it susceptible to rock bursts. Earlier mining experience

suggested that dolerite dyke contacts might function as weak planes, increasing the risk of seismic activity and displacement (Manouchehrian and Cai, 2016; James *et al.*, 2007). Consequently, additional support was considered essential.

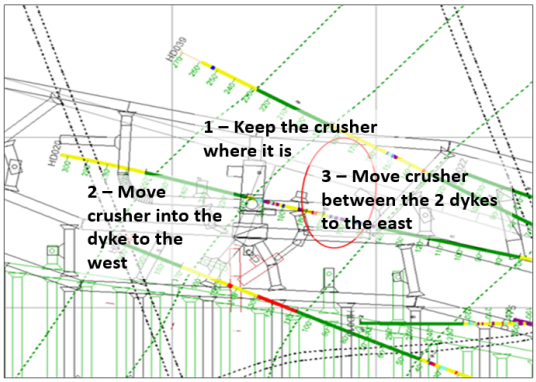


Figure 2. Options considered for the positioning of the crusher chamber at PMC.

Subsequent assessments led to a slight modification of the position and orientation of the chamber to avoid contact between the dolerite dyke and foskorite (see position 3 in Figure 2). These changes improved excavation stability over time. The geotechnical evaluation also provided insights into the support strategies needed to maintain stability for the life of the mine. It indicated that the undercutting method could elevate vertical stresses to two to three times the existing in situ stress. Numerical modelling identified a secure location for the crusher chamber, ensuring it remains clear of abutment stress effects (Sainsbury, 2017; Masole, 2018).

Proposed excavation strategy

The excavation of the crusher chamber was performed in a top-down sequence to minimise unsupported spans and ensure ground stability. The excavation process was divided into multiple stages to allow for systematic support installation and reduce the risk of ground instability during mining. The mining sequence for the crusher chamber followed the benching method and was divided into the following stages, as depicted in Figure 3(a).

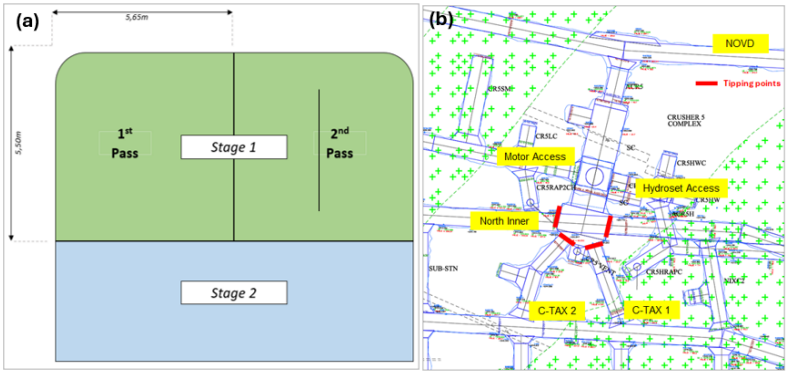


Figure 3. Crusher chamber development at PMC: (a) Mining sequence, (b) Access and tipping layout.

Stage 1 – Initial Excavation: The first pass involved creating a flat tunnel at the top of the chamber, measuring 5.5 m in height, 5.65 m in width, and 55 m in length. This was accessed via the North Inner, crusher tipping access (C-TAX) 1 & 2 tunnels as shown in Figure 3(b). Primary support was installed immediately, including a 50 mm layer of fibre-reinforced shotcrete followed by 2.4 m long roof bolts. The second pass involved slipping the remaining area, but this could only begin after installing two rows of 12 m cable anchors to secure the span.

Stage 2 – Bench Development: Bench development was carried out towards the North Outer Ventilation Drive (NOVD) access, with a 90° orientation and 11.3 m width. This step was completed in successive blasts, with each blast progressively increasing the bench height until it reached the NOVD access. Protective cable anchors were installed in advance to prevent damage during holing.

Stage 3 – Face Creation: After holing through to the NOVD access, excavation continued with three faces (south, east, and west), which were later merged into a single face. A 90° ramp, 11.3 m wide, was mined towards the south to further access the crusher chamber. *Stage 4 – Ramp Stripping and Ripping*: The ramp to the south was stripped, and the excavation process moved towards the southern wall of the chamber.

Stage 5 – Additional Benching: Additional benching at -11° was carried out to provide a safer and more controlled environment for further excavation.

Stage 6 – Crusher Motor Access: Excavation continued from the Crusher Motor Access shown in Figure 3b and Figure 4, with ripping and blasting on both the north and south sides of the excavation.

Stage 7 – Crusher Hydro-set Access: The Crusher Hydro-set Access was excavated, and the ground in the northern and southern sections was ripped and blasted to the required dimensions.

Stage 8 – Silo Excavation: The final stage involved the excavation of the Crusher 5 silo using drop-raising techniques, creating a 6 m diameter and 14 m long silo. This silo was connected to the sacrificial tunnel at the base of the Crusher 5 Complex. Figure 4 depicts these stages in the crusher chamber excavation process and the evolution of the chamber over time.

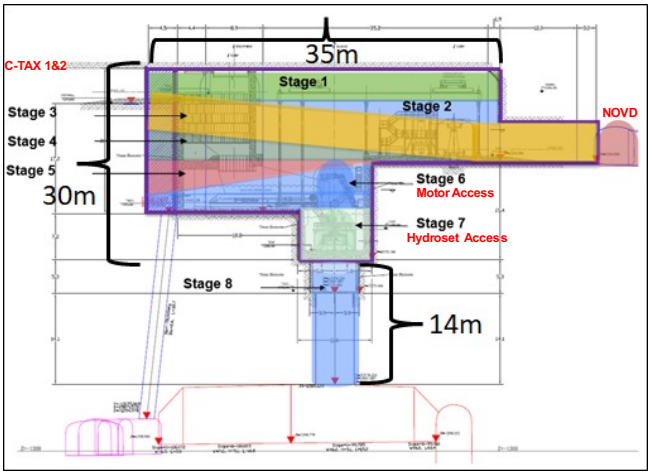


Figure 4. Crusher chamber with multiple mining stages (sequence) with dimensions.

Modelled excavation strategy

The sequence for excavating the crusher chamber was included in the numerical model. Although a specific excavation sequence was not provided, it was determined that the most probable method would be to 'bench' from the top down. As each bench of the crusher chamber is excavated, ground support was installed in a consecutive manner. The five excavation steps for the crusher chamber are illustrated in Figure 5. After the crusher chamber was finished, the propagation of Lift II cave was also simulated progressively in several stages.

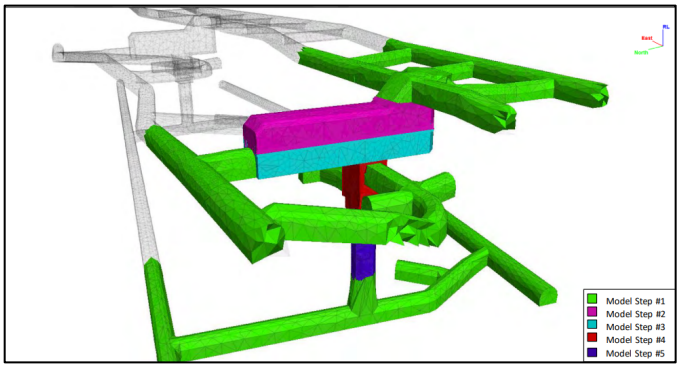


Figure 5. Crusher chamber modelled excavation strategy.

Equipment selection

Selecting the right equipment for developing the crusher chambers was essential for achieving flexibility and reducing costs. The process considered excavation dimensions, equipment functionality, and material handling effectiveness to meet production targets on time while minimising expenses. Equipment was carefully chosen for excavation, transportation, and ground support to ensure safe operations.

Primary excavation equipment included jumbo drills, haul trucks, load-haul-dump (LHD) machines, and cable bolters. Jumbo drills mounted on diesel platforms featured dual booms for rock excavation and support installation. Haul trucks transported up to 30 tons of blasted material from the excavation area to the stockpile. A combination of 17-ton and 14-ton LHD machines assisted in loading and conveying the material, while cable bolters reinforced excavation stability.

In addition to primary excavation equipment, several auxiliary machines assisted in the development process. Shotcreters/Spraymechs applied shotcrete for structural integrity, and agitators delivered pre-mixed shotcrete, increasing efficiency. Integrated Tool carriers moved materials and assisted in personnel transport. Equipment availability was crucial in production planning, as any downtime could affect efficiency and project deadlines.

RESULTS

This section demonstrates effective modelling outcomes and reliable ground support performance, which are essential for maintaining stability and safety within the crusher chamber.

Modelling results

Geotechnical modelling is a critical step in developing large excavation chambers. In this project, one of the key parameters used when modelling was the stress changes in the chamber during three key stages: before undercutting, during the undercutting phase, and at the initiation of cave formation. The effects of cave propagation and subsequent breakthrough into Lift I were also considered. Figure 6(a) and Figure 6(b) illustrates the progression of maximum principal stress and rock mass damage around the crusher chamber, both before and after cave propagation. Upon completing the excavation of the crusher chamber, the maximum principal stress near the excavation site decreased to low levels (10 – 20 MPa), indicating that the rock mass had yielded. In contrast, areas beyond the immediate vicinity of the excavation exhibited high magnitudes of maximum principal stress, ranging between 80 and 90 MPa. As cave propagation continued, the volume of both low-stress and high-stress rock mass surrounding the crusher chamber increased. At the end of the excavation process, minor to moderate rock mass damage was observed in the hanging wall, and moderate damage was noted in the sidewalls. This damage correlates with the regions of low maximum principal stress. As cave propagation progressed, the extent of moderate to highly damaged rock mass in both the hanging wall and sidewall grew. The depth of yielding in the sidewalls was estimated to range from 2.5 to 3.0 m.

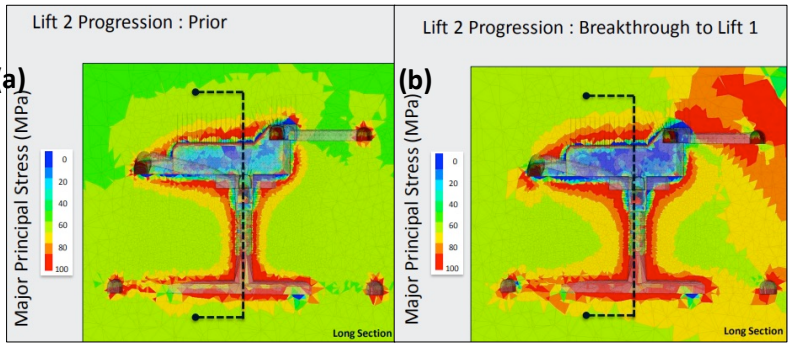


Figure 6. Stress changes around the crusher chamber

Ground support performance

Support design for the crusher chambers was based on benchmark data from Lift I. The geology of the northern footprint, where both Lift I and Lift II crushers are located, is similar, with stable ground conditions observed in the Lift I crushers since their installation. However, the Lift II chambers are slightly larger due to the increased performance capacity of the new crushers, which are twice the size of those in Lift I.

Support requirements were assessed through FLAC 3D, a review of previous 3D numerical modelling, and new 2D modelling (Sainsbury, 2017). These analyses indicated that the caving process would not significantly affect the crusher stations. However, excavation would cause stresses near the chamber to increase to approximately 68 MPa, nearly double the virgin stress of 37 MPa (Handley, 2017). The wedge analysis conducted by Gash (1997) suggested that the potential wedges in the sidewalls would be long and thin, extending no more than 3 m. On the roof, although wedges would be longer, they would not pose a significant risk due to clamping effects. Table II provides a summary of the specific support requirements for Lift II.

Table II: Lift II support requirements

Feature	Span	Cable Anchor Spacing	Cable Anchor Length	Support Spacing	Bolt Length	Welded Mesh	Shotcrete Type & Thickness
Crusher Chamber	11.3 m	2.0 m	12.0 m	1.4 m	2.4 m	2.0 m x 4.0 m x 5.6 mm	FRS 50 -150 mm

The support system recommended for the Lift I crushers, and adapted for Lift II, included:

- 100 mm of fibre-reinforced shotcrete (fibre-crete) with 45 MPa strength.
- Off-surface rock support straps, commonly referred to as OSRO straps for added stability.
- 2.4 m long 20 mm resin rebar bolts installed at 1 m spacing in the roof and sidewalls.
- 9 m long mechanical end-anchored cable anchors in the roof at 2 m spacing.
- 12 m long cable anchors in the sidewalls at 2 m spacing.

The effectiveness of reinforcement was evaluated by measuring the elongation of roof bolts and cable anchors, which is defined as the difference in displacement between the collar and the toe of the roof bolt or cable anchor. The elongation of solid rebar roof bolts and twin-strand cable anchors is illustrated in Figure 7(a) and Figure 7(b), respectively. Generally, the elongation of solid rebar roof bolts and cable anchors was less than 25 mm around the crusher chamber. However, when installed in transgressive carbonatite (TCB), the elongation significantly increased. In TCB, the elongation of roof bolts reached up to 60 mm, while cable anchors experienced elongation of up to 80 mm. This increased support in TCB can be attributed to its geological properties, which cause greater rock deformation and heightened stress on the reinforcement systems.

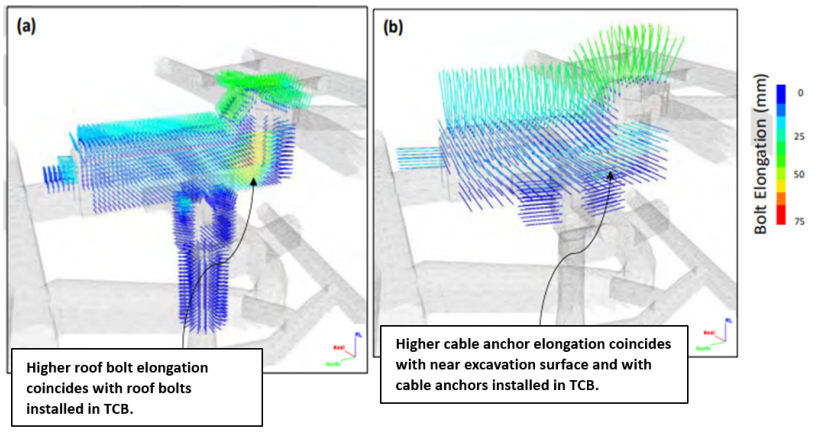


Figure 7. Roof bolt and cable anchor response as a means of ground support.

The forces exerted by solid rebar roof bolts are illustrated in Figure 8(a), while the forces from the twin-strand cable anchors are shown in Figure 8(b). Both sets of forces account for a factor of safety (FoS = 2.0) by reducing the yield capacities of the bolts, which is reflected in the different force scales used. As cave propagation progressed, the force exerted by the solid rebar roof bolts did not exceed 30 kN, and the force from the twin-strand cable anchors did not exceed 90 kN. The yield capacities for the solid rebar roof bolts and twin-strand cable anchors were 210 kN and 400 kN, respectively. Therefore, this design was considered an overdesign, ensuring the maximum performance of the support units, long-term stability, and enhanced safety.

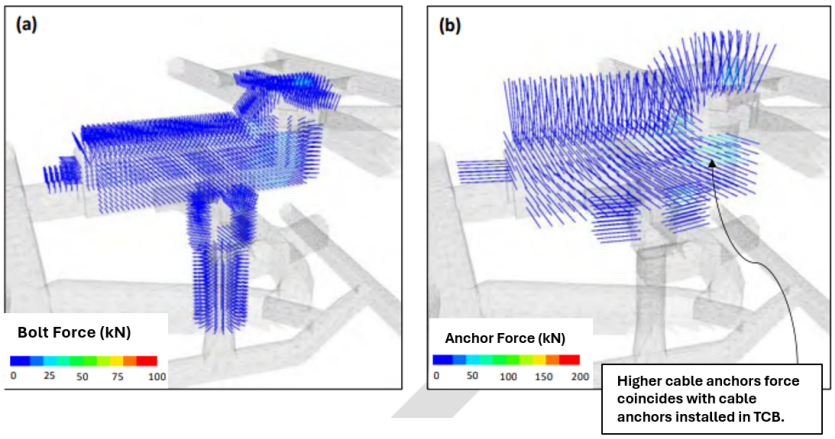


Figure 8. Roof bolt and cable anchor yield capacities.

The support design for the Lift II crusher chambers was informed by the modelled excavation design, ensuring that the structural integrity and stability of the chambers were maintained throughout the excavation process. This approach allowed for effective management of stress redistribution and enhanced the overall safety of the operation, reinforcing the success of the project in meeting its engineering and safety goals.

CHALLENGES ENCOUNTERED AND SOLUTIONS IMPLEMENTED

Several challenges arose during the excavation of the crusher chambers, necessitating adaptive strategies:

Ground Conditions
Although cover drilling was done for the chamber prior to its development, unexpected joints were exposed leading to overmining due to the large-scale nature of the excavation. The presence of joints in the rock mass led to energy losses during blasting creating tight spots with the rock mass remaining intact. Consequently, undermining occurred in certain areas. Targeted rehabilitation strategies, including additional bolting and re-shotcreting, were employed to address overmining. For undermining, secondary blasting had to be carried out with the next blast.

Equipment Breakdowns
The critical equipment for the chamber development were the LHDs, Jumbo Drills and Spraymech (shotcreters). However, due to ageing of the equipment, operational efficiency was impacted. Dedicated critical equipment were prioritised based on their age and reliability over the other mining activities. This was to ensure reliable critical equipment are used to improve operational efficiency.

Mining Layout Deviations
Face marking plays an important role for achieving desired mine layout as it directly affects the drilling and charging-up of shot holes. Unanticipated deviations from marking of shot holes were experienced and sometimes created undermining and overmining similar to as explained above. To remedy this, after each blast and upon installation of primary support, survey profiling was conducted by surveyors to identify high level mining layout deviations. For the identified deviations, secondary blasting was recommended and conducted. However, if there were no mining layout deviations, a survey mark-up was carried out and face marking proceeded. A cavity monitoring system scanner was used for continuous geotechnical and survey monitoring after every third blast. This was to ensure that the excavation plan of the chamber was maintained.

CONCLUSION

The successful development of the multi-stage large excavation crusher chambers at PMC represents a significant milestone in deep-level block cave mining. The project showcases a replicable methodology for designing, excavating, and stabilising large underground chambers, contributing to industry best practices. Upon completion of the first crusher chamber, the installed crusher achieved stable operations with no reported safety incidents, demonstrating the effectiveness of the excavation and support strategies. This project offered various key operational and project management lessons that can enhance the performance of future mining projects:

- Comprehensive planning is vital and includes careful choice of equipment, careful design of support systems, and extensive geological study.
- The stability of the chamber and the safety of the workers, particularly when the crusher is in operation, depend on strong support systems like shotcrete, cable bolts, and roof bolts.
- Regular inspections and stringent quality control measures during excavation are necessary to maintain operational standards and resolve challenges quickly.
- Timely decision-making and smooth operations depend on effective communication and collaboration among all deciplines involved.

While progress persists on the second crusher chamber in the Lift II cave, new and better technological innovations (an underground drone) have been implemented for quick and efficient scanning of excavations. The approaches used in this project consistently offer important insights for enhancing underground infrastructure, especially in South African mining. The insights gained from this project—covering areas like planning, support system design, resource optimisation, and safety management—can greatly improve the productivity, safety, and sustainability of upcoming mining projects. Mining operations can effectively manage challenges, maximise resource use, and guarantee project success by putting these insights to use.

ACKNOWLEDGEMENTS

The authors express their appreciation to Palabora Mining Company for the chance to present their work and expertise. Furthermore, the authors convey their sincere gratitude to their colleagues at Palabora Mining Company and at the University of South Africa for their constructive inputs. Permission to use data and access necessary equipment for this research is also acknowledged with sincere gratitude.

REFERENCES

Barton, N., Lien, R. and Lunde, J. (1974). Engineering classification of rock masses for the design of tunnel support. *Rock Mechanics*, vol. 6, no. 4. pp. 136-189

Campbell, A.D., Lilley, C.R., Waters, S. and Jones, P.A. (2013). Geotechnical analysis and ground support selection for the Ernest Henry crusher chamber. *Proceedings in the Ground Support 2013 Conference, 13-15 May 2013.* Potvin, Y., Brady, B., (eds.). Australian Centre for Geomechanics. Perth, Australia, pp. 437-450

Chen, Y., Geng, X., Li, J., Zhang, M., Zhu, C., Cai, M., Zhao, W., and Wang, T. (2024). Excavation method optimization and mechanical responses investigating of a shallow buried super large section tunnels: a case study in Zhejiang. *Dental Science Reports*, vol. 14, p. 6281

Elrawy, W.R., Abdelhaffez, G.S. and Saleem, H.A. (2020). Stability assessment of underground openings using different rock support systems. *Rudarsko-geološko-naftni Zbornik*, vol. 35, no. 1. pp. 49–63

Feng, J., Meng, L., Jixiong, Z., Xiexing, M. and Zhan, L. (2014). Construction and stability of an extra-large section chamber in solid backfill mining. *International Journal of Mining Science and Technology*, vol. 24, pp. 763-768

Gash, P. (1997). Palabora Copper. *Internal Report*. Palabora Mining Company, Unpublished

Handley, M. (2017). Palabora stress measurement report. *Internal Report*. Palabora Mining Company, Unpublished

Hoek, E. (2006). Practical rock engineering. *Evert Hoek Consulting Engineer Inc.*, North Vancouver, British Columbia

Hoek, E. and Brown, E.T. (2005). Underground excavations in rock – Revised First Edition. *Institution of Mining and Metallurgy*, CRC Press, Taylor & Francis Group, Boca, Raton, London, New York

Hormazabal, E., Pereira, J., Barindelli, G. and Alvarez, R. (2014). Geomechanical evaluation of large excavations at the New Level Mine – El Teniente. *Proceedings in the International Symposium on Block and Sublevel Caving,* Santiago, Chile, 05-06 June 2014, pp. 486-500

James, J.V., Rangasamy, T. and Petho, S.P. (2007). Excess Shear Stress Analysis of Seismicity Associated With Dykes. *In Deep Mining 2007: Proceedings of the Fourth International Seminar on Deep and High Stress Mining*. Australian Centre for Geomechanics, pp. 21-30

Kuschke, O.H. and Tonking, M. (1971). Geology and mining operations at Palabora Mining Company Limited, Phalaborwa, NE Transvaal. *Journal of the Southern African Institute of Mining and Metallurgy*, vol. *72,* no.1. pp.12-23

Liu, X., Xu, D., Jiang, Q. and Ma, X. (2024). Excavation response and reinforcement practice of large underground caverns within high-stress hard rock masses: The case of Shuangjiangkou hydropower station, China. *Tunnelling and Underground Space Technology*, vol. 147, p. 105698

Lv, B. (2024). Analysis of the influence of rock mechanics variables on the stability of tunnel surrounding rock based on engineering mathematics applications. *Journal of Combinatorial Mathematics and Combinatorial Computing,* vol. 122, pp. 173-184

Maloma, M.P. (2016). PMC Lift II mining project overview no. 8. *Internal Report*. Palabora Mining Company, Unpublished

Manouchehrian, A. and Cai, M. (2016). Influence of weak planes on rockburst occurrence. *In 3rd International Symposium on Mine Safety Science and Engineering*, pp. 12-17

Masole, N., 2018. Ground Support Design of the Lift II East Crusher Chamber. *Internal Report*. Palabora Mining Company, Unpublished

Nyarela, M.S., Khumalo, R.B. and Nemathithi, R.C. (2022). Drawpoint loading optimization strategies in block caving: A case study of Palabora Mining Company. *Journal of the Southern African Institute of Mining and Metallurgy*, vol. 122, no. 11, pp. 639-646

Sainsbury, D.P. (2017). Numerical modeling of Palabora Lift II crusher chambers. *Internal Report.* Palabora Mining Company, Unpublished

Sainsbury, D.P., Sainsbury, B.L., Paetzold, H.D., Lourens, P. and Vakili, A. (2016). Caving-induced subsidence behaviour of lift 1 at the Palabora block cave mine. In *Seventh International Conference & Exhibition on Mass Mining. Australasian Institute of Mining and Metallurgy (AusIMM)*. Sydney, Australia

Sharrock, G.B., Ooi, J. and Baasanjav, B. (2022). Geotechnical analysis and ground support selection for the Oyu Tolgoi crusher chamber #2. Australian Centre for Geomechanics, *Potvin, Y., (Eds.), Proceedings in the Caving 2022 Conference, Adelaide, Australia, 30 August – 1 September 2022*, pp. 227-240

Xu, Z., Guo, S., Guo, L., Guo, P., Ding, H., Liu, K., Xu, B., Wu, B., Wu, W. and Wang, Y. (2023). Stability analysis of super-large special-shaped deep excavation in coastal water-rich region considering spatial variability of ground parameters. *Water*, vol. 16, no. 1, p. 98

Zhao, D., Xia, Y., Zhang, C., Tang, C., Zhou, H., Liu, N., Singh, H. K., Zhao, Z., Chen, J. and Mu, C. (2022). Failure modes and excavation stability of large-scale columnar jointed rock masses containing interlayer shear weakness zones. *International Journal of Rock Mechanics and Mining Sciences*, vol. 159, p. 105222

Zvarivadza, T. and Sengani, F. (2018). Support design for large chamber excavations: Case study of mechanized deep to ultra-deep level gold mining. American Rock Mechanics Association, *Proceedings in the 52nd US Rock Mechanics / Geomechanics Symposium, Seattle,* Washington, USA, 17-20 June 2018



Mohlapachila Matsapola

Mining Superintendent
Palabora Mining Company

I am a results-driven Mining Professional with a proven track record of success in managing complex mining operations and projects, leading cross-functional teams and implementing process improvements that drive efficiency, safety and productivity. With 12 years extensive experience combined in underground deep-level gold, and block caving in copper mines I possess a unique blend of project management skills, technical expertise, and leadership acumen.

Throughout my career, I have grown through the mining ranks. In addition, I have held technical roles such as Strata Control Officer and Drill & Blast Engineer for the Palabora Mining Company Lift II Expansion Project. As a seasoned mining professional, I hold a B.Tech Mining Engineering Degree, Mine Manager's Certificate of Competency and Strata Control Certificate. I am serving as a PROTO Captain and affiliated with Association of Mine Managers South Africa (AMMSA).

Effect of pyroxenite layers on the strength of UG2 pillars

T.J. Maphosa and B.P. Watson

University of the Witwatersrand, South Africa

The Bushveld Complex in South Africa is a stratified igneous formation stretching approximately 350 km from east to west. The platinum group metals are found in two gently sloping, narrow ore bodies known as the Merensky and Upper Group 2 (UG2) Reefs. This paper focused on the UG2, which is essentially a chromitite reef with pyroxenite layers of varying thicknesses. Most shallow-depth UG2 operations use a bord and pillar mining method. Extensive research has been carried out to determine the strength of these pillars. Laboratory tests indicate that pyroxenite is stronger than chromitite and possesses different geomechanical properties. The impact of these pyroxenite layers on pillar strength and behaviour remains unknown. This study investigated the effects of these layers using FLAC3D numerical modelling, calibrated from laboratory tests. Importantly, the test data was not downrated as the research took the form of a sensitivity analysis. The results showed a strengthening effect of pyroxenite on UG2 pillars of over 30%. An equation has been developed to determine the strengthening effects as a function of the percentage of pyroxenite in the pillar. The models showed that little damage occurred in the foundations at 100% chromitite, suggesting reasonable results could be obtained using metal platens in a laboratory. It is recommended that further studies be done using carefully prepared laboratory samples to confirm this research.

Keywords: chromitite pillars, UG2 pillars, pillar modelling, strain softening

INTRODUCTION

The Bushveld Complex in South Africa is a vast layered igneous formation stretching approximately 350 km from east to west (Figure 1). This complex contains concentrated platinum group metals in two shallow-dipping, tabular ore bodies known as the Merensky and UG2 Reefs. This paper focused on the UG2.

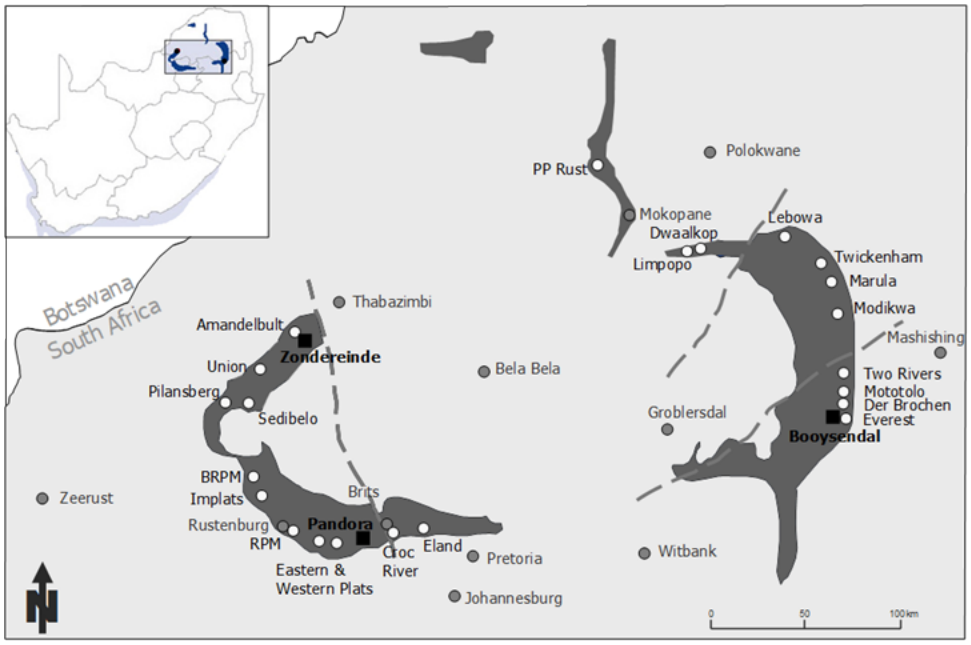


Figure 1. The extent of the Bushveld platinum exposure in South Africa (Northam Platinum Limited, 2020).

Most shallow-depth UG2 operations are mined using a bord and pillar method. These mines, therefore, rely heavily on pillars for support. Much work has been done to determine pillar strength (Watson, 2021a, 2021b and 2024a). UG2 pillars generally consist of chromitite interspersed with pyroxenite layers of variable thicknesses (Figure 2). Laboratory tests show that pyroxenite is stronger than chromitite and has different geomechanical properties (Maphosa, 2021; Watson *et al*., 2024b). The effects of these pyroxenite layers on pillar strength and behaviour are unknown. Pegmatoid is often found near the base of UG2 pillars. It was found to have geotechnical properties like chromitite (Watson *et al*., 2024b) and could therefore be considered chromitite for modelling purposes. This research was done to determine the effects of various thicknesses of pyroxenite as a percentage of the pillar height using FLAC3D (Itasca, 2019) models. The models were calibrated using laboratory tests performed on the reef and foundation rock types.

The Platmine formula is a pillar strength formula developed through a back-analysis of stable and failed UG2 pillars on the Bushveld platinum mines to provide a strength estimation suitable for the UG2 (Watson *et al*., 2024c). Historical pillars in the Bushveld complex were designed using formulas that were developed for other rock types. This resulted in oversized pillars locking away precious resources in the pillars. The Platmine formula is given in Equation 1.

$$Pillar\ strength = Kw_e^{\alpha} h_e^{\beta} \qquad \textit{Equation 1}$$

Where: $h_e \approx \left[1 + 0.2692\left(\frac{w}{h}\right)^{0.08}\right]$ (when there is a gully on one side of the pillar); $w_e \approx {}^{2wL}/_{(w+L)}$; K = in situ cube strength ; w = pillar width; h = pillar height; L = pillar length; α = 0.71; β = 0.71 and K=82 MPa.



Figure 2. Typical UG2 pillar assessed in the PlatMine formula (Watson et al.*, 2021a).*

LITERATURE REVIEW

Underground measurements on Merensky Reef pyroxenite (Watson *et al.*, 2006) and UG2 chromitite pillars (Watson *et al.*, 2021b) suggest that pyroxenite pillars are significantly stronger than chromitite pillars. This strength variation is also confirmed by the Merensky and UG2 pillar formulae shown in Figure 3 (Watson *et al.*, 2021a). Triaxial tests conducted on pyroxenite and chromitite samples obtained from Impala Platinum Mine (Maphosa, 2021) confirm these strength variations (Figure 4).

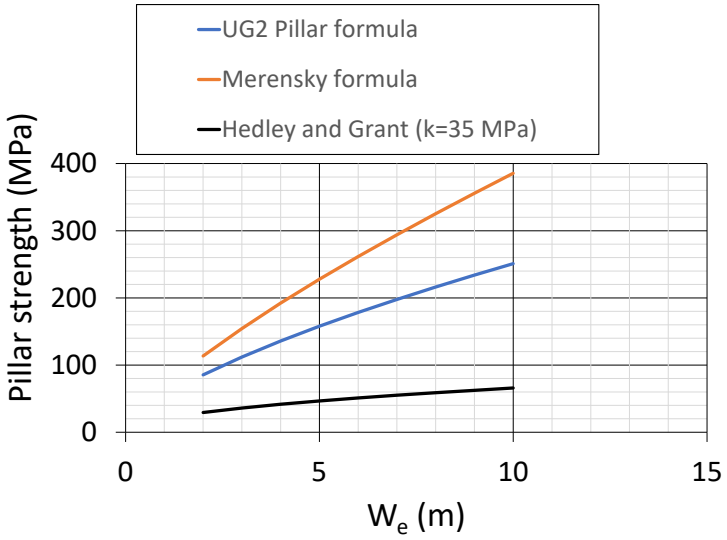


Figure 3. Comparison between the PlatMine formula (UG2), Merensky formula (Watson et al.*, 2008) and Hedley and Grant formula (1972) for square pillars of 2 m height (Watson* et al.*, 2021a).*

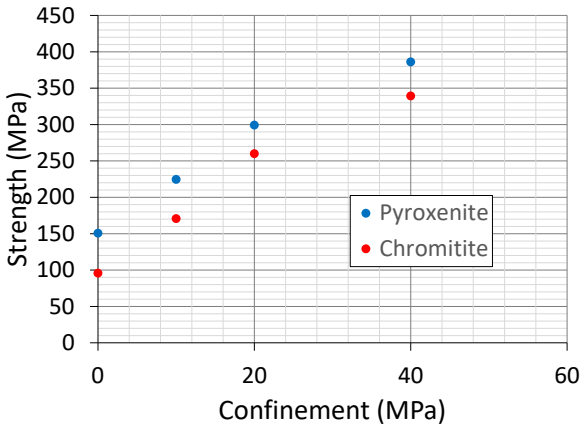


Figure 4. Comparison between strength results of chromitite and pyroxenite from Impala Platinum (after Maphosa, 2021).

The commonly used Hedley and Grant (Hedley, 1972) formula with a downrated k-value (Malan and Napier, 2011) underestimates pillar strength compared to field observations (Roberts and Esterhuyse, 2021; Watson *et al.*, 2021b). This observation is also confirmed by the comparatively lower strength provided by the formula in Figure 3 (Watson *et al.*, 2021a). A proper understanding of UG2 pillar strength will allow for better exploitation and possibly higher extraction ratios while maintaining safe working conditions (Watson *et al.*, 2024c). The PlatMine pillar strength formula inherently includes layers of pyroxenite of up to 43% of the pillar height (Watson *et al.*, 2021b), but the effect of pyroxenite on the behaviour of UG2 pillars has not been studied. This research was done to quantify the effect of the pyroxenite layers on UG2 pillar strength through numerical simulations calibrated by laboratory tests with post-failure behaviour.

LABORATORY TESTING

The following laboratory tests were performed on chromitite, pyroxenite, and anorthosite samples obtained from the UG2 area to determine the input parameters for the models:

- Uniaxial compressive strength (UCS) tests are used to establish the basic rock strength parameters without post-peak behaviour.
- Brazilian tensile (UTB) tests were done without strain measurements, to determine the tensile strength of the rock samples; and
- Triaxial compressive strength (TCS) tests were conducted at confinement levels of 10 MPa, 20 MPa, and 40 MPa for each rock type except anorthosite, which was tested up to 30 MPa (due to oil leakages at 40 MPa).

Testing was conducted using the MTS 815 servo-controlled stiff testing machine. Radial strain control was applied at a deformation rate of 0.09 mm/min to investigate post-peak failure behaviour. All samples were prepared and tested following International Society of Rock Mechanics (ISRM) standards (Ulusay and Hudson, 2007). The results for peak and residual strengths are presented in Figures 5 and 6, respectively. Three TCS tests were performed at each confinement level for all the rock types. Table 1 summarises the average elastic constants of the tested rock types.

Table 1. Elastic constants for the three rock types

Rock types	Elastic (E)	Poisson's ratio (v)
Anorthosite	79.29	0.43
Chromitite	73.98	0.33
Pyroxenite	106.16	0.23

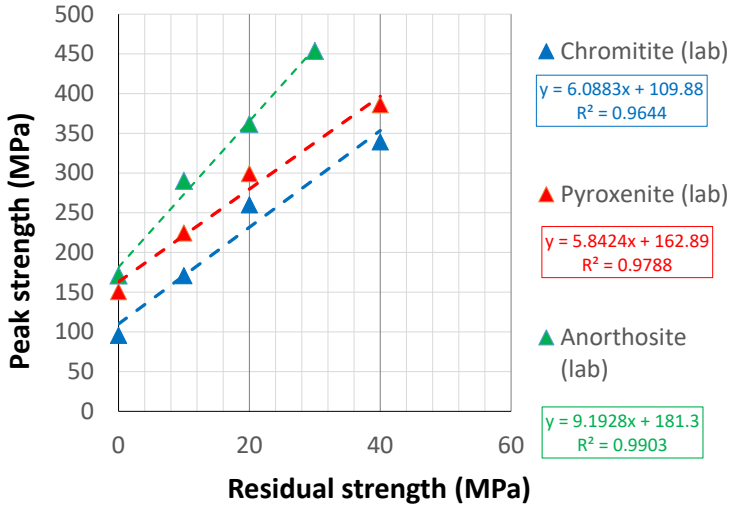


Figure 5. Results of peak strength vs confining pressure for the hangingwall, reef and footwall materials (after Watson et al.*, 2024).*

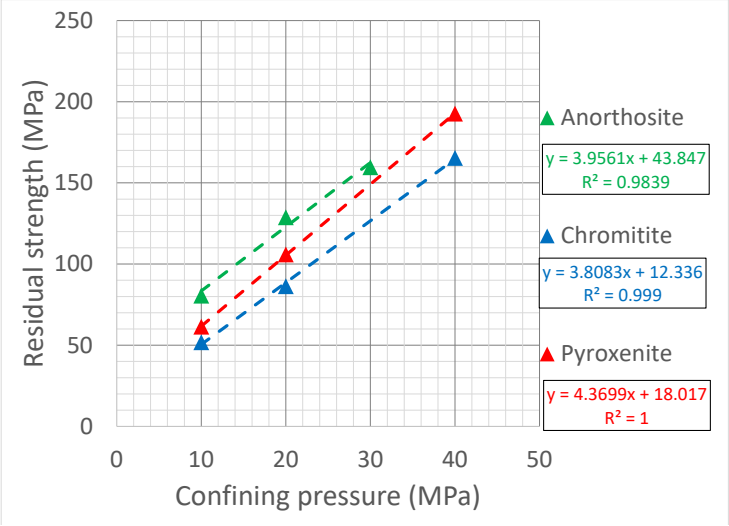


Figure 6. Results of residual strength vs confining pressure for the hangingwall, reef and footwall materials (after Watson et al.*, 2024)*

MODEL DESCRIPTION

A numerical model was built to investigate the effects of pyroxenite layers on UG2 pillar strength using FLAC3D (Itasca, 2019). The pillar dimensions in the model were 6 m × 6 m in plan-view with a height of 2 m. A bord width of 8 m was assumed to be the common distance between pillars (Figure 7b). Roller boundaries were applied to all the lateral sides to simulate repeating geometries of bords and pillars, typical of a mechanised UG2 mine. The base was fixed to allow for the loading of the pillar. A 50 m high

hangingwall and footwall were created (Figure 7a) to minimise the influence of the boundary on the stress distribution.

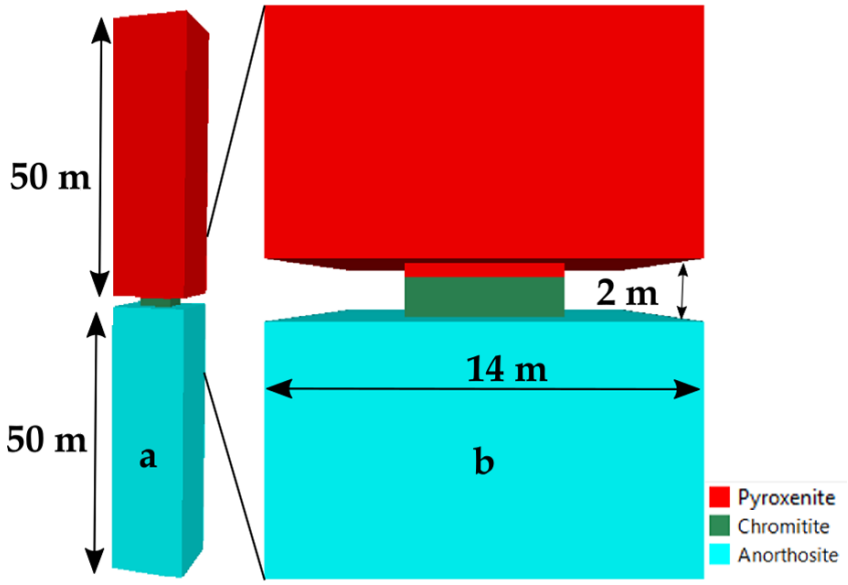


Figure 7. 3D visualisation of the model setup (a=whole model, b=zoomed in model.)

Plastic strain input parameters were derived by calibrating the FLAC3D models against laboratory triaxial test data, ensuring the simulated stress-strain curves closely matched experimental results. An example of chromitite stress-strain curves that were fitted to FLAC3D models is illustrated in Figure 8 (Watson *et al.*, 2024b). The rock mass behaviour was represented using a strain-softening, cohesion-weakening model (Hajiabdolmajid *et al.*, 2002), developed from the laboratory tests (Watson *et al.*, 2024b). The results of the strain-softening and cohesion-weakening investigations are shown in Figure 9. A constant displacement rate of 10^{-6}m/s was applied to the top of the model, and the average pillar stress was recorded at mid-height. Downrating of the test results was not applied to the model inputs. The model configuration is shown in Figure 7. The pyroxenite percentages were increased from 0% to 75% in four equal steps. All models were loaded until residual strength was reached.

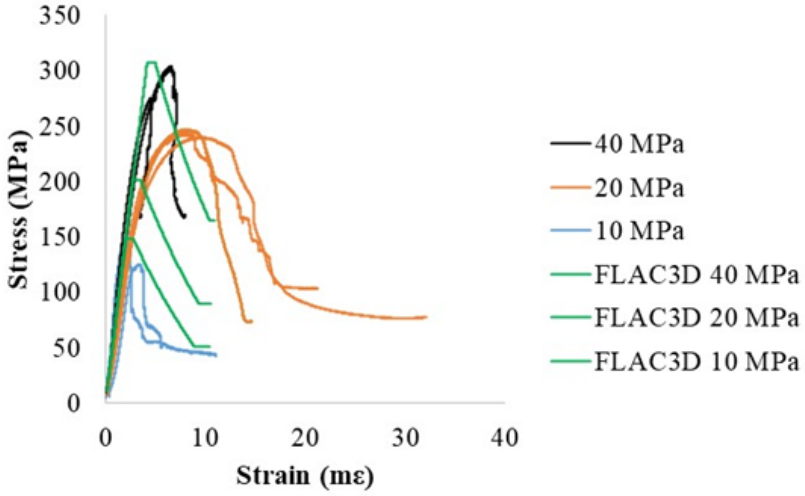


Figure 8. Curve fitting for the chromitite samples (Watson et al.*, 2024b).*

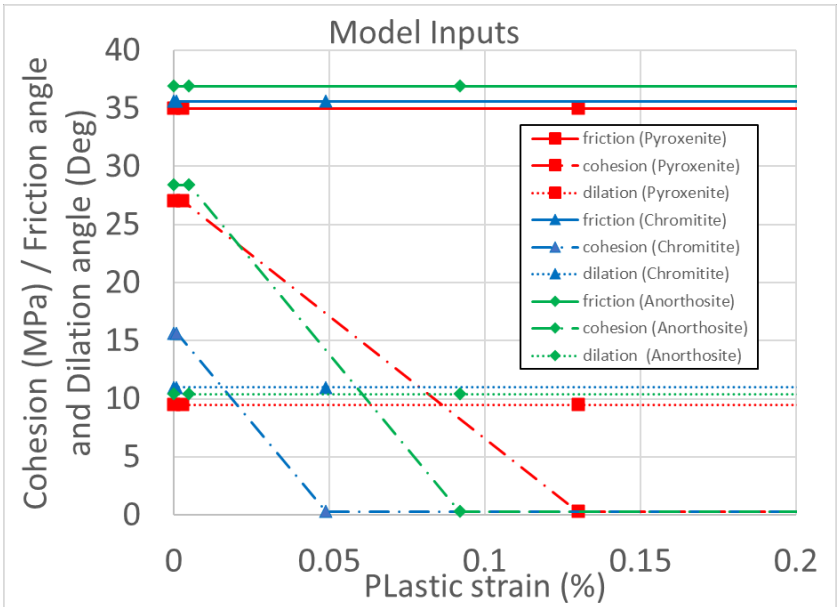


Figure 9. Strain softening parameters from the laboratory tests, used in the FLAC3D modelling (Watson et al.*, 2024b)*

RESULTS

The results of the triaxial test were used to calibrate a FLAC3D triaxial model. The model results for chromite and pyroxenite are shown in Figure 10. The model results show that pyroxenite has a gentler post-peak slope than chromitite, suggesting that pyroxenite is more ductile.

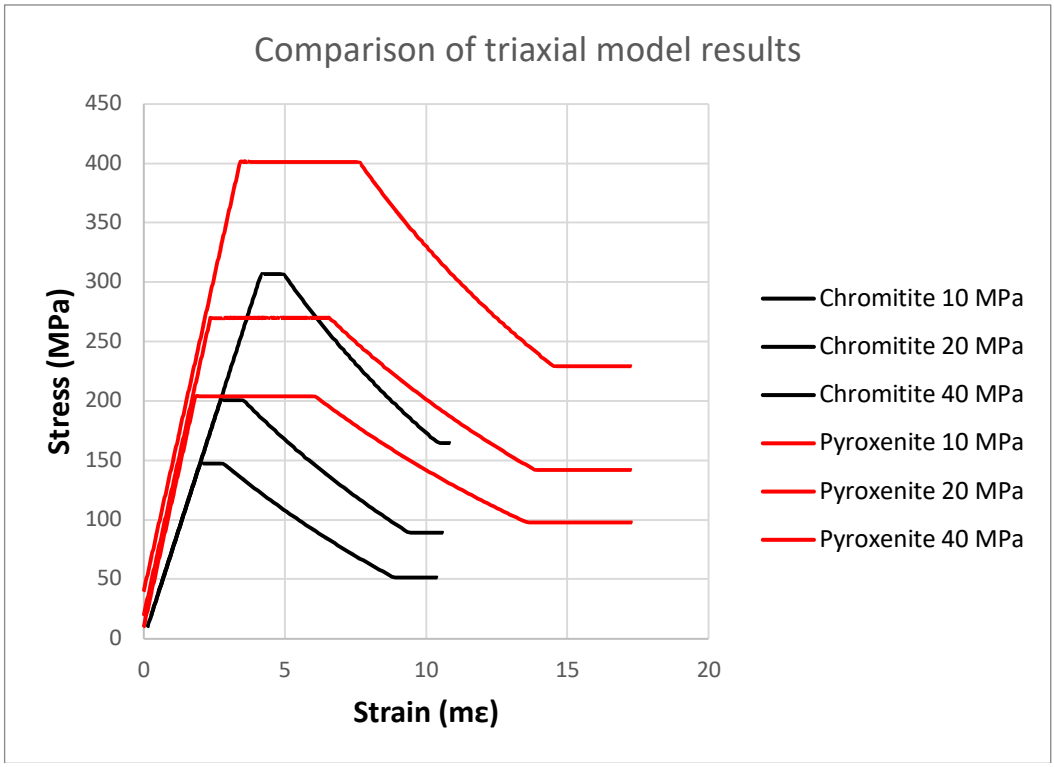


Figure 10. Triaxial model results comparison between chromitite and pyroxenite.

Significant variations in peak pillar strength and post-peak behaviour were observed in the model results as the pyroxenite layer thickness was increased (Figure 11). Pillars with 100% chromitite had a strength of 220 MPa, while the pillars with 75% pyroxenite increased in strength to 320 MPa, a difference of over 30%. Further investigations are needed to establish the effects of interfaces in a pillar. The pillar residual strength also appears to be influenced by the presence of pyroxenite. However, this increase does not seem to be associated with the percentage of pyroxenite.

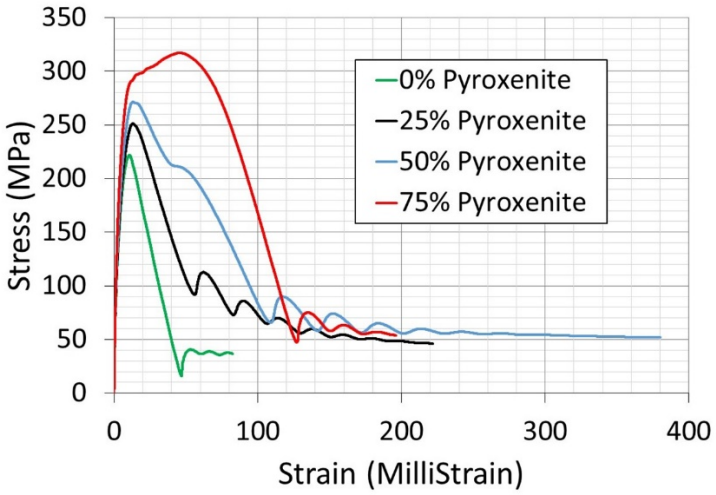


Figure 11. Model results for different pyroxenite compositions.

The model results suggest that the percentage of pyroxenite may also affect foundation damage (Figure 12). However, the observed increase in hangingwall damage may only be a function of the increased pillar strength. As the pillar undergoes loading, it expands laterally due to the Poisson effect, dragging the foundation and tearing it apart. The excessive lateral strain results in the formation of vertical tensile cracks in the foundation, known as Hertzian cracks (Hertz, 1896). Vertical tensile stresses can be observed in the pyroxenite hangingwall, as indicated in Figure 12. Importantly, little damage was observed in the foundation of the 100% chromitite pillar.

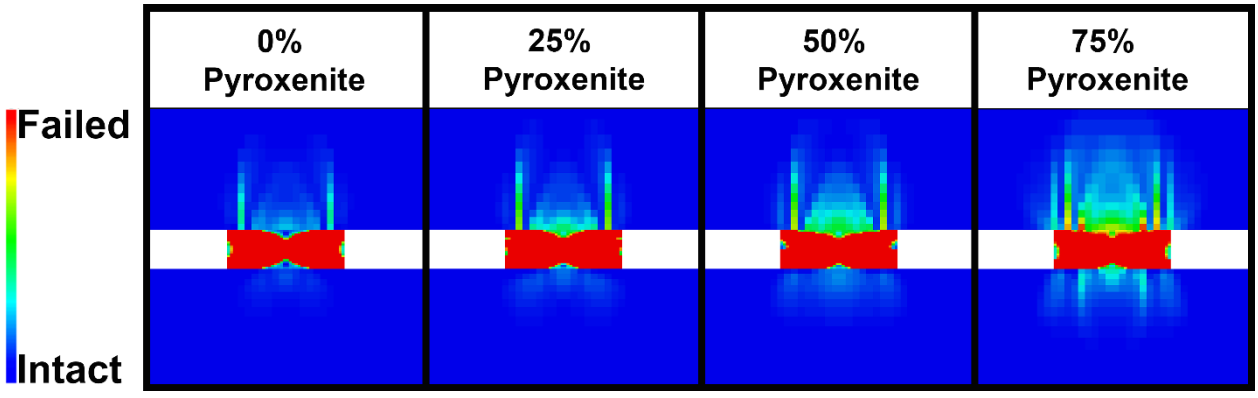


Figure 12. Failure at residual strength for different pyroxenite compositions.

DISCUSSION

The strengthening effects of pyroxenite on UG2 pillars are shown in Figure 13. In this figure, pillar strength is shown as a function of the percentage of pyroxenite to the pillar height. A straight-line function provided a good fit to the model data.

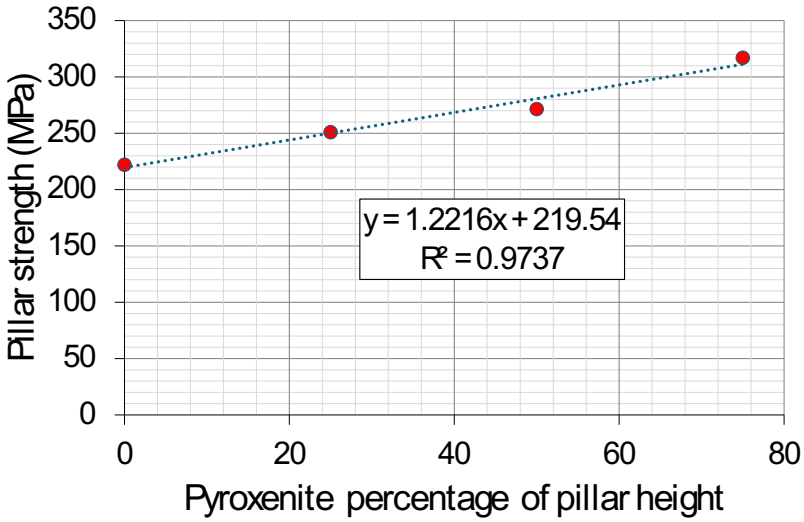


Figure 13. Strengthening effects of pyroxenite on UG2 pillars.

Figure 14 shows that approximately 43% of the instrumented pillar described in Watson *et al.*, (2021b) was pyroxenite. The paper also showed that the PlatMine formula (Watson *et al.*, 2021a) provided a strength that was only slightly less than that which was measured at the instrumentation site (Figure 15). Pillars within the database used to generate the UG2 strength formula contained an unknown percentage of pyroxenite, though observations suggest that this pyroxenite content was probably close to 43% (Figure 2). To demonstrate the impact of the pyroxenite layers on the formula, we assume that the pillars contained the maximum expected/observed 43%. The relationship shown in Figure 13 can then be used to determine a strength reduction for pillars without pyroxenite. An equation has been developed from Figure 13 and a pillar strength formula for UG2 pillars (Watson *et al.*, 2024c), to account for the percentage pyroxenite. The equation assumes the average UG2 pillar to have 43% pyroxenite content.

$$\sigma_p = \left[82\left(\frac{w_e}{h_e}\right)^{0.71}\right][0.0045 \times PP + 0.8065] \qquad \textit{Equation 2}$$

Where: σ_p is the pillar strength, w_e and h_e refer to the effective pillar width and height, respectively, PP is the percentage of pyroxenite layer thickness over the pillar height. The w_e parameter was determined using the Wagner (1974) formula for rectangular pillars:

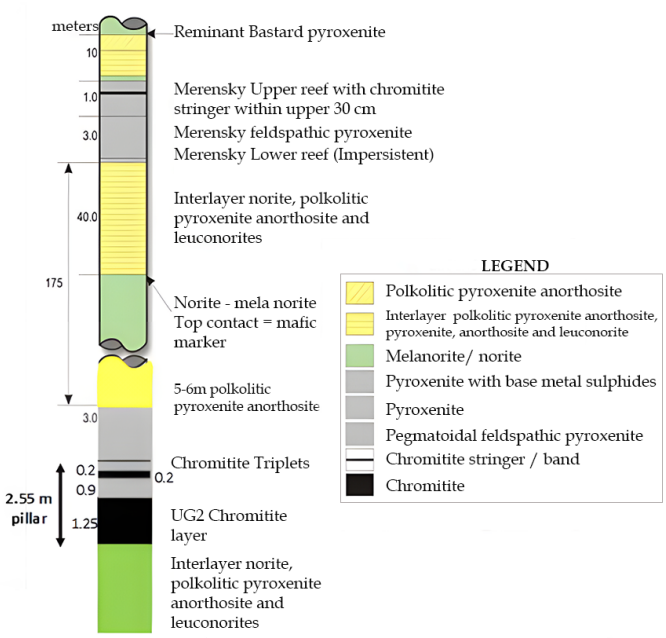


Figure 14. Pillar composition at the Booysendal Instrumentation Site (Watson et al.*, 2021b).*

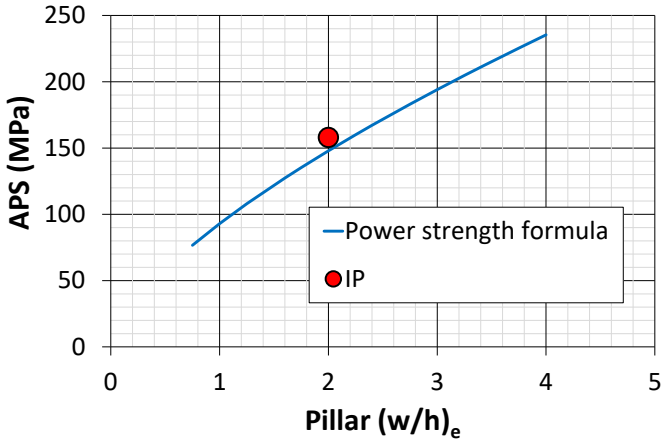


Figure 15. Comparison between the power APS formula and the underground measurement (IP) (Watson et al., 2021b)

A safety factor of 1.6 is commonly applied to in-stope pillars to account for pillars with a strength weaker than the average strength. Figure 16 shows that the reduction in strength provided by the safety factor more than adequately caters for any effects that the pyroxenite layers may have had on pillar strength.

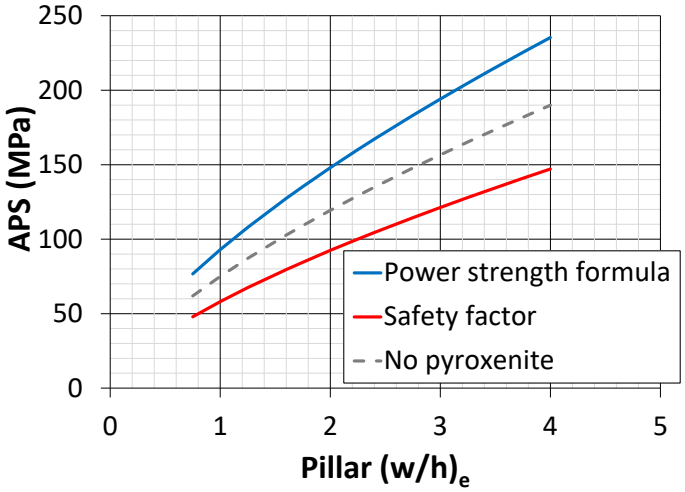


Figure 16. PlatMine pillar strength, reduction in strength due to a safety factor of 1.6 and the maximum strength reduction for pillars with no pyroxenite.

CONCLUSION

FLAC3D models were run to investigate the strengthening effects of pyroxenite on UG2 pillars. The results suggest a linear strengthening effect of pyroxenite layers as a function of pyroxenite percentage. An equation has been developed to determine the change in pillar strength. It was established that a safety factor of 1.6 adequately covers any change in strength resulting from pyroxenite layers. It is recommended that additional studies be carried out using carefully prepared laboratory samples with a width-to-height ratio like those used in this research. The models suggest that little foundation damage occurred during testing, particularly at low ratios of pyroxenite. Where there is little in situ foundation damage, reasonable results may be obtained using properly prepared metal loading platens.

REFERENCES

Hajiabdolmajid, V., Kaiser, P.K., Martin, C.D., 2002. Modelling brittle failure of rock. International Journal of Rock Mechanics and Mining Sciences 39, 731–741.

Hartzenberg, A.G., 2019. Structural Mechanisms Contributing to Large-Scale Hangingwall Instabilities on the UG2 Reef Horizon (master's research report). University of Pretoria, Pretoria.

Hartzenberg, A.G., Du Plessis, M., Malan, D.F., 2019. The Effect of Alteration Layers on UG2 Pillar Behaviour in the Bushveld Complex, in: Rock Mechanics for Natural Resources and Infrastructure Development. Presented at the 14th ISRM Congress, Foz do Iguacu, pp. 2019–278.

Hedley, D.G.F., Grant, F., 1972. Stope-and-Pillar Design for the Elliot Lake Uranium Mines. Canadian Institute of Mining, Metallurgy and Petroleum, Elliot Lake, Ontario.

Hertz, H., 1896. On the contact of rigid solids and on hardness, miscellaneous papers, Macmillan, London.

Itasca, 2019. General Comments FLAC3D 7.0 documentation [WWW Document]. Flac3d. URL http://docs.itascacg.com/flac3d700/flac3d/docproject/source/theory/interfaces/generalcomments.html (accessed 2.10.22).

Malan, D.F., Napier, J.A.L., 2011. Design of stable pillars in the Bushveld Complex mines: A problem solved? Journal of the Southern African Institute of Mining and Metallurgy 111, 821–836.

Roberts, D., Esterhuyse, J., 2021. Technical Services Optimisation - Guidelines for Pillar design in Bord-and-Pillar operations. Mandela Mining Precinct, Johannesburg.

Ulusay, R., Hudson, J.A., 2007. The Complete ISRM Suggested Methods for Rock Characterization, Testing and Monitoring: 1974-2006. ISRM and Turkish National Group of ISRM, Ankara, Turkey.

Wagner, H. (1974). Determination of the complete load-deformation characteristics of coal pillars. Proceedings of 3rd International Congress on Rock Mechanics, ISRM, Denver, Vol. 2B, pp 1076-1082.

Watson, B.P., Lamos, R.A., Roberts, D.P., 2021a. PlatMine pillar strength formula for the UG2 Reef. J. S. Afr. Inst. Min. Metall. 121, 1–12. https://doi.org/10.17159/2411-9717/1387/2021

Watson, B.P., Mabala, M.I., and Kanda, M.J. 2024c. Re-evaluation of the PlatMine chromitite pillar strength database. Journal of the Southern African Institute of Mining and Metallurgy, vol. 124, no.11 pp. 645–652. http://dx.doi.org/10.17159/2411-9717/3382/2024.

Watson, B.P., Maphosa, T., Theron, W., Fernandes, N., Stacey, T., Morgan, A., Carpede, A., Betz, G., 2024a. Establishing a UG2 Pillar Strength Formula in South African Platinum Mines. Minerals 14, 1161. https://doi.org/10.3390/min14111161

Watson, B.P., Maphosa, T.J., Roberts, D.P., Gardner, L.J., 2024b. Determination of strength of UG2 chromitite pillars at Impala Platinum from laboratory tests and FLAC3D. J. S. Afr. Inst. Min. Metall. 124, 437–446. https://doi.org/10.17159/2411-9717/3261/2024.

Watson, B.P., Roberts, M.K.C., Kuijpers, J. and Van Aswegen, L. 2006. The stress-strain behaviour of in stope pillars in the Bushveld Platinum deposits in South Africa. Proceedings of the 41st U.S. Symposium on Rock Mechanics (USRMS): "50 Years of Rock Mechanics - Landmarks and Future Challenges". Golden, Colorado, June 2026.

Watson, B.P., Ryder, J.A., Kataka, M.O., Kuijpers, J.S., Leteane, F.P., 2008. Merensky pillar strength formulae based on back-analysis of pillar failures at Impala Platinum. J. S. Afr. Inst. Min. Metall 108, 449–461.

Watson, B.P., Theron, W., Fernandes, N., Kekana, W.O., Mahlangu, M.P., Betz, G., Carpede, A., 2021b. UG2 pillar strength: Verification of the PlatMine formula. J. S. Afr. Inst. Min. Metall. 121, 449–456. https://doi.org/10.17159/2411-9717/1491/2021

Improvements in stope designs, and sequencing at the Big Gossan sub level open stope mine, Indonesia

A. Febrian, A. Sjadat, J.P.E. Hamman

PT Freeport Indonesia, Indonesia

The Big Gossan (BG) Sub Level Open Stope (SLOS) mine is part of the Grasberg mining complex at PT Freeport Indonesia (PTFI) that consists of an additional two active cave mines and one cave mine being developed. The BG mine started development in 2005 and production in 2010.

The orebody is vertical, approximately 40 m wide, 1,500 m on strike 400 m in depth. The mining method consists of 15 m wide, 40 m high and <60 m long transverse stopes that use cemented paste fill (CPF). The mine design is planned at over 23 production levels, and production will be divided into two mining districts separated by a 20 m wide sill pillar.

The Modified Stability Graph (MSG) method was used to record the stability of almost 171 stopes. The stability levels were classified as stable, minor failures and major failures. Cavity Monitoring Systems (CMS) were used to.

This paper briefly discusses the geotechnical methods used and the results that provided critical insights into the stability characteristics of the SLOS mining method at Big Gossan. The findings indicate areas where a change in stope dimensions or sequencing is required and highlight the importance of strategic sequencing to minimize stope failure risks. This assessment serves as a model for the application of advanced geotechnical tools in sub-level stoping environments, offering practical solutions for stability management in complex underground mining conditions.

Keywords: Big Gossan Mine, Sub Level Open Stope, Stope Stability Assessment, Modified Stability Graph

INTRODUCTION

Big Gossan mine is a sublevel open-stope operation producing approximately 10,000 tons of ore per day. This level of production, typical for the sublevel stoping method, requires advanced geotechnical stability assessments to manage ground conditions and optimize productivity. The challenges associated with maintaining stable stopes in such a high production mining environment are compounded by the varying geological conditions of the Big Gossan ore body.

This study aims to address these challenges by applying the site-specific MSG, stability evaluation of the unsupported stope backs and undercutting sequences. These methods provide a comprehensive framework for assessing geotechnical risks, with the goal of improving stope design, minimizing ground failures, and enhancing operational efficiency at the Big Gossan mine.

BACKGROUND

SLOS operations at the BG mine face geotechnical challenges due to the mine's varying geological conditions, change in stress environments and the presence of structurally controlled very poor to poor rock mass zones. To address these changing conditions, empirical methods like the original stability graph that has been developed by Matthews et al (1981) and the modified stability graph (MSG) by Potvin (1988) and Nickson (1992) have been evaluated at the BG mine to assess stope stability. The MSG was adopted to classify the BG stopes into stable, transitional, and unstable zones based on the rock mass quality, stope geometry, structural orientations, rock strength and induced mining stress levels. Apart from the feasibility studies, the first actual stope stability data from the BG mine was plotted on the MSG in 2018 and consisted of 11 stopes. The second data set was plotted in 2020 and consisted of 64 stopes. Site-specific transition zones were indicated on the BG MSG in 2020.

In 2024 the site-specific BG MSG was again updated based on 171 stopes. It was found that the transition zones followed very similar trends, for hydraulic radii (HR) less than 25, as the work documented as the extended MSG by Mawdesley et al. (2001), Trueman et al. (2000) and Trueman and Mawdesley (2003). This site-specific MSG for the BG mine is currently in use.

The CMS was used extensively to provide overbreak and underbreak data at different interval periods to gain insight into blast-induced overbreak and an improvement in the Equivalent Linear Overbreak Slough (ELOS) graphs.

Additionally, the stand-up time concept for unsupported spans - RMR relationship (Bieniawski, 1993; Lauffer, 1958) and the relationship between unsupported spans and Q-value for different Excavation Support Ratio (ESR) values (Barton et al., 1974) were evaluated to estimate the stability of temporary unsupported stope backs and walls to increase the production by alternating blasting sequences.

Understanding these geotechnical considerations is essential for enhancing the safety and efficiency of the Big Gossan operation, especially given the high demands on production and the challenging underground environment.

The classification of the rockmass, as used in the MSG method, is done using the Modified Stability Number, N', as specified by Potvin (1988), Potvin and Milne (1992) and Bawden (1993). This parameter (N') is similar to value N proposed by Mathews et al. (1981) but has different factor weightings. Canadian mines use Potvin's N', while mines in Australia, use the Mathews' analysis and N value (Suorineni, 2010). Only the Modified Stability Number (N'), will be considered in this study.

UPDATED STABILITY ANALYSIS METHODS

Modified Stability Graph

The MSG (Potvin 1988) method for designing open stopes at the BG mine has been used to present the stability data. The MSG plots the stability number (N') against the hydraulic radius (HR), as defined in Equations [1],[2], and [3] respectively, and illustrated in Figure 1.

$$N' = (Q')\ (A)\ (B)\ (C) \quad [1]$$

$$Q' = \frac{\mathrm{RQD}}{Jn} \times \frac{Jr}{Ja} \quad [2]$$

$$\mathrm{HR} = \frac{Area\ (m^2)}{Perimeter\ (m)} \quad [3]$$

RQD stands for rock quality designation, while (Jn) represents the joint set number, (Jr) is the joint roughness number, and (Ja) denotes the joint alteration number. In Equation (1), the variables (A), (B), and (C) are defined as the stress adjustment factor, joint defect orientation factor, and gravity factor, respectively.

Factor A (Figure 2) is the stress adjustment factor. It accounts for the influence of in-situ stresses on stope stability. Factor A compares the ratio of intact rock strength values against the induced compressive stress. The geotechnical domain for stope extraction is Skarn, for which the intact rock strength values based on geotechnical evaluation for Big Gossan, are 130 MPa. The induced compressive stress value is obtained from the stress model results (Map 3D) at Big Gossan. Stress fields at Big Gossan, and the other underground mines at the Grasberg mining complex, varies from gravitational to tectonic, resulting in a higher horizontal stress at depths below 900 m below the surface.

Factor B (Figure 2) is the joint orientation factor and is based on the understanding that joints parallel and sub-parallel to the stope walls are more prone to instability compared to perpendicular intersected joints.

Factor C (Figure 2) is the gravity adjustment factor that reflects the potential failure methods e.g., gravity, slabbing or sliding, that can affect the stability of the stope walls or back.

The Big Gossan mine operations has been expanding the MSG to determine the stope size stabilities. Over time, several advancements have enhanced the reliability of the stability graph at Big Gossan Mine. The volume of open stope mining at the Big Gossan mine has increased steadily as additional production areas became available. The Big Gossan stope stability results were plotted on the stability zones as proposed by Nickson (1992), and the Big Gossan MSG results from 2018, 2020 and 2024 are summarised in Figures 3a, 3b and 3c. These improvements stem from an expanding database and accumulated experience applying the stope stability methodology at Big Gossan mine.

The stability graph method is empirical, and as the database used to develop it expands, its reliability and accuracy improve. However, caution is needed when using stability graph databases, as they are not all based on the same factors. Notably, the extended Mathews stability graph by Mawdesley, Trueman, and Whiten (2001) relies on the uncalibrated stability graph factors (A), (B), and (C), which were derived from only 26 case histories. While these factors support the stability graph concept, they do not establish confidence and reliability in its application. Nonetheless, the extended Mathews Stability Graph concept was considered where the Big Gossan mine's data was evaluated.

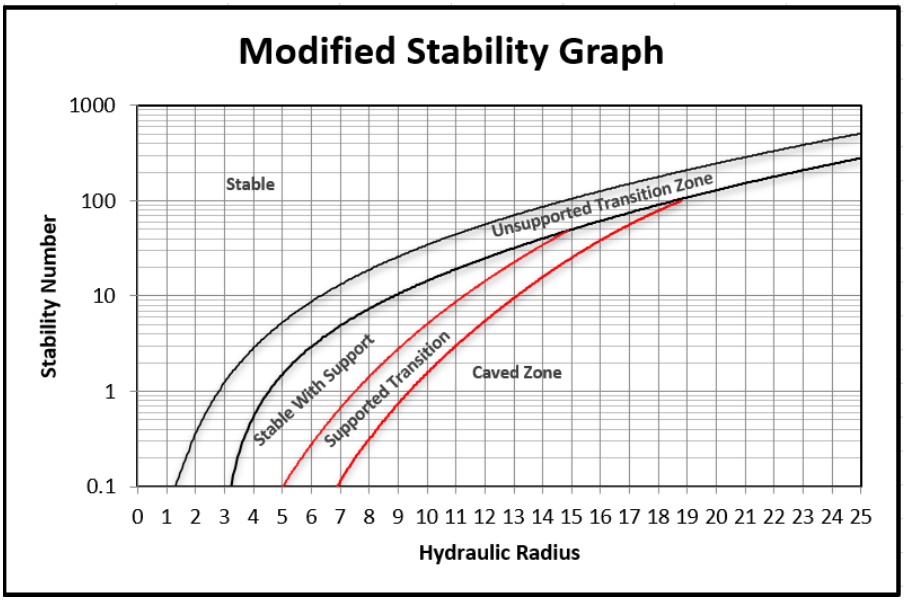


Figure 1. Modified Stability Graph for supported zones (Nickson, 1992)

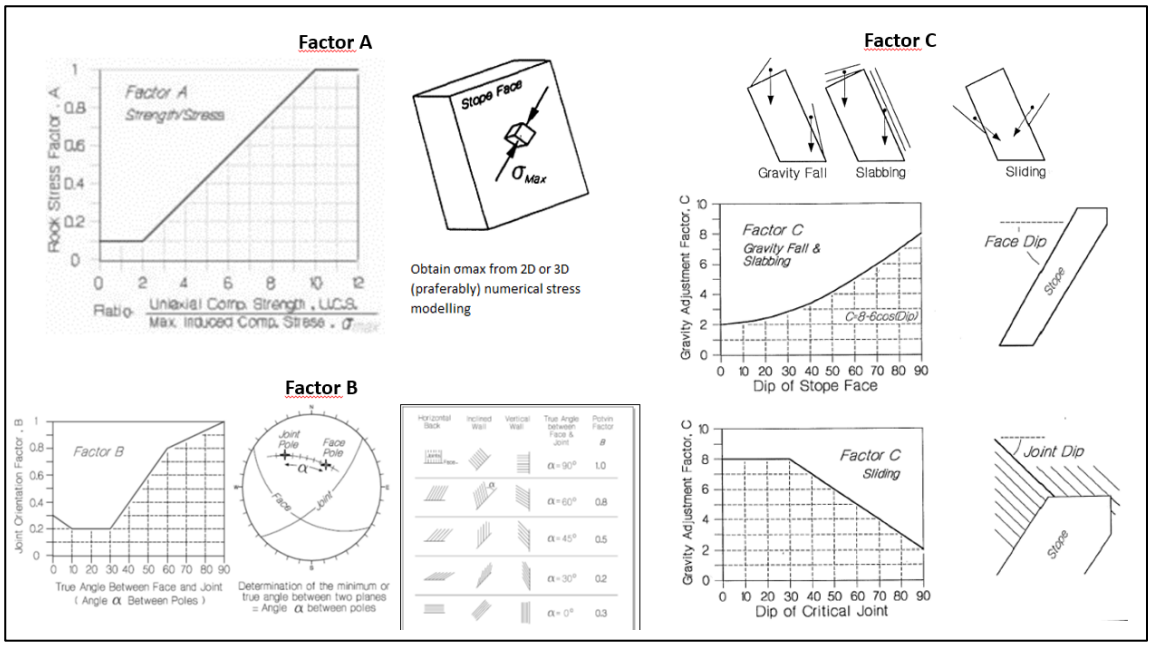


Figure 2. Adjustment factors for determination of the modified stability number. (Potvin, 1988).

The Big Gossan data was plotted on combined graphs of the Modified Stability Graph and the extended Mathews Stability Graph for comparison. When the A, B and C Factors are excluded, the Big Gossan data indicate similar trends to the extended Matthew's Stability Graph. Soureneni (2010) cautioned as to which HR extend the design should be considered, and that stope sizes should not exceed an HR of 25. A maximum possible HR of 20 will be considered for design purposes at Big Gossan mine.

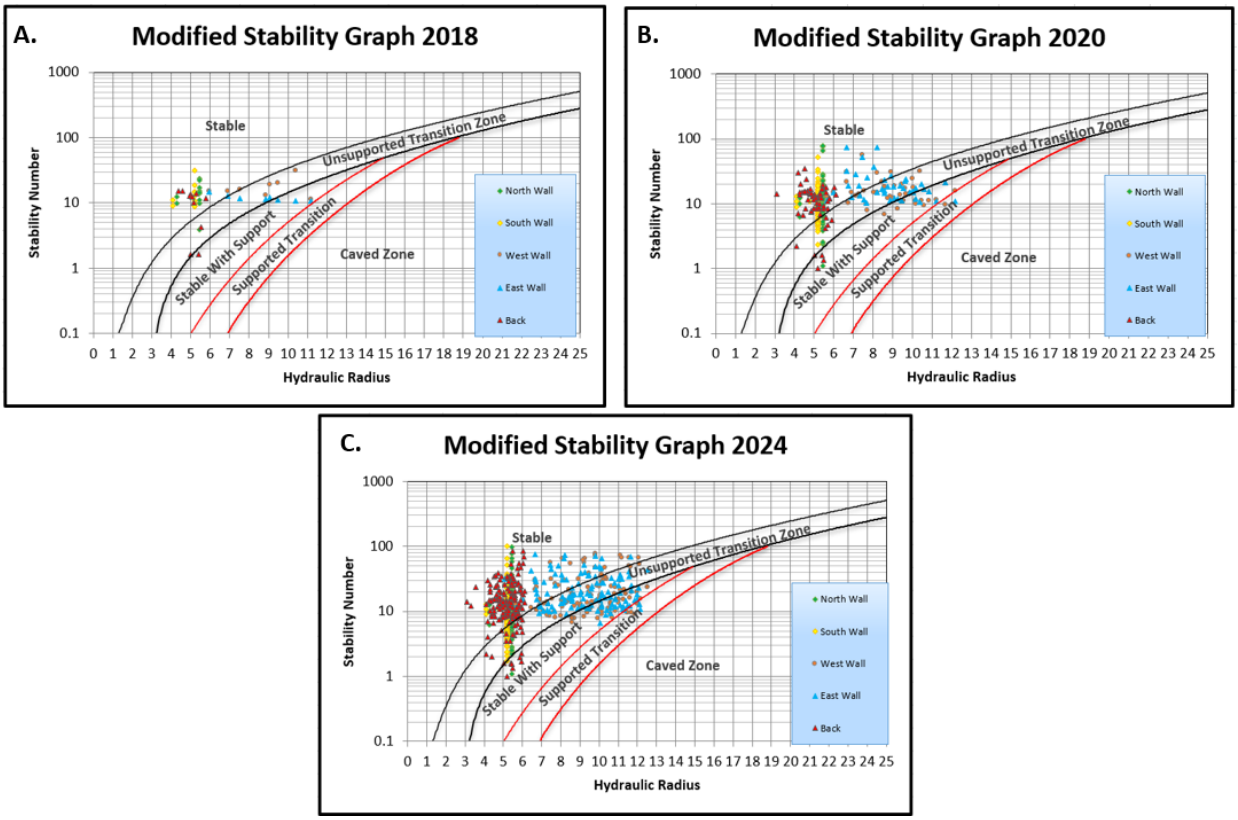


Figure 3. Big Gossan data: (a) MSG Data 2015, (b) MSG Data 2020 and (c) MSG Data 2024

Equivalent Linear Overbreak Slough (ELOS)

The stability analysis conducted for the assessment of each opened stope is validated through a stope reconciliation process. This process aims to determine the accuracy of the calculations and analyses by comparing the actual stope openings with the initial design. The dimensions of the opened stope are obtained from the CMS, which provides accurate measurements of the stope openings (Figure 4). By comparing this survey measurement, it can be determined whether the initial design has been successfully implemented or if there are discrepancies that require further adjustments. This reconciliation process is crucial to ensure that the design and analysis methods are reliable and result in safe and efficient mining operations. The Equivalent Linear Overbreak Slough (ELOS), introduced by Clark and Pakalnis in 1997, serves as an indirect quantitative measure of dilution and overbreak as indicated in Equation [4].

$$\text{ELOS} = \frac{Volume\ of\ Slough}{Stope\ wall\ surface\ area} \quad [4]$$

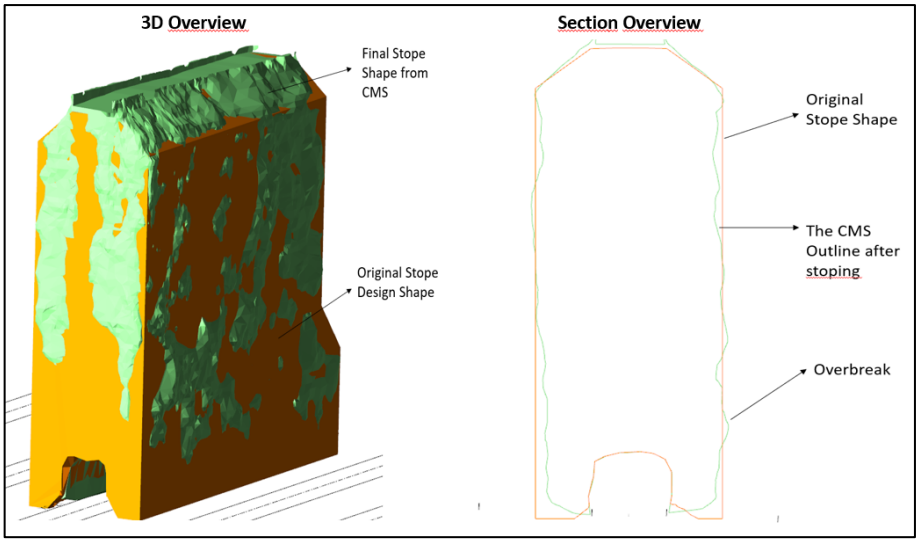


Figure 4. Stope design and Cavity Monitoring Survey at Big Gossan Mine

The Big Gossan mine had the luxury to CMS every stope and this data set was used to correlate with the initial MSG stability zone. The data was separated into the various walls and backs and statistically evaluated. In general, very little overbreak was measured, except for the back wings, but this over- and underbreak was ascribed to inaccurate blasting. These measurements were ignored (Suorineni, 2015) and deleted from the ELOS data set (Figure 5).

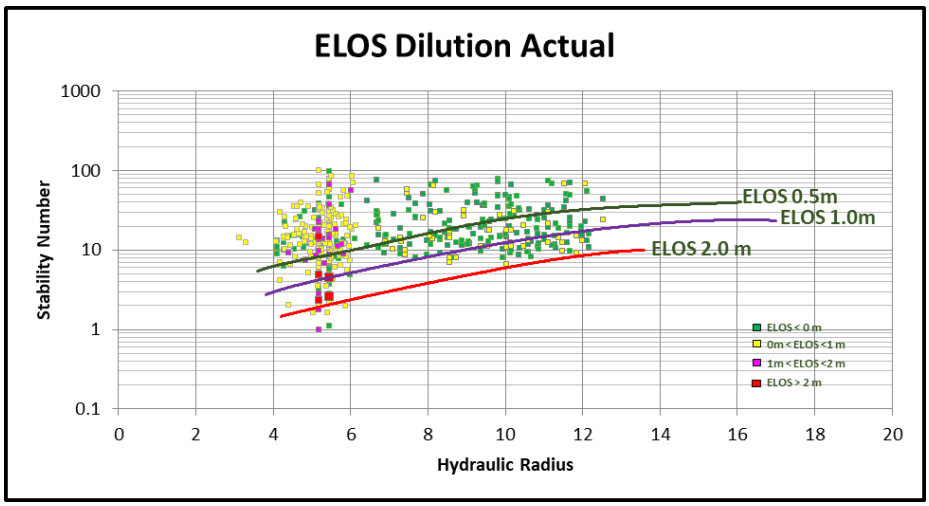


Figure 5. ELOS data showing all data (backs and walls)

Stability and Stand-up Time for temporary Unsupported Backs during Undercutting Sequences
In the Big Gossan SLOS, the blasting sequence is crucial for efficient ore extraction and maintaining stope stability. The initial Big Gossan blast design consisted of an initial slot raise at the furthest end of the stope, whereafter sequences of 3 to 6 rings (±9 m – 18 m) are blasted and mucked (Figure 6a). Each sequence consisted of up- and down holes, creating a complete void from the bottom to the top crosscut. A supported back (Figure 6b) provides stability to the mucking operations. Once this blasting sequence is completed and the stope was completely mucked, the stope is filled with cemented paste fill (CPF) designed at 4.6% cement for primary stopes and 1.5% cement for secondary stopes.

To improve safety related to the length of time a stope was open before CPF, the possibility to mine the stope in two cuts was investigated. It was suggested that the bottom 20 m of a 40 m high stope, be drilled, blasted and mucked from the bottom crosscut, before the top cut of similar dimensions will be mined and mucked before being paste filled.

To address this proposal, an undercutting sequence proposal was initiated. This approach involves creating an undercut below the ore body before the main blasting sequence. The undercut provides a controlled space for the broken ore to collapse into, reducing the risk of large voids and improving overall stability. It was believed that by incorporating the undercutting sequence, the blasting process would become more efficient and safer. This undercutting method also contributes to providing a steady flow of blasted ore, thereby enhancing productivity. This method also allows for better blast control and the fragmentation of the ore, leading to more consistent and predictable results. (Figure 7)

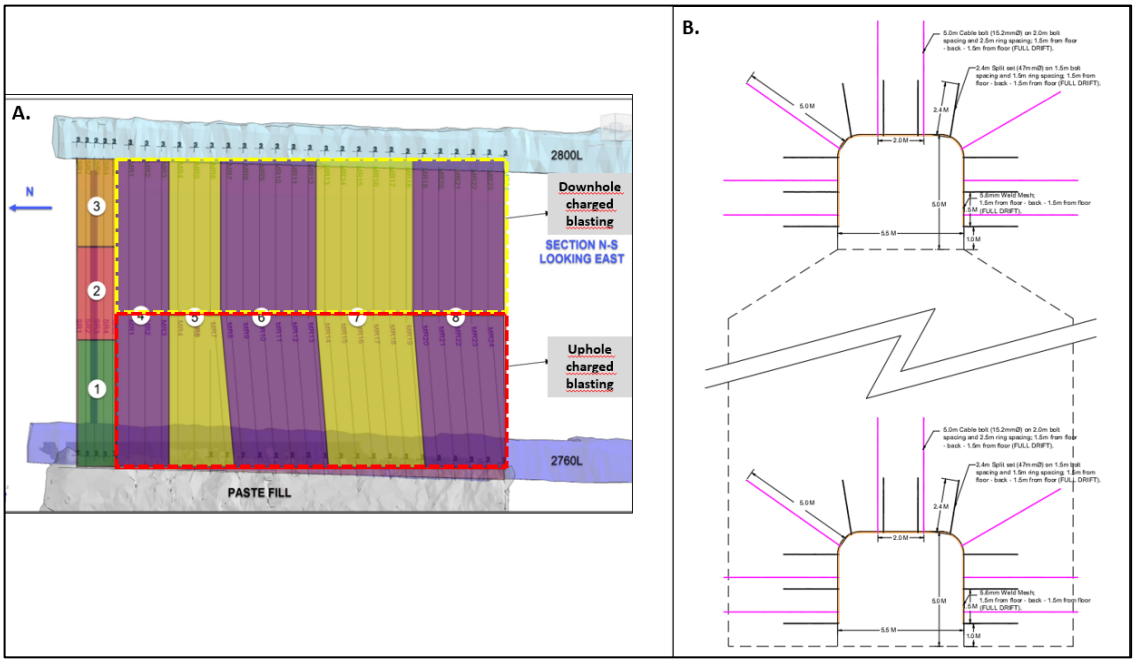


Figure 6. (a) Initial Blasting Design (longitudinal view) and (b) Ground Support Design for top crosscut and stope backs

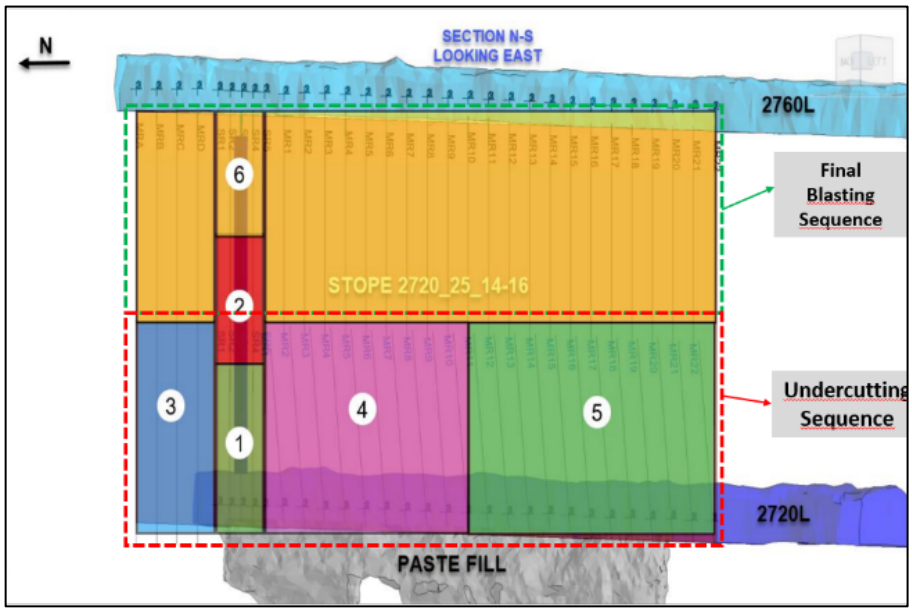


Figure 7. Implemented Undercutting Sequence at Big Gossan Mine (longitudinal view)

When implementing the undercutting sequence in sublevel stoping, several geotechnical concerns must be addressed to ensure the safety and stability of the operation.

1. The length and span of the unsupported back that can be open without any ground support.
2. The duration for which an unsupported back can remain stable without ground support could vary, based on rock quality and stress conditions.

Initially, several empirical methods, although not perfectly suited for this scenario, were evaluated to determine stability and stand-up time periods. These methods included the (a) "Stand-up Time for

Tunnel Spans" (Bieniawski, 1993), (b) "No support Span Limits for Underground Openings" (Barton et al., 1992) and the (c) "Unsupported Stability Graph" (Potvin 1988, Nickson, 1992). Furthermore, the updated site-specific Modified Stability Graph for the Big Gossan, specifically the supported back, was used to compare data.

Methods (b) and (c) gave guidance regarding the back dimensions that could be excavated, and method (a) gave guidance regarding the stand-up time. These three methods use different rock mass classifications methods, e.g. (a) RMR, (b) Q-system and (c) Modified Stability Number N'. The areas identified for the sill mining procedure were studied in detail for rock mass variations and structural disturbances.

The implementation process was sequenced, whereby blasting and mucking were done in stages (Figure 8). The initial stage per stope was a slot raise with a length of 8 m, followed by a cut length of 18 m and a second cut length of 18 m. The final unsupported sill back length was 44 m. When practicable a CMS was taken of each stage, to determine over and underbreak. A final CMS was done before the final upper sill pillar was blasted to determine if there were any sloughing or large failures along the temporary unsupported back.

DATA PROCESSING, VALIDATION AND RECOMMENDATION

Extending the site-specific BG Modified Stability Graph

To extend the site-specific BG Modified Stability Graph (MSG) at the Big Gossan mine, a comprehensive analysis was conducted using data from 171 stopes from 2010-2024. The process began with gathering detailed geotechnical data, including rock mass properties, stope dimensions, and ground conditions. Each data point was meticulously analysed to determine the stability conditions and performance of the stopes. By plotting these data points on the existing MSG (Figure 8a), patterns and trends were identified, highlighting areas where the original graph could be adjusted to better reflect the unique conditions at Big Gossan.

The updated MSG for BG assessed 171 stope data entries, with each stope divided into five walls e.g. North, South, West, East, and Back, the trends reveal critical insights into stability conditions. Preliminary analysis of the dataset indicates that possible unstable conditions could occur along the North, South walls, and the Back, while the West and East walls generally exhibit stable conditions. These potential instabilities were further evaluated by the Equivalent Linear Overbreak/Slough (ELOS) method. The values correlate well with the ELOS chart, although a few data points exceeding 2 m were found to be distributed across the boundaries (Figure 8b). The assessment of the corrected results, for stope wall stability, has shown reasonable outcomes, demonstrating that the validation of stope stability calculations provides fairly accurate results. The indication of potential instability in these regions is supported by ELOS values ranging from 0.5 to 2 m, which suggest low to moderate overbreak. This consistency between calculated stability predictions and actual field conditions reinforces the reliability of the assessment method.

The MSG from the BG has been extrapolated to HR < 20 for feasibility studies to include a potential stope height of 80 m and a stope length of 60 m, including the ELOS, stability and failure zones (Figure 8c).

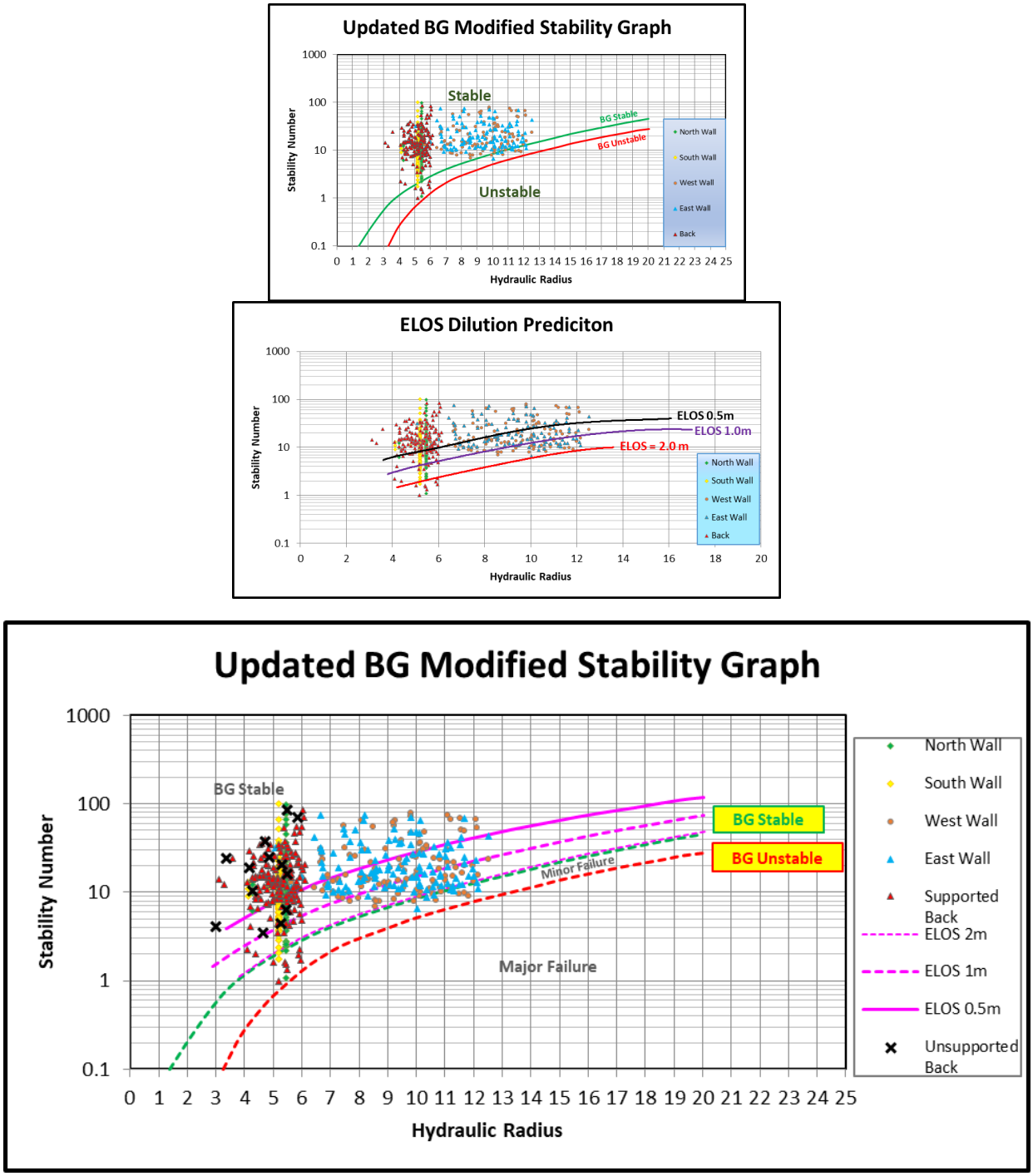


Figure 8. (a) Modified Stability Graph at Big Gossan Mine, (b) ELOS Dilution at Big Gossan Mine Cases, and (c) Extended MSG, updated failure and ELOS zones for all Big Gossan Mine Cases

Stability and Stand-up Time During the Undercutting Sequence

Since March 2024, Big Gossan has implemented 69 undercutting sequences across 22 stopes, with lengths ranging from 5 m to 55 m. The Rock Mass Rating (RMR) for these stopes ranges from 69 to 83, indicating good to very good ground conditions. Similarly, data sets for the N′ stability number and Q have been calculated to create different data sets for the different empirical evaluation methods. A thorough back analysis has been conducted to evaluate any failures that occurred during these

undercutting sequences. The data obtained from this analysis provides critical insights into the stability and performance of the unsupported spans.

The analysis of the entire dataset, confirmed by CMS, indicated that no instability conditions were directly caused by the undercutting sequence. This conclusion is supported by the results of the back reconciliation, which confirm that all observed overbreak occurrences were primarily attributed to blasting effects rather than inherent rock mass conditions. These findings highlight the importance of controlled blasting techniques in minimizing overbreak while ensuring the integrity of the surrounding rock mass. The reconciliation of ELOS data indicates that stopes with undercutting <55 m show no signs of instability.

It can conclude that the unsupported back of the sill pillar sequence is stable and indicate similar MSG and ELOS graph distribution data sets as for the supported backs. Therefore, the ground support in the top crosscut adds little value to the overall stability in relation to the ELOS, indicating that the final stope back and intermediate stope back data sets could be correlated.

Table II. Actual ELOS and stability for the Undercutting Sequences Method at Big Gossan

Stope Id	Dimension				Ground Condition (RMR)	Q-Value	Ground Condition	Elos Calculation		
	Width	length	Height	Undercutting				Elos (Meter)	Status	Stability
2940_23_16	15	65.2	40	54.2	83	33.75	Good Ground	0.22	overbreak	Stable
2940_19_18	15	41.2	40	40.72	78	30	Good Ground	0.35	overbreak	Stable
2860_24_15	15	65	40	56.7	73	10	Fair to Good Ground	0.36	overbreak	Stable
2860_20_15	15	64	40	53.45	75	19.8	Good Ground	1.04	overbreak	Stable
2860_39_11	15	55	40	40.92	73	8.75	Fair Ground	0.74	overbreak	Stable
2720_25_14	15	65.5	40	55.8	80	30	Good Ground	0.38	overbreak	Stable
2720_19_16	15	51	40	44.64	80	30	Good Ground	0.22	overbreak	Stable
2640_18_13-14	15	45.1245	40	41.2	74	13.2	Good Ground	0.33	overbreak	Stable

CONCLUSIONS

The geotechnical assessment at the Big Gossan mine has provided valuable insights into stope stability, undercutting sequences, and the effectiveness of the Modified Stability Graph (MSG). By analysing 171 stope data points collected between 2010 and 2024, the MSG has proven to be a reliable tool for evaluating stability, as confirmed by Equivalent Linear Overbreak/Slough (ELOS). The findings indicate that the North and South walls show lower levels of stability than the East and West walls, with occasional ELOS values exceeding 2 m, whereas the West and East walls generally exhibit stable conditions.

The implementation of 69 undercutting sequences across 22 stopes since March 2024 has also been analysed, revealing that no instability was directly caused by the undercutting sequence. Instead, any observed overbreak was primarily attributed to blasting effects rather than rock mass conditions. Reconciliation of ELOS data further indicates that stopes with undercutting <55 m remained stable. These results establish a strong correlation between back stability and the MSG, reinforcing the reliability of empirical stability assessments. Based on these findings, it can be concluded that if the stability assessment via the Modified Stability Graph remains within acceptable limits, undercutting can be extended to match the full stope span without compromising stability.

Overall, this study underscores the importance of controlled blasting techniques and continuous refinement of geotechnical models in optimizing stope design. The implementation of advanced stability assessment tools, combined with empirical and site-specific data analysis, has enhanced operational safety and efficiency at Big Gossan. Moving forward, ongoing monitoring and adjustments based on geotechnical feedback will be crucial in maintaining and improving underground mining conditions.

REFERENCES

Barton, N, Lien, R and Lunde, J, 1974. Engineering classification of rock masses for the design of rock support, Rock Mechanics, 6(4):189–236.

Barton, N., By, T.L., Chryssanthakis, L., Tunbridge, L., Kristiansen, J., Løset, F., Bhasin, R.K., Westerdahl, H. and Vik, G. 1992. Comparison of prediction and performance for a 62 m span sports hall in jointed gneiss. Proc. 4th. int. rock mechanics and rock engineering conf., Torino. Paper 17.

Bawden, W. F.,1993. The use of rock mechanics principles in Canadian hard rock mine design. Oxford: Pergomon; 1993. Hudson. Comprehensive Rock Engineering.

Bieniawski, Z T, 1973. Engineering classification of jointed rock masses, Trans S Afr Inst Civ Engrs, 5:335–344.

Bieniawski, Z T, 1989. Engineering Rock Mass Classification (Wiley: New York).

Bieniawski, Z.T., 1993, Classification of rock masses for engineering: The RMR system and future trends, In: Hudson, J.A., ed., Comprehensive Rock Engineering, Volume 3: Oxford; New York, Pergamon Press, p. 553-573.

Clark, L M and Pakalnis, R C, 1997. An empirical approach for estimating unplanned dilution from open stope hangingwalls and footwalls, in Proceedings 99th Annual General Meeting, 33 p (CIM: Vancouver).

Lauffer, H., 1958, Gebirgsklassifizierung für den Stollenbau: Geology Bauwesen, v. 24, p.46-51.

Mathews, K E, Hoek, E, Wyllie, D C and Stewart, S B V, 1981. Prediction of stable excavation spans at depths below 1000m in hard rock mines, CANMET report, DSS serial no OSQ80–00081, 127 p.

Mawdesley, C A, Trueman, R and Whiten, W, 2001. Extending the Mathews stability graph for Open-stope design, Transactions of the Institutions of Mining and Metallurgy, Mining Technology, 110(1):A27–A39.

Mawdesley, C A, 2002. Predicting rock mass cavability in block caving mines, PhD thesis, Julius Kruttschnitt Mineral Research Centre, University of Queensland.

Nickson, S D, 1992. Cable support guidelines for underground hard rock mine operations, MSc thesis, Department of Mining and Mineral Processing, University of British Columbia.

Potvin, Y, 1988. Empirical open stope design in Canada, PhD thesis, University of British Columbia.

Y. Potvin, Y, and Milne, D, Empirical cable bolt support design, Proceedings of International Symposium on Rock Mechanics, Sudbury, ON, Canada, 1992.

Suorineni, F T, 2010. The stability graph after three decades in use: experiences and the way forward, International Journal of Mining, Reclamation and Environment, 24(4):307–339.

Suorineni, F T, 2012. A critical review of the stability graph method for open stope design, in Proceedings MassMin 2012, 8 p (Canadian Institute of Mining, Metallurgy and Petroleum: Montreal).